

# Tokamaks

---

THIRD EDITION

JOHN WESSON

with contributions from

D. J. CAMPBELL

J. W. CONNOR

R. D. GILL

J. HUGILL

C. N. LASHMORE-DAVIES

G. M. McCACKEN

H. R. WILSON

and

A. E. COSTLEY    R. J. HASTIE         A. HERRMANN

B. LLOYD              G. F. MATTHEWS    J. J. O'ROURKE

D. F. START          B. J. D. TUBBING   D. J. WARD

CLARENDON PRESS - OXFORD

2004

**OXFORD**  
UNIVERSITY PRESS

Great Clarendon Street, Oxford OX2 6DP

Oxford University Press is a department of the University of Oxford.  
It furthers the University's objective of excellence in research, scholarship,  
and education by publishing worldwide in

Oxford New York

Auckland Bangkok Buenos Aires Cape Town Chennai

Dares Salaam Delhi Hong Kong Istanbul

Karachi Kolkata Kuala Lumpur Madrid Melbourne Mexico City Mumbai  
Nairobi São Paulo Shanghai Taipei Tokyo Toronto

Oxford is a registered trade mark of Oxford University Press  
in the UK and in certain other countries

Published in the United States  
by Oxford University Press Inc., New York

© John Wesson, 1987, 1997, 2004

The moral rights of the author have been asserted

Database right Oxford University Press (maker)

First edition 1987

Second edition 1997

Third edition 2004

All rights reserved. No part of this publication may be reproduced,  
stored in a retrieval system, or transmitted, in any form or by any means,  
without the prior permission in writing of Oxford University Press,  
or as expressly permitted by law, or under terms agreed with the appropriate  
reprographics rights organization. Enquiries concerning reproduction  
outside the scope of the above should be sent to the Rights Department,  
Oxford University Press, at the address above

You must not circulate this book in any other binding or cover  
and you must impose this same condition on any acquirer

A catalogue record for this title is available from the British Library

Library of Congress Cataloguing in Publication Data

(Data available)

ISBN 0 19 8509227

10 9 8 7 6 5 4 3 2 1

Typeset by Newgen Imaging Systems (P) Ltd., Chennai, India

Printed in Great Britain

on acid-free paper by

The Bath Press, Avon

## Preface

When I worked on toroidal devices in the early days of fusion research the plasma temperatures achieved were around 10 eV and the confinement times were perhaps 100 microseconds. In the next thirty years there was steady progress and at the publication of the first edition of this book in 1987 the temperatures in large tokamaks were several keV and a confinement time of one second had been reached.

By then the tokamak had become the predominant device in the attempt to achieve a useful power source from thermonuclear fusion. The accompanying increase in research activity and general interest in tokamaks led to the need for an introductory account of the subject and it was the aim of the first edition to provide such an introduction.

In the subsequent decade up to publication of the second edition the subject was transformed again. There were now areas where the experimental behaviour could be understood in terms of accepted theory, which was encouraging. There had also been substantial research on large tokamaks leading to the long awaited achievement of significant amounts of fusion power. Inevitably this brought us face to face with the problems involved in designing and building a tokamak reactor. The aim of the second edition was to describe these advances, and it is perhaps a measure of the developments in the subject that the second edition was twice the size of the first. When the time came for a reprint the opportunity was taken of bringing the book up to date in this third edition. In the intervening period the emphasis has been on preparing the ground for an experimental reactor but there have also been significant advances in our understanding of the plasma behaviour, for example, the wider experience of internal transport barriers, the appreciation of the role of tearing modes driven by neoclassical effects, and insights from turbulence simulations.

Despite the increasing complexity of the subject it is hoped that the book will still prove useful to those entering the subject, to specialists within tokamak research who wish to acquire knowledge of other areas in the subject, and to those outside tokamak research who would like to learn something of the principal concepts, methods, and problems involved. A further aim is to provide a handbook of equations, formulas, and data which the research worker frequently needs.

I regard it as an honour to have worked with the distinguished physicists who are my co-authors. Their spirit of cooperation has made the endeavour a pleasure.

I am grateful to my wife Olive for her support during the time-consuming preparation of the manuscript. I would like to thank Carol Simmons, Birgitta Croysdale, and Ingrid Farrelly who typed the earlier editions and Lynda Lee who has been unfailingly helpful in the preparation of this edition. I must further thank Stuart Morris who produced most of the figures and Chad Heys who helped with the many new figures required for the present edition. I am also grateful to Graham O'Connor for his careful reading of the text and for the resulting corrections.

Finally, I would like to dedicate this book to my friends and colleagues in the worldwide community of fusion physicists. They have set a splendid example of international collaboration for others to follow.

*England  
July 2003*

JOHN WESSON

---

# Authorship

---

- |  |  |
|--|--|
| 1 J.A. WESSON  | 8 H.R. WILSON  |
| 2 J.A. WESSON<br>2.11 R.J. Hastie  | 9 G.M. McCACKEN  |
| 3 J.A. WESSON<br>3.14 D.F. Start and B. Lloyd  | 10 R.D. GILL<br>10.2 D.J. Ward<br>10.3 J.J. O'Rourke<br>10.4 and 10.5 A.E. Costley<br>10.9 G.F. Matthews |
| 4 J.W. CONNOR<br>4.1-4.5 J.A. Wesson<br>4.8 J.A. Wesson<br>4.11 B.J.D. Tubbings<br>4.13 J.A. Wesson<br>4.23-4.25 J.A. Wesson | 11 J.A. WESSON AND J. HUGILL   |
| 5 J.A. WESSON (5.1-5.5)<br>C.N. LASHMORE-DAVIES (5.6-5.10)   | 12 D.J. CAMPBELL<br>12.6 A. Herrmann   |
| 6 J.A. WESSON  | 13 J.A. WESSON<br>13.5 D.J. Ward   |
| 7 J.A. WESSON  | 14 J.A. WESSON<br>14.13 J.W. Connor  |

---

## Acknowledgements

---

The authors acknowledge the help of many colleagues and in particular as follows:

Tokamak reactor—Roger Hancox and Terry Martin.

Potato orbits—Bill Core and Per Helander.

Current drive—Martin Cox and Martin O'Brien.

Transport barriers—Barry Alper.

Confinement—Ted Stringer and Geoff Cordey.

Neutral beam heating—Andrew Bickley, Ron Hemsworth, Peter Massmann, and Ernie Thompson.

RF heating—Lars-Goran Eriksson, Jean Jacquinot, and Franz Söldner.

Neoclassical tearing modes—Richard Buttery and Tim Hender.

TAE modes—Sergei Sharapov.

Plasma surface interactions—Rainer Behrisch, Richard Pitts, and Peter Stangeby.

Diagnostics—Wolfgang Engelhardt, Ian Hutchinson, and George Magyar.

Tokamak experiments—Karl Heinz Finken, Martin Greenwald, Otto Gruber, Ian Hutchinson, Louis Laurent, Niek Lopes Cardozo, Kent McCormick, William Morris, Jerome Pamela, Chris Schüller, Paul Smeulders, Alan Sykes, Paul Thomas, Fritz Wagner, Henri Weisen, Gerd Wolf and Hartmut Zohm.

ITER—George Vayakis

---

# Contents

---

Units and symbols	xiii	2.15	Collision times	69
		2.16	Resistivity	70
		2.17	Runaway electrons	72
<b>1 Fusion</b>	<b>1</b>	2.18	Electromagnetism	75
1.1 Fusion and tokamaks	2	2.19	Fluid equations	77
1.2 Fusion reactions	3	2.20	Magnetohydrodynamics	79
1.3 Thermonuclear fusion	5	2.21	Physics of plasma fluid	81
1.4 Power balance	8	2.22	Plasma diamagnetism	84
1.5 Ignition	10	2.23	Braginskii equations	88
1.6 Tokamaks	15	2.24	Plasma waves	94
1.7 Tokamak reactor	18	2.25	Landau damping	100
1.8 Fuel resources	24			
1.9 Tokamak economics	25	<b>3 Equilibrium</b>	<b>105</b>	
1.10 Tokamak research	27	3.1	Tokamak equilibrium	106
		3.2	Flux functions	108
		3.3	Grad-Shafranov equation	109
<b>2 Plasma physics</b>	<b>33</b>	3.4	Safety factor, $q$	111
2.1 Tokamak plasma	34	3.5	Beta	115
2.2 Debye shielding	35	3.6	Large aspect-ratio	117
2.3 Plasma frequency	38	3.7	Shafranov shift	119
2.4 Larmor orbits	40	3.8	Vacuum magnetic field	121
2.5 Particle motion along $B$	42	3.9	Electric fields	123
2.6 Particle drifts	44	3.10	Particle orbits	124
2.7 Adiabatic invariants	49	3.11	Particle trapping	127
2.8 Collisions	51	3.12	Trapped particle orbits	129
2.9 Kinetic equations	55	3.13	Plasma rotation	133
2.10 Fokker–Planck equation	57	3.14	Current drive	136
2.11 Gyro-averaged kinetic equations	58			
2.12 Fokker–Planck equation for a plasma	60	<b>4 Confinement</b>	<b>149</b>	
2.13 Fokker–Planck coefficients for Maxwellian distributions	62	4.1	Tokamak confinement	150
2.14 Relaxation processes	65	4.2	Resistive plasma diffusion	152
		4.3	Diffusion in a cylinder	153

x	Contents				
4.4	Pfirsich-Schlüter current	155	5.10	Electron cyclotron resonance heating	290
4.5	Pfirsich-Schlüter diffusion	158			
4.6	Banana regime transport	159			
4.7	Plateau transport	167	<b>6 Mhd stability</b>		<b>303</b>
4.8	Ware pinch effect	169	6.1	Mhd stability	304
4.9	Bootstrap current	172	6.2	Stability theory	306
4.10	Neoclassical resistivity	174	6.3	Growth rates	307
4.11	Ripple transport	175	6.4	Energy principle	309
4.12	Confinement modes and scaling expressions	180	6.5	Tokamak instabilities	311
4.13	H-modes	185	6.6	Large aspect-ratio tokamak	312
4.14	Internal transport barriers	189	6.7	Kink instability	313
4.15	Scaling laws	191	6.8	Tearing modes	318
4.16	Transport coefficients	195	6.9	Tearing stability	324
4.17	Fluctuations	198	6.10	Internal kink	329
4.18	Turbulence-induced transport	202	6.11	Resistive $m = 1$ modes	332
4.19	Radial electric field shear and transport	210	6.12	Localized modes	336
4.20	Candidate modes	213	6.13	Ballooning modes	337
4.21	Turbulence simulations, critical gradients, and temperature pedestals	217	6.14	Ballooning stability	340
			6.15	Axisymmetric modes	342
			6.16	$\beta$ limit	343
4.22	Impurity transport	219	<b>7 Instabilities</b>		<b>351</b>
4.23	Experimental discoveries	223			
4.24	Radiation losses	227	7.1	Instabilities	352
4.25	Impurity radiation	229	7.2	Magnetic islands	354
			7.3	Tearing modes	356
<b>5 Heating</b>		<b>237</b>	7.4	Mirnov instabilities	362
5.1	Heating	238	7.5	Current penetration	364
5.2	Ohmic heating	240	7.6	Sawtooth oscillations	365
5.3	Neutral beam injection	243	7.7	Disruptions	374
5.4	Neutral beam heating	246	7.8	Causes of disruptions	376
5.5	Neutral beam production	253	7.9	Physics of disruptions	382
5.6	Radio frequency heating	258	7.10	Mode locking	390
5.7	Physics of radio frequency heating	261	7.11	Error field instability	394
5.8	Ion cyclotron resonance heating	270	7.12	Vertical instability	396
5.9	Lower hybrid resonance heating	286	7.13	Ergodicity	397
			7.14	Fishbone instability	399
			7.15	Toroidal Alfvén eigenmodes	402

7.16	MARFEs	406	10.6	Ion temperature and the ion distribution function	522
7.17	ELMs	409			
7.18	Operational overview	411	10.7	Radiation from plasmas	531
			10.8	Total radiation measurements	541
<b>8</b>	<b>Microinstabilities</b>	<b>417</b>	10.9	Langmuir probes	<b>546</b>
8.1	Microinstabilities	418	10.10	Measurements of fluctuations	551
8.2	Electron drift wave	420	10.11	Determination of the <i>q</i> -profile	556
8.3	Passing particle instabilities	422			
8.4	Trapped particle instabilities	430			
8.5	Micro-tearing modes	435			
<b>9</b>	<b>Plasma-surface interactions</b>	<b>443</b>	<b>11</b>	<b>Tokamak experiments</b>	<b>561</b>
9.1	Plasma-surface interactions	444	11.1	Tokamak experiments	562
9.2	The plasma sheath	446	11.2	T-3	563
9.3	The scrape-off layer	449	11.3	ST	564
9.4	Recycling	453	11.4	JFT-2	566
9.5	Atomic and molecular processes	457	11.5	Alcator A, Alcator C, and Alcator C-Mod	567
9.6	Wall conditioning	462	11.6	TFR	569
9.7	Sputtering	466	11.7	DITE	570
9.8	Arcing	473	11.8	PLT	572
9.9	Limiters	475	11.9	T-10	572
9.10	Divertors	477	11.10	ISX	573
9.11	Heat flux, evaporation, and heat transfer	489	11.11	FT and FT Upgrade	574
9.12	The behaviour of tritium	492	11.12	Doublet-III	576
			11.13	ASDEX	576
			11.14	TEXT	579
			11.15	TEXTOR	580
			11.16	Tore Supra	581
			11.17	COMPASS	583
			11.18	RTP	584
			11.19	START, MAST, and NSTX	586
			11.20	TCV	589
<b>10</b>	<b>Diagnostics</b>	<b>497</b>	11.21	Tokamak parameters	<b>590</b>
10.1	Tokamak diagnostics	498			
10.2	Magnetic measurements	500			
10.3	Interferometry	507	<b>12</b>	<b>Large Tokamaks</b>	<b>593</b>
10.4	Reflectometry	511	12.1	Large Tokamaks	594
10.5	Measurement of electron temperature	514	12.2	TFTR	597
			12.3	JET	617

xii	Contents				
12.4	JT-60/JT-60U	645	14.3	Units—conversions	724
12.5	DIII-D	665	14.4	Physical constants	725
12.6	ASDEX Upgrade	687	14.5	Coulomb logarithm	725
			14.6	Collision times	729
			14.7	Lengths	731
<b>13</b>	<b>The future</b>	<b>705</b>	14.8	Frequencies	733
13.1	Status	706	14.9	Velocities	734
13.2	Strategy	707	14.10	Resistivity	735
13.3	Reactor requirements	708	14.11	Chang–Hinton formula for $\chi_i$	737
13.4	ITER	711	14.12	Bootstrap current	738
13.5	Prospects	718	14.13	Confinement scaling relations	740
			14.14	Plasma shape	741
<b>14</b>	<b>Appendix</b>	<b>721</b>	14.15	Formulae	742
14.1	Vector relations	722	14.16	Symbols	743
14.2	Differential operators	722	<b>Index</b>		<b>745</b>

---

## Units and symbols

---

The system of units used is m.k.s. Following the convention generally accepted in the subject, temperatures are written either in joules or in electron-volts (or keV). Thus in place of conventional  $kT^\circ$  (where  $k$  is Boltzmann's constant and  $T^\circ$  is in degrees Kelvin) we write  $T$  (joules), so that  $T^\circ = T$  (joules)/ $1.381 \times 10^{-23}$ . The temperature in electron-volts is defined by the potential difference in volts through which an electron must fall to acquire an energy  $T$ , that is  $T(\text{eV}) = T(\text{joules})/e$  where  $e$  is the electronic charge. Thus  $T(\text{eV}) = T(\text{joules})/1.602 \times 10^{-19}$ . Whenever the temperature given is in electron-volts this is explicitly stated.

To avoid continual redefinition of frequently used symbols a list of such symbols is given in Section 14.16.

**1**

# **Fusion**

**1.1****Fusion and tokamaks**

If a nucleus of deuterium fuses with a nucleus of tritium, an  $\alpha$ -particle is produced and a neutron released. The nuclear rearrangement results in a reduction in total mass and a consequent release of energy in the form of the kinetic energy of the reaction products. The energy released is 17.6 MeV per reaction. In macroscopic terms, just 1 kg of this fuel would release  $10^8$  kWh of energy and would provide the requirements of a 1 GW (electrical) power station for a day.

Deuterium is a plentiful resource but tritium does not occur naturally. It should, however, be possible to use the neutrons released in the fusion reaction to breed tritium from lithium, of which there are large reserves.

In order to induce the fusion of nuclei of deuterium and tritium it is necessary to overcome the mutual repulsion due to their positive charges, and as a result the cross-section for fusion is small at low energies. However, the cross-section increases with energy, reaching a maximum at 100 keV, and a positive energy balance is possible if the fuel particles can be made to react before they lose their energy. To achieve this the particles must retain their energy and remain in the reacting region for a sufficient time. More precisely the product of this time and the density of reacting particles must be sufficiently large.

The simple schemes of firing a beam of particles into a solid target or through another beam fail to satisfy this criterion. In the first case the particles lose their energy too rapidly and in the second the density is too low.

The most promising method of supplying the energy is to heat the deuterium-tritium fuel to a sufficiently high temperature that the thermal velocities of the nuclei are high enough to produce the required reactions. Fusion brought about in this way is called thermonuclear fusion. The optimum temperature is not as high as that corresponding to the energy of maximum cross-section because the required reactions occur in the high energy tail of the Maxwellian distribution of heated particles. The necessary temperature is around 10 keV, that is about 100 million degrees centigrade. At such temperatures the fuel is fully ionized. The electrostatic charge of the nuclear ions is neutralized by the presence of an equal number of electrons and the resulting neutral gas is called a plasma.

Since such high temperatures preclude confinement by material walls another method of confinement is needed. The tokamak offers such a method. In a tokamak the plasma particles are confined to a toroidal region by a magnetic field, being held by the field in small gyrating orbits. It is possible by this means to arrange that ions travel a distance a million times the dimensions of the vessel before reaching the wall.

Although the required temperature, density and confinement time have all been obtained in tokamaks, they have not been achieved in the same

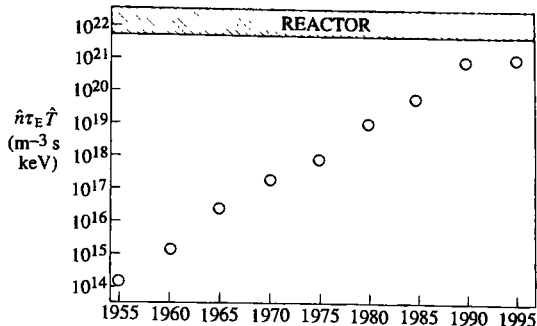


**Fig. 1.1.1** In a reactor the product  $n\tau_E$  of ion density and energy confinement time, and the temperature,  $T$ , must both be in the right range. Taking peak values, the required  $n\tau_E$  is  $2-5 \times 10^{20} m^{-3} s$  and the temperature range is around 10–20 keV. The required value of the product  $\hat{n}\tau_E \hat{T}$  is approximately  $5 \times 10^{21} m^{-3} s \text{ keV}$  (Section 5.1). The figure shows the progress in improving this product, leading to the verge of reactor conditions.

plasma. However, the progress toward this goal has been remarkable, and a thermonuclear power of more than sixty percent of the input power has been produced. A further step is to achieve ignition where, as with fossil fuels, the burning process becomes self-sustaining without further applied heating. The progress toward ignition can be measured by means of a single parameter. The form of the dependence of the fusion cross-section on energy fortuitously allows the requirement for ignition to be expressed approximately by

$$\hat{n}\tau_E \hat{T} > 5 \times 10^{21} m^{-3} s \text{ KeV}$$

where  $\hat{n}$  and  $\hat{T}$  are the peak ion density and temperature in the plasma and  $\tau_E$  is the energy confinement time. The improvement in the achieved value of this parameter over the years is shown in Fig. 1.1.1.

It is now believed that a tokamak can be built which would produce ignition. However, the design of such a reactor raises a wide range of questions. A commercial reactor even more so. Present research is aimed at answering these questions and this book gives an introductory account of our knowledge of the underlying physics.

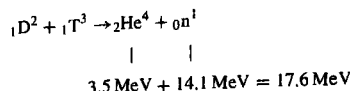
## 1.2

### Fusion reactions

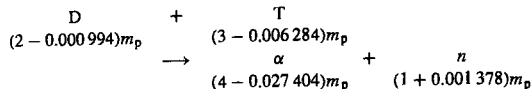
By far the most promising fusion reaction is that in which the nuclei of deuterium and tritium fuse to produce an alpha particle with the release

## 1.2 Fusion reactions

of a neutron, that is



where the energies given are the kinetic energies of the reaction products. The mass-energy balance follows from the overall mass deficit  $\delta m$  in the reaction



where  $m_p$  is the mass of the proton ( $1.6726 \times 10^{-27}$  kg). The mass deficit is  $0.018\,75m_p$ , and so the energy released is

$$\mathcal{E} = \delta m \cdot c^2 = 0.018\,75m_p c^2 = 2.818 \times 10^{-12} \text{ joules} = 17.59 \text{ MeV.}$$

The reaction is induced in collisions between the particles, and the cross-section for the reaction is therefore of fundamental importance. The cross-section at low impact energies is small because of the Coulomb barrier which prevents the nuclei from approaching to within nuclear dimensions as is required for fusion to take place. The potential is illustrated in Fig. 1.2.1.

Because of quantum mechanical tunneling, D-T fusion occurs at energies somewhat less than that required to overcome the Coulomb barrier. The cross-section for the reaction is given in Fig. 1.2.2 and it is seen that the maximum cross-section occurs at just over 100 keV.

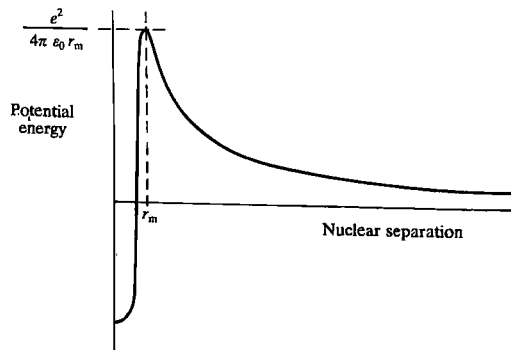
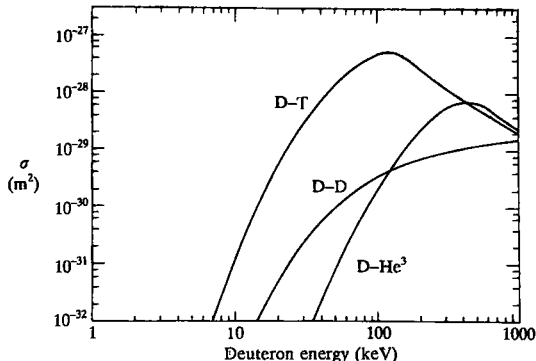
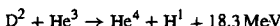
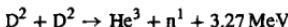


Fig. 1.2.1 Potential energy as a function of nuclear separation.



**Fig. 1.2.2** Cross-sections for the reactions D-T, D-D and D-He<sup>3</sup>. The two D-D reactions have similar cross-sections, the graph gives their sum.

The reason the D-T reaction is preferred to other reactions is clear from Fig. 1.2.2 where the cross-sections for



are also shown. It is seen that these cross-sections are considerably less than that for D-T except at impractically high energies.

## 1.3

### Thermonuclear fusion

Calculation of the reaction rate in a hot D-T plasma requires an integration over the distribution functions of both species. The rate of reaction per unit volume between particles of one species with a velocity  $v_1$  and particles of the other species with velocity  $v_2$  is

$$\sigma(v') v' f_1(v_1) f_2(v_2)$$

where

$$v' = v_1 - v_2$$

and  $f_1$  and  $f_2$  are the distribution functions.

If the distributions are Maxwellian.

$$f_j(v_j) = n_j \left( \frac{m_j}{2\pi T} \right)^{3/2} \exp - \frac{m_j v_j^2}{2T},$$

the total reaction rate per unit volume

$$\mathcal{R} = \iint \sigma(v') v' f_1(v_1) f_2(v_2) d^3 v_1 d^3 v_2$$

may be written

$$\begin{aligned} \mathcal{R} = n_1 n_2 & \frac{(m_1 m_2)^{3/2}}{(2\pi T)^3} \iint \exp \left( -\frac{m_1 + m_2}{2T} \left( V + \frac{1}{2} \frac{m_1 - m_2}{m_1 + m_2} v' \right)^2 \right) \\ & \times \sigma(v') v' \exp \left( -\frac{\mu v'^2}{2T} \right)^2 d^3 v' d^3 V \end{aligned}$$

where

$$V = \frac{v_1 + v_2}{2} \quad \text{and} \quad \mu = \frac{m_1 m_2}{m_1 + m_2},$$

$\mu$  being the reduced mass.

The integral over  $V$  is  $(2\pi T / (m_1 + m_2))^{3/2}$  so that

$$\mathcal{R} = 4\pi n_1 n_2 \left( \frac{\mu}{2\pi T} \right)^{3/2} \int \sigma(v') v'^3 \exp \left( -\frac{\mu v'^2}{2T} \right) dv'. \quad 1.3.1$$

The cross-sections measured in laboratory experiments are usually given in terms of the energy of the bombarding particle, say type 1, that is

$$\epsilon = \frac{1}{2} m_1 v^2$$

so that eqn 1.3.1 may be more conveniently written

$$\mathcal{R} = \left( \frac{8}{\pi} \right)^{1/2} n_1 n_2 \left( \frac{\mu}{T} \right)^{3/2} \frac{1}{m_1^2} \int \sigma(\epsilon) \epsilon \exp \left( -\frac{\mu \epsilon}{m_1 T} \right) d\epsilon. \quad 1.3.2$$

If the cross-section  $\sigma(\epsilon)$  for D-T reactions given in Section 1.2 is substituted into the integral of eqn 1.3.1, the reaction rate  $\mathcal{R} = n_d n_t \langle \sigma v \rangle$  is obtained where  $\langle \sigma v \rangle$  is given in Fig. 1.3.1. For a given ion density the maximum rate is achieved for  $n_d = n_t$ .

At temperatures of interest the nuclear reactions come predominantly from the tail of the distribution. This is illustrated in Fig. 1.3.2 where the

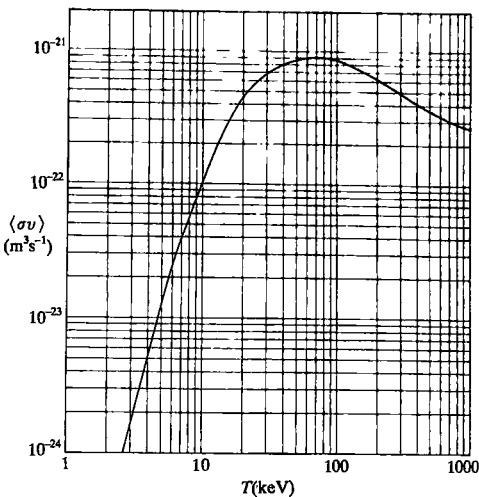


Fig. 1.3.1  $\langle\sigma v\rangle$  for D-T reactions as a function of plasma temperature.

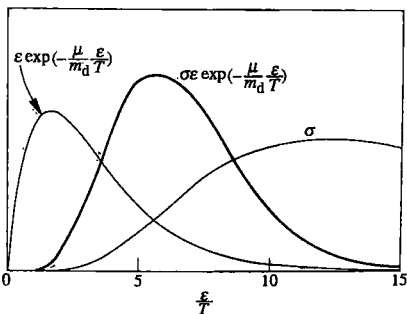
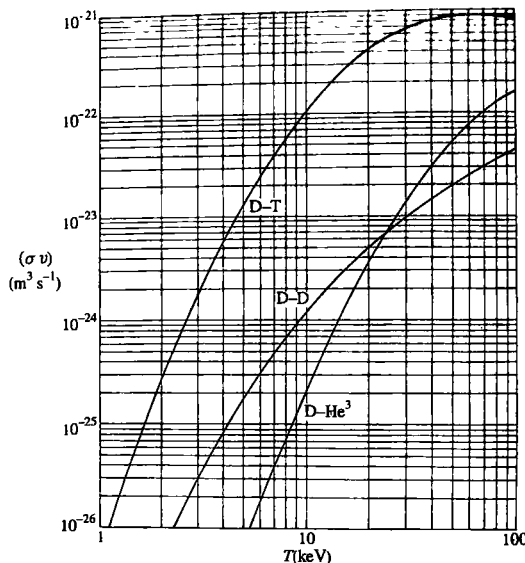


Fig. 1.3.2 Graph of the integrand of eqn 1.3.2 and of its two factors  $\sigma(\varepsilon)$  and  $\varepsilon \exp(-\mu\varepsilon/m_d T)$  against the normalized energy  $\varepsilon/T$  for a D-T plasma at  $T = 10 \text{ keV}$ .

integrand of eqn 1.3.2 is plotted against  $\varepsilon/T$  together with the two factors  $\sigma(\varepsilon)$  and  $\varepsilon \exp(-\mu\varepsilon/m_d T)$  for a D-T plasma at a temperature of 10 keV.

Experiments are more usually carried out using deuterium rather than a deuterium-tritium mixture. A graph of  $\langle\sigma v\rangle$  for deuterium is given in Fig. 1.3.3 together with that for D- $\text{He}^3$ . In the temperature range 5–20 keV the ratio of  $\langle\sigma v\rangle$  for D-T to that of deuterium is around 80.



**Fig. 1.3.3**  $(\sigma v)$  for D-D (total) and D-He<sup>3</sup> reactions as a function of plasma temperature. The values are much smaller than those for D-T which are included for comparison.

## 1.4

### Power balance

#### Thermonuclear power

The thermonuclear power per unit volume in a D-T plasma is

$$P_{Tn} = n_d n_t (\sigma v) \mathcal{E}, \quad 1.4.1$$

where  $n_d$  and  $n_t$  are the deuterium and tritium densities,  $(\sigma v)$  is the rate given in Fig. 1.3.1 and  $\mathcal{E}$  is the energy released per reaction. The total ion density is

$$n = n_d + n_t,$$

so eqn 1.4.1 can be written

$$P_{Tn} = n_d (n - n_d) (\sigma v) \mathcal{E}.$$

For a given  $n$  this power is maximized by  $n_d = \frac{1}{2}n$ , that is equal deuterium and tritium densities. For this optimum mixture the thermonuclear power density is

$$p_{T_0} = \frac{1}{4}n^2 \langle \sigma v \rangle E. \quad 1.4.2$$

### Energy loss

In a tokamak there is a continuous loss of energy from the plasma which has to be replenished by plasma heating. The average energy of plasma particles at a temperature  $T$  is  $\frac{3}{2}T$ , comprised of  $\frac{1}{2}T$  per degree of freedom. Since there is an equal number of electrons and ions, the plasma energy per unit volume is  $3nT$ . The total energy in the plasma is therefore

$$\begin{aligned} W &= \int 3nT \, d^3x \\ &= \overline{3nT} V, \end{aligned} \quad 1.4.3$$

where the bar represents the average value, and  $V$  is the plasma volume. The rate of energy loss,  $P_L$ , is characterized by an energy confinement time defined by the relation

$$P_L = \frac{W}{\tau_E}. \quad 1.4.4$$

In present tokamaks the thermonuclear power is usually small and in steady state the energy loss is balanced by externally supplied heating. Thus if the power supplied is  $P_H$ ,

$$P_H = P_L \quad 1.4.5$$

and eqns 1.4.4 and 1.4.5 give

$$\tau_E = \frac{W}{P_H}.$$

This expression provides a means of determining  $\tau_E$  from experimentally known quantities.

### $\alpha$ -particle heating

The thermonuclear power given by eqn 1.4.2 consists of two parts. Four fifths of the reaction energy is carried by the neutrons and the remainder,  $E_\alpha$ , is carried by the  $\alpha$ -particles. The neutrons leave the plasma without interaction but the  $\alpha$ -particles, being charged, are confined by the magnetic field. The  $\alpha$ -particles then transfer their 3.5 MeV energy to the

plasma through collisions. Thus the  $\alpha$ -particle heating per unit volume is

$$p_\alpha = \frac{1}{4} n^2 (\sigma v) \mathcal{E}_\alpha \quad 1.4.6$$

and the total  $\alpha$ -particle heating is

$$\begin{aligned} P_\alpha &= \int p_\alpha d^3x \\ &= \frac{1}{4} n^2 (\sigma v) \mathcal{E}_\alpha V. \end{aligned} \quad 1.4.7$$

### Power balance

In the overall power balance the power loss is balanced by the externally supplied power plus the  $\alpha$ -particle power. That is

$$P_H + P_\alpha = P_L$$

and using eqns 1.4.3, 1.4.4, and 1.4.7 this balance is given by

$$P_H + \frac{1}{4} n^2 (\sigma v) \mathcal{E}_\alpha V = \frac{3nT}{\tau_E} V. \quad 1.4.8$$

The implications of this equation are described in the next section.

## 1.5

### Ignition

#### Ignition condition

As a D-T plasma is heated to thermonuclear conditions the  $\alpha$ -particle heating provides an increasing fraction of the total heating. When adequate confinement conditions are provided, a point is reached where the plasma temperature can be maintained against the energy losses solely by  $\alpha$ -particle heating. The applied heating can then be removed and the plasma temperature is sustained by internal heating. By analogy with the burning of fossil fuels this event is called ignition.

The power balance is described by eqn 1.4.8 and, taking constant density and temperature for simplicity, this can be written

$$P_H = \left( \frac{3nT}{\tau_E} - \frac{1}{4} n^2 (\sigma v) \mathcal{E}_\alpha \right) V. \quad 1.5.1$$

Equation 1.5.1 provides the condition for ignition, the requirement for the plasma burn to be self-sustaining being

$$n\tau_E > \frac{12}{(\sigma v)} \frac{T}{\mathcal{E}_\alpha}. \quad 1.5.2$$

The right-hand side of inequality 1.5.2 is a function of temperature only and a graph of the temperature dependence of the required value of  $n\tau_E$

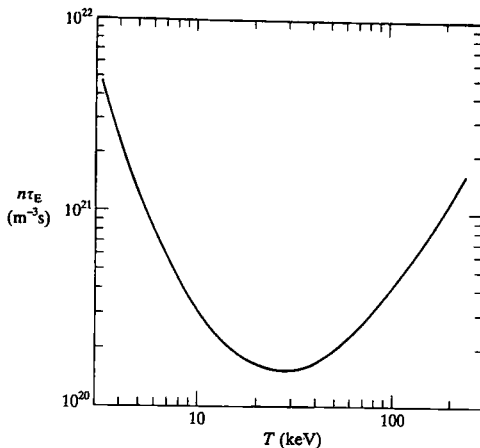


**Fig. 1.5.1** The value of  $n\tau_E$  required to obtain ignition, as a function of temperature.

is given in Fig. 1.5.1. It has a minimum close to  $T = 30 \text{ keV}$  and the requirement for ignition at this temperature is

$$n\tau_E > 1.5 \times 10^{20} \text{ m}^{-3} \text{ s} \quad 1.5.3$$

However, since  $\tau_E$  is itself a function of temperature, the temperature at the minimum is not to be taken as an optimum condition. It turns out that the ignition temperature is likely to be somewhat lower. It is a fortunate coincidence for calculation that in the temperature range 10–20 keV the reaction rate is represented to within 10% by

$$\langle\sigma v\rangle = 1.1 \times 10^{-24} T^2 \text{ m}^3 \text{ s}^{-1}, \quad T \text{ in keV}, \quad 1.5.4$$

so that, using  $E_\alpha = 3.5 \text{ MeV}$ , the ignition condition becomes

$$nT\tau_E > 3 \times 10^{21} \text{ m}^{-3} \text{ keV s}. \quad 1.5.5$$

This is a very convenient form for the ignition condition since it brings out clearly the requirements on density, temperature and confinement time. The condition would be reached for example by  $n = 10^{20} \text{ m}^{-3}$ ,  $T = 10 \text{ keV}$  and  $\tau_E = 3 \text{ s}$ .

The precise value of the constant in condition 1.5.5 depends on the profiles of  $n$  and  $T$  and on the use of average or peak values. The condition 1.5.5 is for flat profiles. For parabolic density and temper-

profiles the ignition requirement on the peak value is

$$\hat{n} \hat{T} \tau_E > 5 \times 10^{21} \text{ m}^{-3} \text{ keV s.} \quad 1.5.6$$

Relation 1.5.3 is reminiscent of the Lawson criterion. In the early days of fusion research Lawson identified the product of density and confinement time,  $n\tau$ , as a critical parameter for a thermonuclear reactor. However, in his calculation he neglected  $\alpha$ -particle heating and assumed that the plasma was heated from an external source. It is then clearly a necessary, but not sufficient, requirement that the power produced by the reactor, after the inefficiencies of transforming to electrical power, should be able to supply the applied heating. In the ignition calculation described above only the  $\alpha$ -particle fraction, 20%, of the total energy is used to heat the plasma. In Lawson's calculation the corresponding factor is related to the power station efficiency,  $\eta$ , with  $\eta \approx 30\%$ . Thus Lawson's necessary  $n\tau$  turns out to be somewhat less stringent than the ignition criterion 1.5.3, requiring  $n\tau > 0.6 \times 10^{20} \text{ m}^{-3} \text{ s}$ . Lawson also took account of hydrogen bremsstrahlung radiation but, as will be shown in Section 4.24, this loss is small for a tokamak plasma.

A measure of the success in approaching reactor conditions is given by the ratio,  $Q$ , of the thermonuclear power produced to the heating power supplied, that is

$$Q = \frac{\frac{1}{4}n^2(\sigma v)\mathcal{E}V}{P_H}.$$

Since the energy  $\mathcal{E}$  released in each reaction is five times the  $\alpha$ -particle energy  $\mathcal{E}_\alpha$ ,  $Q$  may also be written

$$Q = \frac{5P_\alpha}{P_H}.$$

Thus  $Q = 1$  corresponds to an  $\alpha$ -particle power which is 20% of the applied heating power. At ignition, where  $P_H$  is reduced to zero,  $Q \rightarrow \infty$ .

It is seen that although an ignited plasma has the desirable feature that no applied heating is required, it is quite possible to obtain a large  $Q$  without ignition. However, in this case the supplied power  $P_H$  is a cost on the system in that it involves recycling some of the reactor power with a corresponding loss of efficiency.

### Approach to ignition

The approach to ignition can be described by adding the time dependence to eqn 1.5.1. This gives

$$\frac{d}{dt}3nT = \frac{P_H}{V} + \frac{1}{4}n^2(\sigma v)\mathcal{E}_\alpha - \frac{3nT}{\tau_E(n, T)}. \quad 1.5.7$$

If the heating power is increased slowly the solution of eqn 1.5.7 consists of a sequence of quasi-steady states for which the terms on the right-hand side balance to give zero. The result depends on the density and

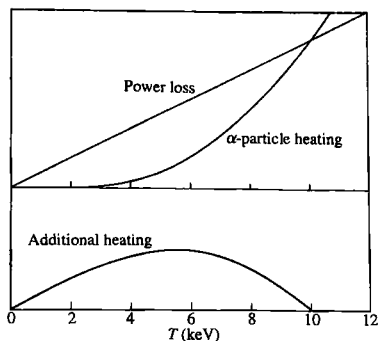


**Fig. 1.5.2**  $\alpha$ -particle heating and power loss from the plasma for constant confinement time, and ignition at 10 keV. The lower graph shows the applied heating required to balance the excess of power loss over  $\alpha$ -particle heating and sustain a steady temperature.

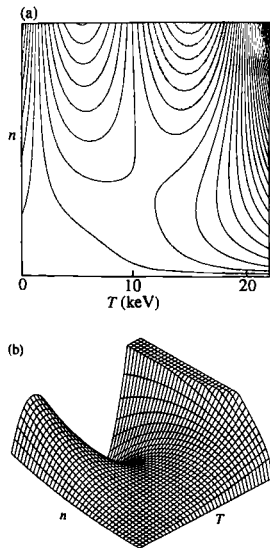


**Fig. 1.5.3** (a) Contours of power needed to maintain a steady state in the  $(n, T)$  plane. The shaded region corresponds to the ignited plasma and within this region the contours give the excess of  $\alpha$ -particle heating over energy losses. (b) A two dimensional graph giving the shape of  $P(n, T)$  corresponding to the contours of Fig. (a).

temperature dependence of the confinement time which is uncertain in the regime of interest.

The general type of behaviour expected is illustrated in Fig. 1.5.2. This gives the temperature dependence of the  $\alpha$ -particle heating and loss terms together with the required power, for a constant confinement time and ignition at 10 keV. It is seen that in this case the maximum applied power is required at about 5 keV and this power is then less than 40% of the  $\alpha$ -particle power at the ignition temperature.

A more general view of the approach to ignition is obtained by considering the power balance in the  $(n, T)$  plane. Using eqn 1.5.1 it is possible to plot contours of equal values of  $P$  required to maintain a given temperature at a given density. Uncertainty over  $\tau_E(n, T)$  prevents the drawing of a precise diagram but Fig. 1.5.3(a) illustrates the general form expected. Figure 1.5.3(b) gives the same information in the form of a two dimensional graph  $P(n, T)$ . It is seen that the trajectory to ignition requiring minimum power is one which goes over the saddle point. This saddle is often called the Cordey pass.

At ignition the applied heating can be switched off and there is an equilibrium between the  $\alpha$ -particle heating and the power lost from the plasma. However, for the case shown in Fig. 1.5.2 this equilibrium is unstable. A small increase in temperature leads to a positive imbalance of heating over losses and this enhances the temperature increase.

This instability can be analysed for the more general situation in which  $\tau_E$  is taken to be a function of temperature and the density is kept constant. Thus taking the time dependent heating eqn 1.5.7 with  $P_H = 0$ ,

$$3n \frac{dT}{dt} = -3n \frac{T}{\tau_E(T)} + \frac{1}{4} n^2 (\sigma v) \mathcal{E}_\alpha. \quad 1.5.8$$

The equilibrium is given by

$$3\frac{T}{\tau_E} = \frac{1}{4}n(\sigma v)\mathcal{E}_\alpha. \quad 1.5.9$$

Considering a small change,  $\Delta T$ , from the equilibrium temperature, and expanding  $\tau_E$  and  $(\sigma v)$  about their equilibrium values, eqn 1.5.8 gives the equation governing stability.

$$3n\frac{d\Delta T}{dt} = \left[ -3n\left(\frac{1}{\tau_E} - \frac{T}{\tau_E^2}\frac{d\tau_E}{dT}\right) + \frac{1}{4}n^2\frac{d(\sigma v)}{dT}\mathcal{E}_\alpha \right] \Delta T. \quad 1.5.10$$

Substituting the equilibrium solution from eqn 1.5.9, eqn 1.5.10 becomes

$$3n\frac{d\Delta T}{dt} = \frac{1}{4}n^2(\sigma v)\frac{\mathcal{E}_\alpha}{T}\left(-1 + \frac{T}{\tau_E}\frac{d\tau_E}{dT} + \frac{T}{(\sigma v)}\frac{d(\sigma v)}{dT}\right)\Delta T.$$

If the right-hand side is positive  $\Delta T$  grows exponentially. Thus the condition for stability is

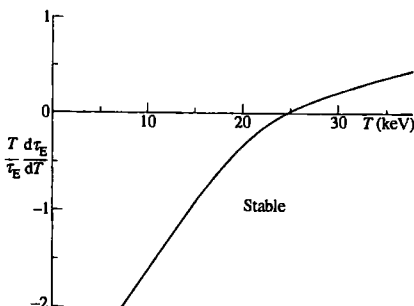
$$\frac{T}{\tau_E}\frac{d\tau_E}{dT} < 1 - \frac{T}{(\sigma v)}\frac{d(\sigma v)}{dT}.$$

Figure 1.5.4 gives a graph of the value of  $(T/\tau_E)d\tau_E/dT$  required for stability.

Experimental results show that the energy confinement time decreases with increasing temperature and typically  $\tau_E \propto 1/T$ . This temperature dependence has  $(T/\tau_E)d\tau_E/dT = -1$  and from Fig. 1.5.4 it is seen that an equilibrium is then stable for  $T > 14.5$  keV. Figure 1.5.5 gives an example of heating and loss graphs for this temperature dependence of  $\tau_E$ . For the case shown there are two equilibrium temperatures, one at  $\sim 13$  keV and the other at  $\sim 16$  keV. At the lower equilibrium temperature the thermonuclear burn is weakly unstable and the temperature would rise to the upper equilibrium temperature which is stable.

Instability can also occur in a sub-ignited plasma once the maximum applied power condition is passed. Stable approach to ignition therefore requires a controlled reduction of the power.

If the ignited plasma is not temperature stable it will be necessary to provide a feedback control which adjusts one of the parameters appearing in the energy balance equation. Thus control could be achieved by adjusting the density, the D-T mixture or the confinement time. Another factor which will play a role is the accumulation of the 'helium ash' in the form of slowed down  $\alpha$ -particles.



**Fig. 1.5.4** Stability for  $\alpha$ -particle heating requires that  $(T/\tau_E) d\tau_E/dT$  be below a critical value. The graph gives its temperature dependence.

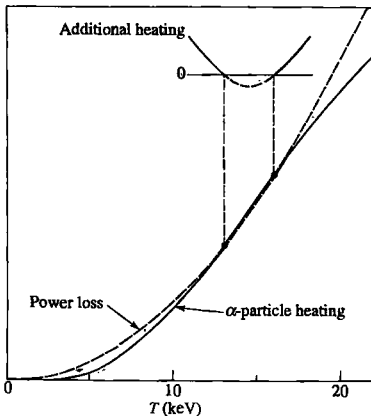


**Fig. 1.5.5** A deterioration of confinement with increasing temperature is a stabilizing effect for  $\alpha$ -particle heating. The figure shows the power loss as a function of temperature for  $\tau_E \propto 1/T$  together with the corresponding  $\alpha$ -particle power. For the case shown the conditions are arranged so that unstable ignition occurs at 13 keV. The instability then takes the temperature to a stable equilibrium 16 keV. The inset graph shows the additional power required to sustain a given temperature.

## 1.6

### Tokamaks

The tokamak is a toroidal plasma confinement system, the plasma being confined by a magnetic field. The principal magnetic field is the toroidal field. However, this field alone does not allow confinement of the plasma. In order to have an equilibrium in which the plasma pressure is balanced

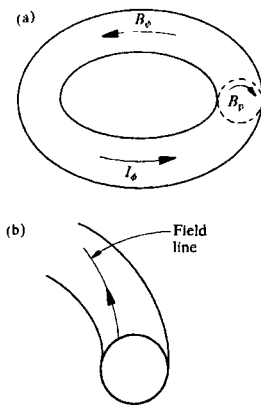


**Fig. 1.6.1** (a) Toroidal magnetic field  $B_\phi$ , and poloidal magnetic field  $B_p$  due to toroidal current  $I_\phi$ . (b) Combination of  $B_\phi$  and  $B_p$  causes field lines to twist around plasma.

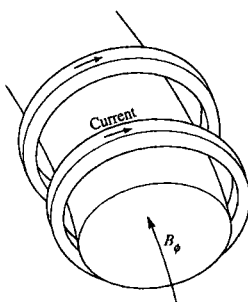


**Fig. 1.6.2** The toroidal magnetic field is produced by current in external coils.

by the magnetic forces it is necessary also to have a poloidal magnetic field. In a tokamak this field is produced mainly by current in the plasma itself, this current flowing in the toroidal direction. These currents and fields are illustrated in Fig. 1.6.1(a). The combination of the toroidal field  $B_\phi$  and poloidal field  $B_p$  gives rise to magnetic field lines which have a helical trajectory around the torus as shown in Fig. 1.6.1(b). The toroidal magnetic field is produced by currents in coils linking the plasma as shown in Fig. 1.6.2.

The plasma pressure is the product of the particle density and temperature. The fact that the reactivity of the plasma increases with both of these quantities implies that in a reactor the pressure must be sufficiently high. The pressure which can be confined is determined by stability considerations and increases with the strength of the magnetic field. However, the magnitude of the toroidal field is limited by technological factors. In laboratory experiments with copper coils both the requirement for cooling and the magnetic forces put a limit on the magnetic field which they can produce. Furthermore in a reactor the Joule heating loss in normal coils is unacceptable and superconducting coils are envisaged. There is a loss of superconductivity above a critical magnetic field and this presents another limitation. With present technology it seems likely that the maximum magnetic field at the coils would be limited to around 12 T, but improved conductors with fields up to 16 T are also considered. This maximum toroidal field appears at the inboard side of the toroidal field coil. Since the toroidal magnetic field is inversely proportional to the major radius the resulting field at the centre of the plasma would be around 6–8 T. The toroidal fields in present large tokamaks are somewhat lower than this value.

For a given toroidal magnetic field the plasma pressure which can be stably confined increases with toroidal plasma current up to a limiting value. The resulting poloidal magnetic fields are typically an order of magnitude smaller than the toroidal field. In present large tokamaks currents of several megamps are used, a current of 7 MA having been produced in the JET tokamak. With conservative assumptions a reactor would require a current of 20–30 MA. Advances in technology and understanding could lead to a lower value.

In present experiments the plasma current is driven by a toroidal electric field induced by transformer action in which a flux change through the torus is generated as illustrated in Fig. 1.6.3(a). The flux change is brought about by a current passed through a primary coil around the torus as shown in Fig. 1.6.3(b). Although not essential, an iron transformer core is often used, reducing the required power supply and having the advantage of reduced stray magnetic fields.

There are advantages for confinement and achievable pressure with plasmas which are vertically elongated. Control of the shape requires additional toroidal currents. Further such currents are required to control the position of the plasma. These toroidal currents are carried by suitably placed coils. The complete system of toroidal and poloidal coils is illustrated in Fig. 1.6.4.

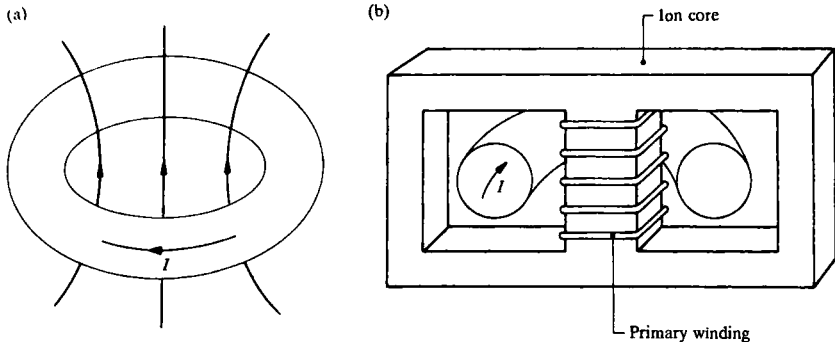


**Fig. 1.6.3** (a) A change of flux through the torus induces a toroidal electric field which drives the toroidal current. (b) The flux change is produced by primary winding often using a transformer core.

The processes limiting the confinement of plasma in tokamaks are not understood. However the expected improvement of confinement with size is found experimentally. Typically the best energy confinement times for existing tokamaks are around  $\frac{1}{2}r_p^2$  where  $r_p$  is the mean minor radius of the plasma. An energy confinement time of greater than one second has been obtained in JET. It is found that the energy confinement time increases with plasma current and, unfortunately, decreases with increasing plasma pressure.

Tokamak plasmas are heated to temperatures of a few keV by the ohmic heating of the plasma current. The required temperatures of  $\gtrsim 10$  keV are then achieved by additional heating by particle beams or electromagnetic waves.

Present tokamak plasmas typically have particle densities in the range  $10^{19}\text{--}10^{20}\text{ m}^{-3}$ . This is a factor  $10^6$  lower than that in the atmosphere. The plasma is contained within a vacuum vessel and to minimize the presence of impurities low background pressures must be maintained.

Impurities in the plasma give rise to radiation losses and also dilute the fuel. The restriction of their entry into the plasma therefore plays a fundamental role in the successful operation of tokamaks. This requires a separation of the plasma from the vacuum vessel. Two techniques are currently used. The first is to define an outer boundary of the plasma with a material limiter as shown in Fig. 1.6.5(a). The second is to keep the particles away from the vacuum vessel by means of a modification of the magnetic field to produce a magnetic divertor as shown in Fig. 1.6.5(b).

A tokamak reactor will require additional elements in the tokamak structure itself and will also need a means of converting the fusion power into electricity. These features are described in Section 1.7.

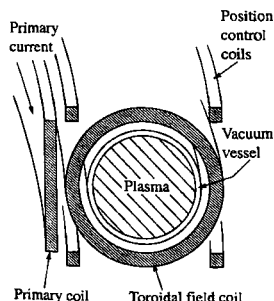


**Fig. 1.6.4** Arrangement of coils in a tokamak.

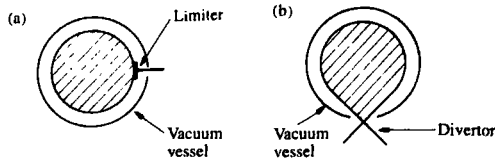


**Fig. 1.6.5** Separation of plasma from vacuum vessel by (a) limiter and (b) divertor.

## 1.7 Tokamak reactor

### Structure of reactor

A tokamak reactor would be considerably more complex than a non-thermonuclear tokamak. The general structure is illustrated in Fig. 1.7.1 and described below.

The plasma is surrounded by a blanket which has three roles. Firstly, it absorbs the 14 MeV neutrons, transforming their energy into heat which is then carried away by a suitable coolant to provide most of the reactor power output. Secondly, in absorbing neutrons the blanket shields the superconducting coils and other outer components. Thirdly, the blanket allows the necessary breeding of tritium to fuel the reactor. In order to accomplish this the blanket is composed of a compound of lithium such as  $\text{Li}_2\text{O}$ . A triton is produced in each neutron-lithium reaction as described in Section 1.8 but it is not possible to engineer the blanket so that all the neutrons undergo such a reaction. In order to make up for this deficiency and achieve an overall breeding ratio greater than unity, it is necessary to employ a neutron multiplier such as beryllium or lead. The neutron flux

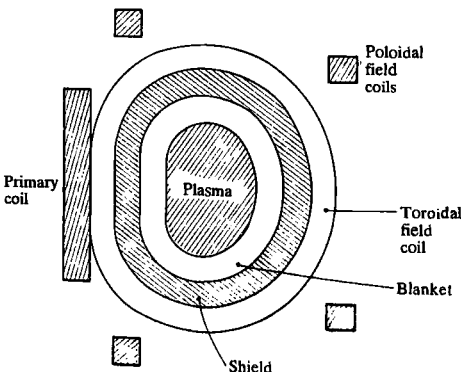


**Fig. 1.7.1** Layout of principal components in a conceptual tokamak reactor.

from the plasma decays with distance into the blanket, a blanket thickness of 0.6–1.0 m being adequate to absorb most of the neutrons.

The energy flux of the neutrons which pass through the outer wall of the blanket must be reduced by a factor  $10^6$ – $10^7$  before reaching the superconducting coils to avoid both radiation damage and heating of the coils. This protection is achieved by placing a shield of about 1 m thickness of high Z material such as steel between the blanket and the coils.

In experimental tokamaks direct contact between the plasma and the first wall is avoided by means of either a material limiter or by a divertor which leads magnetic field lines away from the surface of the plasma to a dump plate more remote from the plasma as described in Section 9.10. In a reactor the power load on the material surfaces will be substantially higher and the need to minimize the flow of impurities into the plasma, together with a greater flexibility of design, appears to favour the divertor system.

Ideally the toroidal current in the plasma would be continuous in time. However with the transformer action, the driving electric field is induced by increasing the magnetic flux linking the torus, and this can only be continued for a limited period. The transformer action might allow pulses of, say, one hour. Although not entirely satisfactory it is possible to accept such pulsed operation provided the shut-down period is sufficiently brief that the repeated thermal stresses arising from cooling are acceptable. The alternative solution is to arrange that a continuous current is driven by other means than an electric field. The current drive requirement is substantially lessened by the fact that the plasma itself will generate part of the required current through a mechanism called the bootstrap effect. The remaining currents would be driven by injected neutral particle beams or electromagnetic waves. These methods of current drive are described in Section 3.14.

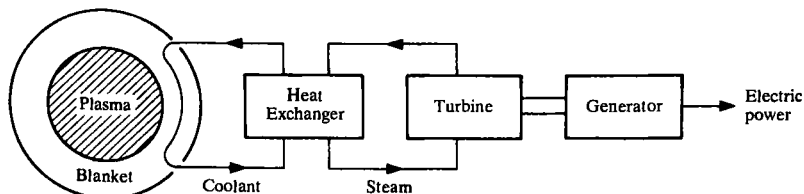
The heat leaving the plasma and that produced in the blanket, would be removed by a liquid or gaseous coolant. It would then be transformed into electrical power by conventional means as illustrated in Fig. 1.7.2.

### Reactor parameters

Sufficient information is now available from experimental tokamaks to be able to estimate the general parameters of a tokamak reactor.

The size and plasma current required for a reactor are basically determined by three considerations. The first is the energy confinement time.

Fig. 1.7.2 Thermonuclear power absorbed in blanket would be converted into electric power by conventional means.



The confinement time must be long enough to satisfy the power balance condition for a reacting plasma as described in Section 1.4. This requires that the plasma be sufficiently large, allowing the improvement in confinement which comes from the increased current carrying capacity of the larger plasma. However, this introduces the second consideration, instability induced plasma disruptions which bring plasma operation to a sudden halt. For a given device the plasma current must be accompanied by a sufficiently large toroidal magnetic field to avoid disruptions. The third constraint is that the toroidal magnetic field is itself limited both by the critical field allowed in superconductors and by the magnetic stresses on the coil. There is some uncertainty associated with each of these factors but it is nevertheless possible to make an approximate calculation of the required parameters.

The reactor plasma must satisfy conditions on density, temperature, and confinement. As shown in Section 1.5, these conditions can be summarized by the requirement

$$\hat{n}\hat{T}\tau_E \gtrsim 5 \times 10^{21} \text{ m}^{-3} \text{ keV s.} \quad 1.7.1$$

To relate this requirement to the plasma parameters an expression is needed for the energy confinement time. Various empirical formulas have been proposed and, as described in Chapter 4, several different modes of operation have been found. It is convenient to start the discussion by introducing an early formula which has stood the test of time. This formula, given by Goldston, can be approximated by

$$\tau_E = \frac{I^2}{nT} f\left(\frac{R}{a}, \frac{b}{a}\right), \quad 1.7.2$$

where  $I$  is the plasma current,  $n$  and  $T$  are the density and temperature,  $R/a$  is the aspect ratio and  $b/a$  is the elongation of the plasma, measured by the ratio of its half-height and half-width.

There are uncertainties in formula 1.7.2 with regard to both the magnitude and scaling. In particular, regimes which have better confinement have been found. Furthermore, because of the limited range of geometries in tokamak experiments, the dependence,  $f$ , on aspect-ratio and elongation is uncertain.

The possibility of operating in a regime of improved confinement will be allowed for by introducing an enhancement factor into eqn 1.7.2. This equation is commonly written in terms of the heating power rather than the temperature. Thus balancing the input power  $P$  with the losses  $3nT/\tau_E$ , eqn 1.7.2 can be equivalently written

$$\tau_E = (3f)^{1/2} \frac{I}{P^{1/2}}.$$

It is usual to introduce the enhancement factor  $H$  into this form so that

$$\tau_E = H(3f)^{1/2} \frac{I}{P^{1/2}}. \quad 1.7.3$$

Returning now to the form of eqn 1.7.2, eqn 1.7.3 becomes

$$\tau_E = \frac{H^2 I^2}{n\bar{T}} f.$$

In present experiments typical geometric ratios are  $R/a = 3$  and  $b/a = 5/3$ . For these values  $f = 2 \times 10^6 \text{ m}^{-3} \text{ keV s A}^{-2}$ . Using this value of  $f$  and taking the density and temperature profiles to be parabolic, with peak values  $\hat{n}$  and  $\hat{T}$ , so that  $n\bar{T} = \frac{1}{3}\hat{n}\hat{T}$ , gives

$$\hat{n}\hat{T}\tau_E = 6 \times 10^6 H^2 I^2 \text{ m}^{-3} \text{ keV s.}$$

Eliminating  $\hat{n}\hat{T}\tau_E$  using relation 1.7.1, the minimum requirement for the tokamak to provide a reacting plasma is

$$I = \frac{30}{H} \text{ MA.} \quad 1.7.4$$

Thus for  $H = 1$  the required current is 30 MA.  $H$  factors of 2–3 have been obtained experimentally and if these could be achieved in a reactor without other deleterious effects the required current would be correspondingly reduced.

It has been found experimentally that to avoid current driven disruptions the toroidal magnetic field must be sufficiently high to satisfy

$$\frac{B_\phi}{B_{\theta s}} \gtrsim 2 \frac{R}{\bar{a}}, \quad 1.7.5$$

where  $B_{\theta s}$  is the mean poloidal magnetic field at the surface of the plasma and  $\bar{a}$  is the mean radius of the plasma.

Approximating Ampère's law by

$$I = \frac{2\pi}{\mu_0} \bar{a} B_{\theta s}, \quad 1.7.6$$

and taking  $\bar{a} = (ab)^{1/2}$ , relations 1.7.4 to 1.7.6, together with  $R/a = 3$  and  $b/a = \frac{5}{3}$ , give the approximate reactor requirement

$$RB_\phi \gtrsim \frac{65}{H} \text{ mT.} \quad 1.7.7$$

The trade-off between size and magnetic field is determined by economic and technical considerations. At low values of  $B_\phi$  the overall cost decreases as  $B_\phi$  is increased, but this dependence is limited by the difficulty of achieving high  $B_\phi$  in superconducting materials. With present technology the optimum  $B_\phi$  has around 12 T at the inner side of the toroidal field coil and allowing for the  $1/R$  dependence this implies a field of approximately 6 T at the centre of the plasma.

Taking  $B_\phi = 6$  T, condition 1.7.7 requires a major radius of  $11/H$  and for  $H$  between 1 and 2 this gives  $R$  between 11 m and 5.5 m. The corresponding range of  $a$  is roughly 3.5–2 m, and of  $b$  is 6–3 m.

However, other considerations enter into the decision as to the best plasma parameters. The avoidance of pulsed operation by exploiting the bootstrap current leads to a higher aspect-ratio design. The condition 1.7.5 for the avoidance of disruptions then implies a higher toroidal magnetic field. This in turn requires the development of advanced superconducting magnets. It is also an advantage to have a lower current to increase the bootstrap current fraction. The possibility of a lower current depends on having a sufficiently high confinement improvement, either through the enhancement factor  $H$  or from an improvement with the increased aspect-ratio.

### Reactor power

The thermonuclear power density for equal deuterium and tritium densities is given by eqn 1.4.2 and so the total reactor power is

$$P = \frac{\pi}{2} \mathcal{E} \int n^2 \langle \sigma v \rangle R dS \quad 1.7.8$$

where  $dS$  is an area element of the poloidal cross-section. This power can clearly be calculated numerically for any particular case but it is instructive to derive an analytic expression by making simplifying approximations. The geometry is simplified by taking  $R$  to be its central value, and the elongated plasma is represented by an equivalent circular plasma with a radius  $\bar{a} = (ab)^{1/2}$ . Equation 1.7.8 then becomes

$$P = \pi^2 R \mathcal{E} \int_0^{\bar{a}} n^2 \langle \sigma v \rangle r dr. \quad 1.7.9$$

For the temperatures of interest  $\langle \sigma v \rangle$  is well represented by eqn 1.5.4. Using this approximation and taking the pressure profile to be of the form

$$nT = \hat{n}\hat{T} \left(1 - \frac{r^2}{\bar{a}^2}\right)^v \quad 1.7.10$$

eqn 1.7.9 gives

$$P = \frac{0.15}{2v+1} Rab \left(\frac{\hat{n}}{10^{20}}\right)^2 \hat{T}^2 \text{MW}, \quad \hat{T} \text{ in keV.}$$

Graphs of this power against  $\hat{n}^2/(2v+1)$  are shown in Fig. 1.7.3 for the cases  $R = 9 \text{ m}$ ,  $a = 3 \text{ m}$ ,  $b = 5 \text{ m}$  and  $R = 6 \text{ m}$ ,  $a = 2 \text{ m}$ ,  $b = 3.3 \text{ m}$ , taking  $\hat{T} = 20 \text{ keV}$ . It is seen that the thermal power produced is in the GW range. The precise value is sensitive to the pressure profile and the density, which are both constrained by stability considerations as discussed in Chapters 6 and 7.

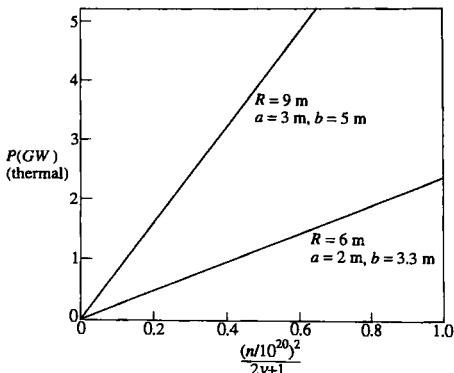


**Fig. 1.7.3** Graphs giving the dependence of the thermonuclear power on the peak density  $\bar{n}$  and the pressure profile shape index  $\nu$  for two reactor sizes with  $\hat{T} = 20 \text{ keV}$ .

### Impurities

One of the most severe problems for a reactor is the presence of impurities in the plasma. The impurities are of two types. Firstly there are impurity ions which have come from solid surfaces and secondly there are the  $\alpha$ -particles,  $\text{He}^4$ , resulting from the fusion process. The design has to be such as to minimize incoming impurities but clearly the  $\alpha$ -particle impurity is intrinsic. The requirement for the 'helium ash' is that it should not have too long a confinement time in the plasma.

Impurities from the wall produce partially stripped ions which then give rise to a plasma energy loss through radiation. This is discussed quantitatively in Section 4.25. In addition there is the problem of fuel dilution. Each ion is associated with a number of free electrons determined by its ionization state. These impurity electrons will have the same temperature as the plasma and, for a given confined plasma energy, can be regarded as having displaced fuel ions of deuterium and tritium. A heavy metallic atom can release tens of electrons in the centre of the plasma.

Control of the impurity influx depends upon a satisfactory design of both the magnetic structure and the material surfaces receiving the outflowing plasma energy. At present this is believed to require a magnetic divertor. The aim of the divertor is to lead the outgoing particles to a 'target' surface well separated from the plasma, and to restrict the impurity back-flow. A difficult problem associated with the divertor is that of limiting the power density flowing to the target surface. This is necessary to avoid high surface temperatures which can lead to surface melting or catastrophic impurity release by evaporation or other processes.

## 1.8

### Fuel resources

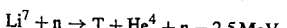
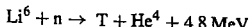
There are two basic questions in judging the availability of fuel resources for a fusion reactor. The first is the size of the natural reserves of the basic fuels and the second is the cost of production. In a complete treatment of the subject the reserves should be regarded as a function of cost but for present purposes this is unnecessary. The answers to these questions must be set against the requirements for power and the cost of that power.

The world annual primary energy consumption is about  $3 \times 10^{11}$  GJ. The world annual electrical energy consumption is about  $3 \times 10^{10}$  GJ. The consumer cost of electricity is typically \$30 per GJ.

The natural abundance of deuterium in hydrogen is one part in 6700. The mass of water in the oceans is  $1.4 \times 10^{21}$  kg and the mass of deuterium is therefore  $4 \times 10^{16}$  kg. In D-T reactors with a thermal efficiency of 1/3 this would allow the production of  $(4 \times 10^{16}/m_d) (17.6/3)$  MeV, that is  $10^{22}$  GJ (el). This is about  $3 \times 10^{11}$  times the world's annual electrical energy consumption. Clearly there is no problem with deuterium resources.

The cost of deuterium is of the order \$1 per gram. One gram of deuterium allows the production of  $(10^{-3}/m_d) (17.6/3)$  MeV, that is 300 GJ (el). The cost contribution of the deuterium fuel is therefore \$0.003 per GJ(el), which is negligible compared to the \$30 per GJ cost of electricity.

The situation regarding tritium is more complex. Tritium has a half-life of only 12.3 years and is virtually non-existent in nature. Tritium, however, can be bred from lithium using the neutron induced fission reactions.



The natural abundances are 7.4% Li<sup>6</sup> and 92.6% Li<sup>7</sup>. With this system the basic fuels are deuterium and lithium.

It is Li<sup>6</sup> which is principally consumed in the blanket and the energy potentially available from 1 kg of Li<sup>6</sup> is roughly  $22 \text{ MeV}/m_{\text{Li}}$ , that is  $3 \times 10^5$  GJ. At a thermal efficiency of 1/3 this gives  $1 \times 10^5$  GJ(el). Thus, allowing for the natural abundance of Li<sup>6</sup>, 1 kg of lithium would provide around  $7 \times 10^3$  GJ(el). The cost of lithium is of the order of \$40 per kg and so the contribution of the lithium fuel to the cost is less than \$0.001 per GJ(el). This cost is very small compared to the cost of electricity and it is clear that it would be possible to tolerate a large increase in the cost of lithium before it became a significant factor.

The estimated United States reserves of lithium at prices comparable to present prices is  $5 \times 10^9$  kg. This amount of lithium could produce

**Table 1.8.1** Estimated world energy resources. The figures are only indicative, being dependent on prices and subject to uncertainty because of incomplete exploration.

	Gigajoules ( $10^9$ joules)	Divided by present world total energy consumption per year
Present world annual primary energy consumption	$3 \times 10^{11}$	1 year
<b>Resources</b>		
Coal	$1.0 \times 10^{14}$	300 years
Oil	$1.2 \times 10^{13}$	40 years
Natural gas	$1.4 \times 10^{13}$	50 years
Uranium 235 (fission reactors)	$10^{13}$	30 years
Uranium 238 and thorium 232 (breeder reactors)	$10^{16}$	30 000 years
Lithium (D-T fusion reactors)		
Land	$10^{16}$	30 000 years
Oceans	$10^{19}$	$30 \times 10^6$ years

$(5 \times 10^9 \text{ kg}) \times (7 \times 10^3 \text{ GJ(eI)}/\text{kg}) \sim 3 \times 10^{13} \text{ GJ (eI)}$  which is of the order of 100 years world primary energy consumption. The world land area is 17 times that of the United States. It is not unreasonable therefore to assume that the world lithium supplies would allow electrical energy generation of a thousand times the present world annual total energy consumption even at the very low lithium price assumed.

To put these figures into the context of the energy available from other fuels, Table 1.8.1 gives a summary of estimated energy resources.

## 1.9

### Tokamak economics

The aim of tokamak research is to build a reliable power producing system. As this goal is approached economic questions will become more insistent. The ultimate question is whether a tokamak reactor will be competitive with other power systems, in particular those based on fossil or fission fuels. This raises the questions of the cost of a tokamak reactor and the competitive environment in the future. There are no definitive answers to these questions but it is possible to address the issues.

The cost of an electricity power station has two basic components. The first part is the heat producer, which is different for the different fuels. The second is the part which transforms the heat into electricity

and consists basically of turbines and generators. In the case of a tokamak fusion station the cost of the reactor itself will dominate that of the conventional plant.

The cost of the components is strongly dependent on their size and therefore on the overall dimensions of the reactor. For a given overall size of reactor the blanket volume is given by the thickness required to stop the neutrons. For coils the size is related to the magnetic forces associated with their currents. The vacuum vessel has to withstand the force of atmospheric pressure and also the force due to currents induced in the vessel by possible rapid changes in the plasma current. Further costs arise from the generators required to drive the coil currents, and the system used to heat the plasma. Table 1.9.1 gives an estimate of the break-down of costs in presently envisaged forms of a reactor.

To make a comparison of the cost of electricity produced by a tokamak reactor with that from other systems it is necessary to know the reactor cost. Costings have been made for a number of reactor designs with a range of results. These typically lie in the range 1–3 times the cost of a comparable fission reactor. In making these cost estimates there is scope for expectations of technological progress and also for understandable over-optimism.

**Table 1.9.1** Components of possible costs for a tokamak reactor. The largest item of the indirect costs is interest charges and the largest cost in the conventional plant is that of the turbogenerators. The blanket cost is for the first installation, several replacements would be necessary during the life of the reactor.

Total cost	
Direct cost	65%
Indirect cost	25%
Contingency	10%
	<u>100%</u>
→ Direct cost	
Reactor	50–60%
Conventional plant	35–30%
Structures	<u>15–10%</u>
	100%
→ Reactor cost	
Coils	30%
Shield	10%
Blanket	10%
Heat transfer	15%
Auxiliary power	15%
Other components	20%
	<u>100%</u>

A further piece of information is provided by the first proposed form of ITER the planned International Toroidal Experimental Reactor which was designed to ignite. Its estimated cost was ~6 billion \$(1989). Since this costing was related to an actual project it is reasonable to take it seriously. A thermonuclear reactor of this size would produce several thermal gigawatts.

The current capital cost of fission power stations including the conventional plant is around \$0.7 billion per thermal gigawatt. However, a comparison is not straightforward since ITER would be the first experimental tokamak reactor whereas fission reactors have had several decades of development.

The other main economic issue is the economic environment which a tokamak reactor would face. Projections tend to place the first commercial reactor around the middle of the twenty-first century. It is difficult to predict what developments will have taken place by then. The present concerns are with the pollution and CO<sub>2</sub> emission from fossil fueled stations, and with uncontrolled reactions and radioactive waste associated with fission reactors. It is possible that factors such as these will either make such stations unacceptable or that necessary modifications will increase the cost, making fusion reactors more competitive.

Perhaps a reasonable view of the situation is that a tokamak reactor looks rather expensive, but given the small cost of a tokamak development programme compared to the world-wide expenditure on electricity power production, the possible benefits justify the expenditure. It is worth reflecting that our inability to predict the future is well established.

## 1.10

### Tokamak research

The word 'tokamak' is derived from the Russian words, *toroidalnaya kamera* and *magnitnaya katushka*, meaning 'toroidal chamber' and 'magnetic coil'.

The device was invented in the Soviet Union, the early development taking place in the late 1950s. At this time research on the toroidal pinch configuration was being strongly pursued in the United Kingdom and the United States. The advantage of the tokamak comes simply from the increased stability provided by its larger toroidal magnetic field.

The successful development of the tokamak was principally the result of the careful attention paid to the reduction of impurities and the separation of the plasma from the vacuum vessel by means of a 'limiter'. This led, during the 1960s, to comparatively pure plasmas with electron temperatures of around 1 keV. By 1970 these results were generally accepted and their significance appreciated.

The early tokamaks had energy confinement times of several milliseconds and ion temperatures of a few hundred eV. The evident need for the 1970s was to find out whether these conditions could be improved. This task was undertaken in several countries and many tokamaks were built.

It soon became apparent that the energy confinement was anomalous. The electron energy losses exceed the collisional transport rate by roughly two orders of magnitude and the ion energy loss is typically several times the collisional rate. Thus, although collisional theory predicts that the energy loss rate will be dominated by the faster ion thermal conduction, in practice the electron and ion energy are typically comparable. It was further found that whereas theoretically the collisional confinement time would fall as  $1/n$ , where  $n$  is the electron density, experimentally the confinement time increased with  $n$ .

As larger tokamaks were built the expected improvement in confinement was achieved and confinement times approaching 100 ms had been obtained by 1980. Since a confinement time of the order of a second is needed for a reactor, it was important to make the best estimate of the conditions required for this. The simplest model consistent with experimental results gave  $\tau_E \propto n a^2$ , where  $a$  is the minor radius of the plasma, and an extrapolation of the experimental data indicated that a minor radius  $\sim 2$  m might be adequate for a reactor.

This requirement on the size of the plasma seemed quite acceptable and the design of large tokamak experiments was undertaken in several countries. The largest of these was the collaborative Joint European Torus experiment, JET, having a mean minor radius of 1.5 m.

The other task of the 1970s was to investigate means of heating the ions to a high temperature. The early experiments relied entirely on the ohmic heating of the plasma resulting from the toroidal current. Unfortunately ohmic heating becomes less effective at higher temperature because the electrical resistivity of the plasma falls as the electron temperature increases, varying as  $T_e^{-3/2}$ . The earliest additional heating method to achieve success was neutral particle injection. Fast neutral atoms are injected into the plasma and give up their energy through collisions. Another method of heating is to launch RF waves into the plasma in such a way that they are absorbed at resonant surfaces within the plasma. Various frequencies were used but the most promising method was that of ion cyclotron resonance heating. Both neutral beam and RF heating had achieved temperatures of several keV in the early 1980s.

The higher temperature produced by the additional heating allowed the dependence of confinement time on temperature to be clarified. A theoretical prediction based on energy transport due to simple collisions would give confinement which deteriorated with increased density and improved with increased temperature. Unfortunately, in these hotter plasmas, the confinement time was found to be a decreasing function of both density and temperature. As power was applied to the plasma the confinement time fell. These results were disappointing but did not present a fundamental obstacle. Using the empirical evidence provided by a range of

experiments the confinement time was predicted to improve with larger tokamaks and their associated higher plasma currents.

A fortunate discovery made in the ASDEX tokamak was the existence of a mode of plasma operation which had a longer confinement time than 'normal' operation. This is called the H-mode. The transition to this state of higher confinement was found in a plasma with a divertor and at a sufficiently high level of plasma heating. The transition occurs abruptly and appears to be associated with improved confinement at the plasma edge.

A problem which has been apparent since the earliest experiments is the occurrence of instabilities. The most serious of these is the 'disruption' in which instability causes a rapid loss of the plasma energy and termination of the discharge. In these events large currents are induced in the vacuum vessel, producing very large forces on the vessel. Disruptions seriously restrict the operating regime of the tokamak, limiting both the density and the plasma current for a given toroidal magnetic field. Another instability, which restricts the current density in the centre of the plasma, is a relaxation oscillation called the sawtooth instability. These oscillations cause repeated loss of energy from the central region.

A further type of instability limits the ratio of plasma pressure to the magnetic energy density. The ratio of these two quantities is called  $\beta$  and the restriction imposed by the instability is called the  $\beta$ -limit. The value of  $\beta$  has been increased to this limit in a number of machines. By manipulation of the operating conditions the  $\beta$ -limit can be increased and a value of  $\beta$  greater than 10% has been obtained in the DIIID tokamak. The  $\beta$ -values required in a reactor are somewhat less than this, encouraging the belief that the  $\beta$ -limit will not be a serious problem.

In the early 1980s two larger tokamaks were built, TFTR and JET. They were designed to carry several megampères and to produce a significant amount of thermonuclear energy in a deuterium-tritium plasma. In these experiments the plasmas were heated up to the temperatures required in a reactor, ion temperatures in excess of 30 keV being reached. In JET a confinement time greater than a second was achieved, and the regime of tokamak operation was also extended with plasma currents up to 7 MA and plasma pulse lengths of up to one minute.

In 1991 a further milestone was passed. Calculations showed that the plasma conditions achieved in deuterium plasmas in JET were such that if the deuterium was replaced by a 50-50 mixture of deuterium and tritium the resulting fusion reaction power would be comparable to the power supplied to heat the plasma. Although this experiment could not be carried out at that time because of the resulting level of radioactivity in the tokamak structure, it was decided to carry out a preliminary tritium experiment. A controlled amount of tritium was injected into a deuterium plasma as a neutral beam. This led to a fusion reaction power in excess of a megawatt for more than a second. Subsequent experiments used a 50-50 mixture of deuterium and tritium, allowing the production of a fusion power of more than 10 MW in the TFTR tokamak and 16 MW in JET.

It is clear that many of the problems of fusion research have been overcome in tokamaks. It is now necessary to look to the future and the next stage of tokamak development. This enterprise will concentrate effort on the critical problems and, if successful, demonstrate the feasibility of a tokamak reactor. It seems likely that the first ignition tokamak will be a joint project involving many countries. There is already worldwide co-operation in an international team, whose task is to design a tokamak which will produce substantial fusion power. This conceptual tokamak is ITER—the International Thermonuclear Experimental Reactor. If it is decided to proceed to construction of this reactor it will be an exciting endeavour.

## Bibliography

Few books have been written with thermonuclear fusion as their principal subject. Of these the earlier ones are to some extent outdated but nevertheless still offer useful information and insights, and are therefore included in the following chronological list:

Glasstone, S. and Loveberg, R.H. *Controlled thermonuclear reactions*. Van Nostrand, Princeton, New Jersey (1960).

Rose, D.J. and Clark, M. *Plasmas and controlled fusion*. MIT Press, Cambridge, Mass. (1961).

Artyukovich, L.A. *Controlled thermonuclear reactions*. Gordon and Breach, New York (1974).

Kammash, T. *Fusion reactor physics*. Ann Arbor Science, Ann Arbor, Michigan (1975).

Teller, E. (ed.). *Fusion*. Academic Press, New York (1981).

Gill, R.D. (ed.). *Plasma physics and nuclear fusion research*. (Culham Summer School on Plasma Physics). Academic Press, London (1981).

Dolan, T.J. *Fusion research*. Pergamon Press, New York (1982).

Gross, J. *Fusion energy*. Wiley, New York (1984).

Miyamoto, K. *Plasma physics for nuclear fusion*, 2nd edn. MIT Press, Cambridge, Mass. (1989).

### Fusion reactions and thermonuclear fusion

A compilation of cross-sections and reaction rates is given in

Miley, G.H., Towner, H., and Ivich, N. *Fusion cross-sections and reactivities*. University of Illinois Nuclear Engineering Report COO-2218-17, Urbana, Illinois (1974).

### Lawson criterion

Lawson, J.D. Some criteria for a power producing thermonuclear reactor, *Proceedings of the Physical Society B70*, 6 (1957).

A derivation of the criterion is given in the first edition of this book.

### Basic tokamak

An early paper describing the basic principles and initial results is

Artsimovitsh, L.A. Tokamak devices. *Nuclear Fusion*, 12, 215 (1972).

### Tokamak reactor

An extensive account of fusion reactors including a discussion of tokamaks is given in the article

Conn, R.W. Magnetic fusion reactors. *Fusion* (ed. E. Teller) Vol. 1, Academic Press, New York (1981).

An overview on fusion reactors is included in Chapter 7 of the book

Gross, J. *Fusion energy*. Wiley, New York (1984).

### Fuel resources

The general subject of fuel resources is discussed in Lapedes, D.N. (ed.) *Encyclopedia of energy*. McGraw-Hill, New York (1971).

The figures in the table of Section 1.8 were obtained from the article entitled 'Outlook for fuel reserves', by M.K. Hubbert in the above book, together with

Hafele, W., Holdren, J.P., Kessler, G., and Kulchinski, G.L. *Fusion and fast breeder reactors*. International Institute for Applied Systems Analysis, Laxenburg, Austria (1977).

### Economics

Analysis of the economics of tokamak reactors seems to allow a wide range of views. A concise assessment of the potential of fusion reactors together with a discussion of possible electricity costs is given in

Conn, R.W. *et al.* Economic, safety and environmental prospects of fusion reactors. *Nuclear Fusion* **30**, 1919 (1990).

A more detailed account is given in

Krakowski, R.A. and Delene, J.G. Connection between physics and economics for tokamak fusion power plants. *J. Fusion Energy* **7**, 49 (1988).

A less optimistic view is expressed by

Pfirsch, D. and Schmitter, K.H. Some critical observations on the prospects of fusion power. *Fourth international conference on energy options*. London, I.E.E. Conference publication No. 233, 350, I.E.E., London (1984).

### Tokamak research

Chapters 11 and 12 are devoted to a description of particular experiments, and references to detailed papers are given there.

A book which summarizes tokamak research and gives a good insight into the underlying physics is

Kadomtsev, B.B., *Tokamak plasma, a complex physical system*. Institute of Physics Publishing, Bristol (1992).

The Goldston scaling is described in

Goldston, R.J. Energy confinement scaling in tokamaks: some implications of recent experiments with ohmic and strong auxiliary heating. *Plasma Physics and Controlled Fusion*, **26**, No. IA, 87 (1984).

### Physical constants

A comprehensive list of fundamental and other physical constants is available in

*Tables of physical and chemical constants*, (originally compiled by) G.W.C. Kaye and T.H. Laby. Longman, London

**2**

# **Plasma physics**

**2.1****Tokamak plasma**

A plasma is an ionized gas. When fully ionized it is composed entirely of ions and electrons. These components have many of the properties of a normal gas. For example they can be described by their particle density and temperature. However, a plasma has two characteristic properties. Firstly the electric charge density of the two species is so large that any substantial separation would lead to a very large restoring force, and as a consequence the ion and electron charge densities in a plasma are almost equal. The second property is the ability to carry a current as result of a relative drift between the ions and electrons. In a tokamak the plasma current produces an important part of the magnetic field. Where the plasma current crosses the magnetic field it gives rise to a magnetic force which can balance the plasma pressure gradient.

When a plasma is in a magnetic field the individual particles are constrained in their motion. They are free to move parallel to the magnetic field, but perpendicular to the field they gyrate in Larmor orbits. In tokamaks the ion orbits typically have a radius of a few millimetres and the electron orbits are smaller by the square root of the electron-ion mass ratio. Although the precise behaviour of the plasma is determined by the motion of the individual particles in the local electromagnetic field, the constraints on the particle motions described above give the plasma fluid-like properties on lengths larger than the Larmor radii. Much of our understanding of tokamaks is based on such fluid models of the plasma.

The particle concentration in tokamaks is typically  $\sim 10^{20} \text{ m}^{-3}$  which is about  $10^{-5}$  of the particle concentration in the atmosphere. Tokamak plasmas typically reach temperatures of several keV, which corresponds to tens of millions of degrees Kelvin. This is of the order  $10^5$  times atmospheric temperatures and consequently the pressure in tokamak plasmas is comparable to that of the atmosphere.

The outward force of the plasma pressure is balanced by the magnetic field. However, the plasma energy density in a tokamak is small compared to that of the magnetic field, typically a few per cent. The basic magnetic field is the toroidal field produced by coils outside the plasma. The poloidal field produced by the toroidal plasma current is typically ten times smaller.

Many processes in the plasma are determined by particle collisions. Collisions between ions and electrons give rise to an electrical resistance, which leads to ohmic heating of the plasma. Collisions also produce transport of particles and energy, leading to losses of both from the plasma. Typically ion collision times are in the range 1–100 ms. Electron collision times are shorter by the square root of the mass ratio. Collision times increase with increasing temperature, varying as  $T^{3/2}$ . As a consequence

**Table 2.1.1** Typical tokamak plasmas.

Plasma volume	1–100 m <sup>3</sup>
Total plasma mass	$10^{-4} - 10^{-2}$ gm
Ion concentration	$10^{19} - 10^{20}$ m <sup>-3</sup>
Temperature	1–40 keV
Pressure	0.1–5 atmospheres
Ion thermal velocity	100–1000 km s <sup>-1</sup>
Electron thermal velocity	0.01c–0.1c
Magnetic field	1–10 T
Total plasma current	0.1–7 MA

ohmic heating becomes less effective at high temperatures. On the other hand collisional plasma losses are reduced.

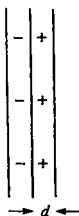
The basic behaviour of tokamak plasma is poorly understood. The energy loss substantially exceeds that predicted on the basis of simple collisions and this is not explained. The anomaly is thought to be due to small scale plasma instabilities.

Typical tokamak plasmas (Table 2.1.1) are far from quiescent and a number of macroscopic instabilities are regularly observed. In some cases the plasma adjusts to the instability and no substantial deterioration of performance results. However, in the case of so-called tokamak disruptions the instability damages the plasma beyond recovery.

The present chapter gives an introduction to the basic physics involved in the analysis and understanding of tokamak plasmas.

## 2.2

### Debye shielding



The electric charge density of the separate ion and electron components of a plasma is large enough to ensure that only small charge separations occur. The magnitude of this effect can be appreciated by imagining the separation of the ions and electrons into sheets of thickness  $d$  as illustrated in Fig. 2.2.1.

If the ions are singly charged and the density of ions and electrons is  $n$ , the charge per unit area in each of the separated sheets is  $dne$ . Ignoring numerical factors the electric field between the sheets is  $\sim dne/\epsilon_0$  and the resulting force per unit area is

$$F \sim \frac{(dne)^2}{\epsilon_0}.$$

**Fig. 2.2.1** Ion and electron charge sheets separated by a distance  $d$ .

2.2.1

In a tokamak the density  $n$  is around  $10^{20} \text{ m}^{-3}$  and for this density

$$F \sim 10^{13} d^2 \text{ Nm}^{-2}.$$

As an example consider a sheet thickness of 1 cm. This gives a force per unit area of  $10^9 \text{ Nm}^{-2}$  or  $10^5 \text{ tonnes m}^{-2}$ .

As a result of the very strong force caused by charge separation, the electron and ion densities are held almost equal throughout the plasma. This is called quasi-neutrality and, for the general case with ions of charge  $Z_i$ , the constraint is expressed by

$$n_e = \sum_i n_i Z_i \quad 2.2.2$$

where the summation is over ion species.

It should be noted that eqn 2.2.2 does not mean that  $\nabla \cdot \mathbf{E} = 0$ . Equation 2.2.2 is almost, but not quite, exact and the small charge difference gives rise to significant electric fields. Thus the electric field cannot be determined from eqn 2.2.2. On the other hand, given the electric field, the charge density,  $\rho_c$ , is determined by  $\nabla \cdot \mathbf{E} = \rho_c/\epsilon_0$ .

It is seen from eqn 2.2.1 that the restoring force decreases with decreasing charge separation length. The argument for quasi-neutrality is therefore invalid for sufficiently small scale-lengths. It is possible to derive a fundamental length characterizing the plasma by calculating the thickness  $d$  for which the internal energy of the plasma could provide the energy for a complete separation of the ions and electrons as shown in Fig. 2.2.1. The required energy is  $Fd$ , the force  $F$  being given by relation 2.2.1, and the internal energy is  $\sim dnT$ . Equating these energies gives the characteristic length  $d = \lambda_D$  where

$$\begin{aligned} \lambda_D &= \left( \frac{\epsilon_0 T}{ne^2} \right)^{1/2} \\ &= 2.35 \times 10^5 \left( \frac{T}{n} \right)^{1/2} \text{ m}, \quad T \text{ in keV.} \end{aligned} \quad 2.2.3$$

This length is called the Debye length. In a typical tokamak plasma  $\lambda_D$  lies in the range  $10^{-2}$ – $10^{-1}$  mm.

Although the charge separation described above is energetically possible over a Debye length, it does not of course occur spontaneously in the body of the plasma because the velocity of the particles are random and the coherence of the particle motions required for the imagined displacement does not arise. One situation for which a substantial charge separation does occur is where a plasma is in contact with a solid surface. Charge separation then appears in a sheath close to the surface and this sheath has a thickness  $\sim \lambda_D$ . The Debye length also arises in a more subtle way inside the plasma, characterizing the phenomenon called Debye shielding.

Consider a particular ion in the plasma and let the ion be singly charged. The electric field of this ion is

$$E = \frac{e}{4\pi\epsilon_0 r^2}.$$

Now although this is the electric field *directly* associated with this ion, the other particles in the plasma adjust to this field and the resulting distribution of their charge shields the charge of the ion and changes the *effective* electric field. The trajectories of the electrons close to the ion are slightly displaced toward the ion and the trajectories of the ions are slightly displaced away from it. The shielding occurs around every ion and the inverse effect occurs for every electron. This behaviour is similar to that which occurs in electrolytes. This case was analysed by Debye and hence the shielding carries his name.

The form of the shielding can be calculated for a stationary ion by solving Poisson's equation for the potential  $\phi$ . In spherical geometry the equation is

$$\frac{1}{r^2} \frac{d}{dr} r^2 \frac{d\phi}{dr} = -\frac{\rho_c}{\epsilon_0}, \quad 2.2.4$$

where the charge density  $\rho_c = \sum_j n_j e_j$ . The ions and electrons will each have a Boltzmann distribution in the potential, and so their densities  $n_j$  will be given by

$$n_j = n_0 \exp -\frac{e_j \phi}{T}, \quad 2.2.5$$

$n_0$  being the electron, and ion, density at a large distance from the chosen ion, where the potential is taken to be zero. Thus substituting eqn 2.2.5 into eqn 2.2.4 and taking singly charged ions

$$\frac{1}{r^2} \frac{d}{dr} r^2 \frac{d\phi}{dr} = -\frac{n_0 e}{\epsilon_0} (e^{-e\phi/T} - e^{e\phi/T}). \quad 2.2.6$$

It will be found that  $e\phi/T \ll 1$  and, anticipating this result, eqn 2.2.6 becomes

$$\frac{1}{r^2} \frac{d}{dr} r^2 \frac{d\phi}{dr} = \frac{2n_0 e^2}{\epsilon_0 T} \phi. \quad 2.2.7$$

Regarding the product  $(r\phi)$  as the variable, eqn 2.2.7 may be written

$$\frac{d^2}{dr^2} (r\phi) = \frac{2}{\lambda_D^2} (r\phi)$$

and the solution which decays at large  $r$  is

$$\phi = \alpha \frac{1}{r} e^{-\sqrt{2}r/\lambda_D} \quad 2.2.8$$

where  $\alpha$  is a constant. Since  $\phi = e/4\pi\epsilon_0 r$  as  $r \rightarrow 0$ , eqn 2.2.8 becomes

$$\phi = \frac{e}{4\pi\epsilon_0 r} e^{-\sqrt{2}r/\lambda_D} \quad 2.2.9$$

This equation describes the Debye shielding. It is seen that the potential  $e/4\pi\epsilon_0 r$  of the single ion is shielded according to the exponential factor, the characteristic length of the shielding being the Debye length. Graphs of the unshielded and shielded potentials are given in Fig. 2.2.2.

From eqn 2.2.9 the approximation  $e\phi/T \ll 1$  used in the calculation implies

$$r \gg \frac{e^2}{4\pi\epsilon_0 T}. \quad 2.2.10$$

The physical nature of this requirement can be made clear by noting that the smallest relevant value of  $r$  is the order of the interparticle separation, that is  $1/n^{1/3}$ . Using this value for  $r$ , inequality 2.2.10 becomes

$$n\lambda_D^3 \gg \left(\frac{1}{4\pi}\right)^{3/2}$$

and so the approximation used is valid if there are many particles in a cube with sides of length  $\lambda_D$ , that is

$$n\lambda_D^3 \gg 1. \quad 2.2.11$$

In a tokamak plasma typical values are  $n \sim 10^{20} \text{ m}^{-3}$  and  $\lambda_D \sim 10^{-4} \text{ m}$ . Thus  $n\lambda_D^3 \sim 10^8$  and inequality 2.2.11 is well satisfied. The quantity  $n\lambda_D^3$  is called the plasma parameter.

The assumption that the test particle is stationary has given a simplified account of the shielding process. In reality each particle has a velocity relative to the mean velocity of the background particles. When the test particle has a velocity comparable to the thermal velocity of the shielding particles there is a delay in the formation of the shielding charge and only partial shielding occurs. In the limit of very fast test particles the shielding response is negligible and the potential associated with the test charge approaches the bare charge form  $e/4\pi\epsilon_0 r$ .

The overall behaviour is such that each particle generates its shielding charge as it moves through the plasma and this results in a fluctuating electric field. The particles also receive energy from the electric field and the equilibrium balance of these driving and damping processes gives the thermal spectrum of electrostatic fluctuations.

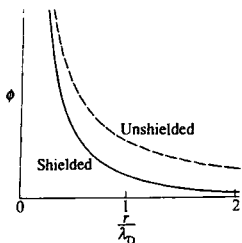
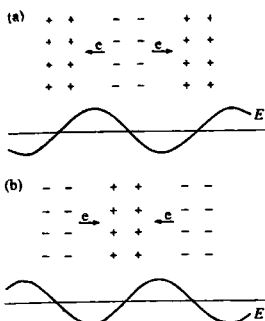


Fig. 2.2.2 Graphs of the unshielded and shielded potential around an ion.

## 2.3

### Plasma frequency

In Section 2.2 it was shown that a plasma has a characteristic length, the Debye length. It also has a characteristic frequency. This can be understood by considering displaced sheets of electrons as shown in



**Fig. 2.3.1** (a) Displaced electrons give rise to restoring force and acceleration, (b) after half a cycle the charges are interchanged.

**Fig. 2.3.1(a).** It is assumed that because of their larger mass the ions are stationary and have uniform density. The positive charges in the figure represent the deficiency of electrons in the layers from which the electrons have been moved. The resulting electric field is shown in the accompanying graph. The electrons are accelerated by the electric field and move to cancel the positive charge. At the time of cancellation the electron momentum is a maximum and this allows the electrons to recreate the charge separation, now in the opposite phase. The process is repeated and the resulting motion of the electrons constitutes plasma oscillations with the characteristic plasma frequency.

The plasma frequency can be calculated using the fluid equations. For a cold plasma the equation of motion for the electron fluid is

$$m_e \frac{\partial v}{\partial t} = -e E \quad 2.3.1$$

and, assuming a small density perturbation  $\tilde{n}$ , the electric field is given by

$$\nabla \cdot \mathbf{E} = -\frac{e\tilde{n}}{\epsilon_0}. \quad 2.3.2$$

Thus taking the divergence of eqn 2.3.1 and eliminating  $\nabla \cdot \mathbf{E}$  using eqn 2.3.2

$$m_e \frac{\partial}{\partial t} \nabla \cdot \mathbf{v} = \frac{e^2}{\epsilon_0} \tilde{n}. \quad 2.3.3$$

The continuity equation is

$$\frac{\partial n}{\partial t} = -\nabla \cdot (n\mathbf{v})$$

and its linearized form is

$$\frac{\partial \tilde{n}}{\partial t} = -n \nabla \cdot \mathbf{v}. \quad 2.3.4$$

Substitution of  $\nabla \cdot \mathbf{v}$  from eqn 2.3.4 into 2.3.3 gives the required equation for plasma oscillations

$$\frac{\partial^2 \tilde{n}}{\partial t^2} = -\omega_p^2 \tilde{n}$$

where  $\omega_p$  is the electron plasma frequency

$$\omega_p = \left( \frac{ne^2}{\epsilon_0 m_e} \right)^{1/2}. \quad 2.3.5$$

A similar frequency is associated with ion oscillations, the ion plasma frequency being

$$\omega_{pi} = \left( \frac{ne_i^2}{\epsilon_0 m_i} \right)^{1/2} \quad 2.3.6$$

where  $e_i$  is the ion charge.

In Section 2.25 a more general account of plasma oscillations is given and it is there shown that eqn 2.3.5 gives the frequency of electron plasma waves in the limit where the wavelength is much larger than the Debye length.

Substituting numerical values into eqn 2.3.5,

$$\omega_p = 56.4 n^{1/2} \text{ s}^{-1}.$$

For a tokamak this frequency is very high. For example a density  $n = 10^{20} \text{ m}^{-3}$  gives  $\omega_p = 5.6 \times 10^{11} \text{ s}^{-1}$  with a characteristic time,  $\omega_p^{-1}$ , less than one hundredth of a nanosecond.

## 2.4 Larmor orbits

The equation of motion of a particle of mass  $m_j$  and charge  $e_j$  in a magnetic field is

$$m_j \frac{dv}{dt} = e_j v \times B.$$

If the magnetic field is uniform and in the  $z$  direction, the components of this equation are

$$\frac{dv_x}{dt} = \omega_{cj} v_y, \quad \frac{dv_y}{dt} = -\omega_{cj} v_x, \quad 2.4.1$$

$$\frac{dv_z}{dt} = 0, \quad 2.4.2$$

where

$$\omega_{cj} = \frac{e_j B}{m_j}$$

is the cyclotron frequency and the  $z$  axis has been chosen to be along the magnetic field. From eqn 2.4.2 the particle velocity,  $v_z$ , along the magnetic field is constant. Separation of the variables in eqns 2.4.1 leads to

$$\frac{d^2 v_x}{dt^2} = -\omega_{cj}^2 v_x, \quad \frac{d^2 v_y}{dt^2} = -\omega_{cj}^2 v_y,$$

and the solutions of these equations may be written

$$v_x = v_\perp \sin \omega_{cj} t, \quad v_y = v_\perp \cos \omega_{cj} t. \quad 2.4.3$$

Using  $v_x = dx/dt$  and  $v_y = dy/dt$ , eqns 2.4.3 can be integrated to give

$$x = -\rho_j \cos \omega_{cj} t, \quad y = \rho_j \sin \omega_{cj} t, \quad 2.4.4$$

where

$$\rho_j = \frac{v_{\perp}}{\omega_{cj}} = \frac{m_j v_{\perp}}{e_j B}$$

is the Larmor radius. Thus the particle has a helical orbit composed of the circular motion of eqns 2.4.4 and a constant velocity in the direction of the magnetic field.

A particle having the mean thermal energy in the plane perpendicular to the magnetic field has  $v_{\perp}^2 = 2v_{Tj}^2$ , where  $\frac{1}{2}m_j v_{Tj}^2 = \frac{1}{2}T_j$ . The factor of 2 appears because two degrees of freedom are involved. Thus, for a thermal particle

$$\rho_j = \sqrt{2} \frac{m_j v_{Tj}}{|e_j| B}. \quad 2.4.5$$

Substituting the values of electronic charge  $e = 1.602 \times 10^{-19}$  C, electron mass  $m_e = 9.11 \times 10^{-31}$  kg, and proton mass  $m_p = 1.673 \times 10^{-27}$  kg, together with  $v_{Tj} = 1.27 \times 10^{-8} (T_j/m_j)^{1/2}$  ms<sup>-1</sup> where the temperature is now expressed in keV, gives

Electron	$ \omega_{ce}  = 1.76 \times 10^{11} B \text{ s}^{-1}$ ,	}
	$\rho_e = 1.07 \times 10^{-4} T_e^{1/2} / B \text{ m}$ ,	
Proton	$ \omega_{cp}  = 9.58 \times 10^7 B \text{ s}^{-1}$ ,	
	$\rho_p = 4.57 \times 10^{-3} T_p^{1/2} / B \text{ m}$ ,	
Particle $j$	$ \omega_{cj}  = 9.58 \times 10^7 (Z/A) B \text{ s}^{-1}$ ,	$T \text{ in keV}$
	$\rho_j = 4.57 \times 10^{-3} (A^{1/2}/Z) T_j^{1/2} / B \text{ m}$ ,	

where  $Z$  and  $A$  are the charge and mass numbers of particle  $j$ .

Tables 2.4.1 and 2.4.2 give some values of  $\omega_c$  and  $\rho$ . It should be noted that the Larmor radius of a thermal particle is sometimes defined without the factor  $\sqrt{2}$  of eqn 2.4.5.

**Table 2.4.1** Values of cyclotron frequency  $\omega_c$  and  $f_c (= |\omega_c|/2\pi)$  for electrons and protons.

Frequency	Magnetic field		
	1 Tesla	3 Teslas	5 Teslas
$ \omega_{ce}  (\text{s}^{-1})$	$1.76 \times 10^{11}$	$5.28 \times 10^{11}$	$8.79 \times 10^{11}$
$ \omega_{cp}  (\text{s}^{-1})$	$9.58 \times 10^7$	$2.87 \times 10^8$	$4.79 \times 10^8$
$f_{ce}$	28 GHz	84 GHz	140 GHz
$f_{cp}$	15 GHz	46 GHz	76 GHz

**Table 2.4.2** Values of Larmor radius,  $\rho$ , for electrons and protons having the thermal velocity

$B$	Larmor radius	Temperature			
		10 eV	100 eV	1 keV	10 keV
3 Teslas	$\rho_e$	0.003 mm	0.011 mm	0.035 mm	0.11 mm
	$\rho_p$	0.15 mm	0.48 mm	1.5 mm	4.8 mm
5 Teslas	$\rho_e$	0.002 mm	0.007 mm	0.021 mm	0.67 mm
	$\rho_p$	0.09 mm	0.29 mm	0.91 mm	2.9 mm

**2.5****Particle motion along  $B$** 

As described in Section 2.4 the motion of a charged particle in a uniform magnetic field is composed of two parts, a circular orbital motion perpendicular to the magnetic field and a uniform velocity along the field. An acceleration of the particle along the magnetic field is introduced if there is an electric field parallel to  $B$  or a gradient of  $B$  parallel to  $B$ .

**Acceleration due to  $E_{||}$** 

A parallel electric field simply provides an acceleration given by

$$\frac{d}{dt}(m_j v_{||}) = e_j E_{||}$$

so that if  $E_{||}$  is a function of  $t$ ,  $v_{||}$  is given by

$$m_j v_{||} = e_j \int E_{||} dt.$$

There are circumstances where the velocity resulting from such acceleration is relativistic and the mass of the particle is then related to its rest mass  $m_{j0}$  by the relation

$$m_j = \frac{m_{j0}}{\sqrt{1 - v^2/c^2}}.$$

If  $E_{||}$  is a function of the distance  $x_{||}$  along the magnitude field and of time, it is then necessary to solve the equation

$$\frac{d}{dt} \left( m_j \frac{dx_{||}}{dt} \right) = e_j E_{||}(x_{||}, t).$$

### Acceleration due to $\nabla_{||}B$

A charged particle moving parallel to a magnetic field is not subject to any magnetic force. However, if the particle also has a velocity perpendicular to the magnetic field and the magnetic field has a gradient parallel to  $B$  there is a force on the particle parallel to the magnetic field at the centre of its gyro-orbit.

The geometry of the situation is shown in Fig. 2.5.1. The force on the particle is  $e_j(v \times B)$ . If the magnetic field is slowly varying, the component of this force parallel to the field line at the guiding centre of the orbit is

$$F = \alpha |e_j(v \times B)| \quad 2.5.1$$

where  $\alpha$  is the small angle between the magnetic field at the position of the particle and that at the guiding centre, and the force is clearly in the direction of the weaker magnetic field.

Taking cylindrical coordinates with the  $z$  axis along the line of the guiding centre motion and a radial coordinate  $r$ , the angle  $\alpha$  is given by

$$\alpha = \frac{B_r}{B_z} \quad 2.5.2$$

where

$$B_r = \frac{\partial B_r}{\partial r} \rho, \quad 2.5.3$$

$\rho$  being the Larmor radius. Since  $\nabla \cdot B = 0$  and  $B_r = r \partial B_r / \partial r$ ,

$$\frac{1}{r} \frac{\partial}{\partial r} (r B_r) = 2 \frac{\partial B_r}{\partial r} = - \frac{\partial B_z}{\partial z} \quad 2.5.4$$

Taking  $\partial B_z / \partial z$  at the guiding centre,

$$\frac{\partial B_z}{\partial z} = |\nabla_{||}B| \quad 2.5.5$$

where  $\nabla_{||}$  is the gradient parallel to  $B$ .

Combining eqns 2.5.2 to 2.5.5 and putting  $B_z = B$ , the angle  $\alpha$  is given by

$$\alpha = \frac{1}{2} \rho \frac{|\nabla_{||}B|}{B}. \quad 2.5.6$$

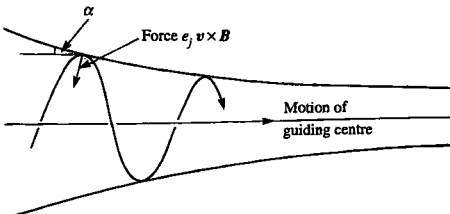


Fig. 2.5.1 Gradient of  $B$  parallel to  $B$  gives rise to a component of the force  $e_j(v \times B)$  along the direction of motion of the guiding centre.

From the force balance of the Larmor orbit

$$|e_j(v \times B)| = \frac{mv_\perp^2}{\rho} \quad 2.5.7$$

and so, using equations 2.5.1, 2.5.6, and 2.5.7 the force arising from  $\nabla_{||}B$  is

$$F = -\frac{\frac{1}{2}mv_\perp^2}{B} \nabla_{||}B. \quad 2.5.8$$

A particle moving into a magnetic field of increasing magnitude can be reflected by this force, this effect being called the mirror effect. If a magnetic field has a minimum along a field line, particles in this region of weaker field can be trapped between the two mirrors which result.

The quantity  $\mu = \frac{1}{2}mv_\perp^2/B$  appearing in eqn 2.5.8 is an adiabatic invariant being almost constant in a slowly varying magnetic field. This invariance is described in Section 2.7.

## 2.6

### Particle drifts

The circular Larmor orbits calculated in Section 2.4 resulted from the assumption of a uniform magnetic field having straight field lines and no electric field. Any deviation from this basic state leads either to acceleration parallel to the magnetic field or to particle drift perpendicular to the magnetic field. The accelerated motions were dealt with in Section 2.5.

On the scale of the Larmor radius charged particles gyrate rapidly about the guiding centre of their motion, but larger scale perpendicular drifts of this guiding centre arise in the presence of any of the following:

- (1) an electric field perpendicular to the magnetic field;
- (2) a gradient in magnetic field perpendicular to the magnetic field;
- (3) curvature of the magnetic field;
- (4) a time dependent electric field.

The drift velocity for each of these cases is derived below.

#### $E \times B$ drift

If there is an electric field perpendicular to the magnetic field the particle orbits undergo a drift perpendicular to both fields. This is the so-called  $E \times B$  drift.

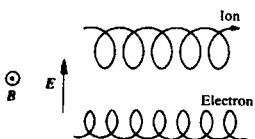


**Fig. 2.6.1**  $E \times B$  drift of ion and electron.  $v_d = E/B$ .

The equation of motion is

$$m_j \frac{dv}{dt} = e_j(E + v \times B). \quad 2.6.1$$

Choosing the  $z$  coordinate along the magnetic field and the  $y$  coordinate along the perpendicular electric field, the components of eqn 2.6.1 are

$$m_j \frac{dv_x}{dt} = e_j v_y B, \quad m_j \frac{dv_y}{dt} = e_j(E - v_x B).$$

The solutions of these equations can be written

$$v_x = v_{\perp} \sin \omega_{cjt} + \frac{E}{B}, \quad v_y = v_{\perp} \cos \omega_{cjt}. \quad 2.6.2$$

This drift is independent of the charge, mass, and energy of the particle. The whole plasma is therefore subject to this drift. The trajectories of an ion and an electron are shown in Fig. 2.6.1.

The  $E \times B$  drift can be further understood by recognizing that the perpendicular electric field is frame dependent. Thus this electric field can be transformed away by moving to a frame having a perpendicular velocity  $v_f$  such that

$$E + v_f \times B = 0. \quad 2.6.3$$

In this frame the particle orbit will simply be circular. It is seen therefore that in the original frame the particle will have its circular motion together with a drift velocity  $v_d = v_f$ . Crossing eqn 2.6.3 with  $B$  now gives the drift velocity

$$v_d = \frac{E \times B}{B^2}$$

as before.

### $\nabla B$ drift

In a magnetic field with a transverse gradient the particle orbit has a smaller radius of curvature on the part of its orbit in the stronger magnetic field, as illustrated in Fig. 2.6.2. This leads to a drift perpendicular to both the magnetic field and its gradient.

Taking the magnetic field to be in the  $z$  direction, and its gradient in the  $y$  direction, the magnitude of the drift can be calculated from the  $y$  component of the equation of motion, that is

$$m_j \frac{dv_y}{dt} = -e_j v_x B. \quad 2.6.4$$

Assuming the gradient of  $B$  to be small so that the magnetic field variation across the Larmor radius is small compared to  $B$ , the magnetic field can

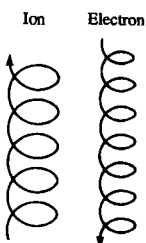


**Fig. 2.6.2** A gradient of  $B$  perpendicular to  $B$  gives ion and electron drifts in opposite directions.

be written

$$\mathbf{B} = \mathbf{B}_0 + \mathbf{B}' y$$

where  $y = 0$  is at the midplane of the particle orbit. Using the smallness of the perturbation of the orbit eqn 2.6.4 becomes

$$\frac{m_j}{e_j} \frac{dv_y}{dt} = -v_{x0}(B_0 + B' y) - v_d B_0 \quad 2.6.5$$

where  $v_d$  is the required drift velocity and the unperturbed motion of a particle with perpendicular velocity  $v_{\perp}$  is given by

$$v_{x0} = v_{\perp} \sin \omega_{cj} t, \quad y = \rho_j \sin \omega_{cj} t$$

where  $\rho_j = v_{\perp}/\omega_{cj}$ . Substituting for  $v_{x0}$  and  $y$  in eqn 2.6.5

$$\frac{m_j}{e_j} \frac{dv_y}{dt} = -v_{\perp} \sin \omega_{cj} t (B_0 + B' \rho_j \sin \omega_{cj} t) - v_d B_0.$$

Taking the time average of this equation with  $(dv_y/dt) = 0$  gives the required drift velocity in the  $x$  direction

$$v_d = -\rho_j \frac{B'}{B} v_{\perp} \quad 2.6.6$$

or in vector form

$$\mathbf{v}_d = \frac{1}{2} \rho_j \frac{\mathbf{B} \times \nabla B}{B^2} \mathbf{v}_{\perp}. \quad 2.6.7$$

The ions and electron have opposite drifts, the sign in eqn 2.6.7 being determined by the sign of  $e_j$  in  $\rho_j = m_j v_{\perp}/e_j B$ .

### Curvature drift

When a particle's guiding centre follows a curved magnetic field line it undergoes a drift perpendicular to the plane in which the curvature lies. This behaviour is illustrated in Fig. 2.6.3.

To calculate the drift it is convenient to transform to a frame rotating with the angular velocity,  $v_{||}/R'$  of the particle, where  $v_{||}$  is the velocity parallel to the magnetic field and  $R'$  is the radius of curvature of the field line. In this frame the particle experiences a centrifugal force  $m v_{||}^2/R'$  and the equation of motion is

$$m_j \frac{dv}{dt} = \frac{mv_{||}^2}{R'} \mathbf{i}_c + e_j (\mathbf{v} \times \mathbf{B}) \quad 2.6.8$$

where  $\mathbf{i}_c$  is the unit vector outward along the radius of curvature. Equation 2.6.8 is similar to eqn 2.6.1 for the case of the  $\mathbf{E} \times \mathbf{B}$  drift

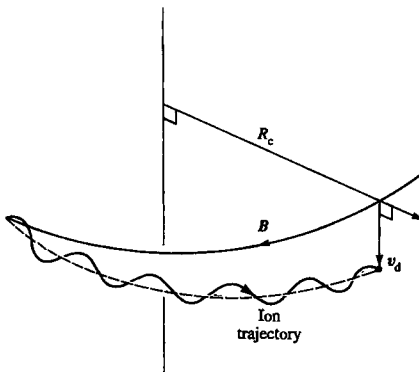


**Fig. 2.6.3** Ion drift due to magnetic field curvature. Electrons drift in the opposite direction.

with the force  $e_j E$  replaced by  $m_j v_{\parallel}^2 / R$ . Thus, by analogy with the  $E/B$  drift, the curvature drift is given by

$$v_d = \frac{v_{\parallel}^2}{\omega_{cj} R}$$

Since  $\omega_{cj}$  takes the sign of the particle charge, the electrons and ions have opposing drifts, the drift direction for the ions being that of  $i_c \times B$ .

If no currents are present the  $\nabla B$  drift is in the same direction as the curvature drift and takes a similar form. In this case  $\nabla B = -i_c B / R$  and the  $\nabla B$  drift velocity given by eqn 2.6.7 is

$$v_d = \frac{1}{2} \frac{v_{\perp}^2}{\omega_{cj} R}.$$

The combined drift is therefore

$$v_d = \frac{v_{\parallel}^2 + \frac{1}{2} v_{\perp}^2}{\omega_{cj} R}$$

or, in vector form

$$v_d = \frac{v_{\parallel}^2 + \frac{1}{2} v_{\perp}^2}{\omega_{cj}} \frac{\mathbf{B} \times \nabla \mathbf{B}}{B^2}. \quad 2.6.9$$

### Polarization drift

When an electric field perpendicular to the magnetic field changes in time it results in what is called the polarization drift. The name arises from the fact that the ion and electron drifts are in opposing directions and give rise to a polarization current proportional to  $dE/dt$ .

The equation of motion is

$$m_j \frac{dv}{dt} = e_j(E(t) + v \times B).$$

The electric field can be transformed away by moving to an accelerated frame having a velocity

$$v_f = \frac{E \times B}{B^2}.$$

The equation of motion is then

$$m_j \frac{dv}{dt} = e_j v \times B - m_j \frac{dv_f}{dt}$$

so that

$$m_j \frac{dv}{dt} = e_j v \times B - \frac{m_j}{B^2} \frac{dE}{dt} \times B. \quad 2.6.10$$

Equation 2.6.10 is similar to eqn 2.6.1 with  $e_j E$  being replaced by

$$-\frac{m_j}{B^2} \frac{dE}{dt} \times B.$$

The polarization drift corresponding to the electric drift ( $E \times B / B^2$ ) is therefore

$$v_d = -\frac{m_j}{e_j B^2} \left( \frac{dE}{dt} \times B \right) \times B,$$

so that, recalling that  $E$  is perpendicular to  $B$ ,

$$v_d = -\frac{1}{\omega_{ci} B} \frac{dE}{dt}. \quad 2.6.11$$

This drift is illustrated in Fig. 2.6.4.

The drift is in the same direction as  $dE/dt$  for ions and the opposite direction for electrons, being much larger for the ions. If the electron density is  $n$  the resulting polarization current density is

$$j_p = \sum_j n e_j v_{dj}$$

and substituting eqn 2.6.11 for each species

$$j_p = \frac{\rho_m}{B^2} \frac{dE}{dt}$$

$\rho_m$  being the mass density.

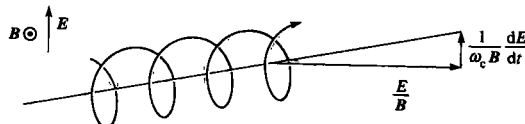


Fig. 2.6.4 Polarization drift of an ion caused by an increasing electric field perpendicular to the magnetic field. The electron drift is in the opposite direction.

## 2.7

### Adiabatic invariants

Adiabatic invariants are quantities associated with the particle motion, which remain almost constant during changes in the motion provided the changes are sufficiently slow. In the case of charged particles in a magnetic field the requirement is that time changes are on a time scale long compared to the gyro-period, and spatial changes are on a length scale much larger than the Larmor radius. There are three principal invariants for a charged particle in a magnetic field, the most important being the magnetic moment.

#### Magnetic moment

The basic definition of the magnetic moment of a current loop is

$$\mu = IA \quad 2.7.1$$

where  $I$  is the current in the loop and  $A$  is its area. The current carried by a charged particle gyrating in its Larmor orbit is

$$I = \frac{\omega_{cj}}{2\pi} e_j \quad 2.7.2$$

and the area,  $\pi\rho_j^2$ , of the orbit is

$$A = \pi \left( \frac{v_\perp}{\omega_{cj}} \right)^2$$

so that

$$\mu = \frac{\frac{1}{2}m_j v_\perp^2}{B}. \quad 2.7.3$$

For a small current loop the force on the loop is

$$\mathbf{F} = -\mu \nabla_B B \quad 2.7.4$$

in agreement with the detailed calculation given in Section 2.5.

The invariance of  $\mu$  is demonstrated by calculating its time derivative, that is

$$\frac{d\mu}{dt} = \frac{1}{B} \left( \frac{d}{dt} \left( \frac{1}{2}m_j v_\perp^2 \right) - \mu \frac{dB}{dt} \right). \quad 2.7.5$$

The conservation of energy gives

$$\frac{d}{dt} \left( \frac{1}{2}m_j v_\perp^2 \right) = e_j \mathbf{E} \cdot \mathbf{v} - m_j v_\parallel \frac{dv_\parallel}{dt} \quad 2.7.6$$

and the change in  $B$  following the guiding centre velocity  $v_{\parallel}$  is given by

$$\frac{dB}{dt} = \frac{\partial B}{\partial t} + v_{\parallel} \cdot \nabla B. \quad 2.7.7$$

Substituting eqns 2.7.6 and 2.7.7 into eqn 2.7.5

$$\begin{aligned} \frac{d\mu}{dt} = \frac{1}{B} & \left\{ \left( -m_j v_{\parallel} \frac{dv_{\parallel}}{dt} - \mu v_{\parallel} \cdot \nabla B + e_j E_{\parallel} v_{\parallel} \right) \right. \\ & \left. + \left( e_j E_{\perp} \cdot v_{\perp} - \mu \frac{\partial B}{\partial t} \right) \right\}. \end{aligned} \quad 2.7.8$$

The acceleration  $dv_{\parallel}/dt$  is produced by the force given in eqn 2.7.4 together with that due to  $E_{\parallel}$  and so, taking the scalar products with  $v_{\parallel}$

$$m_j v_{\parallel} \frac{dv_{\parallel}}{dt} = -\mu v_{\parallel} \cdot \nabla B + e_j E_{\parallel} v_{\parallel}.$$

Thus the terms in the first bracket in eqn 2.7.8 give zero. Since  $v_{\perp} = \omega_{ci} \rho_j$  the gyro-average of  $E_{\perp} \cdot v_{\perp}$  is given by

$$\langle E_{\perp} \cdot v_{\perp} \rangle = \frac{\omega_{ci}}{2\pi} \oint \mathbf{E} \cdot d\mathbf{s} \quad 2.7.9$$

where the integral is around the Larmor orbit and the line element  $d\mathbf{s}$  is along  $v_{\perp}$ . Thus using eqns 2.7.1, 2.7.2 and 2.7.9, eqn 2.7.8 can now be rewritten

$$\frac{d\mu}{dt} = -\frac{e_j}{B} \frac{\omega_{ci}}{2\pi} \left( \oint \mathbf{E} \cdot d\mathbf{s} + A \frac{\partial B}{\partial t} \right). \quad 2.7.10$$

The last term in the bracket of eqn 2.7.10 is the rate of change of flux through the area  $A$ , and from Faraday's law

$$A \frac{\partial B}{\partial t} = - \oint \mathbf{E} \cdot d\mathbf{s}$$

so that

$$\frac{d\mu}{dt} = 0.$$

This shows that, in the limit of slow variations of  $B$ ,  $\mu$  is a constant. That is,  $\mu$  is an adiabatic invariant.

### Second and third adiabatic invariants

The magnetic moment is associated with the Larmor orbit of a particle. When the particle has a larger scale periodic motion there is a second invariant,  $J$ , defined by

$$J = \oint v_{\parallel} dl \quad 2.7.11$$

where the integral is taken over the periodic orbit  $x(t)$  and  $dl = \mathbf{b} \cdot d\mathbf{x}$  where  $\mathbf{b}$  is the unit vector along the magnetic field. In the absence of an electric field the total energy,  $W$ , of the particle is constant, where

$$W = \frac{1}{2}m_f(v_{\perp}^2 + v_{\parallel}^2)$$

and, using the definition for  $\mu$  given by eqn 2.7.3,  $v_{\parallel}$  in eqn 2.7.11 can be written in terms of the constants of the motion and the magnetic field,

$$v_{\parallel} = \left( \frac{2}{m_f}(W - \mu B) \right)^{1/2}.$$

The periodic motion involved in the invariant  $J$  can be subject to a drift and this drift can result in a larger scale periodic motion. The third adiabatic is associated with this motion. If the drift velocity is  $v_d$ , the invariant is defined by the following integral over the periodic motion:

$$J_3 = \int v_d dl.$$

It can be shown that  $J_3$  is proportional to the magnetic flux enclosed by the orbit.

## 2.8

### Collisions

Collisions between particles give rise to plasma diffusion and other transport processes. They also allow transfer of energy between particles and are responsible for the electrical resistivity of the plasma.

The calculation of these processes is complex. First of all the concept of collision in a plasma is rather subtle. Secondly, collisions between particles depend on their relative velocities, and the overall result of collisions is the integrated effect of interactions between particles of all velocities. Finally the effective collision frequency depends upon the process under consideration.

The electric field at a given point in the plasma includes the sum of the contributions from all of the charged particles. Thus each particle is subject to the electric field force of all the other particles. However it turns out that the electric field can be separated into two parts. The first is a smooth macroscopic field, this is the field  $E$  which determines the particle drifts and appears in the equations governing the macroscopic behaviour of the plasma. The second part is a rapidly fluctuating microscopic electric field. For a given particle these fluctuations are the sum of the electric fields of the other particles with which it is 'colliding'. These are the particles which, at that instant, lie inside a Debye sphere surrounding the given particle, their trajectories adjusting to shield out

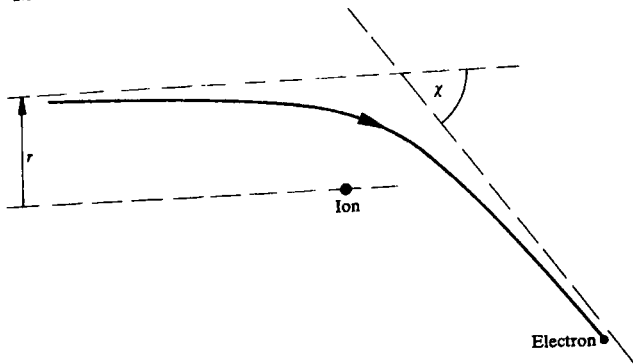


**Fig. 2.8.1** Geometry of electron-ion collision with impact parameter  $r$  and scattering angle  $x$ .

the collisional effect of more distant particles. A complete analysis of this behaviour is very complicated. In the following treatment the interaction of pairs of particles will be described and the sum of these binary Coulomb interactions will be cut-off at the shielding radius.

Consider as an example the case of a plasma electron colliding with a singly charged ion. The force between the particles is an inverse square force and is therefore described by the classical theory of Rutherford. The geometry of the collision is shown in Fig. 2.8.1. The scattering angle  $x$  for an impact parameter  $r$  and incident velocity  $v$  is given by

$$\cot(x/2) = \frac{4\pi\varepsilon_0 m_e v^2 r}{e^2}.$$

The impact parameter for a  $90^\circ$  scatter is therefore

$$r_0 = e^2 / 4\pi\varepsilon_0 m_e v^2.$$

The cross-section for scattering through an angle  $> 90^\circ$  is  $\sigma_0 = \pi r_0^2$  so that

$$\sigma_0 = e^4 / 64\pi\varepsilon_0^2 \delta^2$$

where  $\delta$  is the kinetic energy of the electron.

However, in a plasma the electron is simultaneously interacting with a large number of ions. Each collision leads to a different angle of scatter and to different losses of momentum and energy.

For collision with a single ion the change in momentum parallel to the initial electron motion is

$$\delta p = -\frac{2m_e v}{1 + (r/r_0)^2}.$$

If the ions are taken to be effectively at rest the total rate of change of momentum of the electron is obtained by integrating with respect to the impact parameter,  $r$ . Thus since the rate of collisions per unit area of impact is  $n v$ , where  $n$  is the ion density,

$$\begin{aligned}\frac{dp}{dt} &= -2nm_e v^2 \int \frac{2\pi r}{1 + (r/r_0)^2} dr \\ &= -2nm_e v^2 \sigma_0 \ln(1 + (r/r_0)^2) \Big|_{r_0}^{\lambda_D}.\end{aligned}\quad 2.8.1$$

In eqn 2.8.1 the Debye length,  $\lambda_D$ , has been introduced as the upper limit to remove the divergence which has arisen from the neglect of Debye shielding for collisions with impact parameters larger than the Debye length. Since  $\lambda_D \gg r_0$ , eqn 2.8.1 becomes

$$\frac{dp}{dt} = -4 \ln \Lambda \sigma_0 n m_e v^2 \quad 2.8.2$$

where  $\ln \Lambda = \ln(\lambda_D/r_0)$  is called the Coulomb logarithm. If the length  $r_0$  is less than the quantum mechanical length  $\hbar/2m_e v$  it should be replaced by this length in  $\Lambda$ , leading to a comparatively small change in its numerical value. The value of  $\ln \Lambda$  is typically around 17 in tokamak plasmas. Details of its properties are given in Section 14.5. It is seen that the cumulative effect of the many small angle collisions for impact parameters greater than  $r_0$  gives an effective collision cross-section  $4 \ln \Lambda \sigma_0$ . This is much larger than  $\sigma_0$ , the cross-section for large angle collisions alone.

The above example serves as an introduction to the nature of collisions in plasmas. More generally it is necessary to carry out integrations over the velocity distributions of the species involved. The proper basis for this is provided by the Fokker-Planck equation which is derived in Section 2.10. The effects of collisions can usually be expressed in terms of characterizing collision frequencies or collision times and these are described in Section 2.14.

### Momentum and energy change

Equation 2.8.2 gives the rate of change of momentum for an electron colliding with stationary ions. More generally, for particles of arbitrary mass ratio and relative velocity, the rate of change of momentum for particle  $i$  with velocity  $v_i$  through collisions with particles  $j$  with a velocity  $v_j$ , averaged over all impact parameters, is

$$\left\langle \frac{dp_{ij}}{dt} \right\rangle = -A_{ij} \frac{v_{ij}}{v_{ij}^3} \quad 2.8.3$$

where the relative velocity

$$v_{ij} = v_i - v_j,$$

and

$$A_{ij} = \frac{e_i^2 e_j^2 \ln \Lambda}{4\pi \epsilon_0^2 m_{ij}}$$

the reduced mass,  $m_{ij}$ , being given by

$$m_{ij} = \frac{m_i m_j}{m_i + m_j}.$$

The corresponding rate of change of energy is

$$\left\langle \frac{d\epsilon_{ij}}{dt} \right\rangle = -A_{ij} \frac{(m_i v_i + m_j v_j) \cdot v_{ij}}{(m_i + m_j) v_{ij}^3}. \quad 2.8.4$$

To obtain the average rates of change for a particle  $i$  due to collisions with *all* particles of type  $j$ , it is necessary to integrate eqns 2.8.3 and 2.8.4 over the velocity distribution function  $f_j(v_j)$ . The resulting integral can be written

$$\left\langle \frac{dp_i}{dt} \right\rangle_j = m_i A \nabla_v H \quad 2.8.5$$

where  $\nabla_v$  is the gradient in the  $v_i$  velocity space,

$$H = \left(1 + \frac{m_i}{m_j}\right) \int \frac{f_j(v_j)}{v_{ij}} d^3 v_j.$$

and

$$A = \frac{e_i^2 e_j^2 \ln \Lambda}{4\pi \epsilon_0^2 m_i^2}.$$

It is interesting to note the connection to potential theory, the integral in the expression for  $H$  having the same form as that for the electrostatic potential of a charge distribution  $f_j$ . It is apparent from this that for a spherical distribution of  $f_j$ , only particles with a velocity  $v_j < v_i$  contribute to the force on particle  $i$ .

The corresponding expression for the rate of energy change is

$$\left\langle \frac{d\epsilon_i}{dt} \right\rangle = A(m_i v \cdot \nabla_v H + m_{ij} H). \quad 2.8.6$$

The total rates of change of  $p_i$  and  $\epsilon_i$  are obtained by summing over all species present in the plasma.

The potential  $H$  can be calculated for a given distribution function  $f_j$  and in particular for a Maxwellian distribution. However the discussion of this is best delayed until the kinetic equations have been introduced in the following sections. These equations describe the time development of the distribution function. The collisional contribution to this is given by the Fokker-Planck equation, and the coefficients appearing in this

equation are related to the rates of change of momentum and energy described above. The form of  $H$  for a Maxwellian distribution is given in Section 2.13 and there is further discussion of the momentum and energy change in Section 2.14. Explicit forms for eqns 2.8.5 and 2.8.6 can be obtained from eqns 2.13.1 and 2.14.4.

## 2.9 Kinetic equations

Kinetic theory describes the behaviour of gases and plasmas in terms of the particle motions. Because of the large number of particles involved this description has to be statistical. In practice this is carried out using the distribution function  $f(x, v, t)$  which measures the probability density for a single particle in the six dimensional phase space  $(x, v)$ . The behaviour of the distribution function is described by the kinetic equation. Depending on the circumstances this takes different forms, some of which are described below.

A full account of the kinetic equations starts from the  $N$  particle distribution function which is a function of the positions and momenta of all the  $N$  particles. This includes information about pair correlations, and leads to a separation of the effects of large-scale fields and those varying on the scale of the Debye length, these small-scale fields being responsible for 'collisions'. For present purposes it is adequate to use the single particle distribution function  $f$  and to allow for collisions by introducing a separate collision term.

The distribution function is a function of the position  $q$  and the canonical momentum  $p$ , that is  $f = f(q, p)$ . From the conservation of particles it follows that the rate of change of  $f$  along a trajectory in phase space is given by the divergence of the phase space flow, thus

$$\frac{df}{dt} = -f \left( \frac{\partial}{\partial q} \cdot \dot{q} + \frac{\partial}{\partial p} \cdot \dot{p} \right) \quad 2.9.1$$

where

$$\frac{d}{dt} = \frac{\partial}{\partial t} + \dot{q} \cdot \frac{\partial}{\partial q} + \dot{p} \cdot \frac{\partial}{\partial p}.$$

The divergence term on the right-hand side of eqn 2.9.1 is zero as is readily seen by substituting Hamilton's equations

$$\dot{q} = \frac{\partial H}{\partial p}, \quad \dot{p} = -\frac{\partial H}{\partial q}.$$

The resulting equation is

$$\frac{\partial f}{\partial t} + \dot{q} \cdot \frac{\partial f}{\partial q} + \dot{p} \cdot \frac{\partial f}{\partial p} = 0. \quad 2.9.2$$

Considering a particle species  $j$ , the equation of motion in a plasma is

$$\dot{p}_j = e_j(E + v \times B)$$

and substituting into eqn 2.9.2 leads to the *Vlasov equation*

$$\frac{\partial f}{\partial t} + v \cdot \frac{\partial f}{\partial x} + \frac{e_j}{m_j} (E + v \times B) \cdot \frac{\partial f}{\partial v} = 0. \quad 2.9.3$$

This is the equation which governs the behaviour in the absence of collisions.

The inclusion of collisions requires the addition of a term  $(\partial f / \partial t)_c$  to the right-hand side of eqn 2.9.3. If the collisions in a plasma were hard collisions, localized in space and time, it would be appropriate to use the form of the collision term given by Boltzmann's equation. However, as seen from Section 2.8, this is inappropriate for a plasma. The proper collisional kinetic equation for a plasma is the *Fokker–Planck equation*

$$\frac{\partial f}{\partial t} + v \cdot \frac{\partial f}{\partial x} + \frac{e_j}{m_j} (E + v \times B) \cdot \frac{\partial f}{\partial v} = \left( \frac{\partial f}{\partial t} \right)_c \quad 2.9.4$$

for which the collision term is derived on the basis of multiple small angle collisions as described in Section 2.10.

The *drift kinetic equation* is a form of the Fokker–Planck (or Vlasov) equation which describes the evolution of  $f$  under conditions where it occurs slowly in time compared to the gyro-period and gradually in space compared to the gyro-radius of the particle orbits. The equation is derived from eqn 2.9.4 and involves a reduced phase space of five variables  $(v_{\parallel}, v_{\perp}, x)$ . The *gyro-kinetic equation* is similar, but describes the case where the electromagnetic fields do vary significantly across a Larmor radius, by averaging their effect over the Larmor orbit.

The kinetic equations are used for many purposes. Numerical solutions of the Fokker–Planck equation give the slowing down of a beam of particles injected into the plasma and the resulting heating of the ions and electrons. Approximate forms of the equation allow the calculation of the collisional transport of particles and energy. The linearized form of eqns 2.9.3 and 2.9.4 are used in stability calculations, particularly for micro-instabilities.

The Fokker–Planck equation can also be used to calculate characteristic relaxation times, as described in Section 2.14, by considering the behaviour of test particles in the plasma. By taking moments of the kinetic equations it is possible to derive fluid equations. Although the fluid equations are less generally valid, they are easier to solve and give considerable insight into plasma behaviour.

## 2.10

### Fokker-Planck equation

As described in Section 2.8 the dominant effect of collisions in a plasma occurs through the cumulative contribution of many small angle scatterings. The appropriate equation to describe the effect of these collisions is the Fokker-Planck equation. This provides an explicit form for the collision term  $(\partial f / \partial t)_c$  and hence allows calculation of the behaviour of the particle distribution function.

The rate of change of the distribution function due to collisions during a short time  $\Delta t$  is given by

$$\left( \frac{\partial f}{\partial t} \right)_c = \frac{f(x, v, t + \Delta t) - f(x, v, t)}{\Delta t}. \quad 2.10.1$$

The change in  $f$  results from the integrated effect of scatterings  $\Delta v$  in velocity during this time, thus

$$f(x, v, t + \Delta t) = \int f(x, v - \Delta v, t) \psi(v - \Delta v, \Delta v) d(\Delta v) \quad 2.10.2$$

where  $\psi(v, \Delta v)$  is the probability that a particle with velocity  $v$  will be scattered by  $\Delta v$  in a time  $\Delta t$ .

The integrand of eqn 2.10.2 can be expanded in a Taylor series in  $\Delta v$  to obtain

$$\begin{aligned} f(x, v - \Delta v, t) \psi(v - \Delta v, \Delta v) &= f(x, v, t) \psi(v, \Delta v) \\ &- \sum_{\alpha} \frac{\partial}{\partial v_{\alpha}} (f \psi) \Delta v_{\alpha} + \frac{1}{2} \sum_{\alpha, \beta} \frac{\partial^2}{\partial v_{\alpha} \partial v_{\beta}} (f \psi) \Delta v_{\alpha} \Delta v_{\beta}. \end{aligned} \quad 2.10.3$$

Substituting eqn 2.10.3 into eqn 2.10.2 and using

$$\int \Psi(v, \Delta v) d(\Delta v) = 1$$

gives

$$\begin{aligned} f(x, v, t + \Delta t) - f(x, v, t) &= - \sum_{\alpha} \frac{\partial}{\partial v_{\alpha}} \left( f(x, v, t) \int \psi(v, \Delta v) \Delta v_i d(\Delta v) \right) \\ &+ \frac{1}{2} \sum_{\alpha, \beta} \frac{\partial^2}{\partial v_{\alpha} \partial v_{\beta}} \left( f(x, v, t) \int \psi(v, \Delta v) \Delta v_{\alpha} \Delta v_{\beta} d(\Delta v) \right). \end{aligned} \quad 2.10.4$$

It is convenient to define the Fokker–Planck coefficients

$$\langle \Delta v_\alpha \rangle = \int \psi \Delta v_\alpha d(\Delta v) / \Delta t$$

and

$$\langle \Delta v_\alpha \Delta v_\beta \rangle = \int \psi \Delta v_\alpha \Delta v_\beta d(\Delta v) / \Delta t$$

giving the average time rate of change of  $\Delta v_\alpha$  and  $\Delta v_\alpha \Delta v_\beta$  due to collisions. Substitution of eqn 2.10.4 into eqn 2.10.1 then gives the Fokker–Planck collision term

$$\left( \frac{\partial f}{\partial t} \right)_c = - \sum_{\alpha} \frac{\partial}{\partial v_\alpha} (\langle \Delta v_\alpha \rangle f) + \frac{1}{2} \sum_{\alpha, \beta} \frac{\partial^2}{\partial v_\alpha \partial v_\beta} (\langle \Delta v_\alpha \Delta v_\beta \rangle f). \quad 2.10.5$$

The quantity  $\langle \Delta v_\alpha \rangle$  is called the coefficient of dynamic friction and  $\langle \Delta v_\alpha \Delta v_\beta \rangle$  the diffusion tensor.

## 2.11 Gyro-averaged kinetic equations

Many plasma phenomena involve processes which are slow compared to the Larmor frequency and which vary slowly in space compared to the Larmor radius of the individual ions or electrons. To study such phenomena simpler kinetic equations which average over the fast Larmor motion have been derived.

The advantage of such kinetic equations lies in the reduced dimensionality of the phase space. The Vlasov equation has the six independent variables involved in  $r$  and  $v$  and the gyro-averaging reduces this to five. Under some circumstances there is a periodic motion *along* the magnetic field and if this is sufficiently fast a further averaging over this motion reduces the phase space to four dimensions.

The *drift kinetic equation* is an equation for the gyro-averaged distribution function

$$\bar{f} = \frac{1}{2\pi} \int f d\phi,$$

where  $\phi$  is the rapidly varying gyrophase. It is obtained by expanding the Fokker–Planck equation with  $\omega_c^{-1}\partial/\partial t \ll 1$  and  $\rho/L \ll 1$ , where  $\omega_c$  is the cyclotron frequency,  $\rho$  the Larmor radius and  $L$  is a characteristic plasma length, and the equation then takes the form

$$\frac{\partial \bar{f}}{\partial t} + \mathbf{v}_g \cdot \nabla \bar{f} + \left[ e_f \mathbf{E} \cdot \mathbf{v}_g + \mu \frac{\partial \mathbf{B}}{\partial t} \right] \frac{\partial \bar{f}}{\partial K} = \left( \frac{\partial \bar{f}}{\partial t} \right)_c, \quad 2.11.1$$

where the averaged distribution function  $\bar{f}$  is a function of the five phase space variables  $x, \mu, K$  with the magnetic moment  $\mu = m_j v_{\perp}^2 / 2B$  and the energy  $K = \frac{1}{2} m_j v^2$ . In eqn 2.11.1  $E$  is the electric field and the guiding centre velocity  $v_g$  contains the rapid longitudinal motion, the electric cross-field drift, and the magnetic gradient  $B$  and curvature drifts

$$v_g = v_{\parallel} b + \frac{E \times B}{B^2} + \frac{v_{\parallel}^2 b \times (b \cdot \nabla) b + \mu b \times \nabla B}{\omega_{cj}} \quad 2.11.2$$

where  $b = B / |B|$  and  $\omega_{cj} = e_j B / m_j$ .

In eqn 2.11.1 the first two terms of the left-hand side contain the Lagrangian time derivative convecting along the guiding centre trajectory. The coefficient of  $(\partial \bar{f} / \partial K)$  contains the work done by the electric field on the guiding centre together with the change in the perpendicular energy,  $\frac{1}{2} m v_{\perp}^2$ , experienced by a guiding centre (whose magnetic moment  $\mu$  is conserved) in a changing magnetic field. The right-hand side of eqn 2.11.1 represents the rate of change of  $f$  due to interparticle collisions. An explicit form for  $(\partial \bar{f} / \partial t)_c$  can be obtained by gyro-averaging the Fokker-Planck collision operator, but is somewhat complicated. The resulting operator describes slowing down and diffusion in energy,  $K$ , and diffusion in magnetic moment  $\mu$  (or in the pitch angle variable  $\lambda = \mu/K$ ). It is not usual to retain the effect of classical collisional diffusion which is a second order effect (of order  $v_j \rho_j^2 / L_1^2$  where  $\rho_j$  is the Larmor radius,  $v_j$  the collision frequency and  $L_1$  a characteristic length of variation of  $\bar{f}$  across the magnetic field). This is not an essential weakness and a more complex drift kinetic equation, correct to higher order in  $\rho_j / L$  can be derived which contains both higher order drift velocities like the polarization drift and classical diffusion.

The equation is used in linear and nonlinear studies of low frequency and long wavelength instabilities, and in neoclassical transport theory where the neglect of the ‘classical’ contribution to transport, arising from Larmor gyration, is unimportant.

The *gyro-kinetic equation* extends these averaging procedures to situations in which some components of the electromagnetic fields vary significantly across a particle’s Larmor orbit.

It was first used in linear stability analyses in which the perturbed fields vary as  $\exp(i\mathbf{k} \cdot \mathbf{x})$  and the wavelengths in the directions transverse to the magnetic field are comparable to the Larmor radius, that is  $k_{\perp} v_{\perp} / \omega_c$  is of order unity.

Taking collisionless equations for simplicity and perturbations for which  $k_{\perp} v_{\perp} / \omega_c$  is of order unity and the perturbed quantities vary as  $\exp(-i\omega t + \mathbf{k}_{\perp} \cdot \mathbf{x})$  then, writing  $f = f_0 + \delta f$  and  $E = E_0 - \nabla \phi - i\omega A$ , the distribution function perturbation  $\delta f$  may be obtained in terms of the perturbed potentials  $\phi$  and  $A_{\parallel}$  and the magnetic field perturbation  $B_{\parallel}$  by expanding the linearized Vlasov equation. The result, for isotropic  $f_0$  is

$$\delta f = e_j \phi \frac{\partial f_0}{\partial K} + g e^{iL},$$

where

$$L = \frac{v_{\perp} \times b - k_{\perp}}{\omega_{ci}}$$

and  $g(\mu, K, x)$  satisfies the gyro-kinetic equation

$$\begin{aligned} \frac{\partial g}{\partial t} + v_{\parallel} b \cdot \nabla g + ik_{\perp} \cdot v_g g \\ = - \left[ \omega \frac{\partial f_0}{\partial K} - \frac{b \times \nabla f_0 \cdot k_{\perp}}{\omega_{ci}} \right] \left[ J_0(z) e_j (\phi - v_{\parallel} A_{\parallel}) + \frac{2J_1(z)}{z} \mu B_{\parallel} \right] \end{aligned} \quad 2.11.3$$

with

$$z = k_{\perp} v_{\perp} / \omega_{ci}.$$

In the long wavelength limit,  $z \rightarrow 0$  and  $L \rightarrow 0$  and the results for  $\delta f$  and  $g$  are identical to those which would be obtained by linearizing the drift kinetic equation. The Bessel functions  $J_0(z)$  and  $J_1(z)$ , and the factor  $\exp(iL)$  contain the effects of Larmor averaging over the rapid spatial variation of the perturbed fields.

If the equilibrium possesses magnetic shear this simple picture of the gyro-kinetic equation as a differential equation is invalid because the spatial variation of the perturbed quantities can no longer be represented purely by the eikonal form  $\exp(ik \cdot x)$ . However, many short wavelength linear stability calculations in toroidal geometry introduce the so-called ballooning transformation. This has the important consequence that eikonal representations for the perturbed quantities are valid in the transformed space, even in strongly sheared magnetic fields, so that simple gyro-kinetic equations like 2.11.3 are obtained.

The gyro-kinetic equation appears in linearized studies of low frequency instabilities, but more complicated versions of the equation can be derived for high frequency modes ( $\omega/\omega_c \sim 1$ ) with nonlinear terms included.

For applications to low frequency or slowly evolving phenomena, a second averaging (over the longitudinal motion of the particles) can be performed. This further reduces the dimensionality of the problem to the four variables  $x_{\perp}, \mu, K$  and generates the *bounce averaged drift kinetic equation*, or *bounce averaged gyro-kinetic equation*.

## 2.12

### Fokker-Planck aquation for a plasma

In the case of a plasma the coefficients in the Fokker-Planck equation are calculated for small angle Coulomb collisions and a sum is made over

all the particle species. The coefficients take the form of differentials of integrals over the distribution function. These integrals,  $H_j$  and  $G_j$ , called the Rosenbluth potentials, are given by

$$H_j(v) = \left(1 + \frac{m}{m_j}\right) \int \frac{f_j(v_j)}{|v - v_j|} dv_j \quad 2.12.1$$

and

$$G_j(v) = \int f_j(v) |v - v_j| dv_j \quad 2.12.2$$

the subscript  $j$  referring to the particle species. Written in terms of these potentials the required coefficients are

$$\langle \Delta v_\alpha \rangle = \sum_j A_j \frac{\partial H_j(v)}{\partial v_\alpha} \quad 2.12.3$$

and

$$\langle \Delta v_\alpha \Delta v_\beta \rangle = \sum_j A_j \frac{\partial^2 G_j(v)}{\partial v_\alpha \partial v_\beta} \quad 2.12.4$$

where

$$A_j = \frac{e^4 Z^2 Z_j^2 \ln \Lambda}{4\pi \epsilon_0^2 m^2}.$$

and the subscripts  $\alpha$  and  $\beta$  refer to the Cartesian components of  $v$  and  $v_j$ .

Using eqn 2.10.5 with eqns 2.12.3 and 2.12.4 the Fokker-Planck collision term can now be written

$$\begin{aligned} \left(\frac{\partial f}{\partial t}\right)_c &= \sum_j \frac{e^2 Z^2 Z_j^2 \ln \Lambda}{4\pi \epsilon_0^2 m^2} \left\{ -\frac{\partial}{\partial v_\alpha} \left( \frac{\partial H_j(v)}{\partial v_\alpha} f(v) \right) \right. \\ &\quad \left. + \frac{1}{2} \frac{\partial}{\partial v_\alpha} \frac{\partial}{\partial v_\beta} \left( \frac{\partial^2 G_j(v)}{\partial v_\alpha \partial v_\beta} f(v) \right) \right\} \end{aligned} \quad 2.12.5$$

where summation is taken over double indices of  $\alpha$  and  $\beta$ .

Alternatively, the collision term may be written in the symmetric Landau integral form

$$\begin{aligned} \left(\frac{\partial f}{\partial t}\right)_c &= \sum_j \frac{e^2 Z^2 Z_j^2 \ln \Lambda}{8\pi \epsilon_0^2 m} \\ &\times \frac{\partial}{\partial v_\alpha} \int \left( \frac{f_j(v_j)}{m} \frac{\partial f(v)}{\partial v_\beta} - \frac{f(v)}{m_j} \frac{\partial f_j(v_j)}{\partial v_{j\beta}} \right) u_{\alpha\beta} dv_j \end{aligned} \quad 2.12.6$$

where

$$u = v - v_j \quad \text{and} \quad u_{\alpha\beta} = \frac{u^2 \delta_{\alpha\beta} - u_\alpha u_\beta}{u^3}.$$

The Fokker-Planck equation for a plasma is now obtained by substituting eqn 2.12.5 or 2.12.6 into eqn 2.9.4. Its solution is usually obtained

numerically. However it is possible to obtain useful information of a simpler form by considering the response of test particles to collisions with species having a Maxwellian velocity distribution. This allows the calculation of characteristic times for the slowing and deflection of particles as described in Section 2.14.

## 2.13

### Fokker-Planck coefficients for Maxwellian distributions

Taking a Maxwellian velocity distribution for the ‘background’ species and denoting this species with subscript 1,

$$f_1(v_1) = \frac{n_1}{(2\pi)^{3/2} v_{T1}^3} \exp - \left( \frac{v_1^2}{2v_{T1}^2} \right),$$

the Rosenbluth potentials given by eqns 2.12.1 and 2.12.2 can be calculated. The resulting potentials are

$$H_1 \left( 1 + \frac{m}{m_1} \right) n_1 \frac{\Phi(v/\sqrt{2}v_{T1})}{v}$$

and

$$G_1 = n_1 \left( \frac{v^2 + v_{T1}^2}{v} \Phi(v/\sqrt{2}v_{T1}) + \frac{v_{T1}}{\sqrt{2}} v_{T1} \Phi'(v/\sqrt{2}v_{T1}) \right)$$

where

$$\Phi(x) = \frac{2}{\sqrt{\pi}} \int_0^x e^{-y^2} dy$$

is the error function, and so

$$\Phi'(x) = \frac{2}{\sqrt{\pi}} e^{-x^2}.$$

The corresponding  $\langle \Delta v \rangle$  is parallel to  $v$ , and the diffusion tensor is diagonal. It is therefore convenient to use Cartesian coordinates parallel and perpendicular to a chosen direction as shown in Fig. 2.13.1, the two perpendicular coordinates being written  $v_{\perp\alpha}$  and  $v_{\perp\beta}$ . From eqns 2.10.5 and 2.12.5 the friction and diffusion coefficients are related to the potentials by the equations

$$\langle \Delta v_{||} \rangle = A_1 \frac{\partial H_1}{\partial v}$$

$$\langle (\Delta v_{||})^2 \rangle = A_1 \frac{\partial^2 G_1}{\partial v^2}$$

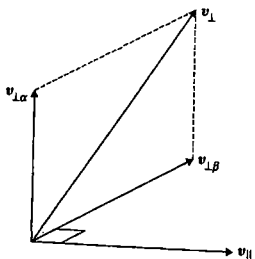


Fig. 2.13.1 Orthogonal velocity coordinates  $v_{||}$ ,  $v_{\perp\alpha}$  and  $v_{\perp\beta}$  with  $v_{\perp} = v_{\perp\alpha} + v_{\perp\beta}$ .

and

$$\langle (\Delta v_{\perp\alpha})^2 \rangle = A_1 \frac{1}{v} \frac{dG_1}{dv}$$

where

$$A_1 = \frac{e^4 Z^2 Z_j^2 \ln \Lambda}{4\pi \epsilon_0^2 m^2}.$$

The form of  $\langle (\Delta v_{\perp\alpha})^2 \rangle$  follows from the relation

$$v^2 = v_{\parallel}^2 + v_{\perp\alpha}^2 + v_{\perp\beta}^2$$

so that

$$\left( \frac{\partial^2 G_1}{\partial v_{\perp\alpha}^2} \right)_{v_{\perp\alpha}=0} = \frac{1}{v} \frac{dG_1}{dv}.$$

The explicit forms are

$$\langle \Delta v_{\parallel} \rangle = -A_D \left( 1 + \frac{m}{m_p} \right) \frac{\Psi(v/\sqrt{2}v_{T1})}{2v_{T1}^2} \quad 2.13.1$$

$$\langle (\Delta v_{\parallel})^2 \rangle = A_D \frac{\Psi(v/\sqrt{2}v_{T1})}{v}$$

$$\langle (\Delta v_{\perp\alpha})^2 \rangle = A_D \frac{\Phi(v/\sqrt{2}v_{T1}) - \Psi(v/\sqrt{2}v_{T1})}{2v} \quad 2.13.2$$

where

$$\Psi(x) = \frac{\Phi(x) - x\Phi'(x)}{2x^2}$$

and

$$A_D = \frac{n_1 e^4 Z^2 Z_1^2 \ln \Lambda}{2\pi \epsilon_0^2 m^2}.$$

It is to be noted that the total perpendicular coefficient  $\langle (\Delta v_{\perp})^2 \rangle$  is given by

$$\langle (\Delta v_{\perp})^2 \rangle = \langle (\Delta v_{\perp\alpha})^2 \rangle + \langle (\Delta v_{\perp\beta})^2 \rangle = 2 \langle (\Delta v_{\perp\alpha})^2 \rangle$$

so that

$$\langle (\Delta v_{\perp})^2 \rangle = A_D \frac{\Phi(v/\sqrt{2}v_{T1}) - \Psi(v/\sqrt{2}v_{T1})}{v} \quad 2.13.3$$

and

$$\langle (\Delta v)^2 \rangle = \langle (\Delta v_{\parallel})^2 \rangle + \langle (\Delta v_{\perp})^2 \rangle = A_D \frac{\Phi(v/\sqrt{Z_{T1}})}{v}.$$

Graphs of  $\Phi(x)$  and  $\Psi(x)$  are given in Fig. 2.13.2. These functions take the limiting forms

$$\Psi(x) \rightarrow \frac{2x}{3\sqrt{\pi}}, \quad \Phi(x) \rightarrow \frac{2x}{\sqrt{\pi}}, \quad x \ll 1,$$

$$\Psi(x) \rightarrow \frac{1}{2x^2}, \quad \Phi(x) \rightarrow 1, \quad x \gg 1.$$

Defining the diffusion coefficients  $D_{\parallel}$  and  $D_{\perp}$  by

$$D_{\parallel} = \frac{1}{2} \langle (\Delta v_{\parallel})^2 \rangle$$

and

$$D_{\perp} = \frac{1}{2} \langle (\Delta v_{\perp\alpha})^2 \rangle = \frac{1}{2} \langle (\Delta v_{\perp\beta})^2 \rangle,$$

the Fokker-Planck collision term given by eqn 2.10.5 can be written in either of the two forms

$$\left( \frac{\partial f}{\partial t} \right)_c = -\nabla_v \cdot [(\Delta v_{\parallel})f - \nabla_{\parallel}(D_{\parallel}f) - D_{\perp}\nabla_{\perp}f] \quad 2.13.4$$

and

$$\left( \frac{\partial f}{\partial t} \right)_c = -\nabla_v \cdot [((\Delta v_{\parallel}) - \nabla_{\parallel}D_{\parallel})f - D_{\parallel}\nabla_{\parallel}f - D_{\perp}\nabla_{\perp}f] \quad 2.13.5$$

where  $\nabla_v$  indicates the divergence operator in velocity space,  $\Delta v_{\parallel}$  is along  $v$ , and  $\nabla_{\parallel}$  and  $\nabla_{\perp}$  are the components of  $\nabla$  parallel and perpendicular to  $v$ . The term 'dynamic friction' is usually applied to  $(\Delta v_{\parallel})$ ,  $((\Delta v_{\parallel}) - \nabla_{\parallel}D_{\parallel})$  in eqn 2.13.4, but sometimes to the coefficient

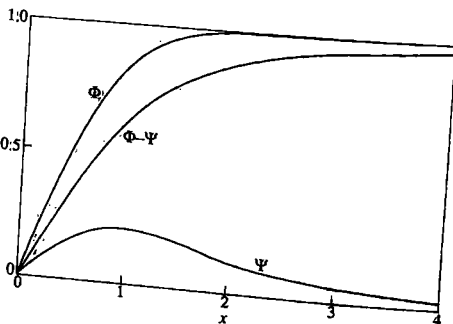


Fig. 2.13.2 Graphs of the error function  $\Phi(x)$ ,  $\Psi(x)$ , and  $\Phi(x) - \Psi(x)$ .

## 2.14

### Relaxation processes

The calculation of the changes in the distribution function described by the Fokker-Planck collision term is generally quite complicated. However, it is possible to obtain some insight by considering the response of a test particle to collisions with remaining particles. These particles are called the field particles and are denoted by the subscript 1. Formally the procedure is to take a delta function at a chosen velocity for the initial distribution function and to calculate the subsequent time development. However, the initial rate of change of momentum loss, and deflection and diffusion of velocity are given by the Fokker-Planck coefficients themselves and it is possible to obtain the associated relaxation times from these coefficients.

The *slowing-down time* for a particles of velocity  $v$  is given by

$$\tau_s = -\frac{v}{(dv/dt)} = -\frac{v}{(\Delta v_{||})}.$$

This time characterizes the rate of change of velocity in the direction of the initial velocity. Using eqn 2.13.1 for  $(\Delta v_{||})$

$$\tau_s = \frac{2v_{T1}^2 v}{(1 + m/m_1) A_D \Psi(v/\sqrt{2v_{T1}})}. \quad 2.14.1$$

The *deflection time* measures the average rate at which the particle velocity is scattered into the direction perpendicular to its initial velocity. This is a diffusion process and the deflection time is defined by

$$\tau_d = \frac{v^2}{(dv_{\perp}^2/dt)} = \frac{v^2}{((\Delta v_{\perp})^2)}.$$

Using eqn 2.13.3

$$\tau_d = \frac{v^3}{A_D (\Phi(v/\sqrt{2v_{T1}}) - \Psi(v/\sqrt{2v_{T1}}))}. \quad 2.14.2$$

Both of the processes described above involve a change in energy of the test particles. The equation for the full rate of change of energy,  $\langle \Delta E \rangle$ , is

$$\langle \Delta E \rangle = \frac{m}{2} \left( 2v(\Delta v_{||}) + ((\Delta v_{||})^2) + ((\Delta v_{\perp})^2) \right). \quad 2.14.3$$

This equation also gives the rate of loss of energy of a particle beam. Substituting for the coefficients from eqns 2.13.1 to 2.13.3

$$\langle \Delta E \rangle = \frac{mA_D}{\sqrt{2v_{T1}}} \left( - \left( 1 + \frac{m}{m_1} \right) x \Psi(x) + \frac{\Psi(x)}{2x} + \frac{\Phi(x) - \Psi(x)}{2x} \right).$$

where  $x = v/\sqrt{2}v_{T1}$ . Rearranging the terms in the bracket

$$\begin{aligned} \langle \Delta E \rangle &= -\frac{1}{2} \frac{m^2}{m_1} A_D \frac{1}{v} \\ &\times \left( \Phi(v/\sqrt{2}v_{T1}) - \left( 1 + \frac{m_1}{m} \right) \frac{v}{\sqrt{2}v_{T1}} \Phi'(v/\sqrt{2}v_{T1}) \right). \end{aligned} \quad 2.14.4$$

The physical processes underlying the energy balance can be understood by writing the dynamic friction force

$$F_d = m(\Delta v_{||})$$

and the rate of energy transfer to the field particles

$$\frac{dE_f}{dt} = -\langle \Delta E \rangle.$$

Equation 2.14.3 can then be written

$$-F_d v = \frac{dE_f}{dt} + \frac{1}{2} m \left( (\Delta v_{||})^2 + (\Delta v_{\perp})^2 \right).$$

The quantity  $-F_d v$  is the work done by the test particles against the dynamic friction force. Part of the energy so released is transferred to the field particles and the remainder appears as increased energy of the test particles through the increased perpendicular and parallel spread in their velocities.

In the limit  $v/v_{T1} \gg 1$

$$\begin{aligned} \frac{dE_f}{dt} &\rightarrow \frac{m^2}{m_1} \frac{A_D}{2v} \\ \frac{1}{2} m (\Delta v_{||})^2 &\rightarrow 0 \\ \frac{1}{2} m (\Delta v_{\perp})^2 &\rightarrow \frac{m A_D}{2v} \\ -F_d v &\rightarrow \left( 1 + \frac{m}{m_1} \right) \frac{m A_D}{2v}. \end{aligned} \quad 2.14.5$$

2.14.6

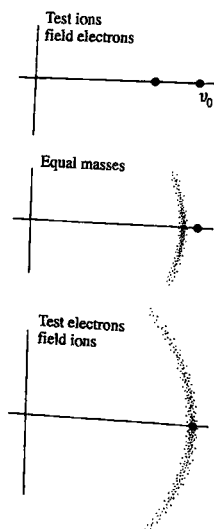


**Fig. 2.14.1** Velocity space behaviour of test particles under collisions with field particles for a test particle velocity much greater than the thermal velocity of the field particles. The field particle distribution is centred at the origin and the test particles initially have a delta function distribution at velocity  $v_0$ .

For ion test particles and electron field particles almost all of the energy is transferred to the electrons, the ions being slowed with negligible scattering. For particles of equal mass half the energy is transferred to the field particles and half appears in the energy of the perpendicular motion. For test electrons and field ions the energy is retained in the electrons, the collisions deflecting the electrons on a sphere of equal velocity. The behaviour in these three cases is illustrated in Fig. 2.14.1.

In the limit  $v/v_{\text{Ti}} \ll 1$

$$\begin{aligned}\frac{dE_f}{dt} &\rightarrow \frac{m A_D}{\sqrt{2\pi} v_{\text{Ti}}} \left( \frac{2}{3} \frac{\frac{1}{2}mv^2}{T_1} - 1 \right) \\ \frac{1}{2}m \langle (\Delta v_{\parallel})^2 \rangle &\rightarrow \frac{1}{3} \frac{m A_D}{\sqrt{2\pi} v_{\text{Ti}}} \\ \frac{1}{2}m \langle (\Delta v_{\perp})^2 \rangle &\rightarrow \frac{2}{3} \frac{m A_D}{\sqrt{2\pi} v_{\text{Ti}}} \\ -F_d v &\rightarrow \frac{m A_D}{\sqrt{2\pi} v_{\text{Ti}}} \frac{2}{3} \frac{\frac{1}{2}mv^2}{T_1}.\end{aligned}$$

In this case energy transfer to the field particles only occurs for test particles which are much more massive than the field particles, to allow  $\frac{1}{2}mv^2 > \frac{3}{2}T_1$ , as with an ion test particle and field electrons. If the particles are of similar mass then, in this limit ( $v/v_{\text{Ti}} \ll 1$ )

$$\frac{1}{2}mv^2 \ll T_1, \quad F_d v \rightarrow 0$$

and the test particles are simply ‘heated’, the distribution function expanding isotropically. The perpendicular energy is twice the parallel energy because two dimensions are involved.

When two species are at different temperatures collisions bring about an exchange of heat between them, lowering the temperature difference. For species  $i$  and  $j$  this process is characterized by the *heat exchange time*  $\tau_{ij}$  defined by

$$\frac{dT_i}{dt} = \frac{T_j - T_i}{\tau_{ij}}. \quad 2.14.7$$

The rate of energy loss from a test particle to field particles is given by eqn 2.14.4. The total transfer of energy from one species with a Maxwellian distribution function to another is obtained by integrating the test particle energy loss over the whole distribution. Thus

$$\frac{3}{2}n_i \frac{dT_i}{dt} = \int \langle \Delta E \rangle_{ij} f_i 4\pi v_i^2 dv_i$$

where  $\langle \Delta E \rangle_{ij}$ , given by eqn 2.14.4, can be written

$$\begin{aligned}\langle \Delta E \rangle_{ij} &= -\frac{n_j e^4 Z_i^2 Z_j^2 \ln \Lambda}{4\pi \epsilon_0^2 m_j} \\ &\times \left( \frac{\Phi(v_i/\sqrt{2}v_{\text{Ti}})}{v_i} - \left( 1 + \frac{m_j}{m_i} \right) \frac{1}{\sqrt{2}v_{\text{Ti}}} \Phi'(v_i/\sqrt{2}v_{\text{Ti}}) \right)\end{aligned}$$

and

$$f_i = \frac{n_i}{(2\pi)^{3/2} v_{\text{Ti}}^3} \exp -\frac{v_i^2}{2v_{\text{Ti}}^2}.$$

Thus

$$\frac{dT_i}{dt} = -\frac{2n_j e^4 Z_i^2 Z_j^2 \ln \Lambda}{3(2\pi)^{3/2} \epsilon_0^2 m_i m_j} I \quad 2.14.8$$

where

$$I = \int \left( v_i \Phi(v_i/\sqrt{2}v_{Tj}) - \left(1 + \frac{m_j}{m_i}\right) \frac{v_i^2}{\sqrt{2}v_{Tj}} \Phi'(v_i/\sqrt{2}v_{Tj}) \right) \times \exp -\frac{v_i^2}{2v_{Ti}^2} dv_i.$$

Integrating the first term by parts

$$I = \frac{m_i}{\sqrt{2}v_{Tj}v_{Ti}^3} \int \left( v_{Ti}^2 - \left(1 + \frac{m_j}{m_i}\right) v_i^2 \right) \Phi'(v_i/\sqrt{2}v_{Tj}) \exp -\frac{v_i^2}{2v_{Ti}^2} dv_i \\ = \sqrt{\frac{2}{\pi}} \frac{m_i}{v_{Tj}v_{Ti}^3} \int \left( v_{Ti}^2 - \left(1 + \frac{m_j}{m_i}\right) v_i^2 \right) \exp -\left(\frac{1}{2} \left(\frac{1}{v_{Ti}^2} + \frac{1}{v_{Tj}^2}\right) v_i^2\right) dv_i$$

so that

$$I = \frac{T_i - T_j}{(v_{Ti}^2 + v_{Tj}^2)^{3/2}}. \quad 2.14.9$$

Substitution of eqn 2.14.9 into eqn 2.14.8 gives  $dT_i/dt$  and comparison with eqn 2.14.7 gives the required heat exchange time

$$\tau_{ij} = \frac{3\sqrt{2}\pi^{3/2}\epsilon_0^2 m_i m_j}{n_j e^4 Z_i^2 Z_j^2 \ln \Lambda} \left( \frac{T_i}{m_i} + \frac{T_j}{m_j} \right)^{3/2}. \quad 2.14.10$$

For electrons and single charged ions the heat exchange time is

$$\tau_{ie} = \tau_{ei} = \frac{m_i}{2m_e} \tau_e \quad 2.14.11$$

where  $\tau_e$  is the electron collision frequency given by

$$\tau_e = 3(2\pi)^{3/2} \frac{\epsilon_0^2 m_e^{1/2} T_e^{3/2}}{ne^4 \ln \Lambda}.$$

In this case the frequency of collisions is determined by the faster component, the electrons. However, because of the difference in mass the energy transfer in a collision is inefficient, only a fraction  $\sim m_e/m_i$  of the electron energy being transferred to the ions.

## 2.15

### Collision times

The characteristic times for the collisional relaxation processes described in Section 2.14 are functions of the velocity of the test particle. Typical values of the times involved may be obtained by taking the test particle to have the average thermal velocity. Thus, putting  $u = v_T$  and using  $m v_T^2 = T$  it is seen that all of the resulting characteristic collision times are proportional to a time having the form

$$\frac{\epsilon_0^2 m^{1/2} T^{3/2}}{ne^4 \ln \Lambda}.$$

It is convenient to define collision times with the numerical factors which occur in the calculation of macroscopic quantities such as the electrical conductivity. For a plasma with ions of charge  $Z$  this leads to an *electron collision time*

$$\tau_e = 3(2\pi)^{3/2} \frac{\epsilon_0^2 m_e^{1/2} T_e^{3/2}}{n_i Z^2 e^4 \ln \Lambda} \quad 2.15.1$$

and an *ion collision time*

$$\tau_i = 12\pi^{3/2} \frac{\epsilon_0^2 m_i^{1/2} T_i^{3/2}}{n_i Z^4 e^4 \ln \Lambda}. \quad 2.15.2$$

The ratio of these times,  $\tau_e/\tau_i$ , is of order  $(m_e/m_i)^{1/2}$  reflecting the faster thermal velocity of the electrons compared with that of the ions.

A further characteristic time is the heat exchange between the electron and ion components of the plasma. This is the *heat exchange time* given by eqn 2.14.11.

Expressing  $T$  in keV the collision times are

$$\left. \begin{aligned} \tau_e &= 1.09 \times 10^{16} \frac{T_e^{3/2}}{n_i Z^2 \ln \Lambda} \text{ s}, \\ \tau_i &= 6.60 \times 10^{17} \frac{(m_i/m_p)^{1/2} T_i^{3/2}}{n_i Z^4 \ln \Lambda} \text{ s}, \end{aligned} \right\} T \text{ in keV} \quad 2.15.3$$

Values of  $\ln \Lambda$  are given in Section 14.5. A graph of collision times is given in Section 14.6 and some typical values are given in Tables 2.15.1 to 2.15.3.

**Table 2.15.1** Values of electron collision time,  $\tau_e$ , for  $Z = 1$ .

$n$	$T$		
	100 eV	1 keV	10 keV
$10^{19} \text{ m}^{-3}$	2.4 $\mu\text{s}$	67 $\mu\text{s}$	1.9 ms
$10^{20} \text{ m}^{-3}$	0.27 $\mu\text{s}$	7.2 $\mu\text{s}$	0.20 ms

**Table 2.15.2** Values of ion collision time,  $\tau_i$ , for deuterium.

$n$	$T$		
	100 eV	1 keV	10 keV
$10^{19} \text{ m}^{-3}$	0.20 ms	5.0 ms	0.13 s
$10^{20} \text{ m}^{-3}$	21 $\mu\text{s}$	0.54 ms	14 ms

**Table 2.15.3** Values of heat exchange time,  $\tau_{ie}$ , for a deuterium plasma.

$n$	$T$		
	100 eV	1 keV	10 keV
$10^{19} \text{ m}^{-3}$	4.4 ms	0.12 s	3.4 s
$10^{20} \text{ m}^{-3}$	0.49 ms	13 ms	0.37 s

## 2.16

### Resistivity

When an electric field is applied to a plasma the electrons accelerate to a drift velocity,  $v_d$ , at which the force due to the field is balanced by the force due to collisions with the ions. This occurs for

$$E_e = \frac{m_e v_d}{\tau_c} \quad 2.16.1$$

where  $\tau_c$  is the time for momentum loss by the electrons.

The resistivity is defined by Ohm's law,

$$E = \eta j$$

so that, using eqn 2.16.1,

$$\eta = \frac{m_e}{n_e e^2 \tau_c}.$$

A rough estimate is obtained by putting  $\tau_c = \tau_e$ , the electron collision time given in eqn 2.15.1. To obtain an accurate value it is necessary to

solve the collisional kinetic equation for the electron distribution function taking account of electron-electron collisions. This was done by Spitzer and his co-workers who found that for singly charged ions the resistivity is approximately a half of the rough estimate referred to above. More precisely

$$\begin{aligned}\eta_s &= 0.51 \frac{m_e}{n_e e^2 \tau_e} = 0.51 \frac{m_e^{1/2} e^2 \ln \Lambda}{3 \varepsilon_0^2 (2\pi T_e)^{3/2}} \\ &= 1.65 \times 10^{-9} \ln \Lambda / T_e^{3/2} \text{ ohm m, } T_e \text{ in keV,} \\ &= 2.8 \times 10^{-8} / T_e^{3/2} \text{ ohm m, } T_e \text{ in keV, } \ln \Lambda = 17.\end{aligned}\quad 2.16.2$$

The plasma resistivity is equal to that of copper for  $T_e \approx 1.4$  keV and is an order of magnitude less at the thermonuclear temperatures required in a tokamak. Numerical values of  $\eta$  from eqn 2.16.2 are given in Section 14.10.

Equation 2.16.2 is appropriate either in the absence of a magnetic field or for the component of current parallel to a magnetic field. In the direction perpendicular to a magnetic field the cyclotron motion makes the electron distribution function more isotropic. The resulting resistivity,  $\eta_{\perp}$ , is almost exactly twice  $\eta_{\parallel}$ . Thus

$$\eta_{\perp} = \frac{m_e}{n_e e^2 \tau_e} = 1.96 \eta_{\parallel}.$$

If the plasma is composed of several ion species, as it is in the case of hydrogen plasma with impurities, equation 2.16.1 becomes

$$Ee = m_e v_d \sum_j \frac{1}{\tau_{cj}}, \quad 2.16.3$$

where  $\tau_{cj}$  is the electron momentum transfer time through collisions with ion species  $j$ . From the requirements of charge neutrality the number of electrons is

$$n_e = \sum_j n_j Z_j$$

and so Ohm's law gives

$$E = \eta \sum_j n_j Z_j e v_d. \quad 2.16.4$$

Thus, combining eqns 2.16.3 and 2.16.4

$$\eta = \frac{m_e}{e^2} \frac{\sum_j \frac{1}{\tau_{cj}}}{\sum_j n_j Z_j}. \quad 2.16.5$$

Now from eqn 2.14.1 the momentum transfer times for species  $j$  is proportional to  $1/n_j Z_j^2$  and for a hydrogen plasma containing small amounts

of impurity equation 2.16.5 becomes

$$\eta = \eta_s \frac{\sum_j n_j Z_j^2}{\sum_j n_j Z_j}$$

where  $\eta_s$  is the resistivity of a pure hydrogen plasma. An effective  $Z$  can then be defined by

$$Z_{\text{eff}} = \frac{\sum_j n_j Z_j^2}{\sum_j n_j Z_j}$$

so that

$$\eta = Z_{\text{eff}} \eta_s \quad 2.16.6$$

with  $Z_{\text{eff}} = 1$  for a pure hydrogen plasma.

It should be noted that eqn 2.16.5 is an approximation based on the assumption that the higher charge states arise from small concentrations of impurity. For plasmas composed of a single species of charge  $Z$  there is a further weak  $Z$  dependence of the resistivity, the resistance being given by

$$\eta(Z) = N(Z) Z \eta(1)$$

with  $N = 0.85$  for  $Z = 2$  and  $N = 0.74$  for  $Z = 4$ .

A further modification arises when the magnetic geometry traps a fraction of the electrons so that they cannot carry a current in response to the electric field. If a fraction  $f$  is trapped the number of current carriers is reduced by a factor  $1 - f$  and the resistivity is increased by a factor  $\sim 1/(1 - f)$ . This is discussed further in Section 4.10.

## 2.17

### Runaway electrons

The resistivity formula given in eqn 2.16.1 is only valid if the relative drift velocity between the electron and ion species is much less than the electron thermal velocity. This is usually the case. For example a current density of  $1 \text{ MA m}^{-2}$  at an electron density of  $10^{20}$  has an electron drift velocity of  $6 \times 10^4 \text{ ms}^{-1}$  whereas the electron thermal velocity at a temperature of  $10 \text{ keV}$  is  $4 \times 10^7 \text{ ms}^{-1}$ , a ratio of  $\sim 10^{-3}$ . However, if the electric field is sufficiently high the approximations assumed in calculating the resistivity are invalid. Indeed the concept of resistivity fails. If the relative velocity between the electron and ion species exceeds the electron thermal velocity the collisional force between them decreases

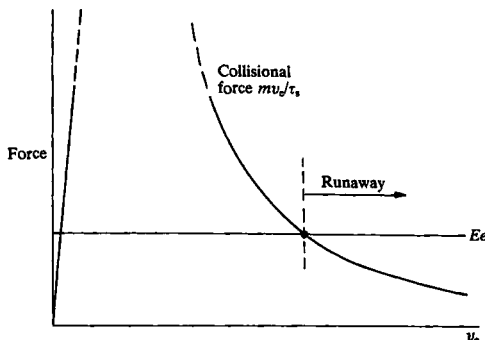


**Fig. 2.17.1** The electric field force,  $Ee$ , and the collisional force for an electron with a velocity  $v_e$ .

rather than increases with velocity. This is clearly an unstable situation and, if the electric field is maintained, the electrons run away.

Even with smaller electric fields such that  $v_d \ll v_{Te}$  for which the bulk of the electrons do not accelerate, it is possible for a smaller number of electrons in the tail of the velocity distribution to runaway.

The requirement for an electron to accelerate is that

$$Ee > \frac{mv_e}{\tau_s} \quad 2.17.1$$

where  $v_e$  is the velocity of the electron and  $\tau_s$  is its slowing down time given by eqn 2.14.1. For  $v_e \gg v_{Te}$ ,  $\tau_s \propto v_e^3$  and hence the collisional drag decreases with increasing velocity as  $1/v_e^2$ . A graph of the two terms in inequality 2.17.1 is shown in Fig. 2.17.1.

For  $v_e \gg v_{Te}$ , the electron slowing down time due to collisions with electrons is

$$\tau_{se} = \frac{4\pi\epsilon_0^2 m_e^2 v_e^3}{ne^4 \ln \Lambda}.$$

The slowing-down time for ion collisions,  $\tau_{si}$ , is a half of  $\tau_{se}$ . Since the drag is proportional to  $1/\tau_s$ , the total slowing-down time is given by

$$\tau_s^{-1} = \tau_{se}^{-1} + \tau_{si}^{-1},$$

and so

$$\tau_s = \frac{4\pi\epsilon_0^2 m_e^2 v_e^3}{3ne^4 \ln \Lambda}. \quad 2.17.2$$

## 2.17 Runaway electrons

Substitution of eqn 2.17.2 into inequality 2.17.1 gives the critical velocity,  $v_c$ , above which runaway would occur

$$\begin{aligned} v_c^2 &= \frac{3ne^3 \ln \Lambda}{4\pi \epsilon_0^2 m_e E} \\ &= 2.3 \times 10^{-4} \frac{n}{E} \text{ m}^2 \text{ s}^{-2}, \quad \ln \Lambda = 17 \end{aligned} \quad 2.17.3$$

This corresponds to a critical energy

$$E_c = 6.6 \times 10^{-19} \frac{n}{E} \text{ keV}.$$

This picture of electron runaway is oversimplified. It gives the velocity above which electrons would run away at the sudden application of an electric field. However, on a longer timescale, the rate of electron runaway is determined by collisional diffusion in velocity space. As the faster electrons runaway they are replaced by electrons diffusing through the tail of the velocity distribution. Detailed calculations give the resulting runaway rate per unit volume

$$R = \frac{2}{\sqrt{\pi}} \frac{n}{v_{te}} \left( \frac{E}{E_D} \right)^{1/2} \exp \left[ -\frac{E_D}{4E} - \left( \frac{2E_D}{E} \right)^{1/2} \right]$$

where the Drieger electric field,  $E_D$ , is given by

$$E_D = \frac{ne^3 \ln \Lambda}{4\pi \epsilon_0^2 m_e v_{te}^2}.$$

When the electric field is sufficiently small the critical velocity calculated from eqn 2.17.3 approaches the velocity of light. The equation is then no longer valid. For relativistic electrons the slowing down time is almost constant and the essential reduction of drag with increased momentum no longer occurs. Thus the runaway process does not occur for electric fields such that

$$E < \frac{ne^3 \ln \Lambda}{4\pi \epsilon_0^2 m_e c^2}.$$

Another process which can put electrons into the runaway region of velocity space arises from close collisions between already existing runaway electrons and the thermal electrons. Although test particles in a plasma are mainly affected by the sum of large impact parameter collisions with small momentum transfer, the smaller number of close collisions which transfer larger momentum are more important in this process. The relevant close collisions in this case are those which lift a slow electron above the critical velocity for runaway.

The momentum transferred to the slow electron by a fast electron is principally perpendicular to the velocity,  $v_f$ , of the fast electron and is given by

$$m_e \Delta v \approx 2m_e v_f \frac{r_0}{r}$$

where  $r$  is the impact parameter and  $r_0 (= e^2 / 4\pi\epsilon_0 m_e v_f^2)$  is its value for a 90° scatter. For the collision to transfer the electron to the runaway region,  $\Delta v$  must be greater than the critical velocity given by eqn 2.17.3, that is  $\Delta v > v_c$ . This requirement gives a cross-section for runaway production

$$\pi r^2 = \frac{Ee}{3nm_e v_f^2 \ln \Lambda}. \quad 2.17.4$$

Taking the fast electrons of the already existing population of runaway electrons to be relativistic, the rate of production of new runaway electrons by close collisions is  $R_f = n\pi r^2 c$ , that is, using eqn 2.17.4

$$R_f = \frac{1}{3} \ln \Lambda \frac{Ee}{m_e c}.$$

Thus, since  $m_e c / Ee$  is the time,  $\tau_0$ , taken for an already existing runaway electron to gain a rest mass energy,  $m_e c^2$ , from the electric field, the average time,  $\tau_r$ , for a relativistic electron to produce a new runaway electron may be written

$$\tau_r = 3 \ln \Lambda \tau_0.$$

During this time the fast electron would increase its energy by an amount  $Eec\tau_r$ , that is

$$\Delta E_f = 3 \ln \Lambda (m_0 c^2),$$

and so a new runaway electron is produced each time an existing runaway increases its energy by this amount. For a constant electric field this process leads to an exponential growth in the runaway electron current with an e-folding time  $\tau_r$ .

## 2.18

### Electromagnetism

The fundamental equations relating the electric and magnetic fields  $E$  and  $B$  are Maxwell's equations

$$\nabla \times B = \mu_0 j + \frac{1}{c^2} \frac{\partial E}{\partial t} \quad 2.18.1$$

$$\nabla \times E = - \frac{\partial B}{\partial t} \quad 2.18.2$$

with

$$\nabla \cdot \mathbf{B} = 0$$

2.18.3

and

$$\nabla \cdot \mathbf{E} = \frac{\rho_c}{\epsilon_0} \quad 2.18.4$$

where  $j$  is the electric current density,  $\rho_c$  is the electric charge density, and

$$\mu_0 = 4\pi \times 10^{-7} \text{ henry m}^{-1},$$

$$\epsilon_0 = 1/\mu_0 c^2 = 8.854 \times 10^{-12} \text{ farad m}^{-1},$$

$$c = 2.998 \times 10^8 \text{ m s}^{-1}.$$

In magnetic and dielectric media it is convenient to separate the atomic and polarization currents from  $j$  and write eqn 2.18.1 in the form

$$\nabla \times \mathbf{H} = j_m + \frac{\partial \mathbf{D}}{\partial t}$$

where  $j_m$  represents the macroscopic currents and, in uniform and isotropic media,

$$\mathbf{B} = \mu \mathbf{H} \quad \mathbf{D} = \epsilon \mathbf{E}$$

where  $\mu$  is the permeability and  $\epsilon$  the dielectric constant.

In a plasma, eqn 2.18.1 is appropriate but when describing linear waves the dielectric tensor  $K$  is defined to include the effect of the oscillating part,  $\tilde{j}$ , of the current-density so that

$$\tilde{j} + \epsilon_0 \frac{\partial \mathbf{E}}{\partial t} = \epsilon_0 K \frac{\partial \mathbf{E}}{\partial t}.$$

Since  $\nabla \cdot \mathbf{B} = 0$ ,  $\mathbf{B}$  can be written

$$\mathbf{B} = \nabla \times \mathbf{A} \quad 2.18.5$$

where  $\mathbf{A}$  is the vector potential. Substitution of eqn 2.18.5 into eqn 2.18.2 gives

$$\nabla \times \left( \mathbf{E} + \frac{\partial \mathbf{A}}{\partial t} \right) = 0.$$

Thus the quantity in brackets may be expressed as the gradient of a scalar potential so that

$$\mathbf{E} = -\nabla \phi - \frac{\partial \mathbf{A}}{\partial t}.$$

2.18.6

The potentials  $A$  and  $\phi$  are not uniquely defined since it is possible to make a gauge transformation

$$A' = A + \nabla f, \quad \phi' = \phi - \frac{\partial f}{\partial t},$$

which leaves the fields  $E$  and  $B$ , calculated from eqns 2.18.5 and 2.18.6, unchanged.

The electromagnetic energy density,  $\mathcal{E}$ , is given by

$$\mathcal{E} = \epsilon_0 \frac{E^2}{2} + \frac{1}{\mu_0} \frac{B^2}{2}.$$

Using eqns 2.18.1 and 2.18.2 it is found that the time rate of change of  $\mathcal{E}$  is given by

$$\frac{\partial \mathcal{E}}{\partial t} = -\nabla \cdot \left( \frac{E \times B}{\mu_0} \right) - E \cdot j.$$

The term  $E \cdot j$  represents the transfer of energy to the charged particles. The first term is the divergence of the flow of electromagnetic energy, this flow being given by the Poynting vector

$$S = \frac{E \times B}{\mu_0}.$$

For static fields the curl of eqn 2.18.5, together with eqn 2.18.1 and the choice of the gauge  $\nabla \cdot A = 0$ , gives

$$\nabla^2 A = -\mu_0 j$$

and the divergence of eqn 2.18.6 together with eqn 2.18.4 gives

$$\nabla^2 \phi = -\frac{\rho_0}{\epsilon_0}.$$

## 2.19

### Fluid equations

The kinetic equations describe the plasma in terms of the distribution function  $f(x, v, t)$  which is a function of seven variables. For many purposes it is adequate to describe the plasma in terms of fluid variables such as the particle density  $n(x, t)$ , fluid velocity  $v(x, t)$ , and pressure  $p(x, t)$  which are functions of only four variables. The required equations are derived for each species of particle from the kinetic eqn 2.9.4

$$\frac{\partial f}{\partial t} + v' \cdot \frac{\partial f}{\partial x} + \frac{F}{m} \cdot \frac{\partial f}{\partial v'} = \left( \frac{\partial f}{\partial t} \right)_c \quad 2.19.1$$

where  $F$  is the force on the particle, the symbol  $v'$  now being used to distinguish the particle velocity from the fluid velocity  $v$ . Equation 2.19.1

is multiplied by chosen functions  $\phi(v')$  and integrated over velocity space to obtain equations for

$$\begin{aligned} n &= \int f(x, v', t) dv', \\ v &= \frac{1}{n} \int f(x, v', t) v' dv', \\ P &= m \int f(x, v', t) (v' - v)(v' - v) dv', \end{aligned}$$

where  $P$  is the pressure tensor. For an isotropic distribution function the pressure is scalar and is given by

$$p = \frac{1}{3} m \int f(x, v', t) (v' - v)^2 dv'.$$

Thus the  $\phi = 1$  moment of eqn 2.12.1 gives

$$\frac{\partial n}{\partial t} + \frac{\partial}{\partial x} \int v' f dv' - \frac{1}{m} \int \frac{\partial F}{\partial v'} f dv' = 0 \quad 2.19.2$$

where the third term has been integrated by parts and, considering only collisions which do not change the number of particles, the integral over the collision term is zero. Since  $\partial F / \partial v'$  is zero for electromagnetic forces eqn 2.19.2 gives the *continuity equation*

$$\frac{\partial n}{\partial t} + \nabla \cdot (nv) = 0. \quad 2.19.3$$

The momentum equation is obtained by taking the  $mv'$  moment of eqn 2.19.1 to obtain

$$m \frac{\partial}{\partial t} (nv) + m \frac{\partial}{\partial x} \int v' v' f dv' - \int \frac{\partial}{\partial v'} (F(v') v') f dv' = \int mv' \left( \frac{\partial f}{\partial t} \right) dv' \quad 2.19.4$$

where again the third term has been integrated by parts. The collision term represents the rate of change of momentum  $R$  due to collisions with all other species. Thus eqn 2.19.4 becomes

$$m \frac{\partial}{\partial t} (nv) + m \frac{\partial}{\partial x} \int v' v' f dv' - nF(v) = R.$$

This equation may now be put in a more convenient form by writing  $v' = (v' - v) + v$  to obtain

$$m \frac{\partial}{\partial t} (nv) + \nabla \cdot P + m \nabla \cdot (nv v) - nF = R.$$

Then eliminating  $\partial n / \partial t$  using the continuity eqn 2.19.3 gives the *equation of motion*

$$nm \left( \frac{\partial v}{\partial t} + v \cdot \nabla v \right) = -\nabla \cdot P + nF + R. \quad 2.19.5$$

In a plasma the force on a particle is  $\mathbf{F} = Ze(\mathbf{E} + \mathbf{v} \times \mathbf{B})$ , where  $Ze$  is the particle charge, and eqn 2.19.5 therefore becomes

$$nm \left( \frac{\partial \mathbf{v}}{\partial t} + \mathbf{v} \cdot \nabla \mathbf{v} \right) = -\nabla \cdot \mathbf{P} + nZe(\mathbf{E} + \mathbf{v} \times \mathbf{B}) + \mathbf{R}. \quad 2.19.6$$

It is seen from the above procedure that the equation for the time dependence of the zeroth moment,  $n$ , introduces the first moment  $\mathbf{v}$ , and that the equation for the time dependence of  $\mathbf{v}$  introduces the second moment  $\mathbf{P}$ . In calculating the equation for  $\mathbf{P}$  the third moment is introduced and so on. This procedure does not therefore lead to a closed set of equations. Closure is usually achieved by making simplifying assumptions in the equation for  $\mathbf{P}$ . For example it is often assumed that the motion is adiabatic or that the third moment, the heat flux vector, may be calculated using a simple form of thermal conduction.

The formal validity of the fluid equations rests on the behaviour being sufficiently localized. This is achieved if the mean free path of the particles is sufficiently small compared to the macroscopic lengths under consideration. At high temperatures the mean free path is long and this justification of the equations fails. For motion perpendicular to the magnetic field the Larmor radius can provide the necessary localization. The fluid equations will also fail when the scale length under consideration is so small that it is comparable with the Larmor radius of the particles.

## 2.20 Magnetohydrodynamics

Magnetohydrodynamics, or mhd, is the name given to the single fluid description of the plasma. In this model the separate identities of the ions and electrons do not appear.

The equation of mass conservation is

$$\frac{\partial \rho}{\partial t} = -\nabla \cdot (\rho \mathbf{v}) \quad 2.20.1(a)$$

or

$$\frac{d\rho}{dt} = -\rho \nabla \cdot \mathbf{v} \quad 2.20.1(b)$$

where  $\rho$  is the mass density,  $\mathbf{v}$  the fluid velocity, and  $d/dt$  is the derivative  $(\partial/\partial t + \mathbf{v} \cdot \nabla)$ . Sometimes the fluid is taken to be incompressible in which case  $d\rho/dt = 0$  and  $\nabla \cdot \mathbf{v} = 0$ .

The rate of change of velocity is given by the equation of motion

$$\rho \left( \frac{\partial \mathbf{v}}{\partial t} + \mathbf{v} \cdot \nabla \mathbf{v} \right) = \mathbf{j} \times \mathbf{B} - \nabla p. \quad 2.20.2$$

In order to calculate the pressure gradient force an equation for  $p$  is required. The simple non-dissipative model usually used assumes

adiabatic behaviour, that is

$$\frac{d}{dt}(p\rho^{-\gamma}) = 0 \quad 2.20.3$$

implying conservation of entropy. If the density is eliminated using eqn 2.20.1 then eqn 2.20.3 becomes

$$\frac{\partial p}{\partial t} = -\mathbf{v} \cdot \nabla p - \gamma p \nabla \cdot \mathbf{v} \quad 2.20.4(a)$$

or

$$\frac{dp}{dt} = -\gamma p \nabla \cdot \mathbf{v}. \quad 2.20.4(b)$$

If the fluid is taken to be incompressible,  $\nabla \cdot \mathbf{v}$  is then zero. However,  $\gamma p \nabla \cdot \mathbf{v}$  is not zero, incompressibility corresponding to the limit  $\gamma \rightarrow \infty$ . The appropriate procedure in this case is to eliminate  $p$  from eqn 2.20.2 by taking the curl of the equation and to use the separate equations  $d\rho/dt = 0$  and  $\nabla \cdot \mathbf{v} = 0$  arising from the continuity equation.

The coupling to the magnetic field arises through the force  $\mathbf{j} \times \mathbf{B}$ . In the mhd model the displacement current in Maxwell's equation is neglected and the current density is therefore given by Ampère's law

$$\mu_0 \mathbf{j} = \nabla \times \mathbf{B}. \quad 2.20.5$$

The rate of change of  $\mathbf{B}$  is given by the induction equation

$$\frac{\partial \mathbf{B}}{\partial t} = -\nabla \times \mathbf{E}. \quad 2.20.6$$

It is now necessary to determine  $\mathbf{E}$  in terms of the other variables. In the model of ideal mhd the plasma is taken to be perfectly conducting. Thus in the local frame of the moving fluid no electric field can be sustained, and consequently

$$\mathbf{E} + \mathbf{v} \times \mathbf{B} = 0. \quad 2.20.7$$

Equations 2.20.1 to 2.20.7, which are summarized in Table 2.20.1, together with  $\nabla \cdot \mathbf{B} = 0$ , constitute the ideal mhd model. A simple modification of these equations leads to the model of resistive mhd. It is only necessary to replace eqn 2.20.7 by Ohm's law

$$\mathbf{E} + \mathbf{v} \times \mathbf{B} = \eta \mathbf{j} \quad 2.20.8$$

and the adiabatic equation by

$$\frac{d}{dt} \left( \frac{p}{\gamma - 1} \right) = -\frac{\gamma}{\gamma - 1} p \nabla \cdot \mathbf{v} + \eta j^2$$

where  $\eta$  is the resistivity of the plasma.

**Table 2.20.1** The equations of ideal mhd.

$\frac{dp}{dt} = -\rho \nabla \cdot v$	$j = \nabla \times B / \mu_0$
$\rho \frac{dv}{dt} = j \times B - \nabla p$	$\frac{\partial B}{\partial t} = -\nabla \times E$
$\frac{dp}{dt} = -\gamma p \nabla \cdot v$	$E + v \times B = 0$

## 2.21

### Physics of plasma fluid

The behaviour of plasma in experiments is usually complicated, and influenced by the particular circumstances of the experiment. However the fluid equations presented in the previous sections give rise to a number of more basic questions. Since the physics involved provides an insight into the properties of plasma some of these matters are discussed below.

#### Fluid velocity

The fluid velocity of a constituent species of a plasma at a given point is simply the mean velocity of the particles of that species in a small volume around that point. However, as described in Section 2.6 the gyro-averaged velocity of particles is the velocity of their guiding centres. Generally the fluid velocity and the velocity of guiding centres at a given point are not the same. For example in a non-uniform plasma in which the ion guiding centres are stationary there will be a finite ion fluid velocity. The relation between these velocities is exemplified in the phenomenon of plasma diamagnetism which is described in Section 2.22.

#### Pressure balance

In a steady plasma with a scalar pressure the force balance for each species is

$$n_j e_j (E + v_j \times B) = \nabla p_j. \quad 2.21.1$$

In the frame for which the velocity of a given species is zero the pressure gradient is balanced by the electric field force, that is

$$n_j e_j E = \nabla p_j.$$

Alternatively, in the frame in which  $E = 0$

$$n_j e_j v_j \times B = \nabla p_j.$$

This freedom of description is removed when the complete plasma is considered. Thus summing eqn 2.21.1 over the species

$$E \sum_j n_j e_j + \sum_j n_j e_j v_j \times B = \nabla p. \quad 2.21.2$$

Since the plasma is almost charge neutral the first term in eqn 2.21.2 is negligible and the equation becomes

$$j \times B = \nabla p. \quad 2.21.3$$

Using Ampère's law for  $j$  in eqn 2.21.3

$$\frac{1}{\mu_0} (\nabla \times B) \times B = \nabla p \quad 2.21.4$$

and using the vector relation

$$(\nabla \times B) \times B = B \nabla B - \nabla B^2 / 2$$

eqn 2.21.4 becomes

$$\nabla p = -\nabla \frac{B^2}{2\mu_0} + \frac{1}{\mu_0} B \cdot \nabla B. \quad 2.21.5$$

The last term in eqn 2.21.5 is the result of field line curvature,  $B \cdot \nabla B$  being along the radius of curvature, and the radius being given by  $R_c^{-1} = |b \cdot \nabla b|$ , where  $b$  is the unit vector along  $B$ . If the magnetic field lines are straight the magnetic field gives a scalar pressure  $B^2/2\mu_0$  and

$$p + \frac{B^2}{2\mu_0} = \text{constant}.$$

### Pressure tensor

The force arising from the pressure tensor  $P$  in eqn 2.19.5 is

$$F_\alpha = - \sum_\beta \frac{d}{dx_\beta} P_{\alpha\beta}.$$

When  $P$  has an isotropic pressure component, it can be written

$$P_{\alpha\beta} = p \delta_{\alpha\beta} + \Pi_{\alpha\beta}$$

$p$  being the scalar pressure. The term  $\Pi_{\alpha\beta}$  results from plasma velocities and can often be written as a linear function of the velocity gradients. When this is the case the term stress tensor is used for both  $P_{\alpha\beta}$  and  $\Pi_{\alpha\beta}$ . It will here be reserved for  $\Pi_{\alpha\beta}$ .

In a normal fluid the linear velocity gradient terms in  $\Pi_{\alpha\beta}$  arise from viscosity and the resulting tensor is called the viscosity stress tensor. For a

plasma in a magnetic field the corresponding tensor is more complicated and includes non-viscous effects. For velocities and gradients along the magnetic field the normal collisional viscous effect occurs, the viscosity being dependent on, and increasing with the mean free path. However, for velocity gradients perpendicular to the magnetic field the momentum transfer is limited by the Larmor orbits and, the effect of the velocity gradients is much reduced. The full pressure tensor for a collisional plasma is given in Section 2.23.

Sometimes the pressure is anisotropic as a result of the magnetic field. Writing  $p_{\parallel}$  and  $p_{\perp}$  for the pressures parallel and perpendicular to the magnetic field the force  $\nabla p$  is replaced by

$$\nabla_{\perp} p_{\perp} + \nabla_{\parallel} p_{\parallel}$$

where  $\nabla_{\parallel}$  and  $\nabla_{\perp}$  are the gradients parallel and perpendicular to the magnetic field.

#### 'Frozen in' magnetic field

In a perfectly conducting fluid the electric field in a frame moving with the fluid velocity,  $v$ , is zero, that is

$$\mathbf{E} + \mathbf{v} \times \mathbf{B} = 0$$

2.21.6

It will be shown below that the magnetic flux through each surface moving with the fluid is constant and consequently that the magnetic flux can be thought of as frozen-in to the fluid and moving with it. Thus although at each point there is a fluid velocity  $v$  and the term  $v \times B$  exists, it is also true that eqn 2.21.6 implies the convection of the magnetic flux with the fluid.

Consider an arbitrary bounded surface  $S$  in the fluid. The magnetic flux through this surface is

$$\Phi = \int \mathbf{B} \cdot d\mathbf{S}.$$

The time derivative moving with the fluid is

$$\frac{d\Phi}{dt} = \int \frac{\partial \mathbf{B}}{\partial t} \cdot d\mathbf{S} + \oint \mathbf{B} \cdot \mathbf{v} \times d\mathbf{s},$$
2.21.7

where the second term describes the change of flux across the surface boundary as the local magnetic field is swept by the line element  $d\mathbf{s}$  at a rate  $\mathbf{v} \times d\mathbf{s}$ .

From Stokes' theorem

$$\oint \mathbf{B} \cdot \mathbf{v} \, d\mathbf{s} = - \int \nabla \times (\mathbf{v} \times \mathbf{B}) \cdot d\mathbf{S}$$

and using Faraday's law,  $\partial \mathbf{B} / \partial t = - \nabla \times \mathbf{E}$ , eqn 2.21.7 becomes

$$\frac{d\Phi}{dt} = - \int \nabla \times (\mathbf{E} + \mathbf{v} \times \mathbf{B}) \cdot d\mathbf{S}$$

Thus, since  $\mathbf{E} + \mathbf{v} \times \mathbf{B} = 0$

$$\frac{d\Phi}{dt} = 0$$

and the magnetic flux through every surface moving with the plasma is constant.

### Polarization

Consider a perfectly conducting fluid in a magnetic field to which an electric field,  $\mathbf{E}(t)$ , is applied perpendicular to the magnetic field. Since  $\mathbf{E} + \mathbf{v} \times \mathbf{B} = 0$  the fluid will move with a velocity

$$v = \frac{E}{B}. \quad 2.21.8$$

This velocity is produced by a current  $j$  in the direction of  $\mathbf{E}$ , through the force  $j \times \mathbf{B}$ . Thus substituting eqn 2.21.8 into the equation of motion

$$\rho \frac{dv}{dt} = j \times \mathbf{B}$$

gives

$$j = \frac{\rho}{B^2} \frac{dE}{dt}. \quad 2.21.9$$

Equation 2.21.9 shows that a polarization current flows and that the fluid has a dielectric constant

$$K = 1 + \frac{c^2}{B^2/\mu_0\rho},$$

where  $c$  is the velocity of light. The velocity  $B/(\mu_0\rho)^{1/2}$  is the velocity characterizing Alfvén waves which are discussed in Section 2.24.

## 2.22

### Plasma diamagnetism

In the early investigations of the magnetic properties of solids it was found that rods of some substances aligned themselves to the magnetic

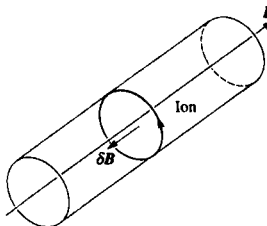


**Fig. 2.22.1** Ions with a given velocity having Larmor orbits on a cylinder produce a magnetic field  $\delta B$  inside the cylinder, this field being in the opposite direction to the total magnetic field  $B$ .

field. These were called paramagnetic. Rods of other substances aligned themselves across the magnetic field and were therefore called diamagnetic. The cause of this behaviour is that in paramagnetic substances the response of the material is to enhance the applied magnetic field whereas in diamagnetic substances the field is diminished.

Plasmas in magnetic fields are naturally diamagnetic, the gyro-orbits of the charged particles being such as to reduce the field. This is easily seen by considering the orbits of particles with a given velocity perpendicular to the magnetic field with the centres of their Larmor orbits on a particular field line as illustrated in Fig. 2.22.1. The figure shows the behaviour of ions. Electron gyrate in the opposite direction but carry a negative current.

The particles lie on a cylinder and each contributes a current  $e_j \omega_{cj} / 2\pi$ . If there are  $\delta n$  particles per unit length, their orbits produce a cylindrical current per unit length

$$\delta i = -\frac{e_j \omega_{cj}}{2\pi} \delta n$$

and using  $\omega_{cj} = e_j B / m_j$ ,

$$\delta i = -\frac{e_j^2}{2\pi m_j} \delta n B.$$

The minus sign indicates that the current is in the opposite direction to that producing the main field  $B$ . From Ampère's law the magnetic field resulting from this current is  $\delta B = \mu_0 \delta i$ , so that

$$\delta B = -\frac{\mu_0 e_j^2}{2\pi m_j} \delta n B,$$

and  $\delta B$  is independent of the sign of the charge as expected.

Considering now the more general case with a distribution of particle velocities, let the magnetic field be in the  $z$  direction and consider those particles with velocity  $v_\perp$  perpendicular to the magnetic field. These particles contribute to the magnetic field at a given point if their orbit centre lies within a Larmor radius,  $v_\perp / \omega_{cj}$ , of that point. The sum of the currents of such particles in a velocity space element  $d^3 v$  gives a current per unit length

$$\begin{aligned} di &= -\pi \left( \frac{v_\perp}{\omega_{cj}} \right)^2 e_j \frac{\omega_{cj}}{2\pi} f_j d^3 v \\ &= -\frac{e_j}{2\omega_{cj}} v_\perp^2 f_j d^3 v \end{aligned}$$

where  $f_j$  is the distribution function. The resulting magnetic field is

$$dB_{sj} = -\frac{\mu_0 m_j}{2B} v_\perp^2 f_j d^3 v$$

2.22.1

and integrating over the velocity distribution

$$\begin{aligned} B_{ij} &= -\frac{\mu_0}{B} \int \frac{1}{3} m_j v_{\perp}^2 f_j d^3 v \\ &= -\frac{\mu_0 p_j}{B} \end{aligned} \quad 2.22.2$$

where  $p_j$  is the particle pressure.

It is seen that the circular orbits of particles of species  $j$  produce a field  $B_{ij}$  in the opposite direction to the applied field, and the full field  $B_s$  is obtained by summing over the species  $j$  to obtain the diamagnetic field

$$B_s = -\frac{\mu_0 p}{B} \quad 2.22.3$$

where  $p$  is the plasma pressure. This result is a low  $\beta$  approximation. If the applied magnetic field is  $B_0$  and the exact diamagnetic field is  $B_d$ , the pressure balance equation

$$\frac{(B_0 + B_d)^2}{2\mu_0} + p = \frac{B_0^2}{2\mu_0}$$

gives the full equation for  $B_d$

$$B_d \left( 1 - \frac{1}{2} \frac{B_d}{B_0} \right) = -\frac{\mu_0 p}{B_0}. \quad 2.22.4$$

In the low- $\beta$  approximation,  $p \ll B_0^2/2\mu_0$ , the term involving  $B_d^2$  is small and  $B_d \approx B_0$ .

The full pressure balance is obtained by recognizing that the gradient in the magnetic field leads to a drift of the particle orbits and the resulting current produces a further magnetic field. The current associated with the magnetic field  $B_s$  arising from the stationary orbits is obtained by applying Ampère's law, with the present geometry, to eqn 2.22.3

$$j_s = b \times \nabla \left( \frac{p}{B} \right).$$

where  $b$  is the unit vector along  $B$ . From the force balance equation  $\vec{j} \times \vec{B} = \nabla p$  and the total current is

$$j = b \times \frac{\nabla p}{B},$$

and so the residual current is

$$j - j_s = b \times \frac{p}{B^2} \nabla \cdot B. \quad 2.22.5$$

That this is equal to the current,  $j_d$ , caused by the magnetic field gradient drift is seen by writing

$$j_d = \sum_j n_j e_j \langle v_{dj} \rangle \quad 2.22.6$$

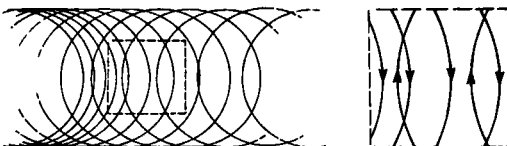


**Fig. 2.22.2** Showing how a density gradient of stationary orbits give rise to a current. The current arises through a local imbalance of upward and downward moving particles as illustrated in the enlarged section.

where  $v_{dj}$  is the drift velocity given by eqn 2.6.6 with  $\rho_j = m_j v_{\perp j} / e_j B$  and  $(v_{\perp j}^2) = 2v_{Tj}^2$  so that

$$\langle v_{dj} \rangle = \frac{m_j v_{Tj}^2}{e_j B^2} \mathbf{b} \times \nabla B$$

and, since  $n_j m_j v_{Tj}^2 = p_j$ , the drift current given by eqn 2.22.6 is

$$\mathbf{j}_d = \mathbf{b} \times \frac{p}{B^2} \nabla B. \quad 2.22.7$$

Thus eqns 2.22.5 and 2.22.7 give the required result

$$\mathbf{j} = \mathbf{j}_s + \mathbf{j}_d$$

showing that the total diamagnetic current is the sum of the current due to the circular orbits and that due to their drift. The primary diamagnetic effect arising from the magnetic field of circular orbits is at first sight surprising since the orbit is stationary and its averaged current is zero. For a uniform plasma the diamagnetically induced magnetic field given by eqn 2.22.2 is constant and the diamagnetic current inside the plasma is indeed zero. However, there has to be a gradient in plasma pressure between such a region and the surrounding vacuum magnetic field and it is this gradient which provides the necessary current from stationary orbits. This is illustrated in Fig. 2.22.2 for the case with a density gradient only. With a temperature gradient the imbalance of neighbouring orbits arises from their different orbital velocities.

The discussion in this section is restricted to the case of straight magnetic field lines but illustrates the care required in keeping a clear distinction between the guiding centre motion of individual particles and the current which they contribute at a given point in space. The two descriptions of the plasma must of course always be consistent but in more complicated geometries the relationship is quite complex.

## 2.23

### Braginskii equations

The fluid equations for a plasma are derived by taking moments of the kinetic equation as described in Section 2.19. However these equations contain quantities which are undetermined. The required quantities are the rate of change of momentum due to collisions, the pressure tensor, the heat flux and the heat generated as a result of collisions. In order to determine these quantities it is necessary to solve the kinetic equation 2.19.1 with the collision term given by the Fokker-Planck equation as given in eqn 2.12.5 or 2.12.6. A complete solution of these equations is not possible. However, if the microscopic variables are taken to vary slowly in space and time, an expansion procedure allows the required quantities to be calculated. Such calculations have been carried out by a number of workers, but Braginskii has given a clear and comprehensive presentation and the resulting equations are often given his name.

The underlying idea is that the distribution functions can be expanded about a Maxwellian distribution. That is

$$f = f_0 + \delta f$$

with

$$f_0 = \frac{n_j}{(2\pi T_j/m_j)^{3/2}} \exp - \left( \frac{m_j}{2T_j} (v' - v)^2 \right).$$

where  $v'$  is the velocity coordinate and  $v$  is the mean velocity of the particles. In a uniform plasma, in which the species are stationary and have the same temperature, the distribution function is Maxwellian and the collision term in the kinetic equation is zero. If small gradients and drift velocities are now introduced the change,  $\delta f$ , in the distribution function makes the collision term in the kinetic equation non-zero. The procedure is to solve the resulting kinetic equation and determine the collisional response to the gradients and drifts. This provides formulas for the collisional drag, viscosity and thermal conduction and closes the set of fluid equation. The unknown fluid variables, including the pressure tensor and heat flux, can then be determined by solving these equations.

The form of the transport coefficients can be partly anticipated. For example the thermal conductivity parallel to the magnetic field is related to the mean free path,  $\lambda$ , and the collision time,  $\tau$ , by the usual random walk relation, giving the familiar result

$$K_{\parallel} \sim n \frac{\lambda^2}{\tau} \sim n v_T^2 \tau \sim \frac{n T \tau}{m}.$$

For conduction perpendicular to the magnetic field the step-length becomes the Larmor radius and

$$K_{\perp} \sim n \frac{\rho^2}{\tau} \sim \frac{1}{\omega_c^2 \tau^2} \frac{n T \tau}{m},$$

the thermal conductivity being reduced by the usually very large factor  $\omega_c^2 \tau^2$ .

The formal calculations determine the precise numerical coefficients and also introduce a number of less familiar physical transport processes. These calculations are quite complex and will not be described here. The equations of continuity, momentum balance and energy balance will be introduced separately with some discussion of the underlying physics.

The equations given are derived on the assumption that the plasma is sufficiently collisional that the mean free path is short compared to the macroscopic lengths involved. The transport coefficients given are for a singly charged species ( $n_i = n_e = n$ ) and for  $\omega_{ce} \tau_e$  and  $\omega_{ci} \tau_i$  much greater than one. The basic electron and ion collision times which appear in the transport coefficients are defined in Section 2.15.

### Continuity equation

The continuity equation for species  $j$ , electrons or ions, is

$$\frac{dn_j}{dt} = -n_j \nabla \cdot v_j \quad 2.23.1$$

where the total derivative

$$\frac{d}{dt} = \frac{\partial}{\partial t} + v_j \cdot \nabla.$$

Thus, moving with the fluid, density changes arise from compressibility. For incompressible motion  $\nabla \cdot v_j$  and  $d n_j / d t = 0$ . Equation 2.23.1 can alternatively be written

$$\frac{\partial n_j}{\partial t} = -\nabla \cdot (n v_j)$$

expressing the density change at a stationary point as the divergence of the particle flux  $\Gamma_j = n v_j$ .

There is no collision time in eqn 2.23.1 because, unlike say ionization collisions, Coulomb collisions do not change the number of particles.

### Momentum equation

The momentum balance equation is

$$n_j m_j \frac{dv_j}{dt} = -\nabla p_j - \frac{\partial}{\partial x_\beta} \Pi_{j\alpha\beta} + n_j e_j (\mathbf{E} + v_j \times \mathbf{B}) + \mathbf{R}_j \quad 2.23.2$$

where the pressure  $p_j = n_j T_j$  and repeated Greek indices imply summation over the repeated index. The stress tensor  $\Pi_{j\alpha\beta}$  is complicated and

will be given below.  $R_e$  is the rate of momentum transfer due to collisions. The total momentum change in collisions is zero and so,  $\sum_i R_i = -R_e$ . The rate of momentum transfer from ions to electrons is given by

$$R_e = R_u + R_T,$$

$R_u$  being the friction force and  $R_T$  the so-called thermal force.

The *friction force* is

$$R_u = -\frac{m_e n}{\tau_e} (0.51 u_{||} + u_{\perp}) = n e (\eta_{||} j_{||} + \eta_{\perp} j_{\perp})$$

where

$$\mathbf{u} = \mathbf{v}_e - \mathbf{v}_i,$$

$\eta$  is the electrical resistivity, and the subscripts  $||$  and  $\perp$  refer to the directions parallel and perpendicular to the magnetic field. This force constitutes the resistivity which was discussed in Section 2.16.

The *thermal force* is

$$R_T = -0.71 n \nabla_{||} T_e - \frac{3}{2} \frac{n}{|\omega_{ce}| \tau_e} \mathbf{b} \times \nabla T_e, \quad 2.23.3$$

$\mathbf{b}$  being the unit vector parallel to the magnetic field. Although the first term does not involve the collision time it is nevertheless a result of collisions. Consider the ions lying in a sheet perpendicular to the magnetic field. Electrons passing through this sheet in the direction of the electron temperature gradient lose momentum at a rate,  $v_e n_e m_e \bar{v}_e$  where  $v_e$  is the collision frequency. Electrons travelling in the opposite direction lose momentum of opposite sign. However, although the fluxes  $n \bar{v}_e$  will be equal, the values of  $v_e$  will be different. The electrons coming from each side will have a collision frequency characteristic of the temperature at their point of origin, that is the position of their last collision a mean free path away. The rate of momentum loss is therefore

$$R_{T||} \sim \Delta v_e n_e m_e \bar{v}_e \quad 2.23.4$$

where  $\Delta v_e$ , the difference in  $v_e$  on the two sides, is given by

$$\Delta v_e \sim \lambda |\nabla_{||} v_e| \quad 2.23.5$$

where  $\lambda$  is the mean free path. Now  $v_e = \tau_e^{-1} \propto T_e^{-3/2}$  and so

$$\nabla_{||} v_e \sim \frac{dv_e}{dT_e} \nabla_{||} T_e \sim -\frac{v_e}{T_e} \nabla_{||} T_e. \quad 2.23.6$$

Using  $\lambda = v_{Te}/v_e$ , eqns 2.23.5 and 2.23.6 give

$$\Delta v_e \sim \frac{v_{Te}}{T_e} |\nabla_{||} T_e|. \quad 2.23.7$$

Since the velocity  $\bar{v}_e \sim v_{Te}$  and  $v_{Te}^2 = T_e/m_e$ , the form of the thermal force on the electrons, given by relations 2.23.4 and 2.23.7 is

$$R_{T\parallel} \sim -n_e \nabla_{\parallel} T_e.$$

The sign of the force on the electrons is clearly in the direction of  $-\nabla_{\parallel} T_e$  because the electrons from the colder side are more collisional and are therefore subject to the larger force.

The absence of the collision time in the expression for  $R_{T\parallel}$  arises from the fact that, although less momentum is transferred by electrons if they have a longer collision time, the *difference* in collision time between the two sides is proportional to the mean free path and this itself is proportional to the collision time. Thus the effects cancel.

The thermal force on the ions is equal and opposite to that on the electrons, the colder electrons transferring more momentum than the hot ones and hence producing a force in the direction of  $\nabla T_e$ . In a steady state the thermal force on the electrons gives rise to an electric field which provides a balancing force. The equal and opposite thermal force on the ions is similarly balanced by this electric force.

The  $b \times \nabla T_e$  term in eqn 2.23.3 has a similar origin. The electrons colliding with ions around a given point have different directions according to the position of their guiding centre as illustrated in Fig. 2.23.1.

As before, the rate of momentum loss is  $\sim \Delta\nu_e n_e m_e \bar{v}_e$  but the length which characterizes  $\Delta\nu_e$  is now the Larmor radius  $\rho_e$  and not the mean free path. Thus

$$\Delta\nu_e \sim \rho_e |\nabla_{\perp} \nu_e| \sim \frac{\nu_{Te}}{\omega_{ce}} \frac{\nu_e}{T_e} |\nabla_{\perp} T_e|. \quad 2.23.8$$

The rate of momentum loss is

$$R_{T\perp} \sim \Delta\nu_e n_e m_e \nu_{Te}$$

and substituting relation 2.23.8 with  $\nu_e = \tau_e^{-1}$  this becomes

$$R_{T\perp} \sim \frac{1}{|\omega_{ce}| \tau_e} n_e |\nabla_{\perp} T_e|.$$

From Fig. 2.23.1 it is seen that, since the colder electrons are subject to the greater force, the thermal force on the electrons is in the direction  $-b \times \nabla T_e$  and consequently

$$R_{T\perp} \sim -\frac{1}{|\omega_{ce}| \tau_e} n_e b \times \nabla T_e.$$

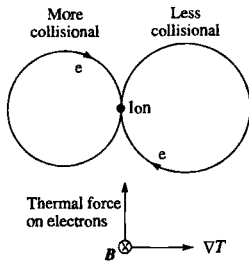


**Fig. 2.23.1** Electrons colliding with an ion have velocities characterized by the temperature an electron Larmor radius away. In the presence of a temperature gradient there is a difference in collisionality between the two sides, the hotter electron having a lower collisionality. The resulting collisional imbalance leads to a force on the ion and an equal and opposite force on the electrons, the force being perpendicular to the temperature gradient.

The stress tensors  $\Pi_{i\alpha\beta}$  and  $\Pi_{e\alpha\beta}$  for ions and electrons appearing in eqn 2.23.2 both take the same form. In a strong magnetic field ( $\omega_c, \tau_i \gg 1$ )

$$\begin{aligned}\Pi_{zz} &= -\eta_0 W_{zz} \\ \Pi_{xx} &= -\frac{1}{2}\eta_0(W_{xx} + W_{yy}) - \frac{1}{2}\eta_1(W_{xx} - W_{yy}) - \eta_3 W_{xy} \\ \Pi_{yy} &= -\frac{1}{2}\eta_0(W_{xx} + W_{yy}) - \frac{1}{2}\eta_1(W_{yy} - W_{xx}) + \eta_3 W_{xy} \\ \Pi_{xy} &= \Pi_{yx} = -\eta_1 W_{xy} + \frac{1}{2}\eta_3(W_{xx} - W_{yy}) \\ \Pi_{xz} &= \Pi_{zx} = -\eta_2 W_{xz} - \eta_4 W_{yz} \\ \Pi_{yz} &= \Pi_{zy} = -\eta_2 W_{yz} + \eta_4 W_{xz}\end{aligned}$$

where the  $z$ -axis is parallel to the magnetic field and the rate-of-strain tensor

$$W_{\alpha\beta} = \frac{\partial v_\alpha}{\partial x_\beta} + \frac{\partial v_\beta}{\partial x_\alpha} - \frac{2}{3}\delta_{\alpha\beta}\nabla \cdot v.$$

The ion viscosity coefficients are

$$\begin{aligned}\eta_0^i &= 0.96n_i T_i \tau_i \\ \eta_1^i &= \frac{3}{10} \frac{n_i T_i}{\omega_{ci}^2 \tau_i} \quad \eta_2^i = 4\eta_1^i \\ \eta_3^i &= \frac{1}{2} \frac{n_i T_i}{\omega_{ci}} \quad \eta_4^i = 2\eta_3^i\end{aligned}$$

and the electron viscosity coefficients for  $Z = 1$  are

$$\begin{aligned}\eta_0^e &= 0.73n_e T_e \tau_e \\ \eta_1^e &= 0.51 \frac{n_e T_e}{\omega_{ce}^2 \tau_e} \quad \eta_2^e = 4\eta_1^e \\ \eta_3^e &= -\frac{1}{2} \frac{n_e T_e}{|\omega_{ce}|} \quad \eta_4^e = 2\eta_3^e.\end{aligned}$$

### Energy equation

The energy balance equation is

$$\frac{3}{2}n \frac{dU_j}{dt} = -p_j \nabla \cdot v_j - \nabla \cdot q_j - \Pi_{j\alpha\beta} \frac{\partial v_{j\alpha}}{\partial x_\beta} + Q_j.$$

The electron heat flux is

$$q^e = q_u^e + q_T^e$$

where

$$q_u^e = n T_e \left( 0.71 u_{||} + \frac{3/2}{|\omega_{ce}| \tau_e} b \cdot \mathbf{x} u \right)$$

and

$$q_T^e = \frac{n T_e \tau_e}{m_e} \left( -3.16 \nabla_{\parallel} T_e - \frac{4.66}{\omega_{ce}^2 \tau_e^2} \nabla_{\perp} T_e - \frac{5/2}{|\omega_{ce}| \tau_e} b \times \nabla T_e \right) \quad 2.23.9$$

and the *ion heat flux* is

$$q_i = \frac{n T_i \tau_i}{m_i} \left( -3.9 \nabla_{\parallel} T_i - \frac{2}{\omega_{ci}^2 \tau_i^2} \nabla_{\perp} T_i + \frac{5/2}{\omega_{ci} \tau_i} b \times \nabla T_i \right)$$

The *heat exchange* between ions and electrons due to collisions gives rise to the ion heating

$$Q_i = \frac{3m_e n}{m_i \tau_e} (T_e - T_i)$$

and the heating of the electrons due to collisions with the ions is

$$\begin{aligned} Q_e &= -R \cdot u - Q_i \\ &= \eta_{\parallel} j_{\parallel}^2 + \eta_{\perp} j_{\perp}^2 + \frac{1}{ne} j \cdot R_T + \frac{3m_e n}{m_i \tau_e} (T_i - T_e). \end{aligned}$$

As explained at the beginning of this section the ratio of parallel to perpendicular thermal conductivity is  $(\omega_{ci} \tau_i)^2$ . This ratio is large for both ions and electrons, typical values being  $10^{13}$  and  $10^{16}$  respectively. In the direction parallel to the magnetic field the electron thermal conductivity is larger than that of the ions by a factor  $\sim (m_i/m_e)^{1/2}$  because of their longer collision time. Perpendicular to the magnetic field the relationship is reversed because of the larger ion Larmor radius, the ion thermal conductivity being larger by  $\sim (m_i/m_e)^{1/2}$ .

The heat fluxes arising from  $b \times \nabla T$  are analogous to the diamagnetic current, the imbalance between the energy carried by particles with their guiding centres in the hotter and colder regions providing a heat flux. The electron and ion fluxes are of opposite sign and cancel at equal temperatures. Furthermore, because the heat flux is perpendicular to  $\nabla T$  it flows along isotherms and does not cool the plasma.

The ohmic heating,  $\eta j^2$ , appears in the electron equation only. This is because an electron colliding with an ion transfers only a small fraction  $\sim m_e/m_i$  of its energy to the ion. Consequently the scattering of the directed relative motion leads to a predominant heating of the electrons.

The same inefficiency of energy transfer explains the appearance of the factor  $m_e/m_i$  in the heat exchange term. Thus the heat exchange between ion and electron species at different temperatures occurs at a slower rate than the other relaxation processes.

The term involving the stress tensor and velocity gradients describes the viscous heating of the plasma.

**2.24****Plasma waves**

The wave properties of plasmas are extremely complex. In this section some of the simpler waves in uniform plasmas are introduced.

The general procedure is to solve Maxwell's equations together with the linearized plasma equations. In the absence of plasma Maxwell's equations give the familiar vacuum electromagnetic waves with a velocity  $c$ . The inclusion of plasma effects introduces the one remaining term to Maxwell's equations, namely the current in the equation for  $\nabla \times B$ . Thus the addition of the plasma effects requires a calculation of the perturbed plasma current in terms of the perturbed electric field. This amounts to a calculation of the dielectric tensor.

Maxwell's equation combine to give the electromagnetic wave equation which may be written

$$\nabla \times \nabla \times E = -\frac{1}{c^2} \frac{\partial^2 E}{\partial t^2} - \mu_0 \frac{\partial j}{\partial t}. \quad 2.24.1$$

In a uniform plasma all of the perturbed quantities can be taken to be sinusoidal in space and time. It is algebraically convenient to write the perturbed quantities in the form

$$A_1(x, t) = \text{Re}[\hat{A}_1 e^{i(-\omega t + kx)}]$$

where  $\hat{A}_1$  is a complex amplitude and  $k$  is the wave vector. For simplicity the symbol  $\text{Re}$  is not written, but is implied, in all of the linearized equations and circumflex on the symbol  $\hat{A}$  is dropped. Thus the curl operator can be replaced by  $ik \times$  and eqn 2.24.1 becomes

$$-k \times k \times E = \frac{\omega^2}{c^2} E + i\omega \mu_0 j. \quad 2.24.2$$

The dielectric tensor  $K$  (sometimes represented by  $\epsilon$ ) is defined by

$$KE = E + \frac{i}{\epsilon_0 \omega} j \quad 2.24.3$$

and eqn 2.24.2 can be written

$$k \times k \times E + \frac{\omega^2}{c^2} KE = 0. \quad 2.24.4$$

When the current  $j$  is determined in terms of  $E$ , eqn 2.24.3 gives  $K$  and substitution of  $KE$  into eqn 2.24.4 gives the relationship between  $\omega$  and  $k$ , that is  $\omega = \omega(k)$ . This is called the dispersion relation. The refractive

index,  $n$ , is defined by  $n = |n|$  where

$$n = \frac{kc}{\omega}$$

is the ratio of the velocity of light to the phase velocity of the wave. Although the procedure described above gives the formal basis of the calculation of the properties of plasma waves, the underlying physics is often seen more clearly by writing each of the relevant Maxwell equations separately, and this method will be followed below.

In each equation the variables are written as the sum of the equilibrium part and the perturbation, that is

$$A = A_0 + A_1.$$

Then taking the perturbations to be sufficiently small the equations are linearized by subtracting the equilibrium equation and dropping nonlinear terms in the perturbed quantities. In the following calculations the basic equations are given together with their linearized forms.

### Plasma oscillations

Plasma oscillations were discussed in Section 2.3. Their frequency will be recalculated here using the formalism described above. Plasma oscillations are longitudinal oscillations, the electrons being displaced in the direction of the wave vector. This gives rise to a restoring electric field resulting in the oscillatory motion. In terms of Maxwell's equation this means that the magnetic field plays no role and the right hand side of the equation for  $\nabla \times B$  is zero. That is, the plasma current and the displacement current cancel.

The oscillations are governed by the equation of motion, Coulomb's equation and the continuity equation, as given below

$$m_e \frac{\partial v_e}{\partial t} = -eE \quad \rightarrow \quad -m_e i\omega_{ei} = -eE_1 \quad 2.24.5$$

$$\nabla \cdot E = -n_e e/\epsilon_0 \quad \rightarrow \quad ik \cdot E_1 = -n_{ei} e/\epsilon_0$$

$$\frac{\partial n_e}{\partial t} = -\nabla \cdot (n_e v_e) \rightarrow \quad -i\omega_{ei} = -in_0 k \cdot v_{ei}.$$

Combination of these equations gives  $\omega = \omega_p$ , where

$$\omega_p = \left( \frac{n_0 e^2}{\epsilon_0 m_e} \right)^{1/2}$$

is the plasma frequency. Although the wave vector appears in the relationships between the physical variables, the oscillation frequency is independent of  $k$ . The effect of finite temperature on the dispersion relation is given in Section 2.25 where the non-collisional damping of thermal plasma oscillations is calculated.

### Transverse electromagnetic waves

In a transverse electromagnetic wave the perturbed electric and magnetic fields are both perpendicular to the wave vector. In a vacuum the magnitude of the electric field is simply  $E = cB$ , but when a plasma is introduced the electric field drives an electron oscillation, again in the direction perpendicular to  $k$ .

When the plasma response is significant the electromagnetic wave can alternatively be thought of as a plasma oscillation with a magnetic induction contribution to the electric field. Whereas in electrostatic plasma oscillations the terms  $\mu_0 j$  and  $(1/c^2)\partial E/\partial t$  cancel, in the electromagnetic oscillations these two terms are unequal and the difference is balanced by  $\nabla \times B$ . The inductive effect of this magnetic field becomes weaker at small  $k$  and as  $k \rightarrow 0$ , the frequency  $\omega \rightarrow \omega_p$ .

Equation 2.24.2 can be written

$$k^2 E_1 = \frac{\omega^2}{c^2} E_1 + i\omega\mu_0 j_1 \quad 2.24.6$$

where

$$j_1 = -n_0 e v_{el}$$

and  $v_{el}$  is given by eqn 2.24.5. Making the substitutions, eqn 2.24.6 gives the dispersion relation

$$\omega^2 = k^2 c^2 + \omega_p^2. \quad 2.24.7$$

It is seen that, for a given frequency, as the density of the plasma is increased to increase  $\omega_p$ , a critical point is reached where  $\omega_p = \omega$  and  $k^2$  becomes negative. This shows that undamped propagation of electromagnetic waves in a plasma can only occur if  $\omega > \omega_p$ . For  $\omega < \omega_p$ ,  $k$  becomes imaginary and under such conditions the wave decays. When an electromagnetic wave enters a plasma with a spatially increasing density, propagation can occur up to the point where  $\omega = \omega_p$  and the wave is then subject to a cut-off.

In the above description the electrons have been taken to be cold. However even at finite temperature the electron pressure will not play a role because the gradients arising from  $k$  are orthogonal to the electron motion.

### Sound waves

In the calculations for plasma oscillations and transverse electromagnetic waves the ions were neglected. At the high frequencies of these waves the large ion mass prevents a significant response. However at lower frequencies ion oscillations become possible in the form of sound waves. These are similar to sound waves in a gas, but the electron pressure contributes to the ion motion through coupling provided by the electric field.

The equation of motion for singly charged ions is

$$n_i m_i \frac{\partial v_{i\parallel}}{\partial t} = n_i e E - \nabla p_i \rightarrow -i\omega n m_i v_{i\parallel} = ne E_\parallel - ik p_{i\parallel}. \quad 2.24.8$$

The inertia of the electrons is negligible and so the force balance equation for the electrons is

$$0 = -n_e e E - \nabla p_e \rightarrow 0 = -ne E_\parallel - ik p_{e\parallel}. \quad 2.24.9$$

Adding eqns 2.24.8 and 2.24.9

$$-i\omega n m_i v_{i\parallel} = -ik(p_{i\parallel} + p_{e\parallel}) = -ik p_{\parallel}. \quad 2.24.10$$

For these waves quasi-neutrality is preserved, and from the continuity equations

$$\frac{\partial n_i}{\partial t} = -\nabla \cdot (n_i v_i) \rightarrow -i\omega n_{i\parallel} = -ink \cdot v_{i\parallel},$$

$$\frac{\partial n_e}{\partial t} = -\nabla \cdot (n_e v_e) \rightarrow -i\omega n_{e\parallel} = -ink \cdot v_{e\parallel}$$

it is seen that the requirement  $n_{e\parallel} = n_{i\parallel}$  implies  $v_{e\parallel} = v_{i\parallel}$  ( $=v_1$ ). To obtain the dispersion relation,  $p_1$  is related to  $v_1$  by assuming the electron and ion motions to be adiabatic so that

$$\frac{\partial p}{\partial t} = -\gamma p \nabla \cdot v \rightarrow -i\omega p_1 = -i\gamma p k \cdot v_1. \quad 2.24.11$$

Substitution of eqn 2.24.11 into eqn 2.24.10, with  $v_{i\parallel} = v_1$ , now gives

$$\omega^2 = k^2 C_s^2$$

where the sound speed  $C_s$  is given by

$$C_s^2 = \gamma \frac{p_1 + p_e}{nm_i}. \quad 2.24.12$$

### Magnetohydrodynamic waves

The waves described so far have been in plasmas with no magnetic field or, if there is a magnetic field the wave direction is such that the particle motions were parallel to it, and therefore unaffected by it.

There is a class of waves described by the MHD equations for which the magnetic field plays a central role. There are three types of wave. Firstly there is the shear Alfvén wave. This is an incompressible wave and it is therefore unaffected by the plasma pressure. The other two involve compression and their wave velocities involve both the Alfvén speed and the sound speed. Because of this they are called magnetosonic waves. These two waves are distinguished by their velocities, being called the fast and the slow magnetosonic waves.

### Shear Alfvén wave

The simplest form of the Alfvén wave occurs when the wave-vector is parallel to the magnetic field. This case is illustrated in Fig. 2.24.1. The elasticity is provided by the magnetic field, the curvature of the bent field lines giving a  $\mathbf{B} \cdot \nabla \mathbf{B}$  force in the opposite direction to the plasma displacement. The inertia is provided by the mass density, coming essentially from the mass of the ions.

A convenient way to describe the general Alfvén wave and its relation to the magnetosonic waves is to assume a uniform magnetic field and to take a coordinate system with the  $x$ -axis along the magnetic field and the wave-vector  $\mathbf{k}$  in the  $(x, y)$  plane. In this coordinate system the fluid displacement of the Alfvén wave is entirely along the  $z$  direction. The geometry is shown in Fig. 2.24.2.

The governing equations are the mhd equations given in Section 2.20. These are written below together with their linearized forms taking the perturbed quantities to vary as  $\exp[i(-\omega t + k_x x + k_y y)]$

$$\begin{aligned}\rho \frac{\partial \mathbf{v}}{\partial t} &= \mathbf{j} \times \mathbf{B} & \rightarrow & -\rho i\omega u_{zt} = -j_{yt} B_0 \\ \mathbf{j} &= \nabla \times \mathbf{B}/\mu_0 & \rightarrow & j_{y1} = -ik_x B_{z1} \\ \frac{\partial \mathbf{B}}{\partial t} &= -\nabla \times \mathbf{E} & \rightarrow & -i\omega B_{z1} = -ik_z E_{y1} + ik_y E_{x1} \\ \mathbf{E} &= -\mathbf{v} \times \mathbf{B} & \rightarrow & E_{x1} = 0, \quad E_{y1} = -v_{z1} B_0.\end{aligned}$$

These equations combine to give

$$\omega = k_x V_A \quad \text{with} \quad V_A = B_0 / \sqrt{\mu_0 \rho}. \quad 2.24.13$$

Thus, independent of the direction of  $\mathbf{k}$ , the shear Alfvén wave has a velocity  $V_A$  along the magnetic field. With  $\mathbf{k}$  parallel to  $\mathbf{B}$ , that is  $k_y = 0$ , the wave takes the form illustrated in Fig. 2.24.1 with the displacement shown there being in the  $z$  direction of the above calculation.

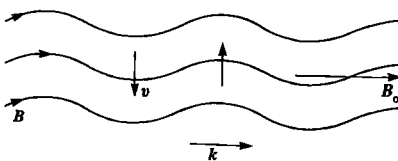


Fig. 2.24.1 Simple Alfvén wave with  $k \parallel B_0$ . The fluid velocity oscillates in the plane of the figure.

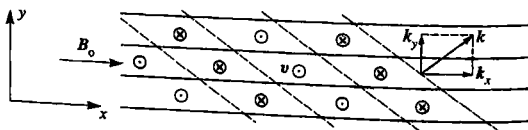
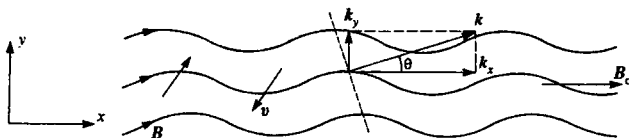


Fig. 2.24.2 General shear Alfvén wave.  $B_0$  and  $\mathbf{k}$  lie in the plane of the figure and the velocity oscillation is perpendicular to this plane. The wave propagates along  $x$  with the Alfvén velocity  $V_A$ .



**Fig. 2.24.3** The magnetosonic wave has velocity oscillations in the plane containing  $B_0$  and  $k$

### Magnetosonic waves

In magnetosonic waves the plasma displacement lies in the plane containing the wave vector and the magnetic field. Thus in the chosen coordinate system shown in Fig. 2.24.3 the fluid velocity has components  $v_x$  and  $v_y$ . The wave motion is governed by the same equations as Alfvén waves with the addition of the adiabatic equation for the pressure. These equations are written below together with their linearized forms

$$\begin{aligned} \rho \frac{\partial \mathbf{v}}{\partial t} &= \mathbf{j} \times \mathbf{B} - \nabla p \rightarrow -\rho_0 i \omega v_{x1} = -ik_x p_1 \\ &\quad -\rho_0 i \omega v_{y1} = j_{z1} B_0 - ik_y p_1 \\ \mathbf{j} &= \nabla \times \mathbf{B} / \mu_0 \rightarrow j_{z1} = i(k_x B_{y1} - k_y B_{x1}) / \mu_0 \\ \frac{\partial \mathbf{B}}{\partial t} &= -\nabla \times \mathbf{E} \rightarrow -i\omega B_{x1} = ik_y E_{z1} \\ &\quad -i\omega B_{y1} = ik_x E_{z1} \\ \mathbf{E} &= -\mathbf{v} \times \mathbf{B} \rightarrow E_{z1} = v_{y1} B_0 \\ \frac{\partial p}{\partial t} &= -\gamma p \nabla \cdot \mathbf{v} \rightarrow -i\omega p_1 = \gamma \rho_0 i (k_x v_{x1} + k_y v_{y1}). \end{aligned}$$

These equations combine to give the dispersion relation

$$(\rho \omega^2 - k_x^2 \gamma p) \left( \rho \omega^2 - k_y^2 \gamma p - k^2 \frac{B^2}{\mu_0} \right) = k_x^2 k_y^2 \gamma^2 p^2$$

or

$$\frac{\omega^2}{k^2} = \frac{1}{2} \left[ C_s^2 + V_A^2 \pm ((C_s^2 + V_A^2)^2 - 4C_s^2 V_A^2 \cos^2 \theta)^{1/2} \right] \quad 2.24.14$$

where  $C_s$  is the sound speed and  $V_A$  is the Alfvén velocity, given by eqns 2.24.12 and 2.24.13, and  $\theta$  is the angle between  $k$  and  $B$ .

The wave with the positive sign in eqn 2.24.14 is the fast magnetosonic wave and that with the negative sign is the slow magnetosonic wave.

For  $\theta = 0$ , that is  $k$  parallel to  $B$ , the waves have

$$\frac{\omega}{k} = V_A \quad (\text{fast})$$

and

$$\frac{\omega}{k} = C_s \quad (\text{slow})$$



**Fig. 2.24.4** The fast magnetosonic with  $\mathbf{k} \perp \mathbf{B}_0$ . The oscillations involve compression of both the fluid and the magnetic field.

The fast wave with  $\mathbf{k} \parallel \mathbf{B}$  is identical to the Alfvén wave with  $\mathbf{k}$  in the same direction, the different directions of  $v_1$  in the above calculations being purely a result of the choice of coordinates.

For  $\theta = \pi/2$ , that is  $\mathbf{k}$  perpendicular to  $\mathbf{B}$ ,

$$\frac{\omega^2}{k^2} = V_A^2 + C_s^2 \quad (\text{fast})$$

$$\omega = 0 \quad (\text{slow})$$

The fast wave is here simply a compressional wave in which both the magnetic field and the fluid are compressed as illustrated in Fig. 2.24.4.

## 2.25

### Landau damping

It might be expected that waves in a collisionless plasma would be free from damping. This is not the case. The interaction between the particles and the field of the wave can lead to a form of damping called Landau damping. As an example, the Landau damping of Langmuir waves is described below.

The linearized form of the electron Vlasov equation for  $f_1(x, t)$  is

$$\frac{\partial f_1}{\partial t} + v \frac{\partial f_1}{\partial x} - \frac{e}{m_e} E_1 \frac{\partial f_0}{\partial v} = 0 \quad 2.25.1$$

and the perturbed electric field,  $E_1(x, t)$  is given by

$$\frac{\partial E_1}{\partial x} = -\frac{e}{\epsilon_0} \int f_1 dv. \quad 2.25.2$$

Fourier and Laplace transforms are now applied to eqns 2.25.1 and 2.25.2 by multiplying by  $\exp[i(-kx + \omega t)]$  and integrating over all space and over time from  $t = 0$  to  $\infty$ . This gives equations for the

transform variables

$$f_1(k, \omega) = \left( f_1(k, t=0) - \frac{e}{m_e} E_1(k, \omega) \frac{\partial f_0}{\partial v} \right) / i(\omega - kv) \quad 2.25.3$$

$$E_1(k, \omega) = (ie/k\epsilon_0) \int f_1(k, \omega) dv \quad 2.25.4$$

where  $f_1(k, t=0)$  is the Fourier transform of  $f_1$  at  $t=0$ . Substitution of 2.25.3 into 2.25.4 now gives

$$E_1(k, \omega) = -\frac{e}{\epsilon_0} \int \frac{f_1(k, t=0)}{v - \omega/k} dv / \left( k^2 - \frac{e^2}{m_e \epsilon_0} \int \frac{\partial f_0 / \partial v}{v - \omega/k} dv \right). \quad 2.25.5$$

Thus the required solution for the Fourier component of the electric field is

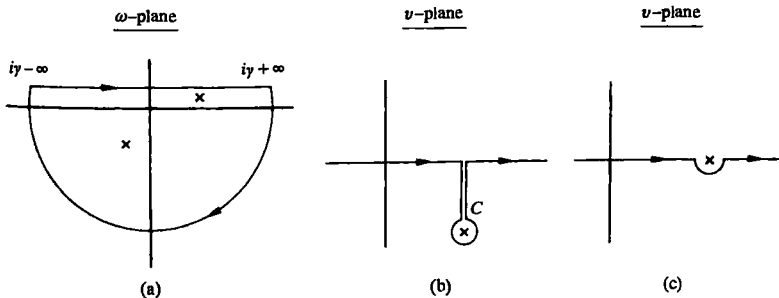
$$E(k, t) = \frac{1}{2\pi} \int_{iy-\infty}^{iy+\infty} \frac{I e^{-i\omega t}}{k^2 - \frac{e^2}{m_e \epsilon_0} \int \frac{\partial f_0 / \partial v}{v - \omega/k} dv} d\omega \quad 2.25.6$$

where  $I$  is the numerator of eqn 2.25.5 and represents the initial conditions.

The normal procedure for evaluating an inverse transform of this type is to extend the line of integration in the  $\omega$ -plane to form a closed contour as shown in Fig. 2.25.1(a). The integral is then equal to  $2\pi i$  times the residues of the enclosed poles. Since the zeros of the denominator of eqn 2.25.5 are such poles, these zeros would then give the eigenvalues of the problem.

However, the integrand of the  $\omega$  integral in eqn 2.25.5 does not have the necessary analytic properties because of the discontinuity arising from the velocity integral at  $v_i = 0$ . As shown by Landau this difficulty may

**Fig. 2.25.1** (a) Integration contour in the  $\omega$ -plane, (b) Landau contour, and (c) contour for calculating Landau damping of the Langmuir waves.



be resolved by deforming the velocity integral to the contour C as shown in Fig. 2.25.1(b).

Thus the eigenvalues are given by the dispersion relation

$$1 - \frac{\omega_p^2}{k^2} \frac{1}{n} \int_C \frac{\partial f_0 / \partial v}{v - \omega/k} dv = 0. \quad 2.25.7$$

It is this Landau integral which leads to collisionless damping. For a Maxwellian distribution the long wavelength limit of eqn 2.25.7 gives the dispersion relation

$$1 - \frac{\omega_p^2}{\omega^2} \left( 1 + \frac{3k^2 v_{te}^2}{\omega_p^2} \right) + \frac{\omega_p^2}{k^2 n} i\pi \left( \frac{\partial f_p}{\partial v} \right)_{v=\omega/k} = 0 \quad 2.25.8$$

where the last term arises from the Landau contour shown in Fig. 2.25.1(c). If the real part of the frequency is determined from the first three terms in eqn 2.25.8 and used to calculate the last term, the dispersion relation becomes

$$\omega = \omega_p (1 + 3k^2 \lambda_D^2)^{1/2} - i \left( \frac{\pi}{8} \right)^{1/2} \frac{\omega_p}{(k\lambda_D)^3} \exp -\frac{1}{2} \left( \frac{1}{k^2 \lambda_D^2} + 3 \right)$$

the last term giving the Landau damping of the waves. It is seen from eqn 2.25.8 that the damping arises through the interaction of the wave with particles travelling at the phase velocity,  $\omega/k$ .

## Bibliography

- The present chapter provides only an introduction to the plasma physics involved in the study of tokamak plasmas. A more general treatment will be found in the following books, listed in chronological order.
- Spitzer, L. *The physics of fully ionized gases*, 2nd edn. Interscience, New York (1962).
  - Thomson, W.B. *An introduction to plasma physics*. Pergamon Press, Oxford (1962).
  - Montgomery, D.C. and Tidman, D.A. *Plasma kinetic theory*. McGraw-Hill, New York (1963).
  - Kunkel, W.B. *Plasma physics in theory and application*. McGraw-Hill, New York (1966).
  - Boyd, T.J.M. and Sanderson, J.J. *Plasma dynamics*. Nelson, London (1969).
  - Clemmow, P.C. and Dougherty, J.P. *The electrodynamics of particles and plasmas*. Addison-Wesley, Reading, Mass. (1969).
  - Ichimaru, S. *Basic principles of plasma physics*. Benjamin, Reading, Mass. (1973).
  - Krall, N.A. and Trivelpiece, A.W. *Principles of plasma physics*. McGraw-Hill, New York (1973).
  - Golant, V.E., Zhilinsky, A.P., and Sakharov, I.E. *Fundamentals of plasma physics*. Wiley, New York (1977).
  - Schmidt, G. *Physics of high temperature plasmas*. Academic Press, New York (1979).
  - Gill, R.D. (ed.) *Plasma physics and nuclear fusion research* (Culham Summer School). Academic Press, London (1981).
  - Rosenbluth, M.N. and Sagdeev, R.Z. (eds.) *Handbook of plasma physics*. North Holland, Amsterdam (1983).
  - Nicholson, D.R. *Introduction to plasma theory*. John Wiley, New York (1983).
  - Chen, F.F. *Introduction to plasma physics and controlled fusion*. Plenum Press, New York (1984).
  - Miyamoto, K. *Plasma physics for nuclear fusion*, 2nd edn. MIT Press, Cambridge, Mass. (1989).
  - Dendy, R.O. *Plasma dynamics*. Clarendon Press, Oxford (1990).

- Goldston, R.J. and Rutherford, P.H. *Introduction to plasma physics*. Institute of Physics Publishing, Bristol (1995).
- Dendy, R.O. (ed.) *Plasma physics: an introductory course (Culham Summer School)*. Cambridge University Press, Cambridge (1993).

An extensive source of material is available in the series of volumes entitled *Reviews of plasma physics* (ed. Leontovich, M.A.). Consultants Bureau, New York. At present there are 18 volumes. Each chapter reviews a different branch of the subject.

### Fokker–Planck equation

The Fokker–Planck equation for a plasma, and the Rosenbluth potentials are derived in

Rosenbluth, M.N., MacDonald, W.M., and Judd, D.L. Fokker–Planck equation for an inverse-square force. *Physical Review* **107**, 1 (1957).

The Landau integral formulation is derived in

Landau, L.D., *Journal of Experimental and Theoretical Physics* **7**, 203 (1937).

### Gyro-averaged kinetic equations

A derivation of the drift kinetic equation is given by

Sivukhin, D.V. Motion of charged particles in electromagnetic field in the drift approximation. *Reviews of Plasma Physics*, Vol. 1, see p. 96, Consultants Bureau, New York (1965).

The linearized gyro-kinetic equation is derived in

Taylor, J.B. and Hastie, R.J., Stability of general plasma equilibria. *Plasma Physics* **10**, 479 (1968).

### Relaxation processes

An introductory account is given in Chapter 5 of

Spitzer, L. *The physics of fully ionized gases*, 2nd edn. Interscience, New York (1962).

The subject is further described by J.J. Sanderson in Chapter 7 of

Gill, R.D. (ed.) *Plasma physics and nuclear fusion research*. Academic Press, London (1981).

### Resistivity

The calculation of the classical resistivity of a uniform plasma was carried out by Spitzer and his co-workers and is given in

Spitzer, L. and Härn, R. Transport phenomena in a completely ionized gas. *Physical Review* **89**, 977 (1953).

The enhancement of resistivity in a tokamak due to trapped particles is discussed in Section 4.10.

### Electromagnetism

A clear discussion of Maxwell's equations is given in Chapters 18 and 32 of

Feynman, R.P., Leighton, R.B., and Sands, M. *Lectures on physics*, Vol. II. Addison-Wesley, Reading, Mass. (1965).

### Braginskii equations

The equations are derived in

Braginskii, S.I. Transport processes in a plasma. *Reviews of plasma physics* (ed. Leontovich, M.A.), Vol. 1, Consultants Bureau, New York (1965).

### Runaway electrons

The seminal paper is

Dreicer, H., Electron and ion runaway in a fully ionized gas. *Physical Review* **117**, 329 (1960).

The runaway rate was calculated by

Gurevich, A.V., On the theory of runaway electrons. *Zhurnal Eksperimentalnoi i Teoreticheskoi Fiziki* **39**, 1296 (1960). [Soviet Physics, *JETP* **12**, 904 (1961)]

and the relativistic effect by

Connor, J.W. and Hastie, R.J., Relativistic limitations on runaway electrons. *Nuclear Fusion* **15**, 415 (1975). The significance of short-range collisions was pointed out by Sokolov, Yu. A., Multiplication of accelerated electrons in a tokamak. *Pis'ma Zhurnal Experimentalnoi i Teoreticheskoi Fiziki* **29**, 244 (1979) [*JETP Letts.* **29**, 218 (1979)].

### Waves

The cases treated in Section 2.24 are elementary examples of a very complex variety of waves which can propagate in a plasma. The subject is treated at length in

Stix, T.H. *Waves in plasmas*. American Institute of Physics,

New York (1992).

Akhiezer, A.I., Akhiezer, I.A., Polovin, R.V., Stienko, A.G. and Stepanov, K.N. *Plasma electrodynamics*, Vol. 1, Pergamon Press, Oxford (1975).

### Landau damping

Landau, L.D. On the vibrations of the electronic plasma. *Journal of Physics (USSR)* **10**, 25 (1946).

A physical picture of Landau damping is given by

Stix, T.H. *Waves in plasmas*. American Institute of Physics, New York (1992).

**3**

# **Equilibrium**

### 3.1

### Tokamak equilibrium

The subject of tokamak equilibrium has two basic aspects. Firstly there is the internal balance between the pressure of the plasma and the forces due to the magnetic field. Secondly there is the shape and position of the plasma, these being determined and controlled by currents in external coils.

As described in Section 1.6 the main component of the magnetic field is the toroidal field produced by poloidal currents in external coils. A smaller, poloidal magnetic field is produced mainly by the toroidal current in the plasma. The full poloidal field is comprised of this internally generated field together with that due to toroidal currents in the primary winding and other coils used for plasma shaping and control. Finally the toroidal magnetic field is modified to a small extent by poloidal currents in the plasma.

The general form of the spatial variation of the magnetic field is illustrated in Fig. 3.1.1. The basic shape of the toroidal field  $B_\phi$  is obtained from Ampère's law. Thus, taking a line integral around a circular toroidal circuit inside the toroidal field coils, and neglecting the small poloidal plasma current

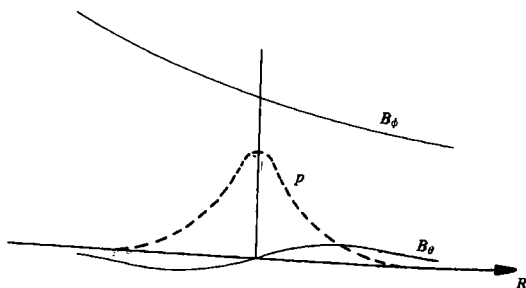
$$2\pi R B_\phi = \mu_0 I_T$$

3.1.1

where  $R$  is the major radius coordinate and  $I_T$  is the total current in the coils. It is seen from eqn 3.1.1 that

$$B_\phi \propto \frac{1}{R}.$$

**Fig. 3.1.1** Basic radial variation of the toroidal magnetic field  $B_\phi$  (with an approximate  $1/R$  dependence), the poloidal magnetic field  $B_\theta$ , due mainly to the plasma current, and the plasma pressure,  $p$ .  $R$  is the distance from the major axis of the torus and the graphs are for the median plane.



In present tokamaks this radial fall off is significant. Taking a minor radius  $a$ , the change in  $B_\phi$  across the plasma is

$$\begin{aligned}\Delta B_\phi &= B_{\phi 0} \left( \frac{R_0}{R_0 - a} - \frac{R_0}{R_0 + a} \right) \\ &\approx B_{\phi 0} \frac{2a}{R_0}\end{aligned}$$

where  $B_{\phi 0}$  is the field at the mid-plane  $R = R_0$ . For an aspect-ratio  $R/a = 3$ ,  $\Delta B_\phi/B_{\phi 0} = \frac{3}{4}$ . This variation of  $B_\phi$  across the plasma has an important effect on the trajectories of the plasma particles as described in Section 3.10.

The distribution of the poloidal magnetic field depends on the toroidal current profile. In the case where this current is driven by a toroidal electric field, the steady state current profile is determined by the electrical conductivity. Since this increases with electron temperature as  $T_e^{3/2}$  the current is peaked in the central region where the temperature is highest. It is possible to drive the current by non-ohmic means using RF waves or particle beams as described in Section 3.14. Another component of the plasma current is the so-called bootstrap current described in Section 4.9. This current arises from a combination of the radial gradients of density and temperature and the toroidal magnetic geometry.

Because the mass density of the plasma is very low, typically  $10^{-4} \text{ gm m}^{-3}$ , and the component internal forces on the plasma are quite large, typically  $10 \text{ tonnes m}^{-3}$ , the internal forces must balance. The plasma pressure exerts an outward force across the minor radius and the poloidal magnetic field exerts an inward force. The imbalance between these two forces is taken up by the magnetic pressure of the toroidal magnetic field. This force may be inward or outward.

The complete magnetic field produces an infinite set of nested toroidal magnetic surfaces. The field lines themselves follow a helical path on their magnetic surface as they wind round the torus. The sound speed in the plasma is typically  $10^5 - 10^6 \text{ m s}^{-1}$  and consequently the pressure is constant along the magnetic field, any imbalance being rapidly removed.

The direction of the magnetic field changes from surface to surface. This shear of the magnetic field has important implications for the stability of the plasma. The average twist of the magnetic field on each surface can be characterized by the so-called safety factor,  $q$ , which is a measure of the pitch of the helical field lines. The shear is then determined by the radial rate of change of  $q$ .

The toroidal geometry of the plasma leads to a hoop force which is in the direction to expand the plasma ring. This force is balanced by applying a vertical magnetic field which interacts with the toroidal current to give an inward force.

The particle motions are quite complex. The basic component is the normal small scale helical motion along the magnetic field as the particles gyrate in their Larmor orbits. At low temperatures the particles suffer frequent collisions and collectively they can be regarded as a fluid.

At higher temperatures collisions are less frequent and the particle orbits are affected by the toroidal geometry of the magnetic field. A substantial fraction of the particles are trapped in the weaker magnetic field on the outer side of the torus, being reflected between turning points in the region of stronger magnetic field.

While the equilibrium is partly determined by the externally imposed conditions such as total current, applied toroidal magnetic field and the applied heating, many characteristics are the result of the plasma behaviour. Thus the density and temperature profiles are governed by the transport properties which in turn are affected by plasma instabilities.

## 3.2

### Flux functions

For axisymmetric equilibria, that is equilibria which are independent of the toroidal angle  $\phi$ , the magnetic field lines lie in nested toroidal magnetic surfaces as illustrated in Fig. 3.2.1.

The basic condition for equilibrium is that the force on the plasma be zero at all points. This requires that the magnetic force balances the force due to the plasma pressure, that is

3.2.1

$$\mathbf{j} \times \mathbf{B} = \nabla p.$$

It is clear from this equation that  $\mathbf{B} \cdot \nabla p = 0$ . Thus, there is no pressure gradient along the magnetic field lines and the magnetic surfaces are surfaces of constant pressure. Furthermore eqn 3.2.1 gives  $\mathbf{j} \cdot \nabla p = 0$ , and consequently the current lines also lie in the magnetic surfaces as shown in Fig. 3.2.2.

In studying tokamak equilibria it is convenient to introduce the poloidal magnetic flux function  $\psi$ . This function is determined by the poloidal flux lying within each magnetic surface and is therefore a constant on that surface. Thus  $\psi$  satisfies

$$\mathbf{B} \cdot \nabla \psi = 0$$

Introducing a cylindrical coordinate system based on the major axis of the torus as shown in Fig. 3.2.3 and defining  $\psi$  to be the poloidal flux per radian in  $\phi$ , the poloidal magnetic field is related to  $\psi$  by

$$B_R = -\frac{1}{R} \frac{\partial \psi}{\partial z}, \quad B_z = \frac{1}{R} \frac{\partial \psi}{\partial R} \quad 3.2.2$$

conforming to the requirement  $\nabla \cdot \mathbf{B} = 0$ , that is

$$\frac{1}{R} \frac{\partial}{\partial R} (RB_R) + \frac{\partial B_z}{\partial z} = 0.$$

The flux function  $\psi$  is arbitrary to an additive constant which may be chosen for convenience.

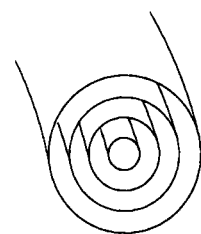


Fig. 3.2.1 Magnetic flux surfaces forming a set of nested toroids.

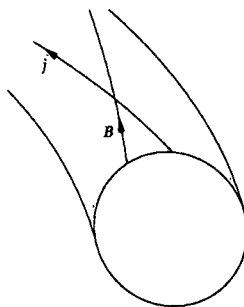


Fig. 3.2.2 Magnetic field lines and current lines lie in magnetic surfaces.

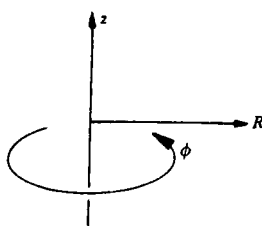


Fig. 3.2.3 Cylindrical coordinate system.  $R = 0$  is the major axis of the torus.

From the symmetry of  $j$  and  $B$  it is clear that a current flux function also exists. This function,  $f$ , is related to the poloidal current density by

$$j_R = -\frac{1}{R} \frac{\partial f}{\partial z}, \quad j_z = \frac{1}{R} \frac{\partial f}{\partial R}. \quad 3.2.3$$

Comparison of eqns 3.2.3 with Ampère's equation,

$$j_R = -\frac{1}{\mu_0} \frac{\partial B_\phi}{\partial z}, \quad j_z = \frac{1}{\mu_0 R} \frac{1}{R} \frac{\partial}{\partial R} (RB_\phi),$$

gives the relation between  $f$  and the toroidal magnetic field as

$$f = \frac{RB_\phi}{\mu_0}. \quad 3.2.4$$

It can be shown that  $f$  is a function of  $\psi$  by taking the scalar product of eqn 3.2.1 with  $j$ , to obtain  $j \cdot \nabla p = 0$ , and then substituting eqn 3.2.3 for  $j$ . Thus

$$\frac{\partial f}{\partial R} \frac{\partial p}{\partial z} - \frac{\partial f}{\partial z} \frac{\partial p}{\partial R} = 0$$

and hence

$$\nabla f \times \nabla p = 0,$$

proving that  $f$  is a function of  $p$ . Then, since  $p = p(\psi)$ , it follows that  $f = f(\psi)$ .

The flux functions as defined here give the poloidal flux associated with a unit angle in  $\phi$ . It is also possible to use the total flux function for the torus which is simply larger by a factor  $2\pi$ .

### 3.3

### Grad-Shafranov equation

The equilibrium equation for an axisymmetric system such as a tokamak can be written as a differential equation for the poloidal flux function  $\psi$ . This equation which has two arbitrary functions,  $p(\psi)$  and  $f(\psi)$ , is usually called the Grad-Shafranov equation.

The equilibrium equation

$$j \times B = \nabla p$$

may be written

$$j_p \times i_\phi B_\phi + j_\phi i_\phi \times B_p = \nabla p \quad 3.3.1$$

where  $j_p$  is the poloidal current density,  $B_p$  is the poloidal magnetic field, and  $i_\phi$  is the unit vector in the  $\phi$  direction,  $\phi$  being the toroidal coordinate.

### 3.3 Grad-Shafranov equation

Equation 3.3.1 can now be written in terms of the poloidal flux function  $\psi$ . Equations 3.2.2 and 3.2.3 may be contracted to

$$B_p = \frac{1}{R}(\nabla\psi \times i_\phi) \quad 3.3.2$$

and

$$j_p = \frac{1}{R}(\nabla f \times i_\phi). \quad 3.3.3$$

Thus, substituting eqns 3.3.2 and 3.3.3 into eqn 3.3.1, and remembering that  $i_\phi \cdot \nabla\psi = i_\phi \cdot \nabla f = 0$ , gives

$$-\frac{B_\phi}{R}\nabla f + \frac{j_\phi}{R}\nabla\psi = \nabla p. \quad 3.3.4$$

Now

$$\nabla f(\psi) = \frac{df}{d\psi}\nabla\psi$$

and

$$\nabla p(\psi) = \frac{dp}{d\psi}\nabla\psi,$$

and substitution of these relations into eqn 3.3.4 leads to

$$j_\phi = R\frac{dp}{d\psi} + B_\phi\frac{df}{d\psi}. \quad 3.3.5$$

Substituting eqn 3.2.4 for  $B_\phi$  into eqn 3.3.5 then gives

$$j_\phi = Rp' + \frac{\mu_0}{R}ff'. \quad 3.3.6$$

It remains to write  $j_\phi$  in terms of  $\psi$ . This is done by introducing Ampère's equation

$$\mu_0 j = \nabla \times B. \quad 3.3.7$$

Substitution of eqns 3.2.2 into the toroidal component of eqn 3.3.7 gives

$$-\mu_0 R j_\phi = R\frac{\partial}{\partial R}\frac{1}{R}\frac{\partial\psi}{\partial R} + \frac{\partial^2\psi}{\partial z^2} \quad 3.3.8$$

and using eqn 3.3.8 to substitute for  $j_\phi$  in eqn 3.3.6 gives the required equation

$$R\frac{\partial}{\partial R}\frac{1}{R}\frac{\partial\psi}{\partial R} + \frac{\partial^2\psi}{\partial z^2} = -\mu_0 R^2 p'(\psi) - \mu_0^2 f(\psi)f'(\psi). \quad 3.3.9$$

This equation is the Grad-Shafranov equation. Figure 3.3.1 shows the flux surfaces and profiles of  $j_\phi$ ,  $p$ , and  $B_\phi$  obtained by numerical solution of the equation for a typical case.

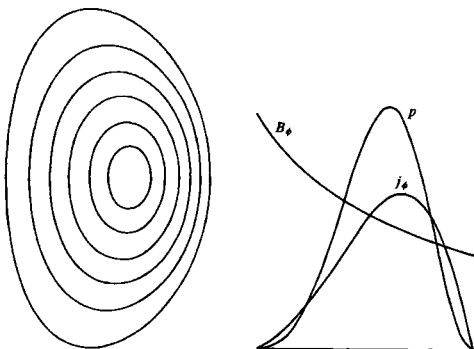


**Fig. 3.3.1** Equilibrium flux surfaces and plots of toroidal current density, plasma pressure, and toroidal magnetic field across the midplane.

## 3.4 Safety factor, $q$

### Safety factor, $q$

The safety factor,  $q$ , is so called because of the role it plays in determining stability. In general terms, higher values of  $q$  lead to greater stability. It also appears as an important factor in transport theory.

In an axisymmetric equilibrium each magnetic field line has a value of  $q$ . The field line follows a helical path as it goes round the torus on its associated magnetic surface. If at some toroidal angle,  $\phi$ , the field line has a certain position in the poloidal plane, it will return to that position in the poloidal plane after change of toroidal angle  $\Delta\phi$ . The  $q$ -value of this field line is defined by

$$q = \frac{\Delta\phi}{2\pi} \quad 3.4.1$$

Thus if a magnetic field line returns to its starting position after exactly one rotation round the torus, then  $q = 1$ . If it moves more slowly in the poloidal direction it has a higher value of  $q$ . Rational values of  $q$  play an important role in stability. If  $q = m/n$ , where  $m$  and  $n$  are integers, the field line joins up on itself after  $m$  toroidal and  $n$  poloidal rotations round the torus. A  $q = 2$  line is illustrated in Fig. 3.4.1(a).

In order to calculate the value of  $q$  it is necessary to use the equation of the field line

$$\frac{R d\phi}{ds} = \frac{B_\phi}{B_p}$$

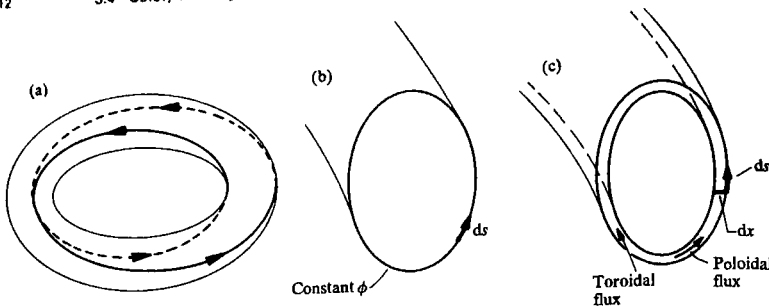


**Fig. 3.4.1** (a) Field line on  $q = 2$  surface. (b) Poloidal integration path for eqn 3.4.2. (c) Flux annulus containing toroidal flux  $d\Phi$  and poloidal flux  $d\Psi$ .

where  $ds$  is the distance moved in the poloidal direction while moving through a toroidal angle  $d\phi$ , and  $B_p$  and  $B_\phi$  are the poloidal and toroidal magnetic fields. Thus from eqn 3.4.1

$$q = \frac{1}{2\pi} \oint \frac{1}{R} \frac{B_\phi}{B_p} ds \quad 3.4.2$$

where the integral is carried out over a single poloidal circuit around the flux surface as illustrated in Fig. 3.4.1(b).

It is clear from eqn 3.4.2 that  $q$  is the same for all magnetic field lines on a magnetic surface. Thus  $q$  is a flux function, that is  $q = q(\psi)$ .

For a large aspect-ratio tokamak of circular cross-section eqn 3.4.2 gives the approximation

$$q = \frac{r B_\phi}{R_0 B_\theta} \quad 3.4.3$$

where  $r$  is the minor radius of the flux surface,  $B_\theta$  is the poloidal magnetic field,  $R_0$  is the major radius, and the toroidal magnetic field is essentially a constant.

An alternative expression for  $q$  can be obtained in terms of the magnetic fluxes. Consider an infinitesimal annulus between two magnetic surfaces as illustrated in Fig. 3.4.1(c). The poloidal flux is

$$d\Psi = 2\pi R B_p dx \quad 3.4.4$$

where  $dx$  is the local separation of the surfaces. The toroidal flux through the annulus is

$$d\Phi = \oint (B_\phi dx) ds. \quad 3.4.5$$

Substituting eqn 3.4.4 for  $B_p$  into eqn 3.4.2 gives

$$q = \frac{1}{d\Psi} \oint (B_\phi dx) ds.$$

and using eqn 3.4.5

$$q = \frac{d\Phi}{d\Psi}.$$

Thus the safety factor can be expressed as the rate of change of toroidal flux with poloidal flux.

An associated quantity is the rotational transform,  $\iota$ , (iota) which is given by  $\iota = 2\pi/q$ . It is often replaced by  $t = \iota/2\pi$ , that is  $t = 1/q$ .

### $q$ profiles

The radial profile of  $q$  usually has its minimum value at, or close to, the magnetic axis and increases outwards. In the case of large aspect-ratio and circular cross-section the behaviour of  $q$  is simply determined by the toroidal current density profile,  $j(r)$ . Thus writing Ampère's law in the form

$$2\pi r B_\theta = \mu_0 I(r),$$

where the current inside  $r$  is

$$I(r) = 2\pi \int_0^r j(r')r' dr',$$

and using eqn 3.4.3 for  $q$  gives

$$q(r) = \frac{2\pi r^2 B_\phi}{\mu_0 I(r) R} \quad 3.4.6$$

Taking  $r = a$ , the edge value of  $q$  is

$$q_a = \frac{2\pi a^2 B_\phi}{\mu_0 I R} \quad 3.4.7$$

where  $I$  is the total current. The central value of  $q$  is obtained by taking the limit  $r \rightarrow 0$  in eqn 3.4.6. In this limit  $I(r) = \pi r^2 j_0$ , where  $j_0 = j(0)$ , and so

$$q_0 = \frac{2B_\phi}{\mu_0 j_0 R}. \quad 3.4.8$$

Equations 3.4.7 and 3.4.8 give the ratio

$$\frac{q_a}{q_0} = \frac{\pi a^2 j_0}{I} = \frac{j_0}{\langle j \rangle_a}$$

where  $\langle j \rangle_a$  is the average current density over the whole plasma.

Equation 3.4.6 can be written

$$q(r) = \frac{2B_\phi}{\mu_0(j)_r R} \quad 3.4.9$$

where  $(j)_r$  is the average current density inside the radius  $r$

$$(j)_r = \frac{\int_0^r j(r')r' dr'}{r^2/2}. \quad 3.4.10$$

Differentiating eqn 3.4.9 with respect to  $r$

$$\frac{q'}{q} = -\frac{(j)'_r}{(j)_r}. \quad 3.4.11$$

Now it follows from eqn 3.4.10 that  $(j)'_r = 2(j - (j)_r)/r$ . Thus, since a monotonically decreasing current profile has  $j < (j)_r$  it is seen from eqn 3.4.11 that such a current profile has  $q' > 0$ .

For plasmas which have a limiter the general behaviour of  $q$  described above persists for non-circular plasmas. However precise values require numerical computation and this usually involves solving the Grad-Shafranov equation. An approximation which is often used is ‘ $q$  cylindrical’ which by analogy with eqn 3.4.7 is defined by

$$q_{cyl} = \frac{2\pi abB_\phi}{\mu_0 IR}$$

where  $a$  and  $b$  are the half-width and half-height of the plasma.

It is convenient to have a simple model for  $q(r)$ . In the case of a large aspect-ratio-circular plasma such a model is provided by the current distribution

$$j = j_0(1 - r^2/a^2)^v.$$

Ampère’s equation,  $\mu_0 j = (1/r) d(rB_\theta)/dr$ , then gives

$$B_\theta = \frac{\mu_0 j_0 a^2}{2(v+1)} \frac{1 - (1 - r^2/a^2)^{v+1}}{r}. \quad 3.4.12$$

Substituting eqn 3.4.12 into the approximation for  $q$  given by eqn 3.4.3 leads to the required  $q(r)$ ,

$$q = \frac{2(v+1)}{\mu_0 j_0} \frac{B_\phi}{R} \frac{r^2/a^2}{1 - (1 - r^2/a^2)^{v+1}}.$$

With this model

$$\frac{q(a)}{q(0)} = v + 1.$$

When plasmas are bounded by a separatrix, as they are in configurations with a divertor, the  $q$  profile is fundamentally modified. The reason is

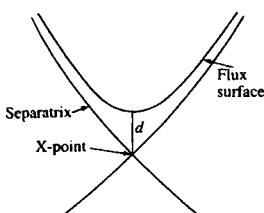


**Fig. 3.4.2** Illustrating the geometry of the flux surfaces around the X-point when the plasma is bounded by a separatrix.

that the value of  $q$  for surfaces close to the separatrix is dominated by the contribution close to the X-point. The poloidal magnetic field,  $B_p$ , has a null at the X-point, and locally its magnitude is proportional to the distance from the X-point. The magnetic geometry around the X-point is illustrated in Fig. 3.4.2. The expression 3.4.2 for  $q$  has  $B_p$  in the denominator of the integrand and this leads to a logarithmic contribution. If the shortest distance of a flux surface from the X-point is  $d$ , the limiting form of  $q$  as  $d \rightarrow 0$  is

$$q \rightarrow \frac{B_\phi}{\pi R |\nabla B_p|} \ln \frac{\lambda}{d} \quad (d \rightarrow 0)$$

where  $\lambda$  is a length characterizing the overall geometry. Thus as the separatrix is approached,  $q \rightarrow \infty$ . The underlying cause is that the smallness of  $B_p$  around the X-point delays the poloidal motion of the field lines, and field lines on surfaces close to the separatrix spend almost all of their trajectory close to the X-point.

## 3.5 Beta

The efficiency of confinement of plasma pressure by the magnetic field is represented in a simple way by the ratio

$$\beta = \frac{P}{B^2/2\mu_0}.$$

However, there are several different measures of this type, some arising from varying choices of definition and others from the need to quantify different equilibrium properties.

For a reactor, the important quantity is the thermonuclear power obtained for a given magnetic field. The reaction rate is proportional to  $n^2(\sigma v)$  which is not generally expressible as a pressure. However, in the temperature range envisaged for a reactor 10–15 keV,  $(\sigma v)$  is roughly proportional to  $T^2$  and the thermonuclear power is then proportional to  $p^2$ . The resulting form of  $\beta$ , called  $\beta^*$ , is defined by

$$\beta^* = \frac{\left( \int p^2 d\tau / \int d\tau \right)^{1/2}}{B_0^2/2\mu_0}$$

where the integrals are over the plasma volume and  $B_0$  is the value of the toroidal magnetic field. Although it is the toroidal magnetic field at the coil which is subject to limitation it is usually more convenient to use the value of the vacuum toroidal magnetic field at the geometric centre of the plasma.

A commonly used  $\beta$  is the average value defined by

$$\langle \beta \rangle = \frac{\int p d\tau / \int d\tau}{B_0^2 / 2\mu_0}.$$

Another expression which arises is the poloidal  $\beta$ , defined by

$$\beta_p = \frac{\int p dS / \int dS}{B_a^2 / 2\mu_0} \quad 3.5.1$$

where the integrals are surface integrals over the poloidal cross-section and

$$B_a = \frac{\mu_0 I}{l}$$

where  $I$  is the plasma current and  $l$  is the length of the poloidal perimeter of the plasma. For a large aspect-ratio circular plasma  $l = 2\pi a$  and eqn 3.5.1 becomes

$$\beta_p = \frac{\int p dS}{\mu_0 I^2 / 8\pi}. \quad 3.5.2$$

An alternative definition uses the volume average of  $p$  rather than the cross-sectional average in eqn 3.5.1.

The significance of  $\beta_p$  may be seen by taking a circular cross-section and integrating the numerator of eqn 3.5.2 by parts to obtain

$$\beta_p = -\frac{8\pi^2}{\mu_0 I^2} \int_0^a \frac{dp}{dr} r^2 dr$$

and substituting  $dp/dr$  from the approximate pressure balance equation

$$\frac{dp}{dr} + \frac{d}{dr} \left( \frac{B_\phi^2}{2\mu_0} \right) + \frac{B_\theta}{\mu_0 r} \frac{d}{dr} (r B_\theta) = 0$$

to obtain, after integration,

$$\beta_p = 1 + \frac{1}{(a B_{\theta a})^2} \int_0^a \frac{dB_\phi^2}{dr} r^2 dr. \quad 3.5.3$$

It is seen that if there are no azimuthal currents, so that the integrand of eqn 3.5.3 is zero, then  $\beta_p = 1$ . If  $dB_\phi^2/dr > 0$ , so that the toroidal field plays a part in confining the pressure, then  $\beta_p > 1$ . On the other hand, if  $dB_\phi^2/dr < 0$ , the magnetic pressure  $B_\phi^2/2\mu_0$  displaces some of the plasma pressure and  $\beta_p < 1$ . This is illustrated in Fig. 3.5.1.

There is no formal limit to the equilibrium value of  $\beta$ . This may be seen by the following thought experiment. Consider a perfectly conducting plasma surrounded by a perfectly conducting shell. Imagine the plasma to be continually heated, increasing the pressure on the flux surfaces. The plasma surfaces will move but their nested topology will remain

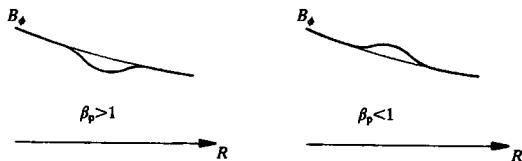


Fig. 3.5.1 Profiles of  $B_\phi$  for cases  $\beta_p > 1$  and  $\beta_p < 1$ .

unchanged. Furthermore the plasma boundary is fixed. In principle there is no limit to this process and therefore to the  $\beta$  which can be obtained. However, it should be noted that this procedure leads to an increased plasma current. The experimental situation is of course more complex and in practice raising  $\beta$  ultimately leads to the formation of a separatrix with an X-point on the high field side of the plasma.

## 3.6 Large aspect-ratio

Tokamak equilibria take a comparatively simple form for low- $\beta$ , large aspect-ratio plasmas of circular cross-section. The ordering of quantities in terms of the inverse aspect-ratio,  $\varepsilon = a/R$ , is

$$\begin{aligned} B_\phi &= B_{\phi 0}(R_0/R)(1 + O(\varepsilon^2)) & B_\theta &\sim \varepsilon B_{\phi 0} \\ j_\phi &\sim \varepsilon B_{\phi 0}/\mu_0 a & j_\theta &\sim \varepsilon^2 B_{\phi 0}/\mu_0 a \\ p &\sim \varepsilon^2 B_{\phi 0}^2/\mu_0, (\beta \sim \varepsilon^2) & \beta_p &\sim 1 \end{aligned}$$

where  $B_{\phi 0}$  is the vacuum toroidal magnetic field at the major radius of the plasma  $R_0$ . The basic pressure balance equation is that of a cylinder,

$$\frac{dp}{dr} = j_\phi B_\theta - j_\theta B_{\phi 0}, \quad 3.6.1$$

the equilibrium being specified by  $j_\phi(r)$  and  $p(r)$  with  $p(a) = 0$ . The azimuthal field is given by Ampère's equation

$$\mu_0 j_\phi = -\frac{1}{r} \frac{d}{dr}(r B_\theta)$$

and  $j_\theta$  is then determined by eqn 3.6.1.

When toroidal effects are included, the flux surfaces form non-concentric circles as illustrated in Fig. 3.6.1(a). Using the coordinate

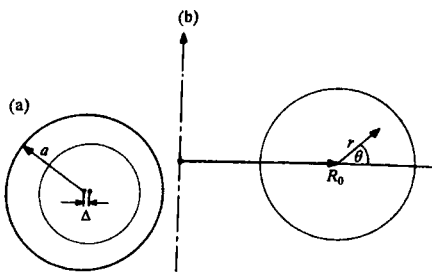


**Fig. 3.6.1** (a) Showing circular flux surface displaced by a distance  $\Delta$  with respect to outer flux surface whose centre is at a distance  $R_0$  from the major axis. (b) Coordinate system  $(r, \theta)$  with centre at major radius  $R_0$ .

system shown in Fig. 3.6.1(b) the Grad-Shafranov equilibrium eqn 3.3.9 may be written

$$\begin{aligned} & \left( \frac{1}{r} \frac{\partial}{\partial r} r \frac{\partial}{\partial r} + \frac{1}{r^2} \frac{\partial^2}{\partial \theta^2} \right) \psi - \frac{1}{R_0 + r \cos \theta} \left( \cos \theta \frac{\partial}{\partial r} - \sin \theta \frac{1}{r} \frac{\partial}{\partial \theta} \right) \psi \\ &= -\mu_0 (R_0 + r \cos \theta)^2 p'(\psi) - \mu_0^2 f(\psi) f'(\psi). \end{aligned} \quad 3.6.2$$

Expanding  $\psi$  in  $\varepsilon$ ,

$$\psi = \psi_0(r) + \psi_1(r, \theta).$$

The flux function  $\psi_0$  is given by the leading order part of eqn 3.6.2, corresponding to eqn 3.5.1, that is

$$\frac{1}{r} \frac{d}{dr} \left( r \frac{d\psi_0}{dr} \right) = -\mu_0 R_0^2 p'(\psi_0) - \mu_0^2 f(\psi_0) f'(\psi_0) \quad 3.6.3$$

and  $\psi_1$  satisfies the first-order part of eqn 3.6.2

$$\begin{aligned} & \left( \frac{1}{r} \frac{\partial}{\partial r} r \frac{\partial}{\partial r} + \frac{1}{r^2} \frac{\partial^2}{\partial \theta^2} \right) \psi_1 - \frac{\cos \theta}{R_0} \frac{d\psi_0}{dr} \\ &= -\mu_0 R_0^2 p''(\psi_0) \psi_1 - \mu_0^2 (f(\psi_0) f'(\psi_0))' \psi_1 - 2\mu_0 R_0 r \cos \theta p'(\psi_0) \\ &= -\frac{d}{dr} (\mu_0 R_0^2 p'(\psi_0) + \mu_0^2 f(\psi_0) f'(\psi_0)) \frac{dr}{d\psi_0} \psi_1 - 2\mu_0 R_0 r \cos \theta p'(\psi_0). \end{aligned} \quad 3.6.4$$

If the flux surface  $\psi$  is displaced a distance  $\Delta(\psi_0(r))$ ,  $\psi$  may be written

$$\begin{aligned} \psi &= \psi_0 + \psi_1 \\ &= \psi_0 - \Delta(r) \frac{\partial \psi_0}{\partial R} \\ &= \psi_0 - \Delta(r) \cos \theta \frac{d\psi_0}{dr}. \end{aligned} \quad 3.6.5$$

Substituting the form for  $\psi_1$  given by eqn 3.6.5 into eqn 3.6.4 leads to

$$\begin{aligned} -\Delta \frac{d}{dr} \left( \frac{1}{r} \frac{d}{dr} \left( r \frac{d\psi_0}{dr} \right) \right) - \frac{1}{r} \left( \frac{dr}{d\psi_0} \right) \frac{d}{dr} \left( r \left( \frac{d\psi_0}{dr} \right)^2 \frac{d\Delta}{dr} \right) - \frac{1}{R_0} \frac{d\psi_0}{dr} \\ = \Delta \frac{d}{dr} (\mu_0 R_0^2 p'(\psi_0) + \mu_0^2 f(\psi_0) f'(\psi_0)) - 2\mu_0 R_0 r \frac{dp_0}{dr} \frac{dr}{d\psi_0} \end{aligned} \quad 3.6.6$$

and, from eqn 3.6.3, the first terms on the two sides of equ 3.6.6 cancel, leaving

$$\frac{d}{dr} \left( r B_{\theta 0}^2 \frac{d\Delta}{dr} \right) = \frac{r}{R_0} \left( 2\mu_0 r \frac{dp_0}{dr} - B_{\theta 0}^2 \right) \quad 3.6.7$$

where the definition of the flux function given by equ 3.2.2 has been used to replace  $(d\psi_0/dr)/R_0$  by  $B_{\theta 0}$ .

The solution of the differential equation 3.6.7 with  $d\Delta/dr = 0$  at  $r = 0$  and  $\Delta(a) = 0$  gives the displacement  $\Delta(r)$  of the flux surfaces for a zero-order pressure  $p_0(r)$  and azimuthal magnetic field  $B_{\theta 0}(r)$ . Together with eqn 3.6.5 this then provides the solution  $\psi(r, \theta)$ .

## 3.7

### Shafranov shift

From the equilibrium calculation of Section 3.6 it is seen that the centres of the magnetic flux surfaces are displaced with respect to the centre of the bounding surface. This displacement,  $\Delta(r)$ , is given by the solution of equ 3.6.7. The displacement of the axis,  $\Delta_s = \Delta(0)$ , is called the Shafranov shift.

The Shafranov shift depends upon the particular forms of  $p_0(r)$  and  $B_{\theta 0}(r)$ , and equ 3.6.7 must be solved for each case. However, some indication of the behaviour can be obtained by using simple analytic forms. Thus, dropping the subscript zero, and taking

$$p = \hat{p} \left( 1 - \frac{r^2}{a^2} \right)$$

and

$$j = \hat{j} \left( 1 - \frac{r^2}{a^2} \right)^v \quad 3.7.1$$

equ 3.6.7 can be written

$$\frac{d\Delta}{dr} = -\frac{1}{RB_\theta^2} \left( \frac{r^3}{a^2} \beta_p B_{\theta a}^2 + \frac{1}{r} \int_0^r B_\theta^2 r dr \right) \quad 3.7.2$$

where  $B_{\theta a} = B_{\theta(a)}$  and the poloidal beta,  $\beta_p$ , is defined by

$$\beta_p = \frac{\tilde{p}}{B_{\theta a}^2/2\mu_0} = \frac{4\mu_0 \int_0^a pr dr}{a^2 B_{\theta a}^2} \quad 3.7.3$$

and  $\beta_p = \mu_0 \hat{p}/B_{\theta a}^2$  in this case. Application of Ampère's law to eqn 3.7.1 gives the required poloidal field

$$B_\theta = B_{\theta a} \frac{1 - \left(1 - \frac{r^2}{a^2}\right)^{v+1}}{r/a}. \quad 3.7.4$$

Using eqn 3.7.4 for  $B_\theta$  equation 3.7.2 can be integrated numerically to obtain  $\Delta_s$  as a function of  $\beta_p$  and  $v$ . However, it is more useful to use the internal inductance,  $\ell_i$ , rather than  $v$ . This is defined by

$$\ell_i = \frac{B_\theta^2}{B_{\theta a}^2} = \frac{2 \int_0^a B_\theta^2 r dr}{a^2 B_{\theta a}^2}. \quad 3.7.5$$

A graph of  $\ell_i(v)$  is given in Fig. 3.7.1, and an empirical fit correct to within 2% is given by

$$\ell_i = \ln(1.65 + 0.89v).$$

The parameter  $v$  is related to the ratio of edge and central  $q$  values through  $q_a/q_0 = v + 1$  and this ratio is also indicated in the figure. The calculated values of the Shafranov shift are plotted in Fig. 3.7.2 in the form of contours of equal  $(R/a)\Delta_s/a$  in the  $(\beta_p, \ell_i)$ -plane.

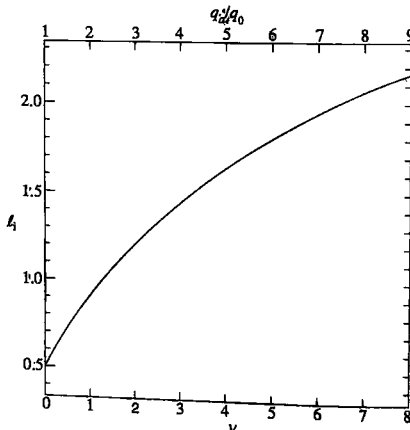
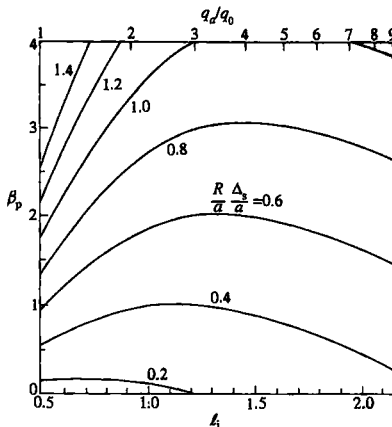


Fig. 3.7.1 Graph of the internal inductance of the current  $f = f(1 - (r/a)^2)^v$  as a function of  $v$ .



**Fig. 3.7.2** Graphs giving the Shafranov shift  $\Delta_z$  in the form of contours of equal values of  $(R/a)\Delta_z/a$  in the  $(\beta_p, \ell_i)$  plane for a parabolic pressure profile and current profiles given by eqn 3.7.1.

## 3.8

### Vacuum magnetic field

The calculation described in Section 3.6 leads to an approximate solution for the plasma equilibrium. This solution gives the variation of the poloidal magnetic field around the plasma surface at  $r = a$ . This in turn determines the vacuum magnetic field and prescribes the externally produced field necessary to maintain the equilibrium.

It is first necessary to determine  $B_\theta(a)$  from the plasma equilibrium using the large aspect-ratio expansion introduced in Section 3.6.  $B_\theta$  is given by

$$B_\theta = \frac{1}{R} \frac{\partial \psi}{\partial r} = \frac{1}{R_0 + r \cos \theta} \frac{\partial \psi}{\partial r} \quad 3.8.1$$

with

$$\psi = \psi_0 - \Delta(r) \frac{d\psi_0}{dr} \cos \theta \quad 3.8.2$$

and  $\Delta(r)$  determined by the solution of eqn 3.6.7. Thus, using  $\Delta(a) = 0$ , eqns 3.8.1 and 3.8.2 give the poloidal field at  $r = a$  as

$$B_\theta(a) = B_{\theta 0}(a) \left[ 1 - \left( \frac{a}{R_0} + \left( \frac{d\Delta}{dr} \right)_a \right) \cos \theta \right]. \quad 3.8.3$$

The quantity  $d\Delta/dr$  must now be calculated. Carrying out an integration of eqn 3.6.7 and integrating by parts on the right-hand side leads to

$$\frac{d\Delta}{dr} = \frac{2\mu_0}{rR_0B_{\theta 0}^2} \left\{ r^2 p_0 - \int_0^r \left( 2p_0 + \frac{B_{\theta 0}^2}{2\mu_0} \right) r dr \right\}. \quad 3.8.4$$

Now, using the definitions of  $\beta_p$  and  $\ell$ , given by eqns 3.8.3 and 3.7.5, and taking  $p_0(a) = 0$ , eqn 3.8.4 gives

$$\left( \frac{d\Delta}{dr} \right)_a = -\frac{a}{R_0} \left( \beta_p + \frac{\ell_1}{2} \right). \quad 3.8.5$$

Substitution of eqn 3.8.5 into eqn 3.8.3 then leads to

$$B_\theta(a) = B_{\theta 0}(a) \left( 1 + \frac{a}{R_0} \Lambda \cos \theta \right) \quad 3.8.6$$

where

$$\Lambda = \beta_p + \frac{\ell_1}{2} - 1.$$

The vacuum magnetic field must now be matched to this solution for  $B_\theta(a)$ . The vacuum field is given by the solution of the equation  $(\nabla \times \mathbf{B})_\phi = 0$ . Using eqns 3.2.2, and the present coordinates,  $(\nabla \times \mathbf{B})_\phi$  takes the form of the left-hand side of eqn 3.6.2. In the large aspect-ratio approximation the solution for  $r \ll R_0$  is

$$\psi - \frac{\mu_0 I}{2\pi} R_0 \left( \ln \frac{8R_0}{r} - 2 \right) + \frac{\mu_0 I}{4\pi} \left( r \left( \ln \frac{8R_0}{r} - 1 \right) + \frac{c_1}{r} + c_2 r \right) \cos \theta, \quad 3.8.7$$

where  $I (= -2\pi a B_{\theta 0}(a)/\mu_0)$  is the plasma current. The values of the constants  $c_1$  and  $c_2$  are determined from the requirements that  $B_\theta(a)$  matches the plasma solution given by eqn 3.8.6 and that  $B_r(a) = 0$ .

Substitution of eqn 3.8.7 into the expanded form of eqn 3.8.1 provides the vacuum solution for  $B_\theta(a)$ . Matching this to eqn 3.8.6 then gives

$$\frac{1}{a^2} c_1 - c_2 = \ln \frac{8R_0}{a} + 2\Lambda. \quad 3.8.8$$

Since  $B_r = -(1/R_0 r) \partial \psi / \partial \theta$ , the requirement  $B_r(a) = 0$  implies that the coefficient of  $\cos \theta$  in eqn 3.8.7 is zero at  $r = a$ . Thus using eqn 3.8.8 the values of  $c_1$  and  $c_2$  are found to be

$$c_1 = a^2 (\Lambda + \frac{1}{2}), \quad c_2 = - \left( \ln \frac{8R_0}{a} + \Lambda - \frac{1}{2} \right)$$

and substitution into eqn 3.8.7 gives

$$\psi = \frac{\mu_0 I}{2\pi} R_0 \left( \ln \frac{8R_0}{r} - 2 \right) - \frac{\mu_0 I}{4\pi} r \left( \ln \frac{r}{a} + \left( \Lambda + \frac{1}{2} \right) \left( 1 - \frac{a^2}{r^2} \right) \right) \cos \theta.$$

The factor  $(\ln(8R_0/r) - 1)$  in eqn 3.8.7 is an approximation, valid for  $r \ll R_0$ , to a function which is zero for  $r \rightarrow \infty$ . Thus for large

$r, \psi$  takes the form  $(\mu_0 I / 4\pi) c_2 r \cos \theta$  corresponding to a vertical field  $(\mu_0 I / 4\pi) c_2 / R_0$ , that is

$$B_\psi = -\frac{\mu_0 I}{4\pi R_0} \left( \ln \frac{8R_0}{a} + \Lambda - \frac{1}{2} \right).$$

This is the vertical magnetic field necessary to maintain the plasma in equilibrium, its effect being to provide an inward force to balance the outward hoop force on the plasma.

## 3.9

### Electric fields

In a tokamak equilibrium the electric field has three components. The two components in the magnetic surface can be regarded as either toroidal and poloidal, or as parallel and perpendicular to the magnetic field. The third component is that which is perpendicular to the magnetic surface, the 'radial' electric field.

Discharges are formed by the application of a toroidal electric field. This electric field at first produces a current in the outer region of the plasma. The current and its associated electric field then diffuse into the plasma. In the simplest model this diffusion is governed by Maxwell's equations and Ohm's law. The actual behaviour however is rather complicated because the temperature dependent electrical conductivity is determined by the ohmic heating and energy transport, and often there are instabilities associated with the process.

Another element in the behaviour is the  $E \times B$  drift. In cylindrical geometry the application of an axial electric field produces an inward drift velocity  $E_z/B_\theta$ . This inward motion leads to the build up of a negative pressure gradient and this in turn drives an outward diffusive plasma flux which, in the resulting equilibrium, balances the inward  $E \times B$  drift. In this steady state the radial velocity is zero and Ohm's law becomes simply  $E = \eta j$ . In a tokamak the behaviour is more complex partly because of the toroidal geometry and partly because the plasma flow across the magnetic field is determined by anomalous transport rather than simple resistivity.

However a simplifying feature is that in the final steady state the magnetic field in the plasma is constant in time and consequently there are no flux changes in the plasma. Thus, from Faraday's equation,  $\nabla \times E = 0$ . Using cylindrical coordinates  $(R, \phi, z)$  with the  $z$ -axis along the axis of symmetry of the torus, the  $z$ -component of this equation is

$$E_\phi = \frac{c}{R}$$

where  $c$  is a constant. The constant toroidal voltage,  $2\pi R E_\phi$ , is maintained by the imposed flux change through the torus.

Faraday's equation also gives a simple result for the poloidal electric field  $E_p$ . In a steady state the toroidal magnetic field is constant and  $\nabla \times E = 0$  implies

$$\oint E_p \cdot ds = 0$$

where the integral is taken around any poloidal circuit in the plasma. However, as will be seen below, this does not mean that  $E_p$  itself is zero.

In equilibrium each species in the plasma must satisfy its own force balance equation. The component perpendicular to the magnetic surface is

$$n_j e_j (E_n + (v_j \times B)_n) = \frac{dp_j}{dx_n}$$

where the subscript  $n$  refers to the perpendicular components. Thus the 'radial' pressure gradient force is balanced by the force from a field which is the sum of the radial electric field and the  $v_j \times B$  field arising from the species flow velocity in the surface. The contribution of the two individual terms is frame dependent. In a frame with velocity equal to  $v_j$  the pressure gradient is balanced entirely by the electric field. On the other hand, summing over species, quasi-neutrality imposes  $\sum_j n_j = 0$ . Thus in any frame the total pressure gradient is balanced by  $\sum_j n_j e_j (v_j \times B)_n$  and this is just  $j \times B$ .

## 3.10

### Particle orbits

In a uniform magnetic field a charged particle gyrates around a magnetic field line and the guiding centre of the particle's orbit moves with constant velocity along the magnetic field. In a tokamak the non-uniformity of the magnetic field leads to drifts of the guiding centre. In the absence of collisions these drifts give rise to two types of guiding centre orbit.

Particles with a sufficiently large velocity parallel to the magnetic field circulate continually round the torus. These are called *passing particles*. The remaining particles are *trapped particles*, being trapped on the outer side of the torus by the magnetic mirrors formed as a result of the poloidal variation of the magnetic field as shown in Fig. 3.10.1. Both types of orbit lie on toroidally symmetric drift surfaces. The poloidal cross-sections of such surfaces are illustrated in Fig. 3.10.2 with the projections of particle orbits. The condition for collisions to be important is derived in Section 3.12.

The orbits are constrained to lie within a distance,  $d$ , of a magnetic surface. This distance can be calculated using the conservation of the canonical angular momentum which follows from the toroidal symmetry.

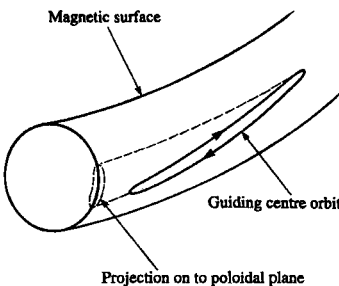


**Fig. 3.10.1** Showing the banana orbit of a trapped particle with its projection onto a poloidal plane.

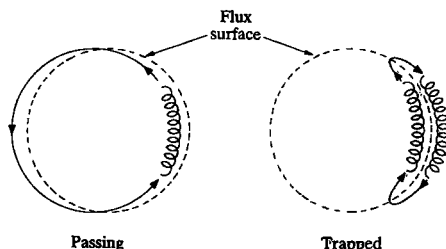


**Fig. 3.10.2** Diagram illustrating drift surfaces for the orbits of a passing particle and the (banana) orbit of a trapped particle. The major axis of the torus is on the left.

The conservation is demonstrated by calculating the change of mechanical momentum using the equation of motion in the toroidal direction

$$m_j \frac{d}{dt}(Rv_\phi) = e_j R(v \times B)_\phi. \quad 3.10.1$$

Using eqn 3.2.2 for  $B$  eqn 3.10.1 can be written

$$m_j \frac{d}{dt}(Rv_\phi) = -e_j v \cdot \nabla \psi, \quad 3.10.2$$

$\psi$  being the poloidal flux function. Since  $d\psi/dt = v \cdot \nabla \psi$ , eqn 3.10.2 becomes

$$\frac{dp_\phi}{dt} = 0$$

where the canonical momentum  $p_\phi$  is given by

$$p_\phi = m_j Rv_\phi + e_j \psi. \quad 3.10.3$$

Returning now to the calculation of the separation of the orbit from the magnetic surface, it is seen from eqn 3.10.3 that the constancy of  $p_\phi$

implies that orbit involves a change in  $\psi$ . This in turn implies a displacement of the particle across the flux surfaces. For a small displacement  $d$  from the flux surface the change in the flux function is

3.10.4

$$|\delta\psi| = |\nabla\psi|d.$$

Using eqn 3.10.3 to obtain  $\delta\psi$ , eqn 3.10.4 gives

$$d = \left| \frac{m_j}{e_j} \frac{\delta(Rv_\phi)}{|\nabla\psi|} \right|. \quad 3.10.5$$

An approximate upper bound on  $d$  may now be obtained using eqn 3.3.2 to write  $|\nabla\psi| = R_0 B_\theta$ , and then, taking the maximum value of  $\delta(Rv_\phi)$  to be  $R_0 v_\phi$ , with  $v_\phi$  the maximum value of the particle's toroidal velocity, eqn 3.10.5 gives

$$d \lesssim \left| \frac{v_\phi}{\omega_{c\theta}} \right| \quad \text{where } \omega_{c\theta} = \frac{e_j B_\theta}{m_j}.$$

The distance  $v_\phi/\omega_{c\theta}$  is the Larmour radius calculated for a particle of velocity  $v_\phi$  using the poloidal magnetic field  $B_\theta$ .

Particles with low velocity parallel to the magnetic field are trapped in the weaker magnetic field on the outer side of the torus. This behaviour is described in Section 3.11 where it is shown that, in the approximation  $(r/R) \ll 1$ , the region of velocity space for particle trapping is the cone  $v_{\parallel 0}/v_{\perp 0} \lesssim (2r/R_0)^{1/2}$  where  $v_{\parallel 0}$  and  $v_{\perp 0}$  are the velocities parallel and perpendicular to the magnetic field at the minimum value of the field on the particle orbit. The orbits of the trapped particles are calculated in Section 3.12.

The drift surfaces of passing particles are determined by two components of the particle motion. The first is the motion parallel to the magnetic field giving rise to a poloidal rotation. For particles which are strongly passing, this rotation has a frequency

$$\omega = (B_\theta/B)v_{\parallel}/r.$$

The second component is the vertical drift due to the gradient and curvature of the toroidal field as given by eqn 2.6.9, that is

$$v_d = \frac{m_j \left( v_\parallel^2 + \frac{1}{2} v_\perp^2 \right)}{e_j R B_\phi}. \quad 3.10.6$$

Combining these motions the equations for the drift orbit are

$$\frac{dR}{dt} = \omega z, \quad \frac{dz}{dt} = -\omega(R - R_c) + v_d$$

where  $z$  is the vertical coordinate and  $R_c$  is the  $R$  coordinate of the centre of the cross-section of the magnetic surface.

The resulting equation for the drift surface is

$$\left( R - R_c - \frac{v_d}{\omega} \right)^2 + z^2 = \text{constant}.$$

This is a circular surface displaced from the magnetic surface by a distance

$$d = -\frac{v_d}{\omega} \simeq -\frac{r}{R} \frac{v_{||}}{\omega_{ce}}$$

which is a factor  $r/R$  smaller than the bound derived above.

## 3.11

### Particle trapping

Since the vacuum toroidal magnetic field is proportional to  $1/R$ , the field is smaller on the outer side of the torus. Particles in this region having a small velocity parallel to the magnetic field undergo a magnetic mirror reflection as they move into the region of higher field. In the absence of collisions the particles are trapped in the low field region, undergoing repeated reflections as they bounce backward and forward between turning points.

The mirror force responsible for the trapping is given by eqn 2.5.8. Its effect is most readily understood by regarding it as the force on the magnetic moment,  $\mu$ , of the particle orbit, that is

$$F = -\mu \nabla_{||} B, \quad \text{where } \mu = \frac{\frac{1}{2} m v_{\perp}^2}{B}. \quad 3.11.1$$

As shown in Section 2.7,  $\mu$  is almost constant during the particle's motion and the criterion for particle trapping can be calculated using this result.

The magnitude of the magnetic field along a particle trajectory has its lowest value,  $B_{\min}$ , in the median plane. Denoting the velocity at this point by a subscript zero, the constancy of  $\mu$  gives

$$\frac{v_{\perp}^2}{B} = \frac{v_{\perp 0}^2}{B_{\min}}. \quad 3.11.2$$

Now, at the bounce point,  $v_{||} = 0$  and so conservation of energy implies

$$v_{\perp}^2 = v_{\perp 0}^2 + v_{||0}^2.$$

Substitution into eqn 3.11.2 then gives the field  $B_b$  at the bounce point,

$$\frac{B_b}{B_{\min}} = 1 + \left( \frac{v_{||0}}{v_{\perp 0}} \right)^2. \quad 3.11.3$$

Thus the smaller the angle  $v_{||0}/v_{\perp 0}$  the shorter the trajectory between bounces.

The condition that a particle be trapped is clearly that, given its pitch angle  $v_{\parallel 0}/v_{\perp 0}$  at the median plane, the magnetic field along the particle trajectory reaches the value  $B_b$  required for reflection as given by eqn 3.11.3. An approximate form for this condition may be obtained taking the toroidal magnetic field to have its vacuum form

$$B = B_0 \frac{R_0}{R}$$

where  $B_0$  is the field at the major radius  $R_0$ . The ratio of the maximum field to the minimum field on a surface of minor radius  $r$  is then

$$\frac{B_{\max}}{B_{\min}} = \frac{R_0 + r}{R_0 - r}.$$

Thus, using eqn 3.11.2, the requirement for trapping,  $B_b < B_{\max}$ , becomes

$$\left( \frac{v_{\parallel 0}}{v_{\perp 0}} \right) < \left( \frac{2r}{R_0 - r} \right)^{1/2}. \quad 3.11.4$$

For an isotropic distribution function such as a Maxwellian the number of the particles which are trapped is determined by the velocity space geometry and the fraction  $f$  is

$$f = \left( \frac{v_{\parallel 0}}{v_0} \right)_{\text{crit}} \quad 3.11.5$$

where  $v_0$  is the total velocity. Using  $v^2 = v_{\parallel}^2 + v_{\perp}^2$  to write

$$\left( \frac{v_{\parallel}}{v} \right)^2 = \frac{(v_{\parallel}/v_{\perp})^2}{1 + (v_{\parallel}/v_{\perp})^2}$$

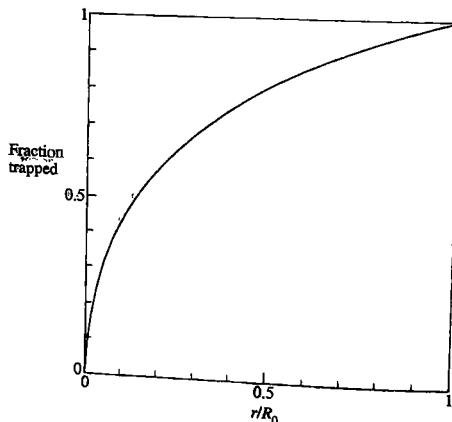


Fig. 3.11.1 Graph of the fraction of the particles which are trapped as a function of the inverse aspect-ratio of the magnetic surface,  $r/R_0$ .

and substituting the critical condition for  $(v_{\parallel}/v_{\perp 0})$  from condition 3.11.4 gives  $(v_{\parallel 0}/v_0)_{\text{crit}}$  and hence, using eqn 3.11.5 the trapped fraction

$$f = \left( \frac{2r}{R_0 + r} \right)^{1/2}.$$

For  $R_0/r < 7$  over half of the particles are trapped. A graph of  $f(r/R_0)$  is given in Fig. 3.11.1.

## 3.12

### Trapped particle orbits

The bounce motion of trapped particles can be calculated using the force given by eqn 3.11.1. Writing the major radius coordinate  $R = R_0 + r \cos \theta$ , the parallel gradient of the magnetic field,  $dB/ds$ , may be obtained using

$$B = B_0 \frac{R_0}{R} = \frac{B_0}{1 + (r/R_0) \cos \theta} \quad 3.12.1$$

which for strongly trapped particles ( $\theta \ll 1$ ), and large aspect-ratio gives

$$\frac{dB}{ds} = \frac{r B_0}{R_0} \frac{d(\theta^2/2)}{ds}. \quad 3.12.2$$

The equation of a field line is  $r d\theta/ds = B_\theta/B$  and so  $\theta = (B_\theta/r B)s$ . Thus substituting eqn 3.12.2 into eqn 3.11.1 the equation of motion is

$$\frac{d^2s}{dt^2} = -\omega_b^2 s \quad 3.12.3$$

where the bounce frequency

$$\omega_b = \frac{v_\perp}{q R_0} \left( \frac{r}{2R_0} \right)^{1/2} \quad 3.12.4$$

with  $q = r B_0 / R_0 B_\theta$ , and so the motion along the magnetic field is given by

$$s = s_b \sin \omega_b t.$$

Since  $\theta \propto s$ , the  $\theta$  component of motion is given by

$$\theta = \theta_b \sin \omega_b t. \quad 3.12.5$$

The turning point  $\theta_b$  is obtained using eqn 3.11.3 for the bounce condition. For  $\theta_b \ll 1$  eqn 3.12.1 gives

$$\frac{B_b}{B_{\min}} = 1 + \frac{r}{R_0} \frac{\theta_b^2}{2}$$

and substitution into eqn 3.11.3 gives

$$\theta_b = \frac{v_{\parallel 0}}{v_{\perp 0}} \left( \frac{2R_0}{r} \right)^{1/2}.$$

The drift surface on which the trapped particle orbit lies is now obtained by including the  $r$  component of the vertical drift due to the toroidal magnetic field as given by eqn 3.10.6. For  $v_{\perp} \gg v_{\parallel}$  this drift,  $v_d = \frac{1}{2}m_j v_{\perp}^2/e_j R B_{\phi}$ , is almost constant and its radial component is

$$\frac{dr}{dt} = v_d \sin \theta \simeq v_d \theta. \quad 3.12.6$$

Equation 3.12.5 gives

$$\frac{d\theta}{dt} = \omega_b \theta_b \left( 1 - \left( \frac{\theta}{\theta_b} \right)^2 \right)^{1/2} \quad 3.12.7$$

and the combination of eqns 3.12.6 and 3.12.7 then leads to the differential equation of the drift surface

$$\frac{dr}{d\theta} = \frac{v_d}{\omega_b \theta_b} \frac{\theta}{\left( 1 - \left( \frac{\theta}{\theta_b} \right)^2 \right)^{1/2}}. \quad 3.12.8$$

Thus, integrating eqn 3.12.8, the equation for the drift surface is

$$(r - r_0)^2 = \left( \frac{\theta_b v_d}{\omega_b} \right)^2 \left( 1 - \left( \frac{\theta}{\theta_b} \right)^2 \right). \quad 3.12.9$$

This surface has the shape of a banana, as illustrated in Fig. 3.10.2, and the orbits are called banana orbits. From eqn 3.12.9 the half-width,  $\Delta r$ , of the orbit is  $\theta_b v_d / \omega_b$ , that is

$$\Delta r = \frac{v_{\parallel 0}}{\omega_{c\theta}} \quad 3.12.10$$

where  $\omega_{c\theta} = e_j B_{\theta} / m_j$ . Thus  $\Delta r$  is equal to the Larmor radius calculated for a particle of velocity  $v_{\parallel 0}$  using the poloidal magnetic field  $B_{\theta}$ .

It is now necessary to determine the conditions of collisionality which allow particle trapping. Potentially trapped particles have velocities lying

within the cone of velocity space satisfying eqn 3.11.4. Collisions cause these particles to diffuse in velocity space and they will diffuse out of the trapping cone in a time proportional to the square of the trapping angle, that is

$$\tau_{\text{detrap}} \approx \frac{2r}{R_0} \tau_{\text{coll}} \quad 3.12.11$$

where  $\tau_{\text{coll}}$  is the collision time for a large angle scatter.

The condition for collisions to prevent trapping is that the detrapping time be shorter than the bounce time  $\omega_b^{-1}$  as given by eqn 3.12.4. Thus, using eqn 3.12.11, the collisionality condition for detrappling is

$$\tau_{\text{coll}} \lesssim \left( \frac{R_0}{r} \right)^{3/2} \frac{q R_0}{\sqrt{2v_\perp}}.$$

This condition can be estimated by using the appropriate collision times  $\tau_e$  and  $\tau_i$  for electrons and ions given in eqns 2.15.3 together with  $v_\perp = \sqrt{2}v_T$  where  $v_T$  is the thermal velocity. For typical tokamak geometry and plasma densities, this gives critical temperatures of a few hundred eV for both ions and electrons. Below the critical temperature collisions detrap the particles.

### Potato orbits

The above analysis of trapped particle orbits assumes that the deviation from a flux surface is sufficiently small that  $r$  is almost constant over the orbit. From eqn 3.12.10 the requirement for this is

$$r^{3/2} \gg q\rho R^{1/2} \quad 3.12.12$$

where  $\rho$  is the Larmor radius. For deuterons,  $q\rho R^{1/2}$  is typically a few centimetres and so, apart from a small central region, trapped deuterons have banana orbits. However,  $\alpha$ -particles, which have a Larmor radius more than an order of magnitude larger and are predominantly produced in the core of plasma, will generally fail to satisfy criterion 3.12.12. These particles have broader orbits, given the name potato orbit.

The general particle orbit can be calculated using the constancy of the particles energy and canonical toroidal angular momentum together with the adiabatic invariant  $\mu = mv_\perp^2/2B$ . Before carrying out this calculation it is instructive to derive the potato orbit for the illustrative case when the bounce point is on the magnetic axis.

The velocity parallel to the magnetic field is given by

$$\begin{aligned} v_\parallel^2 &= v^2 - v_\perp^2 \\ &= \frac{2}{m}(W - \mu B) \end{aligned} \quad 3.12.13$$

where  $W$  is the particle energy. If the turning point,  $v_{\parallel} = 0$ , is on the magnetic axis,  $W = \mu B_0$  and

$$v_{\parallel}^2 = v_{\perp}^2 \left( 1 - \frac{B}{B_0} \right). \quad 3.12.14$$

Using eqn 3.12.1, and examining large aspect-ratio, eqn 3.12.14 becomes

$$v_{\parallel}^2 = v_{\perp}^2 \frac{r}{R_0} \cos \theta. \quad 3.12.15$$

The toroidal equation of motion is

$$m \frac{dv_{\phi}}{dt} = e_j v_r B_{\theta}. \quad 3.12.16$$

Taking  $B_{\theta} = B'_{\theta} r$  and writing  $v_r = dr/dt$ , eqn 3.12.16 becomes

$$m \frac{dv_{\phi}}{dt} = e_j B'_{\theta} r \frac{dr}{dt}$$

and can be integrated to obtain

$$v_{\phi} = \frac{e B'_{\theta}}{2m} r^2. \quad 3.12.17$$

Since  $v_{\phi} = v_{\parallel} B_{\phi}/B \simeq v_{\parallel}$ , eqns 3.12.15 and 3.12.17 now combine to give the particle orbit

$$\left( \frac{r}{R_0} \right)^3 = \left( \frac{2\rho q}{R_0} \right)^2 \cos \theta$$

where  $q = B/R_0 B'_{\theta}$ . The potato orbit is shown in Fig. 3.12.1.

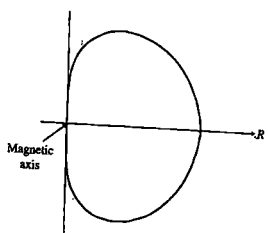


Fig. 3.12.1 Potato orbit for particle passing through the magnetic axis.

### General orbit

A particle's canonical toroidal angular momentum is

$$p_{\phi} = mRv_{\phi} - e_j \psi \quad 3.12.18$$

where  $\psi$  is the poloidal flux function defined by eqn 3.2.2, and taking  $v_{\phi} = v_{\parallel} B_{\phi}/B$

$$v_{\parallel} = \frac{p_{\phi} + e_j \psi \cdot B}{mR} \frac{B}{B_{\phi}}. \quad 3.12.19$$

Eliminating  $v_{\parallel}$  between eqns 3.12.13 and 3.12.19 gives

$$2m(W - \mu B) = \left( (p_{\phi} + e_j \psi) \frac{B}{RB_{\phi}} \right)^2. \quad 3.12.20$$

For specified constants  $W$ ,  $\mu$  and  $p_\phi$ , with the specified spatial dependence of  $B$ , and hence  $B_\phi$  and  $\psi$ , eqn 3.12.20 gives the general particle orbit.

## 3.13

### Plasma rotation

When neutral particle beams are injected into the plasma with a toroidal component to their velocity, the momentum of the beam particles is deposited in the plasma causing it to spin. Figure 3.13.1 gives an experimental example of the spinning-up of the plasma as measured using the Doppler shift of impurity spectral lines. The plasma can also be spun by ion cyclotron waves but the rotation produced is much smaller.

If particles diffusing out of the plasma were simply lost from the surface, the plasma would develop a uniform rotational velocity over the minor cross-section. Figure 3.13.2 shows a typical velocity profile and it is seen that there is a considerable fall-off towards the edge, indicating a drag force at the boundary. The radial gradient of rotation also implies a viscous drag in the plasma with an associated transport of momentum across the plasma radius.

#### Centrifugal effects

The spin of the plasma introduces a centrifugal force, which invalidates the Grad-Shafranov equation. The effect of rotation is to throw the plasma towards the outboard side of the flux surface.

The distribution of plasma on a flux surface can be calculated using the equation of pressure balance parallel to the magnetic field. For a toroidally symmetric plasma this equation reduces to the equation for pressure balance around the magnetic surface in the poloidal plane. Thus, if  $i_\phi$  is the unit vector in the toroidal direction and  $\psi$  is the poloidal flux

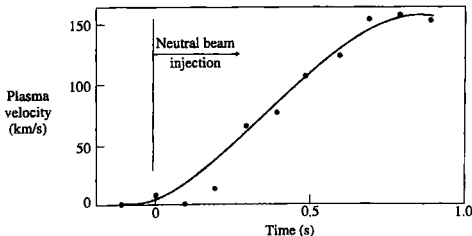


Fig. 3.13.1 Plasma velocity during neutral beam injection as measured by the Doppler shift of the impurity spectral lines (JET).

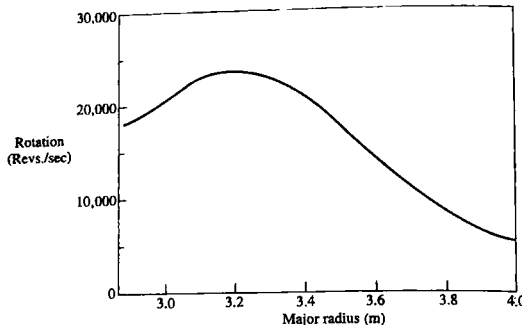


Fig. 3.13.2 Typical radial profile of toroidal rotation of a plasma spun by neutral beam injection (JET).

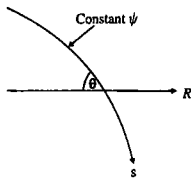


Fig. 3.13.3 Geometry used in the calculation of centrifugal effects.

function, the pressure balance equation is to be applied in the  $i_\phi \times \nabla\psi$  direction.

The geometry is illustrated in Fig. 3.13.3, which shows part of a flux surface. The distance along the surface is  $s$  and the major radius coordinate is  $R$ . At any point on the surface the poloidal angle between the major radius vector and the flux surface is  $\theta$ . For a given surface,  $s = s(R)$  and so for any quantity  $y$

$$\frac{dy}{ds} = \frac{dy}{dR} \frac{dR}{ds} = \frac{dy}{dR} \cos \theta. \quad 3.13.1$$

The pressure balance equation for any species  $j$  is

$$T_j \frac{dn_j}{ds} = n_j m_j \omega^2 R \cos \theta + n_j Z_j e E_s \quad 3.13.2$$

where the temperature  $T_j$  is taken to be constant on a flux surface,  $n_j$  is the particle density,  $m_j$  and  $Z_j e$  are the particle mass and charge,  $E_s$  is the component of electric field along  $s$ , and the toroidal rotation frequency,  $\omega$ , will be taken to be the same for all species.

Using relation 3.13.1

$$\frac{dn_j}{ds} = \frac{dn_j}{dR} \cos \theta \quad 3.13.3$$

and, introducing the electrostatic potential  $\phi$ ,

$$E_s = -\frac{d\phi}{ds} = -\frac{d\phi}{dR} \cos \theta \quad 3.13.4$$

where the derivatives are all at constant  $\psi$ .

Substitution of eqns 3.13.3 and 3.13.4 into eqn 3.13.2 gives

$$T_j \frac{dn_j}{dR} = n_j m_j \omega^2 R - n_j Z_j e \frac{d\phi}{dR}$$

and this equation can be integrated to give the density distribution

$$n_j = n_{j0} \exp \left( \frac{\frac{1}{2} m_j \omega^2 (R^2 - R_0^2) - e Z_j \phi}{T_j} \right) \quad 3.13.5$$

with  $n_j = n_{j0}$  and  $\phi = 0$  at a position on the surface  $R = R_0$ .

There is an eqn 3.13.5 and an unknown density,  $n_j$ , for each species. There is also an additional unknown,  $\phi$ . The required further equation is the equation for quasi-neutrality

$$\sum_j n_j Z_j = 0. \quad 3.13.6$$

Thus eqns 3.13.5 and 3.13.6 define the problem.

For a pure hydrogenic plasma, the ion and electron densities are given by

$$n_i = n_{i0} \exp \left( \frac{\frac{1}{2} m \omega^2 (R^2 - R_0^2) - e \phi}{T_i} \right) \quad 3.13.7$$

and

$$n_e = n_{e0} \exp \left( \frac{e \phi}{T_e} \right) \quad 3.13.8$$

where the centrifugal force on the electrons has been taken to be negligible.

Using quasi-neutrality,  $n_i = n_e (= n)$  eqns 3.13.7 and 3.13.8 give the potential

$$\phi = \frac{T_e}{T_i + T_e} \frac{m_i \omega^2}{2e} (R^2 - R_0^2)$$

and the particle density

$$n = n_0 \exp \frac{m_i \omega^2 (R^2 - R_0^2)}{2(T_i + T_e)} \quad 3.13.9$$

Expanding the exponential in 3.13.9

$$n \approx n_0 \left( 1 - \frac{m_i \omega^2 (R^2 - R_0^2)}{2(T_i + T_e)} \right)$$

and, using the aspect-ratio expansion, the total difference,  $\Delta n$ , in density around a surface is given by

$$\Delta n = n_0 M^2 \frac{2r}{R_m}$$

where  $M = \omega R_m / ((T_i + T_e) / m_i)^{1/2}$ ,  $r$  is the minor radius of the magnetic surface and  $R_m$  is the major radius of the plasma.

The displacement to the outboard side of the plasma is sometimes observed in the soft X-ray emission from impurities. Because impurity ions have a larger mass than hydrogenic ions it is possible for the impurity ion flow to have a Mach number greater than one and for quite large variations of the impurity density to arise on a plasma surface. Figure 3.13.4 shows an experimental example.

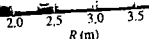


**Fig. 3.13.4** Toroidal rotation of the plasma throws the impurity ions to the outboard side of the plasma. The tomographic reconstruction of the soft X-ray emission shows the resulting asymmetry (Ingesson, L.C. et al., Nuclear Fusion 38, 1675 (1998)).

## 3.14

### Current drive

The concept of a tokamak reactor operating with a current generated by an induced electric field, and therefore as a pulsed device, has substantial drawbacks related to the fatigue stress produced by the thermal cycling and the interruption of the power output. These problems could be removed by a non-inductive current drive system which would make continuous operation feasible. The development of high poloidal beta regimes has produced plasmas in which more than 70% of the plasma current is carried in the form of the plasma self-generated bootstrap current. Such operating scenarios bring the efficiency demanded of the non-inductive current drive system within the range of technical feasibility. Non-inductive current drive is also required for control of the radial profile of the current density in order to avoid or control mhd instabilities and to optimize plasma confinement. Optimization of the plasma current density profile may require a combination of several non-inductive current drive schemes. Current drive in the plasma centre can easily be provided by fast waves, high energy neutral beam injection or electron cyclotron waves, whereas efficient current drive at large minor

radius is more difficult because of the lower electron temperature and the deleterious effects of trapped electrons. However, lower hybrid current drive can be used to generate current efficiently for  $r/a > 0.5$ . There are several current drive schemes available with different attributes and limitations. The following sections describe the features of the main schemes.

### Neutral beam injection

Neutral beam injection produces a current of fast ions circulating around the torus. The slowing down of these fast ions by collisions with electrons causes the electrons to drift toroidally in the same direction as the fast ions. The electron current due to this drift is in the reverse direction to the fast ion current, so there is some cancellation between these two components. The degree of cancellation depends on the charge,  $Z_{fe}$ , of the fast beam ions, the effective plasma ion charge,  $Z_{eff}$ , and the number of trapped electrons. Since there can be near cancellation of the fast ion and electron currents, correct calculation of the net current requires accurate evaluation of the electron current. In the usual regime, where the electron thermal velocity significantly exceeds the fast ion velocity, use of the Fokker–Planck equation to calculate the beam driven current in the large aspect-ratio approximation and in the low collisionality banana regime gives,

$$\frac{I}{I_f} = 1 - \frac{Z_f}{Z_{eff}} + 1.46\sqrt{\varepsilon} \frac{Z_f}{Z_{eff}} A(Z_{eff}) \quad 3.14.1$$

where  $I/I_f$  is the ratio of the net current to the fast ion current and  $\varepsilon = r/R$  is the inverse aspect-ratio. For fast ion velocities which are much less than the electron thermal velocity, as is normally the case, values of the function A range from 1.67 for  $Z_{eff} = 1$ , to 1.18 for  $Z_{eff} = 4$ . In eqn 3.14.1 the second term on the right hand side represents the reverse electron current in the absence of trapped electrons and the third term takes their effect into account. Equation 3.14.1 is normally applied locally in the plasma to calculate the beam driven current density at a given magnetic flux surface. In a tokamak the fast ion current stacks up during the injection period as the fast ions circulate repeatedly around the torus. A steady state is reached when the build up rate of current due to stacking is balanced by the loss rate due to slowing down through collisions with the plasma electrons and bulk ions, or to charge exchange of the fast ions with neutral atoms. In the case where charge exchange dominates the loss process, the fast ions can be considered to be at constant speed so that the fast ion current density on a specific flux surface is given by,

$$j_f = j_i v_{||} \tau_{cx} / 2\pi R$$

where  $j_i$  is the injected current density,  $v_{||}$  is the fast ion velocity parallel to the magnetic field and  $\tau_{cx}$  is the charge exchange time. The fast ion

current density can also be written in terms of the fast ion source rate per unit volume,  $S$ ,

$$j_f = S \tau_{ce} e Z_f v_{f\parallel}$$

It is usually necessary to use a neutral beam power deposition code, which takes into account the injection geometry, to determine the radial profile of the beam deposition.

Furthermore, to compute the local fast ion current density,  $j_f$ , a two-dimensional Fokker-Planck or Monte Carlo calculation of the beam ion velocity distribution is generally necessary, including the effects of trapping of the fast ions. In the absence of trapping, a relatively simple analytic solution can be found and the current density is given by,

$$j_f = \frac{S \tau_s e Z_f v_0}{(1 + u_c^2)} \int_0^1 f_1(u) u^3 du$$

where  $\tau_s$  is the fast ion slowing down time and  $u$  is the fast ion velocity normalized to the injection velocity,  $v_0$ . The distribution function  $f_1$  is the first order Legendre polynomial component of  $f$  given by

$$f_1 = u^{2\beta} \left[ \frac{1 + u_c^3}{u^3 + u_c^3} \right]^{1+2\beta/3}$$

where

$$\beta = \frac{m_i Z_{\text{eff}}}{2 m_f \bar{Z}}$$

$$u_c^3 = \frac{3\sqrt{\pi}}{4} \frac{m_e \bar{Z} v_{fe}^3}{m_i v_0^3}$$

and

$$\bar{Z} = \sum_i \frac{m_i n_i Z_i^2}{m_i n_e}$$

the subscript  $i$  referring to the plasma ions.

The efficiency for generating the fast ion current, defined as  $j_f$  divided by the power per unit volume  $P_d$  ( $= \frac{1}{2} m_f v_0^2 S$ ), is given by

$$\frac{j_f}{P_d} = \frac{2 \tau_s e Z_f}{m_f v_0 (1 + u_c^2)} \int_0^1 f_1(u) u^3 du$$

Evaluation of this expression shows that the highest efficiency is achieved by operating at the highest electron temperature and lowest

electron density in order to maximize  $\tau_e$ , and by choosing the fast ion energy to be close to the so-called critical energy, for which  $u_c \sim 1$ , at which the effects of collisions with electrons and collisions with ions are approximately equal, as described in Section 5.4. In practice, the beam energy is usually determined by beam penetration requirements. The radial profile of the beam driven current is determined by the beam energy, the deposition profile, and the injection angle.

Neutral beam current drive has been observed in most large tokamaks, although in many cases the neutral beam injection systems were not optimized for high current drive efficiency. Experimental measurements are generally in good agreement with theoretical predictions. A neutral beam driven current of 0.34 MA was measured in TFTR for an injected power of 11.5 MW. The bootstrap current was calculated to be 0.5 MA in this case, indicating that the total plasma current of 0.9 MA was predominantly non-inductively driven. In DIII-D and JT-60U, the entire plasma current of 0.35 and 0.5 MA, respectively, has at low density, been maintained by a combination of bootstrap current and neutral beam current drive. In JET, a neutral beam driven current of 0.25 MA has been observed. All these results were obtained using neutral beams based on the acceleration and subsequent neutralization of positive ion beams. However, for the plasma parameters characteristic of a fusion reactor, adequate beam penetration requires very high energy neutral beams with energies  $\sim 1$  MeV. Since the neutralization efficiency of positive ion beams decreases rapidly with increasing energy, systems based on negative ion beams must be deployed in a reactor as explained in Section 5.5. Such a system has been installed on JT-60U where a neutral beam driven current of 1 MA was measured for an injected power of 3.75 MW at a beam energy of 360 keV.

### Lower hybrid current drive

The most effective non-inductive current drive scheme in present day tokamaks is based on current drive by travelling waves in the lower hybrid range of frequencies. Present experiments use frequencies in the range 0.8–8 GHz. By using a phased waveguide array antenna, power may be coupled to lower hybrid waves with high phase velocity parallel to the magnetic field. These waves are resonant with high energy electrons having a parallel velocity which matches the phase velocity of the wave and absorption takes place through Landau damping as described in Section 5.7. The phased array antenna ensures that most of the power is coupled to waves propagating in a particular toroidal direction so that the wave-particle interaction occurs preferentially with electrons travelling in that direction. In the simplest picture, the lower hybrid waves directly impart momentum to these electrons which, in steady state, leads to the generation of a current determined by the balance between the momentum input and the loss by collisions to the ions. However, a more important effect is that the accelerated electrons become less collisional and

lose momentum at a slower rate. Since electrons moving in a particular toroidal direction are preferentially heated, this gives rise to a so-called 'asymmetric resistivity' and accounts for 75% of the driven current.

The action of the lower hybrid wave is to accelerate electrons from a velocity  $v_{\parallel}$ , parallel to the magnetic field, to a velocity  $v_{\parallel} + \Delta v_{\parallel}$ . This requires an incremental energy input per unit volume

$$\Delta E = n_e m_e v_{\parallel} \Delta v_{\parallel}.$$

Assuming that the velocity of an electron  $v$  is randomized by collisions on a momentum destruction timescale  $1/\nu(v)$ , this incremental energy input produces an incremental current density  $j$  that persists for a time  $1/\nu$

$$j = n_e e \Delta v_{\parallel} = \frac{\Delta E e}{m_e v_{\parallel}}.$$

The power density required to refresh this current at time intervals of  $1/\nu$  is

$$p_d = v \Delta E$$

Hence the 'current drive efficiency' is given by

$$\frac{j}{p_d} = \frac{e}{m_e v_{\parallel} \nu}.$$

For  $v_{\parallel} \gg v_{Te}$ ,  $\nu \propto 1/v_{\parallel}^3$ , and so

$$\frac{j}{p_d} \propto v_{\parallel}^2.$$

This simple treatment serves to illustrate the important influence of collisionality leading to a strong dependence of the current drive efficiency on the parallel electron velocity and hence the parallel wave phase velocity (since the parallel phase velocity  $\omega/k_{\parallel} = v_{\parallel}$  at Landau resonance, where  $k_{\parallel}$  is the parallel component of the wave-vector). An accurate calculation of the current drive efficiency requires a two-dimensional treatment of velocity space dynamics. For a general velocity displacement in the direction  $\hat{g}$  it can be shown that

$$\frac{j}{p_d} = \frac{e}{v_0 m_e v_{Te}^3} \frac{2}{(5 + Z_{eff})} \frac{\hat{g} \cdot (\partial/\partial v) (v_{\parallel} v^3)}{\hat{g} \cdot (\partial/\partial v) v^2} \quad 3.14.2$$

where  $v_0$  is a characteristic electron-ion collision frequency given by

$$v_0 = \frac{\omega_{pe}^4 \ln \Lambda}{4\pi n_e v_{Te}^3}.$$

For lower hybrid waves  $\hat{g}$  is in the parallel direction and from eqn 3.14.2

$$\frac{j}{p_d} \propto v_{\parallel}^{-1} (v_{\parallel}^2 + v_{\perp}^2)^{3/2} + 3v_{\parallel} (v_{\parallel}^2 + v_{\perp}^2)^{1/2} \quad 3.14.3$$

where the velocity  $v_{\perp}$ , perpendicular to the magnetic field, is much less than  $v_{\parallel}$  for the resonant electrons. Equation 3.14.3 shows that the term arising from the energy input is three times larger than the term arising from the momentum input. Thus the asymmetric resistivity provides three quarters of the current. This effect requires no momentum input from the wave since the parallel momentum of the current carrying electrons is balanced by an equal and opposite momentum in the ions, which carry a negligible amount of current due to their much higher mass and hence lower velocity for the same momentum.

It is convenient to introduce normalized parameters  $u = v/v_{Te}$ ,  $J = j/(n_e e v_{Te})$  and  $P_d = p_d/(n_e m_e v_0 v_{Te}^2)$ . Equation 3.14.2 then reduces to

$$\frac{J}{P_d} = \frac{2}{(5 + Z_{\text{eff}})} \frac{\hat{s} \cdot (\partial/\partial u) (u_{\parallel} u^3)}{\hat{s} \cdot (\partial/\partial u) u^2}. \quad 3.14.4$$

For lower hybrid waves in the high velocity limit,  $u_{\parallel} \gg u_{\perp}$ , this gives

$$\frac{J}{P_d} \propto u_{\parallel}^2 \propto \frac{(\omega/k_{\parallel})^2}{v_{Te}^2}.$$

The efficiency of any current drive method in practical units is given by

$$\frac{I}{P} = \frac{A j}{2\pi R A p_d}$$

where  $I$  is the total current driven,  $P$  is the total power and  $A$  is the plasma cross-sectional area. In terms of the normalized current and power densities defined above this becomes

$$\frac{I}{P} = 0.061 \frac{T_e}{R(n_e/10^{20}) \ln \Lambda} \left( \frac{J}{P_d} \right) \text{AW}^{-1} \quad T_e \text{ in keV}$$

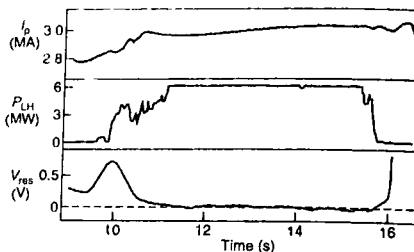
Thus, in the suprathermal, but non-relativistic, limit discussed above for lower hybrid waves  $I/P$  scales quadratically with the phase velocity (through the factor  $J/P_d$ ), inversely with major radius and density, and has only a weak dependence on  $Z_{\text{eff}}$ . In this particular case there is no dependence on electron temperature since  $J/P_d$  varies inversely as  $v_{Te}^2$ . This is not the case for most other schemes which do not generate suprathermal electrons and so have a favourable scaling with  $T_e$ . However, the capability of lower hybrid waves to give high current drive efficiency even in moderate temperature plasmas, due to strong Landau damping on suprathermal electrons, has resulted in an abundant database of results compared with other schemes, giving rise to the convention of defining a current drive figure of merit  $\eta$  in terms of the scaling for suprathermal electrons, namely,

$$\eta = \frac{RI}{P} \frac{\bar{n}_e}{10^{20}} \text{m}^{-2} \text{AW}^{-1}$$

where  $\bar{n}_e$  is the line-average electron density. For most schemes  $\eta$  depends on  $T_e$ . A full treatment of the problem, in which the response of the

**Fig. 3.14.1** Sustainment of the full plasma current in a 3 MA JET discharge by lower hybrid current drive. Signals shown are plasma current  $I_p$ , lower hybrid power  $P_{LH}$  and resistive loop voltage.

$V_{res} = V_{loop} - (1/I_p)d/dt(\frac{1}{2}L_p^2)$ . The resistive voltage is the loop voltage corrected for inductive effects and represents the voltage required to sustain the plasma current. A zero resistive voltage indicates that the plasma current is fully sustained by the lower hybrid waves.  
(Ekedahl, A. et al., *Nuclear Fusion* 38, 1397 (1998)).



electron distribution function to a finite spectrum of launched waves is calculated, requires a solution of the two-dimensional Fokker-Planck equation including electron trapping and relativistic effects.

In many tokamak experiments it has been possible to drive the complete plasma current by lower hybrid waves. Some experiments have also demonstrated discharge start-up by lower hybrid waves. Plasma currents of 3.6 and 3 MA have been fully sustained by lower hybrid current drive in JT-60U and JET (Fig. 3.14.1), respectively. A current drive figure of merit  $\eta > 0.3 \text{ AW}^{-1}\text{m}^{-2}$  has been achieved in these devices. In TRIAM-1 M, a plasma current of 20 kA was sustained for 2 h whilst in Tore-Supra a plasma current of 0.8 MA was sustained for 2 min by lower hybrid waves. Current drive at high density,  $\sim 10^{20} \text{ m}^{-3}$ , has been demonstrated using high frequency lower hybrid waves in Alcator-C and FTU.

In present experiments lower hybrid waves typically transit the plasma many times before full absorption occurs. Nevertheless, the effectiveness of lower hybrid waves for control of the radial profile of plasma current has been demonstrated in many tokamaks. As shown above, waves with the highest phase velocity give the highest current drive efficiency but these waves also have the poorest penetration due to mode conversion. Although lower hybrid waves are expected to be absorbed in a single pass for plasma parameters characteristic of a fusion reactor, strong Landau damping and mode conversion are expected to limit penetration of the waves to the outer half of the plasma in this case.

### Fast wave electron current drive

Fast wave current drive using fast magnetosonic waves in the ion cyclotron frequency range is similar to that by lower hybrid waves in that the waves damp at the Landau resonance. However, the force on the electrons is due not only to the parallel electric field of the wave but also to the interaction between the parallel gradient of the wave's magnetic field and the magnetic moment of the electron arising from its gyro-motion, so-called transit time magnetic pumping (TTMP). The net interaction is much

weaker than for lower hybrid waves. Furthermore, other absorption mechanisms, associated with cyclotron resonances for example, can compete with electron Landau damping and TTMP. Typically only 10–20% of the launched power is absorbed in a single pass through the plasma in existing tokamaks. Power is deposited centrally, typically within  $r/a \sim 0.4$ , and the interaction does not produce suprathermal electrons. The single pass absorption is expected to increase to  $\sim 50\%$  in the next generation of tokamaks such as ITER. A current of about 100 kA has been driven in DIII-D and Tore-Supra using fast waves. In DIII-D the current drive figure of merit,  $\eta$ , was observed to increase linearly with central electron temperature, in agreement with theoretical predictions, reaching values in excess of  $0.04 \text{ AW}^{-1} \text{ m}^{-2}$ . In ITER, a current drive figure of merit in the range  $0.15\text{--}0.25 \text{ AW}^{-1} \text{ m}^{-2}$  is expected, depending on the electron temperature. Unlike some other schemes, fast wave current drive has no penetration problems with the high density plasmas required in reactors.

### Electron cyclotron current drive

In the case of lower hybrid current drive, only 25% of the driven current arises from direct momentum input from the waves (eqn 3.14.3), the remaining 75% resulting from the energy input which gives rise to an ‘asymmetric resistivity’. In fact even waves with negligible momentum, such as electron cyclotron waves, can be used to drive current, by heating only those electrons circulating in a particular toroidal direction. These preferentially heated electrons collide less often with the ions than do those electrons circulating in the opposite toroidal direction. Thus the electron population transfers net parallel momentum to the ions and the two species drift in opposite toroidal directions generating a current.

The effect can be quantified by further analysis of eqn 3.14.4. The action of the electron cyclotron wave is to accelerate electrons primarily in the perpendicular direction. In this case eqn 3.14.4 gives

$$\frac{J}{P_d} = \frac{2}{(5 + Z_{\text{eff}})} \left( \frac{3}{2} u_{\parallel} u \right). \quad 3.14.5$$

For lower hybrid waves which accelerate electrons primarily in the parallel direction eqn 3.14.4 gives

$$\frac{J}{P_d} = \frac{2}{(5 + Z_{\text{eff}})} \left( \frac{u}{2u_{\parallel}} \right) (4u_{\parallel}^2 + u_{\perp}^2). \quad 3.14.6$$

Comparing eqns 3.14.5 and 3.14.6 we see that, in the high velocity limit where  $u_{\parallel} \gg u_{\perp}$  the normalized electron cyclotron current drive efficiency is  $3/4$  of the lower hybrid current drive efficiency. The results of linearized Fokker–Planck theory are shown in Fig. 3.14.2 and agree with the above analysis for suprathermal parallel electron velocities.

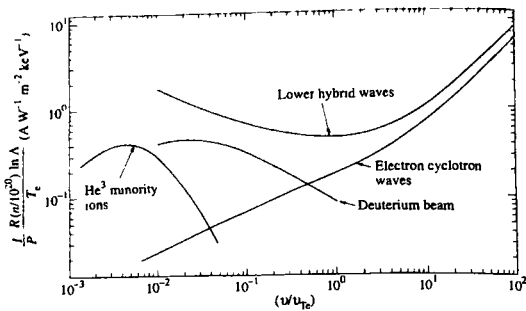


**Fig. 3.14.2** Comparison of theoretical current drive efficiency for (i) deuterium beams injected into a D-T plasma; (ii) Landau damping of lower hybrid waves; (iii) electron cyclotron waves, and (iv) He<sup>3</sup> minority ions in a deuterium plasma. The scale gives the ratio of the total current  $I$  (A) to the total power injected,  $P$  (W), into a tokamak plasma of major radius  $R$  (m), density  $n$  ( $10^{30}$  m<sup>-3</sup>), and temperature  $T_e$  (keV).  $v$  is the wave phase velocity, or beam ion velocity, and  $v_{Te}$  the electron thermal velocity.

The electron cyclotron resonance condition for interaction in the vicinity of the  $l$ th cyclotron harmonic is given by

$$\omega - l\omega_{ce}(R) = k_{\parallel}v_{\parallel} \quad 3.14.7$$

where the electron gyro-frequency  $\omega_{ce}$  is a function of major radius through the dependence of the toroidal magnetic field on  $R$ . The frequency shift of the resonance, represented by the term on the right hand side of eqn 3.14.7, arises due to the Doppler effect. From the resonance condition it can be seen that, for a given directivity (given sign of  $k_{\parallel}$ ), the resonant parallel velocity changes sign on opposite sides of the 'unshifted' resonance,  $\omega = l\omega_{ce}$ , giving rise to opposing toroidal currents. Hence strong single pass absorption is required for high current drive efficiency to ensure that the waves are damped on one side of the resonance layer only. Fortunately this is usually the case in present tokamaks. The strong, localized absorption of waves in the electron cyclotron frequency range, and the ability to control the absorption location by steering of the launched microwave beam or adjustment of the toroidal magnetic field, makes electron cyclotron waves particularly suitable for the control of MHD instabilities by local current drive. Control of sawteeth and stabilization of tearing modes by electron cyclotron current drive has been effectively demonstrated in a number of tokamaks. Current drive efficiencies have been compared with theoretical predictions made using ray tracing codes to obtain the power deposition, coupled to Fokker-Planck calculations of the current density. Measured currents are in reasonable agreement with such calculations if the effects of electron trapping, relativity and radial electron diffusion are included. A current drive figure of merit in excess of  $0.03 \text{ AW}^{-1} \text{ m}^{-2}$  has been reported in T-10, and in TCV a plasma current of  $\sim 150 \text{ kA}$  has been fully sustained using electron cyclotron waves.

Electron cyclotron waves are effective for both current drive in the plasma core and off-axis current drive. For core current drive in ITER,

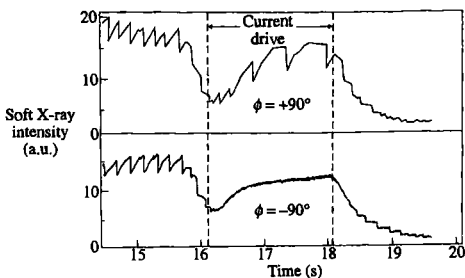
a current drive figure of merit in the range  $0.2\text{--}0.3 \text{ AW}^{-1} \text{ m}^{-2}$  may be achievable, depending on the electron temperature and the electron cyclotron system parameters. However, for current drive at large minor radius, electron trapping can have a strong deleterious effect on the current drive efficiency.

### Fast wave minority ion current drive

The same principles can be applied to current drive, in the ion cyclotron frequency range, by asymmetric heating of a minority species of ions introduced into the plasma. The heating, through its effect on ion-ion collisions, creates oppositely drifting ion species, and a net current flows if the charge to mass ratios of the ions are different. As in the case of neutral beam injection, the friction between the ions and electrons causes an electron current to flow which tends to cancel the ion current. The efficiency for the case of  $\text{He}^3$  minority ions in a deuterium plasma is shown in Fig. 3.14.2, and is similar in magnitude to that for current drive by neutral beams.

Evidence for such current drive has been obtained in JET using directed fast waves and a hydrogen minority resonance touching the  $q = 1$  surface. The minority ion current drive is predicted to produce a local bipolar perturbation to the current density profile, due to absorption either side of the unshifted resonance, which leads to opposing driven currents for a fixed wave directivity. When positioned close to the  $q = 1$  surface, such a local bipolar current density perturbation affects the sawtooth instability. This was the case in the JET experiment, as shown in Fig. 3.14.3. With waves directed anti-parallel to the plasma current the sawtooth oscillations were almost completely stabilized. With waves in the opposite direction the sawtooth oscillations were destabilized and the sawteeth became short and of small amplitude. The plasma temperature profile was flattened inside the sawtooth inversion radius at a value of 4 keV compared with a peaked temperature profile of 6 keV central value for the stabilizing antenna phase. This temperature difference resulted in a factor of two change in the D-D fusion reactivity.

**Fig. 3.14.3** The effect of minority current drive on the stability of sawtooth oscillations, as seen on the soft X-ray intensity, when the current is driven at the  $q = 1$  surface. With the phase of the antenna currents  $\phi = +90^\circ$  the sawteeth are stabilized for extended periods. For  $\phi = -90^\circ$  the direction of driven current is reversed and the sawteeth are less stable, taking the form of very rapid, small amplitude oscillations, the level of the X-ray intensity being the same as that after the sawtooth relaxations in the  $\phi = +90^\circ$  case. (Bhatnagar, V.P. et al. *Nuclear Fusion* 34, 1579 (1994)).



**Summary**

There exists a wide range of non-inductive current drive methods possessing a variety of different characteristics and attributes. For example electron cyclotron current drive offers the potential of localized, controllable non-inductive current drive, well-suited for control of mhd instabilities, whilst lower hybrid current drive offers the potential of high current drive efficiency in the outer half of the plasma. The plasma current has been fully sustained in many tokamaks by non-inductive current drive. Due to the interaction with suprathermal electrons, lower hybrid current drive has produced the largest current so far in existing devices. It is likely that a combination of schemes will be employed in a reactor. Measured current drive efficiencies are generally in good agreement with theory, although the experimental database is rather limited at high plasma densities. The projected non-inductive current drive efficiency in a steady-state tokamak reactor leads to an intolerably high recirculating power unless a large fraction of the plasma current is self-generated by the bootstrap effect. Bootstrap currents of more than 70% of the total plasma current have been established in existing tokamaks.

**Bibliography**

Toroidal equilibrium is described in chapters of the books Miyamoto, K. *Plasma physics for nuclear fusion*. MIT Press, Cambridge, Mass. (1989).

Bateman, G. *MHD instabilities*. MIT Press, Cambridge, Mass. (1978).

Freidberg, J.P. *Ideal magnetohydrodynamics*. Plenum Press, New York (1987).

White, R.B. *Theory of toroidally confined plasmas*. Imperial College Press (2001).

The general equilibrium problem is treated in

Shafranov, V.D. Plasma equilibrium in a magnetic field. *Reviews of plasma physics* (ed. Leontovich, M.A.) Vol. 2, p. 103, Consultants Bureau, New York (1966).

An extensive treatment of the properties of magnetic field configurations is given in

Solovev, L.S. and Shafranov, V.D. Plasma confinement in closed magnetic systems. *Reviews of plasma physics* (ed. Leontovich, M.A.) Vol. 5, p. 1, Consultants Bureau, New York (1966).

A more practical account of the tokamak case is given in the review paper

Mukhovatov, V.S. and Shafranov, V.A. Plasma equilibrium in a tokamak. *Nuclear Fusion* 11, 605 (1971).

**Grad-Shafranov equation**

Which should perhaps be called the SLSG Equation, the original references being

Shafranov, V.D. On magnetohydrodynamical equilibrium configurations. *Zhurnal Experimentalnoi i Teoreticheskoi Fiziki* 33, 710 (1957) [Soviet Physics JETP 6, 545 (1958)].

Lust, R. and Schlüter, A., Axialsymmetrische magnetohydrodynamische gleichgewichtskonfigurationen. *Zeitschrift für Naturforschung* 12A, 850 (1957).

and

Grad, H. and Rubin, H. Hydromagnetic equilibria and force-free fields. *Proceedings of the 2nd United Nations International Conference on the Peaceful Uses of Atomic Energy* Geneva 1958 Vol. 31, 190 Columbia University Press, New York (1959).

**Large aspect-ratio**

Shafranov, V.D. Section 6 of Plasma equilibrium in a magnetic field. *Reviews of plasma physics* (ed. Leontovich, M.A.) Vol. 2, p. 103, Consultants Bureau, New York (1966).

### Vacuum magnetic field

Mukhovatov, M.S. and Shafranov, V.D. Plasma equilibrium in a tokamak. *Nuclear Fusion* 11, 605 (1971).

### Particle orbits and particle trapping

Particle trapping in tokamaks is described in Kadomtsev, B.B. and Pogutse, O.P. Plasma instability of trapped particles in toroidal geometry. *Zhurnal Experimentalnoi i Teoreticheskoi Fiziki* 51, 1734 (1966) [Soviet Physics, *JETP* 29, 1172 (1967)].

and an account is given in Chapter 3 of

Miyamoto, K. *Plasma physics for nuclear fusion*. MIT Press, Cambridge, USA (1989).

Potato orbits were identified and described by

Stringer, T.E. Radial profile of  $\alpha$ -particle heating in a tokamak. *Plasma Physics* 16, 651 (1973).

### Plasma rotation

The centrifugal effects of plasma rotation were described in Wesson, J.A. Poloidal distribution of impurities in a

rotating tokamak plasma. *Nuclear Fusion* 37, 577 (1997).

### Current drive

Current drive by neutral beam injection was suggested by Ohkawa, T. Principles of current drive by beams. *Nuclear Fusion* 10, 185 (1970).

The use of high velocity RF waves was proposed by Fisch, N.J. Principles of current drive by Landau damping of travelling waves. *Physical Review Letters* 41, 873 (1978).

A useful overview of current drive is provided by the *Proceedings of IAEA technical committee meeting on non-inductive current drive in tokamaks*, Culham 1983, Culham Laboratory Report CLM-CD (1983).

A comprehensive and extremely clear review of the theory of most types of non-inductive current drive methods is that of Fisch N.J. *Reviews of Modern Physics*, 59, 175 (1987).

The application of non-inductive methods for optimizing the current drive and profile control is discussed in

*US-Japan Workshop on the Physics Issues for Steady-State Tokamaks*, June 1993, RIAM, Kyushu University, FURKU report 93-02(02).

**4**

# **Confinement**

---

**4.1****Tokamak confinement**

To achieve thermonuclear conditions in a tokamak it is necessary to confine the plasma for a sufficient time, as described in Chapter 1. The global energy confinement time is defined by

$$\tau_E = \frac{\int \frac{3}{2}n(T_i + T_e) d^3x}{P}, \quad 4.1.1$$

where  $P$  is the total power input. Confinement is limited by thermal conduction and convection processes but radiation is also a source of energy loss.

In the absence of instabilities the confinement of a toroidally symmetric tokamak plasma is determined by Coulomb collisions. The transport of particles and energy which would occur under these circumstances has been calculated. Unfortunately the transport which actually occurs does not agree with the calculated values. In particular the thermal transport by electrons can be up to two orders of magnitude higher than predicted.

It is thought that the observed anomalous transport is due to instability of the plasma, which causes the particles and the energy to escape at a higher rate. This could occur either through perturbations which allow transport across the nested magnetic field structure or through a break-up of this structure, allowing particles and energy to flow along magnetic field lines which themselves follow stochastic trajectories. However, although fluctuations of various sorts are observed in tokamaks, their relation to the observed transport is not clear. Furthermore, although a range of instabilities has been predicted theoretically, there is no conclusive agreement between calculations of the resulting transport and the experimental behaviour.

In the absence of a theoretical understanding of confinement, and given the need to predict the confinement properties of future tokamaks, it has been necessary to resort to empirical methods. The simplest of these is to accumulate data from a number of tokamaks, each operated under a range of conditions, and to use statistical methods to determine the dependence of the confinement time on the parameters involved. This provides scaling expressions which, within some error, allow extrapolation to projected tokamaks.

Nevertheless, to explain the so-called anomalous transport is one of the most important challenges to theoretical tokamak physics. It is inevitable, however, that the route to understanding must start with an analysis of the irreducible transport arising from collisions. In particular this provides a basis against which to measure the anomalous effects. Even this basic case, without the complications of instabilities, is quite subtle.

In a cylindrical plasma the collisional transport of particles and energy can be understood in terms of a simple diffusion process, and this is called

classical transport. The particles suffer collisions with a characteristic collision time  $\tau_c$ . A collision allows the particle to step across the magnetic field with a step length equal to the Larmor radius,  $\rho$ . This gives a diffusion coefficient  $D \sim \rho^2/\tau_c$  and hence an approximate confinement time  $\tau \sim a^2/D$ , so that

$$\tau \sim \left(\frac{a}{\rho}\right)^2 \tau_c,$$

where  $a$  is the plasma radius.

Since the collision time and the Larmor radius are both proportional to the square root of the particle mass, the classical energy confinement time associated with the electrons is greater than that for the ions by the ratio  $(m_i/m_e)^{1/2}$ . However because collisions between like particles do not produce net particle diffusion, the electron and ion diffusion rates are both determined by electron-ion collisions and both the species diffuse at the rate given by the random walk argument for electrons.

In a torus the classical transport model described above is inappropriate for a number of fundamental reasons. To keep the distinction clear, the collisional transport in a torus is known as neoclassical. At low temperatures, for which the plasma is very collisional, the fluid equations which describe the behaviour in a cylinder can also be used for the torus. However the behaviour is quite different. There is a toroidally induced force on the plasma outward along the major radius, and this leads to an internal convective flow. The net particle transport resulting from this flow is larger than the 'cylindrical' contribution.

At higher temperatures the fluid model is inapplicable. The lower collision frequency allows particles to have trajectories determined by the toroidal geometry. In particular particles which are trapped in the lower magnetic field on the outer side of the torus have banana orbits whose width is  $(q/e^{1/2})\rho$ . These larger orbits allow a greater diffusion to result from collisions than would occur for a Larmor radius step-length.

The transport in the highly collisional fluid regime is called Pfirsch-Schlüter transport. This regime is connected to the low collisionality *banana* regime by the so-called *plateau* regime in which there is no dependence on the collision frequency. In all of these regimes the mass dependencies of classical transport persist.

The energy confinement time scaling of Pfirsch-Schlüter and banana regime transport with respect to density, temperature, magnetic field and plasma size,  $\ell$ , is

$$\tau_E \sim \frac{T^{1/2} B_p^2}{n} \ell^2, \quad 4.1.2$$

where  $B_p$  is the poloidal magnetic field. Experimental confinement times are not only much shorter than the neoclassical prediction, but also differ in scaling from relation 4.1.2. The experimental data available do not allow a unique scaling to be deduced and several are in use. However, the general behaviour can be illustrated using a scaling obtained by Goldston

for auxiliary heated tokamaks. This scaling, which has proved reasonably satisfactory over a wide range of parameters, has the form

$$\tau_E \propto \frac{B_p^2}{nT} t^{1.8}. \quad 4.1.3$$

Although no generally accepted theoretical basis for scalings such as 4.1.3 has been given, it has been appreciated that dimensional analysis imposes useful constraints on their possible forms. Conversely the empirical scalings can shed light on the physical processes responsible for the anomalous losses.

The difference in temperature dependence between the expected form 4.1.2 and the empirical form 4.1.3 has made the achievement of high temperatures more difficult than might have been hoped. It has meant that as higher heating power is applied, and higher pressures are reached, the confinement deteriorates. Using eqn 4.1.1 with relation 4.1.3, it is seen that the confined energy only increases as the square root of the applied power.

It was found, however, that under certain conditions there is a discontinuous improvement in confinement as the heating power is increased. Typically there is a factor of two increase in the confinement time. This regime of higher confinement is called the H-mode and the previous lower level is called the L-mode. The H-mode is achieved more readily in plasmas bounded by a separatrix. The improvement in confinement is mainly due to the appearance of an edge transport barrier, a region of better confinement at the edge of the plasma. A number of other improved confinement regimes, in particular those involving internal transport barriers with hollow current profiles, have also been identified.

Using internal measurements of the density and temperature, together with a knowledge of the power deposition, it is possible to analyse the local confinement properties of the plasma and determine the plasma diffusivity and the electron and ion thermal diffusivities. This detailed information places strong constraints on possible theoretical models of the transport, to the extent that no generally accepted model has yet emerged.

## 4.2

### Resistive plasma diffusion

The resistive diffusion of plasma across a magnetic field is described by Ohm's law together with the pressure balance equation, that is

$$E + v \times B = \eta j \quad 4.2.1$$

and

$$j \times B = \nabla p, \quad 4.2.2$$

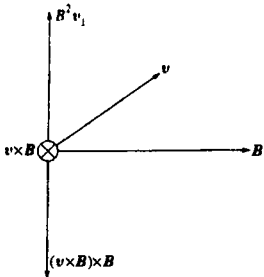


**Fig. 4.2.1** Vector geometry of  $(v \times B) \times B = -B^2 v_{\perp}$ . The vectors  $v$  and  $B$  are in the plane of the paper.

where in general the resistivity is a tensor having a value  $\eta_{||}$  for current parallel to the magnetic field and  $\eta_{\perp}$  for current perpendicular to the field.

The velocity perpendicular to the magnetic field is obtained by taking the cross-product of eqn 4.2.1 with  $B$ . Figure 4.2.1 gives the vector geometry of the term  $(v \times B) \times B$  showing that

$$(v \times B) \times B = -B^2 v_{\perp}.$$

Thus using eqn 4.2.2 to eliminate  $j \times B$ ,

$$v_{\perp} = \frac{E \times B}{B^2} - \eta_{\perp} \frac{\nabla p}{B^2}. \quad 4.2.3$$

In a perfectly conducting plasma  $E + v \times B = 0$  and it was shown in Section 2.21 that this equation implies that the plasma motions are such that the magnetic flux through any element of fluid remains constant. The first term on the right of eqn 4.2.3 gives the velocity which occurs to maintain this condition in the presence of an electric field. The second term gives the deviation from this velocity due to resistivity. This resistive contribution to the velocity is driven by, and proportional to, the pressure gradient. The diffusive nature of this term is seen using the continuity equation. Thus taking  $E = 0$  and constant temperature, the rate of density change ( $= \nabla \cdot n v_{\perp}$ ) is given by

$$\frac{\partial n}{\partial t} = \nabla \cdot \frac{\eta_{\perp} \beta}{2\mu_0} \nabla n,$$

where  $\beta = nT/(B^2/2\mu_0)$ , giving a diffusion coefficient

$$D = \frac{\eta_{\perp} \beta}{2\mu_0}. \quad 4.2.4$$

The two terms in eqn 4.2.3 can also be understood in terms of a particle description. The first term is just the macroscopic effect of the  $E \times B$  drift of all the individual particles as described in Section 2.6. The second term represents the collisional diffusion of the particles.

From Section 2.16,  $\eta_{\perp} \sim m_e/n e^2 \tau_e$  and using  $\rho_e = \sqrt{2m_e v_{Te}/eB}$  with  $\beta \sim n m_e v_{Te}^2 / (B^2/2\mu_0)$  eqn 4.2.4 gives

$$D \sim \frac{\rho_e^2}{\tau_e}.$$

This is the same relation as that derived from a random walk model with a step length  $\rho_e$  and a step time  $\tau_e$ .

## 4.3

### Diffusion in a cylinder

The diffusion velocity in a circular cylinder is given by eqn 4.2.3. The diffusion is radial and so, using cylindrical coordinates  $(r, \theta, z)$ , the

velocity is

$$v_r = \frac{1}{B^2} \left( E_\theta B_z - E_z B_\theta - \eta_\perp \frac{dp}{dr} \right). \quad 4.3.1$$

For a given particle source and known electric and magnetic fields eqn 4.3.1, together with the continuity equation, allows a determination of  $dp/dr$ . In the absence of sources a solution is still possible and in particular there is a steady state solution for which  $v_r = 0$ . In a steady state  $\nabla \times \mathbf{E} = 0$  and this implies  $E_\theta = 0$  and  $E_z = \text{constant}$ . With this condition eqn 4.3.1 gives

$$\frac{dp}{dr} = -\frac{E_z B_\theta}{\eta_\perp}. \quad 4.3.2$$

In a tokamak the axial magnetic field is much larger than the poloidal magnetic field and for  $\beta_p \sim 1$  the axial current density is much larger than the poloidal current density. If the corresponding limit is taken in the cylindrical case it is possible to determine the  $\beta_p$ . With these approximations the parallel component of Ohm's law is

$$E_z = \eta_{||} j_z \quad 4.3.3$$

and substituting eqn 4.3.3 into eqn 4.3.2

$$\frac{dp}{dr} = -\frac{\eta_{||}}{\eta_\perp} j_z B_\theta. \quad 4.3.4$$

Now, from eqn 3.5.1

$$\beta_p = \frac{2 \int_0^a pr dr}{(B_{\theta a}^2 / 2\mu_0) a^2} \quad 4.3.5$$

and for  $p(a) = 0$  an integration by parts gives

$$2 \int_0^a pr dr = - \int_0^a \frac{dp}{dr} r^2 dr. \quad 4.3.6$$

Using Ampère's law

$$j_z = \frac{1}{\mu_0 r} \frac{d}{dr} (r B_\theta)$$

in eqn 4.3.4 and substituting for  $dp/dr$  into eqn 4.3.6 gives

$$2 \int_0^a pr dr = \frac{\eta_{||}}{\eta_\perp} \frac{B_{\theta a}^2}{2\mu_0} a^2$$

so that, from eqn 4.3.5

$$\beta_p = \frac{\eta_{||}}{\eta_\perp}. \quad 4.3.7$$

For  $\eta_{||} = \eta_\perp$  eqn 4.3.7 gives  $\beta_p = 1$ . This is simply a consequence of there being no poloidal current in this case, the axial electric field driving

an axial current. For the classical case  $\eta_{\parallel}/\eta_{\perp} = 1/2$ , a poloidal current arises from the axial electric field, the current being 'deflected' by the anisotropic resistivity. This poloidal current enhances the axial magnetic field, a phenomenon called the paramagnetic effect.

## 4.4

### Pfirsch-Schlüter current

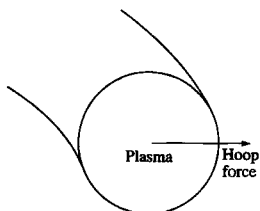


**Fig. 4.4.1** In toroidal geometry plasma pressure leads to an outward hoop force.

Resistive diffusion in a toroidal plasma is considerably more complex than that in a cylinder. The basic reason is that the plasma pressure gives a toroidal hoop force outward along the major radius as shown in Fig. 4.4.1. This force must be balanced by an internal magnetic force, and the currents which produce this force are driven by a plasma flow which is specific to the torus and is absent in the cylinder.

The current required to balance the pressure force is perpendicular to the magnetic field and is essentially a vertical current. This current alone would lead to charge accumulation in the upper and lower parts of the plasma. Charge accumulation is prevented by a return current which flows along the magnetic field and does not therefore affect the force balance. This parallel current was discovered by Pfirsch and Schlüter who showed that, through its resistive dissipation, it plays a fundamental role in the plasma diffusion in a torus. Before calculating the Pfirsch-Schlüter current a heuristic account will be given.

The plasma pressure is constant on each flux surface, but through toroidal geometry the surface area is larger at larger major radii. The resulting pressure imbalance gives rise to a net outward force density along the major radius

$$F \sim -\frac{r}{R} \frac{dp}{dr}.$$

This is balanced by a  $j \times B$  force. Thus the associated perpendicular current,  $j_h$ , has a vertical component

$$j_{hv} \sim -\frac{1}{B} \frac{r}{R} \frac{dp}{dr}. \quad 4.4.1$$

To avoid charge accumulation the Pfirsch-Schlüter current,  $j_{ps}$  parallel to the magnetic field, must be such that its vertical component is equal and opposite to  $j_{hv}$  as illustrated in Fig. 4.4.2. Since this vertical component is

$$j_{\parallel v} \sim \frac{B_p}{B} j_{ps}, \quad 4.4.2$$

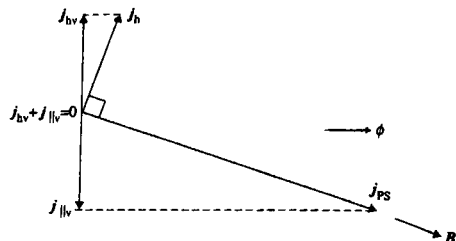


**Fig. 4.4.2** Showing the balancing of the vertical component of the Pfirsch-Schlüter current and the perpendicular hoop force current  $j_h$ .

where  $B_p$  is the poloidal magnetic field, relations 4.4.1 and 4.4.2 give the required current

$$j_{PS} \sim -\frac{1}{B_p} \frac{r}{R} \frac{dp}{dr}. \quad 4.4.3$$

The correct expression for a plasma with a circular cross-section in the large aspect ratio limit has the form of relation 4.4.3 but with a numerical factor 2 as will be shown below. Because the angle of the magnetic field to the vertical varies with the poloidal angle as  $\cos\theta$ , the required vertical component of  $j_{PS}$  implies that  $j_{PS}$  varies as  $\cos\theta$ , its toroidal direction being of opposite signs on the inboard and outboard side of the torus.

The formal calculation requires a more precise form for  $j_\parallel$ . This is obtained by writing the poloidal current density,  $j_p$  as the sum of its components from  $j_\parallel$  and  $j_\perp$ . Thus defining

$$j_\perp = -(j \times B) \cdot B / B^2,$$

$j_p$  can be written

$$j_p = \frac{B_p}{B} j_\parallel - \frac{B_\phi}{B} j_\perp. \quad 4.4.4$$

Equations 3.3.2 and 3.3.3 give

$$j_p = \frac{df}{d\psi} B_p$$

and since

$$\begin{aligned} j_\perp &= \frac{1}{B} |\nabla p| \\ &= -\frac{1}{B} \frac{dp}{d\psi} |\nabla \psi| \\ &= -\frac{RB_p}{B} \frac{dp}{d\psi} \end{aligned}$$

and, from eqn 3.2.4  $RB_\phi = \mu_0 f$ , eqn 4.4.4 can be written

$$j_{\parallel} = f' B - \frac{\mu_0 f p'}{B}, \quad 4.4.5$$

where  $f = f(\psi)$  and the prime denotes a derivative with respect to  $\psi$ . In steady state the quantity  $f'$  is determined by the requirement that, from  $\nabla \times E = -\partial B/\partial t$ ,

$$\oint E_{ps} ds = 0, \quad 4.4.6$$

where  $ds$  is a poloidal line element along the magnetic surface,  $E_{ps}$  is the component of the electric field in the direction of  $B_p$ , and the line integral is taken round a flux surface in the poloidal plane.  $E_{ps}$  is given by the component of Ohm's law parallel to  $B$

$$\eta_{\parallel} j_{\parallel} = \frac{B_p}{B} E_{ps} + \frac{B_{\phi}}{B} E_{\phi}. \quad 4.4.7$$

Using eqn 4.4.5 for  $j_{\parallel}$  and eqn 4.4.7 for  $E_{ps}$ , eqn 4.4.6 gives

$$f' = \mu_0 f p' \frac{(1/B_p)}{\langle B^2/B_p \rangle} + \frac{\langle E_{\phi} B_{\phi}/B_p \rangle}{\eta_{\parallel} \langle B^2/B_p \rangle}, \quad 4.4.8$$

where the averages are defined by

$$\langle x \rangle = \oint x ds / \oint ds$$

and it has been assumed that  $\eta_{\parallel} = \eta_{\parallel}(\psi)$ .

Substituting eqn 4.4.8 into eqn 4.4.5 gives the required equation for  $j_{\parallel}$

$$j_{\parallel} = -\mu_0 f p' \left( \frac{1}{B} - \frac{\langle 1/B_p \rangle}{\langle B^2/B_p \rangle} B \right) + \frac{\langle E_{\phi} B_{\phi}/B_p \rangle}{\eta_{\parallel} \langle B^2/B_p \rangle} B. \quad 4.4.9$$

The last term on the right hand side of eqn 4.4.9 gives the parallel current driven by the applied electric field  $E_{\phi}$ . The other term is the Pfirsch-Schlüter current, that is

$$j_{ps} = -\mu_0 f p' \left( \frac{1}{B} - \frac{\langle 1/B_p \rangle}{\langle B^2/B_p \rangle} B \right). \quad 4.4.10$$

Equation 4.4.10 is exact. The expression for the circular cross-section large aspect-ratio case is obtained by calculating the required averages.

## 4.5 Pfirsch–Schlüter diffusion

Taking  $B_p/B_\phi \sim \epsilon$ , with

$$B_\phi = \frac{B_0}{1 + \epsilon \cos \theta}, \quad 4.4.11$$

where  $\epsilon = r/R_0$ , together with

$$B_p = B_\theta(1 + \epsilon \Lambda(r) \cos \theta), \quad 4.4.12$$

where  $\Lambda(r)$  is determined for a particular equilibrium by eqns 3.8.1 and 3.8.2

$$j_{ps} = -\mu_0 f p' \frac{2\epsilon}{B} \cos \theta + O(\epsilon^2).$$

Substitution of

$$f = RB/\mu_0 \quad \text{and} \quad p' = (dp/dr)/RB_\theta$$

then gives the Pfirsch–Schlüter current

$$j_{ps} = -2 \frac{1}{B_\theta} \frac{r}{R} \frac{dp}{dr} \cos \theta.$$

## 4.5

### Pfirsch–Schlüter diffusion

Plasma diffusion in a cylinder was described in Section 4.3. The fluid equations used there also describe the diffusion in a torus for a low temperature, collisional plasma. The requirement on collisionality is that collisions are sufficiently frequent that the trapping of particles in the region of lower magnetic field is negligible. Under these conditions the diffusion velocity is given by eqn 4.2.3 and in toroidal geometry the velocity perpendicular to the flux surfaces is

$$v_\perp = \frac{E_{ps} B_\phi - E_\phi B_p}{B^2} - \eta_\perp \frac{\nabla_\perp p}{B^2}, \quad 4.5.1$$

where  $\nabla_\perp p$  represents the scalar magnitude of  $\nabla p$ .

It is now necessary to obtain an expression for  $E_{ps}$  in terms of known quantities and this is done using the component of Ohm's law parallel to the magnetic field given in eqn 4.4.7. Substituting for  $E_{ps}$  in eqn 4.5.1,

$$v_\perp = \frac{B_\phi}{B_p B} \eta_\parallel j_\parallel - \eta_\perp \frac{\nabla_\perp p}{B^2} - \frac{E_\phi}{B_p}. \quad 4.5.2$$

Using eqn 4.4.9 with eqn 4.4.10, eqn 4.5.2 becomes

$$v_\perp = \frac{B_\phi}{B_p B} \eta_\parallel j_{ps} - \eta_\perp \frac{\nabla_\perp p}{B^2} + \frac{1}{B_p} \left( \frac{(E_\phi B_\phi / B_p)}{(B^2 / B_p)} B_\phi - E_\phi \right). \quad 4.5.3$$

The last three terms on the right hand side of this equation correspond to pressure gradient and electric field terms in the cylindrical case as they

appear in eqn 4.3.1. The first term is proportional  $j_{\parallel S}$  and this term gives the toroidal contribution called Pfirsch–Schlüter diffusion.

The velocity  $v_{\perp}$  is a function of the poloidal angle and the total plasma flux across a magnetic surface is given by the poloidal line integral around the surface

$$\Gamma = 2\pi n \oint v_{\perp} R \, ds = 2\pi n \langle v_{\perp} R \rangle \oint ds,$$

where  $n$  is the particle density. The required quantity is therefore  $\langle v_{\perp} R \rangle$  and this is obtained using eqn 4.5.3 for  $v_{\perp}$ .

Thus, using eqn 4.4.10, the Pfirsch–Schlüter term contributes

$$\langle v_{\perp} R \rangle_{PS} = -\eta_{\parallel} \mu_0 f p' \left\langle \frac{RB_{\phi}}{B_p} \left( \frac{1}{B^2} - \frac{\langle 1/B_p \rangle}{\langle B^2/B_p \rangle} \right) \right\rangle, \quad 4.5.4$$

where  $p' = dp/d\psi$ . This expression can be evaluated in the large aspect-ratio approximation, using eqns 4.4.11 and 4.4.12. After some algebra the contributions from the poloidal variation of  $B_p$  cancel and the leading order result is

$$\frac{\langle v_{\perp} R \rangle_{PS}}{R_0} = -2 \left( \frac{r}{R} \right)^2 \eta_{\parallel} \frac{dp/dr}{B_{\theta}^2}.$$

The contribution of the electric field term in eqn 4.5.3 is similarly calculated and, using  $q = B_{\phi}r/B_{\theta}R$ , the final result is

$$\frac{\langle v_{\perp} R \rangle}{R_0} = -\frac{dp/dr}{B^2} (\eta_{\parallel} + 2q^2 \eta_{\parallel}) - \frac{E_{\phi} B_{\theta}}{B^2}. \quad 4.5.5$$

It is seen that the Pfirsch–Schlüter diffusion resulting from the parallel currents is  $2q^2 \eta_{\parallel}/\eta_{\perp}$  larger than the cylindrical contribution involving the perpendicular currents.

## 4.6

### Banana regime transport

In the absence of collisions those particles with  $v_{\parallel} \lesssim \varepsilon^{1/2} v_{\perp}$  are trapped in the weaker region of the tokamak magnetic field and execute banana orbits as described in Section 3.10. When a small collisionality is allowed for, it is these trapped particles which dominate the transport, even though the fraction of the particles which are trapped is  $\sim \varepsilon^{1/2}$ . It should be noted that here  $\varepsilon$  is the inverse aspect-ratio of the magnetic surface and therefore varies across the plasma radius. When the collisionality is sufficiently low that particles complete at least one bounce orbit before suffering a collision, the plasma is said to be in the banana regime. Collisions

cause scattering out of the region of velocity space where particles are trapped. This transition requires collisional diffusion in velocity space through an angle  $\Delta\theta \sim \varepsilon^{1/2}$  and so the effective collision frequency for detrapping is  $v/(\Delta\theta)^2 \sim v/\varepsilon$ . Thus the banana regime requirement is that this effective collision frequency be smaller than the bounce frequency  $\omega_b \sim \varepsilon^{1/2} v_T/qR$ , that is

$$v < \frac{\varepsilon^{3/2} v_T}{qR}.$$

It is possible to derive an approximate expression for the diffusion coefficient by considering the random walk behaviour of the electrons as follows.

The collisions which scatter the electrons out of their trapped orbits displace the particles across the flux surface by a distance  $\sim w_{be}$ , the electron banana width. This provides the step length for the diffusion process. Since  $w_{be} \sim (q/\varepsilon^{1/2})\rho_e$  this step length is larger than the Larmor radius step length,  $\rho_e$  associated with classical diffusion.

Using the banana width step length together with the effective collision frequency it is possible to derive an estimate of the resulting diffusion. This gives a diffusion coefficient  $w_{be}^2/(\varepsilon/v_e)$ . However, only a fraction,  $\sim \varepsilon^{1/2}$ , of the particles are trapped and so the effective banana regime diffusion coefficient is

$$D \sim \frac{\varepsilon^{1/2} (\rho_e q / \varepsilon^{1/2})^2}{\varepsilon/v_e} \sim \frac{q^2}{\varepsilon^{3/2}} v_e \rho_e^2.$$

This exceeds the classical diffusion coefficient by the large factor  $q^2/\varepsilon^{3/2}$  and the Pfirsch-Schlüter coefficient by  $1/\varepsilon^{3/2}$ .

A similar estimate can be made for the electron and ion thermal diffusivities. The resulting expression for the electrons is

$$\chi_e \sim D \sim \frac{q^2}{\varepsilon^{3/2}} v_e \rho_e^2$$

and the ion thermal diffusivity is given by the analogous expression

$$\chi_i \sim \frac{q^2}{\varepsilon^{3/2}} v_i \rho_i^2.$$

It is seen that

$$\chi_i \sim \left( \frac{m_i}{m_e} \right)^{1/2} \chi_e$$

with the consequent prediction that the ion thermal conduction would far exceed that of the electrons.

The estimate of the banana width given above is modified when  $\omega_b$  is comparable to the distance from the magnetic axis. In this case we take

the value  $\varepsilon = w/R$ , where  $w$  is the new orbit width. As a result

$$w \sim w_{\text{pot}} \sim (q^2 R \rho^2)^{1/3},$$

where  $w_{\text{pot}}$  is known as a 'potato' width on account of the shape of the orbit in this situation. Since  $w_{\text{pot}} > w_b$  one expects larger transport near the magnetic axis.

The calculation of the transport coefficients is much more complex than the heuristic account given above would suggest. Rather than give a lengthy and detailed derivation it is more appropriate here to outline the general structure of the calculation.

### Kinetic theory

Basically the requirement is to calculate the steady state distribution function in tokamak geometry using the kinetic equation and then use this distribution function to calculate the flux across each magnetic surface. The fundamental kinetic equation is

$$\mathbf{v} \cdot \nabla f + \frac{Ze}{m} (\mathbf{E} + \mathbf{v} \times \mathbf{B}) \cdot \frac{\partial \mathbf{f}}{\partial \mathbf{v}} = C(f), \quad 4.6.1$$

where the collision term on the right is given by the Fokker-Planck equation and  $Ze$  is the particle charge,  $Z$  being  $-1$  for electrons. However, since the detailed motion in the Larmor orbits is not important, eqn 4.6.1 can be replaced by the drift kinetic equation as described in Section 2.11. In the present case this takes the form

$$\mathbf{v}_{\parallel} \cdot \nabla f + v_d \cdot \nabla f + \frac{Ze}{m} E_{\parallel} \frac{\partial f}{\partial v_{\parallel}} = C(f), \quad 4.6.2$$

where the subscript  $\parallel$  refers to the direction parallel to the magnetic field,  $v_{\parallel}$  being the parallel component of the velocity, and  $v_d$  is the toroidal drift velocity given by eqn 2.6.9, that is

$$v_d = \frac{v_{\parallel}^2 + \frac{1}{2} v_{\perp}^2}{\omega_c} \frac{\mathbf{B} \times \nabla \mathbf{B}}{B^2}, \quad 4.6.3$$

where  $\omega_c = ZeB/m$ . When eqn 4.6.2 is solved for  $f$ , the particle flux across a magnetic surface is given by

$$\Gamma = \iint f v_d \cdot dS d^3 v, \quad 4.6.4$$

where  $dS$  is a vector normal to the magnetic surface.

The solution of eqn 4.6.2 uses two expansions. In the first the Larmor radius and the inductive electric field are taken to be small, allowing the expansion

$$f = f^{(0)} + f^{(1)},$$

where  $f^{(1)}$  is of order  $\rho/a$  or  $ZeER/T$ . In the second expansion the ratio of effective collision frequency to trapped particle bounce frequency is

taken to be small and  $f^{(1)}$  is written

$$f^{(1)} = f^{(1)0} + f^{(1)1},$$

$f^{(1)1}$  being of order  $v_{\text{eff}}/\omega_b$  relative to  $f^{(1)0}$ . It is  $f^{(1)1}$  that gives rise to the flux  $\Gamma$ , although, as will be seen, it can be expressed in terms of  $f^{(1)0}$ . However, it is still necessary to consider  $f^{(1)1}$  because it provides a constraint which determines  $f^{(1)0}$ .

The equation for  $f^{(0)}$  is

$$\mathbf{v}_{\parallel} \cdot \nabla f^{(0)} = C(f^{(0)})$$

and the solution is a Maxwellian distribution

$$f^{(0)} = f_M(W) = N \left( \frac{m}{2\pi T} \right)^{3/2} \exp\left(-\frac{W}{T}\right),$$

where

$$W = \frac{1}{2}mv^2 + Ze\phi,$$

$\phi$  being the electrostatic potential,  $N = N(\psi)$  and  $T = T(\psi)$ , with  $\psi$  the poloidal flux function introduced in Section 3.2.

In next order eqn 4.6.2 becomes

$$\mathbf{v}_{\parallel} \cdot \nabla f^{(1)} + \mathbf{v}_d \cdot \nabla f_M + ZeE_{\parallel}v_{\parallel} \frac{\partial f_M}{\partial W} = C(f^{(1)}). \quad 4.6.5$$

To obtain an equation for the flux in terms of  $f^{(1)0}$  eqn 4.6.4 is first written

$$\Gamma = - \iint f \mathbf{v}_d \cdot \nabla \psi \frac{dS}{|\nabla \psi|} d^3v,$$

the outward component of  $\nabla \psi$  being negative.

The factor  $\mathbf{v}_d \cdot \nabla \psi$  is obtained using eqn 4.6.3,

$$\mathbf{v}_d \cdot \nabla \psi = \frac{v_{\parallel}^2 + \mu/mB}{\omega_c} \nabla B \cdot \frac{(\nabla \psi \times B)}{B^2}, \quad 4.6.6$$

where  $\mu$  is the magnetic moment  $\frac{1}{2}mv_{\perp}^2/B$ . The magnetic moment is now expressed in terms of  $v_{\parallel}$  using the conservation of particle energy to write

$$\nabla \left( \frac{1}{2}v_{\parallel}^2 + \frac{\mu}{m}B \right) = 0$$

so that

$$\left( v_{\parallel}^2 + \frac{\mu}{m}B \right) \nabla B = -v_{\parallel}B^2 \nabla \left( \frac{v_{\parallel}}{B} \right). \quad 4.6.7$$

Substituting eqn 4.6.7 into eqn 4.6.6

$$\mathbf{v}_d \cdot \nabla \psi = \frac{v_{\parallel}}{\omega_c} (\mathbf{B} \times \nabla \psi) \cdot \nabla \left( \frac{v_{\parallel}}{B} \right) \quad 4.6.8$$

and writing

$$\mathbf{B} = B_\phi i_\phi + \frac{1}{R}(\nabla\psi \times i_\phi)$$

gives

$$\mathbf{B} \times \nabla\psi = -B_\phi \nabla\psi \times i_\phi + \frac{1}{R}(\nabla\psi)^2 i_\phi.$$

Since, from axisymmetry,

$$i_\phi \cdot \nabla(v_{||}/B) = 0$$

and the poloidal magnetic field is given by

$$B_p = \nabla\psi \times i_\phi/R,$$

eqn 4.6.8 becomes

$$v_d \cdot \nabla\psi = -\frac{v_{||}}{\omega_c} I(\psi) \mathbf{B} \cdot \nabla\left(\frac{v_{||}}{B}\right), \quad 4.6.9$$

where axisymmetry allowed  $B_p \cdot \nabla$  to be replaced by  $\mathbf{B} \cdot \nabla$ , and  $I(\psi) = RB_\phi$ , this symbol being used here in place of the function  $\mu_0 f$ , introduced in Section 3.2, to avoid confusion with the distribution function.

The required form for  $\Gamma$  is now obtained by taking the  $m v_{||}/B$  moment of eqn 4.6.5 and integrating over  $dS/|\nabla\psi|$ . Since

$$d^3v = 2\pi \sum_{\sigma=\pm 1} B d\mu dW/|v_{||}|, \quad 4.6.10$$

where  $\sigma$  is sign( $v_{||}$ ), the first term can be integrated by parts over a magnetic surface and the resulting term is proportional to  $\Gamma$ . The second term integrates to zero so that

$$\Gamma = - \int \left( \frac{m}{ZeB} \int v_{||} C(f^{(1)}) d^3v + n \frac{E_{||}}{B} \right) I \frac{dS}{|\nabla\psi|}. \quad 4.6.11$$

The first term gives the collisional diffusion and it is seen that it is related to the exchange of momentum in collisions. Since like-particle collisions cannot create momentum they do not cause diffusion. Furthermore, multiplying eqn 4.6.11 by  $Ze$ , and recognizing that total momentum is conserved in collisions between electrons and ions, it is seen that the electron and ion fluxes are equal, that is the diffusion is ambipolar. The result 4.6.11 is independent of collisionality regime.

As remarked earlier the flux given by eqn 4.6.11 is determined by  $f^{(1)0}$  bnt  $f^{(1)0}$  itself is constrained by  $f^{(1)1}$ . The physical basis of this constraint is as follows:  $f^{(1)0}$  satisfies a collisionless equation and the solutions correspond to a Maxwellian distribution with ‘diamagnetic’ toroidal drifts for both electrons and ions. If only like-particle collisions are allowed for,

the Maxwellian solutions persist. However, electron-ion collisions would tend to reduce the drift of the passing electrons toward that of the ions and such a form can be constructed from the constants of the motion  $W$ ,  $\mu$ , and  $\sigma$ . But for trapped particles this is impossible because  $\sigma$  is not a constant of the motion and this gives rise to a residual friction between the trapped and passing electrons. The collisional constraint arising from  $f^{(1)1}$  describes the competition between trapped electrons and ions in determining the form of the 'collisionless' electron distribution function  $f^{(1)0}$ .

### Solution of Fokker-Planck equation

To solve for  $\Gamma$  as given by eqn 4.6.11 a solution of eqn 4.6.5 for  $f^{(1)}$  is required. This is obtained making use of the low collisionality expansion  $f^{(1)} = f^{(1)0} + f^{(1)1}$  introduced above and taking the electric field to be of the same order as the collision term. In leading order only the first two terms appear and eqn 4.6.5 becomes

$$\frac{v_{\parallel}}{B} \mathbf{B} \cdot \nabla f^{(1)0} + \frac{m}{Ze} \frac{v_{\parallel}}{B} I \mathbf{B} \cdot \nabla \left( \frac{v_{\parallel}}{B} \right) \frac{\partial f_M}{\partial \psi} = 0, \quad 4.6.12$$

where use has been made of the relation 4.6.9.

Integration of eqn 4.6.12 gives the solution

$$f^{(1)0} = -\frac{m}{Ze} \frac{v_{\parallel}}{B} I \frac{\partial f_M}{\partial \psi} + g, \quad 4.6.13$$

where  $g(\psi, W, \mu, \sigma)$  is a function of the constants of the motion including  $\sigma$ , the sign of  $v_{\parallel}$ . The first term in eqn 4.6.13 represents the diamagnetic drift of the Maxwellian distribution. The second term,  $g$ , is to be determined by the constraint imposed by  $f^{(1)1}$ .

From eqn 4.6.5 the equation for  $f^{(1)1}$  is

$$\frac{v_{\parallel}}{B} \mathbf{B} \cdot \nabla f^{(1)1} + ZeE_{\parallel}v_{\parallel} \frac{\partial f_M}{\partial W} = C(f^{(1)0}). \quad 4.6.14$$

The function  $f^{(1)1}$  must satisfy the constraints imposed by the periodic motion of the particles. These are different for passing and for trapped particles. Passing particles freely complete a periodic motion in the poloidal angle  $\theta$  whereas trapped particles bounce between turning points  $\theta_1$  and  $\theta_2$  where  $v_{\parallel} = 0$ . Thus, for passing particles integration of eqn 4.6.14 over a period  $2\pi$  in  $\theta$  using  $f^{(1)1}(\theta) = f^{(1)1}(\theta + 2\pi)$  gives

$$\oint \left\{ C \left( -\frac{mv_{\parallel}}{ZeB} I \frac{\partial f_M}{\partial \psi} + g \right) - Zev_{\parallel} E_{\parallel} \frac{\partial f_M}{\partial W} \right\} \frac{ds}{v_{\parallel}} = 0. \quad 4.6.15$$

For the trapped particles the integration is carried out between turning points and summed over the two streams  $\sigma \pm 1$  to obtain

$$\int_{s(\theta_1)}^{s(\theta_2)} C(g) \frac{ds}{|v_{\parallel}|} = 0. \quad 4.6.16$$

Here  $ds$  is an element of poloidal arc length along the magnetic surface.

Equations 4.6.15 and 4.6.16 provide the collisional constraint necessary to determine  $g$  and hence  $f^{(1)0}$ , from which the fluxes can be calculated. A full solution requires a lengthy calculation, the results of which will be quoted below. However, the procedure can be illustrated by using a model collision operator to solve eqns 4.6.15 and 4.6.16 explicitly.

The model operator used has the important feature of correctly representing pitch angle scattering and conserving momentum in like-particle collisions. It is also asymptotically correct for distribution functions that are localized in pitch angle, as occurs for the trapped and just passing particles when  $\epsilon \ll 1$  or for the passing particles when  $\epsilon \sim 1$ , where  $\epsilon = r/R$ . For simplicity it is convenient to neglect the energy dependence of the collision frequency, the temperature gradients and the toroidal electric field. Then the ion and electron collision operators are written

$$C_i(f_i) = v_{\parallel}v_{\parallel}\left[\frac{\partial}{\partial\mu}\frac{v_{\parallel}\mu}{B}\frac{\partial f_i}{\partial\mu} + f_{Mi}\frac{m_i}{T_i}u_i\right]$$

and

$$\begin{aligned} C_e(f_e) &= v_{ee}v_{\parallel}\left[\frac{\partial}{\partial\mu}\frac{v_{\parallel}\mu}{B}\frac{\partial f_e}{\partial\mu} + f_{Me}\frac{m_e}{T_e}u_e\right] \\ &\quad + v_{ei}v_{\parallel}\left[\frac{\partial}{\partial\mu}\frac{v_{\parallel}\mu}{B}\frac{\partial f_e}{\partial\mu} + f_{Me}\frac{m_e}{T_e}u_i\right], \end{aligned}$$

where

$$u_j = \int v_{\parallel}f_j d^3v.$$

Substitution into the constraints 4.6.15 and 4.6.16 leads to the ion equation

$$\frac{\partial g_i^{(0)}}{\partial\mu} = -\frac{1}{\langle v_{\parallel}/B \rangle}\left[\frac{Im_i}{Z_ie}\left(\frac{1}{B}\right)\frac{\partial f_{Mi}}{\partial\psi} + f_{Mi}\frac{m_i}{T_i}\langle u_i \rangle\right], \quad 4.6.17$$

where

$$\langle A \rangle = \oint A ds / \oint ds.$$

Using the definition of  $u_i$  and eqns 4.6.13 and 4.6.17, and performing the velocity integral by integrating by parts in  $\mu$  using eqn 4.6.10 gives

$$u_i + \frac{I}{Ze}\frac{T_i}{B}\frac{1}{n}\frac{dn}{d\psi} + \frac{I}{B}\frac{d\phi}{d\psi} = 0, \quad 4.6.18$$

where  $n = N \exp(-Ze\phi/T_i)$ . This represents the role of neoclassical poloidal flow damping in reducing the total ion poloidal velocity to zero. In the presence of a radial temperature gradient eqn 4.6.18 is modified by thermal forces to

$$u_i + \frac{T_i}{ZeB_\theta n}\frac{1}{r}\frac{dn}{dr} - \frac{k}{ZeB_\theta}\frac{dT_i}{dr} + \frac{1}{B_\theta}\frac{d\phi}{dr} = 0,$$

where  $k = 0.172$  and a large aspect ratio expansion for the equilibrium has been used. In the rest frame of the ions, and setting  $Z = 1$  for simplicity,

this yields a radial electric field

$$E_r = \frac{T_i}{en} \frac{dn}{dr} - \frac{0.172}{e} \frac{dT_i}{dr}. \quad 4.6.19$$

Similarly, the electron equation gives

$$u_e - u_i = 1.46\epsilon^{1/2} \frac{T_e}{eB_\theta} \frac{1}{n} \frac{dn}{dr} \left( 1 + \frac{T_i}{T_e} \right) \left( \frac{\nu_{ee} + \nu_{ei}}{\nu_{ei}} \right) \quad 4.6.20$$

where the result

$$\int \frac{\mu B}{T} \frac{\nu_{||}}{(\nu_{||})} f_M d^3v = 1 - 1.46\epsilon^{1/2} + O(\epsilon)$$

has been used.

### Transport coefficients

The equations of particle and electron and ion energy transport take the form

$$\frac{\partial n}{\partial t} + \frac{1}{r} \frac{\partial}{\partial r} (r \Gamma) = 0 \quad 4.6.21$$

$$\begin{aligned} \frac{\partial}{\partial t} \left( \frac{3}{2} n T_e \right) + \frac{1}{r} \frac{\partial}{\partial r} \left[ r \left( q_e + \frac{5}{2} \Gamma T_e \right) \right] \\ = -Q_\Delta - T_i \Gamma \left( \frac{1}{n} \frac{\partial n}{\partial r} - \frac{0.172}{T_i} \frac{\partial T_i}{\partial r} \right) + E_{||} j_{||} \end{aligned} \quad 4.6.22$$

and

$$\begin{aligned} \frac{\partial}{\partial r} \left( \frac{3}{2} n T_i \right) + \frac{1}{r} \frac{\partial}{\partial r} \left[ r \left( q_i + \frac{5}{2} \Gamma T_i \right) \right] \\ = Q_\Delta + T_i \Gamma \left( \frac{1}{n} \frac{\partial n}{\partial r} - \frac{0.172}{T_i} \frac{\partial T_i}{\partial r} \right) \end{aligned} \quad 4.6.23$$

where

$$Q_\Delta = \frac{3n}{\tau_e m_i} (T_e - T_i)$$

is the electron-ion energy equipartition term,  $E_{||} j_{||}$  is the Ohmic heating and the remaining terms, on the right-hand side of eqns 4.6.22 and 4.6.23 are the work done against the radial electric field given in eqn 4.6.19.

Equation 4.6.11 expresses the electron flux  $\Gamma_e$  in terms of the momentum exchange between electrons and ions and, in the absence of thermal forces, this is given by  $-m_e n \nu_{ei} (u_e - u_i)$ . Using eqn 4.6.19, the surface averaged electron flux per unit area is given by

$$\Gamma_e = -0.73 (\nu_{ee} + \nu_{ei}) \epsilon^{-3/2} q^2 \rho_e^2 \frac{dn}{dr} \left( 1 + \frac{T_i}{T_e} \right),$$

where  $\rho_e = (2T_e/m_e)^{1/2}/\omega_{ce}$ .

The heat fluxes for electron and ions can be calculated in a similar way. The more complete variational calculation gives the following results.

$$\Gamma = \frac{\varepsilon^{-3/2} q^2 \rho_e^2 n}{\tau_e} \left[ -1.12 \left( 1 + \frac{T_i}{T_e} \right) \frac{1}{n} \frac{dn}{dr} + \frac{0.43}{T_e} \frac{dT_e}{dr} + \frac{0.19}{T_e} \frac{dT_i}{dr} \right] - \frac{2.44 \varepsilon^{1/2} n E_{||}}{B_\theta} \quad 4.6.24$$

$$q_e = \frac{\varepsilon^{-3/2} q^2 \rho_e^2 n}{\tau_e} T_e \left[ 1.53 \left( 1 + \frac{T_i}{T_e} \right) \frac{1}{n} \frac{dn}{dr} - \frac{1.81}{T_e} \frac{dT_e}{dr} - \frac{0.27}{T_e} \frac{dT_i}{dr} \right] + \frac{1.75 \varepsilon^{1/2} n T_e E_{||}}{B_\theta}. \quad 4.6.25$$

Because the ion thermal diffusivity can sometimes approach the neoclassical value, an improved treatment including finite aspect-ratio effects is justified. Such a calculation leads to somewhat larger values. An interpolation formula which gives the correct asymptotic results for  $\varepsilon \ll 1$  and  $\varepsilon \approx 1$ , when nearly all particles are trapped, is

$$q_i = -0.68 \frac{\varepsilon^{-3/2} q^2 \rho_i^2}{\tau_i} \left( 1 + 0.48 \varepsilon^{1/2} \right) n \frac{dT_i}{dr}, \quad 4.6.26$$

where  $\rho_i = (2T_i/m_i)^{1/2}/\omega_{ci}$ . A more complete result for moderate  $\varepsilon$ , due to Chang and Hinton, is given in Section 14.11. This describes all collisionality regimes and includes the effects of impurities.

Finally, it is noted that the collisional ion toroidal viscosity does not show a neoclassical enhancement. In the banana regime it merely acquires a Pfirsch-Schlüter factor so that

$$\chi_\phi = 0.1 \frac{\rho_i^2 q^2}{\tau_i}.$$

These results serve as a useful basis for comparison with experiments.

## 4.7

### Plateau transport

Figure 4.7.1 displays the variation of diffusion coefficient with collision frequency for the Pfirsch-Schlüter and banana regimes at large aspect ratio,  $\varepsilon = r/R \ll 1$ . These two regimes leave a gap in collision frequency

$$\varepsilon^{3/2} v_T / R q < v < v_T / R q. \quad 4.7.1$$

In this region diffusion is found to be dominated by a class of slowly circulating particles. These are particles which have such a low  $v_{||}$  that

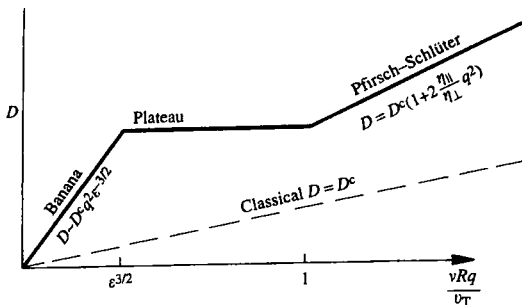


Fig. 4.7.1 Variation of diffusion coefficient with collision frequency.

they suffer a small angle collision with  $\Delta v_{\parallel} \sim v_{\parallel}$  during a single transit round the torus. Since Coulomb collisions are diffusive in velocity space this characteristic value of  $v_{\parallel}$  is determined by equating the effective collision frequency for such small angle collisions to the transit frequency of the particle round the torus:  $(v_{\text{T}}/v_{\parallel})^2 \sim v_{\parallel}/Rq$ . Thus, this so-called resonant velocity is given by

$$\frac{v_{\parallel}}{v_{\text{T}}} \sim (vRq/v_{\text{T}})^{1/3}. \quad 4.7.2$$

As the collision frequency spans the range 4.7.1 from the banana regime to the Pfirsich-Schlüter regime, this velocity changes from the trapped band  $v_{\parallel} \sim \epsilon^{1/2} v_{\text{T}}$  to  $v_{\parallel} \sim v_{\text{T}}$ . A heuristic estimate of the corresponding diffusion can be made by noting that, due to the magnetic drift, a particle with this resonant velocity drifts a radial distance  $\delta \sim v_d \tau$  in a transit time  $\tau \sim Rq/v_{\parallel}$ . Since it suffers a collision during such a transit this is the characteristic step for a random walk estimate. Noting that the fraction of resonant particles is  $\sim v_{\parallel}/v_{\text{T}}$ , the diffusion coefficient

$$D \sim \frac{v_{\parallel}}{v_{\text{T}}} v_d^2 \frac{Rq}{v_{\parallel}} \sim \frac{v_{\text{T}} q}{R} \rho^2.$$

This is the plateau diffusion coefficient. It is independent of collisions and matches the banana and Pfirsich-Schlüter results at the appropriate collision frequencies.

To provide a quantitative expression for the particle and heat fluxes it is necessary to solve the drift kinetic equation 4.6.2 for these particles. It is convenient to use the velocity space variables  $v_{\parallel}$  and  $v_{\perp}$ . For a large aspect-ratio tokamak with circular surfaces eqn 4.6.2 takes the form

$$\frac{v_{\parallel}}{qR} \frac{\partial f}{\partial \theta} + \frac{v_{\parallel}^2 + \frac{1}{2}v_{\perp}^2}{\omega_c R} \sin \theta \frac{\partial f_M}{\partial r} + \frac{Ze}{m} E_{\parallel} \frac{\partial f_M}{\partial v_{\parallel}} = v \frac{v^2}{2} \frac{\partial^2 f}{\partial v_{\parallel}^2}, \quad 4.7.3$$

where the Fokker–Planck collision term has been approximated by the pitch-angle scattering contribution appropriate for scattering of the small  $v_{\parallel}$  particles from the resonant band. Equation 4.7.3 can be solved for  $f$  by Fourier transforming in  $v_{\parallel}$ . Neglecting the  $E_{\parallel}$  term for simplicity, the solution is

$$f(v_{\parallel}, v_{\perp}, \theta) = \frac{q}{\omega_c} \frac{\partial f_M}{\partial r} \frac{v^2}{2} \int_0^{\infty} \sin(v_{\parallel} t - \theta) \exp\left(-\frac{R q v v^2 t^3}{6}\right) dt.$$

The radial flux  $\Gamma = r \int v_{\text{dr}} f d^3 v d\theta$  due to the radial magnetic drift  $v_{\text{dr}}$  can be calculated directly for this distribution function. The major contribution is indeed provided by particles satisfying relation 4.7.2.

Detailed calculations yield a particle flux

$$\begin{aligned} \Gamma = & -\frac{\sqrt{\pi}}{2} \epsilon^2 \frac{T_e}{e B_\theta} \frac{\rho_e n}{r} \left[ \left(1 + \frac{T_i}{T_e}\right) \frac{1}{n} \frac{dn}{dr} + \frac{3}{2 T_e} \frac{dT_e}{dr} + \frac{3}{2 T_e} \frac{dT_i}{dr} \right] \\ & - 1.6 \sqrt{\pi} \epsilon^2 \frac{v_{Te} T_e}{r} \frac{n E_{\parallel}}{B}, \end{aligned} \quad 4.7.4$$

an electron heat flux

$$\begin{aligned} q_e = & -\frac{\sqrt{\pi}}{4} \epsilon^2 \frac{T_e}{e B_\theta} \frac{\rho_e n T_e}{r} \left[ \left(1 + \frac{T_i}{T_e}\right) \frac{1}{n} \frac{dn}{dr} + \frac{15}{2} \frac{1}{T_e} \frac{dT_e}{dr} + \frac{3}{2} \frac{1}{T_e} \frac{dT_i}{dr} \right] \\ & - 2.1 \sqrt{\pi} \epsilon^2 \frac{v_{Te} n T_e E_{\parallel}}{r} \end{aligned}$$

and an ion heat flux

$$q_i = -\frac{3}{2} \sqrt{\pi} \epsilon^2 \frac{T_i}{e B_\theta} \frac{\rho_i}{r} n \frac{dT_i}{dr}.$$

Since

$$\rho_i \sim (m_i/m_e)^{1/2} \rho_e,$$

$q_i$  exceeds  $q_e$  by  $\sim (m_i/m_e)^{1/2}$ .

The plateau region is an idealization based on the large aspect-ratio approximation. Calculations of the transport fluxes have been carried out to describe the transition between banana and plateau regimes when the resonant particles merge with the trapped particles. It is found that for realistic values of  $\epsilon$ , the plateau approximations are valid over only a very narrow region of collisionality.

## 4.8

### Ware pinch effect

Expressions 4.6.24 and 4.7.4 indicate an inward particle transport due to the toroidal electric field. This is known as the Ware pinch effect.

The inward flow occurs for trapped particles and their behaviour follows directly from the toroidal equation of motion. In the banana regime this is

$$\frac{d}{dt} m_j v_\phi = e_j (E_\phi + (v \times B)_\phi). \quad 4.8.1$$

For trapped particles the integral between bounces of the term on the left-hand side of eqn 4.8.1 is zero and consequently the steady state time average is also zero. Thus

$$\langle (v \times B)_\phi \rangle = -E_\phi. \quad 4.8.2$$

Now

$$(v \times B)_\phi = v_\perp B_\theta, \quad 4.8.3$$

where  $v_\perp$  is the component of the velocity perpendicular to the magnetic flux surface, corresponding to the radial velocity in the case of a circular plasma, and  $B_\theta$  is the poloidal magnetic field. Combining eqns 4.8.2 and 4.8.3 the time averaged pinch velocity of the trapped particles is given by

$$\langle v_\perp \rangle = -\frac{E_\phi}{B_\theta}$$

independent of the particle's mass and charge. Thus, since the trapped particle fraction is  $\sim \epsilon^{1/2}$ , there is a flux

$$\Gamma \sim \epsilon^{1/2} n E_\phi / B_\theta.$$

The mechanism underlying this behaviour can be understood by considering the effect of the toroidal electric field on the banana orbits of the particles. Following eqn 3.12.3, the modified equation of motion along the magnetic field lines is

$$\frac{d^2 s}{dt^2} = -\omega_b^2 s + \frac{e_j E_\phi}{m_j}$$

so that

$$s = s_b \sin \omega_b t + \frac{e_j E_\phi}{m_j \omega_b^2}$$

and since  $s = (B/B_\theta)r\theta$

$$\theta = \theta_b \sin \omega_b t + \frac{e_j B_\theta E_\phi}{m_j \omega_b^2 r B}. \quad 4.8.4$$

It is seen that the orbit is displaced by the electric field to have a mean angle

$$\bar{\theta} = \frac{e_j B_\theta}{m_j \omega_b^2 r B} E_\phi$$

as illustrated in Fig. 4.8.1.

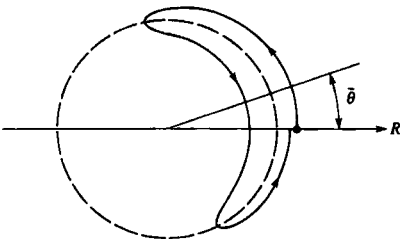


**Fig. 4.8.1** Showing the displacement of a trapped particle orbit arising from the toroidal electric field.

As a consequence, the effect of the  $\nabla B$  and curvature drifts is not symmetric about the mid-plane. The particle therefore experiences a radially inward component of the vertical drift for a longer time than the outward component. If the drift velocity is  $v_{dj}$ , the resulting radial velocity is  $-v_{dj} \sin \theta$  and, considering deeply trapped particles for which  $\theta$  is small,

$$v_r = -v_{dj} \theta.$$

Using eqn 4.8.4

$$v_r = -v_{dj} \theta_b \sin \omega_b t - \frac{e_j v_{dj} B_\theta}{m_j \omega_b^2 r B} E_\phi$$

and the time-averaged  $v_r$  is

$$\langle v_r \rangle = -\frac{\omega_c j v_{dj} B_\theta}{\omega_b^2 r B^2} E_\phi.$$

Substituting  $v_{dj} = \frac{1}{2} m_j v_\perp^2 / e_j R B$  and  $\omega_b = (v_\perp / q R) (r/2R)^{1/2}$  with  $q = r B / R B_\theta$ , the required pinch velocity is obtained

$$\langle v_r \rangle = -\frac{E_\phi}{B_\theta}.$$

Typical values of  $E_\phi$  and  $B_\phi$  are  $10^{-1} \text{ V m}^{-1}$  and  $0.5 \text{ T}$ , giving pinch velocities of  $\sim 0.2 \text{ m s}^{-1}$ . The inward radial displacement per bounce period is very small. The time taken for a radial displacement equal to the banana width  $w_b$  is

$$\tau = \frac{w_b}{E_\phi / B_\theta},$$

and using eqn 3.12.10 for the banana width

$$\tau \sim \frac{m_j v_{Tj}}{e_j E_\phi}.$$

Typical values of  $\tau$  are 0.1 s for ions and 1 ms for electrons.

**4.9****Bootstrap current**

It was shown in Section 4.8 that a radial particle flux results from a toroidal electric field. The Onsager symmetry relations require the existence of a parallel electric current driven by a density gradient. Indeed, the general relation 4.6.11 between diffusion and electron-ion momentum exchange, or friction, parallel to the magnetic field implies such a current. In the Pfirsch-Schlüter regime the friction associated with the Pfirsch-Schlüter currents, which have zero average over a magnetic surface, is consistent with the Pfirsch-Schlüter diffusion. But the additional friction related to the higher transport in the banana regime implies the existence of a unidirectional toroidal current, which is known as the bootstrap, or diffusion driven current. Such a current exists independently of the conventional current driven by an applied electric field. The suggestion that this current, which can be maintained by steady radial diffusion of the plasma, could provide part of the tokamak's poloidal magnetic field has led to the term bootstrap current.

A heuristic explanation of the bootstrap current can be given. For an inverse aspect-ratio  $\varepsilon = r/R$  there is a fraction  $\varepsilon^{1/2}$  of trapped particles and they typically have a parallel velocity  $\varepsilon^{1/2} v_T$ . They execute a banana orbit of width  $w_b \sim \varepsilon^{-1/2} q \rho$ , where  $\rho$  is the Larmor radius. Thus in the presence of a density gradient they carry a current analogous to the diamagnetic current of untrapped particles but here parallel to the magnetic field. This current is

$$j_t \sim -e\varepsilon^{1/2}(\varepsilon^{1/2} v_T) w_b \frac{dn}{dr} \sim -q \frac{\varepsilon^{1/2}}{B} T \frac{dn}{dr}. \quad 4.9.1$$

Both trapped ions and trapped electrons carry such a current and there is a transfer of momentum to the passing particles of both species which adjust their velocities accordingly. The dominant current turns out to be that arising from the difference in velocity between the passing ions and the passing electrons and this is the bootstrap current  $j_b$ .

The momentum exchange between the passing electrons and the passing ions is  $v_{ei} m_e j_b / e$  and for the passing electrons this is balanced by the momentum exchange between the passing and trapped electrons. The trapped electrons are localized to a part  $\sim \varepsilon^{1/2}$  of velocity space and their effective collision frequency is determined by the time for diffusion out of this region,  $\nu_{eff}^{-1} \sim (\varepsilon^{1/2})^2 \nu_{ee}^{-1}$ . Thus the momentum exchange between passing and trapped electrons is  $\sim (v_{ee}/\varepsilon) m_e j_t / e$ . Equating the two expressions for momentum exchange for the passing electrons

$$v_{ei} j_b \sim \frac{v_{ee}}{\varepsilon} j_t$$

and using relations 4.9.1,

$$j_b \sim -\frac{v_{ee}}{v_{ci}} \frac{q}{\epsilon^{1/2}} \frac{T}{B} \frac{dn}{dr}.$$

Since  $v_{ee} \sim v_{ci}$  and  $q = \epsilon B / B_\theta$  the banana regime bootstrap current is given by

$$j_b \sim -\frac{\epsilon^{1/2}}{B_\theta} T \frac{dn}{dr},$$

this current being parallel to the magnetic field.

The precise expression correct to  $\mathcal{O}(\epsilon^{1/2})$  is

$$j_b = -\frac{\epsilon^{1/2} n}{B_\theta} \left[ 2.44(T_e + T_i) \frac{1}{n} \frac{dn}{dr} + 0.69 \frac{dT_e}{dr} - 0.42 \frac{dT_i}{dr} \right]. \quad 4.9.2$$

In the opposite limit,  $\epsilon \rightarrow 1$ , when most particles are trapped, it is found that

$$j_b = -\frac{1}{B_\theta} \frac{dp}{dr} \quad 4.9.3$$

so that, with increasing  $\epsilon$ , the current tends to be driven predominantly by the pressure gradient, rather than the density gradient. Equation 4.9.3

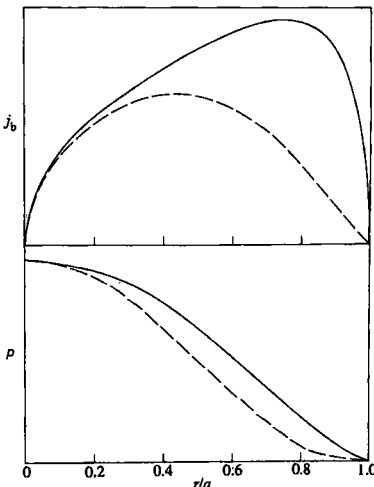


Fig. 4.9.1 Typical bootstrap current profiles for two pressure profiles (with  $T'/T = n'/n$ ).

gives the scaling for the total bootstrap current  $I_b$  as a fraction of the total current  $I$  as

$$\frac{I_b}{I} = c \varepsilon^{1/2} \beta_p$$

with  $c$  typically around 1/3.

Figure 4.9.1 shows two typical bootstrap current density profiles and indicates the sensitivity to the pressure profile. In contrast to the inductively driven current the bootstrap current peaks off-axis. Experimental evidence for the bootstrap current is described in Section 12.2.

In the plateau regime the trapped particle effects diminish as  $\varepsilon^{-1}$ , becoming negligible as the Pfirsch-Schlüter regime is approached. Because of the need to calculate the bootstrap current under realistic conditions, models have been derived which include the trapping fraction, the collisionality and the charge state as parameters. The resulting formulas for  $j_b$  are rather complicated and one such formula is given in Section 14.12 of the Appendix.

## 4.10 Neoclassical resistivity

In a cylindrical plasma the conductivity along the magnetic field is given by its Spitzer value  $\sigma_{Sp} = 1.96ne^2t_e/m_e$ . However, in a tokamak the trapped electrons are unable to move freely along the magnetic field in response to an applied electric field. The current is thus reduced by the presence of trapped particles. In the banana regime the conductivity takes the form  $\sigma = \sigma_{Sp}f(\varepsilon)$  where  $\varepsilon = r/R$ . Thus the conductivity varies over the minor radius through both  $\sigma_{Sp}$  and the variation in  $\varepsilon$ .

In the large aspect-ratio approximation the current density parallel to the magnetic field is given by

$$j_{\parallel} = \sigma_{Sp}(1 - 1.95\varepsilon^{1/2})E_{\parallel} + j_b, \quad 4.10.1$$

where the first term has the trapped particle modification to the resistivity and  $j_b$  is the bootstrap current given by eqn 4.9.2. However, more complete calculations show that the range of applicability of eqn 4.10.1 is rather limited. A more accurate form of the  $\varepsilon$  dependence from the extended calculations is

$$\sigma = \sigma_{Sp}(1 - \varepsilon^{1/2})^2.$$

A more complete empirical representation of numerical calculations which includes the dependence on  $Z_{eff}$  ( $= \sum_i n_i Z_i^2/n_e$ ) and the collision frequency is given in Section 14.10. Experimental evidence for eqn 4.10.1 is described in Section 12.2.

## 4.11 Ripple transport

The finite number of toroidal field coils of a tokamak destroys the perfect axisymmetry of the device. The coils produce a short wavelength 'ripple' in the magnetic field strength as a field line is followed around the torus. For  $N$  coils, the magnetic field can be represented by

$$B = B_0(1 - \varepsilon \cos \theta)(1 - \delta(r, \theta) \cos N\phi)$$

and the resulting magnetic wells are illustrated in Fig. 4.11.1.

An approximation for the value of  $\delta$ , for the case of strongly elongated toroidal field coils, is given by

$$\delta = \left( \frac{R}{R_{\text{outer}}} \right)^N + \left( \frac{R_{\text{inner}}}{R} \right)^N,$$

where  $R$  is the coordinate along the major radius and  $R_{\text{outer}}$  and  $R_{\text{inner}}$  are the major radii of the outer and inner legs of the toroidal field coils.

It is clear from Fig. 4.11.1 that following a field line, for which  $\phi = \phi_0 + q\theta$ , the wells vanish for angles  $\theta$  such that  $|\alpha| \sin \theta | > 1$ , where the parameter  $\alpha = \varepsilon/(Nq\delta)$ . The condition  $\alpha > 1$  divides the poloidal plasma cross-section into two regions, the 'ripple well region', where toroidal wells do exist, and the remainder where they do not. The typical shape of the ripple well region is shown in Fig. 4.11.2.

The ripple affects the transport properties in different ways in these two regions. In the ripple well region the most important effect is due to particles becoming trapped in the local toroidal wells, and subsequently being lost via grad-B drifts in the vertical direction. In particular banana trapped particles with tip positions at the edge of the ripple well region have a high probability of becoming well-trapped. In the remainder of the plasma the ripple modifies the orbits, mainly those of the banana trapped particles, leading to transport.

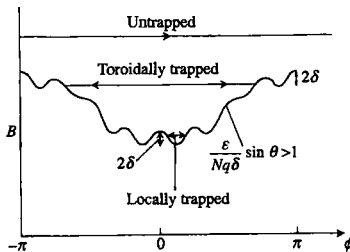
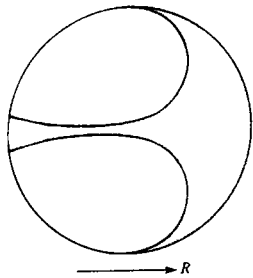


**Fig. 4.11.1** Variation of magnetic field strength along a field line in a tokamak with a rippled field, and the resulting types of particle trapping.



Ripple well transport and ripple banana transport affect both the thermal plasma and highly energetic particles. For thermal particles both forms of transport are mainly collisional (collisional ripple well transport and collisional ripple diffusion), while for fast particles collisionless effects dominate (collisionless ripple well trapping and stochastic diffusion respectively). Because of the larger ion Larmor radius the effects of the ripple are mainly on the ion, rather than the electron, transport. An exception is the ripple effect on very highly energetic runaway electrons.

For a reactor, the main considerations regarding ripple are the loss of fast  $\alpha$ -particles and the associated heat losses to the first wall and in-vessel components. These heat losses can be highly localized. Ripple well losses appear vertically above or below the ripple well regions, depending on the grad- $B$  drift direction. In addition to this poloidal localization, there is a toroidal localization due to the increase in ripple well depth as the particle moves closer to the toroidal field coil.

A second consideration is that of losses of neutral beam injected fast particles. Neutral beam particles ionized in the outer region of the plasma may have banana tip positions which lie inside the ripple well region. This will lead to their rapid loss. In particular for beamlines having large angles with the magnetic field (near perpendicular), a significant proportion of the neutral beam energy may be lost through this mechanism.

For a reactor the ripple amplitude  $\delta$  at the plasma edge typically must not exceed 1 to 2%, in order to avoid excessive ripple well losses, while the ripple at the plasma centre should not be greater than about 0.01%, in order to avoid stochastic diffusion losses. These considerations lead to numbers of toroidal field coils typically between 16 and 24. For smaller numbers of toroidal field coils, the separation between the coils and the plasma needs to be larger than for larger numbers in order to satisfy the criterion on the ripple at the plasma edge. This leads to somewhat larger coils, offsetting the advantage of the smaller numbers. The main arguments for a smaller number of coils are the accessibility of the tokamak for remote handling devices, and the access for tangential neutral beam injection for purposes of non-inductive current drive.

### Collisional ripple well trapping transport

For a particle to be trapped in the ripple wells it has to satisfy the condition that the parallel velocity is sufficiently small that magnetic mirror reflection occurs in the ripple well. This is equivalent to the statement that the banana turning point positions of the particles lie inside the ripple well region. Particles are trapped into and de-trapped out of ripple well trapping by collisional processes, in particular by pitch-angle scattering, which changes the ratio between the parallel and perpendicular velocities. The typical residence time of a particle as ripple well trapped is then of order  $\Delta t \sim \delta/v$ , where  $v$  is the collisional deflection frequency. The fraction of particles which is ripple well trapped is of order  $\delta^{1/2}$ .

Particles which are trapped in the ripple wells drift vertically with a velocity  $v_d \sim \rho v/R$  due to the toroidal field gradient drift, where  $\rho$  is the

Larmor radius and  $v$  is the total particle velocity. Combining the ripple well trapped fraction, the drift velocity and the residence time, a diffusion coefficient for collisional ripple well transport can be estimated as

$$D \sim \delta^{1/2} \left( \frac{\rho v \delta}{R v} \right)^2 \frac{v}{\delta} \sim \frac{\delta^{3/2} \rho^2 v^2}{R^2 v}, \quad 4.11.1$$

where  $D$  is a radial diffusion coefficient for a circular plasma, averaged over the pitch angle. This implies a greater loss rate for ions than for electrons, and an ambipolar electric field will evolve to reduce the ion particle diffusion. Nevertheless, eqn 4.11.1 remains an appropriate estimate. It should however be noted that its validity is restricted to collision frequencies  $v > v_d \delta/a$ , where  $a$  is plasma minor radius, since otherwise particles would drift out of the plasma before suffering a collision, producing a loss cone in velocity space rather than a diffusion. This restriction is particularly stringent as  $D$  is dominated by contributions from the more energetic particles, so that the inequality must hold for these particles (say energies approximately five times the plasma temperature). A second caveat is associated with the poloidal variation in the ripple. As shown in Fig. 4.11.2, ripple wells typically exist only near the low field side and near the plasma mid-plane. The proper poloidal averaging procedure leads to a significant reduction in  $D$  from that given in eqn 4.11.1.

### Ripple well losses of fast particles

For ripple well trapped particles that are sufficiently energetic as not to suffer a collision before being lost ( $v < v_d \delta/a$ ), the ripple well trapping process represents a loss cone. Particles are fed into this loss cone either by (i) collisional processes (pitch-angle scattering), (ii) the processes of ripple transport of banana particles, (iii) acceleration by radio frequency fields, or iv) directly by neutral beam injection. The process responsible for the actual trapping in the ripple wells of these particles is collisionless ripple trapping. This occurs due to the finite banana width of particle orbits in the vicinity of the turning point. The particle feels a different ripple value on approaching the turning point than on leaving it. The difference is approximately  $\Delta w(\delta \partial/\partial z)$ , where  $\Delta w$  represents the vertical displacement which the particle undergoes at the turning point, and  $z$  is the vertical coordinate. If this is a positive number, so that the ripple increases in the direction of the vertical drift, the particle can be trapped, and will remain trapped as long as the ripple well depth increases along its trajectory. The occurrence of trapping further depends on the toroidal position of the turning point with respect to the toroidal field coil location. For a large number of coils and for sufficiently large toroidal banana precession, the toroidal phase of the turning point can be considered random. The rate of collisionless trapping can then be expressed in terms of a trapping probability  $p$  per bounce. Taking into account that

$$\Delta w \sim \frac{v_d R}{N v \delta^{1/2}}$$

then near the ripple well boundary, where  $\alpha \sim 1$ ,

$$p \sim \frac{\rho}{R} (Nq\epsilon)^{1/2},$$

$\epsilon$  being the inverse aspect ratio.

To be trapped the high energy particle needs a finite number of reflections of order  $l/p$ . In practice, with  $p$  in the range of  $10^{-2}$ – $10^{-1}$ , trapping in the ripple wells for particles with banana tips near the ripple well boundary is a very fast process, much faster than slowing down.

### Collisional ripple diffusion

The absence of perfect axisymmetry also modifies the banana orbits. Under conservation of the magnetic moment, the rippled field produces variations in the velocity component parallel to the magnetic field. These cancel over most of the banana orbit, but are significant in modifying the time spent near the banana turning point. This leads to a motion of the position of the banana turning point for successive banana bounces. Because of constancy of energy and magnetic moment, the turning point is constrained to lie on surfaces of constant total magnetic field. In practice, this means that the motion of the turning point is essentially vertical.

The vertical step at one banana turning point is given by  $\Delta z = \Delta \cos(N\phi \pm \pi/4)$ , where the + and – refer to the upper and lower turning points respectively, and  $\phi$  is the toroidal coordinate of the turning point. The amplitude  $\Delta$  is given by:

$$\Delta = \rho(\pi/N)^{0.5} (B_\phi/B_R)^{0.5} \alpha^{-1},$$

where  $B_\phi$  is the toroidal field and  $B_R$  is the major-radial component of the poloidal field. The difference in toroidal angle between consecutive banana turning points is given by the bounce angle and the precession angle of the banana orbit. The difference in steps  $\Delta z$  between consecutive turning points leads to a non-closure of the banana orbits.

For small values of  $\Delta$ , the result is a complicated vertical motion of the banana tip on consecutive bounces. It is determined by two periodicities, namely the toroidal periodicity of the ripple field and the periodicity of the toroidal banana precession motion. This motion is essentially periodic. It does not lead to losses.

Transport of particles can result from collisional de-correlation of the successive steps  $\Delta z$ . An upper estimate of this transport can readily be obtained by assuming full de-correlation of the successive steps. The de-correlation can be produced by collisions and occurs when the collision frequency is large, that is

$$\nu > \frac{\epsilon}{N^2 q^2} \frac{1}{\tau_b},$$

where  $\tau_b$  is the banana bounce time. In this case, the steps  $\Delta z$  are fully de-correlated, and a diffusive transport of order  $\epsilon^{1/2} \Delta^2 / \tau_b$  results, where the fraction  $\epsilon^{1/2}$  represents the fraction of banana-trapped particles.

This regime of complete collisional de-correlation is called the banana plateau regime. At higher temperatures and consequently lower collision frequencies, the behaviour enters the banana drift regime, in which the diffusion rate is suppressed due to partial correlation between consecutive steps. In the banana drift regime, the diffusion coefficient decreases with particle energy. At yet higher particle energies, there is the regime of stochastic diffusion.

### Stochastic diffusion

If the vertical step-size amplitude in the above discussion becomes large, then the step itself leads to a de-correlation of the orbits. The condition for this is that the change in toroidal bounce angle, due to the vertical step, is of the order of the angle between toroidal field coils, or  $\Delta\phi = (\partial\phi/\partial z)\Delta \approx 2\pi/N$ . Consequently, a so-called Chirikov parameter  $\gamma = N\Delta(\partial\phi/\partial z)$  is defined, which describes the level of de-correlation. For large values of  $\gamma$ , full de-correlation of the steps occurs, leading to stochastic motion of the banana tip and to a fast transport. As for the collisional transport above, this transport is of a diffusive nature, and an upper estimate of the diffusion coefficient is given by  $D = \Delta^2/\tau_b$ . This upper estimate is valid for  $\gamma \gg 1$ . For  $\gamma < 1$ , the effective diffusion coefficient is significantly smaller.

The usual method of calculating stochastic diffusion losses is by the use of guiding centre following Monte Carlo codes. On the basis of a large number of such code calculations, an expression for the dependence of the diffusion coefficient on the Chirikov parameter has been formulated:

$$D = \frac{\Delta^2}{\tau_b} \frac{1}{1 + e^{(6.9 - 5.5\gamma)}}, \quad 4.11.2$$

where  $D$  is the diffusion coefficient for vertical diffusion of a banana particle with a given magnetic moment, that is with a given turning point major radius. Figure 4.11.3 shows a set of contours of constant  $D$  for 1 MeV protons in JET with the number of toroidal field coils reduced from 32 to 16.

Expressions such as this make possible the use of codes which follow the history of the bounce-averaged coordinates (rather than the guiding centre coordinates) to study the ripple loss problem.

### Experimental studies

Experimentally, the particle and heat losses of fast particles due to ripple well trapping have been verified. In Tore Supra fast electrons lost from the plasma, and collected by Faraday cups, were shown to be on trajectories originating in the ripple well regions. In JT60-U the heat losses associated mainly with the loss of neutral beam ions were measured, and shown to agree well with the predicted losses.

The most comprehensive experiments on toroidal field ripple were performed on ISX-B and JET. The tokamaks were operated with half the set of toroidal field coils, that is 9 out of 18 and 16 out of 32 respectively.

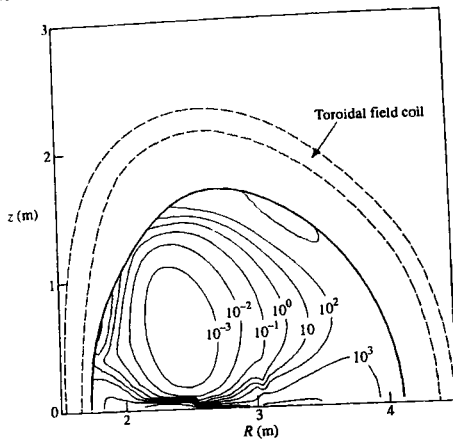


**Fig. 4.11.3** Contours of constant coefficient of stochastic diffusion for 1 MeV protons, as calculated from eqn 4.11.2 for a JET configuration with 16 toroidal field coils. ( $D$  in  $\text{m}^2 \text{s}^{-1}$ )  
(Tubbing, B.J.D. et al., Proc. 20th E.P.S. Conf. on Controlled Fusion and Plasma Physics, Lisbon 1993, Vol. 17C, Part 1 p. 39.)

so that ripple effects could be studied in otherwise identical plasma discharges. In JET, this raises the toroidal field ripple at the edge of the plasma from about 1% to about 10%. Fast particle losses, thermal energy confinement, and plasma rotation were studied. In both ISX-B and JET the effect of ripple on thermal energy confinement and on plasma rotation exceeded theoretical predictions. In addition, it was found in JET that the ripple has a severely deleterious effect on the H-mode of confinement. With 16 toroidal field coils in operation, H-modes without Edge Localized Modes (ELMs, see Section 7.17) could not be obtained with heating powers up to 12 MW, whereas with 32 coils ELM-free H-modes could be readily obtained in otherwise identical plasmas. Finally, in the JET experiment stochastic diffusion was studied by its effect on minority ions accelerated by ion cyclotron resonance heating and on tritons generated by deuterium-deuterium fusion reactions. These experiments led to the conclusion that the stochastic diffusion losses are well modelled with the existing theory. The loss of heating power, and the loss of tritons, could be predicted to within a factor two using calculations with guiding centre or bounce-averaged Monte Carlo codes.

## 4.12

### Confinement modes and scaling expressions

As discussed in Section 4.1 tokamaks do not behave according to the predictions of neoclassical theory described in the previous sections. The

energy confinement, as measured by the confinement time  $\tau_E$ , is found to be much shorter than the neoclassical value. There is a lack of understanding of the underlying cause of this behaviour and as a result it has been necessary to resort to an empirical representation of the confinement time. This usually takes the form of a product of powers of the various parameters involved. Unfortunately even this procedure does not adequately describe the behaviour of the confinement time. It is found that there are several regimes of operation and these are described by a patchwork of scaling expressions. For convenience these regimes are described as modes of confinement.

The confinement behaviour can be conveniently put into four categories. The first covers ohmically heated plasmas and the other three relate to plasmas with additional heating. The two basic modes of additionally heated plasma are the so-called L (for low) and H (for high) confinement regimes. The third category covers a variety of plasmas for which operational procedures have been found which produce enhanced confinement: particularly important examples are those associated with hollow current profiles (or ones almost flat in the centre) known variously as reverse shear, negative central shear or optimized shear. The scalings for these modes will now be described in turn.

### Ohmically heated plasmas

At low density it was found that the energy confinement time scaled as

$$\tau_E = 0.07(n/10^{20})aR^2q \text{ s}, \quad 4.12.1$$

where  $n$  is the average electron density,  $a$  and  $R$  the minor and major plasma radii, and  $q$  is the cylindrical equivalent edge safety factor. The improved confinement with increased density is in conflict with the decrease in confinement predicted by neoclassical theory.

As the density is increased the linear improvement of  $\tau_E$  with  $n$  is lost and  $\tau_E$  saturates at a density

$$n_{\text{sat}} = 0.06 \times 10^{20} I R A^{0.5} \kappa^{-1} a^{-2.5} \text{ m}^{-3} \quad (I \text{ in MA}),$$

where  $I$  is the plasma current,  $A$  is the atomic mass of the ions, and  $\kappa$  is the plasma elongation,  $b/a$ .

By controlling the density in such a way as to maintain a peaked density profile it has proved possible to extend the linear scaling into the so-called Improved Ohmic Confinement (IOC) regime. Results from the ASDEX tokamak are given in Fig. 4.12.1.

It should be noted that, because the level of ohmic heating itself depends on the plasma parameters, there is a freedom to rearrange the form of  $\tau_E$ . Since the ohmic heating has the form  $I^2 R_\eta$ , where  $R_\eta$  is the plasma resistance which scales as

$$R_\eta \sim \frac{R}{ab} \frac{I}{T^{3/2}},$$

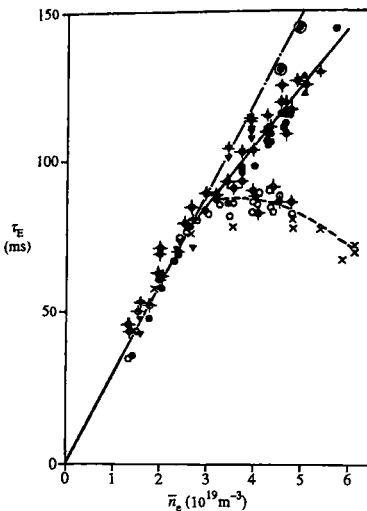


**Fig. 4.12.1** Improved ohmic confinement mode in ASDEX. The broken curve, with open circles and crosses, corresponds to the saturation mode; the upper lines are for two different scans in IOC modes. (Aratari, R. et al., Max-Planck Institut für Plasmaphysik, Annual Report 1988.)

the energy balance relation takes the form

$$\frac{I^2 R}{abT^{3/2}} \sim \frac{nTabR}{\tau_E}.$$

Thus the ohmic heating confinement time given by  $\tau_E$  in eqn 4.12.1 can equally well be represented by  $\tau'_E$  where

$$\tau'_E = \tau_E f \left( \frac{n T^{5/2} a^2 b^2}{I^2 \tau_E} \right)$$

and  $f$  is an unknown function which cannot be determined by the global experimental measurements.

#### L-mode confinement

In order to improve the plasma energy content above that achieved with ohmic heating alone additional heating was applied using beams of energetic neutral particles or RF waves. The results were disappointing in that, for given operational conditions, the confinement was found to degrade with increased heating power. By analysing the results from several tokamaks Goldston obtained the confinement scaling

$$\tau_G = 0.037 \frac{IR^{1.75}k^{0.5}}{P^{0.5}a^{0.37}} \text{ s} \quad (I \text{ in MA}, P \text{ in MW}),$$

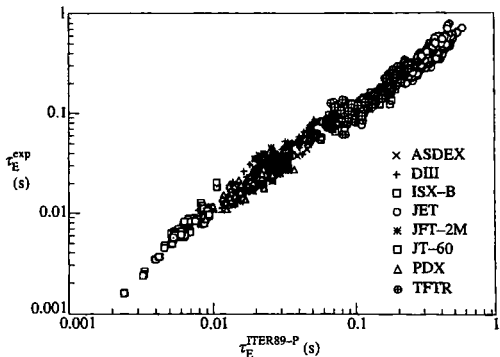


**Fig. 4.12.2** Comparison of the experimental values of confinement time from a number of tokamaks with the L-mode scaling  $\tau_E^{\text{ITER89-P}}$ . (Yushmanov, P.N. et al. *Nuclear Fusion* **30**, 1999 (1990).)

where  $P$  is the applied power. The degradation is apparent through the factor  $P^{0.5}$  in the denominator.

Although this scaling was obtained before the large tokamaks such as JET were operational, it was found to describe the results on these machines quite well. In order to improve the predictive capability for the proposed tokamak reactor ITER an extended data base, including the larger tokamaks, was used to generate a more precise form of Goldston's scaling. The resulting confinement time, which was given the name ITER89-P, is given by

$$\tau_E^{\text{ITER89-P}} = 0.048 \frac{I^{0.85} R^{1.2} a^{0.3} \kappa^{0.5} (n/10^{20})^{0.1} B^{0.2} A^{0.5}}{P^{0.5}} \text{ s} \quad (I \text{ in MA, } P \text{ in MW}), \quad 4.12.2$$

where  $B$  is the toroidal magnetic field. A comparison between this formula and data from a number of tokamaks is shown in Fig. 4.12.2. The results of a later analysis based on an improved data base are given in Appendix 14.13.

It is interesting to note that, using the power balance relation  $P \sim n T a b R / \tau_E$ , the Goldston confinement time takes the approximate form

$$\tau_G \propto \frac{I^2}{n T} g, \quad 4.12.3$$

where  $g$  is a geometrical factor.

### H-mode confinement

The improved confinement of the H-mode was discovered on ASDEX tokamak and its properties are described in Section 4.13. It was found that when sufficient power was applied the discharge made an abrupt

transition in which the edge confinement was improved, leading to edge pedestals in the temperature and density. The effect of this was to produce a doubling of the confinement time.

This behaviour was subsequently obtained in many tokamaks and analogues of the ITER89-P L-mode scaling law have been derived. An example is

$$\tau_{\text{Th}}^{\text{ITER H93-P}} = 0.053 \frac{I^{1.06} R^{1.39} a^{-0.11} \kappa^{0.66} (n/10^{20})^{0.17} B^{0.32} A^{0.41}}{P^{0.67}} \text{ s} \quad (I \text{ in MA, } P \text{ in MW}) \quad 4.12.4$$

where  $\tau_{\text{Th}}$  refers to the confinement time for the *thermal* part of the plasma energy. A different scaling relation holds when ELMs are present. A widely used expression is

$$\tau^{\text{IPB98(y,2)}} = 0.145 \frac{I^{0.93} R^{1.39} a^{0.58} \kappa^{0.78} (n/10^{20})^{0.41} B^{0.15} A^{0.19}}{P^{0.69}} \text{ s.} \quad (I \text{ in MA, } P \text{ in MW}) \quad 4.12.5$$

It is seen that the dependencies are generally similar to those of the L-mode. The results of other analyses are given in Appendix 14.I3.

To relate the confinement in a given plasma to that of the L-mode a factor  $H$  is introduced, defined by

$$H = \frac{\tau_E}{\tau_L^L},$$

where  $\tau_L^L$  is the confinement time given by one of the L-mode scaling laws. While  $H$  is typically 2 in H-modes it is reduced in the presence of ELMs. Unless steps are taken to reduce the effect of ELMs they can seriously degrade performance, in particular at higher densities approaching the density limit.

### Other improved confinement modes

Improved confinement was achieved in the TFTR tokamak in the form of the so-called Snpershot. These discharges are heated by neutral beam injection into a low density plasma, the injection consisting of two oppositely directed, balanced beams. The resulting plasmas have low recycling of particles at the edge and peaked density profiles. Their improvement factor  $H$  is around 3.

The energy confinement of tokamak plasmas has also been improved by narrowing the current profile. This has led to the use of another parameter, the internal inductance  $\ell_i$ , in the scaling formulas for  $\tau_E$ . Thus it is found that

$$\tau_E \propto \ell_i^\alpha \quad 0.67 < \alpha < 0.8.$$

In JET the so-called Pellet Enhanced Performance (PEP) H-mode with peaked pressure profiles was induced by the injection of hydrogen pellets into the plasma giving values of  $H$  up to 3.8.

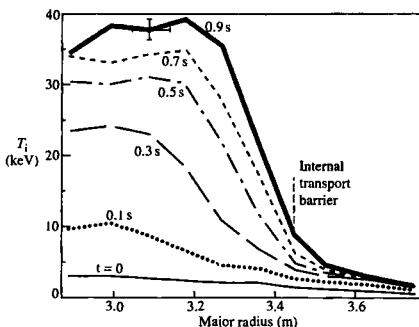


**Fig. 4.12.3** Radial ion temperature profiles from charge exchange spectroscopy for a JET D-T discharge. An internal transport barrier is triggered at 0.35 s after the start of the high power heating phase. (Gomezano, C. *Physical Review Letters* 30, 5544 (1998).)

So-called V-H modes with  $H$  up to 3.6 have been obtained in DIII-D by depositing boron on the walls. Similar results were obtained in JET with beryllium surfaces. In these discharges there is an edge temperature pedestal and a high edge bootstrap current.

A variety of configurations with non-monotonic  $q$ -profiles, or merely weak positive magnetic shear, have achieved  $H > 2$ . They are characterized by a region of good confinement known as an internal transport barrier, shown in Fig. 4.12.3.

The TEXTOR tokamak has obtained the so-called Radiatively Improved Mode by seeding additionally heated plasmas with a small fraction of impurities, such as argon or neon. These discharges maintain good confinement, with  $\tau_E \propto n$  at high density.

The above description of the various regimes clearly demonstrates the lack of understanding of confinement. Ideally, the cause of the enhanced transport would be identified and the resulting transport calculated. This would then provide an understanding in which each mode of behaviour fitted into an overall scheme. This task presents a formidable challenge. In the absence of such understanding it is necessary to look for other theoretical aids. One such is provided by the constraints which dimensional analysis imposes on the scaling laws, and this is discussed in Section 4.14.

## 4.13 H-modes

During neutral beam heating experiments on ASDEX it was found that under certain conditions there was an abrupt transition to higher

confinement. In this higher confinement regime the confinement time was typically twice that of the previous low confinement. Figure 4.13.1 shows an example of the transition from L-mode to H-mode and a comparison of the behaviour of an H-mode and L-mode plasma. This type of behaviour has subsequently been observed on many tokamaks.

The change in confinement is first apparent at the edge of the plasma where there is a rapid increase in the pressure gradient mainly due to an increase in edge density. The associated improvement in edge confinement can be thought of as a transport barrier. When this barrier appears it produces an increase in density over the whole plasma on the timescale of a confinement time, with some further improvement of confinement in the bulk plasma. A sequence of density profiles is shown in Fig. 4.13.2.

This behaviour was unexpected and the reason for it is not clear. One possibility is that the transition is implicit in the basic transport equations, with the solutions having a bifurcation at the critical condition. A more widely held view is that the explanation lies in a sudden change in the stability of the edge plasma associated with a change in the flow profile. It is possible for example that an increase in the flow shear across an unstable region would suppress the instability. Since the perpendicular particle flow velocity  $v_{\perp j}$  for each species, is related to the radial electric field through

$$n_j e_j (E_r + v_{\perp j} B) = - \frac{dp_j}{dr},$$

the behaviour is also discussed in terms of changes in the gradient of the electric field. This view receives support from the observation that edge density fluctuations undergo a sudden decrease over a few cms

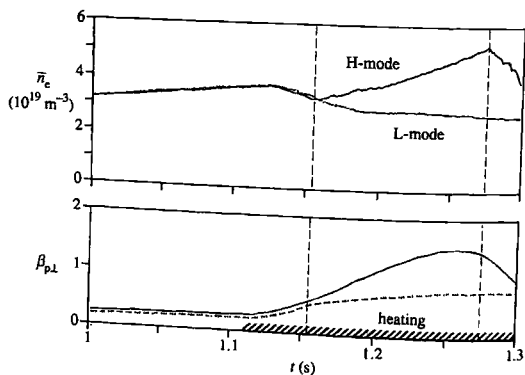


**Fig. 4.13.1** Comparison of H- and L-mode discharges with the same heating power. The L-H transition follows the application of tangential neutral beam heating. After the transition the density and the perpendicular component of  $\beta_p$  rise to around twice the values reached in the L-mode discharge. (ASDEX team, Nuclear Fusion 29, 1959 (1989).)

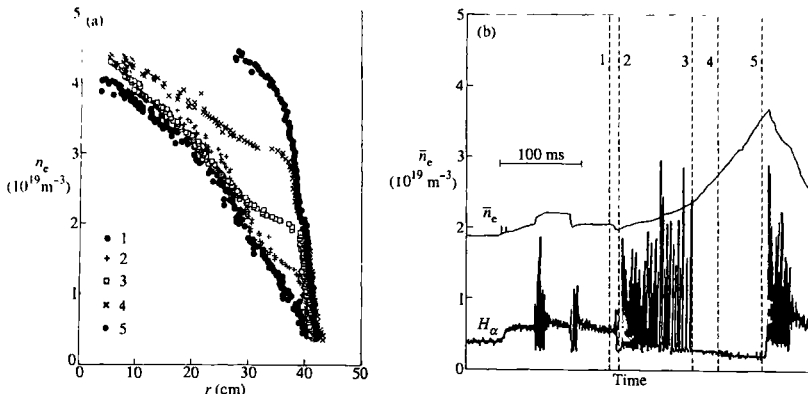
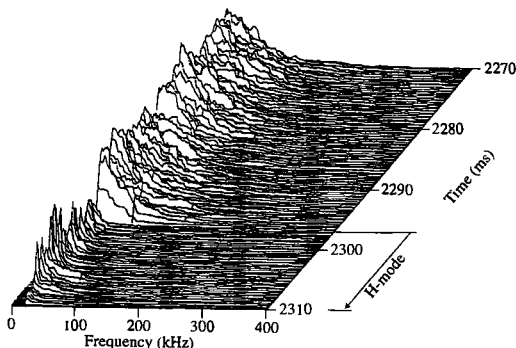


**Fig. 4.13.2** Sequence of density profiles measured on ASDEX through and following an L-H transition. The profiles in (a) are at the times shown in (b), which gives the time dependence of  $\bar{n}_e$  and the  $H_\alpha$  signal. (Wagner, F. et al., *Plasma physics and controlled nuclear fusion research*, (Proc. 13th Int. Conf., Washington, 1990), Vol. I, 277 I.A.E.A. Vienna (1991).)

**Fig. 4.13.3** Showing the fall in density fluctuations, as measured by the reflectometer signal, at the onset of the H-mode in DIII-D. (DIII-D team, *Plasma physics and controlled nuclear fusion research*. (Proc. 13th Int. Conf., Washington, 1990), Vol. I, 69 I.A.E.A. Vienna (1991).)



at the time of the transition as seen in the DIII-D results shown in Fig. 4.13.3. However experiments on JET indicate that the sudden change in confinement can occur over a large part of the outer plasma radius.

The transition to H-mode requires that the heating power be above a certain threshold. An empirical scaling for this threshold power has been obtained by assembling data from a range of tokamaks

$$P_{\text{th}} = 1.38(n/10^{20})^{0.77} B^{0.92} R^{1.23} a^{0.76} \text{ MW.}$$

4.13.1

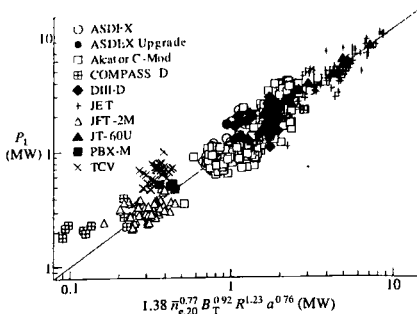


**Fig. 4.13.4** Comparison of experimental power thresholds for the L-H transition with the scaling expression 4.13.1.  $n_{e,20}$  is the line-averaged density in units of  $10^{20} \text{ m}^{-3}$ .  $P_L$  is the loss power in MW when the L-H transition occurs. (ITER Physics Basis, Nuclear Fusion 39, 2175 (1999).)

A comparison with experiment is shown in Fig. 4.13.4. There are further conditions which affect the ease with which the transition occurs. For example it is more readily obtained with a divertor configuration, although it also appears with a separatrix X-point near the wall and in some circumstances in limiter configurations. In configurations with a single X-point the transition occurs at lower power when the toroidal magnetic field is in the direction such that  $\mathbf{R} \times \mathbf{B}$  is toward the divertor,  $\mathbf{R}$  being the major-radius vector. This is commonly described as having the ion grad- $B$  drift toward the divertor.

The improvement in confinement in the H-mode has certain negative aspects. Firstly the increase in density is uncontrolled and can lead to a transition back to the L-mode. There is also an associated enhancement in impurity confinement. Both of these effects are ameliorated in the presence of so-called Edge Localized Modes or ELMs, described in Section 7.17. However ELMs are associated with a loss of confinement and pulsed heat loads.

A characteristic feature of H-modes is the fall in the  $H_\alpha$  signal from the edge of the plasma as seen in Fig. 4.13.2. The  $H_\alpha$  emission comes from neutral hydrogen entering the plasma as part of the recycling process and so the  $H_\alpha$  signal is a measure of the recycling of hydrogen between the plasma and the surrounding surfaces. Thus, the abrupt fall in the  $H_\alpha$  signal marks a sudden decrease in recycling. It is seen from Fig. 4.13.2 that the subsequent deterioration of the H-mode is accompanied by the reappearance of spikes on the  $H_\alpha$  signal. These are associated with the ELMs and indicate bursts of recycling induced by a loss of particles from the plasma. It seems likely that the ELM instability is driven by the steepened edge pressure gradient or current gradient associated with the H-mode.

The ultimate usefulness of the H-mode depends on whether the benefits of improved confinement can be achieved under controlled conditions without the detrimental effects of increased impurity level and a build up of  $\alpha$ -particles in a reacting plasma, or excessive transient heat loads on divertor target plates due to associated ELMs.

## 4.14

### Internal transport barriers

Experiments on TFTR with a non-monotonic  $q$  profile, referred to as reversed shear, sometimes exhibited transitions to states with significant enhancements in confinement over L-mode as a result of the formation of an internal transport barrier as opposed to the edge transport barrier of H-mode. However, the reversed magnetic shear in itself was insufficient as it was found that seemingly identical  $q$  profiles could demonstrate different behaviour. Those discharges with improved confinement were termed enhanced reverse shear (ERS) discharges. This difference indicated that the reverse shear merely facilitated the action of another process, possibly the generation of flow shear which suppresses turbulent transport as in H-mode, as discussed in Section 4.19. Subsequently many tokamaks, both electron heated and ion heated, have achieved improved confinement in situations where the magnetic shear is reversed or just weakly positive and a range of other terms to describe these have been coined, for example, negative central shear in DIII-D, optimized shear in JET. These magnetic configurations can be achieved in a variety of ways: by means of non-inductive current drive or in the transient phase during ohmic current penetration, for example. The requisite flow shear can be provided by momentum input from neutral beams or arise from the radial electric field which balances the ion pressure gradient. Because of the influence of details of the profiles of  $q$  and the deposition of heating power, there appears to be no simple threshold condition for these transitions. There is some evidence for a power threshold increasing with magnetic field strength but this can be strongly modified by appropriate current drive, to produce strongly reversed magnetic shear. The formation of an internal transport barrier is often found to occur in the vicinity of low order rational  $q$ -surfaces, for example  $q = 2, 3$ .

Internal transport barriers are narrow radial regions with greatly reduced transport and steep radial gradients. This reduction can occur in various transport channels, most commonly in the ion thermal channel, where neoclassical levels are obtained as shown in Fig. 4.14.1, and in the density and toroidal momentum channels. However, it is sometimes also seen in the electron thermal channel. Often the transport is also reduced in the core plasma region within the radius of the internal transport barrier. Measurements show that the internal transport barriers are associated with regions of rapid radial variation in the radial electric field as shown in Fig. 4.14.2.

During the later evolution of an internal transport barrier discharge, or with increasing heating power, the position of the barrier moves outward. Sometimes an H-mode edge transport barrier can also form providing a further improvement in confinement. However, these subsequent

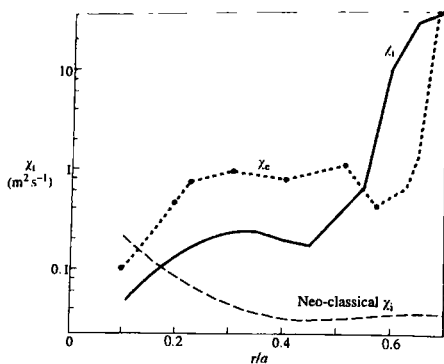


**Fig. 4.14.1** Radial profiles of the ion, electron and neoclassical diffusivities for an optimized shear D-T discharge in JET. (JET Team, *Nuclear Fusion* 39, 1 (1999))

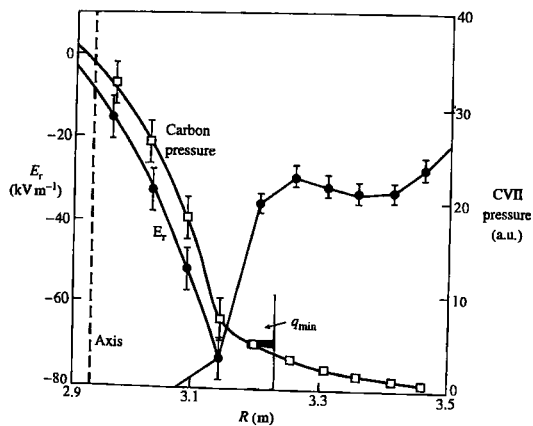


**Fig. 4.14.2** Radial electric field and carbon pressure profiles in an ERS discharge in TFTR. Fluctuations and turbulent fluxes are reduced inside the transport barrier near the minimum in  $q$ . Correspondingly, the carbon pressure profile has a steeper gradient in this region. The transport barrier is associated with a rapidly varying profile of  $E_r$ .

developments can produce profiles which are mhd unstable, leading to a termination of the discharge.

Experiments on JET have demonstrated significant  $\alpha$ -particle production in optimized shear discharges with D-T fuel. The improved confinement of internal transport barrier configurations makes them attractive for a steady state fusion power plant. However, their use in these ways requires the development of current drive and heating systems to control the current and pressure profiles on timescales longer than that corresponding to resistive diffusion.

## 4.15

### Scaling laws

#### Theory

The purely empirical scaling relations described in Section 4.12 were expressed in terms of operational and engineering parameters such as  $I$ ,  $P$ ,  $B$ , and  $a$ . The equations governing the underlying mechanism determining confinement place constraints on the form of these scaling laws, the constraints being dependent on the type of process responsible. These constraints have been derived using the scale invariance technique and are referred to as the Connor-Taylor or Kadomtsev constraints. This technique exploits the invariance of the governing equations under scale transformations. It is related to dimensional analysis but is more systematic and can uncover constraints not readily accessible by that more heuristic method.

An illustrative example is the case where the transport mechanisms are taken to be described by the Vlasov equation with electrostatic potentials determined by the quasi-neutrality condition. Thus electrons and ions satisfy

$$\frac{\partial f_j}{\partial t} + \mathbf{v} \cdot \frac{\partial f}{\partial \mathbf{x}} + \frac{e_j}{m_j} (\mathbf{E} + \mathbf{v} \times \mathbf{B}) \cdot \frac{\partial f_j}{\partial \mathbf{v}} = 0 \quad 4.15.1$$

and

$$\sum_j e_j \int f_j d^3 v = 0. \quad 4.15.2$$

These equations are invariant under just three scaling transformations. In these transformations each of the variables is multiplied by a power of the scale factor such that the equation remains unchanged. The three scale transformations in this case are

$$T1 : \quad f_j \rightarrow \alpha f_j$$

$$T2 : \quad v \rightarrow \beta v \quad t \rightarrow \beta^{-1} t \quad E \rightarrow \beta^2 E \quad B \rightarrow \beta B$$

$$T3 : \quad t \rightarrow \gamma t \quad x \rightarrow \gamma x \quad E \rightarrow \gamma^{-1} E \quad B \rightarrow \gamma^{-1} B.$$

These transformations can now be used to impose constraints on the form of the confinement time scaling. Thus, taking the confinement time to be dependent on characteristic values of the quantities  $n$ ,  $B$ ,  $T$ , and  $a$  in the power law

$$t_E \propto n^p B^q T^r a^s \quad 4.15.3$$

and using the definitions

$$n = \int f d^3 v \quad nT = \frac{1}{3} m \int v^2 f d^3 v,$$

the transformations T1 to T3 can be substituted in turn into eqn 4.15.3. Equating the powers of  $\alpha$ ,  $\beta$ , and  $\gamma$  on the two sides of the resulting equations then provides three constraints on the indices  $p$ ,  $q$ ,  $r$ , and  $s$ .

$$C1 : \quad p = 0$$

$$C2 : \quad q + 2r = -1$$

$$C3 : \quad s - q = 1.$$

Substitution of these constraints into eqn 4.15.3 now gives the required scaling relation

$$\tau_E \propto \frac{1}{B} \left( \frac{T}{a^2 B^2} \right)^r. \quad 4.15.4$$

If  $\tau_E$  is taken to have a general functional dependence on the characteristic quantities, relation 4.15.4 is replaced by

$$\tau_E = \frac{1}{B} F \left( \frac{T}{a^2 B^2} \right). \quad 4.15.5$$

Relations 4.15.4 and 4.15.5 are specific to the model defined by eqns 4.15.1 and 4.15.2. More complex models lead to fewer invariant transformations and fewer constraints on the indices. The most important of these models are summarized in Table 4.15.1.

If in the above example the quasi-neutrality condition is replaced by Poisson's equation, a constraint would be removed. Indeed if the confinement processes also involved the Fokker-Planck equation and finite- $\beta$  effects, there would be no constraints on the form of  $\tau_E$ , and

**Table 4.15.1** Scaling laws for various plasma models.

Plasma model	Scaling law for $B\tau_E$	Constraints on power law scaling (4.15.3)	Number of free exponents
Collisionless low- $\beta$	$F(T/a^2 B^2)$	$p = 0, s = -2r = q + 1$	1
Collisional low- $\beta$	$F(T/a^2 B^2, na^2/B^4 a^5)$	$3p + 2r + s = 0$ $4p + q + 2r + 1 = 0$	2
Collisionless high- $\beta$	$F(na^2, T/a^2 B^2)$	$2p - 2r - s = 0$ $q + 2r + 1 = 0$	2
Collisional high- $\beta$	$F(na^2, Ta^{1/2}, Ba^{5/4})$	$2p + \frac{5}{4}q + \frac{r}{2} - s + \frac{5}{4} = 0$	3
Ideal mhd	$(na^2)^{1/2} F(nT/B^2)$	$2p + q = 0$ $q + 2r + 1 = 0$ $s = 1$	1
Resistive mhd	$(na^2)^{1/2} F(nT/B^2, Ta^{1/2})$	$2p + q = 0$ $p - r + 2s - \frac{5}{2} = 0$	2

in the power law representation the four indices  $p, q, r$ , and  $s$  would be independent.

In general this method does not give information on geometrical ratios such as  $a/R, b/a$ , and the safety factor  $q$ . The procedure is of less value when atomic processes play a significant role.

### Experimental scaling relations

A characteristic time which frequently appears in the discussion of confinement scaling laws is the so-called Bohm time. This is defined by

$$\tau_B = \frac{a^2}{D_B},$$

where  $D_B$  is proportional to the diffusion coefficient introduced by Bohm and is here defined by

$$D_B = \frac{T}{eB}.$$

It is seen that this coefficient can be rewritten in the form

$$D_B \sim \omega_c \rho^2,$$

where  $\omega_c$  is the cyclotron frequency and  $\rho$  is the Larmor radius.

Equation 4.15.5 can be expressed in terms of  $\tau_B$  in the form

$$\tau_E = \tau_B F(\rho_*) \quad 4.15.6$$

where

$$\rho_* = \frac{\rho}{a}$$

is a normalized Larmor radius. More generally  $\tau_E$  can be written

$$\tau_E = \tau_B F(\rho_*, \beta, v_*, \lambda_*) \quad 4.15.7$$

where

$$v_* = \frac{v}{\epsilon^{3/2} v_T / R q}$$

with  $\epsilon = r/R$ , is the ratio of the effective collision frequency for trapped particles to their bounce frequency and

$$\lambda_* = \frac{\lambda_D}{a}$$

is a normalized Debye length.

If  $\lambda_*$  plays no role in confinement, there are only three free indices in a power law form for  $\tau_E$ . This constraint on  $p, q, r$ , and  $s$  in eqn 4.15.3 is known as the Kadomtsev constraint. The ITER89-P and ITER H93-P scaling laws satisfy this constraint approximately. It also follows from eqn 4.15.7 that if the quantities  $\rho_*, \beta$ , and  $v_*$  are the same in different

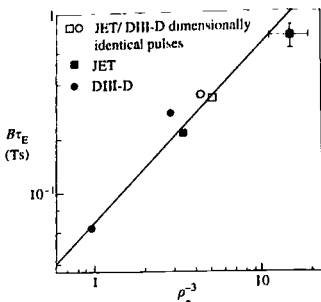


**Fig. 4.15.1** The normalized energy confinement time,  $B\tau_E$ , compared to the gyro-Bohm scaling  $\rho_*^{-3}$ , for discharges in JET and DIII-D with similar values of  $q$  and  $\beta_N$  ( $q$  is the safety factor,  $\beta_N$  the Troyon normalized thermal  $\beta$ ). The solid squares are JET discharges with  $q = 3.4$ ,  $\beta_N = 1.5$ , the solid circles are DIII-D discharges with  $q = 3.8$ ,  $\beta_N = 2.1$ . The open squares and circles relate to dimensionally identical discharges in IET and DIII-D, respectively.

tokamaks, then  $\tau_E \propto B^{-1}$ . Such so-called identity experiments have been carried out between JET and DIII-D and are consistent with this prediction (see Fig. 4.15.1).

If further there is no  $\beta$  dependence, the constraint is that of the low- $\beta$  Fokker-Planck equation. The absence of  $v_*$  would correspond to the constraint of the collisionless high- $\beta$  model. Finally if both  $v_*$  and  $\beta$  play no role the scaling relation is that given by eqn 4.15.6.

In extrapolating from present experiments to a tokamak reactor it is found that the values of  $\beta$  and  $v_*$  will undergo a small change compared to  $\rho_*$ . It is important therefore to determine the  $\rho_*$  scaling.

If confinement is governed by small scale turbulence on the scale of  $\rho$ , the collisionless skin depth  $c/\omega_{pe}$ , or the layer width of resistive instabilities, additional invariant scalings exist, leading to

$$\tau_E = \tau_B \frac{1}{\rho_*} F(\beta, v_*). \quad 4.15.8$$

This is known as gyro-Bohm scaling. At constant  $\beta$  and  $v_*$  eqn 4.15.8 implies  $B\tau_E \propto \rho_*^{-3}$ . This has been demonstrated in similarity experiments between H-mode discharges in JET and DIII-D, as shown in Fig. 4.15.1. If on the other hand the turbulence is on a scale related to  $a$ ,  $\tau_E$  takes the Bohm scaling form

$$\tau_E = \tau_B F(\beta, v_*). \quad 4.15.9$$

The ITER89-P scaling relation 4.12.2 gives Bohm scaling with

$$\tau_E \sim \tau_B \beta^{-1/2} v_*^{-1/4},$$

whereas the H-mode scaling expressions 4.12.4 and 4.12.5 are closer to gyro-Bohm.

It may be that  $\tau_E$  is not best described by a power law expression in  $\rho_*$ ,  $\beta$ , and  $v_*$ . For example, a two term, non-linear form has been

suggested for H-mode. This represents separate contributions from the plasma core and edge pedestal regions.

Even if the functional form  $(\rho_*, \beta, v_*)$  in eqn 4.15.7 is not known it is possible to use the concept of similarity to predict the performance of other tokamaks from the confinement behaviour of existing devices.

For example, a family of similar tokamaks of different sizes but having the same values of  $\rho_*$ ,  $\beta$ , and  $v_*$  would have

$$\tau_E \sim \frac{1}{B} \sim a^{5/4}.$$

If  $\tau_E$  satisfies eqn 4.15.8 then, for the same values of  $\beta$  and  $v_*$ , there is a two parameter family of similar tokamaks with

$$\tau_E \sim Ba^{5/2}$$

while if  $\tau_E$  satisfies eqn 4.15.9, there is another two parameter family with

$$\tau_E \sim B^{1/3} a^{5/3}.$$

Thus knowledge of the performance of one tokamak of a given size can be used to predict the performance of a future device provided conditions are arranged to maintain the similarity, including geometry and profiles.

## 4.16

### Transport coefficients

The energy confinement time  $\tau_E$  represents the result of a number of transport processes. In the centre of the discharge sawteeth play a role, at the edge ELMs have an effect in H-mode and in between transport is usually determined by local processes in which both the electrons and the ions undergo diffusion and convection. Further effects are the exchange of energy between the species and the loss of energy by radiation. Furthermore there is a radial dependence of the processes determining the transport and it is therefore necessary to carry out measurements which allow a determination of the local transport coefficients. In addition to energy transport it is important to investigate the transport of particles, including impurities and energetic particles, and the transport of toroidal angular momentum.

The radial flux densities are the particle fluxes  $\Gamma_j$ , and the heat fluxes  $q_j$  for each species  $j$ . In neoclassical theory these are driven by the radial gradients  $dn_j/dr$  and  $dT_j/dr$ . The observed transport can also be written in these terms, the fluxes being related to the gradients by a

matrix of coefficients. Thus if the fluxes for each species depend only on the gradients for that species, the equations for the fluxes can be written

$$\Gamma_j = -\alpha_{11} \frac{dn_j}{dr} - \alpha_{12} \frac{dT_j}{dr}$$

$$q_j = -\alpha_{21} \frac{dn_j}{dr} - \alpha_{22} \frac{dT_j}{dr}.$$

The diagonal elements of the matrix are the usual  $D_j$  and  $n\chi_j$ . In a more general representation there would be an equation for the toroidal current, introducing the toroidal electric field into the flux equations (for example eqns 4.6.24 and 4.6.25). Furthermore there could be dependencies on gradients of other species.

In an alternative simplified representation the fluxes are expressed as the sum of a diffusive and a convective term. For example the electron particle flux can be written

$$\Gamma_e = -D \frac{dn_e}{dr} - V n_e,$$

where  $D$  is the diffusivity. The second term describes an inward pinch with a velocity  $V$  and could represent the contribution of all the off-diagonal terms. It is not possible to separate  $D$  and  $V$  using steady state measurements but they can be determined by means of transient perturbations using, for example, pellet injection or gas puffs.

Most experimental information relates to the diagonal matrix elements or diffusivities, but the particle and impurity pinches have also been measured. A heat pinch is less commonly invoked. The diffusivities are generally much larger than the neoclassical values. Thus typically

$$\chi_i, \chi_e \sim 1 \text{ m}^2 \text{s}^{-1}$$

and the hydrogen and impurity diffusivities are somewhat lower with,

$$D \sim D_z \sim \frac{1}{4} \chi_e$$

and the pinch velocity

$$V \sim 10 \text{ m s}^{-1}.$$

These values are to be compared with typical neoclassical values

$$\chi_{i \text{ neo}} \sim 0.3 \text{ m}^2 \text{s}^{-1}$$

$$\chi_{e \text{ neo}} \sim D_{e \text{ neo}} \sim \left( \frac{m_e}{m_i} \right)^{1/2} \chi_{i \text{ neo}}$$

$$D_{z \text{ neo}} \sim 0.1 \text{ m}^2 \text{s}^{-1}.$$

Generally

$$\chi_i \sim 1 \text{ to } 10 \chi_{i \text{ neo}} \quad \text{and} \quad \chi_e \sim 10^2 \chi_{e \text{ neo}}.$$

The values of  $D$ ,  $D_z$ , and  $\chi_i$  can approach neoclassical levels in the plasma core and in high confinement regimes but  $\chi_e$  is almost always anomalous.

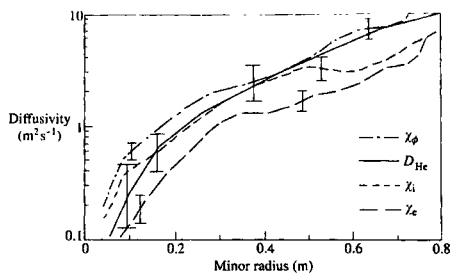


**Fig. 4.16.1** Similarity of the toroidal momentum diffusivity  $\chi_\phi$ , helium diffusion coefficient,  $D_{He}$ , and ion and electron thermal diffusivities,  $\chi_i$  and  $\chi_e$ , in a hot ion L-mode discharge in TFTR. (ITER Physics Basis. *Nuclear Fusion* 39, 2175 (1999).)

Toroidal momentum confinement is also anomalous, with a diffusivity  $\chi_\phi$  which is similar in magnitude to  $\chi_i$  and  $\chi_e$ .

A general feature of the diffusivities is their increase across the radius toward the plasma edge. Results from the TFTR tokamak are shown in Fig. 4.16.1. Experiments on JET indicate a sharp transition from approximately neoclassical values in the core to very anomalous values in the outer region.

The various confinement regimes arise from changes in either  $\chi_i$  or  $\chi_e$ . Thus in ohmic confinement  $\chi_e$  dominates at low  $n_e$  but decreases with  $n_e$  until  $\chi_i$  exceeds it in the saturated confinement regime. In L-mode plasmas  $\chi_i$  is somewhat greater than  $\chi_e$ . H-mode plasmas are characterized by a reduced  $\chi_e$  in the outer region, the enhanced confinement appearing as an edge transport barrier. In Supershots and Improved Ohmic Confinement plasmas density peaking leads to lower values for  $\chi_i$ . Plasmas with non-monotonic  $q$  profiles have neoclassical values of  $\chi_i$  in the core region (see Fig. 4.14.1); sometimes  $\chi_e$  is also reduced.

There is an apparent difficulty in relating the temperature and density dependence of the  $\chi_s$  to the scaling of the energy confinement time. From relation 4.12.2 it is seen that  $\tau_E$  decreases with *increasing* density and temperature whereas  $\chi$  increases with radius and so confinement decreases radially with *decreasing* density and temperature. The reason for this is not known but it could for example be the result of a deterioration with the shear parameter  $(r/q) dq/dr$ .

The  $l^2$  dependence of  $\tau_E$  in relation 4.12.2 indicates local dependence on  $B_\theta$ , possibly  $\chi \sim 1/B_\theta^2$  but again there is considerable uncertainty. In ohmic conditions  $\chi_e$  and  $\chi_i$  are inversely proportional to the ion mass but this dependence is much weaker in L-mode plasmas.

Detailed parameter scans in T-10 provided a fit for  $\chi_e$  for ohmic conditions,

$$\chi_e \sim \frac{T_e^{1/2} r}{n q R} \sim \frac{D_B \rho_*}{\beta q} \left( \frac{r}{R} \right),$$

where  $D_B = T/eB$ . This gyro-Bohm form is contrary to the L-mode scans which, for JET and TFTR, give the Bohm form

$$x_{\text{eff}} \sim D_B \beta^{1/2} v_*^{1/4}.$$

In H-mode, however, results from JET and DIII-D are gyro-Bohm in nature

$$x_{\text{eff}} \sim D_{gB} \beta^{-0.54} v_*^{0.49}.$$

where  $D_{gB} = \rho_* D_B$ .

Experiments in DIII-D with transient off-axis ECRH suggest the existence of an electron heat-pinch, but this conflicts with the results of ICRH experiments in JET. This question is related to that of so-called profile resilience. Experimental results sometimes suggest that the plasma relaxes to a particular type of  $T_e$  profile. This is at variance with experiments in which the transient behaviour is understood in terms of a non-linear conduction law. Furthermore, the  $T_i$  profile is sometimes close to that corresponding to marginal stability for ion temperature gradient modes, discussed in Section 4.20. Heat pulse and pellet injection experiments indicate the importance of off-diagonal elements in the transport matrix.

## 4.17

### Fluctuations

The anomalous transport described in previous sections is believed to arise from turbulent diffusion caused by fluctuations in the plasma. These may be electrostatic or electromagnetic and such fluctuations are expected to appear as the non-linearly saturated state of one or more of the many microinstabilities which have been predicted for a tokamak.

Thus turbulent fluctuations produce an  $E \times B$  drift velocity

$$\delta v_\perp = \frac{\delta E_\perp}{B}$$

and this combines with density fluctuations  $\delta n$  to give a convective particle flux

$$\Gamma = \langle \delta v_\perp \delta n \rangle,$$

where  $\langle \rangle$  is an average over a flux surface.

This average will produce a finite flux except where  $\delta v_\perp$  and  $\delta n$  are exactly out of phase. Similarly temperature fluctuations of species  $j$  will give rise to a heat flux

$$q_j = \frac{3}{2} n_j \langle \delta v_\perp \delta T_j \rangle,$$

where  $n_j$  is the equilibrium density. The electric field fluctuations can be either electrostatic or electromagnetic.

If there are magnetic fluctuations  $\delta B$  with an associated change in magnetic topology, the perturbed velocity  $\delta v_{\parallel}$ , parallel to the magnetic field combines with the perturbed radial magnetic field  $\delta B_r$ , to give a flux

$$\Gamma_j = \frac{n}{B} \langle \delta v_{\parallel} \delta B_r \rangle.$$

Macroscopic mhd phenomena such as sawteeth and low mode number tearing mode islands can also have a significant effect on confinement through a rearrangement of the otherwise toroidally nested magnetic flux surfaces. These phenomena are described in Chapter 7, and this section will concentrate on finer scale fluctuations, often comparable in size to the Larmor radius.

### Observations

At the edge of the plasma, fluctuations in  $\delta n$ ,  $\delta T_e$ , and the electric potential  $\delta\phi$  can be measured by Langmuir probes, and the magnetic perturbation  $\delta B$  can be measured using Mirnov coils. While  $\delta n/n$ ,  $\delta T_e/T_e$ , and  $e\delta\phi/T_e$  rise rapidly towards the plasma edge, reaching values  $\sim 50\%$ , under quiescent conditions the edge value of  $\delta B/B$  is small, typically  $\sim 10^{-4}$ .

Measurements of  $\delta n$  in the plasma interior can be made by a variety of techniques including microwave scattering, Far Infra Red scattering (FIR), Heavy Ion Beam Probes (HIBP), Beam Emission Spectroscopy (BES) and microwave reflectometry. Figure 4.17.1 gives results from TFTR. It is seen that the internal density fluctuations are much lower, falling to  $\sim 1\%$ .

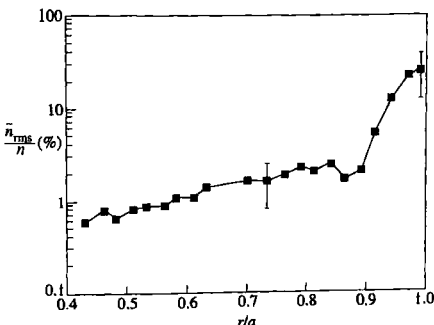


Fig. 4.17.1 Amplitude of normalized density fluctuations in a TFTR Supershot plasma as measured by beam emission spectroscopy. (Fonck, R.J. et al., *Phys. Rev. Letters* **70**, 3736 (1993).)

Measurements of  $\delta\phi$  in the core using a heavy ion beam probe indicate  $c\delta\phi/T_e \sim \delta n/n$ . Direct measurements of internal magnetic fluctuations are in their infancy but a cross polarization scattering measurement on TORE SUPRA suggests  $\delta B_r/B \sim 10^{-4}$ .

The spatial Fourier transform of the fluctuations has wavenumbers  $k_\perp$  and  $k_\parallel$  perpendicular and parallel to the magnetic field. Theoretical models for fluctuations are usually characterized by the predicted  $k$  spectrum. The observed spectrum  $S(k_\perp)$  is dominated by wavelengths greater than the ion Larmor radius. In the radial direction correlation lengths of 2–3 cm are observed with the spectrum peaking at the longest wavelength measurable. The poloidal spectrum is peaked in the region  $k_\perp \rho_s \lesssim 0.3$ , where  $\rho_s$  is the ion Larmor radius at the electron temperature,  $S$  falling off at larger  $k_\perp$ . Typical wavenumbers parallel to the magnetic field have  $k_\parallel L \sim 1$  where  $L$  is the connection length,  $qR$ , around the torus. The fluctuation amplitudes for  $\delta n$  satisfy the simple theoretical mixing-length estimate  $\delta n/n \sim 1/k_\perp L_n$  where  $L_n$  is the density scale-length. This is the amplitude at which the perturbed gradient  $k_\perp \delta n$  balances the equilibrium gradient.

The characteristic frequencies of the fluctuations appear to be  $\sim 100$  kHz. This would be comparable with the diamagnetic frequency  $\omega_s/2\pi$  for poloidal mode number  $m \sim 100$ , though taking account of Doppler shifts from plasma flows may significantly reduce  $m$ .

### Correlations with transport

If the fluctuations described above are to account for the observed transport processes it is necessary to demonstrate a correlation between the fluctuations and confinement.

This can take the form of detailed quantitative comparisons between measured fluxes and those calculated from the fluctuation measurements. However this is usually only possible at the edge of the plasma. For the main plasma it is necessary to resort to a comparison of the radial dependencies of the fluctuation *amplitude* and  $\chi(r)$ . For example it is found that  $(\delta n/n)^2$  and  $\chi$  increase together with radius. More globally it is possible to analyse the correlation between the level of fluctuations and the confinement time  $\tau_E$ . These correlations can take the form of similar scalings with parameters such as  $n$  and  $I$ , or similar behaviour at transitions such as the L–H transition and the formation of an internal transport barrier.

In the edge region a precise analysis of the relationships between transport and electrostatic fluctuations is possible since probes can be used to measure the amplitudes and phases of  $\delta n$ ,  $\delta\phi$ , and  $\delta T_e$ . Detailed studies have been made on TEXT. For particle fluxes, the resulting magnitudes and scalings agree with the observed transport behaviour, indicating that electrostatic fluctuations provide the dominant transport mechanism. The conductive electron heat flux is more uncertain but the measurements of  $\delta T_e$  would allow an explanation in terms of electrostatic fluctuations.

For the edge region the magnetic fluctuations are too small to play a significant part.

Using the heavy ion beam probe in TEXT it has been possible to determine  $\delta\phi$  and  $\delta n$  together with their phase relation further into the core. This allows a calculation of the expected particle flux from electrostatic fluctuations and rough agreement is found with the actual flux over the region  $r/a > 0.6$ . In the absence of information on  $\delta\phi$  theoretical estimates of  $\chi$  based on measurements of the amplitude of the  $\delta n$  fluctuations in the case of TFTR are in reasonable agreement with power balance calculations. Similar agreement is obtained from the estimate  $\chi \sim L_c^2/\tau_c$  using experimental correlation lengths  $L_c$  and times  $\tau_c$ .

A clear correlation between  $\tau_E^{-1}$  and  $(\delta n/n)^2$  was found in ohmic, ion cyclotron, and neutral beam heated plasmas in TFR as shown in Fig. 4.17.2. Detailed studies of the correlation between density fluctuation characteristics and transport have been carried out in TFTR where ohmic, L-mode, and Supershot discharges have all been analysed. The fluctuation power correlates with anomalous transport in that, within the confinement zone, the variation with applied power and plasma current is consistent with  $\tau_E$ . The fluctuation scale-length also decreased from  $\sim 4$  cm in low density ohmic plasmas to  $\sim 2$  cm in Supershots, consistently with the

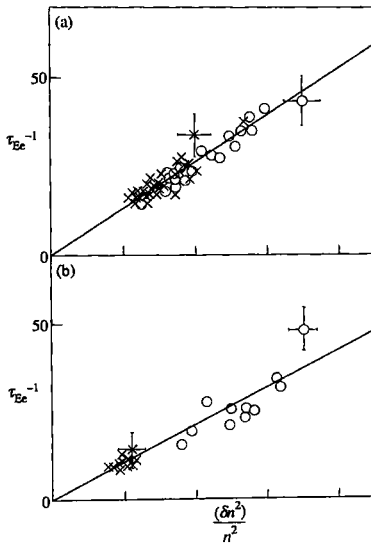


**Fig. 4.17.2** Measurements from TFR showing a correlation between the level of density fluctuations and the electron energy confinement time (with allowance for the effect of sawtooth oscillations). Figure (a) is for ion cyclotron heating and Fig. (b) is for neutral beam heating. Both figures also give results for ohmic heating. (TFR Group and Truc, A. in *Turbulence and anomalous transport in magnetic plasmas*, 1986, p. 141, Eds Grésillon, D. and Dubois, M.A. Editions de Physique, Orsay (1987).)

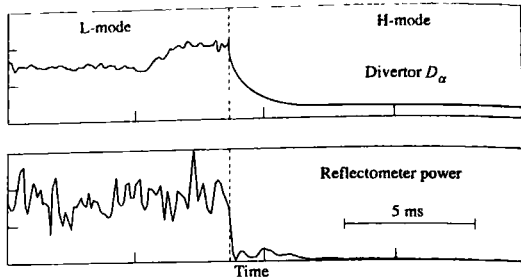


**Fig. 4.17.3** Showing the fall of density fluctuations as measured by reflectometry during an L-H transition in DIII-D.  
(Doyle, E.J. et al. *Plasma Physics and Controlled Nuclear Fusion Research*, (Proc. 14th Int. Conf. Wurzburg, 1992) Vol. I, p. 235 I.A.E.A Vienna (1993))

improved confinement. The longer wavelength fluctuations in L-mode discharges may relate to the Bohm-like scaling of L-mode confinement.

In DIII-D and ASDEX detailed correlations between fluctuation levels and the L-H transition have been observed. As the edge transport barrier forms, the fluctuation level drops within  $100 \mu\text{s}$ . Figure 4.17.3 shows the correlation between the decrease in  $D_\alpha$  emission and the fluctuation level at an L-H transition in DIII-D. Furthermore the improved confinement which develops later for  $r/a \gtrsim 0.7$  is accompanied by a decrease in fluctuations over tens of ms. In L-mode current ramp experiments in TFTR the fluctuations change more rapidly at the edge than in the core, consistently with the changes in heat transport.

## 4.18

### Turbulence-induced transport

The theoretical picture of turbulence-induced transport is that the free energy released by an instability drives a steady level of fluctuations in the associated perturbed quantities. In this turbulent state fluctuations result in a radial transport of particles and energy.

It is possible to attempt a theoretical description at one of two levels. Firstly, the behaviour of the underlying instability can be taken as given. In this case the transport arising from the electromagnetic fluctuations  $\delta E$  and  $\delta B$  such as those described in Section 4.17, is calculated. This procedure is described in the next sub-section where random walk estimates for turbulent transport arising from the fluctuating  $E \times B$  drift velocity  $\delta v_\perp$  and from the parallel motion along stochastic magnetic field lines are given. This is followed by a discussion of quasi-linear theory where turbulent fluxes such as the particle flux  $\Gamma = \langle \delta n \delta v_\perp \rangle$ , are calculated using the linear plasma response to  $\delta E$  and  $\delta B$ .

Secondly, at a more ambitious level, it is possible to attempt a calculation of the non-linearly saturated state of the microinstability and

then the resulting transport. There are several possible procedures available. One general method uses the scale invariance approach described in Section 4.15 to discuss local rather than global transport. Another approach is strong turbulence theory in which saturation is taken to occur when the perturbed gradient  $\nabla \delta n$  is comparable with the equilibrium gradient  $\nabla n$ . Alternatively, for weak turbulence the linear growth of a fluctuation of a particular wavelength is balanced against its decay due to non-linear scattering to other wavelengths. Particular examples arising from candidate instabilities are discussed in Section 4.20. Finally computational simulation of turbulent transport based on the fundamental plasma equations as discussed in Section 4.21, offers the most exact approach.

### Transport due to electrostatic fluctuations

It is convenient to describe the fluctuations in terms of their Fourier components. Thus the electrostatic potential is written  $\delta\phi = \sum_k \delta\phi_k e^{ik \cdot x}$ . A particular component  $\delta\phi_k$  gives rise to a crossfield  $E \times B$  drift velocity

$$\delta v_k = -i \frac{\mathbf{k} \times \mathbf{B}}{B^2} \delta\phi_k.$$

If the particle velocity  $\delta v_k$  persists for a time  $\tau_k$ , known as the correlation time, it leads to a displacement  $\delta r_k \sim \delta v_k \tau_k$ . Summing over the wave-number spectrum, a random walk estimate for the turbulent diffusion is

$$D = \sum_k \frac{(\delta r_k)^2}{\tau_k} = \sum_k \left( \frac{k_{\perp} \delta\phi_k}{B} \right)^2 \tau_k. \quad 4.18.1$$

The correlation time is determined by the process which most rapidly limits the unidirectional  $E \times B$  drift. The possible processes include (i) the time variation of the fluctuation, characterized by  $\tau_k \sim 1/\omega_k$ , (ii) the effect of the linear motion of the particles giving for example  $\tau_k = 1/k_{\parallel} v_T$ , the time for a particle to move along a parallel wavelength of the fluctuations, or  $\tau_k = 1/\omega_d$ , the time for magnetic drifts to carry particles over a perpendicular wavelength, or (iii) the time  $\tau_k = 1/v_{\text{eff}}$  for collisions to change the particle orbit, as for example with trapped particles, which have  $v_{\text{eff}} = v/\varepsilon$ . However, as the level of the turbulence increases the fastest limiting process may become the turbulent velocity  $\delta v_k$  carrying a particle a perpendicular wavelength, that is  $\tau_k = \Omega_k^{-1}$  where

$$\Omega_k = k_{\perp} \delta v_k = \frac{k_{\perp}^2 \delta\phi_k}{B}.$$

Thus for low levels of fluctuations with  $\Omega_k \ll \omega_{\text{eff}k}$ , where  $\omega_{\text{eff}k} = \max(\omega_k, k_{\parallel} v_T, \omega_d, v_{\text{eff}})$ , eqn. 4.18.1 becomes

$$D = \sum_k \frac{1}{\omega_{\text{eff}k}} \left( \frac{k_{\perp} \delta\phi_k}{B} \right)^2$$

which yields the scaling  $D \propto (\delta\phi)^2$ . At higher fluctuation levels when  $\Omega_k \gtrsim \omega_{eff}$ , the diffusion coefficient is given by

$$D = \sum_k \frac{\delta\phi_k}{B}$$

so that  $D$  becomes linear in  $\delta\phi$ .

### Transport due to magnetic fluctuations

When magnetic fluctuations  $\delta B$  are present they can destroy the set of nested toroidal flux surfaces and produce ergodic magnetic fields as described in Section 7.13. The thermal motion of particles along the resulting magnetic field lines can then lead to loss of particles and energy.

As described in Section 7.2 a magnetic field perturbation  $\delta B_r$  at a rational surface at radius  $r_{mn}$ , given by  $m = nq(r_{mn})$ , produces a magnetic island of width

$$w_{mn} = \left( \frac{L_s r_{mn}}{m} \frac{\delta B_r}{B} \right)^{1/2} \quad 4.18.2$$

where the shear length  $L_s = Rq^2/rq' = Rq/s$ , where  $s$  is the magnetic shear. As the perturbation level is raised an increasing part of the regions between resonant surfaces becomes ergodic. The behaviour is determined quantitatively by the parameter

$$\alpha = \frac{1}{2} \frac{w_{mn} + w_{m'n'}}{|r_{mn} - r_{m'n'}|}, \quad 4.18.3$$

where adjacent resonant surfaces are labelled by  $m, n$  and  $m', n'$  respectively. The field line behaviour becomes predominantly ergodic as  $\alpha$  approaches one. When  $\alpha \gg 1$  and many islands overlap the behaviour becomes stochastic. Equation 4.18.3 is then conveniently generalized to

$$\alpha = \frac{\sum_{m,n} w_{mn}}{\Delta r},$$

where the sum is over all modes with rational surfaces in  $\Delta r$ , that is those for which  $nq(r) < m < nq(r) + nq'\Delta r$ . Then for  $w_{mn}$  independent of  $m$

$$\alpha = \sum_n w_n nq'.$$

When  $\alpha \gg 1$  the radial diffusion of the field lines can be described by a magnetic field line diffusion coefficient  $D_M$ . Thus if the field perturbation  $\delta B_r$  remains in the same direction over a distance  $L_c$  in the toroidal direction, that is  $L_c$  is a correlation length, then the field line takes a radial step

$$\delta r \sim \frac{\delta B_r}{B} L_c.$$

If a sequence of such steps is uncorrelated then a random walk estimate for the radial diffusion coefficient as the field line moves around the torus

is given by

$$D_M = \sum_k \frac{(\delta r_k)^2}{L_{ck}} = \sum_k \left( \frac{\delta B_{rk}}{B} \right)^2 L_{ck}. \quad 4.18.4$$

For weak turbulence the correlation length  $L_{ck} \sim 1/k_\parallel \sim Rq$ , leading to  $D_M \propto (\delta B_r)^2$ . More generally

$$k_\parallel = \frac{\mathbf{B}_0}{B} \cdot \nabla + \frac{\delta \mathbf{B}_r}{B} \cdot \nabla$$

and the second term dominates as the fluctuation level increases. Expressing  $\delta B_{rk}$  in terms of the island width  $w_k$  and estimating a radial derivative as  $w_k^{-1}$ , eqn 4.18.4 can be written

$$D_M = \sum_k \frac{k_\perp w_k^3}{L_s}. \quad 4.18.5$$

The motion of particles along these diffusing magnetic field lines leads to radial transport of particles and energy. In the 'collisionless' limit, when the mean free path  $\lambda$  exceeds the correlation length  $L_c$ , a particle moves freely along the radially diffusing magnetic field line with velocity  $v_\parallel$  for a collision time  $\tau_c$ . In this time it moves a radial step distance  $\delta r = \sqrt{D_M \lambda}$ . If a collision displaces the particle's guiding centre to an uncorrelated field line, so that it does not merely retrace its path, it performs a random walk with a diffusion coefficient

$$D = \frac{(\delta r)^2}{\tau_c} = \frac{D_M \lambda}{\tau_c} = v_\parallel D_M.$$

However, if the plasma is more collisional with  $\lambda < L_c$  the particle collisionally diffuses along the magnetic field line with a radial step  $\delta r \sim (\delta B_r/B)\lambda$  for each collision time. A random walk estimate for the radial diffusion then yields

$$D \sim \left( \frac{\delta B_r \lambda}{B} \right)^2 \frac{1}{\tau_c} \sim D_\parallel \left( \frac{\delta B_r}{B} \right)^2,$$

where  $D_\parallel \sim (\lambda^2/\tau_c)$  is the parallel collisional diffusivity.

A number of the theories introduced in Section 4.20 obtain  $w_n \propto 1/n$  and in this case eqns 4.18.4 and 4.18.2 can be used to write eqn 4.18.5 in the form

$$D \sim \frac{v_\parallel R}{q^2 S^2} \left( \frac{r}{R} \right)^2 \left( \frac{\alpha_s}{N} \right)^3, \quad 4.18.6$$

where  $\alpha_s \simeq 1$  and  $N$  is the number of contributing toroidal mode numbers. Because relation 4.18.6 depends on the mobility of a particle along  $B$ , the

transport coefficients for the different species have the following relations

$$\begin{aligned}\chi_e &\sim \sqrt{\frac{m_i}{m_e}} \chi_i, \quad \chi_i \sim D \\ D_z &\sim \sqrt{\frac{m_i}{m_z}} D, \quad D^{E_n}(v) \sim \left(\frac{v}{v_{Th}}\right) D,\end{aligned}$$

where  $\chi_e$  and  $\chi_i$  are the electron and ion diffusivities, and  $D$ ,  $D^{E_n}(v)$ , and  $D_z$  are the diffusion coefficients for the thermal electrons, suprathermal electrons of velocity  $v$  and impurity ions with charge  $Z$  and mass  $m_z$ .

The ambipolarity requirement, that the electron and ion fluxes be equal in order to maintain charge neutrality, is brought about by a positive radial electric field which restrains the more mobile electrons.

### Quasi-linear theory

More precise relationships between fluctuations and transport can be obtained from quasi-linear theory.

Within a fluid description of the plasma, the turbulent density flux can be obtained from the surface-averaged electron density,  $n$ , equation:

$$\frac{\partial}{\partial t} n + \nabla \cdot (\mathbf{V} n) = S, \quad 4.18.7$$

where  $S$  is the particle source. Choosing coordinates with  $x$  and  $y$  perpendicular to the magnetic field, which is in the  $z$ -direction,  $x$  being in the direction of the gradient in density and averaging over the  $y$ -direction with  $n = \langle n \rangle + \delta n$ ,  $\mathbf{V} = \delta \mathbf{V}$ , one has

$$\frac{\partial}{\partial t} \langle n \rangle + \frac{\partial}{\partial x} (\Gamma_x) = S, \quad 4.18.8$$

where the particle flux  $\Gamma_x$  in the  $x$ -direction is

$$\Gamma_x = (\delta V_x \delta n).$$

From the perturbed form of eqn 4.18.7 we have

$$(-i)(\omega_k + i\gamma_k) \delta n_k = -\delta V_{x,k} \frac{\partial}{\partial x} \langle n \rangle, \quad 4.18.9$$

where  $\omega_k$  and  $\gamma_k$  are the frequency and growth rate of the Fourier mode  $k$ . Only the irreversible part of the perturbed density from eqn 4.18.9

$$\delta n_k = -\frac{\gamma_k}{\omega_k^2 + \gamma_k^2} \delta V_{x,k} \frac{\partial}{\partial x} \langle n \rangle,$$

gives a contribution to expression 4.18.8

$$\Gamma_x = -D_\perp \frac{\partial}{\partial x} \langle n \rangle$$

where the diffusion coefficient is

$$D_{\perp} = \sum_k \frac{\gamma_k}{\omega_k^2 + \gamma_k^2} |\delta V_{x,k}|^2. \quad 4.18.10$$

It is more convenient to express  $\delta V_{x,k}$  in terms of the radial displacement  $\xi_x$  of the plasma element using the relation  $d\xi/dt = V_{\perp}$

$$(-i)(\omega_k + i\gamma_k) \xi_{x,k} = \delta V_{x,k}. \quad 4.18.11$$

Again only the irreversible part of the displacement  $\xi$

$$\gamma_k \xi_{x,k} = \delta V_{x,k} \quad 4.18.11$$

is needed in estimating the transport. After substitution of expression 4.18.11 in 4.18.10

$$D_{\perp} = \sum_k \gamma_k |\xi_{x,k}|^2 \frac{\gamma_k^2}{\omega_k^2 + \gamma_k^2}. \quad 4.18.12$$

This is the quasi-linear expression for transport, where  $\xi$  remains to be determined. Further simplification is possible from the fact that the displacement cannot exceed the value  $\xi_{x,k} = \pi/k_{\perp}$ . Supposing that for short wave turbulence  $k_x \approx k_y \approx k_{\perp}$ , the diffusion coefficient becomes

$$D_{\perp} = \frac{(2.4)^2}{2} \left( \frac{\gamma_k}{k_{\perp}^2} \frac{\gamma_k^2}{\omega_k^2 + \gamma_k^2} \right)_{\max k}, \quad 4.18.13$$

where the maximum term in the sum 4.18.12 has been chosen.

In terms of a kinetic description the quasi-linear particle and heat fluxes can be computed from  $\delta f$ ,  $\delta E$ , and  $\delta B$ . For example

$$\Gamma_x = \left( \int \delta f \left( \frac{\delta E_y}{B} + v_{\parallel} \frac{\delta B_x}{B} \right) d^3 v \right). \quad 4.18.14$$

In cylindrical geometry the linearized kinetic equation 4.15.1 can be solved for  $\delta f$  to obtain

$$\delta f_k = -\frac{1}{\omega - k_{\parallel} v_{\parallel}} \frac{k_y}{B} (\delta \phi - v_{\parallel} \delta A_{\parallel})_k \frac{d f_M}{dr} \quad 4.18.15$$

where  $f_M$  is the Maxwellian distribution and  $A$  is the vector potential. Only the imaginary part of  $\delta f$  in eqn 4.18.15 contributes to  $\Gamma$  in eqn 4.18.14 and consequently

$$\Gamma = \left( \int \sum_k \text{Im} \left( \frac{1}{\omega - k_{\parallel} v_{\parallel}} \right) \frac{k_y^2}{B^2} (\delta \phi - v_{\parallel} \delta A_{\parallel})_k^2 \frac{d f_M}{dr} d^3 v \right) \quad 4.18.16$$

with  $A_{\parallel}$  the parallel component of the vector potential. Similar equations hold for the heat flux  $q$ , and the whole transport matrix can be determined

from the density and temperature gradients appearing in  $\partial f_M / \partial r$  provided the spectrum of fluctuations is known. An important modification appears in toroidal geometry when trapped particles are present. For these particles the contribution from parallel motion,  $k_{\parallel} v_{\parallel}$  in the denominator of eqn 4.18.16 averages to zero due to their periodic bounce motion. Then the lower frequencies  $\langle \omega_d \rangle$ , the precessional magnetic drift of trapped particles, and  $\nu_{\text{eff}}$  their detrappling frequency due to Coulomb collisions, play an important role and require the replacement

$$\text{Im} \left( \frac{1}{\omega - k_{\parallel} v_{\parallel}} \right) \rightarrow \text{Im} \left( \frac{1}{\omega - \langle \omega_d \rangle + i\nu_{\text{eff}}} \right)$$

in eqn 4.18.16.

### Saturation levels and transport fluxes

The determination of the fluctuation spectrum is a difficult theoretical task. Analytic approaches involve uncertain assumptions about saturation mechanisms and numerical simulations play an important role in validating these models. Before discussing these calculations it is appropriate to mention the constraints arising from dimensional analysis. If the turbulence is on a microscopic scale, for example on the scale-length of the ion Larmor radius  $\rho_s$  measured at the electron temperature, the collisionless skin depth  $c/\omega_{pe}$ , or resistive layer width  $a/\sqrt{\tau_R/\tau_A}$  then the scale invariance technique can be applied to the equation for the fluctuations. The decoupling of the equilibrium scale-length from the fluctuation scale-length permits more invariant transformations. This procedure leads to scalings for the fluctuations and the corresponding turbulent transport. For example, the potential fluctuation takes the form

$$\frac{e\delta\phi}{T} = \frac{\rho_s}{L_n} f(v_*, \beta, \dots)$$

and the diffusion coefficient

$$D = D_{gB} f(v_*, \beta, \dots)$$

where the gyro-Bohm coefficient is

$$D_{gB} = \frac{\rho_s}{L_n} D_B$$

with  $D_B = T/eB$  the Bohm coefficient. On the other hand, if the fluctuations have a scale  $\ell$  which is proportional to  $a$ , rather than  $\rho_s$ , but still

satisfies  $\ell \ll a$ , then

$$\frac{e\delta\phi}{T} \sim \frac{\ell}{a}$$

and

$$D = D_B f(\nu_*, \beta, \dots).$$

The calculation of specific forms for the function  $f$  requires a model for the non-linear saturation. A simple bound is given by the so-called mixing-length estimate, in which it is assumed that the instability drive is removed when the perturbations reach an amplitude such that the perturbed gradients equal the equilibrium gradient. Thus for drift waves driven by the density gradient this estimate gives

$$k_{\perp} \delta n_k \sim n_0 / L_n \quad 4.18.17$$

and since the density perturbations satisfy the Boltzmann relation the saturated potential fluctuation is

$$\frac{e\delta\phi_k}{T} \sim \frac{1}{k_{\perp} L_n}. \quad 4.18.18$$

A comparison of the estimate 4.18.17 with experimental data is given in Fig. 4.18.1.

Inserting relation 4.18.18 into the quasi-linear formula 4.18.16 for electrostatic drift wave fluctuations with the diamagnetic frequency

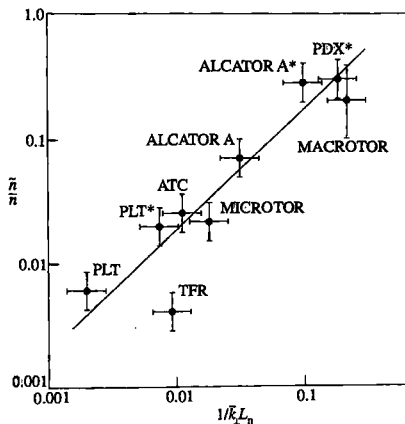


Fig. 4.18.1 Showing a comparison of the normalized fluctuation level  $\bar{n}/n$  with the mixing-length estimate  $1/\bar{k}_{\perp} L_n$  for a number of tokamaks, where  $\bar{k}_{\perp}$  is the mean perpendicular wavenumber of the fluctuations. The asterisks indicate measurements closer to the plasma edge. (Surko, C.M. in *Turbulence and anomalous transport in magnetic plasmas*, 1986, p. 93, Eds Grésillon, D. and Dubois, M.A. Éditions de Physique, Orsay (1987).)

$\omega_*$  ( $= k_{\perp} T / eBL_n$ ) gives

$$D \sim \frac{\gamma}{k_{\perp}^2}. \quad 4.18.19$$

This result can also be interpreted as a balance between the linear growth of a mode and a stabilization from turbulent diffusion,  $k_{\perp}^2 D$ . The expression 4.18.13 reduces to 4.18.19 when  $\gamma_k > \omega_k$ .

Weak turbulence theory allows calculation of a steady state spectrum of fluctuations by balancing wave energy growth  $\gamma_k |\delta\phi_k|^2$  against damping from non-linear wave scattering due to ions. This damping arises from the  $\delta E \times B / B^2 \cdot \nabla \delta f$  non-linearity in the ion kinetic equation and leads to a damping rate  $k_{\perp}^4 |\delta\phi_k|^4 / \omega_* B^2$ .

Precise expressions can be obtained for a particular instability but a qualitative estimate is given by

$$\left| \frac{e\delta\phi_k}{T} \right|^2 \sim \frac{\gamma}{\omega_*} \frac{1}{k_{\perp}^2 L_n^2}. \quad 4.18.20$$

Substitution of eqn 4.18.20 into eqn 4.18.16, gives the weak turbulence estimate for the diffusion coefficient,

$$D \sim \frac{\gamma}{\omega_*} \frac{\gamma}{k_{\perp}^2}.$$

## 4.19

### Radial electric field shear and transport

Experimental evidence from tokamaks indicates that improved confinement is often associated with the development of strongly radially varying profiles of the radial electric field,  $E_r$ , as shown in Fig. 4.14.2. In particular this is evident in the vicinity of transport barriers, both the edge barriers associated with H-mode and internal transport barriers. However, other improved confinement modes such as V-H mode in DIII-D show this feature across much of the plasma radius. These observations suggest that a radially varying  $E_r$  profile reduces anomalous transport.

A theoretical basis for a link between reduced transport and the sheared  $E \times B$  velocity which arises from a radially varying  $E_r$  has been provided. The mechanism is a reduction in the mixing-length estimate for a density fluctuation, eqn 4.18.17, which arises from an increase in the effective perpendicular wavenumber,  $k_{\perp}$ , as a result of the velocity shear. This increase in  $k_{\perp}$  is illustrated in Fig. 4.19.1 where a sheared velocity  $V_y(x) = S_v x$  is superimposed on an isotropic turbulent eddy or vortex of

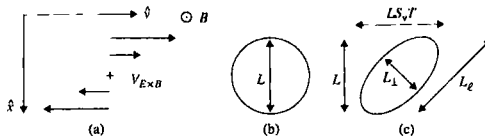


**Fig. 4.19.1** The effect of a sheared  $E \times B$  flow,  $V_{E \times B}$ , on a turbulent eddy: (a) illustrates the  $x$ -variation of the sheared flow in the  $y$ -direction, perpendicular to the magnetic field  $B$ , (b) shows a circular eddy of size  $L$ , and (c) demonstrates how the sheared flow distorts this into an elongated elliptical shape after time  $t$ . The major axis of the ellipse is given by  $L_\ell = L(1 + S_v^2 t^2)^{1/2}$  where,  $S_v$  is the velocity shear, while the minor axis is reduced to  $L_\perp$  preserving the area of the eddy. (Itoh, K., Itoh, S.-I., and Fukuyama, A. *Transport and Structural Formation in Plasma*, I.O.P. Publishing, Bristol, p. 226 (1999).)

size  $L = k_{\perp 0}^{-1}$  in the  $(x, y)$  plane, perpendicular to the magnetic field. After a time  $t$  the eddy becomes distorted, the circular eddy being stretched to an ellipse with major axis  $L_\ell = L(1 + S_v^2 t^2)^{1/2}$ . The area of the eddy is conserved so the minor axis is reduced by the same factor, leading to an effective perpendicular wavenumber,  $k_{\text{eff}} = k_{\perp 0}(1 + S_v^2 t^2)^{1/2}$ . This process persists for a correlation time so  $t = \tau_c = (D_0 k_{\text{eff}}^2)^{-1}$ , where  $D_0$  is the turbulent diffusion coefficient in the absence of velocity shear, and

$$k_{\perp \text{eff}} = k_{\perp 0}(1 + S_v^2 \tau_c^2)^{1/2}. \quad 4.19.1$$

In the limit of strong velocity shear,  $S_v \tau_c \gg 1$ , it follows from eqn 4.19.1 and the definition of the correlation time that

$$\tau_c \sim (D k_{\perp 0}^2)^{-1/3} S_v^{-2/3}.$$

According to the mixing-length estimate the density fluctuation amplitude,  $\tilde{n}$ , is suppressed relative to its value  $\tilde{n}_0$  in the absence of velocity shear, by a factor  $k_{\perp 0}/k_{\text{eff}}$  so that

$$\frac{\langle \tilde{n}^2 \rangle}{\langle \tilde{n}^2 \rangle_0} \simeq \frac{1}{1 + S_v^2 \tau_c^2}.$$

This is a significant reduction if  $S_v \tau_c > 1$ . In cylindrical geometry the  $E \times B$  velocity is given by  $E_r/B$  and the condition  $S_v \tau_c \gg 1$  is expressed in terms of the  $E \times B$  shearing frequency  $\omega_E = r d(E_r/rB)/dr$  as

$$\omega_E > 1/k_{\perp 0}^2 D. \quad 4.19.2$$

For a toroidal flow,  $\omega_E$  takes the form

$$\omega_E = \frac{RB_\theta}{B} \frac{\partial}{\partial r} \left( \frac{E_r}{RB_\theta} \right).$$

For a mixing-length estimate,  $D_0 = \gamma_L/k_1^2$ , where  $\gamma_L$  is the linear growth rate, and inequality 4.19.2 reduces to

$$\omega_E > \gamma_L.$$

4.19.3

Calculations show that this condition on  $\omega_E$  provides linear stability for a range of modes. Non-linear simulations of turbulent transport due to ion temperature gradient turbulence are consistent with condition 4.19.3, providing a 'rule of thumb' for the suppression of transport by sheared flows. The inequality 4.19.3 is often found to correlate with experimental observations on the formation of transport barriers.

The electric field shear can also modify classical and neoclassical transport by a process known as 'orbit squeezing'. This is most easily illustrated for Larmor orbits in a uniform magnetic field  $B$  in the  $z$ -direction. Consider the Hamiltonian for the motion of a particle in this field and a quadratic electrostatic potential well

$$\Phi(x) = \frac{x^2}{2} \Phi'' \quad (\Phi'' > 0)$$

that is

$$H = \frac{m}{2} p_x^2 + \frac{m}{2} (p_y - eBx)^2 + \frac{m}{2} p_z^2 + \frac{e\Phi''x^2}{2},$$

where  $p_x, p_y, p_z$  are the canonical momenta with  $p_y$  and  $p_z$  conserved quantities. Then the normal Larmor orbit appears as motion in the  $x$ -direction in a 'potential well'  $m(p_y - eBx)^2/2$ , leading to an excursion  $x = p_y/eB$  about  $x = 0$ , giving the usual Larmor radius,  $\rho_L$ . Inclusion of the electrostatic potential steepens the potential well and the turning points are modified to  $x = x_L/(1 + S)$  where  $S = m\Phi''/eB^2$  is the squeezing factor. Transport coefficients are correspondingly reduced by a factor  $S^{-1}$  in the limit  $S \ll 1$ . The effect on banana orbits is similar, but more complex.

The radial electric field satisfies the radial force balance equation for any ion of charge  $Ze$

$$E_r = \frac{1}{nZe} \frac{dp_i}{dr} - V_{\theta i} B_\phi + V_{\phi i} B_\theta, \quad 4.19.4$$

where  $V_{\theta i}$  and  $V_{\phi i}$  are the poloidal and toroidal flows, respectively, of the ion species considered.  $E \times B$  flows can be generated by applying a voltage using biased probes at the plasma edge, but eqn 4.19.4 shows they can also be produced indirectly in a number of other ways: applying additional heating to increase the ion pressure gradient contribution  $dP_i/dr$ , using momentum inputs to drive  $V_{\theta i}$  and  $V_{\phi i}$  against viscous damping, and by flows driven by the turbulence itself through the Reynolds stress. These various inputs offer means to control the presence of transport barriers.

Computational simulations of plasma turbulence, described in Section 4.21, indicate that fine scale poloidal  $E \times B$  flows can be generated by the turbulence. These are called zonal flows and are found to reduce the saturated level of the turbulence.

## 4.20

### Candidate modes

The recognition that the transport in tokamaks is 'anomalous' has led to an intensive search for the mode, or modes, of instability which cause this behaviour. So far no candidate has received general acceptance.

Several microinstabilities have been invoked to explain the observed fluctuations and the associated transport. A brief account of the drift mode instabilities is given in Chapter 8 and the fluid-like mhd instabilities are introduced in Chapter 6.

A commonly used model for ohmic and L-mode plasmas assumes electrostatic trapped-electron drift waves and ion temperature gradient modes with a contribution from resistive ballooning modes near the plasma edge. The ion temperature gradient instability involves the quantity  $\eta_i = d \ln T_i / d \ln n$  and is often called the  $\eta_i$ -mode. In toroidal geometry the toroidal curvature plays an important role and the parameter  $L_{Ti}/R$ , where  $L_{Ti} = -(d \ln T_i / dr)^{-1}$  replaces  $\eta_i$  in the theory. The shorter wavelength, electromagnetic electron drift wave instability which involves the analogous quantity,  $\eta_e$ , has also been suggested. This mode gives the required  $\chi \sim 1/n$  scaling for ohmic discharges.

Resistive fluid instabilities such as rippling modes, which are driven by the resistivity gradient, and resistive ballooning modes are generally only relevant near the plasma edge where a number of atomic processes also come into play. Modifications of the resistive ballooning modes in which neoclassical effects or electron inertia play a role would extend their influence into the plasma interior. It has also been suggested that self-sustained magnetic islands could be a cause of enhanced transport.

The principal electron drift wave instabilities arise from trapped particle effects when the normalized collision frequency,  $v_{se} = v_e/\varepsilon^{3/2}(v_{Te}/Rq)$  is such that  $v_{se} < 1$ . They typically have  $\omega \sim \omega_{se}$  and poloidal wave number  $k_\theta$  such that  $k_\theta \rho_s \sim 0.3$ . They are categorized as collisionless when  $v_{eff} < \omega_*$ , and dissipative at high effective collision frequency  $v_{eff} > \omega_*$ , where  $v_{eff} = v/e$ . In more collisional plasmas, with  $v_{se} > 1$ , the mode takes the form of a collisional drift wave driven unstable by circulating particles. There is a variety of expressions for the associated thermal diffusivities, depending on the saturation mechanism invoked and whether or not the mode structure depends on toroidicity. These diffusivities have the gyro-Bohm form

$$\chi_e \sim D_{GB} f(v_*, \text{geometry}).$$

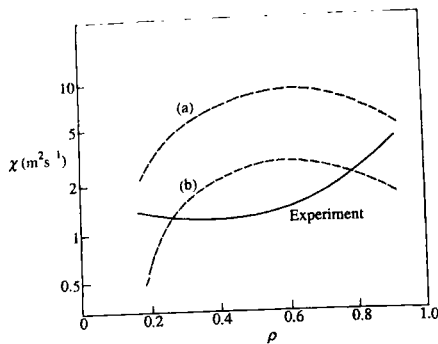


**Fig. 4.20.1** Comparison of theoretical values of thermal diffusivity for trapped-electron modes with experimental values for a JET discharge. The  $\chi$  scale is logarithmic and  $\rho$  is the normalized radius. The theoretical curves are calculated from (a) Romanelli, F., Tang, W.M., and White, R.B. *Nucl. Fusion* 26, 1515 (1986) and (b) Dominguez, R.R. and Waltz, R.E. *Nucl. Fusion* 27, 65 (1987).

A typical expression, based on mixing-length estimates, is

$$\chi_e = \frac{5}{2} \frac{\varepsilon^{3/2}}{v_e} \frac{c_s^2 \rho_s^2}{L_n L_{Te}} \frac{1}{1 + 0.1/v_{se}}, \quad 4.20.1$$

where  $\varepsilon = r/R$ ,  $c_s^2 = T_e/m_i$ ,  $\rho_s = c_s/\omega_{ci}$ , where  $c_s$  is the isothermal sound speed, and  $L_n$  and  $L_{Te}$  are the characteristic scale-lengths for the radial gradients of density and electron temperature. The form 4.20.1 encompasses the transition from the dissipative trapped-electron mode to the collisionless mode driven by the precessional-drift resonance as  $v_{se} \rightarrow 0$ . This model captures some features of the ohmic and L-mode scalings but  $\chi_e$  has a radial profile which decreases toward the plasma edge. A comparison of the form 4.20.1 with JET experimental results is shown in Fig. 4.20.1.

For a sufficiently large temperature gradient the  $\eta_i$  mode with  $k_{\perp} \rho_s \lesssim 1$  becomes unstable. This has been offered as an explanation of the confinement scalings for both the saturated ohmic confinement and the L-mode. In slab geometry instability is predicted for  $\eta_i \gtrsim 1$  but in toroidal geometry the criterion for instability is that the radial scale-length,  $L_{Ti}$ , for the ion temperature is such that  $L_{Ti} < L_{Tic}$  where  $L_{Tic} = cR$  with  $c \simeq 1/6$ . The toroidal mode is more relevant to most tokamaks. Several gyro-Bohm expressions for  $\chi_i$  have been derived, taking the form

$$\chi_i \sim \frac{\rho_s^2 c_s}{L_{Ti}} f(\text{geometry}) H\left(\frac{1}{L_{Ti}} - \frac{1}{L_{Tic}}\right), \quad 4.20.2$$

where  $H$  is the Heaviside function and  $f$  is a function of geometric ratios. One of the forms which has been more successful in reproducing the experimental profiles and current scalings has  $f \propto q$ . A model based on simulations of gyrofluid plasma equations for ion temperature gradient turbulence has a structure like eqn 4.20.2.

In a more collisionless plasma with the normalized collision frequency  $\nu_{\text{ei}} = \epsilon^{-3/2} v_i / (v_{T1} R q)$  such that  $\nu_{\text{ei}} < 1$ , trapped ion modes are predicted to be unstable. An expression for the thermal diffusivity due to the dissipative trapped ion instability is

$$\chi_i = \frac{3}{2\sqrt{2}} \frac{\rho_i^2 c_s R}{L_h^2} \sqrt{\frac{m_e}{m_i}} \frac{\epsilon^{1/2} q}{s^2 \nu_{\text{ei}}}.$$

where  $s = (r/q) dq/dr$ .

In addition to the electron drift waves with  $k_\perp \rho_0 \lesssim 1$ , there is the electromagnetic  $\eta_e$ -mode with  $k_\perp \lesssim \omega_{pe}/c$ , which is unstable for  $\eta_e \gtrsim 1$ , where  $\eta_e = d \ln T_e / d \ln n$ . An expression for the associated gyro-Bohm thermal diffusivity in cylindrical geometry is

$$\chi_e = 0.13 \left( \frac{c}{\omega_{pe}} \right)^2 \frac{v_{Te} s}{q R} \eta_e (1 + \eta_e).$$

Calculations for the toroidal version, the electron temperature gradient mode, lead to a result resembling eqn 4.20.2

$$\chi_e \sim \left( \frac{c}{\omega_{pe}} \right)^2 \frac{v_{Te}}{R} f H \left( \frac{1}{L_{Te}} - \frac{1}{L_{Tec}} \right).$$

Resistive ballooning modes are driven by the pressure gradient in the region of unfavourable curvature of the magnetic field. Although basically electrostatic, the mode has a magnetic component which can lead to a stochastic magnetic field. The resulting thermal diffusivity has the form

$$\chi_e = C \frac{\eta}{\mu_0} \left( \beta \frac{m_i}{m_e} \right)^{1/2} \left( \frac{\alpha}{s} \right)^{3/2}$$

where  $\eta$  is the Spitzer resistivity,  $\alpha = -(2\mu_0 R q^2/B^2) dp/dr$ ,  $\beta = 2\mu_0 p/B^2$ , and  $C \gtrsim 10$ . Replacing resistivity by electron inertia leads to a form of  $\chi_e$  which captures some features of the L-mode scaling. The convective transport in this case leads to

$$\chi_e \sim \frac{V_A}{q R} \left( \frac{c}{\omega_{pe}} \right)^2 \frac{\alpha^{3/2}}{h(s)},$$

where  $V_A$  is the Alfvén speed,  $h(s) = 1.7$  for  $s < 0.7$  and  $h(s) = 2.5s$  for  $s > 0.7$ .

Although micro-tearing modes are generally stable in hot tokamaks there remains the possibility of non-linear instability of magnetic islands. The Rutherford equation for island growth, derived in Section 7.3, is modified by various effects such as finite ion Larmor radius or bootstrap

currents to take the form

$$\frac{dw}{dr} = \eta \left( \Delta' + \frac{\lambda}{w} \right). \quad 4.20.3$$

In the case of bootstrap currents

$$\lambda = 0.6e^{3/2} \frac{\beta_p R}{sL},$$

where  $\beta_p = 2\mu_0 p/B_p^2$ . For large  $m$  numbers the outer solution to the perturbed flux takes the form  $\exp(-|m|x/r)$  where  $x$  is the distance from the resonant surface. Thus  $\Delta' = 2(\psi'/\psi) = -2m/r$  and eqn 4.20.3 gives a saturated island width

$$w = \frac{\lambda}{2m} r.$$

If islands 'overlap' the magnetic field becomes ergodic. A model based on this behaviour was given by Rebut, Lallia, and Watkins. In this model the condition for self-sustainment of the chaotic magnetic field leads to a critical temperature gradient. The model is semi-empirical being constructed from dimensionless quantities in such a way as to reproduce the ohmic and L-mode behaviour in JET. The resulting forms of the transport coefficients have a more complicated form than the familiar power dependencies on the parameters. In particular the enhancement over the neoclassical values is 'switched on' when the electron temperature gradient exceeds a critical value and  $dq/dr > 0$ .

This is illustrated by the radial electron heat flux which takes the form

$$q_e = q_{e,\text{neo}} - n_e \chi_{RLW} \left( \frac{dT_e}{dr} - \left( \frac{dT_e}{dr} \right)_c \right) H \left( \left| \frac{dT_e}{dr} \right| - \left| \left( \frac{dT_e}{dr} \right)_c \right| \right)$$

where  $H$  is the Heaviside function

$$\begin{aligned} \chi_{RLW} = 0.5c^2 \sqrt{\mu_0 m_i} & \frac{(1 - \sqrt{r/R})(1 + Z_{\text{eff}})^{1/2}}{B^2 R^{1/2}} \left( \frac{T_e}{T_i} \right)^{1/2} \\ & \times \frac{(1/T_e)(dT_e/dr) + (2/n_e)(dn_e/dr)}{(1/q^2)(dq/dr)} \end{aligned}$$

and the critical temperature gradient is

$$\left| \left( \frac{dT_e}{dr} \right)_c \right| = 0.06 \frac{e}{(\mu_0 m_e^{1/2})^{1/2}} \frac{1}{q} \left( \frac{n_j B^3}{n_e T_e^{1/2}} \right)^{1/2},$$

where  $\eta$  is the Spitzer resistivity. In addition to the critical temperature gradient the model predicts neoclassical transport when  $dq/dr$  is reversed in sign from its normal positive value.

An opportunity to test transport models is afforded by the International Profile Database.

Attempts to explain the transport barriers which appear in H-mode or internal transport barrier plasmas have generally relied on a reduction of the turbulence by shear in the plasma flow or the associated electric field as discussed in Section 4.19. When  $\Gamma = \omega_S \tau_D > 1$ , where  $\omega_S = k_\theta V'_\theta / \Delta$  and  $\tau_D = \Delta^2 / D$  the turbulence is expected to be reduced. Here  $\Delta$  is the radial width of a fluctuation and  $D$  the turbulent diffusion coefficient so that  $\tau_D$  is the time for turbulent diffusion across  $\Delta$ .  $V'_\theta$  is the radial shear in the poloidal flow and  $k_\theta$  the poloidal wavenumber so that  $\omega_S$  is the width of Doppler shifts across  $\Delta$ .

## 4.21

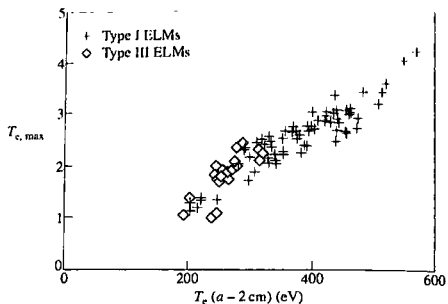
### Turbulence simulations, critical gradients, and temperature pedestals

Analytic estimates of turbulent transport, as described in Section 4.18, are of uncertain validity, so it is important to perform 'first-principles' numerical simulations of plasma turbulence in a tokamak. This approach solves the governing equations for a given plasma model without approximation. Three main models have been studied: one utilizes the Braginskii collisional fluid equations, one a full gyrokinetic description of the plasma and one a simpler so-called gyrofluid model.

The first model has been applied to the edge regions of the tokamak, where simulations of electromagnetic resistive ballooning modes have shown that the resulting turbulence is reduced by finite  $\beta$  and diamagnetic effects. This has led to a theory for the L-H transition. The gyrokinetic and gyrofluid models have been applied to temperature gradient turbulence and have cast light on transport processes in the main plasma core. The seminal gyrofluid study of  $\eta_i$ , or ion temperature gradient, turbulence led to an analytic parameterization of the numerical results, known as the IFS-PPPL model. This model produces high transport once the linear stability criterion is violated. Since this criterion is the form of a critical ion temperature gradient length  $R d(\ln T_i) / dr > c$ , where  $c$  is a constant ( $c \sim 6$ ), such a model tends to force the  $T_i$  profile to lie near this marginally stable profile—hence it is known as a critical gradient model. This model provides a good description of L-mode discharges in TFTR, but is less convincing for H-modes.

However, there is considerable experimental evidence that tokamaks exhibit critical gradient characteristics, the temperature profiles being resilient to changes from the critical gradient profile, a property known as 'stiffness'. In particular, a critical gradient model predicts a strong link of both the central temperature and energy content and the temperature at the edge of the plasma as is shown in Fig. 4.21.1. This edge temperature is taken to be the temperature at the inner side of the H-mode transport barrier, known as the pedestal temperature,  $T_{ped}$ . This linkage means high values of  $T_{ped}$  are important for tokamak performance. A common

**Fig. 4.21.1** Profile stiffness in ASDEX Upgrade. The central electron temperature is plotted against the boundary temperature measured 2 cm inside the plasma edge,  $T_e(a-2 \text{ cm})$ , showing how these are proportional if the edge pressure gradient is near the ballooning limit. It can be seen that this is the case for Type I ELMs. Type III ELMs do not follow this proportionality. (Suttorp, W. et al. *Plasma Physics and Controlled Fusion* 39, 2051 (1997).)



estimate for  $T_{ped}$  is based on the assumption that the good confinement in the H-mode barrier allows the pressure gradient to reach the limit imposed by ideal mhd ballooning stability,  $\alpha = -2\mu_0(Rq^2/B^2)(dp/dr) = \alpha_{crit} \sim 0(1)$ . If the barrier width  $\Delta$  is known then  $T_{ped}$  can be calculated. There is experimental evidence and plausible theoretical arguments that  $\Delta$  scales as a hybrid of the ion poloidal Larmor radius,  $\rho_{i\theta}$ , and the tokamak major radius,  $R$ . For example, if  $\Delta \propto \rho_{i\theta}$ , a scaling for  $T_{ped}$  can be developed:

$$T_{ped} \propto (R/a)(B^2/n^2 R^2 q^2).$$

When  $\alpha > \alpha_{crit}$ , ELMs are triggered.

The gyrofluid simulations were followed by more basic gyrokinetic calculations and differences between the predictions of the two models led to a deeper understanding of the non-linear saturation mechanisms involved. In the gyrokinetic model the ion temperature gradient instabilities first develop as radially elongated structures known as streamers. However, a secondary non-linear Kelvin-Helmholtz instability breaks these up into more isotropic eddies and microscale poloidal flows known as zonal flows build up. These zonal flows limit the growth of the turbulence in much the same way as the equilibrium sheared flows discussed in Section 4.19 lead to lower transport. As a result the critical gradient for ion temperature gradient modes is increased from its linear value, an effect known as the 'Dimits upshift'. In the less accurate gyrofluid model the growth of these zonal flows is impeded and the transport remains high. Nevertheless there is a damping of zonal flows by parallel neoclassical viscosity in a torus and this introduces a collisionality dependence in the gyrokinetic simulations of transport coefficients similar to that observed experimentally. Figure 4.21.2 shows an example of the turbulence calculated by a simulation code.

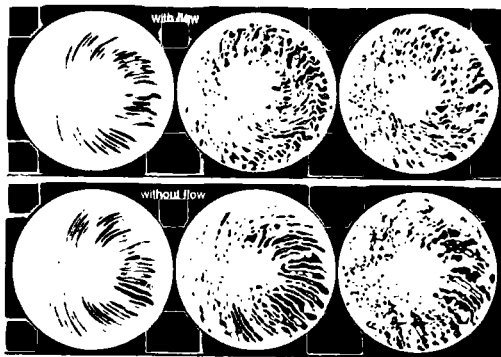


**Fig. 4.21.2** Turbulence simulations with a gyrokinetic code, the turbulence evolving in time from left to right. The behaviour with sheared flow is shown in the upper panel, the initial linear, radially extended structures being broken up by the flow. The lower panel shows the behaviour without sheared flow and the extended structures are seen to persist into the non-linear regime. (Lin, Z. and Tang, W.M. *Physics of Plasmas* 9, 1856 (2002).)

Experimental investigations of electron thermal transport in non-monotonic  $q$  profiles show that it often remains high. A candidate mode to explain electron transport is the electron temperature gradient instability. Electromagnetic gyrokinetic simulations of this turbulence show that radial streamers again develop but in contrast to the case of the ion temperature gradient mode, they persist. Since this implies  $k_r \ll k_\theta$  the transport is much greater than the mixing-length estimate based on eqn 4.18.18 for isotropic turbulence with  $k_r \sim k_\theta$ . However, for small or negative magnetic shear and large values of the normalized pressure gradient,  $\alpha$ , the streamer can be inhibited and low electron transport ensues. This provides an explanation of the experimental observations.

## 4.22

### Impurity transport

The presence of impurities can dilute the fuel ions in a reacting plasma and enhance radiation losses, both effects impairing the performance of a tokamak reactor. Impurities arise from the solid surfaces and, through transport processes, can penetrate to the central plasma. Another serious source is the helium 'ash' necessarily produced by the fusion reactions themselves. The requirement that the fraction of helium ash remains acceptable ( $\lesssim 10\%$ ) can only be met if the outward transport of helium is sufficiently rapid.

A discussion of impurity transport involves consideration of both neoclassical and anomalous processes since experiments show evidence of both effects.

The neoclassical theory of impurity transport, although exceedingly complex for an arbitrary number of species, is highly developed. For simplicity, however, the discussion here will be restricted to one charge state of one impurity species.

The distinctive feature of neoclassical impurity particle transport follows from the relation 4.6.11 between fluxes and momentum exchange. Since the collision frequency of ions with impurities can greatly exceed that for ions with electrons, such collisions can induce a correspondingly greater impurity flux and an oppositely directed ion flux. This will modify the impurity density profile until the frictional forces vanish. The condition for this is

$$\frac{I}{n_z} \frac{dn_z}{dr} = \frac{Z}{n_i} \frac{dn_i}{dr} + \frac{\alpha}{T} \frac{dT}{dr}, \quad 4.22.1$$

where  $n_z$  is the density of an impurity species of charge  $Z$ ,  $n_i$  is the plasma ion density and the coefficient  $\alpha$  depends on the details of the thermal force. In the absence of the thermal force, eqn 4.22.1 implies a concentration of impurities towards the magnetic axis according to the relation

$$\frac{n_z(r)}{n_z(0)} = \left( \frac{n_i(r)}{n_i(0)} \right)^Z.$$

This relation has potentially serious implications for radiation losses from impurities and for the removal of helium ash resulting from fusion reactions. However, these problems may be reduced if the coefficient  $\alpha$  in eqn 4.22.1 is negative, an effect known as 'temperature screening'. The sign of  $\alpha$  depends on the collisional regimes of both plasma ions and impurities.

Impurities are heavier and more highly charged than the plasma ions and hence will tend to lie in the Pfirsch-Schlüter regime. Consequently there is generally no banana-plateau contribution to the impurity diffusion. The so-called principle of detailed balance states that the contributions from banana-plateau and from Pfirsch-Schlüter particle transport are separately ambipolar. Thus the plasma ion transport due to collisions with impurities will be characteristic of the Pfirsch-Schlüter regime since the impurities experience only Pfirsch-Schlüter transport. However, it is still necessary to consider subdivisions of the Pfirsch-Schlüter regime.

The first of these, called the intermediate Pfirsch-Schlüter regime, arises when collisions are insufficient to make the plasma ion distribution Maxwellian. Normally this only applies when the plasma ions are in the banana-plateau regime. In an impure plasma the time for the plasma ion distribution to relax to a Maxwellian can exceed the 90° collision time, and so this situation arises even in the Pfirsch-Schlüter regime. Detailed

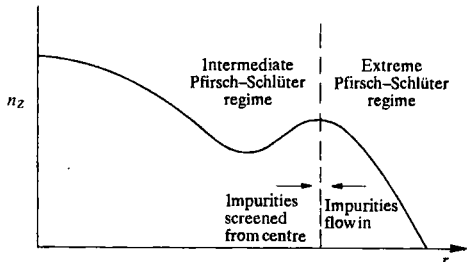


**Fig. 4.22.1** Predicted neoclassical impurity fluxes near plasma edge, showing impurity accumulation.

calculations show that temperature screening occurs in the intermediate Pfirsch–Schlüter regime. When collisions are sufficient to maintain a Maxwellian distribution of the plasma ions, as is usually the case near the edge of the plasma, the conventional fluid (or extreme Pfirsch–Schlüter) description is appropriate and it is found that temperature screening disappears. Figure 4.22.1 indicates the consequences for the radial impurity distribution.

The full neoclassical theory has been implemented in transport codes, allowing for a large number of impurity species and charge states in these various regimes. Experimental situations occur in which impurity transport exhibits these neoclassical features but, more commonly, impurities appear to experience anomalous transport similar to that characteristic of the background plasma. Unfortunately no adequate theory of this anomalous transport exists but surprisingly a simple universal empirical formula appears to satisfactorily model many situations.  $\Gamma_z$ , the radial particle flux averaged over a magnetic surface, is given by the formula

$$\Gamma_z = -D_z \left( \frac{dn_z}{dr} + 2S \frac{r}{a^2} n_z \right),$$

with

$$D_z = 0.25\text{--}6 \text{ m}^2 \text{s}^{-1}, \quad S = 0.5\text{--}2, \quad 4.22.2$$

and has been used in most transport codes. It contains a diffusion coefficient  $D_z$  and an inward velocity similar to that commonly used to model the anomalous particle fluxes of the background plasma.

Detailed experimental studies of the transport of trace impurities injected into tokamak plasmas have been carried out. In the core of the plasma the transport of impurities is very slow in the absence of sawtooth activity. Experiments in JET show that typically  $D_z \sim 0.1 \text{ m}^2 \text{s}^{-1}$ . This is an order of magnitude lower than its value further out, but is still greater

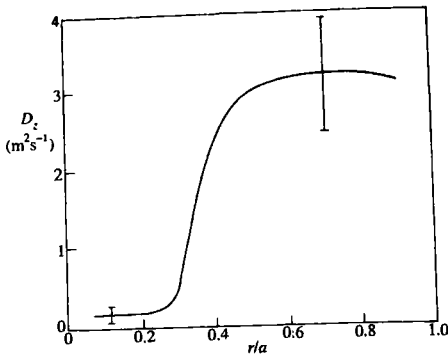


Fig. 4.22.2 Experimental profile of the diffusion coefficient for injected nickel in a JET discharge. The bars indicate the range of uncertainty.

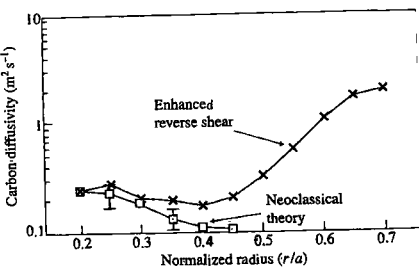
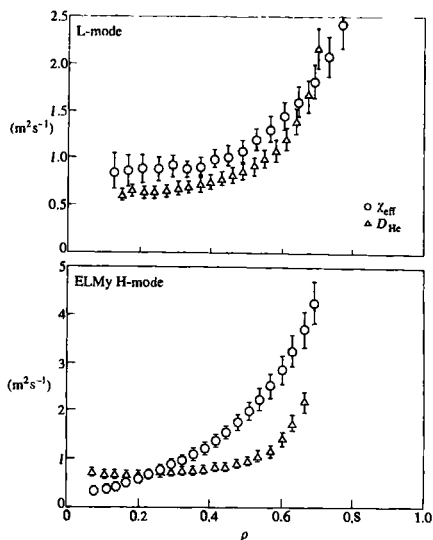


Fig. 4.22.3 Comparison of carbon diffusivity and neoclassical prediction for an enhanced reversed shear plasma in TFTR. (Efthimion, P.C. et al. *Nuclear Fusion* **39**, 1905 (1999)).

than the neoclassical predictions by a factor 2 to 10. In fact  $D_z$  appears to undergo a rapid transition at a particular radius, possibly characterized by a value of the shear parameter,  $s = (r/q)dq/dr$ , of around 0.5. This behaviour is shown in Fig. 4.22.2. Furthermore  $D_z$  increases markedly with the temperature gradient in this outer region. However, impurity transport in non-monotonic  $q$  profiles can be described by neoclassical theory, as shown in Fig. 4.22.3. The diffusivity of helium, significant for the build-up of helium ash which dilutes the fuel in a burning plasma, is comparable to  $\chi_{\text{eff}}$  for L and H-mode plasmas (see Fig. 4.22.4 from DIII-D).

Sawtooth activity in the core is efficient in removing impurities from that region, while ELM activity at the edge can prevent them entering the plasma and accumulating at the centre in the H-mode.



**Fig. 4.22.4** Comparison between the helium diffusivity  $D_{\text{He}}$  and the effective thermal diffusivity,  $\chi_{\text{eff}}$ , in DIII-D for L-mode and ELM My H-mode. (ITER Physics Basis, Nuclear Fusion 39, 2175 (1999)).

## 4.23

### Experimental discoveries

While most attention has been paid to the global confinement and general transport properties of tokamaks there have been several specific experimental results which, because surprising, are worthy of study. Examination of the underlying behaviour in these cases should provide clues to the understanding of the complex nature of transport in tokamaks. Three examples are described below.

#### The X-event and power switch-off experiment

*The X-event.* Figure 4.23.1 shows the time development of the total plasma energy,  $W$ , in a particular type of JET discharge with neutral beam heating. The characterizing feature of the behaviour is the sudden change in  $dW/dr$  from being strongly positive to strongly negative. Because of the problems in understanding this sudden transition it has been called the X-event.

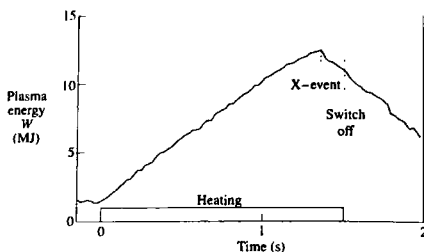


Fig. 4.23.1 Time dependence of the plasma energy in a heated plasma, implying abrupt changes in confinement at the X-event and power switch-off.  
(Wesson, J.A. and Balet, B., *Physical Review Letters*, **77**, 5214 (1996).)

There is always an obvious immediate cause of the X-event in the form of a sawtooth collapse, an ELM, or both. However, these phenomena are very brief and cannot provide an explanation for the very different behaviour of  $W$  immediately before and after the X-event when the gross configuration of the plasma is the same.

The power balance equation is

$$\dot{W} = P - \frac{W}{\tau}, \quad 4.23.1$$

where  $P$  is the heating power, and the energy loss is characterized by the confinement time  $\tau$ . Rearranging eqn 4.23.1 gives an expression for the confinement time

$$\tau = \frac{W}{P - \dot{W}}. \quad 4.23.2$$

In the example of Fig. 4.23.1 the power is 18 MW and considering times immediately before and after the X-event,  $\dot{W} = 8$  MW before and  $-11$  MW after. Equation 4.23.2 gives the ratio of the confinement times  $\tau_1$  before and  $\tau_2$  after to be

$$\frac{\tau_1}{\tau_2} = 2.9.$$

Since the profiles of the temperature and density are essentially the same before and after the X-event this result shows that for plasmas of this type the confinement properties cannot be expressed as a simple function of these variables.

*The switch-off.* Even more surprising is the behaviour when the heating beams are switched off some time after the X-event. From eqn 4.23.1 it is expected that the negative slope of  $\dot{W}$  will increase by  $P$ , in this case 18 MW, but as seen from Fig. 4.23.1 there is no significant change in the slope. Before the switch-off

$$\tau_b = \frac{W}{P - \dot{W}}$$

and after

$$\tau_a = \frac{W}{-W}$$

giving a ratio

$$\frac{\tau_a}{\tau_b} = 1 - \frac{P}{W}.$$

For the present case this gives a ratio of confinement times of approximately 3. Since the plasma configuration is essentially the same before and after switch-off it is again difficult to understand the change in confinement. The simple explanation that the beams were inadvertently switched off at the X-event is not available since the beams are detected directly by charge exchange measurements up to the switch-off.

These results seem to imply that the heat transport and confinement are not single valued functions of the macroscopic plasma properties.

### The L-H transition

As described in Section 4.13 it is found that with increased heating there is a transition to H-mode confinement. This is marked by the formation of large gradients in temperature and density at the edge of the plasma. The fact that large differences in these quantities are sustained over a narrow region implies that the improved confinement can be attributed to a transport barrier formed at the edge of the plasma. Theoretical efforts to provide an explanation of H-modes have concentrated on trying to find a bifurcation between states with and without this barrier.

A study of the phenomenon in JET showed a quite different behaviour. Cases were found in which at the onset of the H-mode an immediate change in the behaviour occurred, not only at the edge but across the outer half of the plasma radius. Figure 4.23.2 shows the time dependence of

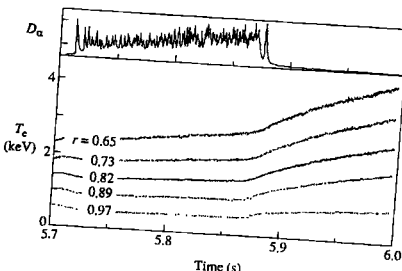


**Fig. 4.23.2** The fall in the  $D_\alpha$  signal marks the onset of the H-mode. The electron temperature undergoes an increase in slope simultaneously over a large part of the radius. The radius  $r$  is normalized to the radius of the plasma. (Neudatchin, S.V., Cordey, J.G., and Muir, D.G. *Proc. 20th E.P.S. Conf. on Controlled Fusion and Plasma Physics*, Lisbon 1993, Vol. I7C Part 1, p. 83.)

the electron temperature at several positions across the plasma radius. It is clear that this behaviour is not just due to the formation of a barrier at the edge of the plasma. Had this been the case the plasma away from the edge would have shown a delayed response over a longer timescale. The almost simultaneous change in the rate of temperature increase over the outer half of the plasma obviously calls for a different explanation. One possibility is that the conductivity is not determined locally. This might be the case, for example, if the anomalous transport is due to radially elongated convective cells.

### Narrow transitions

The temperature gradients associated with internal transport barriers are described in Section 4.14. A remarkable feature of the observed gradients is the narrowness of the transition to the steep gradient. Since the thermal conductivity  $\kappa = -q/(dT/dr)$  where  $q$  is the heat flux, this sudden radial transition implies that the thermal conductivity changes over a very short distance. This is illustrated in Fig. 4.23.3(a) which gives the result of

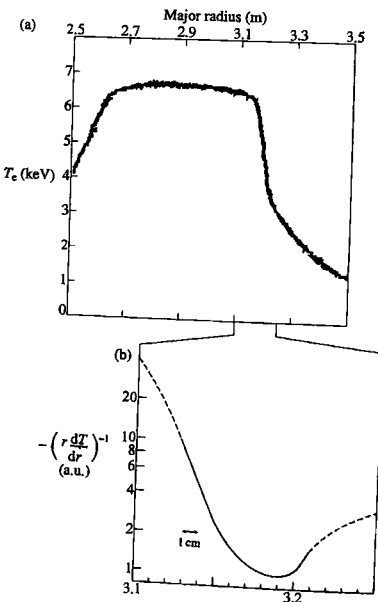


**Fig. 4.23.3** (a) Electron temperature profile in a TFR plasma with an internal transport barrier. (b) Graph of  $-\left(r \frac{dT}{dr}\right)^{-1}$  derived from the temperature profile, implying a large change in thermal conductivity over a short distance. (From Bell, M.G. et al., *Plasma Physics and Controlled Fusion* 41, A719 (1999).)

an electron temperature measurement in TFTR in which a reliable continuous plot of temperature was obtained by moving the plasma across the line of sight of the detector channels.

Over short distances the total heat flux  $Q$  across magnetic surfaces is almost constant. Since  $Q \propto r\dot{q}$ , a good estimate of the local radial variation of the thermal conductivity is obtained from  $\kappa \propto 1/(r dT/dr)$ . Figure 4.23.3(b) gives a graph of  $-1/(r dT/dr)$  carefully derived from Fig. 4.23.3(a). It is seen that there is an order of magnitude change and at its steepest the graph implies a factor of 2 change in  $\kappa$  over 1 cm. This result provides a challenging test for any theory of transport across internal barriers.

## 4.24

### Radiation losses

A pure hydrogen plasma emits electromagnetic radiation. Microscopically this is due to the acceleration of the charged particles. Because of their lighter mass the electrons undergo larger acceleration than the ions. Consequently they radiate much more strongly and only the electrons need be considered.

The electrons are accelerated in two ways. Firstly they are accelerated by collisions, the resulting radiation being called bremsstrahlung. Secondly they are subject to the acceleration of their cyclotron motion and the associated radiation is called cyclotron or synchrotron radiation.

In the presence of impurities the bremsstrahlung is enhanced. There are also further losses due to the atomic processes of line radiation and recombination radiation. These losses are described in Section 4.25.

#### Bremsstrahlung

The power radiated by an electron undergoing an acceleration  $a$  is

$$P = \frac{e^2}{6\pi\epsilon_0 c^3} a^2. \quad 4.24.1$$

The acceleration of an electron during a collision with an ion is caused by the Coulomb force  $Ze^2/4\pi\epsilon_0 r^2$ , where  $r$  is their separation and  $Ze$  the charge on the ion, and so

$$a = \frac{Ze^2}{4\pi\epsilon_0 m_e r^2}. \quad 4.24.2$$

Taking the duration of a collision to be  $2r/v$ , the energy lost per collision is  $\delta E = P2r/v$  and eqns 4.24.1 and 4.24.2 give

$$\delta E = \frac{Z^2 e^6}{6(2\pi\epsilon_0 c r)^3 m_e^2 v}.$$

Thus, integrating over the impact parameter  $r$ , the bremsstrahlung radiation power per unit volume is given by

$$\begin{aligned} P_{\text{br}} &= n_e n_z \int \delta E v 2\pi r \, dr \\ &= \frac{n_e n_z Z^2 e^6}{24\pi^2 \epsilon_0^3 c^3 m_e^2} \int \frac{1}{r^2} \, dr. \end{aligned} \quad 4.24.3$$

The integral is  $1/r$  but the divergence at small  $r$  is removed by quantum mechanical effects so that the lower limit of  $r$  is  $\hbar/m_e v$ . Using this limit in  $1/r$  and replacing  $v$  by its average value from  $1/2 m_e v^2 = 3/2 T_e$ , eqn 4.24.3 gives the required form for  $P_{\text{br}}$ . Substituting the numerical factor obtained from a full calculation then gives the bremsstrahlung power due to ions of charge  $Z$  as

$$P_{\text{br}} = g \frac{e^6}{6(3/2)^{1/2} \pi^{3/2} \epsilon_0^3 c^3 h m_e^{3/2}} Z^2 n_e n_z T_e^{1/2}, \quad 4.24.4$$

where  $g$  is the Gaunt factor which gives a quantum mechanical correction. Under the conditions of interest  $g \simeq 2\sqrt{3}/\pi$  and

$$P_{\text{br}} = 5.35 \times 10^{-37} Z^2 n_e n_z T_e^{1/2} \text{ W m}^{-3}, \quad T_e \text{ in keV.}$$

Figure 4.24.1 gives the ratio of the bremsstrahlung power in a pure D-T plasma to the thermonuclear power produced in  $\alpha$ -particles, as given by eqn 4.6. This shows that although bremsstrahlung is a significant

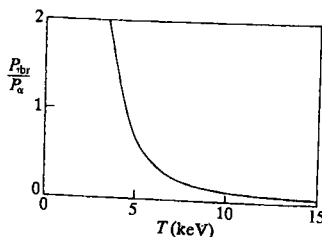


Fig. 4.24.1 Ratio of power radiated in bremsstrahlung to the thermonuclear power produced in  $\alpha$ -particles for a D-T plasma with  $T_i = T_e$ .

loss mechanism it does not present a serious obstacle to ignition in a pure D-T plasma.

### Cyclotron radiation

The theory of cyclotron radiation losses is quite complex, involving emission and absorption at harmonics of the cyclotron frequency in spatially varying plasma and magnetic field. However, the basic elements can be simply described.

The power radiated from a single non-relativistic electron is given by eqn 4.24.1 with the acceleration of the cyclotron orbit,  $a = \omega_{ce}^2 \rho_e$ . Putting  $\rho_e = (2T_e/m_e)^{1/2}/\omega_{ce}$  would then give a radiation power density

$$P_c = (e^4/3\pi\varepsilon_0 m_e^3 c^3) B^2 n_e T_e.$$

This power is very large and under reactor conditions would be more than  $1 \text{ MW m}^{-3}$ . However, this is *not*, the power lost from the plasma because the plasma is optically thick to radiation at the fundamental frequency. The principal energy loss occurs at the harmonics of the cyclotron frequency, these harmonics being generated through relativistic effects. The power in each harmonic falls rapidly with increasing harmonic number  $n$ , being proportional to  $(v_{Te}^2/c^2)^{n-1}$ . However, like the fundamental, lower harmonics are absorbed and the plasma behaves like a black body for these frequencies, radiating according to the Rayleigh-Jeans law. Most of the power loss occurs, therefore, in the harmonics at the transition from optically thick to optically thin behaviour. The resulting power loss is only  $10^{-2}\text{--}10^{-3}$  of the power given above for the fundamental without absorption. In a reactor this power loss would be of the order of  $10^{-2} \text{ MW m}^{-3}$  and would therefore be negligible.

## 4.25

### Impurity radiation

The presence of impurities in the plasma produces energy losses through radiation. There are two types of process involved. The first is the enhancement of bremsstrahlung because of the higher value of the ionic charge for impurities. The second is the radiation which occurs through the atomic processes of fine radiation and recombination.

In a steady state with negligible transport effects (coronal equilibrium), the power radiated from a given impurity species is proportional to the electron density  $n_e$  and to the impurity density  $n_1$ , and the radiated power

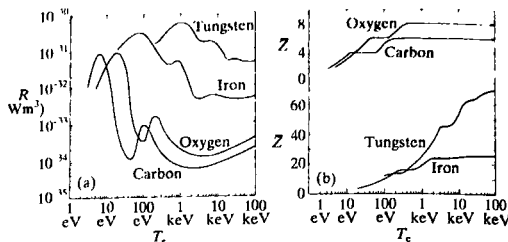


**Fig. 4.25.1** (a) The radiation parameter  $R$  and (b) the mean charge  $\bar{Z}$  as functions of electron temperature for carbon, oxygen, iron, and tungsten.

density may be written

$$P_R = n_e n_I R,$$

where the radiation parameter  $R$  is a function of the electron temperature. Graphs of  $R(T_e)$  are given in Fig. 4.25.1 for a number of elements.

The  $R(T_e)$  curves have a principal maximum together with subsidiary maxima at higher temperatures. For light impurities the principal maximum occurs at a low temperature and above this temperature the radiation is substantially reduced. As the temperature is increased, electrons are successively removed from the impurity ions and when the ions are fully stripped only bremsstrahlung radiation remains. In a reactor low  $Z$  atoms would be fully stripped. At a particular temperature a given impurity species will have a distribution of charge states  $Z$ . A mean value  $\bar{Z}$ , can be defined by

$$\bar{Z} = \sum n_z Z / n_I \quad \text{where } n_I = \sum n_z,$$

$n_z$  being the density of ions in the charge state  $Z$ . Some graphs of  $\bar{Z}(T_e)$  are given in Fig. 4.25.1.

For low  $Z$  impurities such as carbon and oxygen the maximum radiation occurs at a very low temperature, of the order of tens of eV. The ions of these impurities are fully stripped at a temperature of 1 keV and in the hot plasma of a reactor they would only radiate through bremsstrahlung. At the plasma edge radiation losses arise from the incompletely stripped impurities which enter the plasma as neutral atoms.

For high  $Z$  impurities, and these include the metals of which the tokamak is constructed, the first maximum in radiated power occurs at a somewhat higher temperature. For temperatures above 100 eV the radiation per ion is much greater than for low  $Z$  impurities. Even at reactor temperatures these ions are not fully stripped and the radiated power is such that the level of high  $Z$  impurities must be very small in a reactor.

A quantitative assessment of the required impurity levels can be obtained by calculating the radiated power for a particular impurity as

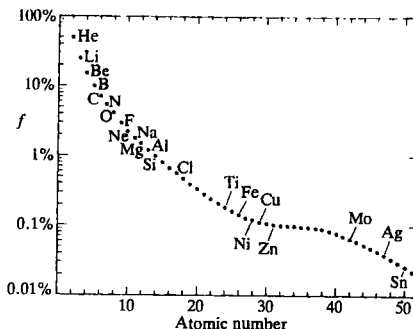


**Fig. 4.25.2** Fractional impurity level which produces a radiation power equal to 10% of the total thermonuclear power.

a fraction,  $F$ , of the thermonuclear power given by eqn 1.4.2

$$F = \frac{n_e n_1 R}{\frac{1}{4} n_H^2 (\sigma v) \mathcal{E}} = \frac{(1 + f \bar{Z}) f R}{\frac{1}{4} (\sigma v) \mathcal{E}},$$

where  $n_H$  is the total density of hydrogenic ions (deuterons plus tritons),  $f$  is the impurity fraction  $n_I/n_H$  and  $\mathcal{E} = 17.6$  MeV. Figure 4.25.2 gives the values of  $f$  which would produce a radiated power fraction  $F = 0.1$  at  $T = 10$  keV. This corresponds to a radiated power loss of 50 per cent of the  $\alpha$ -particle power.

A further problem arising from impurities in a reactor is that, for a given total particle density, there is a displacement of reacting ions by the large number of electrons produced by the impurities.

## Bibliography

A book which provides insights into the physics is

Itoh, K., Itoh, S.-I., and Fukuyama, A. *Transport and structural formation in plasmas*. Institute of Physics Publishing, Bristol (1999).

The theory of purely collisional transport is described in Helander, P. and Sigmar, D.J. *Collisional transport in magnetized plasmas*. Cambridge University Press, Cambridge (2002);

and a further theoretical account is given by Hazeltine, R.D. and Meiss, J.D. *Plasma confinement*, Addison-Wesley, Redwood City, California (1991).

### General review of transport

A summary of theoretical and experimental research on tokamak confinement can be found in

ITER Physics Expert Groups on Confinement and Transport and Confinement Modelling and Databases. ITER Physics Basis, Chapter 2: Plasma confinement and transport. *Nuclear Fusion* 39, 2175 (1999).

Experimental results have been reviewed by Hugill, J. *Transport in tokamaks—a review of experiment*. *Nuclear Fusion* 23, 331 (1983).

- and discussed by Wagner, E. and Stroth U. Transport in toroidal devices – the experimentalist's view. *Plasma Physics and Controlled Fusion* **35**, 1321 (1993).
- Measurements and theories of anomalous transport are discussed by Liewer, P.C. Measurements of micro-turbulence in tokamaks and comparisons with theories of turbulence and anomalous transport. *Nuclear Fusion* **25**, 543 (1985).
- Reviews of neoclassical theory can be found in Hinton, F.L. and Hazeltine, R.D. Theory of plasma transport. *Reviews of Modern Physics* **48**, 239 (1976); and Galeev, A.A. and Sagdeev, R.Z. Theory of neoclassical diffusion. In *Reviews of plasma physics* (ed. Leontovich, M.A.) Vol. 7, p. 257. Consultants Bureau, New York (1979).
- ### Neoclassical transport
- The original paper on Pfirsch-Schlüter transport is Pfirsch, D. and Schlüter, A. Der Einfluss der elektrischen Leitfähigkeit auf das Gleichgewichtsverhalten von Plasmen niedrigen Drucks in Stellaratoren. Max-Planck-Institut, Report MPI/PA/7/62 (1962); and on banana-plateau transport is Galeev, A.A. and Sagdeev, R.Z. Transport phenomena in a collisionless plasma in a toroidal magnetic system. *Zhurnal Experimentalnoi i Teoreticheskoi Fiziki* **53**, 348 (1967) [Soviet Physics JETP **26**, 233 (1968)].
- ### Pfirsch-Schlüter transport
- Treatments can be found in Solovev, L.S. and Shafranov, V.D. Effects of curvature on classical diffusion and thermal conductivity. *Reviews of plasma physics* (ed. Leontovich, M.A.) Vol. 5, p. 145. Consultants Bureau, New York (1970); and Hazeltine, R.D. and Hinton, F.L. Collision dominated plasma transport in toroidal confinement systems. *Physics of Fluids* **16**, 1883 (1973).
- ### Banana regime transport
- A heuristic discussion can be found in Kadomtsev, B.B. and Pogutse, O.P. Trapped particles in toroidal magnetic systems. *Nuclear Fusion* **11**, 67 (1971). The complete variational solution for the fluxes is obtained in Rosenbluth, M.N., Hazeltine, R.D., and Hinton, F.L. Plasma transport in toroidal confinement systems. *Physics of Fluids* **15**, 116 (1972). A clear derivation of the essential results (including plateau and Pfirsch-Schlüter diffusion) is given by Rutherford, P.H. Collisional diffusion in an axisymmetric torus. *Physics of Fluids* **13**, 482 (1970).
- Expressions for ion neoclassical conductivity in a finite aspect-ratio torus, also valid for all collisionality regimes, are given in Chang, C.S. and Hinton, F.L. Effect of impurity particles on the finite aspect-ratio neoclassical ion thermal conductivity in a tokamak. *Physics of Fluids* **29**, 3314 (1986).
- ### Plateau transport
- The complete results are derived in Galeev, A.A. Diffusion-electrical phenomena in a plasma confined in a tokamak machine. *Zhurnal Experimentalnoi i Teoreticheskoi Fiziki* **59**, 1378 (1970) [Soviet Physics JETP **32**, 752 (1971)].
- The transition between banana and plateau transport is investigated in Hinton, F.L. and Rosenbluth, M.N. Transport properties of a toroidal plasma at low-to-intermediate collision frequencies. *Physics of Fluids* **16**, 836 (1973).
- ### Ware pinch effect, bootstrap current, and neoclassical resistivity
- These effects are all implied in the complete banana-plateau transport theory, references given above, but seminal and interesting papers are Ware, A.A. Pinch effect for trapped particles in a tokamak. *Physical Review Letters* **25**, 15 (1970). Bickerton, R.J., Connor, J.W., and Taylor, J.B. Diffusion driven plasma currents and bootstrap tokamak. *Nature Physical Science*, **229**, 110 (1971). Hinton, F.L., and Oberman, C. Electrical conductivity of plasma in a spatially inhomogeneous magnetic field. *Nuclear Fusion* **9**, 319 (1969).
- The effects of finite aspect-ratio on the bootstrap current are to be found in Hirshman, S.P. Finite-aspect-ratio effects on the bootstrap current in tokamaks. *Physics of Fluids* **31**, 3150 (1988), and the subject of bootstrap currents is reviewed in Kikuchi, M. and Azumi, M. Experimental evidence for the bootstrap current in a tokamak. *Plasma Physics and Controlled Fusion* **37**, 1215 (1995).
- Tight aspect-ratio effects on neoclassical conductivity are discussed in Hazeltine, R.D., Hinton, F.L., and Rosenbluth, M.N. Plasma transport in a torus of arbitrary aspect ratio. *Physics of Fluids* **16**, 1645 (1973); and

Boshman, S.P., Hawrylyuk, R.J. and Birge, B. Neoclassical conductivity of a tokamak plasma. *Nuclear Fusion* **17**, 611 (1977).

### Ripple transport

This has been discussed in detail in the review by Kondratenko, L.M. Neoclassical theory of transport processes in toroidal magnetic confinement systems, with emphasis on non-axisymmetric configurations. *Nuclear Fusion* **24**, 851 (1984).

Ripple trapped transport is described in

Stringer, T.E. Effect of the magnetic field ripple on diffusion in tokamaks. *Nuclear Fusion* **12**, 689 (1972).

An account of ripple plateau transport can be found in

Boozer, A.H. Enhanced transport in tokamaks due to toroidal ripple. *Physics of Fluids* **23**, 2283 (1980).

A good account of banana drift transport is included in Goldston, R.J. and Towner, H.H. Effects of toroidal field ripple on suprathermal ions in tokamak plasmas. *Journal of Plasma Physics* **26**, 283 (1981).

A more recent review is

Yushmanov, P.N. Diffusive transport processes caused by ripple in tokamaks. *Reviews of plasma physics* (ed. Kadomtsev, B.B.) Vol. 16, p. 117. Consultants Bureau, New York (1990).

### Confinement modes

A description of different modes of energy confinement is given in

Stambaugh, R.D. et al. Enhanced confinement in tokamaks. *Physics of Fluids* **B2**, 2941 (1990).

The H-mode was first observed in the ASDEX tokamak.

Wagner, F. et al. Regime of improved confinement and high beta in neutral beam heated divertor discharges in the Asdex tokamak. *Physics Review Letters* **49**, 1408 (1982).

Further information can be found in the overviews amongst the papers for the 4th H-mode Workshop (I.A.E.A. Technical Committee Meeting on H-mode Physics), Naka, Japan, November 1993, published in *Plasma Physics and Controlled Fusion* **36**, pp. A3-A74 (1994).

Information on non-monotonic q profile configurations can be found in

Levinton, F.M., Zarnstorff, M.C., Bartha, S.H., Bell, M., Bell, R.E., Budny, R.V., Bush, C., Chang, Z., Fredrickson, E., Jones, A. et al. Improved confinement with reversed shear in TFTR. *Physical Review Letters* **75**, 4417 (1995).

Connor, J.W., Bracco, G., Buttery, R.J., Hidalgo, C., Jacchia, A., Peeters, A.G., and Stroth, U. EU-US Transport Task Force Workshop on Transport in Fusion Plasmas, Transport Barrier Physics. *Plasma Physics and Controlled Fusion* **43**, 355 (2001).

Synakowski, E.J. Formation and structure of internal and edge transport barriers. *Plasma Physics and Controlled Fusion* **40**, 581 (1998).

A review of experimental data on the L-H transition is given in

Carlstrom, T.N. Transition physics and scaling overview. *Plasma Physics and Controlled Fusion* **38**, 1149 (1996).

while theories of the transition are reviewed in

Connor, J.W. and Wilson, H.R. A review of theories of the L-H transition. *Plasma Physics and Controlled Fusion* **42**, R1 (2000).

### Scaling relations for energy confinement

An early review of experimental results was given by Goldston, R.J. Energy confinement scaling in tokamaks: some implications of recent experiments with ohmic and strong auxiliary heating. *Plasma Physics and Controlled Fusion* **26**, No. 1A, 87 (1984).

and more recently by

Kaye, S.M. et al. Status of global energy confinement studies. *Physics of Fluids* **B2**, 2926 (1990).

A compilation of scalings for the energy confinement and L-H power threshold is in

Thomson, K., Bracco, G., Bush, C., Carlstrom, T.N., Chudnovskij, A.N., Cordey, J.G., Deboos, J.C., Fielding, S.J., Fukuda, T., Greenwald, M. et al. Latest results from the ITER H-mode confinement and threshold databases. *Fusion energy* (Proc. 17th Int. Conf., Yokohama 1998) Vol. 3, p. 987 I.A.E.A. Vienna (1999).

Scaling relations for L- and H- mode confinement have been given by

Kaye, S. and the ITER Joint Central Team and Home Team. Projection of ITER performance using the multi-machine L and H mode databases. *Plasma physics and controlled nuclear fusion research* (Proc. 15th Int. Conf. Seville, 1994) Vol. 2, p. 525 I.A.E.A. Vienna (1995).

A theoretical framework for discussing the empirical laws can be found in

Kadomtsev, B.B. Tokamaks and dimensional analysis. *Fizika Plasmy* **1**, 531 (1975) [Soviet Physics—Journal of Plasma Physics] **1**, 295 (1975),

and

Connor, J.W. and Taylor, J.B. Scaling laws for plasma confinement. *Nuclear Fusion* **17**, 1047 (1977).

### Experimental observations on transport coefficients and fluctuations

The correlations between fluctuations and local transport coefficients are discussed in the review by

- Wootton, A.J. *et al.* Fluctuations and anomalous transport in tokamaks. *Physics of Fluids* **B2**, 2879 (1990) and the papers
- Connor, J.W. Tokamak turbulence—electrostatic or magnetic? *Plasma Physics and Controlled Fusion* **35**, B293 (1993).
- Bickerton, R.J. Magnetic turbulence and the transport of energy and particles in tokamaks. *Plasma Physics and Controlled Fusion* **39**, 339 (1979).
- Some experimental results on thermal diffusivities are discussed in
- Perkins, F.W. *et al.* Nondimensional transport scaling in the Tokamak Fusion Test Reactor: Is tokamak transport Bohm or gyro-Bohm? *Physics of Fluids* **B5**, 477 (1993).
- An example of a study of particle transport is given in
- Behringer, K., Engelhardt, W., Fussman, G. *et al.* in *Proc. IAEA Technical Committee on Divertors and Impurity Control*, Max Planck Inst. für Plasma-physik, Garching, 42 (1981).
- The effect of transport barrier on fluctuation is described in
- Mazzucato, E., Batha, S.H., Beer, M., Bell, M., Bell, R.E., Budny, R.V., Bush, C.H., Hahm, T.S., Hammett, G.W., Levinton, F.M., Nazikian, R. *et al.* Turbulent fluctuations in TFTR configurations with reversed magnetic shear. *Physical Review Letters* **77**, 3145 (1996).
- Theories of anomalous transport**
- Some of the principles are discussed in Chapter 4 of
- Kadomtsev, B.B. *Plasma turbulence*. Academic Press, London (1965), and in
- Horton, W. Nonlinear drift waves and transport in magnetized plasma. *Physics Reports* **192**, 1 (1990).
- The effects of stochastic magnetic fields on transport are addressed by
- Rechester, A.B. and Rosenbluth, M.N. Electron heat transport in a tokamak with destroyed magnetic surfaces. *Physical Review Letters* **40**, 38 (1978); and in more depth by
- Krommes, J.A., Oberman, C., and Kleva, R.G. Plasma transport in stochastic magnetic fields. Part 3, Kinetics of test particle diffusion. *Journal of Plasma Physics* **30**, 11 (1983).
- The applications to a number of specific instabilities can be found in
- Kadomtsev, B.B. and Pogutse, O.P. Turbulence in toroidal systems. *Reviews of plasma physics* (ed. Leontovich, M.A.) Vol. 5, Chap. 2. Consultants Bureau, New York (1970).
- and the review by
- Connor, J.W. and Wilson, H.R. Survey of theories of anomalous transport. *Plasma Physics and Controlled Fusion* **36**, 719 (1994).
- The Rebut, Lallia, Watkins model was first described in
- Rebut, P.H., Lallia, P.P., and Watkins, M.L. Electron heat transport in tokamaks. *Plasma Physics and Controlled Fusion* **11** D(I), 172 (1987).
- Simulations of edge turbulence can be found in
- Rogers, B.N. and Drake, J.F. Enhancement of turbulence by magnetic fluctuations. *Physical Review Letters* **79**, 229 (1997), and simulations of ITG turbulence are reported in
- Dimitri, A.M., Bateman, G.A., Beer, M.A., Cohen, B.I., Dorland, W., Hammett, G.W. *et al.* Comparisons and physics basis of tokamak transport models and turbulence simulations. *Physics of Plasmas* **7**, 969 (2000)
- and
- Lin, Z., Hahm, T.S., Lee, W.W., Tang, W.M., and White, R.B. Gyrokinetic simulations in general geometry and applications to collisional damping of zonal flows. *Physics of Plasmas* **7**, 1857 (2000)
- with ETG simulations in
- Jenko, F., Dorland, W., Kotschenreuther, M., and Rogers, B.N. Electron temperature gradient driven turbulence. *Physics of Plasmas* **7**, 1909 (2000).
- These papers discuss zonal flows, critical gradients and streamers.
- Comparison of theory and experiment**
- A comparison of a theory of stochastic magnetic transport with the ISX-B experiment is described in
- Carreras, B.A., Diamond, P.H., Murakami, M., Dunlap, J.L. *et al.* Transport effects induced by resistive ballooning modes and comparison with high- $\beta_p$  ISX-B tokamak confinement. *Physical Review Letters* **50**, 503 (1983).
- Comparisons of various theories with JET experimental results can be found in
- Connor, J.W. *et al.* An assessment of theoretical models based on observations in the JET tokamak: I Ion heat transport due to  $V\bar{T}_i$  instabilities. *Plasma Physics and Controlled Fusion* **35**, 319 (1993)
- and
- Tibone, F., Connor, J.W., Stringer, T.E., and Wilson, H.R. An assessment of theoretical models based on observations in the JET tokamak. II Heat transport due to electron drift waves, electromagnetic and resistive fluid turbulence and magnetic islands. *Plasma Physics and Controlled Fusion* **36**, 473 (1994).
- A comparison of a theory for ion temperature gradient turbulence with the TFTR tokamak can be found in

- Kotschenreuther, M., Dorland, W., Beer, M.A., and Hammel, G.W. Quantitative predictions of tokamak energy confinement from first principles simulations with kinetic effects. *Physics of Plasmas* 2, 2380 (1995).
- and a comparison of a number of theories with the International Profile Database in
- Connor, J.W., Alexander, M., Attenberger, S.E., Bateman, G., Boucher, D., Chudnovskij, N., Dnestrovskij, Yu. N., Dorland, W. et al. Validation of 1D transport and sawtooth models for ITER. *Fusion energy* (Proc. 16th Int. Conf., Montreal, 1996) Vol. 2, p. 935 I.A.E.A. Vienna (1997).
- The role of  $E \times B$  shear flow in improved confinement modes is discussed in
- Burrell, K. H. Tests of causality: Experimental evidence that sheared  $E \times B$  flow alters turbulence and transport in tokamaks. *Physics of Plasmas* 6, 4418 (1999).
- and
- Burrell, K.H. Effects of  $E \times B$  velocity shear and magetic shear on turbulence and transport in magetic confinement devices. *Physics of Plasmas* 4, 1499 (1997).
- Experimental results on the edge temperature pedestal are reviewed in
- Hubbard, A.E. Physics and scaling of the H-mode pedestal. *Plasmas Physics and Controlled Fusion* 42, A15 (2000).

### Impurity transport

- The complex and complete neoclassical theory has been reviewed by
- Hirshman, S.P. and Sigmar, D.J. Neoclassical transport of impurities in tokamak plasmas. *Nuclear Fusion* 21, 1079 (1981).

An example of experimental measurements of impurity transport can be found in

Cianella, R. et al. Role of current profile in impurity transport in JET L-mode discharges. *Nuclear Fusion* 34, 1185 (1994).

### Radiation losses

- A precise calculation of bremsstrahlung losses was given by Karzas, W.J. and Latter, R. Electron radiative transitions in a Coulomb field. *Astrophysical Journal Supplement* number 55, 6, 167 (1961); and a more introductory account is given in
- Tucker, W.H. *Radiation processes in astrophysics*. MIT Press, Cambridge, Mass. (1975).
- An early calculation of electron cyclotron emission from plasmas was made by
- Trubnikov, B.A. *Magnetic emission of high temperature plasma*. Thesis, Institute of Atomic Energy, Moscow (1958). [English trans. USAEC Techn. Information Service AEC-tr; 4073 (1960)]; and a more recent review paper is
- Bornatici, M., Caro, R., De Barbieri, O., and Engelmann, F. Electron cyclotron emission and absorption in fusion plasmas. *Nuclear Fusion* 23, 1153 (1983).
- The impurity radiation losses under coronal conditions are given in
- Post, D.E., Jensen, R.V., Tarter, C.B., Grasberger, W.H., and Lokke, W.A. Steady-state radiative cooling rates for low-density, high-temperature plasmas. *Atomic data and nuclear data tables* 20, 397 (1977).

**5**

# **Heating**

## 5.1

### Heating

In an ignited D-T plasma the energy losses are balanced by the plasma heating from the slowing down of the  $\alpha$ -particles resulting from the fusion reactions. However, the fusion reaction rate is a strong function of temperature and is negligible at low temperatures. Thus, to reach the temperature required for ignition it is necessary to provide some form of heating. There are several proposed methods of achieving this, but before describing these it is instructive to estimate the amount of heating needed.

As shown in Section 1.4 the power balance in a thermonuclear D-T plasma is given by

$$P_H = \left( \frac{3nT}{\tau_E} - \frac{1}{4} n^2 \langle \sigma v \rangle E_\alpha \right) V \quad 5.1.1$$

where the energy loss and  $\alpha$ -particle heating terms in the bracket represent spatial averages. At ignition these two terms are equal, the additional power  $P_H$ , by definition, being zero. Thus, for a tokamak plasma to ignite  $\tau_E$  must be sufficiently large and because, for chosen ignition conditions, the confinement time increases with size, this essentially determines the plasma dimensions. It is seen from eqn 5.1.1 that the additional power required to raise the plasma temperature to ignition depends on both the plasma volume and the temperature dependence of the  $\alpha$ -particle heating and energy loss terms. The temperature dependence of  $\langle \sigma v \rangle$  has been determined precisely but the dependence of  $\tau_E$  is less accurately known.

Before considering the total heating power requirements the temperature dependence of the required heating per unit volume will be calculated for constant  $\tau_E$  and  $\tau_E \propto 1/T$ . Using the values of  $\langle \sigma v \rangle$  given in Fig. 1.3.1 the two terms in the bracket of eqn 5.1.1 are shown in Fig. 5.1.1(a) for a given density and an ignition temperature of 10 keV. The difference between these two terms gives the required additional heating per unit volume and this is shown in Fig. 5.1.1(b). The powers are normalized to the  $\alpha$ -particle heating at ignition and the total powers required in the two cases will depend on the functional dependence of  $\tau_E$ . At temperatures below 4 keV the  $\alpha$ -particle heating is small.

For each GW of thermonuclear power at ignition, the  $\alpha$ -particle power is 200 MW. For the cases considered above, the peak additional power requirement was approximately 40 per cent of the ignition  $\alpha$ -particle heating for constant  $\tau_E$  and 15 per cent for  $\tau_E \propto 1/T$ . These correspond to total required heating powers of 80 and 30 MW per GW of thermonuclear power.

The initial heating in all tokamaks comes from the ohmic heating caused by the toroidal current. At low temperatures ohmic heating is quite powerful and, in large tokamaks, easily produces temperatures of a few keV. However, as the temperature increases, the collision frequency

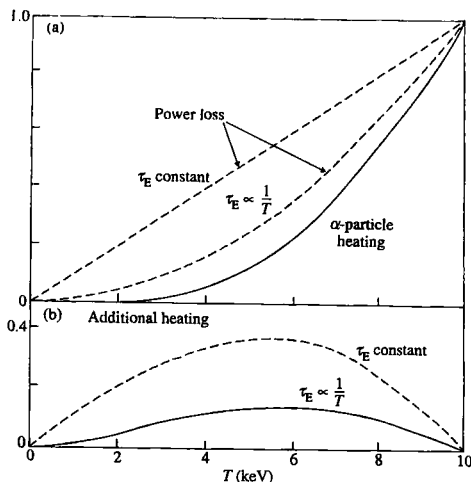


**Fig. 5.1.1** Showing the power balance for a tokamak which would ignite at a temperature of 10 keV. Figure (a) gives the rate of power loss per unit volume for  $\tau_E = \text{constant}$  and  $\tau_E \propto 1/T$ , together with the corresponding  $\alpha$ -particle heating. Figure (b) gives the additional heating per unit volume to provide a steady state power balance in the two cases. The powers are normalized to the  $\alpha$ -particle heating (and therefore to the power loss) at ignition.

and the resistivity fall. Consequently, at the temperatures required for ignition the ohmic heating is much reduced, leading to the requirement for additional heating. Nevertheless under some conditions it is possible for ohmic heating to contribute significantly to the heating required for ignition.

The two main methods which are envisaged for heating to ignition temperatures are the injection of energetic neutral beams and the resonant absorption of radio frequency (RF) electromagnetic waves. With the level of confinement found experimentally both of these methods would in principle be capable of providing heating of the required magnitude, and both have been successfully tested at power levels of tens of MW.

The beams used for injection heating have to be composed of neutral particles because ions would be reflected by the tokamak magnetic field. Heating with neutral beams is a complex process. Ions must first be produced and accelerated to the required energy. They are then neutralized by charge exchange in a gas target, and the unwanted residual ions removed. In the plasma the neutral particles become charged again and as a result are confined by the magnetic field. They are then slowed by collisions with the plasma particles, giving up their energy in the process.

There are several types of RF heating, the three principal ones involving waves at around the ion cyclotron frequency, the electron cyclotron frequency, and the lower hybrid frequency. The design of the system must be such that the waves propagate to the central region of the plasma and are

then absorbed. This requires calculation of the propagation of the waves in the non-uniform plasma and non-uniform magnetic field, and the transfer of wave energy to the plasma particles. Some schemes involve the introduction of an additional ion species to absorb wave energy. Another method, which is less developed, uses the low frequency shear Alfvén resonance.

It is also possible to achieve a transient heating of the plasma by plasma compression. If the plasma is compressed in a time short compared with the confinement time the compression is adiabatic. The behaviour then depends upon whether the compression is sufficiently slow that equipartition occurs between the degrees of freedom. If it is, the pressure change and therefore the energy density change is related to the volume change by the adiabatic law  $p \propto V^{-5/3}$ . If equipartition does not occur then the heating depends upon the number of degrees of freedom involved in the compression. Compression of both the plasma minor radius and the major radius are possible.

## 5.2

### Ohmic heating

The toroidal current which is necessary for equilibrium in a tokamak is also a source of plasma heating through the resistance to the current caused by electron-ion collisions. At low temperatures this ohmic heating is very strong but, because the resistance of the plasma varies with temperature as  $T_e^{-3/2}$ , it is less effective at high temperatures.

The ohmic heating density is

$$P_\Omega = \eta j^2$$

where  $\eta$  is the resistivity of the plasma and  $j$  the current density. There are two limitations on  $j$  arising from mhd stability requirements. The first is the necessity of avoiding disruptions. This imposes a constraint on the safety factor at the edge of the plasma which, for a circular plasma is approximated by  $q_a > 2$ . Thus, since  $q_a = aB_\phi/RB_{\theta a}$  and, from Ampère's law,  $B_{\theta a} = \mu_0 I/2\pi a$  the average current density must satisfy

$$(j) < \frac{1}{\mu_0} \frac{B_\phi}{R}. \quad 5.2.1$$

Since the local ohmic heating density is proportional to  $j^2$  the requirement 5.2.1 would not, by itself, limit the total ohmic heating. Concentration of the current density provides another degree of freedom. However, this is subject to a limitation arising from instability in the central region of plasma, particularly the sawtooth instability.

It was once thought that the sawtooth instability limited the central current density to a value which maintained the central safety factor,  $q_0$ , at a value equal to or greater than one. As explained in Sections 7.6 and 7.14, it appears that this limitation is not so firm. This is firstly because measurements of  $q_0$  give values less than one even during sawtooth oscillations and secondly because the oscillations can be stabilized.

In the absence of instability a steady state current of a given value would require a certain toroidal electric field,  $E$ . The ohmic heating density can then be written

$$P_\Omega = E j.$$

However, both the electric field and the current distribution depend upon the confinement properties of the configuration through the dependence of the resistivity on temperature.

A further complication arises from the form of the resistivity. The Spitzer resistivity,  $\eta_s$ , is independent of the geometry but neoclassical resistivity has a strong aspect-ratio dependence, taking the form

$$\eta_n = \frac{\eta_s}{\left(1 - \left(\frac{r}{R}\right)^{1/2}\right)^2}. \quad 5.2.2$$

This neoclassical effect increases the resistivity substantially but, because it falls to zero at  $r = 0$ , the current concentrates toward the axis, driving  $q_0$  down. There is some uncertainty as to the actual resistivity in tokamaks but the experimental evidence indicates that it is neoclassical.

It is seen from the above account that it is not easy to make a precise calculation of the ohmic heating and its resulting temperature. To illustrate the basic features a simple approximate calculation will be used. Since the volume within small radii is small and the current at the plasma edge is small the effective resistivity is taken to be that at half the plasma radius. Thus, taking  $R/a = 3$ , the geometric factor in eqn 5.2.2 enhances the Spitzer resistivity by approximately a factor 3. Using eqn 2.16.2, this gives

$$\eta \approx 8 \times 10^{-8} Z_{\text{eff}} T_e^{-3/2}, \quad T_e \text{ in KeV.} \quad 5.2.3$$

Using this approximation the average ohmic heating density is

$$P_\Omega = \eta \langle j^2 \rangle.$$

Taking the current profile to be

$$j = j_0 \left(1 - \frac{r^2}{a^2}\right)^\nu,$$

$\langle j^2 \rangle$  is given by

$$\langle j^2 \rangle = \frac{j_0^2}{2\nu + 1}. \quad 5.2.4$$

Ampère's law gives

$$B_\theta = \frac{\mu_0 a^2 j_0}{2(v+1)r} \left[ 1 - \left( 1 - \frac{r^2}{a^2} \right)^{v+1} \right] \quad 5.2.5$$

and eqn 5.2.5 together with  $q(r) = (B_\phi/R)/(B_\theta/r)$  leads to

$$v+1 = \frac{qa}{q_0}. \quad 5.2.6$$

Using  $j_0 = 2B_\phi/Rq_0\mu_0$  and eqn 5.2.6, eqn 5.2.4 becomes

$$(j^2) = 2 \left( \frac{B_\phi}{\mu_0 R} \right)^2 \frac{1}{q_0(q_a - \frac{1}{2}q_0)}. \quad 5.2.7$$

The temperature which would be achieved by ohmic heating alone is now obtained by substituting eqn 5.2.7 into the energy balance equation

$$\eta(j^2) = \frac{3nT}{\tau_E}$$

where  $\eta$  is given by eqn 5.2.3. This gives an average temperature. If the peak temperature,  $\hat{T}$ , is taken to be twice this value then

$$\hat{T} = 2.7 \times 10^8 \left( \frac{Z_{\text{eff}} \tau_E}{n q_a q_0} \right)^{2/5} \left( \frac{B_\phi}{R} \right)^{4/5} \text{ keV} \quad 5.2.8$$

where the small contribution from  $\frac{1}{2}q_0$  in eqn 5.2.7 has been neglected.

There is uncertainty as to what scaling to use for  $\tau_E$ . Since the conditions in a large reactor tokamak would be different from present experiments there is a range of possible outcomes. One scaling used for ohmically heated plasmas is the so-called Alcator scaling

$$\tau_E = \frac{1}{2}(n/10^{20})a^2 \text{ s}. \quad 5.2.9$$

Substitution of eqn 5.2.9 into eqn 5.2.8 gives

$$\hat{T} = 2.1 \left( \frac{Z_{\text{eff}}}{q_a q_0} \right)^{2/5} \left( \frac{a}{R} B_\phi \right)^{4/5} \text{ keV}.$$

Taking  $Z_{\text{eff}} = 1.5$ ,  $q_a q_0 = 1.5$  and  $R/a = 3$ ,

$$\hat{T} = 0.87 B_\phi^{4/5} \text{ keV}$$

and values for this case are plotted in Fig. 5.2.1.

It is seen that for a magnetic field of 6 T the temperature is 3.6 keV and that very high fields are needed to reach temperatures required for ignition. However, the use of scaling 5.2.9 is for illustration and a different scaling could significantly affect the result.

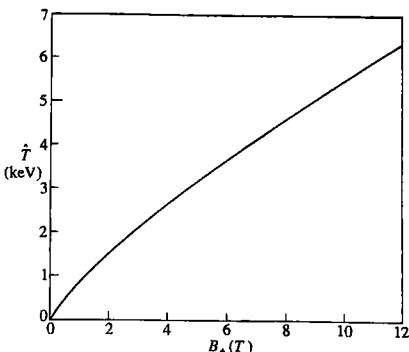


**Fig. 5.2.1** Temperature predicted for ohmic heating as a function of the toroidal magnetic field using Alcator scaling.

Plasmas with a substantial amount of impurity have a higher value of  $Z_{\text{eff}}$  which increases the ohmic heating and leads to a higher temperature. Of course the presence of impurities also leads to additional power loss through radiation as described in Section 4.25.

The ohmic heating in an ignited plasma is quite small. It can be estimated using eqns 5.2.3 and 5.2.7 to obtain

$$\eta(j^2) = 0.10 Z_{\text{eff}} T^{-3/2} \left( \frac{B_\phi}{R} \right)^2 \frac{1}{q_0(q_a - \frac{1}{2}q_0)} \text{MWm}^{-3}, \quad T \text{ in keV.}$$

Taking  $Z_{\text{eff}} = 1.5$ ,  $B_\phi/R = 1$  and  $q_0(q_a - \frac{1}{2}q_0) = 1.5$

$$\eta(j^2) = \frac{0.10}{T^{3/2}} \text{MWm}^{-3}, \quad T \text{ in keV.}$$

In a reactor with a plasma volume of  $2000 \text{ m}^3$  this would give an ohmic heating power of  $\sim 6 \text{ MW}$  for  $T = 10 \text{ keV}$ .

## 5.3

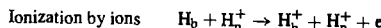
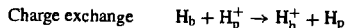
### Neutral beam injection

Neutral atoms injected into a plasma travel in straight lines, being unaffected by the magnetic field. The atoms become ionized through collisions with the plasma particles and the resulting ions and electrons are then held by the magnetic field. Since the ions and electrons have the same velocity the energy is carried almost entirely by the more massive ions. Once ionized the ions have orbits in the magnetic field determined by their energy, angle of injection and point of deposition. The energy of

the injected ions is gradually transferred to the plasma electrons and ions through Coulomb collisions. Thus the injected ions are initially slowed and then thermalized.

It is clearly desirable that as much of the deposition as possible should take place in the central region of the plasma. This means avoiding both too strong absorption, which leads to heating of the plasma edge, and too weak absorption which allows transmission of the beam through the plasma to produce heating and particle sputtering at material surfaces.

There are three basic atomic processes leading to beam absorption: charge exchange, ionization by ions, and ionization by electrons. These processes are listed below using the symbol H to represent the species. In a reactor the beam would probably be deuterium and the target plasma a deuterium-tritium mixture. Thus, using subscripts b and p for beam and plasma, the processes are



The absorption of the beam depends upon the cross-section for these processes. Thus if the intensity of the beam is

$$I(x) = N_b(x)v_b$$

where  $N_b$  is the number of beam particles per unit length and  $v_b$  their velocity, its decay is governed by the equation

$$\frac{dI}{dx} = -n \left( \sigma_{ch} + \sigma_i + \frac{\langle \sigma_e v_e \rangle}{v_b} \right) I$$

where  $n(x)$  is the electron (and ion) density,  $\sigma_{ch}$  and  $\sigma_i$  are the cross-sections for charge exchange and ionization by ions, and  $\langle \sigma_e v_e \rangle$  is the electron ionization rate coefficient. The different form of the electron ionization term is due to the fact that the electrons will generally have velocities greater than the particles in the beam while the plasma ion velocities, of course, are less.

The cross-sections for the various processes are shown in Fig. 5.3.1, the electron ionization being represented by the effective cross-section  $\langle \sigma_e v_e \rangle / v_b$ . Below 90 keV, charge exchange is the most effective process for a deuterium beam. Above this energy, ionization by ions becomes dominant.

In a reactor the electron density will be around  $10^{20} \text{ m}^{-3}$ . For a deuterium beam energy of 100 keV the combined cross-section for charge exchange and ionization by ions is  $3 \times 10^{-20} \text{ m}^2$  giving a decay length,  $(\sigma n)^{-1}$ , of 30 cm. Since a reactor would have a plasma radius an order of magnitude larger this represents a serious problem because, using conventional methods, there are difficulties in producing neutral beams with high energies. The proposed solution is to use negative ion beams, which can

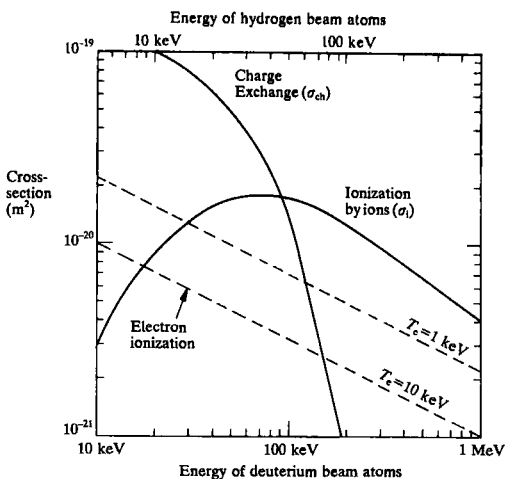


**Fig. 5.3.1** Cross-sections for charge exchange and ionization by plasma ions (protons, deuterons, or tritons) and the effective cross-section  $(\sigma_e v_e)/v_b$  for ionization by electrons, as functions of the neutral beam energy. The cross-sections for a hydrogen beam are the same as those for a deuterium beam having twice the energy.

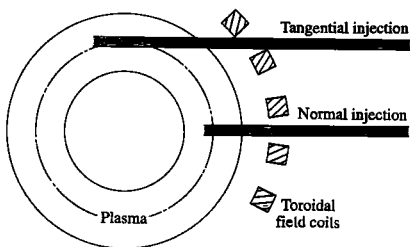


**Fig. 5.3.2** Illustrating the increased neutral beam absorption length with tangential injection, and the increased difficulty of access through the toroidal field coils.

be efficiently produced and neutralized at substantially higher energies. The techniques of neutral beam production are described in Section 5.6.

If the neutral beam is injected along the major radius of the tokamak, that is perpendicular to the magnetic field, the resulting ions are subject to losses arising from the ripple in the magnetic field as described in Section 4.11. In smaller tokamaks there is also the problem that the beam is not completely absorbed in the plasma and impinges on the far wall. These difficulties are ameliorated by a more tangential injection as shown in Fig. 5.3.2. However the ability to do this is restricted by the difficulty of access between the toroidal field coils and the increased pumping requirement in the longer drift ducts. The chosen injection angle is therefore a compromise between these constraints.

A disadvantage of neutral beam systems is the large scale of the equipment. On the other hand they have the advantages that, in the main, they can be developed and tested separately from the tokamak itself, and the heating profile can be predicted independently of the magnetic configuration.

## 5.4

### Neutral beam heating

Once the neutral beam particles entering the plasma have become ionized, the resulting fast ions are slowed down by Coulomb collisions. As the slowing down occurs energy is passed to the particles of the plasma, causing heating of both electrons and ions. At high injection velocity the electron heating is initially dominant. Then, as the beam ions slow down, the heating is transferred to the ions.

Because the electron mass is much smaller than that of the ions, collisions with the electrons cause only a small scattering of the beam ions. Consequently if the drag force which the electrons transmit to the beam ion is  $F_{be}$ , and beam ion velocity is  $v_b$ , the heating of the plasma electrons is given by

$$P_e = -F_{be}v_b. \quad 5.4.1$$

The force is given by the rate of momentum loss, that is

$$\begin{aligned} F_{be} &= m_b(\Delta v_{\parallel})_e \\ &= -\frac{m_b v_b}{\tau_{se}} \end{aligned}$$

where  $m_b$  is the mass of the beam ions,  $(\Delta v_{\parallel})_e$  is the friction coefficient introduced in Section 2.13, and  $\tau_{se}$  is given by eqn 2.14.1. Thus eqn 5.4.1 becomes

$$P_e = \frac{m_b v_b^2}{\tau_{se}}. \quad 5.4.2$$

Taking the case where  $v_b$  is less than the electron thermal velocity,

$$\tau_{se} = \frac{3(2\pi)^{1/2} T_e^{3/2}}{m_e^{1/2} m_b A_D} \quad 5.4.3$$

with

$$A_D = \frac{n e^4 \ln \Lambda}{2\pi \epsilon_0^2 m_b^2}.$$

Substituting eqn 5.4.3 into eqn 5.4.1 gives the electron heating

$$P_e = \frac{2m_e^{1/2} m_b A_D \delta_b}{3(2\pi)^{1/2} T_e^{3/2}}. \quad 5.4.4$$

where  $\delta_b$  is the beam energy  $\frac{1}{2} m_b v_b^2$ .

A similar heating of the ions occurs through beam ion collisions with the plasma ions. However, in this case the comparability of their masses means that the slowing down of the beam ions is accompanied by a scattering of the beam ion velocities principally perpendicular to the initial direction of the beam. This spreading of the perpendicular velocities constitutes a 'heating' of the beam ions which will ultimately contribute to the plasma energy but does not appear in the initial direct heating. Thus the rate of direct heating of the plasma ions is

$$P_i = -F_{bi} v_b - \frac{1}{2} m_b \langle v_{\perp}^2 \rangle \quad 5.4.5$$

where  $F_{bi}$  is the drag force on the beam ion due to the plasma ions, the velocity diffusion coefficient  $\langle v_{\perp}^2 \rangle$  is given by eqn 2.13.3, and

$$\begin{aligned} F_{bi} &= m_b (\Delta v_{\parallel})_i \\ &= -\frac{m_b v_b}{\tau_{si}} \end{aligned}$$

where the slowing-down time,  $\tau_{si}$ , is given by eqn. 2.14.1. Since the beam ion velocity is much greater than the plasma ion thermal velocity

$$\tau_{si} = \frac{m_i}{m_b + m_i} \frac{2v_b^3}{A_D}$$

the appropriate limiting forms, given by eqns 2.14.5 and 2.14.6 are

$$-F_{bi} v_b = \frac{m_b A_D}{2v_b} \frac{m_b + m_i}{m_i} \quad 5.4.6$$

and

$$\frac{1}{2} m_b \langle v_{\perp}^2 \rangle = \frac{m_b A_D}{2v_b}.$$

Thus, from eqn 5.4.5, only the fraction  $m_b/(m_b + m_i)$  of  $F_{bi} v_b$  appears as direct heating of the plasma ions, and

$$P_i = \frac{m_b^{5/2} A_D}{2^{3/2} m_i \delta_b^{1/2}} \quad 5.4.7$$

Combining eqns 5.4.4 and 5.4.7 the total direct heating per beam ion,  $P = P_e + P_i$ , is

$$P = m_b A_D \left( \frac{2m_e^{1/2} \delta_b}{3(2\pi)^{1/2} T_e^{3/2}} + \frac{m_b^{3/2}}{2^{3/2} m_i \delta_b^{1/2}} \right). \quad 5.4.8$$

It is seen that at higher values of  $\delta_b$ , the first term, representing the electron heating, predominates and that as the beam ions lose energy the ion

heating takes over. Equation 5.4.8 can be written

$$\begin{aligned} P &= \frac{2m_e^{1/2} m_b A_D}{3(2\pi)^{1/2} T_e^{3/2}} \mathcal{E}_b \left( 1 + \left( \frac{\mathcal{E}_c}{\mathcal{E}_b} \right)^{3/2} \right) \\ &= 1.71 \times 10^{-18} \frac{n}{A_b T_e^{3/2}} \mathcal{E}_b \left( 1 + \left( \frac{\mathcal{E}_c}{\mathcal{E}_b} \right)^{3/2} \right) \text{ keV s}^{-1}, \end{aligned}$$

$T_e, \mathcal{E}_b, \mathcal{E}_c$  in keV,

where  $A_b$  is the atomic mass of the beam ions,  $\ln \Lambda$  has been put equal to 17 and

$$\begin{aligned} \mathcal{E}_c &= \left( \frac{3\sqrt{\pi}}{4} \right)^{2/3} \left( \frac{m_i}{m_e} \right)^{1/3} \frac{m_b}{m_i} T_e \\ &= 14.8 \frac{A_b}{A_i^{2/3}} T_e \end{aligned} \quad 5.4.9$$

where  $A_i$  is the atomic mass of the plasma ions. At the critical beam energy,  $\mathcal{E}_b = \mathcal{E}_c$ , the electron and ion heating rates are equal. For  $A_b = A_i = 2$  the critical energy is 19  $T_e$ . Figure 5.4.1 shows the fraction of the direct heating by a beam ion going to electrons and ions as a function of  $\mathcal{E}_b/T_e$  for  $A_b = A_i = 2$ . In present experiments typical injection energies are of the order of the critical energy and the electron and ion heating are of comparable magnitude.

### Beam slowing

Using the beam-ion power balance equation

$$P = -\frac{d\mathcal{E}_b}{dt},$$

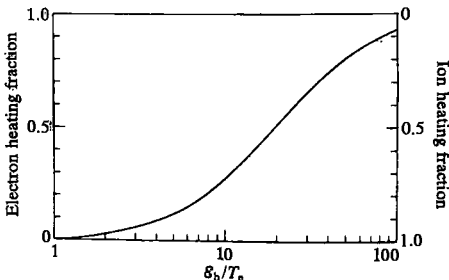


Fig. 5.4.1 Electron and ion heating by deuterium beam ions with energy  $\mathcal{E}_b$  as fractions of the total heating plotted against  $\mathcal{E}_b/T_e$  for a deuterium plasma.

with equations 5.4.3 and 5.4.9, eqn 5.4.8 can be written

$$\frac{d\delta_b}{dt} = -\frac{2}{\tau_{se}} \delta_b \left( 1 + \left( \frac{\delta_c}{\delta_b} \right)^{3/2} \right) \quad 5.4.10$$

and the solution for the beam energy is

$$\delta_b = \delta_{b0} \left[ e^{-3t/\tau_{se}} - \left( \frac{\delta_c}{\delta_{b0}} \right)^{3/2} \left( 1 - e^{-3t/\tau_{se}} \right) \right]^{2/3} \quad 5.4.11$$

where  $\delta_{b0}$  is the initial value of  $\delta_b$ . Equation 5.4.11 is not valid at very small  $\delta_b$  but gives a satisfactory value of the time for the beam ions to slow down to the thermal energy. Thus putting  $\delta_b = 0$  the characteristic time is

$$\tau = \frac{\tau_{se}}{3} \ln \left( 1 + \left( \frac{\delta_{b0}}{\delta_c} \right)^{3/2} \right).$$

The graph in Fig. 5.4.1 gives the fraction of the heating going to ions and electrons for a beam ion of a given energy. It is also possible to calculate the overall heating fractions allowing for the time dependent energy of the beam ions, as below.

### Ion-electron heating fractions

The second term in eqn 5.4.10 represents power transferred to the ions and so the rate of ion heating is

$$P_i = \frac{2}{\tau_{se}} \delta_b \left( \frac{\delta_c}{\delta_b} \right)^{3/2}$$

and using eqn 5.4.10

$$P_i = -\frac{\delta_c^{3/2}}{\delta_c^{3/2} + \delta_b^{3/2}} \frac{d\delta_b}{dt}.$$

Thus the total energy delivered to the ions is

$$\int P_i dt = \delta_c^{3/2} \int_0^{\delta_{b0}} \frac{d\delta_b}{\delta_c^{3/2} + \delta_b^{3/2}}$$

and the fraction of the initial ion beam energy which goes to the ions is

$$\begin{aligned} \frac{1}{\delta_{b0}} \int P_i dt &= \frac{\delta_c}{\delta_{b0}} \int_0^{\delta_{b0}/\delta_c} \frac{\delta_c d(\delta_b/\delta_c)}{1 + (\delta_b/\delta_c)^{3/2}} \\ &= \phi(\delta_{b0}/\delta_c). \end{aligned} \quad 5.4.12$$

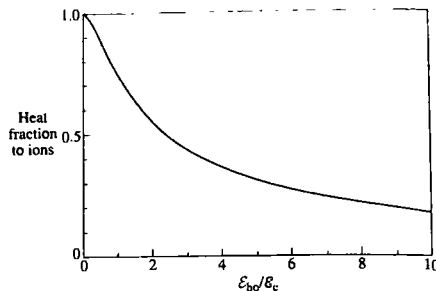


Fig. 5.4.2 Fraction of the initial beam energy which is directly transferred to the plasma ions as a function of the ratio  $\epsilon_{bo}/\epsilon_c$ .

where

$$\phi(x) = \frac{1}{x} \left[ \frac{1}{3} \ln \frac{1 - x^{1/2} + x}{(1 + x^{1/2})^2} + \frac{2}{\sqrt{3}} \left( \tan^{-1} \frac{2x^{1/2} - 1}{\sqrt{3}} + \frac{\pi}{6} \right) \right].$$

Thus eqn 5.4.12 gives the fraction of the plasma heating which is received by the plasma ions as a function of the ratio of the initial beam energy to the critical energy and a graph of  $\phi(\epsilon_{bo}/\epsilon_c)$  is shown in Fig. 5.4.2.

### Distribution function

The steady state distribution function of the slowing beam ions can be calculated using the fact that the flux in energy-space is uniform and given by the source rate  $S$ . Thus distribution of energies  $f(\epsilon_b)$  is given by

$$-\frac{d\epsilon_b}{dt} f(\epsilon_b) = S.$$

Using eqn 5.4.10

$$f(\epsilon_b) = \frac{\tau_{se} S}{2\epsilon_b (1 + (\epsilon_c/\epsilon_b)^{3/2})},$$

a graph of which is shown in Fig. 5.4.3.

As the beam ions lose their energy, their velocities are increasingly scattered in the perpendicular direction, so-called pitch angle scattering. The slowing and scattering ultimately lead to a thermalization of the beam at the plasma temperature. The scattering is predominantly caused by collisions with the ions and can be illustrated by an approximate calculation using the associated form of  $\langle (\Delta v_\perp)^2 \rangle$  as represented by the deflection time  $\tau_d$  given by eqn 2.14.2. Thus the resulting rate of energy increase due to the perpendicular spread in velocities is

$$\frac{d}{dt} \frac{1}{2} m_b v_\perp^2 = \frac{\epsilon_b}{\tau_d}. \quad 5.4.13$$

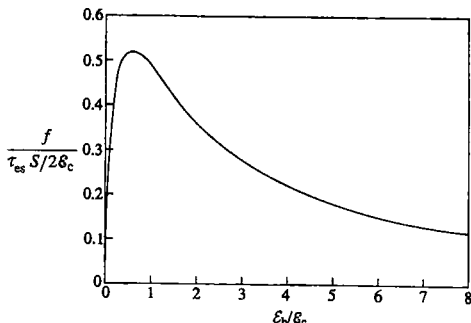


Fig. 5.4.3 Graph of the steady state energy distribution function resulting from the slowing-down of an ion beam.

This represents the part of the power  $F_{bi}\nu_b$  which is not transmitted to the plasma ions. Using eqns 5.4.13 and 5.4.10,

$$\frac{d}{d\delta_b} \left( \frac{1}{2} m_b v_\perp^2 \right) = -\frac{\tau_{se}}{2\tau_d} \left( 1 + \left( \frac{\delta_c}{\delta_b} \right)^{3/2} \right)^{-1}. \quad 5.4.14$$

For  $v \gg v_{Ti}$

$$\tau_d = \frac{v^3}{A_D}$$

and using eqn 5.4.3 for  $\tau_{se}$ , eqn 5.4.14 becomes

$$\frac{d}{d\delta_b} \left( \frac{1}{2} m_b v_\perp^2 \right) = -\frac{m_i/m_b}{1 + (\delta_b/\delta_c)^{3/2}} \quad 5.4.15$$

so that

$$\frac{1}{2} m_b v_\perp^2 = \frac{m_i}{m_b} \delta_c^{3/2} \int_{\delta_b}^{\delta_{b0}} \frac{d\delta_b}{\delta_c^{3/2} + \delta_b^{3/2}}.$$

It is seen from eqn 5.4.15 that the scattering is small for  $\delta_b \gg \delta_c$  and increases as  $\delta_b$  falls. Figure 5.4.4 illustrates schematically the time development of the velocity distribution of a set of ions injected at a given time.

### Experiments

The first steps in the neutral beam heating of tokamaks were reported in 1973. Injection with tens of kW of power was carried out in the ATC,

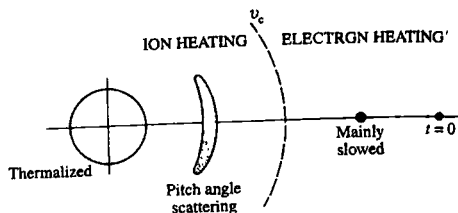


**Fig. 5.4.4** Sketch of the time development of the velocity distribution of beam ions injected at  $t = 0$ , showing the change in behaviour when the ions are slowed below the critical velocity  
 $v_c = (2\epsilon_c/m_b)^{1/2}$ .

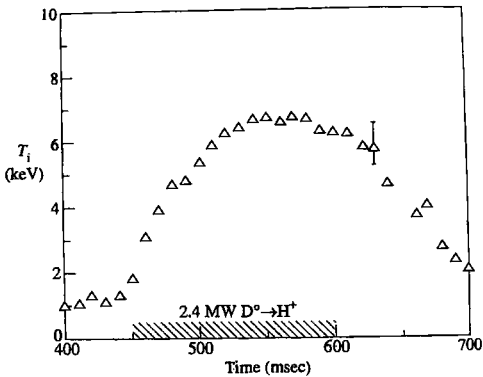


**Fig. 5.4.5** Heating of PLT plasma by neutral beam injection. The ion temperature was measured by analysis of charge-exchange neutrals for 2.4 MW deuterium injection into a plasma with a central density  $n(0) = 4.5 \times 10^{19} \text{ m}^{-3}$ . (Eubank, H. et al. *Physical Review Letters* 43, 270 (1979).)

CLEO, and ORMAK devices. Typically plasmas with temperatures of  $\sim 200 \text{ eV}$  were heated through a temperature increase of  $\sim 50 \text{ eV}$ .

Subsequent development of the beam systems led to megawatt beam powers and by 1979 temperature increases of several keV had been obtained. Figure 5.4.5 shows results from the PLT tokamak in which 2.4 MW of deuterium beam injection increased the ion temperature from 1 keV to over 6 keV.

As the available beam power was increased to tens of MW, the plasma temperatures moved into the reactor relevant range and temperatures of tens of keV were achieved. A further development was the use of tritium beams in JET. Figure 5.4.6 shows the time development in one such discharge. A peak beam power of 14 MW, including 1.5 MW in the tritium beams, raises the ion temperature to 19 keV. The resulting fusion power was  $\sim 1.5 \text{ MW}$ .

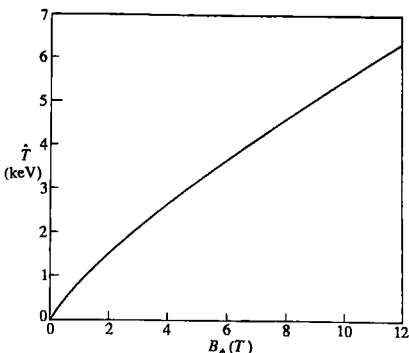


**Fig. 5.2.1** Temperature predicted for ohmic heating as a function of the toroidal magnetic field using Alcator scaling.

Plasmas with a substantial amount of impurity have a higher value of  $Z_{\text{eff}}$  which increases the ohmic heating and leads to a higher temperature. Of course the presence of impurities also leads to additional power loss through radiation as described in Section 4.25.

The ohmic heating in an ignited plasma is quite small. It can be estimated using eqns 5.2.3 and 5.2.7 to obtain

$$\eta(j^2) = 0.10 Z_{\text{eff}} T^{-3/2} \left( \frac{B_\phi}{R} \right)^2 \frac{1}{q_0(q_a - \frac{1}{2}q_0)} \text{MWm}^{-3}, \quad T \text{ in keV.}$$

Taking  $Z_{\text{eff}} = 1.5$ ,  $B_\phi/R = 1$  and  $q_0(q_a - \frac{1}{2}q_0) = 1.5$

$$\eta(j^2) = \frac{0.10}{T^{3/2}} \text{MWm}^{-3}, \quad T \text{ in keV.}$$

In a reactor with a plasma volume of  $2000 \text{ m}^3$  this would give an ohmic heating power of  $\sim 6 \text{ MW}$  for  $T = 10 \text{ keV}$ .

## 5.3

### Neutral beam injection

Neutral atoms injected into a plasma travel in straight lines, being unaffected by the magnetic field. The atoms become ionized through collisions with the plasma particles and the resulting ions and electrons are then held by the magnetic field. Since the ions and electrons have the same velocity the energy is carried almost entirely by the more massive ions. Once ionized the ions have orbits in the magnetic field determined by their energy, angle of injection and point of deposition. The energy of

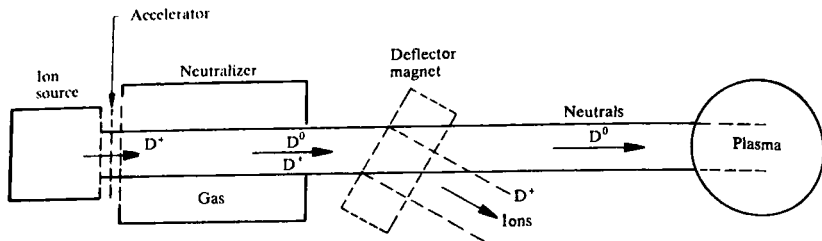


**Fig. 5.5.1** Layout of neutral injection system.

the same energy. However, because of their higher mass, the velocity of the molecules will be lower. The molecules are dissociated in the neutralizer and the resulting atoms have energies of one-half and one-third of the energy of the main component. These particles will therefore penetrate the plasma less well and will produce more heating at the plasma edge.

The most commonly used system is the so-called bucket source. For efficient confinement of the source plasma this utilizes a multipolar cusp magnetic field around the boundary of the source as illustrated in Fig. 5.5.2. The magnetic field, which is produced by permanent magnets, falls to a low value in the central region. A plasma is generated using tungsten filaments, and the ions are then extracted through a grid. In such a source the atomic fraction of the extracted ions can be 90%. A possible development of the source for long pulse or steady state operation is the replacement of the filament by RF excitation of the plasma.

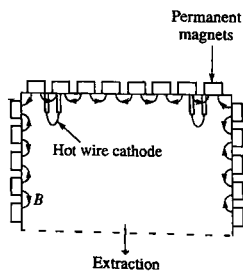


**Fig. 5.5.2** Schematic diagram of bucket ion source.

#### Accelerator

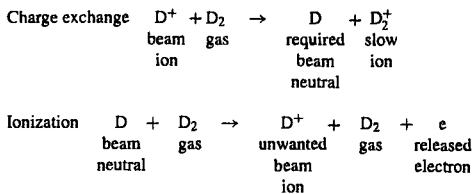
The ions are accelerated from the source through a multi-aperture system of either slots or circular holes which are carefully designed to minimize the aberrations of each beamlet. The structure undergoes heating from incident ions and requires a cooling system between the apertures.

Although the divergence of the individual beamlets emerging from each aperture is quite low ( $\sim 0.5^\circ$ ), the long path to the torus requires some extra beamlet steering. This can be achieved by an aperture offset between two consecutive grids or geometrical shaping of the grids, or by combination of both.

#### Neutralizer

The neutralizer gas allows the neutralization of beam ions by charge exchange, but unfortunately also produces re-ionization of the neutralized

particles. There are therefore two competing processes:



In a sufficiently thick target an equilibrium is reached in which the ratio of the charged and uncharged components is given by the ratio of the cross-sections for the two processes, that is

$$\frac{N^0}{N^+} = \frac{\sigma_{ch}}{\sigma_i}.$$

This ratio is a function of the beam energy and, unfortunately, the fraction of the particles which are neutrals decreases rapidly with increasing energy. This is shown in Fig. 5.5.3 together with the plasma penetration capability of the beam as indicated by the penetration distance in a plasma ( $H$ ,  $D$ , or  $D-T$ ) with  $n = 10^{20} \text{ m}^{-3}$  calculated using the cross-sections of Fig. 5.3.1. It is seen that it is not possible, using positive ions, to produce neutral beams efficiently at energies required to penetrate a plasma having a radius of 2–3 m, as would be required for a reactor.

The unwanted charged fraction of the beam leaving the neutralizer has a power of the same order as that of the neutral beam used to heat

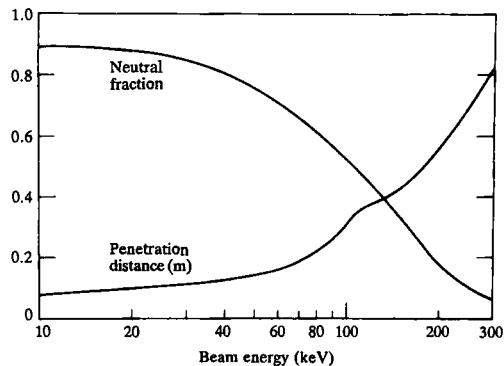


**Fig. 5.5.3** Graphs showing the energy dependence of (i) the equilibrium neutral fraction in a deuterium beam and (ii) the penetration distance of the neutrals in a plasma of density  $n = 10^{20} \text{ m}^{-3}$ . The change of behaviour of the penetration distance at around 100 keV indicates the transition from charge exchange dominance to ionization dominance.

the plasma. The charged particles are therefore deflected by a magnet and dumped before entering the influence of the tokamak magnetic fields where they would otherwise be deflected on to the walls of the injection port.

### Negative ion beams

Although present neutral injection systems are based on positive ion sources, it is envisaged that the problem of producing high energy beams with a high neutral fraction can be overcome by using negative ion sources. Such sources allow the achievement of much higher neutral fractions at high energy than is possible with positive ion beams. The negative ions are produced either by double charge-changing at surfaces with a low work function or by volume production in a low density plasma.

The negative ions are passed through a neutralizing gas. Unlike the positive ion beam case the neutral fraction at first increases and then decays as the beam passes through the neutralizing gas. There are six cross-sections describing the possible transitions between the charge states  $-e$ ,  $0$ , and  $+e$ , but only three are significant. Initially the dominant process is  $D^- \rightarrow D$ , creating the desired neutrals. This is followed by an attrition, through  $D \rightarrow D^+$ . The transition  $D^- \rightarrow D^+$  also occurs but plays a small role. The cross-sections are given in Fig. 5.5.4.

The essential features of the process can be calculated using a simple model based on the two dominant processes with cross-sections  $\sigma_{-10}$  and  $\sigma_{01}$ , so that

$$\frac{dN^-}{dx} = -n\sigma_{-10}N^- \quad 5.5.1$$

and

$$\frac{dN^0}{dx} = n(\sigma_{-10}N^- - \sigma_{01}N^0) \quad 5.5.2$$

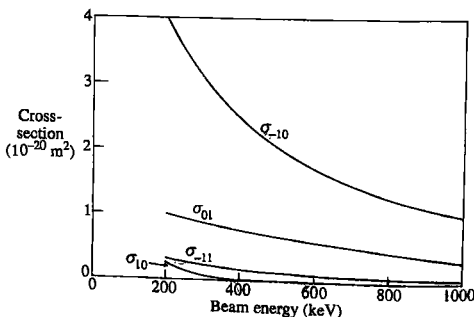


Fig. 5.5.4 Cross-sections for  $D^- \rightarrow D$ ,  $D \rightarrow D^+$ ,  $D^- \rightarrow D^+$  and  $D^+ \rightarrow D$ .

where  $N^-$  and  $N^0$  are the densities of the negative ions and neutral atoms, and  $n$  is the density of the neutralizing gas. The solution of eqns 5.5.1 and 5.5.2 for  $N^0$  is

$$N^0 = N_0^- \frac{\sigma_{-10}}{\sigma_{-10} - \sigma_{01}} (e^{-n\sigma_{01}x} - e^{-n\sigma_{-10}x}) \quad 5.5.3$$

where  $N_0^-$  is the initial negative ion density.

The maximum value of  $N_0$  occurs for

$$x_m = \frac{\ln(\sigma_{-10}/\sigma_{01})}{n(\sigma_{-10} - \sigma_{01})} \quad 5.5.4$$

and the maximum value of  $N_0$  is given by

$$\frac{N_{\max}^0}{N_0^-} = \alpha^{\alpha/(1-\alpha)} \quad 5.5.5$$

where

$$\alpha = \frac{\sigma_{01}}{\sigma_{-10}}.$$

The small effect of the cross-section  $\sigma_{-11}$  can readily be included in the calculation, the cross-section  $\sigma_{-10}$  simply being replaced by  $(\sigma_{-10} + \sigma_{-11})$ .

The experimental values of the cross-sections for beam energies  $\delta_b$  between 0.5 and 1.0 MeV are represented approximately by

$$\sigma_{-10} = \frac{1.04 \times 10^{-20}}{\delta_b (\text{MeV})} \text{m}^2, \quad \sigma_{01} = \frac{0.34 \times 10^{20}}{\delta_b (\text{MeV})} \text{m}^2. \quad 5.5.6$$

Using these values in eqn 5.5.3 gives  $N^0$  as a function  $nx/\delta_b$ , and the resulting graph is shown in Fig. 5.5.5. From eqn 5.5.5 the maximum value

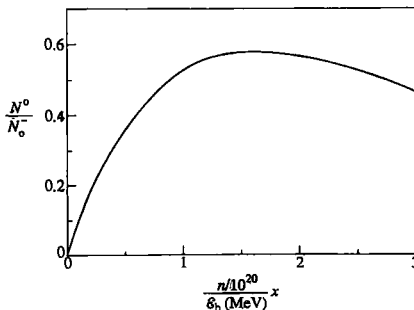


Fig. 5.5.5 Neutral density as a function of  $nx/\delta_b$  using the cross-sections from eqns 5.5.6.

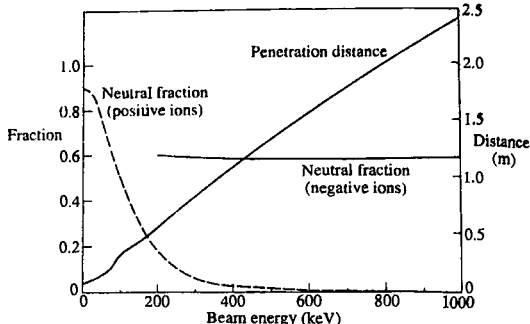


Fig. 5.5.6 Showing the advantage of the higher neutral fraction of negative ion beams when deep penetration is needed. The graphs are for deuterium beams.

of  $N_0$  has a neutral fraction,  $N_{\max}^0/N_0^-$ , of 58%, and using eqn 5.5.4 the maximum occurs at

$$x_m = 1.6 \frac{\delta_b(\text{MeV})}{n/10^{20}}.$$

The benefit of negative ion beams is illustrated in Fig. 5.5.6 which gives the maximum neutral fraction in a negative ion beam neutralizer together with the beam penetration into a plasma.

## 5.6

### Radio frequency heating

Radio frequency heating transfers energy from an external source to the plasma by means of electromagnetic waves. When an electromagnetic wave propagates through a plasma the electric field of the wave accelerates the charged particles which then heat the plasma through collisions. The collisional absorption scales as  $T_e^{-3/2}$  so that, just as for ohmic heating, collisional absorption of electromagnetic waves is ineffective as a direct heating mechanism for hot plasmas.

However, electromagnetic waves in plasmas are subject to resonant absorption which is a collisionless process and produces strong heating. A magnetized, multispecies plasma has a number of resonant frequencies which give rise to absorption of the energy of an incident wave. Due to the non-uniformity of the tokamak magnetic field, each resonance is associated not only with absorption but also reflection, that is resonant reflection. Thus when the wave approaches the resonance from the

high magnetic field side strong absorption takes place. When the wave approaches from the low magnetic field side strong reflection may occur. This phenomenon will be described in Section 5.7.

The variety of wave modes in a magnetized plasma allows many different radio frequency heating schemes. However, all consist of the same general layout, namely, an efficient high power generator remote from the plasma, a low-loss transmission line and an efficient antenna which couples the electromagnetic energy to the plasma.

Once the energy has been coupled to the plasma it is required to propagate, with negligible loss, to a localized absorption zone where, ideally, it will be deposited in one transit of the absorption region. A desirable property for any heating scheme is that the location of the absorption zone should be externally controllable.

The cold plasma model provides a good first approximation to the propagation of electromagnetic waves in a plasma. It gives accurate information except in certain critical regions in the vicinity of plasma resonances, which will be discussed at length. In these regions, close to a resonance, thermal corrections become important either because the wave phase speed has become comparable with the thermal speed of a particular species or because the perpendicular wavelength is no longer negligible compared with the Larmor radius. However, as will be seen, even for such critical regions, it is still possible to extract some useful information from the cold plasma model. This model can therefore be used to describe the propagation of energy to the resonance region and hence to determine the accessibility of the resonance. The cold plasma dispersion relation serves also to identify the three principal radio frequency heating schemes. In a slab approximation it takes the form

$$\varepsilon_{\perp} n_{\perp}^4 - [(\varepsilon_{\perp} - n_{\parallel}^2)(\varepsilon_{\perp} + \varepsilon_{\parallel}) + \varepsilon_{xy}^2] n_{\perp}^2 + \varepsilon_{\parallel} [(\varepsilon_{\perp} - n_{\parallel}^2)^2 + \varepsilon_{xy}^2] = 0 \quad 5.6.1$$

where the equilibrium magnetic field is in the  $z$ -direction,  $x$  and  $y$  represent the radial and poloidal coordinates, and  $n_{\parallel}$  ( $= ck_{\parallel}/\omega$ ) and  $n_{\perp}$  ( $= ck_{\perp}/\omega$ ) are the components of the refractive index parallel and perpendicular to the equilibrium magnetic field, with  $\omega$  the wave frequency,  $k_{\parallel}$  the wave number parallel to the magnetic field and  $k_{\perp}$  the 'radial' wave number. The dielectric tensor has components

$$\varepsilon_{xx} = \varepsilon_{yy} = \varepsilon_{\perp} = 1 - \sum_j \frac{\omega_{pj}^2}{(\omega^2 - \omega_{cj}^2)}, \quad \varepsilon_{zz} = \varepsilon_{\parallel} = 1 - \sum_j \frac{\omega_{pj}^2}{\omega^2}, \quad 5.6.2$$

$$\varepsilon_{xy} = \sum_j \frac{i\omega_{pj}^2 \omega_{cj}}{\omega(\omega_{cj}^2 - \omega^2)}, \quad \text{and} \quad \varepsilon_{yx} = -\varepsilon_{xy} \quad 5.6.3$$

all other elements being zero. The summation is over electrons and all ion species, the gyrofrequency,  $\omega_{cj}$  ( $= Z_j e B / m_j$ ), contains the sign of

the charge, and

$$\omega_{pj} = \left( \frac{n_j Z_j^2 e^2}{\epsilon_0 m_j} \right)^{1/2}$$

Since  $n_{||}$  is determined by the antenna and  $\omega$  is fixed by the generator, eqn 5.6.1 can be solved for  $n_{\perp}^2$ . An approximate solution to the problem of the propagation of a wave through an inhomogeneous plasma can be obtained by computing the solutions of eqn 5.6.1 as the density and magnetic field change slowly as functions of the radial coordinate. These solutions yield information on the propagation of a given wave across the equilibrium magnetic field from the edge plasma to the centre of the discharge. A wave will only propagate when the solution of eqn 5.6.1 satisfies  $n_{\perp}^2 > 0$ . For certain values of the frequency, density, and magnetic field, a resonance occurs as  $n_{\perp} \rightarrow \infty$ . As already remarked, a resonance is associated with absorption. In the vicinity of a resonance the cold plasma model becomes invalid since for  $k_{\perp} \rightarrow \infty$ , the perpendicular phase velocity can no longer be much larger than the particle thermal speeds. Consequently the physics of the resonance region, and in particular the absorption mechanism, requires a kinetic treatment. Nevertheless, even within the cold plasma model it is possible to calculate the energy lost by an incident wave in crossing the resonance region as described in Section 5.7.

The kinetic model distinguishes two channels through which an incident wave can lose energy in the resonant region. The first is by transferring some of its energy to another propagating wave of the plasma which is resonant in the same region as the incident wave. This is a reactive process and is referred to as mode conversion. It is this process which is responsible for resonant absorption. The second is through a collisionless, wave-particle resonant interaction which is a dissipative process.

For particular values of the density, equilibrium magnetic field and  $n_{||}$ , the square of the perpendicular refractive index,  $n_{\perp}^2$  can change sign and therefore it will be equal to zero on some surface,  $n_{\perp}^2 = 0$ . The plasma conditions for which either  $n_{\perp} \rightarrow \infty$  or  $n_{\perp} \rightarrow 0$  define critical surfaces for the propagation of a given wave. The former are referred to as resonance surfaces, where wave absorption occurs, and the latter as cut-off surfaces at which an incident wave is reflected. In addition to the cut-off associated with a resonance, isolated cut-offs can also occur. Beyond a cut-off point a wave decays exponentially. This does not imply the wave is damped but simply that the plasma is unable to support wave propagation. Such a region of non-propagation is referred to as evanescent. If an evanescent region is of finite extent some of the wave energy can leak through to the propagation region and the wave is said to tunnel through the evanescent zone. This phenomenon will be discussed in Section 5.7. If the evanescent region is too large the wave will be unable to cross this region and will be totally reflected. When the antenna is situated in an evanescent region, efficient transfer requires that the evanescent region

be minimized and that the antenna should be part of a low-loss resonant circuit where high RF voltage is applied.

## 5.7

### Physics of radio frequency heating

Radio frequency heating has been used to heat magnetically confined plasmas since the early days of fusion research. Three schemes have emerged as the most successful, namely, ion cyclotron, lower hybrid and electron cyclotron heating. Each method has been tested at the megawatt level in major tokamak installations.

The principle radio frequency heating methods can be identified by using eqn 5.6.1 to obtain the resonances associated with each regime. Since eqn 5.6.1 is a quadratic in  $n_{\perp}^2$ , one of the solutions will tend to infinity when  $\varepsilon_{\perp}$ , the coefficient of  $n_{\perp}^4$ , becomes zero. Thus,  $\varepsilon_{\perp} = 0$  is the condition for a perpendicular, cold plasma resonance to occur.

The lowest frequency scheme is *ion cyclotron resonance heating* (ICRH) for frequencies  $\omega \sim \omega_{ci}$ . In this case a resonant frequency only occurs when two or more ion species are present. It is called the ion-ion hybrid, or Buchsbaum, resonance. The resonant frequency  $\omega_{ii}$  with two ion species is

$$\omega_{ii}^2 = \frac{\omega_{ci}\omega_{cz}(1 + n_2m_2/n_1m_1)}{(m_2Z_1/m_1\bar{Z}_2 + n_2Z_2/n_1Z_1)} \quad 5.7.1$$

which gives a frequency in the range 30–120 MHz, depending on the magnetic field and the species.

The *lower hybrid-resonance* frequency lies between  $\omega_{ci}$  and  $\omega_{ce}$ , where  $\omega_{ce}$  is the unsigned electron cyclotron frequency. For the central regions of a tokamak where  $\omega_{pi}^2 \gg \Omega_i^2$ , and neglecting terms  $\sim m_e/m_i$ ,

$$\omega_{LH}^2 \approx \omega_{pi}^2 / (1 + \omega_{pe}^2/\omega_{ce}^2). \quad 5.7.2$$

This defines the lower hybrid resonance heating scheme which utilises the frequency range  $\sim 1$ –8 GHz.

Finally, the highest frequency scheme is *electron cyclotron resonance heating* (ECRH) for frequencies  $\omega \sim \omega_{ce}$ . For a cold plasma and perpendicular propagation the only resonant frequency in this regime occurs at the upper hybrid frequency,  $\omega_{UH}$ , where

$$\omega_{UH}^2 = \omega_{pe}^2 + \omega_{ce}^2. \quad 5.7.3$$

The electron density and magnetic field in a tokamak discharge are such that  $\omega_{pe}$  is much less than  $\omega_{ce}$  at the plasma edge whereas  $\omega_{pe} \gtrsim \omega_{ce}$  at the centre. Hence the upper hybrid frequency is just above the electron

cyclotron frequency. The electron cyclotron resonance heating scheme requires sources in the range 100–200 GHz. The above resonances will be described in more detail in the following sections where the three heating schemes are treated separately.

### Wave polarization

An important factor which influences the strength of the damping of a given wave mode in the resonance region is its electric field polarization. For cyclotron resonance, a wave will be strongly absorbed if a significant fraction of the wave energy resides in electric fields rotating in the same sense as the cyclotron resonant particles. In addition, the strength of the electric field parallel to the equilibrium magnetic field will also be important for electron dissipation. As noted in Section 5.6, a slab geometry is considered in which the equilibrium magnetic field is taken as the  $z$ -axis, the radial direction is represented by the  $x$ -axis and the poloidal direction is therefore given by the  $y$ -axis. For simplicity, waves are assumed to propagate in the  $x - z$  plane where the  $x$ -direction is the direction of inhomogeneity.

In the vicinity of a resonance,  $E_x \gg E_y$  where  $E_x$  and  $E_y$  are the components of the wave electric field perpendicular to the equilibrium magnetic field. This result can be obtained from Maxwell's equations and the dielectric tensor,  $\epsilon$ , which yield the linearized equation

$$(n^2 \mathbf{I} - nn - \epsilon) \mathbf{E} = 0 \quad 5.7.4$$

where  $n = ck/\omega$  and  $\mathbf{I}$  is the unit dyadic.

The determinant of the matrix multiplying the electric field vector gives the dispersion relation, eqn 5.6.1. The electric field polarization of one of the eigen-solutions of eqn 5.6.1 is given by the ratios of the electric field components obtained from eqn 5.7.4. When  $k_{\parallel} = 0$ ,  $E_x$  and  $E_y$  are related by

$$\frac{E_y}{E_x} = -\frac{\epsilon_{\perp}}{\epsilon_{xy}}. \quad 5.7.5$$

Clearly  $E_y \ll E_x$  near to a perpendicular resonance surface where  $\epsilon_{\perp} \rightarrow 0$ . This inequality is valid over a wider range of conditions for the two-ion hybrid resonance. In this case, when  $k_{\parallel} \neq 0$ , and assuming a cold plasma, eqn 5.7.4 gives the relation between  $E_x$  and  $E_z$

$$n_{\perp} n_{\parallel} E_x + (\epsilon_{\parallel} - n_{\perp}^2) E_z = 0. \quad 5.7.6$$

For the ion cyclotron range of frequencies,  $\epsilon_{\parallel} \gg n_{\perp}^2$  and therefore

$$\frac{E_z}{E_x} \simeq -\frac{n_{\perp} n_{\parallel}}{\epsilon_{\parallel}} \ll 1.$$

The relation between  $E_x$  and  $E_y$  is now given by

$$\frac{E_y}{E_x} \simeq -\frac{(\epsilon_{\perp} - n_{\parallel}^2)}{\epsilon_{xy}}. \quad 5.7.7$$

Near to the two-ion hybrid resonance,  $\epsilon_{\perp} - n_{\parallel}^2 \rightarrow 0$  and again  $E_y \ll E_x$ . Away from a resonance region,  $E_y \sim E_x$ , corresponding to a wave whose electric field polarization is partially transverse ( $E_y$ ) and partially longitudinal ( $E_x$ ). In the resonance region, the polarization becomes predominantly longitudinal. This is important for two reasons. First, since a longitudinal polarization can be decomposed into an equal mixture of right- and left-hand circular polarization, cyclotron absorption by either electrons or ions may result, depending on the wave frequency and on the proximity of the hybrid resonance to the cyclotron resonance region. Second, the longitudinal polarization facilitates the coupling of the incident wave to a longitudinal wave which propagates at frequencies in a narrow band around the hybrid resonance frequency. These longitudinal waves are members of a class of waves known as Bernstein waves whose significance for the resonance region is discussed below.

### Local description

In this subsection the information presented is obtained from solutions of the local dispersion relation for each wave mode treated separately. Several features characteristic of all radio frequency heating schemes are illustrated in Fig. 5.7.1 which gives the square of the perpendicular refractive index for the extraordinary electron cyclotron wave propagating across the toroidal magnetic field for  $\omega \sim \omega_{ce}$ . The extraordinary electron cyclotron wave is the mode which, in the limit of perpendicular propagation, illustrated in Fig. 5.7.1, is polarized with its electric field entirely in the plane perpendicular to the equilibrium magnetic field. This is in contrast to the ordinary electron cyclotron wave which in the same limit is linearly polarized with its electric field aligned parallel to the equilibrium magnetic field. These two modes are discussed more fully in Section 5.10. In Fig. 5.7.1 the magnetic field increases from the low field side on the right to the high field side on the left, and  $n_{\perp}^2$  is plotted against the major radius over the full width of the plasma. The density varies from zero on either side to a maximum at the centre. The expression for

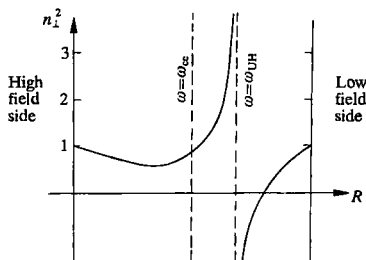


Fig. 5.7.1  $n_{\perp}^2$  versus major radius for the electron cyclotron X-mode for  $n_{\parallel} = 0$  and  $\omega \sim \omega_{ce}$ .

$n_{\perp}^2$  is easily obtained from eqn 5.6.1 by putting  $n_{\parallel} = 0$  and neglecting the ion contribution. The most notable feature of Fig. 5.7.1 is a resonance, where  $n_{\perp} \rightarrow \infty$ , with its associated cut-off. This is often referred to as a back-to-back, cut-off resonance pair. The separation between the cut-off on the low field side and the upper hybrid resonance is a function of density. The lower the density, the closer the cut-off is to the resonance. The existence of the cut-off on the low field side of the resonance means that if an extraordinary wave (with  $\omega \sim \omega_{ce}$ ) is to reach the upper hybrid resonance from this side it must tunnel through the evanescent layer. The larger the separation between the cut-off and the resonance, the smaller the fraction of incident energy which tunnels through the layer. On the other hand, since there are no cut-offs on the high field side of the resonance, an extraordinary mode launched from the high-field side will propagate directly to the upper hybrid resonance. In doing so, the wave would also cross the fundamental electron cyclotron resonance where absorption can also occur, although the cold plasma model does not exhibit a resonance at this frequency. In order to obtain a perpendicular resonance at the cyclotron frequency, and its harmonics, a kinetic model of a hot, magnetized plasma must be used.

### Full wave description

Diagrams such as Fig. 5.7.1 are only approximations to the local properties of one solution to the wave equation for a particular frequency and polarization. In the vicinity of cut-offs and resonances, it is no longer sufficient to consider a single wave mode. Clearly, in the vicinity of a cut-off it is necessary to take account, not only of an incident wave, but also a reflected wave. If the incident wave is not totally reflected, which is usually the case, there will also be a transmitted wave which tunnels through the evanescent region to a propagating region deeper in the plasma.

The simplest description of resonant absorption and tunnelling is given by the Budden model which describes the physics of the back-to-back cut-off resonance pair referred to above. This model consists of a second order differential equation of the Schrödinger type,

$$\frac{d^2\phi}{d\xi^2} + \frac{k_0^2(\xi - \xi_c)}{\xi}\phi = 0, \quad 5.7.8$$

where  $\phi$  is a normalized wave amplitude,  $\xi$  is a normalized spatial coordinate and  $k_0$  is the wave number for  $|\xi| \gg \xi_c$ . The wave potential is singular at  $\xi = 0$  and has a zero at  $\xi = \xi_c$ . Hence the resonance occurs at  $\xi = 0$  and the cut-off at  $\xi = \xi_c$ . If the local dispersion relation is obtained from eqn 5.7.8 the wave number has a resonance and cut-off at these points. The transmission coefficient,  $T$ , is defined as the fractional power transmitted across the resonance for unit incident power. It can be obtained from the solution of eqn 5.7.8 by calculating the ratio of the

intensities ( $|\phi|^2$ ) of the transmitted and incident waves and is given by

$$T = \exp(-\pi k_0 \xi_c). \quad 5.7.9$$

$T$  depends only on the separation of the cut-off and resonance and does not depend on whether the wave encounters the cut-off or resonance first. However, there is an asymmetry with regard to reflection. When the incident wave meets the cut-off first, the reflection coefficient  $R$ , is related to the transmission coefficient,  $T$ , by  $R = (1 - T)^2$ . When the wave is incident from the opposite direction,  $R = 0$ . It should be noticed that  $T + R < 1$ . The missing energy is 'absorbed' at the resonance (by a mechanism not specified in the cold plasma model).

In the Budden model the incident wave loses energy due to the resonance where the perpendicular phase velocity of the wave becomes zero. This behaviour is a result of including only the incident and reflected waves in the second order eqn 5.7.8. A more accurate theory must allow for the presence of another mode of propagation which becomes degenerate with the incident wave in the resonance region. The degeneracy of the two waves means that they have the same frequency and wave number in the resonance region and can therefore couple. As a result, the incident wave gives up a fraction of its energy to the second mode. This is the reactive loss mechanism associated with the resonance region. The inclusion of a second propagating mode in the resonance region removes the singularity from the wave equation but raises the order of the equation from second to fourth. The additional wave can be the shear Alfvén wave. It can also be one of the family of hot plasma modes known as Bernstein waves. These are predominantly electrostatic waves which propagate for a small range of angles around ninety degrees to the equilibrium magnetic field at harmonics of the ion and electron cyclotron frequencies.

For the hot plasmas characteristic of tokamak discharges the Bernstein waves are usually the most important. For example, in the vicinity of the two-ion hybrid resonance, the incident fast wave couples to an ion hybrid wave (which belongs to the ion Bernstein family) rather than to the shear Alfvén branch when the plasma beta is greater than the electron to ion mass ratio. An example of such a coupling mechanism is illustrated schematically in Figs 5.7.2(a) and (b) which show the  $(\omega, k_{\perp})$  diagram in the vicinity of the upper hybrid resonance for the extraordinary electron cyclotron wave (X-mode) propagating across the equilibrium magnetic field with  $n_{\parallel} = 0$ .

In Figs 5.7.2(a) and (b) the X-mode is shown to bifurcate in the vicinity of the upper hybrid resonance,  $\omega_{UH}/\omega_{ce} = \sqrt{2}$  for  $\omega_{pe}/\omega_{ce} = 1$ . The bifurcation is caused by the coupling of the X-mode to an electron Bernstein (upper hybrid) wave. All Bernstein waves have cut-offs at harmonics of the cyclotron frequency *except* the one at a hybrid frequency. In the short wavelength limit, *all* Bernstein waves, including the hybrid wave, are resonant at a cyclotron harmonic.

Although Figs 5.7.2(a) and (b) have been obtained from a uniform plasma model, they can be used to interpret the behaviour in an inhomogeneous plasma. This can be done by considering a wave launched

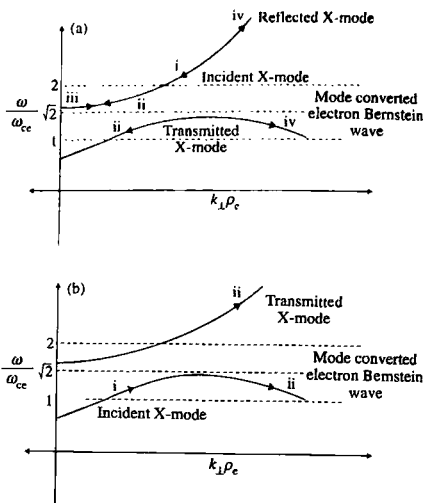


**Fig. 5.7.2** Full wave properties of X-mode propagating perpendicular to the magnetic field in the vicinity of the upper hybrid resonance (a) X-mode launched towards the upper hybrid resonance from the low-field side (b) X-mode launched from the high-field side. In both cases  $\omega_{pe}/\omega_{ce} = 1$ , and the Roman numerals give the causal sequence.

across a tokamak discharge by an antenna outside the plasma. The source supplies power at a fixed frequency which is transmitted through the inhomogeneous plasma where the equilibrium quantities vary as a function of the radial coordinate. As the wave propagates into the plasma it will be subject to an increasing toroidal magnetic field. As it travels across the magnetic field, the ratio  $\omega/\omega_{ce}$  will therefore decrease. This characterizes waves travelling from the low field to the high field side of a tokamak. Conversely, for a fixed frequency wave propagating from the high field to the low-field side,  $\omega/\omega_{ce}$  will increase.

A wave incident from the low-field side will thus correspond to a point moving down the dispersion curve in Fig. 5.7.2(a). The causal sequence of events is shown by the Roman numerals (i)–(iv). The incident X-mode starts at point (i). On reaching the vicinity of the upper hybrid resonance the wave is partially transmitted, (ii), and partially mode converted to an upper hybrid wave (also (ii)). The fraction of the incident X-mode energy which is transmitted across the resonance region is denoted by  $T$  and, assuming both waves are undamped in the coupling region, a fraction  $1 - T$  is converted to the upper hybrid wave. The upper hybrid wave then encounters its cut-off where it is reflected (iii) and returns to the coupling region. For this crossing it is the upper hybrid wave which is the incident wave. However, the transmission coefficient is independent of the direction of travel or of the wave mode for a given coupling. Therefore, a fraction  $T$  of the incident upper hybrid energy ( $1 - T$ ) is transmitted on

the upper hybrid branch (iv) and the remainder  $1 - T - T(1 - T)$  is mode converted to an X-mode (iv) which returns to the low-field side as the reflected wave. The net result is that a fraction  $T$  of the incident X-mode is transmitted, a fraction  $(1 - T)^2$  is reflected and a fraction  $T(1 - T)$  is mode converted. Since the mode converted upper hybrid wave remains in the plasma, this energy is equivalent to the absorbed energy even though it was assumed that the waves are undamped in the coupling region. Clearly the energy gained by the upper hybrid wave has been lost by the incident wave. It can also be verified that the total wave energy is conserved.

When the upper hybrid region is well separated from the cyclotron resonances, which will be the case when  $\omega_{pe} \sim \omega_{ce}$ , the waves will be undamped in the resonance region. The mode converted upper hybrid wave will then be absorbed at the fundamental electron cyclotron resonance by a relativistic wave-particle cyclotron interaction. This will be discussed in Section 5.10.

The case where the X-mode is incident from the high field side is illustrated in Fig. 5.7.2(b). Here, the incident wave is shown moving in the direction of increasing  $\omega/\omega_{ce}$ , (i). For this situation there is clearly no reflection since the mode converted upper hybrid wave travels away from the cut-off directly to the fundamental resonance. This is the reason for the asymmetry in the reflection coefficient. Thus, a fraction  $T$  is transmitted and a fraction  $1 - T$  mode-converted or equivalently absorbed. The Roman numerals in Fig. 5.7.2(b) again show the causal sequence. It is clear that the key quantity for the above phenomena is the transmission coefficient  $T$ . This must be calculated from a solution of the relevant differential equation in the resonance region, and can be obtained from theories of varying levels of complexity. The simplest is the second-order Budden equation 5.7.8. More complicated fourth order systems yield the same value for  $T$  as the Budden equation. If detailed information on the Bernstein waves is required then a fourth-order system must be solved.

### Wave-particle collisionless dissipation

The above qualitative discussion of the upper hybrid resonance illustrates the nature of the physical phenomena which occur in the resonance region. This description of the upper hybrid resonance will be used as a reference model when the resonance phenomena of each of the principal heating schemes are described. The extension of such models to include the effect of collisionless wave dissipation in the resonance (coupling) region will also be described.

The collisionless dissipation of an electromagnetic wave for ion cyclotron, lower hybrid and electron cyclotron heating schemes is governed by the wave-particle resonance condition

$$\omega - k_{\parallel} v_{\parallel j} - \ell |\omega_{cj}| = 0 \quad 5.7.10$$

where  $\ell = 0, 1, 2, 3, \dots$ . The Landau (or Cerenkov) resonance condition is given by  $\ell = 0$ . For this resonance, wave energy is transferred to the

parallel degree of freedom of the resonant particles by the component of the electric field parallel to the equilibrium magnetic field. Electron Landau damping is significant for lower hybrid waves and for the fast wave in the ion cyclotron range of frequencies. Wave energy can also be transferred by the component of the wave magnetic field parallel to the equilibrium magnetic field through the mechanism known as transit time damping (or magnetic pumping) under the Landau resonance condition. Transit time damping is significant for the fast wave in the ion cyclotron range of frequencies and makes a contribution to the direct electron dissipation of this wave which is comparable to that due to electron Landau damping.

In all these cases the parallel phase velocity of the wave is required to be resonant with electron velocities. Both the lower hybrid wave and the fast wave can have parallel phase velocities ranging from the electron thermal speed to the velocity of light. Hence, these waves can couple to both thermal and superthermal electrons making them relevant to heating and current drive.

On the other hand  $\ell \neq 0$  corresponds to electron or ion cyclotron resonance. For these cases it is the perpendicular energy of the resonant particle which is increased. An important point to note is that, unlike the Landau resonance, a particle can be in cyclotron resonance with a wave irrespective of whether it is slow or fast ( $\omega/k_{\parallel} < c$  or  $\omega/k_{\parallel} > c$ ). The condition to be satisfied by a cyclotron resonant particle is, from eqn 5.7.10

$$v_{\parallel j} = \frac{\omega}{k_{\parallel}} - \frac{\ell|\omega_{ci}|}{k_{\parallel}}. \quad 5.7.11$$

For  $\ell > 0$ , the resonance is sometimes referred to as the normal Doppler resonance and requires a particle with a parallel velocity less than the parallel phase speed. The particle may even be travelling in the opposite direction to the wave depending whether it is in resonance on the high-field or low-field side. For  $\ell < 0$ , the resonance is known as the anomalous Doppler resonance. In this case the parallel velocity of the particle must be greater than the parallel phase velocity of the wave. Hence, a particle may only come into anomalous Doppler resonance with a slow wave. The anomalous Doppler resonance has the interesting property that the flow of the energy takes place from the parallel motion of the resonant particle to both the wave and the perpendicular degrees of freedom of the particle.

It is useful to distinguish between the cold plasma resonances discussed at the beginning of this section and wave-particle resonances. The physical significance of a cold plasma resonance becomes clear when thermal corrections are included. It is then found that the resonance is replaced by a mode conversion to another wave branch which propagates as a result of the thermal effects. Since a natural wave mode of a plasma is supported by all the particles of at least one species, it is clear that the response of the plasma at a resonance will involve all the particles of at least one species. On the other hand, it has just been noted that a

wave-particle resonance is associated with a small sub-set of resonant particles of one species.

However, a wave-particle resonance does result in the dissipation of wave energy whereas a cold plasma resonance does not, by itself, produce dissipation. The energy which is mode converted from the launched wave to the hot plasma mode at a plasma resonance will eventually propagate to a region where the wave satisfies the conditions for a wave-particle resonance and the wave is then damped. A cold plasma resonance will have its most pronounced effect when it is situated at a position which is well separated from wave-particle resonances (see Section 5.8). There are also hot plasma resonances where mode conversion can occur such as the second harmonic cyclotron resonance. However, these harmonic resonances are always associated with the corresponding harmonic wave-particle resonance which will result in local dissipation except for the case, of perpendicular propagation. For the electrons local dissipation occurs even for exactly perpendicular propagation. This will be discussed in Section 5.10.

For each of these collisionless absorption mechanisms, only those particles which have the velocity required by the resonance condition will gain energy from the wave. For a given collisionless absorption mechanism the evolution of the plasma depends on the collision rate and the power input. Since the resonant particles are a small sub-set they will collide mainly with non-resonant particles. If these collisions occur sufficiently rapidly the Maxwellian distribution is preserved, the power absorption is maintained and bulk heating results. If the power level is increased, collisions may be too infrequent to maintain a thermal distribution and a hot tail can develop.

A small population of energetic particles can have both beneficial and deleterious effects. Energetic ion tails produced by minority ion cyclotron heating can reach energies of 1 MeV and above. Provided they are confined, these tails eventually relax by colliding with the bulk electrons. Hence, strong ion cyclotron heating can result in bulk electron heating. For some applications, such as radio frequency current drive and tail-enhanced non-thermal fusion schemes, the creation of a superthermal population is advantageous.

### **Evolution of the equilibrium distribution function**

The evolution of the equilibrium distribution function under the simultaneous influence of radio frequency heating and collisional relaxation can be described by a modified Fokker-Planck equation:

$$\frac{\partial f}{\partial t} = C(f) + Q(f), \quad 5.7.12$$

where  $C(f)$  represents Coulomb collisions as discussed in Sections 2.10 and 2.12, and  $Q(f)$  describes the interaction of the radio frequency fields with the resonant particles and is referred to as the quasi-linear term. The quasi-linear interaction is the lowest-order nonlinear effect obtained by

averaging the nonlinear terms in the kinetic equation over a number of wave periods in space and time, and yields the time evolution of the equilibrium distribution function on a time scale long compared with the time period of the radio frequency fields. The term quasi-linear is used because the perturbed distribution and electromagnetic fields are taken from linear theory. Mode coupling and higher-order nonlinear effects are neglected. Quasi-linear theory was first derived for an unmagnetized plasma and was later generalized to a magnetized plasma. For a magnetized plasma the distribution function is also averaged over the gyro-phase angle in velocity space. The quasi-linear term  $Q(f)$  is proportional to the intensity of the incident electromagnetic wave and contains  $\delta(\omega - k_{\parallel}v_{\parallel} - \ell|\omega_{ci}|)$ , under an integral over  $k_{\parallel}$  for the uniform magnetic field under discussion. The latter dependence is simply an expression of the fact that only the resonant particles are directly influenced by the wave.

In the general case, the solution of eqn 5.7.12 represents a formidable computational problem. However, there are situations where a simplified description can still represent the most important features of the problem. One such case is that of fundamental ion cyclotron heating of a minority ion species. For this situation, eqn 5.7.12 can be reduced to a one-dimensional differential equation in velocity space for the heated (isotropic) minority ion distribution function. This will be described at the end of Section 5.8.

## 5.8

### Ion cyclotron resonance heating

The resonance frequency of a deuteron in a magnetic field of 5 T is 38 MHz. In a tokamak, the toroidal field falls off with major radius as  $R^{-1}$  and the ion cyclotron resonance is localized at a value of  $R$  for which the wave frequency,  $\omega$ , satisfies  $\omega = \omega_{ci}(R)$ . The resonance is subject to Doppler broadening, resulting in a resonance width  $\delta\omega = (k_{\parallel}v_{Ti}/\omega_{ci})R$ . In all practical cases this is much smaller than the plasma dimensions. Ion cyclotron resonance heating has therefore the desirable feature that the absorption region can be positioned simply by matching the wave frequency to the known toroidal field.

Ion cyclotron heating in tokamaks relies on the fast magnetosonic (compressional Alfvén) wave to transport energy from the antenna to the absorption region. The fast wave is the only wave in this frequency range which can propagate directly across the magnetic field, requiring only that the density be above the cut-off density, which is defined in the next paragraph. The ion cyclotron (shear Alfvén) wave is not suitable for ion cyclotron heating of tokamaks. There are two main reasons for this. The first is that it will not propagate above the ion cyclotron frequency and would therefore have to be launched from the high field side of the

tokamak. Second, even in this case it would not penetrate beyond the edge plasma due to mode conversion to an electrostatic wave.

The propagation of the fast wave can be described by means of the approximate dispersion relation

$$n_{\perp}^2 = (\varepsilon_{\perp} + i\varepsilon_{xy} - n_{\parallel}^2)(\varepsilon_{\perp} - i\varepsilon_{xy} - n_{\parallel}^2)/(\varepsilon_{\perp} - n_{\parallel}^2). \quad 5.8.1$$

Equation 5.8.1 can be obtained from eqn 5.6.1 by retaining only terms proportional to  $\varepsilon_{\parallel}$  since  $\varepsilon_{\parallel} \gg \varepsilon_{\perp}, \varepsilon_{xy}, n_{\perp}^2$ . Physically, this means that  $E_{\parallel}$  is neglected compared with  $E_{\perp}$ , where  $E_{\parallel}$  and  $E_{\perp}$  are the amplitudes of the fast wave electric fields parallel and perpendicular to the equilibrium magnetic field. This is a good approximation in the ion cyclotron range of frequencies and requires  $\omega^2 \ll \omega_{pe}^2$ .

For the central regions of a tokamak discharge,  $m_e/m_i \ll \omega_{pe}^2/\omega_{ce}^2 \leq 1$ . It therefore follows that  $\omega_{pi}^2 \gg \omega_{ci}^2$ . In the ion cyclotron range of frequencies,  $\omega \sim \omega_{ci}$  and therefore the contribution of the electrons to  $\varepsilon_{\perp}$  is negligible. Thus, for the cold plasma description,  $\varepsilon_{\perp} \simeq -\sum_j \omega_{pj}^2/(\omega^2 - \omega_{cj}^2)$ . However, the electrons do make a contribution to  $\varepsilon_{xy}$ . Using the condition of charge neutrality, which can be written as  $\omega_{pe}^2/\omega_{ce}^2 = \sum_j \omega_{pj}^2/\omega_{cj}^2$  where the summation over  $j$  refers only to the different ion species, the electron contribution to  $\varepsilon_{xy}$  can be included in the ion term. The result is  $\varepsilon_{xy} \simeq -\sum_j i\omega_{pj}^2/\omega/\omega_{cj}(\omega^2 - \omega_{cj}^2)$ .

Substituting these expressions for  $\varepsilon_{\perp}$  and  $\varepsilon_{xy}$  into eqn 5.8.1, the fast wave dispersion relation can be written as

$$n_{\perp}^2 = \frac{\left[ \sum_j \frac{\omega_{pj}^2}{\omega_{cj}(\omega + \omega_{cj})} - n_{\parallel}^2 \right] \left[ \sum_j \frac{\omega_{pj}^2}{\omega_{cj}(\omega - \omega_{cj})} + n_{\parallel}^2 \right]}{\left[ \sum_j \frac{\omega_{pj}^2}{(\omega^2 - \omega_{cj}^2)} + n_{\parallel}^2 \right]}. \quad 5.8.2$$

It can be seen from eqn 5.8.2 that  $n_{\perp}^2 = 0$  when the first bracket on the right-hand side of this equation is zero. This gives the fast wave cut-off condition,  $\sum_j \omega_{pj}^2/\omega_{cj}(\omega + \omega_{cj}) = n_{\parallel}^2$ . For a pure deuterium plasma and a wave frequency  $\omega \sim 2\omega_{cD}$  the above condition reduces to  $\omega_{pD}^2 > 0.75c^2k_{\parallel}^2$  where  $\omega_{pD}$  and  $\omega_{cD}$  are the deuteron plasma and cyclotron frequencies. A typical value of  $k_{\parallel}$  set by antennas in large tokamaks is  $\sim 5 \text{ m}^{-1}$  so that for such an experiment the fast wave would only propagate for electron densities  $n_e > 2 \times 10^{18} \text{ m}^{-3}$ . The significance of this result is that the fast wave is evanescent at the antenna which must therefore be placed within a few centimetres of the cut-off density for efficient coupling.

In the centre of a tokamak plasma,  $\omega_{pi}^2/(\omega^2 - \omega_{ci}^2) \gg n_{\parallel}^2$ . However, as discussed in Section 5.7, for a two-ion species plasma the hybrid resonance occurs when  $\sum_j \omega_{pj}^2/(\omega^2 - \omega_{cj}^2) = 0$ . Thus, in the vicinity of the hybrid resonance, the denominator of eqn 5.8.2 can vanish and

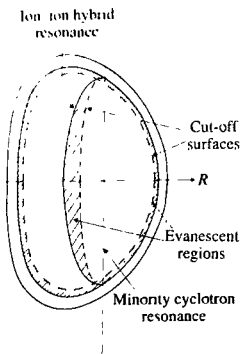


**Fig. 5.8.1** Loci of cut-off and resonances in the poloidal cross-section of a tokamak. The fast wave is evanescent in the hatched regions.

$n_1 \rightarrow \infty$ . Wherever there is a resonance, there must be an associated cut-off,  $n_j = 0$ , and this is given by the vanishing of the second bracket in the numerator of eqn 5.8.2. A poloidal cross section of the cut-off and resonant surfaces of the fast wave is shown in Fig. 5.8.1. The hatched regions denote zones of evanescence. Also shown in the figure is a resonance of a minority species which occurs along a vertical chord. The relationship between a hybrid and minority resonance is discussed in the next subsection.

Since the wave can propagate directly across the magnetic field, the illumination of the resonance surface depends on the poloidal location of the antenna. Generally the antennas are located near the equatorial plane on the low field side so that the intensity of the wave has its maximum value on the central part of the resonance surface. This results in peaked power deposition profiles which favour the achievement of high heating efficiency. Such an antenna arrangement is illustrated in Fig. 5.8.2 which shows the power flow refracted to the centre of the minority resonance surface by the plasma.

In a single ion species plasma the damping of the fast wave is weak at the fundamental resonance due to the fact that the electric field rotates almost entirely in the opposite sense to the ions. However, at the second harmonic resonance ( $\omega = 2\omega_{ci}$ ) in a single ion species plasma, or in the presence of a second ion species, a significant fraction of the perpendicular electric field possesses the polarization required to couple to the ions. As a result the main heating scenarios for the ion cyclotron range of frequencies are the second harmonic and minority schemes.

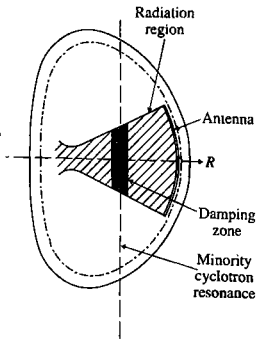


**Fig. 5.8.2** Contour of the wave power emitted by an antenna located on the low field side. Refraction concentrates the power near the centre of the resonance chord.

### Heating regimes in a two ion species plasma

There are two regimes of heating in a two ion species plasma. The two regimes are differentiated by the ratio of the densities of the ion species. In the first regime, referred to as minority heating, the two-ion hybrid resonance does not occur. In the second scheme, the mode conversion regime, the two-ion hybrid resonance is present.

The minority ion concentration is defined by the ratio,  $\eta = n_{\min}/n_{\maj}$ , of the densities of the minority and majority ion species. For very low minority ion concentrations,  $\eta \lesssim 0.1\%$ , the fast wave will undergo weak cyclotron damping at the minority fundamental resonance. As the minority concentration is increased the damping is increased until the absorption reaches a maximum value at a critical concentration  $\eta_c$ . For further increases of the minority concentration beyond this critical value the hybrid resonance occurs and the wave polarization becomes less favourable for cyclotron damping in the vicinity of the minority resonance. In addition, the cut-off associated with the hybrid resonance produces strong reflection of the fast wave. Because the hybrid cut-off is on the low-field side of the hybrid resonance, the fast wave must be launched from the high-field side of the tokamak to propagate unimpeded to the resonance. On the other hand, the minority resonance (for a light ion minority) is accessible with a low-field side antenna.

The two regimes are illustrated by the dispersion diagrams shown in Fig. 5.8.3. In Fig. 5.8.3(a) the concentration ratio is less than the critical value with the result that there is no hybrid resonance and the fast wave is able to propagate everywhere between the fast wave cut-offs on the high and low field sides. The wave is most strongly damped on the high field side of the minority resonance where the wave polarization is most favourable. In Fig. 5.8.3(b), the concentration ratio is above the critical value and the hybrid resonance and cut-off now appear. The minority resonance is still accessible from the low field side but the damping decreases as  $\eta$  increases due to the less favourable polarization. A wave launched from the high field side will be mode converted to an ion hybrid wave at the hybrid resonance and will damp on electrons due to electron Landau damping. When the separation of the hybrid resonance and cut-off is not too large some of the fast wave energy excited by a low field side antenna can tunnel through the evanescence zone to the hybrid resonance and undergo mode conversion. However, there is an upper limit of twenty five per cent to the fraction of energy incident on the hybrid cut-off which can be mode converted in a single transit compared to one hundred per cent from the high field side. When the hybrid resonance occurs, minority heating schemes can still be operated with a low field side antenna, but the absorption at the minority resonance will be weakened and strong reflection will be produced at the hybrid cut-off.

The effect of the hybrid resonance on fast wave heating is demonstrated in Fig. 5.8.4 which gives results from experiments performed on the TFR tokamak which had an antenna on the high field side. In each figure the position of the hybrid and minority (proton) resonance is shown together with the neutron counting rate which gives a measure of the heating. The counting rate is only high when the hybrid resonance is at the centre of the discharge, as in Figs 5.8.4(a) and (c). In Fig. 5.8.4(b), when the proton resonance is at the centre but the hybrid resonance is at the edge, the counting rate is low. This indicates that for the mode conversion regime, it is the position of the hybrid resonance which is vital for strong absorption, and also that the minority ion cyclotron damping is weak.

In order to understand how the two regimes of heating arise in a two-ion species plasma and to obtain a quantitative theory of cyclotron damping it is necessary to take account of the kinetic response of the minority ion species. For the present discussion, only the kinetic modification to the  $\epsilon_{\perp}$  element of the dielectric tensor is required. The cold plasma expression given by eqn 5.6.2 is replaced by

$$\epsilon_{\perp} = -\frac{\omega_{p1}^2}{(\omega^2 - \omega_{ci}^2)} + \frac{\omega_{p2}^2}{2\sqrt{2}\omega k_{\parallel} v_{T2}} [Z(z_{12}) + Z(z_{-12})] \quad 5.8.3$$

where the subscripts 1 and 2 refer to the majority and minority ion species and  $v_{T2}$  is the minority ion thermal speed,  $v_{T2} = (T_2/m_2)^{1/2}$  and  $Z$ ,  $z_{12}$  and  $z_{-12}$  are defined below. The vacuum and electron contributions to eqn 5.8.3 have again been neglected. It should also be noted that only the effect of the thermal motion of the minority ions along the equilibrium

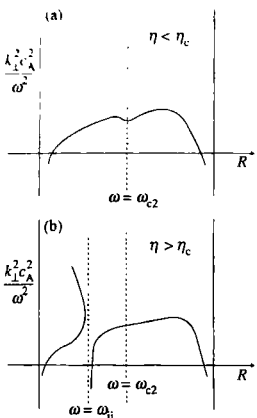


**Fig. 5.8.3** Plot of the square of the fast wave perpendicular refractive index as a function of major radius (a) minority concentration is below the critical value,  $\eta < \eta_c$  and the ion-ion hybrid resonance is not present, (b) minority concentration is, above the critical value,  $\eta > \eta_c$  and the ion-ion hybrid resonance is present.

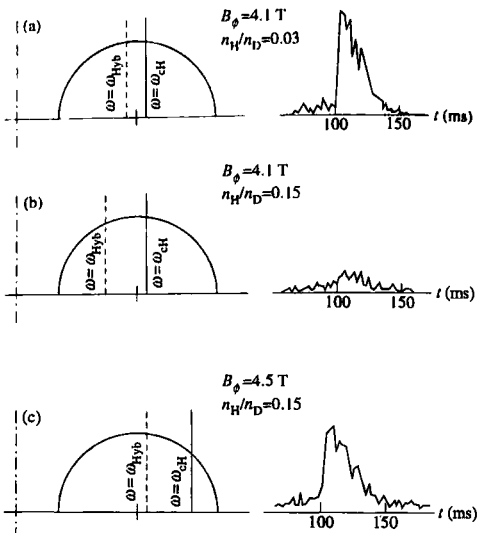


**Fig. 5.8.4** Effect of  $n_H/n_D$  on the neutron rate at different values of the magnetic field in 'low density' plasmas. Strong absorption (high count) only occurs when the ion-ion hybrid resonance is at the centre of the discharge. [Adam J. and Equipe T.F.R., Proceedings of 9th European Conference on Controlled Fusion and Plasma Physics, Oxford 1979, Invited Papers, UKAEA Culham Laboratory, p. 355.]

magnetic field is included. The effect of finite ion Larmor radius, which is important for second harmonic resonance, has been neglected.

The function  $Z(z)$  appearing in eqn 5.8.3 is known as the plasma dispersion function and was first obtained by Landau in his theory of the collisionless damping of electron plasma waves in unmagnetized plasmas. The plasma dispersion function is defined as

$$Z(z) = \pi^{-1/2} \int_C \frac{\exp(-t^2) dt}{(t - z)} \quad 5.8.4$$

where  $C$  is known as the Landau contour and was chosen in order to satisfy causality requirements. In other words, the Landau contour is such that there is no response until the field has been switched on, ensuring that the cause must precede the effect. This choice of contour provides a prescription for integrating around the singularity which occurs on the real  $t$ -axis and which yields the collisionless damping decrement. The plasma dispersion function, which is a complex function, even for a real argument, has been tabulated by Fried and Conte. This function always arises in a kinetic description of wave phenomena in hot plasmas.

In eqn 5.8.3 the arguments of the plasma dispersion function are  $z_{12} = (\omega + \omega_{c2})/\sqrt{2}k_{\parallel}v_{T2}$  and  $z_{-12} = (\omega - \omega_{c2})/\sqrt{2}k_{\parallel}v_{T2}$ . Since  $\omega$  and  $\omega_{c2}$  are both defined as positive quantities,  $z_{12} \gg 1$ . On the other hand,

for the spatially varying equilibrium magnetic fields relevant to tokamak plasmas,  $z_{-12}$  can pass through zero when  $\omega = \omega_{c2}$ .

The plasma dispersion function can also be written as

$$Z(z) = -2e^{-z^2} \int_0^z \exp(t^2) dt + i\pi^{1/2} \exp(-z^2) \quad 5.8.5$$

which is valid for a real argument and shows explicitly the real and imaginary parts of the function. It is clear from eqn 5.8.5 that when  $z \gg 1$  the imaginary part of the function is negligible. Under these conditions the function can be expanded asymptotically as  $Z(z) \sim -1/z$ . Thus, in eqn 5.8.3,  $(\omega_{p2}^2/2\omega k_{\parallel} v_{T2})Z(z_{12}) \sim -\omega_{p2}^2/2\omega(\omega + \omega_{c2})$ . This is referred to as the non-resonant part of the minority ion response and describes those minority ions which do not come into cyclotron resonance with the (fast) wave. The minority ion temperature does not appear in the non-resonant response which can therefore be obtained from a cold plasma model. For low minority ion concentrations the non-resonant response can be neglected.

The resonant minority ion response is described by the term  $(\omega_{p2}^2/2\omega k_{\parallel} v_{T2})Z(z_{-12})$  in eqn 5.8.3 for which the exact plasma dispersion function must be retained. The physical significance of the resonant argument,  $z_{-12}$ , is that it is the ratio of the parallel velocity of a resonant ion to the minority thermal speed. Once this ratio exceeds about three for a thermal population of minority ions the number of resonant ions rapidly becomes negligible. Since  $\omega_{c2}$  is spatially varying,  $(\omega - \omega_{c2})/k_{\parallel}$  can match the velocities of thermal minority ions as well as more energetic ones.

### The critical minority concentration

The above account of the thermal effects of the minority ions can be used to explain how the critical concentration ratio of the two ion species arises. Referring to eqn 5.8.1, it can be seen that the fast wave will have a resonance when  $\varepsilon_{\perp} - n_{\parallel}^2 = 0$ . For a single ion species plasma,  $\varepsilon_{\perp} \gg n_{\parallel}^2$  in the centre of a tokamak discharge. However, as discussed in Section 5.7,  $\varepsilon_{\perp} = 0$  at the two-ion hybrid resonance which can occur at the centre of the discharge. Thus,  $\varepsilon_{\perp} - n_{\parallel}^2 = 0$  can be satisfied at the centre of a tokamak plasma near to the two-ion hybrid resonance.

The condition for a resonance of the fast wave, allowing for the parallel thermal motion of the minority ions is therefore given by

$$\frac{-\omega_{p1}^2}{(\omega^2 - \omega_{c1}^2)} - n_{\parallel}^2 + \frac{\omega_{p2}^2}{2\sqrt{2}\omega k_{\parallel} v_{T2}} Z(z_{-12}) = 0. \quad 5.8.6$$

When cold plasma theory is used to describe the minority ions, their response becomes singular as  $\omega \rightarrow \omega_{c2}$ , with the result that the minority response can always balance that of the majority ions, no matter how low the minority density. However, the minority ion response, given by the

third term in eqn 5.8.6, is no longer singular as  $\omega \rightarrow \omega_{c2}$  (or  $z_{-12} \rightarrow 0$ ). Hence, for low minority concentrations, the minority response cannot balance the majority response. Furthermore, the minority response contributes an imaginary term corresponding to minority damping. In other words, cold plasma theory breaks down for low minority concentrations.

In Sections 5.6 and 5.7 the propagation of an electromagnetic wave through an inhomogeneous tokamak plasma was approximated by a one-dimensional slab model in which the direction of the inhomogeneity represented the radial coordinate. For the present discussion, the only inhomogeneity which need be considered is that of the magnetic field which is assumed to vary as  $B(x) = B_0(1 - x/R)$  where  $R$  is the major radius. Taking  $\omega = \omega_{c2}(0)$ , the resonant argument,  $z_{-12}$ , of the plasma dispersion function in eqn 5.8.6 is given by  $z_{-12} = wx/\sqrt{2k_{\parallel}v_{T2}R}$ . The condition for a resonance of the fast wave, given by eqn 5.8.6, yields the position of resonance,  $x = x_{\text{res}}$ . Since  $\text{Re } Z(z_{-12}) < 0$  for  $z_{-12} > 0$  and  $\text{Re } Z(z_{-12}) > 0$  for  $z_{-12} < 0$ , the (hybrid) resonance can only occur on the high field side of the minority ion cyclotron resonance where  $x < 0$ . A further condition to be satisfied for resonance of the fast wave is  $\text{Im } Z(z_{-12}) \ll 1$  which requires  $|z_{-12}| \gg 1$ .

Solutions of eqn 5.8.6 are illustrated in Fig. 5.8.5. This figure has been obtained by writing eqn 5.8.6 in the alternative form,

$$Z(z_{-12}) = \frac{2}{\eta} \frac{k_{\parallel}v_{T2}}{\omega} \frac{m_1}{m_2} \left[ \frac{\alpha^2}{(1 - \alpha^2)} + \frac{k_{\parallel}^2 c_A^2}{\omega^2} \right] \quad 5.8.7$$

where  $\alpha = Z_1 m_2 / Z_2 m_1$ . The real part of  $Z$  is shown as a function of  $z_{-12}$  in Fig. 5.8.5. The quantity on the right-hand side of eqn 5.8.7 is independent of  $z_{-12}$  and is therefore represented by a horizontal line in Fig. 5.8.5 whose height above the  $z_{-12}$ -axis is governed by the size of  $\eta$  for given ion species and minority temperature. Three horizontal lines are shown corresponding to three values of the minority to majority ion density ratio  $\eta$ . For  $\eta < \eta_c$ , there is no intersection of the horizontal

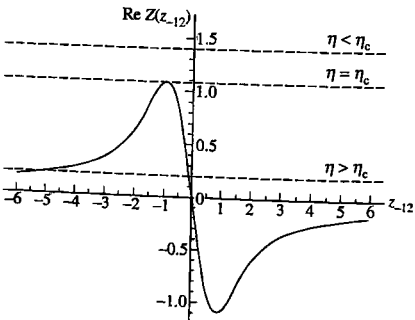


**Fig. 5.8.5** Plot of eqn 5.8.7. The curve shows  $\text{Re } Z(z_{-12})$ . The three horizontal lines represent the right-hand side of the equation for three different minority concentrations. Intersections of the horizontal line with  $\text{Re } Z(z_{-12})$  produce the ion-ion hybrid resonance when  $\text{Im } Z(z_{-12}) \ll 1$  at the intersection.

line with  $\text{Re } Z(z_{-12})$  and hence no resonance. This is called the minority regime, shown in Fig. 5.8.3(a). For  $\eta > \eta_c$ , the horizontal line intersects  $\text{Re } Z(z_{-12})$  twice, once for  $|z_{-12}| < 1$  and once for  $|z_{-12}| > 1$ , making a resonant solution possible. This is referred to as the mode conversion regime, shown in Fig. 5.8.3(b). For  $\eta = \eta_c$ , the horizontal line is tangent to the curve,  $\text{Re } Z(z_{-12})$ . This condition marks the transition between the two regimes.

The physical interpretation of Fig. 5.8.5 is as follows. The argument  $z_{-12}$  is proportional to the distance from the position where the fast wave frequency is equal to the fundamental minority ion cyclotron frequency. For low minority ion concentrations  $\eta < \eta_c$ , the condition for fast wave resonance, eqns 5.8.6 or 5.8.7, cannot be satisfied. For  $\eta > \eta_c$ , there are two possible positions where the resonance conditions could be satisfied. The first position is close to the minority ion cyclotron resonance where  $\text{Im } Z$  is significant and is therefore ruled out. For the second position where  $|z_{-12}| > 1$ , resonance of the fast wave is possible. The larger the value of  $|z_{-12}|$ , the smaller the value of  $\text{Im } Z$  and the stronger the effect of the resonance. The increase in the magnitude of  $|z_{-12}|$  is equivalent to an increase in the separation of the two-ion hybrid resonance from the minority cyclotron resonance. The former is a region of mode conversion and weak ion damping and the latter a region of potentially strong, wave-particle, ion cyclotron damping. The larger the value of the minority to majority concentration ratio the larger the separation of the hybrid from the minority resonance. The critical concentration,  $\eta = \eta_c$ , illustrated by the tangent line in Fig. 5.8.5, gives the condition where hybrid resonance first becomes possible. However, the effect of hybrid resonance, namely mode conversion, will not be strong for  $\eta = \eta_c$  because there will be strong cyclotron damping under these conditions. In fact, minority absorption is close to its maximum value for  $\eta = \eta_c$ . As  $\eta$  increases beyond the critical value  $\eta_c$ , the minority damping region occurs further from the hybrid resonance and the influence of the hybrid resonance increases.

The critical density ratio which marks the beginning of the transition between the two regimes of heating can be obtained from eqn 5.8.7 by using the fact that the maximum value of  $\text{Re } Z$  is approximately unity. Thus

$$\eta_c = \frac{2k_{\parallel}v_{T2}}{\omega} \frac{m_1}{m_2} \left[ \frac{\alpha^2}{(1 - \alpha^2)} + \frac{k_{\parallel}^2 c_A^2}{\omega^2} \right] \quad 5.8.8$$

which shows that the occurrence of the two-ion hybrid resonance requires higher minority concentrations as the minority temperature is increased or as the parallel wave number is increased, both of which result in an increase in minority ion cyclotron damping.

As a specific example, consider the case of a deuterium plasma with a hydrogen minority which is often denoted as D(H). When the minority density is above the critical value, a full-wave calculation for the propagation of the fast wave across the two-ion hybrid resonance gives

a transmission coefficient

$$T = \exp(-\pi \eta \omega_{\text{CI}} R / 4c_A) \quad 5.8.9$$

where  $\eta = n_H/n_D$  and  $c_A$  is the Alfvén speed corresponding to the deuterium plasma. The expression for  $T$  given by eqn 5.8.9 has been obtained by neglecting the weak damping in the region of the hybrid resonance. In general there will still be cyclotron damping in the vicinity of the hydrogen minority fundamental resonance. For typical JET parameters,  $B_0 = 3.4 \text{ T}$ ,  $R = 3 \text{ m}$ ,  $n_D = 5 \times 10^{19} \text{ m}^{-3}$  with  $n_H/n_D = 0.05$  the transmission coefficient  $T \ll 1$ . This means that the fast wave energy launched from the low field side which reached the hybrid cut-off would be totally reflected. Under these conditions the fast wave would be subject to damping by the hydrogen minority both as an incident wave and as a reflected wave. Conversely, fast wave energy reaching the hybrid resonance from the high field side would be totally mode converted to an ion hybrid wave.

For a D(H) plasma, the deuteron will also have a second harmonic resonance which is degenerate with the hydrogen fundamental resonance. Including the majority second-harmonic terms the transmission coefficient is

$$T = \exp \left[ -\frac{\pi}{4} \left( \eta + \frac{2v_{TD}^2}{c_A^2} \right) R \frac{\omega}{c_A} \right]. \quad 5.8.10$$

It is clear from this result that the hybrid resonance will dominate the second harmonic majority resonance provided  $\eta > \beta_D$  where  $\beta_D = 2v_{TD}^2/c_A^2$ . In a pure deuterium plasma the second harmonic resonance has similar properties to the hybrid resonance. Thus, for large enough values of  $\beta_D$  or small enough  $k_{\parallel}$ , the fast wave will be mode converted to an ion Bernstein wave for high field side incidence and reflected for low field side incidence. Similarly, as  $k_{\parallel}$  is increased, the region of cyclotron damping will eventually overlap the mode conversion region, progressively increasing the damping and reducing the reflection from the low field side.

However, there is still another possibility to consider in a plasma with two, or more, ion species. The discussion of mode conversion given above is based on the Budden model of a resonance and its associated cut-off illustrated by Fig. 5.8.3(b), which shows the square of the perpendicular refractive index of the fast wave as a function of the major radius. This figure also shows the fast wave cut-off on the high field side of the resonance. The effect of the high field side cut-off on the mode conversion process had been ignored. It is now clear that this cut-off plays a significant role in the conversion process. Thus, instead of two critical points there are now three to consider, the fast wave cut-off on the high field side, the ion-ion hybrid resonance and its associated cut-off. This is often referred to as a triplet configuration. Depending on the ion species and the value of  $k_{\parallel}$ , conditions exist for which the reflected energy is

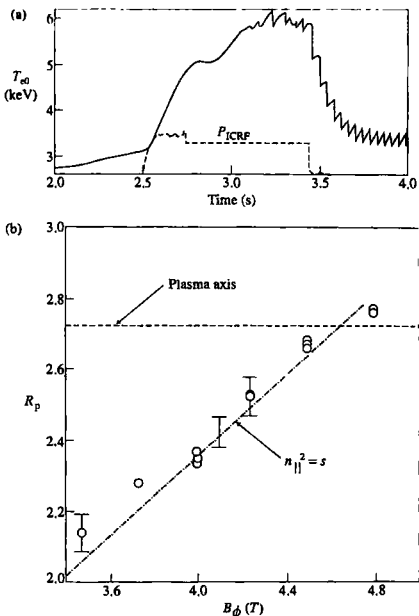


**Fig. 5.8.6** (a) Time development of the electron temperature at the Shafranov-shifted axis from electron cyclotron emission during mode conversion heating in TFTR, with peak ICRF power of 4.4 MW. (b) Variation of the radius,  $R_p$ , of peak electron power for mode conversion heating during a scan of the toroidal magnetic field. Also shown is the location of the mode conversion surface. [Majeski, R. et al., *Physical Review Letters* 76, 764 (1996).]

reduced to zero. The incident fast wave is then totally converted to the ion hybrid wave. It should be noted that for other values of  $k_{||}$  the converted energy is minimized and the reflected energy is maximal. For low values of electron beta, the electron dissipation of the ion hybrid wave is significantly stronger than the electron dissipation of the fast wave. Hence this mechanism can lead to enhanced electron heating and possibly current drive. Furthermore, as the absorption is associated with the ion-ion hybrid resonance, which is a cold plasma resonance, this offers the possibility of both on and off-axis heating and current drive. It is also worth emphasizing that mode conversion heating and current drive uses a low field side antenna.

Results from an experiment carried out on the TFTR tokamak are shown in Fig. 5.8.6. The ICRF antenna launched a fast wave with a parallel wave number  $k_{||} \sim 10 \text{ m}^{-1}$  for symmetric phasing or  $6 \text{ m}^{-1}$  with directed phasing for current drive. The figure shows a doubling of the central electron temperature and demonstrates that the peak electron

heating scaled with the position of the ion–ion resonance for a scan of the toroidal magnetic field. The on and off-axis currents derived from differences in loop voltage were somewhat in excess of the theoretically predicted currents

Another version of fast wave heating has been proposed specifically to produce non-inductive current drive in spherical tokamaks, which achieve a higher plasma beta than conventional tokamaks. This is called high harmonic fast wave heating which, as the name implies, operates in a frequency range where  $\omega \gg \Omega_i$ . In a region of the discharge outside an ion cyclotron harmonic resonance, the damping of the fast wave is due to the electrons through the Landau resonance and  $\text{Im } k_{\perp}/\text{Re } k_{\perp} \sim \pi^{1/2} \beta_e \xi_{0e} \exp(-\xi_{0e}^2)$  where  $\beta_e = 2\mu_0 n T_e / B^2$  and  $\xi_{0e} = \omega/k_{\parallel} v_{te}$ . Under conditions of high electron beta the electron dissipation is strong so that both on and off-axis current drive appear to be possible. For this application ion absorption is to be avoided. Under conventional tokamak conditions, the ion damping at high ion cyclotron harmonics ( $n > 5$ ) would be negligible. For the high beta conditions of a spherical tokamak where values of  $n$  up to 20 can occur the damping as the fast wave crosses many ion cyclotron harmonics can be significant. This is because, for the low magnetic fields present in a spherical tokamak the ion Larmor radius can be of the order or larger than the perpendicular wavelength of the fast wave. For a deuterium plasma in NSTX with a toroidal magnetic field  $\sim 0.25$  T, a density  $5 \times 10^{19} \text{ m}^{-3}$ , and a harmonic number of  $n = 20$ ,  $k_{\perp}^2 \rho_D^2 \cong 64 T_D (\text{keV})$ . Hence, for a modest deuterium temperature  $T_D = 0.5 \text{ keV}$ ,  $k_{\perp}^2 \rho_D^2 \gg 1$ . Although the high beta conditions produce strong electron dissipation (through transit time damping and electron Landau damping) the ion cyclotron damping can also be strong. Strong electron or ion dissipation requires different ranges of  $k_{\parallel}$ . One of the challenges to high harmonic heating in a spherical tokamak is to design an antenna system which will result in a predominantly electron absorption.

The ion cyclotron damping mechanism is due to those ions which experience the wave electric field at the cyclotron frequency in their guiding centre rest frame. The resonance condition is given in eqn 5.7.4. Since the number of collisions experienced by resonating ions due to collisions with the background species decreases with increasing energy, their distribution function does not remain Maxwellian. Such distributions can be calculated by solving the Fokker–Planck equation containing an appropriate wave diffusion operator. The deviation from a Maxwellian distribution can be substantial with a high energy tail extending above the thermal ion energy by 1 to 3 orders of magnitude (up to several MeV in a large tokamak).

### Heated minority distribution function

Before describing the calculation of the heated minority ion distribution function some further observations on the absorption mechanism and its

consequences will be given. Each wave absorption mechanism depends on the properties of the particular wave and on the wave-particle resonance. The properties of the wave are influenced by all the particles in the plasma whereas the wave-particle resonance depends on a small group of resonant particles.

Although the wave-particle resonance can be derived from a single particle description, the net flow of energy between the wave and the plasma can only be obtained by taking into account the equilibrium velocity distribution of the resonant particles. This is because for any wave-particle resonance, some particles gain energy from the wave and others lose energy to the wave. For example, in ion cyclotron resonance a resonant ion will receive an impulse mainly in the direction perpendicular to the equilibrium magnetic field, and this impulse can be either retarding or accelerating depending on the phase between the ion motion and the wave. Averaging the ion impulses over all velocities, and assuming a thermal distribution of the resonant particles, a net gain of energy by the plasma is obtained. This causes an evolution of the heated particle distribution as outlined in Section 5.7. In addition, for cyclotron resonance, the resonant particles are constrained to move along certain paths in velocity space. In the non-relativistic limit, these paths are given by the circles.

$$v_{\perp}^2 + \left( v_{\parallel} - \frac{\omega}{k_{\parallel}} \right)^2 = C \quad 5.8.11$$

where  $C$  is a constant. This result is easily obtained, as follows. The change in energy  $\delta E$  of a non-relativistic, resonant particle is given by

$$\delta E = mv_{\perp}\delta v_{\perp} + mv_{\parallel}\delta v_{\parallel}. \quad 5.8.12$$

However, from quantum mechanics, this gain in energy must be equal to the energy lost by the wave  $\delta E = \hbar\omega$  where  $\omega$  is the wave frequency and  $\hbar$  is Planck's constant divided by  $2\pi$ . Since the wave has a parallel wave number  $k_{\parallel}$ , it also loses parallel momentum,  $p_{\parallel} = \hbar k_{\parallel}$  which is gained by the resonant particle. Hence

$$\frac{\delta E}{\delta E_{\parallel}} = \frac{\omega}{k_{\parallel} v_{\parallel}}$$

giving

$$\delta E = \frac{\omega m \delta v_{\parallel}}{k_{\parallel}}. \quad 5.8.13$$

Combination of eqns 5.8.12 and 5.8.13 gives

$$v_{\perp}\delta v_{\perp} + \left( v_{\parallel} - \frac{\omega}{k_{\parallel}} \right) \delta v_{\parallel} = 0. \quad 5.8.14$$

Integration of eqn 5.8.14 immediately yields eqn 5.8.11. Making use of the cyclotron resonance condition, eqn 5.8.14 also shows that  $\delta v_{\perp}/\delta v_{\parallel} = \Omega/k_{\parallel}v_{\perp} \gg 1$ . It is important to emphasize that the velocity contours given by eqn 5.8.11 only have physical significance when the cyclotron resonance condition is simultaneously satisfied.

The distribution function for the heated, resonant ions can be calculated starting from eqn 5.7.12. As already mentioned, this is a complicated time dependent, nonlinear partial-differential equation in three spatial and three velocity variables. In addition, the plasma is embedded in a non-uniform equilibrium magnetic field. However, the problem can be greatly simplified for the case of fundamental ion cyclotron heating of a minority ion species. Since the minority ions relax collisionally on the bulk electrons and ions, they can be treated as test particles. This means that the Fokker–Planck term  $C(f)$ , which involves the Coulomb scattering potentials can be evaluated explicitly in terms of the bulk ion and electron distribution functions which can be assumed to be Maxwellian. The scattering term  $C(f)$  is independent of the test ion distribution function. The problem is further simplified by assuming that the cyclotron interaction occurs in a uniform magnetic field.

The Fokker–Planck equation given by eqn 5.7.12 is therefore reduced to an equation for  $f(v_{\perp}, v_{\parallel}, t)$  where  $v_{\perp}$  and  $v_{\parallel}$  refer to the velocity perpendicular and parallel to the uniform, equilibrium magnetic field. It is convenient to express  $f$  in terms of spherical velocity coordinates  $(v, \xi)$  where  $\xi = v \cdot \mathbf{B}_0/|v||\mathbf{B}_0|$ . Since Legendre functions  $P_{2\ell}(\xi)$  are eigenfunctions of the operator  $C(f)$  it is useful to expand  $f$  as a sum of Legendre functions. Even though the  $P_{2\ell}(\xi)$  are not eigenfunctions of  $Q(f)$  this procedure is still very helpful since the expansion reduces the partial-differential equation for  $f(v, \xi, t)$  to a coupled system of differential equations  $f(v, t)$ . In fact, the zeroth  $\xi$ -moment yields significant physical information and makes possible an analytic evaluation of the heated, pitch-angle averaged minority ion distribution function. This was obtained by Stix who reduced eqn 5.7.12 to the following magnetic-surface, pitch-angle averaged small Larmor-radius equation for the evolution of  $f(v, t)$  for minority ions, assumed to be passing particles, subject to fundamental cyclotron resonance heating and collisional relaxation

$$\frac{\partial f}{\partial t} = \frac{1}{v^2} \left[ -\alpha v^2 f + \frac{1}{2} \frac{\partial}{\partial v} (\beta v^2 f) + \frac{1}{2} H_{01} v^2 \frac{\partial f}{\partial v} \right] \quad 5.8.15$$

where  $\alpha$  and  $\beta$  are the coefficients of the Fokker–Planck equation discussed in Section 2.12. These diffusion coefficients have been represented by analytic approximations. The quantity  $H_{01}$  comes from the quasi-linear term and is given by  $H_{01} = \langle P_{\perp} \rangle / 2n_s m_s$  where  $\langle P_{\perp} \rangle$  is the radio frequency power absorbed due to the fundamental minority ion cyclotron resonance, averaged over a magnetic surface, and  $n_s$  and  $m_s$  are the density and mass of the resonant ions on the magnetic surface.  $\langle P_{\perp} \rangle$  has been assumed proportional to  $|E^+|^2$  where  $E^+ = \frac{1}{2}(E_x + iE_y)$  is the component of the transverse electric field rotating in the same sense as the ions

$E^- (= \frac{1}{2}(E_x - iE_y))$  and  $E_z$  have been neglected, as has the effect of the parallel velocity in the quasi-linear operator. The final approximation is to assume that the radio-frequency pulse is of sufficient duration to produce a steady state. Under these conditions  $\partial f/\partial t$  is set equal to zero in eqn 5.8.15 and the following explicit solution for  $f(v)$  obtained

$$\ln f(v) = -\frac{E}{T_e(1+\zeta)} \left[ \frac{1+R_f(T_e-T_f+\zeta T_e)}{T_f(1+R_f+\zeta)} K(E/E_f) \right] \quad 5.8.16$$

where a single species of background ion has been assumed, denoted by subscript  $f$ ,

$$\zeta = \langle P_{\perp} \rangle t_s / 3nT_e, \quad R_f = n_f Z_f^2 \ell_f / n_e \ell_e,$$

where

$$\ell_f = 1/\sqrt{2}v_{T_f}, \quad \ell_e = 1/\sqrt{2}v_{T_e}$$

and

$$E = mv^2/2, \quad E_f = \frac{mT_f}{m_f} \left[ \frac{3\sqrt{\pi}}{4} \frac{(1+R_f+\zeta)}{(1+\zeta)} \right]^{2/3}$$

with

$$K(x) = \frac{1}{x} \int_0^x \frac{du}{(1+u^{3/2})}$$

$n$  and  $m$  being the density and mass of the test ions and  $t_s$  the slowing down time given by eqn 2.14.1.

The solution for  $f(v)$  given in eqn 5.8.16 allows an effective temperature to be defined for each value of  $E$ , given by

$$T_{\text{eff}} = -[\text{d}(\ln f)/\text{d}E]^{-1}. \quad 5.8.17$$

For  $E \ll E_f$ ,  $T_{\text{eff}}$  is somewhat above the background ion temperature. For  $E \gg E_f$ ,  $T_{\text{eff}}$  approaches asymptotically the value  $T_e(1+\zeta)$ , since for these energies the wave-induced test ion diffusion is balanced by electron drag. The theoretical distribution function given by eqn 5.8.16 has been compared with data from minority ion heating experiments carried out on PLT and JET. The PLT comparison is shown in Fig. 5.8.7.

At high energies, where the dominant slowing down process of the minority ions is on the electrons, the minority ion distribution function is expected to become anisotropic since the electron relaxation does not involve angular scattering. Anisotropic minority ion distributions where

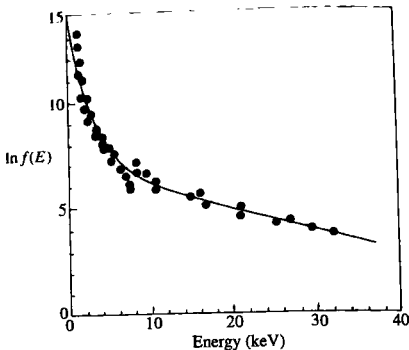


**Fig. 5.8.7** PLT experimental data for hydrogen minority heating in a deuterium plasma. Hydrogen charge exchange spectrum is shown together with theoretical curve based on  $Z_{\text{eff}} = 2.2$  and  $\zeta = 13.8$ . [Hosea, J.C. et al., *Physical Review Letters* 43, 1802 (1979).]

the perpendicular energy exceeds the parallel energy will be generated above a critical energy  $E_{\text{crit}}$  given by

$$E_{\text{crit}} = 14.8 T_e \left[ \frac{A_m^{3/2}}{n_e} \sum_j n_j \frac{Z_j^2}{A_j} \right]^{2/3} \quad 5.8.18$$

where the summation is over the field (bulk) ions and  $A_m$  is the atomic number of the minority ions. Those ions with energies above  $E_{\text{crit}}$  transfer their energy to plasma electrons. Those with energies below  $E_{\text{crit}}$  produce bulk ion heating. The relative transfer of power to electrons or bulk ions can be controlled by choosing the minority ion concentration.

It is remarkable that such a simple model can describe the experimental results so well. The cyclotron resonance interaction is described by means of a uniform magnetic field model in contrast to the non-uniform magnetic field of the experiment. For a uniform field a particle is either never in resonance or always in resonance, whereas in the magnetic field of the experiment particles are only in cyclotron resonance for a finite time but many more particles can come into resonance than in the uniform field case. Furthermore, the uniform field theory can only deal with passing particles whereas strong ion cyclotron heating tends to push resonant ions into the magnetically trapped regime. Such a case is illustrated in Fig. 5.8.8, which gives a solution of the Fokker-Planck equation for a tokamak magnetic field including the effect of both passing and trapped resonant ions for second-harmonic cyclotron resonance of the bulk ions. Finally, the distribution function given by Stix's theory is averaged over a single magnetic surface whereas the experimental distribution functions were obtained from line-averaged measurements which include the effects of many magnetic surfaces.

**Fig. 5.8.8** Contours of the steady state ion distribution represented in midplane velocity space coordinates ( $v_{||0}$ ,  $v_{\perp 0}$ ) for a majority ion excited at its second harmonic cyclotron frequency. The oblique lines mark the trapped-passing boundary and both figures show the accumulation of heated ions which turn (have their banana tips) in the resonance region. A similar result has also been obtained for fundamental ion cyclotron resonance of minority ions. [From Kerbel, G.D. and McCoy, M.G., *Physics of Fluids* **28**, 3269 (1985).]

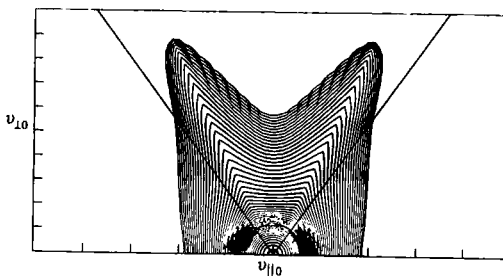
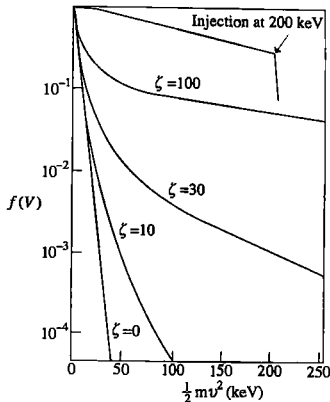


**Fig. 5.8.9** Plots of  $f(v)$  versus  $E$  based on eqn. 5.8.16 for different levels ( $\zeta$ ) of RF excitation at the minority-species cyclotron frequency, with  $Z_{\text{eff}} = 3$ . The ion velocity distribution for injection at 200 keV into the same plasma is also shown. [Stix, T.H., *Nuclear Fusion* **15**, 737 (1975).]



A closely related problem is the calculation of the distribution function for neutrally injected ions. In this case there is no quasi-linear driving term but instead a source of monoenergetic injected ions at a given energy (see Section 5.4). Solutions for the test ion distribution as a function of energy for various levels of radio frequency power are shown in Fig. 5.8.9. Also shown in this figure, for comparison, is the solution for a 200 keV deuteron neutral beam injected into a 4 keV tritium plasma.

#### Summary of experimental progress

Ion cyclotron resonance heating by means of the fast wave has made continual progress since the mid-seventies. In 1979 the state of the art was demonstrated on the TFR tokamak where 200 kW pulses of duration

20 ms were injected with a high-field side antenna. This resulted in ion temperature increases  $\sim 150$  eV at an average density of  $3 \times 10^{19} \text{ m}^{-3}$ . In 1980, with an upgraded TFR600, 500 kW were coupled producing increases of both electron and ion temperatures  $\sim 200$  eV. At lower density ( $\sim 5 \times 10^{19} \text{ m}^{-3}$ ) a temperature increase of 500 eV was obtained. However, increases of the plasma density, loop voltage, radiated power, and impurity content were also observed. By 1982 the level of injected power in the ion cyclotron range of frequencies (ICRF) into TFR was 1.5–2 MW. At this power level the ion temperature saturated during the radio frequency (RF) pulse due to the accumulation of metallic impurities. The electron temperature even began to decrease (after 25–30 ms) during the pulse. The limitation of the heating by impurity accumulation observed on TFR is now thought to have been due to the small dimensions of TFR and the lower single pass absorption.

In 1984, 2.6 MW of ICRF from a low-field side antenna on PLT produced a central ion temperature of 3.6 keV at a central density of  $5 \times 10^{19} \text{ m}^{-3}$ . A 7.2 MW, 10 s pulse was coupled to JET in 1986, also with a low-field side antenna. The best heating occurred with the minority fundamental resonance on axis. In 1988, 18 MW of ICRF power was coupled to JET discharges producing central electron and ion temperatures of 11.5 and 8 keV respectively.

Ion cyclotron heating on JET has not been limited by impurity accumulation as it was in TFR. Nevertheless the production of an H-mode plasma by ICRF alone and the coupling of large amounts of ICRF power to such discharges was not achieved until the RF induced influx of impurities had been significantly reduced. This has been brought about by the introduction of beryllium as a wall and limiter material. Of equal importance has been the covering of the nickel Faraday screens for the antenna by beryllium. Impurity release has also been found to depend on the antenna phasing. The dipole antenna in combination with a beryllium screen reduces the beryllium influx to negligible proportions. The reduction of RF produced impurities in JET has been one of the most significant developments in the subject of ion cyclotron heating allowing very successful operation of high power ICRF heating with good prospects for future large tokamaks.

## 5.9

### Lower hybrid resonance heating

Lower hybrid resonance heating utilizes electromagnetic power in the frequency range 1–8 GHz. At 3 GHz the vacuum wavelength is 0.1 m thus allowing the energy to be transmitted and launched by means of wave guides operating in their fundamental mode. This is one of the principle advantages of this scheme.

The lower hybrid range of frequencies satisfies  $\omega_{ci} \ll \omega \ll \omega_{ce}$ . Propagation in this frequency range is again well described by eqn 5.6.1 where the dielectric tensor elements are approximately

$$\epsilon_{\perp} \approx 1 + \frac{\omega_{pe}^2}{\omega_{ce}^2} - \frac{\omega_{pi}^2}{\omega^2}, \quad \epsilon_{\parallel} \approx 1 - \frac{\omega_{pe}^2}{\omega^2}, \quad \epsilon_{xy} \approx -\frac{i\omega_{pe}^2}{\omega\omega_{ce}}.$$

The use of lower hybrid waves was originally proposed with the object of heating the ions. For this purpose it is essential to choose conditions such that the lower hybrid resonance occurs in the plasma. The condition for this is, from eqn 5.7.2,

$$n_{res} = \frac{2.3 \times 10^{19} A_i f^2}{(1 - 2.3 A_i f^2/B_0^2)} \text{ m}^{-3}, \quad f \text{ in GHz,} \quad 5.9.1$$

where  $n_{res}$  is the electron density at the lower hybrid resonance,  $A_i$  is the atomic mass number of the ions,  $f$  is the frequency, and  $B_0$  is the magnetic field. Tokamaks operate in the range of densities  $10^{19}$  to  $5 \times 10^{20} \text{ m}^{-3}$ . The frequency must be chosen so that  $n_{res}$  matches the plasma density. Thus, the location of the resonance which governs the ion absorption is not completely under the control of the experimenter.

However, bulk ion heating by lower hybrid waves has proved to be problematical and unreproducible. Nevertheless, interest in the use of lower hybrid waves has increased very significantly since it was demonstrated to be very effective in driving the equilibrium plasma current in a tokamak discharge (see Section 3.13). As a result, most lower hybrid research has concentrated on coupling the wave energy to electrons rather than to ions. For electron heating, a symmetric spectrum of  $n_{\parallel}$  is launched, whereas for current drive an asymmetric spectrum is required.

For electron coupling and current drive it is no longer essential for the lower hybrid resonance to be present in the plasma. However, for lower hybrid waves to reach the centre of the plasma the wave must be excited with  $n_{\parallel} > 1$ . Thus, in common with the fast wave in the ion cyclotron range of frequencies, the lower hybrid wave is evanescent at the edge of the plasma requiring the lower hybrid antenna to be positioned close to the plasma. The antenna is required to excite the slow electromagnetic wave in preference to the fast wave which does not have a resonance. Since the slow wave has a component of  $E$  parallel to the magnetic field it is excited by aligning the wave-guide antenna with its short side parallel to the toroidal field and using the appropriate transverse electric field (TE) guide mode.

Once the slow wave has tunneled through the evanescent layer at the plasma edge it is required to propagate unimpeded to the plasma centre. However, when the parallel refractive index is less than a critical value,  $n_c$ , defined below in eqn 5.9.2, a confluence of the slow wave with the fast wave occurs between the cut-off and the centre of the plasma. Since the slow wave is a backward wave (the group velocity is opposite in sign from the phase velocity) conversion from the slow wave to the fast results

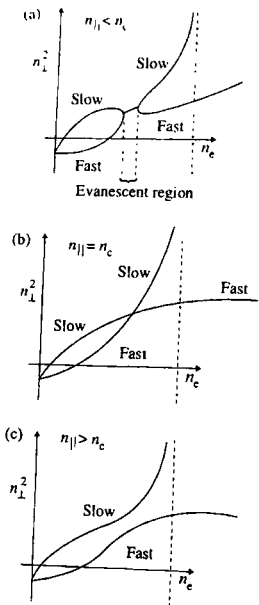


Fig. 5.9.1 Perpendicular refractive index squared versus density for  
(a)  $n_{\parallel} < n_c$ , (b)  $n_{\parallel} = n_c$  and (c)  $n_{\parallel} > n_c$ .

in the energy being reflected. Under these circumstances an additional non-propagating region prevents the slow wave from penetrating further into the plasma. This is illustrated in Figs 5.9.1(a), (b), and (c), where (a) shows the confluence of the fast and slow waves for  $n_{\parallel} < n_c$ , (b) shows the critical condition,  $n_{\parallel} = n_c$ , where the two branches just touch, and (c) where no confluence occurs and the slow wave propagates freely to the centre of the plasma (or the hybrid resonance if it is present). For the critical condition, the energy of the incident slow wave is divided equally between the transmitted slow wave and the reflected fast wave. However, as soon as  $n_{\parallel}$  is even a few tenths of one per cent below the critical value, the transmitted energy becomes completely negligible and total reflection occurs. The critical value  $n_c$  is given by the Stix-Golant accessibility condition

$$n_{\parallel}^2 > 1 + (\omega_{pe}^2/\omega_{ce}^2)_{res} (= n_c^2). \quad 5.9.2$$

In view of the above discussion this condition is very much an on-off condition for a wave to reach the centre.

Another important characteristic of lower hybrid heating is that the slow wave has the property that  $v_{g\perp}/v_{g\parallel} = k_{\parallel}/k_{\perp}$ , where  $v_{g\perp}$  and  $v_{g\parallel}$  are the perpendicular and parallel group velocities. This means that the energy does not go directly across the magnetic field but only reaches the centre of the plasma (or the resonance, if it is present) after travelling a number of times around the torus since  $k_{\parallel} \ll k_{\perp}$ .

The standard method of exciting the required spectrum of  $n_{\parallel}$  of lower hybrid waves satisfying the Stix-Golant accessibility criterion, is the lower hybrid grill launcher. A simplified diagram of the grill antenna is given in Fig. 5.9.2. This shows an array of appropriately phased wave guides arranged in two sets in which the small sides of the wave guides are oriented to be parallel to the toroidal magnetic field. This arrangement maximizes the coupling of the wave guide electric field to the lower hybrid wave. The array is driven by klystrons, one for each wave guide, all klystrons operating at the same frequency. Two vertically adjacent guides should be excited in phase and two horizontally adjacent guides excited in quadrature. The appropriate phase for each high power source is imposed at a low power level after the first amplifier. The resulting  $n_{\parallel}$  spectrum is shown in Fig. 5.9.2(b) in which the power is concentrated around a value satisfying eqn 5.9.2. Because the group velocity of the lower hybrid wave is predominantly in the toroidal direction there is a need to use a number of launching structures around the torus. Thus unlike the cyclotron heating schemes, lower hybrid systems use a single launching position.

Since the original proposal for the grill antenna, lower hybrid launchers have become increasingly sophisticated. As an illustration the lower hybrid launcher on JET will be described. This consists of 384 wave guides arranged in 12 rows with 32 wave guides in each row. The rows are divided into 3 groups allowing the possibility of radiating three different lower hybrid spectra simultaneously. Each of the 3 groups

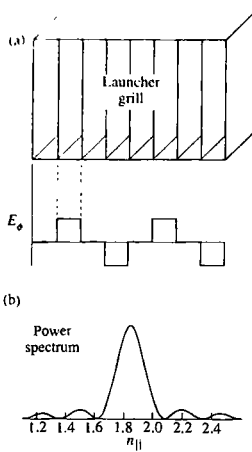


**Fig. 5.9.2** (a) Schematic diagram of a lower hybrid 'grill' antenna. (b) A typical Fourier spectrum for JET.

sub-divided into 16 wave guides in a  $4 \times 4$  array. Each  $4 \times 4$  array is fed by one klystron, and the phase between the four horizontal wave guides increases by  $90^\circ$  at each wave guide. The four guides in the same column have the same phase. The next group of 16 wave guides may repeat the previous phase change to give a periodic variation or it may advance or retard the phase by  $90^\circ$ . These three phase settings are referred to as  $\Delta\phi = 0$ ,  $90^\circ$ , or  $-90^\circ$  and give the three independent spectra referred to above.

The lower hybrid launcher operates at a frequency of 3.7 GHz with a maximum power of 15 MW in the generator supplied in 20 second pulses. The grill is driven by 24 klystrons each one operating at 650 kW and the surface power density at the plasma interface is  $40 \text{ MW m}^{-2}$ . The launcher is fed by transmission lines through a distance of 40 m.

Lower hybrid coupling to the plasma is determined by the electron density and its gradient in front of the launcher. Hence, the distance between the plasma and the antenna has to be adjusted. This is facilitated by curving the front ends of the wave guides toroidally and poloidally to match the shape of the plasma surface. The system has independent control of the launcher position and the plasma position. The launcher can be moved radially over a distance of 210 mm during shots with a maximum velocity of  $100 \text{ mm s}^{-1}$ . Fast changes of the plasma parameter in front of the launcher can be accommodated by a feedback loop acting on the plasma position. In practice, the launcher is only expected to be moved radially by  $\pm 10 \text{ mm}$  during a discharge. The optimum coupling occurs for an electron density in front of the launcher of  $1 \times 10^{18} \text{ m}^{-3}$ . Good coupling has been obtained with a reflection coefficient as low as 1%. In an H-mode discharge the lower hybrid system has driven a 1 MA current with a reflection coefficient of  $\sim 3\%$ .

When the lower hybrid resonance is present in the plasma the perpendicular wave number will increase as the wave approaches the resonance. This increases the coupling of the lower hybrid wave to the high ion Bernstein harmonics due to finite Larmor radius effects. The wave is totally absorbed at the lower hybrid resonance. If the resonance is not present, the lower hybrid wave will still be subject to strong ion cyclotron damping in a fusion plasma due to the presence of  $\alpha$ -particles. These particles will have much larger Larmor radii than thermal ions and so will couple to the lower hybrid wave at high Bernstein harmonics regardless of whether the lower hybrid resonance is present.

Since the lower hybrid wave has a much higher frequency than the fast wave in the ion cyclotron range of frequencies it will have a larger parallel electric field. This causes the wave to damp strongly on the electrons through Landau damping. The condition for electron Landau damping to occur is  $n_{\parallel} T_e^{1/2} \sim 5$  where  $T_e$  is in keV. The resultant electron heating is not confined either to the vicinity of the lower hybrid resonance, or to the central regions of the plasma, and moves to the edge of the plasma for  $T_e > 5 \text{ keV}$ .

By concentrating the  $n_{\parallel}$ -spectrum at lower values, but still consistent with the Stix-Golant accessibility condition, lower hybrid waves will also couple to superthermal electrons which are important for current

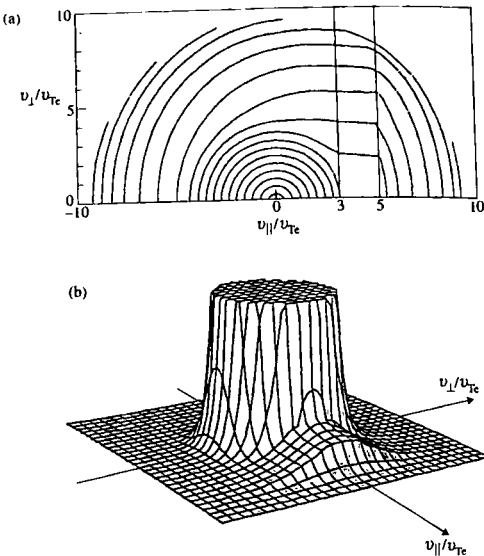


**Fig. 5.9.3** Contours of steady state electron distribution in  $(v_{\parallel}, v_{\perp})$  space for lower hybrid current drive. (a) represents contours of constant  $f(v_{\parallel}, v_{\perp})$  where  $v_{\parallel}$  and  $v_{\perp}$  have been normalized to  $v_{te}$  and (b) shows the surface  $f(v_{\parallel}, v_{\perp})$  truncated at 0.02 times the maximum in  $f$ , in order to show the plateau more clearly. [From Karney, C.F.F. and Fisch, N.J., *Physics of Fluids* 22, 1817 (1979).]

drive. A striking feature associated with lower hybrid waves is the generation of a superthermal tail when the antenna is phased to drive current. The tail generation mechanism has no generally accepted explanation even though it is the basis of lower hybrid current drive, and this is referred to as the spectral gap problem. Several tokamaks have reported the sustainment of the full plasma current by lower hybrid waves and the corresponding reduction of the loop voltage to zero. A discussion of non-inductive current drive, including lower hybrid current drive, is given in Section 3.13. The electron velocity distribution function generated by lower hybrid waves is shown in Fig. 5.9.3. This clearly illustrates the tail in the direction parallel to the magnetic field.

## 5.10

### Electron cyclotron resonance heating

Electron cyclotron resonance heating is the simplest of the radio frequency heating methods. In contrast to ion cyclotron and lower hybrid heating, there is no evanescent region between the antenna and the plasma,

although cut-offs can exist within the plasma. As a result, the antenna can be retracted into a less hostile environment than for the other schemes.

Electron cyclotron heating has been made possible by the invention of the gyrotron millimetre wave source. This and related devices have only emerged since the mid-1970s. Gyrotron tubes capable of 0.5–1 MW output and with frequencies in the range 100–200 GHz are now under intense development. The frequency required for a reactor would be in the range 100–200 GHz which corresponds to vacuum wavelengths of 1–2 mm.

Since  $\omega_{ce} \gtrsim \omega_{pe}$  only the electrons respond to electron cyclotron waves and only the electrons are heated directly. However, under reactor-like conditions the ions will be heated collisionally by the electrons. As the density is increased, a limit is encountered above which electron cyclotron waves cannot penetrate to the central regions of a tokamak. Propagation is again described by eqn 5.6.1,

$$n_\perp^2 = 1 - \frac{\omega_{pe}^2}{\omega^2} \quad (\text{O-mode}) \quad 5.10.1$$

$$n_\perp^2 = \frac{\left(1 - \frac{\omega_{pe}^2}{\omega^2} - \frac{\omega_{ce}}{\omega}\right) \left(1 - \frac{\omega_{pe}^2}{\omega^2} + \frac{\omega_{ce}}{\omega}\right)}{\left(1 - \frac{\omega_{pe}^2}{\omega^2} - \frac{\omega_{ce}^2}{\omega^2}\right)} \quad (\text{X-mode}) \quad 5.10.2$$

where only propagation perpendicular to the equilibrium magnetic field  $\mathbf{B}$  is considered ( $n_\parallel = 0$ ). Equation 5.10.1 corresponds to a linearly polarized wave with  $E \parallel \mathbf{B}$  and is called the O-mode. Equation 5.10.2 corresponds to an elliptically polarized wave where  $E \perp \mathbf{B}$  and is referred to as the X-mode.

Both the O-mode and the X-mode are able to propagate directly across the equilibrium magnetic field and so either may be used to heat the plasma. In the cold plasma description the O-mode does not possess a resonance, whereas the X-mode has a resonance at  $\omega = \omega_{UH}$  referred to in Section 5.7. However, when hot plasma effects are included both modes are found to have resonances at  $\omega = l\omega_{ce}$  where  $l$  is an integer. It is these resonances together with the upper hybrid resonance which are utilized for heating.

The accessibility conditions for the O- and X-modes are given by eqns 5.10.1 and 5.10.2. When  $\omega \approx l\omega_{ce}$  the O-mode condition is  $\omega_{pe}^2/\omega_e^2 = l^2$  and the X-mode condition is  $\omega_{pe}^2/\omega_{ce}^2 = l(l \pm 1)$ . The significance of the two X-mode cut-offs, at low and high density, and the accessibility information in general is best illustrated by means of a Clemmow–Muñiz–Allis (CMA) diagram, shown in Fig. 5.10.1, which, for fixed  $\omega$ , gives a plot of the square of the magnetic field  $\omega_{ce}^2/\omega^2$  against the density  $\omega_{pe}^2/\omega^2$ .

Three wave trajectories, labelled 1–3, are shown in the diagram. The first corresponds to the fundamental X-mode launched from the low magnetic field side which does not reach any resonance since it first

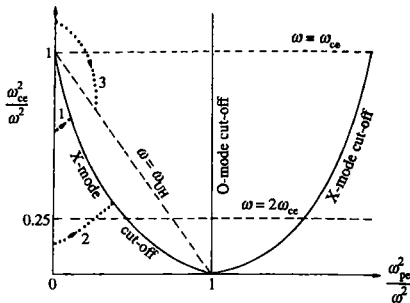


**Fig. 5.10.1** CMA diagram (plot of square magnetic field versus density) showing accessibility to X-mode and O-mode resonances (— cut-offs, - - - resonances, . . . X-mode trajectories).

encounters the low density cut-off, where it is reflected. The second corresponds to the second-harmonic X-mode ( $l = 2$ ) which is able to reach the second harmonic resonance (but not the upper hybrid) from the low field side. The third again corresponds to the fundamental X-mode but from the high field side. In this case the wave can propagate to the fundamental and the upper hybrid resonance. Finally, the O-mode is indifferent to the launching and will penetrate freely to the resonance provided the density is below the cut-off value.

The three trajectories described in the last paragraph have been interpreted in terms of the single mode WKB theory. As discussed in Section 5.7, a more accurate approach requires a full wave theory. It is then found that the X-mode, launched from the low field side, may be able to tunnel through the evanescent layer to reach the upper hybrid resonance. The fraction of the incident power which reaches the upper hybrid resonance depends on the plasma density. The transmission coefficient for this process is given by

$$T = \exp(-\pi k_0 \xi_c)$$

where

$$k_0^2 = \frac{\left[ 1 + \left( 1 + \frac{\omega_{pe}^2}{\omega_{ce}^2} \right)^{1/2} \right] \left[ \left( 1 + \frac{\omega_{pe}^2}{\omega_{ce}^2} \right)^{1/2} + \frac{\omega_{pe}^2 R}{\omega_{ce}^2 L} \right]}{2 \left[ 1 + 2 \frac{\omega_{pe}^2 R}{\omega_{ce}^2 L} \right]} \frac{\omega_{ce}^2 R^2}{c^2},$$

$$\xi_c = \frac{\left[ \left( 1 + \frac{\omega_{pe}^2}{\omega_{ce}^2} \right)^{1/2} - 1 \right]}{\left[ \left( 1 + \frac{\omega_{pe}^2}{\omega_{ce}^2} \right)^{1/2} + \frac{\omega_{pe}^2 R}{\omega_{ce}^2 L} \right]}.$$

$R$  is defined at the beginning of Section 5.8 and  $L$  is the scale length of the equilibrium density. For large tokamaks the transmission is zero for all practical conditions. The tunnelling to the upper hybrid resonance from the low magnetic field side would therefore be negligible. When the density is low, such that  $\omega_{pe}^2 \ll \omega_{ce}^2$ , the transmission coefficient takes the form  $T \simeq \exp(-\pi \omega_{pe}^2 R / 2\omega_{ce} c)$  which shows that  $\omega_{pe}^2 / \omega_{ce}^2 \lesssim c / R \omega_{ce}$  before significant tunnelling can take place.

The cut-off conditions for the O- and X-modes show that  $n/B^2$  is constant. This means that electron cyclotron heating cannot produce values of local  $\beta_e (= p_e/(B^2/2\mu_0))$  in excess of  $0.004 \alpha T_e$  (keV) where  $\alpha = l^2$  for the O-mode, and  $\alpha = l(l \mp 1)$  for the X-mode, the  $\mp$  referring to the low and high density cut-offs respectively.

The discussion of accessibility for the O- and X-modes has been restricted to the rather special case of propagation exactly perpendicular to the equilibrium magnetic field. For the more general case of oblique propagation, where  $n_{\parallel} \neq 0$ , the high and low density X-mode cut-offs are given by  $\omega_{pe}^2 / \omega_{ce}^2 = l(l \pm 1)(1 - n_{\parallel}^2)$ . Thus, perpendicular propagation gives access to the highest density. The O-mode cut-off at the electron plasma frequency is unchanged by finite  $n_{\parallel}$ . It should also be noted that for oblique propagation, the two linearly independent modes, which are still referred to as the O- and X-modes, possess both  $E_{\parallel}$  and  $E_{\perp}$  electric fields.

For conditions relevant to a tokamak reactor ( $T_e \gtrsim 10$  keV) the most strongly absorbing resonances are the X-mode fundamental and second harmonic, and the O-mode fundamental. At higher harmonics the absorption becomes progressively weaker and the source development problem greater. It is therefore expected that electron cyclotron heating will be restricted to the fundamental O-mode or the second-harmonic X-mode since both of these resonances are accessible from the low magnetic field side of a tokamak.

The resonance condition, which determines the absorption region, is given by eqn 5.7.10 with the suffix  $j$  now referring to electrons. An electron cyclotron wave will be undamped outside this region but in crossing the resonance zone will have its energy reduced by a factor  $\exp(-\tau)$ ,  $\tau$  being the optical depth. Like ion cyclotron heating, electron cyclotron heating has the great advantage that the absorption region is controlled by matching the wave frequency to the vacuum toroidal magnetic field, the wave being resonant along the whole of a vertical chord in the minor cross-section.

The fundamental resonance of the O-mode and the second harmonic resonance of the X-mode are both due to finite electron Larmor radius effects of a hot plasma. An important property of both these waves is that they are very strongly damped in the cyclotron resonance region even for propagation perpendicular to the equilibrium magnetic field. This property is due to the relativistic variation of the electron mass with speed. In contrast to ion cyclotron absorption, this variation is significant for electron temperatures of only one or two keV. The higher the electron temperature the stronger the absorption. For perpendicular propagation

the electron cyclotron resonance condition is

$$\omega - \frac{I\omega_{ce}}{\gamma} = 0 \quad 5.10.3$$

where  $\omega_{ce}$  is the magnitude of the electron cyclotron frequency calculated with the rest mass and  $\gamma$  is the usual relativistic factor  $(1 - v^2/c^2)^{-1/2}$ . In the non-relativistic limit,  $\gamma = 1$ , eqn 5.10.3 would be satisfied by all the electrons at one radial location, say  $R = R_c$ , assuming  $B$  depends only on the radial coordinate  $R$ . The resonance would therefore have zero width and would give rise to a singularity (or resonance) in the corresponding wave equation. However, using the fact that for almost all tokamak conditions the equilibrium energy of the electrons is small compared with the rest energy,  $v^2/c^2 \ll 1$ , the  $\gamma$ -factor can be expanded to give the approximate resonance condition:

$$\omega - I\omega_{ce}(x) + I\omega_{ce} \frac{v^2}{2c^2} \simeq 0 \quad 5.10.4$$

where a local spatial dependence of the magnetic field has been included in the second term but neglected in the (small) third term. The resonance condition is now velocity dependent which is the characteristic feature of a wave-particle resonance. Clearly, the resonance now has a finite width and electrons with different energies satisfy the resonance condition at different positions. If the zero energy electrons are resonant at  $x = x_0$  where  $\omega - I\omega_{ce}(x_0) = 0$ , then the more energetic electrons will be resonant further from this point. It is also clear that the resonance condition can only be satisfied when  $\omega - I\omega_{ce}(x) < 0$ . In other words, electron cyclotron resonance for perpendicular propagation is asymmetric with respect to the cold resonance and can occur only on the high magnetic field side of the resonance. A wave incident from the low field side will come into resonance with low energy electrons first, whereas a wave incident from the high field side will be resonant with the most energetic electrons before the less energetic ones. The width of the resonance  $\delta x$  can be estimated by substituting the thermal speed into eqn 5.10.4 and assuming a linear magnetic field profile in the resonance region,  $\omega_{ce}(x) = \omega_{ce}(0)(1 + x/R)$  giving  $\delta x/R \simeq v_{Te}^2/2c^2$ . For a wave propagating obliquely to the magnetic field, Doppler broadening will eventually dominate over relativistic broadening. In this limit electron cyclotron waves are absorbed on both sides of the cold resonance and the width is then given by  $\delta x/R \simeq (v_{Te}/c) \cos \theta$  assuming  $k \simeq I\omega_{ce}/c$  for low density ( $\omega_{pe} \ll \omega_{ce}$ ). For higher densities the value of  $k$  must be taken from the appropriate dispersion relation.

As already noted, a consequence of the relativistic absorption of the O-mode fundamental and X-mode second harmonic is that these modes can be used for heating by launching directly across the magnetic field from the low field side. In contrast to ion cyclotron heating where the second harmonic undergoes significant reflection for perpendicular incidence from the low field side, the relativistic absorption removes the reflection of the incident O- or X-mode from the low field side.

Returning to the resonance condition given by eqn 5.10.4 it is seen that the weakly relativistic correction has resulted in the wave resonance being replaced by a wave-particle resonance. Such singular integrals in velocity space must be evaluated using Landau's prescription described in Section 5.8. Carrying out this procedure for the fundamental O-mode gives the following expression for the optical depth

$$\tau_{01} = \frac{\pi}{2} \frac{\omega_{pe}^2}{\omega_{ce}^2} \left( 1 - \frac{\omega_{pe}^2}{\omega_{ce}^2} \right)^{1/2} \frac{v_{te}^2 \omega_{ce}}{c^2} R. \quad 5.10.5$$

The optical depths,  $\tau_{O,X}$ , maximized with respect to the density for the fundamental O-mode and second harmonic X-mode can also be written in the form  $\tau_{O,X} = \gamma_{O,X} R(m) f(\text{GHz}) T_e(\text{keV})$  where  $\gamma_O = 0.025$  and  $\gamma_X = 0.15$ . Due to the relativistic broadening, energy incident from the low field side is totally absorbed in one transit of the resonance and there is no transmitted wave (or reflected wave) for typical tokamak conditions.

Electron Bernstein waves could also be used for heating and current drive. Very little attention has been paid to this alternative because the O- and X-modes can be launched in vacuum, remote from the hot plasma, and will penetrate to the core of the discharge of a conventional tokamak, whereas coupling to electron Bernstein waves is more difficult since they do not propagate in vacuum. However, in the case of spherical tokamaks, where  $\omega_{pe}^2 \gg \Omega_e^2$ , the O- and X-modes are not accessible to the centre of the discharge for the fundamental or second harmonic. The higher harmonics do have accessibility but these modes are very weakly damped and this makes the conventional use of ECRH unsuitable for a spherical tokamak.

Electron Bernstein waves do not have any density limits and all harmonics are damped very strongly making these waves promising candidates for heating and current drive in spherical tokamaks. The main problem for this scheme is to develop a reliable and effective coupling method. There are two possibilities.

The first was originally discussed for ionospheric applications. Power is launched on the O-mode in the usual way. If the launch angle is arranged so that  $n_{||}$  has the critical value,  $n_{cr}$ , where  $n_{cr}^2 = \omega_{ce}/(\omega + \omega_{ce})$ , then the high density X-mode and O-mode cut-offs are degenerate and the O-mode is totally converted to the X-mode. The X-mode then propagates to lower density where it meets the upper hybrid resonance and is converted to an electron Bernstein wave (EBW). Finally, the converted electron Bernstein wave propagates towards the plasma centre and is totally absorbed at the first electron cyclotron resonance it encounters. This is referred to as the O-X-EBW scheme.

The second possibility is based on the triplet scheme proposed for mode conversion heating by the fast wave in a two ion species plasma. In this case the X-mode low density cut-off, upper hybrid resonance and high density cut-off form the triplet of critical points. For sufficiently steep edge density gradients it is possible, in principle, to convert all the

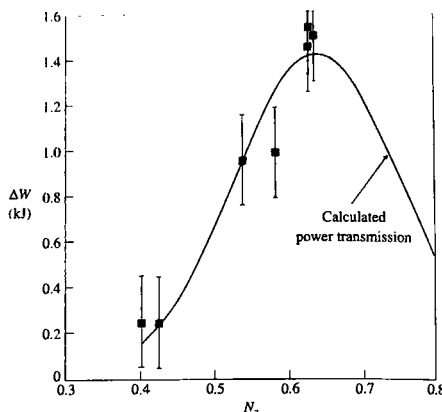


**Fig. 5.10.2** Dependence of the increase in plasma energy from O-X-B heating on the longitudinal vacuum refractive index  $N_z$  of the incident O-wave. The solid line is the calculated transmission function multiplied by the maximum energy increase. [Laqua, H.P. et al., *Physical Review Letters* **78**, 3467 (1997).]

incident X-mode energy from the low field side to the electron Bernstein wave. This is referred to as the X-EBW scheme.

The O-X-EBW scheme has been demonstrated on the W7-As Stellarator and produced heating at densities more than twice the cut-off value. Figure 5.10.2 shows the measured increment in the plasma energy by O-X-B heating as a function of the vacuum parallel refractive index which gives the variation with the launch angle. The measured values lie close to the theoretical curve, shown for comparison.

Electron cyclotron resonance in a tokamak heats the electrons in a similar manner to the heating of the ions by ion cyclotron resonance. An electron which is in cyclotron resonance with the O- or X-mode experiences an impulse predominantly in the direction perpendicular to the magnetic field. Whether a given electron gains or loses energy depends on the phase of the gyration of the electron relative to the phase of the wave. The resonant electrons will again be constrained to move along certain paths in velocity space as discussed in Section 5.8.

The electron paths will differ from the corresponding ion cyclotron contours due to the relativistic corrections. However, the heated electron distribution function can be calculated by solving the electron Fokker-Planck equation with an appropriate, weakly relativistic, quasi-linear term. The result of such a calculation for a toroidal magnetic field is shown in Fig. 5.10.3. This illustrates an important difference between electron and ion cyclotron heating. Comparing Fig. 5.8.8 with Fig. 5.10.3 it can be seen that the ion velocity contours have undergone much greater distortion from the thermal lines than the corresponding electron velocity

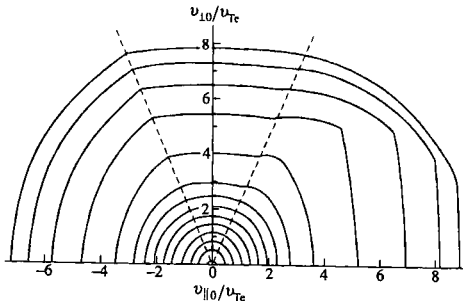


**Fig. 5.10.3** Contours of electron distribution function for second-harmonic X-mode heating in the COMPASS tokamak for an injected power of 1.5 MW. The other parameters are,  $n_e = 10^{19} \text{ m}^{-3}$ ,  $T_e = 1.5 \text{ keV}$ ,  $f = 60 \text{ GHz}$  and  $\rho/R = 0.08$ , where  $\rho$  is the radius of the resonant flux surface. The dashed lines show the boundaries between trapped and passing electrons. [From O'Brien, M.R., Cox, M., and Start, D.F.H., *Nuclear Fusion* **26**, 1625 (1986).]

contours. This is due to the dependence of the electron cyclotron resonance condition on  $v_\perp$  through the relativistic variation of the electron mass which causes a heated electron to fall out of resonance before it is driven to very high energy. In contrast, the relativistic mass dependence of a thermal ion is negligible. Hence, an ion can remain in cyclotron resonance and continue to gain perpendicular energy. It is also worth noting that the electron distribution remains Maxwellian near to the origin because of the large collision frequency in this region. The main distortion of the electron distribution occurs between  $4v_{Te}$  and  $8v_{Te}$ . The distortion diminishes for larger velocities because these electrons cannot come into cyclotron resonance on this particular flux surface of radius  $\rho = 4.4 \text{ cm}$ .

An experiment designed to test the weakly relativistic hot plasma theory of electron cyclotron absorption was carried out in PLT. Transmitting and receiving horns were positioned on opposite sides of the mid-plane. Both horns were oriented such that their axes were perpendicular to the equilibrium magnetic field. The experiment was therefore arranged to detect the O-mode for perpendicular propagation.

The incident 4 mm microwave power was supplied by a klystron at a fixed frequency of 71 GHz. The transmitted power detected by the receiving horn was compared with the incident power to obtain the optical depth,  $\tau_{\text{exp}}$ . The electron cyclotron resonance position was altered by varying the central value of the equilibrium magnetic field. The experiment was corrected for refraction losses which could exceed absorption for lower densities and temperatures. This was done by repeating the transmission measurements for lower magnetic fields such that no electron cyclotron resonance was present in the plasma. The results are shown in Table 5.10.1 where the experimentally determined optical depth  $\tau_{\text{exp}}$  is compared with the theoretical value  $\tau_0$  given by eqn 5.10.5. The theoretical values of the optical depth were obtained by using the values of the local density and temperature,  $n_e(r)$ ,  $T_e(r)$ , obtained from laser Thomson scattering.

**Table 5.10.1** A comparison of the measured experimental values of the optical depth,  $\tau_{\text{exp}}$ , with the corresponding quantity,  $\tau_{01}$ , calculated for the propagation of the fundamental ordinary mode [see eqn 5.10.5]. The data were collected over two separate experimental runs and are partitioned in this table.

$B(R_0)$ (Tesla)	$T_e(r)$ (eV)	$n_e(r)$ ( $10^{19} \text{ m}^{-3}$ )	$\tau_{01}$	$\tau_{\text{exp}}$
1.9	160	0.38	$0.5 \pm 0.03$	0
2	290	0.7	$0.21 \pm 0.16$	$0.09 \pm 0.03$
2.15	240	0.7	$0.14 \pm 0.04$	0.11
2.4	650	1.1	$0.57 \pm 0.06$	$0.38 \pm 0.05$
2.5	900	1.3	$0.98 \pm 0.16$	$0.88 \pm 0.06$
2.15	270	1.30	$0.29 \pm 0.06$	$0.3 \pm 0.03$
2.3	420	0.96	$0.35 \pm 0.18$	$0.33 \pm 0.07$
2.4	760	2.6	$1.43 \pm 0.13$	$1.5 \pm 0.15$
2.5	850	2.7	$1.65 \pm 0.30$	1.9

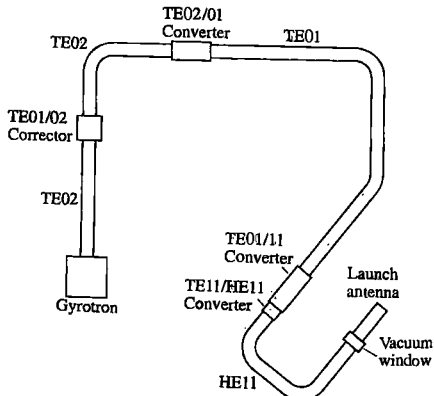


**Fig. 5.10.4** Schematic diagram of the layout of the ECRH system for low field side injection into COMPASS.

It is apparent from Table 5.10.1 that there is generally good agreement between the theory and the experiment.

A representative example of an ECRH system is given schematically in Fig. 5.10.4. This shows an ECRH layout for COMPASS with the gyrotron, transmission system and antenna for low field side launch. The salient features of Fig. 5.10.4 are the following. The power emerging from the

gyrotron is mainly in the TE<sub>02</sub> mode (~90%) with somewhat less than 10% carried by the TE<sub>01</sub> and the remainder in higher modes. The TE<sub>mn</sub> notation refers to a mode of a cylindrical wave guide with a transverse electric field where  $m$  and  $n$  are the azimuthal and radial mode numbers. It should be noted that at the high frequencies characteristic of ECRH the wave guide transmission systems operate in over moded conditions. This means many different modes can propagate requiring considerable care in ensuring only the desired mode is present. The TE<sub>01/02</sub> mode corrector and the TE<sub>01/02</sub> mode convertor result in the conversion of more than 95% of the power to the TE<sub>01</sub> mode, which is the desired mode for transmission because of its very low loss. The power remains in the TE<sub>01</sub> mode until it nears the tokamak where mode conversion to the launching mode is required. This occurs in two stages. First, the power is transformed from the circular TE<sub>01</sub> mode to the approximately linear polarized TE<sub>11</sub> mode. The final mode conversion is from TE<sub>11</sub> to HE<sub>11</sub> which is a mode which only exists in a corrugated wave guide but which is almost ideal for coupling to the plasma. This is because the HE<sub>11</sub> mode has an exact linear polarization where the plane of polarization can be selected to match to the O-mode or to the X-mode. The transmission system carries high power over a length of 50 m, and round five bends before being coupled to the plasma. The total loss between the gyrotron and the plasma is no more than 15%. The vacuum window, occurring just before the antenna, is one of the critical components for an ECRH system for a tokamak reactor. For the higher frequency systems required by a reactor, quasi-optical transmission lines offer an alternative to wave guides.

In conclusion, it should be mentioned that electron cyclotron resonance heating has been successfully operated at the MW level. Central electron temperatures up to 10 keV have been observed on T-10 using 2.5 MW at 81 GHz and 1.1 MW at 75 GHz for a line averaged density of  $1.5 \times 10^{19} \text{ m}^{-3}$ . The resonance lines of the two frequencies were placed symmetrically about the centre of the plasma ( $r/a = \pm 0.2$ ). In DIII-D, central temperatures of 5 keV were obtained with 1 MW at 60 GHz for a density of  $0.7 \times 10^{19} \text{ m}^{-3}$ . Electron cyclotron resonance heating is a very versatile scheme which has various other applications in addition to bulk heating. It has been successfully employed to pre-ionize discharges and assist the start-up. Even though electron cyclotron waves carry little momentum they can be used to drive the equilibrium plasma current, in principle with comparable efficiency to lower hybrid waves. Another important application is the control of the current profile, either by localized heating or by local current drive. Finally, electron cyclotron resonance absorption is capable of selective heating of energetic electrons through the relativistic resonance condition and vertical incidence. To date very little use has been made of this unique property for tokamak experiments. It is worth noting that the relativistic cyclotron resonance condition is the basis of the gain mechanism of a gyrotron, albeit for a highly non-thermal distribution of electrons possessing an energy in the range  $\sim 80$  keV with  $v_{\perp 0} \gtrsim 2v_{\parallel 0}$ .

## Bibliography

### Ohmic heating

A proposal for an experiment (Ignitor) in which ohmic heating plays a major role was made by

Coppo, B., Compact experiment for  $\alpha$ -particle heating. *Comments on Plasma Physics and Controlled Fusion* Vol. III, 47 (1977)

### Neutral beam heating

Introductory accounts of the subject are given by Sweetman, D.R., Cordey, J.G., and Green, T.S.. Heating and plasma interactions with beams of energetic neutral atoms, *Philosophical Transactions of the Royal Society A* 300, 589 (1981); and

Hemsworth, R.S., In *Plasma physics and nuclear fusion research* (ed. Gill, R.D.). Academic Press, London (1981).

A more recent review is that by

Stork, D., Neutral beam heating and current drive systems. *Fusion Engineering and Design* 14, 111 (1991).

The physics of the beam-plasma interaction is described in the article, Trapping and thermalization of fast ions, by Cordey, J.G., *Applied atomic and collision physics* Vol. 2, Eds Barnett, C.F. and Harrison, M.F.A. Academic Press, Orlando (1984).

The technological aspects are described in the article, Neutral-beam formation and transport, by Green, T.S., *Applied atomic and collision physics* Vol. 2 (eds Barnett, C.F. and Harrison, M.F.A.). Academic Press, Orlando (1984).

The early heating experiments were reported at the 6th European Conference on Controlled Fusion and Plasma Physics, Moscow, 1973 and published in Vol. II of the proceedings as follows  
Furth, H.P., Tokamak heating by neutral beams and adiabatic compression, p. 51.

Sheffield, J. et al. Neutral injection on the CLEO tokamak, p. 328.

Barnett, C.F. et al. ORMAK and neutral injection, p. 330. Experiments in which substantial heating was achieved are described in

Eubank, H., Goldston, R.J. et al. PLT neutral beam heating results. *Plasma physics and controlled nuclear fusion research* (Proceedings 7th International Conference, Innsbruck, 1978) Vol. I, 167. I.A.E.A. Vienna (1979); and

Kitsunezaki, A., Angel, T. et al. High pressure plasma with high-power NBI heating in Doublet III. *Plasma physics and controlled nuclear fusion research* (Proceedings 10th International Conference, London, 1984) Vol. I, 57. I.A.E.A. Vienna (1985).

The higher power heating on large tokamaks is described in Chapter 12.

### Radio frequency heating

Two state-of-the-art summaries are

Porkolab, M., Review of RF heating. In *Theory of magnetically confined plasmas. Proceedings of the International School of Plasma Physics*, Varenna 1977, p. 339. Pergamon Press, Oxford (1979); and

Hwang, D.Q. and Wilson, J.R., Radio frequency wave applications in magnetic fusion devices. *Proceedings of IEEE* 69, 1030 (1981).

The first of these outlines the theory and its experimental status whilst the second also contains information on the technology.

An introduction to the subject is given in the book Cairns, R.A., *Radio frequency heating of plasmas* Adam Hilger, Bristol (1991),

and another general account including much experimental information is given in Golant, V.E. and Fedorov, V.I., *RF plasma heating in toroidal fusion devices*, Consultants Bureau, New York (1989).

### Physics of radio frequency heating

The standard work on waves in plasmas which has been issued in its second edition with a detailed discussion of developments in the subject is Stix, T.H., *Waves in plasmas*, American Institute of Physics (New York), 1992. The theory of waves with particular reference to radio frequency heating is given in

Swanson, D.G., *Plasma waves*, Academic Press, San Diego (1989).

A detailed and comprehensive account of the theory of linear waves in magnetized, uniform plasmas is provided by Akhiezer, A.I., Akhiezer, I.A., Polovin, R.V., Sitenko, A.G., and Stepanov, K.N., *Plasma electrodynamics* Vol. I. Pergamon Press, Oxford (1975).

Reviews of the three main heating schemes and current drive are given in

*Wave heating and current drive in plasmas*, Eds Granatstein, V.L. and Coletstock, P.L., Gordon and Breach, New York (1985).

A rigorous discussion of the Budden equation is given in Budden, K.G., *The propagation of radio waves*, Cambridge University Press, Cambridge (1985), pp. 596-602.

The first account of Bernstein waves was given in Bernstein, I.B., Waves in plasma in a magnetic field, *Physical Review* **109**, 10 (1958).

The original derivation of Landau damping, which is the fundamental physical process underlying the absorption of radio frequency power in hot plasmas, is given in Landau, I.D., On the vibrations of the electronic plasma, *Journal of Physics (USSR)* **10**, 25 (1946).

An early account of linear mode conversion (in a plasma physics context) is given in

Stix, T.H., Radiation and absorption via mode conversion in an inhomogeneous collision free plasma, *Physical Review Letters* **15**, 878 (1965).

Later discussions of mode conversion are given in

Cairns, R.A. and Lashmore-Davies, C.N., A unified theory of a class of mode conversion problems, *Physics of Fluids* **26**, 1268 (1983); Colestock, P.L. and Kashuba, R.J., The theory of mode conversion and wave damping near the ion cyclotron frequency, *Nuclear Fusion* **23**, 763 (1983); Stix, T.H. and Swanson, D.G., Propagation and mode-conversion for waves in non-uniform plasmas, in *Handbook of plasma physics*, Eds Rosenbluth, M.N. and Sagdeev, R.Z., Vol. I, North-Holland, Amsterdam, p. 335 (1983).

An interesting discussion of the anomalous Doppler (cyclotron) resonance is given by

Nezlin, M.V., Negative-energy waves and the anomalous Doppler effect, *Usp. Fiz. Nauk* **120**, 481 (1976) [*Sov. Phys. Usp.* **19**, 946 (1976)].

The original derivation of the quasi-linear theory was given independently by

Vedenov, A.A., Velikhov, E.P. and Sagdeev, R.Z., Nonlinear oscillations of a rarefied plasma, *Nuclear Fusion* **1**, 82 (1961)

and

Drummond, W.E. and Pines, D., Nonlinear stability of plasma oscillation, *Nuclear Fusion* **1**, Supplement, Part 3, 1049 (1962).

### **Ion cyclotron resonance heating**

The first account of the two ion hybrid resonance was given by

Buchsbaum, S.J., Resonance in a plasma with two ion species, *Physics of Fluids* **3**, 418 (1960).

A very thorough and detailed account of the fundamentals of ion cyclotron heating by means of the fast wave is

Stix, T.H., Fast-wave heating of a two component plasma, *Nuclear Fusion* **15**, 737 (1975).

Later reviews are given in

Swanson, D.G., Radio frequency heating in the ion-cyclotron range of frequencies, *Physics of Fluids* **28**, 2645 (1985) and in Hwang, D.Q., Colestock, P.L. and Philips, C.K. The theory of minority species fast magnetosonic wave heating in a tokamak. In *Wave heating and current drive*

*in plasmas*, Gordon and Breach, New York (1985), Eds Granatstein, V.L. and Colestock, P.L., p. 1.

The quasi-linear theory generalized to a magnetized plasma was given first by

Kennel, C.F. and Engelmann, F., Velocity space diffusion from weak plasma turbulence in a magnetic field, *Physics of Fluids* **9**, 2377 (1966).

A comprehensive account of the solution of the Fokker-Planck equation with a quasi-linear wave term in a tokamak plasma is given by

Kerbel, G.D. and McCoy, M.G., Kinetic theory and simulation of multispecies plasmas in tokamaks excited with electromagnetic waves in the ion-cyclotron range of frequencies, *Physics of Fluids* **28**, 3629 (1985).

Some early results using ion cyclotron heating are given by Equipe, TFR, ICRF Heating in TFR 600. *Proceedings of the 8th International Conference on the Physics of Plasmas and Controlled Nuclear Fusion* (Brussels, 1980), Vol. 2, p. 75, IAEA, Vienna (1981).

A later review of experiments is given by

Colestock, P.L., An overview of ICRH experiments in *Wave heating and current drive in plasmas*, Gordon and Breach, New York (1985) Eds Granatstein, V.L. and Colestock, P.L., p. 55.

Attention was drawn to the significance of the high field side fast wave cut-off to mode conversion from the low field side by

Majeski, R., Phillips, C.K., and Wilson, J.R., Electron heating and current drive by mode converted slow waves, *Physical Review Letters* **73**, 2204 (1994).

An explicit calculation demonstrating the possibility of 100% mode conversion from the low field side was given by Fuchs, V., Ram, A.K., Schultz, S.D., Bers, A. and Lashmore-Davies, C.N., Mode conversion and electron damping of the fast Alfvén wave in a tokamak at the ion-ion hybrid frequency, *Physics of Plasmas* **2**, 1637 (1995).

The high harmonic scheme for electron heating and current drive in spherical tokamaks is proposed by

Ono, M., High harmonic fast waves in high beta plasmas, *Physics of Plasmas* **2**, 4075 (1995).

### **Lower hybrid resonance heating**

The two original discussions of the lower hybrid accessibility condition are by

Stix, T.H., *The theory of plasma waves*, McGraw-Hill, New York (1962).

Golant, V.E., Plasma penetration near the lower hybrid frequency, *Zhurnal Technicheskoi Fisiki* **41**, 2492 (1971) [*Soviet Physics-Technical Physics* **16**, 1980 (1972)].

Summaries of the theory of lower hybrid heating and experiments are given by

Bonoli, P. Linear theory of lower hybrid waves in tokamak plasmas and Porkolab, M. Lower hybrid wave propagation, heating and current drive experiments, in *Wave heating and current drive in plasmas*, Gordon and Breach, New York (1985) Eds Granatstein, V.L. and Colestock, P.L., p. 175 and p. 219 respectively.

The original proposal to use a phased array of wave guides (the grill) as the lower hybrid antenna was made by

Lallia, P. A LHR heating slow wave launching structure suited for large toroidal experiments. *Proceedings of 2nd Topical Conference on RF Plasma Heating* (Texas Tech Univ, Lubbock, Texas) Paper C3 (1974)

The first experiment which succeeded in driving the whole of the plasma current in tokamak by means of lower hybrid waves is described in

Bernabei, S., et al. Lower hybrid current drive in the PLT tokamak. *Physical Review Letters* 49, 1255 (1982).

### Electron cyclotron resonance heating

The first experiment to utilize high power electron cyclotron heating (with a gyrotron) is described in

Alikava, V.V., Bobrovskii, G.A., Poznyak, V.I., Razumova, K.A., Sannikov, V.V., Sokolov, Yu A., and Shmarin, A.A., ECR plasma heating in the TM-3 tokamak in magnetic fields up to 25kOe, *Fizika Plasmy* 2, 390 (1976) [*Soviet Journal of Plasma Physics* 2, 212 (1976)].

The effect of relativity on electron cyclotron absorption was first noted in the Russian literature. One of the first treatments is given in

Dnestrovskii, Yu N., Kostomarov, D.P., and Skrydlov, N.V., Plasma waves in cyclotron resonant regions, *Zhurnal Tekhnicheskoi Fiziki* 33, 922, (1963) [*Soviet Physics Technical Physics* 8, 691 (1964)].

One of the early and most thorough treatments of the relativistic effects on electron cyclotron absorption was given by Shkarofsky, I.P., Dielectric tensor in Vlasov plasmas near cyclotron harmonics. *Physics of Fluids* 9, 561 (1966).

A very readable introduction to electron cyclotron heating is contained in the review

Manheimer, W.M., *Electron cyclotron heating in tokamaks, infra-red and millimeter waves*, Vol. II (ed. Button, K.J.). Academic Press, New York (1979).

A comprehensive review is given by

Bornatici, M., Cano, R., DeBarbieri, O., and Engelmann, F., Electron cyclotron emission and absorption in fusion plasmas, *Nuclear Fusion* 23, 1153 (1983).

The CMA diagram is described in

Stix, T.H., *Waves in plasmas*, American Institute of Physics, New York (1992), p. 14. Swanson, D.G., *Plasma waves*, Academic Press, San Diego (1989), p. 29.

Other accounts of the theory and experimental results are given by

Chu, K.R., Theory of electron cyclotron resonance heating and England, A.C., and Hsuan, H., Electron cyclotron heating in tokamaks and tokamak reactors, in *Wave heating and current drive in plasmas*, Gordon and Breach, New York (1985) Eds Granatstein, V.L., and Colestock, P.L., p. 317 and p. 459 respectively.

A more recent account of ECRH experiments is given by Prater, R., Recent results on the application of electron cyclotron heating to tokamaks, *Journal of Fusion Energy* 9, 19 (1990).

The comparison given in Section 5.10 of the theoretical value for the optical depth of the O-mode fundamental with experiment is taken from

Efthimion, P.C., Arunasalam, V., and Hosea, J.C., Ordinary-mode fundamental electron-cyclotron resonance absorption and emission in the Princeton Large Torus, *Physical Review Letters* 44, 396 (1980).

Attention was drawn to the relevance of the conversion of the ordinary mode to the extraordinary mode at the plasma resonance for a particular incident angle to high density heating in a paper by

Preinhaelter, J. and Kopecký, V., Penetration of high frequency waves into a weakly inhomogeneous magnetised plasma at oblique incidence and their transformation to Bernstein waves. *Journal of Plasma Physics* 10, 1 (1973)

An experimental demonstration of heating above the cut-off density in the W7-As stellarator is described by

Laqua, H.P., Erckmann, V., Hartfuss, H.J., and Laqua, H., Resonant and non-resonant electron cyclotron heating at densities above the plasma cut-off by O-X-B mode conversion at the W7-As stellarator. *Physics Review Letters* 78, 3467 (1997).

Electron Bernstein wave heating of spherical tokamaks through the X-EBW (triplet) scheme was proposed by

Bers, A., Ram, A.K., and Schultz, S.D., Coupling to electron Bernstein waves in tokamaks. *Proc. 2nd Europhysics Topical Conf. on Radio Frequency Heating and Current Drive of Fusion Devices*, Brussels 1998, edited by Jacquinot J., Van Oost, G. and Weynants, R.R. (*European Physical Society, Petit-Lancy*, 1998) p. 237.

# **6**

# **Mhd stability**

---

## 6.1

### Mhd stability

The strongest instabilities in tokamaks are those which, in their simplest form, are described by the magnetohydrodynamic model of the plasma.

The basic destabilizing forces arise from:

- (i) *Current gradients* and
- (ii) *Pressure gradients combined with adverse magnetic field curvature*.

The resulting instabilities are divided into two categories:

- (i) *Ideal modes*—instabilities which would occur even if the plasma were perfectly conducting, and
- (ii) *Resistive modes*—which are dependent on the finite resistivity of the plasma.

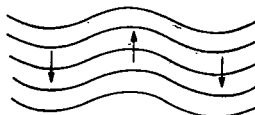
Both ideal and resistive instabilities have an infinite spectrum of possible modes, each member being characterized by its mode numbers. In the case of a circular, large aspect-ratio tokamak the modes take the form  $\exp i(m\theta - n\phi)$ ,  $m$  and  $n$  being the poloidal and toroidal mode numbers.

The stabilizing effects for mhd modes are illustrated in Fig. 6.1.1. They arise from

- (i) *Magnetic field line bending*—the production of a perturbed magnetic field perpendicular to the equilibrium field. This effect is larger for shorter wavelengths, that is it increases with  $m$ ,
- (ii) *Magnetic field line compression*—the production of a perturbed magnetic field parallel to the equilibrium field, and
- (iii) *Good magnetic field curvature*—the centre of curvature being in the opposite direction to the pressure gradient.

The stabilizing effect of line bending is minimized on magnetic surfaces for which the magnetic field helix matches that of the mode. This resonance occurs for rational surfaces on which  $m = nq$ , where  $q$  is the safety factor. Although the stabilizing effect is stronger for

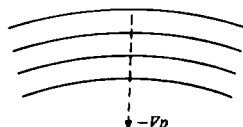
**Fig. 6.1.1** Magnetic field line bending and magnetic field compression are stabilizing for mhd modes. The magnetic field curvature is stabilizing if the negative pressure gradient is in the direction of the centre of curvature.



Bending of magnetic field lines



Compression of magnetic field



$-V_p$

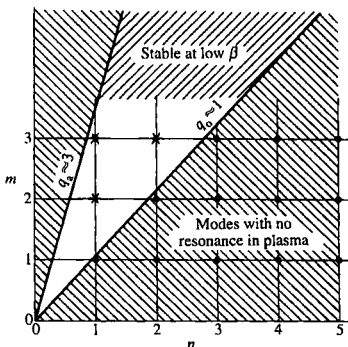


**Fig. 6.1.2** Showing how exclusion of resonant surfaces from the tokamak plasma reduces the number of potential modes of instability. These modes are restricted to  $q_0 < m/n \lesssim q_4$  and are indicated by asterisks. At low  $\beta$ , high  $m$ -modes are stabilized by line bending and by good average field line curvature.

high- $m$  modes, instability can occur if they are localized around a resonant surface.

In the limit of  $m$  and  $n$  approaching infinity the modes are sufficiently localized that stability becomes a magnetic surface property. In this case the stability criterion must be applied to all magnetic surfaces.

For low mode numbers the modes are not localized. However, for instability, their resonant surfaces must satisfy  $m/n = q$  for a value of  $q$  existing inside the plasma or close to its surface. Part of the stability of tokamaks derives from the exclusion of resonances for all but a few of the low  $m$ -modes by the limited range of  $q$ -values across the plasma. This is illustrated in Fig. 6.1.2 for a case where the highest value of  $q$  is around 3 and the lowest value is just greater than unity.

The present chapter deals with linear stability theory. Its main purpose is to locate the boundaries in parameter space between stable and unstable regions. It might be thought that it would be necessary to operate in a stable region. However the matter is more subtle and for some modes it is possible that a certain level of instability is acceptable in order to achieve otherwise better conditions. Experimentally, tokamaks usually display signs of mhd instability. It is the task of nonlinear theory, introduced in Chapter 7, to determine the level of saturation of these instabilities and to calculate their deleterious effects.

The three principal theoretical procedures for determining stability are:

- (i) The *energy principle*, in which the potential energy change resulting from a plasma displacement  $\xi(x)$  is examined.
- (ii) Calculation of the *eigenfunctions* and corresponding *eigenvalues* for the frequency,  $\omega$ . The sign of the imaginary part of  $\omega$  then determines stability.

- (iii) Solution of the *marginal stability* equation ( $\omega_l = 0$ ). Its solution satisfies the required boundary conditions for a configuration on the stability boundary.

## 6.2

### Stability theory

The basic method of determining the stability properties of a system is to analyze the behaviour of perturbations to a chosen state. In tokamaks this state is usually one given by a time independent solution of the governing equations. The linear stability of the system is determined by examining the behaviour of infinitesimal perturbations which satisfy the governing equations and the boundary conditions. It is plausibly assumed that all possible perturbations which satisfy these conditions will arise from microscopic fluctuations of the initial state. Thus if the system is unstable to any form of infinitesimal perturbation the corresponding instability will appear. Simple theory predicts that such instabilities have an exponential growth which will continue until the assumption of a linear perturbation fails. The perturbation is then limited in amplitude, that is 'saturated', by nonlinear processes, the nature of which depends on the particular case.

Linearization of the governing equations is accomplished by writing each factor in the equations as the sum of its equilibrium value and the small perturbation. Thus

$$p = p_0 + p_1.$$

The products of two such factors  $p$  and  $q$  is

$$pq = p_0q_0 + p_0q_1 + q_0p_1 + p_1q_1$$

and similarly for the product of more factors. When the governing equations are written in this form, the leading terms in each expression, such as  $p_0q_0$ , describe the equilibrium solution and cancel. The terms which are linear in the perturbed quantities, such as  $p_0q_1$  and  $q_0p_1$  are retained, and the higher order terms, such as  $p_1q_1$ , are clearly negligible if the perturbation is sufficiently small. Mathematically, at least, the perturbation can be taken to be infinitesimal and this provides a rigorous basis for the linearization procedure.

The formal procedure for calculating the behaviour of small perturbations by solving the linearized equations involves taking Laplace transforms. The resulting solution has a part which depends on the initial conditions and a part which is a homogeneous solution of the equations. The homogeneous solution is comprised of the eigenfunctions of the system, each having as an eigenvalue the quantity  $\omega$  appearing in the time

dependent factor  $e^{-i\omega t}$  of the solution. In general  $\omega$  is complex and

$$e^{-i\omega t} = e^{-i\omega_1 t + i\omega_2 t}.$$

It is seen therefore that the real part of  $\omega$  describes the real frequency of the mode and the imaginary part determines stability, instability corresponding to  $\omega_1 > 0$ . A common procedure for determining stability is therefore to take the time dependence to be  $e^{-i\omega t}$  and to solve the governing equations for the eigenfunctions and the corresponding eigenvalues of  $\omega$ . Since the factors  $e^{-i\omega t}$  are the only time dependent factors in the solutions, time derivatives in the equations are simply replaced by  $-i\omega$ . By analogy with the theory of waves the equation  $D(\omega) = 0$  which gives the eigenvalues is called the dispersion relation. Indeed, formally the dispersion relation governing stability is just an extension of the wave dispersion relation.

In the ideal mhd model the above procedure can be followed, or alternatively the change in potential energy corresponding to a given plasma displacement  $\xi(x)$  can be calculated. This does not involve any time dependence. The plasma is unstable to any perturbation  $\xi(x)$  which makes the potential energy change  $\delta W[\xi]$  negative. An account of this method is given in Section 6.4.

In all methods the calculation is simplified if there are coordinates along which the equilibrium is constant. In a tokamak the toroidal symmetry means that the toroidal angle  $\phi$  is such a coordinate. In this case the perturbations can be Fourier analysed in  $\phi$ . Each component has the form  $e^{-in\phi}$  and can be treated separately, the component being characterized by the mode number  $n$ . Sometimes the equilibrium variation in the poloidal angle  $\theta$  is sufficiently small that the Fourier components in  $\theta$  are separable. The eigenfunctions then have the form  $e^{i(m\theta - n\phi)}$ . More generally the Fourier components in  $\theta$  are coupled.

Some confusion arises from the use of the symbol  $m$  to describe both the mode number and the Fourier components. The mode number is an integer 'eigenvalue' which characterizes the eigenmode. In the case of a vibrating string the harmonic mode numbers of a given mode, determined by counting nodes, does not change if the mass distribution of the string is varied but a Fourier decomposition would have many components. Similarly, the plasma modes with a given mode number  $m$  can be described in terms of Fourier components. In a tokamak the structure of the eigenfunction involves the coupling of these components.

## 6.3

### Growth rates

The simplest theoretical approach to stability is first to decide which equilibria are stable and which unstable, and then to calculate the growth

rate of the unstable cases. This procedure is theoretically sound but often does not relate to reality.

The missing element is the time dependence of the equilibrium. If an equilibrium is in an unstable state it is necessary to ask how it reached that state. In principle an unstable configuration can be established so rapidly that the instability growth during the setting-up phase is negligible. In this case the simple exponential growth,  $e^{\gamma t}$ , associated with this configuration will occur. However, in a tokamak the time scale for equilibrium changes is usually very long compared to typical linear growth times. Looked at on this time-scale it becomes apparent that when the unstable regime is entered the growth rate is zero and that the early growth will be at a very low growth rate.

This behaviour can be illustrated by a simple model. Let the growth rate,  $\gamma(p)$ , be proportional to the amount by which some equilibrium parameter,  $p$ , exceeds a critical value  $p_c$ , that is

$$\gamma = (p - p_c) \frac{dp}{dp} \quad 6.3.1$$

and take

$$p - p_c = \dot{p}(t - t_0), \quad 6.3.2$$

where  $t_0$  is the time at which the stability boundary is passed. If the characteristic time,  $\tau$ , for equilibrium change is defined by writing

$$\dot{p} = \frac{p_c}{\tau} \quad 6.3.3$$

eqns 6.3.1–6.3.3 allow the equation for the growth of a small perturbation  $\xi$  to be written

$$\frac{d\xi}{dt} = \gamma \xi = \frac{\gamma^*}{\tau} (t - t_0) \xi, \quad 6.3.4$$

where  $\gamma^*$  characterizes the linear growth rate through

$$\gamma^* = \frac{dp}{dp} p_c.$$

The solution of eqn 6.3.4 is

$$\xi = \xi_0 \exp \frac{\gamma^*(t - t_0)^2}{2\tau}.$$

The behaviour is illustrated graphically in Fig. 6.3.1 for a case for which  $\gamma^*\tau = 100$ , and nonlinear effects become important at a level  $\xi/\xi_0 = 10$ .

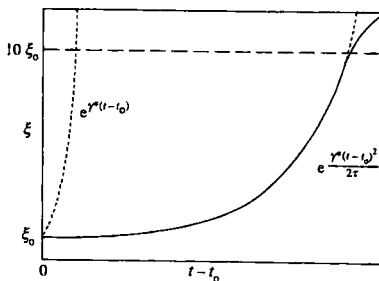


**Fig. 6.3.1** Illustration of instability growth following passage of the equilibrium through marginal stability at  $t = t_0$  with a growth rate  $\gamma$  proportional to  $(t - t_0)$ . The dashed curve gives the associated simple exponential growth for comparison. The ratio of the equilibrium time  $\tau$  to the characteristic instability time  $\gamma^{-1}$  is taken to be 100.

## 6.4 Energy principle

The energy principle of ideal mhd is based on the concept that if a physically allowable perturbation of an equilibrium lowers the potential energy, then the equilibrium is unstable. The instabilities it describes are called ideal modes. The potential energy change due to an arbitrary displacement will be calculated using the equations given in Section 2.20.

The energy change resulting from a displacement  $\xi(x)$  of the plasma is given by the volume integral.

$$\delta W = -\frac{1}{2} \int \xi \cdot F \, d\tau, \quad 6.4.1$$

where  $F(x)$  is the force arising from the displacement.

From eqn 2.20.2 the linearized force is

$$F = j_1 \times B_0 + j_0 \times B_1 - \nabla p_1, \quad 6.4.2$$

where the subscripts 0 and 1 refer to the equilibrium and the perturbation. The pressure change  $p_1$  is related to the displacement by integrating the linearized adiabatic eqn 2.20.4 to give

$$p_1 = \gamma p_0 \nabla \cdot \xi - \xi \cdot \nabla p_0. \quad 6.4.3$$

The perturbed magnetic field is obtained by integrating Faraday's induction eqn 2.20.6 together with the perfect conductivity eqn 2.20.7

## 6.4 Energy principle

to give

$$\mathbf{B}_1 = \nabla \times (\xi \times \mathbf{B}_0). \quad 6.4.4$$

The perturbed current density may now be obtained from Ampère's eqn 2.20.5

$$\mathbf{j}_1 = \nabla \times \mathbf{B}_1 / \mu_0. \quad 6.4.5$$

Substitution of eqns 6.4.2–6.4.5 into eqn 6.4.1 then gives  $\delta W$  in terms of  $\xi$

$$\begin{aligned} \delta W = & -\frac{1}{2} \int \left( \xi \cdot \nabla (\gamma p_0 \nabla \cdot \xi + \xi \cdot \nabla p_0) \right. \\ & + \frac{1}{\mu_0} \xi \cdot [(\nabla \times \nabla \times (\xi \times \mathbf{B}_0)) \times \mathbf{B}_0 \\ & \left. + (\nabla \times \mathbf{B}_0) \times \nabla \times (\xi \times \mathbf{B}_0)] \right) d\tau \end{aligned}$$

and using the vector relationships 3 and 5 of Section 14.1 together with Gauss's theorem this equation may be written

$$\begin{aligned} \delta W = & \frac{1}{2} \int \left( \gamma p_0 (\nabla \cdot \xi)^2 + (\xi \cdot \nabla p_0) \nabla \cdot \xi \right. \\ & + \frac{1}{\mu_0} \mathbf{B}_1^2 - \mathbf{j}_0 \cdot (\mathbf{B}_1 \times \xi) \Big) d\tau \\ & \left. + \frac{1}{2} \int \left( p_1 + \frac{1}{\mu_0} \mathbf{B}_0 \cdot \mathbf{B}_1 \right) \xi \cdot dS \right) \quad 6.4.6 \end{aligned}$$

The surface term is zero if the normal displacement at the surface is zero, as it would be at a perfect conductor. When there is a vacuum region outside the plasma (and there are no surface currents in the equilibrium configuration) the surface term represents the transfer of energy to the vacuum region. This energy is  $\int \mathbf{B}_v^2 / 2\mu_0 d\tau$  where  $\mathbf{B}_v$  is the perturbed magnetic field, and the integral is over the vacuum region. Equation 6.4.6 for  $\delta W$  may therefore be written

$$\begin{aligned} \delta W = & \frac{1}{2} \int_{\text{plasma}} \left( \gamma p_0 (\nabla \cdot \xi)^2 + (\xi \cdot \nabla p_0) \nabla \cdot \xi \right. \\ & \left. + \frac{\mathbf{B}_1^2}{\mu_0} - \mathbf{j}_0 \cdot (\mathbf{B}_1 \times \xi) \right) d\tau + \int_{\text{vacuum}} (\mathbf{B}_v^2 / 2\mu_0) d\tau \quad 6.4.7 \end{aligned}$$

where  $\mathbf{B}_1(\xi)$  is given by eqn 6.4.4 and  $\mathbf{B}_v$  satisfies  $\nabla \times \mathbf{B}_v = 0$  together with the required,  $\xi$ -dependent, boundary conditions.

If  $\delta W$  is negative for any physically allowable  $\xi$  the plasma is unstable. If, on the other hand,  $\delta W$  is positive for all allowable  $\xi$  the plasma is stable.

It is sometimes possible to use the energy principle to obtain a sufficient criterion for stability. This is done by arranging the terms of  $\delta W$  in a

form such that, when the criterion is satisfied,  $\delta W$  is positive for all displacements. A more common procedure is to use a trial function to make  $\delta W$  negative and hence demonstrate instability.

If the eigenfunctions and eigenvalues,  $\omega$ , of a problem are required it is necessary to introduce the kinetic energy

$$K = \int \frac{1}{2} \rho \omega^2 \dot{\xi}^2 dt$$

and to obtain an extremum of the Lagrangian

$$L = K - \delta W.$$

This is equivalent to solving the full linearized ideal mhd equations. An example of such a solution is shown in Fig. 6.4.1.

## 6.5

### Tokamak instabilities

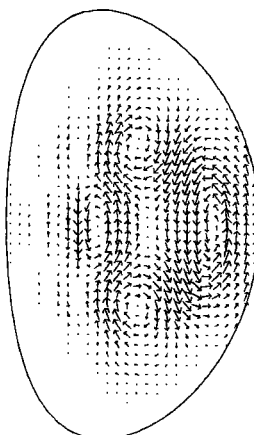


**Fig. 6.4.1** Showing the poloidal component of the displacement  $\xi$  for an ideal mhd instability in a tokamak.

The first class of instabilities consists of the so-called ideal mhd modes. In the theory of these modes it is assumed that the plasma is perfectly conducting. Since the plasma is *not* perfectly conducting the implications of ideal mhd stability analysis require some comment. If the ideal mhd theory predicts instability then it is to be expected that instability will occur, but there is no reason to believe that resistivity will not be important in the nonlinear development of the instability. These instabilities are 'ideal' in the sense that instability would occur even if the plasma were perfectly conducting.

On the other hand, if the plasma is predicted to be ideal mhd stable, the plasma may or may not be stable. In particular there is the possibility of resistive modes of instability. These are usually paired with the types of ideal mode since, for a particular ideal mode, the source of free energy is still available when the constraint of perfect conductivity is relaxed. For example, it will be seen that the tearing mode is the resistive analogue of the kink instability.

The remaining part of the present chapter will introduce the various mhd instabilities and establish their stability boundaries as determined by linear stability theory.

The instabilities which will be described are:

- (i) *Kink instability* An ideal mhd instability driven at low  $\beta$  by the current gradient. At high  $\beta$ , pressure gradients also contribute to the instability.
- (ii) *Tearing mode* The resistive form of the kink instability.

## (iii) Internal kink

This instability has mode number  $m = 1$ . It principally affects the plasma core where  $q \lesssim 1$  and is driven by the pressure gradient in that region.

(iv) Resistive  $m = 1$  instability

Similar to the internal kink, principally affecting the plasma core, but with a different energy source.

## (v) Ballooning modes

A localized instability driven by the pressure gradient.

## (vi) Mercier instability

A limiting case of the ballooning mode.

## (vii) Vertical instability

An instability arising from plasma elongation, in which the whole plasma is subject to a vertical motion.

**6.6****Large aspect-ratio tokamak**

Tokamaks typically have an aspect ratio,  $R/a$ , of 3–4 and large tokamaks usually have vertically elongated cross-sections. Precise mhd stability calculations for these configurations are carried out using numerical computer codes. However, the understanding of the underlying structure of the problem, involving the types of instability and stability limits, derives from calculations for a large aspect-ratio, circular cross-section tokamak. In this limit much of the calculation can be carried out analytically and such calculations provide both a good introduction to mhd stability and a terminology to discuss more complex cases.

It might be expected that in the limit of very large aspect-ratio the stability of a tokamak plasma would be the same as that of a cylinder. It turns out that although this is the case for some modes, for others the toroidal nature of the instability persists even at large aspect ratio. The explanation follows from the fact that a tokamak, by definition, has a safety factor  $q$  of order 1. This means that

$$\frac{B_\theta}{B_\phi} \sim \frac{a}{R}.$$

Thus, as the aspect ratio is increased the ratio of poloidal to toroidal field must be decreased. Geometrically this means that no matter how large  $R/a$ , the field lines still traverse only  $q \sim 1$  times around the torus to complete a poloidal transit. As the aspect ratio is increased this toroidal feature persists. Had the ratio  $B_\theta/B_\phi$  been held constant  $q$  would be proportional to  $a/R$ , and in the large aspect-ratio limit the plasma would be described by cylindrical theory and would have the stability of a pinch configuration. The two basic consequences of the tokamak ordering are (i) the number of low-mode number resonant surfaces is restricted, and

(ii) the curvature of the magnetic field lines on the inboard (smaller major radius) side of the plasma is away from the plasma, in contrast to a cylinder where the curvature is everywhere toward the plasma.

A further assumption which can substantially simplify the calculations is that of low  $\beta$ . When this assumption is made the equilibrium pressure balance leads to further simplifications. In leading order the equilibrium equation  $\nabla p = j \times B$  takes the form

$$\frac{dp}{dr} + \frac{d}{dr} \frac{B_\phi^2}{2\mu_0} + \frac{1}{\mu_0} \frac{B_\theta}{r} \frac{d}{dr} r B_\theta = 0. \quad 6.6.1$$

In the low- $\beta$  approximation  $p$  is taken to be of order  $B_\theta^2/2\mu_0$ , that is  $\beta_p \sim 1$ , and since  $B_\phi \sim (R/a)B_\theta$ , eqn 6.6.1 implies

$$\begin{aligned} \frac{dB_\phi}{dr} &\sim \mu_0 \frac{1}{B_\phi} \frac{dp}{dr} \\ &\sim \beta \frac{B_\phi}{a}. \end{aligned}$$

Thus writing  $a/R = \varepsilon$ , the large aspect-ratio, low- $\beta$  ordering can be summarized as follows:

$$\begin{aligned} q &\sim 1, & \frac{B_\theta}{B_\phi} &\sim \varepsilon, \\ \beta_p &\sim 1, & \beta &\sim \varepsilon^2 \end{aligned}$$

and

$$\frac{dB_\phi}{dr} \sim \varepsilon^2 \frac{B_\phi}{a}, \quad j_\theta \sim \varepsilon j_\phi.$$

This set of assumptions simplifies the basic stability equations. In carrying out the stability analysis the ordering also implies an expansion of the perturbed quantities. For example  $\delta W$  can be expanded in powers of  $\varepsilon$ , and in the simplest cases only the leading order term need be considered.

## 6.7

### Kink instability

The potentially strongest ideal mhd instability is the kink mode. It is so named because it leads to the kinking of the magnetic surfaces and the plasma boundary. At low  $\beta$  its driving force comes from the radial gradient of the toroidal current. At higher  $\beta$  the pressure gradient contributes to the instability.

For a circular, large aspect-ratio tokamak with low  $\beta$  ( $\sim \varepsilon^2$ ) the potential energy of a perturbation can be derived using the form of  $\delta W$

## 6.7 Kink instability

given by eqn 6.4.7. In this case  $B_\phi$  and  $R$  are taken to be constants. A full calculation using this ordering shows that the leading order term in  $\delta W$  is essentially that of a cylinder with a number of small terms removed. Thus the calculation can be carried out using coordinates  $(r, \theta, \varphi)$  where  $(R\phi)$  corresponds to the  $z$  coordinate of a cylinder. Taking  $\partial/\partial r \sim (1/r) \partial/\partial\theta \gg (1/R) \partial/\partial\phi$ , the minimizing perturbation has  $\nabla \cdot \xi = 0$ ,  $\xi_r \sim \xi_\theta \gg \xi_\phi$  and  $B_{r1} \sim B_{\theta1} \gg B_{\phi1}$ . In this approximation eqn 6.4.7 gives

$$\begin{aligned}\delta W = \pi R \int_0^a & \left( \frac{B_1^2}{\mu_0} - j_{z0}(B_{r1}\xi_\theta - B_{\theta1}\xi_r) \right) d\theta r dr \\ & + \pi R \int_a^b \frac{B_v^2}{\mu_0} d\theta r dr,\end{aligned}\quad 6.7.1$$

where  $B_1^2 = B_{r1}^2 + B_{\theta1}^2$ ,  $a$  is the radius of the plasma and  $b$  the radius of a perfectly conducting wall. The first integral term in eqn 6.7.1 gives the plasma contribution  $\delta W_p$  and the second gives the vacuum contribution  $\delta W_v$ .

The perturbations are Fourier analysed in the form  $e^{i(m\theta - n\phi)}$ , and  $\nabla \cdot \xi = 0$  becomes

$$\xi_\theta = -\frac{i}{m} \frac{d}{dr}(r\xi_r). \quad 6.7.2$$

Then, using eqn 6.4.4, the magnetic perturbations are

$$B_{r1} = -\frac{imB_\phi}{R} \left( \frac{n}{m} - \frac{1}{q} \right) \xi_r \quad 6.7.3$$

and

$$B_{\theta1} = \frac{B_\phi}{R} \frac{d}{dr} \left[ \left( \frac{n}{m} - \frac{1}{q} \right) r \xi_r \right], \quad 6.7.4$$

where  $q (= rB_\phi/RB_\theta)$  is the safety factor.

It is convenient to take the Fourier amplitude  $\xi_r$  to be real, and then  $B_{\theta1}$  is real, and  $\xi_\theta$  and  $B_{r1}$  are imaginary. Allowing for the phases, substitution of eqns 6.7.2 to 6.7.4 in the plasma part of eqn 6.7.1 gives

$$\begin{aligned}\delta W_p = \frac{\pi^2 B_\phi^2}{\mu_0 R} \int_0^a & \left\{ m^2 \left( \frac{n}{m} - \frac{1}{q} \right)^2 \xi_r^2 + \left( \frac{d}{dr} \left[ \left( \frac{n}{m} - \frac{1}{q} \right) r \xi_r \right] \right)^2 \right. \\ & + \frac{1}{r} \frac{d}{dr} (r B_\theta) \frac{R}{B_\phi} \left[ \left( \frac{n}{m} - \frac{1}{q} \right) \xi_r \frac{d}{dr} (r \xi_r) \right. \\ & \left. \left. + \frac{d}{dr} \left[ \left( \frac{n}{m} - \frac{1}{q} \right) r \xi_r \right] \xi_r \right] \right\} r dr.\end{aligned}\quad 6.7.5$$

After some cancellation, and integration by parts to remove terms involving  $\xi_r \frac{d\xi_r}{dr} (= \frac{1}{2} d\xi_r^2/dr)$ , eqn 6.7.5 becomes

$$\begin{aligned}\delta W_p = & \frac{\pi^2 B_\phi^2}{\mu_0 R} \int_0^a \left[ \left( r \frac{d\xi}{dr} \right)^2 + (m^2 - 1) \xi^2 \right] \left( \frac{n}{m} - \frac{1}{q} \right)^2 r dr \\ & + \left[ \frac{2}{qa} \left( \frac{n}{m} - \frac{1}{qa} \right) + \left( \frac{n}{m} - \frac{1}{qa} \right)^2 \right] a^2 \xi_a^2,\end{aligned}\quad 6.7.6$$

where the subscript on  $\xi_r$  has now been dropped and the subscript  $a$  indicates the value at  $r = a$ .

The vacuum contribution to  $\delta W$  is most readily calculated by solving for the flux function  $\psi$  defined by  $B_{r1} = -(1/r)\partial\psi/\partial\theta$  and  $B_{\theta 1} = \partial\psi/\partial r$ . Then  $\psi$  satisfies Laplace's equation

$$\frac{1}{r} \frac{d}{dr} \left( r \frac{d\psi}{dr} \right) - \frac{m^2}{r^2} \psi = 0 \quad 6.7.7$$

and since

$$\begin{aligned}B_v^2 &= B_{r1}^2 + B_{\theta 1}^2 \\ &= \frac{m^2}{r^2} \psi^2 + \left( \frac{d\psi}{dr} \right)^2\end{aligned}$$

the vacuum term can be written

$$\begin{aligned}\delta W_v &= \frac{\pi^2 R}{\mu_0} \int_a^b B_v^2 r dr \\ &= \frac{\pi^2 R}{\mu_0} \left\{ \int_a^b \left[ \frac{m^2}{r^2} \psi^2 - \psi \frac{1}{r} \frac{d}{dr} \left( r \frac{d\psi}{dr} \right) \right] r dr + \left( r \psi \frac{d\psi}{dr} \right) \Big|_a^b \right\}\end{aligned}$$

and using eqn 6.7.7

$$\delta W_v = \frac{\pi^2 R}{\mu_0} \left( r \psi \frac{d\psi}{dr} \right) \Big|_a^b. \quad 6.7.8$$

The solution of eqn 6.7.7 is

$$\psi = \alpha r^m + \beta r^{-m}. \quad 6.7.9$$

For a conducting wall at  $r = b$ ,  $B_r(b) = 0$ , and so the outer boundary condition is

$$\psi = 0, \quad r = b. \quad 6.7.10$$

At  $r = a$ ,  $B_r$  is continuous so that, taking  $B_{r1}$  from the plasma equation 6.7.3 with the vacuum solution  $B_{r1}(a) = -im\psi_a/a$ , the inner

boundary condition for the vacuum region is

$$\psi_a = B_{\theta a} \left( \frac{nq_a}{m} - 1 \right) \xi_a. \quad 6.7.11$$

Substituting boundary conditions 6.7.10 and 6.7.11 into eqn 6.7.9 gives the solution

$$\psi = B_{\theta a} \left( \frac{nq_a}{m} - 1 \right) \frac{\left(\frac{r}{b}\right)^m - \left(\frac{b}{r}\right)^m}{\left(\frac{a}{b}\right)^m - \left(\frac{b}{a}\right)^m} \xi_a \quad 6.7.12$$

and substituting eqn 6.7.12 into eqn 6.7.8

$$\delta W_v = \frac{\pi^2 B_\phi^2}{\mu_0} m \lambda \left( \frac{n}{m} - \frac{1}{q_a} \right)^2 a^2 \xi_a^2 \quad 6.7.13$$

where

$$\lambda = \frac{1 + (a/b)^{2m}}{1 - (a/b)^{2m}}.$$

The complete form of  $\delta W$  is now obtained by adding eqns 6.7.6 and 6.7.13 and this gives

$$\begin{aligned} \delta W = & \frac{\pi^2 B_\phi^2}{\mu_0 R} \left\{ \int_0^a \left[ \left( r \frac{d\xi}{dr} \right)^2 + (m^2 - 1)\xi^2 \right] \left( \frac{n}{m} - \frac{1}{q} \right)^2 r dr \right. \\ & \left. + \left[ \frac{2}{q_a} \left( \frac{n}{m} - \frac{1}{q_a} \right) + (1 + m\lambda) \left( \frac{n}{m} - \frac{1}{q_a} \right)^2 \right] a^2 \xi_a^2 \right\}. \end{aligned} \quad 6.7.14$$

If there is a conducting wall at the surface of the plasma, the boundary condition is  $\xi_a = 0$ . It is seen from eqn 6.7.14 that in this case  $\delta W > 0$  and the plasma is stable. For any position of the conducting wall, including  $b \rightarrow \infty$ ,  $\delta W$  is positive for all modes having  $m/n < q_a$ . If  $q$  is an increasing function of  $r$ , modes having a resonant surface within the plasma will have  $m/n < q_a$  and will therefore be stable.

Since outside the plasma  $q \propto r^2$ , modes with resonant surfaces outside the plasma have  $m/n > q_a$ . Such modes can therefore be unstable. A straightforward way to determine stability for a particular case is to solve the eigenmode equation

$$\frac{d}{dr} \left[ (\rho \omega^2 - F^2) r \frac{d}{dr} (r \xi) \right] - \left[ m^2 (\rho \omega^2 - F^2) - r \frac{dF^2}{dr} \right] \xi = 0,$$

where  $\rho$  is the plasma density,  $F = (m - nq) B_\theta / r \mu_0^{1/2}$ , and the mode has a time-dependence  $\exp -i\omega t$ . The boundary condition to be applied at the origin is  $\xi \propto r^{m-1}$ , and that at the plasma surface is

$$\frac{d}{dr} (r \xi) = \frac{m(m - nq_a)^2}{(\mu_0 \rho \omega^2 a^2 / B_\theta^2) - (m - nq_a)^2} \left( \lambda - \frac{2}{m - nq_a} \right) \xi, \quad (r = a).$$

This condition represents the requirement of pressure balance and the condition that the plasma boundary remains a flux surface.

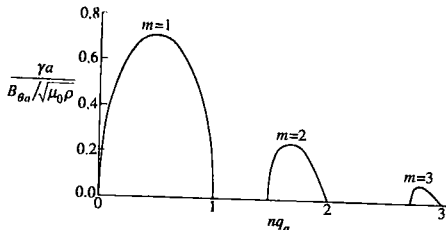


**Fig. 6.7.1** Growth rate of modes  $m = 1, 2$ , and  $3$  for the parabolic current profile  $j = j_0(1 - (r/a)^2)^v$ , as a function of  $nq_a$ .

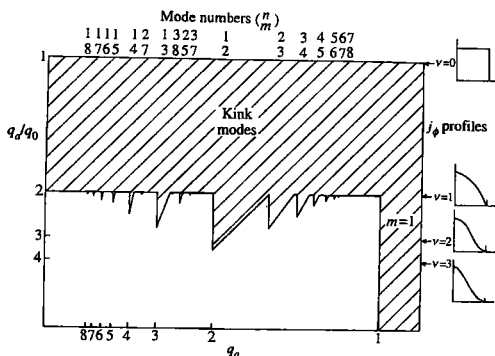


**Fig. 6.7.2** Stability diagram for kink modes for the current distributions  $j = j_0(1 - (r/a)^2)^v$ . The vertical axis measures the peaking of the current as given by  $q_a/q_0 = v + 1$  and the horizontal coordinate is proportional to  $1/q_a$  and therefore to the total current.

Figure 6.7.1 gives growth rate,  $\gamma (= \omega_r)$ , for a parabolic current distribution and Fig. 6.7.2 shows the regime of stability for the class of current profiles  $j = j_0(1 - (r/a)^2)^v$ . The broad band of instability in the upper part of this diagram is due to the destabilizing effect of the current gradient close to the surface of the plasma arising from the flatness of the current profiles. The protrusions of instability into the lower part of the diagram, where the current profiles are more peaked, are due to the proximity of the external resonance surfaces of the various modes to the surface of the plasma and hence to the current gradients in the plasma.

The onset of stability as the resonant surface reaches the plasma surface from outside, that is  $q_a \rightarrow m/n$ , is a misleading feature resulting from the ideal MHD model. It can be seen from Section 6.9, on the stability of tearing modes, that the inclusion of resistive effects removes this stability boundary and leads to instabilities with resonant surfaces inside the plasma.

## 6.8

### Tearing modes

The tearing instability in a tokamak is driven by the radial gradient of the equilibrium toroidal current density. The name derives from the tearing and rejoining of magnetic field lines which occur during the instability as a consequence of finite resistivity.

The growth of the instability is sufficiently slow that, over most of the plasma, inertial effects are negligible. Also, over most of the plasma the resistivity is negligible and the motion conforms to ideal mhd. However, at the resonant surface for the mode the  $v \times B$  contribution to Ohm's law goes to zero and, in the neighbourhood of this surface, the  $\eta j$  term becomes important in balancing the induced electric field,  $E$ .

Thus the theory of tearing modes involves solving one set of equations over most of the plasma and another set in a resistive layer around the resonant surface. The complete eigenfunction then requires a matching of the resulting solutions and the condition for matching determines the growth-rate eigenvalue. The matching procedure is illustrated in Fig. 6.8.1.

#### Outer region

In the outer region inertia is negligible and the perturbed plasma is in force equilibrium, that is

$$\mathbf{j} \times \mathbf{B} = -\nabla p,$$

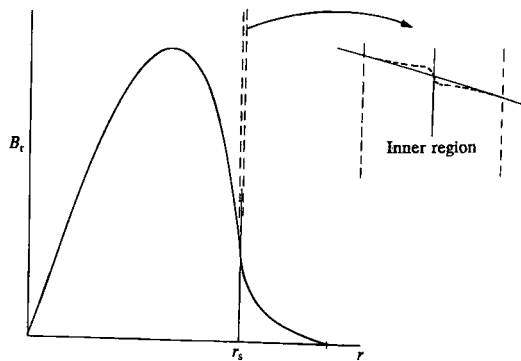


**Fig. 6.8.1** Showing a typical form of  $B_r(r)$ . The full line in the expanded view of the inner region is the actual (resistive) solution. The dashed line shows the continuation of the outer (ideal) solution.

and since the curl of a gradient is zero

$$\nabla \times j \times B = 0. \quad 6.8.1$$

Using the vector relation 14.1.7 with  $\nabla \cdot B = 0$  and  $\nabla \cdot j = 0$ , eqn 6.8.1 becomes

$$B \cdot \nabla j - j \cdot \nabla B = 0. \quad 6.8.2$$

The large aspect-ratio ordering will now be applied. Taking  $\varepsilon = a/R \ll 1$ , the ordering of the equilibrium quantities is

$$B_\theta \sim \frac{1}{r} \frac{dB_\phi}{dr} \sim \varepsilon B_\phi$$

$$j_\theta \sim \varepsilon j_\phi$$

and the appropriate ordering of the perturbed quantities is

$$B_{\phi 1} \sim \varepsilon B_{r1} \sim \varepsilon B_{\theta 1}$$

$$j_{r1} \sim j_{\theta 1} \sim \varepsilon j_{\phi 1},$$

where the suffix 1 refers to the linear perturbations.

With this ordering the required component of eqn 6.8.2 is the toroidal component and since  $j \cdot \nabla B_\phi \ll B \cdot \nabla j_\phi$  the equation governing the outer region is

$$(B \cdot \nabla j_\phi)_1 = 0. \quad 6.8.3$$

It is convenient now to introduce a magnetic flux function. In the present ordering  $\nabla \cdot B = 0$  gives

$$\frac{\partial(rB_{r1})}{\partial r} + \frac{\partial B_{\theta 1}}{\partial \theta} = 0$$

and so the appropriate flux function,  $\psi$ , is defined by

$$B_{r1} = -\frac{1}{r} \frac{\partial \psi}{\partial \theta}, \quad B_{\theta 1} = \frac{\partial \psi}{\partial r}. \quad 6.8.4$$

Thus, substituting eqns 6.8.4 into Ampère's law,

$$\mu_0 j_{\phi 1} = \nabla^2 \psi = \frac{1}{r^2} \frac{\partial}{\partial r} r \frac{\partial \psi}{\partial r} + \frac{1}{r^2} \frac{\partial^2 \psi}{\partial \theta^2}. \quad 6.8.5$$

Writing eqn 6.8.3

$$B \cdot \nabla j_{\phi 1} + B_1 \cdot \nabla j_\phi = 0 \quad 6.8.6$$

and taking the perturbations to have the form  $e^{i(m\theta - n\phi)}$ , eqns 6.8.4 – 6.8.6 give

$$\frac{1}{\mu_0} \left( \frac{m B_\theta}{r} - \frac{n B_\phi}{R} \right) \nabla^2 \psi - \frac{m}{r} \frac{d j_\phi}{dr} \psi = 0$$

and so, using  $q = r B_\phi / R B_\theta$ , the equation for the outer region is

$$\frac{1}{r} \frac{d}{dr} r \frac{d\psi}{dr} = \frac{m^2}{r^2} \psi - \frac{dj_\phi/dr}{\frac{B_\theta}{\mu_0} \left(1 - \frac{nq}{m}\right)} \psi = 0. \quad 6.8.7$$

If eqn 6.8.7 is multiplied by  $r\psi$  and integrated over a region  $r_1$  to  $r_2$  it gives

$$\int_{r_1}^{r_2} \left\{ B_{\theta 1}^2 + B_{r1}^2 + \frac{dj_\phi/dr}{(B_\theta/\mu_0)(1-(nq/m))} \psi^2 \right\} r dr = \left( r\psi \frac{d\psi}{dr} \right) \Big|_{r_1}^{r_2}.$$

The first two terms represent the stabilizing effect of line bending and the third represents the energy associated with the destabilizing effect of the equilibrium current gradient. The boundary term describes the Poynting flux.

Equation 6.8.7 can be integrated outward from  $r = 0$  and inward from  $r = a$  using the appropriate boundary conditions. However, the equation has a singularity at the resonant surface,  $r = r_s$ , where  $q = m/n$ . It is in a layer around this surface that eqn 6.8.7 fails and a separate analysis taking account of resistivity and inertia is required. The matching of the inner and outer solutions is carried out by equating the values of  $d\psi/dr$  and of  $\psi$  in the region of overlap. More precisely, because the solution is linear, it is only the ratio  $(d\psi/dr)/\psi$  which is involved. Equation 6.8.7 is solved in the two regions  $r > r_s$  and  $r < r_s$  and these solutions determine the discontinuity,  $\Delta'$ , in  $\psi'/\psi$  across  $r = r_s$ ,  $\Delta'$  being defined by

$$\Delta' = \frac{\psi'}{\psi} \Big|_{r=r_s-\epsilon}^{r=r_s+\epsilon}, \quad \epsilon \rightarrow 0.$$

This procedure is not quite straightforward and the details will be described in Section 6.9. Having obtained  $\Delta'$ , it is equated to the change in  $\psi'/\psi$  across the inner layer as determined from the solution of the full equations, including resistivity and inertia, in this layer.

### Resistive layer

Two equations govern the behaviour in the resistive layer, Ohm's law and the equation of motion. The required form of Ohm's law is

$$\mathbf{E} + \mathbf{v} \times \mathbf{B} = \eta \mathbf{j}.$$

Taking the curl of this equation and using Faraday's and Ampère's laws gives

$$-\frac{\partial \mathbf{B}}{\partial t} + \nabla \times (\mathbf{v} \times \mathbf{B}) = \frac{\eta}{\mu_0} \nabla \times \nabla \times \mathbf{B}. \quad 6.8.8$$

The linearized form of the radial component of eqn 6.8.8 relates the linear quantities  $B_r$  and  $v_r$

$$-\frac{\partial B_r}{\partial t} + \mathbf{B} \cdot \nabla v_r = -\frac{\eta}{\mu_0} \nabla^2 B_r. \quad 6.8.9$$

The separate modes are obtained by taking the perturbed variables to have the form  $\exp(\gamma t + im\theta - in\phi)$ . Thus, using eqn 6.8.4 to write  $B_r = -im\psi/r$  and regarding  $r$  as constant in the layer, eqn 6.8.9 becomes

$$\gamma\psi + B_\theta \left(1 - \frac{nq}{m}\right) v_r = \frac{\eta}{\mu_0} \nabla^2 \psi. \quad 6.8.10$$

The resistive layer is narrow and so the radial derivatives in  $\nabla^2$  dominate. Equation 6.8.10 then gives the required form of Ohm's law

$$\frac{d^2\psi}{dr^2} = \frac{\mu_0\gamma}{\eta}\psi + \frac{\mu_0 B_\theta}{\eta} \left(1 - \frac{nq}{m}\right) v_r. \quad 6.8.11$$

Equation 6.8.11 will be solved in conjunction with the equation of motion, and the resulting solution determines the change,  $\Delta'_{in}$ , in  $\psi'/\psi$  across the layer. The solution has an almost constant  $\psi$  through the layer and this allows eqn 6.8.11 to be integrated across the layer to give

$$\Delta'_{in} = \frac{\mu_0\gamma}{\eta} \int \left(1 + \frac{B_\theta}{\gamma} \left(1 - \frac{nq}{m}\right) \frac{v_r}{\psi}\right) dr. \quad 6.8.12$$

Because the layer is narrow the equilibrium quantities are to be regarded as constants except that, since  $(1 - nq/m) = 0$  at the resonant surface, this factor must be expanded in the form

$$\left(1 - \frac{nq}{m}\right) = -\left(\frac{q'}{q}\right)_{r_s} s \quad \text{where } s = (r - r_s).$$

Equation 6.8.12 then becomes

$$\Delta'_{in} = \frac{\mu_0\gamma}{\eta} \int \left(1 - \frac{B_\theta q'}{q} s \frac{v_r}{\psi}\right) ds. \quad 6.8.13$$

It is now necessary to evaluate  $v_r/\psi$  from the equation of motion

$$\rho \frac{\partial v}{\partial t} = j \times B - \nabla p.$$

Taking the curl of this equation gives

$$\nabla \times j \times B = \nabla \times \rho \frac{\partial v}{\partial t}. \quad 6.8.14$$

Equation 6.8.14 is the same as eqn 6.8.1 with the addition of the inertial term. Thus, again taking the axial component of the equation and assuming incompressibility, the dominant additional term in the inner layer is

given by

$$\begin{aligned} \left( \nabla \times \rho \frac{\partial \mathbf{v}}{\partial t} \right)_\phi &= \gamma \rho \frac{dv_\theta}{dr} \\ &= \frac{\gamma \rho}{m} ir \frac{d^2 v_r}{dr^2}. \end{aligned}$$

Including this term in the analysis, eqn 6.8.7 becomes

$$\frac{\gamma \rho r^2}{m^2} \frac{d^2 v_r}{dr^2} = \frac{B_\theta}{\mu_0} \left( 1 - \frac{nq}{m} \right) \frac{d^2 \psi}{dr^2} - \frac{dj_\phi}{dr} \psi. \quad 6.8.15$$

Using eqn 6.8.11 to eliminate  $d^2 \psi / dr^2$  in eqn 6.8.15 gives

$$\frac{d^2 v_r}{ds^2} - \left( \frac{B_\theta^2 m^2 q'^2}{\rho \eta \gamma r^2 q^2} \right) s^2 v_r = -\frac{B_\theta m^2 q'}{\rho \eta r^2 q} s \psi - \frac{m^2}{\rho \gamma r^2} \frac{dj_\phi}{dr} \psi. \quad 6.8.16$$

Since  $\psi$  is taken to be constant, eqn 6.8.16 is an inhomogeneous equation for  $v_r$ . The solution is a sum of parts which are odd and even in  $s$ . Only the odd part, arising from the first term on the right hand side of eqn 6.8.16, contributes to the integral in eqn 6.8.13.

Equation 6.8.16 is written in a more convenient form by introducing the characteristic length  $d$  and new variables  $x$  and  $y$  defined by

$$d = \left( \frac{\rho \eta \gamma r^2 q^2}{B_\theta^2 m^2 q'^2} \right)^{1/4}, \quad 6.8.17$$

$$x = \frac{s}{d} \quad \text{and} \quad y = -\frac{\rho \gamma r^2 q}{m^2 B_\theta q' d^3} \frac{v_r}{\psi}$$

where  $y$  and  $v_r$  here represent only the odd part of the solution of eqn 6.8.16. Thus, making the substitutions, eqn 6.8.16 becomes

$$\frac{dy}{dx^2} = -x(1 - xy) \quad 6.8.18$$

and equation 6.8.13 becomes

$$\Delta'_{in} = \frac{\mu_0 \gamma d}{\eta} \int_{-\infty}^{+\infty} (1 - xy) dx. \quad 6.8.19$$

The limits of the integral have now become effectively  $\pm\infty$  on the scale of the layer. Substitution of the solution  $y(x)$  of eqn 6.8.18 into the integral of eqn 6.8.19 gives the required quantity  $\Delta'_{in}$ .

The solution  $y$  and the form of the integrand in eqn 6.8.19 are shown in Fig. 6.8.2. The integral of eqn 6.8.19 is equal to 2.12 and hence, equating  $\Delta'_{in}$  to  $\Delta'$  yields the dispersion relation for the tearing mode

$$\Delta' = 2.12 \frac{\mu_0 \gamma d}{\eta}. \quad 6.8.20$$

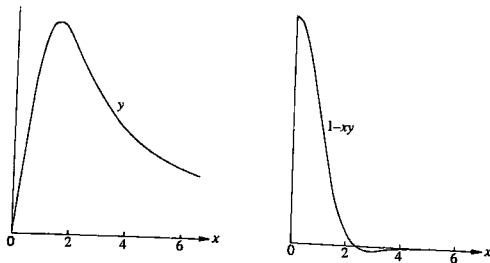


**Fig. 6.8.2** Solutions for  $y$  and  $(1 - xy)$  across the resistive layer.

Substitution for  $d$  from eqn 6.8.17 into eqn 6.8.20 gives the growth rate

$$\gamma = 0.55 \left( \left( \frac{\eta}{\mu_0} \right)^{3/5} \left( \frac{m B_\phi}{(\mu_0 \rho)^{1/2}} \frac{q'}{r q} \right)^{2/5} \right)_{r=r_i} \Delta'^{4/5}.$$

Written as a function of the characteristic resistive diffusion time

$$\tau_R = \frac{\mu_0 a^2}{\eta}$$

and the Alfvén transit time

$$\tau_A = \frac{a}{B_\phi / (\mu_0 \rho)^{1/2}}$$

the growth rate is

$$\gamma = \frac{0.55}{\tau_R^{3/5} \tau_A^{2/5}} \left( \pi \frac{a}{R} \frac{aq'}{q} \right)^{2/5} (a \Delta')^{4/5}. \quad 6.8.21$$

For  $B_\phi = 5$  T, a deuterium plasma with  $n_e = 10^{20} \text{ m}^{-3}$ ,  $T_e = 5 \text{ keV}$  and  $a = 1 \text{ m}$  has characteristic times  $\tau_R \sim 10 \text{ mins}$  and  $\tau_A \sim 0.1 \mu\text{s}$ , giving a growth time  $\gamma^{-1} \sim \tau_R^{3/5} \tau_A^{2/5} \sim 70 \text{ ms}$ . The layer width can be determined using eqns 6.8.17 and 6.8.20. This gives  $d \sim a(\tau_A/\tau_R)^{2/5}$  and for the above example the width is  $\sim 0.15 \text{ mm}$ . This is an order of magnitude less than the ion Larmor radius and it is seen therefore that the simple model of the resistive layer is of limited applicability. However, the outer solutions retain their validity and, as will be described in Section 7.3, the resistive layer analysis can be replaced by a more satisfactory nonlinear treatment.

## 6.9

### Teering stability

The stability of tearing modes is determined by the solution of eqn 6.8.7 and the resulting value of  $\Delta'$ . It is seen from eqn 6.8.21 that marginal stability corresponds to  $\Delta' = 0$ . Instability occurs for  $\Delta' > 0$ . To determine stability therefore it is only necessary to find the sign of  $\Delta'$ . However, eqn 6.8.7 is singular at the resonant surface and some care is needed in the calculation.

If eqn 6.8.7 is expanded about the radius,  $r_s$ , of the resonant surface, with

$$\left(1 - \frac{nq}{m}\right) \rightarrow -\left(\frac{q'}{q}\right)_{r_s} (r - r_s)$$

then, keeping only the dominant terms, eqn 6.8.7 becomes

$$\frac{d^2\psi}{dr^2} + \left(\frac{dj/dr}{B_\theta/\mu_0 q'}\right)_{r_s} \frac{\psi}{r - r_s} = 0$$

or

$$\frac{d^2\psi}{ds^2} - \frac{\kappa}{s}\psi = 0, \quad 6.9.1$$

where  $s = r - r_s$  and  $\kappa = -(\mu_0 j' q / B_\theta q')_{r_s}$ . Equation 6.9.1 has a singularity at  $s = 0$  and the general solutions are also singular at this point. The leading terms of the two independent solutions have the form

$$\psi = 1 + \kappa s \ln |s| + \dots$$

$$\psi = A(s + \frac{1}{2}\kappa s^2 + \dots)$$

and so the expanded solutions for  $r < r_s$  and  $r > r_s$  are given by

$$\psi = 1 + \kappa s \ln |s| + \dots + A^- s + \dots \quad r < r_s$$

$$\psi = 1 + \kappa s \ln s + \dots + A^+ s + \dots \quad r > r_s,$$

where  $A^-$  and  $A^+$  are constants to be determined. It is seen that, although  $\psi$  is finite at  $s = 0$ , the solutions have the singular derivatives

$$\psi' = \kappa(\ln |s| + 1) + A^- \quad r < r_s$$

$$\psi' = \kappa(\ln s + 1) + A^+ \quad r > r_s.$$

However, in calculating the jump in  $\psi'$  between  $s = \pm \varepsilon$  the singular terms cancel leaving

$$\Delta' = A^+ - A^-.$$

Thus  $\Delta'$  can be calculated numerically by determining the value of  $A^-$  which gives a solution of eqn 6.8.7 which satisfies the regularity condition,

$\psi = 0$  at  $r = 0$ , and the value of  $A^+$  which gives a solution which satisfies the chosen boundary condition at the edge of the plasma.

This outer boundary condition is dependent on the position of any conductor, such as the vacuum vessel, outside the plasma and this will be discussed in more detail later in this section. For the case of a conducting shell at the surface of the plasma the boundary condition is

$$\psi' = \left( -\frac{m}{a} + \gamma \mu_0 \sigma \delta \right) \psi \quad r = a, \quad 6.9.2$$

where  $\gamma$  is the growth rate,  $\sigma$  is the conductivity of the shell and  $\delta$  its thickness. In the limit of a perfectly conducting shell  $\sigma \rightarrow \infty$ , and condition 6.9.2 becomes  $\psi(a) = 0$ . In the opposite, high resistance, limit  $\sigma \rightarrow 0$  and the boundary condition becomes  $\psi'(a) = -(m/a)\psi(a)$  giving the solution which falls to zero as  $r \rightarrow \infty$ .

Thus, given the boundary condition,  $\Delta'$  can be calculated numerically by solving eqn 6.8.7. One procedure is to start solutions at  $r = r_s$  with trial values of  $A^-$  and  $A^+$  and to adjust these values until the resulting solutions satisfy the boundary conditions at  $r = 0$  and  $r = a$ .

For sufficiently large  $m$ , depending on the current profile, tearing modes are stable. This is due to the  $m^2$  dependence of the stabilizing line bending term in eqn 6.8.7.

Values of  $r_s \Delta'$  for the  $m = 2$  mode are given in Fig. 6.9.1 for a parabolic current profile with and without a perfectly conducting wall. Without a conducting wall  $\Delta' > 0$  and the mode is unstable for all positions of the resonant surface. The presence of a conducting wall only affects  $\Delta'$  for values of  $r_s$  close to  $a$ . For resonant surfaces sufficiently close to the plasma edge the conducting wall makes the mode stable.

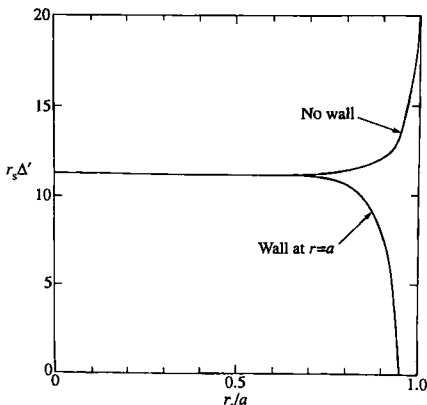
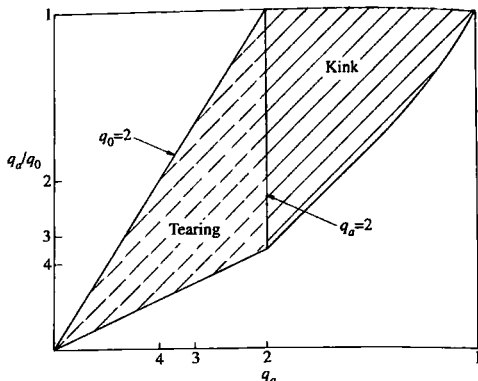


Fig. 6.9.1 Plots of  $r_s \Delta'(r_s)$  for  $m = 2$  and toroidal current density  $J = J_0(1 - (r^2/a^2))$ .  $\Delta' > 0$  gives instability. The lower curve shows the stabilizing effect of a perfectly conducting wall at  $r = a$ .



**Fig. 6.9.2** Stability diagram for the  $m = 2$  kink and tearing modes for current distributions  $j = j_0(1 - (r^2/a^2))^\nu$ . Stability for  $q_0 > 2$  results from the absence of a resonant ( $q = 2$ ) surface.

In Fig. 6.9.2 the region of instability of the  $m = 2$ -mode is shown for current profiles of the form

$$j = j_0 \left( 1 - \left( \frac{r}{a} \right)^2 \right)^\nu.$$

It is seen that the tearing instability is continuous with the kink instability as the resonant surfaces pass through the plasma boundary. For these profiles and normal tokamak operation ( $q_0 \approx 1$ ) the presence of a  $q = 2$  surface in the plasma implies instability of the  $m = 2$  tearing mode.

The values of  $r_s \Delta'$  for low  $m$  modes, in the limit  $r_s \rightarrow 0$ , are

$m$	$r_s \Delta'$
2	11.22
3	2.46
4	-2.01

#### Conducting wall boundary condition

When  $m = 2$  tearing modes are observed at low amplitude they usually have a finite real frequency. This is due either to a natural frequency of the mode arising from effects not included in the above analysis, or to a rotation imparted to the plasma by, say, neutral beam injection. This affects the influence of a conducting shell because the penetration of magnetic perturbations into the shell is a strong function of the frequency. At low frequency the field penetration is characterized by a resistive time  $\tau_s \sim \mu_0 \sigma b \delta$  where  $b$  is the radius of the shell,  $\delta$  its thickness and  $\sigma$  its

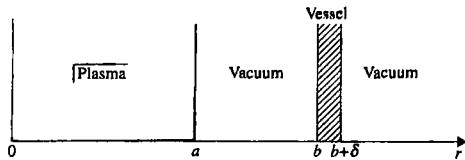


**Fig. 6.9.3** Showing the geometry involved in calculating the plasma boundary condition in the presence of a conducting vessel.

conductivity. At sufficiently high frequencies  $\omega\tau_s \gg 1$  field penetration does not occur because eddy currents shield out the perturbation.

Figure 6.9.3 gives the geometry. The required boundary condition at the surface of the plasma is obtained by solving the equations for  $\psi$  in the outside regions. Ampère's law can again be written in the form of eqn 6.8.5. In the vacuum region this becomes

$$\frac{1}{r} \frac{d}{dr} r \frac{d\psi}{dr} = \frac{m^2}{r^2} \psi. \quad 6.9.3$$

In the conducting shell  $j = \sigma E$  and in the large aspect-ratio approximation the required component is that in the  $\phi$  direction. Thus

$$\frac{1}{r} \frac{d}{dr} r \frac{d\psi}{dr} = \frac{m^2}{r^2} \psi + \mu_0 \sigma E_\phi. \quad 6.9.4$$

From Faraday's equation,  $\nabla \times E = -\partial B/\partial t$  so that, using the definition of  $\psi$  given in eqns 6.8.4,

$$E_\phi = \frac{\partial \psi}{\partial t}. \quad 6.9.5$$

Thus, taking the time dependence to be  $\exp -i\omega t$ , eqns 6.9.4 and 6.9.5 give the equation for the conducting shell:

$$\frac{1}{r} \frac{d}{dr} r \frac{d\psi}{dr} = \left( \frac{m^2}{r^2} - i\omega \mu_0 \sigma \right) \psi. \quad 6.9.6$$

Considering the first vacuum region the solution of eqn 6.9.3 has the form

$$\psi = Cr^m + Dr^{-m} \quad a < r < b$$

and consequently

$$\left( \frac{\psi'}{\psi} \right)_a = -\frac{m}{a} \frac{1+f(a/b)^{2m}}{1-f(a/b)^{2m}} \quad 6.9.7$$

where

$$f = \frac{(\psi'/\psi)_b - (m/b)}{(\psi'/\psi)_b + (m/b)}. \quad 6.9.8$$

## 6.9 Tearing stability

It remains to calculate  $(\psi'/\psi)_b$  by matching the solution through the resistive shell to the outer vacuum solution which has the form

$$\psi = Fr^{-m} \quad b + \delta < r < \infty. \quad 6.9.9$$

For frequencies of interest the effect of the resistive shell is to produce a change in  $\psi'$  across the width  $\delta$  with only a small change in  $\psi$ . It is convenient therefore to integrate eqn 6.9.6 across the shell using a constant  $\psi$  approximation. Thus

$$\left(\frac{\psi'}{\psi}\right)_{b+\delta} - \left(\frac{\psi'}{\psi}\right)_b = \left(\frac{m^2}{r^2} - i\omega\mu_0\sigma\right)\delta. \quad 6.9.10$$

Using eqn 6.9.9 and taking  $\delta \ll b$

$$\left(\frac{\psi'}{\psi}\right)_{b+\delta} = -\frac{m}{b}. \quad 6.9.11$$

Substitution of eqn 6.9.11 into eqn 6.9.10 gives  $(\psi'/\psi)_b$ , and substitution of this expression into eqn 6.9.8 with the approximation  $\delta \ll b/m$  gives

$$f = \frac{1}{1 + (im/\omega\tau_s)} \quad 6.9.12$$

where

$$\tau_s = \frac{\mu_0\sigma b\delta}{2} \quad 6.9.13$$

is the characteristic resistive time constant of the shell. Equation 6.9.7 together with eqn 6.9.12 now provide the boundary condition to be applied at the surface of the plasma.

For  $\omega_r\tau_s \gg 1$ ,  $f \rightarrow 1$  and  $(\psi'/\psi)_b \rightarrow \infty$  implying  $\psi_b \rightarrow 0$ . This is the result of the decreasing penetration of the magnetic field perturbation at high frequency, making the resistive shell behave as a perfect conductor. In the opposite limit  $\omega_r\tau_s \rightarrow 0$ ,  $f \rightarrow \gamma\tau_s/(m + \gamma\tau_s)$  and the shell appears as a good conductor ( $f \approx 1$ ) for high growth rates and loses its effect completely for  $\gamma \rightarrow 0$ . Thus for  $\omega_r = 0$  the conducting shell does not affect the stability-boundary, at which  $\gamma = 0$  and therefore  $f = 0$ , it only affects the growth rate.

For finite perturbations interaction with the vacuum vessel can cause a lowering of the frequency of an instability and at large amplitude the mode locks to the vessel, bringing the frequency to zero. This in turn introduces the possible effect of static error fields arising from the structure of the external coils. These effects are described in Sections 7.10 and 7.11.

## 6.10 Internal kink

The internal kink instability is characterized by having the azimuthal mode number  $m = 1$ , and toroidal mode number  $n = 1$ . Consequently the resonant surface for this mode, given by  $m = nq$ , is  $q = 1$ . Thus the instability only occurs if there is a  $q = 1$  surface in the plasma, and consequently a sufficient condition for stability is that the minimum value of  $q$  be greater than unity. With a current density which decreases monotonically with radius the minimum value of  $q$  is  $q_0$ , the value on axis. The internal kink mode is then stable if  $q_0 > 1$ .

The internal kink mode is distinguished from other modes by the fact that  $m = 1, n = 1$  implies a radial displacement whose azimuthal variation is given by  $\cos(\theta - \phi)$ . For each poloidal plane this corresponds to a simple displacement of each flux surface as illustrated in Fig. 6.10.1(a). The significance of this becomes apparent from the large aspect-ratio approximation,  $\varepsilon = a/R \ll 1$ , for the potential energy for internal modes given by eqn 6.7.6.

$$\delta W = \frac{\pi^2 B_\phi^2}{\mu_0 R_0} \int_0^a \left[ \left( r \frac{d\xi}{dr} \right)^2 + (m^2 - 1)\xi^2 \right] \left( \frac{n}{m} - \frac{1}{q} \right)^2 r dr + O(\varepsilon^2), \quad 6.10.1$$

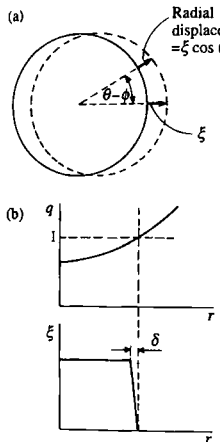


Fig. 6.10.1 Showing (a) the displacement of a circular flux surface for an  $m = 1$  perturbation and (b) the radial dependence of  $\xi$  for an unstable displacement.

where  $\xi$  is the amplitude of the radial displacement, and the small term is  $O(\varepsilon^2)$  with respect to the leading term.

It is seen that for  $m = 1$ , a rigid displacement,  $\xi = \text{constant}$ , reduces the integrand to its minimum value, that is zero. However, eqn 6.10.1 is for internal modes having  $\xi = 0$ , the surface terms in  $\delta W$  having been neglected. Thus a constant  $\xi$  is not allowed. Figure 6.10.1(b) shows a form for  $\xi(r)$  which is wholly internal and makes  $\delta W$  zero. The displacement is rigid within the  $q = 1$  surface and zero outside. The inevitable distortion between these two regions is taken up at the  $q = 1$  surface. At this surface the perturbation has the same helicity as the magnetic field. Consequently the energy change can be made arbitrarily small by localization of  $d\xi/dr$ . From eqn 6.10.1 the resulting energy change is proportional to

$$\int_{-\delta}^0 \left( \frac{\xi}{\delta} \right)^2 (q' x)^2 dx$$

and this is  $O(\delta)$ , going to zero as  $\delta \rightarrow 0$ .

It is seen therefore that, in the leading order in  $\varepsilon$ , the minimum value of  $\delta W$  is zero. Thus the mode is marginally stable to this order and stability depends upon the sign of the  $O(\varepsilon^2)$  term in eqn 6.10.1. This term can be straightforwardly calculated for a cylinder but the toroidal result is

completely different. This can be seen from the toroidal  $\delta W$  which can be written in the form

$$\delta W = \left(1 - \frac{1}{n^2}\right) \delta W_C + 2\pi^2 R \xi_0^2 \frac{B_\phi^2}{\mu_0} \left(\frac{r_1}{R}\right)^4 \delta \tilde{W}_T,$$

where  $\xi_0$  is the zero order constant displacement described above,  $\delta W_C$  is the value of  $\delta W$  for a cylinder,  $\delta \tilde{W}_T$  is a dimensionless representation of the toroidal contribution and  $r_1$  is the radius of the  $q = 1$  surface. It is seen that for the important  $n = 1$  mode only the toroidal term remains.

The toroidal calculation is quite complicated. For the large aspect-ratio case with simple current profiles and small  $r_1/a$  the result for  $\delta \tilde{W}_T$  is

$$\delta \tilde{W}_T = 3(1 - q_0) \left( \frac{13}{144} - \beta_{p1}^2 \right), \quad 6.10.2$$

where

$$\beta_{p1} = \frac{\int_0^{r_1} (p - p_1) 2r \, dr}{(B_{\theta 1}^2 / 2\mu_0) r_1^2},$$

where  $p_1 = p(r_1)$  and, since  $q(r_1) = 1$ ,  $B_{\theta 1} = (r_1/R) B_\phi$ . Equation 6.10.2 gives instability for  $\beta_{p1} > 0.3$ . For larger  $r_1/a$  instability is predicted for lower values of  $\beta_{p1}$ , as shown in Fig. 6.10.2.

The result described above is dependent on the profiles having the assumed form. In particular it was assumed that the  $q$  profile is similar to that in Fig. 6.10.1. However, for  $q$  profiles which are flat within the  $q = 1$  surface the result is different. For  $m = n = 1$  the factor  $(n/m - 1/q)^2$  in

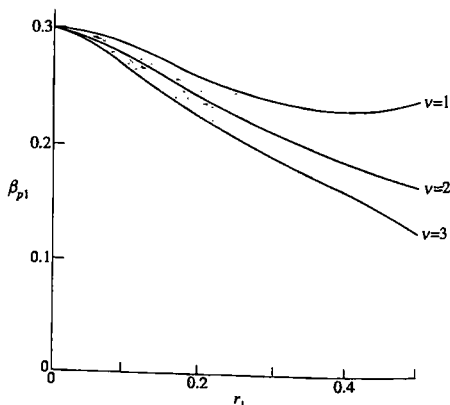
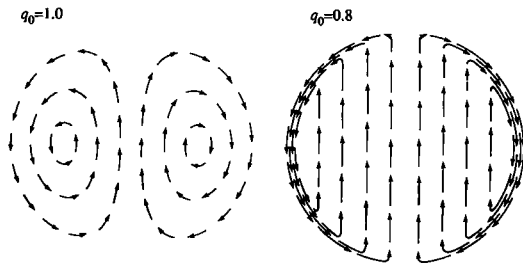


Fig. 6.10.2 Critical value of  $\beta_{p1}$  as a function of  $r_1$  for current profiles  $j = j_0(1 - (r^2/a^2))^\nu$ . (Bussac, M.N. et al., Phys. Rev. Lett. 35, 1638 (1975).)

eqn 6.10.1 becomes  $(1 - 1/q)^2$  and if  $q$  remains sufficiently close to 1 this factor is reduced to  $O(\varepsilon^2)$ . This invalidates the separation of the leading term in eqn 6.10.1 from the  $O(\varepsilon^2)$  term. When the analysis is carried out with the changed ordering a different type of instability is found. Physically the term involving  $(1 - 1/q)^2$  describes the stabilizing effect of magnetic field line bending, and the constant  $\xi$  solution allows this stabilizing effect to be avoided. When  $q \approx 1$  the line bending contribution becomes less important and is comparable with the destabilizing terms. The most unstable mode then takes the form of a convective cell as shown in Fig. 6.10.3 rather than a rigid shift. The magnetic field lines are almost parallel to the perturbation helix and the convection almost interchanges the field lines. For this reason this form of the  $m = 1$  instability is called a quasi-interchange instability.

When the  $m = 1$  mode is taken into account, the stability diagram 6.7.2 is modified to the form given in Fig. 6.10.4, further restricting the predicted stable region. The experimentally observed behaviour of the



**Fig. 6.10.3** Flow pattern of quasi-interchange ( $q_0 = 1.0$ ) and rigid shift ( $q_0 = 0.8$ ).

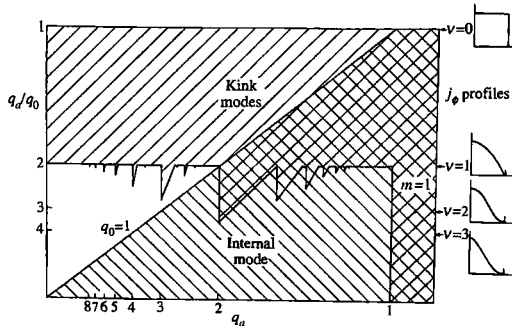


**Fig. 6.10.4** Kink stability diagram (Fig. 6.7.2) with inclusion of internal kink stability boundary.

$m = 1$  instability is described in Section 7.6 which deals with sawtooth oscillations.

## 6.11

### Resistive $m = 1$ modes

As with the  $m > 1$  kink mode described in Section 6.7 the introduction of resistivity extends the instability of the internal kink mode. The effect of resistivity again appears in the behaviour of a narrow layer about the resonant surface, in this case the  $q = 1$  surface. The degree of instability is measured by the potential energy  $\delta W$  characterizing the configuration. For  $\delta W < 0$  the ideal mode described in Section 6.10 is unstable. As  $\delta W$  is increased there is a range of small  $\delta W$  around zero where a resistive form of the kink mode is unstable. As  $\delta W$  becomes more positive the instability persists as an  $m = 1$  tearing mode. This behaviour is illustrated schematically in Fig. 6.11.1 which shows the dependence of the growth rate on  $\delta W$ .

The separation of the regimes is determined by a number of variables, the range over which the resistive kink is unstable having the ordering

$$\frac{\delta W}{\pi R \xi_0^2 (B_\theta q' r)_{q=1}^2 / \mu_0} \sim \left( \frac{\tau_H}{\tau_R} \right)^{1/3},$$

where  $\xi_0$  is the core displacement

$$\tau_H = \left( \frac{\sqrt{\mu_0 \rho}}{q' B_\theta} \right)_{q=1} \quad \text{and} \quad \tau_R = \left( \frac{\mu_0 r^2}{\eta} \right)_{q=1}.$$

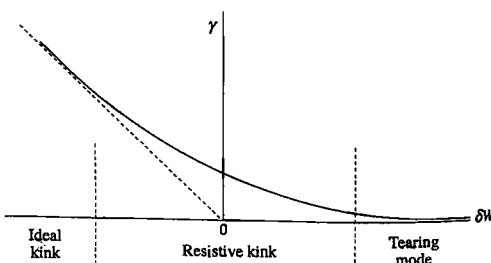


Fig. 6.11.1 Schematic graph of the dependence of the growth rate of the  $m = 1$  mode on  $\delta W$ , illustrating the transition from the ideal kink ( $\delta W < 0$ ) to the tearing mode ( $\delta W > 0$ ) through the resistive kink mode.

In all cases the basic eigenfunction has the form of the ideal mode, that is

$$\xi = \xi_0 \quad r < r_1, \quad \xi = 0 \quad r > r_1, \quad 6.11.1$$

where  $q(r_1) = 1$ . The resistive kink and the tearing mode will now be described in turn.

### Resistive $m = 1$ kink mode

In the resistive layer, Ohm's law and the equation of motion take the forms derived for the tearing mode layer as given by eqn 6.8.11 and eqn 6.8.15 without the small  $dj_\phi/dr$  term. With  $m = n = 1$  these equations can be expanded around  $r = r_1$  to obtain

$$\tilde{\eta} \frac{d^2\tilde{\psi}}{dx^2} = \tilde{\gamma}\tilde{\psi} + \tilde{\gamma}x\tilde{\xi}, \quad 6.11.2$$

$$\tilde{\gamma}^2 \frac{d^2\tilde{\xi}}{dx^2} = x \frac{d^2\tilde{\psi}}{dx^2}, \quad 6.11.3$$

where

$$\tilde{\psi} = -\frac{\psi}{q'(r_1)B_\theta(r_1)}, \quad \tilde{\xi} = \frac{v_r}{\gamma r_1},$$

$$x = \frac{r - r_1}{r_1} \quad \text{and} \quad \tilde{\gamma} = \gamma \tau_H.$$

The solution of eqns 6.11.2 and 6.11.3 which matches the outer solutions given by eqns 6.11.1 is

$$\tilde{\xi} = \frac{1}{2}\xi_0 \left( 1 - \operatorname{erf} \frac{x}{\sqrt{2}\tilde{\eta}^{1/3}} \right),$$

where

$$\operatorname{erf}(s) = \frac{2}{\sqrt{\pi}} \int_0^s e^{-\sigma^2} d\sigma,$$

and the eigenvalue is given by

$$\tilde{\gamma} = \tilde{\eta}^{1/3}.$$

Thus the growth rate of the resistive kink instability is

$$\tilde{\gamma} = \frac{(q/B_\theta/\sqrt{\mu_0\rho})_{r_1}^{2/3}}{(\mu_0 r^2/\eta)_{r_1}^{1/3}} \quad 6.11.4$$

and this may also be written

$$\gamma = \tau_H^{-2/3} \tau_R^{-1/3}.$$

It is seen that the growth rate is closer to the mhd time than the resistive time. If  $q$  is assumed to be parabolic around the axis and  $r_1$  is sufficiently

### 6.11 Resistive $m = 1$ modes

small,  $q'(r_1) = 2(1 - q_0)/r_1$ . Using Spitzer resistivity and noting that  $B_\theta(r_1) = (r_1/R)B_\phi$ , eqn 6.11.4 then gives

$$\gamma = \frac{6 \times 10^3}{T_e^{1/2}(n/10^{20})^{1/3}} \left( \frac{(1 - q_0)B_\phi}{r_1 R} \right)^{2/3} T_e \text{ in keV}, \quad 6.11.5$$

where  $n$  is the electron density. For typical experimental values the growth time  $\gamma^{-1}$ , lies in the range

$$\gamma^{-1} = \frac{10 - 100}{(1 - q_0)^{2/3}} \mu\text{s}, \quad 6.11.6$$

small tokamaks having the faster growth rates.

#### The $m = 1$ tearing mode

As with the higher  $m$ -number tearing modes described in Section 6.8, the growth rate of the  $m = 1$  tearing mode is determined by matching outer solutions to resistive layer solutions using the quantity  $\Delta'$ . The resulting relationship is the same and is given by eqn 6.8.20 which, for the present case, takes the form

$$\Delta' = \sqrt{2} \left( \Gamma \left( \frac{3}{4} \right) \right)^2 \gamma^{5/4} \tau_H^{1/2} \tau_R^{3/4} / r_1, \quad 6.11.7$$

where  $\Gamma$  is the gamma function and  $\sqrt{2} \left( \Gamma \left( \frac{3}{4} \right) \right)^2 = 2.12$ . It remains to calculate  $\Delta'$ , and for  $m = 1$  this can be done analytically.

The radial component of  $\nabla \times (E + v \times B) = 0$  together with  $B_r = -(1/r) \partial \psi / \partial \theta$  gives

$$\psi = B_\theta(q - 1)\xi.$$

For  $r < r_1$ ,  $\xi$  can be separated into its zero order constant part  $\xi_0$ , and an additional part  $\xi_1$ , so that

$$\psi = B_\theta(q - 1)(\xi_0 + \xi_1). \quad 6.11.8$$

Now  $\xi_1$  is localized to the  $q = 1$  surface and its value can be obtained from the equation for  $\delta W$  which from eqn 6.10.1 can be written

$$\delta W(r) = \pi^2 R \int_0^r \left[ \frac{B_\theta^2}{\mu_0} r (1 - q)^2 \left( \frac{d\xi}{dr} \right)^2 + g\xi^2 \right] dr. \quad 6.11.9$$

The minimizing solution is given by the Euler-Lagrange equation

$$\frac{d}{dr} \left( \frac{B_\theta^2}{\mu_0} r (1 - q)^2 \frac{d\xi}{dr} \right) = g\xi \quad 6.11.10$$

and substitution of eqn 6.11.10 into eqn 6.11.9 followed by an integration by parts gives

$$\delta W(r) = \pi^2 R \frac{B_\theta^2}{\mu_0} r (1 - q)^2 \xi \xi'. \quad 6.11.11$$

Since  $\xi \xi' = \xi_0 \xi'_1$ , and close to  $r = r_1$ ,  $(1 - q) = -q'x$ , eqn 6.11.11 can be written

$$\xi'_1 = \frac{\delta W(r_1)}{\pi^2 R(rq'^2 B_\theta^2 / \mu_0)_{r_1} \xi_0} \frac{1}{x^2}$$

so that

$$\xi_1 = -\frac{\delta W}{\pi^2 R(rq'^2 B_\theta^2 / \mu_0)_{r_1} \xi_0} \frac{1}{x}. \quad 6.11.12$$

Thus, using eqns 6.11.8 and 6.11.12, the forms of  $\psi$  and  $\psi'$  as  $r \rightarrow r_1$  are

$$\psi = (B_\theta q')_1 x \xi_1$$

$$\psi' = (B_\theta q')_1 \xi_0$$

so that

$$\left(\frac{\psi'}{\psi}\right)_{r_1-\epsilon} = \frac{\xi_0}{x \xi_1}. \quad 6.11.13$$

Substitution of eqn 6.11.12 into eqn 6.11.13 now gives

$$\left(\frac{\psi'}{\psi}\right)_{r_1-\epsilon} = -\frac{\pi^2 R(rq'^2 B_\theta^2 / \mu_0)_{r_1} \xi_0^2}{\delta W}. \quad 6.11.14$$

For  $r > r_1$  the constant term in  $\xi$  is zero and consequently

$$\left(\frac{\psi'}{\psi}\right)_{r_1+\epsilon} = 0. \quad 6.11.15$$

Equations 6.11.14 and 6.11.15 give the required  $\Delta'$ ,

$$\Delta' = \frac{\pi^2 R(rq'^2 B_\theta^2 / \mu_0)_{r_1}}{\delta W / \xi_0^2}. \quad 6.11.16$$

The tearing mode only occurs for  $\delta W > 0$ , giving the unstable positive sign to  $\Delta'$ . The stabilizing role of  $\delta W$  in  $\Delta'$  is clear from its appearance in the denominator of eqn 6.11.16. The growth rate of the  $m = 1$  tearing mode is now obtained by substituting for  $\Delta'$  from 6.11.16 in eqn 6.11.7. This gives

$$\gamma = 0.55 \left( \frac{\pi^2 R(rq'^2 B_\theta^2 / \mu_0)_{r_1}}{\delta W / \xi_0^2} \right)^{4/5} \tau_H^{-2/5} \tau_R^{-3/5}. \quad 6.11.17$$

As  $\delta W \rightarrow 0$  the mode is transformed into the resistive kink instability described earlier and when  $\delta W < 0$  the mode becomes an ideal kink.

**Unified  $m = 1$  theory**

The ideal kink, resistive kink, and  $m = 1$  tearing mode can be analysed together. This results in a single dispersion relation from which the three modes appear in different limits. The dispersion relation is

$$\gamma \tau_H = \delta W_H \left\{ \frac{1}{8} \left( \frac{\gamma}{\gamma_{\eta k}} \right)^{9/4} \frac{\left( \frac{\Gamma(\gamma/\gamma_{\eta k})^{3/2} - 1}{4} \right)}{\left( \frac{\Gamma(\gamma/\gamma_{\eta k})^{3/2} + 5}{4} \right)} \right\}, \quad 6.11.18$$

where a normalized potential energy is defined by

$$\delta W_H = \frac{\delta W / \xi_0^2}{2R(r)B_\theta q')^2 / \mu_0}$$

and  $\gamma_{\eta k}$  is the resistive kink growth rate  $\tau_H^{-2/3} \tau_R^{-1/3}$ . The ideal kink is obtained in the limit of large  $\gamma$ . The quantity inside the outer bracket in eqn 6.11.18 is then equal to one, and  $\gamma = \delta W_H / \tau_H$ . As  $\delta W_H \rightarrow 0$  eqn 6.11.18 gives the resistive kink growth rate,  $\gamma = \gamma_{\eta k}$ , since  $\Gamma(x) \rightarrow 1/x$  as  $x \rightarrow 0$ . The tearing mode occurs for  $\delta W_H > 0$ , that is ideal mode stable, and for  $\gamma \ll \gamma_{\eta k}$ . The gamma functions are then equal to constants and the growth rate becomes that of the tearing mode as given by eqn 6.11.17.

## 6.12

### Localized modes

In the description of kink modes in Section 6.7 it was implicitly assumed that the mode numbers  $m$  and  $n$  were small.

High- $n$  modes tend to be strongly stabilized by the energy required to perturb the magnetic field. However, the component of the equilibrium magnetic field which is involved in the stabilization is that parallel to the wave vector, and at a resonant surface this component is zero. Consequently high- $n$  modes are concentrated around their resonant surfaces, that is the surfaces for which  $q = m/n$ . In the limit  $n \rightarrow \infty$  the number of such surfaces becomes infinite and their separation approaches zero. This limit allows a theoretical treatment of localized modes.

In a cylindrical plasma the relevant part of the potential energy  $\delta W$  is

$$\delta W = \pi \int \frac{1}{k^2} \left[ \frac{1}{2\mu_0} \left( \mathbf{k} \cdot \mathbf{B} \frac{d\xi_r}{dr} \right)^2 + \frac{k_z^2}{r} \frac{dp}{dr} \xi_r^2 \right] r dr,$$

where  $\mathbf{k} = (m/r)\mathbf{i}_\theta + k_z \mathbf{i}_z$ . A necessary condition for the contribution of the stabilizing first term to exceed that of the destabilizing pressure

gradient term is given by the Suydam criterion

$$\frac{rB_t^2}{8\mu_0} \left(\frac{q'}{q}\right)^2 > (-p'),$$

where here,  $q'/q = (B_z/rB_\theta)'/(B_z/rB_\theta)$ .

In a tokamak the situation is much more complicated. The principal difference is that, unlike the cylinder, the effective curvature of the magnetic field lines changes sign along their length. On the inner side of the torus the curvature is away from the plasma and is stabilizing whereas on the outer side it is toward the plasma and is destabilizing. Calculation of stability involves the appropriate averaging of these curvatures for the most unstable displacement.

For a large aspect-ratio tokamak of circular cross-section the analogous criterion for stability is the Mercier criterion

$$\frac{rB_\phi^2}{8\mu_0} \left(\frac{q'}{q}\right)^2 > (-p')(1 - q^2). \quad 6.12.1$$

The term  $p'q^2$  represents the stabilizing contribution of the average curvature of the toroidal magnetic field. For  $q > 1$  this is sufficiently large that the resultant curvature is good and a negative pressure gradient is stabilizing.

Inequality 6.12.1 is only a necessary stability condition. This is because the toroidal geometry has only been partially allowed for. A complete treatment requires that the perturbations be more fully optimised to extract the free energy associated with the destabilizing curvature on the outer side of the torus. The resulting instabilities are called ballooning modes and these are described in the following section.

## 6.13

### Ballooning modes

The localized modes described in Section 6.12 are stabilized when the appropriate average curvature of the magnetic field lines with respect to the pressure gradient is sufficiently stabilizing. The curvature is stabilizing on the inner (smaller  $R$ ) side of the torus and destabilizing on the outer side of the torus, as shown in Fig. 6.13.1. At low pressures the average effect is stabilizing provided  $q > 1$ . However, if the pressure gradient is too high a different situation arises. It is then possible for the perturbation to be concentrated in the region of destabilizing curvature. The potential energy thus released can be greater than that required for the line bending inherent in the variation of the perturbation along a field line. The resulting instability is the ballooning mode.

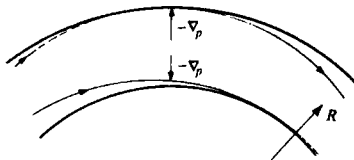


**Fig. 6.13.1** Showing the stabilizing curvature on the inner side of the torus and the destabilizing curvature on the outer side.

The ballooning instability is quite complex, but it is possible to estimate the conditions for ballooning to be important from the following simple picture. The destabilizing energy available from the pressure gradient is

$$\delta W_d \sim \frac{-dp/dr}{R_c} \xi^2,$$

where  $R_c$  represents the destabilizing curvature of the magnetic field line and  $\xi$  the radial displacement. The energy required for line bending is

$$\delta W_s \sim k_{\parallel}^2 (B_{\phi}^2 / \mu_0) \xi^2,$$

where  $\pi/k_{\parallel}$  characterizes the length parallel to the magnetic field over which the displacement varies. This is given by the distance along a field line from the inside to the outside of the torus and so  $k_{\parallel}$  is of order  $1/qR$ . Thus, taking  $R_c$  to be the radius of curvature of the toroidal magnetic field ( $\sim R_0$ ) is seen that ballooning becomes important when the pressure gradient is sufficiently large that

$$\frac{dp}{dr} \sim \frac{B_{\phi}^2 / \mu_0}{q^2 R_0}$$

corresponding to an ordering  $\beta \sim \varepsilon/q^2$  where  $\varepsilon$  is the inverse aspect-ratio.

The determination of ballooning mode stability starts from the equation for  $\delta W$  in the limit of large mode number. This is written in an orthogonal coordinate system  $(\psi, \chi, \phi)$  based on the magnetic surfaces.

The poloidal flux  $\psi$  labels the magnetic surface,  $\chi$  is an angle around the surface and  $\phi$  is the toroidal angle. There is freedom to choose the measure of the coordinate  $\chi$ . The poloidal area element of the coordinate system is given by  $J d\psi d\chi$ ,  $J$  being the Jacobian.

In this coordinate system the required expression for  $\delta W$  is

$$\begin{aligned} \delta W = \frac{\pi}{\mu_0} \int & \left[ \frac{B^2}{R^2 B_p^2} |k_{\parallel} X|^2 + R^2 B_p^2 \left| \frac{1}{n} \frac{\partial}{\partial \psi} k_{\parallel} X \right|^2 \right. \\ & \left. - 2\mu_0 \frac{dp}{d\psi} \left( \frac{\kappa_n}{RB_p} |X|^2 - \frac{i f B_p}{BB_{\phi}} \kappa_s \frac{X \partial X^*}{n \partial \psi} \right) \right] J d\chi d\psi. \quad 6.13.1 \end{aligned}$$

The perturbation  $X$  is defined by  $X = RB_p \xi_{\psi}$  where  $B_p$  is the poloidal magnetic field and  $\xi_{\psi}$  is the displacement normal to the flux surface.

The operator  $ik_{\parallel}$  is defined by  $ik_{\parallel} = (JB)^{-1}(\partial/\partial\chi + i\nu)$  where  $n$  is the toroidal number and  $\nu = JB_{\phi}/R$ .  $\kappa_n$  and  $\kappa_s$  are the normal and geodesic components of the magnetic field line curvature, the geodesic curvature being the curvature of the field line within the magnetic surface. The first and second terms give the energy involved in bending the magnetic field lines and the third and fourth terms give the energy arising from the coupling of the pressure gradient with the normal and geodesic curvatures. The first and third terms correspond to the contributions used in the introductory description of ballooning given above. To relate the coordinates to the more familiar variables of cylindrical geometry,  $\psi$  corresponds to the radial coordinate  $r$ , and  $\chi$  to  $\theta$ .

Minimization of eqn 6.13.1 leads to an Euler equation. This equation can be solved by extending the periodic variable  $\chi$  to the infinite range  $-\infty < y < +\infty$  and using the eikonal transformation

$$X = F \exp \left( -in \int^y v d\chi \right)$$

to give

$$\begin{aligned} \frac{1}{J} \frac{d}{dy} \left\{ \frac{1}{JR^2B_p^2} \left[ 1 + \left( \frac{R^2B_p^2}{B} \int^y \frac{\partial v}{\partial \psi} d\chi \right)^2 \right] \frac{\partial F}{\partial y} \right\} \\ + \frac{2\mu_0}{RB_{\phi}} \frac{dp}{d\psi} \left( \kappa_n - \frac{fRB_p^2}{BB_{\phi}} \kappa_s \int^y \frac{\partial v}{\partial \psi} d\chi \right) F = 0. \end{aligned} \quad 6.13.2$$

Marginally stable states will have solutions which are zero at  $y \rightarrow \pm\infty$  but have no other zeros. The condition for instability is that a solution of eqn 6.13.2 which is zero at  $y \rightarrow -\infty$  has a zero for a finite value of  $y$ . A symmetric solution for a marginally stable case is shown in Fig. 6.13.2.

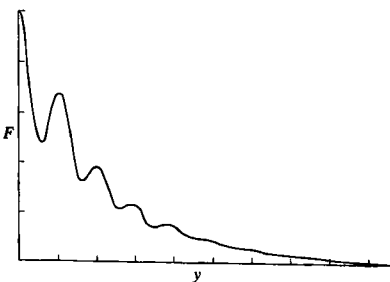


Fig. 6.13.2 Solution of eqn 6.13.2 for a marginally stable configuration.

**6.14****Ballooning stability**

Calculation of stability against ballooning modes requires the solution of eqn 6.13.2 at each flux surface. Usually the stability of a set of representative surfaces is determined by numerical computation.

A simple model which can be analysed more directly is the large aspect-ratio tokamak with circular flux surfaces. In the calculation of  $\delta W$  for this case it is assumed that the equilibrium has  $\beta \sim (a/R)^2$ . However, instability occurs for  $(r dp/dr)/(B^2/2\mu_0) \sim a/R$ . The results obtained are therefore formally only applicable when the local pressure gradient is enhanced. Nevertheless this model brings out important results and provides a conceptual framework for discussing ballooning modes.

For this case  $\delta W$  takes the form

$$\delta W = \int \left[ (1 + \Lambda^2) \left( \frac{dF}{d\theta} \right)^2 - \alpha (\Lambda \sin \theta + \cos \theta) F^2 \right] d\theta, \quad 6.14.1$$

where

$$\Lambda = s\theta - \alpha \sin \theta$$

$$s = \frac{r}{q} \frac{dq}{dr} \quad \text{and} \quad \alpha = -\frac{2\mu_0 R q^2}{B^2} \frac{dp}{dr},$$

$s$  being the surface average magnetic shear and  $\alpha$  a measure of the pressure gradient responsible for the instability. The term proportional to  $(dF/d\theta)^2$  represents the stabilizing effect of line bending and the  $\alpha \cos \theta F^2$  term gives the destabilizing effect of the pressure gradient coupled with the  $\cos \theta$  dependent normal curvature of the magnetic field lines. The  $\alpha \Lambda \sin \theta F^2$  term gives the shear dependent contribution arising from the geodesic curvature,  $\Lambda$  being related to the shear by the equation

$$\frac{d\Lambda}{d\theta} = s - \alpha \cos \theta,$$

$\alpha \cos \theta$  giving the  $\theta$  dependence of the shear around the surface.

Minimization of  $\delta W$  leads to the Euler equation

$$\frac{d}{d\theta} \left[ (1 + (s\theta - \alpha \sin \theta)^2) \frac{dF}{d\theta} \right] + \alpha [(s\theta - \alpha \sin \theta) \sin \theta + \cos \theta] F = 0 \quad 6.14.2$$

and the form of the solution of eqn 6.14.2 determines stability. Marginally stable surfaces have values of  $s$  and  $\alpha$  for which the solution has  $F \rightarrow 0$  at  $\theta \rightarrow \pm\infty$  and no other zeros. The stability boundary in  $(s, \alpha)$  space

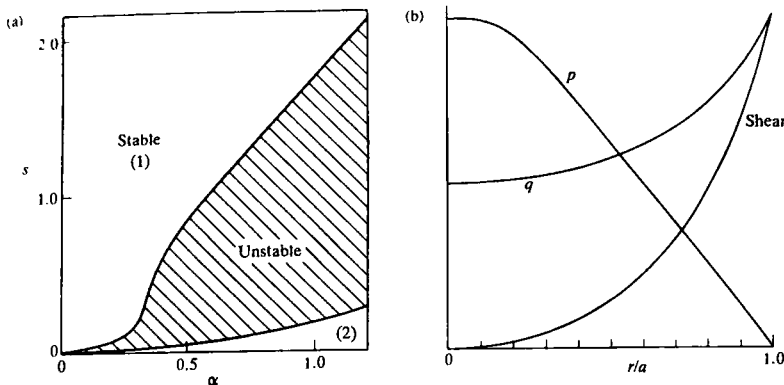


**Fig. 6.14.1** (a) Ballooning mode stability diagram for circular flux surfaces showing the first (1) and second (2) stability regions. (b) Marginally stable pressure for a parabolic current profile. The associated  $q$  and  $s$  profiles are also shown.

has been determined by numerical calculation and the result is shown in Fig. 6.14.1(a).

The stable region at large  $s$  and small  $\alpha$  is due to the stabilizing effect of line bending. As the shear is decreased and the pressure gradient is increased instability arises as might be expected. However, surprisingly, further reduction of shear leads to a second region of stability. The origin of this can be seen from eqn 6.14.1. In the limit of small  $s$  and large  $\alpha$ ,  $\delta W$  takes the stable positive definite form

$$\delta W = \int \alpha^2 \sin^2 \theta \left[ \left( \frac{dF}{d\theta} \right)^2 + F^2 \right] d\theta. \quad 6.14.3$$

The two terms in eqn 6.14.3 have arisen from the  $\theta$  dependent part of the shear as represented by the  $\alpha \sin \theta$  contribution to  $\Lambda$ . Thus the second region of stability is generated by a modification of the toroidal equilibrium at low shear caused by the pressure gradient.

Each point in the  $(s, \alpha)$  diagram corresponds to a particular flux surface in the plasma. Thus a complete plasma configuration is represented in this diagram by a line. This line will start from the origin and, in the case with zero pressure gradient and zero current density at the boundary, will terminate at the point  $\alpha = 0, s = 2$ .

For a given current profile the shear is determined. Figure 6.14.1(a) may then be used to calculate a pressure profile which is at the margin of stability for the first region at all radii across the plasma. Figure 6.14.1(b) gives the result for a parabolic current profile, this profile corresponding to a shear  $s = 1/(a/r)^2 - \frac{1}{2}$ .

The second region of stability can be obtained either by adjusting the required pressure and  $q$  profiles in a tokamak of usual cross-section, or by shaping the plasma boundary to a 'bean' shape as illustrated in Fig. 6.14.2.

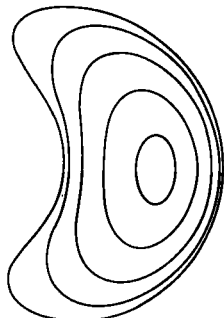


**Fig. 6.14.2** Bean configuration for achieving second region stability.

The introduction of resistivity leads to a resistive ballooning mode. In the absence of other physical effects such as finite Larmor radius and viscosity these modes are universally unstable but have a small growth rate.

The high- $n$  analysis described above does not comprehensively deal with ballooning modes. The low mode number pressure driven instabilities need to be treated separately. This becomes especially the case when the magnetic shear is small. The plasma is then susceptible to instability if the region with slowly varying  $q$  has a  $q$  value which is close to a rational value  $m/n$  for low mode numbers. These instabilities are often called infernal modes.

## 6.15

### Axisymmetric modes

Elongated tokamak plasmas are susceptible to an axisymmetric instability in which the plasma undergoes a basically vertical motion. Since the eigenmodes have a toroidal dependence  $e^{-in\phi}$  such instabilities are also called  $n = 0$  modes.

In the absence of a conducting wall a circular cylindrical plasma is neutrally stable to a rigid displacement. If however the plasma is elongated it is unstable to a motion in the direction of elongation. In the presence of a perfectly conducting wall there is a critical elongation for instability.

The practical case is more complicated. Firstly because of toroidal effects and secondly because of the presence of adjacent structures of varying degrees of conductivity.

The elongation of the plasma is due to currents in external conductors. A simple example of such an equilibrium is shown in Fig. 6.15.1. If the plasma is displaced there will be a perturbed vertical force on the plasma.

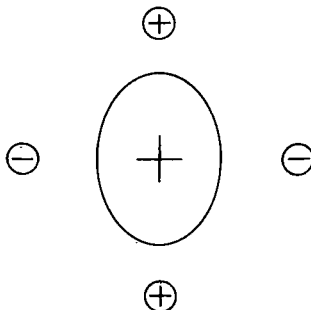


Fig. 6.15.1 Elongated equilibrium with external conductors.

resulting from the changed position of the plasma and from currents induced in the plasma and possibly in the external conductors. The plasma is unstable if the resultant force is such as to increase the displacement.

In simple cases the instability can be described in terms of the equilibrium magnetic field produced by external currents. Thus in the case of an almost circular, large aspect-ratio plasma without stabilizing conductors, stability is determined by the magnetic field decay index  $n = -(R/B_z) dB_z/dR$  where  $B_z$  is the vertical magnetic field and  $R$  the major radial coordinate. The criterion for stability is that  $n > 0$ .

The stability analysis for practical cases requires a numerical calculation. However, some insight may be obtained from simpler cases for which an analytic treatment is possible. Figure 6.15.2 shows a cylindrical elliptical plasma with minor and major semi-axes  $a$  and  $b$  surrounded by a perfectly conducting confocal elliptical shell with semi-axes  $a'$  and  $b'$ . The current density in the plasma is uniform. The criterion for stability against a vertical motion is

$$\frac{b-a}{b+a} < \left( \frac{b+a}{b'+a'} \right)^2. \quad 6.15.1$$

If this criterion is violated instability occurs on an inertial time-scale.

If the surrounding shell has a finite conductivity, failure to satisfy criterion 6.15.1 leads, as before, to an inertial instability. If, on the other hand, the criterion is satisfied, instability still results, but now with a growth rate related to the resistive penetration time of the shell,  $\tau_R$ . For large  $\tau_R$  the growth rate is given by  $\gamma = (D\tau_R)^{-1}$  where the quantity

$$D = \frac{b+a}{b-a} \left( \frac{b+a}{b'+a'} \right)^2 - 1$$

measures the extent to which criterion 6.15.1 has been satisfied.

It has been found from numerical calculations that there is a toroidal stabilizing effect. This increases the critical elongation at which there is a transition from inertial growth to growth on the resistive time-scale,  $\tau_R$ .

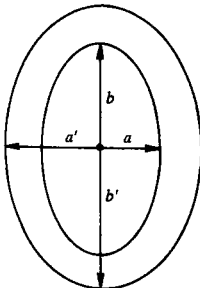
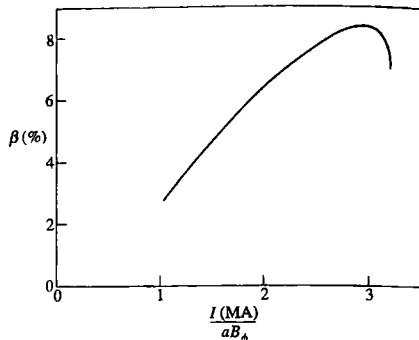


Fig. 6.15.2 Elliptical plasma and conducting shell.

## 6.16

### $\beta$ limit

$\beta$  is a basic inhd parameter measuring the confined pressure and, since there are inhd instabilities driven by pressure gradients, it is natural to expect that  $\beta$  will be subject to a stability limitation. However, the concept of a  $\beta$  limit is not precise. Stability depends on profiles, and any optimization introduces the questions of which modes of instability to include and what mode numbers to allow. Furthermore there is



**Fig. 6.16.1** Early calculation of  $\beta$  limit for JET showing an approximate linear dependence on  $I/aB_\phi$  for  $I/aB_\phi \lesssim 3$ . (Wesson, J.A. in Stringer, T.E. *Computer Physics Communications* **24**, 337 (1981).)

uncertainty as to the severity of the nonlinear consequences of the various modes. Nevertheless the intrinsic usefulness of a concise analytic  $\beta$  limit in assessing possible tokamak performance has prompted a number of investigations.

The simplest case to consider is the limit imposed by ballooning modes. In the introductory discussion of ballooning mode stability in Section 6.13 it was seen that a limit  $\beta \sim \varepsilon/q^2$  might be expected, where  $\varepsilon = a/R$ . In terms of operational parameters this would mean  $\beta \sim (I/aB_\phi)^2/\varepsilon$ . However, this is not correct.

The first indication of the correct scaling came from optimized stability calculations for JET. When plotted against  $I/aB_\phi$ , the  $\beta$  dependence was found to have the essentially linear dependence shown in Fig. 6.16.1. The turnover at high  $\beta$  is due to the instability, at low  $q$ , of the low- $m$  modes included in the calculation.

The approximate linear scaling can be understood by considering the case of a large aspect-ratio circular plasma. The definition of  $\beta$  is

$$\beta = \frac{2\pi \int_0^a pr dr}{\pi a^2 B_\phi^2 / 2\mu_0}$$

and integrating by parts

$$\beta = \frac{2\mu_0}{a^2 B_\phi^2} \int_0^a -\frac{dp}{dr} r^2 dr. \quad 6.16.1$$

The pressure gradient stability limit plotted in Fig. 6.14.1 can be represented reasonably well by a straight line as shown in Fig. 6.16.2. This line is  $s = 1.67\alpha$ , which can be written

$$-\frac{dp}{dr} = 0.30 \frac{B_\phi^2}{\mu_0 R} \frac{r}{q^3} \frac{dq}{dr}.$$

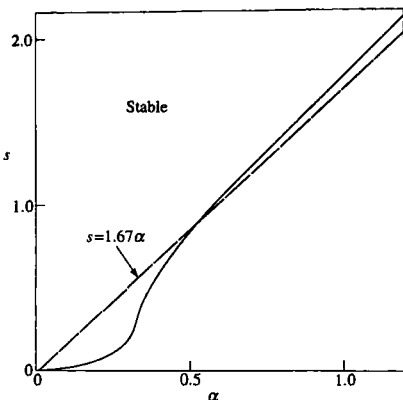


Fig. 6.16.2 Approximation of the ballooning mode stability boundary  $s(\alpha)$  by a straight line.

An equilibrium which satisfies this equation everywhere has a  $\beta$  determined by eqn 6.16.1, that is

$$\beta = -0.30 \frac{1}{Ra^2} \int_0^a \frac{d}{dr} \left( \frac{1}{q^2} \right) r^3 dr. \quad 6.16.2$$

Taking the central value of  $q$  to be limited, this  $\beta$  is maximized with respect to  $q(r)$  by a configuration in which the current is carried within a constant current density central region, outside which the current is zero. This limiting case is physically unrealistic but it serves to illustrate the essential features. The shear is stabilizing, and is most effective in producing a high  $\beta$  when used to produce a pressure gradient in the outer region. In the inner region where  $dq/dr = 0$  the contribution to the integral in eqn 6.16.2 is zero, and the whole contribution comes from the outer region,  $(r/a) > (q_0/q_a)^{1/2}$ , where  $q = q_a(r/a)^2$ . Taking  $q_0 = 1$ , eqn 6.16.2 gives

$$\beta_m = 1.2 \frac{\epsilon}{q_a^2} (q_a^{1/2} - 1). \quad 6.16.3$$

Equation 6.16.3 for the maximum  $\beta$  has the expected  $\epsilon/q_a^2$  factor but the radial dependence resulting from optimization has introduced the further factor  $(q_a^{1/2} - 1)$ . The function  $\beta_m/\epsilon$  is plotted against  $1/q_a$  in Fig. 6.16.3 where it is seen that  $\beta_m$ , expressed as a percentage, is quite well represented by the linear relation

$$\% \beta_m = 28 \frac{\epsilon}{q_a}$$

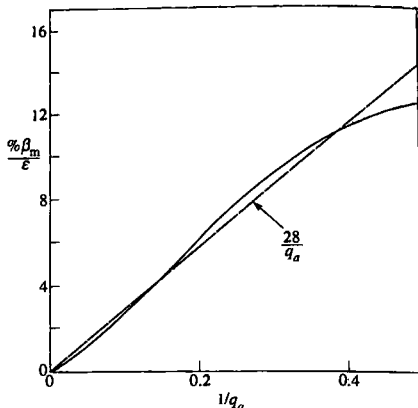


**Fig. 6.16.3** Plot of  $\beta_m/\epsilon$  as a function of  $q_a$  from eqn 6.16.3 together with straight line approximation.

or, in terms of operational variables,

$$\% \beta_m = 5.6 \frac{I}{a B_\phi}, \quad I \text{ in MA.}$$

This result is unrealistically optimistic, the current profile is singular and would be unstable to tearing modes. A more reasonable numerical value can be obtained by retaining the scaling

$$\% \beta_m = c \frac{\epsilon}{q_a} \quad 6.16.4$$

and calculating the value of  $c$  by substituting into eqn 6.16.2 the  $q(r)$  resulting from a parabolic current distribution with  $q_0 = 1$ , that is

$$q = \frac{1}{(1 - \frac{1}{2}r^2/a^2)}.$$

This current distribution is weakly unstable to kink modes but can be made stable by a small modification. The result is  $\beta = 0.077\epsilon$ . The constant  $c$  is now determined using the fact that for this case  $q_a = 2$ . Thus eqn 6.16.4 becomes

$$\% \beta_m = 15 \frac{\epsilon}{q_a}.$$

If this result is expressed in terms of the plasma current, using  $q_a = (B/R)(2\pi a^2/\mu_0 I)$ , the limit becomes

$$\% \beta_m = 3 \frac{I}{a B_\phi}, \quad I \text{ in MA.} \quad 6.16.5$$

Computer calculations by Sykes and by Troyon have shown this result to have wider applicability and to include elongated and D-shaped plasmas. The stability limit for a given configuration can be written

$$\% \beta_m = g \frac{I}{aB_\phi}, \quad I \text{ in MA},$$

where  $g$  is often called the Troyon factor. The value of  $\% \beta$  with  $g = 2.8$  is called the Troyon limit. The quantity

$$\beta_N = \frac{\% \beta}{I/aB_\phi}, \quad I \text{ in MA},$$

is called the normalized  $\beta$  and the stability limit is then expressed as  $\beta_N < g$ .

Experiments have been found to be limited to a  $\beta$  value around that given by eqn 6.16.5 except when the pressure and  $q$  profiles allow entry into the second region of stability. More generally however the current profile will not be close to the optimum. The optimization procedure led to concentration of the current toward the axis. This is the same as increasing the internal inductance  $\ell_i$ . Indeed the pre-optimization formula 6.16.2 can be rearranged to show the  $\ell_i$  dependence and in the simplest approximation this leads to a linear dependence on  $\ell_i$ .

This result is borne out experimentally and Fig. 6.16.4 shows a comparison of experimental results with the formula

$$\% \beta = 4\ell_i \frac{I}{aB}, \quad I \text{ in MA}. \quad 6.16.6$$

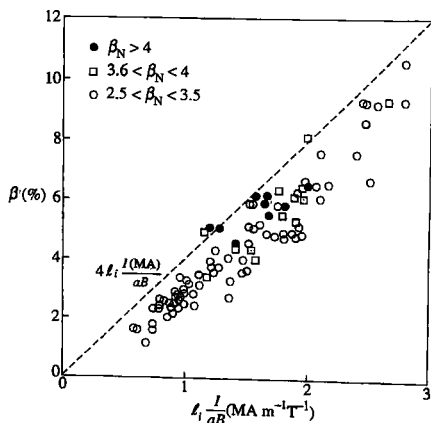


**Fig. 6.16.4** Experimental values of  $\beta$  plotted against  $\ell_i I / aB$  for discharges in DIII-D. (Taylor, T.S. et al., *Plasma Physics and Controlled Nuclear Fusion Research* (Proc. 13th Int. Conf. Washington 1990) Vol. 1 p. 177 I.A.E.A. Vienna (1991).)

When configurations are such that part of their profile lies in the second stability region the above considerations are not appropriate. Furthermore, for realistic configurations the stability diagram of Fig. 6.14.1 oversimplifies the situation, there being no exact stability relation  $s(\alpha)$ . However, in general terms the first and second stability regions are joined in the low shear region. This allows access to substantially higher  $\beta$  values, and  $\beta = 12.5\%$  has been achieved in DIII-D. The aspect-ratio scaling of the  $\beta$  limit favours low aspect-ratio and a  $\beta$  of 40% was obtained in the START experiment described in Section 11.19.

## Bibliography

An excellent account of ideal mhd stability is given in the book *Ideal magnetohydrodynamics* by Freidberg, J.P. Plenum Press, New York (1987). The book *MHD instabilities* by Bateman, G. MIT Press (1978) includes a detailed discussion of tokamak stability, and this subject is reviewed in the article Wesson, J.A. Hydromagnetic stability of tokamaks, *Nuclear Fusion* **18**, 87 (1978). A useful set of reprints is included in the book by Jeffrey, A. and Tanuti, T. *Magnetohydrodynamic stability and thermonuclear containment*, Academic Press, New York (1966). A general article on ideal mhd stability is given in the chapter, *Hydromagnetic stability of a plasma* by Kadomtsev, B.B. in *Reviews of plasma physics* (ed. Leontovich, M.A.) Vol. 2 Consultants Bureau, New York (1966). The book *Theory of toroidally confined plasmas* by White, R.B., Imperial College Press, London (2001) has several chapters devoted to stability.

### Mhd stability

In the early work the stability problems were made tractable by employing the large aspect-ratio expansion. The references to these contributions will be given under the appropriate headings below. The solution for general geometry became possible when numerical techniques were introduced in Sykes, A. and Wesson, J.A. Two-dimensional calculation of tokamak stability. *Nuclear Fusion* **14**, 645 (1974). Later developments of computational methods are described in

Grimm, R.C., Greene, J.M., and Johnson, J.L. Computation of the magnetohydrodynamic spectrum in axisymmetric toroidal confinement systems. *Methods of computer physics* Vol. 16 p. 253. Academic Press, New York (1976); and Gruber, R., Troyon, F., Berger, D., Bernard, L.C., Rousset, S., Schreiber, R., Kerner, W., Schneider, W., and Roberts, K.V. Erato stability code. *Computer Physics Communications* **21**, 323 (1981).

The codes referred to in the above papers deal with ideal mhd. An extension to resistive instabilities is described in Charlton, L.A. et al. Compressible linear and nonlinear resistive mhd calculations in toroidal geometry. *Journal of Computational Physics* **86**, 270 (1990).

### Energy principle

The original papers are

Bernstein, I.B., Frieman, A.E., Kruskal, M.D., and Kulsrud, R.M. An energy principle for hydromagnetic stability problems. *Proceedings of the Royal Society A223*, 17 (1958).

Hain, K., Lüst, R., and Schlüter, A. Zur Stabilität eines plasmas. *Zeitschrift für Naturforschung* **12A**, 833 (1957).

### Kink stability

The basic paper for tokamaks is Shafranov, V.D. Hydromagnetic stability of a current-carrying pinch in a strong longitudinal magnetic field. *Zhurnal Tekhnicheskoi Fiziki* **40**, 241 (1970) [Soviet Physics—Technical Physics] **15**, 175 (1970).

A summary with results for a range of cases is given in Wesson, J.A., Hydromagnetic stability of tokamaks. *Nuclear Fusion* **18**, 87 (1978).

### Tearing modes

The fundamental paper on resistive instabilities is Furth, H.P., Killeen, J., and Rosenbluth, M.N. Finite resistivity instabilities of a sheet pinch. *Physics of Fluids* **6**, 459 (1963).

A numerical treatment is given in

Wesson, J.A., Finite resistivity instabilities of a sheet pinch. *Nuclear Fusion* 6, 130 (1966).

### Tearing stability

Methods and results for the tokamak case are given in Furth, H.P., Rutherford, P.H., and Selberg, H. Tearing mode in the cylindrical tokamak. *Physics of Fluids* 16, 1054 (1973).

### Internal kink

The cylindrical problem is described in Shafranov, V.D. Hydromagnetic stability of a current carrying pinch in a strong toroidal field. *Zhurnal Tekhnicheskoi Fiziki* 40, 241 (1970) [*Soviet Physics—Technical Physics* 15, 175 (1970)].

Rosenbluth, M.N., Dagazian, R.Y., and Rutherford, P.H. Nonlinear properties of the internal kink instability in the cylindrical tokamak. *Physics of Fluids* 16, 1894 (1973).

The toroidal problem is analysed in Bussac, M.N., Pellat, R., Edery, D., and Soule, J.L. Internal kink modes in toroidal plasma with circular cross-section. *Physical Review Letters* 35, 1638 (1975).

### Resistive $m = 1$ modes

These modes are analysed in

Coppi, B., Galvao, R., Pellat, R., Rosenbluth, M., and Rutherford, P. Resistive internal kink modes. *Fizika Plasmy* 2, 961 (1976) [*Soviet Journal of Plasma Physics* 2, 533 (1976)].

Reviews of  $m = 1$  stability are given in

Ara, G. et al. Magnetic reconnections and  $m = 1$  oscillations in current carrying plasmas. *Annals of Physics* 112, 443 (1978).

and more recently in

Migliuolo, S. Theory of ideal and resistive  $m = 1$  modes in tokamaks. *Nuclear Fusion* 33, 1721 (1993).

### Localized modes

The original paper is

Mercier, C. Un critère nécessaire de stabilité hydromagnétique pour un plasma en symétrie de révolution. *Nuclear Fusion* 1, 47 (1960)

and a detailed derivation is given in

Mercier, C. and Luc, H. The magnetohydrodynamic approach to the problem of plasma confinement in closed magnetic configurations EUR 5127e. Commission of the European Communities, Luxembourg (1974).

The criterion for resistive localized modes was given by Mikhalovskij, A.B. The stability criteria for the g-mode in a toroidal plasma. *Nuclear Fusion* 15, 95 (1975).

The Suydam criterion is derived in

Suydam, B.R. Stability of a linear pinch. *Proceedings of Second United Nations International Conference on the Peaceful Uses of Atomic Energy*, Geneva 1958, Vol. 31, p. 157. Columbia University Press, New York (1959).

### Ballooning modes

The problem of ballooning modes in tokamaks was addressed in the papers

Todd, A.M.M., Chance, M.S., Greene, J.M., Grimm, R.C., Johnson, J.L., and Manickam, J. Stability limitations on high-beta tokamaks. *Physical Review Letters* 38, 826 (1977); and

Coppi, B. Topology of ballooning modes. *Physical Review Letters* 39, 939 (1977).

A precise derivation of the ballooning mode criterion is given in

Connor, J.W., Hastie, R.J., and Taylor, J.B. Shear, periodicity and plasma ballooning modes. *Physical Review Letters* 40, 396 (1978).

The instability of resistive ballooning modes was described by

Bateman, G. and Nelson, D.B. Resistive-ballooning-mode equation. *Physical Review Letters* 41, 1804 (1978).

The modification to ballooning mode theory for reduced shear is discussed in

Hastie, R.J. and Taylor, J.B. Validity of ballooning representation and mode number dependence of stability. *Nuclear Fusion* 21, 187 (1981);

and a numerical analysis of infernal modes is described in Manickam, J., Pomphrey, N., and Todd, A.M.M. Ideal mhd stability properties of pressure driven modes in low shear tokamaks. *Nuclear Fusion* 27, 1461 (1987).

A helpful discussion of ballooning modes is provided in the book

Freidberg, J.P. *Ideal magnetohydrodynamics*. Plenum Press, New York (1987).

### Ballooning stability

The large aspect-ratio ballooning mode eqn 6.10.1 was derived by

Connor, J.W., Hastie, R.J., and Taylor, J.B. Shear, periodicity and plasma ballooning modes. *Physical Review Letters* 40, 396 (1978)

and the curves of Fig. 6.10.1 were given by

- Lortz, D. and Nührenberg, J. Ballooning stability boundaries for the large aspect-ratio tokamak. *Physics Letters* **68A**, 49 (1978).
- The second region of stability is discussed in Greene, J.M. and Chance, M.S. The second region of stability against ballooning modes. *Nuclear Fusion* **21**, 453 (1981).

### Axisymmetric modes

- A simple model is described in Laval, G., Peillat, R., and Soule, J.L. Hydromagnetic stability of a current-carrying pinch with noncircular cross-section. *Physics of Fluids* **17**, 835 (1974).
- The subject is reviewed in Wesson, J.A. Hydromagnetic stability of tokamaks. *Nuclear Fusion* **18**, 87 (1978) and calculations for a practical case are given in Perrone, M.R. and Wesson, J.A. Stability of axisymmetric modes in JET. *Nuclear Fusion* **21**, 871 (1981).

### $\beta$ -limit

- Ideal mhd  $\beta$  limits are best determined using two-dimensional computer codes together with the ballooning mode criterion. This was first carried out in Bernard, L.C., Dobrott, D., Helton, R.J., and Moore, R.W. Stabilization of ideal mhd modes. *Nuclear Fusion* **20**, 1199 (1980). and an analysis of these results indicating the  $\beta$ -limit scaling was carried out by Wesson, J.A. and presented in

- Stringer, T.E. Mhd problems relevant to JET. *Computer Physics Communications* **24**, 337 (1981).
- The substantiation of the  $\beta$ -limit scaling is based on detailed calculations given in the papers Troyon, F., Gruber, R., Sauremann, H., Semenzato, S., and Succi, S. Mhd limits to plasma confinement. *Plasma physics and controlled fusion* **26** (1A) 209 (1984) (Proc. 11th European Physical Society Conference, Aachen, 1983); and Sykes, A., Turner, M.F., and Patel, S. Beta limits in tokamaks due to high- $n$  ballooning modes. *Proc. 11th European Conference on Controlled Fusion and Plasma Physics II*, 363 (Aachen 1983).
- An analytic explanation of the  $\beta$  limit was given by Wesson, J.A., and Sykes, A. Tokamak beta limit. *Nuclear Fusion* **25**, 85 (1985).
- A discussion of the experimental evidence and its relation to theory is presented in the paper.
- Strait, E.J. Stability of high beta tokamak plasmas. *Physics of Plasmas* **1**, 1415 (1994).
- Experimental results on the  $\beta$  limit are described in Troyon, F. and Gruber, R. A semi-empirical scaling law for the  $\beta$  limit in tokamaks. *Physics Letters* **110A**, 29 (1985); and McGuire, K.M. *Observations of finite- $\beta$  mhd in tokamaks*. Report PPPL-2134, Plasma Physics Laboratory, Princeton, N.J. (1984).
- The use of bean shaping to achieve higher  $\beta$  is described in Miller, R.L. and Moore, R.W. Shape optimization of tokamak plasmas to localized magnetohydrodynamic modes. *Physical Review Letters* **43**, 765 (1979).

# 7

# Instabilities

---

## 7.1

### Instabilities

From the earliest experiments it was clear that tokamaks are subject to a variety of macroscopic instabilities. Although these instabilities are not fully understood they can mainly be attributed to identifiable MHD modes.

During the current rise it is often found that bursts of magnetic oscillations occur. Following the discovery of this activity using magnetic coils around the plasma surface, the oscillations are called Mirnov oscillations. The azimuthal variation of the magnetic fluctuations allowed them to be identified with a decreasing sequence of  $m$  numbers. It seems likely that these modes are tearing modes, having resonant surfaces  $q = m$  close to the surface of the plasma. The magnetic oscillations also occur throughout the pulse and an example is shown in Fig. 7.1.1.

The plasma emits soft X-rays with an intensity dependent on the electron temperature and density. It is usually found that, at sufficiently large currents, this emission undergoes oscillations having a sawtooth time dependence as shown in Fig. 7.1.2. The cause of these oscillations is an  $m = 1$  instability occurring in the central region of plasma. The sawtooth form of the observed X-ray emission is attributed to repeated relaxation to a stable state, the relaxation being brought about by the instability.

The two instabilities described above do not prevent satisfactory operation of the tokamak. Disruptions, however, can involve a sudden loss

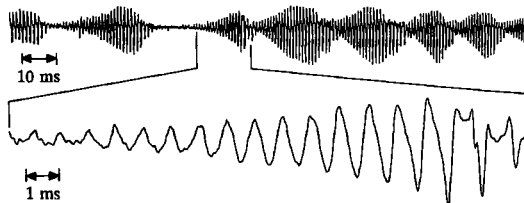


**Fig. 7.1.1** Oscillations of the poloidal magnetic field measured outside the plasma (JET).

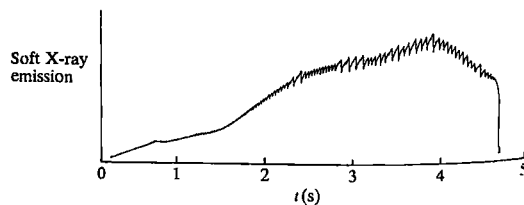


**Fig. 7.1.2** Sawtooth oscillations of the soft X-ray emission (JET).

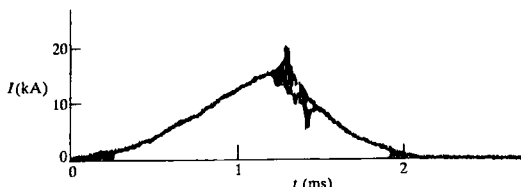


**Fig. 7.1.3** Early experimental observation of current collapse brought about by a plasma disruption. (Gorbulov, E.P. and Razumova, K.A. *Plasma Physics* 6, 515 (1964) from *Atomnaya Energiya* 15, 363 (1963))

of confinement and a rapid decay of the whole current, leading to an end of the discharge. An example of the current collapse is shown in Fig. 7.1.3. Disruptions occur over a range of conditions and are a complex phenomenon involving a sequence of only partially understood events. The instability usually involves the growth of an  $m = 2$  mode to a large amplitude.

The interaction of magnetic perturbations with the vacuum vessel reduces the rotation frequency of tearing modes and often leads to a locking to magnetic error fields. These error fields can then be the seed for the growth of an instability which leads to a full disruption.

It is seen that tearing modes play an important part in the observed instabilities. They appear in their nonlinear form in which the magnetic topology within the plasma is substantially changed. The simple nesting of the axisymmetric toroidal surfaces is broken and so-called magnetic islands appear in the plasma.

When islands of different modes interact, magnetic surfaces are destroyed. The magnetic field lines no longer map out a surface but instead follow a space filling trajectory. Under such conditions the field is said to be ergodic. Ergodicity clearly changes the confinement properties of the magnetic field and may lead to enhanced transport.

The axisymmetric instability described in Section 6.15 is stabilized by feedback control, but the loss of control can lead to a vertical instability followed by a disruption.

Other instabilities are driven by the presence of fast ions. The fishbone instability is caused by the fast ions resulting from neutral beam injection, and a potential instability for a reactor plasma is the toroidal Alfvén mode driven unstable by  $\alpha$ -particles.

The edge localized mode, or ELM, is a transient instability which can lead to a repetitive loss of energy from the plasma edge. It appears in various forms, the cause of which is not clear. Another instability which appears at the edge of the plasma is the so-called MARFE. This is not an mhd instability, its mechanism being the unstable energy loss arising from the increase of impurity radiation with reduced temperature at low temperatures.

## 7.2

### Magnetic islands

When mhd instabilities occur in a plasma they usually bring about a change in the magnetic topology. This occurs at surfaces with rational values of  $q$ . At these surfaces the magnetic field lines break and reconnect to form magnetic islands as illustrated in Fig. 7.2.1. The formation of magnetic islands is generally associated with resistive instabilities and particularly tearing modes. However, since the plasma is not perfectly conducting, island formation will occur to some extent in the nonlinear development of all mhd instabilities with a resonant surface in the plasma.

Consider the equilibrium configuration around a resonant surface,  $s$ , having  $q = q_s = m/n$ . The magnetic field lines on this surface define a helix. A perturbation resonant with this surface has the form  $\exp im\chi$  where

$$\chi = \theta - \frac{n}{m}\phi$$

is an angular coordinate orthogonal to the helix. The equilibrium field in this orthogonal direction is

$$B^* = B_\theta \left( 1 - \frac{n}{m}q(r) \right)$$

and close to the magnetic surface this may be written

$$B^* = - \left( B_\theta \frac{q'}{q} \right)_s z \quad 7.2.1$$

where  $z = r - r_s$ .

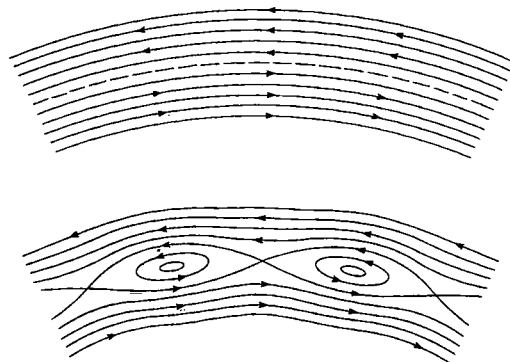


**Fig. 7.2.1** Reconnection of magnetic field producing magnetic islands.

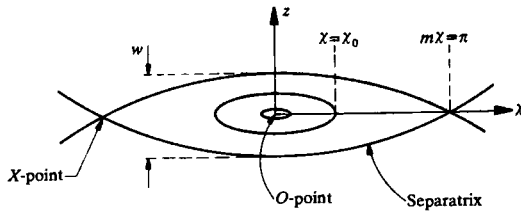


**Fig. 7.2.2** Geometry of magnetic field lines of a magnetic island in the  $(z, x)$  plane.

The geometry of the change in the magnetic topology arising from the resonant perturbation is illustrated in Fig. 7.2.2. It can be calculated by determining the trajectory of a magnetic field line from the equation

$$\frac{dr}{r_s d\chi} = \frac{B_r}{B^*}. \quad 7.2.2$$

The radial field perturbation may be taken to have the form

$$B_r = \hat{B}_r(r) \sin mx \quad 7.2.3$$

so that, substituting eqns 7.2.1 and 7.2.3 into eqn 7.2.2, the differential equation for the field line is

$$-\left(B_\theta \frac{q'}{q}\right) z dz = r_s \hat{B}_r \sin mx d\chi. \quad 7.2.4$$

Taking  $\hat{B}_r$  to be essentially constant over the radial extent of the island, integration of eqn 7.2.4 gives the equation of the field line

$$z^2 = \frac{w^2}{8} (\cos mx - \cos mx_0)$$

where

$$w = 4 \left( \frac{rq' \hat{B}_r}{mq' B_\theta} \right)_s^{1/2} \quad 7.2.5$$

is the width of the magnetic island and  $x_0$  is the value of  $\chi$  for which the field line under consideration has  $z = 0$ .

The magnetic field lines within the magnetic island lie on a set of helical magnetic surfaces with their own magnetic axis. This is labelled the *O-point* in Fig. 7.2.2. The island is bounded by the separatrix, the two parts of which meet at the *X-points*. The distance between the *X-points* is one full wavelength.

For  $B_\theta = \frac{1}{2}T$  and  $rq'/q = 1$  an  $m = 2$  mode would have an island size  $w/r = 4\hat{B}_r^{1/2}$ , so that a field perturbation  $\hat{B}_r = 10$  gauss would give

an island width  $\sim 10\%$  of the radius. The magnetic island can also be described in terms of the helical flux, defined by

$$B_r = -\frac{1}{r} \frac{\partial \psi}{\partial \chi} \quad B^* = \frac{\partial \psi}{\partial r}.$$

The flux function is

$$\psi = \psi_0(r) + \hat{\psi} \cos m\chi \quad 7.2.6$$

where

$$\psi_0 = -\frac{1}{2} \left( B_\theta \frac{q'}{q} \right)_s z^2 \quad 7.2.7$$

and

$$\hat{\psi} = \frac{r \hat{B}_r}{m}.$$

From eqns 7.2.6 and 7.2.7 the equation of a flux surface is

$$z^2(\psi) = \frac{2q}{B_\theta q'} (\hat{\psi} \cos m\chi - \psi)$$

and, since the separatrix has  $\psi = -\hat{\psi}$ , the full island width at  $x = 0$  is

$$w = 4 \left( \frac{q \hat{\psi}}{q' B_\theta} \right)_s^{1/2}. \quad 7.2.8$$

## 7.3 Tearing modes

In tokamak plasmas tearing modes take the form of magnetic islands. The growth of these islands is usually driven by the same destabilizing effect as linear tearing modes, that is current gradients in the plasma. However, the growth is limited by resistive diffusion, inertia generally playing a negligible role.

It is seen from eqn 7.2.5 that the island width is proportional to  $B_r^{1/2}$ , so that growth of the island implies growth of perturbed radial magnetic field. The island growth is limited by the diffusion of this field and a simple description of the growth can be obtained from the resistive diffusion equation for  $B_r$ . From Maxwell's equations 2.20.5 and 2.20.6 and

Ohm's law,  $E = nj$ ,

$$\frac{\partial \mathbf{B}}{\partial t} = \frac{\eta}{\mu_0} \nabla^2 \mathbf{B}. \quad 7.3.1$$

In the region of the magnetic island the radial derivatives are dominant and the  $r$  component of eqn 7.3.1 becomes

$$\frac{\partial B_r}{\partial t} = \frac{\eta}{\mu_0} \frac{\partial^2 B_r}{\partial r^2}. \quad 7.3.2$$

Integrating eqn 7.3.2 over the island width,  $w$ , and taking  $B_r$  to be approximately constant across the island, gives

$$w \frac{\partial B_r}{\partial t} = \frac{\eta}{\mu_0} \frac{\partial B_r}{\partial r} \Big|_{r_s-w/2}^{r_s+w/2}. \quad 7.3.3$$

Now from eqn 7.2.5,  $B_r \propto w^2$ , and eqn 7.3.3 can therefore be written

$$\frac{dw}{dt} \simeq \frac{\eta}{2\mu_0} \frac{1}{B_r} \frac{\partial B_r}{\partial r} \Big|_{r_s-w/2}^{r_s+w/2}. \quad 7.3.4$$

Since  $B_r$  is related to the helical flux function  $\psi$  by the relation  $B_r = -im\psi/r$ , eqn 7.3.4 can be written

$$\frac{dw}{dt} \simeq \frac{\eta}{2\mu_0} \frac{\psi'}{\psi} \Big|_{r_s-w/2}^{r_s+w/2}.$$

Introducing a generalization of the quantity  $\Delta'$  defined in the linear theory of Section 6.8,  $\Delta'(w)$  is defined by

$$\Delta'(w) = \frac{\psi'}{\psi} \Big|_{r_s-w/2}^{r_s+w/2} \quad 7.3.5$$

$\Delta'(w)$  being determined from the outer solutions. Equation 7.3.5 now gives the equation describing the growth of the island:

$$\frac{dw}{dt} \simeq \frac{\eta}{2\mu_0} \Delta'(w). \quad 7.3.6$$

Equation 7.3.6 is only an approximation. A more precise calculation has given

$$\frac{dw}{dt} = 1.66 \frac{\eta}{\mu_0} (\Delta'(w) - \alpha w) \quad 7.3.7$$

where the changed numerical factor results from the inclusion of the plasma flow and the term  $\alpha w$  comes from a more detailed treatment of the magnetic island region,  $\alpha$  being related to the local plasma properties.

It is seen that the saturated island size  $w_s$  is given by

$$\Delta'(w_s) = \alpha w_s.$$

A typical plot of  $\Delta'(w)$  and  $\alpha w$  is shown in Fig. 7.3.1. The simple relation  $\Delta'(w_s) = 0$  is often used to obtain an approximate value of  $w_s$ .

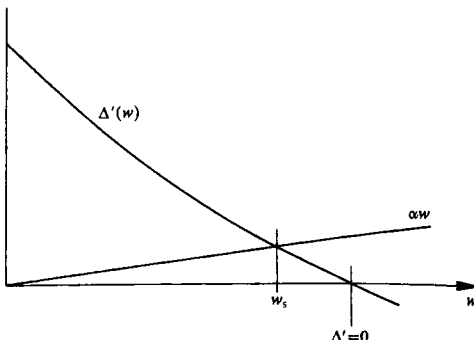


**Fig. 7.3.1** Plots of  $\Delta'(w)$  and  $\alpha w$ , which determine the growth and saturation of tearing mode magnetic islands.

The strongest instability usually occurs for the  $m = 2$  mode. This typically has a value of  $r_s \Delta'(0) \sim 10$ . Thus, from eqn 7.3.7, the characteristic growth time may be taken as  $\tau_g \sim 0.1(w/a)\tau_R$  where  $\tau_R$  is the resistive diffusion time  $(\mu_0/\eta)a^2$ ,  $a$ , being the plasma radius. Using Spitzer resistivity, given by eqn 2.16.2, this becomes

$$\tau_g \sim 4.5 \left( \frac{w}{a} \right) a^2 T_e^{3/2} \text{ s}, \quad T_e \text{ in keV.} \quad 7.3.8$$

In a small plasma with  $a = 0.25 \text{ m}$  and  $T_e = 500 \text{ eV}$ , an  $m = 2$  island covering 10% of the radius would have a typical growth time  $\sim 10 \text{ ms}$ . This is much shorter than the typical duration of the discharge and it is likely that the actual size of an island will be close to its saturation value. In a larger plasma at a higher temperature it is likely that the resistivity will be neoclassical and taking a neoclassical enhancement factor of 3, eqn 7.3.8 becomes

$$\tau_g \sim 1.5 \left( \frac{w}{a} \right) a^2 T_e^{3/2} \text{ s}, \quad T_e \text{ in keV.}$$

For  $w/a = 0.1$ , a plasma with a radius of 1 m would have a growth time of  $\sim 1 \text{ s}$  at 3 keV and 5 s at 10 keV. It is again likely that the islands will grow to their saturation size. However, at the time of disruption, conditions are dramatically different as described in Section 7.7.

### Internally driven tearing

In the analysis given above the tearing is driven by forces external to the island, and the drive is represented by the value of  $\Delta'$  as calculated from the tearing mode equation 6.8.7. It is also possible for a drive to arise within the island as a result of mechanisms which modify the current distribution.

The simplest case results from a modification of the resistivity within the island. This could for example arise from enhanced impurity radiation or the effect of an injected pellet. The behaviour is most clearly seen in terms of the helical flux, introduced in Section 7.2, and the associated helical current density  $j_h$ . Faraday's law gives the electric field  $E_h$  arising from the helical perturbation

$$\frac{\partial \psi}{\partial t} = E_h.$$

Thus using Ohm's law,  $E = \eta j$ ,

$$\frac{\partial \psi}{\partial t} = (\eta j)_h \quad 7.3.9$$

The simple tearing mode analysis, taking  $\eta$  constant, uses the term  $\eta j_h$  but if there is a helical perturbation,  $\eta_h$ , to the resistivity there is a further contribution. For small perturbations eqn 7.3.9 can then be written.

$$\frac{\partial \psi}{\partial t} = \eta j_h + \eta_h j. \quad 7.3.10$$

The new term is destabilizing when the resistivity in the island is increased. In the steady state  $\partial \psi / \partial t = 0$  and the helical current is given by

$$j_h = -\frac{\eta_h}{\eta} j \quad 7.3.11$$

and the associated flux perturbation which defines the resulting magnetic island is given by Ampère's law

$$\nabla^2 \psi = \mu_0 j_h.$$

### Neoclassical tearing modes

Another form of tearing mode arises from the modification of the bootstrap current as a result of the reduction in the temperature and density gradients which drive this current. Thus, when these gradients are reduced within the magnetic island by transport parallel to the field lines, the resulting reduction of the bootstrap current leads to a helical current  $\delta j_b$ .

The electric field perturbation is given by

$$E_h = \eta(j_h - \delta j_b), \quad 7.3.12$$

and the behaviour can be illustrated by considering the case of strong particle trapping. The bootstrap current is then proportional to the pressure

gradient, being given by

$$j_h = \frac{\varepsilon^{1/2}}{B_\theta} \left( -\frac{dp}{dr} \right).$$

If the pressure gradient were completely removed in the magnetic island the perturbed current would be  $\delta j_b = -j_h$  and eqn 7.3.12 becomes

$$E_h = \eta \left( \frac{1}{\mu_0} \frac{\partial^2 \psi}{\partial r^2} + \frac{\varepsilon^{1/2}}{B_\theta} \left( -\frac{dp}{dr} \right) \right). \quad 7.3.13$$

where eqn 7.3.11 has been used to give  $j_h$ .

Faraday's eqn 7.3.9 now becomes

$$\frac{\partial \psi}{\partial t} = \eta \left( \frac{1}{\mu_0} \frac{\partial^2 \psi}{\partial r^2} + \frac{\varepsilon^{1/2}}{B_\theta} \left( -\frac{dp}{dr} \right) \right). \quad 7.3.14$$

Integrating eqn 7.3.14 across the island and using the same procedure as that following eqn 7.3.2 leads to the equation for island growth

$$\frac{dw}{dt} = \frac{\eta}{2\mu_0} \left( \Delta' + \frac{\alpha \varepsilon^{1/2} \beta_p}{w} \right) \quad 7.3.15$$

where  $\beta_p = B_\theta^2 / 2\mu_0$ , and  $\alpha = (-8p'q/pq')$  and is usually positive. Figure 7.3.2 gives results of an experiment showing the growth in island width of a neoclassical tearing mode, followed by a decay as  $\beta_p$  falls.

The bootstrap term in eqn 7.3.15 approaches infinity as  $w$  approaches zero and for positive  $\alpha$  would always predict instability. The instability

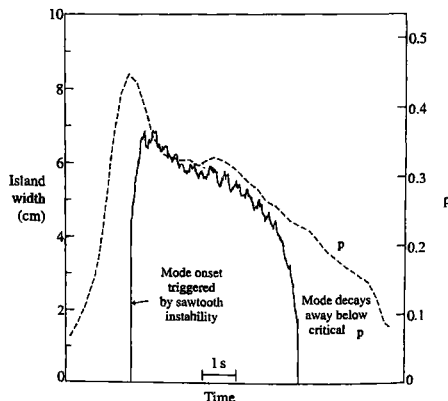


**Fig. 7.3.2** Evolution of a neoclassical tearing mode in JET. The mode is triggered by a sawtooth collapse and evolves in response to the changing  $\beta_p$ .

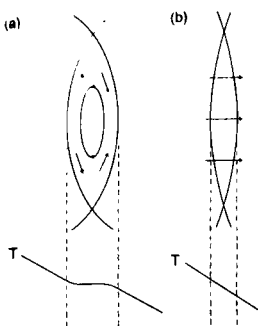


**Fig. 7.3.3** Schematic drawing showing how the magnetic island short-circuits the heat flow for a larger island (a) flattening the temperature, whereas the heat flow for a narrower island (b) is essentially unaffected.

would grow until the right hand side of eqn 7.3.15 is zero, giving the equation for the saturated island width

$$\Delta'(w) = -\frac{\alpha \varepsilon^{1/2} \beta_p}{w}$$

Equation 7.3.15 predicts that every resonant surface would be unstable. However, the connection length along the magnetic field within the island increases with decreased island width and for sufficiently small islands the connection length is too long for effective short-circuiting of the heat and particle fluxes, as illustrated in Fig. 7.3.3. This means that for small islands the destabilizing effect is essentially removed and that consequently there will be a critical 'seed' island size required for neoclassical tearing modes to grow.

The parallel thermal conduction will be effective in removing the radial temperature gradient when the radial heat flow parallel to the field is larger than the normal heat flow  $-\kappa_{\perp} dT/dr \sim \kappa_{\perp} \Delta T/w$  where  $\Delta T$  is the temperature difference across the island. The radial heat flow from parallel conduction is  $\sim -\kappa_{\parallel} (\Delta T/\Delta x) B_r/B$ , where the parallel connection length  $\Delta x \sim 4R/ns(w/r)$  with  $s = rq'/q$ ,  $n$  is the toroidal mode number and from eqn 7.2.5,  $B_r/B \sim ns w^2/16rR$ . Combining these results, the condition for temperature flattening is

$$w > \left( \frac{\kappa_{\perp}}{\kappa_{\parallel}} \right)^{1/4} \left( \frac{8rR}{ns} \right)^{1/2}.$$

With anomalous perpendicular transport the threshold island width for ion temperature flattening to occur is typically of the order of a millimetre. However, at typical tokamak temperatures collisions are ineffective in restricting the heat flow parallel to the magnetic field and the appropriate radial heat flux is  $n_j v_T \Delta T B_r/B$  where  $n_j$  is the particle density and  $v_T$  the thermal velocity. Under these conditions the critical island size for temperature flattening is

$$w > \left( \frac{16 \chi_{\perp} r R}{v_T n s} \right)^{1/3}$$

where the thermal diffusivity  $\chi_{\perp} = \kappa_{\perp}/n_j$ . The resulting critical island size for ion temperature flattening is typically of the order of a centimetre.

Another mechanism which could provide a critical island size for growth comes from the additional currents which flow due to ion polarization. These arise from the different  $E \times B$  flows of the ions and electrons because of the difference in the size of their banana orbits.

The neoclassical drive for the tearing of small islands is further reduced if the island width is less than the width of the ion banana orbit. This typically occurs for island widths less than 1–3 cms. The drive from electrons, with their much smaller banana orbit, is basically unaffected.

## 7.4

## Mirnov instabilities

Magnetic fluctuations found to occur during the current rise are shown in Fig. 7.4.1 together with their observed spatial structure. The decreasing values of the mode number,  $m$ , are associated with the decreasing value of  $q$  at the surface of the plasma. This decrease follows from the definition  $q_a = B_\phi a / B_{\theta a} R$  which together with the relation  $\mu_0 I = 2\pi a B_{\theta a}$  gives

$$q_a = \frac{2\pi a^2 B_\phi}{\mu_0 R I}.$$

As the current is increased there will be a negative current gradient at the plasma surface. During this time the integral  $q$  surfaces move outward toward the plasma edge, and tearing mode instabilities with  $m \simeq q_a$  are then expected to occur as the resonant surfaces meet the destabilizing current gradient.

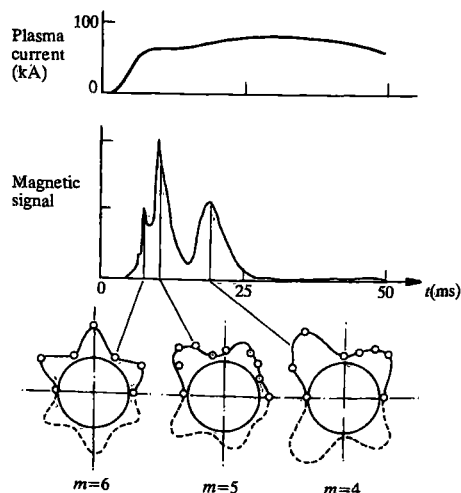


**Fig. 7.4.1** Development of magnetic fluctuations during the current rise, together with their spatial dependence indicating, successively, modes  $m = 6, 5$ , and  $4$ . (Mirnov, S.V. and Semenov, I.B., *Soviet Atomic Energy* **30**, 22 (1971), from *Atomnaya Energiya* **30**, 20 (1971).)

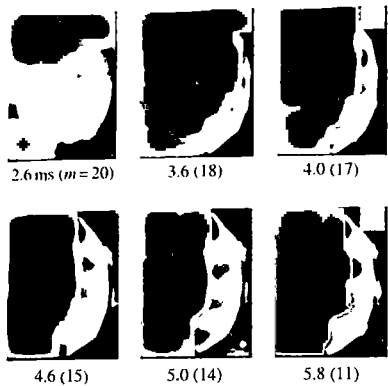
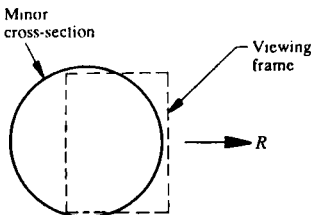


**Fig. 7.4.2** Cine photographs of instability observed during the current rise in the DITE tokamak. The time from the start of the pulse is given together with the poloidal mode number,  $m$ . (Goodall, D.J.H. and Wesson, J.A. *Plasma Physics* 26, 789 (1984).)



Further evidence of such instabilities has also been obtained by cine photography of the plasma during the current rise. The sequence of frames in Fig. 7.4.2 shows the deformation of the plasma surface. The associated mode numbers are found to satisfy  $m \approx q_a$ .

If the current rise is sufficiently fast, a skin current is produced. This gives rise to a  $q$  profile having a minimum. Such a profile allows two resonances for the same values of  $m$  and  $n$ , and this configuration leads to the possibility of a double tearing mode. The region between the resonant surfaces has only a small shear and if the surfaces are sufficiently close instability occurs. It is possible that this explains the observation that the skin current can penetrate faster than simple resistive diffusion would allow. This is described in Section 7.5.

Mirnov oscillations of the magnetic field can persist beyond the current rise and are then observed as continuous oscillations as illustrated in Fig. 7.1.1. They occur most strongly at low  $m$ , particularly  $m = 2$ . The magnetic fluctuations are measured on pick-up coils outside the plasma but they imply magnetic perturbations inside the plasma and these in turn imply the existence of magnetic islands on the surfaces having  $q = m/n$ .

The frequency of the oscillations is typically 1–10 kHz and the propagation velocity normally has the sign of the electron drift velocity. An extended theory of tearing modes including finite Larmor radius effects predicts a mode frequency of the order of the electron drift frequency  $\omega_{se} = (mT_e/eBrn_e)dn_e/dr$ , where  $m$  is the mode number. This is in rough agreement with the observations.

## 7.5

### Current penetration

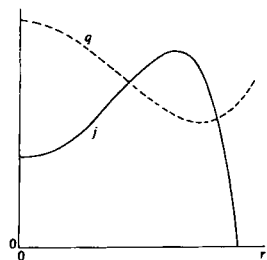


Fig. 7.5.1 Skin current profile and associated  $q$ -profile.

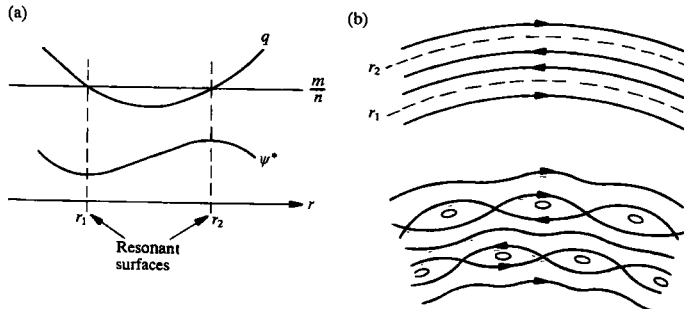
The instabilities which occur during the current rise are believed to be driven by the destabilizing current gradient. If the current rise is sufficiently rapid it is expected that these instabilities will cause anomalous penetration of the current. There is experimental evidence that such current penetration can occur.

In the absence of instability the normal current penetration time is of order  $\mu_0 a^2 / \eta$ . If the current rise is sufficiently slow compared to this time the current profile is peaked around the plasma axis. If however the current rise is faster, a skin current is formed as shown in Fig. 7.5.1. The corresponding  $q$  profile has a minimum. This allows two resonances close to the minimum having the same value of  $m/n$ , and the configuration is unstable if the two resonances are sufficiently close. The reason for this is easily seen from the tearing mode equation

$$\nabla^2 \psi = \frac{dj/dr}{\frac{B_\theta}{\mu_0} \left(1 - \frac{nq}{m}\right)} \psi.$$

The term on the right represents the effect of the current gradient and is destabilizing when the coefficient of  $\psi$  is negative. The region between the resonances combines a destabilizing current gradient and a small value of  $1 - (nq/m)$ .

It seems likely that this instability would accelerate current penetration. A simple model of the process is obtained by considering the helical flux of the equilibrium configuration associated with the resonant surfaces under consideration. This flux is that of the helical field  $B^*$  defined in Section 7.2,



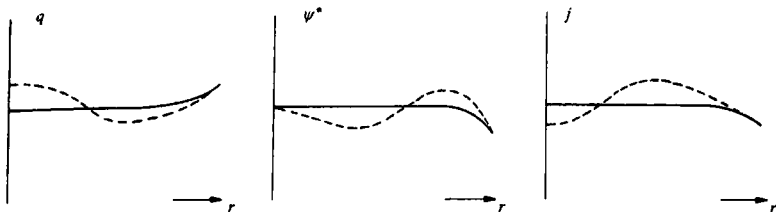


**Fig. 7.5.3** Graphs of  $q(r)$ ,  $\psi^*(r)$ , and  $j(r)$  before the instability (dashed lines) and after the instability (full lines). The instability flattens  $q$  and enhances the current penetration.

$$B^* = B_\theta \left( 1 - \frac{nq}{m} \right).$$

The flux function,  $\psi^*$ , associated with this field is defined by

$$\frac{d\psi^*}{dr} = B^*. \quad 7.5.1$$

It is seen that at resonant surfaces  $\psi^*$  has a maximum or a minimum. An example is given in Fig. 7.5.2(a). The resulting instability will initially produce islands on both of the resonant surfaces as shown in Fig. 7.5.2(b).

The instability ultimately leads to the resistive reconnection of parts of the flux, reducing the current gradient in the unstable region and flattening the  $q$  profile as illustrated in Fig. 7.5.3. It is seen that this produces an enhanced penetration of the current.

## 7.6

### Sawtooth oscillations

Under a wide range of operating conditions tokamaks are subject to a relaxation oscillation in the centre of the plasma. This appears as a sawtooth oscillation of the temperature and density and is also observed on other diagnostics. Figure 7.6.1 shows the sawtooth temperature variation in the centre of the plasma together with the inverted behaviour which occurs in the outer region. It is clear that during the stable ramp phase heating raises the temperature and that at the collapse the associated thermal energy is released to the outer part of the plasma in the form of a heat pulse.

The collapse is due to an instability which has an  $m = 1, n = 1$  structure and is associated with the existence of a  $q = 1$  surface in the plasma. The sawtooth oscillations usually start when a  $q = 1$  surface first appears. The  $q$  profile also oscillates with a sawtooth-like behaviour. During the ramp

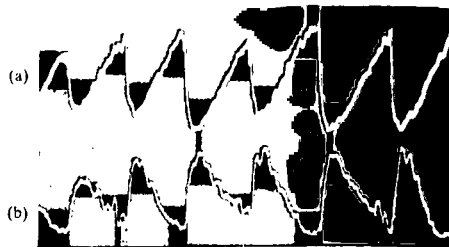


**Fig. 7.6.1** X-ray emission from (a) the central region of the plasma and (b) the outer region. (TPR.)

phase the current density around the axis increases and at the collapse it is reduced. Correspondingly the central value of  $q$  falls during the ramp and rises at the collapse. The change is typically a few per cent.

When the instability was first observed it was realized that the collapse phase was much shorter than the characteristic resistive time  $\tau_R = \mu_0 r_1^2 / \eta$  where  $r_1$  is the radius of the  $q = 1$  surface. Whereas  $\tau_R$  was typically 10 ms the collapse times could be  $\sim 100 \mu\text{s}$ . Thus if the collapse is associated with a magnetic rearrangement an explanation of its rapidity was required. A model which included a fast magnetic reconnection was proposed by Kadomtsev. Initially this model was thought to provide a complete explanation of the process but subsequent analysis has given rise to some difficulties. These will be examined later. First it is necessary to describe Kadomtsev's model.

#### Kadomtsev's model

The magnetic field lines on the  $q = 1$  surface define a helix and the reconnection process is concerned with the flux perpendicular to this helix. These magnetic field lines wind around the torus with  $d\theta/d\varphi = 1$ . A helical sheet which has  $d\theta/d\varphi = 1$  can be defined and this is shown in Fig. 7.6.2. The magnetic field lines at the  $q = 1$  surface lie in this sheet. For  $q \neq 1$  the field lines intersect the sheet, giving rise to a helical flux. Since the unit normal to the sheet has components

$$i_\theta = \frac{1}{\sqrt{1 + r^2/R^2}} \quad i_\varphi = -\frac{r/R}{\sqrt{1 + r^2/R^2}},$$

the leading order expression for the helical magnetic field,  $B^* = i_\theta B_\theta + i_\varphi B_\varphi$ , is

$$\begin{aligned} B^* &= B_\theta - (r/R) B_\varphi \\ &= B_\theta(1 - q), \end{aligned}$$

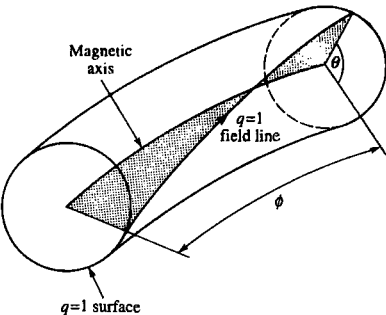


Fig. 7.6.2 Schematic diagram of the geometry of the helical sheet which contains the magnetic axis and the  $q = 1$  field line.

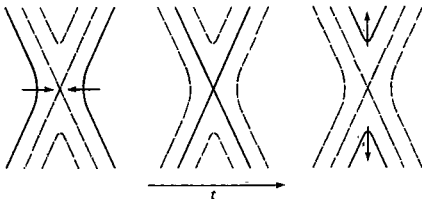


Fig. 7.6.3 The flux surfaces indicated by the full lines approach the X-point where they break and join to form a reconnected flux surface.

the corresponding helical flux being given by  $d\psi^*/dr = B^*$ . The helical field changes sign at the  $q = 1$  surface and in Kadomtsev's model the helical flux between the axis and the  $q = 1$  surface reconnects with an equal and opposite flux outside the  $q = 1$  surface. The process of reconnection is illustrated schematically in Fig. 7.6.3. The flux is progressively reconnected, the structure passing through the states illustrated by the sequence shown in Fig. 7.6.4. The reconnected flux forms an island which grows and ultimately takes the place of the original nested flux surfaces. The reconnection actually takes place in a narrow layer of thickness  $\delta$  as illustrated in Fig. 7.6.5. There is a current sheet in this layer driven by the electric field  $v_1 B^*$  where  $v_1$  is the velocity of the incoming plasma, thus

$$j \sim v_1 B^*/\eta. \quad 7.6.1$$

From Ampère's law

$$j \sim B^*/\mu_0 \delta \quad 7.6.2$$

and so, combining expressions 7.6.1 and 7.6.2

$$v_1 = \frac{\eta}{\mu_0 \delta}. \quad 7.6.3$$

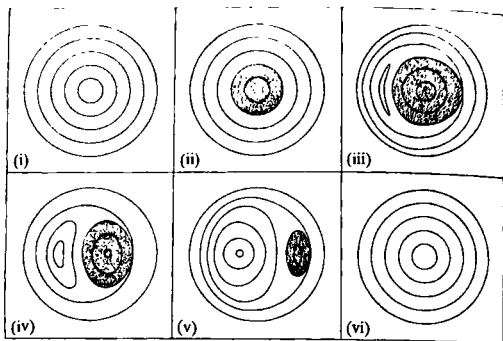


**Fig. 7.6.4** Development of the magnetic field structure during the sawtooth instability according to Kadomtsev's model (following Sykes, A. and Wesson, J.A., *Physical Review Letters* 37, 140 (1976)). The  $m = 1$  instability displaces the  $q < 1$  region (shown shaded) and restores  $q_0$  to a value  $> 1$ .

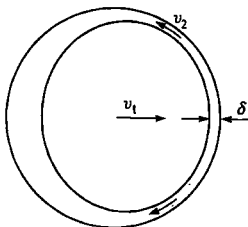


**Fig. 7.6.6** Reconnection takes place in narrow layer of thickness  $\delta$ , the central core moves into the layer with velocity  $v_1$  and the plasma leaves the layer with velocity  $v_2$ .

The displaced core transmits a pressure  $\sim B^{*2}/2\mu_0$  which causes a flow along and out of the layer with a velocity,  $v_2$ , given by

$$\rho v_2^2 \sim B^{*2}/2\mu_0. \quad 7.6.4$$

Taking the flow into the layer to take place over a length  $\sim r_1$ , continuity requires

$$v_1 r_1 \sim v_2 \delta \quad 7.6.5$$

and using relations 7.6.3 and 7.6.4 to eliminate  $v_1$  and  $v_2$  in 7.6.5 gives an expression for  $\delta$

$$\delta^2 \sim \frac{\eta}{\mu_0} \frac{\sqrt{\mu_0 \rho}}{B^*} r_1$$

or, writing

$$\tau_R = \frac{\mu_0 r_1^2}{\eta} \quad \text{and} \quad \tau_A = \frac{r_1}{B^*/\sqrt{\mu_0 \rho}},$$

$$\delta \sim \left( \frac{\tau_A}{\tau_R} \right)^{1/2} r_1. \quad 7.6.6$$

The characteristic time of the collapse is given by the time for the core to move across the radius  $r_1$ ,

$$\tau_K \sim \frac{r_1}{v_1}. \quad 7.6.7$$

The velocity  $v_1$  is obtained using relations 7.6.3 and 7.6.6 to give

$$\tau_K \sim (\tau_R \tau_A)^{1/2}, \quad 7.6.8$$

that is, the collapse time is the geometric mean of the resistive diffusion time and the Alfvénic time. Since  $\tau_A \ll \tau_R$  this model was able to bring the

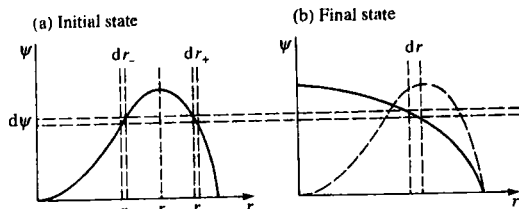


**Fig. 7.6.6** Mapping of the flux from the initial state to the final state in Kadomtsev's model of the sawtooth collapse.

predicted collapse time close to the experimental values. Typical values were  $\tau_R \sim 10 \text{ ms}$ ,  $\tau_A \sim 1 \mu\text{s}$  and  $\tau_K \sim 100 \mu\text{s}$ .

The reconnection of the flux can be calculated from the flux diagram for  $\psi(r)$  shown in Fig. 7.6.6. The flux element  $d\psi$  covers region  $dr_-$  at  $r = r_-$  on the inner side of the  $q=1$  surface and is equal to the flux covering  $dr_+$  at  $r = r_+$  on the outer side. These two fluxes will connect and will finally cover a region of  $dr$  at a radius  $r$ , both to be calculated. The reconnection starts at  $r_1$  where  $\psi = \psi_{\max}$ , and this first reconnected flux will form the new centre of the plasma. Thus  $\psi(0)$  in the final state is equal to  $\psi_{\max}$  in the initial state.

The incompressibility of the toroidal magnetic field means that the sum of the poloidal areas covered by the initial fluxes must equal the area covered by the final flux, that is

$$r dr = r_- dr_- + r_+ dr_+. \quad 7.6.9$$

From Fig. 7.6.6 it is seen that the initial radial dependence of the flux  $\psi(r)$  gives the inverse relations  $r_-(\psi)$  and  $r_+(\psi)$  and hence  $r_-^2(\psi)$  and  $r_+^2(\psi)$ . The final flux distribution,  $\psi_f$ , can therefore be calculated from  $r^2(\psi_f)$  after integrating eqn 7.6.9 to obtain

$$r^2(\psi_f) = \int_{r_1}^{r_+} dr_+^2(\psi) + \int_{r_-}^{r_1} dr_-^2(\psi).$$

This solution holds out to the radius at which the initial and final values of  $\psi$  are equal. Beyond this radius  $\psi$  is unchanged.

Figure 7.6.7 summarizes the changes in the magnetic field from the initial to the final state. It is seen that there are discontinuities at a radius somewhat larger than  $r_1$  and in particular that there is a discontinuity in  $B_{\theta f}$ , which implies a current sheet in the reconnected state.

Numerical simulations essentially verify Kadomtsev's model as a solution of the resistive MHD equations. However experimental results have arisen which seem to be in conflict with various aspects of the resistive MHD model and these will be described in turn.

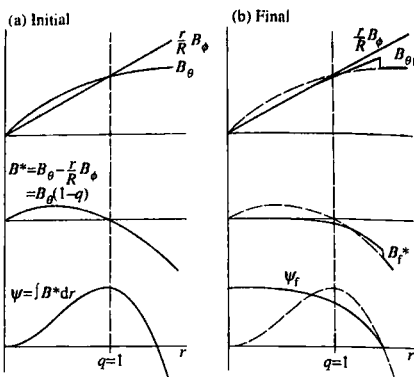


**Fig. 7.6.7** Changes of the magnetic fields and the helical flux in Kadomtsev's model of the sawtooth collapse, the subscript f referring to the final state.

### i) The collapse time

From relation 7.6.8 it is seen that the Kadomtsev collapse time is proportional to  $r_1^{3/2}$ . Thus for larger tokamaks such as JET there should be a large increase in the collapse time as compared with the smaller devices in which sawtooth oscillations were first observed. However, the collapse times are comparable. For JET the predicted collapse times are typically  $\sim 10$  ms whereas the observed times are  $\sim 100 \mu\text{s}$ . A re-examination of the theory led to the realization that in high temperature plasmas the electrical impedance of the reconnection layer is not resistive and that the reconnection is collisionless, the rate being determined by electron inertia.

Using relations 7.6.4 and 7.6.5

$$v_1 \sim \frac{\delta}{\tau_A} \quad 7.6.10$$

and substitution into the relation  $\tau = r_1/v_1$  gives the reconnection time

$$\tau \sim \frac{r_1 \tau_A}{\delta}. \quad 7.6.11$$

The physics of the reconnection now enters through the calculation of the layer thickness  $\delta$ .

When electron inertia is dominant there are two possible cases depending on the factor determining the duration of the electron's acceleration. In the simplest case the time is just the residence time as the plasma passes through the layer. In the other case the time is determined by 'collisionless viscosity'. The electrons travel along the magnetic field with their thermal velocity, and the shear in the magnetic field causes them to move out of phase with the accelerating electric field.

In the layer, Ohm's law can be written

$$v_1 B^* = \eta j + \frac{m}{ne^2} \left( \frac{dj}{dt} + \frac{v_{Te}}{\ell} j \right) \quad 7.6.12$$

where  $\ell$  is the length available for acceleration, which is  $\sim (B/B^*)r_1 \sim R/(1-q_0)$ . The dominant term in  $dj/dt$  is  $v \cdot \nabla j$  where  $v \cdot \nabla$  is approximately the residence time  $v_1/\delta$ . Since  $\eta = 1/\epsilon_0 \omega_p^2 \tau_e$  where  $\tau_e$  is the electron collision time, eqn 7.6.12 becomes

$$v_1 B^* \sim \frac{1}{\epsilon_0 \omega_p^2} \left( \frac{1}{\tau_e} + \frac{v_1}{\delta} + \frac{v_{Te}}{\ell} \right) j. \quad 7.6.13$$

Using eqn 7.6.2 for  $j$  and eqn 7.6.10 for  $v_1$ , eqn 7.6.13 gives the layer thickness  $\delta$

$$\delta \sim \frac{c}{\omega_p} \left( \frac{1}{\tau_e} + \frac{1}{\tau_A} + (1-q_0) \frac{v_{Te}}{R} \right)^{1/2} \tau_A^{1/2}. \quad 7.6.14$$

The relation 7.6.14 shows clearly the regimes in which the different impedances dominate. For electron inertia to be more important than resistivity requires  $\tau_A < \tau_e$  and typically this requires  $T(\text{keV}) > (n/10^{20})$ . The condition for electron viscosity to dominate electron inertia is  $(1-q_0)v_{Te}/R > 1/\tau_A$ , and this can be written approximately

$$\beta_e > \frac{m_e}{m_i} \quad 7.6.15$$

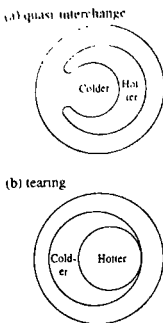
where  $\beta_e = nT_e/(B_\phi^2/2\mu_0)$ . The inequality 7.6.15 is easily satisfied and electron viscosity provides the dominant mechanism in high temperature tokamaks.

Substitution of 7.6.14 into 7.6.10 gives a general formula for the collapse time and shows the relationship of the three regimes.

$$\tau \sim \frac{\tau_A}{\left( \tau_A/\tau_R + (c/r_1 \omega_p)^2 (1 + (\beta_e/(m_e/m_i))^{1/2}) \right)^{1/2}}$$

### ii) Quasi-interchange

Because of the high electrical conductivity of the plasma the slow redistribution of current during the ramp phase would only lead to a small change in  $q$  in the central region, typically 0.02–0.05. If  $q$  were approximately equal to one following the collapse, as predicted by Kadomtsev's model, it would still be quite close to one at the end of the ramp phase when the instability occurred, giving a rather flat  $q$ -profile. A configuration with a sufficiently flat  $q$ -profile would be unstable to an ideal quasi-interchange instability with a fast growth rate. This argument is modified somewhat by the effect of neoclassical resistivity, which if it is operative, leads to a further localized reduction of  $q$  around the magnetic axis.



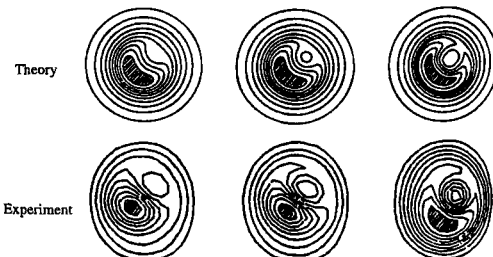
**Fig. 7.6.8** Showing the contrasting non-linear development for (a) the quasi-interchange and (b) the reconnecting tearing mode.

Figure 7.6.8 illustrates the difference between the form of a quasi-interchange instability and that of a reconnection. An identifying feature of the quasi-interchange is the formation of a cold bubble. When the JET soft X-ray images of the plasma during the collapse were examined they were found to agree with the quasi-interchange model. The comparison of a non-linear simulation of the quasi-interchange instability with the soft X-ray images in Fig. 7.6.9 makes the similarity clear. The initial JET soft X-ray diagnostic gave rather poor resolution but a subsequent high resolution system confirmed the earlier result. However, there is a problem with this interpretation of the collapse. This arises from the measurement of the  $q$ -profile, which will now be examined.

### iii) Measurement of $q_0$

When accurate measurements of  $q$  became possible they led to a number of difficulties. The first definitive measurement, using polarimetry, gave values of  $q_0$  well below one, typically between 0.7 and 0.8. This is in conflict with the calculation predicting only a small change from  $q_0 = 1$  during the ramp phase. Even more problematical, the value of  $q_0$  remains well below one during the whole sawtooth period as shown in Fig. 7.6.10. The difficulty is that, although the small change in  $q$  observed during the ramp phase is consistent with that calculated from resistive diffusion of the equilibrium,  $q_0$  remaining below one implies that full reconnection does not occur. It should be noted, however, that in some experiments measurements do give  $q_0$  close to one.

$q_0$  was measured in JET using both polarimetry and the motional Stark effect. Under conditions where the observed instability had the appearance of quasi-interchange the value of  $q_0$  was typically around 0.7, completely inconsistent with the requirement,  $q_0 \approx 1$ , for a quasi-interchange instability.



**Fig. 7.6.9** Comparison of a quasi-interchange simulation (P. Kirby) with the deformation as reconstructed from the soft X-ray emission on JET (R. Granetz).

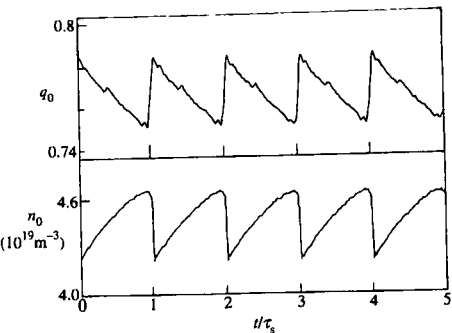


**Fig. 7.6.10** Time dependence of  $q_0$  during sawtooth oscillations on TEXTOR as measured by Faraday rotation. The noise level has been reduced by overlaying many sawteeth to give the averaged behaviour during the sawtooth period,  $\tau_s$ , shown in the figure. (Soltwisch, H. and Stodiek, W. presented at 29th Annual Meeting of A.P.S. Division of Plasma Physics, San Diego (1987).)

#### iv) The spontaneous onset

The sawtooth collapse is often preceded by growing oscillations. These oscillations arise from the finite frequency of the mode, and their presence indicates that the growth time is longer than the period. However, in other cases the instability appears without such precursors implying a sudden onset of the growth.

Whatever the cause of the instability, it would be expected that it would arise through a change in the equilibrium during the ramp phase. Instability would first arise at marginal stability and hence zero growth rate. The growth rate would then increase as the underlying equilibrium developed. However, the time for an equilibrium change to produce a configuration having a growth rate equal to that observed is very much longer than the sawtooth collapse time. In JET the discrepancy in these times is typically two orders of magnitude. This spontaneous onset of the instability is not understood.

#### v) Stability during the ramp phase

There is a difficulty in understanding the stability of the  $m = 1$  mode during the ramp phase if  $q_0$  is substantially below one. Such a configuration is expected to be unstable to the resistive kink mode which has a growth rate proportional to the two-thirds power of  $q'$  at the  $q = 1$  surface. A simple  $q$  profile gives a growth time of typically less than a millisecond while the ramp phase can be hundreds of milliseconds.

A possible explanation is that the  $q$  profile is flattened around the  $q = 1$  surface, and there is some experimental evidence for this. This flattening could be the result of the previous collapse phase. However no consistent model of this behaviour has been found.

### vi) The thermal collapse

If the magnetic reconnection process is not completed, as implied by  $q_0$  remaining well below one, it would be expected that the unconnected core would remain confined. However, the flattening of the temperature across the whole of the  $q < 1$  region is in conflict with this conclusion. A possible explanation seemed to be that, although the simple model predicts that the magnetic surfaces in the remnant core would remain nested, the magnetic surfaces become broken and the resulting ergodization could then allow the plasma energy to escape along the magnetic field lines.

However, a well-known phenomenon is the rapid inward movement of impurities into the core at the time of a sawtooth collapse. The timescale for this redistribution can be as short as the flattening of the temperature profile. If ergodization of the magnetic field were the explanation of the electron temperature collapse in the collapse time  $\tau_c$ , the electrons would travel a distance  $\sim v_{Te} \tau_c$  along the magnetic field lines during the collapse. For a 100  $\mu$ s collapse at a temperature of 10 keV the electrons would travel 4 km. Taking nickel impurity as an example, nickel atoms would have a thermal velocity 330 times smaller than that of the electrons. During the collapse they would therefore travel only 12 m along the field. Clearly they cannot reach the centre of the plasma on this timescale by motion along the ergodic field.

This result implies that the impurity inflow must be due to motion which is essentially in the poloidal plane and if the impurities move in this way it seems likely that the plasma electrons and ions do also. While there is no explanation of this behaviour it should be noted that such poloidal motion is precisely that observed in the soft X-ray, quasi-interchange like, images of the sawtooth collapse in JET.

It is seen from the above enumeration of the difficulties in explaining sawtooth behaviour that there is uncertainty about the  $q$  profile, both as to its central value and its shape. This directly leads to uncertainty as to the nature of the  $m = 1$  instability involved. From Sections 6.10 and 6.11 it is seen that the stability of the internal kink depends critically on the level of shear and therefore  $q_0$ , and that the resistive kink depends on the value of  $q'$  at the  $q = 1$  surface and therefore on the shape of the  $q$  profile around this surface.

It is remarkable that a phenomenon which initially appeared to have a simple and elegant explanation should give rise to such difficulties of understanding.

## 7.7

### Disruptions

The tokamak disruption is a dramatic event in which the plasma confinement is suddenly destroyed. In a major disruption this is followed by a

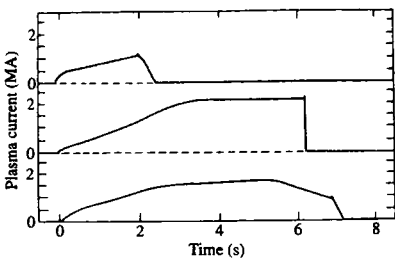


**Fig. 7.7.1** Current traces showing disruptions on the current rise, flat-top and current fall (JET).

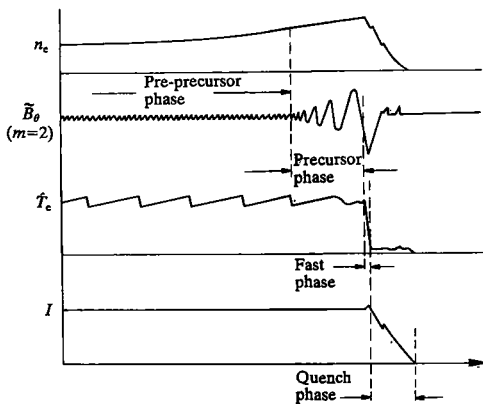


**Fig. 7.7.2** Showing typical time dependence of the  $m = 2$  magnetic fluctuations, central temperature, and plasma current during the period of a disruption. In this example the disruption is precipitated by a density increase as shown.

complete loss of the current as shown in Fig. 7.7.1. Disruptions pose a serious problem for tokamak development. This is firstly because they limit the range of operation in current and density, and secondly because their occurrence leads to large mechanical stresses and to intense heat loads.

The sequence of events is illustrated in Fig. 7.7.2. There are essentially four phases and these are summarized below. The physical processes involved are described in Section 7.9.

#### Pre-precursor phase

There is a change in the underlying conditions leading toward a more unstable configuration. This change is often clear, as in the case of

an increase in total current or plasma density. Sometimes however a disruption is precipitated without an identified change in the conditions.

#### Precursor phase

When the underlying change reaches a critical point there is an onset of mhd instability. This is most obvious in the growth of the magnetic oscillations of an  $m = 2$  mode which had previously been absent, or had saturated at a low amplitude. The time during which the growth occurs is variable but is typically  $\sim 10$  ms in medium sized tokamaks. Other low- $m$  modes are also observed.

#### Fast phase

After the mhd instability has undergone considerable growth a second critical point is reached at which much more rapid developments occur. The central temperature collapses on a timescale typically of the order of a millisecond. A rapid flattening of the radial current profile is observed and this gives rise to a characteristic short negative voltage pulse, typically 10–100 times the applied positive voltage.

#### Quench phase

Finally the plasma current decays to zero. The decay time depends upon the particular conditions and on the plasma position control but current decay rates greater than  $100 \text{ MA s}^{-1}$  occur.

## 7.8

### Causes of disruptions

There are several identified causes of disruptions. Operating limits for steady operation are imposed by both low- $q$  disruptions and density limit disruptions. These are thought to be due to unstable current profiles which lead to large amplitude tearing modes. These instabilities can also lead to disruptions if the current rise is too rapid. Another cause of disruptions is the existence of magnetic field errors which seem to provide a seed for the growth of tearing modes. Disruptions can also be caused by solid fragments which fall into the plasma. Finally, the vertical instability, described in Section 7.12, can end in a disruption.

In the absence of a detailed theoretical understanding of disruptions it is convenient to have an operation-based description which describes the operational limits. The low- $q$  and high-density limits can be combined in a diagram which was found by Hugill to give some pattern to the

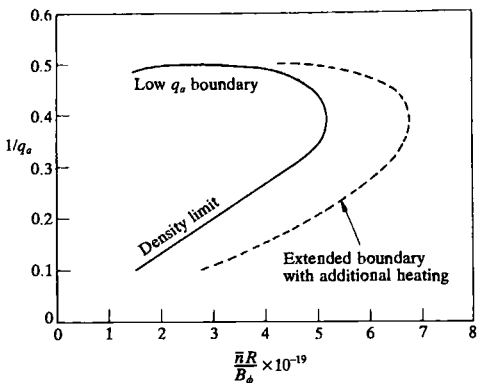


**Fig. 7.8.1** Typical Hugill diagram showing the operating regime as limited by disruptions.  $q_a$  is the safety factor at the surface of the plasma and  $\bar{n}$  the mean electron density. The parameter  $10^{-19}\bar{n}R/B_\phi$  is called the Murakami parameter.

experimental behaviour. In this diagram the boundary of operation as limited by disruptions is plotted against  $1/q_a$  and  $\bar{n}R/B_\phi$ , this latter parameter having been introduced by Murakami. Such a plot is shown in Fig. 7.8.1. It is found that disruptions generally restrict operation to a region  $q_a \gtrsim 2$ , and to electron densities such that  $(10^{-19}\bar{n}R/B_\phi)q_a$  is below a critical value in the range  $10\text{--}20\text{ m}^{-2}\text{ T}^{-1}$ . Some improvement in this density limit is found with the application of additional heating.

Using the relationship  $B_\phi/Rq_a = (\pi/5)J$ , where  $J = I_{MA}/\pi a^2$  is the average current density in megamps per square metre, the density limit can be written  $\bar{n}/10^{20} = (1\text{ to }2)(\pi/5)J\text{ m}^{-3} \sim 1\text{ J m}^{-3}$ .

Using data from a number of tokamaks Greenwald has generalized this empirical result to give a critical value  $\bar{n}/10^{20} = \kappa J$  where  $\kappa$  is the plasma elongation and  $J$  is now the average current density in megamps per square metre over the plasma cross-section. For an elliptical plasma  $J = I_{MA}/\pi ab$  and the critical density is then given by  $\bar{n}/10^{20} = I_{MA}/\pi a^2$ .

The basic causes of disruptions will now be examined in turn and the physics of the disruption process and its consequences will be described in the next section.

### Low- $q$ disruptions

The underlying cause for low- $q$  disruptions is probably the increasing incompatibility of stability of  $m = 1$  and  $m = 2$  modes as  $q_a$  is lowered. If the value of  $q_0$  is restricted by an  $m = 1$  sawtooth instability, then increasing the current, and hence lowering  $q_a$ , forces the  $q$  profile to be more unstable. This can be seen from Fig. 6.10.4 where the stability line  $q_0 = 1$  meets the  $m = 2$  kink stability boundary at  $q_a = 2$ .

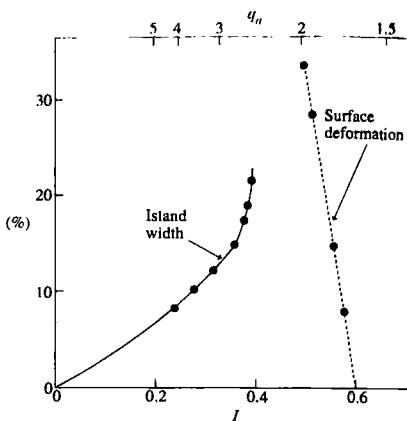


**Fig. 7.8.2** Saturated helical perturbations arising from the  $m = 2$  instability given as a percentage of the minor radius, ( $I$  is the total current normalized to  $\pi a^2 j_0$ ). For  $q_a > 2$  the graph gives the tearing mode island width, and for  $q_a < 2$  it gives the surface deformation of the kink mode with a conducting wall at  $r = 1.2a$ . (Sykes, A. and Wesson, J.A., *Plasma physics and controlled nuclear fusion research, Proc. 8th International Conference, Brussels 1980 Vol. 1, 237, I.A.E.A Vienna (1981)*.)

In the absence of the sawtooth instability, increasing the total current would increase the current density at the axis. However the sawtooth oscillations restrict  $q_0$  by flattening the central  $q$  profile. The natural consequence of this is an increased current gradient in the outer part of the plasma. As  $q_a = 2$  is approached the  $q = 2$  surface moves outward toward the surface of the plasma and sees an increasing destabilizing effect of this current gradient. The resulting tearing/kink instability then grows to a catastrophic level.

Numerical calculations have brought out this  $m = 1, m = 2$  incompatibility and a graph of the nonlinear amplitude of the tearing and kink modes is shown as a function of  $q_a$  in Fig. 7.8.2. It is seen that the calculated amplitude becomes very large as  $q_a$  approaches 2.

Evidence for the role of the  $m = 2$  mode was provided by an experiment in JET. The surface value,  $q_a$ , of the safety factor was reduced during the discharge until disruption occurred and this was repeated for a range of values of the Murakami parameter. The trajectories of the discharges up to the disruption are plotted in Fig. 7.8.3. It is seen that the disruptions all occur close to  $q_a = 2$ .

### Density limit disruptions

One mechanism for disruptions at high density results from the increase in impurity radiation as the density is increased. This radiation appears predominantly at the edge of the plasma where low  $Z$  impurity atoms are not fully stripped. The resulting cooling of the plasma produces a contraction

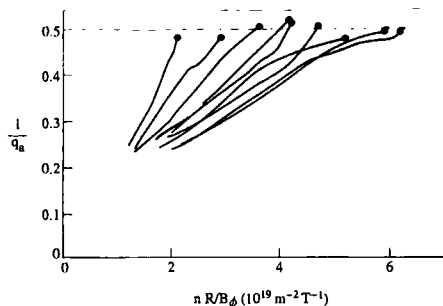


**Fig. 7.8.3** Trajectories of JET discharges in the Hugill diagram showing a disruption boundary close to  $q_a = 2$ . (Wesson, J.A. et al. *Nuclear Fusion* 29, 641 (1989).)

of the current profile which leads to an increased destabilizing current gradient inside the  $q = 2$  surface as described in Section 7.9.

As the density is increased and an increasing fraction of the heat loss is in the form of radiation, a smaller fraction is conducted out of the plasma boundary. In the limit of 100% radiation there is no conduction loss and the plasma becomes thermally disconnected from the boundary. It is then possible for the plasma to contract. As it does so the current profile adjusts and the value of  $q$  at the contracted edge of the plasma approaches an unstable value.

A simple model of the radiation process can be obtained from the energy balance equation applied to the outer region of the plasma,

$$\frac{d}{dr} \left( K \frac{dT}{dr} \right) = n_e n_z R(T) \quad 7.8.1$$

where  $K$  is the thermal conductivity, taken to be constant,  $n_e$  is the edge electron density,  $n_z$  is the impurity density and  $R(T)$  is the radiation function.

Multiplying both sides of eqn 7.8.1 by  $K(dT/dr)$  gives

$$\frac{1}{2} \frac{d}{dr} \left( K \frac{dT}{dr} \right)^2 = n_e n_z K R(T) \frac{dT}{dr}. \quad 7.8.2$$

Taking  $n_e$  and  $n_z$  to be constant and integrating eqn 7.8.2,

$$\mathcal{Q}_{\text{plasma}}^2 - \mathcal{Q}_{\text{edge}}^2 = 2n_e n_z K \int_0^\infty R(T) dT \quad 7.8.3$$

where the heat flux  $\mathcal{Q} = -KdT/dr$ ,  $\mathcal{Q}_{\text{plasma}}$  is the heat conducted from the core of the plasma, and  $\mathcal{Q}_{\text{edge}}$  is that conducted from the plasma at the edge. The form of  $R(T)$  is taken to be such that  $R$  is negligible at both the low edge temperature and the high internal plasma temperature so that the integral can effectively be taken over all  $T$ . Examples of this function

## 7.8 Causes of disruptions

for coronal radiation are given in Section 4.21. When 100% radiation is reached  $Q_{\text{edge}} \rightarrow 0$  and eqn 7.8.3 gives

$$Q_{\text{plasma}} = \alpha_1 (n_e n_z)^{1/2} \quad 7.8.4$$

where  $\alpha_1$  is a constant.

This condition can be used to derive a plausible model of the disruption boundary for ohmic heating. First the energy balance equation is written.

$$2\pi a Q_{\text{plasma}} = \pi a^2 \eta j^2$$

where  $\eta$  and  $j$  refer to average values so that, using eqn 7.8.4 and  $\eta \sim T^{-3/2}$ , the critical condition has the form

$$(n_e n_z)^{1/2} \propto \frac{aj^2}{T^{3/2}}. \quad 7.8.5$$

It is now necessary to determine  $T$ , and this is done using the energy balance relation

$$nj^2 \propto \frac{nT}{\tau_E}. \quad 7.8.6$$

Using the ohmic confinement relation,  $\tau_E \propto na^2$ , eqn 7.8.6 gives

$$T \propto (aj)^{4/5}, \quad 7.8.7$$

and eliminating  $T$  using relations 7.8.5 and 7.8.7 gives

$$(n_e n_z)^{1/2} \propto \frac{j^{4/5}}{a^{1/5}}. \quad 7.8.8$$

Using Ampère's law,  $j$  is related to  $q_a$  by

$$j \propto \frac{B_\phi}{\mu_0 R q_a}. \quad 7.8.9$$

Neglecting the factor  $a^{1/5}$ , eqns 7.8.8 and 7.8.9 now give the disruption condition

$$\frac{1}{q_a} = \alpha \frac{(n_e n_z)^{5/8} R}{B_\phi} \quad 7.8.10$$

where  $\alpha$  is a constant. If  $n_z$  is taken to be proportional to  $n_e$  the quantity on the right of eqn 7.8.10 is almost the Murakami parameter. Since this parameter is based on an empirical description of the experimental results, a precise relation is not to be expected. The derivation of eqn 7.8.10 brings out clearly that it is the edge values of the electron and impurity densities which are relevant in this disruption process. When additional heating or  $\alpha$ -particle heating predominates, eqn 7.8.4 indicates that the achievable density increases with the heating power.

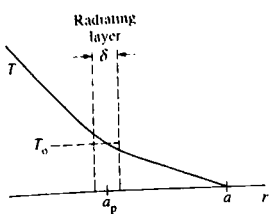


Fig. 7.8.4 Temperature profile in the neighbourhood of the radiating layer as assumed in the contraction instability model.

When the 100% radiation condition is reached the subsequent inward movement of the radiation layer and contraction of the current channel can in principle develop in either of two ways. In the first the contraction follows a continuing increase either in the electron or the impurity density. In the second the contraction is an unstable process. This instability can be understood in terms of a simple model in which the radiation is idealized to take place in a narrow layer around a radius  $a_p$ , and stability is then determined by analysing the power balance for this layer. Figure 7.8.4 shows the form of the temperature around the layer. The power balance equation is

$$\frac{d}{dt} \mathcal{E}(a_p) = I^2 \rho(a_p) - C n^2(a_p) a_p \delta - \frac{K T_0}{a - a_p} a_p. \quad 7.8.11$$

The left-hand side gives the rate of change of the plasma energy per unit length,  $\mathcal{E}$ . The first term on the right is the ohmic heating,  $\rho$  being the resistance per unit length. The second term gives the power radiated from the layer of thickness  $\delta$ ,  $n$  being the electron density in the layer and the radiation being taken to be proportional to  $n^2$  with  $C$  a constant. The final term describes the power loss from the layer through thermal conduction,  $T_0$  being the temperature characterizing the layer and  $a - a_p$  is the distance over which the temperature falls to a negligible value. In equilibrium the three terms on the right-hand side of eqn 7.8.11 are in the ratio  $1 : \varphi : (1 - \varphi)$  where  $\varphi$  is the radiated power fraction.

Linearizing eqn 7.8.11 at constant current yields the stability equation

$$\frac{a_p}{\mathcal{E}} \frac{d\mathcal{E}}{da_p} \gamma \tau_E = \left\{ \frac{a_p}{\rho} \frac{d\rho}{da_p} - \varphi \left( 1 + \frac{2a_p}{n} \frac{dn}{da_p} \right) - (1 - \varphi) \frac{a_p}{a - a_p} \right\}$$

where  $\gamma$  is the growth rate of a perturbation of  $a_p$ ,  $\tau_E = \mathcal{E}/I^2 \rho$  is the energy confinement time, and only the dominant contribution to the last term has been retained. Stability to contraction is determined by the sign of  $\gamma$  and depends on the changes in plasma resistance and the electron density in the radiating layer as the contraction takes place. If the plasma resistance is taken to be proportional to  $1/a_p^2$ , and the experimental observation that  $d\mathcal{E}/da_p > 0$  is used, the criterion for instability is

$$-\frac{a_p}{n} \frac{dn}{da_p} > \frac{1}{2} + \frac{1}{\varphi} + \frac{1 - \varphi}{2\varphi} \frac{a_p}{a - a_p}.$$

The final term on the right-hand side is normally strongly stabilizing, the large factor  $1/(a - a_p)$  representing the need for the radiating layer to be close to the boundary to conduct the power out of the plasma. However as the radiated fraction increases this term decreases and as  $\varphi \rightarrow 1$  it becomes negligible, the requirement to conduct power to the boundary being removed. For  $\varphi = 1$  the plasma can be said to be disconnected from the boundary. When this condition is reached the criterion for instability

becomes

$$-\frac{a_p}{n} \frac{dn}{da_p} > \frac{3}{2}.$$

This criterion is difficult to apply because of the uncertainty as to how the density changes in response to a change in the radius of the radiation layer. However, it clearly exhibits the destabilizing effect of the layer moving into a region of higher density to produce increased radiation.

The mhd destabilization of the contracting current channel can be understood by writing the safety factor  $q$  in terms of the plasma current and the effective plasma radius  $a_p$ . Thus

$$qa_p = \frac{2\pi a_p^2 B_\phi}{\mu_0 I R}$$

and it is seen that  $qa_p$  decreases as  $a_p^2$ . The effect is to produce a more unstable configuration in a similar way to that brought about by approach to the low- $q$  disruption boundary.

## 7.9

### Physics of disruptions

The physical processes involved in disruptions are not understood in detail but the general pattern of the behaviour can be described.

The basic events are:

- (i) The evolution of an unstable current profile leading to the growth of a tearing mode, the  $m = 2$  mode being particularly important.
- (ii) The nonlinear growth of this tearing mode.
- (iii) A sudden relaxation of the equilibrium in which the current profile is flattened and there is a dramatic loss of confinement with a collapse of the plasma temperature.
- (iv) The total current decays.
- (v) Under some circumstances the increased toroidal electric field associated with the increased plasma resistance produces runaway electrons. These electrons can carry a large current which sometimes persists after the plasma current decay phase.
- (vi) Both the loss of plasma energy and the current decay induce currents in the vacuum vessel which can produce very large forces on the vessel.

These events will be described in turn.

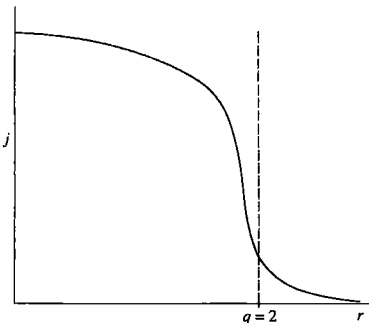


**Fig. 7.9.1** Illustrating the destabilizing form of a current profile with a negative current gradient inside the  $q = 2$  surface.

### Tearing mode instability

The common feature of the causes of disruptions listed in Section 7.8 is that they lead to a current profile which is unstable to tearing modes and in particular to an  $m = 2$  mode. Thus, in the pre-precursor phase a slow change in the equilibrium moves the current profile to marginal stability and the onset of precursor oscillations marks the crossing of the stability boundary.

It is seen from eqn 6.8.7 that a negative current gradient is destabilizing for radii inside the resonant surface and most destabilizing when close to this surface. Figure 7.9.1 shows a current profile which has these features. The steep current gradient is in part due to the constraint on  $q_0$  imposed by sawtooth oscillations. This causes a flattening of the current profile in the central region and increases the current gradient outside this region. A similar effect would be produced by increased resistivity arising from a concentration of impurities in the central region.

With  $q_0$  constrained, increasing the total current and hence lowering  $q_a$  leads to an increasingly unstable current profile brought about by a combination of the increased current gradient and the outward movement of the  $q = 2$  surface. If the current is increased rapidly there is not sufficient time for the current to diffuse into the plasma and a skin current forms as shown in Fig. 7.9.2. This enhances still further the current gradient at the edge of the plasma and under these circumstances the normally stable higher  $m$  modes can be driven unstable as a resonant surface with  $q = m$  passes through the steep edge current gradient.

As described in Section 7.8 a density limit is imposed by the contraction of the plasma current profile caused by increased surface radiation. A contraction of the current profile can also result from a loss of confinement in the outer region. A further enhancement of this effect can result from the loss of confinement brought about by the instability itself, the magnetic island formed by the instability leading to increased transport.

**Fig. 7.9.2** A skin current leads to a large current gradient at the plasma edge making the configuration susceptible to a kink/tearing instability through the neighbouring resonant surface.

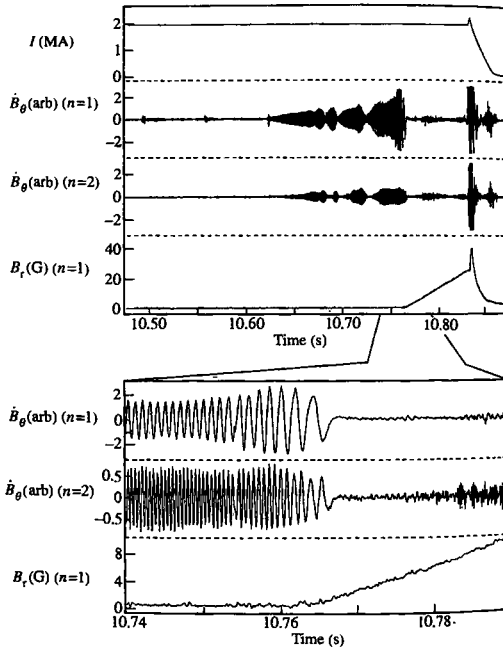
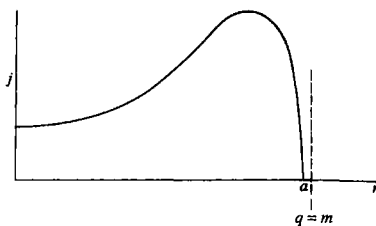


**Fig. 7.9.3** An example of the growth of mhd instabilities in a disruption, with expanded traces around the time of mode-locking. The bottom trace gives the time integrated  $\dot{B}_r$  signal, showing the continued instability growth following mode-locking. (Wesson J.A. et al., Nuclear Fusion 29, 641 (1989).)

### Growth of the tearing mode

Figure 7.9.3 presents the time development of a tearing mode instability during the precursor phase of a disruption. The instability first appears as low level magnetic oscillation. The oscillatory form of the growth derives

from the motion of the helical instability around the torus. The velocity of this motion, and therefore the frequency, is given by the sum of the natural propagation velocity of the instability and the mass velocity of the plasma. The mass velocity of the plasma can be produced, for example, by the injection of momentum associated with neutral beam heating.

The oscillatory magnetic signal displayed in Fig. 7.9.3 is the time derivative of the poloidal magnetic field at the edge of the plasma as measured by the voltage induced in a pick-up coil.

The instability is seen to grow in a sporadic way, each burst constituting a minor disruption. The oscillatory signal then disappears. However, this is not due to a departure of the instability, it is due to the removal of the oscillation. This is caused by the phenomenon called mode-locking, described in Section 7.10. Essentially mode-locking occurs when the amplitude of the instability is sufficiently large for it to interact with external conductors, such as the vacuum vessel, in such a way as to extract momentum from the plasma bringing the mode propagation to a halt.

The subsequent growth of the instability to a large amplitude can be followed by integrating the induced signal,  $B$ , to give the amplitude of the perturbed magnetic field. It is seen from Fig. 7.9.3 that following locking  $B_r$  grows continuously as the fast phase of the instability is approached.

The growing magnetic perturbation implies the growth of a magnetic island in the plasma. A precise calculation of the island size from the externally measured magnetic perturbation requires a knowledge of the radial dependence of the eigenfunction. However, in calculating the change in the perturbed magnetic field between the plasma surface and the  $q = 2$  surface, it is often a good approximation to neglect the current gradient term in the tearing mode equation 6.8.7. The perturbed flux  $\psi$  for the  $m = 2$  mode then varies as  $r^{-2}$  and so, since  $B_r \sim \psi/r$ , the radial magnetic field at the resonant surface is

$$B_{rs} = B_r(a) \left( \frac{a}{r_s} \right)^3.$$

The corresponding island size is then given by eqn 7.2.5.

Magnetic Islands 'short circuit' the radial transport through parallel transport around the magnetic surfaces as illustrated in Fig. 7.9.4. Apart from a narrow layer close to the separatrix of the island the high electron thermal conductivity parallel to the magnetic field ensures that the temperature is constant on each magnetic surface. As a consequence the electron temperature is almost constant across the magnetic island. This flattening of the temperature profile through the island has been observed experimentally. A similar but weaker effect flattening effect is to be expected for the plasma density.

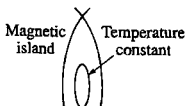


Fig. 7.9.4 The temperature across the midplane of a magnetic island is flattened through the equalization of the temperature around the interior flux surfaces.

### The fast phase

The calculated, and directly observed,  $m = 2$  magnetic island size grows to a width of typically 20% of the plasma radius. This by itself is not adequate to explain the sudden energy loss from the central region and the general loss of confinement. The explanation of this behaviour is not clear. There are two pieces of experimental evidence.

The first is that there is a flattening of the current profile which leads to the idea that a broad break up of magnetic surfaces has occurred with multiple magnetic reconnections taking place. This is a generalization of the single reconnection which leads to current profile flattening in Kadomtsev's sawtooth model. The growth of tearing mode islands on many surfaces could lead to an ergodization of the magnetic field structure as described in Section 7.13. An account of the evidence for the current flattening will be given below.

The second experimental result relating to the rapid energy loss is that there is a gross  $m = 1$  structure to the soft X-ray perturbation at the time of the energy loss. This seems to be in conflict with the concept of a multi-mode turbulence imagined to underlie the current flattening.

The evidence for the current flattening is the observation of a negative spike in toroidal voltage at the time of the rapid phase as shown in Fig. 7.9.5. This is measured as a negative voltage induced in a toroidal voltage loop on the vacuum vessel, close to the surface of the plasma. This voltage is the opposite of that expected since Lenz's law requires that the increased resistance of the plasma, indicated by the subsequent current decay, would lead to a positive voltage to maintain to current. The geometry is illustrated in Fig. 7.9.6. The voltage on the primary winding, which lies some distance outside vacuum vessel, is very small and so the large negative voltage in the voltage loops means the magnetic flux

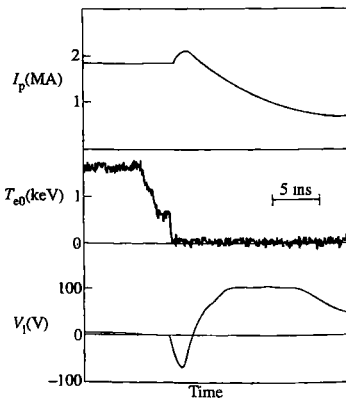


**Fig. 7.9.5** At the time of disruption, indicated by the fall in  $T_e$ , there is an increase in plasma current and an associated negative voltage spike. (Wesson, J.A., Ward, D.J., and Rosenbluth, M.N. *Nuclear Fusion* 30, 1011 (1990).)

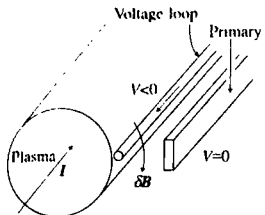


**Fig. 7.9.6** The negative voltage spike measured on the voltage loop is due to the flux change induced by the *increase* in plasma current.

through the space between the loop and the primary has increased. Since  $\int \mathbf{B} \cdot d\mathbf{l} = \mu_0 I$ , this increase in the magnetic field linking the plasma current means that the plasma current itself has increased. As seen from Fig. 7.9.5, this is observed.

That the current profile is flattened now follows from a consideration of the magnetic energy associated with the plasma current. This energy is

$$\mathcal{E} = \frac{1}{2} L I^2$$

where  $L$  is the inductance associated with the plasma current. More precisely it is the inductance given by the sum of the magnetic energy inside the plasma and the magnetic energy between the plasma and the primary. On the timescale of the negative voltage spike the magnetic energy is essentially conserved and so the observed increase in current implies a lowering of the inductance. Since the external part of the inductance is determined by the geometry, this lowering of the inductance must be due to a flattening of the current profile. Alternatively it can be said that the negative electric field at the surface of the plasma implies an outward Poynting flux. Since  $I$  increases, this outward flow of energy implies lowering of the internal inductance of the plasma and again of a flattening of the current profile.

### Current decay

After the rapid energy loss phase the plasma current falls, usually decaying to zero. Since the temperature drops during the energy loss the resistance of the plasma increases and, unless the primary voltage is able to adjust, some current decay is expected from this cause. However the current decay is usually faster than such a mechanism would allow. It has long been conjectured that the increased plasma resistance implied by the current decay could be due to an impedance arising from mhd turbulence persisting from the energy loss phase.

However the irreversibility of the current decay implies that some other process is involved. This is probably a cooling due to impurity radiation. The cooling could be caused by the temperature falling to a level where radiation is substantially increased. In the more rapid current decays the explanation lies in an influx of impurities into the plasma, probably resulting from the outflowing heat pulse arising from the rapid energy loss. The rapid current decay is then due to a very low electron temperature, typically a few eV. The extremely high ohmic heating implied by such a low temperature is balanced by radiation from the impurity atoms.

### Runaway electron current

Figure 7.9.7 shows the runaway electron current which sometimes persists after the current decay phase, the electrons carrying this current are relativistic and probably received their initial acceleration during the

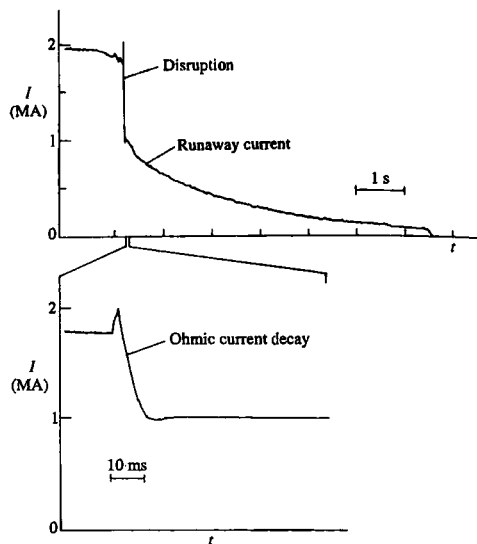


**Fig. 7.9.7** Runaway electron current formed at a disruption together with an expanded trace showing the decay of the ohmic current (JET).

rapid cooling of the plasma by impurities. The electric field during this time is

$$E = \eta j_\Omega$$

where  $j_\Omega$  is the ohmic component of the current. Since  $\eta \propto T_e^{-3/2}$

$$E = \frac{c_1}{T_e^{3/2}} j_\Omega. \quad 7.9.1$$

From Section 2.17 the criterion for electron runaway has the form

$$E > c_2 \frac{n}{T_e}$$

and substituting for  $E$  from eqn 7.9.1 electron runaway is expected for

$$T_e^{1/2} < c_3 \frac{j_\Omega}{n} \quad 7.9.2$$

Counter-intuitively a low electron temperature is required, the increase in the ohmic electric field outweighing the increased collisional drag. Initially  $j_\Omega$  takes its pre-disruption value. The electron density  $n$  is increased through the influx of impurities but at temperatures of a few

eV criterion 7.9.2 allows a large and immediate runaway current to arise. The precise behaviour is quite complex because the runaway current,  $j_r$ , subtracts from the total current,  $j$ , to give a reduced ohmic current. Thus, the electric field driving the runaway current is diminished according to

$$E = \eta(j - j_r).$$

The ohmic current decays away leaving the runaway component which has a very slow decay rate. The runaway electrons are ultimately lost to the vacuum vessel with the production of hard X-rays.

Another mechanism which can be involved in the production of runaway electrons is the scattering of plasma electrons into the runaway region of velocity space as a result of close collisions with already existing runaway electrons as described in Section 2.17.

### Vacuum vessel currents

Disruptions cause large forces on the vacuum vessel. These are  $\mathbf{j} \times \mathbf{B}$  forces, the currents being induced by transient electric fields produced in the vessel during the rapid energy loss and the current decay. The forces arise in three ways.

Firstly the loss of plasma pressure leads to an increase in toroidal magnetic field pressure inside the plasma,  $\delta(B_\phi^2/2\mu_0) \sim \delta p$ , and from flux conservation this lowers the toroidal magnetic field between the plasma and the vacuum vessel. The resulting difference in magnetic field across the vacuum vessel implies a poloidal current which crossed with the toroidal magnetic field produces an inward force. The inward pressure is approximately equal to the volume average change in plasma pressure,  $\delta p$ .

The subsequent current decay also produces a rearrangement of the toroidal magnetic field. In a rapid current decay the toroidal magnetic field pressure  $\delta(B_\phi^2/2\mu_0)$  which initially balances the poloidal magnetic field,  $\sim B_{\theta a}^2/2\mu_0$ , is transferred to the vacuum vessel. The relative magnitude of this force and the opposing force due to the loss of plasma pressure depends on the poloidal  $\beta$ . For  $\beta_p = 1$  the forces are equal but have different time dependences.

The third force arises from a toroidal current driven during the plasma current decay, the induced voltage is  $L_v i$  where  $L_v$  is the effective inductance of the vacuum vessel and  $i$  is the plasma current. The current induced in the vessel is therefore

$$I_v = \left( \frac{L_v}{R_v} \right) i$$

where  $R_v$  is the toroidal resistance of the vessel. This current, coupled to the poloidal magnetic field  $B_{\theta a}$ , leads to a pressure on the vessel

$$p_v \sim \frac{B_{\theta a}^2}{\mu_0} \frac{\tau_{\text{vessel}}}{\tau_{\text{decay}}}$$

where  $\tau_{\text{vessel}} = L_v/R_v$ ,  $\tau_{\text{decay}}$  is the plasma current decay time, and  $\tau_{\text{vessel}} \ll \tau_{\text{decay}}$ .

All of the forces typically have pressure of the order  $\frac{1}{3}B_{\theta a}^2/2\mu_0$  and for a safety factor  $q_a = 2$  this pressure is  $\sim (a/R)^2 B_\phi^2/24\mu_0$ . For  $a/R = \frac{1}{3}$  and  $B_\phi = 5\text{ T}$  this pressure is  $\sim 10^5\text{ N m}^{-2}$ , that is 10 tonnes  $\text{m}^{-2}$ . For present large tokamaks this leads to hoop forces of several hundred tonnes and in a reactor tokamak the force would be an order of magnitude larger.

## 7.10

### Mode locking

The influence of a conducting shell on stability was analysed in Section 6.9. In a tokamak the vacuum vessel provides such a shell. For finite amplitude perturbations there is a further interaction between the plasma and the wall resulting from a drag force which acts to reduce the phase velocity of the instability, and therefore its frequency. When the phase velocity is reduced to zero, the mode is locked to the vessel. However there is always a small driving effect tending to increase the frequency to its 'natural' value and this would introduce a very low residual frequency were it not for small error fields which, if large enough, intervene to completely lock the mode. An example of the growth and subsequent locking of a tearing mode is shown in Fig. 7.10.1 and the geometry is illustrated in Fig. 6.9.3.

The interaction which reduces the phase velocity is due to currents induced in the vacuum vessel by the magnetic field perturbation of the instability. For a stationary instability the relative phase of the currents and fields is such that they  $j \times B$  force in the direction of the wave vector is zero. However a finite propagation velocity introduces a phase shift and the resulting force on the vessel is in the direction of the wave. It is quite straightforward to calculate this force and this will be done

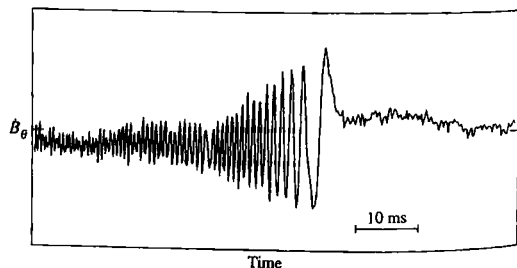


**Fig. 7.10.1** The magnetic signal  $\dot{B}_\theta$  shows the frequency and growth of an  $n = 1$  tearing mode. The reduction in frequency corresponds to a fall of the propagation speed, and the removal of the gross oscillation indicates the final mode locking (JET).

below. Because the magnetic perturbations have their origin in currents in the plasma there is also a force on the plasma. This is more difficult to calculate but for a simple analysis it is sufficient to use the conservation of momentum to deduce that the force on the plasma is equal and opposite to that in the vessel. The force on the plasma, being in the opposite direction to the wave velocity, is the force which brings about the slowing of the wave and the reduction in its frequency. The rate of slowing is basically described by Newton's equation of motion. Because the mass of the plasma is very small, in present tokamaks  $\lesssim 10^{-2}$  g, the electromagnetic forces required to slow the instability are correspondingly small, typically the weight of 1 kg.

Neglecting for the moment the effects of viscous damping and of error fields, and using the large aspect-ratio approximation, the rate of change of the observed frequency is related to that of the plasma velocity by

$$\frac{d\omega}{dt} = k \cdot \frac{dv}{dt} \quad 7.10.1$$

where

$$k = \frac{m}{r} i_\theta - \frac{n}{R} i_\phi. \quad 7.10.2$$

The acceleration is determined by the equation of motion. Integrating the force over the plasma volume and taking the motion to be rigid the toroidal equation is

$$R \int \rho dV \frac{dv_\phi}{dt} = T_\phi = R \int F_\phi dV \quad 7.10.3$$

where  $T_\phi$  is the toroidal torque,  $F_\phi$  the toroidal force density and  $\rho$  is the density of the plasma involved in the rotation. In the poloidal direction the equation of motion is

$$\int \rho r^2 dV \frac{dv_\theta}{r dt} = T_\theta = \int F_\theta r dV \quad 7.10.4$$

$T_\theta$  being the poloidal torque,  $F_\theta$  the poloidal force density and the poloidal rotation frequency  $v_\theta/r$  is taken to be constant in  $r$ .

Equations 7.10.1–7.10.4 now combine to give

$$\frac{d\omega}{dt} = \frac{m T_\theta}{\int \rho r^2 dV} - \frac{n T_\phi}{R^2 \int \rho dV}. \quad 7.10.5$$

As discussed above it is more straightforward to calculate the balancing forces in the vessel and this procedure will be used.

Thus, using the subscript  $v$  to refer to the vessel,  $T_\phi = -T_{\phi v}$  and  $T_\theta = -T_{\theta v}$ , where  $T_{\phi v}$  and  $T_{\theta v}$  are given by integrals over the vessel,

$$T_{\phi v} = R \int F_{\phi v} dV \quad 7.10.6$$

and

$$T_{\theta v} = \int F_{\theta v} r dV. \quad 7.10.7$$

Since there is no contribution from the vacuum regions the inner and outer radial limits on the integrals can be conveniently extended to  $r = a$  and  $r \rightarrow \infty$ , the only contribution actually arising in the vessel. The force density along  $k$  is

$$F = \tilde{j} \tilde{B}_r \quad 7.10.8$$

where  $\tilde{j}$  is the perturbed current along the perturbation, that is, perpendicular to  $k$ . In the large aspect-ratio approximation this force is basically in the  $\theta$  direction and so, in leading order,

$$F_{\theta v} = F \quad 7.10.9$$

and the  $\phi$  component of the force density,  $(k_\phi/k)F$ , is

$$F_{\phi v} = -\frac{n}{m} \frac{r}{R} F. \quad 7.10.10$$

Thus, using eqns 7.10.6 to 7.10.10, eqn 7.10.5 can be written

$$\frac{d\omega}{dt} = -\frac{J}{m} \int_a^\infty Fr^2 dr d\theta \quad 7.10.11$$

where

$$J = \frac{m^2}{\int \rho r^3 dr} + \frac{n^2}{R^2 \int \rho r dr}. \quad 7.10.12$$

The current  $\tilde{j}$  is given by Ampère's law, which takes the same form as eqn 6.8.5, and  $\tilde{B}_r$  is similarly given by eqn 6.8.4. Thus, substituting into eqn 7.10.8

$$F = -\frac{1}{\mu_0 r} \frac{\partial \psi}{\partial \theta} \nabla^2 \psi. \quad 7.10.13$$

Substituting eqn 7.10.13 into the integral of eqn 7.10.11 gives

$$\int \int_a^\infty Fr^2 dr d\theta = -\frac{a}{\mu_0} \int \left( \frac{\partial \psi}{\partial \theta} \frac{\partial \psi}{\partial r} \right)_a d\theta. \quad 7.10.14$$

This is calculated by writing

$$\psi = \text{Re}(\hat{\psi}(r)e^{im\theta})$$

where  $\hat{\psi}$  is complex. Equation 7.10.14 then becomes

$$\int \int_a^\infty Fr^2 dr d\theta = \frac{a}{2\mu_0} \text{Im}(\hat{\psi}^* \hat{\psi}')_a \quad 7.10.15$$

and substituting eqn 7.10.15 into eqn 7.10.11

$$\frac{d\omega}{dt} = -\frac{aJ}{2\mu_0} \text{Im}(\hat{\psi}^* \hat{\psi}')_a \quad 7.10.16$$

Using eqn 6.9.7 for  $\psi'/\psi$  with eqn 6.9.12, eqn 7.10.16 can now be written

$$\frac{d\omega}{dt} = -\frac{J}{\mu_0} \hat{\psi}_a^2 \left(\frac{a}{b}\right)^{2m} \frac{\omega\tau_v}{1 + \frac{1}{m^2} \left(1 - \left(\frac{a}{b}\right)^{2m}\right)^2 \omega^2 \tau_v^2} \quad 7.10.17$$

where  $\tau_v$  is the resistive time constant of the vessel, given by eqn 6.9.13.

In general the time dependence of  $\omega$  is determined by eqn 7.10.17 together with an equation for the growth of  $\hat{\psi}_a$  ( $= aB_r(a)/m$ ). The result of such a calculation is shown in Fig. 7.10.2. However, it is seen directly from eqn 7.10.17 that in the absence of a driving term  $\omega$  will decrease monotonically, and if  $\hat{\psi}_a$  is saturated  $\omega$  will finally decay exponentially to zero.

Equation 7.10.12 implies that the first term in  $J$  dominates. This is because the force is principally poloidal and the inertia of poloidal rotation is much less than that of toroidal motion. However, there are strong

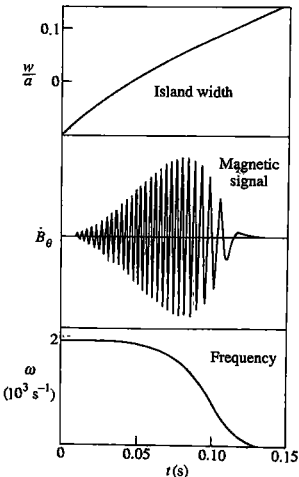


**Fig. 7.10.2** Self-consistently calculated growth and mode-locking for an  $m = 2$  tearing mode. (Nave, M.F.F. and Wesson, J.A. *Nuclear Fusion* **30**, 2575 (1990).)

polaroidal damping mechanisms resulting from toroidal effects whereas the toroidal motion suffers no such damping. It appears from the experimental results that it is more appropriate to retain only the second term in  $J$ . The integral in this term depends upon the radial extent of the accelerated plasma. This can be localized around the magnetic island formed by the instability or, through viscosity, involve most of the plasma.

The presence of a pre-existing magnetic perturbation, arising for example from small magnetic field errors, can play a role in determining the phase of the locking process. For example an error field giving rise to a force  $\sim \beta \cos(\phi - \phi_0)$ , where  $\phi$  is the phase of the oscillation and  $\beta > 0$ , would transform the small  $\omega$  form of eqn 7.10.17 to

$$\frac{d^2\phi}{dt^2} = -\alpha \frac{d\phi}{dt} + \beta \cos(\phi - \phi_0) \quad 7.10.18$$

where  $\omega$  has been replaced by  $d\phi/dt$ . It is seen from eqn 7.10.18 that as  $d\phi/dt \rightarrow 0$  the final locked phase will be  $\phi = \phi_0 + (\pi/2)$ .

## 7.11

### Error field instability

It has been found that small deviations from toroidal symmetry of the magnetic field can lead to the growth of  $m = 2$  tearing modes and terminate the discharge with a disruption. Field errors can arise from (i) the internal winding structure of the coils, (ii) the connections to the coils, and (iii) misalignment of the coils. Although the field errors can be made as small as a few gauss it turns out that, under some circumstances, such errors can cause disruptions.

The deviation from coil current symmetry introduces perturbing components to the magnetic field. Thus, for example, the non-symmetric part of the currents can produce an  $m = 2, n = 1$  contribution to the magnetic field. The radial component,  $B_r(b)$ , provides an inhomogeneous boundary condition for the tearing mode equation 6.8.7 at a radius  $b$  outside the plasma. Solution of this equation for a given current profile allows a calculation of the saturated island width using the criterion  $\Delta'(w) = 0$  described in Section 7.3.

A simple estimate of the modification to  $\Delta'$  can be obtained by assuming the plasma current outside the resonant surface to be negligible. The solution of eqn 6.8.7 is then

$$\psi = \alpha r^{-m} + \psi_{es} \left( \frac{r}{r_s} \right)^m \quad r > r_s$$

where the first term represents the perturbed magnetic flux due to plasma currents and the second term is that due to the error currents in the coils.

$\psi_{es}$  is the value of the error component at the radius,  $r_s$ , of the resonant surface. Putting  $\psi = \psi_s$  at this surface gives

$$\psi = (\psi_s - \psi_{es}) \left( \frac{r_s}{r} \right)^m + \psi_{es} \left( \frac{r}{r_s} \right)^m \quad r > r_s.$$

Thus the contribution to  $(\psi'/\psi)_{r,+e}$  from the error field is  $2(m/r)\psi_{es}/\psi_s$ . The solution for  $r < r_s$  is determined by the boundary condition  $\psi(0) = 0$  and its form is therefore unaffected by the error field, and so the resulting  $\Delta'$  can be written

$$\Delta' = \Delta'_0 + 2 \frac{m}{r_s} \left( \frac{\psi_{es}}{\psi_s} \right) \quad 7.11.1$$

where  $\Delta'_0$  is the value of  $\Delta'$  in the absence of the error field. Since the island width,  $w$  is proportional to  $\psi_s^{1/2}$ , eqn 7.11.1 can be rewritten

$$\Delta' = \Delta'_0 + 2 \frac{m}{r_s} \left( \frac{w_e}{w} \right)^2 \quad 7.11.2$$

where  $w_e$  is the island width which would result from the error field alone which, using eqn 7.2.8, is given by

$$w_e = 4 \left( \frac{q'}{q} \frac{\psi_e}{B_\theta} \right)_{r=r_s}^{1/2}.$$

An estimate of the saturated island width is now given by  $\Delta'(w) = 0$  and eqn 7.11.2 gives the formula for  $w$ ,

$$\Delta'_0(w) + 2 \frac{m}{r_s} \left( \frac{w_e}{w} \right)^2 = 0$$

$\Delta'_0$  being determined from the solution of eqn 6.8.7.

If the plasma is spun toroidally, say by neutral beams, it is to be expected that the island size will be substantially diminished if the angular frequency of rotation,  $\omega$ , is sufficiently high that  $\omega\tau \gg 1$  where  $\tau$  is the nonlinear growth time of the tearing mode island. Calculations predict such an effect and it is observed in experiments that spinning the plasma can indeed prevent disruptions which would otherwise occur.

Even without spinning, tearing modes are observed to rotate toroidally, typically at a frequency around the electron diamagnetic frequency. For very small error fields this rotation prevents large island growth, but if the error field is above a critical level the tearing mode locks to the frame of the error field and the island grows to a large size. The critical level of error field is dependent on the plasma density, higher densities allowing a larger error field.

The requirement that the  $m = 2$  error field be small, with  $B_r$  of the order of a gauss, presents a difficult requirement for a reactor. If error field instabilities persist under such conditions the instability must be prevented by active means, for example by spinning the plasma or by feedback control.

The saturated island width is clearly dependent not only on the error field, but also on the intrinsic tearing mode stability of the current profile. To explain the observed behaviour it is necessary for the error field to have a strong additional effect to that of the intrinsic tearing mode. Calculations for specific cases generally give only small error field increments to the island size and it is not understood how such small modifications cause the observed growth to large islands and to disruption. However it is quite clear that the error fields are responsible, because disruption can be avoided by reducing the magnitude of the error.

## 7.12

### Vertical instability

The instability of elongated plasmas to a gross vertical displacement was discussed in Section 6.15. Because of this instability tokamaks with elongated plasmas have feedback control to hold the vertical position of the plasma. Nevertheless the vertical instability can occur, either through a failure of the control system, or as a result of the gross perturbation resulting from a disruption. The potential threat of this instability became clear on JET when it led to forces on the vacuum vessel of several hundred tonnes.

For small vertical displacements of the plasma a toroidal current is induced in the vacuum vessel as the poloidal flux is compressed between the plasma and the vessel. For these small displacements the flux of the toroidal magnetic field is not compressed because it does not link the plasma. Consequently the poloidal current induced in the vessel is small. However, for the large displacements which are observed experimentally the plasma can make substantial contact with the vessel. The toroidal field is then trapped between the plasma and the vessel driving a large poloidal current in the vessel. The resulting force can dominate that of the toroidal currents.

The geometry of this behaviour is illustrated in Fig. 7.12.1. It is seen that the outer flux surfaces intersect the vessel over a 'halo' region. Because the plasma is cold at this stage there is no pressure gradient and the plasma current in the halo flows parallel to the magnetic field lines. On entering the vessel the current circuit is completed along a path determined by the conductance of the metal structures. The resulting forces can therefore be a threat to other components inside the vessel.

In the overall force balance the destabilizing force is due to the interaction between the poloidal field coil currents and the plasma current. Let this force be  $F_{p,c}$ . Since the total force on the plasma must be zero, the destabilizing force must be balanced by the force  $F_{p,v}$  on the plasma due

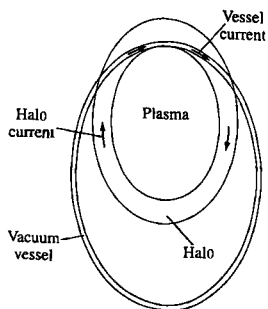


**Fig. 7.12.1** Showing the intersection of the plasma with the vacuum vessel in a vertical instability, resulting in a halo which carries current to the vessel.

to the vessel currents. Thus

$$F_{\text{plasma}} = F_{\text{p,c}} + F_{\text{p,v}} = 0. \quad 7.12.1$$

The total force on the vessel is the sum of the force from the plasma,  $-F_{\text{p,v}}$ , and the force from the coils  $F_{\text{v,c}}$ , so that using eqn 7.12.1 the force on the vessel is

$$F_{\text{vessel}} = F_{\text{p,c}} + F_{\text{v,c}} = -F_{\text{coils}}. \quad 7.12.2$$

It is seen from eqns 7.12.1 and 7.12.2 that the force is transmitted from the poloidal field coils to the vessel via the plasma.

## 7.13 Ergodicity

When an instability with a given helicity occurs in the plasma, the magnetic topology is changed at any magnetic surface which is resonant with the instability. The magnetic perturbation produces a magnetic island as described in Section 7.2.

If the perturbation has more than one helicity then, at small amplitude, each helicity produces narrow islands on its resonant surface. Although the magnetic topology is changed, each island has magnetic surfaces and the regions between the islands retain their laminar magnetic surfaces. However, if the amplitude of the multiple helicity perturbation is increased, a fundamental change arises. The field lines around the separatrices no longer lie on magnetic surfaces. If a field line is followed, its trajectory is found to remain within a certain region but moves throughout this region. After sufficient distance the field line will approach any points in the region arbitrarily closely. In the limit the field line 'fills' the volume concerned. This space-filling property of the field line is called ergodicity.

An example of this behaviour is illustrated in Fig. 7.13.1. The model is in slab geometry, the magnetic field being

$$B_x = B'_x y$$

$$B_z = B_0 = \text{constant}$$

$$\begin{aligned} B_y &= \hat{y}(\cos(k_z z + k_x x) + \cos(k_z z - k_x x)) \\ &= 2\hat{B}_y \cos k_z z \cos k_x x. \end{aligned}$$

This is a sheared magnetic field with two perturbations at an angle to each other. These perturbations are resonant at the surfaces

$$y = \pm \frac{k_z}{k_x} \frac{B_0}{B'_x}.$$

The magnetic field is periodic in  $z$  with periodicity length  $2\pi/k_z$ .

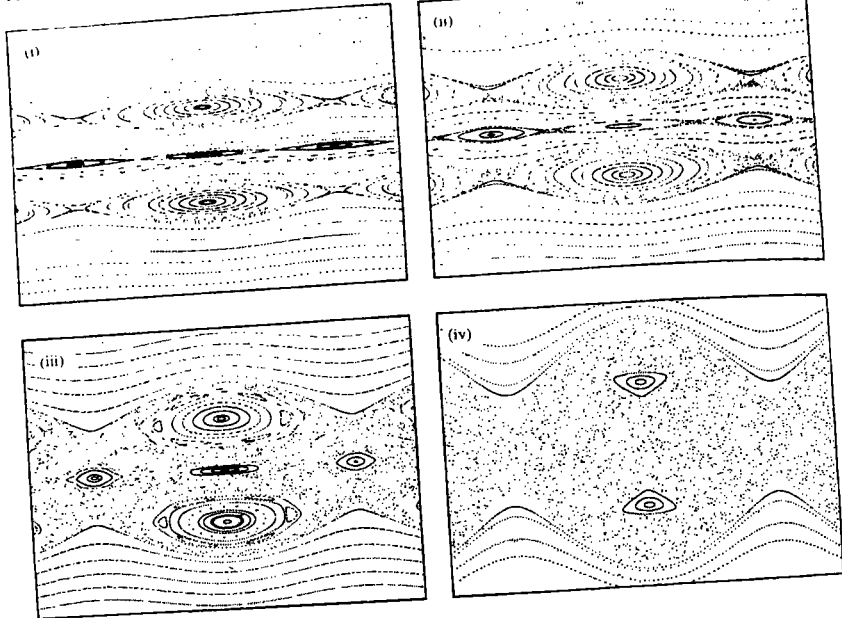


**Fig. 7.13.1** Diagrams showing change in magnetic field topology as the magnitude of the perturbing magnetic field is increased.

The trajectories of the magnetic field *lines* do not of course have this periodicity. These trajectories are determined by the equations,

$$\frac{dx}{dz} = \frac{B_x}{B_z}, \quad \frac{dy}{dz} = \frac{B_y}{B_z},$$

and their  $(x, y)$  position can be plotted at the periodic planes  $z = n(2\pi/k_z)$ ,  $n = 1, 2, \dots$  (In the analogous tokamak problem these planes would be a single plane,  $\phi = \text{constant}$ .) Figure 7.13.1 gives such plots for four levels of perturbation. For Fig. 7.13.1(i) the perturbation amplitude,  $B_y$ , is such that the island width is equal to half the separation between the resonant surfaces. Figures 7.13.1(ii), (iii), and (iv) have perturbations twice, three times, and ten times this value.

In (i) the two island strings are well separated and the magnetic field lines map out laminar surfaces. In (ii) a region around the separatrix is seen to be ergodic. In (iii) and (iv) the ergodic region covers a substantial part of the volume between the original resonant surfaces, and field lines now join these two surfaces.

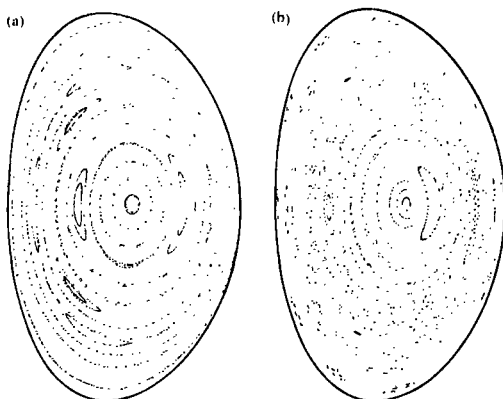


Fig. 7.13.2 Calculated intersections of magnetic field lines with a chosen poloidal plane in a tokamak. In (a) mhd perturbations produce magnetic islands and in (b) a higher level of perturbation leads to a substantial region of ergodic behaviour.

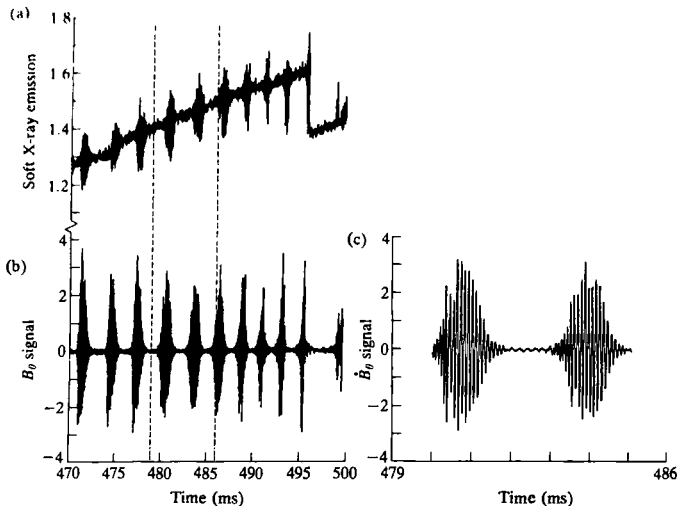
The condition for the regions of ergodicity to join is essentially that the island widths become comparable with their separation—so-called island overlap. If many surfaces are involved the behaviour of the field lines becomes increasingly stochastic, allowing a description in terms of field line diffusion. It is of course difficult to observe this type of behaviour directly in an experiment but it is widely supposed to play a role in the plasma behaviour by increasing transport.

Figure 7.13.2 illustrates the effect of mhd perturbations on a tokamak magnetic field. The two parts show the calculated intersections of a number of field lines with a given poloidal plane. In (a) the perturbations have broken the singly nested structure and have produced magnetic islands. In (b) a higher level of perturbation has given rise to a large ergodic region such as might occur during a disruption.

## 7.14

### Fishbone instability

It has been found that under certain conditions the injection of a high energy neutral beam to heat the plasma can lead to an instability and consequent energy loss. The instability is apparent from several diagnostics. The bursts of soft X-ray emission which are superimposed on the usual sawtooth oscillations are shown in Fig. 7.14.1(a) and the magnetic oscillations which are observed during a burst are shown in Fig. 7.14.1(b)



**Fig. 7.14.1** Fishbone instability: (a) soft X-ray emission; (b) poloidal magnetic field fluctuations; and (c) an expanded trace of these fluctuations. (McGuire, K. et al. *Physical Review Letters* **50**, 891 (1983).)

and (c). It is the form of these oscillations which has given the name fishbone to this instability.

It seems that the instability is due to an interaction between the injected particles and an  $m = 1, n = 1$  mhd perturbation. The interaction is of the resonance type characterized by Landau damping, but here causing growth. The resonance is between the toroidal wave velocity of the instability and the toroidal drift experienced by trapped particles, in this case trapped energetic particles from the injected beam. Since the requirement for a particle to be trapped is that its velocity be sufficiently perpendicular to the magnetic field, this instability would not occur for injection parallel to the magnetic field.

The toroidal drift is most easily seen as the drift of the banana orbit of the trapped particles. At each successive bounce point the orbit is shifted in the toroidal direction. Considering a strongly trapped particle  $v_{\perp} \gg v_{\parallel}$ , the vertical drift velocity  $v_d = \frac{1}{2}v_{\perp}^2/\omega_c R$ , given by eqn 3.10.6, leads to a poloidal displacement between bounces of  $r\Delta\theta = v_d\tau_b$ , where  $\tau_b$  is the bounce period. Since  $d\phi/d\theta = q$ , the associated toroidal displacement between bounces is  $R\Delta\phi = (qv_d R/r)\tau_b$ . Thus the toroidal drift velocity of the banana orbit,  $R\Delta\phi/\tau_b$ , is

$$v_{d\phi} = \frac{qv_{\perp}^2}{2\omega_c r}.$$

For particles which are not strongly trapped the expression is more complicated.

The stability analysis leads to a dispersion relation for  $\omega$  of the form

$$-\frac{i\omega}{\omega_A} + \delta\tilde{W}_p + \omega \int \frac{\phi(\omega, v, r)}{\omega_d - \omega} \frac{\partial f}{\partial r} d^3v dr = 0 \quad 7.14.1$$

where  $\omega_A = (B_\phi/R)/(\mu_0\rho)^{1/2}$  and  $\delta\tilde{W}_p$  is the normalized mhd potential energy change of the plasma. The last term is the contribution from the trapped particles. The instability is driven by  $\partial f/\partial r$ , the radial gradient in the fast particle distribution function. The velocity space integral has a resonance at velocities for which  $\omega = \omega_d(v_\perp)$  where  $\omega_d = v_{d\phi}/R$ .

The first two terms of eqn 7.14.1 describe the mhd  $m = 1$  internal kink mode. The additional term introduces a new root to the dispersion relation. The instability associated with this root requires a sufficiently high energy density of the trapped particles. This energy is measured by an effective beta for these particles,  $\beta_h$ . The precise stability condition depends on the distribution function of the fast particles but approximate solutions can be obtained for particular cases. For the steady state distribution function which results from fast particle injection at a particular energy and the associated slowing down, the dispersion relation takes the form

$$-\frac{i\omega}{\omega_A} + \delta\tilde{W}_p + \alpha\beta_h \frac{\omega}{\omega_{dm}} \ln \left( 1 - \frac{\omega_{dm}}{\omega} \right) = 0 \quad 7.14.2$$

where  $\alpha$  is a quantity of order unity and  $\omega_{dm}$  is the value of  $\omega_d$  at injection.

At marginal stability  $\omega$  is real and the imaginary part of eqn 7.14.2 gives the critical value of  $\beta_h$  for the fishbone instability. Recalling that, for real  $x$ ,  $\ln x = \ln|x| + \pi i$  the criterion for instability is

$$\beta_h > \frac{\omega_{dm}}{\alpha\pi\omega_A}. \quad 7.14.3$$

For the case of marginal mhd stability, that is  $\delta\tilde{W}_p = 0$ , and eqn 7.14.2 can be solved to give

$$\frac{\omega}{\omega_{dm}} = \frac{1}{2} \left( 1 + \frac{i}{\tan(\omega_{dm}/2\alpha\beta_h\omega_A)} \right).$$

This demonstrates the instability criterion 7.14.3, instability occurring for  $\omega_i > 0$ , and gives a real frequency of half the toroidal drift frequency of the injected ions.

More generally the dispersion relation takes the form

$$-\frac{i(\omega(\omega - \omega_{*i}))^{1/2}}{\omega_A} + \delta\tilde{W}_p + \delta\tilde{W}_k = 0 \quad 7.14.4$$

where the diamagnetic frequency  $\omega_{*i}$  arises from the finite Larmor radius of the plasma ions and  $\delta\tilde{W}_k$  represents the contribution of the fast ions. Depending on the circumstances, a range of instabilities is possible with frequencies from  $\omega_d$  down to  $\omega_{*i}$ .

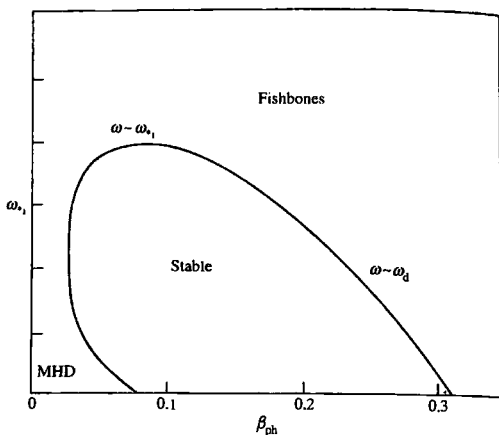


**Fig. 7.14.2** Stability diagram in the  $(\omega_i, \beta_{ph})$  plane where  $\beta_{ph}$  is the poloidal beta of the hot particles. Outside the stable region there is the fishbone instability, with the real frequencies indicated, and the MHD  $m = 1$  kink mode which appears at small  $\beta_{ph}$ . (From Coppi, B. et al., *Physical Review Letters* 63, 2733 (1989).)

The presence of fast ions and the corresponding term in eqn 7.14.4 also allows for stabilization of the  $m = 1$  mode under conditions where it would be otherwise unstable. Such stabilization was observed in JET during ICRH heating. The stabilization took the form of so-called monster sawteeth and is described in Section 12.3. The general features of the stability boundary predicted by eqn 7.14.4 are shown for a typical case in Fig. 7.14.2.

## 7.15

### Toroidal Alfvén eigenmodes

The simple forms of mhd waves were described in Section 2.24. In a tokamak these waves take a more complex form, partly because of the toroidal geometry and partly because of the shear in the magnetic field.

The effect of shear is included in the large aspect-ratio eigenmode equation

$$\frac{d}{dr} \left[ (\rho \omega^2 - F^2) r^3 \frac{d\xi}{dr} \right] - (m^2 - 1)[\rho \omega^2 - F^2] r \xi + \omega^2 r^2 \frac{d\rho}{dr} \xi = 0$$

7.15.1

where  $\xi$  is the radial displacement and  $F = (m - nq)B_\theta/\mu_0^{1/2}r$ . For a given frequency the coefficient of the highest derivative in eqn 7.15.1 has a zero at the radius  $r$  for which

$$m - nq = \pm \frac{\omega r}{B_\theta/(\mu_0 \rho)^{1/2}}. \quad 7.15.2$$

The corresponding solutions to eqn 7.15.1 are therefore singular. Thus rather than having a spectrum of discrete eigenmodes, the solutions form a continuous spectrum. For each  $(m, n)$  the frequency  $\omega(r)$  is given by eqn 7.15.2. Figure 7.15.1 gives a typical graph of  $\omega(r)$  for several mode numbers.

In toroidal geometry there is an interaction between the Fourier components. For a given  $n$ , the curves  $\omega(r)$  break and join at their intersections, to leave gaps in  $\omega(r)$  as shown in Fig. 7.15.2. In addition there is a single mode within the gap, this *Toroidal Alfvén Eigenmode* (TAE) sometimes being referred to as the gap mode.

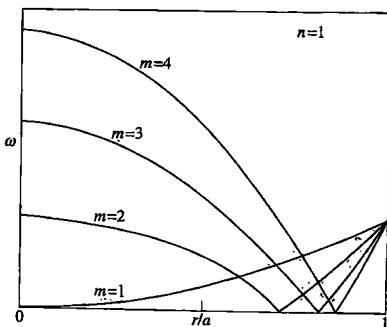


Fig. 7.15.1 Typical form of the spectrum  $\omega(r)$  in a cylinder. The curves are for a given axial wavenumber, and there is a separate curve for each  $m$ .

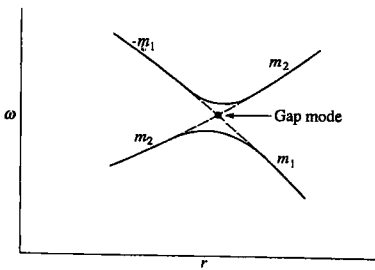


Fig. 7.15.2 Showing how, for a given toroidal mode number  $n$ , the  $\omega(r)$  curves, which are separate for each  $m$  in a cylinder, are modified in a torus. The curves for the cylindrical modes  $m_1$  and  $m_2$  'reconnect' and also produce a discrete 'gap' mode at the intersection.

Whereas the shear Alfvén waves of the continuum are strongly damped, the weaker damping of the TAE can be overcome by a destabilizing interaction with fast particles.

In particular it is thought that the  $\alpha$ -particles produced in a reacting plasma could produce an instability in which a resonance between the  $\alpha$ -particles and the wave leads to a release of the free energy associated with the radial  $\alpha$ -particle density gradient.

Calculation of the driving and damping leads to a growth rate  $\gamma$  given by

$$\frac{\gamma}{\omega_0} \simeq \frac{9}{4} \beta_\alpha \left( \frac{\omega_{*\alpha}}{\omega_0} - \frac{1}{2} \right) F \left( \frac{V_A}{V_\alpha} \right) - D \quad 7.15.3$$

where

$$\omega_0 \simeq \frac{V_A}{2qR_0} \quad 7.15.4$$

is the real frequency of the basic Alfvén mode, with  $V_A = B/(\mu_0\rho)^{1/2}$ ,  $\beta_\alpha$  is the beta value of the  $\alpha$ -particles and  $\omega_{*\alpha}$  is their diamagnetic frequency, given for poloidal mode number  $m$  by

$$\omega_{*\alpha} = -\frac{m}{r} \frac{T_\alpha}{e_\alpha B} \frac{d \ln p_\alpha}{dr}. \quad 7.15.5$$

$V_\alpha$  is the average  $\alpha$ -particle velocity and  $F(x) = x(1+2x^2+2x^4)e^{-x^2}$ . The damping term  $D$  in general has contributions from several effects.

The form of  $F(V_A/V_\alpha)$  shows that the instability is predominantly associated with  $\alpha$ -particle velocities around or above the Alfvén velocity. In a 50:50 deuterium-tritium plasma with  $n = 10^{20} \text{ m}^{-3}$  and  $B = 5 \text{ T}$  the Alfvén velocity is  $7 \times 10^6 \text{ m s}^{-1}$ .  $\alpha$ -particles, formed with an energy 3.5 MeV, have an initial velocity of  $1.3 \times 10^7 \text{ m s}^{-1}$  and so the potential for instability exists.

In a reactor the  $\alpha$ -particle production rate balances the loss of fast  $\alpha$ -particles through slowing down. Thus the density of fast  $\alpha$ -particles has the form

$$n_\alpha \sim n^2 \langle \sigma v \rangle \tau_s$$

where  $\langle \sigma v \rangle$  is given in Fig. 1.3.1 and  $\tau_s$  is the slowing down time. Since  $\tau_s \propto T^{3/2}/n$  and, approximately,  $\langle \sigma v \rangle \propto T^2$

$$n_\alpha \propto nT^{7/2}. \quad 7.15.6$$

Using relation 7.15.6 and substituting typical reactor values into eqn 7.15.5 it is found from eqn 7.15.3 that, in the absence of the damping term, the TAEs would be unstable to all  $m$  numbers. Stability therefore depends on the magnitude and  $m$  dependence of the damping.

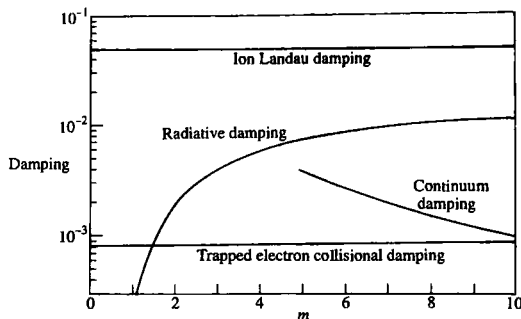


**Fig. 7.15.3** Graphs showing the  $m$ -dependence of the contributions to the normalized damping rate of TAE modes for an ITER equilibrium (from Connor, J.W. et al., Proc. 21st European Phys. Soc. Conf. on Controlled Fusion and Plasma Physics, Montpellier 1994).

There are four important contributions to the damping term  $D$  in eqn 7.15.3:

- (i) Coupling to the damped continuum, damping operating predominantly at low  $m$  and varying as  $m^{-3/2}$  at high  $m$ .
- (ii) Ion Landau damping with little  $m$  dependence.
- (iii) Trapped-electron collisional damping which is proportional to  $m^2$ .
- (iv) Radiative damping due to coupling with Alfvén waves, scaling as  $e^{-1/m}$ .

These contributions are shown in Fig. 7.15.3. In addition to the damping, finite orbit effects limit the increase of the driving term in eqn 7.15.3 with  $m$ . The combined effect of these contributions is such that in present large tokamaks small  $m$  numbers, typically 3–6, are most unstable. In a reactor the  $m$  number would be higher.

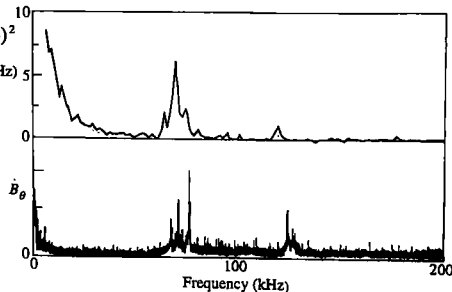


**Fig. 7.15.4** Spectrum of TAE density fluctuations as measured by beam-emission spectroscopy on TFR together with that of the magnetic fluctuations,  $\dot{B}_\theta$ , measured by a Mirnov coil. (Wong, K.L. et al., Physical Review Letters 66, 1874 (1991).)

TAEs were first observed experimentally in TFTR in an experiment using neutral beam injection to provide the fast ions. Figure 7.15.4 shows the frequency spectrum of density fluctuations together with that of the magnetic fluctuation  $\dot{B}_\theta$ . The experimentally observed frequencies showed agreement with eqn 7.15.4 within the experimental uncertainty.

## 7.16 MARFEs

The MARFE is a radiation instability which appears in tokamaks as a toroidally symmetric ring of enhanced radiation. It usually occurs on the inner side of the torus but also appears around the X-point of divertor configurations. The underlying cause is an instability in which the plasma is locally cooled by radiation in circumstances where the cooling itself leads to increased radiation and hence further cooling.

The main element in this process is provided by the increase in line radiation from impurities with decreasing temperature. An example of this is given by the coronal radiation of low  $Z$  impurities such as carbon and oxygen as shown in Fig. 4.25.1. It is seen that for temperatures in the range 10–40 eV the radiated power can rise by orders of magnitude. A second contribution to the instability arises when, in order to maintain pressure balance along the magnetic field, plasma flows into the MARFE thus increasing the density and hence the radiation. The counterbalancing effect is thermal conduction, both parallel and perpendicular to the magnetic field. Figure 7.16.1 illustrates the geometry.

The basic equation describing the behaviour is the energy balance equation

$$\frac{\partial}{\partial t}(3nT) = \nabla \cdot K \nabla T - P_R \quad 7.16.1$$

where  $K$  is the thermal conductivity and  $P_R$  is the radiated power density. Stability can be determined by linearizing this equation together with those describing the plasma dynamics and solving these equations to determine the sign of the time derivative. This procedure can be simplified by finding the condition of marginal stability, this being that the



Fig. 7.16.1 The MARFE region, shown shaded, is cooled by radiation and heated by the stabilizing perpendicular and parallel heat fluxes.

right hand side of eqn 7.16.1 is equal to zero, that is

$$\frac{\partial}{\partial x} K_{\perp} \frac{\partial T}{\partial x} + \frac{\partial}{\partial z} K_{\parallel} \frac{\partial T}{\partial z} = n_i n_e R(T). \quad 7.16.2$$

In eqn 7.16.2,  $x$  is the coordinate perpendicular to the magnetic field, and  $z$  that along the field,  $n_i$  is the impurity density and  $R$  is the radiation function which is taken to be a function of the temperature only. For the MARFE,  $x$  is the radial coordinate. The Fourier components along the magnetic field have the form  $e^{ik_{\parallel} z}$  where for periodicity  $k_{\parallel} = 1/Rq$ . Thus linearizing eqn 7.16.2 and denoting the linear parts with tildes,

$$k_{\perp} \frac{d^2 \tilde{T}}{dx^2} - k_{\parallel}^2 K_{\parallel} \tilde{T} = \tilde{n}_i n_e R(T) + n_i \tilde{n}_e R(T) + n_i n_e \tilde{R}(T). \quad 7.16.3$$

At marginal stability there is pressure balance along the magnetic field lines and so  $\tilde{n}_e$  is determined by the equation.

$$\tilde{n}_e T + n_e \tilde{T} = 0. \quad 7.16.4$$

A detailed calculation would be required for  $\tilde{n}_i$  but for present purposes it is adequate to take

$$\frac{\tilde{n}_i}{n_i} = \frac{\tilde{n}_e}{n_e}. \quad 7.16.5$$

Thus substitution of eqns 7.16.4 and 7.16.5 in to eqn 7.16.3 gives the equation governing stability

$$k_{\perp} \frac{d^2 \tilde{T}}{dx^2} = \left( k_{\parallel}^2 K_{\parallel} - n_i n_e \left( 2 \frac{R}{T} - \frac{dR}{dT} \right) \right) \tilde{T}$$

and the last two terms can be combined to give

$$k_{\perp} \frac{d^2 \tilde{T}}{dx^2} = \left( k_{\parallel}^2 K_{\parallel} - n_i n_e T^2 \frac{d}{dT} \left( \frac{R}{T^2} \right) \right) \tilde{T}. \quad 7.16.6$$

It is seen from the last term that the effect of the density perturbations is effectively to enhance the temperature dependence of the radiation.

Equation 7.16.6 can readily be solved for any particular case but some basic features can be extracted using a simple model. Thus the coefficient of  $\tilde{T}$  on the right hand side is taken to be constant over the region where  $d(R/T^2)/dT < 0$  and the solution is taken to be small outside this region. Taking the width of the region to be  $\Delta$ , this gives a rough condition for instability

$$-n_i n_e T^2 \frac{d}{dT} \left( \frac{R}{T^2} \right) > \frac{\pi^2}{\Delta^2} K_{\perp} + k_{\parallel}^2 K_{\parallel}. \quad 7.16.7$$

Each of the terms in eqn 7.16.7 has a sensitive parameter. For low  $Z$  impurities the radiation term varies by orders of magnitude in the temperature range of tens of eV. The perpendicular thermal conduction varies

as  $1/\Delta^2$ ,  $\Delta$  being determined in part by the width of region over which the radiation is substantial and this in turn depending on the temperature gradient. Finally the parallel thermal conduction is sensitive to the temperature since  $K_{\parallel}$  is proportional to  $T_e^{5/2}$ . Because of these sensitivities, and uncertainties about both the transport and the coronal or non-coronal form of the radiation, no precise calculation of stability is possible. However, to obtain some insight and ascertain the general plausibility, simple assumptions will be made to estimate the size of the terms in the stability criterion.

Since the perpendicular conduction is anomalous the value of  $K_{\perp}$  is uncertain. Using  $K_{\perp} = n\chi_{\perp}$ , the typical measured values of  $n \sim 3 \times 10^{19} \text{ m}^{-3}$  and  $\chi_{\perp} \sim 3 \text{ m}^2 \text{ s}^{-1}$  give  $K_{\perp} \sim 10^{20} \text{ m}^{-1} \text{ s}^{-1}$  and the first term on the right hand side of inequality 7.16.7 is

$$\frac{\pi^2}{\Delta^2} K_{\perp} \sim \frac{10^{21}}{\Delta^2} \text{ m}^{-3} \text{ s}^{-1}. \quad 7.16.8$$

The parallel thermal conductivity is given by eqn 2.23.9 and so, taking  $\ln \Lambda = 12$  and writing the temperature in eV,

$$K_{\parallel} = 1.6 \times 10^{22} T_{\text{eV}}^{5/2} \text{ m}^{-1} \text{ s}^{-1}.$$

For a large tokamak  $k_{\parallel} \sim 0.1 \text{ m}^{-1} \text{ s}^{-1}$  and so

$$k_{\parallel}^2 K_{\parallel} \sim 10^{20} T_{\text{eV}}^{5/2} \text{ m}^{-3} \text{ s}^{-1}. \quad 7.16.9$$

Comparing relations 7.16.8 and 7.16.9 it is seen that perpendicular thermal conduction is dominant on the right hand side of inequality 7.16.7 for  $\Delta \lesssim 3/T_{\text{eV}}^{5/4} \text{ m}$ .

Using the coronal radiation curve of Fig. 4.25.1 for carbon to estimate the radiation term in inequality 7.16.7 a typical value at  $n = 3 \times 10^{19} \text{ m}^{-3}$  and  $T \sim 20 \text{ eV}$  might be

$$-n_i n_e T^2 \frac{d}{dT} \left( \frac{R}{T^2} \right) \sim 10^{25} f \text{ m}^{-3} \text{ s}^{-1} \quad 7.16.10$$

where  $f$  is the fractional impurity level  $n_i/n_e$ . Taking perpendicular thermal conduction to be dominant and comparing relations 7.16.8 and 7.16.10 it is seen that with these assumptions instability would occur for

$$f \gtrsim \frac{1}{\Delta^2} \quad \Delta \text{ in cm}$$

so that a 10% impurity level would sustain a MARFE with a width greater than 3 cm.

## 7.17 ELMs

The discovery of the H-mode of tokamak operation was accompanied by the observation of short bursts of a new, Edge Localized Mode of instability—ELMs. These bursts were detected by magnetic pick-up coils and soft X-ray diodes, and have subsequently been found in association with H-modes in other tokamaks. Each burst of instability causes a reduction in density and temperature in the outer zone of the plasma, and the periodic behaviour constitutes a relaxation oscillation. A fall in temperature across most of the plasma radius is sometimes observed and the existence of ELMs causes some deterioration of confinement through the time-averaged reduction of the H-mode transport barrier.

With each ELM there is a burst of  $H_{\alpha}$  radiation, caused by the influx of hydrogen released from the wall as a result of the instability. Figure 7.17.1 shows such  $H_{\alpha}$  bursts in two ASDEX discharges with neutral beam injection. In the first case each burst is continuous, and such ELMs are often called 'grassy'. In the second case the  $H_{\alpha}$  pulses are single and larger,

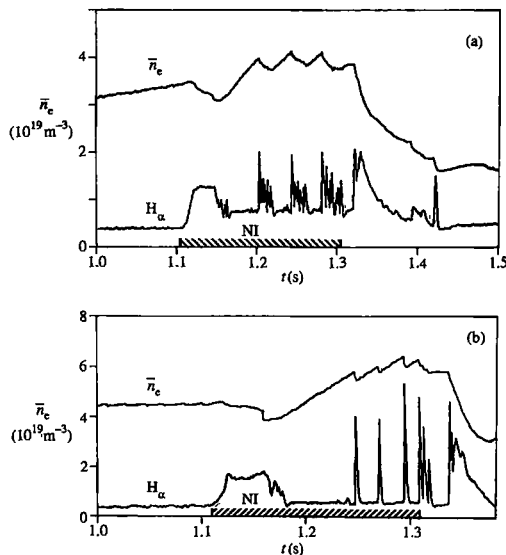


**Fig. 7.17.1**  $H_{\alpha}$  emission showing ELM activity during H-modes with neutral injection in ASDEX. (a) with continuous bursts, and (b) with separated large ELMs. The figure also shows the response of the electron density. (ASDEX Team, *Nuclear Fusion* 29, 1959 (1989).)

giving rise to the name 'giant' ELMs. In both cases the associated restraint on the growth of the electron density is seen.

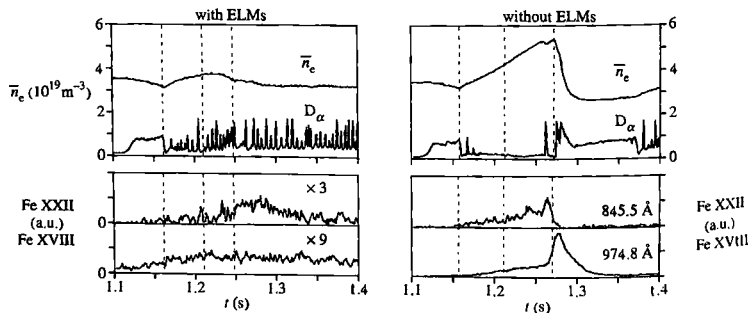
An attempt has been made to categorize the types of ELMs more precisely. Although useful, the definitions are somewhat imprecise.

- Type I ELMs are essentially giant ELMs. This type is a particular threat because of the large heat loss pulse involved and the consequent unacceptably high heat load on the divertor.
- Type II ELMs are intermediate category which avoid the heat pulse of type I but do not lead to a severe loss of general confinement.
- Type III ELMs are continuous 'grassy' ELMs which are associated with a substantial deterioration of confinement.

Another feature is brought out in Fig. 7.17.2 which shows results from two discharges, one with ELMs and one without. The ELM restriction on density is again seen, but the continuous increase in  $\bar{n}_e$  in the ELM-free discharge is seen to be accompanied by an increase in the iron impurity line radiation. The increase in impurity level is also apparent from a comparison of the behaviour of the total radiation. It is found quite generally that ELM-free H-modes lead to impurity accumulation and, in discharges with ELMs, there is a trade-off between the reduced impurity level and deteriorated confinement.

The cause of ELMs is not clear. It is perhaps not surprising that the increase edge gradients in H-modes leads to instability, but no unequivocal identification of the type of instability has been made. The existence of a magnetic perturbation indicates an MHD source. The candidate instabilities include tearing modes driven by the current gradient, ballooning modes driven by the pressure gradient, and a surface kink instability. It is difficult to know the form of the current profile at the edge, but measurements of the pressure gradient have been made. The indications are that the pressure gradient is of the order of that required for ballooning modes but is somewhat below the critical level. The

**Fig. 7.17.2** Discharges with and without ELMs, showing the increase in electron density and impurity accumulation associated with the ELM-free case. Note that the iron emission line signals are amplified in the case with ELMs. (ASDEX Team, *Nuclear Fusion* 29, 1959 (1989).)



observed mode numbers, with  $m$  typically around 10, are consistent with a ballooning mode interpretation, but the relaxation oscillation form of the instability is not understood.

## 7.18

### Operational overview

Chapter 6 and the present chapter give an introduction to mhd stability theory and an account of the observed behaviour of the instabilities.

These instabilities limit the operating regime of the tokamak. The precise form of the limitation depends upon the details of operational procedures and the resulting profiles, but there is a general pattern to the behaviour which can be described in an approximate way.

The simplest procedure is to use the framework provided by the stability diagram of Fig. 6.10.4 to map the current profile parameter  $\nu$  of that diagram on to the internal inductance  $\ell_i$ . Stability can then be discussed in terms of an  $(\ell_i, q_{\text{edge}})$  diagram. The variable  $q_a$  has been replaced by  $q_{\text{edge}}$  to encompass the case of divertor plasmas. Thus, whereas for a large aspect-ratio circular plasma  $q_{\text{edge}} = q_a$ , for a plasma with a bounding separatrix  $q_{\text{edge}}$  will be taken to be  $q_{95}$ , the value of  $q$  on the flux surface containing 95% of the poloidal flux.

The resulting diagram is shown in Fig. 7.18.1. The first constraint is that due to  $m = 2$  instability which generally presents a hard disruptive boundary at  $q_{\text{edge}} \approx 2$ . As  $q_{\text{edge}}$  approaches 2 from above the resonant surface,  $q = 2$ , approaches the plasma boundary from inside the plasma and the  $m = 2$  tearing mode is transformed into a  $m = 2$  kink. The region unstable to tearing modes is not shown in the diagram. Their stability is

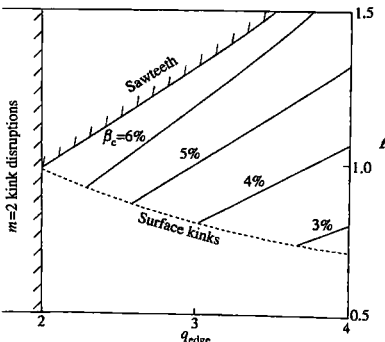


Fig. 7.18.1 Illustrating the operational boundaries imposed by mhd constraints and the values of the mhd  $\beta$  limit within the operating region. The figure is only indicative, the precise values depending on geometry and profiles.

dependent on the current profile and the predicted magnetic island sizes can be quite small. The  $m = 2$  tearing mode becomes important when  $q_{\text{edge}} \rightarrow 2$ , or for a narrow current profile with higher  $\ell_i$ , which has  $q \approx 2$  at the edge of the effective current channel.

The central value of  $q$  is usually limited by sawteeth. Simple theory would put the boundary at  $q_0 = 1$  but, as described in Section 7.6, the boundary is probably better placed at  $q_0 = 0.7$ . This limits the value of  $\ell_i$  and, as shown in Fig. 7.18.1, is most stringent at low  $q$ .

The surface kinks present a less precise boundary and for this reason the corresponding line in the diagram is shown dashed. Both the stability and the consequences of these modes depend upon the edge current profile which itself depends on a variety of factors. In particular a fast current rise produces a high edge current density gradient as a result of the skin current effect.

Having indicated the general position of the stability boundaries it is now possible to determine the  $\beta$  limitation. Taking the form of the  $\beta$  limit given by relation 6.16.6, that is

$$\beta_c(\%) = 4\ell_i \frac{I}{aB} \quad I \text{ in MA},$$

and using the approximate empirical relation

$$q_{95} = \frac{5a^2 B}{2RI} \left(1 + \frac{b^2}{a^2}\right) \left(1 + \frac{2}{3} \left(\frac{q}{R}\right)^2\right) \quad I \text{ in MA},$$

the critical  $\beta$  for  $R/a = 3$  and  $b/a = \frac{5}{3}$  is

$$\beta_c(\%) = 15 \frac{\ell_i}{q_{95}}.$$

The resulting lines of constant  $\beta_c$  are plotted in Fig. 7.18.1.

The diagram is only indicative and the use of specially chosen profiles together with contributions from the second region of stability can allow substantially higher values  $\beta$  to be obtained.

## Bibliography

Although the instabilities described in this chapter have been subject to intensive experimental study, the understanding of the phenomena involved is incomplete and uncertain. As a result there is a shortage of review articles. There is a comparison of theory and experiment in Chapter 11 of Bateman, G. *MHD instabilities*. MIT Press, Cambridge, Mass. (1978);

and a more extensive theoretical treatment by White, R.B. Resistive instabilities and field line reconnection, in Section 3.5 of *Handbook of plasma physics* (eds Galeev, A.A. and Sudan, R.N.) Vol. 1. North Holland, Amsterdam (1983). A general account of nonlinear effects is given in Biskamp, D. *Nonlinear magnetohydrodynamics*, Cambridge University Press (1993).

### Tearing modes

The nonlinear growth of tearing modes was first described by Rutherford, P.H. Nonlinear growth of the tearing mode. *Physics of Fluids* **16**, 1903 (1973).

A more detailed treatment of the quasi-linear theory is given by

White, R.B., Monticello, D.A., Rosenbluth, M.N., and Waddell, B.V. Saturation of the tearing mode. *Physics of Fluids* **20**, 800 (1977).

Two-dimensional calculations of saturated island widths are described in

Sykes, A. and Wesson, J.A. Saturated kinks and tearing instabilities in tokamaks. *Plasma physics and controlled nuclear fusion research* (Proc. 8th International Conference, Brussels 1980) Vol. I, 237. I.A.E.A. Vienna (1981).

The internally driven mode is discussed in the context of disruptions in

Rebut, P.H. and Hugon, M. Thermal instability and disruptions in a tokamak. *Plasma physics and controlled nuclear fusion research* (Proc. 10th Int. Conf., London, 1984) Vol. 2, 197. I.A.E.A. Vienna (1985).

and the neoclassical tearing mode is analysed in

Carrera, R., Hazeltine, R.D., and Kotschenreuter, M. Island bootstrap current modification of the nonlinear dynamics of the tearing mode. *Physics of Fluids* **29**, 899 (1986).

The neoclassical tearing mode was first reported by Chang, Z. et al. Observation of nonlinear neoclassical pressure-gradient-driven tearing modes on TFTR. *Physical Review Letters* **74**, 4663 (1995)

The small island stabilization effects are discussed in Fitzpatrick, R. Helical temperature perturbations associated with tearing modes in tokamak plasmas. *Physics of Plasmas* **2**, 825 (1995)

Wilson, H.R., Connor, J.W., Hastie, R.J., and Hegna, C.C. Threshold for neoclassical magnetic islands in a low collision frequency tokamak. *Physics of Plasmas* **3**, 248 (1996).

and

Poli, E. et al. Reduction of the ion drive and  $\rho_\theta^*$  scaling of the neoclassical tearing mode. *Physical Review Letters* **88**, (2002).

### Mirnov instabilities

Mirnov, S.V. and Semenov, I.B. Investigation of the instabilities of the plasma string in the Tokamak-3 system by means of a correlation method. *Atomnaya Energiya* **30**, 20 (1971) [Soviet Atomic Energy **30**, 22 (1971)].

### Current penetration

The idea of double tearing modes leading to current penetration was described by

Stix, T.H. Current penetration and plasma disruption.

*Physical Review Letters* **36**, 521 (1976).

Numerical simulations of the nonlinear development of double tearing modes were carried out by

Carreras, B., Hicks, H.R., and Waddell, B.V. Tearing mode activity for hollow current profiles. *Oak Ridge National Laboratory Report ORNL/TM6570*, Oak Ridge, Tennessee (1978).

Experimental observations on the instabilities are described in

Granetz, R.S., Hutchinson, I.H., and Overskei, D.O. Disruptive mhd activity during plasma current rise in Alcator A tokamak. *Nuclear Fusion* **19**, 1587 (1979).

### Sawtooth oscillations

Experimental observations on the sawtooth behaviour of the soft X-ray emission were described by

von Goeler, S., Stodiek, W., and Sauthoff, N. Studies of internal disruptions and  $m = 1$  oscillations in tokamak discharges with soft X-ray techniques. *Physical Review Letters* **33**, 1201 (1974).

The fast reconnection model was proposed in

Kadomtsev, B.B. Disruptive instability in tokamaks. *Fizika Plasm* **1**, 710 (1975) [Soviet Journal of Plasma Physics **1**, 389 (1976)].

Numerical calculations on the reconnection were carried out by

Danilov, A.F., Dnestrovsky, Yu. N., Kostomarov, D.P., and Popov, A.M. *Fizika Plasmay* **2**, 187 (1976) [Soviet Journal of Plasma Physics **2**, 93 (1976)].

and calculations demonstrating the relaxation oscillation behaviour by

Sykes, A. and Wesson, J.A. Relaxation instability in tokamaks. *Physical Review Letters* **37**, 140 (1976).

A role for turbulence was suggested in

Dubois, M. and Samain, A. Evolution of magnetic islands in tokamaks. *Nuclear Fusion* **20**, 1101 (1980).

Early doubts about the full reconnection model were expressed in

Dubois, M.A., Marty, D.A., and Pochelon, A. Method of cartography of  $q = 1$  islands during sawtooth activity in tokamaks. *Nuclear Fusion* **20**, 1355 (1980).

Further doubts were reported by

Edwards, A.W. et al. Rapid collapse of a plasma sawtooth oscillation in the JET tokamak. *Physical Review Letters* **57**, 210 (1986)

The quasi-interchange model was introduced in

Wesson, J.A. Sawtooth oscillations. *Plasma Physics and Controlled Fusion Research* **28** (IA), 243 (1986).

- The key aspects of the attempts to understand sawtooth oscillations are reviewed in
- Hastie, R.J. Sawtooth instability in tokamak plasmas. *Astrophysics and Space Science* **256**, 177 (1998).
- Collisionless reconnection was proposed in
- Wesson, J.A. Sawtooth reconnection. *Plasma Physics and Controlled Fusion Research* (Proc. 13th Int. Conf., Washington, 1990) Vol. 2, 79. I.A.E.A. Vienna (1991). and the importance of collisionless electron viscosity was pointed out by
- Yu, Q. A new theoretical model for fast sawtooth collapse and confirming its interchange structure. *Nuclear Fusion* **35**, 1012 (1995).
- The sawtooth 'trigger' problem was described by
- Wesson, J.A., Edwards, A.W., and Granetz, R.S. Spontaneous  $m = 1$  instability in the JET sawtooth collapse. *Nuclear Fusion* **31**, 111 (1991).
- The possible role of stochasticity was discussed by
- Lichtenberg, A.J. Stochasticity as the mechanism for the disruptive phase of the  $m = 1$  tokamak oscillations. *Nuclear Fusion* **24**, 1277 (1984).
- The literature on the sawtooth instability is now very extensive. A review of  $m = 1$  stability theory with some discussion of nonlinear effects is given in
- Migliuolo, S. Theory of ideal and resistive  $m = 1$  modes in tokamaks. *Nuclear Fusion* **33**, 1721 (1993).
- Many numerical simulations have been carried out.
- Toroidal calculations are described in
- Aydemir, A.Y., Wiley, J.C., and Ross, D.W. Toroidal studies of sawtooth oscillations in tokamaks. *Physics of Fluids* **B1**, 774 (1989).
- ### Disruptions
- The phenomenon of disruptions was observed by
- Gorbunov, E.P. and Razumova, K.A. Effect of a strong magnetic field on the magnetohydrodynamic stability of a plasma and the confinement of charged particles in the 'Tokamak' machine. *Atomnaya Energaya* **15**, 363 (1963). [*Journal of Nuclear Energy*, Part C, **6**, 515 (1964)].
- A substantial experimental investigation is described by
- Sauthoff, N.R., von Goeler, S., and Stodiek, W. A study of disruptive instabilities in the P.L.T. tokamak using X-ray techniques. *Nuclear Fusion* **18**, 1445 (1978).
- The Murakami parameter  $nR/B_\phi$  was introduced in
- Murakami, M., Callen, J.D., and Berry, L.A. Some observations on maximum densities in tokamak experiments. *Nuclear Fusion* **16**, 347 (1976).
- and the Hugill diagram was introduced in
- Fielding, S.J., Hugill, J., McCracken, G.M., Paul, J.W.M., Prentice, P., and Stott, P.E. High-density discharges with gittered torus walls in DITE. *Nuclear Fusion* **17**, 1382 (1977).
- The Greenwald formulation of the density limit was introduced in
- Greenwald, M. et al. A new look at density limits. *Nuclear Fusion* **28**, 2199 (1988).
- and a comprehensive review of density limits was given by
- Greenwald, M. Density limits in toroidal plasmas. *Plasma Physics and Controlled Fusion* **44**, R27 (2002).
- Numerical simulations of the interaction of tearing modes, leading to the fast phase of the disruption were carried out at the Oak Ridge National Laboratory and are described in several papers including
- Carreras, B., Hicks, H.R., Holmes, J.A., and Waddell, B.V. Nonlinear coupling of tearing modes with self-consistent resistivity evolution in tokamaks. *Physics of Fluids* **23**, 1811 (1980).
- A model of the precursor phase was developed at the Culham Laboratory and is summarized in
- Wesson, J.A., Sykes, A., and Turner, M.R. Tokamak disruptions. *Plasma Physics and Controlled Fusion Research* (Proc. 10th Int. Conf., London, 1984) Vol. 2, 23. I.A.E.A. Vienna (1985).
- The role of radiation in the precipitation of disruptions is discussed by
- Rebut, P.H. and Green, B.J. Effect of impurity radiation on tokamak equilibrium. *Plasma Physics and Controlled Nuclear Fusion Research* (Proc. 6th Int. Conf., Berchtesgaden 1976) Vol. 2, 3. I.A.E.A. Vienna (1977).
- Ohyabu, N. Density limit in tokamaks. *Nuclear Fusion* **9**, 1491 (1979); and
- Ashby, D.E.T.F. and Hughes, M.H. The thermal stability and equilibrium of peripheral plasmas. *Nuclear Fusion* **81**, 911 (1981).
- The role of impurity influx in fast disruptions was first recognized by
- Ward, D.J., and Wesson, J.A. Impurity influx model of fast tokamak disruptions. *Nuclear Fusion* **32**, 1117 (1992).
- and evidence for a low temperature and large density increase produced by an impurity influx is described in
- JET Team, Sawtooth Oscillations and Disruptions in JET. Proc. 14th Int. Conf. on Plasma Physics and Controlled Nuclear Fusion Research, Wurzburg 1992, vol. 1, p. 437.
- A paper giving results of internal measurements during a disruption is
- Hutchinson, I.H. Magnetic probe investigation of the disruptive instability in LT-3. *Physical Review Letters* **37**, 338 (1976).
- An account of various experimental aspects of disruptions is given in
- Wesson, J.A. et al. Disruptions in JET. *Nuclear Fusion* **29**, 641 (1989).
- and a numerical simulation is described in
- Bondeson, A., Parker, R.D., Hugon, M., and Smeulders, P. *Nuclear Fusion* **31**, 1695 (1991).

## Mode locking

The basic physics is outlined in  
Nave, M.F.E. and Wesson, J.A. Mode locking in tokamaks.  
*Nuclear Fusion* **30**, 2575 (1990).

## Error field instability

Instabilities associated with error fields were described in  
Scoville, J.T. et al. Locked modes in DIII-D and a method for  
prevention of the low density mode. *Nuclear Fusion* **31**,  
875 (1991).

An introductory account of the theory was given by  
Lee, J.K. et al. Magnetic islands driven by external sources.  
*Nuclear Fusion* **23**, 63 (1983).

and a more complete analysis is given in  
Fitzpatrick, R. Interaction of tearing modes with external  
structures in cylindrical geometry. *Nuclear Fusion* **33**,  
1049 (1993).

## Vertical instability

The first observations of the serious consequences of the  
vertical instability were reported in

Noll, P. et al. Stabilization of vertical position and control  
of plasma shape in JET. *Proc. 11th Symposium on Fusion  
Engineering*, Texas, 1985 Vol. I p.33.

A more detailed account of the behaviour is given by

Lao, L.L. and Jensen, T.H. Magnetohydrodynamic equilibria  
of attached plasmas after loss of vertical stability in  
elongated plasmas. *Nuclear Fusion* **31**, 1909 (1991).

## Ergodicity

An introduction is given in the article

White, R.B. Resistive instabilities and field line reconnection.  
*Handbook of plasma physics* (eds Galeev, A.A.  
and Sudan, R.N.) Vol. 1, Section 3.5. North Holland,  
Amsterdam (1983).

## Fishbone instability

The experimental observation of the fishbone instability was  
described in

McGuire K. et al. Study of high- $\beta$  magnetohydrodynamic  
modes and fast ion losses in PDX. *Physical Review Letters*  
**50**, 891 (1983);

and the proposed theoretical interpretation was given by  
Chen, L., White, R.B., and Rosenbluth, M.N. Excitation  
of internal kink modes by trapped energetic beam ions.  
*Physical Review Letters* **52**, 1122 (1984).

## Toroidal Alfvén eigenmodes

The TAE spectrum was described by  
Cheng, C.Z., Chen, Liu and Chance, M.S. High- $n$  ideal  
and resistive shear Alfvén waves in tokamaks. *Annals of  
Physics* **161**, 21 (1985).

The possibility of  $\alpha$ -particle driven instability was discovered by

Fu, G.Y. and Van Dam, J.W. Excitation of the toroidicity-  
induced shear Alfvén eigenmode by fusion alpha particles  
in an ignited tokamak. *Physics of Fluids B* **1**, 1949 (1989).

## MARFEs

The observation of a cold, dense region on the inboard side of  
the plasma was the first reported by  
Baker, D.R., Snider, R.T., and Nagami, M. Observation of  
cold, high density plasma near the Doublet III limiter.  
*Nuclear Fusion* **22**, 807 (1982).

Further observations and analysis, and the designation  
MARFE, appeared in

Lipschultz, B., Marmar, E.S., Pickrell, M.M., Terry, J.L.,  
Watterson, R., and Wolfe, S.M. *Nuclear Fusion* **24**, 977  
(1984).

In this paper the name MARFE is said to be an abbreviation  
of 'Multifaceted Asymmetric Radiation From the Edge'.  
However, it may not be a coincidence that it is also formed  
by the first three letters of one author's name and the last  
two letters of another's.

The first theoretical treatments of the phenomenon were  
Stringer, T.E. A theory of MARFEs *Proc. 12th European  
Conference on Controlled Fusion and Plasma Physics I*,  
86 (Budapest 1985).

and

Neuhäuser, J., Schneider, W., and Wunderlich, R. Thermal  
instabilities and poloidal asymmetric in the tokamak edge  
plasma. *Nuclear Fusion* **26**, 1679 (1986).

## ELMs

The ELM instability was mentioned in

Wagner, F. et al. Regime of improved confinement and  
high beta in neutral beam heated divertor discharges of  
the ASDEX tokamak. *Physical Review Letters* **49**, 1408  
(1982),

and was designated an 'ELM' in

Keilhacker, M. et al. Confinement studies in L and H-type  
ASDEX discharges. *Plasma Physics and Controlled  
Fusion* (Proc. 11th European Conf, Aachen, 1983) Vol. 26,  
1A, p.49 (1984).

A more complete account is to be found in the review  
ASDEX Team, The H-mode of ASDEX. *Nuclear Fusion* **29**,  
1959 (1989).

# 8

# Microinstabilities

---

## 8.1

### Microinstabilities

Instabilities predicted by the single fluid MHD model are described in Chapters 6 and 7. However, calculations which include finite Larmor radius and kinetic dissipation effects indicate that additional instabilities should occur in a tokamak. There is a class of such instabilities which have a wavelength comparable to the ion Larmor radius and these are termed *microinstabilities*.

Microinstabilities provide a mechanism for the generation of fine scale plasma turbulence and may therefore be important for an understanding of anomalous transport in tokamaks. While a full calculation of the turbulence saturation level must involve nonlinear effects, the linear mode characteristics are useful for identifying possible drives and conditions for this turbulence. Furthermore, when the resulting particle and heat transport is high, the plasma density and temperature profiles may adjust to be close to the threshold predicted by linear theory. Linear mode characteristics, such as time and length scales, may also be relevant for characterizing the turbulent state, to provide estimates for the plasma transport as described in Section 4.18. The linear properties of a variety of microinstabilities are introduced in the following sections, but first it is worthwhile describing some more general properties of this class of instability.

Because of their disparate masses, electrons and ions respond differently to electromagnetic field perturbations and they therefore play different roles in the evolution of the microinstability. Typically, one species will provide the drive, while the other provides the damping. Dissipation often plays a crucial role in causing instabilities; this can be either collisional as in a low temperature plasma, or due to a Landau resonance when the collision frequency is low. The resulting instabilities are classed as *dissipative*. However, some microinstabilities are *reactive* and do not require dissipation. The ion temperature gradient mode, which is described in Section 8.3, is an example of this type.

The properties of microinstabilities are often dependent upon the geometry of the confining magnetic field. However, for a tokamak the stability analysis is usually complicated and it is often helpful to use simple models for the geometry in order to identify the important physical mechanisms. The level of simplification depends on the importance of the various particle drifts and trapped particle effects. If magnetic curvature drifts are expected to be important for the instability mechanism, the toroidal geometry must be taken into account. The simplest geometry is then that of the large aspect ratio, circular cross-section, low  $\beta$ , tokamak equilibrium described in Section 3.6. The major and minor radii are then denoted by  $R$  and  $r$  respectively, while  $\theta$  and  $\phi$  denote the poloidal and

toroidal angles. Perturbations can be Fourier analysed in the poloidal and toroidal angles, with mode numbers  $m$  and  $n$ . In toroidal geometry the equilibrium is independent of  $\phi$ , and  $n$  is a precise quantum number. However, the curvature drifts couple the poloidal harmonics so that instabilities for which curvature drifts are important typically involve several poloidal harmonics.

When curvature drifts are not important, the qualitative aspects of the instability can be studied without the effects of toroidal geometry. In such cases it is convenient to analyse the instability using a 'slab' model of the magnetic geometry. This results from considering an annulus which is centred on the rational surface of interest as shown in Fig. 8.1.1a. This is then cut and opened to form the slab of plasma shown in Fig. 8.1.1b. It is conventional to define a new orthogonal coordinate system  $x$ ,  $y$ , and  $z$ , where  $x = r - r_s$  is the coordinate measuring the radial distance from the rational surface  $r = r_s$ , at which the safety factor  $q = m/n$ ,  $z$  is in the direction of the magnetic field at the rational surface (approximately the toroidal direction) and  $y$  is in the direction perpendicular to both of these (approximately the poloidal direction). Note that neither the poloidal nor the toroidal Fourier harmonics are coupled in a plasma slab so a perturbation,  $\tilde{f}$ , can be expressed in the form  $\tilde{f} = \tilde{f}(x) \exp[ik_y y + ik_z z]$ , where  $k_y y$  and  $k_z z$  represent  $m\theta$  and  $-n\phi$  respectively. The parallel wavenumber is given by  $ik_{\parallel} = (1/B) \mathbf{B} \cdot \nabla$ . In toroidal geometry

$$k_{\parallel} = \frac{m - nq}{Rq}$$

and the slab equivalent is

$$k_{\parallel} = -\frac{k_y x}{L_s},$$

where  $k_y = m/r$  is the poloidal mode number, and  $L_s = Rq/s$  is the shear length, with  $s = (r/q) dq/dr$  the magnetic shear.

The class of microinstabilities can be divided into those which are predominantly electrostatic and those for which electromagnetic perturbations are important. They can be further categorized according to the basic plasma wave from which they develop. Examples to be described later are given in Table 8.1.1. Electrostatic modes are described in Sections 8.3 and 8.4, and the electromagnetic instabilities are covered in Section 8.5.

**Table 8.1.1** Plasma waves and their associated instabilities

Electron drift wave	Alfvén wave	Sound wave
'Universal', Trapped electron	Microtearing	Ion temperature gradient

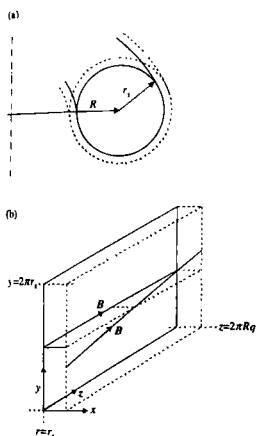


**Fig. 8.1.1** Annulus of tokamak plasma  
(a) cut and opened to form a 'sheared slab'  
plasma (b).

## 8.2

### Electron drift wave

Drift instabilities are a particularly important class of microinstabilities which have often been invoked as the source of plasma turbulence responsible for anomalous transport in tokamaks. These modes, discussed in Sections 8.3 and 8.4, are essentially electrostatic in nature and result from tapping the free energy of the density and temperature gradients of the plasma.

Drift instabilities develop from a basic wave of the plasma, called the electron drift wave. The electron drift mode, described in the next section, is a particularly important example. This drift wave can be illustrated by considering a slab of plasma in a shearless, uniform magnetic field. The geometry is shown in Fig. 8.2.1 which illustrates the plasma slab with the magnetic field in the  $z$  direction and an equilibrium density gradient along the  $x$  direction. A wave having the form  $\exp i(-\omega t + k_y y)$  has surfaces of constant density as shown in the figure. Thus regions of increased density lie in the planes of constant  $x$ . In Fig. 8.2.1 these are labelled by  $\tilde{n} > 0$ , while the regions of low density are labelled by  $\tilde{n} < 0$ .

Because of their low inertia, electrons flow rapidly along the field lines, generating an electric field parallel to the magnetic field in order to establish force balance along the magnetic field given by

$$neE_{||} + \nabla_{||}p_e = 0, \quad 8.2.1$$

where  $p_e$  is the electron pressure,  $E$  is the electric field and  $||$  denotes the component in the direction of the magnetic field. Linearizing eqn 8.2.1 leads to a relation between the perturbed electron density  $\tilde{n}_e$ , and electrostatic potential  $\varphi$

$$\frac{\tilde{n}_e}{n_e} = \frac{e\varphi}{T_e}. \quad 8.2.2$$

where  $n_e$  and  $T_e$  are the equilibrium density and temperature respectively. The electrostatic potential implies a perturbed electric field in the  $y$  direction, directed from the regions of increased density to those of decreased density as indicated in Fig. 8.2.1. The associated  $E \times B$  drift enhances the density in the less dense regions and reduces it in the more dense regions, causing the density and potential perturbations to oscillate in time. The resulting wave, which propagates in the  $y$  direction, is the drift wave.

The diamagnetic drift  $v_{dj} = B \times \nabla p_i / n_i B^2$  does not give rise to a perturbed density. This can be seen from the continuity equation

$$\frac{\partial n_i}{\partial t} = -\nabla \cdot n_i v_i, \quad 8.2.3$$

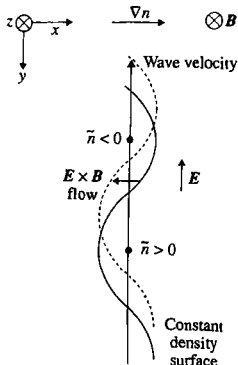


**Fig. 8.2.1** Movement of the constant density surface due to the  $E \times B$  motion in an electron drift wave, represented by the full curve at an initial time and the dashed curve at a later time.

where  $v_i$  is the ion velocity. Substituting for  $n_i v_{di}$  it is seen that the diamagnetic flow has zero divergence and does not therefore contribute to  $\partial n_i / \partial t$ .

The wave frequency is obtained using the quasi-neutrality condition  $\bar{n}_e = \bar{n}_i$ , with  $\bar{n}_i$  being determined from eqn 8.2.3. For waves such that  $\omega/k_{\parallel} \gg v_{Ti}$ , so that the parallel ion motion is negligible, the continuity eqn 8.2.3 for the ions becomes

$$i\omega\bar{n}_i = \bar{v}_{Ex} \frac{dn}{dx}, \quad 8.2.4$$

where  $\bar{v}_{Ex} = -(1/B)\partial\tilde{\varphi}/\partial y$  is the  $x$  component of the perturbed  $E \times B$  drift. Now, choosing the equilibrium frame in which  $E_x = 0$  and equating the values of  $\bar{n}_e$  and  $\bar{n}_i$  given by eqns 8.2.2 and 8.2.4, leads to the frequency

$$\omega = \omega_{*e},$$

where  $\omega_{*e}$  is the electron diamagnetic frequency

$$\omega_{*e} = -\frac{k_y T_e}{e B n} \frac{dn}{dr}.$$

No damping or growth of the mode is predicted by this simple model. However, the introduction of electron dissipation either through collisions or Landau damping will destabilize the drift wave in the shearless slab geometry. The resulting microinstability is called the *electron drift mode*. Because it was originally thought to be unstable in all relevant tokamak conditions it is sometimes referred to as the *universal instability*. Actually the magnetic geometry has a significant influence on the electron drift mode stability. Introducing a sheared magnetic field stabilizes the mode in slab geometry through so-called *shear damping*, and the term ‘universal instability’ is therefore a misnomer. However, in toroidal geometry shear damping is suppressed and additional drives exist due to the presence of trapped electrons. Instability occurs when these additional drives exceed the residual shear damping as is discussed in Section 8.3.

The two classes of particles in a tokamak, trapped and passing, behave differently in the electrostatic potential perturbation. Consequently, different dispersion relations are obtained, depending on whether it is the passing or trapped particle dynamics which is important. In particular, when the mode frequency  $\omega$  exceeds the particle bounce frequency,  $\omega_{bj}$ , for a particular species  $j$ , trapping can be neglected for that species. This leads to a natural categorization into passing and trapped particle instabilities, and examples of these will be considered in turn in the following two sections.

## 8.3

### Passing particle instabilities

Two of the most important drift instabilities that result from the passing particle dynamics are the electron drift mode, and the  $\eta_l$  or ion temperature gradient (ITG) mode. Their dispersion relation is derived in this section using the gyro-kinetic equation described in Section 2.11. A related instability called the  $\eta_c$  mode is also discussed.

The electron drift and ITG modes are described first. It is necessary to identify certain characteristics of their mode structure, as this allows considerable simplification in the derivation of the dispersion relation. Trapped particle effects are neglected here and this implies modes with  $\omega \gg \omega_{bj}$ , where  $\omega_{bj}$  is the bounce frequency of the trapped particles. The assumed ordering is

$$k_{\parallel} v_{Te} \gg \omega \gg k_{\parallel} v_{Ti}, \quad 8.3.1$$

so the electrons move rapidly to respond to the electrostatic potential. Following the derivation of eqn 8.2.2, this allows their response to be written as a Boltzmann distribution

$$\frac{\bar{n}}{n} = \frac{e\bar{\varphi}}{T_e},$$

where  $\bar{n}$  is the electron density perturbation and  $\bar{\varphi}$  is the perturbation in the electrostatic potential. The ordering of  $k_{\parallel} v_{Ti}$  above will be used later to simplify the equation for the ion response. It is also assumed that the drift frequency associated with the ion magnetic curvature drifts,  $\omega_{di}$ , is much smaller than the mode frequency, so that

$$\omega_{di} = 2\varepsilon_n \omega_{*i} \ll \omega, \quad 8.3.2$$

where  $\varepsilon_n = L_n/R$ ,  $L_n = (d \ln n/dr)^{-1}$  is the density scale length and  $\omega_{*i}$  is the ion diamagnetic frequency. Equation 8.3.2 implies peaked density profiles, though some comments will also be made on the flat density profile limit.

The ion dynamics are particularly important for the radial mode structure of electron drift and ITG modes and finite ion Larmor radius (FLR) effects must be included in order to determine this. Though a description of the essential characteristics of the ITG mode can be obtained using the Braginskii fluid equations, care is necessary to take account of cancellations which occur between components of the FLR stress tensor and the diamagnetic drift contribution to the convective derivative, and it turns out that less algebra is involved in the kinetic approach. Thus assuming a leading order Maxwellian velocity distribution,  $f_M$ , for the ions, the

perturbed ion distribution function can be written

$$f_i = -\frac{e\tilde{\varphi}}{T_i} f_M + g \exp \left[ \frac{i k_\perp v_\perp}{\omega_{ci}} \sin \alpha_g \right]$$

where  $g$  is independent of the gyro-phase angle,  $\alpha_g$ , and the subscript  $\perp$  denotes the component perpendicular to the magnetic field. Integrating over velocity space and ensuring quasi-neutrality,  $n_e = n_i$ , then requires

$$\frac{n e \tilde{\varphi}}{T_e} (1 + \tau) = 2\pi \int_{-\infty}^{\infty} \int_0^{\infty} v_\perp g J_0(z) dv_\perp dv_\parallel,$$

where  $\tau = T_e/T_i$ ,  $z = k_\perp v_\perp / \omega_{ci}$  and the Bessel Function

$$J_0(z) = \frac{1}{2\pi} \oint e^{-iz \cos \phi} d\phi.$$

The function  $g$  is to be evaluated by solving the gyro-kinetic equation for the ions which can be written

$$v_\parallel \frac{\partial g}{\partial l} - i(\omega - \mathbf{k} \cdot \mathbf{v}_d)g - i \frac{e\tilde{\varphi}}{m_i} J_0(z) \left[ \frac{k_\theta}{\omega_{ci}} \frac{d f_M}{dr} + \omega \frac{d f_M}{dK} \right] = 0, \quad 8.3.3$$

where  $dl$  is the poloidal arc length element of a flux surface and  $r$  is the flux surface radius. Spatial derivatives are at constant particle energy,  $K$  and  $\mathbf{k}$  is the wave-vector. The equilibrium drift velocity,  $v_d$ , results from the inhomogeneity of the magnetic field in the torus and is given by

$$v_d = \frac{e}{\omega_{ci}} \times \left[ v_\parallel^2 \frac{\partial \mathbf{e}}{\partial l} + \frac{\mu}{m_i} \nabla B \right],$$

where  $\mathbf{e}$  is a unit vector parallel to the magnetic field and the magnetic moment  $\mu = m_i v_\perp^2 / 2B$ . For a large aspect ratio, low  $\beta$  tokamak, with  $B^2 = B_0^2(1 - 2(r/R)\cos\theta)$ , the drift term in eqn 8.3.3 is

$$\mathbf{k} \cdot \mathbf{v}_d = \frac{\omega_{di}}{2} \left[ \left( \frac{v_\parallel}{v_{Ti}} \right)^2 + \left( \frac{v_\perp}{2v_{Ti}} \right)^2 \right] \left( \cos\theta + \frac{k_r}{k_\theta} \sin\theta \right),$$

where  $k_r$  and  $k_\theta$  are the radial and poloidal wave numbers. Equation 8.3.3 then simplifies to the following equation to be solved for  $g$

$$-v_\parallel \frac{\partial g}{\partial l} + i(\omega - \bar{\omega}_{di})g = i \frac{e\tilde{\varphi}}{T_i} J_0(z)(\omega - \omega_{*i}^T) f_M, \quad 8.3.4$$

where  $\bar{\omega}_{di} = \mathbf{k} \cdot \mathbf{v}_d$  and the velocity-dependent drift frequency,  $\omega_{*i}^T$ , is defined by

$$\omega_{*i}^T = \omega_{*i} \left[ 1 + \left( \frac{v^2}{2v_{Ti}^2} - \frac{3}{2} \right) \eta_i \right]$$

and  $\eta_i = n T'_i / T_i n'$  is the ratio of the density scale length to the temperature scale length, the prime denoting a radial derivative. The parameter  $\eta_i$  plays

### 8.3 Passing particle instabilities

a crucial role in the stability of one of the passing particle modes, which is therefore often referred to as the ' $\eta_i$  mode'.

The 'drift wave ordering' of inequality 8.3.1 exploits the slow parallel velocity of the ions. This allows a solution of eqn 8.3.4 to be obtained by treating the parallel derivative term as small so that, expanding to second order in this term,

$$g = J_0(z) f_M \frac{\omega - \omega_{\text{si}}^T}{\omega - \tilde{\omega}_{\text{di}}} \left[ 1 - i \frac{v_{\parallel}}{\omega - \tilde{\omega}_{\text{di}}} \frac{\partial}{\partial l} - \frac{v_{\parallel}^2}{(\omega - \tilde{\omega}_{\text{di}})^2} \frac{\partial^2}{\partial l^2} \right] \frac{e\tilde{\varphi}}{T_i}. \quad 8.3.5$$

Equation 8.3.5 can be further simplified by making use of eqn 8.3.2 and performing a subsidiary expansion in  $\omega_{\text{di}}/\omega$ . In this limit the velocity integrals in the quasi-neutrality expression can be evaluated to give the eigenvalue equation

$$\left\{ \rho_i^2 \frac{\partial^2}{\partial x^2} - \left( \frac{\epsilon_n}{b^{1/2} \tau q \Omega} \right)^2 \left( \frac{\partial}{\partial \theta} + ik_{\theta} s x \right)^2 - \frac{2\epsilon_n}{\tau \Omega} \left( \cos \theta + \frac{i \sin \theta}{k_{\theta}} \frac{\partial}{\partial x} \right) - \left( \frac{\Omega - 1}{\tau \Omega + (1 + \eta_i)} + b \right) \right\} \tilde{\varphi} = 0. \quad 8.3.6$$

where  $s$  is the magnetic shear,  $b = (k_{\theta} \rho_i)^2$  and the radial variable  $x$  is the distance from a reference mode rational surface,  $r = r_s$ , defined by  $m = nq(r_s)$  where  $n$  is the toroidal mode number.  $J_0$  has been expanded for small  $k_{\perp} \rho_i$ , where  $\rho_i$  is the ion Larmor radius evaluated with the thermal velocity, and  $k_r$  has been interpreted as a radial derivative, which then determines the radial mode structure. The parallel derivative has become the second operator on the left hand side, and  $\Omega$  is the mode frequency normalized to the electron drift frequency,  $\omega_{se}$ .

Equation 8.3.6 can be used to illustrate the properties of the electron drift and  $\eta_i$  modes as follows. In order to balance the last bracketed term with the rest (which are small,  $\ll 1$ ) either  $\Omega \approx 1$  or  $\eta_i \gg 1$ . For  $\eta_i \gg 1$  two modes can be identified depending on the strength of the toroidal coupling term (that involving  $\cos \theta$  and  $\sin \theta$ ). For very weak toroidal coupling, a balance of the second and last terms yields a mode frequency  $\omega \sim (k_{\parallel}^2 v_{\parallel}^2 \omega_{ki} \eta_i)^{1/3}$ . This solution is called the slab branch of the  $\eta_i$  mode because it does not involve toroidal coupling effects. In a shearless slab  $k_{\parallel}$  is constant. However, for a sheared slab the effective  $k_{\parallel}$  depends on the radial mode width which can be calculated from eqn 8.3.6. Then  $k_{\parallel}^2 = ib\tau\Omega/L_n L_s$ , which gives  $\omega = (i\epsilon_n s \eta_i/q)^{1/2} \omega_{se}$  for the ITG mode

in a sheared slab. In a torus, a second type of  $\eta_i$  mode structure can occur, resulting from a balance between the toroidal coupling term and the last term. This has a mode frequency  $\omega \sim (\eta_i \omega_{*i} \omega_{\text{di}})^{1/2}$  and is known as the toroidal branch of the  $\eta_i$  mode. Finally, the ordering  $\Omega \sim 1$  gives rise to a branch with  $\omega \sim \omega_{*e}$ , and this is called the slab branch of the electron drift mode. Other orderings exist which give rise to more branches (for example a toroidal electron drift mode), but the three modes introduced above provides a convenient illustration of the principal mode characteristics. These modes will now be described in turn, using eqn 8.3.6 to illustrate the discussion.

### Electron drift mode

It is interesting to review the history of this mode, which was first analysed in a shearless slab geometry. In this case the mode structure is derived from an equation which is similar to the Schrödinger equation. Maintaining this analogy, the potential is found to form a 'well' in the radial direction when variations in the density profile are taken into account. This leads to a confined mode, known as the Krall–Rosenbluth mode, which is unstable. However, on the introduction of a sheared magnetic field in the slab, the mode structure is completely different. In this geometry it can be deduced from eqn 8.3.6 by dropping the curvature term (so that poloidal Fourier harmonics are not coupled) and Fourier analysing in the poloidal direction. The resulting equation, which describes the radial mode structure, is

$$\left\{ \frac{\rho_i^2}{(nq)^2} \frac{\partial^2}{\partial x^2} + \left( \frac{\epsilon_n s k_\theta}{b^{1/2} \tau q} \right)^2 x^2 - \left[ \frac{\Omega - 1}{\tau + 1} + b \right] \right\} \tilde{\varphi} = 0,$$

where the electron drift wave ordering,  $\Omega \sim 1$ , is assumed. For typical tokamak values, the radial variation due to the magnetic shear dominates that due to the density profile which has therefore been neglected. The radial structure is still described by a Schrödinger equation with a parabolic potential but now with a potential hill rather than a well. Such a potential is not able to confine the mode and it was therefore originally thought that the electron drift wave branch could not exist in the presence of magnetic shear. However, an 'outgoing wave' solution is physically acceptable provided there is a dissipation mechanism at large distances from the mode rational surface which can act as a sink for this energy and localize the mode. Such a mechanism does indeed exist. In deriving eqn 8.3.6 a large  $\omega/k_{\parallel} v_{T\parallel}$  expansion was made and so ion Landau damping was neglected. However,  $k_{\parallel}$  increases with  $x$  and at large  $x$  ion Landau damping does become an important dissipation mechanism. Although it does not appear explicitly in eqn 8.3.6, it conceptually justifies selecting the 'outgoing wave' solution. This is illustrated in Fig. 8.3.1. Because the outgoing wave is transferring energy from the mode to the Landau resonance, it is stabilizing. For this reason, and because of the important intermediary role of the magnetic shear, the effect is known

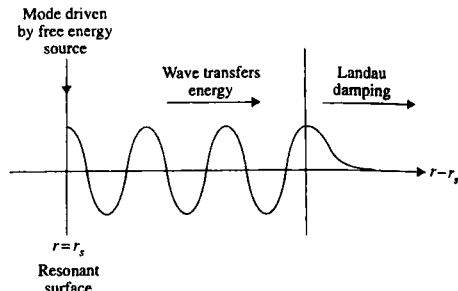


**Fig. 8.3.1** Sketch of the energy flow for the electron drift mode showing the free energy source driving the mode at the rational surface,  $r = r_s$ , and the outgoing wave transferring the energy to target distances where it is dissipated by ion Landau damping.

as *shear damping*. Initial analytic calculations indicated that for values of shear typically found in a tokamak, this shear damping is small and the perturbative inclusion of drive terms from the electron Landau resonance led to the belief that the electron drift mode was unstable. However, subsequent numerical calculations showed that the perturbative treatment inadequately described the effects of the electron Landau resonance and the mode is in fact stable.

### Toroidal electron drift mode

In a torus the mode structure can be quite different from that in a slab. However, the ideas which have been developed in the analysis of the slab mode remain useful for discussing this mode. An important method of analysing the structure of toroidal modes is the ‘ballooning’ transformation, which gains its name from its use in the analysis of mhd ballooning modes (Section 6.13). A simplified treatment can be derived by expanding  $\tilde{\varphi}$  in poloidal Fourier harmonics

$$\tilde{\varphi} = \sum_m e^{-im(\theta-\theta_0)} u_m(y),$$

where the (as yet) arbitrary free parameter,  $\theta_0$ , will be needed to determine the radial structure of  $\tilde{\varphi}$ . It is convenient to define the new radial variable  $y = sk\theta x$  so that eqn 8.3.6 yields a differential-difference equation for  $u_m(y)$ :

$$\begin{aligned} \frac{d^2 u_m}{dy^2} + \frac{\sigma^2}{\Omega^2} (y - m)^2 u_m - \lambda u_m \\ = \frac{\alpha}{2\Omega} \left[ e^{i\theta_0} \left( 1 + s \frac{d}{dy} \right) u_{m+1} + e^{-i\theta_0} \left( 1 - s \frac{d}{dy} \right) u_{m-1} \right] = 0. \end{aligned}$$

where  $\alpha = 2\epsilon_n/b\tau^2 s$ ,  $\sigma = \epsilon_n/b\tau q s$  and  $\lambda$  is the eigenvalue, related to the complex mode frequency by

$$\lambda = \frac{1}{bs^2} \left( \frac{\Omega - 1}{\tau\Omega + 1 + \eta_1} + b \right).$$

Note that  $\alpha$  results from the toroidal geometry and this provides the coupling of the Fourier harmonics,  $u_m$ . For high toroidal mode number  $\tilde{\varphi}$  is radially localized and equilibrium variations other than shear can be neglected. A solution then exists which is of the form  $u_m(y) = u_0(y - m)$ . Fourier transforming

$$u_0(y) = \frac{1}{2\pi} \int_{-\infty}^{\infty} e^{i\eta y} \tilde{u}(\eta) d\eta$$

the eigenmode equation becomes

$$\left\{ \left( \frac{\sigma}{\Omega} \right)^2 \frac{\partial^2}{\partial \eta^2} + \eta^2 + \left( \frac{\sigma}{\Omega} \right) [\cos(\eta - \theta_0) + s\eta \sin(\eta - \theta_0)] + \lambda(\theta_0) \right\} \tilde{u} = 0. \quad 8.3.7$$

At this level,  $\theta_0$  is an arbitrary free parameter, frequently referred to as the 'ballooning angle'. The mode frequency depends on  $\theta_0$ , and a full determination of this frequency requires a higher order calculation in which the finite radial width of the mode and radial variations in  $\omega_*$  are taken into account. A self-consistent ordering is possible if the mode is localized at a radial position where the electron diamagnetic frequency  $\omega_{*e}$  is maximum. The higher order theory then predicts that  $\theta_0$  must be chosen so that the eigenvalue  $\lambda$  is stationary. Equation 8.3.7 can be solved for the mode frequency,  $\Omega$  and contains information about the mode structure in a torus. First, a connection can be made with the slab results discussed above by setting  $\alpha = 0$ . The mode structure is described by a Schrödinger equation and for  $\alpha = 0$  has the same anti-well potential in  $\eta$  derived for the slab mode. Hence the same travelling wave solution is obtained, though an outgoing wave in real  $x$ -space maps onto an incoming wave in  $\eta$ -space. Increasing  $\alpha$  leads to a completely different mode structure which results from the modifications to the potential due to the curvature term. In particular, as  $\alpha$  is increased, the  $s\eta \sin \eta$  term leads to minima in the 'potential' which help to confine the mode. Two examples, one for  $\alpha = 0$  and one for  $\alpha = 3$ , of the 'potential' and the corresponding eigenfunction in  $\eta$  are shown in Fig. 8.3.2. For  $\alpha = 0$  the potential is a hill and shear damping is strong. This is indicated by the eigenfunction, which represents a wave whose amplitude increases toward large  $|\eta|$ . For larger  $\alpha$  a local well forms in the potential and the eigenfunction can be partially confined within this. However, some of the eigenfunction 'tunnels out', though its amplitude is reduced and the shear damping is

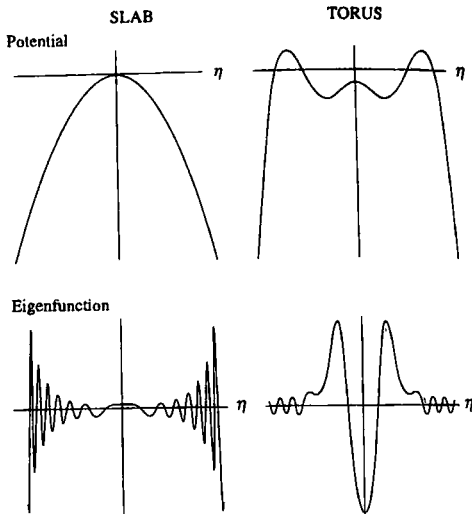


**Fig. 8.3.2** Plots showing the 'potential' for the electron drift mode and the corresponding eigenfunction as a function of the ballooning coordinate  $\eta$ , for the toroidal coupling parameter  $\alpha = 0$  (left) and  $\alpha = 3$  (right).

then less effective. Thus the electron drift wave is generally more unstable in a toroidal plasma than in the slab. This situation is shown in Fig. 8.3.2 for  $\alpha = 3$ .

#### The $\eta_i$ , or ion temperature gradient, mode

The existence of two types of ITG mode structure has been illustrated below eqn 8.3.6: a 'slab' branch, which evolves from the sound wave with  $\omega \sim (k_{\parallel}^2 v_{\text{A}}^2 \omega_{ci} \eta_i)^{1/3}$ , and a toroidal branch with  $\omega \sim (\eta_i \omega_{ci} \omega_{di})^{1/2}$ . In contrast to the electron drift wave, the mode frequency is different from  $\omega_{se}$  and in fact is complex. This results in a different mode structure for the ITG modes than that found for the electron drift wave. The reason for the difference is that the shear damping parameter,  $\sigma/\Omega$ , depends on  $\omega$  so that it now becomes complex. The mode structure is found to be governed by a 'Schrödinger' equation with a potential well, which results in a confined mode and does not exhibit the 'outgoing wave' nature of the electron drift mode. This suppresses the shear damping so that the ITG modes can be readily destabilized.

The properties of the ITG mode, whose growth rate depends on the value of  $\eta_i$ , have been derived above by solving the ion gyro-kinetic equation under the assumption that the resonance associated with the magnetic

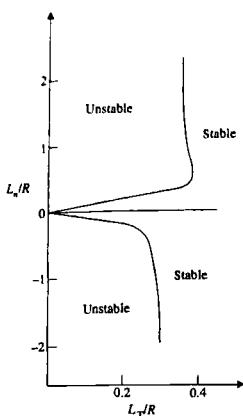


Fig. 8.3.3 Stability diagram for the toroidal ITG mode (from Biglari H., et al., *Physics of Fluids* B1 109 (1989)).

curvature drift is negligible. It was seen that this requires the toroidal coupling term to be small, which in turn requires \$\eta\_i\$ to be large. Equation 8.3.6 predicts that this branch is unstable for all positive \$\eta\_i\$, but when a more complete analysis is performed, in which the curvature drift resonance is retained, it is found that this is not the case. In fact the mode is stable for \$\eta\_i < \eta\_{ic}\$ where \$\eta\_{ic} \sim 1\$. The specific form of \$\eta\_{ic}\$ depends on the branch being considered. For example, by employing the ballooning transformation, it is possible to derive the threshold for the toroidal \$\eta\_i\$ mode

$$\eta_{ic} = \begin{cases} 1.2 & \varepsilon_n < \varepsilon_{nc} \\ \frac{4}{3}(1 + \tau^{-1})(1 + 2s/q)\varepsilon_n & \varepsilon_n > \varepsilon_{nc} \end{cases}$$

where

$$\varepsilon_{nc} = \frac{0.9}{(1 + \tau^{-1})(1 + 2s/q)}.$$

This expression exhibits the interesting feature that when the density profile is sufficiently flat the threshold is a critical temperature gradient rather than a critical \$\eta\_i\$. For this reason, this instability is also referred to as the ion temperature gradient (or ITG) mode. The full stability diagram is illustrated in Fig. 8.3.3.

### The \$\eta\_e\$ mode

There is another passing particle instability, which is similar to the ITG mode, but where the roles of the ions and electrons are reversed. This is the \$\eta\_e\$, or ETG (electron temperature gradient), mode. This mode can be classified as 'electrostatic' because its existence can be demonstrated without addressing the associated electromagnetic perturbations. However, for typical tokamak conditions the electromagnetic perturbations are important and can have significant implications for electron heat transport.

The perpendicular wavelength of the \$\eta\_e\$ mode lies between the electron and ion Larmor radii. Thus \$k\_{\perp}\rho\_i \gg 1\$ so that in eqn 8.3.3 \$J\_0(z) \rightarrow 0\$, resulting in \$g = 0\$ and the ion response being a Boltzmann distribution. The electron response can be calculated from the gyro-kinetic eqn 8.3.3 with the subscripts i replaced by e. Following a similar analysis to that of the ITG mode, the eigenvalue equation is the same as eqn 8.3.6, but with the subscripts i and e interchanged. Taking the slab limit of eqn 8.3.6 corresponds to dropping the third term (that involving \$\cos \theta\$ and \$\sin \theta\$). Neglecting finite electron Larmor radius effects and assuming \$T\_e = T\_i\$ then results in the following dispersion relation for \$\eta\_e\$ modes:

$$-\frac{k_{\parallel}^2 v_{Te}^2}{\omega^2} \left( 1 - \frac{\omega_{*e}}{\omega} (1 + \eta_e) \right) + 1 + \frac{\omega_{*e}}{\omega} = 0.$$

In the limit \$\eta\_e \gg 1\$ an unstable mode exists whose complex frequency is \$\omega \simeq (-k\_{\parallel}^2 v\_{Te}^2 \eta\_e \omega\_{\*e})^{1/3}\$.

The above analysis of the  $\eta_e$  mode neglected the electromagnetic perturbations to allow a simple picture of the essential elements of the instability. The importance of the electromagnetic perturbations can be illustrated by considering Ampère's law

$$k_\perp^2 A_\parallel = \mu_0 j_\parallel,$$

where  $A_\parallel$  is the perturbed vector potential and  $j_\parallel$  is the perturbed current. In a collisionless plasma the current is obtained from the parallel force balance equation for the electrons

$$m_e \omega v_{\parallel e} = e(k_\parallel \tilde{\varphi} - \omega A_\parallel) - k_\parallel \tilde{p},$$

where  $v_{\parallel e}$  is the electron velocity perturbation parallel to the magnetic field and  $\tilde{p}$  is the pressure perturbation. The ions move slowly along the field lines because of their high inertia so that the current is given by  $j_\parallel = nev_{\parallel e}$ . Substituting this expression for the current into Ampère's law and neglecting the pressure perturbation for simplicity results in the following relation between  $A_\parallel$  and  $\tilde{\varphi}$

$$\frac{\omega A_\parallel}{k_\parallel \tilde{\varphi}} = \frac{1}{1 + k_\perp^2 (c/\omega_{pe})^2},$$

where  $c/\omega_{pe} = (m_e/\mu_0 n e^2)^{1/2}$  is the collisionless skin depth. For perpendicular wave-lengths above the electron gyro-radius this ratio is close to unity for typical tokamak parameters and the magnetic perturbations must be taken into account for an accurate quantitative description of the  $\eta_e$  mode. Note that the difference between the  $\eta_i$  mode and  $\eta_e$  mode is that electrons satisfy force balance along the magnetic field lines for the  $\eta_i$  mode and so there is no perturbed parallel electron flow and no significant perturbed parallel current to drive the magnetic perturbations. The importance of the electromagnetic perturbations may have significant implications for the electron heat transport.

## 8.4

### Trapped particle instabilities

Trapped and passing particles behave differently in an electrostatic plasma wave. In particular, trapped particles effectively average out their parallel velocity over a bounce period and therefore the parallel dynamics are less important than for passing particles for modes with  $\omega < \omega_b$ . Secondly, in their bounce orbit they do not explore the full poloidal and toroidal circumferences and they therefore exhibit some stability characteristics which are similar to those experienced by particles confined by a magnetic mirror. This leads to a new class of instabilities—the trapped particle

modes. These can be separated into two classes, dissipative, where the collision frequency plays an important role in the stability, and collisionless, where collisions are not necessary for instability. Theory predicts that the dissipative modes are more dangerous, and are therefore more likely candidates for the tokamak plasma micro-turbulence. However, the physics responsible for the collisionless mode is more transparent and serves as a useful illustration of the different dynamics of the trapped and passing particles. The next subsection is devoted to a description of a collisionless trapped particle mode, and dissipative trapped particle modes are then described in the subsequent subsection.

### Collisionless trapped particle instability

The essential characteristics of the collisionless trapped particle instability can be illustrated by considering plasma oscillations which have a sufficiently low phase velocity,  $\omega/k_{\parallel} \ll v_{Tj}$ , that it can be neglected relative to the parallel velocity of both passing particle species. Thus, the passing particle dynamics are dominated by their parallel motion and, as for the electrons in the passing particle instabilities, they take up a Boltzmann distribution

$$\tilde{n}_{pj} = -n(1 - \sqrt{2\varepsilon}) \frac{e_j \tilde{\varphi}}{T_j},$$

where the subscript  $p$  indicates the passing particle contribution and the fraction of trapped particles is approximated by  $\sqrt{2\varepsilon}$ ,  $\varepsilon$  being the inverse aspect ratio. The trapped particles have zero bounce averaged parallel velocity and the particle drifts are more important for these than for the passing particles. They are trapped between magnetic mirrors and therefore spend most of their time in the bad curvature region on the outboard side of the tokamak. This makes them susceptible to instabilities which resemble flute-like modes as follows. Consider an initial density perturbation which has a long parallel wavelength, as illustrated in Fig. 8.4.1. The magnetic curvature drift is in the opposite direction for electrons and ions and the component in the flux surface results in the charge polarization shown in the figure. Note, that because the trapped particles spend

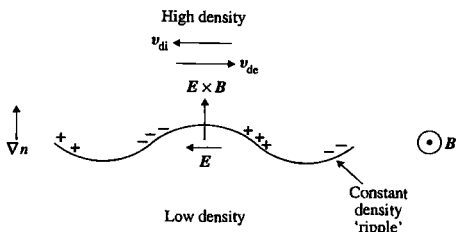


**Fig. 8.4.1** The physical mechanism for the trapped particle instability. The charge polarization caused by the curvature drift of the trapped particles results in an  $E \times B$  flow which enhances the amplitude of an initial density wave and results in an instability.

most of their time on the outboard side, the curvature drift of a particular species has a preferred direction, whereas the passing particles experience both the good and bad curvature regions and average this effect out. The associated local electric fields drive small-scale  $E \times B$  flows which enhance the initial perturbation and lead to instability. The passing particles provide a background 'sea' which does not respond in this way and tends to reduce the instability growth so it is important to retain their contribution. Thus, to describe the instability it is essential to retain the physics of both the magnetic curvature and  $E \times B$  drifts as well as the dominant passing particle dynamics.

For this collisionless trapped particle mode finite Larmor radius effects are not important and the trapped particle response to the electrostatic perturbation is described by the drift kinetic equation. The bounce-averaged parallel dynamics are neglected to obtain the trapped particle response

$$\tilde{n}_{lj} = -\sqrt{2\varepsilon n} \frac{e_j \bar{\varphi}}{T_j} + \sqrt{2\varepsilon} \int g_{lj} d^3 v$$

with

$$(\omega - \bar{\omega}_{dj}) g_{lj} = (\omega - \omega_{*j}^T) f_M \frac{e_j \bar{\varphi}}{T_j},$$

where the subscript t indicates the trapped particle contribution and the bar over a quantity indicates a bounce average. The non-Boltzmann part of the distribution function,  $g_{lj}$ , the magnetic drift frequency  $\omega_{dj}$  and velocity dependent diamagnetic frequency  $\omega_{*j}^T$  are defined in Section 8.3. Assuming quasi-neutrality and averaging any remaining quantities over the trapped particle bounce orbits results in the dispersion relation:

$$\frac{1}{\sqrt{2\varepsilon}} \left( \frac{1}{T_i} + \frac{1}{T_e} \right) = \frac{1}{T_i} \frac{\omega - \omega_{*i}}{\omega - \bar{\omega}_{di}} + \frac{1}{T_e} \frac{\omega - \omega_{*e}}{\omega - \bar{\omega}_{de}}. \quad 8.4.1$$

This equation can easily be solved for  $\omega$ , but a particularly simple illustrative expression for the complex mode frequency,  $\omega$  is obtained by taking  $T_e = T_i$  and  $\omega_{*j} \gg \bar{\omega}_{dj}$ , which is relevant in the large aspect ratio limit, to obtain

$$\omega^2 = \bar{\omega}_{de}(\bar{\omega}_{de} + \sqrt{2\varepsilon}\omega_{*e}).$$

For a density which decreases with minor radius  $\omega_{*e} > 0$  while  $\bar{\omega}_{de} < 0$ , and instability then occurs for  $\sqrt{2\varepsilon}R/L_n > 1$ . The crucial role of the perturbed  $E \times B$  and magnetic curvature drifts is apparent through the dependence of the growth rate on  $\omega_{*e}$  and  $\bar{\omega}_{de}$ .

### Dissipative trapped particle instabilities

The condition for collisions to be important is that the effective collision frequency be of the same order as the relevant drift frequency. In this regime collisions provide a mechanism whereby trapped particles can

be scattered into passing and vice versa. This leads to collisional, or dissipative, trapped particle modes and two examples of such modes will be described below. For the trapped ion mode, both the trapped electrons and ions play a role in the instability which is a dissipative version of the collisionless mode described in the previous subsection. The ion collisions are found to be stabilizing, while the electrons are destabilizing. In the second example, the trapped ions do not play a role and stability is determined by the trapped electron dynamics. This mode is classified as a dissipative trapped electron mode. In both cases, although collisions are important, they must not be so frequent as to prevent the trapped particles completing a banana orbit. This requires that the collision frequency satisfies,  $\nu_j < \varepsilon\omega_{bj}$  for the species being considered, where  $\omega_{bj}$  is the bounce frequency.

### Trapped ion mode

This instability evolves from the collisionless trapped particle mode. It occurs when the effective collision frequency of the trapped particles exceeds the magnetic drift frequency,  $\omega_{dj}$ . The collision frequency then replaces  $\omega_{bj}$  in eqn 8.4.1. In equilibrium the particle species adopt a Maxwellian velocity distribution and the fraction of trapped particles is then  $\sim\sqrt{2\varepsilon}$ . Furthermore, an electrostatic perturbation will cause the distribution function to deviate from a Maxwellian, while collisions tend to restore it. Thus, a simple model which retains the essential physics of the collisions can be incorporated by a term in the continuity equation for the trapped particles, as follows

$$\frac{\partial n_{tj}}{\partial t} + \frac{(\mathbf{B} \times \nabla \varphi)}{B^2} \cdot \nabla n_{tj} = -\frac{\nu_j}{\varepsilon}(n_{tj} - \sqrt{2\varepsilon}n), \quad 8.4.2$$

where the second term on the left represents convection due to the  $\mathbf{E} \times \mathbf{B}$  drift. The effective trapped particle collision frequency is  $\nu_j/\varepsilon$  which acts to maintain the trapped particle density fraction at  $\sim\sqrt{2\varepsilon}n$ . Note that the magnetic drift frequency is not retained for the modes considered since this is dominated by the effective collision frequency,  $\nu_j/\varepsilon > \omega_{dj}$ , that is

$$1 > \nu_{*j} > \frac{(k_\theta \rho_j)q}{\sqrt{\varepsilon}},$$

where  $\nu_{*j} = \nu_j/\varepsilon\omega_{bj}$  is the species collisionality. Linearizing eqn 8.4.2 and neglecting the equilibrium electric field, the non-Boltzmann part of the trapped particle density perturbation is given by

$$\frac{\tilde{n}_{tj}}{n} = \sqrt{2\varepsilon} \left( \frac{\omega - \omega_{*j}}{\omega + i\nu_j/\varepsilon} \right) \frac{e_j \tilde{\varphi}}{T_j}.$$

The passing particle response is again described by a Boltzmann distribution for both species and then quasi-neutrality results in the dispersion relation

$$\frac{1}{\sqrt{2\varepsilon}} \left( \frac{1}{T_e} + \frac{1}{T_i} \right) = \frac{1}{T_i} \left( \frac{\omega - \omega_{*i}}{\omega + i\nu_i/\varepsilon} \right) + \frac{1}{T_e} \left( \frac{\omega - \omega_{*e}}{\omega + i\nu_e/\varepsilon} \right).$$

This can have an unstable root, whose characteristics are easily illustrated by considering the limit  $\nu_e/\varepsilon \gg \omega$  and treating the last term on the right as a perturbation. The relevant root is then

$$\omega = \frac{\sqrt{2\varepsilon}}{1+\tau} \omega_{*e} - i \frac{\nu_i}{\varepsilon} + i \frac{\varepsilon^2}{(1+\tau)^2} \frac{\omega_{*e}^2}{\nu_e}.$$

The competing nature of the two species collision frequencies is clear, the electrons being destabilizing while the ions are stabilizing. For the high electron collision frequency assumed here, the ions 'win' and the mode is stable. However, the imaginary part of  $\omega$  is maximized for  $\nu_e \approx \varepsilon^{3/2}/\omega_{*e}$  in which case it is positive and the mode is unstable. This is illustrated for a typical set of parameters in Fig. 8.4.2 where the growth rate is plotted as a function of the electron collision frequency.

### Dissipative trapped electron mode

Another type of dissipative trapped-particle mode is related to the electron drift mode described in the previous section. Trapped ions do not play an essential role in this mode, which is driven by the combined effects of the trapped-electron collisions and an electron-temperature gradient. The perturbed  $E \times B$  drift is the only drift retained in this simple model. The main contribution to the instability drive results from the low energy trapped electrons and it is essential to retain the velocity dependence of the electron collision frequency. In the simplest model the trapped-particle effective collision frequency has the form  $\nu_{\text{eff}} = \nu_e v_{Te}^3 / ev^3$  and the non-Boltzmann part of the trapped-electron distribution function,  $g_{te}$

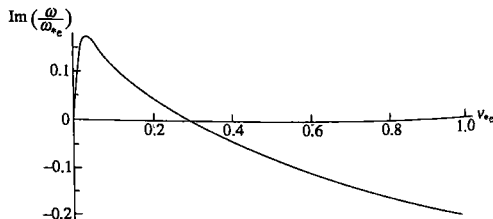


Fig. 8.4.2 Variation of growth rate with electron collisionality,  $\nu_e$ , for the trapped ion mode where  $v_i = (m_e/2m_i)^{1/2} v_e$  is assumed and the other parameters are fixed.

can be calculated from the drift equation

$$(\omega + i\nu_{\text{eff}})g_{te} = \sqrt{2\varepsilon} \frac{e\phi}{T_e} f_M(\omega - \omega_{*e}^T).$$

The parallel motion of the trapped electrons has dropped out on bounce averaging, whereas this parallel motion dominates the passing electron dynamics which therefore adopt a Boltzmann distribution. In keeping with the drift wave ordering introduced in eqn 8.3.1, the ion parallel velocity is neglected and, using the ion continuity equation, the following expression for the ion density perturbation is obtained

$$\bar{n}_i = n \frac{\omega_{*e}}{\omega} \frac{e\phi}{T_e}.$$

Quasi-neutrality then yields the dispersion relation

$$\frac{\omega}{\omega_{*e}} = 1 - \sqrt{2\varepsilon} \int \frac{\omega - \omega_{*e}^T}{\omega + i\nu_{\text{eff}}} f_M d^3 v, \quad 8.4.3$$

where the integral term of eqn 8.4.3 is assumed to be  $\ll 1$ . Thus the mode frequency is close to  $\omega = \omega_{*e}$  and in the limit  $\nu_{\text{eff}} \gg \omega_{*e}$  the growth rate is given by

$$\gamma = \sqrt{2\varepsilon} \omega_{*e} \int \frac{\omega_{*e}^T - \omega_{*e}}{\nu_{\text{eff}}} f_M d^3 v.$$

The key role of the velocity dependence of the collision frequency is now apparent, since without it there is no growth. However, with the collision frequency model assumed here, instability is found with a growth rate

$$\gamma \sim \varepsilon^{3/2} \frac{\omega_{*e}^2}{\nu_e} \eta_e.$$

The main drive for this instability comes from the electron temperature gradient although for  $\eta_e \sim \varepsilon$  the magnetic curvature becomes important and results in a slower instability.

## 8.5

### Micro-tearing modes

The micro-tearing mode differs from the modes described in Sections 8.3 and 8.4 in that magnetic perturbations are important and can result in small scale magnetic islands. In this respect these modes are similar to the gross tearing mode which has been described in Section 6.8. However the modes considered here have short wavelength with high poloidal mode number,  $m$ . In this case the tearing parameter,  $\Delta' \simeq -2m/r$  and

is therefore negative. Thus the standard tearing mode theory, which is based on resistive MHD, predicts stability. Two effects can compete with  $\Delta'$  and result in growth of a magnetic perturbation to a saturated island. First, the nonlinear effects of the island structure can modify the plasma equilibrium and particle drifts and so produce drive mechanisms which are absent in the linear theory. The saturated magnetic island width results from the balance between the dominant nonlinear drive and the stabilizing  $\Delta'$ . These nonlinear islands are discussed later. In the second case, kinetic effects can lead to micro-tearing instability driven by an electron temperature gradient in a sufficiently collisional plasma. These modes are described by linear theory and will be addressed first.

Electrons and ions respond differently to a magnetic perturbation, largely as a result of their differing masses. The different charge flows lead to a current perturbation which must satisfy Ampère's law

$$\frac{\partial^2 A_{\parallel}}{\partial x^2} = -\mu_0 j_{\parallel}, \quad 8.5.1$$

where  $x$  represents the radial distance from the rational surface and  $A_{\parallel}$  and  $j_{\parallel}$  are the components of the perturbed magnetic potential and current density parallel to the equilibrium magnetic field. Equation 8.5.1 is an approximation in which the dominant variation is assumed to be in the  $x$  direction. In fact, the current is highly localized around the rational surface. To illustrate this, it is convenient to introduce a helical magnetic perturbation of the form

$$A_{\parallel} = -\bar{\psi} e^{-ik_z y} e^{iyt}, \quad 8.5.2$$

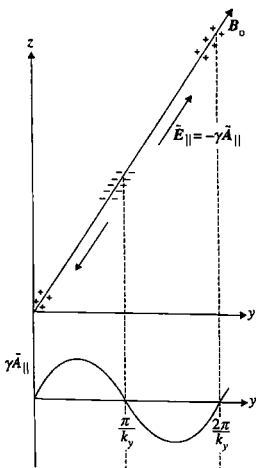


**Fig. 8.5.1** Charge accumulation in response to a time-dependent perturbation in the parallel component of the vector potential,  $A_{\parallel}$ .

where  $\xi = m(\theta - \phi/q_s)$  with  $q_s = m/n$  the safety factor at the rational surface,  $\theta$  and  $\phi$  are the poloidal and toroidal angles and  $\gamma$  is the growth rate. In this approximation  $A_{\parallel}$  is related to the radial magnetic field perturbation by  $B_r = (in/r)A_{\parallel}$ . The time varying magnetic perturbation leads to an electric field,  $E_{\parallel} = -\gamma A_{\parallel}$  which accelerates the electrons along the magnetic field. The ions are much heavier and are not affected by this electromagnetic contribution to the electric field. Thus charge accumulations arise and result in a perturbed electrostatic potential,  $\varphi$ , as illustrated in Fig. 8.5.1. The resulting electrostatic electric field opposes the electromagnetic contribution and the net electric field is

$$E_{\parallel} = -\gamma A_{\parallel} - ik_{\parallel}\varphi.$$

In the region of phase space defined by  $v_{\parallel} > \omega/k_{\parallel}$  the electron speed parallel to the magnetic field is fast relative to the phase velocity of the wave and the electrons effectively 'short out' the electromagnetic contribution to  $E_{\parallel}$  so that  $k_{\parallel}\varphi \simeq i\gamma A_{\parallel}$  and no current results. Thus the current only flows where  $\omega/k_{\parallel}v_{\parallel} > 1$ . Because  $k_{\parallel} = (m/r)x/L_s$ , this corresponds to a narrow layer around the rational surface for thermal velocities.

Equation 8.5.1, can be integrated across the current layer to give

$$\frac{\partial A_{\parallel}}{\partial x} \Big|_{x=l} - \frac{\partial A_{\parallel}}{\partial x} \Big|_{x=-l} = -\mu_0 j_{\parallel} d, \quad 8.5.3$$

where the integration limit,  $l$  is much larger than the current sheet width  $d$ , but small compared with the equilibrium scale lengths. The left hand side of eqn 8.5.3 is the jump in the radial derivative of  $A_{\parallel}$  across the current layer, which must be matched to the jump in the outer solutions as represented by

$$\Delta' = \frac{1}{A_{\parallel}^{\text{out}}} \left[ \frac{\partial A_{\parallel}^{\text{out}}}{\partial x} \Big|_{r=r_s^+} - \frac{\partial A_{\parallel}^{\text{out}}}{\partial x} \Big|_{r=r_s^-} \right], \quad 8.5.4$$

where  $r_s^{\pm}$  is the limit as the minor radius tends to the rational surface,  $r = r_s$  from  $r > r_s$  and  $r < r_s$  respectively. The required  $A_{\parallel}^{\text{out}}$  are solutions of the ideal mhd equations outside the current layer. Equations 8.5.3 and 8.5.4 are matched to give the dispersion relation

$$\Delta' A_{\parallel} = -\mu_0 j_{\parallel} d. \quad 8.5.5$$

For the high  $m$  perturbations considered here  $A_{\parallel}^{\text{out}} \sim r^m$  for  $r < r_s$  and  $\sim r^{-m}$  for  $r > r_s$  and so  $\Delta' = -2m/r$ . In general the external solutions are determined as described in Section 6.8 for the global tearing mode.

In the layer region, kinetic effects must be included to calculate the current,  $j_{\parallel}$ , and the layer width,  $d$ . The growth rate is derived from the matching condition 8.5.5 as described shortly for a simple analytic model. The results of accurate numerical calculations of the linear micro-tearing growth rate are shown in Fig. 8.5.2. It is seen that the micro-tearing mode is stable at both low and high collision frequencies, but a window exists for intermediate collision frequencies in which the mode is unstable in the presence of an electron temperature gradient.

The detailed mechanism responsible for micro-tearing mode instability is complicated. However, a useful model which demonstrates the essential physics of the micro-tearing mode can be described in the 'semi-collisional' regime. In this regime the electron flow velocity,  $v_{\parallel}$  along the field lines is limited by collisions with the ions. Thus the parallel flux  $n v_{\parallel} = D_e k_{\parallel} n$ , where  $D_e = v_{\text{te}}^2/v_e$  is the collisional diffusion coefficient, so that  $v_{\parallel} = k_{\parallel} D_e$ . As discussed above, the current layer exists in the region for which the electron parallel flow is less than the phase velocity of the perturbation, resulting in the following relation between the layer width and the growth rate

$$k_{\parallel} v_{\parallel} = k_{\parallel}^2 v_{\text{te}}^2 / v_e = k_{\parallel}^2 d^2 v_{\text{te}}^2 / L_s^2 v_e = \gamma. \quad 8.5.6$$

In early calculations, the electrostatic potential,  $\varphi$  was neglected within this layer, and then the current perturbation is simply

$$j_{\parallel} = E_{\parallel}/\eta = -\gamma A_{\parallel}/\eta. \quad 8.5.7$$

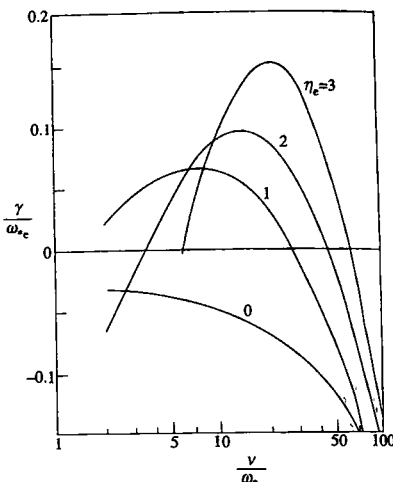


**Fig. 8.5.2** Numerical calculation of the growth rate of the linear micro-tearing mode as a function of electron collision frequency,  $v_e$ , for four different values of the electron temperature gradient parameter,  $\eta_e$ . (Gladd N.T., et al., *Physics of Fluids* 23 1182 (1980).)

where  $\eta$  is the plasma resistivity. Combining eqns 8.5.5, 8.5.6 and 8.5.7 leads to the growth rate

$$\gamma \sim \gamma_0^{2/3} v_e^{1/3},$$

where  $\gamma_0$  is the growth rate in the collisionless limit

$$\gamma_0 \sim \frac{k_y v_{Te} \Delta'}{L_s} \left( \frac{c}{\omega_{pe}} \right)^2$$

with  $c/\omega_{pe}$  the collisionless skin depth. However, later more detailed calculations show that the electrostatic perturbation is important in the layer and then the high  $m$  mode is stable in the absence of plasma density and temperature gradients. When these gradients are introduced, an extra drive for the magnetic perturbation results from the cross-field drifts which modifies the parallel current through  $\nabla \cdot \mathbf{j}_{\parallel} = -\nabla \cdot \mathbf{j}_{\perp}$ . The drive comes from the electron temperature gradient parameter,  $\eta_e$ . In the electron drift kinetic equation the coefficient of  $\eta_e$  is velocity dependent and care must be taken when performing the velocity integrals to weight this coefficient with the correct velocity dependence. Indeed, if no velocity weighting exists the coefficient of  $\eta_e$  is zero. However, by taking the velocity dependence of the collisions into account a micro-tearing instability can occur for a sufficiently high  $\eta_e$ . This corresponds to retaining

the so-called 'thermal force', discussed in Section 2.23. An approximate analytic form for the growth rate in the semi-collisional regime is:

$$\frac{\gamma}{\omega_{se}} = \left[ \frac{2\Gamma(17/4)}{\sqrt{\pi}\Gamma(11/4)} \right] \frac{\eta_e(1+5\eta_e/4)}{(v_e/\omega_{se})} + \left[ \frac{3}{8\sqrt{2}\pi^{1/4}\Gamma(11/4)} \right] \frac{\Delta'}{\rho_e} \left( \frac{c}{\omega_{pe}} \right)^2 \left( \frac{L_n}{L_s} \right) \frac{(v_e/\omega_{se})^{1/2}}{(1+5\eta_e/4)^{1/2}}. \quad 8.5.8$$

Equation 8.5.8 shows the competition between the field line bending measured by  $\Delta'$ , which is stabilizing, and the electron temperature gradient drive measured by  $\eta_e$ . Equation 8.5.8 demonstrates that the temperature gradient has two effects. It reduces the field line bending term and provides the drive for the destabilizing term. The mode is stable for  $\eta_e = 0$ .

For sufficiently high collision frequency eqn 8.5.8 predicts stability, while for low collision frequency the drive dominates and the mode is unstable. Equation 8.5.8 was derived using an expansion in  $\omega_{se}/v_e$  and so is invalid in the limit  $v_e \rightarrow 0$ . However, in the absence of collisions there is no thermal force and then stability is expected. The growth rate is therefore maximised at an intermediate electron collision frequency, in qualitative agreement with the numerical results illustrated in Fig. 8.5.2.

In the above discussion of microtearing modes a narrow 'layer' around the rational surface has been identified in which the plasma inertia and resistivity are important. If the island width associated with a perturbation in the radial component of the magnetic field exceeds the width of this so-called 'resistive layer' then the linear theory is inadequate and the effect of the island structure on the plasma density and temperature profiles must be taken into account. These nonlinear effects can lead to extra drives for the island growth and theory suggests that small scale magnetic islands may be present in tokamaks even in the low and high collision frequency regimes in which the linear theory predicts stability.

The simplest nonlinear theory, applicable to large scale islands with a width much greater than the ion Larmor radius and driven by the current gradient outside the island, has been described in Section 7.3. Island growth results when  $\Delta' > 0$  and the island width,  $w$ , is predicted to evolve at a rate proportional to the parameter  $\Delta'$ . In the case of microtearing modes,  $m \gg 1$  and then  $\Delta' \simeq -2m/r$  so that this simplest theory predicts that such islands will not occur. However, the island itself can perturb the equilibrium current density parallel to the equilibrium magnetic field and this can provide an additional drive for the island growth. The saturated island width is determined by a balance between this drive and the stabilizing negative  $\Delta'$ .

There are several candidates for the drive mechanism. First, the reconnected flux within the island allows the density and temperature profiles to be flattened across the island and this reduces the bootstrap current. The resulting perturbation provides the drive for the neoclassical tearing mode discussed in Section 7.3. Second, the presence of a magnetic island may alter the plasma resistivity in its vicinity through an

electron temperature perturbation. This temperature perturbation results from a balance between the net local power density input,  $P$  (that is, the difference between the ohmic and auxiliary heating sources and the radiation and electron-ion heat transfer sinks) against the electron heat conduction. The different topologies of the field lines inside and outside the island affect the power balance relation and a current perturbation results from the change in resistivity caused by the temperature perturbation. This current sustains the magnetic island provided the ratio of the net input power within the island to the magnetic shear,  $P/s$ , is negative. The resulting saturated magnetic islands are called 'thermal islands'. A further example of a drive mechanism arises from the effect of the island structure on the ion and electron drifts. Finite ion Larmor radius effects result in different cross-field drifts for the two species. This gives rise to a perpendicular current which, through  $\nabla \cdot j = 0$ , implies a parallel current capable of sustaining the island against the  $\Delta'$  stabilization. Detailed calculations indicate that the existence of these so-called 'drift' magnetic islands again depends on the parameter  $\eta_e$ , which is the ratio of the electron density scale length to the temperature scale length. In particular, drift effects can sustain magnetic islands provided  $\eta_e$  lies within a certain range. This range is determined by the propagation velocity of the islands, which in turn depends on the dominant dissipation mechanism. Therefore the  $\eta_e$  range in which drift effects can lead to island growth depends on the collision frequency regime of the tokamak plasma and the identification of this regime is rather subtle.

## Bibliography

### Microinstabilities

General surveys of microinstabilities in tokamaks have been given by

Kadomtsev, B.B. and Pogutse O.P., Turbulence in toroidal plasmas. *Reviews of plasma physics* (ed. Leontovich, M.A.), Consultants Bureau, New York, Vol. 5, 249 (1975).

Tang, W.M. Microinstability theory in tokamaks. *Nuclear Fusion* **18**, 1089 (1978).

and

Connor, J.W. and Wilson, H.R. Survey of theories of anomalous transport. *Plasma Physics and Controlled Fusion* **36**, 719 (1994).

### Passing particle instabilities

The first paper to identify the electron drift mode in a sheared slab of plasma and realize the importance of shear damping was

Pearlstein, L.D. and Berk, H.L., Universal eigenmode in a strongly sheared magnetic field. *Physical Review Letters* **23**, 220 (1969).

The instability drive due to the electron Landau resonance was not treated correctly in this first work, as pointed out in papers by

Ross, D.W. and Mahajan, S. M. Are drift waves unstable? *Physical Review Letters* **40**, 324 (1978).

and

Tsang, K.T., et al. 'Absolute universal instability' is not universal. *Physical Review Letters* **40**, 327 (1978).

The role of the toroidal geometry in suppressing the shear damping in a tokamak plasma was first addressed by Taylor, J.B. Does magnetic shear stabilize drift waves? *Plasma physics and controlled nuclear fusion research* (Proc. 6th Int. Conf., Berchtesgarten 1976) Vol. 2, 323 I.A.E.A. Vienna (1977).

and later studied in more detail using the ballooning transform in papers by Hastie, R.J., Hesketh, K.W., and Taylor, J.B. Shear damping of two-dimensional drift waves in a large aspect ratio tokamak. *Nuclear Fusion* **19**, 1223 (1979).

and then in an important paper by

Cheng, C.Z. and Chen, L. Unstable universal drift eigenmodes in toroidal plasmas. *Physics of Fluids* **23**, 1771 (1980).

who demonstrated the existence of a new class of electron drift mode in a tokamak, the toroidal branch, which does not exist in a plasma slab. These toroidal treatments were only valid at a radial position in the tokamak plasma where the diamagnetic frequency is a maximum. A development in the theory of these instabilities in a tokamak identifies a more general class of toroidal mode, which can exist at any radial location. They exhibit a shear damping which is comparable to that of the slab mode, as shown in the paper

Connor, J.W., Taylor, J.B., and Wilson, H.R. Shear damping of drift waves in toroidal plasmas. *Physical Review Letters* **70**, 1803 (1993).

Early work on the ITG mode is described by

Galeev, A.A., Oraevskii, V.N., and Sagdeev, R.Z. 'Universal' instability of an inhomogeneous plasma in a magnetic field. *Zhurnal-Experimentalnoi i Teoreticheskoi Fiziki* **44**, 903 (1963) [Soviet Physics JETP **17**, 615 (1963)].

and a good description of the mode in a slab geometry is given by

Horton, W. and Varma, R.K. Electrostatic slab theory of tokamaks from two-component fluid equations. *Physics of Fluids* **15**, 620 (1972).

The ITG mode properties in a toroidal geometry were first addressed by

Horton, W., Choi, D., and Tang, W.M. Toroidal drift modes driven by ion pressure gradients. *Physics of Fluids* **24**, 1077 (1981).

while a detailed description of the linear mode characteristics in a torus is given by

Guo, S.C. and Romanelli, F. The linear threshold of the ion-temperature-gradient-driven mode. *Physics of Fluids* **B5**, 520 (1993).

A general class of ITG mode has also been identified in a paper by

Romanelli, F. and Zonca, F. The radial structure of the ion-temperature-gradient-driven mode. *Physics of Fluids* **B5**, 4081 (1993).

which has a similar mode structure to the general toroidal electron drift mode discussed above. The  $\eta_e$  mode has been addressed in some detail in the paper by

Lee, Y.C., et al. Collisionless electron temperature gradient instability. *Physics of Fluids* **30**, 1331 (1987).

## Trapped particle instabilities

The trapped particle modes are described in a general review article on the subject by

Kadomtsev, B.B. and Pogutse, O.P. Trapped particles in toroidal magnetic systems. *Nuclear Fusion* **11**, 67 (1971).

In that article the trapped ion mode was considered in the absence of an ion temperature gradient,  $\eta_i = 0$  and ion collisions are then destabilizing. In a later paper by

Biglari, H., Diamond, P.H., and Rosenbluth, M.N. Toroidal ion pressure gradient driven drift instabilities and transport revisited. *Physics of Fluids* **B1**, 109 (1989),

the effects of  $\eta_i > 0$  were investigated and it was found that for  $\eta_i > 4/3$  ion collisions become destabilizing, tapping the free energy source of the ion pressure gradient. An analytic threshold for the trapped electron mode has been derived by Manheimer, W.M., et al. Marginal stability calculation of electron temperature profiles in tokamaks. *Physical Review Letters* **37**, 287 (1976).

A more complete, numerical investigation of trapped electron instabilities (and other modes) is described in

Rewoldt, G., Tang, W.M., and Chance, M.S. Electron kinetic toroidal eigenmodes for general magnetohydrodynamic equilibria. *Physics of Fluids* **25**, 480 (1982).

## Micro-tearing modes

The linear theory of micro-tearing instabilities has been studied in a series of papers by Drake *et al.* In particular, physical 'pictures' of the instability are presented in Drake, J.F. and Lee, Y.C. Kinetic theory of tearing instabilities. *Physics of Fluids* **20**, 1341 (1977).

A review which summarizes the nonlinear theory of micro-tearing instabilities and gives an exhaustive source of references is the article by

Smolyakov, A.I. Non-linear evolution of tearing modes in inhomogeneous plasmas. *Plasma Physics and Controlled Fusion* **35**, 657 (1993).

# 9

# Plasma-surface interactions

---

## 9.1

### Plasma-surface interactions

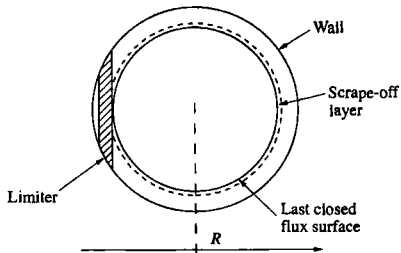
Impurities present a number of problems in tokamak plasmas. One is the radiative power loss, principally due to line radiation from partially stripped ions. Another is fuel dilution. This arises because impurity atoms produce many electrons and, for a given plasma pressure, these electrons take the place of fuel particles. At high concentrations impurities prevent the plasma being heated. This is particularly a problem during the plasma start-up phase since impurities radiate most strongly at low temperatures before they become highly ionized. Impurities can also lead to disruptions as a result of edge cooling and consequent current profile modification. The fractional impurity level which produces a radiation power equal to 10% of the total thermonuclear power is presented in Fig. 4.21.2. Impurities of low atomic number are clearly a much less serious problem than those of high atomic number.

Impurities originate either from the material surfaces facing the plasma due to a variety of plasma surface interactions or, in a reactor, to helium from the fusion reactions. The impurities most easily released are those adsorbed on the surfaces with low binding energies, for example water and carbon monoxide molecules. There are also bulk impurities in the solid, such as carbon, chlorine, and sulphur which can migrate to the surface. These species may be desorbed thermally or by the impact of ions, atoms, electrons, or photons. They can normally be removed from the system by baking the vacuum vessel or by cleaning with glow discharges. It is also possible for the wall material to be introduced into the plasma by such processes as sputtering, arcing, and evaporation. *Sputtering* is a momentum transfer process which releases atoms when energetic ions, either hydrogen or impurities, strike solid surfaces. The walls can also be sputtered by neutrals arising from resonant charge exchange between hot ions in the plasma with cold neutrals. *Arcing* can occur between the plasma and the wall or limiter, driven by the sheath potential. *Evaporation* occurs when the power load is sufficient to heat the surfaces to temperatures near their melting point. Details of these processes are given in subsequent sections of this chapter.

The particle flow to material surfaces is primarily due to diffusion from the plasma core into the boundary region or to ionization of neutrals in the boundary plasma. In the boundary layer the plasma flows along the magnetic field and then interacts with a solid surface. Ions which are incident at this surface may then be neutralized and backscattered or released in other ways to re-enter the plasma. This process is known as *recycling*. When a neutral atom from the surface arrives in the plasma it is excited and ionized by collisions with electrons.

In magnetic confinement devices the plasma is confined within closed magnetic flux surfaces, normally generated by a combination of fields

(a) Limiter operation



(b) Single null divertor operation

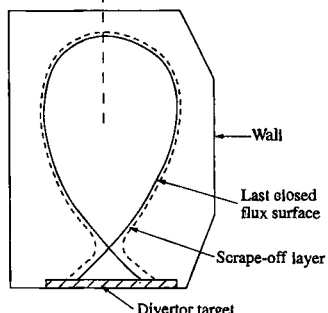


**Fig. 9.1.1** Schematic diagram of poloidal flux surfaces in a tokamak (a) with a limiter and (b) with a divertor. The toroidal field is normal to the page.

due to external conductors and by currents flowing in the plasma. Such fields can only be generated within a restricted volume, and there is therefore a boundary determined by the Last Closed Flux Surface (LCFS). The shape of the LCFS is determined by the magnetic fields. However, closed magnetic surfaces may be interrupted by a solid surface which then determines the position of the last closed flux surface. Such a solid surface is called a limiter. Alternatively the closed surface may be determined entirely by the magnetic fields so that outside the LCFS, the plasma flows towards and eventually interacts with a solid surface. This is the basic geometry of a divertor. The two situations are compared in Fig. 9.1.1. The essential difference between the two is that with a limiter the LCFS is in contact with a solid surface, while with a divertor the solid surface is removed some distance from the LCFS.

## 9.2

### The plasma sheath

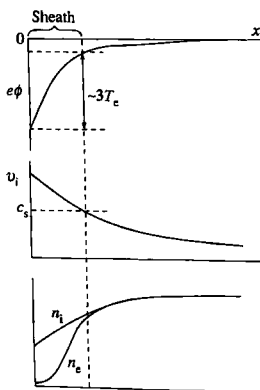
A neutral gas in contact with an absorbing surface flows to the surface at a velocity characterized by the thermal velocity. This velocity differs from the sound speed only by a numerical factor. In the case of a plasma the flow velocity to an absorbing surface is again around the sound speed but the underlying behaviour is more complicated.

The electron thermal velocity is larger than that of the ions by the square root of the mass ratio. However, an electric field is set up which brings the two flows to equality by decreasing the electron flow and enhancing the ion flow. The resultant flow is driven by the combined electron and ion pressures and is restrained by the ion inertia. The principal electric field is located in a narrow sheath near the surface, its width being several Debye lengths. A small electric field, the presheath, extends more deeply into the plasma. Figure 9.2.1 shows the spatial variation of electric potential, ion and electron densities.

The electric potential is described by Poisson's equation

$$\frac{d^2\phi}{dx^2} = \frac{e}{\epsilon_0} (n_e - n_i) \quad 9.2.1$$

where  $n_e$  and  $n_i$  are the electron and ion densities. Defining the potential to be zero at the sheath edge the electrons take up a Boltzmann distribution given by



A simple form for  $n_i$  can be obtained if the ion energy is represented by

$$\frac{1}{2}m_i v_i^2 = \frac{1}{2}m_i v_0^2 - e\phi$$

where  $v_0$  is the velocity with which the ions enter the sheath. Then, since the ion flux  $n_i v_i$  is a constant,  $n_i$  is given by

$$n_i = n_0 \left( \frac{\frac{1}{2}m_i v_0^2}{\frac{1}{2}m_i v_0^2 - e\phi} \right)^{1/2} \quad 9.2.3$$

where  $n_0$  is the plasma density outside the sheath.

Equations 9.2.1 to 9.2.3 give the differential equation for  $\phi$

$$\frac{d^2\phi}{dx^2} = \frac{n_0 e}{\epsilon_0} \left[ \exp \frac{e\phi}{T_e} - \left( \frac{\frac{1}{2}m_i v_0^2}{\frac{1}{2}m_i v_0^2 - e\phi} \right)^{1/2} \right] \quad 9.2.4$$

The value of  $v_0$  is determined by requiring that the solution of eqn 9.2.4 over the narrow sheath region matches the slowly varying small potential

**Fig. 9.2.1** Typical spatial variation of the electric potential, ion velocity and the ion and electron densities across the plasma sheath.

outside the sheath. Thus, taking small  $\phi$ , eqn 9.2.4 becomes

$$\frac{d^2\phi}{dx^2} = \left(1 - \frac{T_e/m_i}{v_o^2}\right) \frac{\phi}{\lambda_D^2} \quad 9.2.5$$

where  $\lambda_D$  is the Debye length. A slowly varying solution of eqn 9.2.5 requires

$$v_o \simeq (T_e/m_i)^{1/2}. \quad 9.2.6$$

The above calculation has implicitly neglected the ion temperature. The generalization of eqn 9.2.6 is

$$v_o = c_s \quad 9.2.7$$

where, within the limitations of the model,  $c_s^2 \simeq (T_e + T_i)/m_i$ . Thus the plasma enters the sheath at the sound speed.

The potential,  $\phi_0$ , across the sheath is determined by the requirement that the total current to the surface be zero. The ion current density into the sheath, and therefore to the material surface, is

$$j_i = n_o e c_s. \quad 9.2.8$$

The electron flux from the sheath to the material surface is  $1/4n_e \bar{c}_e$ , where  $n_e$  is the electron density at the surface and  $\bar{c}_e = (8T_e/\pi m_e)^{1/2}$ . Thus, using eqn 9.2.2 to relate  $n_e$  to  $n_o$ , the electron current density is

$$j_e = -\frac{1}{4} n_o e (8T_e/\pi m_e)^{1/2} \exp \frac{e\phi_0}{T_e}. \quad 9.2.9$$

Substitution of eqns 9.2.8 and 9.2.9 into the requirement  $j_i + j_e = 0$  now gives

$$\frac{1}{4} \left( \frac{8T_e}{\pi m_e} \right)^{1/2} \exp \frac{e\phi_0}{T_e} = \left( \frac{T_e + T_i}{m_i} \right)^{1/2},$$

and so  $\phi_0$  is given by

$$-\frac{e\phi_0}{T_e} = \frac{1}{2} \ln \left[ \frac{m_i/m_e}{2\pi(1+T_i/T_e)} \right]. \quad 9.2.10$$

For a deuterium plasma with  $T_i = T_e$ ,  $-e\phi_0 = 2.8T_e$ .

More generally it is necessary to include the effect of secondary electrons produced at the surface by electron and ion bombardment. Such electrons are accelerated out of the sheath by the electric field. The modified form of eqn 9.2.10 is

$$-\frac{e\phi_0}{T_e} = \frac{1}{2} \ln \left[ \frac{(1-\delta)^2 m_i/m_e}{2\pi(1+T_i/T_e)} \right], \quad 9.2.11$$

where  $\delta$  is the total secondary electron emission coefficient due to ions and electrons.

Ion impact on the surface can cause erosion by sputtering, desorption, and other mechanisms. In addition the thermal loading can lead to sublimation or evaporation. Impurities are transported into the plasma and cause energy loss by radiation. These processes are described in Sections 9.6 to 9.8 and 9.11. If the plasma is in contact with a solid surface at a fixed potential, the plasma potential is determined by the sheath potential. Electric fields can, however, appear in the boundary by having two or more surfaces in contact with the plasma at different potentials. For example the electron temperature can vary radially in the boundary layer in contact with a conducting limiter. The plasma potential thus varies radially, setting up an electric field. Electric fields, either externally induced or occurring naturally in the boundary, can have a significant effect on transport.

The energy of the plasma ions reaching the surface is determined by their thermal energy and the sheath potential through which they fall, given by eqn 9.2.11. The ions are accelerated by the sheath and when they reach the surface their energy distribution is very approximately an accelerated and truncated Maxwellian. The electrons are decelerated by the sheath, their distribution remaining Maxwellian but with a reduced density. It is important to note that, because of the sheath potential, only the high energy tail of the electrons arrives at the wall and is observed experimentally. Examples of experimentally measured distributions are shown in Fig. 9.2.2. The sheath also influences the flow of power to a surface. The energy transported to a surface by a Maxwellian distribution of ions or electrons is  $2T$  per particle. Adding the energy due to the acceleration of ions in the sheath, the power flux to the surface,  $P$ , is given by

$$P = n_e c_s T_e \left[ \frac{2T_i}{T_e} + \frac{2}{1-\delta} + \frac{1}{2} \ln \left( \frac{(1-\delta)^2 m_i/m_e}{2\pi(1+T_i/T_e)} \right) \right]. \quad 9.2.12$$

Equation 9.2.12 can be conveniently written

$$P = \gamma_s \Gamma T_e$$

where  $\Gamma$  is the ion flux density and  $\gamma_s$  is the sheath power transmission factor. The factor  $\gamma_s$  is approximately 6.5 for a hydrogen plasma with  $T_i = T_e$  and  $\delta = 0$ . At high density, collisions within the sheath can reduce the effective value of  $\gamma_s$ .

In practice  $\delta$  is often close to unity and the sheath power transmission coefficient  $\gamma_s$  can be significantly enhanced. Equation 9.2.11 shows that as  $\delta$  increases the sheath potential drops. Thus there is a large uncertainty in the sheath power transmission coefficient, although the *effective* value of  $\delta$  cannot exceed  $\sim 0.8$  because of space charge effects.

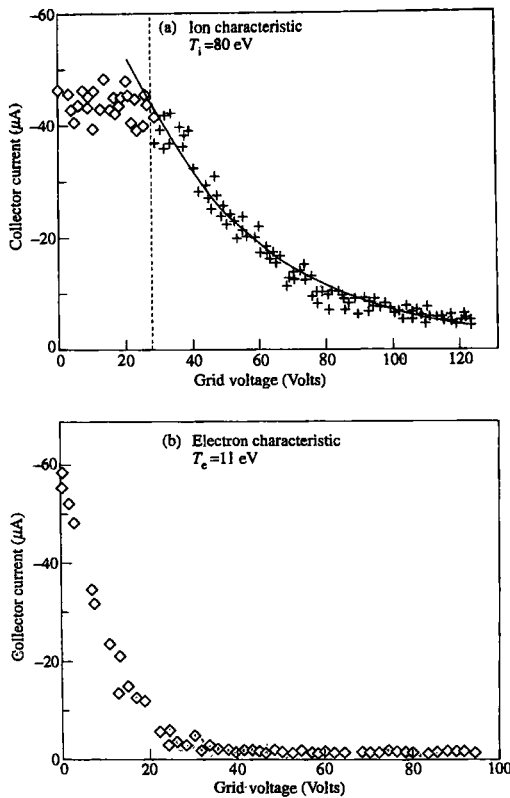


Fig. 9.2.2 Integral energy distributions measured in the plasma boundary of the DITE tokamak (a) ions, (b) electrons. (Pitts, R.A. *Physics of Fluids* 3, 2871 (1991).)

### 9.3

### The scrape-off layer

#### Radial distribution of $n_e$ and $T_e$ in the scrape-off layer

In the scrape-off layer (SOL) perpendicular flow across the magnetic field is balanced by parallel flow along the open field lines towards the

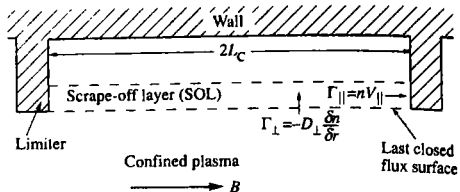


**Fig. 9.3.1** Schematic diagram of the plasma flow from the confined plasma into the SOL by cross-field diffusion and along the field in the SOL to the limiters or divertor target.

limiter or divertor target plate. These flows are illustrated schematically in Fig. 9.3.1. The diffusion coefficient for both power and particles across the field is generally ‘anomalous’, being higher than predicted by neoclassical theory. In steady state, provided there are no other sources or sinks (such as ionization) in the scrape off layer, the loss along the field into the flux tube is balanced by the net flow across the field into the flux tube. We can thus write

$$\frac{d}{dr} \left[ D_{\perp} \frac{dn}{dr} \right] = \frac{n c_s}{L_c} \quad 9.3.1$$

where  $D_{\perp}$  is the cross-field diffusion coefficient and  $L_c$  is the connection length along the flux tube to the flow stagnation point. With the assumption that  $D_{\perp}$  and  $c_s$  are independent of radius, eqn 9.3.1 is readily integrated to obtain

$$n(r) = n(a) \exp\{-(r-a)/\lambda_n\} \quad 9.3.2$$

where

$$\lambda_n = \left[ \frac{D_{\perp} L_c}{c_s} \right]^{1/2}, \quad 9.3.3$$

$a$  is the minor radius at the limiter or last closed flux surface, and  $\lambda_n$  is the scrape-off thickness, or e-folding length, for density.

The electron heat balance can be considered in an analogous way leading to a temperature profile.

$$T_e(r) = T_e(a) \exp\{-(r-a)/\lambda_T\} \quad 9.3.4$$

where approximately

$$1 + \frac{\lambda_n}{\lambda_T} = \frac{\delta}{5/2 + \chi_{\perp} \lambda_n / D_{\perp} \lambda_T}, \quad 9.3.5$$

$\lambda_T$  is the electron temperature e-folding length, and  $\chi_{\perp}$  is the cross-field thermal diffusivity. Equations 9.3.2 and 9.3.4 lead to a radial distribution for the power flux similar to those for  $n_e$  and  $T_e$ .

Equations 9.3.3 and 9.3.5 give the e-folding lengths in the scrape-off layer in terms of the cross field transport parameters. In practice,

since the cross-field transport coefficients are not known, the measured values of  $\lambda_n$  and  $\lambda_T$  are used to deduce  $D_\perp$  and  $\chi_\perp$ . Measurements of the e-folding length for  $n_e$  and  $T_e$  can be made with electrical probes, provided the impurity content is small. Typical values are  $\sim 10$  mm. If there are no sources in the scrape-off layer, this measurement together with the assumption that  $T_e = T_i$ , enables  $c_s$  to be calculated and a value for  $D_\perp$  deduced. This is typically  $\sim 1\text{m}^2\text{s}^{-1}$ . There is experimental evidence that  $D_\perp$  is inversely proportional to density. However, since density and temperature changes in the boundary are correlated, this behaviour can also be interpreted as a temperature dependence of  $D_\perp$ . Absolute values of  $D_\perp$  comparable with the Bohm diffusion coefficient,  $D_B = T/16eB$ , are frequently obtained, although the scaling with  $T_e$  and  $B$  is not. If either particle or energy sources are present in the SOL then the calculation of transport coefficients is much more difficult.

It is possible to make rough estimates of the expected values of the density and temperature at the LCFS by using global particle and energy balances. The integrated particle flux to the limiter must be equal to the total flux diffusing out from the confined plasma. A particle replacement time,  $\tau_p$ , can be defined as

$$\Gamma_n = \frac{\bar{n}V}{\tau_p} \quad 9.3.6$$

where  $\Gamma_n$  is the total particle outflux,  $\bar{n}$  is the average plasma density and  $V$  the plasma volume.

Using eqn 9.3.2 the total flux to a single poloidal limiter is

$$\Gamma_L = 4\pi a \int_a^\infty n(a) \exp(-(r-a)/\lambda_n) c_s dr. \quad 9.3.7$$

Carrying out the integration in eqn 9.3.7 assuming  $c_s$  does not vary with radius and equating  $\Gamma_n$  from eqn 9.3.6 to  $\Gamma_L$  gives the edge density

$$n(a) = \frac{\bar{n}V}{\tau_p} \frac{1}{4\pi a \lambda_n c_s}. \quad 9.3.8$$

Using a simple edge transport model for  $\tau_p$ , taking into account the ionization mean free path of atoms entering the plasma,

$$n(a) = \frac{\overline{\sigma v_i}}{6\bar{v}_n} \lambda_\Gamma \bar{n}^2 \approx 5 \times 10^{21} \bar{n}_e^2 \text{ m}^{-3} \quad 9.3.9$$

where  $\overline{\sigma v_i}$  is the ionization rate coefficient,  $v_i$  is the initial neutral velocity and  $\lambda_\Gamma$  is the flux e-folding length. This expression gives a remarkably good fit to a wide range of limiter experiments, as illustrated in Fig. 9.3.2. However, for scans at constant current on any one machine the slope of the data is less than  $n(a) \propto \bar{n}_e^2$ . This is probably due to decreasing edge temperature as the density increases.

To obtain an upper bound to the edge temperature  $T_e(a)$ , it can be assumed that all the power is lost by particle flow across the sheath, that

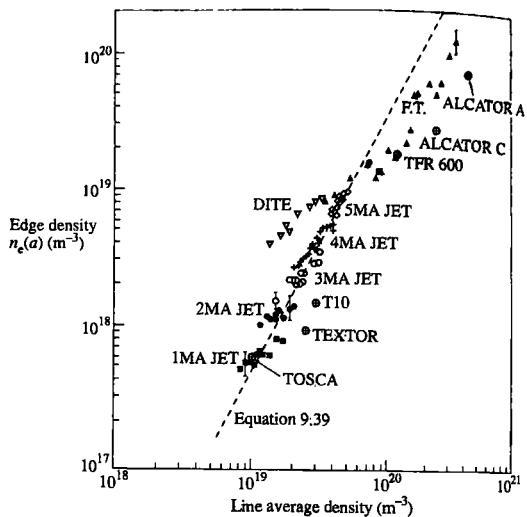


**Fig. 9.3.2** Relationship between the edge density  $n_e(a)$  and line average density  $n_a$  for a range of tokamaks with limiters. The line represents the model of eqn 9.3.9. (Everts, S.K., et al., *Nuclear Fusion* 28, 1209 (1988), Pericoli-Ridolfini, V. *Nuclear Fusion* 31, 127 (1991). Matthews, G. E., et al., *Nuclear Fusion* 28, 2209 (1988).)

is there is no radiation. Equations 9.3.7 and 9.3.9 are used to calculate the particle flux and eqn 9.2.12 is used for the power lost per ion/electron pair. Such a calculation is only valid for limiter tokamaks. The case of divertors is more complex because much of the recycling takes place in the scrape-off layer near the target plates (see Section 9.10).

#### Parallel transport outside the LCFS

The simplest model capable of reproducing the main features of transport along the magnetic field in the scrape-off layer is the isothermal fluid model. Steady-state, inviscid, isothermal one-dimensional flow is determined by conservation of particles and momentum

$$\frac{d}{dz}(nv) = S \quad 9.3.10$$

and

$$nmv \frac{dv}{dz} = -\frac{dp}{dz} - mvS \quad 9.3.11$$

where  $S$  is the source rate of particles due to cross-field transport or ionization,  $p = n(T_e + T_i)$ , and  $m$  is the ion mass. The second term on

the right hand side of eqn 9.3.11 is the drag due to acceleration of the ions from the source. Equations 9.3.10 and 9.3.11 give

$$\frac{dM}{dz} = \frac{S}{nc_s} \frac{(1 + M^2)}{(1 - M^2)} \quad 9.3.12$$

where  $M = v/c_s$  is the Mach number.

From eqn 9.3.12 it is seen that, as  $M$  tends to unity,  $dM/dz$  tends to infinity and the plasma solution breaks down.  $M = 1$  indicates the start of the plasma sheath. Equations 9.3.10 and 9.3.11 give the conservation of momentum

$$\frac{d}{dz}(p + nmv^2) = 0$$

so that

$$\frac{n(M)}{n(0)} = \frac{1}{1 + M^2} \quad 9.3.13$$

where  $n(0)$  is the density at the stagnation point  $v = 0$ . It is seen that  $n(M)/n(0)$  tends to 0.5 as  $M$  tends to 1.

The electron density distribution is given by the Boltzmann relation, eqn 9.2.2, and so using eqn 9.3.13 the plasma potential  $\phi(M)$  is given by

$$\phi(M) = -\frac{T_e}{e} \ln(1 + M^2), \quad 9.3.14$$

and  $\phi$  tends to  $-0.69 T_e/e$  as  $M$  tends to 1.

Many other models, both fluid and kinetic, have been proposed for parallel flow. However, for the most important parameters the predictions of the different models are similar.

Impurities which are produced at surfaces in contact with the plasma and flow into the scrape-off layer are also subject to the presheath electric field and their own pressure gradient. In addition, they are subject to the frictional force of the ion flow towards the limiter. The flow velocity is difficult to calculate and there is little experimental information.

## 9.4

### Recycling

In most tokamaks the pulse length is at least an order of magnitude longer than the particle replacement time. Thus on average each plasma ion goes to the divertor target plate or limiter and returns to the plasma many times during the discharge. This process is called recycling. A global particle replacement time may be defined as the ratio of the total particle content within the last closed flux surface to the total particle influx (and

therefore efflux) across this surface. This time should not be confused with the central particle confinement (or equilibration) time which is the time for a particle to be lost from the centre of the plasma and is therefore of order  $a^2/D_{\perp}$ , where  $a$  is the plasma minor radius. For a limiter tokamak the recycled particles enter the plasma predominantly as neutrals but are ionized and then trapped by the magnetic field after traversing only a fraction of the plasma radius, as discussed in Section 9.5. The situation is more complicated in the case of the divertor, where most of the ionization may take place near the target. Under some conditions there may be no particle source in the core plasma and the density at the LCFS is determined by the density gradient along the separatrix from the target (see Section 9.10). The particle confinement, or replacement time, then has little meaning.

Although the recycling of particles involves processes both in the plasma and in the surface layer of the solid, the present section will concentrate primarily on the processes occurring in the solid. When a plasma ion or neutral arrives at a solid surface it undergoes a series of elastic and inelastic collisions with the atoms of the solid. It may either be backscattered after one or more collisions, or slow down in the solid and be trapped. The trapped atoms can subsequently reach the plasma again after diffusion back to the solid surface. The ratio of the flux returning to the plasma from the solid, to the incident flux, is known as the recycling coefficient. In addition, the flux of plasma particles and radiation may release gas which was previously adsorbed on the wall as described in Section 9.6. This additional influx of particles can lead to effective recycling coefficients which are significantly greater than unity. Large quantities of hydrogen can be built up in wall materials in contact with the plasma, the equilibrium concentration depending on the incident flux, the ion energy, and the wall material and temperature. These processes are discussed in Section 9.12.

The backscattering of ions incident on a surface depends primarily on the ion energy and on the ratio of the masses of the surface atom and the incident ion. Scaling laws which depend on ion energy give an approximate value of the particle backscattering coefficient  $R_p$  for ions incident on all materials. A similar general law can be obtained for the energy reflection coefficient,  $R_E$ . Values of  $R_E$  and  $R_p$  as functions of reduced energy are given in Fig. 9.4.1. The curves are derived from Monte Carlo calculations for a wide range of ion-target combinations. The scatter in experimental data is typically 25% and the Monte Carlo calculations generally agree with the available experimental data within these limits. It is seen that both particle and energy reflection coefficients increase with increasing mass ratio, as expected from simple conservation of momentum. The data in Fig. 9.4.1 are unreliable for energies below about 10 eV because at very low energies the use of sequential binary collisions in the calculations is no longer valid.

The particles which are backscattered are predominantly neutral since an incident ion normally picks up an electron from the solid. The average

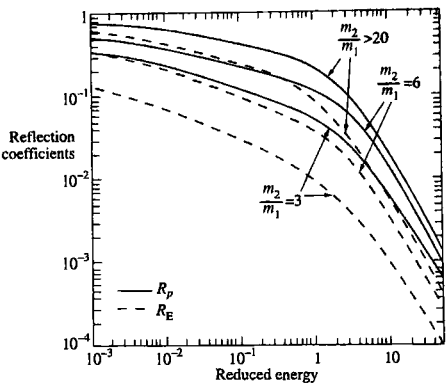


**Fig. 9.4.1** Particle and energy reflection coefficients of ions backscattered from solid surfaces as a function of reduced energy,  $\varepsilon$ , for 3 different ratios of the target to incident mass. The reduced energy is defined as

$$\varepsilon = \frac{32.5m_2 E}{(m_1 + m_2)Z_1 Z_2 (Z_1^{2/3} + Z_2^{2/3})^{1/2}}$$

where  $E$  is the energy of the incident particle. (Thomas, E.W., Janev, R.K. and Smith, J., *Nuclear Instruments and Methods in Physics Research* **B69**, 427 (1992).)

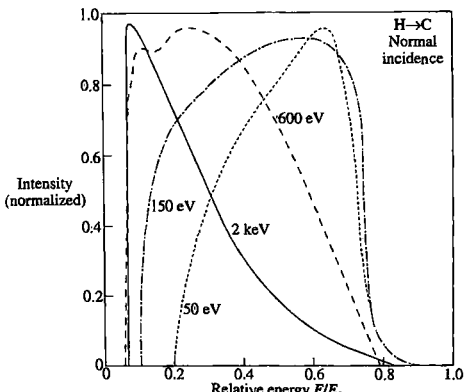


**Fig. 9.4.2** Measured energy distribution of hydrogen atoms backscattered from carbon, for different incident ion energies,  $E_0$ . The distributions are normalized at their maximum intensity. (Aratari, R. and Eckstein, W., *J Nuclear Materials* **910**, 162–4 (1989).)

energy of the backscattered particles is determined by the ratio  $R_E/R_P$ , the mean energy being typically 30–50% of the incident energy. The energy distribution has been experimentally measured down to about 0.1 keV and calculated down to even lower energies. Some results are shown in Fig. 9.4.2. The distribution is continuous, typically having a maximum, the position of which depends on both the energy and the angle of incidence of the primary ion.

The atoms which come to rest within the solid reside either in interstitial sites or in defects in the metal, such as vacancies. For hydrogen, however, diffusion readily occurs at temperatures above 300 K in many materials. Carbon, carbides, and oxides are notable exceptions. When diffusion occurs, the behaviour of the hydrogen depends on the heat of solution of hydrogen in the material. In the exothermic case there is an effective potential barrier at the surface preventing hydrogen atoms being released. The hydrogen thus diffuses into the solid, eventually becoming distributed over the whole volume. In the endothermic case hydrogen atoms diffuse to the surface and escape from it after recombination to form molecules. Since the penetration range of the incident ions slowing down in the solid is small compared with the thickness of material, in most practical cases the concentration gradient, and hence the diffusive flow, is largest towards the surface facing the plasma. The hydrogen ions which have slowed down in the solid are usually released from the surface as molecules, having thermal energies characteristic of the solid surface.

The details of hydrogen diffusion in solids is complex. In both metals and non-metals the diffusing atom can be trapped at lattice vacancies, interstitials, or other imperfections with binding energies much larger than the activation energy for diffusion. The concentration of hydrogen in interstitial sites  $C(x, t)$  can be described by the following equations

$$\frac{\partial C}{\partial t} = D \frac{\partial^2 C}{\partial x^2} - k_{st}C(C_{T0} - C_t) + k_t C_t + S(x) \quad 9.4.1$$

where  $D$  is the diffusion coefficient,  $C_t(x, t)$  is the concentration of hydrogen in traps,  $C_{T0}$  is the concentration of traps,  $k_{st}$  is the rate coefficient for entering traps,  $k_t$  is the rate coefficient for thermal desorption from the traps and  $S(x)$  is the range profile of the implanted ions. The concentration  $C_t$  is determined by

$$\frac{\partial C_t(x, t)}{\partial t} = k_{st}C(C_{T0} - C_t) - k_t C_t \quad 9.4.2$$

with the boundary condition

$$D \frac{\partial C}{\partial x} \Big|_{x=0} = k_r C(0)^2,$$

where  $k_r$  is the surface recombination rate coefficient. The rate coefficients,  $k$ , are all temperature dependent with characteristic activation energies. There are considerable differences between the parameters for different materials. For example in metals  $C_T \sim 0.01$  to  $0.05$  whereas in carbon  $C_T \sim 0.4$ . In carbon at room temperature  $D$  is negligible whereas in some metals, for example nickel, diffusion is significant on a timescale of 10 s. The surface recombination rate is very sensitive to surface conditions and can change by orders of magnitude with the

presence of a submonolayer of impurity. The coupled equations 9.4.1 and 9.4.2 require numerical solution. They have been successful in describing experimental results in many cases both for metals and non-metals.

In steady state the ion flux to the solid is balanced by the outflow. This outflow is determined by the diffusive flow towards the surface and the molecular recombination rate at the surface. Depending on the materials and operating temperature, either may be the rate limiting process. In many practical cases a dynamic equilibrium is set up in which the recycled particles entering the plasma consist of  $\sim 50\%$  backscattered atoms with energies  $\lesssim 5T_e$  (taking into account the sheath potential accelerating the incident ions and the energy reflection coefficient  $R_E$ ) and  $50\%$  of slow molecules with energies  $\sim 0.03$  eV. With light element wall materials the proportion of the particles backscattered as atoms is lower,  $\sim 30\%$ .

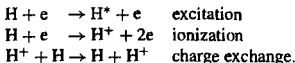
While the recycling flux density is highest at the limiter or divertor target, recycling also occurs at the walls due to charge exchange neutral fluxes. Because charge-exchange and ionization rate coefficients for hydrogen are roughly equal in the temperature range of interest, the integrated neutral recycling at the wall is of the same order as the integrated ion flux to the limiter or divertor target. The distribution of neutral flux can be calculated with Monte Carlo codes. Local measurements of the energy distribution of neutral fluxes to the wall indicate mean energies in the range 100–500 eV.

## 9.5

### Atomic and molecular processes

In the processes of recycling and fuelling, many atomic and molecular reactions occur in the boundary layer as the incoming hydrogen isotopes meet the energetic ions and electrons of the plasma. Further reactions occur when impurities created by sputtering and by other plasma–surface interactions enter the plasma. In most cases the dominant atomic reactions are excitation and ionization. These lead to emission of radiation and cooling of the edge plasma. This is beneficial since it lowers the incident ion energy and reduces the physical sputtering rate.

Considering first the recycling of hydrogen isotopes from the wall, the important atomic reactions are excitation, ionization, and charge exchange,



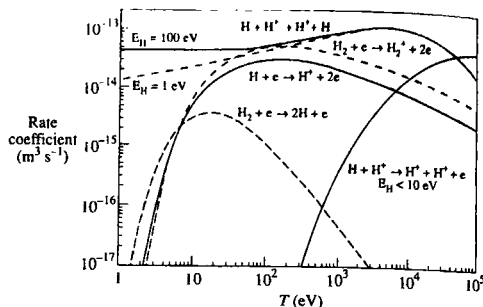
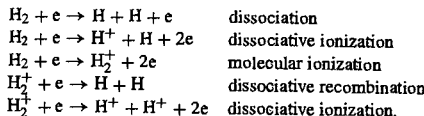


**Fig. 9.5.1** Rate coefficients for hydrogen atoms and molecules for a number of common reactions. The first symbol refers to the test particle and the second refers to the thermal species, the rate coefficient being integrated over the Maxwellian distribution of this species.  $E_H$  is the energy of the test particle (R.K. Janev et al. *Elementary processes in hydrogen–helium plasmas, cross sections and reaction rate coefficients*, Springer-Verlag, Berlin, 1987).

The main molecular reactions are



The relative reaction rates for the different processes are functions of plasma temperature and density. Some rate coefficients are shown in Fig. 9.5.1. Although atomic and molecular processes are complex they have been extensively studied. The cross-sections are well known and in most cases there is good agreement between theory and experiment. Thus good models of the boundary layer atomic physics processes can be made, provided the plasma physics can be sufficiently well described.

When atoms or molecules enter the plasma, the collision rate with the plasma species is  $nn_0\langle\sigma v\rangle$  where  $n$  is the plasma density,  $n_0$  the neutral density and  $\langle\sigma v\rangle$  is the reaction rate averaged over the electron velocity distribution. Considering a simple one-dimensional model with the source at the wall, the flux of neutrals as a function of radial position decreases due to ionization. The neutral flux  $F(r)$  at a given radius is given by

$$F(r) = F(a) \left( 1 - \int_r^a \frac{n_e(r)\langle\sigma v\rangle}{v_0} dr \right)$$

where  $F(a)$  is the initial flux and  $\langle\sigma v\rangle$  is determined by the local electron temperature. The local ionization source function is  $dF(r)/dr$ . Thus if the plasma density and temperature profiles are known, it is possible to determine the penetration into the plasma of both the recycling species and impurity species. However, ionization in the boundary immediately modifies its density and temperature and more complex models

usually have to be used to obtain a self-consistent solution. Charge exchange is a further complication which is particularly important in the case of hydrogen. Because the rate coefficient for charge-exchange is greater than that for ionization, (see Fig. 9.5.1) the penetration of neutral hydrogen is dominated by charge exchange. When the incoming particle undergoes charge exchange an energetic plasma ion becomes a fast neutral and subsequent charge exchange reactions between neutrals and plasma ion leads to a random walk and diffusion to the centre of the plasma. This can be analysed either by transport codes or by Monte Carlo methods.

Ionization of impurities occurs in the same way as for hydrogen species but charge exchange can be neglected in most cases. After the first ionization event the impurity ion is confined by the magnetic field and it can then become multiply ionized in a series of collisions with electrons. The dominant charge state of the impurity ions at any position is determined by the local electron temperature, the electron density and the time for which the impurity is in the plasma. The ratio of the excitation to ionization rate can be calculated for any given ionization state at a given electron temperature. This ratio gives rise to the useful concept of photon efficiency, the ratio of the number of photons emitted in a given transition per ionization event. The inverse photon efficiency (number of ionization events per photon emitted) is shown for a number of ions in Fig. 9.5.2. Knowledge of the photon efficiency together with absolute measurements of the radiation enables the influx of ions to be directly calculated.

By summing over all transitions the average energy lost per ionization event can be obtained. For hydrogen atoms this varies from 150 eV for  $T_e = 2$  eV to 25–30 eV for  $T_e > 20$  eV. At low  $T_e$  it is also dependent on  $n_e$ . For impurities the situation is more complicated as there are many possible charge states and excitation can occur in all of these until the ion is fully stripped of electrons. For a carbon atom entering a typical tokamak plasma the energy lost in producing a fully stripped ion is in the range 1–10 keV per atom, depending on the electron temperature.

As an impurity particle enters the plasma and is raised into successively higher ionization states it is also heated by collisions with the background plasma, principally with the plasma ions. The classical thermalization time, given by eqn 2.14.10, is

$$\tau_{th} = 2.2 \times 10^{17} \frac{m_1 T_B^{3/2}}{m_B^{1/2} n_B Z_B^2 Z_1^2 \ln \Lambda} \text{ s} \quad T_B \text{ in KeV}$$

where  $m_1$  and  $m_B$ ,  $Z_1$  and  $Z_B$  are the masses and charge states of the impurity and plasma ions and  $n_B$  and  $T_B$  are the density and temperature of the background plasma. The characteristic time for ionization is

$$\tau_{ion} = (n_e \langle \sigma v \rangle_{ion})^{-1}.$$

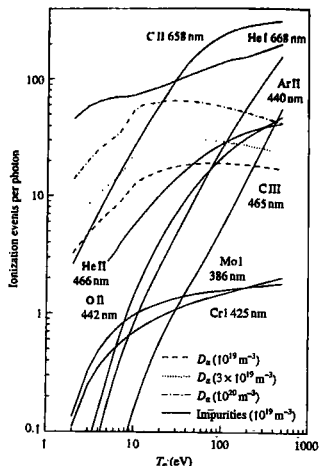


**Fig. 9.5.2** Ionization events per emitted photon for some common impurity lines used for flux measurements, calculated as a function of focal electron temperature. Data derived from the ADAS database at an electron density of  $1 \times 10^{19} \text{ m}^{-3}$  for the impurity lines and at the three densities indicated for deuterium atoms. (Summers, H.P., *The ADAS users manual, Version 2.2*, (2000). <http://adas.phys.strath.ac.uk/adas/>)

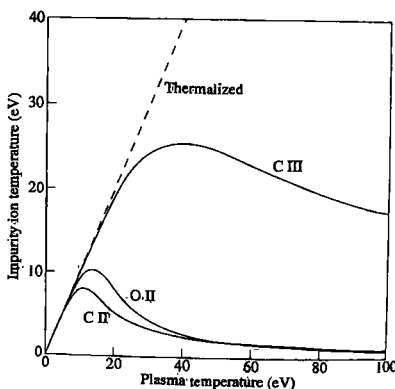


**Fig. 9.5.3** Calculated temperature of CII, OII and CIII impurity ions as a function of background plasma temperature. ( $T_i = T_e$ , initial impurity/ion temperature = 0.)

The temperature which an ion reaches before being ionized to the next charge state is determined by  $\tau_{\text{ion}}/\tau_{\text{th}}$ , which is independent of density. The calculated temperature of some typical impurity ion species as a function of background plasma temperature is shown in Fig. 9.5.3. All

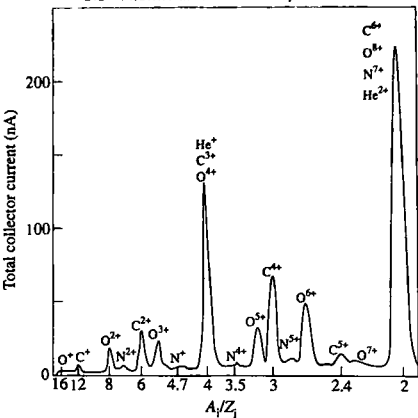


**Fig. 9.5.4** Mass spectrum of impurity ions in the SOL of the DITE tokamak, measured with a plasma ion mass spectrometer. (Matthews, G.F., et al. *Nuclear Fusion* 31, 1495 (1991).)

low temperatures the collision rate is high, the ionization rate is low and the impurities are rapidly thermalized. For increased plasma temperature the ionization rate increases and the thermalization rate decreases so that ionization occurs before thermalization is complete. In equilibrium the charge state distribution of the ions is determined by the local electron temperature.

Impurity ions moving out of the plasma and arriving at the plasma boundary are accelerated through the sheath potential and consequently the energy of an ion arriving at a material surface is a strong function of the ion charge state. Measured values of the distribution of charge state are shown in Fig. 9.5.4. The charge state calculated as a function of  $T_e$  is shown for oxygen in Fig. 9.5.5 for coronal equilibrium conditions.

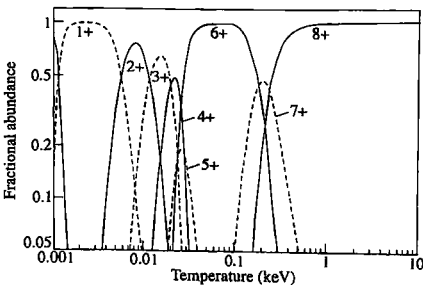


**Fig. 9.5.5** The oxygen ionization state distribution in coronal equilibrium. (Carolan, P.G. and Piotrowicz, V.A., *Plasma Physics* 25, 1065 (1983).)

The residence time can be quite short ( $\lesssim 1 \text{ ms}$ ) if the ions are ionized in the scrape-off layer and stream back along field lines into the divertor or limiter

## 9.6

### Wall conditioning

Under normal vacuum conditions a surface will be covered by a layer of adsorbed gas coming from the surrounding atmosphere. The adsorbed atoms have binding energies ranging from weakly bound physical adsorption,  $\sim 0.3 \text{ eV}$ , to strongly bound chemical absorption  $\sim 3 \text{ eV}$ . The weakly bound species can be removed thermally and at any given temperature there will be a dynamic equilibrium between the arrival rate and the desorption rate. The removal of a single monolayer of gas, with a surface density of  $\sim 10^{19} \text{ atoms m}^{-2}$ , from a circular boundary of 1 m minor radius would, if taken up by the plasma, lead to a density increase of  $\sim 10^{19} \text{ m}^{-3}$ . Although hydrogen can be absorbed on the surfaces, impurity species such as carbon monoxide and water molecules are the typical adsorbents, accounting for the carbon and oxygen frequently observed as impurities in tokamak plasmas. Impurities can dominate the energy balance by radiating most of the power put into the plasma. During the start-up phase of a tokamak, when the walls are covered with adsorbed gas, the various desorption processes can lead to levels of radiation from oxygen and carbon which prevent the plasma being heated. Thus the release of adsorbed gas is a serious impurity source.

Impurities can be desorbed by incident ions, neutrals, electrons, and photons. The electron and photon processes are predominantly electronic in nature and their yields are low, particularly in the case of photons. The yield from electrons is typically two or three orders of magnitude lower than for ions, ions and neutrals having similar yields. The desorption process for ions and neutrals is by momentum transfer, similar to the process for sputtering, (described in Section 9.7) and can have a cross-section,  $\sigma$ , as high as  $10^{-18} \text{ m}^2$ . Typical cross-sections, obtained experimentally for adsorbed species desorbed by ions are shown in Fig. 9.6.1. A simple, approximate expression for the yield of desorbed species,  $Y$ , is

$$Y = \sigma c J \exp(-J\sigma r)$$

where  $J$  is the incident ion flux density and  $c$  is the surface concentration. In practice there is a range of binding energies of the adsorbed species and consequently  $\sigma$  is not a constant.

Desorption can lead to impurity accumulation in the plasma or, in the case of desorption of the plasma species, to lack of density control. In order to minimize the desorption processes various procedures have

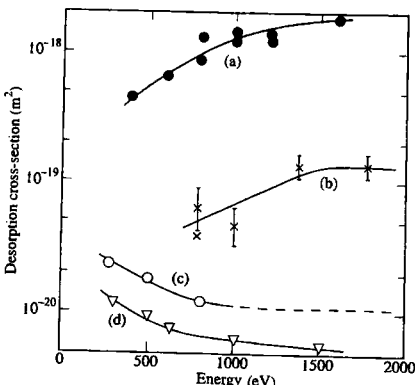


Fig. 9.6.1 Energy dependence of experimental desorption cross sections:  
 (a)  ${}^4\text{He}^+$  incident, carbon monoxide on nickel;  
 (b)  ${}^3\text{He}^+$  incident, hydrogen on tungsten;  
 (c)  ${}^4\text{He}^-$  incident, hydrogen on molybdenum;  
 (d)  $\text{H}^+$  incident, deuterium on nickel (Taglauer, E., in *Nuclear Fusion Special Issue*, ed. Langley, R.A., I.A.E.A., Vienna (1984).)

been adopted for reducing adsorption on the wall. These are frequently referred to as *wall conditioning*. They include (i) baking the vacuum vessel, typically to 200–350 °C, (ii) using a variety of plasma discharges to remove the adsorbed gas from the wall, (iii) gettering, in which the wall is covered with a clean metal film by evaporation, and (iv) covering the wall with a low Z film such as carbon or boron, known as *carbonization* and *boronization*. These processes are described below.

### Discharge cleaning

Surfaces are cleaned by particle bombardment in discharges carried out prior to the main tokamak discharge. The cleaning discharge can be of various types, including glow discharges, pulsed discharges and discharges excited by radiation at the electron cyclotron frequency. In each case the aim is to optimize the removal of wall impurities by energetic ions, neutrals, electrons, or photons. These processes are more effective than simple thermal desorption because more energy is transferred to the adsorbed species. The cleaning process can be further enhanced by operating discharge cleaning with a hot vessel to minimize re-adsorption.

Glow discharge cleaning is the most widely used technique because it is effective and simple to carry out. The DC glow discharge is commonly combined with RF radiation at 10–20 MHz. The RF radiation provides additional ionization, allowing the glow discharge to be operated at lower

pressure, typically  $10^{-1}$  Pa, resulting in fewer collisions within the sheath and hence higher incident ion energies.

The tokamak ohmic heating system can be used to obtain pulsed discharges with no toroidal field, thus producing poor particle confinement and more bombardment of the walls. Although useful in conjunction with other discharge cleaning methods, these pulsed discharges tend to have more localized bombardment than glow discharge cleaning. Excitation of a continuous discharge using microwaves, at the electron cyclotron resonance has also been shown to produce effective cleaning. The spatial position of the cyclotron resonance can be moved by varying the toroidal magnetic field strength.

Although many gases have been used for discharge cleaning, the light ions hydrogen and helium have generally been used as this reduces sputtering of the substrates, which can lead to thin films of sputtered material being deposited on windows and insulators. When using hydrogen, surface cleaning is enhanced by chemical action with the formation of hydrocarbons, such as  $\text{CH}_4$  and  $\text{C}_2\text{H}_4$ , together with  $\text{H}_2\text{O}$  and CO. Since these species are volatile they can be pumped away. In systems with mainly carbon walls, glow discharge cleaning in helium has been found to release oxygen, usually by forming CO. Helium glow discharge cleaning also desorbs implanted hydrogen isotopes in the wall, thus reducing recycling. Helium atoms are not trapped in graphite at temperatures above 300 K.

### Thin metallic films

Evaporation of wires to produce thin metallic films has been widely used for many years as a technique for improving the vacuum, particularly in sealed-off vacuum tubes. This process is referred to as gettering. Fresh layers of chemically active metals react with active gases such as  $\text{O}_2$ , CO,  $\text{H}_2$ , and  $\text{CO}_2$  binding them tightly to the surface. Sequential deposition results in the adsorbed gas being buried. Many different metals have been used, but those with high chemical reactivity and relatively high vapour pressures at modest temperatures, typically 1500–2000 K, are most convenient. Titanium and chromium have been most widely used in tokamaks, but beryllium has also been used successfully. Beryllium is attractive in being both a good getter and having a low atomic number, but has the disadvantage of high toxicity.

In tokamaks gettering appears to work by reducing outgassing from the substrate as well as by removing unwanted impurity species from the gas phase. It is necessary to cover at least 30% of the area of the vacuum vessel for a significant reduction in impurity level to be observed. A disadvantage of gettering is that the adsorption process quickly saturates and it is sometimes necessary to getter between consecutive discharges. A further difficulty is that the films flake off when they reach thicknesses of 10–100  $\mu\text{m}$ . This results in impurities entering the plasma in a random manner which can cause disruptions. Beryllium appears to be less

troublesome than high Z materials in this respect, presumably because it results in lower radiation.

### Non-metallic films

Low Z non-metallic films, such as carbon and boron, have been used to coat the walls of tokamaks in order to minimize the release of high Z impurities. The techniques are termed *carbonization* and *boronization*. To carry out carbonization a gaseous carbon compound, typically methane, is introduced into the vacuum vessel and dissociated in a glow discharge, depositing a thin layer of amorphous carbon on the wall. The optimum wall temperature is about 300 °C and at this temperature a hard, adherent film is formed, typically containing 40% hydrogen. This technique can result in an order of magnitude reduction in metal concentration in the plasma but has the drawback of initially increasing the hydrogen in the walls, making density control difficult. The recycling can be controlled by following the carbonization with a glow discharge in helium. A further problem is that the optimum thickness for good adhesion is  $\sim 1 \mu\text{m}$  and such a film has a limited life before local erosion necessitates renewal of the layer.

Boronization is similar to carbonization. In one approach boranes such as  $\text{B}_2\text{H}_4$  and  $\text{B}_2\text{H}_6$  are introduced into the vacuum vessel at 400 °C. They thermally decompose and deposit a layer of boron on the wall. Boron acts as a getter and thin boron films pump both oxygen and hydrogen. Trimethyl boron,  $\text{B}(\text{CH}_3)_3$ , has also been used to introduce a mixed film of carbon and boron. If a lower vessel temperature is used the rate of decomposition of the gaseous boron compound is decreased. It can however be enhanced by using a glow discharge. The beneficial effects of boronization continue even after the vessel has been exposed to atmosphere and re-evacuated. This is attributed to the low affinity of boronized surfaces for water vapour. A similar technique uses silane,  $\text{SiH}_4$ , to deposit a layer of silicon on the walls. Silicon is also effective as a getter but it has a significantly higher atomic number and so the tolerable impurity concentration is lower.

The advantage of carbonization and boronization for depositing thin films, as opposed to evaporation, is that a more uniform coverage can be achieved. Both boranes and silane have the practical disadvantage of being both explosive and highly toxic.

Successful wall conditioning removes impurities and generally results in access to a much wider range of operating conditions. In particular it allows higher densities to be obtained without excessive radiation. Higher densities in themselves tend to reduce the impurity concentration because, for a given power input, an increase in density reduces edge temperatures and hence sputtering yields. The thin film techniques are valuable in present experiments, allowing machines to be conditioned relatively quickly and reproducibly, but they are unlikely to be satisfactory under reactor conditions because erosion and redeposition would reduce their effectiveness.

## 9.7

### Sputtering

#### Physical sputtering

Sputtering is the removal of atoms from the surface of a solid as a result of impact by ions or atoms. It gives rise to impurities which cause power to be radiated from the plasma and make ignition more difficult. It also leads to erosion of surfaces at a rate which is expected to be a limiting factor in tokamak reactor design. Sputtering can occur due to both physical and chemical processes.

When an energetic ion or neutral atom is incident on a solid surface it produces a collision cascade among the lattice atoms. Physical sputtering takes place when this cascade results in a surface atom receiving sufficient energy to exceed the surface binding energy. Thus sputter yields decrease with increasing sublimation energy of the solid and increase with increasing energy transferred from the incident ion to the lattice atom. For light ions such as hydrogen and helium the sputter yields are small due to low energy transfer, the energy being dissipated mainly in inelastic processes.

There is in general a threshold energy,  $E_T$ , of the incident ion below which insufficient energy is transferred to the lattice atoms for sputtering to occur. Its theoretical value is

$$E_T = \frac{E_s}{\gamma_{sp}(1 - \gamma_{sp})}$$

where  $E_s$  is the sublimation energy of the target solid and  $\gamma_{sp} = 4m_1m_2/(m_1 + m_2)^2$ , where  $m_1$  and  $m_2$  are the masses of the incident and target atoms respectively. The energy necessary to transfer  $E_s$  to the target atom in a head-on collision is  $E_s/\gamma_{sp}$ . The additional fraction of  $(1 - \gamma_{sp})$  takes account of the reflection process, which is important for light ions.

Figure 9.7.1 gives some results for sputter yields obtained from Monte Carlo code calculations. These are generally in good agreement with experimental data except for carbon at low energy, where no threshold is found experimentally, due to chemical effects. Above the energy threshold the sputter yield  $Y$  first increases approximately linearly, reaches a maximum and then decreases at high energies. The decrease in yield is due to the collision cascade taking place deeper in the solid so that there is a lower probability of atoms at the surface receiving sufficient energy to be sputtered. It is found that the position of the maximum yield moves to higher energy as the mass of the target atom increases. The dominant effect in determining the absolute magnitude of the sputter yield in different targets for the same incident ion is the surface binding energy. There is a considerable spread in the measured values of sputter yields for nominally the same system. This is due to uncontrolled factors such

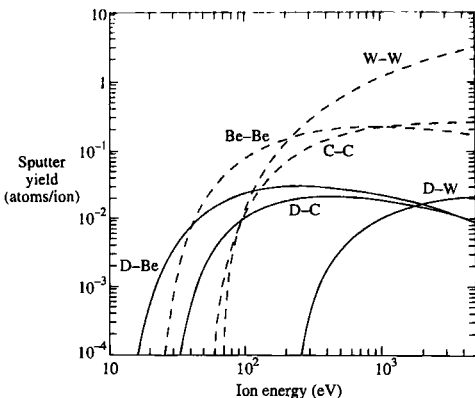


**Fig. 9.7.1** Energy dependence of the physical sputter yield for beryllium, carbon, and tungsten by deuterium and self sputter ions, calculated using a Monte Carlo code. (Eckstein, W., *Sputtering data*, Report PP9/82 Max Planck Institut für Plasmaphysik Garching, 1993.)

as surface structure and impurity levels, which can effectively change the binding energy of the surface atoms.

The experimental results can be summarized by plotting the sputter yield against  $E/E_T$ . There is a general semi-empirical curve which describes the sputter yield of all ions over a wide range. This has the form

$$Y(E) = Q S_n(E/E_{TF}) g(E/E_T)$$

9.7.1

where  $Q$  is the yield factor, depending only on the incident ion and target atom combination,  $S_n(E/E_{TF})$  is the nuclear stopping cross section, where  $E_{TF}$  is a characteristic Thomas–Fermi energy and  $g(E/E_T)$  is a threshold function. Analytical forms are available for  $S_n(E/E_{TF})$  and  $g(E/E_T)$ . A prediction of sputtering yields at normal incidence can be obtained for any ion–solid combination from known values of  $Q$ ,  $E_T$ , and  $E_{TF}$ , using eqn 9.7.1.

The sputter yield increases as the angle of incidence,  $\theta$ , increases from the normal ( $\theta = 0$ ). To first order this increase varies as  $\cos^{-1} \theta$ . However for light ions incident on heavier substrates the yield  $S(\theta)$  increases faster than  $\cos^{-1} \theta$  and  $dS(\theta)/d\theta$  increases with incident energy. This behaviour can be explained qualitatively by the increased probability of the incident ions being backscattered to the surface. Numerical codes based on both transport theory and Monte Carlo calculations give good agreement with laboratory experiments. At low energies,  $E \lesssim 300$  eV, the variation of yield with incident angle is negligible and this is the region of most interest in many plasma surface interactions. In practice it is difficult to calculate the distribution in angle of incidence of ions arriving at a limiter or divertor target. The situation is complicated by the effects of the ion Larmor radius, the acceleration in the plasma sheath and the surface roughness. The surface roughness also varies with time during

operation. Typically when comparing code results with tokamak experiments it is found that the effective yield is about twice that predicted for normal incidence.

The angular distribution of atoms sputtered from randomly oriented target atoms is given to a good approximation by a simple  $\cos\theta$  distribution, though strong crystalline effects are observed in single crystal targets, leading to preferential directions of emission. The energy distribution of sputtered atoms has been quite extensively investigated. Theoretically it has a most probable energy of  $0.5E_s$  ( $\sim 2$  to  $5$  eV) with an energy distribution varying as  $E^{-2}$  at high energies as illustrated in Fig. 9.7.2. This result has been confirmed by experiments in tokamaks as well as in laboratory experiments using monoenergetic ion beams. Atoms sputtered by heavier ions have a higher mean energy due to the larger momentum transfer.

### Chemical sputtering

Chemical reactions between incident ions or neutrals and a solid surface can also lead to erosion of surfaces. In fusion devices the most common of such reactions, is that between hydrogen isotopes and carbon, for example:



Carbon is widely used as a limiter and divertor material because of its refractory qualities and the fact that it does not melt. However it has

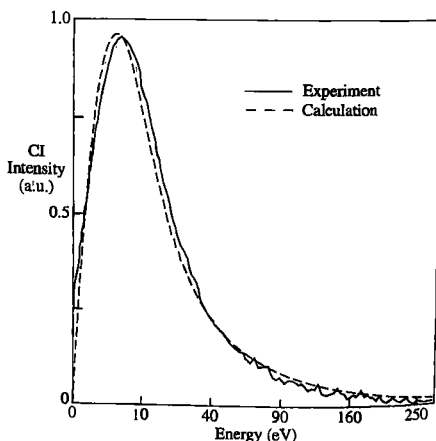


Fig. 9.7.2 Energy distribution of carbon atoms sputtered from the limiter of the TEXTOR tokamak,  $n_e = 1.7 \times 10^{19} \text{ m}^{-3}$ ,  $I_p = 350 \text{ kA}$ . A calculated distribution, assuming a surface binding energy of 9.3 eV, is shown for comparison. (Bogen, P. and Rusbridg, D., *Journal of Nuclear Materials* 179, 196-8 (1992).)

chemical sputtering yields which are comparable and sometimes higher than physical sputtering yields in terms of atoms removed per incident ion or atom. The chemistry depends on hydrogen atoms, on or in the surface, combining with one or more carbon atoms to form a hydrocarbon molecule. Because the hydrocarbons have a low binding energy to the surface they may be thermally released at temperatures as low as 300 K. The chemical reaction rate depends on the surface temperature of the solid as well as the energy of the incident ions. The dependence on ion energy for a fixed surface temperature and on surface temperature for a fixed ion energy are illustrated in Fig. 9.7.3. During ion bombardment, methane is the primary hydrocarbon produced, but lesser amounts of heavier hydrocarbons, such as  $C_2H_4$ ,  $C_3H_6$ , can also be formed as shown in Fig. 9.7.3. Unlike physical sputtering there is no well defined threshold energy below which the yield goes to zero and so at low plasma temperatures chemical sputtering is frequently dominant in the presence of carbon. Experiments in tokamaks with helium plasmas show that the yield of carbon is lower than for hydrogen isotopes, indicating that chemical sputtering is significant.

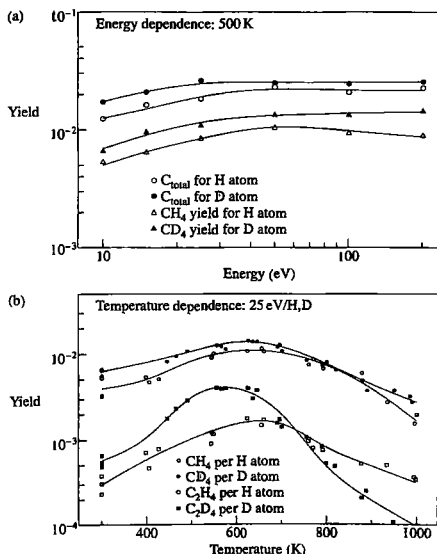


Fig. 9.7.3 Chemical erosion yield of pyrolytic graphite by energetic hydrogen and deuterium ions as a function of (a) incident ion energy for a fixed surface temperature of 500 K, and (b) surface temperature for an incident ion energy of 25 eV. In (a) the  $C_{\text{total}}$  curves refer to the total yield of  $CH_4$ ,  $C_2H_2$ ,  $C_2H_4$ ,  $C_3H_6$ , and  $C_3H_8$  hydrocarbons due to hydrogen impact and equivalent deuterium yields. (Mech B. V. et al., Journal of Nuclear Materials 255, 153 (1998).)

The break-up reactions of the hydrocarbon molecules entering the plasma is complicated and not fully documented. However it is known that the carbon atom or ion released has a significantly lower energy than the energy of the physically sputtered atoms, see Fig. 9.7.2. Thus the chemically sputtered species will penetrate less far into the plasma and consequently will have a shorter mean residence time. The prompt redeposition of molecular fragments is not well documented, but may significantly reduce the effective chemical sputtering yield.

### Sputtering models

It is clear from the above discussion that sputtering processes can release impurities from the wall or limiter by an incident ion, whether hydrogenic or impurity. The energy of the incident ions is the sum of their thermal energy and their flow energy including that due to acceleration through the sheath potential. Since impurity ions are usually multiply-ionized, the acceleration through the sheath potential can result in energies greater than 100 eV. The possibility arises of impurity self-sputtering and a consequent runaway process. Since the physics of the physical sputtering process is well understood it can be readily incorporated into numerical models of plasma confinement. It is routinely included in most transport codes.

In order to illustrate the important interactive effects which occur, a simple global model will be described using physical sputtering. The steady state impurity concentration can be deduced from the equation for the balance of flow into and out of the plasma

$$\frac{n_m}{\tau_m} = \eta \left\{ \frac{n_p}{\tau_p} Y_p + \frac{n_m}{\tau_m} Y_m \right\} \quad 9.7.2$$

where  $n_m$  and  $n_p$  are the impurity and plasma densities,  $\tau_m$  and  $\tau_p$  are their respective replacement (or global confinement) times,  $Y_m$  and  $Y_p$  their sputtering coefficients, and  $\eta$  is the probability of a sputtered atom entering the confined region of the plasma.

Rearranging eqn 9.7.2

$$\frac{n_m}{n_p} = \eta \frac{\tau_m}{\tau_p} \frac{Y_p}{1 - \eta Y_m} \quad 9.7.3$$

and it is seen that if  $\eta Y_m \geq 1$  no steady state solution is possible. This puts an upper limit on the practical edge temperature for a steady state solution. It is also seen that if  $\eta Y_m \ll 1$ , the impurity fraction is proportional to the plasma ion sputtering coefficient  $Y_p$ . A global model for sputtering can be derived self-consistently using eqn 9.7.3 together with the energy balance between the total input power,  $P_H$ , the radiated power,  $P_R$ , and

the power,  $P_C$ , transported to the limiter or divertor targets

$$P_H - P_R = P_C = \gamma_s T_e(a) n_p V / \tau_p \text{ watts},$$

where  $T_e(a)$  is the edge temperature,  $\gamma_s T_e(a)$  is the energy transported to the surface per ion/electron pair, as discussed in Section 9.2, and  $V$  is the plasma volume. Using coronal equilibrium calculations of  $P_R$  and assumed radial profiles of density and temperature it is possible to calculate the edge temperature and hence the sputter yields. A solution for eqn 9.7.4 as a function of density or heating power for assumed values of  $\eta$ ,  $\tau_m$ , and  $\tau_p$  can thus be obtained.

An illustrative calculation to show the marked difference between low and high  $Z$  materials is shown in Fig. 9.7.4. High radiation and high  $Z_{\text{eff}}$  occur at low density for tungsten because the self sputter yield approaches unity, leading to unacceptably high effective sputter yields. Only edge

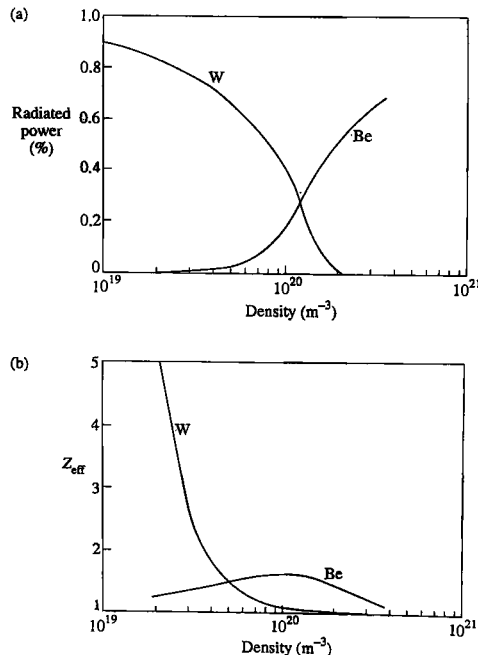


Fig. 9.7.4 Comparison of radiated power and  $Z_{\text{eff}}$  for a tokamak with beryllium and tungsten limiters, modeled using the effective sputter yield defined by eqn 9.7.3 and the energy balance eqn 9.7.4. Assumed parameters:  $P_H/V = 1 \text{ MW m}^{-3}$ ,  $\tau_p = \tau_E = 0.01 \text{ s}$ ,  $\eta = 0.2$ , with radiation functions,  $R = 4 \times 10^{-34} \text{ W m}^3$  for Be,  $R = 1 \times 10^{-32} \text{ W m}^3$  for W,  $Z = 3$  for Be and W at the limiter.

temperatures less than about 80 eV give steady state solutions. On the other hand high density leads to edge temperatures less than the threshold for sputtering, and the impurity influx due to sputtering approaches zero. In the case of beryllium, the effective yield never exceeds unity (at least for normal incidence) and so in principle steady state solutions are possible with arbitrarily high edge temperature. As the density decreases and the edge temperature increases above the value corresponding to the peak in the sputter yield, both the radiation and  $Z_{\text{eff}}$  decrease, all the power being removed by particle convection. As the plasma density increases, causing a decrease in temperature, the sputter yield rises until the ion energy is below 200 eV (plasma temperature  $< 40$  eV). Since the radiation is proportional to both electron density and to sputter influx, the radiation peaks at a much higher plasma density than for tungsten. Only when the edge temperature reaches about 2 eV does the sputter yield go to zero.

The above model of sputtering is much simplified and numerical calculations are necessary to obtain a more detailed understanding and to make reliable estimates of the screening parameter  $\eta$  and the ion charge state. Nevertheless the simple model illustrates the qualitative importance of the various parameters, the interplay between radiated and transported power and the relative advantages of high and low atomic mass materials.

### Choice of materials

The choice of plasma facing materials is a compromise between many different criteria. These include impurity production rates, structural strength, neutron activation, and thermal shock resistance. The increase of radiation from an impurity atom with increasing nuclear charge makes it desirable to minimize both  $Z$  and the sputter yield. A suggested figure of merit,  $M_m$ , is

$$M_m = f_i \frac{1 - Y_m}{Y_p} \quad 9.7.5$$

where  $f_i$  is the maximum allowed impurity concentration in the plasma. The larger  $M_m$  is, the less power will be radiated.

Both the sputter yield and  $f_i$  are functions of  $T_e(a)$ . A plot of  $M_m$  is shown as a function of edge temperature for various materials in Fig. 9.7.5. It is seen that, for low plasma edge temperatures, high  $Z$  refractory metals are best while at high edge temperatures only low  $Z$  materials are practical. This conclusion is consistent with the sputter yield curves shown in Fig. 9.7.1. The plasma edge temperature can be calculated with certain simplifying assumptions as discussed in Section 9.3. It increases with increasing power and decreases with increasing plasma density. A further factor to be considered is the probability of an impurity entering the confined plasma. Detailed analysis would also take into account impurity transport in the plasma.

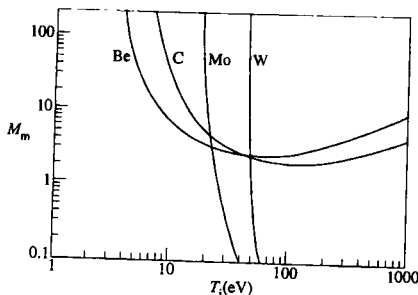


**Fig. 9.7.5** The figure of merit  $M_m$  (equation 9.7.5), as an estimate of the degree of contamination of the plasma by limiter or divertor target materials.  $M_m$  is calculated as a function of plasma ion temperature for Be, C, Mo, and W. An ion charge  $Z$  of 3 is assumed. (From Laszlo, J. and Eckstein, W., *Journal of Nuclear Materials* 184, 22 (1991).)

## 9.8 Arcing

An arc can strike between two electrodes in vacuum if a sufficiently large potential is applied between them. The essential feature of the arc is that material is evaporated from the cathode and is ionized, allowing the flow of current. Arc initiation often occurs at a sharp point or edge where the electric field due to the applied potential is enhanced. The voltage required to strike an arc is very dependent on the state of the surface but once the arc has struck the voltage between the two electrodes is in the range 10 to 20 volts and is dependent only on the electrode material. A flow of current in the solid to a localized point in the surface causes Joule heating, and electrons are produced at the surface by a combination of field emission and thermionic emission. The arc occurring as a result of an externally applied potential is known as a power arc. The presence of a plasma can produce a 'unipolar arc', for which the required applied potential is produced by the plasma sheath, described in Section 9.2. Since the sheath potential is  $\sim 3T_e$  a local electron temperature of only 5–10 eV is necessary to sustain an arc. When the arc is initiated, electrons from the cathode spot are accelerated away from the surface by the sheath potential. The flow of current locally reduces the sheath potential and therefore increases the flow of electrons in the tail of the Maxwellian distribution across the sheath in the area surrounding the arc. The circulating current,  $I$ , can be derived by summing the electron flow towards and away from the solid surface

$$I = A n_e e \left( \frac{T_e}{2m_e} \right)^{1/2} \left\{ \exp \left( -\frac{eV_c}{T_e} \right) - \exp \left( -\frac{eV_s}{T_e} \right) \right\} \quad 9.8.1$$

where  $A$  is the electrode area,  $V_c$  is the critical potential to sustain an arc, and  $V_i$  is the sheath potential. A minimum current,  $\sim 10\text{ A}$ , is required to sustain an arc, determined by the balance between energy deposition from the arc, joule heating, and thermal conduction. Equation 9.8.1 thus shows that a minimum surface area is required to sustain the unipolar arc.

Arches give rise to erosion at the cathode spots. The material is released in the form of ions, neutral vapour, molten and solid drops. The ion current is typically 7 to 10% of the total arc current. The ions are released with typical energies of 50–100 eV and in charge states up to 4 or 5. The higher charge states tend to occur for refractory high  $Z$  metals, such as Ti, Zr, and Mo. It is not understood why the ion energies are significantly higher than the arc voltage drop. Erosion due to vapour emission and droplets is more probable for low melting point metals. The droplets range in size from  $2\text{--}6\text{ }\mu\text{m}$  and are ejected at low angles, typically  $10\text{ to }20^\circ$ , to the surface. They are thought to come from the molten rim of the arc crater. At higher surface temperatures enhanced erosion due to ejection of large droplets is observed.

The erosion of surfaces by arcing in a vacuum diode has been measured for a wide range of materials and different conditions. It is found that the erosion is proportional to the total charge transmitted. From Table 9.8.1 it is seen that the erosion rate varies from  $0.5 \times 10^{-7}\text{ kg/C}$  for molybdenum to  $2.2 \times 10^{-7}\text{ kg/C}$  for zinc. It is commonly assumed that because of the similarity of the cathode spot conditions the erosion rates for bipolar and unipolar arcs are similar. Although this appears a reasonable assumption, there is an absence of any reliable experimental data for unipolar arcs.

The presence of a magnetic field causes a force to be exerted on an arc column, although in the vacuum or unipolar arc the motion is,

**Table 9.8.1** Erosion due to arcing.

Element	Erosion rate $10^{-7}\text{ kg/C}$
Cadmium	6.55
Zinc	2.15
Aluminium	1.2
Copper	1.15
Nickel	1.0
Silver	1.5
Iron	0.73
Tungsten	0.62
Titanium	0.52
Chromium	0.4
Molybdenum	0.47
Carbon	0.17

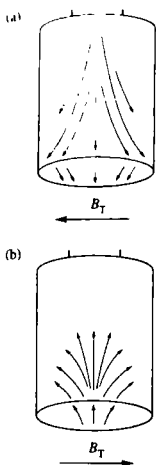


**Fig. 9.8.1** Schematic representation of arc tracks observed on curved surfaces of a cylindrical probe exposed in the tokamak boundary. The direction of the arc depends on the direction of the magnetic field.

surprisingly, in the direction opposite to the  $j \times B$  force. This retrograde motion is seen on the limiters and walls of tokamaks. Two types of arc are observed, called type I and type II arcs. Type I arcs are formed on surfaces having some contamination while type II occur on clean surfaces. The type I arc runs in the impurity vapour and causes comparatively little damage to the surface. Arcs are less likely to be initiated on a clean surface, but when they do form they result in deeper craters and more severe erosion of the surface. The occurrence of arcs removes contaminating layers from a surface, leading to a gradual transition from type I to type II arcs and an increase in the required breakdown potential. The arc current in a unipolar arc is normal to the surface and, if the surface is curved, the direction of the force changes as the arc moves across the surface. This results in a characteristic pattern frequently seen in tokamaks, as illustrated in Fig. 9.8.1. On a surface normal to a magnetic field, since the current and the magnetic field are in the same direction there is no net force and the arc moves about in a random manner.

Arcing is commonly observed in tokamaks, but normally occurs during the current rise phase, when the plasma is unstable. It is difficult to assess the impurity level produced by arcing both because of the irregular nature of the arcing initiation process and because of the problem of measuring the current flow in the unipolar arc. Fortunately, since arcing usually takes place at the start of the discharge and the pulse lengths of tokamak discharges have steadily increased, arcing has become relatively less important as an impurity production mechanism.

## 9.9

### Limiters

A limiter is a solid surface which defines the edge of the plasma. Limiters take various geometrical forms as illustrated in Fig. 9.9.1. The simplest concept is a circular hole in a diaphragm normal to the toroidal field, the hole diameter being smaller than the diameter of the vacuum chamber. This is known as a poloidal limiter. Because magnetic field lines in a tokamak form closed surfaces, even a local or point interaction will in principle define a boundary. In either case there will be a decreasing plasma density radially outside the limiting surface, due to parallel losses in the scrape-off layer, as described in Section 9.3. In the case of a complete poloidal limiter the connection length,  $L$ , will be approximately the circumference of the torus,  $2\pi R$ . In practice such matching of the limiter with the plasma boundary is not possible. In the case of the toroidal limiter the connection length is  $\sim 2\pi Rq$  where  $q$  is the safety factor. The plasma scrape-off layer will thus be broader since, from Section 9.3, the scrape-off layer decay length  $\lambda_n = (D_\perp L/c_s)^{1/2}$ . For the localized, or

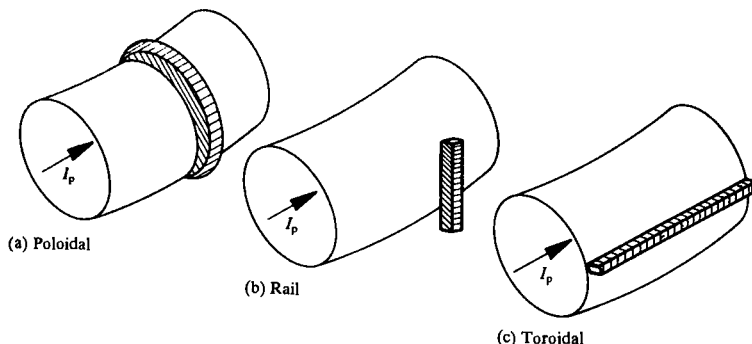


**Fig. 9.9.1** Schematic representation of different types of limiter.

rail limiter, depending on its size and the edge value of  $q$ , the connection length, and hence  $\lambda_n$ , will be longer still.

A limiter plays a number of roles in tokamak operation. It serves primarily to protect the wall from the plasma when there are disruptions, runaway electrons, or other instabilities. For this reason it is commonly made of a refractory material, such as carbon, molybdenum or tungsten, capable of withstanding high heat loads. Secondly, the limiter localizes the plasma-surface interaction. The high power and particle density at the limiter surface causes rapid removal of adsorbed gas, oxide layers and other easily desorbed impurities. When only the clean substrate remains it is possible to maintain plasmas with lower impurity levels. Thirdly, the limiter localizes the particle recycling. A higher neutral density and more radiation is observed in the region near the limiter, than at other positions around the torus.

As the power level in tokamaks has increased, particularly with additional heating, thermal loads on limiters have become large, resulting in many cases in gross melting of the surface. This has been controlled to some extent by increasing the surface area in the toroidal direction and by shaping the limiter so that the power density is more uniformly distributed. In practice it is difficult to calculate the decay length for the power distribution, since there is no satisfactory model for the transport coefficients,  $D_{\perp}$  and  $\chi_{\perp}$ .

Materials for limiters have to satisfy a number of criteria. Firstly, they must withstand thermal shock since high power deposition rates may occur during disruptions. Secondly, they must produce as low an impurity flux as possible, implying low sputter yields and low arcing rates. Thirdly, the impurities produced should preferably have low atomic number in order to reduce radiation losses from the plasma. Finally, limiters must have good thermal conductivity for heat transfer. These are difficult criteria to satisfy simultaneously. Of the low  $Z$  materials, only carbon and

beryllium are suitable for high heat loads. High Z materials such as tungsten and molybdenum have good thermal properties and low sputtering yields, see Section 9.7. In particular they have a high energy threshold for sputtering and for this reason they have been considered for reactor limiters and divertor materials. Nevertheless, because of their high Z, only very low concentrations can be tolerated in the plasma. They can thus only be used if low plasma edge temperatures can be maintained.

Generally tokamak plasmas have been of such short duration, ( $< 10$  s), that the thermal capacity of the limiter has been sufficient to tolerate the total energy deposited. However longer pulses, ( $> 60$  s), have been achieved and for future machines, steady state operation has to be considered. The design of such systems is a major engineering exercise.

The extension of the limiter area naturally leads to the idea of a toroidal limiter running around the circumference of the torus as shown in Fig. 9.9.1(c). Such limiters have been operated successfully in a number of tokamaks. In addition to spreading the heat load, the toroidal limiter minimizes toroidal asymmetries and simplifies the modelling of the boundary compared to a localized limiter.

The main disadvantage of the limiter is that impurities leaving its surface as neutrals penetrate into the confined plasma and become ionized there. The use of a divertor is one way of overcoming this problem. Whether impurity shielding due to a divertor is sufficiently effective to justify the extra complexity and expense of the divertor has still to be resolved.

## 9.10

### Divertors

In the case of a limiter the last closed flux surface (LCFS) is defined by a solid surface and consequently neutral impurity atoms released from the surface can enter directly into the confined plasma, see Section 9.9. In a divertor the LCFS is defined solely by the magnetic field and plasma surface interactions are remote from the confined plasma as illustrated in Fig. 9.1.1. In the divertor configuration impurities released from the target are ionized and may be swept back to the target by the plasma flow before they can reach the LCFS and enter the confined plasma. The divertor also reduces the impurity influx in two further ways, (a) by reducing the flux of neutrals which can reach the main plasma and therefore reducing the flux of charge-exchange neutrals to the walls of the main chamber and (b) by ionizing impurities resulting from any residual wall interactions in the scrape-off layer (SOL) where they then flow along the field lines into the divertor.

There are several possible magnetic configurations for divertors, but the most successful has been the toroidally symmetric or poloidal field

divertor. The required magnetic field is produced by toroidal conductors which create a null in the poloidal field and a separation of open and closed magnetic surfaces. These divertors have the advantage of preserving the essential axisymmetry of the tokamak and can be combined with D-shaped or elliptical cross-sections. It has been found experimentally that use of this divertor configuration often results in a significant improvement in the energy confinement time, the plasma being in a state known as the H-mode (see Section 4.13).

One of the major concerns in fusion reactor design is that of controlling the power reaching the solid surfaces. In an ignited plasma the power entering the scrape-off layer will be determined by the alpha particle fusion power, less any power radiated from the confined plasma. This power then flows in a layer whose width is determined by the cross-field thermal diffusivity,  $\chi_{\perp}$ , and the energy loss time which characterizes the heat flux along the scrape-off parallel to the magnetic field. With present estimates of  $\chi_{\perp}$  the power e-folding length in the scrape-off layer,  $\lambda_p$ , is typically 10 mm. A reactor sized device with a total output of 3 GW (thermal) would produce 600 MW of alpha power and have a toroidal circumference of  $\sim 50$  m. Allowing for the scrape-off layer feeding two limbs of the divertor this gives a poloidal heat flux density in the scrape-off layer of  $\sim 600 \text{ MWm}^{-2}$ , far beyond the power handling capability of any solid material in steady state operation.

Possible ways of reducing the power density are (i) placing the target tiles at an oblique angle to the field lines, (ii) flux expansion of the field lines as they approach the divertor target, (iii) magnetically sweeping the strike point over a width large compared to  $\lambda_p$ , (iv) radiating power in the divertor before it is carried by conduction to the target, and (v) transferring the energy to neutral particles in the divertor. These approaches, however, have not yet led to a fully acceptable solution and the design of the divertor remains one of the most difficult problems in the path of fusion power development.

A further problem is the erosion of the divertor target surface. Even if the impurities produced by sputtering or other erosion processes are prevented from entering the confined plasma, erosion of the target can still be serious. Changes in the target thickness, due both to erosion and to deposition of the eroded material elsewhere, make design of cooling systems very difficult.

The objectives of divertor design are

- (i) Minimizing the impurity content of the plasma by having the plasma surface interactions remote from the confined plasma and designing the divertor particle flow so that any impurities produced at the target cannot enter the confined plasma.
- (ii) Removing the alpha particle power by heat transfer through a solid surface to a fluid transfer medium which will allow it to be transferred from the reactor and used to generate electrical power.
- (iii) Removing the helium ash resulting from the fusion reactions so that the reacting fuel is not seriously diluted.

Under most circumstances the impurity production rate is determined primarily by physical sputtering, which is in turn determined by the flux and energy of the ions arriving at solid surfaces. Achievement of a low plasma temperature at the target is desirable because it reduces the sputtering yield and hence both erosion of the target and the possibility of contamination of the confined plasma. A model is thus required which shows how the divertor density and temperature scale with the experimentally controllable parameters, such as central plasma density and total input power.

### One-dimensional model of the scrape-off layer

The basic parameters of a simple divertor plasma can be represented by a fluid model which takes into account momentum conservation, electron heat conduction, and the boundary conditions on plasma flow at the target. In order to obtain a simple relationship between the densities and temperatures at the LCFS and at the target it is assumed for the present that there are no energy or momentum sources or sinks in the scrape-off layer. Specifically radiation is neglected, although in a more realistic model it can play an important role. The model uses a simplified geometry, treating only the region between the X-point and the target, as illustrated in Fig. 9.10.1. The energy flow comes across the separatrix from the confined plasma.

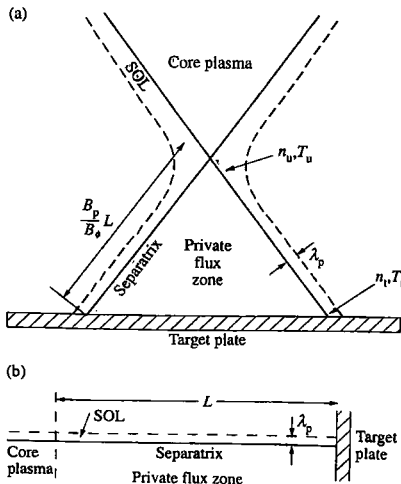


**Fig. 9.10.1** Diagram of the geometry used for the one-dimensional, 2 point flow model of the scrape-off layer. Figure (a) shows the geometry in the *poloidal* cross-section and figure (b) gives the simplified geometry with the horizontal coordinate now *along* the magnetic field.

Momentum conservation along the magnetic field requires

$$nT(1 + \gamma M^2) = \text{constant} \quad 9.10.1$$

where  $M$  is the Mach number of the flow and  $\gamma$  is the ratio of specific heats. It is assumed in the following that  $\gamma = 1$ .  $M$  is taken to be zero on the LCFS and is assumed to be unity at the sheath edge in accordance with sheath theory, described in Section 9.2. Thus eqn 9.10.1 gives

$$n_u T_u = 2n_t T_t \quad 9.10.2$$

where  $n_u$  and  $T_u$ ,  $n_t$  and  $T_t$  are the density and temperature of the plasma at the LCFS and target plate respectively.

Taking heat transport along the SOL to be predominantly by conduction,

$$\kappa \frac{dT_e}{dz} = -q_{\parallel} \quad 9.10.3$$

where  $z$  is the coordinate along the magnetic field line,  $q_{\parallel}$  is the parallel heat flux density and the parallel heat conduction coefficient  $\kappa = \alpha T_e^{5/2}$  with  $\alpha \sim 2000 \text{ W m}^{-1} \text{ s}^{-1} \text{ eV}^{-5/2}$  (see Section 2.23). If there is no net particle flow across the LCFS into the scrape-off layer it is implicit that there must be a source to balance the flow out across the sheath. In practice this is supplied by particle recycling at the target, as described in Section 9.3. The ionization source function determines the profile of the density along the field. Because conduction is independent of density the temperature equations can be solved without explicitly specifying this source, other than saying that it must be close to the target, parallel heat convection being neglected. The effect of particle sources is discussed in more detail later in this section.

For constant  $q_{\parallel}$ , eqn 9.10.3 can be integrated to give

$$T_u^{7/2} = T_t^{7/2} + \frac{7q_{\parallel}L}{2\alpha} \quad 9.10.4$$

where  $L$  is the connection length between the LCFS and the target. Taking  $T_e = T_t$ , the power density transmitted across the plasma sheath at the target is given by

$$q_{\parallel} = \gamma_s n_t T_t c_{st} \quad 9.10.5$$

where  $\gamma_s$  is the sheath power transmission factor and  $c_{st} (= (2T_t/m_i)^{1/2})$  is the sound speed at the target plate, as discussed in Section 9.2.

Taking the parameters  $q_{\parallel}$  and  $n_u$  to be known, eqns 9.10.2, 9.10.4, and 9.10.5 can be solved for  $T_t$ ,  $n_t$  and  $T_u$ . The equation for  $T_t$  is

$$T_t^{7/2} + \frac{7q_{\parallel}L}{2\alpha} = \left( \frac{q_{\parallel}}{n_u \gamma_s (2T_t/m_i)^{1/2}} \right)^{7/2}$$

where  $m_i$  is the ion mass. Solutions for the three parameters are plotted in Fig. 9.10.2. At low density  $n_t$  is proportional to  $n_u$  and at high density it

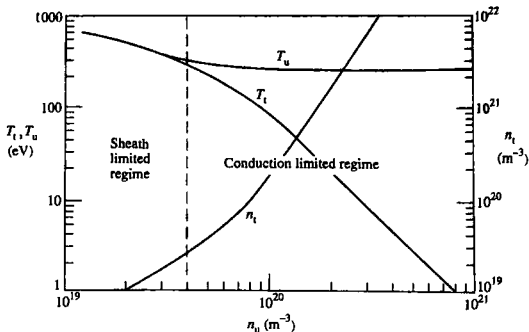


**Fig. 9.10.2** Upstream and target temperatures,  $T_u$  and  $T_t$ , and the target plasma density  $n_t$ , as a function of upstream density,  $n_u$ , calculated for the one-dimensional model described by eqns 9.10.2, 9.10.4, and 9.10.5. Input power flux  $q = 1000 \text{ MVm}^{-2}$ ,  $L = 50 \text{ m}$ .  $\gamma_{\text{th}} = 10$  and ion mass,  $A = 2$ .

is proportional to  $n_u^3$ . When there is a sufficiently large temperature drop that  $T_u^{7/2} \gg T_t^{7/2}$ ,  $n_t$  and  $T_t$  have the solutions,

$$n_t = 2.7 \times 10^{33} \frac{L^{6/7} \gamma_s^2 n_u^3}{A q_{||}^{8/7}} \text{ m}^{-3} \quad 9.10.6$$

and

$$T_t = 3.1 \times 10^{28} \frac{A q_{||}^{10/7}}{L^{4/7} \gamma_s^2 n_u^2} \text{ keV} \quad 9.10.7$$

where  $A$  is the ion mass in atomic mass units.

The high sensitivity of  $n_t$  and  $T_t$  to the input parameters implies sensitivity to the details of the model. If for example the momentum balance along the field line is not described by eqn 9.10.2, it could have a marked effect on  $n_t$  and  $T_t$ . This could arise for example from ion-neutral collisions or from viscosity. There is experimental evidence of such a departure at high density when the plasma may detach from the target plate, as discussed later.

When  $T_u^{7/2} \gg T_t^{7/2}$ , eqns 9.10.4 and 9.10.7 give the ratio of the temperature at the target to the upstream value

$$\frac{T_t}{T_u} = 1.9 \times 10^{32} \frac{A q_{||}^{8/7}}{L^{6/7} \gamma_s^2 n_u^2}$$

from which it should be noted that a large temperature ratio requires a low power, a long connection length or high density.

**Radial power distribution in the scrape-off layer**

The steady state power flow in the scrape-off layer is determined by the requirement that the divergence of the heat flux be zero, that is

$$\nabla \cdot q = \nabla \cdot q_{\perp} + \nabla \cdot q_{\parallel} = 0 \quad 9.10.8$$

where  $q_{\perp}$  and  $q_{\parallel}$  are the heat flux vectors perpendicular and parallel to the magnetic field. A simple one-dimensional radial model for the scrape-off layer can be obtained by writing  $\nabla \cdot q_{\parallel} = q_{\parallel t}/L$ , where  $q_{\parallel t}$  is the value of  $q_{\parallel}$  at the target plate. The parallel energy loss time  $\tau_{\parallel}$  is obtained by taking the ratio of the energy content of the SOL to the power loss at the target

$$\tau_{\parallel} = \frac{3\pi T L}{q_{\parallel t}}. \quad 9.10.9$$

Using eqn 9.10.9, eqn 9.10.8 can be written approximately

$$2\pi \chi_{\perp} \frac{d^2 T}{dr^2} = \frac{3\pi T}{\tau_{\parallel}} \quad 9.10.10$$

where  $r$  is the coordinate perpendicular to the magnetic field and  $\chi_{\perp}$  is the thermal diffusivity. The solution of eqn 9.10.10 is

$$T = T_s \exp(-r/\lambda_p) \quad 9.10.11$$

where  $T_s$  is the temperature at the separatrix, and the scrape-off thickness,  $\lambda_p$  is given by

$$\lambda_p = (\chi_{\perp} \tau_{\parallel}/3)^{1/2}. \quad 9.10.12$$

From eqns 9.10.10 and 9.10.11,  $\lambda_p$  can be written in terms of the value of  $q_{\perp}$  at the separatrix,  $q_{\perp s} = -n_s \chi_{\perp} dT/dr$ , thus

$$\lambda_p = \frac{\chi_{\perp} n_s T_s}{q_{\perp s}}. \quad 9.10.13$$

Taking eqn 9.10.9 for  $q_{\parallel t}$  and substituting in eqn 9.10.12 for  $\tau_{\parallel}$ , with  $\lambda_p$  given by eqn 9.10.13, gives

$$q_{\parallel t} = \frac{q_{\perp s}^2 L}{\chi_{\perp} n_s T_s}. \quad 9.10.14$$

Setting  $T_s = T_u$  and  $q_{\parallel} = q_{\parallel t}$ ,  $T_s$  can be eliminated from eqns 9.10.13 and 9.10.14 using eqn 9.10.4 in its approximate form,  $T_u = (7q_{\parallel} L/2\alpha)^{2/7}$ ,

to obtain

$$\lambda_p = 5.0 \times 10^{-16} \frac{L^{4/9} (\chi_{\perp} n_s)^{7/9}}{q_{\perp s}^{5/9}} \text{ m} \quad 9.10.15$$

and

$$q_{\parallel t} = 2.0 \times 10^{15} \frac{L^{5/9} q_{\perp s}^{14/9}}{(\chi_{\perp} n_s)^{7/9}} \text{ W m}^{-2}. \quad 9.10.16$$

Equation 9.10.16 may now be used in eqns 9.10.6 and 9.10.7 to calculate the values of  $T_i$  and  $n_t$  in terms of the energy flux,  $q_{\perp s}$ , crossing the separatrix, which in turn can be calculated from experimental quantities. The values  $q_{\perp s} = 0.5 \text{ MW m}^{-2}$ ,  $L = 150 \text{ m}$ ,  $\chi_{\perp} = 1 \text{ m}^2 \text{s}^{-1}$  and  $n_s = 1 \times 10^{20} \text{ m}^{-3}$ , give  $\lambda_p = 0.01 \text{ m}$ , and  $q_{\parallel t} = 7 \text{ GW m}^{-2}$ . The poloidal heat flux density is lower by the factor  $B_p/B_\phi$  but is still of the order of hundreds of  $\text{MW m}^{-2}$ . The high power density in the divertor, resulting from the narrowness of the predicted power channels, is one of the main problems in the development of fusion reactors. As discussed later the power flux to a solid surface must not exceed  $\sim 5 \text{ MW m}^{-2}$ . Eqn 9.10.16 shows that it is advantageous to work at high density to minimize the heat load. When flux expansion is included it is found that it is also advantageous to have a long connection length.

### Volume losses of power in the divertor

A possible approach to minimizing power deposition on the target plates is to radiate the power so that it can be distributed over a surface area large compared to the plasma interaction area at the target plate. Some radiation occurs due to recycling of the plasma through excitation and de-excitation of the atoms and molecules returning to the plasma after being neutralized at the target plate. However simple estimates show that this is unlikely to be sufficient to radiate a significant fraction of the power, even at high density operation. An alternative is to introduce an impurity of medium to high atomic number to enhance the radiation. The impurity radiation from a plasma can be written

$$P_r = \int n_m n_e R(T_e) dV \quad 9.10.17$$

where  $n_m$  is the impurity concentration and  $R(T)$  is the radiation parameter, dependent on the impurity species and plasma temperature, discussed in Section 4.21. Maximum values for  $R(T_e)$  are about  $10^{-31} \text{ W m}^3$ . Thus considering average values of the quantities in eqn 9.10.17, a radiated power of 1 GW requires

$$n_m n_e V \gtrsim 10^{40} \text{ m}^{-3} \quad 9.10.18$$

where  $V$  is the volume of the divertor radiating region. For  $V \sim 10 \text{ m}^3$  and  $n_e \sim 10^{20} \text{ m}^{-3}$ , an impurity fraction  $n_m/n_e \sim 10\%$  is required. Such high

concentrations may lead to impurities flowing into the confined plasma, causing radiation from the centre and fuel dilution. It could also cause an unacceptable increase in the target physical sputtering rate, since heavy impurities have a higher yield and a lower energy threshold for sputtering than hydrogen isotopes, due to the higher momentum transfer (see Section 9.7).

Two other volume loss mechanisms which have been considered are charge exchange neutral losses and ion-neutral collisions. However the ratio of charge exchange to ionization rate coefficients indicates that the plasma temperature must already be low ( $< 10$  eV) to obtain a significant power loss by charge exchange. Radiation appears to be the only way to obtain this low temperature. Moreover, charge exchange cools only the ions. Ion-neutral collisions can produce significant cooling if the neutral density is raised sufficiently. While such an effect has been demonstrated in plasma simulators where there is independent control of density, it has not yet been observed in a tokamak and it is unlikely that sufficiently high neutral density can be achieved without losing control of the central plasma density.

More detailed consideration of energy loss by radiation shows that there is a limit to the fraction of the total energy which can be lost by this mechanism, due to the competition with convection across the sheath. If pressure balance is maintained, the losses due to radiation and to conduction both depend linearly on density. Only at temperatures below  $< 5$  eV are the losses due to radiation significantly greater than those due to conduction. There is also a temperature instability at low temperature which may make it difficult to obtain stable radiating conditions. This behaviour is similar to that of MARFES, described in Section 7.16.

Another possible approach to distributing the power in the divertor is to produce a 'detached divertor plasma'. Such a condition has been demonstrated experimentally in most divertor tokamaks. The neutral density is raised until, at a critical density, which depends linearly on the power input, both the plasma density and temperature near the target fall. It is found that pressure balance, as given by eqn 9.10.2, no longer holds, probably due to friction of the plasma with neutral gas. In this respect the situation differs from the conditions when a plasma detaches from a limiter. Although divertor detachment behaviour is not fully understood, it appears that the momentum and energy must be transferred from the plasma to a neutral gas 'blanket' near the target, leading to a drop in pressure along the field lines.

When the plasma detaches from the divertor target the distribution of the radiation moves towards the confined plasma. Because the density at the target falls, the conducted power convected across the sheath also falls and the ratio of radiated power to convected power increases. Under these conditions there is no longer any obvious limit to the fraction of power which can be radiated, although the absolute amount still depends on impurity concentration and temperature as described in eqn 9.10.17. The increased radiation upstream leads to very low plasma temperatures at the target plate and the power flux to the plate drops dramatically.

Ion-electron recombination is observed spectroscopically. The detached regime occurring at high densities can be contrasted with the sheath limited regime at low densities and the conduction limited regime at intermediate densities. It offers a possible solution to the power exhaust although the drop in particle flux to the target means that the pumping of helium ash from the fusion reactions will be made more difficult.

### Flow in the divertor

During normal divertor operation, ions are neutralized at the target and return into the plasma as backscattered neutrals or thermal molecules, as described in Section 9.3. The plasma source arising from ionization of these neutrals near the target enhances the flow back to the target. At high densities, when the flow across the separatrix is small, ionization near the target is the dominant particle source.

A simple picture of the one-dimensional particle flow is presented in Fig. 9.10.3. The ion source due to recycling is localized near the target plate and so the density peaks near the plate and the temperature falls. The plasma flow velocity along the field is low up to the point where ionization occurs, and then accelerates to reach  $M = 1$  at the sheath edge, as shown

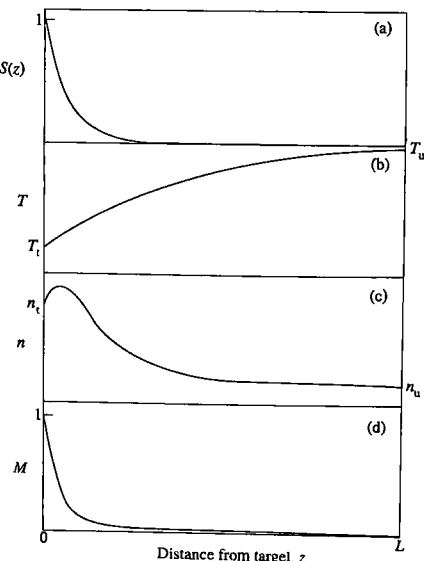


**Fig. 9.10.3** Plots of plasma parameters along the field in the scrape-off layer of a divertor, based on the one-dimensional model described in the text, with  $T_e = T_i$ . The target plate is at  $z = 0$  and the last closed flux surface at  $z = L$ . (a) Assumed plasma source function due to recycling at the target plate. (b) Plasma temperature. (c) Plasma density. (d) Mach number of the plasma flow.

schematically in Fig. 9.10.3d. The flow towards the target provides a frictional drag on the impurities, accelerating them back towards the target, provided they do not escape beyond the region where the plasma is ionized. However, a complication is that there are temperature gradient forces, described in Section 2.23, which can drive the impurities along field lines towards the LCFS. Effective design of the divertor depends on making the frictional force due to the plasma flow towards the divertor target large enough to overcome the temperature gradient force. For a given power input, a high recirculating flow at the target also reduces the average ion temperature.

One of the objectives of divertor design is the removal of the helium ash arising from fusion reactions. Direct pumping of helium from the plasma edge is difficult because the helium neutral density is low and consequently a very high pumping speed is required. However, by transporting the plasma to the separate divertor chamber and transforming from a low density to a high density, the pumping restrictions are significantly eased. The total helium production rate is given by the ratio of the power output of a reactor to the power released per fusion reaction,  $\varepsilon$ . Taking  $\varepsilon = 17.6 \text{ MeV}$  the helium production rate is  $3.6 \times 10^{20} \text{ atoms/GW}$ . The maximum helium concentration which can be tolerated in the plasma without significant fuel dilution is around 10%. Thus taking the confinement time to be the same for helium and deuterium the total particle flow rate will be  $3.6 \times 10^{21} \text{ ions/GW}$ . This constitutes the minimum flow rate across the separatrix and hence the minimum particle flux which must be pumped at the divertor to remove the helium. Such a flow may have to be induced by particle fuelling of the central plasma for example by neutral beams or by deuterium or tritium pellets.

Flow in the divertor becomes much more complicated when two-dimensional effects are considered. The particle source distribution at the target is determined by the ionization rate. The radial profile of density cannot be described by a simple model because there are sources in the scrape-off layer and the behaviour is strongly affected by the geometry of the target plate in relation to the magnetic field structure. A high local density or temperature results in a high ionization rate. Under some conditions the ionization rate near the separatrix may locally exceed the flow rate to the target, resulting in a reverse flow back towards the LCFS, as shown in Fig. 9.10.4. Such an effect is frequently predicted in two-dimensional fluid models, although experimental evidence for it remains sparse. The reverse flow is expected to occur near the separatrix where the electron density and temperature and hence ionization rate are highest. If such a reverse flow occurred under normal operating conditions, it could allow impurities to flow easily to the LCFS.

The complex behaviour of the particles contrasts with the relatively simple power distribution. Because the power is generated near the centre of the plasma and diffuses out to the LCFS, there is no significant power source in the scrape-off layer and the power flux falls off radially with a characteristic length  $\lambda_p$  given by eqn 9.10.15. Thus, in the absence of radiation, the power distribution is rather robust, independent of the geometry.

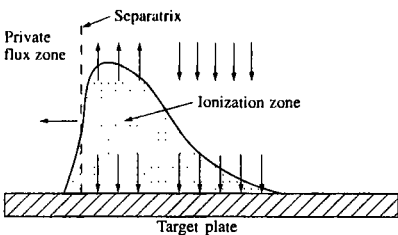


**Fig. 9.10.4** Schematic diagram of particle flows in the poloidal plane of the outer scrape-off layer, near the target plate.

A widely observed experimental result is a strong asymmetry in the power flux to the inner and outer divertor target plates. The plasma at the inner target generally has a lower electron temperature, radiates more strongly and detaches at a significantly lower main plasma density than the outer target plasma. This asymmetry can largely be accounted for by a longer connection length from the outer midplane to the inner than the outer divertor targets, the larger surface area on the low field side of the plasma due to its larger major radius, and the flux compression towards the outside of the plasma due to the Shafranov shift. The longer connection length leads to the inner divertor often being in the conduction regime when the outer divertor is still in the sheath limited regime and results in higher density and higher radiation at the inner target. The asymmetry also depends on the relative direction of the toroidal field and the plasma current, and is most marked when the ion grad  $B$  drift direction is towards the divertor plates. This is the preferred mode of operation because it has a lower power threshold for H-modes. When operating with the ion grad  $B$  drift pointing away from the target plates, slightly more power generally goes to the inner plate but the asymmetry is much less marked. The effect of the ion grad  $B$  drift is not fully understood but plasma flow in the SOL is expected to be influenced by edge toroidal rotation in the plasma direction, radial drift related to parallel temperature gradients and thermoelectric currents due to temperature differentials between inner and outer target plates. The complexity of these effects has meant that they are difficult to incorporate in existing fluid codes. Reducing the asymmetry will be important in next generation tokamaks as the high local heat flux leads to serious engineering problems.

#### General design considerations

There are many complex problems to be considered when designing a practical divertor and no definitive solutions are yet available. In this section the most important factors are described. Both double null and single null poloidal field geometries must be considered. Double null, with an X-point at the top as well as the bottom, allows the wall interaction

area to be doubled, but halves the connection length to the target. It also allows a more triangularly shaped plasma to be obtained, which is beneficial in obtaining high  $\beta$  and high energy confinement. However it increases the complexity of the poloidal field system and decreases the volume of the confined plasma. Stabilizing the plasma so that power flow is balanced between top and bottom is difficult. Both present tokamaks and future tokamak designs favour single null configurations.

Divertor operation has been obtained with a number of different target geometries, varying from flat plates to enclosed chambers. The flat plate target has the advantages of simplicity, good diagnostic access and of enabling the target plates to be designed on a simple rigid structure. The argument in favour of enclosing the divertor is that it reduces the flow of neutral species back to the main confinement chamber, where they may undergo charge exchange reactions in the plasma and cause sputtering of the wall. Having an enclosed divertor chamber allows a higher neutral pressure to be maintained at the target plate for a given plasma density. Extensive variations in the geometrical design of divertors have been tested, for example in ASDEX-upgrade, JET, and Alcator C-Mod. While more enclosed geometries do result in divertor detachment at up to  $\sim 20\%$  lower main plasma densities, the overall operation of the divertor and the main plasma is surprisingly little affected by the divertor geometry. It is still unclear whether neutral density in the main plasma chamber is predominantly due to gas flowing back from the divertor or to plasma interactions in the main chamber itself.

Because the target tiles are heated to high temperatures there is significant thermal expansion. This is a particular problem because the heating is non-uniform, due to the gradient of the power distribution in the scrape-off layer. To minimize stress in the tiles they are normally small,  $\sim 20\text{--}30\text{ mm}$  square. The angle of the tiles with respect to the field lines at the target is made as small as possible in order to increase the effective area of the target surface. Angles as low as  $1^\circ$  have been used. However, due to the finite gap between the tiles, when the angle comes close to grazing a fraction of the tile edge is exposed to the field lines at normal incidence. This problem may be overcome by machining a chamfer on each tile and displacing each one with respect to its neighbour, so that the edges are shielded, as shown in Fig. 9.10.5. This has the disadvantages that it works for only one field direction and it reduces the effective area of the tiles. The optimum design depends on how well the tiles can be

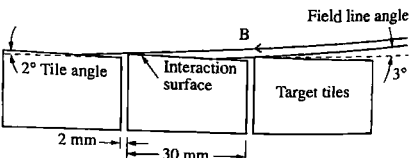


**Fig. 9.10.5** Diagram of target tiles, showing adjacent tiles displaced to protect the edges at gaps. The effective interaction area is reduced depending on the accuracy of the tile placement.

aligned. Alignment is difficult due to thermal expansion, movement due to magnetic and vacuum forces and the large area over which the alignment is necessary.

A further factor to be considered in reactor designs is the erosion of the surface and consequent redeposition of eroded material elsewhere. The gross erosion can be estimated from the incident particle flux density. Considering an upper limit to the energy density of  $\sim 20 \text{ MW m}^{-2}$ , determined by thermal cooling considerations, and a plasma temperature at the target of  $10 \text{ eV}$ , the particle flux is  $\sim 1 \times 10^{24} \text{ ions m}^{-2}\text{s}^{-1}$ . With a typical sputter yield of  $10^{-2}$  atoms/ion this corresponds to a gross erosion rate of  $\sim 3$  metres/year. Such a net erosion rate would be intolerable in the design of the target cooling system. Because the sputter yield is roughly proportional to energy at low energies, variations in the plasma temperature for a constant parallel power density do not affect this estimate until the ion energy is less than the sputter threshold, (see Section 9.7). In practice the net erosion is much less than the gross figure, because eroded material is ionized in the plasma and returns to the surface to be redeposited. However, the location of the deposition depends critically on the transport of the impurities in the plasma.

Experimental observation shows that erosion is greatest near the 'strike point' on the outer target and deposition is largest on the inner target, consistent with the lower plasma temperature there. In fact much of the deposition occurs on cooler surfaces, adjacent to the divertor target but away from the line of sight of the ions. This is now thought to be due to the higher sticking coefficient of the hydrocarbons on the cooler surfaces. There is some experimental evidence that net erosion occurs at the inner wall of the main chamber resulting in transport of wall material onto the inner target. The deposition areas play an important role in locking up tritium within the vessel.

## 9.11

### Heat flux, evaporation, and heat transfer

The power which is produced in the plasma either by ohmic heating, additional heating or by fusion reactions, must be lost to the solid surfaces either by radiation or by transport in the plasma. Radiation tends to result in a uniform deposition of the power. Transport, either by conduction or convection, results in localized power deposition at the limiters or in the divertor since the power transfer is predominantly along field lines. It is common in high power tokamak systems that the power transported to the divertor or limiter is close to the limits which solid materials can withstand. The main factors determining the integrity of a solid are firstly evaporation, leading to erosion of the surface and contamination of

the plasma and secondly thermal shock, leading to the loss of structural strength of the component.

In pulsed systems ( $t \leq 5$  s), where the heat pulse is short compared with the heat diffusion time through the solid, the power to a surface is initially balanced by heat conduction into the bulk. The surface temperature rise  $\Delta T$  due to a power flux density  $P(t)$  is given by

$$\Delta T = \frac{1}{(\pi \kappa \rho C)^{1/2}} \int_0^t \frac{P(t-\tau)}{\tau^{1/2}} d\tau \quad 9.11.1$$

where  $\kappa$  is the thermal conductivity,  $C$  the specific heat and  $\rho$  the density of the solid, and these quantities have been assumed to be independent of temperature. For constant  $P$  eqn 9.11.1 gives

$$\Delta T = 2P \left( \frac{t}{\pi \kappa \rho C} \right)^{1/2}.$$

The materials which can withstand the highest heat fluxes are graphite and the refractory metals with high thermal conductivity such as tungsten and molybdenum. The surface temperature must be such that evaporation is negligible. The evaporation rate,  $R_e$ , is given by

$$R_e = 1.7 \times 10^{24} (AT)^{-1/2} p \text{ atoms m}^{-2} \text{s}^{-1}$$

where  $A$  is the atomic mass,  $T$  the surface temperature in degrees Kelvin and  $p$  the vapour pressure in pascals. Vapour pressure data are available for steady state conditions and results for candidate limiter and wall materials are given in Fig. 9.11.1. However, such data may not be reliable under pulsed conditions or where there are impurities on the surface.

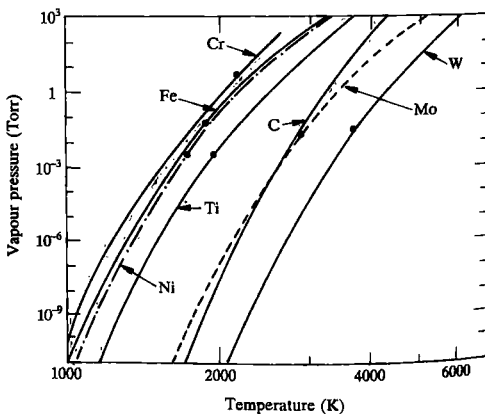


Fig. 9.11.1 Vapour pressure of a range of first wall materials as a function of surface temperature. (Honig, R.E., and Kramer, D.A., Vapour pressure data for the solid and liquid elements. *RCA Review* 30, 285 (1969).)

In steady state the maximum tolerable heat flux is determined by the stress due to temperature gradients between the heated surface and the coolant. Consequently, high thermal conductivity is important. In some designs attempts have been made to combine a low sputter yield plasma-facing surface with a high heat conduction substrate. In these cases thermal stress at the brazed joint may be the limiting factor in the design. The design of such components is complex, calling for finite element analysis of the particular geometric structure. The upper limit to what can presently be achieved in the best designs for steady state heat transfer is 10 to 20 MW m<sup>-2</sup> and, for high reliability, values of 2 to 5 MW m<sup>-2</sup> are more usual. Since the design of such components depends on the basic properties of materials, these limits are unlikely to be significantly improved.

One of the most important factors in designing limiter and divertor surfaces is the power distribution. Since the power density falls approximately exponentially with radius outside the last closed flux surface it is possible, by varying the angle of the surface to the magnetic field lines, to design the surface of the limiter or divertor so that the power per unit area is uniform. On limiters it has been found that this principle works down to angles of  $\sim 3^\circ$  between the field line and the solid surface. At more grazing angles cross-field transport appears to be enhanced, maintaining approximately constant heat flux per unit area exposed. In order to handle the high power densities expected, tiles have to be positioned with an accuracy better than 0.5 mm over distances of order  $2\pi R$ . Gaps between tiles can give rise to field lines being normally incident on surfaces causing unacceptably high heat fluxes as discussed in Section 9.10. Consideration has also to be given to the distribution of the ionization of recycled species and to pumping, particularly in the case of divertors.

Power can also be deposited on the walls during malfunctions, such as the occurrence of disruptions or runaway electrons. Efforts have been made to calculate the energy transported to the surface during disruptions but it is difficult to assess due to the problem of estimating the area of the wall likely to be involved. For a given power density the main problem is estimating the effect of radiation due to the evaporated material from the wall. This radiation reduces the direct power flux to the wall by spreading it more uniformly over a wider area. A problem which may occur during abnormal operation is the production of a thin melted layer at the surface. The hydromagnetic stability of this layer when carrying induced currents which cross the equilibrium magnetic field, is also a matter of concern.

A further difficulty is the erosion of components. Even in the absence of evaporation, erosion occurs due to sputtering. The impurities injected into the plasma are ionized and travel along field lines to be deposited in regions remote from the point of erosion. This leads to areas of net erosion and net deposition. While not a problem in current tokamaks this could be a major difficulty in designing machines for steady-state operation. Quantitative calculations of the net erosion

depend critically on impurity transport coefficients which are not known accurately.

## 9.12

### The behaviour of tritium

Tritium is one of the fuels for fusion reactors. Because it does not occur naturally it is proposed that neutrons from the fusion reactions are used to breed tritium in a lithium containing blanket (see Section 1.8). Loss of tritium into the walls of the reactor is an economic disadvantage as well as being a potential radioactive hazard. Very large concentrations of gas exist in the walls of tokamaks. This gas inventory occurs due to a number of processes including both implantation of ions and charge exchange neutrals and to co-deposition of tritium with the vessel material in the net redeposition regions mentioned above. Ions are implanted into surfaces in contact with the plasma along field lines after acceleration by the sheath potential. The implanted species slow down in the lattice and are distributed according to the range distribution. In many metals hydrogen has a high diffusion coefficient so that after thermalizing in the lattice the atoms diffuse under the concentration gradient through the lattice both towards and away from the surface as discussed in Section 9.4. The equilibrium distribution depends on the boundary conditions at the surface. For metals in which hydrogen isotopes are dissolved exothermically the surface produces a potential barrier. Such metals as titanium, zirconium, and niobium are probably not tolerable because little gas is released and the tritium inventory builds up. In metals where hydrogen is dissolved endothermically the rate of release may be determined by a surface recombination coefficient since, energetically, hydrogen is normally released as molecules rather than atoms. At temperatures above 1000 K dissociation can take place so that atoms rather than molecules are released. The equilibrium concentration of hydrogen isotopes in the wall thus depends on the wall material, its temperature and the ratio of plasma pulse length to the time between pulses.

The distribution of hydrogen in the metal in the steady state is shown schematically in Fig. 9.12.1 for the case where diffusion rather than surface recombination is the rate limiting process. In the idealized situation where the tritium is initially uniformly distributed in the solid there is an analytical solution to the diffusion equation which gives the release rate as a function of time

$$R = At^{-1/2}.$$

In practice, with a non-uniform distribution the release rate is often a power law of similar form but with the exponent in the range

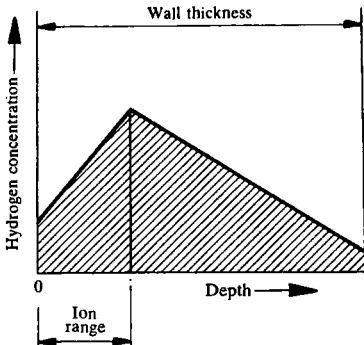


**Fig. 9.12.1** Steady state concentration distribution of hydrogen isotopes implanted in a solid.

-0.5 to -1.0. This is consistent with the implanted tritium being near the surface. By raising the temperature sufficiently the hydrogen can be thermally desorbed from the solid. The high diffusivity of hydrogen isotopes in many metals, while generally leading to low tritium inventory in the vessel structure, is a disadvantage from the point of view of tritium permeation. This can be overcome by using a double wall structure with a pumped interspace.

Understanding the implantation of hydrogen in non-metallic materials is a more difficult problem. The diffusivity of hydrogen isotopes in carbon and many carbides is very low. As implantation progresses the concentration profile increases in a way determined by the range distributions of the incident species. At a given hydrogen concentration saturation occurs locally. Similar behaviour occurs in metals at temperatures below 200 K. The saturated region expands as different parts of the depth distribution increase to the saturated level. For graphite, a commonly used limiter or target material, the saturation level is about 0.44 H atoms per carbon atom. The saturation level per unit area is determined by the energy of the incident ions since the higher energy ions can penetrate further and saturate a deeper layer.

Because graphite is porous, tritium can permeate into the bulk of the material and become trapped at lattice defects. The production of defects by continuous neutron bombardment may increase the tritium inventory significantly above the values extrapolated from present operational conditions. Where the tritium is implanted close to the surface it may be possible to remove it either by heating to 900–1100 K or by erosion of the surface layer by sputtering. Both methods involve difficulties and will have implications for the duty cycle of a reactor.

Another mechanism which can lead to an increase of the tritium inventory is co-deposition of tritium with wall or divertor plate material.

The preferential erosion in some areas of the target plate and the main chamber wall, resulting in impurity transport in the plasma and re-deposition elsewhere (Section 9.10), can result in the build up of hydrogen isotopes within the vessel which cannot be easily removed. Unlike in the implantation process, the tritium resulting from this co-deposition does not tend to saturate but builds up linearly with time. The effect has been particularly noticed in experiments which have used tritium and where a careful inventory has been kept. In experimental measurements the ratio of deuterium to carbon atoms in the deposited layers which continue to be subjected to ion or neutral bombardment is typically 0.1–0.4. In regions shadowed from these energetic fluxes deuterium to carbon ratios in the range 0.5–1.0 have been observed. The layers build up in the coolest areas of the machine as the hydrocarbons released have low sticking coefficients on hot surfaces. After reaching a thickness of  $\sim 10\text{ }\mu\text{m}$  the deposits tend to exfoliate, resulting in the collection of dust in the vessel. The dust is radioactive due to the presence of the tritium and is therefore hazardous. This mechanism has serious implications for future machines operating in tritium and in particular for reactors. The tritium inventory has to be strictly limited for both economic and safety reasons.

## Bibliography

There have been several reviews of plasma surface interactions. The most comprehensive are:

- (A) Stangeby, P.C. *The plasma boundary of magnetic fusion devices*. Institute of Physics, Bristol (2000).
- (B) Stangeby, P.C. and McCracken, G.M., Plasma boundary phenomena in tokamaks. *Nuclear Fusion* 30, 1225 (1991).
- (C) Atomic and plasma material interaction data for fusion, *Supplement to Nuclear Fusion*, R.K. Janev (ed.), I.A.E.A., Vienna.
- Vol. 1 Particle surface interaction data for fusion (1991).
- Vol. 2 Atomic and molecular processes in edge plasmas (1992).
- Vol. 3 Atomic collision processes of helium, beryllium and boron atoms and ions in fusion plasmas (1992).
- (D) Behrisch, R. and Post, D.E., (eds) *Physics of plasma wall Interactions in controlled fusion*. Proceedings of a NATO Advanced Study Institute, Plenum Press, New York (1986).
- (E) Langley, R.A., Bohdansky, J., Eckstein, W., Mioduszewski, P., Roth, J., Taglauer, E., Thomas, E.W., Verbeek, H., and Wilson, K.L., Data compendium for plasma surface interactions, *Nuclear Fusion*, Special Issue, 9–117 (1984).
- (F) McCracken, G.M. and Stott, P.E., Plasma surface interactions in tokamaks. *Nuclear Fusion* 19, 889 (1979).

In addition there has been a series of biennial conferences specifically on plasma surface interactions, which provide a useful source of more detailed information. The proceedings are published in the *Journal of Nuclear Materials* under the title 'Plasma surface interactions in controlled fusion devices'. Some recent conferences have been

Bournemouth, UK	Vols 176–177	1990
Monterey CA, USA	Vols 196–198	1992
Mito, Japan	Vols 220–222	1995
St. Raphael, France	Vols 241–243	1997
San Diego CA, USA	Vols 266–269	1999
Rosenheim, Germany	Vols 290–293	2001
Gifu, Japan	Vols 313–316	2003

## The plasma sheath

A very large literature is devoted to the plasma sheath. However, the high magnetic field present in tokamaks changes the behaviour of the sheath, and particularly the operation of probes. A comprehensive review of the sheath and of probes is given in Stangeby, P.C., in *Plasma Diagnostics*, Vol. 2, (1989), edited by Auciello, O. and Flamm, D.L., Academic Press NY. The subject is also discussed in detail in reference A.

### The scrape-off layer

This subject is discussed in many papers of the current literature and in the conference proceedings mentioned above. It is reviewed in references A and B.

### Recycling

An account of the basic processes is given in reference F. Data on backscattering are given in reference C. More recent summaries of data are given in:  
 Thomas, E.W., Janev, R.K., and Smith, J., *Nuclear Instruments and Methods in Physics Research* **B69**, 427 (1992) and International Nuclear Data committee Report INDC(NDS)-249 Particle reflection from surfaces—A recommended data base, I.A.E.A., Vienna (1991).

Tabata, T., Ito, R., Hakawa, Y., Itoh, N., and Morita, K., *Data on the backscattering coefficients of ions from solids*, Report IPPJ-AM18, Nagoya University (1981).

### Atomic and molecular processes

A comprehensive account of the physics is given by Harrison, M.F.A., The plasma boundary region and the role of atomic and molecular processes in *Atomic and molecular physics of controlled thermonuclear fusion* (eds Joachain, C.J. and Post, D.E.), Plenum Press, New York, 441 (1983).

Much of the atomic data necessary is given in reference C vols 2 and 3 and in

Janev, R.K., Langer, W.D., Evans, K. Jr, and Post, D.E., *Elementary processes in hydrogen-helium plasma, cross sections and reaction rate coefficients*, Springer-Verlag, Berlin, (1987).

A comprehensive review of fundamental atomic data and analytical techniques is available in H. P. Summers *The ADAS users manual*, Version 2.2. (2000). <http://adas.phys.strath.ac.uk/adas/>

### Wall conditioning

Wall conditioning is discussed extensively in the conference proceedings mentioned above. A comprehensive review is given by

Winter, J., *J Nuclear Materials* 176–7, 14 (1990).

### Sputtering

This subject has a wide literature. A very comprehensive account is given in the series of volumes

Behrisch, R., (ed) *Sputtering by particle bombardment*. Springer-Verlag, Berlin, Vol. I (1981), Vol. II (1983), Vol. III (1991).

Data have been collated in

Matsuhashi, N., Yamamura, Y., Itakawa, Y., et al. *Energy dependence of the yields of ion induced sputtering of subatomic solids*, Report IPPJ-AM-32, Nagoya University (1983).

Yamamura, Y., Takaguchi, T., and Tawara, H., *Data compilation of angular distribution of sputtered atoms*, Report NIFS-DATA-1, Nagoya University (1990).

Eckstein, W., *Sputtering data*, Report IPP9/82, Max Planck Institut für Plasmaphysik Garching, (1993).

### Arcing

Mioduszewski, P., Unipolar arcing, Chapter 10 of reference C Vol 1.

### Limiters

Cecchi, J.L., Cohen, S.A., Dylla, H.F., and Post, D.E., (eds) *Energy removal and particle control in fusion devices, Proceedings of a symposium in Princeton, NJ, Journal of Nuclear Materials* 121 (1984).

### Divertors

A recent review of the divertor experiments has been published by

Pitcher, C.S. and Stangeby, P.C., *Plasma physics and controlled fusion* 39, 779 (1997).

For earlier reviews see general references A and B.

### Heat flux, evaporation, and heat transfer

Data on evaporation is given in Chapter 5 of reference C, Langley, R.A., Evaporation.

More comprehensive data on vapour pressure of the elements is given by

Honig, R.E. and Kramer, D.A., Vapour pressure data for the solid and liquid elements, *RCA Review* 30, 285 (1969).

### Tritium inventory

A good survey of hydrogen permeability and solubility under fusion conditions is given by

Moller, W., in reference D and in the general references above (C) vol. 1, and (E).

**10**

# **Diagnostics**

## 10.1

### Tokamak diagnostics

Diagnostics for tokamak plasmas have generally been developed to study particular topics in tokamak research. Five major areas of investigation have been:

- (i) Study of methods of setting up stable plasmas and the investigation of mhd instabilities.
- (ii) Determination of energy and particle containment times, and transport coefficients.
- (iii) Development of supplementary plasma heating methods.
- (iv) Study and control of plasma impurities.
- (v) Investigation of plasma fluctuations to determine their rôle in plasma transport.

The diagnostics to be discussed in this chapter will now be related to each of these areas of research.

Because a current carrying plasma may be in an unstable configuration, the earliest priority of tokamak research was to establish methods of setting up and controlling discharges free from gross mhd or positional instabilities. To achieve this aim, a set of basic electromagnetic diagnostics was developed to measure the plasma current, position, shape, and mhd properties. Even when gross stability is achieved the plasma can still exhibit mhd activity. This activity has been studied with coils at the edge of the plasma which measure the magnetic field perturbations. Internal mhd effects have also been extensively studied with X-ray diode systems which measure the emission from the hot central regions of the plasma. These measurements have been of particular value in studying the sawtooth instability, and the disruptive instability which sometimes terminates tokamak discharges. Although the methods of establishing grossly stable tokamak plasmas are now well developed, there is a need to extend the range of operation. There is also continuing interest in a variety of mhd effects, with new phenomena still being discovered.

A subject of particular interest is the measurement of the energy confinement time. This may be carried out using a diamagnetic loop to determine the energy content,  $W$ , and calculating the confinement time from  $\tau_E = W/P$ , where  $P$  is the power input to the plasma. However, this is not as reliable as obtaining the plasma energy directly from measurements of the density and temperature profiles. The electron density has generally been obtained using microwave phase shift methods although reflectometry is increasingly used, particularly in the outer regions of the plasma. A major step forward was made when the electron temperature was first deduced from Thomson scattering experiments in which the spectrum of light scattered by the plasma electrons from a ruby laser beam was measured. The measurements can also determine the electron

density. In present tokamaks the electron temperature is often determined from electron cyclotron emission measurements. The ion temperature is often determined from the Doppler broadening of radiation produced by the decay of levels that are populated following charge exchange with neutral beams. In addition,  $T_i$  may be found from the emission of neutrals following charge exchange, or from Doppler broadening of impurity lines excited by plasma electrons. In deuterium or deuterium-tritium plasmas the neutrons flux and its spectrum can also determine  $T_i$ .

In experiments using RF or neutral beam heating the particle distribution functions are non-Maxwellian. In order to understand the heating mechanisms, the electron velocity distributions have been studied using X-ray pulse height spectrometers and the ion distributions have been measured with neutral particle analysers operating at high neutral energies.

The importance of impurities was realized early in the tokamak programme when it was found that it was not possible to obtain a stable tokamak discharge in an insufficiently clean vessel. Plasma impurities radiate strongly and the resulting reduction of  $\tau_E$  could prevent ignition in a reactor, and substantial impurity content would also dilute the fuel. It was also recognized that the production of reproducible discharges depended strongly on the control of impurities. These problems led directly to a substantial development of spectroscopic diagnostics to examine the production and behaviour of impurities. In present experiments, spectrometers measure radiation at all wavelengths from the visible through to the X-ray region. Because impurity atoms originate from the tokamak vessel walls, limiter and divertor tiles, a set of diagnostics has been developed to study plasma-surface interactions and the basic physics of impurity production. Langmuir probes are used to measure the properties of the edge and divertor plasma.

The diagnosis of the plasma in the divertor region is of increasing importance. In this region the temperature and density are generally much lower than in the plasma centre but many of the standard techniques can still be used, especially those exploiting spectroscopy.

Measurements of high frequency plasma fluctuations have been undertaken chiefly to establish possible mechanisms to account for the anomalous transport observed in tokamaks. The principal techniques involve the use of heavy ion beam probes, the scattering of electromagnetic radiation, and edge probes. Both magnetic and electrostatic turbulence are regarded as possible causes of anomalous transport. The evaluation of these effects requires measurements of the fluctuations of density, temperature and field strength throughout the plasma volume and, although considerable progress towards making the necessary measurements has been made in recent years, further work is still required.

A great variety of other diagnostics has been developed including measurements using pellets of solid hydrogen, beams of neutral or charged particles, and various methods of determining the internal fields in the plasma leading to a determination of the  $q$ -profile.

There is always a continuing need for the development of new techniques. For example, in reacting D-T plasmas high energy  $\alpha$ -particles are produced. The study of the slowing down and containment of these particles is of critical importance and the development of suitable diagnostics is continuing. The large tokamak experiments lead to plasma conditions in which very large fluxes of neutrons are produced. Under these circumstances radiation hardened diagnostics are required and their development is receiving increasing attention.

An enormous challenge is posed by the design of robust, reliable, and radiation hardened diagnostics for the next generation tokamaks such as ITER. There are many difficulties of access to the plasma, and high engineering standards will be essential.

## 10.2

### Magnetic measurements

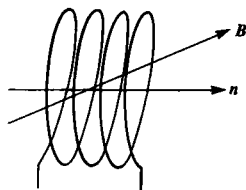


**Fig. 10.2.1** Schematic diagram of coil for measuring the component of  $B$  along  $n$ .

Many properties of a tokamak plasma can be determined using simple loops or coils of wire. Basic measurements are the plasma current, loop voltage, plasma position and shape, stored plasma energy, and current distribution. Information is also obtained about instabilities.

The local magnetic field can be measured using a small coil as illustrated in Fig. 10.2.1. The principle is to determine the flux linking the coil from the induced voltage  $V$

$$\Phi = - \int_{t_0}^t V(t') dt' \quad 10.2.1$$

and to calculate the average value of the normal component of the magnetic field  $B$  from the flux using

$$B \cdot n = \frac{\Phi}{NA},$$

where  $N$  is the number of turns and  $A$  is their average area. All components of the magnetic field may be measured using sets of orthogonal coils.

The toroidal field outside the plasma is determined by the external field coils and is usually measured by only a few detector coils. The strength and direction of the field in the poloidal plane depends strongly on the plasma behaviour and is of more interest. Magnetic coils are placed on a measuring surface, usually the vacuum vessel, to determine the local field in the direction normal to and parallel to the measuring surface. The pick-up coils measuring the field parallel to the surface are best located inside the vessel to detect fast changes which otherwise are much reduced in amplitude by the screening effect of the vessel. Such magnetic field changes are important in the study of instabilities.

Magnetic coils can be accurately calibrated, for instance by comparison with a standard coil of known area. The main source of error in measurements of the poloidal field is the unwanted pick-up of a small part of the strong toroidal field. This can be corrected for by making measurements in the absence of plasma with only toroidal field coils energized.

In addition to the coils determining  $B$  on the measuring surface there are also Rogowski coils to determine current, and toroidal and poloidal flux loops to determine the total enclosed flux and the loop voltage.

### Plasma current

Ampère's law relates the integral of the magnetic field strength round a closed loop to the total current enclosed by the loop:

$$I = \frac{1}{\mu_0} \oint B \cdot dI, \quad 10.2.2$$

where  $dI$  is an element of length of the loop. The toroidal current is usually determined using a continuous Rogowski coil as illustrated in Fig. 10.2.2. The coil consists of a multiple turn coil of wire which, instead of fully encircling the plasma, returns along the axis of the coil to avoid enclosing any net flux parallel to the current.

If the individual turns are small compared with the total size of the coil, then  $B$  varies only slightly across a turn and the flux measured per unit length of coil is given by

$$d\Phi = -nAB \cdot dI,$$

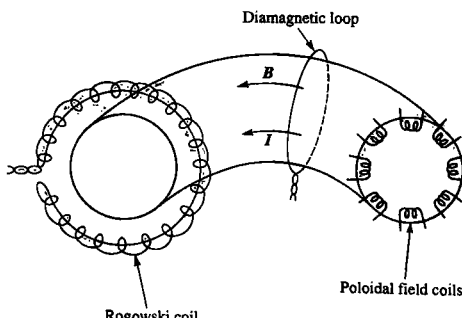


Fig. 10.2.2 Schematic diagram of magnetic diagnostics.

where there are  $n$  turns per unit length, each of area  $A$ . The total flux linking the Rogowski coil is then

$$\Phi = nA \oint \mathbf{B} \cdot d\mathbf{l}. \quad 10.2.3$$

Using eqns 10.2.1, 10.2.2, and 10.2.3 the enclosed current is obtained

$$I(t) = -\frac{\int_{t_0}^t V(t') dt'}{nA\mu_0}.$$

An alternative to a full Rogowski coil is to use a number of discrete magnetic coils surrounding the plasma as shown in Fig. 10.2.2 and approximate the integral 10.2.3 by a summation over the coils. The plasma current can be feedback controlled by adjusting the toroidal loop voltage induced by the primary coil to bring the measured current to the required value.

### Loop voltage

The simplest of all measurements is that of the toroidal loop voltage which is determined by measuring the voltage round a toroidal loop of wire parallel to the plasma. The loop voltage is useful in determining the resistance and the Joule heating of the plasma although the interpretation is not always simple.

The voltage is induced by flux changes due both to currents in the primary circuit and the plasma current itself, and consequently internal rearrangement of the plasma current or a change in its magnitude leads to a toroidal voltage which varies across the plasma. Only when the plasma current and the current density profile are constant in time is the toroidal voltage uniform across the plasma and equal to the loop voltage measured at the surface.

### Plasma surface

The shape and position of the outermost closed magnetic surface of the plasma can be determined from the toroidal loop voltage and poloidal field measured at many points on the vacuum vessel. Since the loop voltages can be integrated to yield flux measurements and the local value of poloidal field gives the gradient in flux, it is possible to extrapolate across a current-free region to find nearby surfaces that enclose constant flux and consequently to identify the last closed flux surface. This requires an extrapolation from the measured poloidal flux,  $\psi$ , at the wall using  $\nabla^2\psi = 0$ . This procedure relies on measurements being made relatively close to the plasma surface, otherwise errors in extrapolation become large.

### Plasma position and shape

In addition to giving the position of the plasma surface the magnetic measurements can be used to give the position of the centre of the current channel. One method is to evaluate moments of the current density profile. In the same way that eqn 10.2.2 relates the integral of the current density over the plasma cross-section to the integral of measurements at the boundary, other moments of the current density are related to surface quantities and consequently can be determined. The first current moment, for instance, gives the position of the current centre,  $R_c$  defined by

$$R_c^2 = \frac{1}{I} \int j_\phi R^2 dA.$$

In the simplest case where the measuring surface is a flux surface,  $R_c$  is given by

$$R_c^2 = \frac{1}{\mu_0 I} \oint B_p R^2 d\ell,$$

where  $j_\phi$  is the toroidal current density and  $B_p$  is the poloidal field at the surface. Higher moments give information on the shape of the current channel. The second moment gives the elongation, the third moment the triangularity.

### Plasma energy and internal inductance

The plasma energy can be determined from magnetic measurements using the force balance between the magnetic field and the kinetic pressure. There are two methods, one using the force balance along the major radius, the other the force balance along the minor radius.

The quantities which require to be measured to determine the energy and internal inductance are the magnitude and direction of the magnetic field at the measuring surface, and the diamagnetic flux. The diamagnetic flux is the difference between the total toroidal flux with plasma and that in the absence of plasma. This flux is measured with a loop enclosing the plasma, encircling it poloidally, as illustrated in Fig. 10.2.2. The vacuum flux is determined either by measuring the current flowing in the toroidal field coils or, equivalently, the toroidal field outside the vacuum vessel.

The equilibrium equations are derived by taking components of

$$\frac{(\nabla \times B) \times B}{\mu_0} = \nabla p$$

and integrating over the plasma volume. The resulting equations relate volume integrals, such as plasma energy and diamagnetic flux, to surface integrals of the field strength. The two main equations are written in

a non-dimensional form for a static isotropic plasma as

$$3\beta_p + l_i - \mu = 2(S_1 + S_2) \quad 10.2.4$$

$$\beta_p + l_i + \mu = 2S_2 \frac{R_T}{R_0}, \quad 10.2.5$$

where  $\beta_p$  is the poloidal beta, related to the plasma energy through  $W = \frac{3}{8}\mu_0 R_0 \beta_p I^2$ , and  $l_i$  is the internal inductance. The diamagnetic parameter  $\mu$  is given approximately by

$$\mu = \frac{8\pi B_0 \Delta\phi}{\mu_0^2 I^2},$$

where  $B_0$  is the toroidal field on axis and  $\Delta\phi$  is the diamagnetic flux.  $S_1$  and  $S_2$  are integrals of the magnetic field over the surface which, when evaluated on a flux surface, simplify to

$$S_1 = \frac{1}{\mu_0^2 I^2 R_0} \int B_p^2 \mathbf{r} \cdot d\mathbf{S}$$

and

$$S_2 = \frac{1}{\mu_0^2 I^2 R_0} \int B_p^2 \mathbf{R} \cdot d\mathbf{S},$$

where  $\mathbf{r}$  and  $\mathbf{R}$  are the minor and major radius vectors and  $d\mathbf{S}$  is an outward facing surface element.  $R_T$  is a characteristic radius of the toroidal configuration involving an integral over the plasma volume which is sometimes approximated by the radius of the current centre discussed above.  $R_0$  is the major radius of the centre of the vacuum vessel.  $S_1$  and  $R_T/R_0$  are both close to unity, while  $S_2$  is related to the  $m = 1$  component of the poloidal field and increases from a small value at low values of pressure and inductance to  $\sim R/a$  at high values.

Care is required when using eqns 10.2.4 and 10.2.5 because there is an arbitrariness introduced in normalizing the equations. All items are normalized to the square of an edge poloidal field,  $B_a^2$ , which, in a non-circular plasma in particular, may be defined in different ways. Here  $B_a^2$  has been chosen as

$$B_a^2 = \frac{\mu_0^2 I^2}{4\pi A}$$

with  $A$  the plasma area. A common alternative is

$$B_a^2 = \frac{\mu_0^2 I^2}{\ell^2}$$

with  $\ell$  the length of the poloidal perimeter. For a given plasma the latter choice gives a higher  $\beta_p$ .

Equations 10.2.4 and 10.2.5 can be rearranged to give

$$\beta_p = S_1 + S_2 \left( 1 - \frac{R_T}{R_0} \right) + \mu \quad 10.2.6$$

and

$$\beta_p + \frac{l_i}{2} = \frac{S_1}{2} + \frac{S_2}{2} \left( 1 + \frac{R_T}{R_0} \right). \quad 10.2.7$$

Equation 10.2.6 is routinely used to determine the plasma energy from diamagnetic flux measurements. In a cylinder  $S_1 = 1$  and  $R_T/R_0 = 1$ , and eqn 10.2.6 reduces to

$$\beta_p = 1 + \mu$$

showing that if  $\beta_p = 1, \mu = 0$  and the diamagnetic flux is zero.

Equation 10.2.7 allows the determination of the sum  $\beta_p + l_i/2$  from magnetic measurements made at the measuring surface. A further relationship exists between  $\beta_p$  and  $l_i$  which only gives additional information in non-circular plasmas. This relation allows the separation of  $\beta_p$  and  $l_i$  in eqn 10.2.7 and consequently there are two independent values of  $\beta_p$ , one from eqn 10.2.6, often called  $\beta_{\text{dia}}$ , and one from eqn 10.2.7, referred to as  $\beta_{\text{mhd}}$ .

For a plasma with isotropic pressure  $\beta_{\text{dia}} = \beta_{\text{mhd}}$  but in a plasma with anisotropic pressure the two are different because the major radius and minor radius force balance are different. The perpendicular and parallel components of  $\beta_p$ ,  $\beta_{p\perp}$ , and  $\beta_{p\parallel}$ , are associated with the perpendicular and parallel pressures and are related to the measured betas by

$$\begin{aligned} \beta_{\text{dia}} &= \beta_{p\perp} \\ \beta_{\text{mhd}} &= \frac{1}{2}(\beta_{p\perp} + \beta_{p\parallel}). \end{aligned} \quad 10.2.8$$

In the presence of a large toroidal rotation velocity, eqn 10.2.8 is modified to include the rotational energy.

### Instability measurements

Several mhd instabilities occur in tokamaks and they can be detected and studied by measuring their magnetic perturbations. Using coils these perturbations can be detected at the plasma edge even when the amplitude of the instability is quite small. This is because the instabilities usually rotate due to the plasma velocity and the diamagnetic velocity, leading to timescales  $10^3$ – $10^4$  times shorter than typical timescales for changes in the equilibrium magnetic field. Since magnetic coils detect the time derivative of  $B$ , instabilities can be detected even when their magnetic perturbations are only  $10^{-4}$ – $10^{-3}$  of the equilibrium poloidal field. Instabilities at still higher frequencies can be detected at correspondingly lower amplitude.

Magnetic perturbations sometimes become stationary in the laboratory frame due to a process referred to as mode locking. The detection of such stationary perturbations is more difficult and relies on integrating the output of several coils combined in such a way as to eliminate the equilibrium field, and only detect toroidal harmonic perturbations such as  $n = 1$  or  $2$ . Detection of stationary instabilities is difficult at low amplitude but this is usually not a problem because mode locking usually occurs only when the instability has grown to a large amplitude.

By making measurements at different poloidal and toroidal locations the structure of magnetic perturbations can be determined as well as their amplitude and frequency. It is important to recognize that the structure may vary across the radius, for instance there may be an  $m = 1, n = 1$  structure in the centre and an  $m = 3, n = 1$  structure near the plasma edge. The magnetic coils will then be dominated by the  $m = 3$  perturbation as the perturbation from the more distant  $m = 1$  component falls off with distance.

Interesting examples of magnetic activity are observed during the current rise phase. As the value of the safety factor at the edge falls, perturbations with decreasing  $m$  values are observed. Figure 10.2.3 shows an example from Alcator A. The poloidal structure of magnetic perturbations is shown along with the toroidal loop voltage, showing minor disruptions caused by the instabilities.

Important results on Alfvén eigenmodes have recently been obtained from magnetic coils systems with a frequency response up to 1 MHz. Analysis of this data has depended on Fourier analysis of large volumes of data.

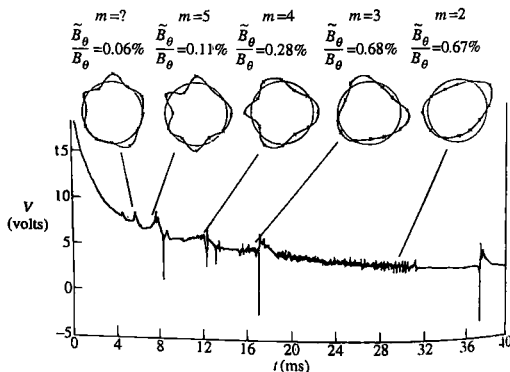


Fig. 10.2.3 The evolution of the loop voltage trace and observed structure of magnetic perturbations during the current rise in Alcator A. (Granetz, R.S. et al., Nuclear Fusion 19, 1587 (1979).)

## 10.3

### Interferometry

The refractive index for an electromagnetic wave propagating in a collisionless magnetized plasma with its electric vector parallel to the magnetic field ('ordinary mode') is given by

$$\mu = [1 - (\omega_p^2/\omega^2)].$$

At frequencies which are large compared with the plasma frequency, the change in the phase of a beam of coherent radiation passing through a plasma compared with that of a reference beam is proportional to the electron density integrated along the beam probing the plasma

$$\Delta\phi = [\lambda e^2/(4\pi\varepsilon_0 m_e c^3)] \int n_e dl, \quad 10.3.1$$

where  $\lambda$  is the wavelength of the radiation. This phase difference can, for example, be measured by a Mach-Zehnder interferometer arrangement as shown in Fig. 10.3.1. A laser or microwave beam of radiation is divided into two components. One of these is shifted in frequency (using, say, a rotating grating). The second component is subdivided further into a reference beam and a number of probing beams. If the detector is nonlinear in the wave amplitude, (for example if it is a 'square law' detector which gives rise to a signal proportional to the incoming power) recombination of a reference or probing beam with the frequency shifted radiation produces a beat signal at the difference frequency  $\Delta\omega_0$ . The variation of the phase of the probing beat signals with respect to the reference beat signal is given by eqn 10.3.1, from which the line integral of the density may be deduced. The beat frequency is chosen to be sufficiently high to allow a good time resolution in the phase measurement and sufficiently low to be electronically tractable (typically 10 kHz–1 MHz for far infrared systems).

The requirement that the interferometer should be sensitive to the electron density and insensitive to mechanical vibrations favours long

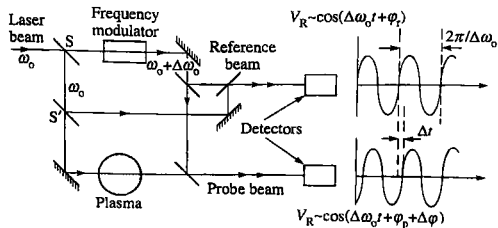


**Fig. 10.3.1** Schematic layout of a Mach-Zehnder interferometer. The laser beam is split at S and S' and recombined at the detectors. The phase differences  $\varphi_0$  and  $\varphi_p$  reflect the different path lengths whereas  $\Delta\varphi$  is caused by the refractive effects of the plasma only.

wavelengths. The requirement that refraction of the beams by transverse density gradients be minimized favours short wavelengths. The choice of the radiation source is determined as a compromise between these competing requirements. For the diagnostics of tokamak plasmas, wavelengths between 10 and 2000  $\mu\text{m}$  have been used. Several types of square-law detector can be used at these wavelengths: room temperature pyroelectric crystals that are simple and inexpensive; liquid helium-cooled indium antimonide crystals that have high sensitivity; or Schottky diodes that have good response at high frequencies. When possible, the interferometer frame is built to stand independently of the tokamak to avoid vibrations of the optics. When this is not possible two interferometers operating at different wavelengths but using the same optical path may be used. The phase shift due to the electron density is proportional to the wavelength,  $\lambda$ , while that due to vibrations is inversely proportional to  $\lambda$ , so that a measurement of the net phase shift at two wavelengths allows the mechanical displacements and the electron density to be determined separately. Figure 10.3.2 shows an example of such a 'two-colour' phase measurement.

Given a large number of sight lines viewing the plasma from several different directions, it is possible to deduce the local electron density from the line-integrated interferometric measurements by tomographic inversion (see Section 10.8). However, access restrictions often give rise to a limit of 5–10 vertical lines of sight. To obtain the local electron density from such a small number of measurements, it is necessary to assume that the surfaces of constant density are known. Usually it is

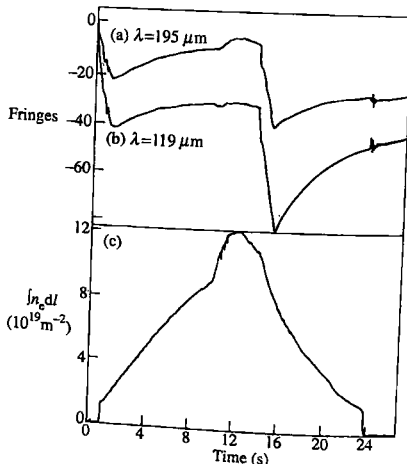


**Fig. 10.3.2** Typical data from a 2-wavelength interferometer on JET:  
 (a) phase shift versus time ( $\lambda = 195 \mu\text{m}$ ),  
 (b) phase shift versus time ( $\lambda = 195 \mu\text{m}$ ), ( $\lambda = 119 \mu\text{m}$ ), (c) net line-integrated electron density versus time.

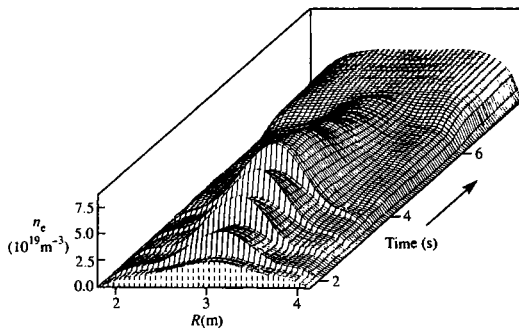


**Fig. 10.3.3** Time evolution of the density profile in a pellet fuelled discharge in JET. Each pellet produces a discontinuous increase in plasma density. The first pellet is injected at 2 s and the three subsequent ones lead to a maximum density at about 3.5 s. At later times the density profile broadens.

assumed that they coincide with the tokamak flux surfaces, since these are isobars and, due to the high parallel heat conductivity, isotherms. If the iso-density surfaces are concentric circles, the local density,  $n_e(r)$ , is given analytically in terms of its line integral along the  $x$ -direction,  $N_e(x)$ , by the Abel transform

$$n_e(r) = -\frac{1}{\pi} \int_r^a \frac{dN_e(x)}{dx} \frac{1}{(x^2 - r^2)^{1/2}} dx.$$

For more complicated iso-density contours a numerical procedure analogous to the Abel transform is performed. Contributions arising from density on the outer surfaces are subtracted for chords probing progressively further into the plasma to obtain the contributions of the inner surfaces. Figure 10.3.3 shows the time evolution of the local electron density obtained by Abel-inversion in a discharge fuelled by injection of frozen deuterium pellets.

### Polarimetry

Coherent radiation is characterized by its polarization as well as its phase. For propagation parallel to a magnetic field in a plasma there is a difference in the refractive indices of right and left circularly polarized radiation, arising from the gyration of plasma electrons, which in one case is in the same direction as that of the polarization while in the other it is counter to it. It can be shown that

$$\mu_{\pm} = 1 - \frac{\omega_p^2}{\omega^2} \frac{\omega}{(\omega \pm \omega_{ce})}.$$

A linearly polarized wave can be decomposed into right and left circularly polarized components. The difference in the refractive indices of these

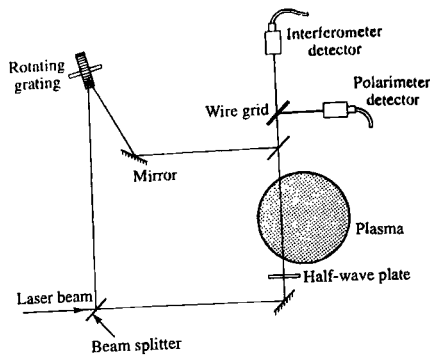


**Fig. 10.3.4** Schematic layout of the TEXTOR polarimeter (from *Interferometry and Faraday rotation measurements on tokamaks*, Soltwisch, H., International School of Plasma Physics, Varenna, CEC, Brussels).

components gives rise to a rotation of the polarization vector known as the Faraday effect. The angle of rotation is given by

$$\theta_F = \frac{\lambda^2 e^3}{8\pi^2 c^3 \epsilon_0 m_e^2} \int n_e B_{||} dl$$

and can be used to measure the internal poloidal magnetic field of a tokamak.

The wavelengths which are used for interferometric measurements are also suitable for measuring the Faraday effect, although the rotation angles tend to be rather small ( $\sim 1^\circ$ ) except in large tokamaks where the path length is long. Figure 10.3.4 shows a typical polarimeter. A polarizing grid, made of uniformly spaced tungsten wires, placed in front of the interferometer detector reflects the component of the probing beam arising from the Faraday rotation into the polarimeter detector. For small rotation angles, the ratio of the amplitudes of the signals at the two detectors is proportional to the angle. Unlike the interferometer measurement, this measurement makes use of the relative amplitude of the signals. It therefore requires a calibration, which is performed by rotating the polarization of the probing beam by a known angle using a quartz half-wave plate and recording the signal amplitudes. Other possible arrangements involving modulation of the polarization angle only require a phase measurement (analogous to the interferometric measurement), thus obviating the necessity of calibration of the system. The lack of efficient polarization modulators has meant that the polarization modulation technique has found few applications in tokamaks.

Faraday rotation measurements of the poloidal magnetic field distribution have been made on several machines (for example see Fig. 10.3.5) and this has led to a major reassessment of the theory of sawtooth instabilities. The original theory of Kadomtsev postulated that a sawtooth leads

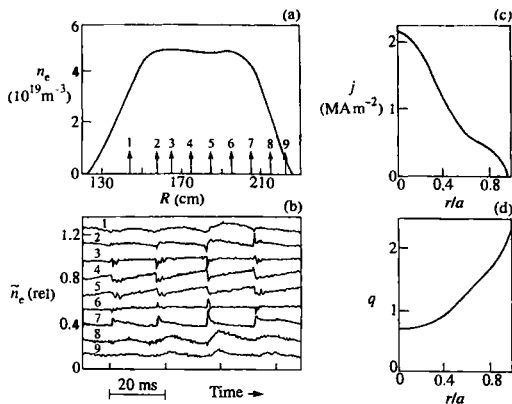


**Fig. 10.3.5** (a) Profile of electron density across major radius. (b) Measured fluctuating part of  $n_e$  at different radii. (c) Deduced current density profile. (d) Safety factor profile. The data was taken for a sawtooth discharge in TEXTOR. (Soltwisch, H. et al., *Plasma Physics and Controlled Nuclear Fusion Research* (Kyoto) 1, 263, IAEA (1987).)

to complete reconnection of the poloidal flux within the sawtooth region, raising the safety factor above 1 everywhere. In contrast, several experiments beginning with TEXTOR concluded from polarimetric measurements that the safety factor can remain well below unity ( $\sim 0.7$ ) throughout the sawtooth period (see Section 7.6).

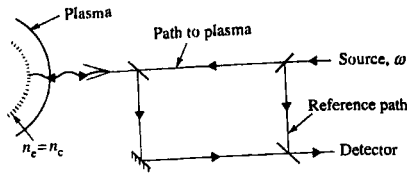
## 10.4

### Reflectometry

An alternative method for measuring the electron density is reflectometry. In this method microwave radiation with frequency  $\omega$  is launched into the plasma along the density gradient and reflected at the layer where the electron density equals a critical value,  $n_c$ . A diagram of a reflectometer system is shown in Fig. 10.4.1. Phase changes in the reflected radiation are measured by mixing this radiation with a reference beam in a detector. The relative positions of the different density layers in the electron density profile are determined by making the measurement with a range of different probing frequencies. Alternatively, movements of a single layer are measured by holding the source frequency constant and measuring the phase output of the reflectometer.

At microwave frequencies the radiation can propagate in two independent modes: the ordinary mode and the extraordinary mode, and this gives different possibilities for reflectometry. For propagation at right angles to

**Fig. 10.4.1** Schematic diagram of a microwave reflectometer. Radiation at angular frequency  $\omega$  is reflected at the critical density layer and combined with a reference beam. Movements of the critical density layer, or changes in  $\omega$ , give rise to fringes in the reflectometer detector.



the magnetic field, the ordinary mode is polarized with the electric vector parallel to  $\mathbf{B}$  and total reflection occurs at the critical density when

$$\omega = \omega_{pe},$$

where

$$\omega_{pe} = \left( \frac{n_e e^2}{\epsilon_0 m_e} \right)^{1/2}$$

is the plasma frequency. The extraordinary mode is polarized with the electric perpendicular to  $\mathbf{B}$  and in this case, total reflection occurs when

$$\omega = \omega_{U,L}$$

where

$$\omega_{U,L} = \left( \frac{\omega_{ce}^2}{4} + \omega_{pe}^2 \right)^{1/2} \pm \frac{\omega_{ce}}{2},$$

$\omega_{ce} = eB/m_e$  is the electron cyclotron frequency, and  $\omega_U$  and  $\omega_L$  are known as the upper and lower cut-off frequencies. The corresponding critical densities may be found from the equations assuming that  $B$  is known. Since the electron density and magnetic field are a function of position,  $\omega_{pe}$ ,  $\omega_U$ , and  $\omega_L$  depend on position. In principle, the layers corresponding to  $\omega_{pe}$ ,  $\omega_U$ , and  $\omega_L$  can all be used for reflectometry. In practice, most measurements have been performed thus far using the  $\omega_{pe}$  layer, with a few using the  $\omega_U$  layer.

Full wave calculations show that the total phase delay of an ordinary mode wave during propagation in the plasma and reflection at the cut-off layer is

$$\phi = 2\frac{\omega}{c} \int_{R_c}^{R_{ant}} \mu(R) dR - \frac{\pi}{2},$$

where the integral is along the major radius,  $R$ , and

$$\mu(R) = \left( 1 - \frac{\omega_{pe}^2(R)}{\omega^2} \right)^{1/2}$$

is the refractive index for the ordinary mode.  $R_{ant}$  is the position of the launch and receive antenna, and  $R_c$  is the position of the reflecting layer.

Differentiation with respect to  $\omega$  and application of the Abel integral equation gives

$$R_c(\omega_{pe}^2) = R_{\text{ant}} - \frac{c}{\pi} \int_0^{\omega_{pe}} \frac{d\phi}{d\omega} \frac{1}{(\omega_{pe}^2 - \omega^2)^{1/2}} d\omega.$$

Hence, in order to determine the position of the reflecting layers, it is necessary to measure  $d\phi/d\omega$  for the range of frequencies between 0 and  $\omega_{pe}$ . In practice, measurements will not be possible down to zero frequency and the missing data have to be provided from other sources, for example by extrapolating measurements made with Langmuir probes.

Two approaches to implementing reflectometry have been developed. In one, the frequency is swept over a broad range and  $d\phi/d\omega$  is measured as a function of frequency. In the other, the output from an array of independent sources with different probing frequencies is combined into the same waveguide, and the frequency of each source is swept over a narrow range to give  $d\phi/d\omega$  at each frequency. The dependence of  $d\phi/d\omega$  on frequency is constructed by interpolation. Each method has its own strengths and weaknesses and areas of optimum application.

Figure 10.4.2 gives an example of measurements using a multiple frequency, narrow band sweep system or JET. The system has twelve frequencies probing densities in the range  $4 \times 10^{18}$ – $8 \times 10^{19} \text{ m}^{-3}$ . It has an effective time resolution of 5 ms and can measure several hundred profiles in a plasma pulse.

Experiments have shown that the electron density is a rapidly fluctuating quantity. Measurements of the characteristics of the fluctuations are important because of their role in the transport of energy and particles. Reflectometry has the potential to provide information on the density fluctuations and a special technique, correlation reflectometry, is being

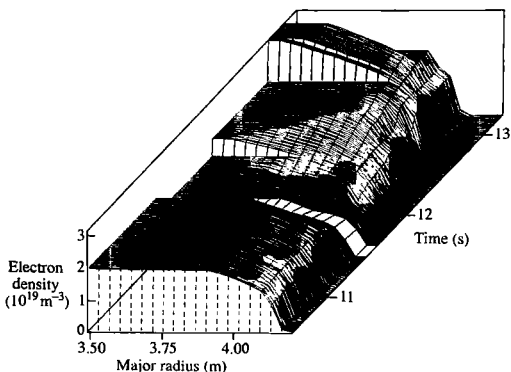


Fig. 10.4.2 Electron density profiles measured with the multiple frequency, narrow band sweep system on JET. In the flat regions no measurements were made

developed specifically for this purpose. In this technique relatively small sampling volumes are chosen at two or more different locations in the plasma. Fluctuations in the electron density in the sample volumes give rise to fluctuations in the measured reflected signals. By choosing the sample volumes at different locations, and by analysing the measured signals using correlation techniques, the size and movement of the density perturbations can be determined. Preliminary measurements on a number of tokamaks have shown that fine-scale density structures exist in the plasma and that the size and movement of the structures depend on plasma conditions.

## 10.5

### Measurement of electron temperature

The electron temperature is measured routinely on most tokamak plasmas by two independent methods: the scattering of laser light from the electrons (Thomson scattering), and the measurement of the emission due to the Larmor motion of the electrons around the magnetic field lines (electron cyclotron emission).

#### Thomson scattering

In the case of Thomson scattering, the electron temperature is determined from the degree of broadening of the spectrum of the scattered laser radiation. The power scattered per unit solid angle in the frequency bandwidth  $d\omega$  can be calculated from electromagnetic theory and is given by

$$P_s = P_0 r_e^2 \sin^2 \theta n_e L S(k, \omega) d\omega,$$

where  $P_0$  is the total incident laser power,  $r_e = e^2 / 4\pi \epsilon_0 m_0 c^2 = 2.82 \times 10^{-15}$  m is the classical electron radius,  $\theta$  is the angle between the incident and scattered rays,  $L$  is the interaction length, and  $S(k, \omega)$  is the spectral density function, which depends on the Fourier spectrum of the fluctuations giving rise to the scattering and has to be calculated for individual cases. In the spectral density function  $\omega$  is the difference between the scattered and incident frequencies, and  $k$  is the magnitude of the scattering vector  $k$  which is the difference between the incident and scattered wave vectors. For a thermal plasma

$$S(k, \omega) d\omega = \Gamma_e(x_e) dx_e + Z \left( \frac{\alpha^2}{1 + \alpha^2} \right)^2 \Gamma_i(x_i) dx_i,$$

where  $Z$  is the ion atomic number,  $x_e = \omega / k v_{T_e}$ ,  $x_i = \omega / k v_{T_i}$ , and  $\alpha = (k \lambda_D)^{-1}$  is the scattering parameter.  $\Gamma$ , the Salpeter function, is strongly dependent on  $e^{-x^2}$ . In the scattered spectrum, the two terms in

this expression produce a narrow peak with a width of order of magnitude  $kV_T$ , superimposed on a broad peak with a width of order  $kT_e$ . When  $\alpha$  is small (short wavelengths) the spectrum is dominated by the broad peak and so  $T_e$  can be determined. The dependence of  $P_s$  on  $n_e$  allows its determination by measuring the absolute level of the scattered power.

Neglecting relativistic effects when  $\alpha \ll 1$ , the function  $S(k, \omega)$  is simply related to the one-dimensional Maxwell velocity distribution of the electrons along the direction of the scattering vector,  $k$ . This approximation produces only small errors at temperatures below  $\sim 1$  keV. At temperatures of several keV relativistic effects have to be taken into account and it is necessary to use the relativistic Maxwell distribution when calculating the scattered radiation frequency spectrum. The spectrum has a characteristic blue shift and departs from the Gaussian shape associated with low temperature Maxwellian distributions, both effects increasing with temperature.

The expression for the scattered power includes a factor  $r_e^2$  ( $8 \times 10^{-30} \text{ m}^2$ ) and so the scattering effect is very weak. Multimegawatt pulsed lasers (ruby or neodymium) are therefore needed. Stray laser light scattered in the apparatus and emission from the plasma are potential causes of large spurious signals and so great care has to be taken in the design of scattering systems to minimize these effects. Very efficient dispersing instruments, such as a set of tilted interference filters, and sensitive detectors, such as gated photomultipliers, are employed.

A multipulse Thomson scattering system is installed on the ASDEX tokamak. Light from a high repetition rate Nd:YAG (neodymium: yttrium aluminium garnet) 60 Hz laser with a 1064 nm wavelength passes vertically through the plasma as shown in Fig. 10.5.1. Sixteen separate three channel polychromators fitted with avalanche silicon photo-diodes

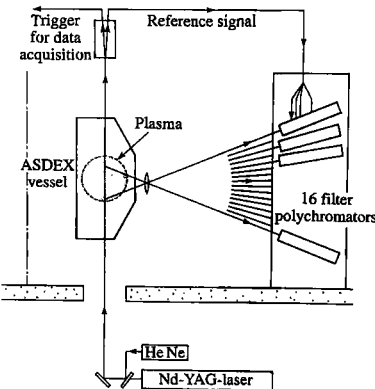


**Fig. 10.5.1** High repetition rate laser scattering system on the ASDEX tokamak. Light from the Nd-YAG laser is scattered by the plasma into one of the polychrometer detecting systems.  
 (Röhr, H., Steuer, K.-H., Murmann, H., and Metzsel, D. Proc. of High-Power Solid State Lasers and Applications, Ed. Ireland, C.L.M., SPIE 1277, 154 (1990).)

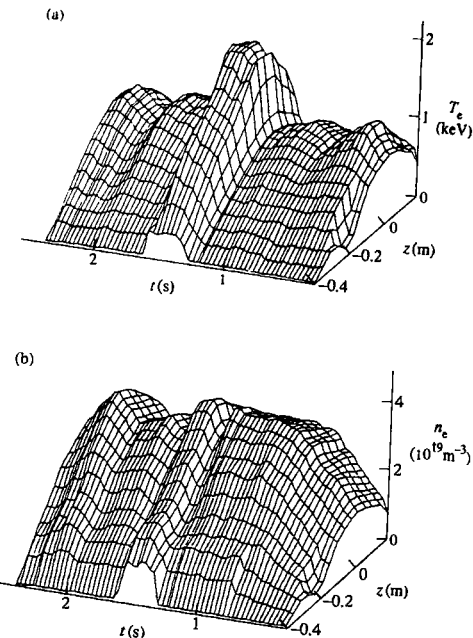
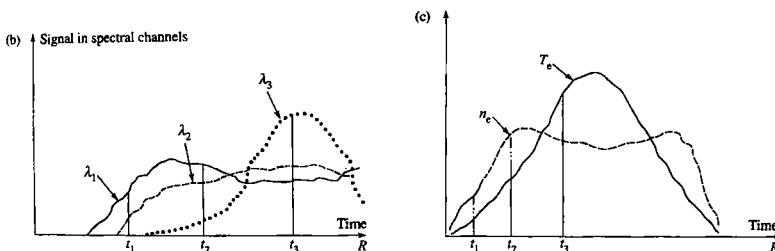
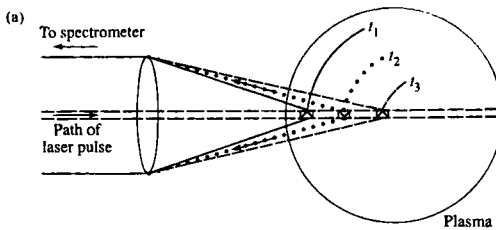


**Fig. 10.5.2** Three-dimensional plots of  $T_e$  and  $n_e$ , during an ASDEX discharge with neutral injection heating applied from 1.3 to 1.6 s.  $z$  is the vertical position coordinate. (Röhr, H., Steuer, K.-H., Murmann, H., and Meisel, D. *Proc. of High-Power Solid State Lasers and Applications*, Ed. Ireland, C.L.M., SPIE 1277, 154 (1990).)

spectrally analyse and detect the scattered radiation. Stray laser light is rejected with dielectric interference filters. The electron temperature and electron density are measured at 16 spatial points along the vertical chord, and the measurements are repeated every 17 ms during the duration of the plasma pulse. Typical results are shown in Fig. 10.5.2.

Another method of measuring the  $T_e$  and  $n_e$  profiles by Thomson scattering has been introduced. The LIDAR (Light Detection and Ranging) time-of-flight principle is used to obtain the spatially resolved information. The spectrum of the backscattered light, generated by a short laser pulse as it traverses the plasma, is recorded as a function of time by a fast detection and recording system. Analysis of the scattered spectrum at each time point yields  $T_e$  and  $n_e$  in the usual way. The position of the laser pulse within the plasma is known at each time point and so the spatial dependences of  $T_e$  and  $n_e$  are obtained. The principle of the technique is illustrated in Fig. 10.5.3.

**Fig. 10.5.3** (a) The principle of LIDAR is shown. The very short laser pulse successively illuminates different parts of the plasma at  $t_1$ ,  $t_2$ ,  $t_3$ . (b) The dispersed signals of the scattered radiation at three different wavelengths as a function of time, or, equivalently, major radius. (c) Electron density and temperature profiles deduced from the scattered spectra at different times. The considerable rise in  $n_e$  and  $T_e$  was a consequence of the 13.5 MW of additional heating which was applied at 6 s.



An operational LIDAR Thomson scattering system is installed on the JET tokamak. The ruby laser has a pulse energy of 3 J, a pulse duration of 300 ps and repetition rate of 0.5 Hz. The laser and all sensitive components of the detection system are located outside the concrete biological shield. The laser beam and the collected scattered light are passed in and out through a labyrinth penetration in the torus hall ceiling. In the torus hall the laser beam is directed towards the torus inner wall by a dielectric mirror mounted outside the torus. The backscattered light is collected by a folded spherical mirror system through an array of six windows surrounding the laser input window on the vessel. The light is spectrally resolved with a spectrometer which utilizes a stack of edge interference filters irradiated at slightly offset angles of incidence. The light is detected with a gated microchannel plate photo-multipliers and the signals are recorded with fast transient recorders with an 800 MHz bandwidth. The spatial resolution is determined by the combination of the laser pulse length with the detector response time and is  $\sim 10$  cm. This is considerably less than the 1.2 m minor radius of JET and so the  $T_e$  and  $n_e$  profiles are well resolved. Typical results are shown in Fig. 10.5.4.

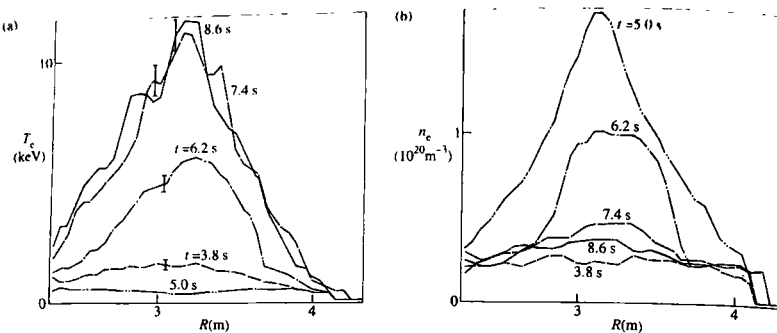


Fig. 10.5.4 Typical measurements of  $T_e$  and  $n_e$  at different times for a JET plasma.

### Electron cyclotron emission

In contrast to Thomson scattering, the measurement of electron cyclotron emission (ECE) is a passive technique. The electrons of a magnetically confined plasma gyrate around the field lines and as a consequence emit electromagnetic radiation. This radiation occurs at discrete angular frequencies  $\omega = n\omega_{ce}$ , where  $n$  is the harmonic number. Under some circumstances, the intensity of the emission is directly related to  $T_e$ .

In order to calculate the observed emission it is first necessary to calculate the emission per unit volume,  $j_n(\omega)$ , and then to take into account the transport of the radiation as it propagates through the plasma including, in particular, the effect of re-absorption.

One method of calculating  $j_n(\omega)$  begins with the equation of motion of an electron moving under the influence of the Lorentz force in a static magnetic field. Classical electrodynamics is then used to compute the coefficient of spontaneous emission for a single particle,  $\eta_n(\omega)$ . An integration over the electron velocity distribution then gives  $j_n(\omega)$ .

The calculation is extremely complicated in the general case. A wide range of electron energies and densities can be involved. The emission is broadened by collisions, particle motions, and relativistic changes in the electron mass, and it can be affected by the dielectric nature of the plasma. The electron velocity distribution need not necessarily be Maxwellian and the plasma will not generally be in complete thermodynamic equilibrium.

In present tokamak plasmas the electron temperatures are usually  $\lesssim 10\text{ keV}$ . The plasmas are usually observed at angles close to perpendicular to the confining magnetic field. The electron densities are  $\lesssim 10^{20}\text{ m}^{-3}$  so that the single particle emissivity is generally applicable. Under these conditions, and assuming a Maxwellian electron velocity distribution, the

emission is given by

$$j_n^i(\omega, \theta) = \frac{\pi}{2} \frac{\omega_{pe}^2}{c} \frac{n^{2n-1}}{(n-1)!} \left( \frac{T_e}{2m_e c^2} \right)^{n-1} I_B(\omega) (\sin \theta)^{2n-2} \\ \times (1 + \cos^2 \theta) \delta(\omega - n\omega_{ce}) F_i(n, \theta), \quad 10.5.1$$

where  $\omega_{pe}$  is the electron plasma frequency,  $\theta$  is the angle between the direction of emission and the confining magnetic field, and  $I_B(\omega)$  is the black-body radiation intensity.  $F_i(n, \theta)$  is a complicated function of  $n$  and  $\theta$ . The index  $i$  signifies that the function is different for the ordinary and the extraordinary modes.

Some characteristics of ECE are immediately obvious from eqn 10.5.1. The strength of the emission depends on  $\theta$  and, as stated above, it has a line spectrum. The relative intensities of the harmonics are independent of the electron density but are a strong function of the electron temperature. The emission is predominantly in the extraordinary mode (polarized emission) and the two modes have different angular dependences.

Transport and re-absorption of the radiation need to be taken into account using a model of the radiating medium. Usually, the classical model of a radiating plasma is employed. This shows that the radiation transport is governed by the equation

$$\mu^2 \frac{d}{ds} \left[ \frac{I(\omega)}{\mu^2} \right] = j(\omega) - \alpha(\omega) I(\omega), \quad 10.5.2$$

where  $I(\omega)$  is the radiation intensity,  $\alpha(\omega)$  is the absorption coefficient, and  $\mu$  is the refractive index. In a plasma in local thermodynamic equilibrium Kirchhoff's law gives a simple relationship between  $j(\omega)$  and  $\alpha(\omega)$

$$\frac{j(\omega)}{\mu^2 \alpha(\omega)} = I_B(\omega). \quad 10.5.3$$

For a homogeneous slab of plasma of thickness  $L$  eqn 10.5.2 can then be integrated using 10.5.3 to give

$$I(\omega) = I_B(\omega) [1 - e^{-\tau(\omega)}],$$

where

$$\tau(\omega) = - \int_L^0 \alpha(\omega) ds$$

is the optical depth. When  $\tau \ll 1$  the emitted radiation suffers negligible re-absorption and the plasma is said to be optically thin. When  $\tau \gtrsim 1$  substantial re-absorption occurs and  $I(\omega) = I_B(\omega)$ . Under this condition the radiation intensity is simply related to the plasma temperature and this forms the basis of the emission as a means of measuring  $T_e$ .

Tokamak plasmas have a spatially dependent magnetic field and this leads to the possibility of obtaining spatially resolved information from

a measurement of ECE. The main component of the magnetic field is the toroidal field,  $B_\phi$ . This field varies inversely with the major radius  $R$  and is constant along a vertical chord, that is

$$B_\phi(R) = \frac{B_0 R_0}{R},$$

where  $B_0$  and  $R_0$  are the values of  $B_\phi$  and  $R$  at the centre of the plasma. This spatially dependent magnetic field has a substantial effect on the character of the ECE. It means that for observation at right angles to the magnetic field and along  $R$ , there is a simple relationship between the frequency of the emitted radiation and the location of the point of emission,

$$\omega = \frac{n e B_0 R_0}{m_e R},$$

where  $n$  is the harmonic number. For tokamak plasmas, some of the emission lines are optically thick, some optically thin and some are intermediate. Because of the magnitude of the magnetic fields employed, ECE occurs at long wavelengths (typically millimetres) and at these wavelengths the Rayleigh-Jeans law applies. The intensity in an optically thick harmonic is therefore

$$I_n(\omega) = \frac{\omega^2 T_e(R)}{8\pi^3 c^2}$$

and so a measurement of the intensity of the emission in an optically thick harmonic gives  $T_e(R)$ . The optically thin harmonics give other diagnostic possibilities, for example the determination of the electron density profile  $n_e(R)$ .

In practice several effects can reduce the usefulness of the measurements: (i) the variation of the magnetic field across the plasma can be so large that two or more harmonics are resonant at the same frequency from different spatial locations (harmonic overlap), (ii) the current in the plasma generates a magnetic field which can be 10% or more of the toroidal field, (iii) finite density effects can prevent the radiation from propagating, and (iv) refraction can give uncertainty in the direction of view. The consequences of these effects can be quite substantial and have to be taken into account in any application of this diagnostic.

The magnetic fields used in present tokamaks are usually in the range  $2\text{ T} < B < 8\text{ T}$  and so the electron cyclotron emission occurs in the frequency range  $60\text{ GHz} < f < 600\text{ GHz}$  ( $5\text{ mm} > \lambda > 0.5\text{ mm}$ ). Four different instruments for measuring the emission have been developed: microwave heterodyne radiometers, Fourier transform spectrometers, Fabry-Perot interferometers, and diffraction grating spectrometers. These instruments have different characteristics. For example, the microwave heterodyne radiometers are very sensitive, have a high spectral resolving power and fast time-response, but current technology limits the application to frequencies below about 150 GHz. On the other hand,

Fourier transform spectrometers are well suited to measuring the whole spectrum of the emission at moderate time and frequency resolution. Present ECE systems usually incorporate more than one type of instrument and view the plasma along several different sightlines. The radiation is transmitted to the measurement instruments using either waveguides with dimensions much longer than the wavelength or with beams having a Gaussian shaped intensity pattern (quasi-optical beams).

An example of a modern system is that installed on JET. Radiation from the plasma is collected by antennas mounted in the vacuum vessel and transmitted to the torus hall with long ( $\sim 40$  m) oversized waveguide runs. There are ten different sightlines in the poloidal cross-section. The system incorporates all four types of measuring instrument and is calibrated by mounting large area calibration sources in the vacuum vessel.

Measurements of ECE are used routinely in the determination and assessment of plasma performance, and in studies of a wide range of plasma physics phenomena. The capability to measure  $T_e$  continuously in time with a time resolution  $\lesssim 10 \mu\text{s}$ , and localized in space with a spatial resolution of a few cm, makes measurements of ECE a powerful technique for the study of a range of phenomena including mhd oscillations, sawtooth activity, and ELMs. One important application is the measurement of the speed of outward propagation of the heat pulse following a sawtooth collapse from which the electron thermal conductivity is determined. Some measurements which illustrate the capability of the technique are shown in Fig. 10.5.5.

A comparison of the Thomson scattering and ECE measurements allows a check on the measurements. On some tokamaks, such comparisons are made automatically and routinely. An example is given in Fig. 10.5.6.

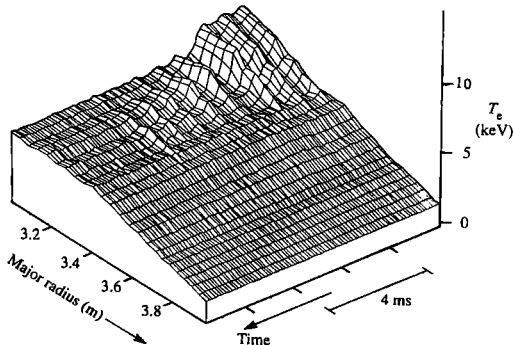


**Fig. 10.5.5** ECE measurement of electron temperature in JET as a function of time and radius. Mhd oscillations associated with a sawtooth crash give rise to variations of  $T_e$  which are clearly visible towards the plasma centre ( $R \sim 3.1$  m).

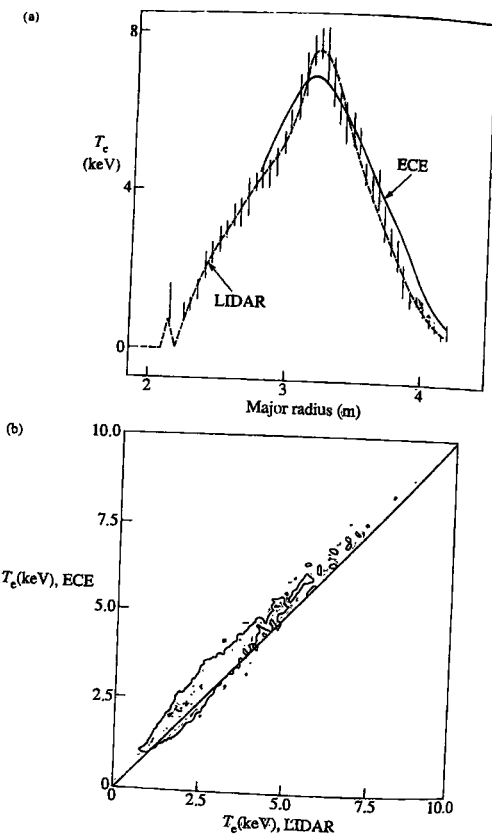


**Fig. 10.5.6** Comparison of  $T_e$  determined by ECE and LIDAR measurements. Good agreement is found for both (a) the profiles for a particular discharge and (b) the averaged central temperature for a wide range of different discharges. The contour shows the region within which 90% of the measurements lie.

## 10.6

### Ion temperature and the ion distribution function

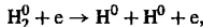
The ion temperature,  $T_i$ , and the ion distribution function are important plasma quantities. Often  $T_i \neq T_e$  because the ion-electron equilibration

time is comparable with or longer than the ion energy confinement time. Ion distribution functions in additionally heated discharges generally depart from a Maxwellian distribution. In small and medium size tokamaks, neutral particle detectors have been used to measure both the thermal and non-thermal parts of the ion distribution function, but in the larger tokamaks these measurements become much less useful because neutrals produced at the plasma centre are absorbed before reaching the plasma periphery. In D and DT plasmas, the ion temperature and some features of the distribution functions are also determined from neutron and gamma-ray measurements. In tokamaks with neutral beams,  $T_i$  is now generally determined from the Doppler broadening of line radiation observed in charge exchange spectroscopy.

### Neutral particle production

The ion temperature in a hydrogen plasma can be measured by analysing the energy distribution of charge-exchanged fast neutrals escaping from the plasma. The method depends on the existence in the plasma of a low density of neutral atoms. A brief outline will be given of their origin and transport within the plasma. The neutrals arise from atoms or molecules released by the walls of the vessel. Recombination of electrons and ions within the plasma can also form neutrals but this mechanism is of less importance except at very high plasma densities and at the centre of large plasmas.

At the plasma edge, many processes can contribute to the production of neutral hydrogen atoms. One process leading to neutral atom production is dissociation by electrons of hydrogen molecules released from the wall



where the neutral atoms formed will have an energy of at least a few eV. Some of these neutrals will immediately escape from the plasma, but others will undergo further charge-exchange reactions with plasma ions, in each case producing a new neutral atom. These secondary neutrals will either escape from the plasma or undergo a further charge exchange reaction, with the process continuing until the secondary neutral becomes ionized or escapes. At low neutral energies, charge exchange is much more probable than ionization, thus allowing several generations of neutrals. By this means a low density of hydrogen atoms can penetrate to the centre of the tokamak plasma. Monte Carlo calculations are used to model the radial distribution of the neutral density,  $n_0$ , which is typically many orders of magnitude less at the plasma centre compared with the edge.

The neutral density gives rise to a flux of neutral energetic plasma particles escaping from the plasma. The source function for the escaping flux is

$$S(v_i) = n_i n_0 f_i(v_i) \int \sigma_{01} |v_i - v_0| f_0(v_0) d^3 v_0,$$

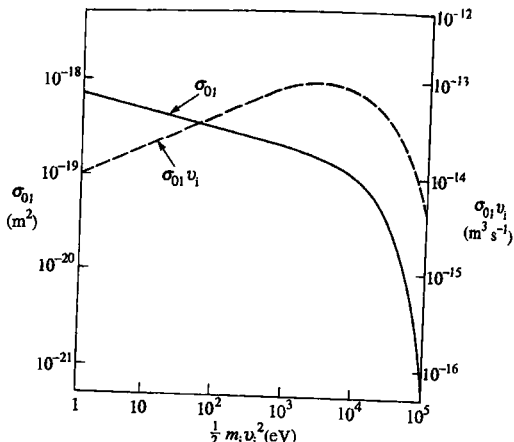


**Fig. 10.6.1** Charge-exchange cross-section  $\sigma_{01}$  and  $\sigma_{01}v_i$  for  $H^0 + H^+$ .

where  $\sigma_{01}$  is the charge-exchange cross-section and  $f_i$  and  $f_0$  are the velocity distribution functions of the ions and neutrals.  $S$  can be written in terms of the averaged charge exchange rate as

$$S(v_i) = n_i n_0 (\sigma_{01} v_i) f_i(v_i). \quad 10.6.1$$

As can be seen from Fig. 10.6.1, neither  $\sigma_{01}$  nor  $\sigma_{01}|v_i - v_0|$  vary rapidly with neutral velocity over the range of interest in typical tokamaks and  $S$  is consequently approximately proportional to  $f_i(v_i)$ . Analysis of the source function,  $S$ , gives the ion distribution function and in particular allows the determination of  $T_i$ , as discussed below.

### $T_i$ from neutral particle analysis

For a Maxwellian plasma the source function for the distribution of the escaping flux is, from eqn 10.6.1,

$$S(E_0) = n_0 n_i (\sigma_{01} v_i) \frac{2E_0^{1/2}}{\pi^{1/2} T_i^{3/2}} e^{-E_0/T_i},$$

where  $E_0$  is the energy of the neutrals. A measurement of the intensity of  $S(E_0)$  as a function of energy will therefore determine  $T_i$  and  $n_0$  assuming a knowledge of  $n_i$ . In practice, the integral of  $S(E_0)$  along the line of sight of the detection system will be measured.

If the flux of escaping particles is to give a correct value of  $T_i$  it is important that the mean free path of the neutrals is much greater than the

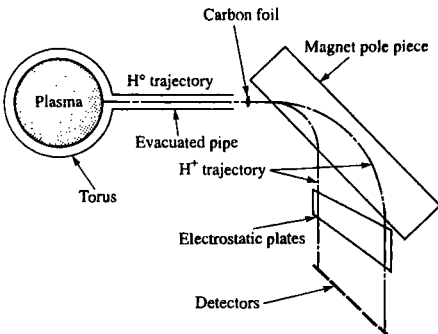


**Fig. 10.6.2** Schematic diagram of neutral particle analyser with  $E \parallel B$  (Corti, S. p. 477, *Diagnostics for contemporary fusion experiments* (Eds Stott, P.E., et al.), Editrice Compositori, Bologna (1991)).

plasma minor radius,  $a$ . That is

$$\frac{1}{n_1 \sigma_{01}} > a.$$

This condition is most likely to be satisfied at higher energies because  $\sigma_{01}$  decreases with energy.

Typical detection systems for measuring the neutral flux will contain a gas stripping cell or thin carbon foil to ionize the incident neutrals and a combination of electrostatic and magnetic fields to determine the particle's energy and momentum, and hence its mass. In some systems the neutrals are electrostatically analysed and then their velocity is measured using the time of flight for the ions to pass from the carbon foil to the detector. The efficiency of these systems depends on their geometry and the efficiency of their stripping cells and detectors. It is usual to measure this efficiency with a neutral beam of known intensity.

The instrument shown in Fig. 10.6.2 is designed for measuring high energy neutrals produced in neutral injection heating experiments. The neutral particles are ionized by a carbon foil and then deflected by magnetic and electric fields, both perpendicular to the plane of the figure, with detection in an array of channeltron electron multipliers.

Neutral particle detectors usually view the plasma along a nearly radial line-of sight and thus provide line-of-sight average values of  $T_i$  and  $n_0$ . In some experiments this limitation has been overcome by using a neutral diagnostic beam perpendicular to the line-of-sight to enhance the neutral density at a chosen point along the line-of-sight of the analyser. This then provides a spatially localized measurement of  $T_i$ . In other experiments, arrays of analysers are used to make direct measurements of the profile of neutral particle emission and local values of  $T_i$  and  $n_0$  are obtained by an inversion procedure.

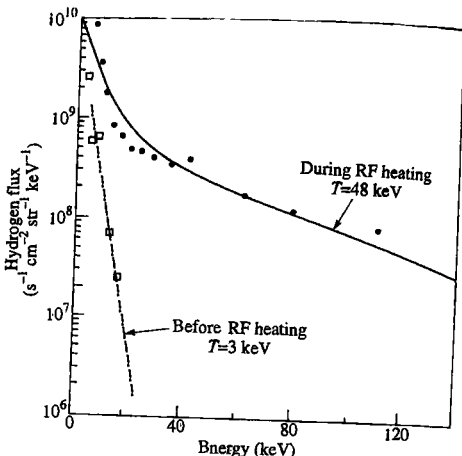


**Fig. 10.6.3** Measured neutral hydrogen flux as a function of energy in an experiment with RF heating. (Bhatnagar, V.P. et al., *Nuclear Fusion*, 33, 83 (1993).)

Typical results from JET are shown in Fig. 10.6.3 for an experiment in which ICRH heating power of 6.5 MW was applied to the plasma. Before application of the ICRH the gradient of the energy spectrum gave  $T_i = 3.0 \text{ keV}$ . With heating, the distribution function develops a high energy tail which is characterized by an effective temperature of 48 keV. The solid line gives a calculated hydrogen flux from a model of the ICRH heating process, showing reasonable agreement with the experiment.

#### $T_i$ from neutron emission

In plasmas containing D, T, or  $\text{He}^3$ , nuclear reactions will occur if the ion temperature is sufficiently high. The most important reactions, several of which produce neutrons, are listed below

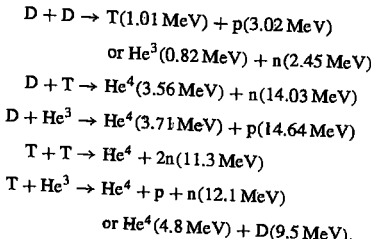


Figure 1.3.3 shows some of these reaction rates which are all strongly dependent on the particle energy. For ions species 1 and 2 described by Maxwellian distribution functions the reaction rate per unit volume is given by

$$R = 4\pi \delta_{12} n_1 n_2 \int f(\mu v^2/2, T_i) v^3 \sigma(v) dv = \gamma n_1 n_2 \langle \sigma v \rangle, \quad 10.6.2$$

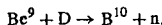
where  $\sigma$  is the nuclear reaction cross-section,  $f$  is the Maxwellian distribution function,  $\mu$  is the reduced mass  $\mu = m_1 m_2 / (m_1 + m_2)$ , and  $\delta_{12}$  is 1/2 when species 1 and 2 are the same and otherwise 1. Because the averaged reaction rate  $\langle \sigma v \rangle$  has a strong dependence upon  $T_i$  an experimental evaluation of  $R$  by measuring the number of neutrons produced allows  $T_i$  to be determined provided  $n_1$  and  $n_2$  are known.

In the integrand of eqn 10.6.2,  $f$  falls rapidly with increasing  $v$  while  $\sigma$  increases with  $v$ . The integral therefore has appreciable contributions only from a range of values of  $v$  in the tail of the distribution function. Most of the neutron producing reactions will occur at the most effective energy for fusion reactions given by

$$E_i = 6.3(Z_1 Z_2 A_\mu T_i^2)^{1/3} \text{ keV}, \quad T_i \text{ in keV},$$

where  $A_\mu$  is the reduced atomic mass of the ions and  $Z_1$  and  $Z_2$  their atomic numbers. Generally  $E_i > T_i$  and this can lead to serious problems in the interpretation of neutral yield measurements if there is any distortion of the distribution function away from a Maxwellian, particularly at low  $T_i$ .

Some caution is required in the interpretation of the measurements on neutrons as they can also be produced by non-thermonuclear reactions between high energy injected or accelerated ions and the plasma ions. In plasmas containing low  $Z$  ions, for example beryllium, nuclear reactions between these and ions accelerated by RF heating to MeV energies can also produce a substantial number of neutrons. A typical reaction is



In some discharges large currents of runaway electrons are generated which produce a copious number of neutrons when they interact with the vessel walls. These neutrons are produced in a two stage process: the energetic electrons produce high energy  $\gamma$ -radiation by bremsstrahlung interactions in the vessel walls and the neutrons are then produced following  $(\gamma, n)$  reactions with the surrounding materials.

The energy distribution of the thermonuclear neutrons is

$$F(E) = \exp - \left( \frac{E - \bar{E}}{\Delta E} \right)^2,$$

where  $E$  is the neutron energy and  $\bar{E}$  is the mean energy of the neutrons. The distribution function consists of a single sharp peak broadened by an

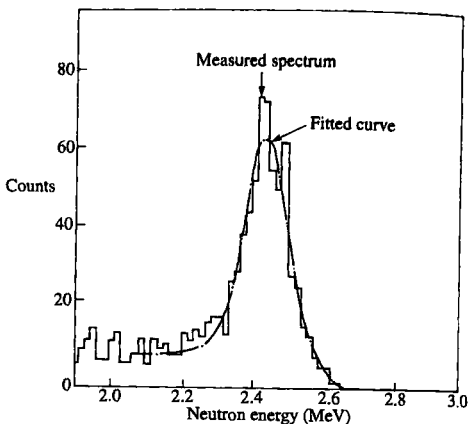


Fig. 10.6.4 Pulse height spectrum as a function of neutron energy taken with a  $\text{He}^3$  neutron spectrometer. (Jarvis, O.N. et al., *Review of Scientific Instruments* 57, 1717 (1986).)

amount which depends on  $T_i$  with a  $1/e$  half-width of

$$\Delta E = 2 \left( \frac{m_n T_i \bar{E}}{m_n + m_i} \right)^{1/2},$$

where  $m_n$  and  $m_i$  are the masses of the neutron and other reacting particle. For the D-D reaction with  $T_i = 10 \text{ keV}$  the  $1/e$  full width is  $314 \text{ keV}$ . The measurement of this width is experimentally quite difficult and detector systems with very high resolving power are required. Both time of flight systems and  $\text{He}^3$  recoil neutron spectrometers have been employed. In Fig. 10.6.4 an energy spectrum is shown taken during a series of ohmically heated discharges in JET with a  $\text{He}^3$  spectrometer having a resolution of  $44 \text{ keV}$ . An ion temperature of  $2.2 \text{ keV}$  was deduced from an analysis of the width of the peak.

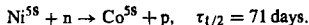
A wide variety of detectors can be used for measuring neutron yields. On large tokamaks  $\text{U}^{235}$  and  $\text{U}^{238}$  fusion chambers embedded into hydrogenous moderating material are suitable for the very high neutron fluxes encountered. Good time resolution is obtained with solid state detectors even though these have a low efficiency. In order to interpret the yield measurements, substantial corrections to the data are required to allow for the effects of absorption and scattering from the transformer core, the field coils and other mechanical structures. Alternatively the detectors can be calibrated by placing a neutron emitting source at different toroidal positions within the torus and measuring the count rate in the detectors.

Use is also made of activation techniques which deduce the integrated neutron yield from measurements of the total radioactivity induced in

one discharge via reactions induced by the neutrons. Reactions leading to nuclei with appropriate decay times must be selected and typical examples are



or



The yield of the decay of the 0.333 MeV isomeric state or of the  $\beta$ -decay of the  $\text{Co}^{58}$  then determines the incident neutron fluxes. Interpretation of these results requires neutron transport calculations to establish the relationship between the total yield and the local neutron flux. Results of a neutron yield measurement are shown in Fig. 10.6.5. The data was taken during a JET experiment in which tritium was introduced into the deuterium plasma by one of the neutral injection systems. The yield of 14 MeV neutrons was determined with a silicon solid state detector and the results show good agreement with the results of a plasma transport model which included reactions induced directly by the beam ions as well as the thermonuclear reactions.

In some experiments collimated neutron detectors have been used to determine emissivity profiles. Because of the long mean free path of neutrons in matter the collimators have very considerable dimensions and weight.

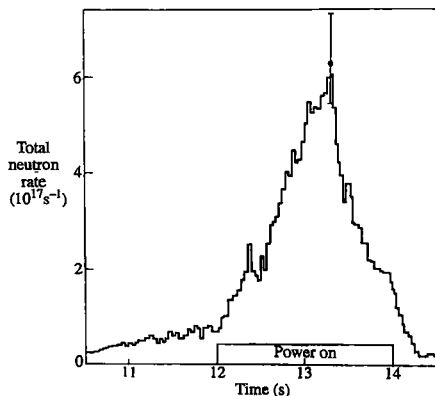


Fig. 10.6.5 Measured total 14 MeV neutron rate in a D-T plasma with neutral beam heating. The full power was turned on at 12 s and off at 14 s. (JET team. Nuclear Fusion 32, 1s7 (1992).)

### $T_i$ from charge exchange spectroscopy

Many interesting diagnostic opportunities are provided by the injection into a tokamak plasma of neutral beams, usually hydrogen or deuterium, with particle energies of tens to hundreds of kiloelectronvolt (keV). As these penetrate the plasma, radiation is produced as a result of excitation of the beam, and also following charge exchange reactions between the beam neutrals and plasma ions. If this radiation is observed at an angle to the beam, localized measurements of plasma parameters can be made. These measurements have been particularly exploited with observations in the visible region of the spectrum because of the simplicity and versatility of the instrumentation at these wavelengths.

In a typical experimental set up, as illustrated in Fig. 10.6.6, a neutral beam is injected across the lines of sight of the optical system of the viewing spectrometer. The collected light is often removed from the immediate vicinity of the tokamak by optical fibres to spectrometers outside the radiation wall. This has advantages of easy access to the experimental equipment. The spectrometers are generally equipped with charged coupled devices to record the dispersed spectra.

The determination of the plasma ion temperature depends on the emission of radiation following a charge exchange reaction. A typical reaction

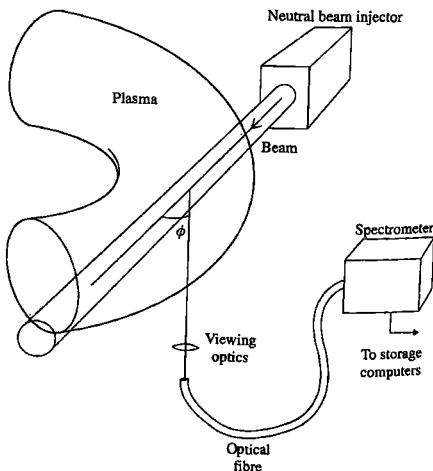


Fig. 10.6.6 Schematic diagram showing the geometry of the injected neutral beam, the plasma, the viewing optics and the spectrometer.

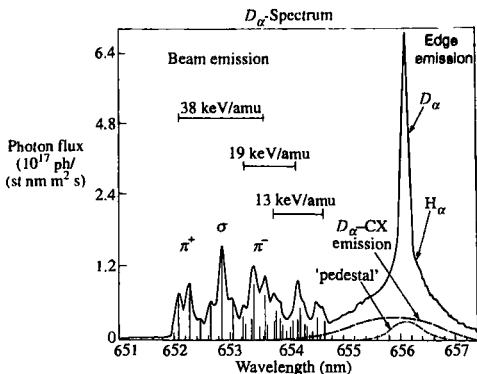


Fig. 10.6.7 Spectrum near the deuterium Balmer-alpha line during beam injection.  $T_i$  is found from the broadened feature at about 656 nm. The features at shorter wavelengths are Doppler shifted from the beam. (Wolf, R., et al., *Nuclear Fusion* 33, 1835 (1993).)

of interest is



where the plasma ion  $X$  was in charge state  $s+$  before the exchange. After the reaction, the electron received by the plasma ion may be in a state with a high principal quantum number and will decay with the emission of visible radiation. The plasma ion  $X^{(s-1)+}$  may also radiate following subsequent excitation by plasma particles. A typical spectrum following charge exchange between the deuterium beam and deuterium ions is given in Fig. 10.6.7. It shows an unshifted Balmer-alpha line that has contributions both from the charge exchange reaction and from cold edge neutrals. The spectrum also shows features corresponding to excitation of the incident beam, but these are Doppler shifted well away from the thermal features. The ion temperature can be extracted from function fitting to the Doppler broadened line at about 656 nm after taking into account the narrow contribution to this feature from the edge neutrals. This determination of  $T_i$  has become the main diagnostic for ion temperature profiles in many tokamak experiments.

## 10.7

### Radiation from plasmas

Tokamak plasmas nearly always contain significant concentrations of impurity ions in addition to hydrogen and helium ions. The impurities

originate from the torus wall, the limiter, or from the dump-plates of an X-point or divertor configuration. Typical impurities are beryllium, carbon and oxygen with low  $Z$ , and iron and nickel with high  $Z$ . This distinction in  $Z$  is made because at the plasma centre the low  $Z$  ions are fully ionized whereas the high  $Z$  ions are usually not quite fully ionized even in very high temperature tokamak plasmas. Towards the plasma edge all the ions are in low states of ionization. The interest in impurities arises from their role in the overall plasma energy balance, since a significant fraction of the input energy is often lost through radiation processes. The impurities also dilute the hydrogen plasma. The study of the radiation from these ions can often also produce valuable information both about the atomic physics of the ions and about processes within the plasma. An outline will be given of the factors which contribute to the ionization balance in the plasma and the mechanisms leading to the production of both line and continuous radiation.

### **Ionization states**

The ions and electrons in a tokamak plasma are not in a thermal equilibrium with a balance between a radiation field and the particle energies. The plasma is transparent to the radiation and, at the densities which generally prevail in tokamaks, the ionization balance is similar to that encountered in the solar corona where a balance is established between ionization and recombination processes. Ionization from state  $Z - 1$  to  $Z$  can take place by direct electron impact, and the ions can recombine by radiative processes. Dielectronic recombination is also an important process for complex ions and occurs in two stages. First, an electron is captured into an excited state together with simultaneous excitation of the ion. Secondly, this configuration can then either lose the electron by autoionization or be stabilized by the emission of a photon which then makes it energetically impossible for an electron to escape and this completes the recombination processes.

As all processes are proportional to the electron density, the equilibrium distribution among the ionization states is independent of  $n_e$  and, for a steady state the impurity charge state densities are given by

$$\frac{n_{z-1}}{n_z} = \frac{\alpha_z}{S_{z-1}},$$

where  $\alpha_z$  and  $S_{z-1}$  are the recombination and ionization rates respectively. Typical values of these rates are shown in Fig. 10.7.1 for hydrogen and the hydrogenic states of beryllium and oxygen. The  $S$  and  $\alpha$  values may be used to determine the relative concentrations,  $f_z$ , of different ionization states as a function of electron temperature. Graphs of  $f_z(T_e)$  for oxygen are shown in Fig. 10.7.2. A tokamak plasma can have strong gradients of  $T_e$  in its outer regions and the impurity density of a particular charge state,  $n_z$ , therefore changes rapidly with minor radius leading to a series of concentric shells each with a different predominant ionization state.

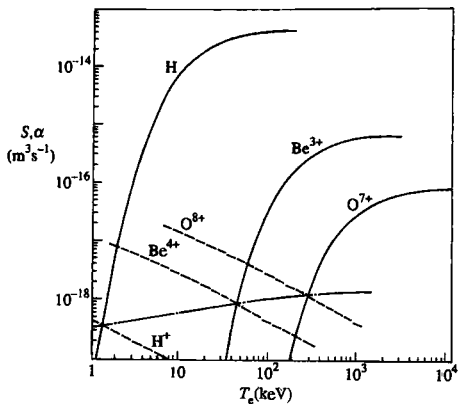


Fig. 10.7.1 The ionization ( $S$ , full line) and recombination ( $\alpha$ , dotted line) coefficients are shown for hydrogen and the hydrogenic states of beryllium and oxygen. The dot-dash line joins the points at which  $S = \alpha$ .

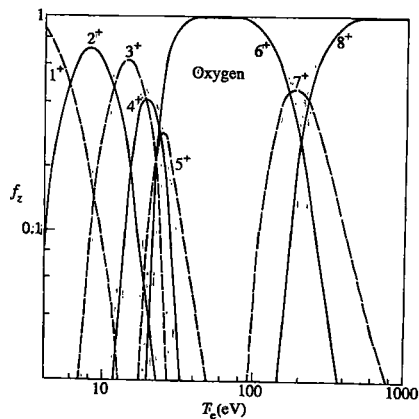


Fig. 10.7.2 The relative concentrations of the different ionization stages,  $f_z$ , are shown as a function of electron temperature.

Each shell appears where  $T_e$  is approximately one-third of the ionization energy.

This simplified situation is modified if the effects of ion diffusion are included. The ionization balance in cylindrical geometry is then governed

by the equation

$$\frac{\partial n_z}{\partial t} + \frac{1}{r} \frac{\partial}{\partial r} (r \Gamma_z) = -n_z n_e S_z + n_{z-1} n_e S_{z-1} + n_{z+1} n_e \alpha_{z+1} - n_z n_e \alpha_z, \quad (10.7.1)$$

where the radial ion fluxes,  $\Gamma_z$ , are driven by both diffusion and convection.

$$\Gamma_z = -D \frac{\partial n_z}{\partial r} - n_z v,$$

where the second term on the right describes an inward pinch characterized by velocity,  $v$ . It is found from experiment that the diffusion coefficients are anomalously large and that typically  $v$  is between 1 and  $10 \text{ m s}^{-1}$  for all ions. The largest modifications to the radial distribution of the ionization states caused by diffusion and convection are in the outer regions of the plasma.

### Production of radiation

Many processes contribute to the production of radiation in a plasma and if it is magnetized, synchrotron radiation is also emitted as discussed briefly in Section 10.5. Line radiation arises from excitation by electron impact followed by the radiative decay of the excited state and also from de-excitation following radiative or dielectronic recombination of plasma electrons with ions. Line radiation can represent a major source of energy loss from the plasma and offers an important method of identification of the impurities from the characteristic wavelengths of the radiation.

Continuum radiation arises from electron-ion collisions, which produce bremsstrahlung, and also from recombination. The recombination radiation spectrum is continuous above a threshold energy corresponding to the binding energy of the captured electron. Measurements of the continuous radiation spectrum are chiefly used to determine the plasma electron temperature and effective charge  $Z_{\text{eff}} = \sum n_z Z^2 / \sum n_z Z$  with the summation running over all charge states of all ion species.

The line excitation rate averaged over a Maxwellian distribution of electrons for a transition in an ion from state  $m$  to state  $n$  requiring energy  $E_{nm}$  (eV) is given by

$$X_{mn} = 5 \times 10^{-16} f_{nm} \bar{g}_{nm} \frac{1}{E_{nm} T_e^{1/2}} \exp(-E_{nm}/T_e) \quad \text{m}^3 \text{s}^{-1},$$

$E_{nm}, T_e$  in keV.

where  $f_{nm}$  is the oscillation strength and  $\bar{g}_{nm}$  is the averaged Gaunt factor. Radiative excitation of dipole transitions from the ground state produces the most intense radiation seen from plasmas.

Radiative recombination occurs when an ion with charge  $Z$  combines with an electron to produce a lower ionization state ( $Z - 1$ ) with the excess energy of the electron radiated by quanta which will have a continuous energy spectrum. The ion with charge ( $Z - 1$ ) will often be left in an excited state and this can decay by the emission of one or more quanta with discrete energy. Dielectronic recombination processes are also important.

The calculation of the impurity-ion recombination radiation is complicated as a detailed knowledge of the atomic structure of the impurity ions is required. These calculations have often been carried out using a very much simplified hydrogenic model for the impurity ions. Recombination with an ion with  $\xi$  vacancies in its lowest  $n$ -shell will give rise to a continuous spectrum

$$\frac{dN}{dE_\nu} = 3 \times 10^{-21} Z^2 n_e n_z \frac{\bar{g}_{fb} e^{-E_\nu/T_e}}{E_\nu \sqrt{T_e}} F(\xi, n, T_e) \text{ m}^{-3} \text{ s}^{-1} \text{ keV}^{-1},$$

$$= n_e n_z Z^2 \bar{g}_{fb} P_b F(\xi, n, T_e) \quad E_\nu, T_e \text{ in keV},$$

where  $N$  is the number of quanta of radiation of energy  $E_\nu$  and  $P_b = 3 \times 10^{-21} \exp(-E_\nu/T_e)/E_\nu \sqrt{T_e}$   $\text{m}^3 \text{ s}^{-1} \text{ keV}^{-1}$ . The temperature averaged Gaunt factor,  $\bar{g}_{fb}$ , is of order of unity and the function  $F$  depends upon the atomic structure of the ion and the electron temperature. The temperature dependence of  $F$  is such that at very high temperatures radiative recombination becomes unimportant compared with bremsstrahlung.

Continuum radiation can also be produced by electron-ion collisions where the incident electron with energy  $E_e$  loses part of its energy by the emission of an electromagnetic quantum via the bremsstrahlung radiation process. The energy spectrum of this process is continuous up to  $E_e$  and for collisions between electrons and ions with charge  $Z$  in a Maxwellian plasma is given by

$$\frac{dN}{dE_\nu} = n_e n_z \bar{g}_{ff}^2 P_b \text{ m}^{-3} \text{ s}^{-1} \text{ keV}^{-1}, \quad E_\nu, T_e \text{ in keV},$$

where the averaged Gaunt factor,  $\bar{g}_{ff}^2$ , is of order of magnitude unity.

#### Total radiated power

The total radiated power from a low density plasma may be found by adding and integrating the radiation from the various processes above. Because all the processes involved depend on the product  $n_e n_z$  it is possible to write the total radiated power for a single impurity species as

$$P_R = \sum n_e n_z f(Z, T_e) = n_e n_I \sum \frac{n_z}{n_I} (Z, T_e) = n_e n_I R(T_e),$$

where  $n_I = \sum n_z$  and the summations run over all the ionization stages. These have relative concentrations of  $n_z/n_I$  which are dependent only

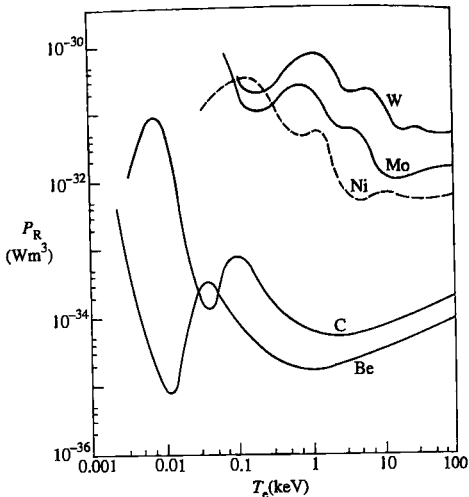


**Fig. 10.7.3** The total radiated power function,  $R$ , is shown as a function of temperature for various elements.

on  $T_e$ . Extensive tabulations of  $P_R$  are available for various impurity ions. In Fig. 10.7.3 data is given for a number of low  $Z$  and high  $Z$  impurities and it can be seen that the high  $Z$  impurities are much more efficient radiators for a given impurity level than the low  $Z$  impurities. It is because of this that especial efforts are made to exclude high  $Z$  ions from tokamak plasmas.

### Measurements of radiation

Because there is an electron temperature gradient in a tokamak, from edge values of a few eV to central values of keV, both line and continuum radiation are emitted over a wide spectral range. At the plasma edge, visible radiation is emitted, and at the plasma centre mainly UV and X-rays. There is a correlation between the plasma temperature, the radiation wavelength and the position of origin of the radiation, and this allows the designation of three principle regions of the plasma. This distinction is useful as the wide spread of wavelengths leads to the requirement of very different instruments to make an experimental investigation of the emitted radiation.

- (a) *Edge region and visible spectroscopy* Here  $T_e$  is small, atoms are neutral or in states of low ionization, and the radiation is emitted mainly in line radiation which can be observed with visible light spectrometers or monochromators. In the visible region it is easy

to make measurements as a wide range of instruments is available, often using ruled gratings as dispersing elements and solid state or photomultiplier tubes as detectors. In addition, pinhole cameras have been used with interference filters to isolate lines of particular interest. The aim of much of this work is to determine impurity influxes and, in particular, the particle confinement time from the  $H_\alpha$  line intensity. High resolution measurements can be used to measure the isotopic content of the plasma, and its impurity content is often determined from the intensity of the visible continuum radiation. Because visible lines are emitted primarily from ions with low ionization these lines are often used to monitor impurity changes in the plasma edge and the interactions between the plasma edge and the limiters and divertor plates.

Examples of visible spectroscopic measurements will be given for the determination of the particle confinement time and the plasma effective charge. The various parameters which can be found from charge-exchange measurements will also be discussed.

- (i) The hydrogen particle confinement time can be found from the  $H_\alpha$  line intensity and a knowledge of excitation and ionization rates. This measurement is standard on all tokamaks. Equation 10.7.1 can be integrated and, assuming that the recombination rate is much less than the ionization rate at the plasma edge, the flux of hydrogen ions at the plasma radius,  $a$ , is given by

$$a\Gamma = \int_0^a S_0 n_e n_{\text{nor}} \, dr.$$

The line of sight integrated intensity of the  $H_\alpha$  line is

$$I_\alpha = \int_{-a}^{+a} n_0 n_e X B \, dr,$$

where  $X$  is the excitation rate and  $B$  is the branching ratio for the de-excitation. The neutral density is appreciable only at the plasma edge and the ratio  $S_0/XB$  is only weakly dependent on temperature and electron density. Both integrals above are then proportional to  $\int_0^a S_0 n_e n_{\text{nor}} \, dr$  and this allows the approximate evaluation of their ratio. The particle confinement time,  $\tau_p$ , is then given by

$$4\pi^2 a R \Gamma = \frac{N_e}{\tau_p} = 2\pi^2 a R \frac{S_0 I_\alpha}{XB},$$

where  $N_e$  is the total number of electrons, and  $R$  and  $a$  are the major and minor radius of the plasma.

- (ii) Bremsstrahlung radiation is emitted in the visible region due to electron-ion collisions. Its intensity at wavelength  $\lambda (\gg hc/T_e)$

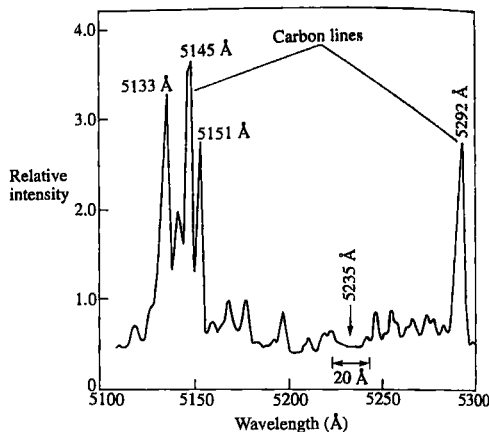


**Fig. 10.7.4** Visible spectrum from the JIPP T-IIU tokamak which shows the region of the spectrum, well clear of prominent lines, which is used to determine  $Z_{\text{eff}}$ . [Ida, K., et al., *Nuclear Fusion* **30**, 665 (1990).]

is given by

$$\frac{dN}{d\lambda} = 3 \times 10^{-21} \bar{g} n_e^2 Z_{\text{eff}} \frac{m^{-3} s^{-1} nm^{-1}}{\lambda \sqrt{T_e}}, \quad T_e \text{ in keV},$$

where  $\bar{g}$  is the temperature averaged Gaunt factor and  $\lambda$  is in nm. Line of sight integrals of this intensity must be measured over the full plasma cross-section for a determination of the  $Z_{\text{eff}}$  profile. In addition, the plasma temperature and density must also be known. One difficulty of the method is to find a region of the visible spectrum unaffected by impurity line radiation. Figure 10.7.4 shows the spectral region used on the JIPP T-IIU tokamak which is selected with a 20 Å interference filter at 5235 Å.

- (iii) Line emission occurs in the visible region following charge exchange reactions between plasma ions or highly ionized impurity ions, and diagnostic or heating beams with energies of 20–200 keV as described in Section 10.6. A typical reaction used for charge exchange recombination spectroscopy is



The cross-sections for these reactions are very large but are often obtained from calculations as the necessary measurements have not been made. The  $O^{5+}$  ions are formed in states with high principal quantum number which radiate in the visible region when they decay. If the line of sight of the viewing optics is orthogonal to the beam then a spatially resolved measurement is

obtained. The ion temperature and plasma rotation velocity can be found from the Doppler broadening and shift of the observed lines. The intensity of the light also determines the impurity density if the attenuation of the beam within the plasma can be accurately calculated.

- (b) *Intermediate region* Here the temperature is higher, tens to hundreds of eV, and the radiation is emitted in the UV to soft X-ray region typically from nearly fully ionized hydrogen or helium ions, and partially ionized higher atomic number atoms. Low Z impurities such as carbon or oxygen may be partly or fully ionized, depending on the temperature.

At the longer wavelengths, materials such as quartz are still transparent to the radiation and instruments similar to those for the visible region can be used. At shorter wavelengths the radiation is strongly absorbed by air. It is necessary therefore to use vacuum paths for the radiation, reflecting gratings for dispersion, and windowless photomultipliers, scintillators or channel plates as detectors.

The purpose of these measurements is generally to determine the plasma impurity composition and to assess the effects of impurity transport by studying departures of the distribution of the different impurity ionization states from a coronal equilibrium. As all the measurements are line-of-sight integrals, it is generally necessary to make spatial scans of the spectra over the plasma cross-section and invert the data.

A typical spectrum from JT60 (Fig. 10.7.5) shows a multitude of lines, mainly from carbon and oxygen impurities, from which impurity concentrations were found.

- (c) *Plasma centre* Here, all atoms except those with very high Z are fully ionized and the radiation is predominantly at X-ray wavelengths. High resolution crystal spectrometers relying on Bragg reflection are used to determine concentrations from line intensities. The Doppler broadening and shifting of these lines are used to determine ion temperatures and plasma rotation velocities.

The continuous radiation spectrum is also measured in the X-ray region where there are contributions both from bremsstrahlung and recombination radiation. The energy spectrum is given by

$$\frac{dN}{dE_\nu} = n_e^2 \zeta P_b \text{ m}^{-3} \text{ s}^{-1} \text{ keV}^{-1}, \quad E_\nu, T_e \text{ in keV},$$

where  $\zeta$  is the X-ray anomaly factor which is dependent on the impurity concentration of the plasma. This factor approximately represents the enhancement of the emission above that for a pure hydrogen plasma. X-ray measurements of this spectrum are generally made with a Si(Li) or Ge crystal cooled to liquid nitrogen temperature. The detector measures the energy of individual quanta with 100% detection efficiency. A typical energy spectrum taken on JT60 (Fig. 10.7.6) shows the continuous spectrum at high energies and prominent K lines at lower energy from almost fully stripped titanium and nickel.

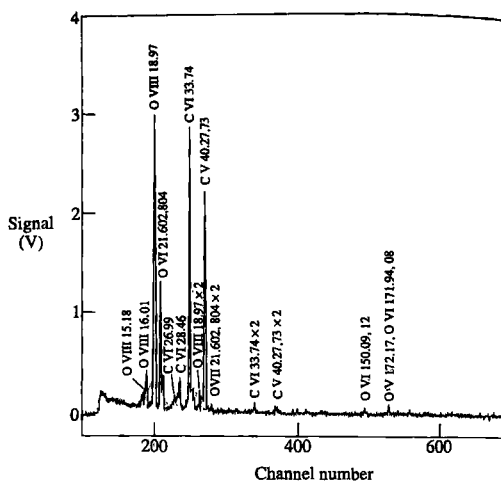


**Fig. 10.7.5** UV spectrum in the 5–500 Å region taken on JT60 with a multichannel spectrometer during a discharge with 19 MW of beam heating. (Kubo, H., et al. *Nuclear Fusion* 29, 571 (1989).)

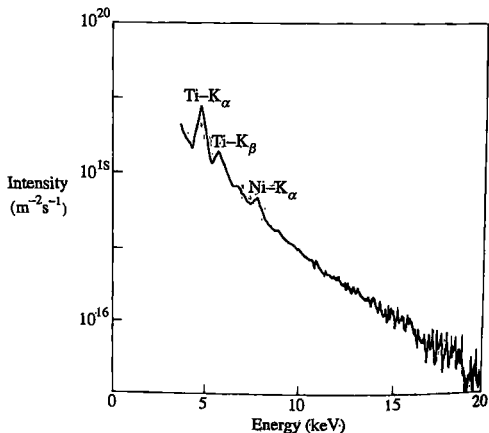


**Fig. 10.7.6** X-ray pulse height spectrum for an ohmically heated discharge in JT60. (Kubo, H., et al. *Nuclear Fusion* 29, 571 (1989).)

The absolute magnitude of the spectrum determines  $\zeta$ , and  $T_e$  can be found from the gradient of the line free part of the spectrum. The K line intensity can be used to identify and measure the concentration of the impurity ions.

## 10.8

### Total radiation measurements

#### Bolometry

A measurement of the total radiation emitted from the plasma is important for evaluation of the energy balance. These measurements have been made with a wide variety of different sensors including thermistors, thermopiles, pyroelectric detectors and thin film bolometers. The sensors are often arranged in one or more pinhole camera configurations with a complete view of the plasma cross-section as shown in Fig. 10.8.1. As the observed signals are integrals over a line-of-sight, the total radiated power from the plasma may be found by integrating over the viewing angle of a single camera. If the spatially resolved radiated power is required, the observed data must be Abel or otherwise inverted. An example is given in Fig. 10.8.2. This shows a pronounced poloidal asymmetry near the plasma inner edge due to the presence of a marfe. It is also possible for the radiated power to have toroidal asymmetries due to preferential interaction with limiters and this complicates the interpretation of the measurements. The detectors usually have a slow time response and are also sensitive to neutral particle fluxes.

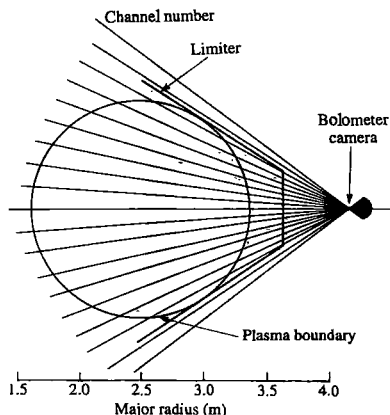


**Fig. 10.8.1** Bolometer camera with 20 channels on the TFR tokamak.  
(Schivell, J. *Review of Scientific Instruments* **S8**, 12 (1957).)

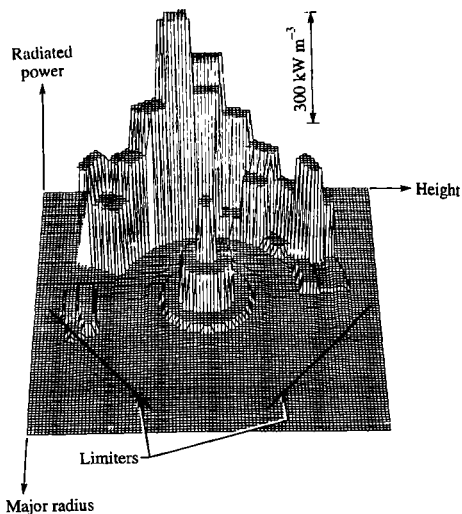


**Fig. 10.8.2** Spatially resolved radiated power showing a mafre at the plasma edge.  
(Schivell, *J. Review of Scientific Instruments* **58**, 12 (1987).)

### Soft X-rays

Soft X-rays are usually detected by silicon diodes which, in contrast to the bolometers, have an extremely fast time response, typically a fraction of a microsecond, and measure the integrated X-ray power above a threshold energy determined by a thin metallic foil, usually beryllium, placed in front of the detectors. The detectors receive most of their power from the hot dense plasma core and have proved invaluable in the study of mhd phenomena and impurity transport effects. Pinhole cameras with more than 100 sensors have been used, often viewing the plasma from orthogonal directions as shown in Fig. 10.8.3. The main advantage of this diagnostic is its excellent spatial and temporal resolution. Many detailed studies of tokamak plasmas have been made particularly of the sawtooth instability, major and minor disruptions, mhd modes, high- $\beta$  mhd effects, impurity transport, the snake and pellet injection.

The signals from *individual* channels often show pronounced mhd effects. These include the sawtooth oscillation which appears at the plasma centre, and mhd oscillations associated with the magnetic surfaces with  $q = m/n$ . The mode number may be found by comparing the phases of signals viewing different parts of the plasma. Figure 10.8.4 shows a sawtooth collapse following strong  $m=1$  oscillations.

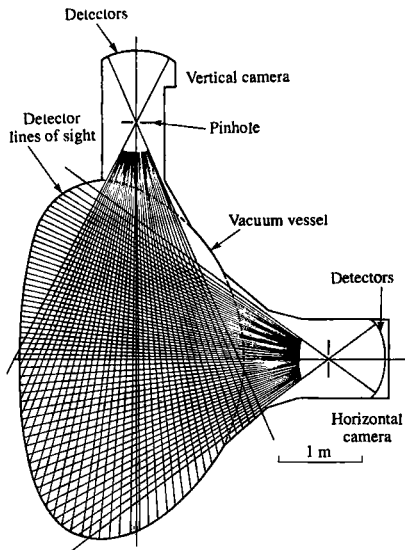


**Fig. 10.0.3** Soft X-ray pinhole cameras on JET. (Edwards, A. W. et al. *Review of Scientific Instruments* 57, 2142 (1986).)

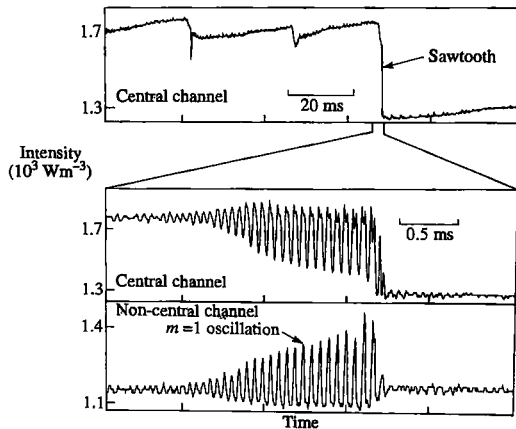


**Fig. 10.0.4** Signals from individual detectors of the JET soft X-ray cameras showing a sawtooth in the upper figure and pronounced MHD activity in the lower figures which are on an expanded timescale. On the rapid timescale the sawtooth precursor activity can be clearly seen both at the plasma centre and at the inversion radius.

### Tomography

The observed soft X-ray signals are integrals along a line of sight. The intensity is

$$I = \Omega \int \varepsilon(x) \alpha(E_x) dx dE_x,$$

where  $\Omega$  is the solid angle factor of the detector,  $\varepsilon(x)$  the plasma emissivity,  $E_x$  the X-ray energy and  $\alpha(E_x)$  the transmission coefficient of the X-ray filter. The geometry and the coordinates are shown in Fig. 10.8.5. For many purposes the spatially resolved emissivity,  $G(r, \theta)$ , is required and this can be obtained by a tomographic inversion of the raw data. Many different techniques have been used for this purpose. One of the most useful procedures is that proposed by Cormack which is based on an expansion in Zernicke polynomials,  $R_{m\ell}$ , to describe the inverted data:

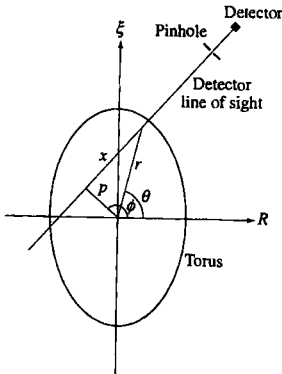


**Fig. 10.8.5** Geometry of detectors for tomographic inversion. The relationship is shown between the plasma coordinates  $(r, \theta)$  and the detector's coordinates,  $(p, \phi)$ .

$$G(r\theta) = \sum_{\ell m} (A_{m\ell}^s \sin m\theta + A_{m\ell}^c \cos m\theta) R_{m\ell}(r).$$

The Zernicke polynomials are given by

$$R_{m\ell}(r) \equiv \sum_{s=0}^{\ell} \frac{(-\ell)^s (m+2\ell-s)!}{s!(m+\ell-s)!(\ell-s)!} r^{m+2\ell-2s}.$$

The observed line of sight data can be described by

$$F(p, \chi) = \sum_{\ell m} (A_{m\ell}^s \sin m\chi + A_{m\ell}^c \cos m\chi) S_{m\ell}(p)$$

with  $S_{m\ell}(p) = 2 \sin[(m+2\ell+1) \cos^{-1} p]/(m+2\ell+1)$  and  $\chi$  the detector angle. The tomography problem can then be solved by determining the coefficients  $A_{m\ell}^{s,c}$  from a fit to the experimental data. The maximum values of  $\ell$  and  $m$  which can be used in the summations depend on the experimental assembly, with  $\ell$  determined by the radial resolution of the X-ray detectors and  $m$ , the poloidal mode number, from the maximum number of independent views of a particular surface of constant  $p$ . The two cameras shown in Fig. 10.8.3 provide essentially four independent views, because for a given value of  $p$  there are detectors with four different values of  $\phi$ . This determines a maximum of 4 coefficients  $A_{m\ell}^{s,c}$  which are typically  $A_{00}^{s,c}, A_{1\ell}^{s,c}, A_{2\ell}^{s,c}$ . Higher  $m$ -number modes cannot generally be determined but will appear from the tomographic analysis to be combinations of lower  $m$ -modes.

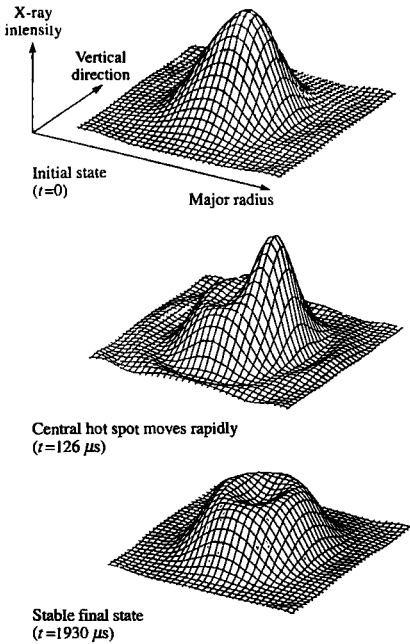


**Fig. 10.8.6** Tomographic reconstructions of the soft X-ray emission in a sawtooth crash in JET.

Tomography has been used extensively to study the fast phase of the sawtooth collapse and throw light on possible sawtooth crash collapse mechanisms. Reconstructed images of soft X-ray emission before, during and after a sawtooth collapse are shown in Fig. 10.8.6. Sequences of reconstructions similar to those shown in the figure have been put onto video cassettes to provide movies. Similar displays of long pulse discharges have also been made using real time data processing techniques to carry out the tomography.

The restriction to low  $m$ -numbers can be avoided either by introducing more views of the plasma or, in some cases, by making use of plasma rotation, effectively producing additional views of the plasma as it moves in front of the detectors. By this means the emissivity of complicated high  $m$ -number or localized features may be reconstructed. An example of this is the strongly localized radiation from the so-called snake, shown in Fig. 10.8.7.

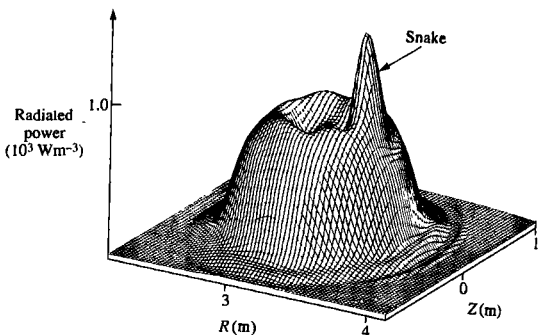


**Fig. 10.8.7** Tomographic reconstruction of the snake which is a small region of enhanced plasma density in JET produced on the  $q = 1$  magnetic surface following injection of a solid D<sub>2</sub> pellet.

## 10.9

### Langmuir probes

In its simplest form the Langmuir probe consists of a single electrode which can be inserted into the plasma. A voltage is applied to the probe with respect to the vessel and the current is measured. From the current-voltage ( $I-V$ ) characteristic of such a probe the electron temperature  $T_e$  and density  $n_e$  can be deduced. In large tokamaks the use of Langmuir probes is limited to the plasma edge because of the large power fluxes in the interior.

The interpretation of Langmuir probes is based on the theory of the electrostatic sheath (see Section 9.2) which is established at the surface of the probe element. Combination of eqns 9.2.8 and 9.2.9 leads to an expression for the current to a probe  $I$  which is biased to voltage  $V$

$$I = (j_i + j_e)A = j_i(1 - \exp(e(V - V_f)/T_e))A, \quad 10.9.1$$

where  $j_i$  and  $j_e$  are the electron and ion current densities and  $A$  is the projected surface area of the probe. In the limit where the probe dimensions are large compared to the ion and electron gyro-radii and the Debye length,  $A = \int \mathbf{B} \cdot d\mathbf{S}/B$ .  $V_f$  is the floating potential discussed below. When the probe is biased sufficiently negatively all electrons are repelled and all that remains is the ion current. This current is independent of voltage and is called the ion saturation current. Saturation of the ion current occurs because all the bias potential appears across the thin sheath and the ion flux is simply determined by the flux of ions crossing the sheath edge at the ion sound speed.

The floating potential  $V_f$  is the potential at which the probe would float if it were electrically isolated. If an external potential is applied to

the probe then  $V_f$  is determined by the applied potential at which the net current is zero. As the probe voltage is swept positive with respect to  $V_f$ , it is seen from eqn 10.9.1 that the electron current rises exponentially. However, eqn 10.9.1 is only applicable when the probe potential lies below the plasma potential. When the probe potential equals the plasma potential there is no sheath electric field and the electrons flow to the probe surface with a thermal velocity distribution. This point in the characteristic is called electron saturation, and the electron saturation current is given by  $I_{es} = \frac{1}{4} n_0 e \bar{c}_e A$ , where  $\bar{c}_e$  is the electron thermal speed. In non-magnetized plasmas, Langmuir probe characteristics often follow this ideal picture with electron to ion saturation current ratios in hydrogen plasmas around 50:1, as expected from the ratio of electron thermal speed to ion sound speed.

Figure 10.9.1 shows an  $I-V$  characteristic obtained from a single Langmuir probe in the T10 tokamak. The data is fitted up to the point where the roll over into electron saturation occurs using eqn 10.9.1. In this case the electron to ion saturation current ratio is 6.5 but ratios as low as 1:1 are sometimes observed. As yet there is no adequate theory for this behaviour and for this reason it is usually advisable to ignore data from the net electron collecting side of the characteristic. The consequence of this is that usually only the tail of the electron distribution, comprising around 5% of the total, is measured.

Assuming equal ion and electron temperatures, the electron density at the sheath edge may be derived from eqn 9.2.8 to give

$$n_0 = \frac{J_i}{e} \left( \frac{m_i}{2T_e} \right)^{1/2}. \quad 10.9.2$$

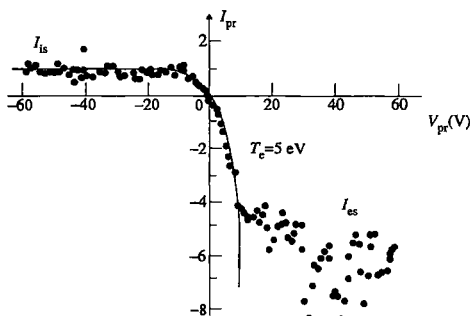


Fig. 10.9.1 Single Langmuir probe characteristic from the T10 tokamak showing low electron to ion saturation current ratio as compared with the value predicted by eqn 10.9.1.

### Probe assemblies

The two main ways that probes of various types can be introduced into a tokamak are illustrated in Fig. 10.9.2:

1. Arrays of fixed probes can be built into limiters and divertor targets with the purpose of characterizing the plasma contacting the material surfaces. Since such probes do not modify the sheath already existing at the limiter or divertor targets, it is normal to quote the density at the sheath edge, given by eqn 10.9.2.

2. Probes can be mounted on drives which can map out a profile of the edge plasma on a pulse by pulse basis (slow drive) or during a pulse (fast reciprocating drive). Fast drives are essential in large tokamaks where prolonged exposure of the Langmuir probe head leads to vaporization. Probes of this type act as sinks for plasma ions and so locally perturb the plasma. This density perturbation occurs over a distance called the collection length  $L_{\text{col}}$  which is determined by the rate at which the parallel flow of ions to the probe can be supplied by cross-field diffusion

$$L_{\text{col}} \simeq \frac{d^2 c_s}{D_\perp},$$

where  $d$  is the projected probe width,  $c_s$  the ion sound speed and  $D_\perp$  the diffusion coefficient perpendicular to the magnetic field. Provided that  $L_{\text{col}}$  is less than the distance along  $B$  to the next material object the unperturbed density can be obtained by multiplying the density at the sheath edge, given by eqn 10.9.2, by  $\sim 2$ . This factor allows for the drop in density which occurs when the ions are accelerated up to the ion sound speed at the edge of the sheath created by the probe.

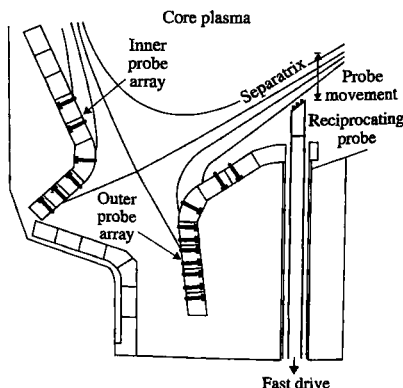


Fig. 10.9.2 Fixed probe arrays and fast reciprocating probe in the divertor region of C-mod tokamak.

### Single probes

When current is drawn from a plasma through a probe tip an equal current of opposite sign must be returned to the plasma through a second electrode. In the case of single Langmuir probes in tokamaks, the torus is often taken as the reference electrode. The main requirement is for a surface area sufficiently large that a negligible potential change across the reference electrode sheath is needed for the return current to flow. This requires that the surface carrying the return current does not reach the ion-saturation limit before the probe reaches electron saturation. In a uniform hydrogenic plasma the reference electrode would need an area which is larger than the probe area by a factor in excess of the ideal electron to ion saturation current ratio, which is typically  $\sim 50:1$ . Despite the large surface area within a tokamak, currents flow much more readily along the magnetic field than across it and so the area of surface from which the return current flows may actually be very restricted. This restriction of the current channel has been put forward as a possible explanation for the low electron to ion saturation current ratios which have been observed in many tokamaks and can be seen in the example of Fig. 10.9.1.

### Double probes

Double Langmuir probes consist of a pair of probe tips located close enough together that they can be considered to be exposed to the same plasma conditions. A swept isolated power supply drives current in one tip and out the other so that  $I_1 + I_2 = 0$ . Defining  $I_1$  and  $I_2$  with eqn 10.9.1 and the power supply voltage as  $V_s = V_1 - V_2$ , the following equation is obtained for an asymmetric double probe characteristic

$$I_1 = \frac{j_i A_1 (1 - \exp(eV_s/T_e))}{1 + (A_1/A_2) \exp(eV_s/T_e)}.$$

If the areas are equal, that is  $A_1 = A_2$  then

$$I_1 = j_i A_1 \tanh(V_s/2T_e).$$

The only advantage that a double probe would appear to have over a single probe is that the return path for the current can be less ambiguous. In practice however, no real benefits have been demonstrated which would justify the added complexity and loss of information about the electron collecting side of the characteristic.

### Triple probes

Triple Langmuir probes consist of three probe tips each of which must be exposed to the same plasma parameters. One tip provides the floating potential whilst the other two are differentially biased with a constant potential as an isolated pair such that one tip draws an ion saturation current  $j_i A_1$  and the other a net electron current  $-j_i A_1$ . This arrangement

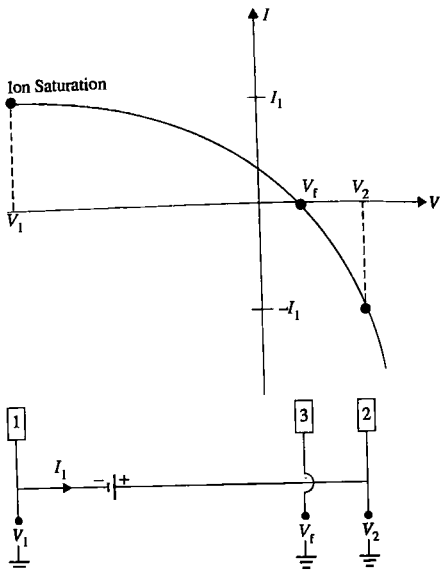


**Fig. 10.9.3** Schematic illustrating the principle of the triple Langmuir probe. The circuit diagram is shown together with the positions of the three probes on the  $I(V)$  curve.

is shown in Fig. 10.9.3. The potential of the electron collecting side of the circuit  $V_2$  adjusts itself such that the electron side draws an equal but opposite current to the ion side. Applying eqn 10.9.1 to tips 1 and 2 and using the continuity equation  $I_1 + I_2 = 0$ , the following equation is obtained

$$(1 - e^{(V_1 - V_f)/T_e})A_1 + (1 - e^{(V_2 - V_f)/T_e})A_2 = 0. \quad 10.9.3$$

In the limit where the supply voltage is large  $e|V_1 - V_f| \gg T_e$ , eqn 10.9.3 gives a simple expression for the electron temperature,

$$T_e = (V_2 - V_f) / \ln \left( 1 + \frac{A_1}{A_2} \right).$$

The advantage of the triple probe method is high time resolution since  $V_2$ ,  $V_f$ , and  $j_i$  can be measured simultaneously. This contrasts with swept probes where the current and voltage may need to be recorded at up to 100 time points to define a single characteristic from which averaged parameters may be extracted. Figure 10.9.4 shows an example of high time resolution divertor triple probe measurements from an ELM My discharge in JET. Triple probe data is however unreliable under conditions where the ion and electron saturation currents are comparable, or the plasma parameters vary across the three tips.

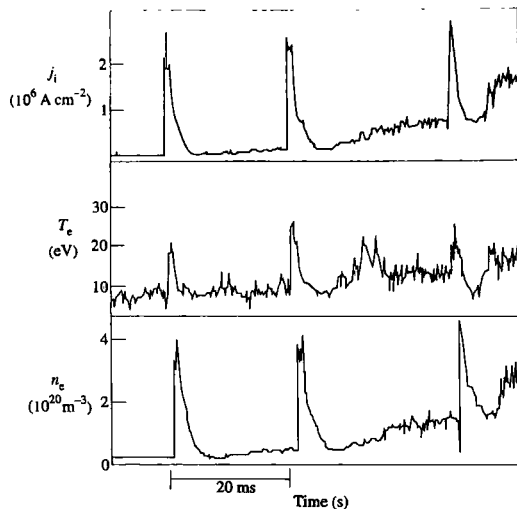


**Fig. 10.9.4** Divertor triple probe data from an ELMy discharge in JET.

## 10.10 Measurements of fluctuations

The experimentally determined energy and particle transport coefficients in a tokamak greatly exceed those calculated from collision theory. It is generally accepted that plasma turbulence is responsible for this anomaly and a considerable experimental effort has been made to try to understand the mechanisms operating, to distinguish between different theoretical models, and to try to show that the experimentally determined turbulence does indeed account for the observed transport.

Electrostatic fluctuations affect both particle transport and heat conduction. The particle flux may be written as

$$\Gamma_j = \frac{\langle \tilde{E}_\perp \tilde{n}_j \rangle}{B},$$

where  $B$  is the magnetic field,  $\tilde{E}_\perp$  and  $\tilde{n}_j$  are the fluctuating parts of the electric field and the particle density respectively. The triangular brackets denote averaging. The heat flux is also affected and the turbulence gives

rise to a term

$$q_j = \frac{3}{2} \frac{n_j \langle \tilde{E}_\perp \tilde{T}_j \rangle}{B},$$

where  $\tilde{T}_j$  is the temperature fluctuation.

Magnetic fluctuations mainly affect the heat flux which is increased by a contribution

$$q_j = -k \left( \frac{\tilde{b}_r}{B} \right)^\alpha \frac{d\tilde{T}_j}{dr},$$

where  $k$  depends on plasma parameters and  $\tilde{b}_r$  is the fluctuating component of the radial magnetic field. The index  $\alpha$  is 1 or 2 depending on the collisionality of the plasma and whether the plasma is in the quasi-linear or strong turbulence regime.

In order to properly evaluate the importance of fluctuations, measurements  $\tilde{n}$ ,  $\tilde{T}_j$  and  $\tilde{E}_\theta$  are required together with their correlations. Measurements of  $\tilde{b}_r$  are also necessary. To determine all of these is clearly a daunting task and the experimental investigations have so far been of a more limited extent. The most comprehensive measurements have been made at the plasma edge where the fluctuations are at their greatest. Much of this work has been done using magnetic and Langmuir probes. Towards the plasma centre this technique will not work as the probes perturb the plasma too greatly and would be melted by high heat fluxes. At the centre more limited data is available from scattering experiments and heavy ion beam probes. The few measurements of the temperature fluctuations show that they are small. Density fluctuations can also be investigated using reflectometry. The information about  $\tilde{b}_r$  is also very limited with data coming only from fairly indirect sources such as the containment properties of runaway electrons. In the paragraphs below some typical fluctuation measurements will be described.

### Heavy ion beam probe

This diagnostic was originally developed to determine the electric potential within a plasma. The basic principles of its operation may be seen in Fig. 10.10.1. An incident beam of singly charged ions is accelerated to energy  $E$  and allowed to enter the plasma perpendicular to the toroidal field. The ions move on an orbit with Larmor radius  $\rho_i$ , until at point I in the interaction zone they become further ionized due to collisions with plasma electrons and then move onto an orbit with smaller radius,  $\rho_i/2$ , and become separated from the primary beam. It is clear that for this diagnostic to work  $\rho_i$  must be comparable with the tokamak minor radius. This is achieved by using a singly charged probe beam, often thallium, with high  $Z$  and with energies typically in the 100s of keV to MeV range.

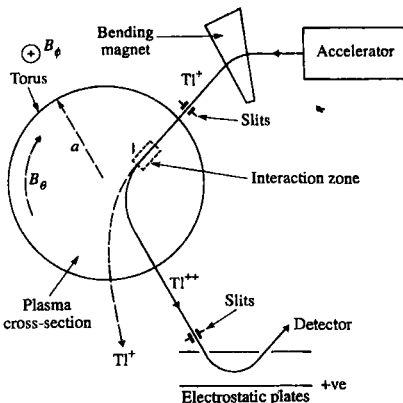


**Fig. 10.10.1** Schematic diagram of a thallium heavy ion beam probe. The accelerated ions are selected in energy by the bending magnet and then enter the plasma where they charge exchange and move on a new trajectory, entering the electrostatic energy analyser and detector.

The diagnostic has not yet been applied to the largest tokamaks, mainly because of the very high energies required.

If the potential difference between the point  $I$  and the exterior of the plasma is  $\phi$  then the doubly charged ions emerge with energy  $E + e\phi$  and a measurement of this energy, with an electrostatic energy analyser, determines  $\phi$  and its fluctuations. The difficulty of the measurement arises from the fact that  $e\tilde{\phi} < e\phi \ll E$ .

Other quantities may also be measured with this diagnostic. For example, the intensity of the secondary beam will be proportional to the plasma electron density in the interaction volume, and, more interestingly, its fluctuations will reflect the density fluctuations,  $\tilde{n}_e$ . The effective interaction volume will be determined by the incident beam divergence and the solid angle of the detection system.

In addition, the beams will be deflected out of the plane perpendicular to  $B_\phi$  by the poloidal magnetic field. A measurement of this deflection can determine information about the components of  $B$  perpendicular to  $B_\phi$  and their fluctuations.

In Fig. 10.10.2 an example is shown of the radial profiles of the relative density ( $\tilde{n}_e/n_e$ ) and potential fluctuations ( $e\tilde{\phi}/T_e$ ) measured on the TEXT tokamak using a heavy ion beam probe technique.

### Scattering measurements of $\tilde{n}_e$

A beam of electromagnetic radiation traversing a plasma will scatter from individual charged particles and it will also scatter from plasma waves and fluctuations due to collective effects. An incident beam with frequency

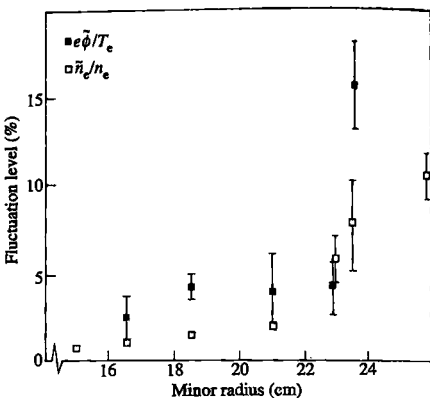


Fig. 10.10.2 Radial profiles showing the fluctuation levels of  $\bar{n}_e/n_e$  and  $e\bar{\phi}/T_e$  in the TEXT tokamak in the outer regions of the plasma. (Forster, J. FRC Report 301, University of Texas, Austin (1987).)

$\omega_0$  and wave number  $k_0$  will collectively scatter from fluctuations with  $(\omega, k)$  to give a scattered beam with  $\omega_s, k_s$  where energy and momentum conservation give the relations

$$\omega_s = \omega_0 \pm \omega, \quad k_s = k_0 \pm k.$$

If the probing beam is chosen so that  $|k_0| \approx |k_s|$  then

$$k^2 = 4k_0^2 \sin^2(\theta_s/2),$$

where  $\theta_s$  is the angle of the scattering. Collective scattering occurs when the electromagnetic beam interacts with the plasma on a scale length greater than the Debye length,  $\lambda_D$ . That is when

$$\frac{1}{k} > \lambda_D.$$

For reasonable scattering angles this relation implies the use of millimetre or submillimetre wavelengths. The scattered power is given by

$$P_s = P_0 r_0^2 n_e V \Omega \int S(k, \omega) d\omega / 2\pi,$$

where  $P_0$  is the incident power,  $V$  is the scattering volume,  $r_0$  the classical electron radius and  $\Omega$  is the solid angle.  $S(k, \omega)$  contains the

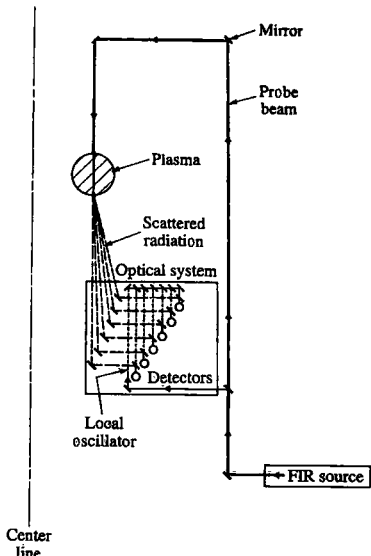


Fig. 10.10.3 Multichannel far infrared scattering apparatus used on the TEXT tokamak. (Park, H., Brower, D.L., Peebles, W.A., Luhmann, Jr., N.C. et al., *Review of Scientific Instruments* 56, 1055 (1985).)

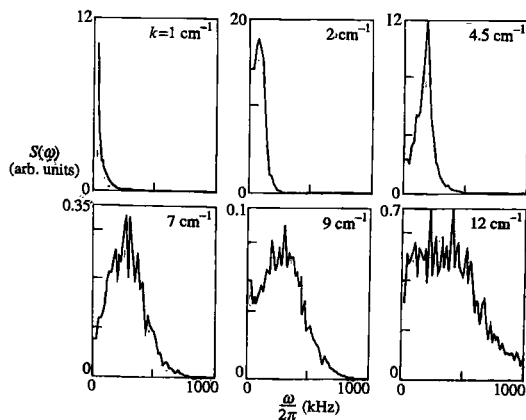
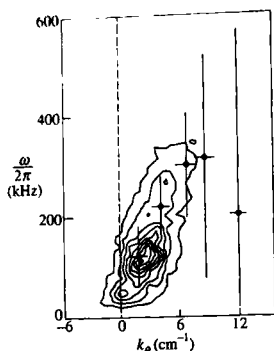


Fig. 10.10.4 Scattered frequency spectra for different values of  $k$ . The spectra peak at gradually increasing values of  $\omega$  as  $k$  increases. (Ritz, Ch.P., Brower, D.L., Rhodes, T.L., Bengtson, R.D., et al., *Nuclear Fusion* 27, 1125 (1987).)



**Fig. 10.10.5**  $S_k(\theta, \omega)$  spectrum at  $r = 0.26 \text{ m}$  in TEXT from scattering experiments (crosses which represent FWHM) and from Langmuir probe measurements (contours). (Wootton, A.J., Austin, M.E., Bengtson, R.D., Boedo, J.A., et al. FRCR#310, University of Texas, Austin (1988).)

## 10.11

### Determination of the $q$ -profile

A knowledge of the  $q$ -profile in a tokamak is fundamental for the understanding of the mhd properties of the plasma. Near the plasma edge,  $q$  may be determined with accuracy from magnetic measurements, but this becomes increasingly inaccurate as extrapolations are made towards the plasma centre. Several methods of determining  $q(r)$  have been developed. The Faraday rotation method has already been discussed in Section 10.3.

An early determination of  $q(r)$  was made using a ruby laser scattering technique. An incident beam with wave vector  $k_0$  was allowed to scatter from the plasma electrons to produce a scattered wave  $k_s$ , with the detector geometry arranged such that  $\mathbf{k} = \mathbf{k}_s - \mathbf{k}_0$  was very nearly perpendicular to the magnetic field,  $\mathbf{B}$ . The spectrum of the scattered radiation has the usual Doppler broadening of approximately  $|k|v_{Te}$  due to the thermal motion of the electrons, but it is strongly modulated in intensity when  $\mathbf{k} \cdot \mathbf{B}$  is very small because of the oscillatory motion of the electrons around the magnetic field lines. These modulations are separated in frequency by  $\omega_{ce}$ . However, this effect cannot be observed in a tokamak directly from the scattered spectrum because, as  $\omega_{ce} \ll |k|v_{Te}$ , the modulations are very closely spaced and each separated peak in the scattered spectrum has a very small number of photons. This difficulty was overcome by using forward scattering together

information about the plasma fluctuation spectrum and is the quantity which needs experimental determination.

In a typical experimental arrangement such as that employed on the TEXT experiment (Fig. 10.10.3), a probe beam enters the plasma after reflection in mirrors mounted in a stainless-steel tower. Part of the probe beam is separated to provide six equal power local oscillator beams which are then mixed in the detectors with the six scattered beams to produce an intermediate frequency signal at the difference frequency which corresponds to the frequency of the density fluctuations. The arrangements of the mirrors allows the measurements to be made over most of the plasma cross-section. Heterodyne detection may also be used and allows the determination of the direction of  $\mathbf{k}$ . The system needs to be calibrated. The scattered radiation is used to determine the spectrum  $S$ , which is shown in Fig. 10.10.4 for various values for  $k$ . At the plasma edge the fluctuations are also measured by Langmuir probes, and a comparison with the scattering results is shown in Fig. 10.10.5.

with detection optics which incorporated a Fabry-Perot interferometer which matched the electron cyclotron frequency. Results from this technique showed a  $q(r)$  profile descending below unity at the plasma centre. Although this method is based on very sound physical principles, it has been little used due to considerable practical difficulties encountered in its execution.

The best established method of measuring the pitch angle of the magnetic field exploits the motional linear Stark effect. The experimental arrangement is similar to that described at the end of Section 10.6, and, again, spatial resolution is obtained from the intersection of the beam and viewing optics. Atoms in an injected neutral beam of deuterium or hydrogen are excited by the plasma particles and emit Balmer-alpha radiation. In their rest frame the atoms experience a Lorentz electric field  $E_L = V \times B$ . For injected deuterium neutrals of  $\sim 100$  keV, this field splits spectral lines into  $\pi$  and  $\sigma$  components more strongly than the Zeeman effect which can be ignored. The beam emission can be easily distinguished from plasma emission by its Doppler shift although the measurements are complicated by the presence in the beam half of and third energy components.

The determination of the direction of the magnetic field comes from the polarisation properties of the spectrum. Viewed transversely to the electric field, the  $\pi$  components are linearly polarised parallel to  $E_L$ , and the  $\sigma$  components are linearly polarised perpendicular to  $E_L$ . The direction of the magnetic field is determined from the direction of the linearly polarised  $\sigma$  components.

In a typical experimental arrangement on the PBX-M experiment the viewing optics intersect the 40–80 keV diagnostic beam injector. A radial profile of the magnetic field pitch angle is obtained by rotation of the

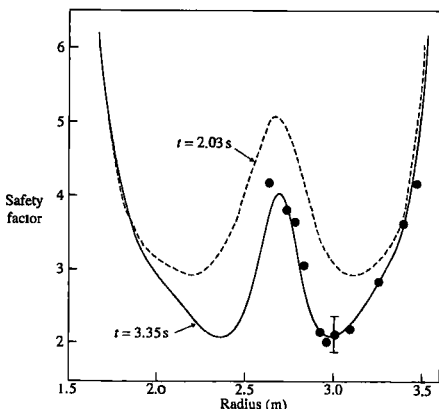


Fig. 10.11.1 Profile of  $q$  during neutral beam experiments in TFR. The remarkably hollow profile is clearly demonstrated. (Levington, F.M. et al., *Physical Review Letters* 75, 4417 (1995).)

beam direction. In other experiments spatial resolution is obtained by viewing the beam at different positions. A lens focuses the light through a polarimeter and interference filter that transmits the  $\sigma$  components only. The polarimeter is based on a photo-elastic modulator and accuracies of 0.1–0.2 degrees are obtained. Some further knowledge of the plasma flux surfaces is needed to determine the  $q$ -profile and the measurements are also slightly sensitive to the radial electric field which can also be determined.

Measurements with this technique were originally used to study the central  $q$ -profile in sawtooth discharges. More recently the measurements have become of much greater importance for setting up and understanding high performance discharges with reversed magnetic shear. A  $q$ -profile determined by this technique is shown in Fig. 10.11.1.

## Bibliography

### Tokamak diagnostics

There is an extensive literature on tokamak diagnostics. The general principles of operation of a wide range of diagnostics are discussed by

Hutchinson, I.H. *Principles of plasma diagnostics*. Cambridge University Press (1987).

A good review of the diagnostics installed on the large tokamaks is by

Orlinskij, D.V., and Magyar, G. Plasma diagnostics on large tokamaks. *Nuclear Fusion* **28**, 611 (1988).

Valuable information on the development and 'state of the art' of diagnostics has been published in the proceedings of the International School of Plasma Physics 'Piero Caldirola' held at Varenna, Italy. The seventh of these is devoted to the new diagnostic challenges arising from the ITER project.

Stott, P.E., Gorini, G., Prandoni, P., and Sindoni, E. (eds). *Diagnostics for experimental thermonuclear fusion reactors 2*. Plenum Press, New York and London (1998).

Many recent developments may be found in

Barnes, C.W. and Snider, R. Proceedings of the 13th topical conference on high-temperature plasma diagnostics. *Review of Scientific Instruments* **72** 285 (2001). The proceedings of earlier conferences in this series, held biannually, also provide valuable material.

### Magnetic measurements

The derivation of equilibrium quantities from magnetic measurements is discussed by

Shafranov, V.D., Determination of the parameters  $\beta_I$  and  $l_i$  in a tokamak for arbitrary shape of plasma pinch cross section. *Plasma Physics* **13**, 757 (1971).

Zakharov, L.E. and Shafranov, V.D. Equilibrium of a toroidal plasma with non-circular cross-section. *Soviet Physics—Technical Physics* **18**, 151 (1973).

Lao, L.L., St. John, H., Stambaugh, R.D., and Pfeiffer, W. Separation of  $\beta_p$  and  $l_i$  in tokamaks of non-circular cross section. *Nuclear Fusion* **25**, 1421 (1985).

A more general overview of magnetic diagnostics is given by Wootton, A.J. in *Diagnostics for contemporary fusion experiments*. Stott, P.E., Akulina, D.K., Gorini, G., and Sindoni, E. (eds). Editrice Compositori, Bologna (1991).

### Interferometry

This is one of the most essential of diagnostics and has been used since the beginning of tokamak research. Useful further information may be found in

Jahoda, F.C. and Sawyer, G.A. Optical refractivity of plasmas. In *Methods of experimental physics*, Vol. 9B, Plasma physics (eds Griem, H.R. and Lovberg, R.H.) Chapter 11. Academic Press, New York (1971).

Veron, D. High sensitivity HCN laser interferometer for plasma electron density measurements. *Optics Communications* **10**, 95 (1974).

### Reflectometry

An overview of reflectometry measurements may be found in Manzo, M.E. Reflectometry in fusion devices. *Plasma Physics and Controlled Fusion* **35**, B141 (1993).

The first reflectometry measurements of density fluctuations are reported in TFR Group. Local density fluctuations measurements by microwave reflectometry on TFR. *Plasma Physics and Controlled Fusion* 27, 1299 (1984).

### Measurements of electron temperature

Measurements of  $T_e$  using laser light scattering are discussed by Evans, D.E. and Katzenstein, J. Laser light scattering in laboratory plasmas. *Reports on Progress in Physics*, 32, 207 (1969).

Peacock, N.J., Robinson, D.C., Forrest, M.J., Wilcock, P.D., and Sannikov, V.V. Measurements of the electron temperature by Thomson scattering in tokamak T3. *Nature* 244, 488 (1969).

Sheffield, J. *Plasma scattering of electronic radiation*. Academic Press, New York (1975).

The physics of electron cyclotron emission is discussed by Beketi, G. *Radiation processes in plasmas*. Wiley, New York (1966).

Bomati, M., Cano, R., De Barbieri, O., and Engelmann, F. Electron cyclotron emission and absorption in fusion plasmas. *Nuclear Fusion* 23, 1153 (1983).

ECE methods to determine  $T_e$  may be found in

Engelmann, F. and Curatolo, M. Cyclotron radiation from a rarefied inhomogeneous magnetoplasma. *Nuclear Fusion* 13, 497 (1973).

Costley, A.E., Hastie, R.J., Paul, J.W.M., and Chamberlain, J. Electron cyclotron emission from a tokamak plasma: experiment and computation. *Physical Review Letters* 33, 758 (1974).

Costley, A.E. Electron cyclotron emission from magnetically confined plasmas: I—Diagnostic potential; II—Instrumentation and measurement. In *Diagnostics for fusion reactor conditions* (eds Stott, P.E., Akulina, D.K., Leotta, G.G., Sindoni, E., and Wharton, C.) Vol. 1, 129 EUR 8351-1EN, CEC, Brussels (1982).

### Neutral particle analysis

The transport of neutrals within a plasma is discussed in detail in

Hughes, M.H., and Post, D.E. A Monte Carlo algorithm for calculating neutral gas transport in cylindrical plasmas. *Journal of Computational Physics* 28, 43 (1978).

### $T_i$ from neutron emission

Calculations of charged particle reaction rates and neutron spectra are given by

Brysk, H. Fusion neutron energies and spectra. *Plasma Physics* 15, 611 (1973).

### Radiation emission from plasmas

An excellent and up-to-date overview of plasma spectroscopy is given by Grein, H.R. *Principles of plasma spectroscopy*. Cambridge University Press, UK (1997).

The physics of the different sources of radiation is discussed by Tucker, W.M. *Radiation processes in astrophysics*. MIT Press, Cambridge, Mass. (1975).

Bremsstrahlung emission from a Maxwellian plasma is discussed by Karzas, W.J., and Latter, R. Electron radiative transitions in a Coulomb field. *Astrophysical Journal Suppl.* Ser. 6, 167 (1961).

Several useful articles explaining the general principles of plasma spectroscopy may be found in Barnett, C.F. and Harrison, M.F.A. (eds) *Applied atomic collision physics*, vol. 2, Plasmas. Academic Press, New York (1984).

Calculations of the power loss from a plasma in coronal equilibrium are given by Post, D.E., Jensen, R.V., Tarter, C.B., Grasberger, W.H., and Lokke, W.A. Steady-state radiative cooling rates for low-density, high temperature plasmas. *Atomic Data and Nuclear Data Tables* 20, 397 (1977).

### Particle influx measurements

The determination of hydrogen influxes from line intensities is discussed by

Johnson, L.C., and Hinov, E. Ionization, recombination, and population of excited levels in hydrogen plasmas. *Journal of Quantitative Spectroscopy and Radiative Transfer* 13, 333 (1973).

Impurity influx determination is discussed in Behringer, K., Summers, H.P., Denne, B., Forrest, M., and Stamp, M. Spectroscopic determination of impurity influx from localised surfaces. *Plasma Physics and Controlled Fusion* 31, 2059 (1989).

### Impurities

The general principles of impurity determination in tokamaks are explained in the review article

Ister, R.C. Impurities in tokamaks. *Nuclear Fusion* 24, 1599 (1984).

A useful review specializing on the X-ray region is de Michelis, C., and Mattioli, M. Soft X-ray spectroscopic diagnostics of laboratory plasmas. *Nuclear Fusion* 21, 677 (1981).

### Tomography

The theory and practice of tomography as applied to tokamak plasmas are reviewed by  
Graneitz, R.S., and Smeulders, P. X-ray tomography on JET.  
*Nuclear Fusion* **28**, 457 (1988).

### Langmuir probes

A thorough review of the application of Langmuir probes in tokamaks is provided by  
Stangeby, P.C., *Plasma diagnostics Volume 2, Surface analysis and interactions*, Edited by O. Auciello, D.L. Flamm,  
Academic Press (Boston, 1989) p. 157.

More recent developments in the theory and application of Langmuir probes, along with a review of advanced electrical probes such as retarding field analysers and mass-spectrometers, are described in  
Matthews, G.F., *Plasma Physics and Controlled Fusion* **36**, 1595 (1994).

### Fluctuations

Much useful information about turbulence and transport may be found in

Grésillon, D. and Dubois, M.A. (eds). *Turbulence and anomalous transport in magnetized plasmas*. (Proc. of the international workshop on small scale turbulence

and anomalous transport, 1986, Cargèse). Editions de physique, Les Ulis, France.

An extremely useful review article is  
Liewer, P.C. Measurements of microturbulence in tokamaks and comparison with theories of turbulence and anomalous transport. *Nuclear Fusion* **25**, 543 (1985).

An early paper on the heavy ion beam probe is  
Jobes, F.C., Hickok, R.L. A direct measurement of plasma space potential. *Nuclear Fusion* **10**, 195 (1970).

### *q*-profile

The determination of  $q(r)$  by laser scattering is described in  
Forrest, M.J., Carolan, P.G., and Peacock, N.J. Measurement of magnetic fields in a tokamak using laser light scattering. *Nature* **271**, 718 (1978).

The determination of  $q(r)$  using the motional Stark effect is described by

Levington, F.M. et al. Magnetic field pitch-angle measurements in the PBX-M tokamak using the motional Stark effect. *Physical Review Letters* **63**, 2060 (1989).

A useful review in this area is

Soltwisch, H. Current density measurements in tokamak devices. *Plasma Physics and Controlled Fusion* **34**, 1669 (1992).

**11**

# **Tokamak experiments**

**11.1****Tokamak experiments**

The earliest experiments aimed at confining a high temperature plasma were carried out in the United Kingdom. The idea of avoiding electrodes by using a toroidal vessel, and of using a transformer action to induce a toroidal current led, to a series of so-called pinch experiments with currents of several kiloamps. However, it was found that the resulting plasmas were grossly unstable. It was subsequently realized that the addition of a toroidal magnetic field would improve stability and this concept was implemented in a number of experiments such as Zeta. However, in modern terminology, the value of  $q$  was less than one. Consequently strong instabilities still occurred, although not on the gross scale of the earlier experiments.

The development of tokamaks in the Soviet Union followed from theoretical ideas of Tamm and Sakharov. The conceptual development was the opposite of that in the United Kingdom. The initial conception was of a toroidal confining magnetic field. The realization that this would not allow an equilibrium led to the suggestion that the problem would be solved by passing a toroidal current through the plasma.

Calculations by Shafranov and Kruskal indicated that improved stability was associated with having  $q > 1$ . This is the essential difference between tokamaks and pinches, and the appreciation of this fact is central to the comparative success of the tokamak concept. It should however be remarked that had the range of instabilities now known to beset tokamaks been discovered by theoreticians before the experimental programme was undertaken, there might have been some hesitation.

The initial tokamak experiments were spoiled by impurities resulting from interaction of the plasma with the vessel. The plasmas were much improved by the use of a conducting shell to reduce the major radius shift of the plasma, and the use of limiters to control the plasma-surface interaction.

These early developments were crucial. In a sequence of experiments carried out under the leadership of Artsimovitch, the impurity problem was largely overcome and the work culminated in the achievement of plasmas with temperatures approaching 1 keV. Since the temperatures were derived from indirect measurements, there were uncertainties. These were removed when experimentalists from the United Kingdom confirmed the electron temperatures using Thomson scattering.

This was a turning point in both fusion and tokamak research. The conviction that the tokamak offered the best way forward rapidly spread around the world. Since then there has been an increasing

concentration on tokamak research which has led to a large scale world-wide programme.

The improvement in confinement has mainly been due to increased size with the best energy confinement time in each device being given approximately by  $\tau_E = \frac{1}{2}r_p^2$  where  $r_p$  is the average poloidal radius. However, these best confinement times have only been possible through the introduction of various control techniques and methods of cleaning and conditioning the vacuum vessel. Other developments were the use of continuous gas feed, the injection of solid deuterium pellets, and the use of low atomic number materials, such as carbon, for the limiter.

Methods of heating the plasma have been developed to raise the temperature from its ohmic heating values of  $\sim 1$  keV and, using a neutral beam injection and ion cyclotron heating, progressively higher temperatures have been reached. It is now possible to obtain ion temperatures in excess of the 10–20 keV required for a reactor.

The following sections of this chapter describe the contributions made by small and medium sized tokamaks. The next chapter gives an account of the results obtained from the four large tokamaks which have brought plasma parameters close to those needed in a reactor.

## 11.2

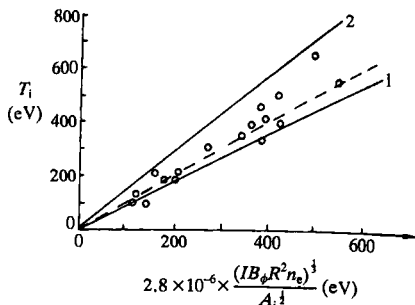
### T-3—Kurchatov Institute, Moscow, USSR

Tokamak-3 was the largest of a series of such devices, built at the Kurchatov Institute in the 1960s, which established the tokamak as the leading contender for a thermonuclear confinement system. Its main features were an iron transformer core, a vacuum system with a bakeable stainless-steel wall, a limiting aperture made of refractory metal, and a thick copper shell.

T-3 and similar devices were first used to explore the conditions necessary to obtain stable operation without excessive interaction with the vacuum vessel walls. A high degree of cleanliness of the vacuum wall was required. This was achieved by baking and conditioning by repetitive 'training discharges', now referred to as discharge cleaning. In addition the theory and practice of controlling the plasma equilibrium, using the copper shell plus applied vertical fields, allowed the discharge to be accurately centred in the limiter aperture; thus minimizing impurity release by plasma-wall interaction. The performance of the discharge was monitored by measuring its electrical resistance, an approximate indication of the mean temperature.

In the best discharges, this so-called conductivity temperature reached values of  $\sim 100$  eV. However, gradually improving diagnostic techniques demonstrated that this was a considerable underestimate of the

**Fig. 11.2.1** A comparison of the ion temperatures measured in various tokamaks with theory. This assumes that the ions are heated by collisions with much hotter electrons and lose energy by thermal conduction, calculated from the neoclassical theory of Galeev and Sagdeev. Line 1 is for flat profiles of plasma current and temperature and line 2 for parabolic profiles. The best fit to the experimental points, shown by the dashed line and by the formula on the abscissa, is called Artsimovich's scaling law. (Artsimovich, L.A. *Nuclear Fusion* 12, 215 (1972).)



temperatures achieved. Among these techniques, pioneered of T-3 and other devices at the Kurchatov, were the measurement of plasma diamagnetism, giving the total energy content of the discharge, the analysis of energetic neutrals produced by charge-exchange reactions, the detection of neutrons from thermonuclear reactions, and the measurement of electron temperatures by Thomson scattering of laser light. These measurements all showed that the tokamak was capable of confining plasma at temperatures of order 1 keV and stimulated the world-wide expansion of tokamak research from 1970 to the present.

The variation of the ion temperature as a function of the plasma density, current, toroidal field, and ion mass could be explained by a balance between collisional energy transfer from the electrons and ion conduction losses calculated using the newly developed neoclassical theory (Artsimovich scaling, Fig. 11.2.1). The electron losses, however, were anomalously high; a problem which is incompletely understood today. They were shown to decrease with increasing density, poloidal field, and minor radius (Mirnov scaling). Studies of particle confinement were also made by the then novel technique of measuring the plasma response to a puff of gas introduced at the discharge boundary.

## 11.3

ST—Princeton Plasma Physics Laboratory, USA

After encouraging results on the T-3 tokamak the model-C stellarator was converted to a tokamak. It featured a rather high aspect-ratio of approximately 10.

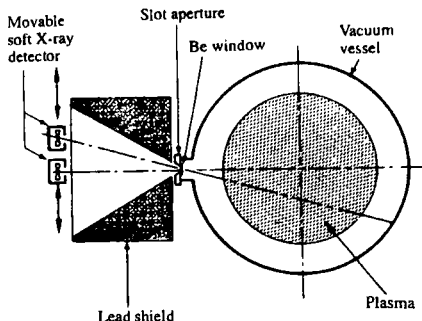
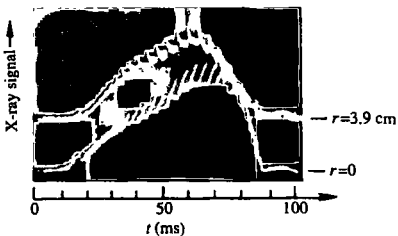


**Fig. 11.3.1** Sawtooth oscillations in the soft X-ray emission from the ST tokamak measured across various chords with collimated detectors. The emission is a sensitive function of the maximum electron temperature on each chord. The rapid collapse of the central chord signal and the increase at larger radii indicates a sudden outflow of energy. On some traces growing precursor oscillations can be seen. The instability is associated with a fall of the safety factor below unity in the centre of the plasma column. (von Goeler, S. et al. *Physical Review Letters* 33, 1201 (1974).)



Initial experiments concentrated on confirming the high values of central electron temperature measured on T-3 using Thomson scattering of ruby laser light. The temperature profiles on ST were considerably narrower than those on T-3. This is now understood in terms of stronger edge cooling by radiation from impurities with low atomic number, such as oxygen, in the relatively less well conditioned vacuum vessel. The value of  $Z_{eff}$ , the measured plasma resistance enhancement over the Spitzer value for a pure hydrogen plasma, was  $\sim 5$  in some discharges. Detailed spectroscopic studies of impurity content showed that this could be explained by the presence of highly stripped impurity ions, approximately in coronal equilibrium with the electrons.

Studies of the disruptive instability showed that it was preceded by the growth of an MHD mode rotating in the direction of electron diamagnetic drift and that it could be provoked by a puff of impurity gas, such as air.

A flattening of the electron temperature profile was observed and, on the assumption  $j \sim T_e^{3/2}$ , this appeared to correspond with a reduction of the central value of  $q$  to unity. The nature of the instability responsible

for this effect was revealed when measurements were made in the soft X-ray region of the radiated spectrum ( $h\nu \sim 1 - 10$  keV). An internal 'disruption' or 'sawtooth' relaxation was observed which caused a rapid flattening of the temperature in the central region in a time of  $\sim 10\mu s$ , repeating at intervals of about 1 ms (Fig. 11.3.1). The precursors to this disruption were also observed to have a poloidal mode number of unity, confirming the correspondence with the  $q = 1$  surface.

The first direct measurements of the local potential of the plasma were made on ST using a high energy thallium ion beam. The escaping ions which had been ionized from  $\text{Th}^+$  to  $\text{Th}^{++}$  suffered a measurable change in energy which could be related to the local space potential, where the incoming and outgoing orbits crossed. The intensity of the escaping beam could also be used to measure a local value of the electron density. This diagnostic showed the discharge centre to be several hundred volts negative with respect to the walls.

## 11.4

### JFT-2—Japanese Atomic Energy Research Institute, Tokyo, Japan

The design of Jaeri Fusion Torus 2 was based on the scalings for ion temperature and confinement time obtained on the T-3 and TM-3 tokamaks at the Kurchatov Institute. Thus the aspect-ratio was low in order to maximize the plasma radius and the plasma current. Great attention was given to removing impurities from the vacuum vessel by baking and discharge conditioning. These efforts were rewarded by exceptionally good values of the energy confinement time, up to 15 ms, and low effective ion charge and plasma resistance.

The importance of the plasma boundary conditions was recognized and experiments to measure and to change the plasma-limiter interaction were devised. An attempt was made to detach the limiters from the plasma by rapidly withdrawing them. However, it proved difficult to move the limiters faster than the plasma boundary expanded by diffusion, and the results were inconclusive.

Measurements were made using Langmuir probes in the scrape-off layer which is the relatively thin shell of plasma on magnetic surfaces which intersect the limiter. The radial decay lengths of the plasma density and temperature in this region provide information on heat and particle transport perpendicular and parallel to the magnetic field. The diffusion coefficient was shown to be comparable with the so-called Bohm value ( $D_B = T(eV)/16B$ ). This result has since been confirmed on several other devices with poloidal limiters. The probe measurements also allowed estimates to be made of the particle fluxes to the limiters and hence the particle confinement times independently of the usual spectroscopic methods.

## 11.5

### Alcator A, Alcator C, and Alcator C-Mod—Massachusetts Institute of Technology, Cambridge, USA

The Alcator series of tokamaks features very high values of the toroidal field, exploiting the technology of high field magnets developed at MIT. This allows impressive values of the plasma pressure to be obtained at relatively low  $\beta$ , even without additional heating.

In Alcator-A, with  $B_\phi$  up to 10 T and  $R = 0.54$  m, the plasma current density (proportional to  $B_\phi/R$  at constant  $q$ ), was an order of magnitude larger than in conventional tokamaks. Since it is found experimentally that the plasma density which can be achieved is proportional to the current density, discharges with a wide range of densities up to  $10^{21} \text{ m}^{-3}$  could be produced. The energy containment time was found to increase almost linearly with the plasma density over more than a factor of ten, a scaling which is now called Alcator scaling (Fig. 11.5.1).

At the highest densities classical electron-ion equipartition is strong enough to equalize the electron and ion temperatures and the major energy loss from the centre is due to neoclassical ion heat conduction rather than electron conduction. The discharge becomes almost impermeable to neutrals so that the rate of ionization at the centre due to gas feed at the boundary is very small. In spite of this, centrally peaked density profiles were found, implying substantial inward convection of plasma comparable to, or larger than, the neoclassical pinch effect.

At low density, where the electron drift velocity is an appreciable fraction of the thermal velocity, the discharge behaviour changed. The electron distribution function was found to be strongly distorted and anomalous electron-ion coupling was observed. This regime is called 'slideaway' to distinguish it from a 'runaway' discharge in which the plasma current may be carried by a small number of very energetic electrons.

In the somewhat larger Alcator-C tokamak the toroidal field was even higher, up to 12 T. At first it was found that the energy confinement time did not continue to increase with density, but 'saturated' at relatively low values. This effect was observed on other devices and was ascribed to neoclassical ion losses, which increase with density. Sometimes these had to be multiplied by a factor of several times to fit the results, and later results indicated that ion transport is also anomalous with a thermal conduction coefficient similar in magnitude to that for electrons.

Experiments using injection of solid deuterium pellets which can penetrate to the discharge centre showed that more peaked density profiles can be recovered by using this technique. In these discharges the energy confinement time was improved and values of  $n_{TE} \sim 10^{20} \text{ m}^{-3} \text{ s}$  were achieved.

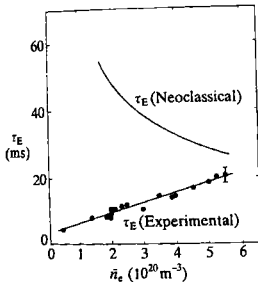


Fig. 11.5.1 Comparison of the observed confinement time with neoclassical theory for an ohmically heated discharge in Alcator. (Gondhalekar, A. et al. *Proceedings of 7th I.A.E.A. International Conference*, Innsbruck, 1978, Vol. 1, 199. I.A.E.A., Vienna (1979).)

### Alcator C-mod

Alcator C-Mod was first operated in 1993. It is a compact high-field tokamak with a closed divertor and capabilities for strong plasma shaping. Research is centred on the following areas. (1) Transport studies on C-Mod provide tests of theoretically based interpretations and empirical scalings at unique plasma parameters. (2) Divertor studies with high-scrape-off layer power density and high divertor plasma density. (3) Ion-cyclotron radio frequency power is used for the investigation of wave absorption, parasitic losses, and mode conversion processes. (4) Mhd studies focusing on disruption effects and mitigation.

C-Mod has a major radius of 0.68 m and a minor radius of 0.22 m. The toroidal field ranges from 2.6 to 8.0 T and plasma current from 0.4 to 1.5 MA. The high current density allows operation at high plasma density, and line averaged densities of  $1.2 \times 10^{21} \text{ m}^{-3}$  have been reached. The auxiliary heating method is ICRF, employing hydrogen minority in deuterium plasmas at  $B_\phi = 5.3$  T as the principal scenario. Up to 5 MW of RF power have been coupled to the plasma. The first wall is fabricated with molybdenum tiles and is designed to take the very high power loadings which occur in this experiment. H-modes are easily obtained with both ohmic and RF heating, and over a wide range of plasma conditions.

A new H-mode has been discovered and studied. Called EDA for Enhanced D-Alpha H-mode it combines good energy confinement with moderate particle transport, avoiding impurity concentration. There are no large ELMs, the H-mode edge gradients apparently being relaxed by a continuous mode localized in the pedestal region. Ion temperature profiles show 'self-similarity' in both L-mode and H-mode,  $T/\text{grad}T$  being approximately constant, consistent with transport models featuring a sharp increase in turbulence when the temperature gradient length drops below a critical value. The formation of internal transport barriers has been observed under a variety of conditions. Their formation produces strongly peaked density profiles, with a minimum in the density scale-length occurring near  $r/a = 0.5$ , and significantly reduced transport in the core region.

In divertor operation three regimes of transport along the magnetic field have been identified—sheath limited, conduction limited with the formation of temperature gradients along the field lines, and the detached divertor plasma with pressure drop along the field. In moderate and low-density discharges the scrape-off layer exhibits a two-layer structure with a steep profile near the separatrix and a flat profile further out. Figure 11.5.2 gives typical temperature and pressure profiles across the flux surfaces measured simultaneously at the outer divertor target plate and a position upstream of the outer divertor. As the plasma density is increased the electron temperature gradients along the field lines increase, being highest near the separatrix. At high plasma density the electron temperature at the divertor target can be reduced to a few eV. Under those conditions ion-neutral collisions remove momentum lowering the electron pressure at the target plate. This 'detached' plasma region develops first near the divertor strike-point location and significantly reduces the

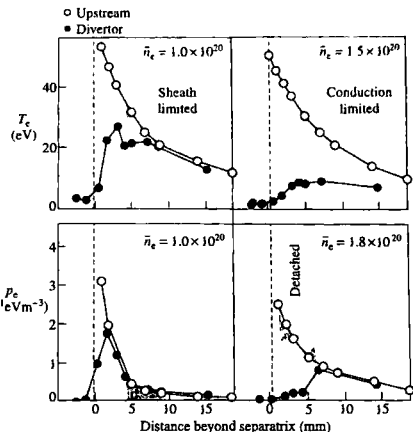


Fig. 11.5.2 Showing the change in electron temperature and pressure profiles with increased plasma density. The profiles are measured across the flux surfaces near the separatrix both upstream and at the divertor.

peak heat flux onto the divertor target. The cross-field transport in the outer zone occurs largely through intermittent bursts. Radially correlated structures extending to the outer wall are seen in the video images of the plasma turbulence. As a result of the rapid cross-field particle transport in this zone, operation is predominantly in the 'main chamber recycling regime' where particle fluxes to main chamber surfaces are large compared to the particle flow along field lines to the divertor. At densities approaching the density limit the zone of bursty cross-field transport is found to extend inside the closed surfaces, indicating a possible role in determining the density limit.

Virtually all disruptions in Alcator C-Mod are either caused by, or result in, fast vertical displacement of the plasma, eventually terminating in contact with internal hardware at the top or bottom of the vacuum vessel. Spatially resolved measurements of the halo currents reveal significant toroidal asymmetry, usually an  $n = 1$  component superimposed on an  $n = 0$  background with comparable amplitudes.

## 11.6

### TFR—Commission d'Energie Atomique, Fenteenay-aux-Roses, France

The first embodiment of the tokamak at Fontenay-aux-Roses, TFR-400 was built along the classical lines developed at the Kurchatov Institute. It was of a similar size to T-4 but with a toroidal magnetic field of 6.0 T.

This allowed plasma currents up to 400 kA to be used, making it for some time the most powerful tokamak in the world.

Initial experiments at relatively low density produced large fluxes, of runaway electrons. Measurements of the radioactivity induced in the limiter by photonuclear processes showed that electrons with energies up to 17 MeV must have been confined.

Plasma heating by up to 1 MW of neutral beam injection at a small angle to the major radius was used. This is an efficient method of heating, provided the plasma density and current are high enough to prevent shine-through of the injected beam and losses of fast ions on banana orbits. Ion temperatures up to 1.8 keV were achieved and studies of the ion energy balance indicated thermal conduction coefficients several times higher than the neoclassical values.

A major modification to the experiment, renamed TFR-600, involved the removal of the copper shell and the installation of a larger, high resistance vacuum vessel made of inconel. Plasma equilibrium was maintained by a fast feed-back system for the vertical field. The use of discharge cleaning in addition to baking of the vacuum vessel, which had been the main method of conditioning on TFR-400, resulted in cleaner, higher density plasma.

An intensive programme was undertaken to develop ion cyclotron resonance (ICRH) as a heating method for tokamak plasmas. The relatively large space between the limiters and the vacuum vessel allowed antennas of increasing sophistication to be installed. However, there appear to be some residual problems with impurity generation due to heating of the plasma near the antenna-plasma interface, where coupling of electromagnetic energy into plasma waves takes place.

ICRH has a tendency to produce ions with high perpendicular velocity, trapped in mirrors produced by individual toroidal field coils which then escape by drifting vertically. These were detected on TFR using specially designed Faraday cups. Similar effects are produced by resonance with impurity ions, which in principle provides a method for selective impurity transport, albeit at the expense of considerable power.

## 11.7

### DITE—Culham Laboratory, Abingdon, UK

DITE stands for Divertor Injection Tokamak Experiment, which describes its main features. It was a medium-sized device equipped with a unique 'bundle divertor' and with plasma heating by tangential neutral beam injection.

The divertor action was produced by two small coils designed to make a localized loop in the toroidal field near the outside edge of the discharge. Only a part of the toroidal flux was diverted by this means, forming a

tube of field lines which is referred to as the diverted flux bundle. The rotational transform produced by the plasma current connects the diverted flux bundle to an annular region around the central part of the discharge, which is relatively unaffected by the short-range divertor field.

Observations of plasma and energy exhaust through the divertor, and of a reduction in contamination of the discharge by metallic impurities from the wall were made, demonstrating the main divertor functions for this configuration.

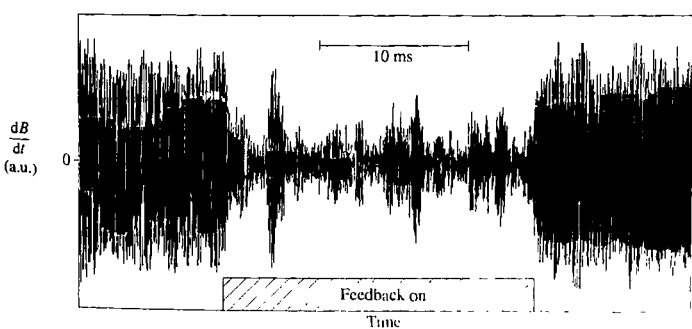
Studies of confinement and neutral beam injection in non-diverted discharges were also made. For much of this work the torus was gettered with evaporated titanium to reduce contamination by low atomic number impurities such as oxygen. This allowed higher current ( $q_a \sim 2$ ) and higher densities to be achieved, especially when combined with neutral beam injection.

The maximum density could not be extended indefinitely by increasing the power input to the discharge and could be represented by the formula  $M q_a \leq 20 \text{ m}^{-2} T^{-1}$ , where  $M = (\bar{n}_e / 10^{19}) R / B_\phi$  is the Murakami parameter. This formula implies a linear increase of the number of particles per unit length of the discharge with plasma current, independent of the toroidal field.

Tangential neutral beam injection gives rise to a circulating current of fast ions which can be used to aid or oppose the plasma current. This effect, predicted by Ohkawa, was demonstrated on DITE using  $\sim 1 \text{ MW}$  of 25 keV hydrogen beams injected into target plasmas of deuterium and helium.

Magnetic feedback was used to explore the stabilization of disruptions, and experiments demonstrated a substantial reduction of the saturated level of  $m = 2$  tearing mode as shown in Fig. 11.7.1. The feedback loop used 32 pick-up coils and fed stabilizing currents to eight saddle coils placed inside the vacuum vessel. This system also allowed the investigation of other features of MHD stability by the imposition of controlled magnetic perturbations.

**Fig. 11.7.1** Showing the reduction in the  $m = 2$  component of the magnetic field fluctuations in DITE on the application of feedback control. The bursts of increased signal during the stabilized period are coincident with sawteeth.



**11.8****PLT—Princeton Plasma Physics Laboratory, USA**

Following the successful operation of smaller tokamaks in the early 1970s, a second generation of larger devices was built of which the first were the T-10 tokamak and the Princeton Large Torus. The approximately two-fold increase in linear dimensions increased the energy confinement time from a maximum of  $\sim 25$  ms to  $\sim 100$  ms, the scaling expected from diffusive loss processes. The plasma current was also increased to more than 0.5 MA.

The plasma temperature achieved by ohmic heating alone was not substantially higher than that obtained in smaller tokamaks. However, the relatively good access to the torus allowed more than 2 MW of tangential neutral beam heating to be applied. When the plasma density and impurity content were held down by 'gettering' the torus with titanium, the additional heating raised the ion temperature to record values of 7 keV. The corresponding value of the ion collisionality parameter, the number of collisions during a trapped ion orbit, is comparable to that required for a reactor.

The momentum input due to neutral beam injection caused plasma rotation in the toroidal direction at velocities of typically  $10^5$  ms $^{-1}$ . Measurements of the Doppler shift of spectral lines due to various impurities give the radial profile of the toroidal velocity and hence the damping due to viscosity. The momentum damping time was measured to be  $\sim 20$  ms at the centre of the discharge. As with particle and energy confinement, this is much shorter than can be explained by classical collisional processes.

Plasma heating at the lower hybrid frequency was also tried. Here, the heating is less efficient. However, using LH waves propagating in the toroidal direction, it was possible to sustain plasma currents of  $\sim 300$  kA for several seconds, demonstrating the principle of a DC tokamak. The current was carried by electrons of several times 100 keV energy, whose velocity matched that of the wave. The process by which thermal electrons achieved these energies was then not understood.

**11.9****T-10—Kurchatov Institute, Moscow, USSR**

Tokamak-10 is of conventional design with a modest aspect-ratio. The main programme of work has been a study of transport processes, with the emphasis on ohmically heated discharges.

The particle transport has been extensively studied by a variety of techniques, following work on the earlier T-3 and T-4 tokamaks. A multi-chord microwave interferometer was used to study the transient response to a change in the particle source term produced by suddenly increasing, decreasing, or modulating the gas feed to the discharge. Analysis of this response allows the variation of the mean fluid velocity with radius to be found. It can be modelled by a combination of diffusion and inward convection. Similar results have been obtained for the transport of impurity ions. In this case small quantities of gaseous or solid impurities which do not occur naturally were injected into the discharge. Their subsequent transport was studied by spectroscopic methods.

Using powerful gyrotron oscillators, up to 1 MW of power has been applied at the electron cyclotron resonance frequency. The central electron temperature increases from 1.4 to 4 keV, while the change in ion temperature is consistent with electron-ion energy transfer by Coulomb collisions. The slight decrease in global energy confinement can be explained by an electron thermal conductivity which is proportional to  $\sqrt{T_e}$ .

The localized heating which can be applied at the electron cyclotron resonance frequency allows appreciable modification of the electron temperature profile. This in turn leads to a redistribution of the plasma current and to changes in the mhd stability of the discharge. For example, by applying localized heating near or just outside the magnetic surfaces where  $q = 1$  and  $q = 2$ , the sawtooth oscillation and the  $m = 2, n = 1$  tearing mode instabilities are suppressed. Since the latter mode is almost always observed as a precursor to a major disruption, the most dangerous form of tokamak instability, this result offers the potential for its control.

More recent work has focussed on the use of electron cyclotron wave current drive for modifying the current profile and also driving a substantial fraction of the plasma current non-inductively. It is less efficient than using lower hybrid waves but has much greater potential for application to reactor-scale devices. The programme on T-10 contributed very significantly to the development of powerful gyrotron sources for fusion application.

## 11.10

### ISX—Oak Ridge National Laboratory, USA

The Impurity Study Experiment was built as a successor to the successful ORMAK (Oak Ridge Tokamak).

Studies of the energy confinement time as a function of density provided the first clear demonstration of a saturation or decrease of global confinement at high density, which was attributed to the increasing importance of neoclassical ion conduction losses.

The second assembly, ISX-B, allowed discharge cross-sections of vertically elongated form and was equipped with tangential neutral beam injection at a power level up to 2.5 MW, and later with electron cyclotron resonance heating. In addition to impurity transport, ion and electron heating, and energy and momentum confinement were studied.

The large power to volume ratio allowed record values of toroidal  $\beta$  of  $\sim 2.5\%$  to be achieved early in the programme. However, it was soon realized that a 'soft'  $\beta$  limit occurs which can be expressed as a degradation of the confinement time as the power input increases. This effect is ascribed to pressure-driven mhd instabilities and is correlated with increased fluctuations of the magnetic field measured at the discharge boundary.

The decrease in confinement time observed with neutral beam heating is not due to toroidal rotation. This is clear from observations with co-injection plus counter-injection in which the toroidal rotation is small but the degradation of confinement is still present.

## 11.11

### FT and FT Upgrade—Centro Ricerche Energia, ENEA, Frascati, Italy

The Frascati Tokamak, FT, was designed for operation at toroidal fields of up to 10 T. In this respect it was similar to the Alcator tokamaks at MIT, though somewhat larger. As a consequence of the high field the ohmic power density was relatively high, allowing operation at high plasma density.

The dependence of the plasma parameters on density in ohmically heated discharges has been a subject of particular study. The constancy of the loop voltage suggested a scaling for the electron energy confinement of the form given by Coppi and Mazzucato. Comparison with the smaller Alcator-A tokamak shows that the confinement time increases with at least the square of the linear dimensions and confirms that, at high density, the losses from the discharge centre can be entirely accounted for by neoclassical ion conduction.

At low density, the central electron temperature was increased by about 700 eV using lower hybrid wave heating at 2.45 GHz. The electron heating efficiency dropped sharply as the density was increased and the RF power was absorbed by hydrogen ions.

#### FT upgrade

The very good confinement obtained in relatively small, high field tokamaks led to the construction of Frascati Tokamak Upgrade with a minor radius of 0.3 m and a major radius of 0.93 m. The machine operates up to the design parameters of 8 T toroidal magnetic field and

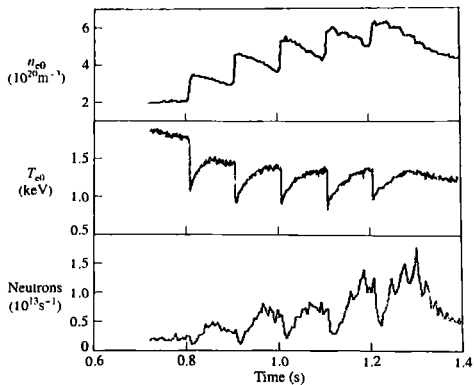


**Fig. 11.11.1** Five pellets injected at 100 ms intervals raise the central electron density to  $6 \times 10^{20} \text{ m}^{-3}$ , while the electron temperature periodically recovers with an increasing neutron yield. (Frignani, D. et al. *Nuclear Fusion* 41, 1613 (2001).)

1.6 MA plasma current, and at high density. A high-speed multiple pellet injection system which injects up to eight pellets at  $1.3 \text{ km s}^{-1}$  has allowed the achievement of a quasi-steady state lasting a few energy confinement times and improved confinement properties with  $\tau_E \approx 100 \text{ ms}$ , which is 1.7 times  $\tau_{\text{ITER-89P}}$ . These discharges have peaked density profiles with a central electron density up to  $8 \times 10^{20} \text{ m}^{-3}$ , equal ion and electron temperatures of 1.5 keV, and  $Z_{\text{eff}}$  down to 1.3. An example is shown in Fig. 11.11.1. Transport analysis shows that in the post-pellet phase the core electron thermal diffusivity is substantially reduced, with  $\chi_e < 0.1 \text{ m}^2 \text{s}^{-1}$ , and the transport, which is dominated by the ion channel, drops to neoclassical levels. The resulting values of the fusion product,  $n \tau_E T_i$ , are around  $10^{20} \text{ m}^{-3} \text{ keVs}$ .

Various RF heating schemes are installed and applied at magnetic fields between 5 and 8 T. The 8 GHz lower hybrid system with a pulse length of 1 s and power up to 3 MW has been used for current drive and plasma heating in various conditions including relatively high density, high field plasmas with  $n = 1.2 \times 10^{20} \text{ m}^{-3}$  at a toroidal field of 7.9 T. The density dependence of the efficiency is in agreement with theory.

At 5 T, stabilization of tearing modes has been obtained using 140 GHz ECRH with powers up to 1.6 MW with a subsequent improvement of the energy confinement. Electron temperatures up to 14 keV have been obtained at a density  $5 \times 10^{19} \text{ m}^{-3}$  using ECRH during the current ramp. Ion Bernstein wave injection at 433 MHz has produced a reduction of the electron thermal conductivity in the region inside the absorption radius possibly due to the formation of an internal transport barrier.

Synergy studies have been performed with simultaneous injection of lower hybrid and ICRH waves well above the electron cyclotron resonance with a toroidal field of 7.2 T. Evidence has been obtained of ECRH wave absorption by the electron tails produced by the lower hybrid waves.

## 11.12

### Doublet-III—General Atomic Company, San Diego, USA

The name of this experiment refers to the proposed shape of the plasma cross-section which originally was designed to take the form of two pear shaped lobes joined by a narrow waist. This had a large peripheral length which allowed a very small effective aspect-ratio. The advantages are a high current capability with a modest toroidal field and hence operation at high  $\beta$ .

The flexibility of the poloidal field allowed the ellipticity and triangularity of the discharge cross-section to be varied over wide ranges, the main interest being in the effects of these changes on the stability and confinement properties. It also allowed several divertor-like configurations to be produced with a poloidal field null-point near the waist in the vacuum vessel. These proved surprisingly effective in preventing recycled neutrals and impurities from entering the main discharge, in spite of the relatively large aperture of the vacuum vessel at the waist. This is explained by the large thickness of plasma in the region of poloidal flux stagnation which provides an effective barrier to recycling impurities.

The installation of up to 7 MW of additional heating by neutral beam injection allowed the effects of ellipticity and triangularity on the maximum  $\beta$  to be explored. In general good agreement with the ideal theory of kink and ballooning modes was found. The maximum  $\beta$ -value obtained was 4.5%, in the range required for an economic fusion reactor.

Approximately 1 MW of electron cyclotron resonance heating was also used. The same reduction in confinement time was obtained as with neutral beam injection at the same power level, strongly suggesting that this is a property of the discharge rather than the method of heating.

## 11.13

### ASDEX—Max-Planck Institut für Plasmaphysik, Garching, Germany

The Axial Symmetric Divertor Experiment, ASDEX, was operated from 1980 to 1990. The divertor field was produced by multiple coils, parallel to the plasma current, positioned at the top and bottom of the discharge

This gives rise to a separatrix which limits the plasma and avoids the direct plasma contact with material surfaces. Both double-null and single-null operation was possible, the cross-section inside the separatrix being nearly circular.

The heating was by NBI, ICRH, and LH. The NBI power was up to 4.5 MW, the ICRH supplied 3 MW to the plasma and the lower hybrid system provided initially 1.5 MV at 1.3 GHz and later 2 MW at 2.45 GHz.

In very clean plasmas the ohmic energy confinement time saturated at densities greater than  $3 \times 10^{19} \text{ m}^{-3}$ , but this saturation could be overcome in so-called IOC (Improved Ohmic Confinement) discharges which had low-Z impurity radiation from the plasma edge with associated peaked density profiles. The level of saturated ohmic confinement in clean plasmas was dependent on the isotope mass, deuterium having better confinement than hydrogen.

Auxiliary heating led to the expected degradation of confinement but in 1982 a regime of improved, or H-mode, confinement was discovered. This was first observed in a single-null discharge with the ion grad-B drift toward the X-point and a heating power of 3 MW. The improvement in confinement was a factor of two above the previous, L-mode, results. Figure 11.13.1 shows the response of the electron temperature to the application of NBI for an H-mode as compared with an L-mode. The H-mode was subsequently obtained using ICRH.

The H-mode was subject to a power of 1 MW with a single-null and 1.8 MW with a double-null. The threshold was typically increased by a factor of two when the ion grad-B drift was directed away from the X-point in the single-null configuration, or when the H-mode was operated in hydrogen rather than deuterium plasmas. Additionally the H-mode required an electron density above around  $2-3 \times 10^{19} \text{ m}^{-3}$ . It was found that the H-mode is associated with an edge transport barrier inside the separatrix, leading to steep gradients in density and temperature. The density fluctuations were strongly reduced in this region. A new instability appeared in the H-mode and was termed the ELM (Edge Localized Mode). The H-mode is further discussed in Section 4.13 and ELMs in Section 7.17. The H-mode has become a central feature of fusion research and is now reproduced on a regular basis in other tokamaks.

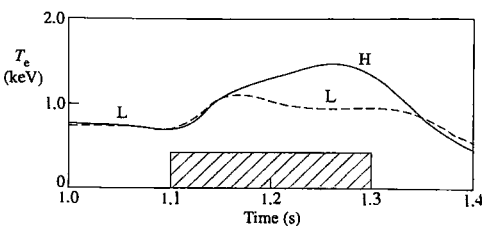


**Fig. 11.13.1** Time dependence of central electron temperature for L and H discharges. The neutral injection heating phase is indicated by the hatched time interval. (Wagner, F., et al. *Physical Review Letters* 49, 1408 (1982).)

Stationary non-inductive currents up to 480 kA were driven using lower hybrid waves, the efficiency agreeing well with theory. The current profile depends upon the wavenumber spectrum ( $n_{\parallel} = k_{\parallel}c/\omega$ ) and is different from the ohmic current profile. It was possible therefore to modify the current profile and in particular to flatten it in the central region. This led to  $q_0 > 1$  with a consequent stabilization of sawtooth oscillations and a strong central electron heating with  $T_e$  up to 8 keV.

The disruption density limit was highest for values of  $q_{\text{cyl}}$  below 2 and could be further increased by NBI heating and pellet injection. Clear evidence was found that the density limit occurs at radiation power levels below the input power.

With the closed divertor configuration, reliable and flexible plasma operation with good confinement and low impurity levels was possible. When, for a time, bypasses for neutral gas from the divertor to the main chamber were introduced, it was found that access to the H-mode was severely restricted and the quality of the H-mode was reduced.

The power loading to the divertor plates had an imbalance between the outer and inner separatrices. Under L-confinement the asymmetry ratio was typically 3 or 4 to 1, but when the grad- $B$  drift was away from the X-point the ratio fell to 2:1, and with counter injection to nearly 1:1. From 20% to 65% of the power entering the scrape-off-layer,  $P_{\text{sol}}$ , could be dissipated in the divertor through the volume-loss processes of radiation and charge-exchange, the larger values being associated with higher density and lower isotope mass.

In the latter phase of ASDEX, when systematic investigations of the divertor plasma were carried out using a reciprocating Langmuir probe, the width of the power-carrying layer in the divertor, an important parameter in determining the power flux at the target plate, was found to scale as  $T_{\text{ed}}^{-0.6} q_a^{0.5}$  with a range of 1–4 cm,  $T_{\text{ed}}$  being the peak electron temperature in the divertor. For moderate  $q_a$  and conditions far from the density limit the width was typically 1 cm.

At the density limit the values of  $T_{\text{ed}}$  were in the vicinity of 5–7 eV. The edge density limit could be raised with heating power, roughly as  $P_{\text{sol}}^{0.5}$ , such that at maximum heating the peak density in the divertor,  $n_{\text{ed}}$ , could be driven to near  $1 \times 10^{20} \text{ m}^{-3}$  before a disruption occurred.

For ohmic and L-confinement plasmas,  $n_{\text{ed}}$  was related to the mid-plane separatrix density  $n_{\text{es}}$  as  $n_{\text{ed}} \sim n_{\text{es}}^{1.7}$ , whereas  $T_{\text{ed}} \sim n_{\text{es}}^{-0.8} P_{\text{sol}}^{0.6}$ . Since the line density of the divertor plasma never significantly exceeded  $2 \times 10^{18} \text{ m}^{-2}$ , neutrals could penetrate this plasma, thereby limiting access to the high recycling regime to plasmas with strong additional heating. Thus,  $n_{\text{ed}}$  was generally only marginally in excess of  $n_{\text{es}}$ .

The scrape-off layer/divertor-parameters appear to be consistent with classical heat transport along the magnetic field. The perpendicular transport was anomalous with typical coefficients  $D \sim 0.5\text{--}1.0 \text{ m}^2\text{s}^{-1}$  and  $\chi_i \sim D \sim \chi_e/3$ .  $D$  is close to Bohm diffusion

in magnitude, but there is no convincing evidence that transport is indeed Bohm-like.

#### ASDEX upgrade

ASDEX Upgrade is the successor to the 'closed' divertor ASDEX experiment and was designed to develop a reactor-compatible open divertor configuration. The device is similar in size to ASDEX but has an elongated plasma and a larger current and toroidal magnetic field. Operation started in 1991. A full description is given in Section 12.6.

## 11.14

### TEXT—University of Texas, Austin, USA

The principal aim of the TEXT experiment was to advance the understanding of turbulence and transport through diagnostic development and the comparison of experiment with theory.

Comparison of the particle flux, determined from measurements of H <sub>$\alpha$</sub>  emission and the calculated flux expected from the turbulence measured with Langmuir probes, indicated that most, if not all, of the particle flux at the edge was driven by electrostatic turbulence. A large part of the total heat flux was carried by the resulting convective heat flow but generally the heat flux is less well accounted for by electrostatic perturbations. In the main plasma the fluctuations were found to decrease toward the plasma centre.

In an examination of the role of the radial electric field in determining the fluctuation level and hence confinement it was found that in the edge plasma the turbulent transport mechanisms are reduced due to the shear in the naturally occurring  $E \times B$  velocity.

The diffusion coefficient of runaway electrons was estimated by modifying the plasma equilibrium either with a simple shift of the plasma or by applying magnetic perturbations to ergodize the outer region. The response of the hard X-ray signal was interpreted using a diffusive model and gave a diffusion coefficient  $\sim 1 \text{ m}^2 \text{ s}^{-1}$ . A study was made of the modifications to transport resulting from the application of perturbing magnetic fields. A detailed comparison was made, both with numerical calculations using test particles, and with analytic models of transport in stochastic fields.

An investigation of the growth and saturation of  $m = 2$  tearing modes showed general agreement with Rutherford's model for the nonlinear growth of the magnetic island. Strong tearing mode instability was found to be associated with the absence of sawtooth oscillations and

this appeared to be due to the dependence of tearing mode stability on  $q(0)$ .

## 11.15

### TEXTOR—Forschungszentrum, Jülich, Germany

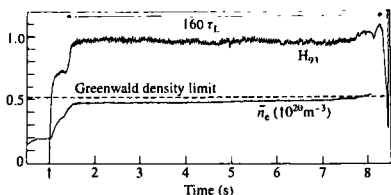
TEXTOR has been used for research into the deposition of low Z materials on to plasma facing surfaces, and this work has been influential in the move to the use of such materials in other tokamaks. The initial experiments introduced carbonization, a technique in which carbon is deposited over the entire inner wall by means of a flow of methane ( $\text{CH}_4$  or  $\text{CD}_4$ ) into a radio-frequency assisted, DC glow discharge. This procedure led to a significant improvement in performance, with an increase of 50% in the density limit. The impurity release from the walls during discharges was greatly reduced, with reduction factors of 5–8 for oxygen and 10–20 for metals. In further experiments boronization and siliconization were used, leading to lower oxygen and carbon contamination.

The careful measurement of the  $q$ -profile on TEXTOR using Faraday rotation had a crucial impact on the analysis of sawtooth oscillations. Theoretical models predicted that after a sawtooth collapse the central value of  $q$  would be close to one. The experimental measurement showed that  $q_0$  remained well below one throughout the sawtooth cycle as described in Section 7.6.

A concept introduced and studied experimentally on TEXTOR is that of the pump limiter. Such a limiter presents a wedge shape to the scrape-off layer, the near face of the wedge leading to a pump. This allows improved control of the density and the study of the exhaust of injected helium and gaseous impurities. The combined helium transport in the plasma core, in the boundary layer and in the pump limiter led to an overall dwell-time of helium of about ten energy confinement times a value just short enough to satisfy reactor requirements.

The problem of avoiding excessive heat loads at the leading edge of the pump limiter has been overcome by generating a cold radiative plasma boundary employing injected neon as radiating impurity. With a well controlled neon level, up to 90% of the total power has been radiated from the plasma boundary in stable and quasi-stationary discharges without degradation of energy confinement or helium exhaust efficiency. These radiatively cooled discharges led to the discovery of the Radiative Improved confinement mode (RI-mode). Figure 11.5.1 gives an example with a confinement quality of the ELM-free H-mode at a density near the Greenwald limit. This mode can be obtained at poloidal  $\beta$  up to 1.5 and

**Fig. 11.15.1** Temporal evolution of H-mode enhancement factor  $H_{93}$  and line averaged electron density  $\bar{n}_e$  in a long pulse RI-mode discharge in TEXTOR ( $I_p = 350\text{ kA}$ ,  $B_\phi = 2.25\text{ T}$ ,  $q_a = 3.8$ ,  $P_{\text{rad}}/P_{\text{tot}} = 70\%$ )



at edge  $q$  values down to 2.8. The radiated power fraction is typically in the range of 70–90% without signs of detrimental accumulation of the applied impurities in the core. Benefiting from the exhaust option due to the pump limiter, the RI-mode becomes stationary over the discharge duration of up to 10 seconds.

An experiment introduced into TEXTOR is the dynamic ergodic divertor which combines the conventional ergodic divertor with the rotation of the underlying perturbation field. The resulting increase of the electron density and the decrease of the electron temperature at the plasma boundary in conjunction with enhanced radial transport lead to improved radiation efficiency of impurities and better impurity screening. The rotation of the perturbation field was introduced because of the excessive heat load at the ‘footprints’ on the divertor plate. This increased the ‘wetted’ area by more than an order of magnitude.

## 11.16

### Tore Supra—CEA Cadarache, France

Tore Supra was built to investigate physics and technology issues related to steady-state plasmas. Its main features are (i) superconducting field coils cooled by superfluid helium at 1.8 K, (ii) actively cooled plasma facing components made of graphite and later of carbon fibre composite reinforced graphite elements, brazed on a metallic substrate cooled by a pressurized water loop, (iii) long pulse lower hybrid current drive (8 MW generator power), and ICRH (12 MW generator power). Particle injection involves a continuous pellet injector and supersonic gas injection. This machine was originally equipped with an ergodic divertor and a set of discrete limiters. These have now been replaced by a toroidal pump limiter with ability to deal with a high power density, raising the power handling capability to more than 20 MW in steady state.

The actively cooled plasma facing components which allow the extraction of heat in steady-state conditions have been successfully tested with the development of power density handling in the  $10\text{--}15 \text{ MW m}^{-2}$  range. Investigations have also been carried out to examine plasma-wall heat transfer both by plasma convection to limiters and by radiation. In the latter domain, promising results were obtained with the ergodic divertor which produces stable radiative layers at the expense of a modest core pollution. Additional beneficial effects are the particle screening in the ergodic field, and a higher radiation efficiency of impurity ions at the plasma edge. In addition to heat exhaust, particle exhaust schemes have been examined in limiter and divertor configurations. In all cases a significant particle exhaust (5–10% of the recycling flux) was obtained.

Lower hybrid waves (3.7 GHz) have been used to drive current and to modify the current profile. Discharges lasting 120 s were produced with a 0.8 MA current at a central electron density of  $2 \times 10^{19} \text{ m}^{-3}$  using 2.5 MW of lower hybrid waves. Results for the longest such plasma are shown in Fig. 11.16.1. The plasma was fully non-inductive for the first 180 s, when a drop in the Lower Hybrid power necessitated the reapplication of 0.1 V per turn. The behaviour of the fast electrons has been investigated, and it was found that their radial transport was slow compared to the collisional relaxation time.

The fast wave (48 MHz) has been successfully coupled to the electrons and the results were found to be in good agreement with theory. Strong central electron heating was observed and also a driven current (80 kA) when an appropriate phasing was applied. Scenarios have been tested in which up to 70% of the plasma current was bootstrap current.

The plasma stability and confinement can be enhanced using the various systems designed to control the plasma and its profiles. In many cases, current drive experiments increase the magnetic shear at the edge. This results in an improvement of the plasma confinement. Similarly shear

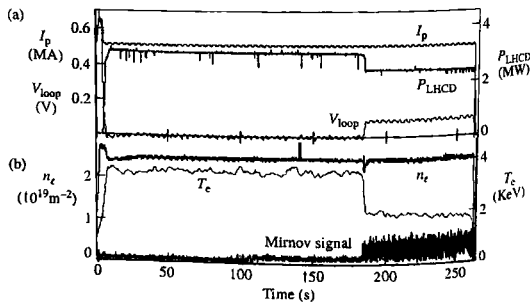


**Fig. 11.16.1** Tore-Supra discharge with a duration of 4 min 25 s in which 0.75 GJ was exhausted from the plasma. Time evolution of (a) plasma current, loop voltage, and LHCD power (b) central line integrated density, electron temperature at normalized radius 0.3 and the Mirnov coil signal.

cancellation or reversal close to the axis leads to improved plasma core performance.

The ergodic divertor stabilized the mhd activity around the  $q = 2$  surface, probably by expelling the current from the exterior. In addition a transport barrier (temperature pedestal), was observed between the ergodic zone and the plasma core. Whilst this was accompanied by a decrease of the turbulence, it is thought more likely that the barrier was caused by the inward drift associated with the strong radial gradient of the ergodic fields.

## 11.17

### COMPASS—UKAEA Culham Science Centre, Abingdon, UK

COMPASS (COMPAct ASSEMBly) started operation in 1989, and in 1992 there was a major upgrade when the circular vacuum vessel (COMPASS-C) was replaced by a D-shaped continuous inconel vessel (COMPASS-D). The programme has focused on addressing key issues for Next Step tokamaks, in particular the onset and control of performance limiting instabilities such as neoclassical tearing modes, the impact of error fields, disruption effects such as halo current generation and the characteristics of H-mode plasmas with strong electron heating.

COMPASS-D is equipped with 2 MW, 60 GHz electron-cyclotron heating and current drive together with 0.6 MW, 1.3 GHz lower hybrid current drive. The magnetic field system allows a range of plasma configurations to be established, including those foreseen in a burning plasma. It is also equipped with a saddle coil set which can be used to apply a wide range of helical resonant magnetic perturbations to the plasma.

Upon application of such resonant magnetic perturbations, it is observed that there is a sharp threshold amplitude above which large stationary magnetic islands are induced. This is consistent with a model in which a rotating plasma resists the penetration of the externally applied perturbation until the plasma velocity in the vicinity of the resonant surface is sufficiently reduced. This model allows the prediction of the effects of error fields in future large tokamaks and predicts a very low threshold for penetration in ITER.

Resonant magnetic perturbations have also been used to provide measurable and controllable 'seed islands' for neoclassical tearing mode growth in high beta electron-cyclotron heated plasmas. In this way the critical seed island size can be directly measured leading to increased understanding onset criteria. Furthermore, current profile control by lower hybrid current drive has been successfully used to fully stabilize neoclassical tearing modes, allowing higher beta. An example is shown in Fig. 11.17.1.

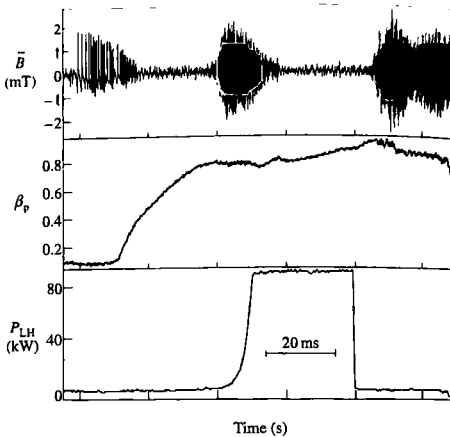


**Fig. 11.17.1** Stabilization of an  $m = 2$ ,  $n = 1$  neoclassical tearing mode by lower hybrid current drive in COMPASS-D: the traces show the mode activity as indicated by the fluctuating poloidal magnetic field, poloidal beta, and lower hybrid power (Warrick, C.D. et al. *Physical Review Letters* **85**, 574 (2000)).

H-mode access and confinement has been studied with and without electron-cyclotron heating which heat electrons, does not inject significant momentum, and does not contribute to fuelling. In these respects ECH has many similarities with alpha particle heating in a burning plasma. A comprehensive set of edge pedestal diagnostics has allowed a study of the evolution of key pedestal parameters, including plasma rotation and radial electric field, with a time resolution of 0.1–2 ms, and spatial resolution of 2–5 mm, giving information on the dynamics of the H-mode transition and the factors governing the power threshold. In particular, it has been demonstrated that the H-mode transition is not preceded by development of a large radial electric field,  $E_r$ , but rather that changes in  $E_r$  occur simultaneously with the development of the edge pedestal.

## 11.18

RTP—FOM Institute of Plasma Physics,  
Rijnhuizen, The Netherlands

The FOM Institute for plasma physics 'Rijnhuizen' operated the tokamak RTP (Rijnhuizen Tokamak Project) from 1989 to 1998. The main parameters of this device were major radius 0.72 m, minor radius 0.16 m, circular cross-section with a boronized vessel, a toroidal field on axis up to 2.4 T and a toroidal plasma current up to 120 kA. The research programme

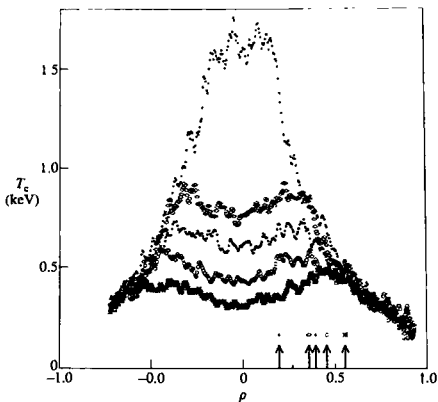


**Fig. 11.18.1** Profiles of the electron temperature of electron-cyclotron heated plasmas, measured with high resolution Thomson scattering.  $\rho$  is the normalized radius. The arrows indicate the power deposition radius for each profile.

focused on anomalous transport phenomena, and in particular electron heat transport.

The special conditions of the RTP tokamak allowed experiments on pure electron transport to be carried out. Power was supplied by electron-cyclotron resonance heating, with 500 kW at 110 GHz. Because of the modest machine size this electron heating exceeded the ohmic input by a factor 4 with off-axis heating and 7 with on-axis heating. The electron-ion energy transfer was negligible and consequently the energy balance essentially involved only the electrons.

The heating pulse duration was typically 50 energy confinement times and 10 global current diffusion times, so that real steady-state conditions could be reached. Furthermore, the tokamak was large enough to allow good localization of the ECRH power to within 10% of the minor radius.

The high resolution electron diagnostics included a Thomson scattering system, giving full profiles of  $n_e$  and  $T_e$  with 3 mm spatial resolution. Figure 11.18.1 shows measured  $T_e$  profiles obtained for different settings of the ECRH deposition radius. As expected, the profiles outside the deposition radii coincide. For deposition far from the axis the steady-state temperature profiles become distinctly hollow. The hollowness could not be explained by heat losses from the plasma centre.

A striking observation is that the  $T_e$  profiles obtained by varying the ECRH deposition radius do not change smoothly. Figure 11.18.2 shows the central  $T_e$  as a function of the deposition radius, which for this experiment was varied with 1 mm steps. This shows that the plasma makes sharp transitions between one type of profile and the

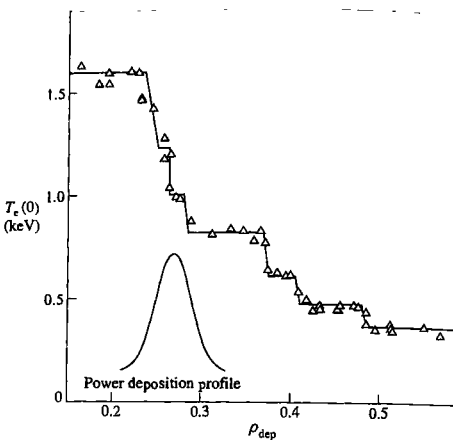


**Fig. 11.18.2** A shot-to-shot scan of the ECH deposition radius revealed step-wise changes of the electron temperature profile. Five main levels and two sub-levels of  $T_e(0)$  were identified. The triangles are the data points and the line is drawn to guide the eye.

next. An analysis of measured  $T_e$  profiles on either side of a transition clearly shows that a transition corresponds to the loss of a narrow region with a steep  $T_e$  gradient, with its implied electron transport barrier. These transitions, and hence the barriers, could be associated—through the appearance of mhd modes—to rational  $q$  values,  $q = 1, \frac{4}{3}, \frac{3}{2}, 2, \dots$ . It is noteworthy that the transitions occur for a change of the deposition radius that is much smaller than the actual width of the deposition pattern indicating that the transitions correspond to bifurcations of the equilibrium. The transitions are also sharp in time. When the deposition was moved dynamically a distinct hysteresis was found.

## 11.19

**START and MAST—UKAEA Culham Science Centre, Abingdon, UK and NSTX—Princeton Plasma Physics Laboratory, USA**

Tokamaks usually have an aspect-ratio,  $R/a$ , of 3 to 4. The purpose of the Small Tight Aspect Ratio Tokamak, START, was to explore the possible advantages of a much smaller aspect-ratio. The device had  $R = 0.2$  m



**Fig. 11.19.1** Photograph of a plasma in START. The full width is about 1 m and the plasma current is 100 kA. Coils at the top and bottom produce a magnetic separatrix and the pairs of bright rings show the intersection of the separatrix with the coil cases.

and  $a = 0.15$  m with a resulting aspect-ratio,  $R/a$ , of 1.3. The scaling of plasma current in a tokamak is  $I \sim (aB_\phi/q)/(R/a)$  and it is seen that any advantages of high current are more readily obtained with a small aspect-ratio. However, such tokamaks have little space for the toroidal field coil. An alternative view of the scaling is that for a given  $q$  and plasma current a smaller toroidal field is required and this reduces the space required for the toroidal field coil.

Figure 11.19.1 shows a photograph of a plasma taken in visible light. The plasmas have co-injection which is better than predicted by the neo-Alcator scaling, and is comparable to that predicted by L-mode scaling laws.

The discharges were found to be free from termination by disruptions although a large internal magnetic reconnection was frequently observed. The plasmas could have an elongation of  $\sim 2$  with active feedback control.

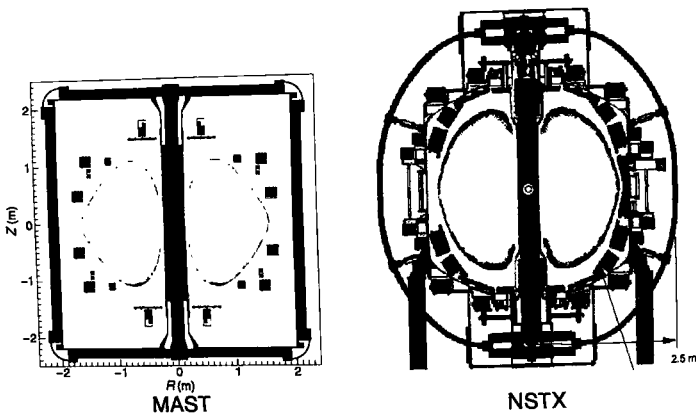
START achieved record beta values of around 40% before ceasing operation in 1998. It was then followed by the scaled-up spherical tokamaks, the National Spherical Torus Experiment, NSTX in 1999 and the Mega-Amp Spherical Tokamak, MAST in 2000. These experiments are comparable in plasma current and cross-section to conventional tokamaks such as DIIID and ASDEX Upgrade. The key parameters of START, MAST, and NSTX are compared in Table 11.19.1.

MAST and NSTX possess a number of complementary features, as seen in Fig. 11.19.2. For example, the close fitting wall in NSTX helps to stabilize mhd instabilities whereas MAST has a large plasma-wall separation and internal poloidal field coils, giving operating flexibility. In both devices the primary heating is provided by high power neutral beam

## 11.19 START, MAST and NSTX

**Table 11.19.1** Comparison of key parameters of START, MAST, and NSTX

	START	MAST	NSTX
Major radius (m)	0.32	0.85	0.85
Aspect ratio	$\geq 1.2$	$\geq 1.3$	$\geq 1.25$
Elongation	$\leq 3$	2.5	2.5
Plasma current (MA)	0.31	2	1.5
Toroidal field (T)	0.31	0.52	0.6
Auxiliary heating $P_{NBI}$ (MW), $P_{RF}$ (MW)	1, 0.2	5, 1.4	>5, 6
Pulse length (s)	$\leq 0.06$	5	5

**Fig. 11.19.2** Cross-sectional drawings of MAST and NSTX.

injection, but whereas in NSTX this is supplemented by high harmonic ion-cyclotron heating, in MAST electron Bernstein wave heating is installed.

Initial results from MAST and NSTX have confirmed and further extended the results from START with normalized beta values which approach theoretical limits being achieved. H-modes are readily obtained and the energy confinement times are comparable with those predicted on the basis of scaling derived from conventional tokamaks. Furthermore, many features of conventional tokamak operation, for example,

transport barriers, edge localized modes, and neoclassical tearing modes, are also observed in MAST and NSTX, allowing tests of physics models under extreme conditions. As a result, these devices also provide insight into plasma behaviour in conventional tokamaks and help to improve predictions of plasma performance in future devices such as ITER.

## 11.20

### TCV—Centre de Recherches en Physique des Plasmas, Ecole Polytechnique Fédérale de Lausanne, Switzerland

Tokamak à Configuration Variable, which has a major radius 0.89 m and a minor radius 0.25 m, began operation in 1992. The scientific programme is devoted to the creation and control of shaped plasmas, particularly of highly elongated plasmas, and to investigating their confinement and mhd properties. The device has a nearly rectangular vacuum vessel with a height-to-width ratio of 2.9, surrounded by 16 shaping coils. A wide variety of shaped limited and divertor plasmas have been produced with elongations up to 2.8. Examples of the shapes obtained are shown in Fig. 11.20.1. Much of the range of shapes obtained cannot be investigated in any other tokamak. Plasma heating, current drive, and profile control are provided by X-mode electron-cyclotron heating and current drive. This is produced by six gyrotrons operating at 82.7 GHz, each delivering 0.5 MW of second harmonic X-mode RF power using poloidally and toroidally steerable launching mirrors. For heating above the second harmonic cut-off density a further set of three gyrotrons at 118 GHz for third harmonic heating is available, each delivering 0.5 MW of power.

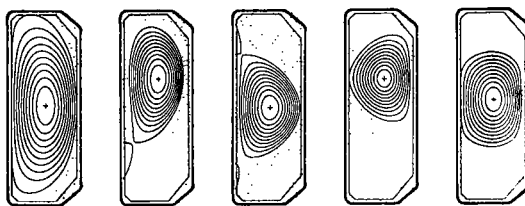


Fig. 11.20.1 Examples of plasma configurations created on TCV, demonstrating the extreme shaping capability of the device, including elongations up to 2.8 (left).

Experience gained on TCV contributes to the optimization of the tokamak as a reactor concept. One of the main attractions of operating at high elongation stems from the possibility of raising the plasma current, since  $I_p \propto (1 + \kappa^2)/2$ , for a fixed value of the edge safety factor. Normalized currents,  $I_p/aB_T$  of up to  $3.6 \text{ MAm}^{-1} \text{ T}^{-1}$  have been obtained at the highest elongations. High plasma current contributes to an increased beta limit and improves confinement, as expected from confinement scaling laws. A direct improvement of confinement with elongation has also been found. Research on TCV has contributed to establishing ECCD as a current drive method, by demonstrating for the first time fully current driven, steady state discharges, with currents up to 210 kA.

## 11.21

### Tokamak parameters

Device name	Year	Major radius (m)	Minor radius (m)	Toroidal field (T)	Plasma* current (MA)	Divertor	Transformer core type	Additional heating (MW)				Device name
								NBI	ICRH	LHRH	ECRH	
Alcator-A	1973	0.54	0.10	10.0	0.31		Air	0.1	0.1			Alcator-A
Alcator-C	1979	0.64	0.17	12.0	0.90		Air			4		Alcator-C
Alcator-C MOD	1993	0.67	0.22	9.0	0.64†(1.1)	Divertor	Air			4		Alcator-C MOD
ASDEX	1980	1.54	0.40	3.0	0.52	2-null	Air	4.5	3	2		ASDEX
ASDEX upgrade	1991	1.65	0.50	3.9	1.0†(1.4)	Divertor	Air	10	6		0.5	ASDEX Upgrade
ATC	1972	0.88-0.35	0.17-0.11	2.0-5.0	0.11-0.28		Air	0.01	0.16		0.2	ATC
Cleo	1972	0.90	0.18	2.0	0.12		Iron	0.04			0.4	Cleo
COMPASS	1989	0.56	0.21	2.1	0.28†	Divertor	Air			0.6	2	COMPASS
Doublet-III	1980	1.45	0.45	2.6	0.61†	1-null	Air	7			1-2	Doublet-III
DIII-D	1986	1.67	0.67	2.1		Divertor	Air	20	4.4		2	DIII-D
DITE	1975	1.17	0.26	2.7	0.26	bundle	Iron	2.4				DITE
DIVA	1974	0.60	0.10	2.0	0.06	1-null						DIVA
FT	1975	0.83	0.20	10.0	0.80		Air			1.0		FT
FT Upgrade	1990	0.93	0.30	8.0	1.3		Air	2††	4	1		FT Upgrade
HT-6B	1983	0.45	0.12	0.75	0.04		Air			0.1	0.1	HT-6B
HT-6M	1985	0.65	0.2	1.5	0.15		Air			1.0	0.15	HT-6M
HT-7***	1993	1.22	0.3	3.0	0.4		Iron	2.0	2.0			HT-7***
ISX-A	1977	0.92	0.26	1.8	0.22		Iron					ISX-A
ISX-B	1978	0.93	0.27	1.8	0.24†		Iron	2.5			0.2	ISX-B
JET	1983	3.0	1.25	3.5	3.0†(7)		Iron	20	20	7		JET
JFT-2	1972	0.90	0.25	1.8	0.23		Iron	1.5	1.0	0.3	0.2	JFT-2
JIPP-T2	1976	0.91	0.17	3.0	0.16		Iron	0.1		0.2		JIPP-T2
JT-60U	1985	3.0	0.95	4.5	2.3	1-null		20	2.5	7.5		JT-60U
LT-1	1968	0.4	0.10	1.0	0.04	Divertor	Air	40	7	8		LT-1
							Iron					

*Continued*

Device name	Year	Major radius (m)	Minor radius (m)	Toroidal field (T)	Plasma* current (MA)	Divertor	Transformer core type	Additional heating (MW)			Device name
								NBI	ICRH	LHRH	
LT-4	1981	0.5	0.10	3.0	0.10	Iron			0.5		LT-4
Macrotor	1977	0.90	0.40	0.4	0.12						Macrotor
MAST	2000	0.85	0.65	0.52	(2.0)	Divertor	Air	5.0		1.4	MAST
Microtor	1976	0.30	0.10	2.5	0.14				0.5		Microtor
NSTX	1999	0.85	0.68	0.60	(1.5)	Divertor	Air	5.0	6.0		NSTX
Ormak	1971	0.80	0.23	1.8	0.20		Iron	0.34			Ormak
PDX	1979	1.40	0.45	2.5	0.60†	4-null	Air		7		PDX
Petula	1974	0.72	0.16	2.7	0.16		Iron			0.5	
PLT	1975	1.30	0.40	3.5	0.72		Air	3	5	1	PLT
Pulsator	1973	0.70	0.12	2.7	0.093		Iron				Pulsator
RTP**	1989	0.72	0.16	2.5	0.16		Iron			0.9	RTP**
ST	1970	1.09	0.14	4.4	0.13		Iron				ST
START	1991	0.32	0.27	0.31	(0.31)	Divertor	Air	1.0		0.2	START
TEXT	1981	1.00	0.27	2.8	0.34	Divertor	Air			0.6	TEXT
TEXTOR	1983	1.75	0.46	3.0	0.6	Pump limiter	Iron	4	4		TEXTOR
T-3	1962	1.0	0.12	2.5	0.06		Iron				T-3
T-4	1970	1.0	0.17	5.0	0.24		Iron				T-4
T-6	1971	0.7	0.25	1.5	0.22		Iron				T-6
T-7	1981	1.22	0.31	3.0	0.39		Iron			0.25	T-7
T-10	1975	1.5	0.37	4.5	0.68		Iron			1.0	T-10
T-11	1975	0.7	0.22	1.5	0.17		Iron				T-11
T-12	1972	0.36	0.08	1.0	0.03†	2-null	Air				T-12
TCV	1992	0.89	0.25	1.5	0.17	1 or 2 null	Air			4.5	TCV
TFR-400	1973	0.98	0.20	6.0	0.41		Iron				TFR-400
TFR-600	1978	0.98	0.20	6.0	0.41		Iron		1.5	0.6	TFR-600
TFR	1982	2.4	0.80	5.0	2.2		Air	40	11		TFR
TM-3	1963	0.4	0.08	4.0	0.11		Iron				TM-3
TNT-A	1976	0.4	0.10	0.44	0.02†		Air				TNT-A
TO-1	1972	0.6	0.13	1.5	0.07		Iron				TO-1
Tore Supra	1984	2.37	0.80	4.5	2.0	(Ergodic)	Iron	1.7	12	8	Tore Supra
Tosca	1974	0.3	0.09	0.5	0.02†		Air			0.2	Tosca
Tuman II	1971	0.4	0.08	2.0	0.05		Iron				Tuman II
Tuman III	1978	0.55	0.15	3.0	0.20		Iron				Tuman III
Versator	1978	0.4	0.13	1.5	0.11					0.1	Versator

\*Value for  $q = 3$  circular discharge ( $I_1 = (5a^2 B_\phi / 3R)$ ) and higher current achieved in brackets

\*\*Formerly Petula \*\*\*Formerly T-7. †Non-circular cross-section ‡Ion-Bernstein waves

## Bibliography

Most experimental groups report their latest work at the biennial international conferences organized by the I.A.E.A. Conference proceedings are published by the I.A.E.A., Vienna under the title *Plasma physics and controlled nuclear fusion research*. The venues and dates of these

conferences are as follows

1st Salzburg	1961	5th Tokyo	1974
2nd Culham	1965	6th Berchtesgaden	1976
3rd Novosibirsk	1968	7th Innsbruck	1978
4th Madison	1971	8th Brussels	1980

9th	Baltimore	1982	10th	London	1984
11th	Kyoto	1986	16th	Montreal	1996
12th	Nice	1988	17th	Yokohama	1998
13th	Washington	1990	18th	Sorrento	2000
14th	Wurzburg	1992	19th	Lyon	2002
15th	Seville	1994			

The European Physical Society also has regular meetings with international representation. The proceedings are usually published by the host organization under the title *Controlled fusion and plasma physics*. These were held as follows

1st	Munich	1966	11th	Aachen	1983
2nd	Stockholm	1967	12th	Budapest	1985
3rd	Utrecht	1969	13th	Schliersee	1986
4th	Rome	1970	14th	Madrid	1987
5th	Grenoble	1972	15th	Dubrovnick	1988
6th	Moscow	1973	16th	Venice	1989
7th	Lausanne	1975	17th	Amsterdam	1990
8th	Prague	1977	18th	Berlin	1991
9th	Oxford	1979	19th	Innsbruck	1992
10th	Moscow	1981	20th	Lisbon	1993

21st	Montpellier	1994	26th	Maastricht	1999
22nd	Bournemouth	1995	27th	Budapest	2000
23rd	Kiev	1996	28th	Madeira	2001
24th	Berchtesgaden	1997	29th	Montreux	2002
25th	Prague	1998	30th	St. Petersburg	2003

Since 1989 invited papers from the annual meeting of the Plasma Physics Division of the American Physical Society have been collected and published in a special issue of the journals *Physics of Fluids B* (1989–1992) and *Physics of Plasmas* (1993–1995). The relevant conferences are as follows,

31st	Anaheim	1989	39th	Pittsburgh	1997
32nd	Cincinnati	1990	40th	New Orleans	1998
33rd	Tampa	1991	41st	Seattle	1999
34th	Seattle	1992	42nd	Quebec	2000
35th	St Louis	1993	43rd	Long Beach	2001
36th	Minneapolis	1994	44th	Orlando	2002
37th	Louisville	1995	45th	Albuquerque	2003
38th	Denver	1996			

**12**

# **Large Tokamaks**

## 12.1

### Large Tokamaks

The generation of large tokamaks which came into operation in the 1980s and 1990s has achieved substantial improvements in almost all aspects of performance. This group of devices, consisting of the Tokamak Fusion Test Reactor at Princeton, the Joint European Torus at Culham, JT-60 in Naka, DIII-D in San Diego, and ASDEX Upgrade in Garching, has been supported by wide-ranging studies at the small and moderate sized tokamaks discussed in Chapter 11. The extensive co-operation between laboratories in many countries which has been a feature of this period reflects the enlarged international dimension which fusion research has acquired. Comparative studies of plasma behaviour and performance, involving both the large devices and many of the smaller tokamaks, have made a fundamental contribution to the development of the physics basis for the design of the International Thermonuclear Experimental Reactor discussed in Chapter 13. Considerable progress has been made, including the achievement of values of the fusion triple product within an order of magnitude of that required for ignition, and the production of more than 10 MW of fusion power in experiments utilizing a deuterium-tritium fuel mixture.

As tokamak plasmas approach the regime in which significant levels of thermonuclear power can be produced, the fusion power quotient,  $Q_{DD}$  or  $Q_{DT}$ , is a useful measure of fusion performance. For deuterium plasmas,  $Q_{DD}$  can be simply defined as the ratio of the fusion power to the applied heating power. It is often converted to an equivalent  $Q_{DT}$ , based on calculations of the predicted fusion reactivity in a 50:50 mixture of deuterium and tritium under the same plasma conditions, as described in Section 13.1. Two critical values are then identified,  $Q_{DT} = 1$ , corresponding to effective breakeven, and  $Q_{DT} \rightarrow \infty$ , corresponding to ignition.

The improvement in fusion performance in the large experimental devices is due mainly to their increased size and power capability. Major and minor radii have doubled relative to the previous generation of devices, leading to an order of magnitude increase in plasma volume and a commensurate improvement in energy confinement. Plasma current and heating power have risen similarly, with JET attaining 7 MA in limiter operation and the three largest tokamaks, JET, JT-60 Upgrade, and TFTR, ultimately acquiring an installed heating capacity of  $\sim 50$  MW. An important aspect of the high current capability of JET and TFTR, both of which were designed for D-T experiments, is that a large fraction of the  $\alpha$ -particles produced by fusion reactions should be confined, permitting studies of  $\alpha$ -particle behaviour in thermonuclear plasmas.

A steady improvement in wall conditioning techniques has also made a major contribution to improved performance. The vacuum vessel walls

have been coated with thin, usually <100 nm, films of carbon, boron, beryllium, lithium, or silicon. These coatings, to varying degrees, prevent sputtering of high-Z metals, reduce hydrogen recycling, and getter oxygen. Maintaining low levels of hydrogen recycling has proved to be an essential ingredient for obtaining plasmas with the highest fusion performance, although there is no satisfactory explanation of why this should be so. More generally, the appreciation that the control of particle fluxes, including those of impurities, is a key step on the route to the construction of a reactor has stimulated extensive studies on this issue. The divertor has emerged as the most favoured solution to this problem and the programmes of the large tokamaks have focused increasingly on experimental investigations of this approach. This is illustrated by the fact that only two of the five devices discussed here were originally conceived as divertor tokamaks, but ultimately four operated almost exclusively as divertor experiments.

The ability to perform detailed quantitative comparisons between experimental measurements and the predictions of theory has been a notable feature of recent tokamak research, as more sophisticated diagnostic techniques have been applied. Increases in plasma parameters and size, technological advances, and an enormous expansion in computing power have all been exploited to improve plasma measurements. Diagnostics of neutrons and energetic particles have probably benefited most from the advance towards the thermonuclear regime, and the study of these facets of plasma behaviour has been an important aspect of the large experiments: studies of energetic particle confinement, their interactions with the thermal plasma and their influence on mhd stability have been conducted using energetic ions produced by auxiliary heating systems and  $\alpha$ -particles produced in D-T experiments. Advances in diagnostics for analysis of the current profile and of internal electric fields have also had a profound impact on the understanding of plasma behaviour.

Improvements in fusion relevant technology, such as heating and current drive systems, fuelling and pumping systems, power handling surfaces and control techniques, have also made substantial contributions to progress on the large devices. Many subsystems of the large tokamaks have developed from their experimental origins to the stage where their operation can be regarded as routine, if not yet at the level of reliability required for reactor applications. This is illustrated by the auxiliary heating and current drive systems. For example, neutral beam systems based on positive ion source and accelerator technology have operated at injected power levels of 40 MW, while negative ion based systems, which are expected to provide the technology required for reactors, have operated at power levels of several megawatts. Ion cyclotron resonance heating of over 20 MW has been coupled into tokamak plasmas, and the associated impurity generation problems have been overcome. In addition, electron cyclotron resonance heating systems capable of producing megawatts of heating power are available. Finally, current drive using lower hybrid waves has reached the 3 MA level.

Due to these developments, there has been a substantial expansion in the accessible operating space. Although tokamaks with a material limiter are still, in the main, restricted to operation in the L-mode confinement regime, the discovery in TFTR of the 'supershot' regime of enhanced confinement has opened an important new area of fusion research. Quasi-steady-state regimes with energy confinement quality greater than that predicted by L-mode scalings, such as the radiation improved mode discovered in TEXTOR, have also extended the operational space of limiter devices. The H-mode regime is readily attainable in plasmas with an internal magnetic separatrix, provided that the vessel conditioning and input power level are adequate. Moreover, the level of confinement enhancement has progressed to the point where plasma regimes have been found in which confinement can increase by up to a factor of 4 relative to that in the L-mode. H-modes have also been achieved in magnetic configurations limited by the vessel wall on the high field side and in ohmically heated plasmas. Combinations of regimes in which, for example, the highly peaked profiles typical of supershots are added to the edge transport barrier of the H-mode have been exploited to improve fusion performance.

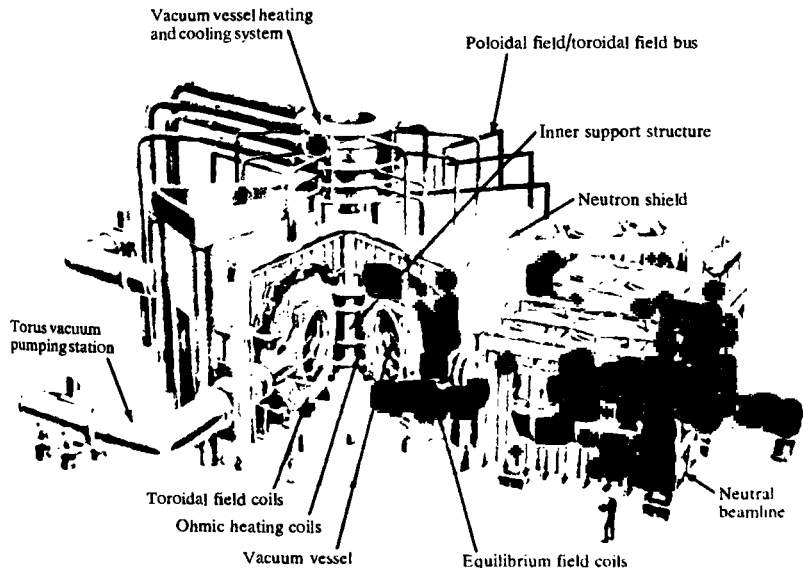
As a result of the intense efforts expended to develop plasmas with confinement enhanced beyond the L-mode level, as defined either by the Goldston or ITER89-P scalings, a wide range of plasma regimes is recognized and studied. In this chapter, the distinction between L-mode and H-mode will refer to the conditions at the plasma edge, rather than to the level of confinement enhancement. The term 'H-mode' will be applied to plasmas which exhibit certain edge characteristics. These often include the formation of steep gradients in edge density and temperature, which have been linked in many experiments to a change in the radial electric field gradient at the edge, but the simplest, and virtually universal, indication is a fall in the  $H_\alpha$  emission from hydrogenic recycling.

Confinement studies have concentrated increasingly on the optimization of plasma profiles, particularly the current profile, with the aim of obtaining enhanced confinement while at the same time improving plasma mhd stability properties. Energy confinement has been enhanced both by increasing the internal inductance,  $\ell_i$ , at fixed current and by establishing current profiles with negative shear in the plasma centre. Although such improvements are transient in the absence of active current profile control techniques, these results suggest an alternative concept for a reactor in which operation at relatively low current is compensated by exploiting current profile control to optimize energy confinement, mhd stability, and hence fusion performance. The advantages of such an approach, often referred to as the 'advanced tokamak scenario', include lower disruption forces at reduced current and a lower current drive requirement for steady-state operation. This latter follows both from the absolute level of current and the increased fraction taken up by the bootstrap current. Many challenges remain, however, among them the need to demonstrate the requisite steady-state control of the current profile and to show that particle transport and divertor requirements are compatible with such regimes.

**12.2****TFTR—Princeton Plasma Physics Laboratory, USA**

Plasmas were initially obtained in the Tokamak Fusion Test Reactor late in 1982, making it the first of the large tokamaks to come into operation, and the experimental programme was completed in April 1997, following a highly successful series of experiments in D-T plasmas. This device, of circular poloidal cross-section (Fig. 12.2.1), with  $R/a = 2.4/0.8$ , used carbon limiters on both the low and high field side of the plasma and was capable of high magnetic field, 6 T, and plasma current, 3 MA. It had a substantial additional heating capability, with NBI power of up to 40 MW at injection energies of up to 120 keV, and an installed ICRF generator power of 16 MW. The principal aim of the experiment was the investigation of plasma heating and confinement, including  $\alpha$ -particle effects, in regimes close to breakeven conditions. Much of the experimental programme concentrated on studying plasma behaviour and optimizing fusion performance in deuterium plasmas, but experiments with 50:50 mixtures of deuterium and tritium began in 1993.

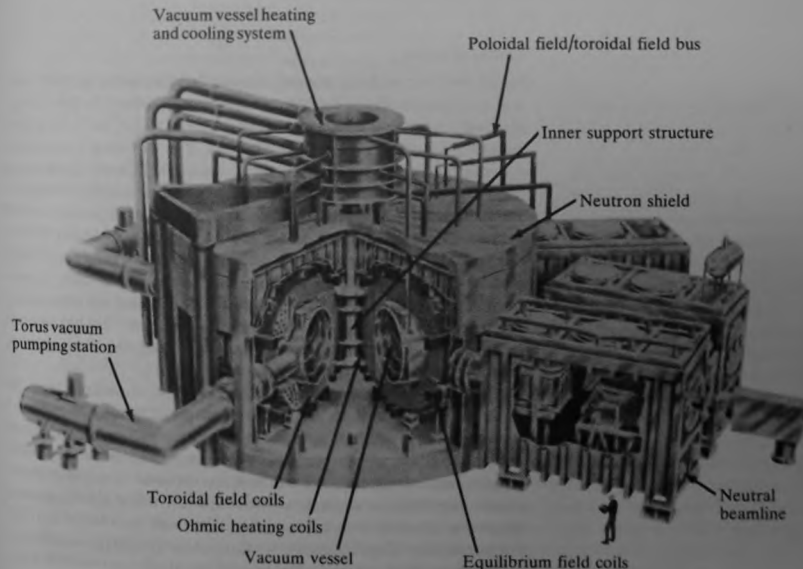
Fig. 12.2.1 Layout of the TFTR experiment.



**12.2****TFTR—Princeton Plasma Physics Laboratory, USA**

Plasmas were initially obtained in the Tokamak Fusion Test Reactor late in 1982, making it the first of the large tokamaks to come into operation, and the experimental programme was completed in April 1997, following a highly successful series of experiments in D-T plasmas. This device, of circular poloidal cross-section (Fig. 12.2.1), with  $R/a = 2.4/0.8$ , used carbon limiters on both the low and high field side of the plasma and was capable of high magnetic field, 6 T, and plasma current, 3 MA. It had a substantial additional heating capability, with NBI power of up to 40 MW at injection energies of up to 120 keV, and an installed ICRF generator power of 16 MW. The principal aim of the experiment was the investigation of plasma heating and confinement, including  $\alpha$ -particle effects, in regimes close to breakeven conditions. Much of the experimental programme concentrated on studying plasma behaviour and optimizing fusion performance in deuterium plasmas, but experiments with 50:50 mixtures of deuterium and tritium began in 1993.

Fig. 12.2.1 Layout of the TFTR experiment.



Many experiments have demonstrated that plasma confinement and, ultimately, fusion performance depend sensitively on the level of recycling of hydrogen isotopes. Therefore, although the usual techniques of vessel baking, glow discharge cleaning, pulse discharge cleaning, and disruptive discharge cleaning were used in preparation of the vacuum vessel for plasma operation, the TFTR group emphasized the conditioning, or degassing, of the torus walls as a means of attaining plasma regimes with the highest performance. Experiments showed that conditioning of the vessel wall on the inner, high magnetic field, side of the plasma was particularly important. This was achieved by means of extensive series of low density discharges, often in helium, which reduced the recycling factor from its usual value close to unity, to  $\sim 0.5$ . The limiter degassing was believed to be due to bombardment of the limiter by energetic helium and carbon ions. Boronization and the injection of lithium pellets were also applied to improve conditioning. Lithium pellet conditioning involved the injection, both before and after the NBI heating phase, of several pellets, each containing sufficient atoms,  $\sim 4 \times 10^{20}$ , to cover the limiter surface with a monolayer of lithium. This evolved into a major conditioning technique as it reduced the carbon and deuterium influxes, led to lower edge densities, and was associated with increased energy confinement in supershots.

### Ohmic plasmas

Initial operation in ohmic plasmas showed that the plasma impurity content increased as the ratio of the average current density to the average electron density,  $j/\bar{n}$ . At electron densities below  $5 \times 10^{19} \text{ m}^{-3}$ , the global energy confinement time increased as  $nq_e R^2 a$ , reaching a maximum value of 0.44 s in gas-fuelled plasmas. As found in many gas-fuelled experiments, the confinement time saturated at higher densities, though in pellet-fuelled discharges an energy confinement time of 0.5 s was attained at densities above  $10^{20} \text{ m}^{-3}$ . Adiabatic compression, achieved by driving the plasma ring towards the high magnetic field side of the torus through a rapid,  $\sim 20 \text{ ms}$ , increase in the vertical field, was successfully demonstrated in ohmic plasmas. Both the plasma density and ion temperature increased in accordance with theoretical expectations, but the electron temperature rise was lower than expected, indicating an enhancement of electron transport during the compression.

The improved confinement in ohmic plasmas associated with the increase in plasma dimensions has produced ohmic temperatures of several keV in the largest tokamaks. In this parameter range the electrons and ions are in the banana regime over a large fraction of the plasma cross-section. Trapped particle effects are expected to manifest themselves, therefore, for example in the resistivity, which should increase above the classical Spitzer formulation. This was confirmed for TFTR ohmic plasmas, where the resistivity agreed closely with the neoclassical formulation. More precisely, the ratio of the single turn voltage at the

plasma surface calculated using neoclassical resistivity to that measured was  $1.01 \pm 0.06$ , while the ratio obtained using the classical form was lower by a factor of  $\sim 2$ . In addition, the evolution of the  $q = 1$  surface, derived from measurements of the sawtooth inversion radius, was in agreement with that deduced from the neoclassical resistivity in many cases where calculations based on classical resistivity predicted that  $q$  should be everywhere above unity.

### High power heating experiments

Neutral beam injection is the main form of additional heating in large tokamaks, and the majority of the experiments in TFTR were dedicated to understanding plasma behaviour in the presence of intense beam heating. When the plasma was limited on the outer limiter, or when the inner wall limiter exhibited high recycling, plasmas were invariably in the L-mode. A systematic study of the variation of global energy confinement with plasma size and aspect ratio revealed the surprising result that the energy confinement was almost independent of minor radius, varying as  $a^\alpha$ , with  $-0.22 \leq \alpha \leq 0.06$ . This weak dependence contrasted with the  $a^2$  scaling expected for diffusive heat transport. Moreover, analysis of local transport in these plasmas showed that the single fluid thermal diffusivity was better described as a function of  $r/R$  than as a function of  $r/a$ , suggesting that toroidicity played a significant role in local heat transport.

The attainment of high fusion yields was pursued predominantly in the supershot regime, which was formed by high power neutral beam injection into a low density,  $\bar{n} < 1.5 \times 10^{19} \text{ m}^{-3}$ , target plasma limited on the inner wall. As noted previously, careful conditioning of the carbon inner wall was a prerequisite for this regime, since control of both carbon and deuterium recycling was crucial. Further reductions in recycling were obtained in experiments in which the inner wall was conditioned by injection of lithium pellets before neutral beam injection. These yielded a 5–10% improvement in fusion reaction rate and achieved the highest D-D reaction rates in TFTR,  $10^{17} \text{ s}^{-1}$  with 33 MW of injected power. For many years, a broadening of the plasma profiles at higher plasma currents, possibly due to sawtooth activity and the increase of the ohmic target density with current, restricted the supershot regime to currents below 2 MA. However, the improved wall conditioning following lithium pellet injection allowed supershots to be established at currents close to 3 MA. A requirement for near-balanced NBI, in which the power injected parallel to the plasma current approximately balanced that injected anti-parallel to the current, was an additional constraint on the accessibility of the regime. The advantage of balanced injection arose in part from classical effects, in that the large rotation velocity driven by unbalanced injection degraded the NBI heating efficiency due to the reduction of relative velocities between plasma particles and injected particles.

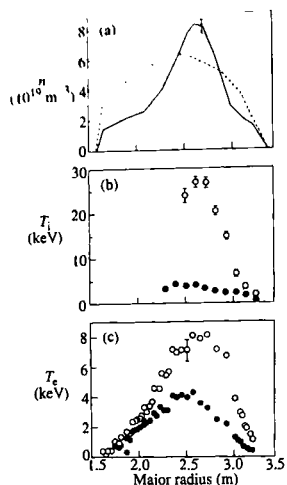


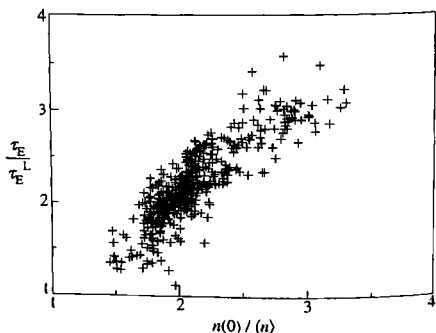
**Fig. 12.2.2** Measured profiles of (a) electron density, (b) ion temperature, and (c) electron temperature for a supershot (solid curve, open points) and a helium target plasma with L-mode confinement (dashed curve, solid points). Both discharges have

$I_p = 1.4 \text{ MA}$ ,  $P_{NBI} = 22 \text{ MW}$ , and  $B = 4.8 \text{ T}$  [Zamstorf, M.C. et al. *Plasma Physics and Controlled Nuclear Fusion Research 1988* (Proc. (2th Int. Conf., Nice, 1988) Vol 1, 183. I.A.E.A., Vienna (1989)].

Strong central beam fuelling and improved confinement in supershot plasmas produced high central electron densities,  $n(0)$  up to  $10^{20} \text{ m}^{-3}$ , and very peaked density profiles (Fig. 12.2.2), with  $n(0)/(n)$  generally in the range 2–3. The peaking correlated well with the improvement in confinement (Fig. 12.2.3), and the confinement enhancement relative to L-mode scaling reached factors of  $\sim 3$  at density profile peaking factors of  $\sim 3$ . Global energy confinement did not degrade with heating power and exhibited little variation with plasma current, in contrast to L-mode behaviour. The ion temperature profile was also very peaked and central values reached 35 keV, while the electron temperature profile was broader, with peak values of only 12 keV. Saturation of the electron temperature at values well below those of the ion temperature was explained by the fact that both direct NBI heating of the electrons and equipartition power transfer from the ions fall as the electron temperature rises. Such hot ion modes, with  $T_i \gg T_e$ , have been widely exploited in modern tokamak research to maximize fusion performance. Enhanced energy confinement and centrally peaked profiles are optimal for high fusion yield, and the fusion triple product in deuterium supershots was up to a factor of 20 greater than in equivalent L-mode plasmas. Values of the triple product up to  $n(0)T_i(0)\tau_E \sim 3 \times 10^{20} \text{ keV sm}^{-3}$  were obtained, corresponding to  $QDT \sim 0.3$ .

The principal reduction in local transport in supershots relative to L-mode plasmas occurred in the ion channel, as might be expected from the very substantial differences in ion temperature between the two regimes. So fundamental was the change in ion thermal diffusivity that, in the core of supershots, the diffusivity fell with increasing ion temperature, in contrast to L-mode plasmas, in which a systematic increase in diffusivity with the local value of  $T_i$  was usual (Fig. 12.2.4). Electron thermal diffusivity was also reduced, but only by a factor of  $\sim 2$ . A notable aspect of the supershot regime is that a transition to a limiter H-mode was sometimes observed. In deuterium plasmas, these H-modes were always

**Fig. 12.2.3** Enhancement of energy confinement time,  $\tau_E$ , over the prediction of Goldston L-mode scaling,  $\tau_E^L$ , as a function of density profile peaking,  $n(0)/(n)$ , for a variety of supershots with  $R = 2.45 \text{ m}$ ,  $a = 0.8 \text{ m}$ ,  $B = 4.8\text{--}5.1 \text{ T}$ , and  $I_p = 0.8\text{--}1.8 \text{ MA}$  [Meade, D.M. et al. *Plasma Physics and Controlled Nuclear Fusion Research 1990* (Proc. 13th Int. Conf., Washington, 1990) Vol 1, 9. I.A.E.A., Vienna (1991)].



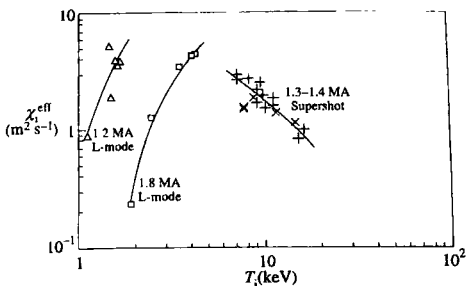


**Fig. 12.2.4** Comparison of the total ion thermal diffusivity,  $\chi_i^{eff}$  ( $r = a/3$ ), which includes ion conduction and convection, versus ion temperature,  $T_i$  ( $r = a/3$ ), for L-mode plasmas and supershots  
 [Meade, D.M. et al. *Plasma Physics and Controlled Nuclear Fusion Research 1990* (Proc. 13th Int. Conf., Washington, 1990) Vol 1, 9. I.A.E.A., Vienna (1991)].

ELMy and so maintained quasi-steady-state conditions for periods of  $\sim 1.5$  s. Energy confinement changed little from that of the supershot, with a confinement enhancement of  $\sim 2.5$  relative to the L-mode level.

Enhanced confinement regimes are often transient and, at the highest powers, supershot performance declined after 1–2 s of heating. In some cases the degradation was linked to a decay of the density profile. In others the growth of MHD activity, usually due to pressure driven modes, was responsible. Another type of performance degradation was caused by localized overheating of the power-handling surfaces which generated a catastrophic influx of impurities, the carbon bloom, so-called because the light emitted from the overheated region caused a ‘bloom’ on the infrared camera image of the plasma-wall interaction region. Although the sublimation temperature for graphite is  $2700^\circ\text{C}$ , the bloom was often observed at limiter surface temperatures in the range  $1700$ – $2400^\circ\text{C}$ . The phenomenon of radiation enhanced sublimation, in which sputtered ions return to the surface and cause further sputtering, leading to runaway impurity production, has been advanced in explanation of this.

The carbon bloom was first reported as a limiting mechanism in TFTR supershots and changes were made to the inner wall limiter to improve its power-handling capability. Deviations from toroidal symmetry of the graphite tiles which formed the limiting surface caused high spots which preferentially intercepted the power flux in the scrape-off layer. The power-handling of the limiter was then constrained by localized heating of these spots, rather than by the toroidally averaged power flux in the SOL. To increase the power-handling capability of the inner wall, the tile alignment was improved, so that deviations from toroidal symmetry were only  $\pm 0.5$  mm. In addition, graphite tiles were replaced by carbon fibre composite tiles, which have a higher thermal conductivity and better thermal shock resistance. These measures virtually eliminated carbon blooms, even at power levels of 35 MW for 1 s.

Following these changes, supershots were more commonly limited by the growth of MHD activity which caused a gradual deterioration in

fusion performance. The mhd modes had low poloidal and toroidal mode numbers,  $m/n$ , and were identified as non-linear neoclassical pressure-gradient-driven tearing modes. Usually a hierarchy of mhd activity was observed. Modes with  $m = 3/n = 2$  had the most severe effect, degrading neutron yield by up to 30% and stored plasma energy by up to 15%, while  $m = 4/n = 3, m = 5/n = 4$  modes, and  $m = 1/n = 1$  fishbone instabilities had less impact on plasma performance. This activity occurred in the vicinity of a boundary formed by the conditions  $\beta_N = 10^8 \beta/(I/aB) < 2.4$  and  $\epsilon\beta_p < 0.7$  (Fig. 12.2.5). In a small percentage of pulses,  $\sim 10\%$ , neutron emission decayed only after the NBI heating, which lasted  $\sim 1$  s, was switched off, and a small fraction of discharges was terminated by major disruptions with rapidly growing precursors lasting  $\sim 5$  ms.

A significant feature of supershot plasmas was that while  $\beta_N$  was limited to 2.4, the peaked pressure profiles imply a substantially better fusion performance. In plasma regimes of interest in reactors, the fusion reactivity varies approximately as  $(n_i T_i)^2$ , and the relevant figure of merit is  $\beta_N^* = 10^8 \beta^*/(I/aB)$ , where  $\beta^* = \langle p^2 \rangle^{1/2} / (B^2 / 2\mu_0)$  and  $\langle p^2 \rangle$  represents the volume average of the square of the plasma pressure. Values of  $\beta_N^* = 3.9$  were attained in supershots.

The normal supershot stability boundary was exceeded in a regime which was characterized as 'high- $\beta_p$ ' (Fig. 12.2.5), and was achieved by ramping the plasma current down rapidly, by as much as 50%, prior to NBI heating. This produced an increase in the plasma internal inductance,

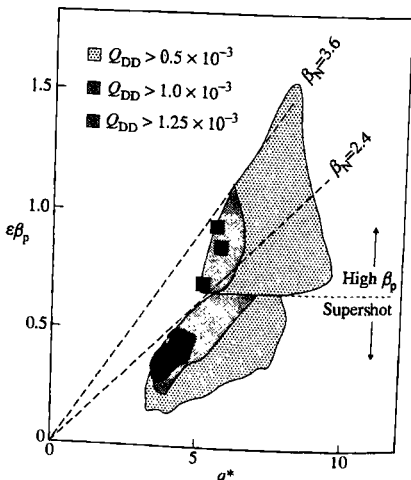


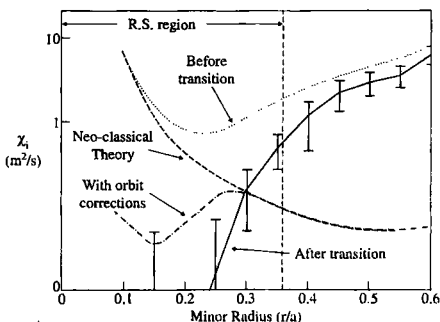
**Fig. 12.2.5** Operational diagram for two high performance regimes in TFTR, supershot and high- $\beta_p$  plasmas, illustrating the accessible range of  $\epsilon\beta_p$  as a function of  $q^*$ , the cylindrical safety factor [Mauel, M.E. et al. *Plasma Physics and Controlled Nuclear Fusion Research 1992* (Proc. 14th Int. Conf., Würzburg, 1992) Vol 1, 205. I.A.E.A., Vienna (1993)].

which was accompanied by a considerable enhancement of energy confinement, the confinement time rising to  $\sim 3.7\tau_E^{\text{ITER89-P}}$ . The plasma stability also improved transiently, allowing  $\beta_N$  to rise to  $\sim 3.6$  and  $\epsilon\beta_p$  to reach  $\sim 1.5$ . However, as  $\ell_i$  decayed, stability was eventually lost, via either a disruption or a collapse in  $\beta$  associated with intense mhd activity.

Further improvements in plasma confinement were observed in plasmas in which the central shear,  $s \approx (r/q)(dq/dr)$ , was reversed. In these plasmas, established by injecting neutral beams during the current ramp-up, a transition to a regime of enhanced plasma confinement and improved mhd stability was observed at high input power,  $P_{\text{NBI}} \sim 20$  MW. During the reversed shear phase, the  $q$ -profile typically had  $q(a) \sim 6$ ,  $q_{\min} \sim 2$ , and  $q(0) \sim 3-4$ , and the pressure profile often became significantly more peaked than in supershots,  $p(0)/(p)$  reaching 8, compared with values of  $\sim 5$  for supershots. Both thermal and particle transport were reduced throughout the reversed shear region (Fig. 12.2.6), the electron particle diffusivity falling by a factor of  $\sim 40$  to the level predicted by neoclassical theory, and the ion thermal diffusivity falling by approximately 2 orders of magnitude to values well below the conventional neoclassical prediction which was thought to be the minimum achievable level of transport. More recent calculations of neoclassical transport include the effect of ion orbit dimensions which are comparable with the pressure scale lengths and appear to have resolved this discrepancy, as illustrated in Fig. 12.2.6. This 'enhanced reversed shear' regime was sustained transiently and many of the best discharges, which reached  $\beta_N \sim 1.7$  and  $\beta_N^* \sim 3.5$ , suffered a major disruption due to an  $n = 1$  mode.

Similar results were obtained simultaneously in DIII-D experiments, and these observations confirmed analysis of PEP H-modes in JET which

**Fig. 12.2.6** Radial profile of the ion thermal diffusivity,  $\chi_i$ , in a reversed shear discharge before and after the transition to the enhanced reversed shear regime. The conventional neoclassical prediction for  $\chi_i$  is also shown, together with a more recent refinement of the neoclassical prediction which includes orbit dimensions comparable with the pressure scale length. 'R.S. region' refers to the region in which the magnetic shear is reversed [from Levinton, F.M. et al. *Physical Review Letters* 75, 4417 (1995) and Lin, Z. et al. *Physical Review Letters* 78, 456 (1997)].



indicated that reduced transport in the plasma core was associated with a central region of reversed shear. Together, these results laid the basis for extensive experimental and theoretical investigations of 'internal transport barriers' in both tokamak and stellarator plasmas. Such studies have provided much insight into local transport processes in toroidal plasmas and have identified a potential route to steady-state operation of a tokamak reactor. Several mechanisms can contribute to the reduction of transport in the plasma core in such plasmas: central shear reversal can stabilize certain small-scale instabilities contributing to transport, and the large Shafranov shift of the central magnetic flux surfaces due to the high central pressure can also contribute, but suppression of turbulence by sheared plasma flows arising from a gradient in the radial electric field in the region of the internal transport barrier has been suggested as the dominant process. The importance of this effect was illustrated by experiments in which varying proportions of co- and counter-NBI were used to influence the duration of the enhanced confinement phase, emphasizing the role of externally applied torque in modifying the plasma toroidal velocity and hence the radial electric field. The essential physics associated with this mechanism for turbulence suppression is discussed in Section 12.5 in relation to the H-mode transition.

At the pressures which obtain in plasmas with high fusion performance, pressure gradients play a significant role in determining the plasma behaviour. The most obvious effect is the observation in many tokamaks of a global limit to  $\beta$ . In addition, a substantial bootstrap current is expected. Experimental evidence for the bootstrap mechanism was unconvincing until the advent of the current generation of large tokamaks with improved diagnostics. Although NBI produced a significant fraction of the total current in TFTR, even in cases of balanced injection, the behaviour of the surface loop voltage in high power discharges

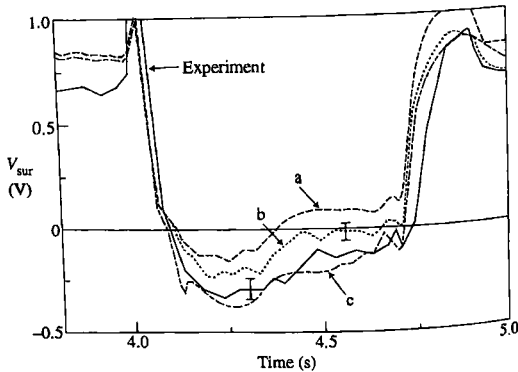


**Fig. 12.2.7** The time variation of the surface loop voltage,  $V_{\text{sur}}$ , determined experimentally from magnetic measurements, shown by the solid line, and calculated under various assumptions: (a) ohmic current only, (b) NB1-driven and ohmic currents, and (c) bootstrap, NB1-driven and ohmic currents [Zarnstorff, M.C. et al., *Physical Review Letters* 60, 1306 (1988)].

could only be explained by invoking the bootstrap current (Fig. 12.2.7). Moreover, the broadening of the current profile produced by the bootstrap current, which, like the trapped particle population, is maximal at some distance from the plasma centre, provided a ready explanation of the transient negative phase of the loop voltage. In the supershot regime up to 70% of the plasma current was driven by the bootstrap mechanism.

### Mhd studies

Considerable advances in the diagnostic capabilities of the large tokamaks stimulated much more detailed quantitative and qualitative analyses of plasma behaviour than had hitherto been possible. In the mhd area, studies of sawtooth oscillations and disruptions were revolutionized by the availability of multichannel electron cyclotron emission (ECE) and soft X-ray detectors coupled to sophisticated computer-based reconstruction techniques. For example, in TFTR, reconstructions of sawtooth collapses using multichannel radially resolved ECE data yielded images which are consistent with the Kadomtsev full reconnection model. Nevertheless, analysis of the  $q$ -profile using the motional Stark effect confirmed observations made on other tokamaks that the central value of  $q$  remains well below unity throughout the sawtooth cycle. Motional Stark effect measurements of the  $q$ -profile were incorporated into a stability analysis of sawtoothing and sawtooth-free plasmas in TFTR. This study found good agreement between the occurrence of sawteeth and a stability criterion, based on  $(rdq/dr)_{q=1}$ , predicted by a two-fluid collisionless  $m = 1$  reconnection model of the sawtooth instability which includes stabilization of the  $m = 1$  mode due to diamagnetic effects.

Similar techniques were applied to the study of the pre-disruptive plasma. The causes of disruptions in TFTR were broadly similar to those in other large tokamaks, as outlined in Section 7.8, though the role of ideal instabilities was perhaps of greater operational importance due to the emphasis on experiments at high- $\beta_p$ . In major disruptions at high density or low  $q(a)$ , an  $m = 1$  deformation of the plasma core developed in the last millisecond before the current quench which, in ECE reconstructions of the electron temperature profile, appeared consistent with the penetration of a cold plasma bubble into the core (Fig. 12.2.8). However, the relationship between this rapidly growing  $m = 1$  mode, with  $\gamma \sim 5 \times 10^3 \text{ s}^{-1}$ , and the more slowly growing  $m = 2/n = 1$  mode identified in most other tokamaks as the precursor to the majority of disruptions remained unresolved.

Disruptions at high- $\beta$  were initiated by a toroidally and poloidally localized ballooning mode, with  $n \sim 10-15$ , which appeared to be destabilized through local modifications of the magnetic shear and pressure gradient by an internal  $n = 1$  kink (Fig. 12.2.9). The growth of this mode generated a rapid,  $\sim 100 \mu\text{s}$ , collapse of the central electron temperature, and the current quench followed within a few tens of milliseconds. Further evidence of pressure profile effects was provided by the observation of

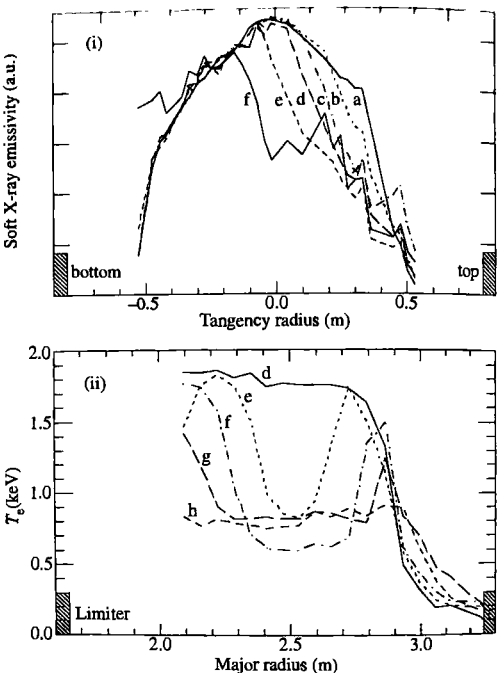


**Fig. 12.2.8** (i) Vertical profiles of chord integrated soft X-ray emissivity showing the downward penetration, at this toroidal location, of an  $m = 1$  deformation of the plasma core. (ii) Profiles of electron temperature, derived from ECE measurements in the horizontal midplane, showing the  $m = 1$  deformation appearing as a 'cold bubble'. Profiles are taken at 50  $\mu\text{s}$  intervals during the last 500  $\mu\text{s}$  before the thermal quench [Fredrickson, E.D. et al. *Nuclear Fusion* 33, 141 (1993)].

medium- $n$  ballooning modes, with  $4 \leq n \leq 10$ , in high- $\beta_p$  plasmas. For example, in discharges with  $\beta_p > 2$  a toroidally and poloidally localized mode, which has been modelled as a fragment of an  $m = 7/n = 6$  helical structure, was associated with a collapse in central electron temperature. As in the high- $\beta$  disruptions, the unusually high toroidal mode numbers, the strong outwardly asymmetric amplitude distribution, and the short growth time of the mode,  $\sim 20 \mu\text{s}$ , provided evidence for the ballooning character of this activity.

Coherent mhd activity potentially represents one of the major anomalous loss mechanisms for energetic fusion products. Two principal types of activity have emerged as possible causes for concern: low  $m/n$  mhd activity including sawtooth oscillations, fishbone instabilities and disruptions; and high frequency Alfvén eigenmodes. D-D reactions produce tritons and protons with MeV energies, and these particles have orbits and spatial profiles, and experience drag forces, similar to those of 3.5 MeV  $\alpha$ -particles. Their behaviour is expected, therefore, to provide

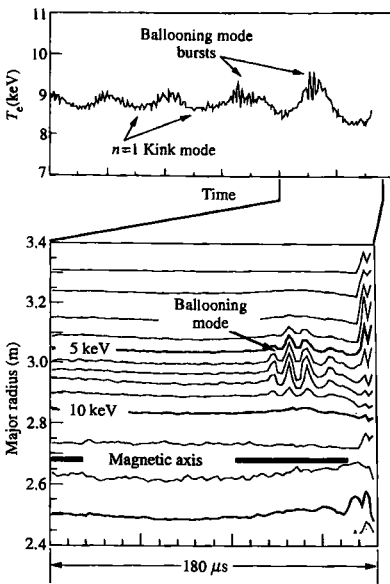


**Fig. 12.2.9** Contours of electron temperature in the  $180 \mu\text{s}$  preceding a disruption at high- $\beta$ , showing  $n = 1$  kink and ballooning mode precursor oscillations [from McGuire, K.M. et al. *Physics of Plasmas* 2, 2176 (1995)].

information on the confinement of  $\alpha$ -particles in D-T plasmas. Measurements of triton burnup, in which the triton reacts with a background deuterium ion producing a 14.1 MeV neutron, is an especially important diagnostic technique. In TFTR it was found that the observed 14.1 MeV neutron production was about a factor of two below that expected, even allowing for fuel dilution by impurities and for the long slowing-down time of the tritons. This discrepancy, which was greater in plasmas with longer triton slowing-down times, could be explained by a diffusion rate for fast particles of  $\sim 0.1 \text{ m}^2 \text{ s}^{-1}$ , although this appeared to be inconsistent with other experimental evidence on fast particle confinement.

The possibility that prompt triton losses were anomalously high, or that triton diffusion was anomalously fast, was excluded by direct measurements of losses of energetic tritons from the plasma edge. These showed that, in the absence of large amplitude coherent MHD activity, prompt losses were consistent with those expected from first orbit losses. Furthermore, the emission rates of 2.4 MeV neutrons and charge exchange neutrals during the decay phase of a short NBI pulse confirmed that the background diffusivity of energetic particles was less than  $0.1 \text{ m}^2 \text{ s}^{-1}$ .

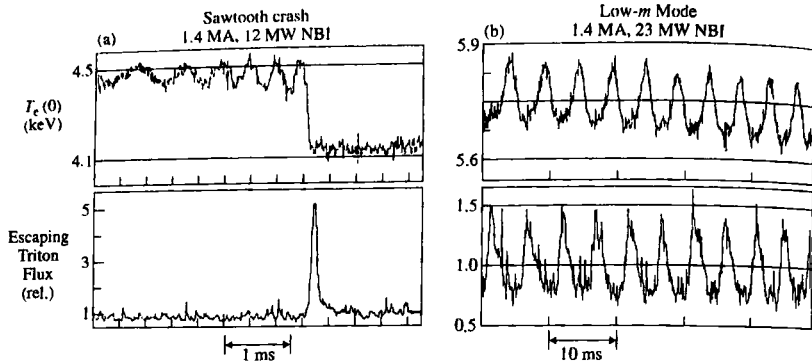


**Fig. 12.2.10** Experimental evidence of 1 MeV triton losses correlated with MHD activity: (a) a sawtooth collapse, (b) an MHD mode with  $m = 2/n = 1$  [from Strachan, J.D. et al. *Plasma Physics and Controlled Nuclear Fusion Research 1988* (Proc. 12th Int. Conf., Nice, 1988) Vol 1, 257. I.A.E.A., Vienna (1989)].

In contrast, cases with MHD activity did exhibit clear evidence of enhanced fast particle losses (Fig. 12.2.10). In such plasmas the prompt loss rate was  $\sim 5\text{--}10$  times the expected first orbit loss rate, and was of a level which might give rise for concern in a reactor.

Toroidal Alfvén eigenmodes (TAE modes), which were described in Section 7.15, have been identified as a potential cause of anomalous  $\alpha$ -particle losses which would reduce the efficiency of  $\alpha$ -particle heating and threaten damage to the first wall of a reactor. Densities of energetic particles with velocities high enough to satisfy the TAE resonance condition are usually too low for mode excitation at normal tokamak operating parameters. However, the resonance condition can be satisfied for the energetic ions produced by NBI if the toroidal magnetic field is reduced to  $\sim 1$  T. Under such conditions, bursts of magnetic fluctuations with frequencies in the region of 100 kHz were observed in experiments with up to 14 MW of balanced NBI using 100 keV injection energy. The bursts had dominant toroidal mode numbers  $n = 2$  and  $n = 3$ , and the mode frequency varied with toroidal field and plasma density in the manner expected for TAE modes,  $\omega \sim V_A/2qR_0$ . Their detrimental impact on the fast particle population was illustrated by global neutron measurements which showed a decrease of  $\sim 7\%$  associated with the growth of the fluctuation on the magnetic signals. Experimental evidence was also obtained that the energetic trapped protons created by ICRF heating could excite TAE modes, leading to losses of up to 10% of the fast protons.

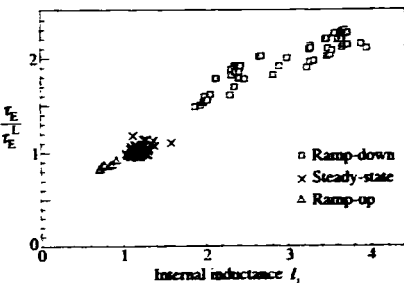
### Transport and confinement

Extensive experiments were carried out to elucidate the processes involved in determining transport in both supershot and L-mode regimes.

These investigations involved analysis of steady-state transport parameters and the use of perturbation techniques. One of the most striking results came from a series of L-mode discharges in which the plasma current was ramped to study how energy confinement is influenced by the current and the current profile. At a given power, the linear relationship between the L-mode energy confinement time and the plasma current is consistently reproducible in tokamaks. It might be expected, therefore, that the plasma energy would respond immediately to a change in the current. However, when the plasma current was ramped up or down, the change in stored energy was significantly delayed relative to the time of the current ramp. The plasma energy changed on a timescale closer to that characteristic of resistive diffusion, rather than the considerably shorter, energy confinement time. While a good correlation was found between the enhancement of the energy confinement and the plasma inductance, producing a scaling of the form  $\tau_E/\tau_E^{\text{L-mode}} \sim 0.4 + \ell_i/2$  (Fig. 12.2.11), a quantitative analysis of the time evolution of energy confinement in these experiments suggested that  $\ell_i$  was not the fundamental parameter describing the influence of the current profile. Nevertheless, this correlation between more peaked current profiles and improved confinement has been reproduced in other tokamaks.

As discussed in Section 4.14, two general forms of the anomalous thermal diffusivity have been explicitly identified, denoted as gyro-Bohm and Bohm. The crucial experimental test to distinguish between the two relies on how the diffusivity, or more precisely the thermal power flow through a magnetic surface, varies with the normalized Larmor radius,  $\rho_s = \rho_s/a$ . With care, a sequence of discharges can be established in which only  $\rho_s$  varies, primarily through the variation of the toroidal field, while other relevant dimensionless parameters are maintained nearly constant. The results of such an experiment clearly supported the conclusion that local transport in the L-mode regime is governed by Bohm, as opposed to gyro-Bohm, transport (Fig. 12.2.12).

Fig. 12.2.11. Results of current ramp experiments showing the ratio of the measured energy confinement time,  $\tau_E$ , obtained from the diamagnetic loop, to the Goldman L-mode scaling prediction,  $\tau_E^L$ , plotted against the internal inductance,  $\ell_i$ . Zarzuelo, M.C. et al. Plasma Physics and Controlled Nuclear Fusion Research A2: Proc. 14th Int. Conf., Wurzburg, 1992, Vol. I, 111 (IAEA, Vienna) (1993).



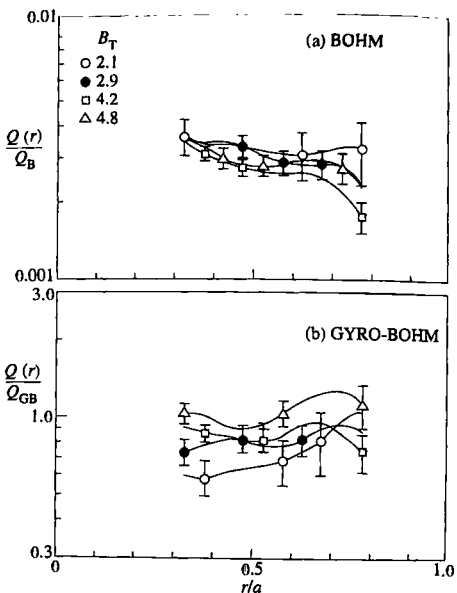


**Fig. 12.2.12** The thermal power flow,  $Q(r)$ , through a given flux surface normalized to the power flow predicted by Bohm scaling in (a), and by the gyro-Bohm scaling in (b), for a series of discharges in which the normalized Larmor radius was varied by changing the toroidal field. The smaller scatter in (a) is taken as evidence that L-mode transport is better described by Bohm than by gyro-Bohm scaling [Scott, S.D. et al. *Plasma Physics and Controlled Nuclear Fusion Research 1992* (Proc. 14th Int. Conf., Würzburg, 1992) Vol 3, 427. I.A.E.A., Vienna (1993)].

Further insight into local transport processes was derived from perturbative analyses of heat and particle transport, the former making use of the heat pulse due to the sawtooth collapse and the latter exploiting gas puffs from the plasma edge. Use of the sawtooth heat pulse to probe thermal transport was first attempted at the ORMAK tokamak, where good agreement was obtained between the measured thermal diffusivity and that resulting from the conventional power balance calculation. In TFR the thermal diffusivity deduced from sawtooth heat pulse propagation using soft X-ray and electron cyclotron emission measurements was up to an order of magnitude greater than that calculated from a steady-state power balance for ohmic and L-mode plasmas. Although it was initially concluded that the heat pulse perturbation propagates diffusively, subsequent investigations found that the sawtooth collapse contributed a 'ballistic', or non-diffusive, component to the thermal transport following the collapse, at least within  $r_{\text{mix}} < r < 1.5r_{\text{mix}}$ , where  $r_{\text{mix}}$  is the radius within which flux reconnection occurs in the Kadaomtsev model of sawtooth oscillations. This calls into question the simple interpretation of the heat pulse propagation in terms of a thermal diffusivity.

The temperature dependence of local transport coefficients was investigated in perturbative studies of electron particle transport in L-mode

helium plasmas heated by NBI. Small quantities of helium gas were puffed into a series of plasmas in which the NBI power was varied at constant plasma density. A significant aspect of this experiment was the use of a generalized form of the particle transport equations to account for variations in the particle diffusivity and pinch terms associated with changes in the perturbed density gradient. Analysis was restricted to the region  $0.43 < r/a < 0.75$  to eliminate uncertainties due to sawtooth activity in the plasma centre and due to the particle source term at the plasma edge. The resultant form of the particle transport coefficients, analogous to the particle diffusion coefficient and the pinch velocity, scaled strongly with local electron temperature, varying as  $T_e^\alpha$ , with  $1.5 < \alpha < 2.5$ . Power balance analysis yielded similar scalings for the ion and electron thermal diffusivities. This form of temperature dependence was taken as strong evidence that L-mode transport is governed by electrostatic drift-type microinstabilities.

The factors influencing transport in supershots were tested in experiments in which the density profile was transiently broadened, either by a helium gas puff, or by pellet injection. The motivation for such tests was the suggestion that supershot plasma profiles lie near the marginal stability limit for ion temperature gradient driven turbulence, for which the parameter  $\eta_i (= d \ln T_i / d \ln n_i)$  plays a determining role. A broadening of the density profile, leading to an increase in  $\eta_i$ , would be expected to generate an increase in the turbulence level and a broadening of the ion temperature profile, to return the plasma to marginal stability. In fact, the ion temperature gradient scale length,  $T_i/\nabla T_i$ , decreased, although  $\eta_i$  was well beyond the theoretically predicted stability limit, calling the original conjecture into question. It seems likely that an understanding of the reduced level of transport in supershots will rely on a self-consistent treatment of the neoclassical radial electric field shear associated with the pressure gradient and flow shear in the plasma and its influence on the stability of ion temperature gradient turbulence, as discussed in Section 12.5 in relation to the improved confinement of H-mode plasmas.

Developments in diagnostics of plasma turbulence, particularly in the areas of beam emission spectroscopy and microwave reflectometry, have allowed more precise comparisons between the underlying plasma turbulence and the measured plasma heat fluxes than was previously possible. It was shown that the relative level of density fluctuations at long wavelengths,  $k_\perp < 2\text{ cm}^{-1}$ , in the core of L-mode plasmas was inversely correlated with  $T_E$ . In addition, a random walk estimate of the local diffusivity, based on beam emission spectroscopy measurements of fluctuation correlation length and correlation time, was in rough agreement with power balance calculations of thermal diffusivity. However, the characteristics of turbulence in the plasma edge,  $r/a > 0.6$ , differed strongly from those at smaller radii and did not correlate with global energy confinement. This transition between core and edge turbulence was observed at all levels of NBI power and was maintained into the supershot regime, though the transition region moved outwards with increasing central temperature, reaching  $r/a \sim 0.9$  in supershots.

One of the key parameters in fusion research, the rate at which thermalized  $\alpha$ -particles are convected out of the plasma, can be determined by measuring the particle diffusivity of helium. This has become possible due to experimental and theoretical advances in the analysis of charge exchange spectra of helium. Helium transport was studied in the L-mode and supershot regimes using edge gas puffs and charge exchange measurements of helium profiles. While an inward pinch caused peaking of the helium density profile in supershots, the transport of helium was sufficiently fast in both regimes to be compatible with sustained ignition in a reactor.

### Experiments with deuterium-tritium mixtures

In late 1993 TFTR became the first tokamak to produce plasmas with a 50:50 mixture of deuterium and tritium. An extended series of experiments was performed to optimize fusion power production and to address important physics issues, such as the control of isotopic concentration, the isotopic dependence of confinement,  $\alpha$ -particle heating, and the existence of collective  $\alpha$ -particle effects. The programme also dealt with technological issues such as tritium handling, neutral beam injection of tritium, demonstration of ICRF heating scenarios, and tritium retention in the first wall.

To maximize fusion power and to access regimes of relevance to an ignited plasma, D-T studies concentrated on the supershot regime. The use of a D-T fuel mixture naturally leads to a factor of  $\sim 100$  increase in fusion power as compared to deuterium plasmas, but the D-T phase was also accompanied by developments in supershot plasmas. Some of these arose from advances in conditioning techniques, such as lithium pellet injection, and others were benefits deriving from the use of tritium. In particular, energy and particle confinement in supershots improved with increasing atomic mass. Thus, the ratio of D-T to D-D fusion power at constant plasma energy was  $115 \pm 15$ , while the ratio at constant NBI power was  $135 \pm 7$ . As a result, a maximum fusion power of 10.7 MW was achieved in a 2.7 MA/5.5 T supershot with 39.5 MW of mixed deuterium and tritium NBI. This pulse, which is illustrated in Fig. 12.2.13, had an instantaneous  $Q_{DT}$  of 0.27, neglecting  $\alpha$ -particle heating, and reached a normalized  $\beta$  of 1.8. Central fusion power densities in D-T supershots reached  $2.8 \text{ MW m}^{-3}$ , which is comparable to that expected in a reactor, while the maximum fusion yield was 7.6 MJ.

In experiments at moderate power, the combination of better conditioning and higher confinement allowed a gain of almost a factor of 3 in fusion triple product relative to the best deuterium plasmas. In a discharge heated by 17 MW of pure tritium NBI,  $n_{\text{hyd}}(0)T_i(0)\tau_E^* = 8.7 \times 10^{20} \text{ keV sm}^{-3}$  was attained, with  $T_i(0) = 44 \text{ keV}$ ,  $n_e(0) = 8.5 \times 10^{19} \text{ m}^{-3}$ , and  $\tau_E^* = 0.33 \text{ s}$ , where  $n_{\text{hyd}}(0)$  is the total density of all hydrogen isotopes in the plasma centre and  $\tau_E^*$  is the ratio of total stored energy to total input power, the time rate of change of the stored energy being neglected.

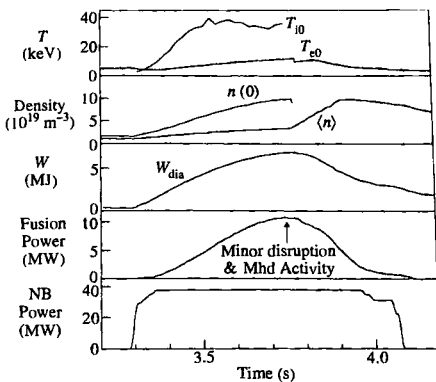


Fig. 12.2.13 Overview of the supershot with the highest D-T fusion power production, showing the central ion and electron temperatures,  $T_{i0}$ ,  $T_{e0}$ , the central and volume averaged electron densities,  $n(0)$ ,  $\langle n \rangle$ , the stored plasma energy,  $W_{dia}$ , the fusion power output, and the neutral beam heating power [Princeton Plasma Physics Laboratory].

Processes limiting fusion performance in D-T supershots were very similar to those observed in deuterium plasmas. At the highest power, the performance was limited by mhd stability, rather than confinement or heating power, and in particular by minor or major disruptions associated with the high values of  $\beta_N$ . At lower power levels, a range of mhd activity with low poloidal and toroidal mode numbers degraded confinement by up to 30%, as in deuterium supershots, though at currents above 2 MA their influence was usually weaker, causing a degradation of perhaps 5%. Further limitations arose from hydrogen, as opposed to deuterium and tritium, recycling from the limiter. In some cases this amounted to 20% of the recycling flux and diluted the plasma fuel mixture.

While the behaviour of D-T discharges was, in many respects, indistinguishable from that of deuterium plasmas, the global confinement and local transport were substantially modified in supershots with a significant tritium content. In D-T supershots both ion and electron temperatures increased with respect to equivalent deuterium cases, leading to increases of up to 22% in the stored plasma energy in D-T plasmas. Approximately 70% of the gain in stored energy was due to the thermal plasma, and both the thermal and total energy confinement times increased approximately as  $A^{0.9}$ , where  $A$  is the volume average isotopic mass of the hydrogenic ions in the region  $r/a < 0.5$ . Local transport coefficients in the core region,  $r/a \sim 1/3$ , scaled even more strongly with isotopic mass. At fixed injection power, the effective ion thermal diffusivity, which is proportional to the ratio of the total ion heat flux to the ion temperature gradient, scaled as  $A^{-2.6 \pm 0.3}$ , while the electron diffusion coefficient varied as  $A^{-1.4 \pm 0.2}$ . D-T limiter H-modes exhibited similar improvements and the energy confinement times reached  $\sim 4\tau_E^{\text{ITER89-P}}$ . In L-mode plasmas, isotopic effects were weaker, but both the thermonuclear and total energy

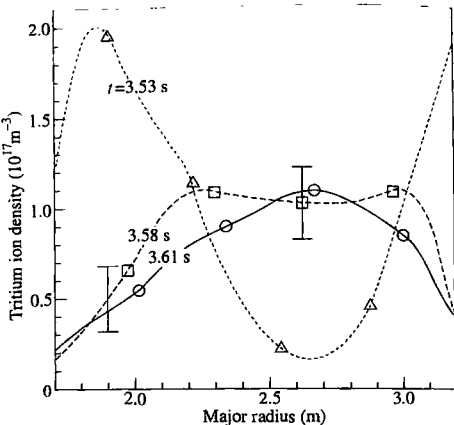


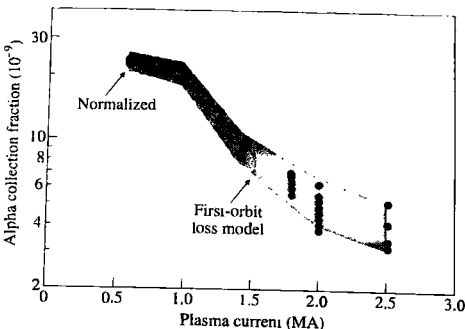
Fig. 12.2.14 Evolution of the tritium density profile inferred from neutron emissivity profiles following a tritium gas puff at 3.5 s [from Eftimion, P. C. et al. *Physical Review Letters* 75, 85 (1995)].

confinement times scaled at least as strongly as the  $A^{0.5}$  dependence of the ITER89-P scaling.

The large fusion cross-section for D-T reactions allows the resultant 14.1 MeV neutrons to be used as a sensitive diagnostic of the spatial profile of tritium within the plasma. The evolution of the tritium profile following a tritium gas puff can be deduced from the neutron emission profile, and the tritium transport coefficients can then be calculated. This technique was applied to supershots with tritium concentrations as low as 1% of that of deuterium. Fig. 12.2.14, showing the inferred evolution of the tritium profile following a tritium gas puff, illustrates how the initially hollow tritium profile becomes peaked on a timescale of  $\sim 100\text{ ms}$ . The local tritium particle diffusivity and convective velocity derived from these measurements are very similar, both in magnitude and radial profile, to He transport coefficients obtained under similar conditions. The tritium diffusivity,  $D_T$ , rises from  $\sim 0.6\text{ m}^2\text{ s}^{-1}$  in the plasma centre to  $\sim 2.5\text{ m}^2\text{ s}^{-1}$  at  $r/a \sim 0.9$ , while the inward convective velocity is close to zero, and consistent with neoclassical values, for  $r/a < 0.65$ , but exceeds the neoclassical prediction at larger radii.

Several important issues concerning the behaviour of energetic  $\alpha$ -particles were investigated. The energy distribution formed as the  $\alpha$ -particles slow from their 3.5 MeV birth energy was measured by several methods. Active charge exchange spectroscopy allowed measurements in the region up to 0.7 MeV. In addition, analysis of neutral helium lost from the plasma following the injection of a lithium or boron pellet, which provided a double charge exchange source, was used for  $\alpha$ -particle energies above 0.7 MeV. During the  $\alpha$ -thermalization phase, after the tritium NBI was switched off, the observed energy distribution followed that expected

**Fig. 12.2.15**  $\alpha$ -particle loss fraction captured by a lost  $\alpha$ -particle detector located at the bottom of the vacuum vessel, that is in the direction of the ion  $\nabla B$  drift. The first orbit loss falls with increasing plasma current in the manner predicted by model calculations. Note that the calculations are normalized to the experimental results at 0.5 MA [Hawryluk, R.J. et al. *Plasma Physics and Controlled Nuclear Fusion Research 1994* (Proc. 15th Int. Conf., Seville, 1994) Vol 1, II. IAEA, Vienna (1995)].



on the basis of collisional slowing-down and transport processes. In plasmas with monotonic shear profiles, the rate at which  $\alpha$ -particles were lost directly from the plasma was, in part, consistent with this. First orbit loss measured by a detector situated  $90^\circ$  below the plasma midplane fell by an order of magnitude as the plasma current increased from 0.5 to 2.5 MA (Fig. 12.2.15), in agreement with model calculations, and at 2 MA the total first orbit losses were only 3%. However, losses to detectors closer to the midplane were higher than expected, and it was suggested that the discrepancy involved additional loss mechanisms such as toroidal field ripple. Prompt losses of  $\alpha$ -particles in plasmas with reversed central shear were up to a factor of 2 greater than in equivalent discharges with monotonic shear. Code calculations showed that for some plasma conditions the higher value of  $q(0)$  could cause all  $\alpha$ -particles born on trapped orbits to be lost, either because they were on unconfined orbits, or due to stochastic ripple diffusion.

In D-T plasmas the loss of  $\alpha$ -particles due to coherent mhd activity was, for the most part, similar to the fusion product loss rate from deuterium plasmas, and affected only a small fraction of the total  $\alpha$ -particle population. At major disruptions, however, up to 20% of the energy stored in the  $\alpha$ -particles was lost in  $\sim 2$  ms during the thermal quench phase, with the loss predominantly downwards, that is in the ion  $\nabla B$  drift direction. Such localized energy losses will require specific measures to protect the first wall of a reactor. Loss rates comparable with first orbit losses were also observed in discharges with ICRF heating. It was proposed that  $\alpha$ -particles on marginally passing orbits could resonate with the RF waves and gain perpendicular energy, a process which transferred them to loss orbits.

TAE modes pose yet another threat to  $\alpha$ -particle confinement, but little evidence for TAE excitation by  $\alpha$ -particles was found in initial D-T experiments. For these conditions, code predictions indicated that

Landau damping, particularly by thermal and beam ions, exceeded the destabilizing contribution of the  $\alpha$ -particles. To explore the conditions for  $\alpha$ -particle excitation of TAE modes, a plasma discharge scenario was developed with weak central magnetic shear and  $q(0) > 1$ , following the predictions of theoretical calculations that the threshold for  $\alpha$ -driven TAE modes should be sensitive to the  $q$ -profile. In these discharges the high power heating phase was terminated before the high confinement phase, resulting in a rapid decay of the thermal and beam ion pressure, while the  $\alpha$ -particle pressure decayed on the longer  $\alpha$ -slowing-down timescale. Under these optimized conditions, it was possible to observe  $\alpha$ -driven TAE modes with low toroidal mode numbers, in the range  $n = 1-6$ , even at low central  $\alpha$ -particle pressure,  $\beta_\alpha(0) \sim 10^{-4}$  (Fig. 12.2.16). Due to the low amplitude of the excited TAE modes, no anomalous  $\alpha$ -particle losses were detected. On the other hand, a small enhancement, by approximately a factor of 2, of the rate of  $\alpha$ -particle losses above the first orbit losses was observed in the presence of kinetic ballooning modes, which are destabilized by steep pressure gradients in the thermal plasma.

Overall, the confinement of  $\alpha$ -particles in high current, mhd quiescent discharges with monotonic shear profiles, where first orbit losses were small, confirmed earlier measurements of energetic particle confinement based on neutral beam injected ions and fusion products in deuterium

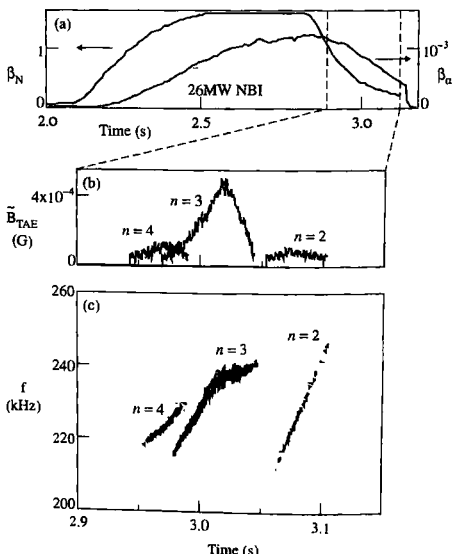


**Fig. 12.2.16** Observations of toroidal Alfvén eigenmodes excited by  $\alpha$ -particles in the NBI afterglow phase of a TFTR D-T plasma with weak central magnetic shear and  $q(0) \sim 1.1$ : (a) normalized plasma beta,  $\beta_N$ , and  $\alpha$ -particle pressure,  $\beta_\alpha$ , together with the NBI heating waveform, (b) amplitude of the magnetic field fluctuations,  $\bar{B}_{TAE}$ , for TAE modes having toroidal mode numbers  $n = 2, 3, 4$  modes, (c) frequency of  $n = 2, 3, 4$  modes. The increase in mode frequency correlates with the decrease in central density following the termination of NBI heating [Nazikian, R. et al., *Fusion Energy 1996* (Proc. 16th Int. Conf., Montreal, 1996) Vol 1, 281. I.A.E.A., Vienna (1997)].

plasmas: the radial diffusion coefficient for  $\alpha$ -particles was up to an order of magnitude smaller than that of thermal ions.

The TFTR D-T programme afforded the first opportunity in magnetic fusion research to investigate the effectiveness of plasma heating by  $\alpha$ -particles, which is an indispensable component of a D-T fusion reactor. During the high power heating phase of supershots, heating of electrons by  $\alpha$ -particles added only  $\sim 1$  MW to a total electro heating of  $\sim 10$  MW from beam heating and ion-electron equipartition. Although this contribution to electron heating was difficult to detect directly, steady-state power balance calculations concluded that  $\sim 50\%$  of the 2 keV rise in electron temperature in D-T relative to deuterium plasmas was explained by  $\alpha$ -particle heating. A more direct determination was made in the decay phase following NBI switch-off by injecting a lithium or boron pellet, which raised the density and caused a fall in electron temperature. The subsequent rate of reheat of the electrons was found to be  $\sim 85\%$  higher in D-T than in deuterium plasmas, in agreement with transport code analysis which included  $\alpha$ -particle heating. Finally, a detailed analysis of the scaling of electron temperature with plasma parameters in deuterium, tritium and D-T experiments revealed that, when the database of electron temperatures was corrected for the change in temperature associated with the isotopic dependence of energy confinement in supershots, the residual change in electron temperature was consistent with the predicted level of  $\alpha$ -particle heating of electrons.

## 12.3

### JET—Joint European Torus, Abingdon, UK

JET was constructed and operated between 1978 and 1999 as a joint undertaking by 16 European states under the auspices of EURATOM. Since 2000, the scientific and technical programme has been conducted under the European Fusion Development Agreement (EFDA) and the device has been operated on behalf of EFDA by the United Kingdom Atomic Energy Authority. The principal aims of the experiment are the investigation of heating and confinement in reactor relevant plasma conditions, the investigation of plasma-wall interactions and the study of  $\alpha$ -particle production, confinement, and consequent plasma heating.

The JET tokamak (Fig. 12.3.1), in which the first plasma was produced in June 1983, has a D-shaped poloidal cross-section to minimize stresses in the toroidal field coils. Its original aspect ratio was  $R/a = 2.96/1.2$ , though the minor radius was subsequently reduced to  $\sim 1$  m following the installation of the pumped divertor. The device operates with magnetic fields of up to 3.8 T and has reached plasma currents of 7 MA in limiter experiments. It is unusual among large tokamaks in that it has an iron

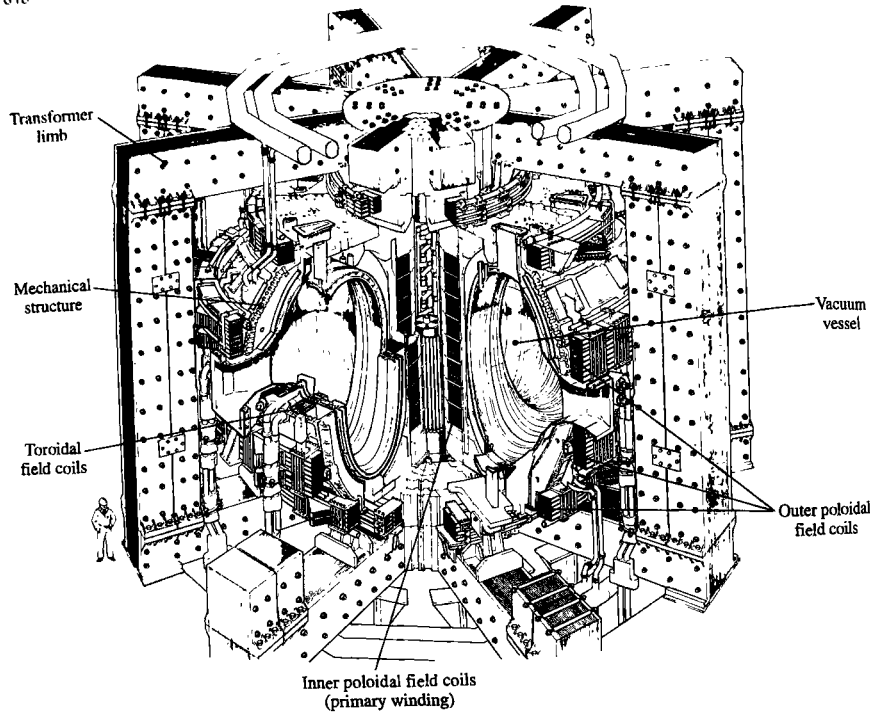


**Fig. 12.3.1** Layout of the initial configuration of the JET experiment.

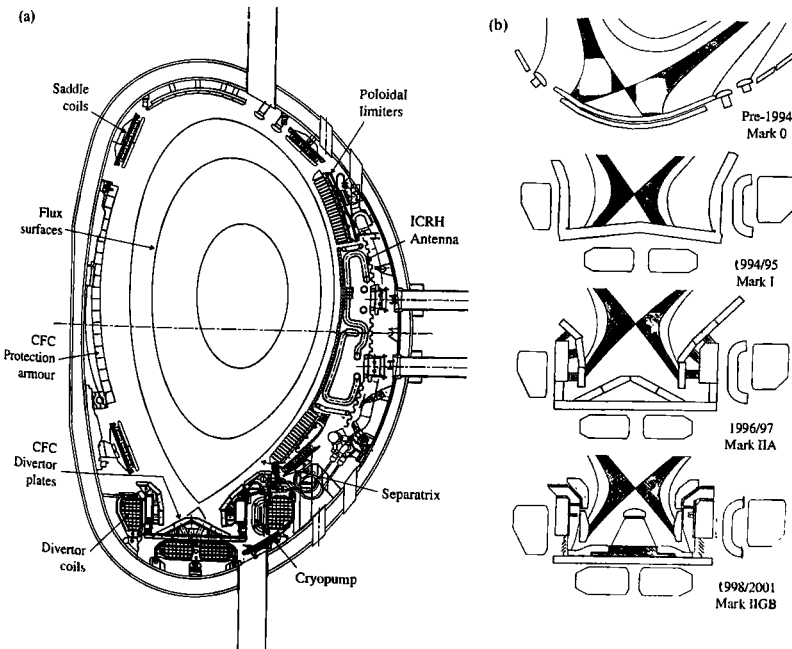
transformer core, which improves the efficiency of the primary circuit and reduces stray fields.

JET was originally envisaged as an elongated limiter tokamak, but was subsequently adapted for magnetic separatrix experiments and was eventually transformed, following a major upgrade in the period 1992–1993, to a pumped divertor configuration. This modification involved a substantial remodelling of the interior of the vacuum vessel (Fig. 12.3.2a) in order to facilitate investigations of the problems of heat exhaust and impurity control. The new arrangement incorporates internal divertor coils to generate a wide range of plasma equilibria and divertor geometries. In addition, a cryopump, with an in situ pumping capacity of  $\sim 200 \text{ m}^3 \text{ s}^{-1}$  for deuterium, permits the study of fuelling and impurity control strategies. The target arrangement has a power-handling surface designed to avoid overheating of tile edges and a capability for sweeping the divertor

strike points at 4 Hz, which allows long pulse, high power heating studies. Both carbon fibre and beryllium divertor targets have been used, though the latter for only a limited period, and the divertor geometry has been progressively modified to improve the power and particle control capabilities (Fig. 12.3.2b). Plasma performance has been studied in the pumped divertor configuration at currents of up to 6 MA.

The JET heating systems have been designed for high power, long pulse operation. The ICRF system has an installed generator capacity of 32 MW for 20 s and can be tuned in the ranges 23–39 MHz and 41–57 MHz so as to permit heating over a range of magnetic fields and minority resonance positions. The antennas can be operated as a phased array for current drive studies. NBI provides the second major source of heating, with a total capability of ~20 MW for 10 s at injection energies of up to 140 keV with deuterium and up to 160 keV with tritium. The main approach to current drive is the lower hybrid system, operating at 3.7 GHz, which has a generator capacity of 12 MW for 20 s.

**Fig. 12.3.2** (a) Poloidal cross-section of the JET pumped divertor configuration showing the divertor coils, the target plates for the Mark II A configuration and the cryopump. (b) The three principal pumped divertor configurations studied, in chronological order: Mark I, Mark II A, Mark II GB (Gas Box). From 2002 on, experiments were conducted without the central septum dividing the inner and outer divertor legs in the Mark II GB. The original X-point configuration, subsequently referred to as the 'Mark 0', is also shown for comparison.



### Limiter experiments

Experiments have been performed using either the outer limiters or the inner wall as limiting surfaces. The former originally consisted of eight discrete graphite poloidal limiters, but these were later replaced by two toroidal belt limiters approximately 1 m above and below the equatorial plane of the vessel. The inner wall limiter consisted of a continuous region of carbon tiles extending 1 m above and below the equatorial plane. Initially all power-handling surfaces were fabricated from graphite or carbon fibre, but solid beryllium has been used for limiter and/or divertor targets in several experimental campaigns from 1989 onwards. The principal techniques for conditioning of the vessel and plasma-facing surfaces have been baking to 350 °C and glow discharge cleaning in deuterium and helium. Carbonization has also been used, but from 1989 onwards beryllium gettering has been preferred since it has proved to be a highly efficient conditioning method.

Initial experiments characterizing the confinement and impurity content of ohmic discharges showed that the variation of  $\tau_E$  and  $Z_{eff}$  with plasma parameters was very similar to that in TFTR. As a result of the larger dimensions of JET and the increased current capability, the maximum energy confinement time in ohmic plasmas reached values of  $\sim 1$  s. Analysis of plasma loop voltage and equilibrium evolution led to the conclusion that, as in TFTR, the resistivity is described by the neoclassical, rather than Spitzer, formulation.

It is well known that elongated plasmas are vertically unstable, as discussed in Section 7.12, and a feedback controlled stabilization circuit is used to maintain the plasma vertical position. Nevertheless, at the limits of stabilization and following sudden changes in equilibrium, such as occur at a disruption, control of the vertical position is often lost. A particularly severe case was encountered during the first year of operation. At 2.7 MA and an elongation of 1.7, a force of several hundred tonnes was transmitted to the vacuum vessel, which weighs  $\sim 100$  tonnes, causing a vessel displacement of  $\sim 1$  cm. Subsequent analysis indicated that a substantial poloidal current flowing through the plasma and the vacuum vessel was required to maintain force balance. The existence of these 'halo currents', discussed in Section 7.12, which are driven by the voltage induced as the plasma crosses the magnetic field in the course of the instability, has been demonstrated by direct measurement of the resultant fields and of the currents flowing in interior vessel components. Experiments have also shown that the distribution of halo currents and forces may not be toroidally symmetric and this is believed to be associated with the growth of a non-axisymmetric MHD instability during the vertical motion. The large vertical and radial forces to which the vacuum vessel and in-vessel structures were subjected led to improvements in the arrangements for supporting the vacuum vessel and a more cautious approach to operation at the limits of vertical stability control.

LHCD and ICRF heating have been used to reduce the plasma resistivity, both by raising the electron temperature and by accelerating electrons to high energy, thereby extending the duration of the current flat-top. For

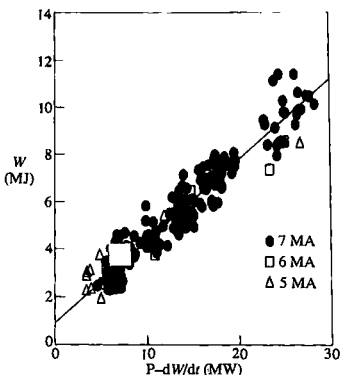
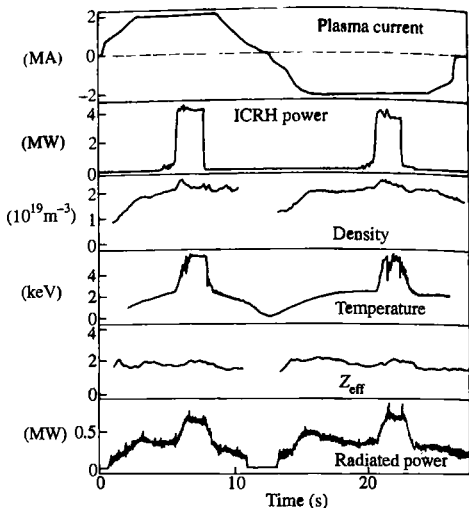


Fig. 12.3.3 Thermal stored energy plotted against loss power for plasmas at 7 MA. Data taken at 5 and 6 MA in the same series of pulses are also shown [The JET Team (presented by P. J. Lomas) *Plasma Physics and Controlled Nuclear Fusion Research 1992* (Proc. 14th Int. Conf., Würzburg, 1992) Vol 1, 181. IAEA, Vienna (1993)].

example, by exploiting LHCD during the current ramp-up, a flat-top duration of 8.5 s was attained at a plasma current of 7 MA. In addition, at 2 MA the plasma pulse was sustained for 60 s, which allowed the plasma behaviour to be investigated on timescales commensurate with those for resistive diffusion and plasma-wall interactions to reach steady-state. The most significant observation was that particle pumping by the plasma walls saturated after  $\sim 30$  s and thereafter the plasma density rose, emphasizing the need for active means of particle control in long pulse experiments.

Confinement data in limiter plasmas cover the range from 1 to 7 MA, with  $q(a)$  in the range 2 to 15 and with total input powers of up to 35 MW using NBI, ICRF, and LHCD. The maximum energy in a 7 MA plasma was 12 MJ, corresponding to an energy confinement time of 0.4 s. Energy confinement of 7 MA discharges at the highest powers was consistent with L-mode scalings, but with considerable scatter in the data. This was particularly noticeable at moderate powers (Fig. 12.3.3), where data in the range 5–7 MA showed no significant variation with current. A rise in the plasma density with increasing current, leading to a broadening of the NBI power deposition profile, was suggested as an important factor in this behaviour. Sawtooth oscillations were also proposed as an element in the confinement degradation, since the sawtooth mixing-radius increases with decreasing  $q(a)$ . In consequence, 7 MA plasmas produced fusion triple products of  $\sim 1 \times 10^{20} \text{ keV sm}^{-3}$ , but the best triple product in limiter plasmas was obtained in 3 MA discharges, which exhibited more peaked plasma profiles and yielded a value of  $n_i(0)T_i(0)\tau_E \sim 2 \times 10^{20} \text{ keV sm}^{-3}$ .

Pulsed AC operation of the tokamak has been suggested as a possible alternative to the requirement that a fusion reactor should operate



**Fig. 12.3.4** Parameters of a full AC plasma cycle at 2 MA [from Tubbing, B.J.D. et al. *Nuclear Fusion* **32**, 967 (1992)].

as a steady-state device. This mode of operation was first demonstrated on the STOR-1M tokamak at a plasma current of 4 kA and was further investigated in JET in 2 MA discharges (Fig. 12.3.4). The aim of these experiments was to demonstrate that two plasma discharges with equal and opposite plasma currents could be produced with essentially zero delay between the termination of the first and initiation of the second. A major concern was that the termination of the first plasma would adversely affect the breakdown conditions for the second. However, it was found that the second breakdown could be achieved for delays of between 50 ms and 6 s following the termination of the forward cycle, even after disruptions at several 100 kA. No significant differences in plasma parameters, including impurities and radiated power, were observed between the two cycles and the overall gas consumption was the same as in a long, uninterrupted tokamak pulse.

#### Magnetic separatrix experiments

Although JET was conceived as a limiter tokamak, it was recognized that its shaping capability permitted operation with a magnetic separatrix within a limited current range. Such plasmas, also known as X-point plasmas, were widely exploited before the installation of the pumped divertor, principally for investigation of H-mode and high performance plasmas, but also for initial studies of divertor physics. Both single null and double null X-point configurations were studied. In ELM-free H-modes global

energy confinement is typically twice as high as that in equivalent L-mode plasmas, but degrades with power as in the L-mode. For plasma currents ranging up to 4 MA in the original JET configuration, energy confinement increased linearly with current at fixed power, consistent with the empirical scaling expressions, but between 4 and 5 MA, the confinement time varied little.

In contrast to plasmas in other tokamaks, H-modes in the original JET configuration were generally ELM-free and the improvement in particle confinement caused a rise in the plasma density, leading to a monotonic increase in radiation. This eventually terminated the H-mode after a period of 3–5 s when the radiated power equalled the input power. ELMs H-modes were produced by puffing gas throughout the H-mode, leading to the establishment of a steady-state regime lasting up to 18 s, which was limited in duration by stresses in the shaping field windings rather than plasma physics constraints. A gradual rise in the density towards the end of these plasmas emphasized yet again the need for active pumping to control particle influxes. Energy confinement in these plasmas was in the range  $1.4\text{--}1.8\tau_{E}^{\text{ITER89-P}}$ , with the best confinement in discharges which were free of large amplitude  $n = 1$  mhd activity.

### Mhd and operational limits

Major disruptions, which are the principal limitation to the operating space accessible to JET plasmas, have several main causes: current rise instabilities,  $q(a)$  reaching 2, error field modes, density limits, neoclassical tearing modes and, especially in plasmas with internal transport barriers, ideal kink instabilities. To this list must be added the vertical instability, which involves rather different physics, but has equally serious consequences. Large amplitude ELMs, such as those observed at the termination of the high fusion performance phase of hot ion H-modes, which are discussed later, emerged as a particularly troublesome source of vertical instabilities during pumped divertor operation. Disruptions in JET follow a well defined sequence of events, and the general behaviour has been described in Sections 7.8 to 7.10. Many of the disruptions can be understood by following the plasma trajectory in the  $\ell_i$ - $q(a)$  diagram in which various, empirical, stability boundaries are plotted (Fig. 12.3.5). The vertical legs of the triangular-shaped lower boundary occur at integer values of  $q(a)$  and correspond to the growth of modes with  $m/n = q(a)/1$ , which can be destabilized if the current ramp rate is too great. Modes growing at  $q(a) = 3, 4$  are particularly dangerous as these can cause disruptions. Experiments have shown that plasmas invariably disrupt at  $q(a) = 2$ , indicating the existence of a hard barrier. The upper stability boundary represents plasmas in which the current channel has contracted to within  $q = 2$ . This is usually the situation in plasmas at the density limit after the radiated power fraction reaches unity.

In JET the L-mode density limit is associated with the radiated power reaching 100% of the input power, due to over-fuelling, to impurities

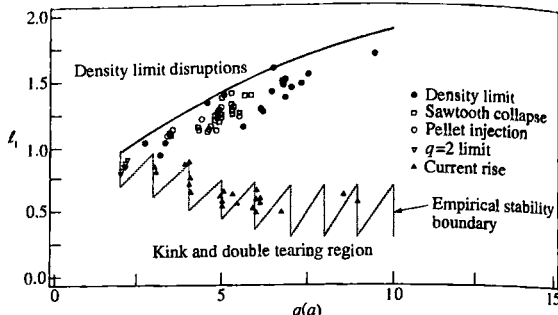


**Fig. 12.3.5** Diagram of loci in the  $\ell_1$ - $q(a)$  plane at which an  $n = 1$  locked mode first occurred in disruptive plasmas under a variety of circumstances. The vertical legs of the lower stability boundary occur at integer values of  $q(a)$  [Snipes, J.A. et al. *Nuclear Fusion* **28**, 1085 (1988)].

entering the plasma, or to a loss of auxiliary heating power. In experiments with carbon plasma-facing materials, before beryllium gettering was applied routinely the limit did not increase significantly with additional heating. The density limit parameter,  $10^{-19} \bar{n} R q(a)/B$ , rose from  $12$  to  $20 \text{ m}^{-2} \text{T}^{-1}$ , with little evidence of a systematic improvement with power. Increased impurity generation with additional heating was thought to be responsible for the robust nature of the limit. The introduction of beryllium as a limiter material produced very different behaviour, with density limit parameters in the range  $30$ – $40 \text{ m}^{-2} \text{T}^{-1}$ , densities 50% in excess of the Greenwald density,  $\bar{n}_{\text{GW}}(10^{20} \text{ m}^{-3}) = I(\text{MA})/\pi a^2$ , and MARFEs playing an important role at the limit. Moreover, the plasma density was often observed to fall in response to the formation of a MARFE. In limiter configurations, therefore, the frequency of disruptions was very much reduced. In addition, a clear correlation was found between the limiting density at the plasma edge,  $n_{\text{edge}}$ , and the total input power,  $P$ , with  $n_{\text{edge}} \propto P^{0.5}$ . This observation is in agreement with theoretical expectations for a limit determined by impurity radiation.

Small deviations from axisymmetry in the externally applied magnetic field give rise to non-rotating  $m = 2/n = 1$  modes which cause disruptions, as discussed in Section 7.11. In JET, field errors, which arise principally from the structure of the poloidal field coils, have been calculated to be  $\sim 1 \text{ G}$  at the  $q = 2$  surface. However, the resulting  $m = 2$  mode grows to saturation levels of  $\sim 10 \text{ G}$ . The mode grows at low plasma density and sets a lower density limit for plasma operation, which increases as  $q(a)$  falls below 4. Experiments have been conducted, by varying the number of active turns in the vertical field coils, to investigate how variation of the magnitude of the field error influences the threshold density. As expected, raising the field error by a factor of  $\sim 2.5$  significantly increases the density range over which the mode grows. In contrast, with the installation of the pumped divertor coils, the total  $n = 1$  component

of the error field has fallen, allowing an expansion of the operating space at low density. Since such modes grow from a stationary field error, spinning of the plasma by NBI is often used to suppress their growth and permit operation below the threshold density. It has also been possible to exploit the internal saddle coils, installed at the time of the pumped divertor upgrade, both to investigate the dependence of the critical error field for instability growth on plasma parameters and to partially correct the  $n = 1$  component of the error field.

The forces applied to the vacuum vessel during disruptions are outlined in Section 7.9. These are a source of great concern, and there has been considerable incentive to avoid regions of operating space in which disruptions occur, or else to minimize the impact of disruptions when they are unavoidable. In JET, the growth of a locked  $m = 2/n = 1$  precursor to a radial disruption has allowed the implementation of a disruption amelioration system. This is triggered when the amplitude of the  $m = 2/n = 1$  mode exceeds a threshold value and it is intended primarily to reduce disruption forces. Since the elongation determines the severity of the force associated with the vertical instability which often accompanies disruptions, and since the resultant force scales quadratically with the plasma current, the main action of the system is to reduce the plasma elongation and current. In this way the force applied to the vacuum vessel has been reduced by up to an order of magnitude.

Sawtooth oscillations have been studied at some length using two-dimensional reconstructions of soft X-ray emission and local electron temperature measurements from electron cyclotron emission. These have revealed that the sawtooth collapse has two main phases. The first consists of a rapidly growing  $m = n = 1$  displacement of the plasma core, and the second is a rapid redistribution of energy, leading to flattening of the central temperature profile on a timescale of  $100 \mu\text{s}$  (Fig. 12.3.6). The initial  $m = 1$  instability apparently takes different forms, in some cases appearing as a classic  $m = 1$  island, indicative of reconnection, in others resembling a convective cell, as illustrated in the figure. In all cases, the onset of the mode is too rapid to be explained by conventional theories of resistive reconnection and, although theoretical analyses of collisionless reconnection have brought calculated and measured values of the collapse time into closer agreement, the rapid growth of the  $m = 1$  instability at the sawtooth collapse remains problematic. It is clear, moreover, that the transport of energy which leads to the flattening of the temperature profile occurs without a full magnetic reconnection, implying that some additional rapid transport mechanism is required. The theoretical implications of the JET observations relating to the sawtooth collapse are discussed in detail in Section 7.6.

Other questions concerning the  $m = 1$  instability are raised by pellet injection experiments which have revealed that a very localized density perturbation, the 'snake', can persist for several seconds following ablation of the pellet (Fig. 12.3.7). It has  $m = n = 1$  symmetry, is located at the  $q = 1$  surface, and can undergo a substantial shift in minor radius,  $\Delta r/r \sim 30\%$ , in the course of a sawtooth period. The inference that

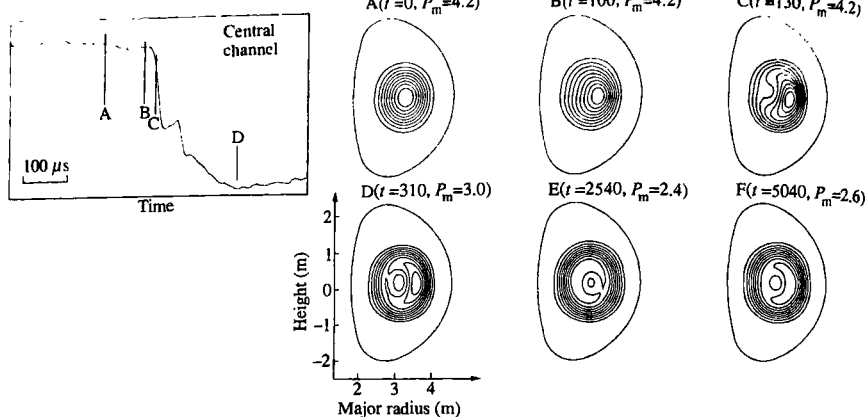


**Fig. 12.3.6** Contour plots of X-ray emissivity during a sawtooth collapse with time slices shown in microseconds ( $\mu s$ ). Core displacement is seen in frames A and B, and poloidal spreading in frame C. The peak emissivity falls significantly between frames C and D, corresponding to rapid core cooling. Frames E and F show a residual asymmetry several milliseconds after the collapse. The time intervals associated with the contour plots are in microseconds and the maximum power density,  $P_m$ , is in kilowatts per cubic metre [Campbell, D.J. et al. *Plasma Physics and Controlled Nuclear Fusion Research 1986* (Proc. 11th Int. Conf., Kyoto, 1986) Vol 1, 433. I.A.E.A., Vienna (1987)].

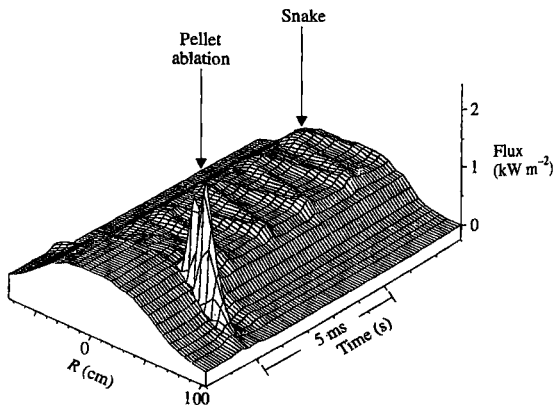


**Fig. 12.3.7** Three dimensional contour plot of soft X-ray emission, as viewed from a camera situated above the plasma, showing the snake-like perturbation of the emission following the injection of a deuterium pellet. The plasma centre is at  $R = 0$  [from Weller, A. et al. *Physical Review Letters* **59**, 2303 (1987)].

the  $q = 1$  surface undergoes a similar displacement would appear<sup>10</sup> imply that the central  $q$ -profile is flat, with  $q(0)$  within a few per cent of unity, in contradiction of polarimetric measurements, which show that  $q(0)$  is typically  $\sim 0.7$  in sawtooth discharges and remains well

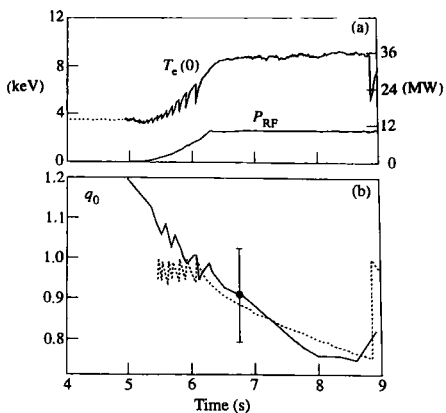


**Fig. 12.3.8** (a) Central electron temperature,  $T_e(0)$ , and ICRF heating power,  $P_{RF}$ , illustrating stabilization of sawtooth oscillations by central ICRF heating. (b) Evolution of the central safety factor,  $q_0$ , as determined by polarimetric measurements (solid line) and resistive diffusion calculations (dashed line) [from Campbell, D.J. et al. *Plasma Physics and Controlled Nuclear Fusion Research 1988* (Proc. 12th Int. Conf., Nice, 1988) Vol. 1, 377. I.A.E.A., Vienna (1989)].

below unity throughout the sawtooth collapse. Unfortunately, the two measurements cannot be made simultaneously. The persistence of the perturbation through many sawtooth collapses confirms, however, that the region inside  $q = 1$  cannot be fully reconnected during the collapse. A final problem is raised by the persistence of the snake for times much longer than its collisional confinement time.

Concern over sawtooth modulation of the central fusion reactivity of the plasma has stimulated studies of methods for stabilizing the sawtooth instability. Modification of the current profile to maintain  $q(0) > 1$ , for example, by lower hybrid current drive, appears to be the most reliable technique. However, sawtooth oscillations have been stabilized by a variety of other methods, some of which provide insight into novel aspects of the physics. For example, in plasmas with central heating and significant fast particle populations, sawtooth oscillations can be stabilized for periods of several seconds (Fig. 12.3.8). Although the phenomenon can be obtained in neutral beam heated plasmas, the appropriate conditions are particularly straightforward to achieve using ICRF minority heating with a central resonance. The ICRF can accelerate minority ions to energies of  $\sim 1$  MeV and a fast ion population with substantial total energy can develop. Detailed experimental results, including the reduction in the efficiency of the stabilization as the minority resonance is moved off-axis, are consistent with a theory which proposes that the fast ion population is responsible for the stabilization, essentially as a result of the conservation of the third adiabatic invariant of the energetic ions, defined in Section 2.7.

Further understanding of factors influencing the stability of sawtooth oscillations has emerged from experiments on the feasibility of ICRF fast wave current drive using minority ions. As discussed in Section 3.13,

this is expected to drive anti-parallel currents on either side of the ICRF resonance position, causing changes in the local current gradient. By varying the relative phasing of the current straps in the ICRF antenna so as to either reduce the current gradient at  $q = 1$ , using phase  $\phi = +90^\circ$ , or to increase it, using  $\phi = -90^\circ$ , a significant change in sawtooth behaviour occurs (see Fig. 3.14.3). In the former case large amplitude sawtooth activity with extended periods is observed, while in the latter case small, rapid sawtooth activity results. These observations support theoretical predictions that the current gradient at  $q = 1$  influences the stability of the  $m = 1$  mode responsible for sawtooth oscillations.

The phenomenon of sawtooth stabilization and the ability of minority ion current drive to control the sawtooth period have been exploited to provide insight into the relationship between sawtooth activity and the limitation on  $\beta$  set by neoclassical tearing modes. Although  $\beta$  values of  $\sim 6\%$  and  $\beta_N$  values of  $\sim 3.8$  have been achieved in JET, these modes are often observed to degrade plasma confinement at  $\beta_N$  values significantly below the ideal stability limit, as is the case in many tokamak experiments. It has been shown that in plasmas with long periods of sawtooth stabilization, typically longer than 600 ms, the terminating collapse triggers the growth of the modes at  $\beta_N$  values as low as 0.5–1. When localized minority current drive is used to shorten the sawtooth period, as described above, the attainable  $\beta_N$  can be increased by a factor of 2 or more. The growth of neoclassical tearing modes generally requires a seed island of a critical size, which is generated by other forms of mhd such as sawteeth, and it has been proposed that collapse terminating a long sawtooth-free period causes a larger magnetic perturbation, thereby producing a larger seed island for a given value of  $\beta_N$ . This approach to controlling the value of  $\beta_N$  at which neoclassical tearing modes occur may provide an important method of influencing the  $\beta$ -limit in reactor-scale plasmas, where  $\alpha$ -particles are predicted to stabilize sawteeth for tens of seconds.

TAE modes have been investigated in considerable detail, principally by a novel application of internal saddle coils which were originally envisaged as a means for stabilizing the  $m = 2/n = 1$  mode responsible for major disruptions, in the manner first explored on the DITE tokamak and discussed in Section 11.7. These were adapted for the excitation of small amplitude ( $\delta B/B \sim 10^{-5}$  in the plasma core), high frequency (20–500 kHz) perturbations with  $|n| = 1, 2$ , and used as an active probe of the frequency and damping rate of Alfvén eigenmodes in the plasma by means of a resonance detection circuit which analysed signals from magnetic pick-up coils at the plasma edge. Figure 12.3.9(a) illustrates the variation in frequency of a TAE mode analysed in this way as the toroidal field was swept in time. This technique has allowed the net damping rate of Alfvén eigenmodes to be investigated over a wide range of plasma conditions in ohmic and additionally heated plasmas and led, in particular, to the first unambiguous measurement of ellipticity-induced Alfvén eigenmodes (EAE). In high temperature plasmas, kinetic effects such as the finite ion Larmor radius can cause the Alfvén continuum in the vicinity of each TAE mode to split into a series of closely spaced kinetic TAE

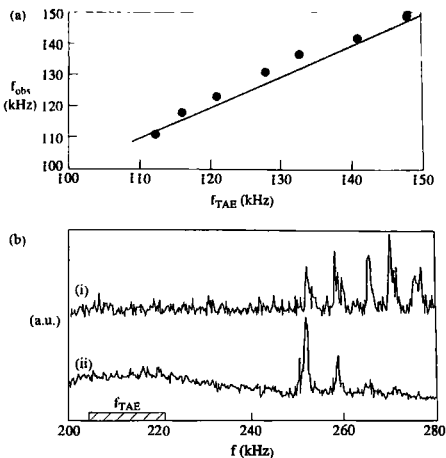


**Fig. 12.3.9** (a) A comparison of the measured eigenmode frequency,  $f_{\text{obs}}$ , as detected by the active magnetic perturbation technique, with the calculated TAE frequency at the  $q = 3/2$  surface,  $f_{\text{TAE}}$ , during a toroidal magnetic field sweep [from Fasoli, A. et al. *Physical Review Letters* 75, 645 (1995)]. (b) Frequency spectrum of (i) magnetic and (ii) density perturbations during additional heating, illustrating the fine splitting of the TAE spectrum associated with the occurrence of kinetic TAEs [from Fasoli, A. et al. *Physical Review Letters* 76, 1067 (1996)].

modes. The first observations of such behaviour were also obtained using this technique (Fig. 12.3.9(b)).

### Transport and confinement studies

The exploitation of heat and density pulses generated by sawtooth collapses to probe the local transport properties of the region outside  $q = 1$  was a particular feature of early JET experiments. As in TFTR, the values of transport coefficients derived by this method were larger than those deduced from power balance calculations. In the case of the thermal diffusivity, the heat pulse value,  $\chi_e^{\text{hp}}$ , was typically a factor of 1–4 greater than  $\chi_e^{\text{pb}}$ , the value calculated from the steady-state power balance. This stimulated the development of a description of  $\chi_e^{\text{hp}}$  which identified this quantity with an incremental diffusivity,  $\chi_e^{\text{inc}}$ , which determines heat transport in response to a perturbation of the temperature profile.

Several perturbation techniques have been applied to the investigation of the particle diffusion coefficient,  $D$ . The most complete calculation used measurements of temperature and density profile perturbations to include the possibility of direct coupling between heat and particle transport. Deduced values of  $\chi_e^{\text{hp}}$  and  $D$  were in agreement with independent analyses of the individual perturbations. However, the coupled analysis suggested that an additional particle pinch driven by  $\nabla T_e$ , or a diffusion coefficient which is a decreasing function of  $\nabla T_e$ , was required to explain the response of the density to the temperature perturbation.

A model of the H-mode transition in which a sudden change in transport at the very edge of the plasma, within  $\sim 1$  cm of the separatrix, is followed by a gradual improvement in transport at smaller minor radii has become generally accepted as a result of extensive experimental observations, particularly in ASDEX and DIII-D. Nevertheless, measurements of electron and ion temperature profile evolution in JET have shown that confinement changes very rapidly over a broad region at the H-mode transition. This effect is particularly pronounced in high performance plasmas, characterized as hot ion H-modes, in which high power injection into a low recycling target plasma permits the temperature change at the L-H transition to be observed clearly. The observed behaviour cannot be explained by a simple model which assumes a change in temperature at the plasma edge followed by heat pulse propagation towards the core. Instead, a rapid reduction in transport over the outer half of the minor radius is required, suggesting that the underlying turbulence responsible for L-mode transport has a radial scale length of order the plasma minor radius.

The response of the heat flux to positive and negative temperature gradients was studied by comparing the conducted heat fluxes in cases where the heating profiles were peaked either on or away from the plasma centre. ICRF was used to compare discharges in which the heating profile was peaked at  $r = 0$  and  $r/a = 0.5$ . This experiment showed that the heat flux was close to zero when  $n\nabla T_e$  was small, implying a negligible heat pinch. In addition, the heat flux rose roughly parabolically with  $-n\nabla T_e$ , suggesting that  $x$  was simply proportional to  $|\nabla T_e|$ , although a dependence on  $T_e^\alpha$ , with  $\alpha \sim 2.5$ , could not be excluded.

Fundamental information on the nature of thermal transport and how it scales to next generation experiments can be obtained from dimensionless scaling experiments in which many key non-dimensional plasma parameters are fixed while  $\rho_*(=\rho_i/a)$  is varied. In a series of ICRF heated L-mode discharges in which both plasma current and toroidal magnetic field were varied so as to keep  $q$ , collisionality, and beta constant, the total conducted heat flux was compared with that expected on the basis of Bohm and gyro-Bohm scalings. As in TFTR, better agreement was obtained with Bohm scaling. Similar experiments performed in NBI heated H-mode plasmas showed that the effective thermal diffusivity exhibited a clear gyro-Bohm dependence, and this conclusion has been confirmed for H-mode plasmas in other tokamaks and in comparisons between tokamaks. Further such experiments performed during the DTE1 deuterium-tritium studies, discussed later, confirmed the gyro-Bohm nature of the confinement scaling and yielded favourable fusion performance extrapolations to ITER.

Following the installation of the pumped divertor, it was found that H-modes, previously ELM-free, exhibit regular giant ELMs, which have enabled steady-state H-modes of up to 20 s duration to be established. In addition, ELMy H-modes were demonstrated at 6 MA with stored energies of 13 MJ, at that time the highest plasma energy achieved in any tokamak (Fig. 12.3.10). Detailed investigations have revealed that the level of recycling influences ELM behaviour, but that the magnetic

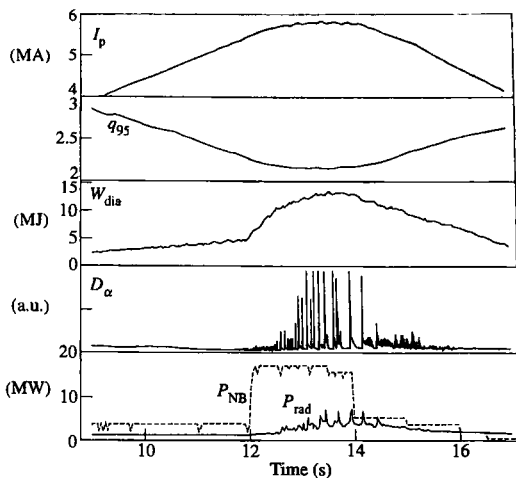


**Fig. 12.3.10** Parameters of a JET 6 MA H-mode showing the plasma current,  $I_p$ , the safety factor at the 95% flux surface,  $q_{95}$ , the plasma diamagnetic energy,  $W_{dia}$ , the  $D_\alpha$  emission, the neutral beam power,  $P_{NB}$ , and the radiated power,  $P_{rad}$ .

shear at the plasma edge is probably more fundamental. Long ELM-free H-modes can be obtained in equilibria with higher edge shear, which more closely resemble plasmas typical of the previous configuration. Mhd analysis suggests that the onset of ELMs occurs close to the ballooning limit at the plasma edge and that this limit can be raised by increasing the edge shear.

Investigation of the H-mode power threshold scaling in hydrogen, deuterium, and tritium plasmas confirmed that the inverse dependence of the power required for H-mode access on the ion atomic mass, previously observed in comparisons of hydrogen and deuterium plasmas, extended to tritium plasmas and, crucially, to D-T mixtures (Fig. 12.3.11). Global confinement analysis was also performed in plasmas with various hydrogen isotope mixtures and it was deduced that the thermal confinement time was approximately independent of mass, scaling as  $A^{0.03 \pm 0.1}$ . However, separation of the stored energy into contributions associated with the H-mode pedestal and the plasma core showed that while the former exhibited a strong mass dependence, scaling as  $A^{0.5}$ , the latter varied as  $A^{-0.17 \pm 0.1}$ , which was consistent with the  $A^{-0.2}$  dependence expected from a gyro-Bohm scaling of local transport in the core.

The range of densities at which H-mode level performance can be maintained was significantly extended by exploiting increased plasma triangularity. Experiments at plasma singularities of up to  $\delta_X = 0.46$ ,

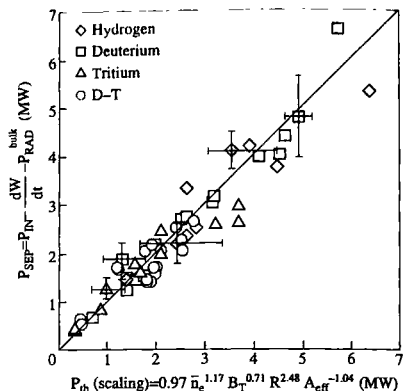


**Fig. 12.3.11** Scaling analysis of the power crossing the separatrix,  $P_{\text{SEP}}$ , at the L-H-mode transition, as defined by total input power,  $P_N$ , corrected for radiation losses,  $P_{\text{RAD}}^{\text{bulk}}$ , and the time derivative of the stored energy,  $dW/dt$ . The abscissa represents a standard H-mode power threshold scaling corrected by a best fit calculation of the experimental dependence of  $P_{\text{SEP}}$  on the effective atomic ion mass,  $A_{\text{eff}}$  [from Righi, E. et al. *Nuclear Fusion* 39, 309 (1999)].

where  $\delta_X$  is the triangularity at the separatrix, demonstrated that the deterioration in H-mode confinement normally observed as the Greenwald density is approached can be delayed to higher densities and that plasmas with confinement close to that expected on the basis of the standard scaling can be obtained at densities in the vicinity of the Greenwald value. In addition, systematic studies of the variation of plasma confinement with plasma elongation showed that the thermal energy confinement time increases significantly with elongation, varying approximately as  $\kappa_X^{0.8 \pm 0.3}$ , where  $\kappa_X$  is the separatrix elongation. The strong dependence of H-mode confinement on plasma shaping provides important guidance to the design of future experiments such as ITER.

Substantial changes in the confinement properties of thermal and fast particles were observed in toroidal field ripple experiments in which 16 rather than 32 coils were utilized. This increased the central toroidal field ripple from  $<10^{-6}$  to  $10^{-3}$ , and the edge ripple from  $\sim 1\%$  to  $\sim 10\%$ . In neutral beam heated L-mode plasmas, the diamagnetic energy fell by  $\sim 30\%$  and the plasma toroidal rotation was entirely suppressed to within measurement errors. Both effects were considerably greater than theoretically predicted, since estimated losses of neutral beam injected fast ions which were either born in, or scattered into, the ripple well loss cone amounted to only 10%. Analysis of the confinement of fast particles, both energetic protons produced by ICRF second harmonic minority heating and tritons resulting from D-D fusion reactions, found that stochastic diffusion losses were well modelled by existing theory. The increased ripple also had a very deleterious impact on H-mode confinement. In experiments with 16 toroidal field coils, ELM activity persisted at power levels of up to 12 MW, while in equivalent plasmas with 32 coils, ELM-free

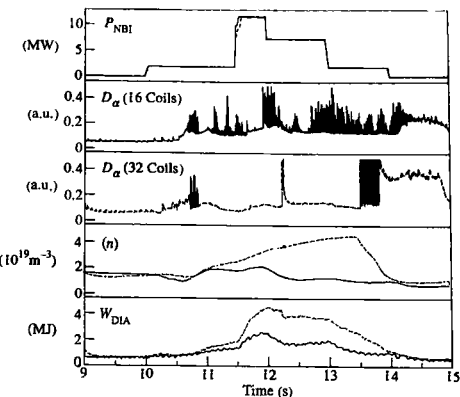


**Fig. 12.3.12** Comparison of NBI H-modes with 16 coils (high toroidal field ripple—solid traces) and 32 coils (low toroidal field ripple—dashed traces). Shown are NBI power,  $P_{\text{NBI}}$ ,  $D_\alpha$  emission signals for 16 and 32 coil cases, volume averaged density,  $\langle n \rangle$ , and stored energy from diamagnetic measurements,  $W_{\text{DIA}}$  [The JET Team (presented by B.J.D. Tubbing) *Plasma Physics and Controlled Nuclear Fusion Research 1992* (Proc. 14th Int. Conf., Würzburg, 1992) Vol 1, 429, I.A.E.A., Vienna (1993)].

H-modes were established at  $\sim 3$  MW (Fig. 12.3.12). Energy confinement in the former case was substantially less than in the latter and was barely improved over L-mode confinement.

### Divertor studies and plasma-surface interactions

Much experience on the relative merits of graphite and beryllium as power-handling and plasma-facing materials has been acquired. In the original JET configuration, both the materials and the design of the limiters and X-point targets were varied to investigate the optimum combination for power handling and impurity control. Beryllium was first introduced into JET as a getter material, with layers of  $\sim 100$  Å being applied by overnight evaporation. Previously,  $Z_{\text{eff}}$  in plasmas using carbon limiters reached values of 2–3 after conditioning by prolonged operation and He glow discharge cleaning (Fig. 12.3.13), with the principal impurities being carbon, oxygen, and nickel. Beryllium gettering led to a reduction in  $Z_{\text{eff}}$  to  $\sim 1.5$ . This resulted from a temporary reduction of the plasma carbon content and a long-lived reduction of the oxygen concentration, which fell by more than an order of magnitude and became almost negligible. The lower oxygen level was beneficial both in decreasing the radiative losses from the plasma and in reducing the sputtering of carbon and nickel. An enduring benefit of beryllium evaporation was that recovery from disruptions was more rapid and specific disruption recovery pulses were rarely required.

The use of beryllium metal as either a limiter or divertor target material led both to a sustained reduction in the level of carbon and in  $Z_{\text{eff}}$

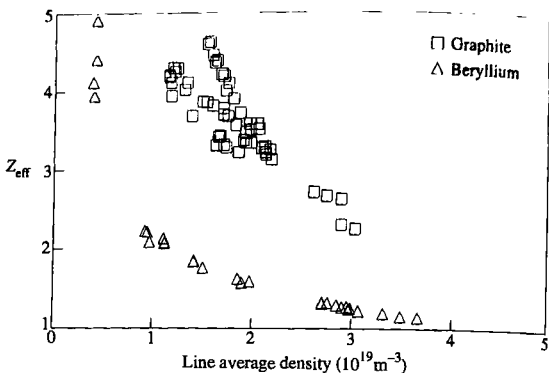


Fig. 12.3.13  $Z_{\text{eff}}$  as a function of density for ohmic discharges using either graphite or beryllium limiters [from The JET Team (presented by K.J. Dietz) *Plasma Physics and Controlled Fusion* 32, 837 (1990)].

(Fig. 12.3.13), and to a substantial increase in the density limit. Further improvements in plasma purity were observed when the nickel Faraday screens of the ICRF antennas were replaced with beryllium screens. This eliminated nickel as a significant contaminant in ICRF experiments and greatly improved the quality of ICRF H-modes. Particle control also benefited from the efficient pumping of hydrogenic species by beryllium. Recycling from graphite surfaces could be reduced by plasma conditioning in helium, but this was effective for only a few pulses. With beryllium evaporation, equally good pumping rates could be obtained which lasted for a day's operation. The use of beryllium metal greatly increased this effect, so that recycling, as determined from the global particle confinement time,  $\tau_p^*$ , decreased by a factor of several and the particle pump-out time fell to 1–2 s. Note that  $\tau_p^* = \tau_p/(1-\mathcal{R})$ , where  $\tau_p$  is the plasma particle confinement time in the absence of recycling and  $\mathcal{R}$  is the recycling coefficient. Overall, the use of beryllium had a major impact on plasma operation, allowing ready access to a wider range of plasma regimes, at both the highest and lowest densities, than previously attainable.

Whereas graphite and carbon fibre surfaces sublime at temperatures in the range 1500–2700 °C, a phenomenon often manifested in the form of a carbon bloom in experiments at the highest heating power, beryllium melts at the rather low temperature of 1270 °C. It is essential to avoid melting in order to minimize impurity influxes and to avoid surface damage. Since surface melting of beryllium and sublimation of carbon are exacerbated by high power fluxes on tile edges exposed by mechanical misalignments, considerable efforts have been expended, both in the original JET configuration and in the several pumped divertor configurations, to improve the alignment of power-handling surfaces to shield tile edges from direct exposure to plasma. By this means, by exploiting the possibility of sweeping the plasma strike points radially in the pumped divertor and by optimizing the exhaust of power via impurity

radiation, as discussed below, it was possible to establish plasmas into which  $\sim 150$  MJ of energy were injected without overheating of the power handling surfaces.

Detailed measurements of power deposition at the divertor target strike points in lower density L- and H-mode plasmas revealed asymmetries in the power distribution which were affected by the direction of the toroidal magnetic field. This is believed to be related to the change in direction of the ion  $\nabla B$  drift relative to the divertor target. When the ion  $\nabla B$  drift was towards the target, the peak power on the outer strike zone was approximately double that on the inner strike zone, while reversal of the toroidal field resulted in an almost symmetric distribution of power. This variation was exploited in high performance plasmas to increase the duration of the additional heating phase which preceded the carbon bloom.

Retention of hydrogen isotopes in first wall materials was highlighted as a key issue for the routine operation of fusion reactors by measurements in TFTR and JET which showed that a non-negligible fraction of the tritium introduced into the torus in the course of D-T experiments remained even after the extensive application of 'clean-up' techniques, such as hydrogen and deuterium operation, and exposure to air. In JET D-T experiments approximately 40% of the tritium introduced was initially retained, although clean-up procedures ultimately reduced this level to  $\sim 10\%$  (4 g out of 35 g). A significant fraction of the remaining tritium was effectively trapped in 'codeposited' layers of carbon and hydrogen isotopes which form preferentially in cool ( $\sim 40^\circ\text{C}$ ) areas of the inner divertor. Strong plasma flows observed in the scrape-off layer are believed to contribute to the in/out asymmetry in codeposited layer formation. The layers, first observed during deuterium experiments, can contain up to 0.8 atoms of deuterium per carbon atom and can form in regions remote from plasma contact, creating difficulties for conventional wall-conditioning techniques. Establishing methods for avoidance of their formation, or for the subsequent removal of tritium, or the replacement of carbon by alternative materials, is a key issue for the development of future tokamaks designed to operate routinely in D-T.

The pumped divertor (Fig. 12.3.2) has been extensively exploited to address many reactor relevant issues in the areas of power handling, particle exhaust, and impurity control. The gradual modification of the geometry towards a more 'closed' configuration, illustrated in Fig. 12.3.2(b), has been a particular feature of the programme which has permitted detailed studies of the relationship between divertor geometry and divertor plasma behaviour. In L-mode plasmas, fully detached steady-state operation, lasting  $\sim 5$  s, has been sustained using deuterium puffing. The radiated power fraction was  $\sim 70\%$  and the peak heat flux at the divertor target fell by an order of magnitude. Langmuir probe measurements of the electron pressure in the scrape-off layer near the plasma midplane and at the divertor target have confirmed that a substantial pressure drop, of more than a factor of 10, develops along the scrape-off layer as the plasma detaches (Fig. 12.3.14). This fall in divertor pressure

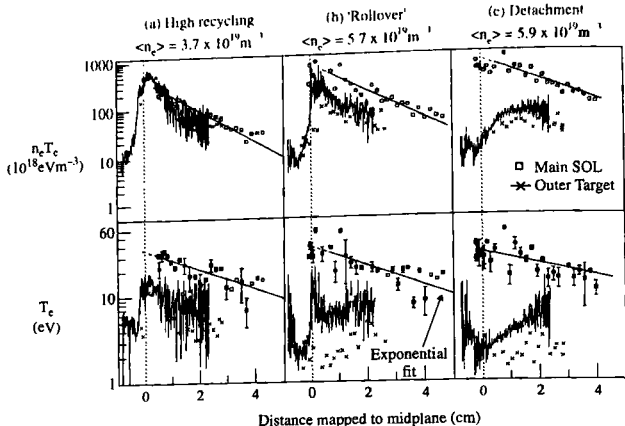


**Fig. 12.3.14** Profiles of electron temperature,  $T_e$ , and electron pressure,  $n_e T_e$ , as a function of distance from the plasma separatrix mapped to the plasma midplane. Three timeslices are shown during an L-mode density ramp: (a) the 'high recycling' attached phase; (b) the 'rollover' as detachment is initiated close to the separatrix; (c) the detached phase. In each case a comparison is made between Langmuir probe measurements made in the SOL close to the plasma midplane and Langmuir probe measurements at the outer divertor target, illustrating the significant fall in temperature at the divertor associated with detachment, together with the substantial pressure drop which develops along the SOL from the midplane to the target [from Loarte, A. et al. *Nuclear Fusion* **38**, 331 (1998)].

is accompanied by a substantial increase in divertor radiation and by a displacement of the peak radiation away from the divertor target towards the X-point.

Studies of the influence of divertor geometry on divertor plasma behaviour have confirmed that increased closure provides some of the expected benefits. For example, detachment is achieved more readily in more closed divertor configurations, though with the result that the L-mode density limit can occur more abruptly. In plasmas using vertical, rather than horizontal, targets, detachment is initiated in the vicinity of the separatrix, as expected from analysis of the distribution of recycling neutrals in the two cases. In addition, with increasing closure, the divertor neutral pressure increases, leading to more efficient particle exhaust. This is reflected in the efficient helium exhaust achieved in ELMMy H-mode plasmas: using the 'argon frosting' technique discussed in Section 12.5, values of  $\tau_{He}^*/\tau_E \sim 8$  have been obtained, where  $\tau_{He}^*$  is the residence time for helium in the plasma chamber. Increased divertor closure was also found to reduce the plasma impurity content in L-mode plasmas when the influence of surface temperature on the chemical sputtering of carbon was properly corrected. However, there was no evidence of a significant difference in H-mode plasmas, possibly as a result of the additional contribution to main chamber impurity production associated with ELMs. A specific effect of geometry was identified in the Marx IIIB divertor, where the presence of a septum separating the inner and outer strike points (Fig. 12.3.2(b)) allowed the use of differential gas fuelling to produce more symmetric detachment behaviour than previously observed.

In ELMMy H-modes it is possible to achieve detachment between ELMs, but H-mode confinement cannot be maintained at the high deuterium flow rates required to establish full detachment, and an alternative scenario has

been explored. Based on results from the TEXTOR and ASDEX Upgrade tokamaks, a mixture of deuterium and impurity gases has been used to raise the level of radiation in higher confinement plasmas. Nitrogen has proved to be the most suitable impurity for JET and long,  $\sim 5$  s, 'radiative divertor' plasmas with total input powers of 27 MW and radiated power fractions of greater than 70% have been produced. In such plasmas the conducted power is further reduced by neutral particle losses, which can reduce the fraction of input power conducted to the target to  $\sim 10\%$ , and lead to the development of detachment in the divertor. Confinement in these discharges is reduced relative to that of normal ELM-free H-modes, the best examples reaching 1.5, rather than 1.9, times  $\tau_E^{\text{ITER89-P}}$ . Analysis of the  $\rho_\star$ -dependence of the global confinement also suggests a Bohm-like, rather than a gyro-Bohm-like, scaling, although a possible influence of collisionality cannot be excluded. More seriously, nitrogen penetrates the main plasma and, at the highest powers,  $Z_{\text{eff}} \sim 3$  is typical, which is an unacceptably high value for a reactor. It is necessary, therefore, to develop techniques for retaining impurities in the divertor plasma.

### Current drive and profile control experiments

The principal current drive techniques which have been explored are lower hybrid waves at 3.7 GHz and bootstrap current drive. Emphasis has been given to optimizing synergistic effects between LHCD and ICRF waves. Detailed studies were carried out in combined LHCD and ICRF experiments, in which currents of up to 1.5 MA were sustained with zero loop voltage. High energy bremsstrahlung spectra from such discharges showed that the fast electrons responsible for the current drive had a parallel temperature of 800 keV, far above that produced in full current drive experiments with LHCD only. Direct damping of the ICRF waves on fast electrons generated by LHCD, either by transit time magnetic pumping or mode conversion, was proposed as a possible mechanism for the acceleration of electrons to such high energies. Current drive efficiencies rose linearly with  $n(T_e)/(5 + Z_{\text{eff}})$ , reaching values of  $\eta_{\text{CD}} = 0.22 \times 10^{20} \text{ Am}^{-2} \text{ W}^{-1}$ , where  $\eta_{\text{CD}} = RnI_{\text{CD}}/P_{\text{tot}}$  and  $P_{\text{tot}} = P_{\text{LH}} + P_{\text{ICRF}}$ . Increases in the coupled LHCD power subsequently allowed full current drive at plasma currents of 3 MA.

JET ELM-free H-mode plasmas normally have a bootstrap current fraction of up to  $\sim 30\%$ . In a series of ICRF heated discharges at 1 MA/2.8 T, ELM-free H-modes with  $\beta_p$  values of up to 2 were produced in which the calculated bootstrap current reached values of  $700 \pm 150$  kA. Although the duration of the ELM-free phase was only 2–3 s and the current profile did not reach steady-state, the broadening of the current profile under the influence of the bootstrap current was sufficient to stabilize sawtooth oscillations. A significant aspect of these plasmas was their high thermal confinement, ranging up to  $1.7\tau_E^{\text{JET/DIII-D}}$ , where  $\tau_E^{\text{JET/DIII-D}}(s) = 0.106 I(\text{MA})^{1.03} R(\text{m})^{1.48} P(\text{MW})^{-0.46}$ . This regime

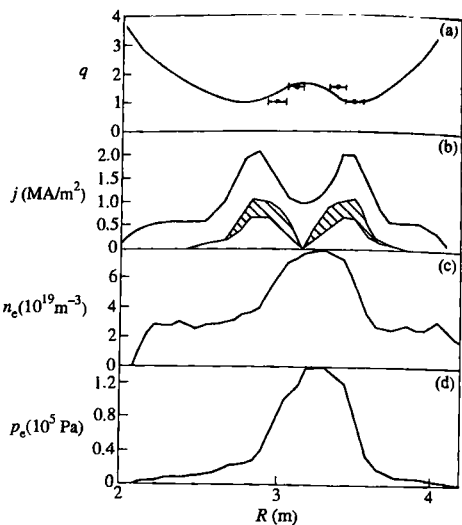


**Fig. 12.3.15** Profiles of (a) safety factor, (b) current density, (c) electron density, and (d) electron pressure for a PEP H-mode plasma. The experimental points in (a) are deduced from the radial localization of mhd activity, while the curve is derived from a reconstruction of the magnetic equilibrium. The shaded area in (b) represents the limits on the experimental uncertainties in the calculated bootstrap current contribution to the total current density [Hugon, M. et al. *Nuclear Fusion* 32, 33 (1992)].

has parallels with experimental observations from high- $\beta_p$  plasmas in other large tokamaks, but was the first case of a bootstrap dominated plasma without a strong central particle source.

Profile control via fuelling, heating, and current drive has become an important tool for the control of plasma confinement. For example, in addition to the standard L- and H-mode discharges, plasmas with reduced central transport have been observed in both regimes. This phenomenon was first identified in a scenario which was referred to as 'pellet enhanced plasma', or PEP. The regime developed following deep pellet injection during the early phase of a discharge, before the onset of sawtooth activity. Rapid central heating created a plasma in which a raised central  $q$  value was effectively frozen and a very peaked pressure profile with a steep gradient at  $r/a \sim 0.4$  was produced (Fig. 12.3.15). Transport in such discharges was distinguished from that in normal L- and H-modes by a significant reduction in the central thermal diffusivity, with  $\chi_i$  approximately 1–3 times the neoclassical value. It was suggested that this transient change in the core transport was associated with an inversion of the central magnetic shear, which was observed via polarimetric measurements of the  $q$ -profile and from observations of the radial distribution of mhd modes. This inversion was consistent with the high bootstrap current density in the vicinity of the steep pressure gradient shown in the figure.

The PEP regime is recognized as the first indication that plasmas with flat or inverted central shear can exhibit reduced transport in the central

region, although later analysis in TFTR and DIII-D showed that additional factors, such as the development of radial electric field shear, appear implicated. Wide ranging studies of the properties of plasmas having low or reversed central shear and internal transport barriers have been undertaken in all major tokamaks. In JET, successor regimes to PEP scenarios were initially developed by using rapid heating during the current rise, as in TFTR and DIII-D, but latterly LHCD has been used to provide reliable access to a greater range of  $q$ -profiles in the plasma core. Plasmas with reduced ion and electron thermal transport and reduced particle transport in the central 'optimized shear' region can then be analysed systematically. These experiments have confirmed the fundamental properties of ITB regimes reported from other devices, including the suppression of turbulence associated with the reduced transport at the onset of the transport barrier and the accumulation of high-Z impurities in the plasma core, though the JET results have also highlighted the fact that the formation of an internal transport barrier is often associated with the presence of a low order rational  $q$ -surface at the foot of the barrier. As in other tokamaks, these studies often deal with 'double barrier' plasmas, in which the internal transport barrier is combined with the H-mode edge transport barrier to optimize confinement and stability properties: a specific goal of the JET experiments has been the exploitation of the improved core confinement to optimize fusion performance, as discussed later.

In the course of experiments to establish target current profiles having reversed central shear, it was observed that, under some circumstances, the central current density could fall to zero in the plasma centre (Fig. 12.3.16). This 'current hole' occurred in plasmas in which off-axis LHCD was applied to assist the formation of a negative shear region during the current ramp. Motional Stark effect measurements of the poloidal field pitch angle showed that it fell to zero over the central region of the plasma and the reconstructed current profile was found to be zero, within

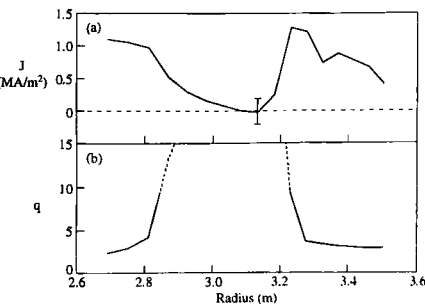


Fig. 12.3.16 Radial profiles of: (a) plasma current density,  $J$ , reconstructed from MSE measurements, (b) the resulting safety factor,  $q$ . The data illustrate the formation of a region of zero current density in the centre of a discharge in which off-axis LHCD was used during the current ramp to establish a central region of reversed shear [from Hawkes, N.C. et al. *Physical Review Letters* 87, 115001 (2001)].

measurement errors, over a region with a radius of up to 20 cm. The current hole is explained in terms of the response of the parallel electric field to the strong off-axis current drive produced by the LHCD, which causes a reversal of the electric field in the plasma core. Since the phenomenon persists for several seconds, due to the long current diffusion time in the hot central region, this could, in principle, lead to a reversal of the central current density. However, no reversal has been observed and it has been proposed that the growth of  $m = 1/n = 0$  resistive mhd modes in the region of zero poloidal field could cause a redistribution of current, preventing a reversed current region developing.

Enhancements in current drive capability, particularly through improved coupling of the LH system, together with improvements in systems for active feedback control of plasma parameters, have allowed the optimized shear scenario to be developed towards the ultimate goal of establishing steady-state tokamak operation. Identification of a reliable means of controlling the formation and location of internal transport barriers has also made a significant contribution. On the basis of theories of microturbulence, a local dimensionless Larmor radius,  $\rho_{T*} = \rho_s/L_T$ , where  $\rho_s = C_s/\omega_{ci}$  is the Larmor radius at the sound speed and  $L_T = T/(dT/dR)$  is the temperature gradient scale length, with  $C_s$  the sound speed and  $\omega_{ci}$  the ion cyclotron frequency, has been defined. An experimental criterion,  $\rho_{Te*} > 1.4 \times 10^{-2}$ , has subsequently been established as a reliable measure for the existence of a transport barrier in the (electron) temperature profile in JET, and it has been experimentally verified that it is possible to control the location of an internal transport barrier in real-time by acting on the auxiliary heating systems. In experiments where LHCD is also used in a preprogrammed mode to delay the relaxation of the reversed shear profile, with ICRF feedback control of the transport barrier temperature gradient and NBI feedback control of the neutron yield, it has been possible to maintain a quasi-stationary ITB scenario for periods of up to 11 s, a significant fraction of the global current diffusion timescale and a duration limited by hardware constraints. Fully non-inductive current drive has been sustained for several seconds in such discharges, with significant contributions from bootstrap, lower hybrid, and neutral beam currents.

### High performance plasmas and deuterium-tritium experiments

Before the introduction of tritium into tokamak plasmas, the highest fusion power output was obtained not from D-D reactions, but from D-He<sup>3</sup> reactions. In deuterium plasmas with a small, ~5%, concentration of He<sup>3</sup> minority, ICRF can accelerate minority ions to energies in the MeV range, greatly enhancing the cross-section for the D-He<sup>3</sup> reaction above that of a thermal plasma. Although the products of this reaction are charged particles, the fusion power can be determined by measurements of  $\gamma$ -ray emission from the very weak D(He<sup>3</sup>,  $\gamma$ )Li<sup>5</sup> branch of the reaction. In L-mode experiments in which up to 15 MW of ICRF power

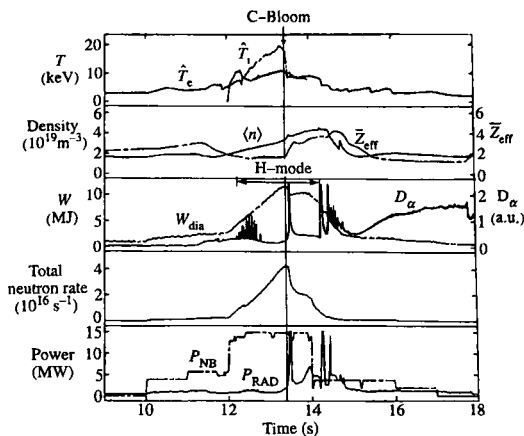


**Fig. 12.3.17** The time development of the central electron and ion temperatures,  $\hat{T}_e$  and  $\hat{T}_i$ , the volume averaged electron density,  $\langle n \rangle$ , the line-averaged  $\bar{Z}_{\text{eff}}$ , the plasma diamagnetic energy,  $W_{\text{dia}}$ , the  $D_\alpha$  emission, the total neutron rate, the NBI power,  $P_{\text{NB}}$ , and the radiated power,  $P_{\text{RAD}}$ , for the deuterium pulse with the highest fusion triple product [The JET Team *Nuclear Fusion* 32, 187 (1992)].

was coupled to the plasma, a peak fusion power of 140 kW was reached, corresponding to a reaction rate of  $4.8 \times 10^{16} \text{ s}^{-1}$ . It is unlikely that this reaction can be exploited for net power production in the near term, but the experiment provided an important test of many aspects of RF absorption and fast particle confinement.

JET high performance plasmas may be classified into two separate regimes, broadly characterized as hot ion H-mode and optimized shear. Hot ion H-modes are established by using high power NBI in low density target plasmas, with  $\langle n \rangle < 2 \times 10^{19} \text{ m}^{-3}$ . A well-conditioned torus is essential and this is usually produced by overnight beryllium evaporation. These H-modes can exhibit thermal confinement times up to twice those calculated from the JET/DIII-D scaling and have attained fusion triple product values of  $\sim 9 \times 10^{20} \text{ keV sm}^{-3}$ , corresponding to  $Q_{\text{DT}} \approx 1$  in a plasma with an optimum mixture of deuterium and tritium. The principal characteristics of the hot ion H-mode (Fig. 12.3.17) include the development of centrally peaked ion and electron temperatures, with  $T_i(0) \sim 20\text{--}30 \text{ keV}$  and  $T_e(0) \sim 10\text{--}15 \text{ keV}$ . While the density profile is more peaked than in normal JET H-modes, it is not as peaked as in TFTR supershots. As noted previously, confinement improves suddenly over the outer half of the plasma at the H-mode transition. Following this, the ion thermal conductivity falls across the entire plasma cross-section, a condition which persists for 1–2 s. This regime resembles the VH-mode of DIII-D, which is described in Section 12.5.

The physics underlying the termination of the high performance phase of the hot ion H-mode is not fully understood, but the several key features are recognized. Initial hot ion H-mode experiments were limited by the

occurrence of a carbon bloom, sometimes linked to mhd events, as in TFTR supershots. The resultant influx of impurities, coupled with the rise in core transport, prevented any recovery in plasma performance and confused the analysis of the core behaviour. Following the development of improved power handling surfaces, in particular the installation of the pumped divertor, the behaviour became more complex. It was then recognized that the termination is usually triggered by mhd events such as an ELM, a sawtooth collapse plus an ELM, or the growth of an 'outer mode', which is typically an  $n = 1$  external kink mode. However, the link between this mhd activity and the subsequent reduction in confinement, which can also be accompanied by a rise in the plasma impurity content and which leads to a substantial fall in neutron emission, remains unclear.

By injecting high power neutral beams into a low density optimized shear plasma,  $\langle n \rangle \sim 2 \times 10^{19} \text{ m}^{-3}$ , a strong ion transport barrier can be formed and many of the characteristics of the hot ion H-mode can be reproduced, with central ion temperatures reaching values as high as 40 keV and central electron temperatures of up to 15 keV. These discharges generally evolve through an initial L-mode to an H-mode phase, which improves the plasma stability by reducing the peaking of the pressure profile and allows higher values of  $\beta_N$  to be achieved. Values of the fusion triple product of up to  $11 \times 10^{20} \text{ keV sm}^{-3}$  have been attained by this approach. As with all high performance regimes, the high confinement decays on a timescale of 1–2 s, often due to mhd activity, the most virulent form being a global  $n = 1$  pressure driven kink having a growth time as short as 200  $\mu\text{s}$ , which typically causes a disruption.

The projection that the best H-mode plasmas could achieve effective breakeven, as defined in Section 12.1, in a 50:50 D-T mixture prompted a short series of experiments in late 1991 in which tritium concentrations of up to 11% were used. This preliminary tritium experiment, or PTE, which involved the introduction of significant amounts of tritium into a tokamak for the first time, was intended to test the accuracy of extrapolations from D-D to D-T fusion yield, to produce in excess of 1 MW of D-T fusion power and to demonstrate the safe and reliable operation of tritium handling systems. Tritium was introduced into the discharges using two neutral beam sources capable of injecting tritium at 78 keV, providing a total of 1.5 MW of injected power. In addition, the sources could be adapted for trace injection studies with 1% tritium in deuterium. The target discharge used for the PTE was a typical hot ion H-mode, a 3 MA/2.8 T single null X-point plasma, with the ion  $\nabla B$  drift away from the divertor target to exploit the superior power-handling capability of this arrangement. A series of trace experiments was carried out to establish a suitable discharge and to investigate tritium diffusion, but, in order to limit activation of the torus, only two high power pulses were performed. These two discharges, at 15 MW of NBI power and a tritium concentration of 11%, achieved very similar fusion yields, with a peak 14 MeV neutron production rate of  $6 \times 10^{17} \text{ s}^{-1}$ , corresponding to a peak power of 1.7 MW and a fusion triple product of  $3.8 \times 10^{20} \text{ keV sm}^{-3}$ . A total fusion energy of 2 MJ was released in each pulse. The plasmas resembled

deuterium hot ion H-modes, and there was no evidence that the tritium or  $\alpha$ -particle populations affected their behaviour.

A more extensive and ambitious series of D-T experiments, referred to as DTE1, was performed in the Mark II A divertor configuration in 1997 with the aims of exploring plasma characteristics over a range of D-T mixtures, extending fusion power production at optimized D:T ratios, that is close to 50:50, studying the influence of  $\alpha$ -particles on plasma behaviour, investigating plasma-wall interaction issues in D-T, including in-vessel tritium retention, and demonstrating the technology of tritium injection, extraction, and processing. Nevertheless, to allow subsequent modifications of the device, the total neutron yield was limited to  $2.5 \times 10^{20}$  neutrons.

The highest fusion power of 16.1 MW was obtained in a 4 MA/3.6 T hot ion H-mode plasma heated by 22.3 MW of mixed deuterium and tritium NBI and 3.1 MW of H-minority ICRF heating. This pulse reached an instantaneous  $Q_{DT}$  of 0.62, without allowance for plasma transients or the power losses due to beam shine-through, with 60% of the fusion power produced by the thermal plasma, the remainder arising from beam-plasma reactions. The plasma achieved  $n_{D+T}(0)T_i(0)\tau_E = 8.7 \times 10^{20} \text{ keV sm}^{-3}$  and a total stored energy of 17 MJ, the highest of any experiment to date. As illustrated in Fig. 2.3.18, the high fusion performance phase lasted for  $\sim 1.5$  s, the duration being limited by similar phenomena to those discussed previously. In optimized shear experiments, although a higher value of  $n_{D+T}(0)T_i(0)\tau_E = 11 \times 10^{20} \text{ keV sm}^{-3}$  was attained in a 3.2 MA/3.45 T plasma, the maximum fusion power produced was 8.2 MW, with the high performance phase again lasting  $\sim 1.5$  s (Fig. 12.3.18). The lower fusion power reflects the lack of optimization of this regime in D-T mixtures: the detailed time evolution of the current profile and the time at which an L to H transition occurs is found to have a significant influence on the performance of such plasmas, and the limited neutron budget available during the DTE1 experiments did not allow this scenario to be re-optimized to accommodate the influence of the different isotopic mixture in D-T plasmas.

Exploration of fusion performance and plasma behaviour under quasi-steady-state conditions was performed in a series of ELMy H-mode experiments. As discussed previously, comparative studies in hydrogen and in D-T mixtures, ranging from 100% deuterium to 90% tritium, allowed the influence of isotopic mass on the H-mode threshold and energy confinement to be addressed. Additional information on local transport processes came from tritium puffing experiments, similar to those performed in TFTR, which showed that in ELMy H-modes the tritium particle diffusivity appeared to follow a gyro-Bohm scaling. Experimental uncertainties prevented an unambiguous distinction between Bohm and gyro-Bohm scaling in L-mode plasmas.

High fusion power was demonstrated in a 3.8 MA/3.8 T ELMy H-mode with an input power of 23 MW in which  $\sim 4$  MW of fusion power was produced for 4 s (Fig. 12.3.18), with  $Q_{DT} = 0.18$  for 3.5 s. This pulse, in which approximately 30% of the fusion power was of thermal

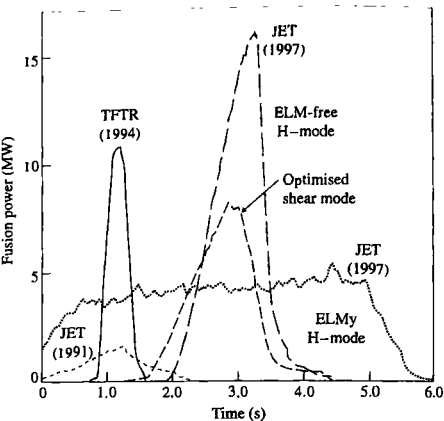


**Fig. 12.3.18** Comparison of the maximum fusion power achieved in various plasma scenarios during the major D-T experimental campaigns performed to date. The 1991 JET experiments (PTE) used only 11% tritium while the remaining experiments employed approximately 50:50 D-T mixtures. The JET ELMy H-mode plasma produced the highest fusion energy of any pulse [Keithacker, M. et al. *Plasma Physics and Controlled Fusion* 41, B1 (1999)].

origin, yielded the largest integrated fusion energy of 22 MJ. A somewhat higher  $Q_{DT}$  of 0.22 was achieved in a similar 3.8 MA/3.8 T plasma using a 9:91 D-T mixture and only 6 MW of ICRF D-minority heating to produce 1.5 MW of fusion power for several seconds. Acceleration of the deuterium minority tail to average energies of 120 keV implied that the majority of the fusion reactions in this scenario were of non-thermal origin. Nevertheless, both of these plasmas were distinguished from the hot ion H-mode and optimized shear experiments by having durations limited only by constraints based on the permitted neutron production, rather than plasma instabilities, and by having  $T_i(0) \approx T_e(0)$  ( $\sim 7$ – $8$  keV), which is a regime of more relevance to fusion reactors. Additional ICRF heating scenarios which are also considered relevant to ITER and which were successfully demonstrated included second harmonic tritium heating and ion heating via ICRF coupling to a He<sup>3</sup> minority at the 5–10% level. In the latter case  $T_i(0) = 13$  keV and  $T_e(0) = 12$  keV were sustained for several seconds with  $\sim 8$  MW of ICRF heating.

As in the TFTR D-T experiments, the investigation of  $\alpha$ -particle effects was a key aspect of the JET studies. No evidence was found for Alfvén eigenmodes excited by  $\alpha$ -particles in any of the standard plasma regimes analysed. This was in agreement with analysis using numerical codes, which identified a variety of stabilization mechanisms contributing to the suppression of AE modes and concluded that the  $\alpha$ -particle pressure in the JET experiments was insufficient to overcome the damping processes. Clear evidence of electron heating by  $\alpha$ -particles was obtained from a series of hot ion H-modes in which the tritium concentration was varied between 0 and 92%, involving careful control of the gas, neutral beam injection, and recycling fueling of the plasma. While the thermal

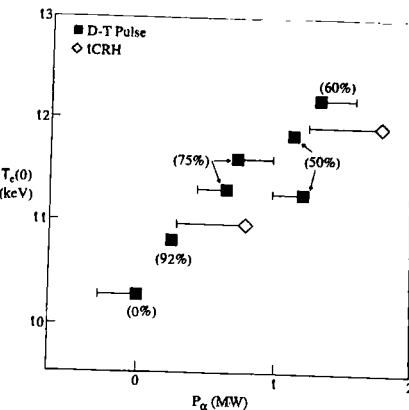


**Fig. 12.3.19** Central electron temperature,  $T_e(0)$ , as a function of  $\alpha$ -particle power,  $P_\alpha$ , in a series of D-T hot ion H-modes in which the tritium concentration was varied between 0 and 92%, as indicated by the figures in brackets. The bars indicate the shortfall in NBI power relative to the nominal value of 10.6 MW and the open diamonds indicate the results of two pure deuterium pulses in which ICRF minority heating was used to simulate the effect of  $\alpha$ -particle heating [The JET Team (presented by P.R. Thomas) *Fusion Energy 1998* (Proc. 17th Int. Conf., Yokohama, 1998) Vol 1, 265. I.A.E.A., Vienna (1999)].

energy confinement time was found to depend only weakly on the isotopic mixture, a clear maximum in both the stored (thermal and total) plasma energy and central electron temperature was observed at a tritium concentration of 50–60% (Fig. 12.3.19), where the fusion power was maximized. A regression fit to the experimental dataset yielded a change of  $\Delta T_e(0) = 1.3 \pm 0.23$  keV in response to the increase in  $\alpha$ -particle heating power of 1.3 MW. Moreover, comparison of the observed increment in the rate of increase of energy density during the highest fusion power pulse with the expected rate of electron heating due to  $\alpha$ -particles supported the conclusion that  $\alpha$ -particles were confined and slowed down classically.

## 12.4

### JT-60/JT-60U—Japan Atomic Energy Research Institute, Naka, Japan

JT-60, in which the first plasma was obtained in April 1985, differed from other large devices in having a triplet of internal coils which formed an enclosed divertor chamber situated on the large major radius side of the plasma. In its original form, 3.2 MA was achieved in limiter discharges, and the maximum toroidal field was 4.8 T. The vacuum vessel was fabricated from inconel and the plasma-facing components consisted initially of molybdenum coated with 20  $\mu\text{m}$  of titanium carbide. Later the molybdenum was replaced by graphite tiles to reduce metallic influxes. The

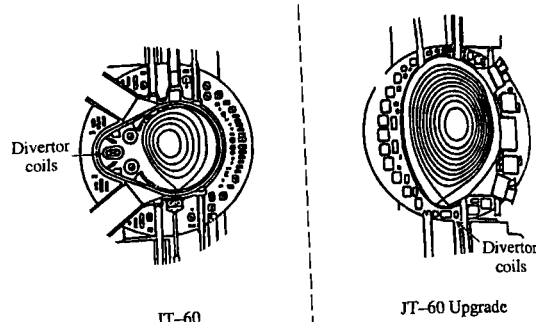


**Fig. 12.4.1** Comparison of the final layout of the JT-60 tokamak (left hand side) with the JT-60U (Upgrade) geometry. Note the original triplet of divertor coils at the large major radius side of JT-60 [from JT-60 Team (presented by M. Nagami) *Plasma Physics and Controlled Nuclear Fusion Research 1990* (Proc. 13th Int. Conf., Washington, 1990) Vol 1, 53. I.A.E.A., Vienna (1991)].

tokamak was equipped with a high power, long pulse heating capability consisting of 22 MW of hydrogen neutral beam injection, 15 MW of lower hybrid current drive operating in the range 1.74–2.23 GHz, and 6 MW of ion cyclotron radiofrequency power in the frequency range 110–130 MHz. Each system had a design pulse length of 10 s.

It was found that this configuration did not allow H-mode operation, and the poloidal circuit was modified in early 1988 to permit the formation of an X-point in the bottom of the vacuum vessel, as shown on the left-hand side of Fig. 12.4.1. This constituted an interim step in a much more extensive modification of the tokamak, which began in late 1989. The vacuum vessel was replaced, eliminating the original divertor, and the poloidal circuit was extensively upgraded within the existing toroidal field coil set. Fig. 12.4.1 compares the final JT-60 configuration with the upgraded JT-60U geometry, and Fig. 12.4.2 shows an overview of the JT-60U device, which began operation in March 1991. As discussed later, a pumped 'W-shaped' divertor was installed in 1997 to enhance the capability for power and particle control studies.

JT-60U has a substantially larger plasma volume than JT-60 and has produced single null X-point plasmas with currents of up to 5 MA. In addition, it is capable of deuterium operation, whereas the previous device was limited to hydrogen and helium plasmas. The first wall is completely lined with graphite, with carbon fibre tiles in the divertor region. While the basic neutral beam geometry is unchanged from JT-60, several neutral beam lines were re-oriented to provide more tangential injection, and the use of deuterium raised the installed neutral beam injection power to 40 MW at 120 keV injection energy. Following the assignment of three neutral beam ports to pumping for the W-shaped divertor, the power from the positive ion based system was reduced to 28 MW, but in 1996 the neutral beam capability was significantly upgraded with the installation of the first operational negative ion based NBI (N-NBI) system. This is

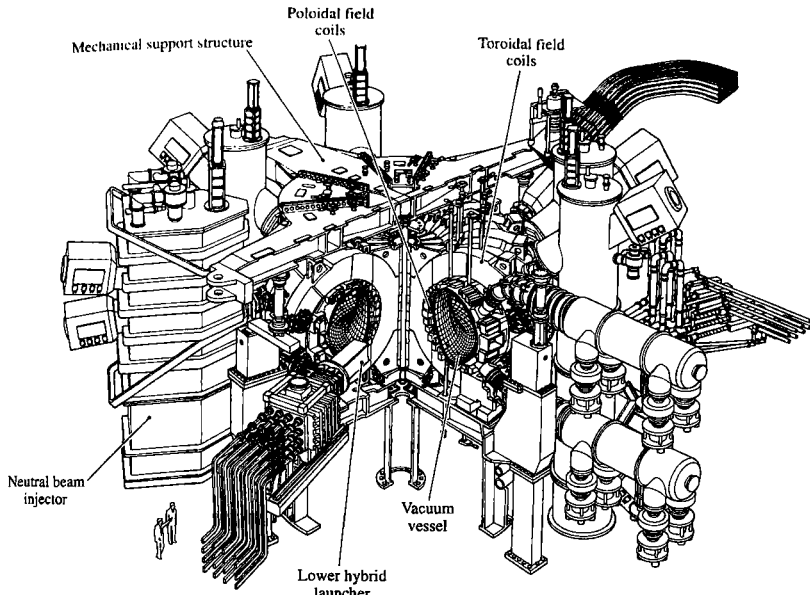
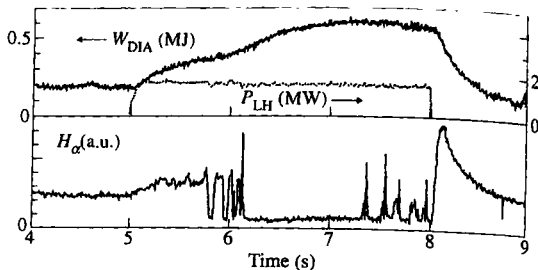


Fig. 12.4.2 Layout of the JT-60U experiment.

designed to provide 10 MW of power at 500 keV for 10 s, though this level of performance has not yet been achieved. Improvements have also been made to the lower hybrid and ion cyclotron RF systems, but the power delivered to the plasma is similar to that in JT-60. The most recent upgrade to the auxiliary heating involves the installation of four gyrotron sources for electron cyclotron resonance heating and current drive. This system can provide up to 3 MW of power at 110 GHz for several seconds.

### Heating and confinement in JT-60

The heating capability of JT-60 allowed a variety of confinement regimes to be investigated. With certain exceptions discussed below, energy confinement was generally found to be close to L-mode, although an offset linear dependence on power gave a better description of the relationship between stored energy and power than the conventional L-mode  $P^{1/2}$



**Fig. 12.4.3** Overview of a limiter H-mode induced by LHCD. Shown are the LH power,  $P_{LH}$ , the diamagnetic measurement of the plasma stored energy,  $W_{DIA}$ , and the  $H_\alpha$  emission [from Tsuji, S. et al. *Physical Review Letters* 64, 1023 (1990)].

variation. No significant differences in energy confinement were found between the three configurations studied, that is limiter, outer X-point and lower X-point, though the volume of lower X-point plasmas was approximately 40% smaller than that of the other two configurations. At neutral beam powers above 18 MW, short H-mode periods, as indicated by a fall in the edge  $H_\alpha$  signal, occurred in both outer and lower X-point plasmas, but their duration did not exceed 200 ms and the confinement was only 10% better than L-mode scaling. In lower X-point plasmas enhanced confinement appeared at injected powers above 15 MW. This regime was characterized by an increase in recycling in the divertor, associated with the formation of a radiating divertor, and led to an improvement of up to 30% in energy confinement relative to equivalent L-mode X-point discharges.

The clearest demonstration of H-mode behaviour was obtained in limiter plasmas using lower hybrid current drive (Fig. 12.4.3). This scenario was optimized at input powers above 1.2 MW when two RF frequencies were applied simultaneously. A minimum threshold density of  $\bar{n} \sim 2 \times 10^{19} \text{ m}^{-3}$  was also required. ELM-free H-modes of up to 3.3 s duration were produced, with an energy confinement enhancement of  $\sim 30\%$  relative to equivalent L-mode plasmas, due primarily to the density rise following the L to H transition. This regime exhibited features common to H-modes in X-point plasmas in other tokamaks, mainly a fall in  $H_\alpha$  light, a fall in edge density fluctuations, and an improvement in particle confinement. Surprisingly, H-modes could not be established in X-point plasmas using this technique. It was proposed that the limiter H-mode might have been triggered by an electric field gradient resulting from losses of fast electrons.

Conventional H-modes proved elusive in JT-60, but enhanced confinement was achieved in neutral beam heating experiments at high- $\beta_p$  in which a centrally peaked hot ion plasma was produced. In these lower null X-point plasmas, helium conditioning was exploited to permit operation at low target density,  $\bar{n} \sim 0.5 \times 10^{19} \text{ m}^{-3}$ . High power neutral beam injection, at the 20 MW level, was used to form centrally peaked profiles in plasmas at currents of up to 1.2 MA. Optimum performance was found in the region of 0.7 MA, where  $q_{cyl} \sim 10$ , sawteeth were absent, and very

peaked ion temperature profiles,  $T_i(0)/(T_i) \sim 3.5$ , and electron density profiles,  $n(0)/(n) \sim 2.5$ , were formed. Such discharges attained  $\beta_p \sim 3$  and  $e\beta_p \sim 0.7$ , and energy confinement times were up to 60% above those predicted by Goldston L-mode scaling. Improved confinement was also observed in the course of pellet injection into neutral beam heated limiter plasmas, where increases of 40% in energy confinement time over equivalent gas-fuelled discharges were obtained. A sequence of pellets was injected into plasmas at up to 3 MA to form very peaked density profiles,  $n(0)/(n) \sim 3$ , with central densities of up to  $2.7 \times 10^{20} \text{ m}^{-3}$  and central plasma pressures of up to  $2 \times 10^5 \text{ Pa}$ .

### Divertor studies

In JT-60 experiments with the outer divertor chamber, low levels of oxygen contamination were observed. This allowed operation with low values of  $Z_{eff} \sim 1-2$ , and of bulk plasma radiation, which was  $\sim 10\%$  of the input power, even at heating powers in the region of 20 MW. Nevertheless, molybdenum influxes degraded plasma performance, in spite of TiC coatings on the molybdenum divertor targets and limiter surfaces. This necessitated a change to graphite divertor targets and first wall components. In addition, the difficulty of achieving H-mode confinement with the outer divertor prompted the development of a more conventional configuration with an open divertor at the bottom of the main plasma chamber. In plasmas using this arrangement  $Z_{eff}$  was usually greater than 4, with carbon and oxygen as the dominant impurities and bulk plasma radiation accounting for at least 20% of the input power.

Two specific observations made in JT-60 have particular relevance to divertor physics. Firstly, it was noted that during neutral beam heating experiments at powers above 15 MW, a highly radiating region developed in the divertor with  $n_{e,\text{div}} \sim 1 \times 10^{20} \text{ m}^{-3}$  and  $T_{e,\text{div}} \sim 20 \text{ eV}$ . This was termed 'remote radiative cooling'. Simultaneously, bulk plasma energy confinement improved by up to 30% relative to standard L-modes. The second observation relates to helium exhaust measurements made using a 30 keV helium beam. In experiments with 10 MW of neutral beam injection, the neutral pressures of hydrogen and helium in the divertor region rose as  $\bar{n}^3$ . Moreover, the enrichment factor for helium, defined as  $\eta = (p_{He}/2p_{H_2})_{\text{div}}/(n_{He}/n_e)_{\text{pl}}$ , where 'div' refers to pressure measurements in the divertor and 'pl' to density measurements in the plasma, increased with density, reaching 0.5 at the highest densities. Although the plasma conditions for these experiments differed from those expected in a power plant plasma, these results suggested that helium ash can be removed efficiently from the divertor in a fusion reactor.

In JT-60U, the care taken in the alignment of the divertor target tiles to avoid exposure of tile edges has provided the experiment with a target capable of accepting high heat loads. Total energies of up to 200 MJ have been deposited into the plasma with no evidence of tile overheating. In addition to boronization, which is used to reduce recycling, individual

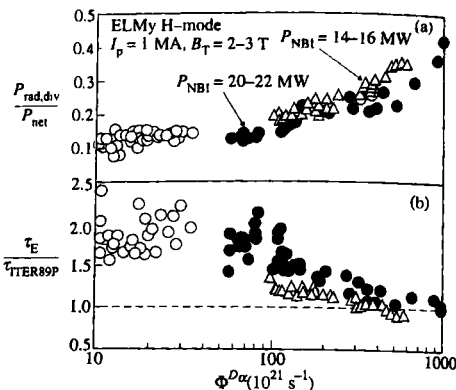


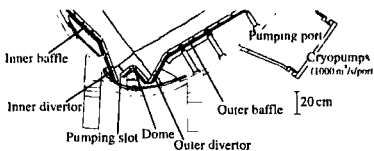
**Fig. 12.4.4** Variation of (a) radiated power fraction from the divertor,  $P_{rad,div}/P_{net}$ , and (b) confinement enhancement factor relative to ITER89-P scaling,  $\tau_E/\tau_{ITER89P}$ , as a function of the total recycling flux in the divertor,  $\Phi^{D\alpha}$ . Open circles represent discharges without gas puffing, while solid circles and open triangles correspond to discharges with gas puffing [Asakura, N. et al. *Plasma Physics and Controlled Nuclear Fusion Research 1994* (Proc. 15th Int. Conf., Seville, 1994) Vol 1, 515. I.A.E.A., Vienna (1995)].

rows of carbon fibre tiles coated with up to  $300 \mu\text{m}$  of  $\text{B}_4\text{C}$  have been installed to investigate the effect of such treatment on plasma performance. Most significantly, this reduced oxygen concentrations to  $< 1\%$  in high power heating experiments.

The feasibility of combining radiative cooling in the divertor with enhanced confinement plasmas has also been addressed. In ELM My H-modes the deuterium fuelling rate required to achieve a substantial radiated power fraction produces an order of magnitude increase in divertor recycling compared to standard, low radiation, ELM My H-modes. Furthermore, as the divertor recycling flux rises, the confinement enhancement factor decreases, until the plasma exhibits L-mode confinement when the divertor radiated power fraction is  $\sim 50\%$  of the input power (Fig. 12.4.4). This confirms the conclusion drawn from experiments in several tokamaks that it is difficult to maintain confinement much above L-mode levels in the presence of strong deuterium recycling fluxes.

Power and particle control capabilities were further enhanced in 1997 with the installation of the W-shaped divertor (Fig. 12.4.5). This semi-closed configuration allows operation up to  $3 \text{ MA}/4 \text{ T}$  and has an installed pumping speed for deuterium of  $16 \text{ m}^2 \text{ s}^{-1}$  via inboard and outboard pumping slots which feed three cryopumping ports previously used by the neutral beam system. Initial experiments with the new configuration showed that the plasma impurity content could be reduced to values of  $Z_{eff} \sim 2$  when the plasma was established with the inboard separatrix  $\sim 2 \text{ cm}$  from the pumping slot and gas puffing in the main chamber was employed. In addition, the improved closure reduced the backflow of neutrals to the main chamber, so that the main chamber recycling flux

**Fig. 12.4.5** Poloidal cross-section of the lower part of the JT-60U torus showing the main elements of the W-shaped divertor. An outboard pumping slot was subsequently added to the divertor dome [Ishida, S. et al. *Fusion Energy 1998* (Proc. 17th Int. Conf., Yokohama, 1998) Vol. 1, IAEA, Vienna (1999)]



could typically be reduced by a factor of 2–3 relative to that in equivalent conditions in the earlier, open, configuration. It was suggested that these improvements have been responsible for the measured reduction of ~30% in the H-mode power threshold relative to plasmas in the original configuration. However, as in several other experiments, the reduced main chamber recycling was found to have no impact on the confinement quality of ELMMy H-modes.

Studies of techniques for the efficient dissipation of exhaust power while maintaining high confinement have been continued in the new configuration. As in other medium to large tokamaks, impurity seeding with various noble gases has yielded the most promising results. The range of densities over which good confinement can be maintained in ELMMy H-mode plasmas has been extended by combined deuterium and argon puffing. In high triangularity plasmas,  $\delta_X = 0.5$ , radiated power fractions of ~80% have been achieved while maintaining  $\tau_E \sim \tau_E^{IPB98(y,2)}$  at densities of 65% of the Greenwald value. In these discharges, the pulsed heat load on the divertor due to ELMs was also considerably reduced. However, the  $Z_{eff}$  rose to values of ~4, so that techniques must be developed to reduce impurity contamination of the main plasma.

Helium exhaust studies in JT-60U have focussed on ELMMy H-mode and internal transport barrier experiments. Following the installation of the W-shaped divertor, systematic analysis of helium exhaust became possible by using argon frosting of the cryopumps (see Section 12.5). Experiments in which a 60 keV He beam was injected for several seconds, that is periods considerably longer than the vessel residence time of helium, showed that in ELMMy H-modes values of  $\tau_{He}^*/\tau_E \sim 4$  could be achieved using only inboard pumping (Fig. 12.4.6), with the core helium concentration maintained in steady-state at ~4%. In addition, the helium enrichment factor was found to be of order unity, significantly higher than in JT-60 experiments. When the ion  $\nabla B$  drift was reversed, the normal enhancement in recycling at the inner strike point relative to the outer strike point was reversed, the helium exhaust efficiency fell and the plasma helium concentration increased by a factor of ~3. With the addition of an outboard pumping slot to the divertor, the helium exhaust efficiency was further improved and  $\tau_{He}^*/\tau_E \sim 3$  has been achieved. Helium exhaust measurements in discharges with an internal transport barrier revealed that the helium diffusion coefficient was reduced inside the transport

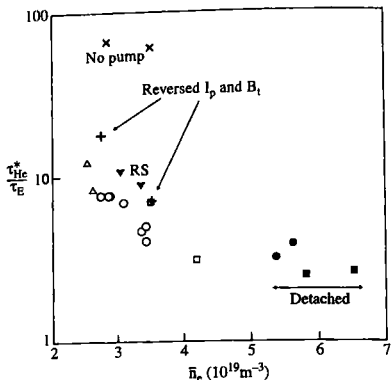


**Fig. 12.4.6** Values of helium residence time normalized to energy confinement time,  $\tau_{He}^*/\tau_E$ , as a function of plasma density,  $\bar{n}_e$ , for various plasma conditions, using inboard pumping only [Sakasai, A. et al. *Fusion Energy 1998* (Proc. 17th Int. Conf., Yokohama, 1998) paper IAEA-CN-69/EX6/5. I.A.E.A., Vienna (2001)].

barrier and, as a result, helium was exhausted more slowly. Values of  $\tau_{He}^*/\tau_E \sim 15$  were obtained in ITB plasmas with high confinement,  $\tau_E \sim 2\tau_{ITER89-P}$ , and although reactor-relevant values of  $\tau_{He}^*/\tau_E (< 10)$  could be obtained by gas puffing, which raised the divertor recycling flux by a factor of 5–10, the energy confinement enhancement was lost, with  $\tau_E \sim 1.2\tau_{ITER89-P}$  resulting.

### Current drive and steady-state operation

Exploration of current drive techniques, principally via lower hybrid waves, negative-ion neutral beams and the bootstrap effect, has been a particular concern of JT-60 and JT-60U experiments. JT-60 was equipped with three lower hybrid launchers, two optimized for current drive and one for heating. The maximum power input was 9.5 MW, and full current drive was achieved at 2 MA. Current drive efficiency improved when the parallel refractive index,  $n_{||}$ , of the waves was reduced and the spectrum narrowed. The efficiency,  $\eta_{CD}$  (see Section 12.3), rose with electron temperature and a maximum value of  $\eta_{CD} = 0.34 \times 10^{20} \text{ m}^{-2} \text{ AW}^{-2}$  was attained. A significant saving in primary flux swing was demonstrated in current ramp experiments with lower hybrid current drive. By injecting up to 2 MW of power during a 2.5 s current ramp, a flux saving,  $\Delta\phi_F$ , of up to 2.5 Vs was obtained. This corresponded to the resistive flux plus ~10% of the inductive flux during the current drive pulse. By neglecting the contribution to the inductive flux and using the known current drive efficiency, the experimental scaling,  $\Delta\phi_F(\text{Vs}) = 0.55 \int [P_{LH}(\text{MW})/\bar{n}(10^{19} \text{ m}^{-3})] dt$ , was shown to be consistent with simple current drive theory.

It was originally expected that current profile broadening induced by a high  $n_{||}$  wave spectrum would prove the most effective approach to

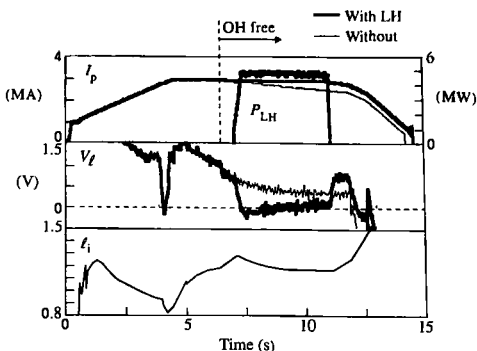


**Fig. 12.4.7** Comparison of plasma parameters during two 3 MA plasma pulses, one with full non-inductive current drive using LHCD (dark curve) and the other without LHCD (light curve). The LHCD power,  $P_{\text{LH}}$ , the plasma current,  $I_p$ , the loop voltage,  $V_L$ , and the internal inductance,  $I_i$ , are shown. Note that the ohmic input power is turned off at 6.5 s in both pulses [from Ikeda, Y. et al. *Plasma Physics and Controlled Nuclear Fusion Research 1994* (Proc. 15th Int. Conf., Seville, 1994) Vol 1, 415. I.A.E.A., Vienna (1995)].

suppressing sawtooth oscillations, but experiments with lower hybrid current drive in neutral beam heated plasmas found that current drive at low  $n_{\parallel}$  readily produced sawtooth stabilization. There was some evidence of current profile modification from the reduction of the sawtooth inversion radius preceding stabilization. Although this appeared insufficient to raise  $q(0)$  above unity, it could not be entirely excluded that  $q(0) > 1$ . Alternative explanations proposed for the stabilization mechanism included the possibility that local current profile modifications could affect the sawtooth stability, or that the presence of energetic electrons in the vicinity of the  $q = 1$  surface could play a role in stabilizing sawtooth oscillations.

In JT-60U experiments current drive performance has been considerably extended using a second multi-junction launcher with a narrower  $n_{\parallel}$  spectrum,  $\Delta n_{\parallel} \sim 0.2$ . The scaling of current drive efficiency, as well as its absolute level, is similar to that in JT-60, with full current drive being achieved up to 3.6 MA. Fig. 12.4.7 illustrates a case in which lower hybrid waves drove the full plasma current at 3 MA. High energy negative-ion neutral beams (300–500 keV/nucleon) provide access to higher current drive efficiencies than the positive ion based systems conventionally used. Hydrogen N-NBI experiments at injected energies of up to 360 keV have achieved  $\eta_{\text{CD}} = 0.16 \times 10^{20} \text{ m}^{-2} \text{ AW}^{-2}$  in plasmas with  $T_e(0) \sim 10 \text{ keV}$ , in agreement with theoretical calculations and resulting in a total beam driven current of up to 1 MA. Electron cyclotron current drive (ECCD) generates localized current drive which can be applied, for example, in the control of mhd instabilities. Measurements of the ECCD efficiencies and profiles for both on- and off-axis current drive yielded good agreement with Fokker-Planck calculations. The very localized nature of the current drive profile,  $\Delta r/a \leq 0.1$ , was confirmed and  $\eta_{\text{CD}} = 0.05 \times 10^{20} \text{ m}^{-2} \text{ AW}^{-2}$  was obtained at  $r/a = 0.2$  for a local electron temperature of 7 keV.

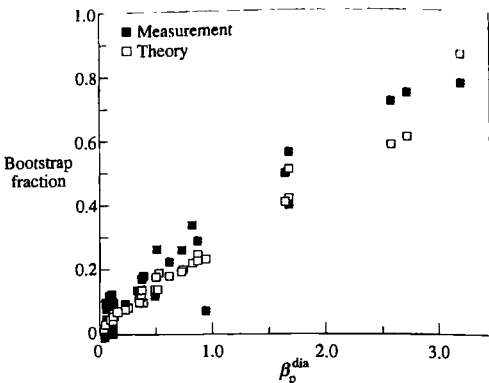


**Fig. 12.4.8** Bootstrap current fraction as a function of  $\beta_p^{\text{dia}}$ , showing both measured values and values derived from neoclassical theory including the bootstrap current contribution [Ishida, S. et al. *Plasma Physics and Controlled Nuclear Fusion Research 1990* (Proc. 13th Int. Conf., Washington, 1990) Vol 1, 195. I.A.E.A., Vienna (1991)].

As in the other large devices, regimes have been developed in which the bootstrap current constitutes a substantial fraction of the total current and, as already noted, such plasmas often exhibit energy confinement up to several times the L-mode value. A detailed investigation of the high- $\beta_p$  regime in JT-60 covered the range of  $\beta_p$  up to 3.2 and included bootstrap current fractions of up to 80%, giving good agreement between theoretical estimates of the bootstrap current fraction, including fast ion effects, and that deduced from analysis of the loop voltage (Fig. 12.4.8). Neutral beam injection in JT-60 was almost perpendicular to the magnetic field, so the calculation was not complicated by contributions from neutral beam driven current, which amounted to only  $\sim 1\%$  of the total current. This analysis also demonstrated that the plasma resistivity in JT-60 was neoclassical.

The extensive current drive capabilities of the JT-60U device have supported the development of steady-state operating regimes with full non-inductive current drive. Two distinct plasma scenarios have been pursued: the first is a high- $\beta_p$  regime having weak positive shear with  $q(0) > 1$  and the second is a reversed shear plasma. Both approaches combine an ITB core plasma with an H-mode edge. In the former case, the highest performance has been achieved at  $q_{95} = 4.1$  in a 1.8 MA/4.1 T plasma, using positive and negative-ion neutral beam injection and electron cyclotron resonance heating, in which fully non-inductive operation has been sustained for  $\sim 2$  s, with  $\sim 50\%$  of the current driven by N-NBI and  $\sim 50\%$  by the bootstrap effect. This plasma maintained  $\beta_N = 2.3\text{--}2.5$ ,  $\tau_E \sim 1.3 \tau_E^{\text{IPB98(y,2)}}$  and reached a fusion triple product of  $3 \times 10^{20} \text{ keV sm}^{-3}$  during the non-inductive phase. In the reversed shear scenario, fully non-inductive current drive has been sustained for 2.5 s with 80% of the current driven by the bootstrap effect in a 0.8 MA/3.4 T plasma at  $q_{95} \sim 9$ . Though the fusion triple product of this plasma

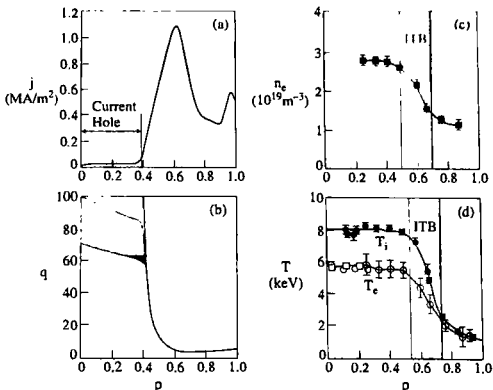


**Fig. 12.4.9** Radial profiles of plasma parameters from a plasma with zero current density over the region  $r/a \leq 0.4$ : (a) plasma current density,  $j$ , (b) safety factor,  $q$ , for which the shaded band indicates the experimental uncertainties, (c) electron density,  $n_e$ , (d) ion and electron temperatures,  $T_i$  and  $T_e$  respectively [Fujita, T. et al. *Physical Review Letters* 87, 245001 (2001)].

was a factor of 4 below that in the high- $\beta_p$  case, the confinement and stability parameters were nevertheless striking, with  $\tau_E \sim 2.2\tau_{E,\text{IPB98(y,2)}}$ ,  $\beta_N \sim 2$  and  $\beta_p \sim 3$  during the full current drive phase.

As in JET, studies of reversed shear operation have led to the development of a regime in which a significant region of the core plasma has zero current density (Fig. 12.4.9). In discharges at 1.35 MA with  $q_{95} \sim 5$ , in which neutral beam injection provides the major form of auxiliary heating, the region of zero current density can extend up to  $r/a = 0.4$  and can persist for many ( $\geq 5$ ) seconds, though with a gradual shrinking in radius. Development of the current hole is driven by the growth of a strong off-axis bootstrap current which develops in the region of steep pressure gradient associated with an internal transport barrier. Motional Stark effect measurements of the poloidal field indicate that  $q(0) > 70$  and that the integrated current within  $r/a = 0.4$  is no more than 12 kA. In cases with moderate values of  $q_{95}$ , the plasma remains stable to global MHD modes throughout the duration of the current hole. As in the JET experiments, no reversal of the central current density has been observed to date.

### MHD studies

Major disruptions in JT-60U usually develop as discussed in Sections 7.8 to 7.10. As in JET, density limits, current rise instabilities, and error field modes are frequent triggers for disruptions. Additional causes include the occurrence of high- $\ell_i$  in the current ramp-down and high- $\beta_p$  collapses caused by ideal kink ballooning modes, particularly in experiments at high fusion performance. Operation at the highest values of  $\beta_N$  is often limited by disruptions and, as in other tokamaks, neoclassical tearing

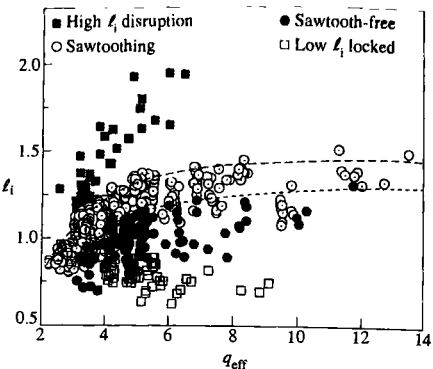


**Fig. 12.4.10**  $\ell_i$ - $q_{\text{eff}}$  diagram summarizing the general stability properties of plasmas in JT-60U. The open squares represent pulses which form a locked mode at low  $\ell_i$ , while the closed squares represent the disruptive boundary at high  $\ell_i$ . The dotted curve indicates the approximate boundary above which sawtooth oscillations occur, and the dashed curve corresponds to the locus of plasmas in quasi-steady-state [Kamada, Y. et al. Nuclear Fusion 33, 225 (1993)].

modes can set the  $\beta_N$ -limit in long pulse operation. The L-mode density limit was studied in JT-60 experiments which confirmed that the limit was due to excessive radiated power and could, therefore, be characterized as an edge density limit. Consequently, pellet injection was used to extend the line average density by a factor of 2, with the density limit parameter,  $10^{-19} \bar{n} R q_{\text{eff}} / B$ , increasing from 15 to  $28 \text{ m}^{-2} \text{ T}^{-1}$ . The behaviour at the density limit in JT-60U is similar.

The general stability properties of JT-60U plasmas at low- $\beta$  are summarized in the  $\ell_i - q_{\text{eff}}$  diagram shown in Fig. 12.4.10. The principal disruption boundaries lie at low- $\ell_i$ , due to modes growing during the current rise, and at high- $\ell_i$ , where density limit and current ramp-down disruptions occur. Between these limits, the plane can be further subdivided according to the presence or absence of sawtooth activity. One subdivision, indicated by a dotted curve, marks the threshold for the onset of sawtooth oscillations. Another, indicated by the dashed curve, represents the locus of plasmas in quasi-steady-state, in which the current profile is fully diffused except in the plasma centre, where it is controlled by sawtooth oscillations.

Considerable attention has been given to the development of strategies for the avoidance of disruptions and for reducing their impact wherever possible. Since the major difficulties during the current rise are associated with passing through  $q_{\text{eff}} \sim 4$ , this is normally crossed during the first 200 ms by forming a small bore inner wall plasma and subsequently expanding the plasma aperture. With this method, current ramp rates of  $2 \text{ MAs}^{-1}$  have been achieved during ramps from 0.5 to 3.5 MA. Minor disruptions can occur for ramp rates in excess of  $1 \text{ MAs}^{-1}$ , but the plasma survives. Similarly, current ramp-down disruptions can be avoided by shrinking the plasma aperture to reduce  $\ell_i$ . It is also found that in some cases the plasma current profile can be broadened, and disruptions prevented, during this phase by applying an external static helical field with

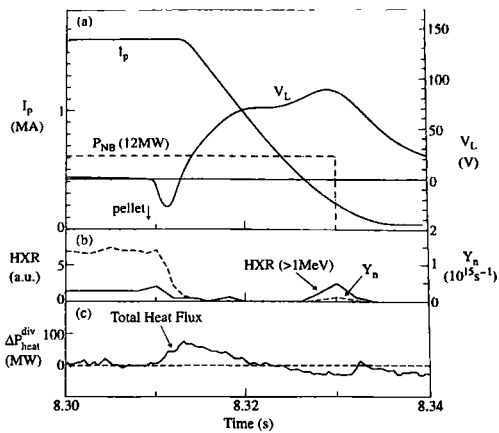


**Fig. 12.4.11** Disruptive behaviour following the injection of a cryogenic neon 'killer' pellet: (a) the plasma current,  $I_p$ , the loop voltage,  $V_L$ , and the NB1 heating power,  $P_{NB}$ , (b) hard X-ray, HXR, and neutron yield,  $Y_n$ , signals, (c) change in power deposited on the divertor targets,  $\Delta P_{heat}^{div}$  [from Yoshino, R. et al. *Plasma Physics and Controlled Fusion* 39, 313 (1997)].

principal mode numbers  $m = 3/n = 2$ . This must be used with care, however, as application of the external field can provoke disruptions for  $r_{q=1}/a > 0.3$ .

Infrared measurements of the heat flux to the divertor at the thermal and current quenches have revealed that it suddenly increases to values above  $100\text{MWm}^{-2}$  several hundred microseconds before the quench, and this is followed by a rapid rise in carbon impurity emission from the bulk plasma. In addition, the timescale for the current decay, defined by  $I_p/(dI_p/dt)$ , increases as the plasma stored energy decreases, where the energy is measured just before the quench. These observations lend support to the idea that the fast current quench is driven by radiation cooling of the plasma.

Experiments to mitigate the effects of disruptions have dealt with the three key issues: the thermal quench, the generation of runaway electrons, and the vertical instability and associated halo currents. It has been demonstrated that the peak heat flux to the divertor plate can be significantly reduced by the injection of cryogenic neon 'killer' pellets before the thermal quench (Fig. 12.4.11). In studies in which one or more neon pellets was injected into ohmic and neutral beam heated discharges, the peak heat divertor flux during the thermal quench was reduced from values in the range  $100\text{--}300\text{MWm}^{-2}$  to  $20\text{--}50\text{MWm}^{-2}$ . Extension of neutral beam heating through the current quench phase is also found to be beneficial in reducing the current decay rate, though the mechanism is not understood.

During the disruption current quench, in particular following the injection of neon pellets, substantial currents of runaway electrons can be

generated with energies extending beyond 30 MeV. In some cases, however, the runaway electrons can be suppressed by the intrinsic magnetic fluctuations occurring during the disruption. This has been exploited by using external saddle coils to apply a predominantly  $m = 3/n = 2$  magnetic perturbation, with  $B_{r(3/2)} < 7 \times 10^{-4}$  T at the plasma centre. This causes bursts of magnetic activity in the plasma, possibly associated with further disruptive events, which suppress the development of the runaway electron current. The occurrence of a rapid vertical instability following major disruptions has also been substantially reduced by adjusting the plasma vertical position to the 'null point' of the vacuum vessel. It was shown that asymmetries in the eddy currents induced in the vacuum vessel at a major disruption can contribute significantly to an enhancement of the growth rate of the subsequent vertical instability. By identifying the plasma position at which these asymmetries are minimized, it has been possible to establish an optimum position, the 'null point', for plasma operation at which the likelihood of a vertical instability following disruptions is small.

In high- $\beta_p$  L-mode experiments in JT-60 and JT-60U,  $\beta$  values were limited by rapid collapses in the plasma core. Although values of  $\varepsilon\beta_p$  as high as 1.2 were reached in JT-60 without a collapse, the high confinement deteriorated after several seconds due to mhd modes with  $m = 1, 2, 3$ . At  $\beta_N \sim 1.1$  an internal collapse, which occurred on a timescale of 100  $\mu$ s with no detectable precursor activity, degraded confinement. Calculations suggested that the large bootstrap current fraction gave rise to a negative shear region in the plasma centre with a minimum  $q$  value just below 3, and it was proposed that this destabilized an ideal low- $n$  kink or ballooning mode which triggered the  $\beta$ -limiting collapse. In JT-60U experiments,  $\beta$  was limited by an internal collapse at values of  $\beta_N \sim 2.3$ . ECE measurements of  $T_e$  showed that the collapse exhibited rapidly growing  $m = \text{odd}$  precursor activity, with a significantly higher amplitude on the outboard side of the plasma centre, and that this mode propagated to the plasma centre in a time of  $\sim 200$   $\mu$ s. Stability analysis indicated that low- $n$  ideal kink ballooning modes were unstable under these conditions, with a dominant  $m = 3/n = 2$  mode at the  $q = 1.5$  surface. In several discharges at lower values of  $q^*(\sim 4.5)$ , where  $q^* = \pi a^2 B (1 + \kappa^2) / (\mu_0 R I)$  is a cylindrical equivalent value of  $q$ , and  $\kappa$  is the plasma elongation,  $\beta_p$  collapses were responsible for inducing major disruptions. Similar limitations were encountered in ITB plasmas with negative central shear and an L-mode edge, where  $\beta_N$  was limited to values of  $\sim 2$  in experiments with  $q_{\min} \sim 2$ .

These problems are alleviated in H-modes due to their broader pressure profiles. For example, in the high- $\beta_p$  H-mode regime, values of  $\beta_N = 4.8$  have been achieved transiently. In these cases,  $\beta$  is limited by pressure driven modes, with  $n = 1-2$  and  $m = 2-5$ , which grow as the current profile broadens under the influence of the bootstrap current, leading to a gradual degradation of confinement. The highest sustainable values of  $\beta_N$  in quasi-steady-state discharges ( $> 5\tau_E$ ) are lower, with  $\beta_N = 3.05$  having been achieved in moderate triangularity plasmas ( $\delta_X = 0.34$ ).

Studies of  $\beta$ -limiting phenomena in JT-60U H-modes show that the global behaviour can be understood primarily in terms of the pressure profile peaking factor,  $p(0)/\langle p \rangle$ , and the plasma triangularity. At low values of  $p(0)/\langle p \rangle$ , the  $\beta_N$ -limit is linked to an edge pressure limit associated with ELMs, although neoclassical tearing modes appear at the highest values of  $\beta_N$ , while at high values of  $p(0)/\langle p \rangle$  the limit is determined by the internal  $\beta_p$  collapses discussed above. Higher triangularity increases the magnetic shear at the plasma edge, improving the edge stability and allowing access to increased values of  $\beta_N$  at low pressure peaking factor.

Further improvements in the plasma shaping capability have extended the range of plasma triangularities up to  $\delta_X = 0.6$  at 1 MA, which may further expand the accessible range in  $\beta_N$ : for example, in a 1 MA/1.8 T high- $\beta_p$  H-mode with  $\delta_X = 0.45$ ,  $\beta_N = 2.7$  was sustained for 7.4 s under quasi-stationary conditions. In this case, the  $\beta$ -limit was determined by a neoclassical tearing mode with  $m = 3/n = 2$  which persisted for the duration of the high- $\beta$  phase. A capability for stabilization of such modes by localized electron cyclotron current drive, as first demonstrated in ASDEX Upgrade, has been successfully tested in JT-60U with the aim of allowing access to higher values of  $\beta_N$ .

### Confinement and fusion performance in JT-60U

L-mode confinement in JT-60U is similar to that in other tokamaks and broadly follows the ITER89-P scaling. However, for  $q_{eff} < 5$ , energy confinement in conventional L-mode plasmas falls below the ITER89-P scaling and degrades with decreasing  $q_{eff}$ . Analysis suggests that this is related to current profile variations, which can be expressed through  $\ell_i$  and  $q_{eff}$ . Some of the dependence on  $q_{eff}$  reflects the observation that  $\ell_i$  tends to decrease as  $q_{eff}$  falls, but there is an additional contribution to transport from the expansion of the sawtooth inversion radius with decreasing  $q_{eff}$ . L-mode plasmas have also been studied using ion cyclotron second harmonic minority heating at power levels of up to 6 MW, with similar results to those in JET first harmonic minority heating experiments. Observations include the production of sawtooth stabilization by on-axis heating and the destabilization of toroidal Alfvén eigenmodes by fast minority ions. Bursts of TAE modes, leading to drops of several percent in neutron emission, are also excited by 360 keV hydrogen ions injected during negative-ion neutral beam heating in reversed shear plasmas.

Following boronization of the torus, H-modes have been established at plasma currents of up to 4.5 MA with a variety of heating scenarios. The power threshold for the L- to H-mode transition increases linearly with toroidal field as in other tokamaks and lies close to the generally accepted scaling. Performance in H-mode plasmas has improved with the gradual upgrading of the poloidal field shaping capability to allow higher triangularity operation. The observation that the nature of the ELM behaviour changes significantly with increasing triangularity and edge safety factor is particularly significant, since the type I ELMs normally

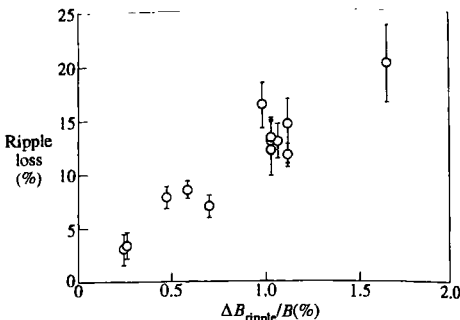


**Fig. 12.4.12** Experimentally measured ripple loss fraction, defined as the ratio of the ripple loss power to the neutral beam input power, as a function of the toroidal field ripple size on the midplane,  $\Delta B_{\text{ripple}}/B$  [Tobita, K. et al. *Physical Review Letters* **69**, 3060 (1992)].

observed are expected to cause enhanced erosion of the divertor targets in a fusion reactor. At high- $\beta_p$  ( $\beta_p \geq 1.6$ ), high triangularity ( $\delta_X \geq 0.45$ ) and in the region  $q_{95} \geq 6$ , complete suppression of type I ELMs is observed and an irregular, 'grassy', behaviour, possibly associated with type II ELMs, is observed. This results in a significant reduction of the pulsed heat flux to the divertor generated by the ELMs. There is some evidence that, as triangularity is further increased, the grassy ELM behaviour can be obtained at  $q_{95} \sim 4$ . Mhd stability analysis of the edge indicates that the transition to the grassy ELM regime is associated with access to the second stability regime for ballooning modes and that the grassy ELM behaviour may be associated with the occurrence of ideal modes with  $n > 10$ , while modes with  $n$  in the range 5–10 may be responsible for type I ELMs. Further progress in ameliorating the divertor heat flux during ELMMy H-modes has been attained via the use of noble gas seeding, as discussed previously. The use of inboard pellet injection, as pioneered in ASDEX Upgrade, has allowed high confinement ELMMy H-modes to be maintained at higher densities, and  $\tau_E \sim \tau_E^{\text{IPB98(y,2)}}$  has been sustained at approximately 70% of the Greenwald density.

JT-60U has only 18 toroidal field coils, and so full bore plasmas experience a large toroidal field ripple,  $\delta B/B \sim 3\%$ , at the plasma edge. Ripple losses of beam injected fast ions or fusion products can, therefore, be substantial, and this provides an opportunity for testing the theoretical understanding of the processes involved. Controlled experiments were performed by expanding the outside edge of the plasma into the high ripple region and monitoring the losses of energetic particles, either by measurements of loss power on the first wall of the torus, or by observations of 2.4 and 14 MeV neutron emission. A linear relationship between the fraction of injected beam ions lost in this way and the ripple at the outer edge was derived from infrared camera measurements of the heat flux on the outer wall of the torus (Fig. 12.4.12). Detailed calculations using an orbit-following Monte Carlo code, which included losses due to ripple trapping and banana drifts, yielded good agreement with the

measured loss fractions. Additional information came from the decay of 2.4 MeV neutrons following a short beam pulse. This showed that the discrepancy between the calculated neutron decay rate and that predicted by classical beam slowing-down calculations increased as the plasma edge was expanded into regions of larger toroidal field ripple, indicating a rise in ripple induced losses with increasing ripple amplitude as expected.

In a related experiment, in which the influence of the toroidal field ripple losses on the quality of hot ion H-mode confinement was analysed, no correlation was observed between the magnitude of ripple losses and the H-mode energy confinement enhancement factor after correcting for the injected power losses caused by the ripple. In contrast, the impact of TF ripple on fast particle confinement in reversed shear plasmas was clearly demonstrated in an experiment which compared the burnup of 1 MeV tritons produced by D-D reactions in a plasma with  $q_{\min} = 2.1$  and  $q(0) = 3.6$  with that measured in a conventional sawtooth plasma. As the plasma edge was expanded into the high ripple region on the outward side of the torus ( $\delta B/B \sim 1\%$ ), the fraction of confined tritons fell by more than a factor of 3 in the reversed shear case, but by only 25% in the conventional scenario, in good agreement with calculations using the orbit following Monte Carlo code.

The two regimes explored as potential steady-state scenarios, the high- $\beta_p$  H-mode and the reversed shear mode, have also been developed towards high fusion performance. The former regime is similar to high performance scenarios in other large experiments in that it is established by high power neutral beam injection into a low density target plasma. As in other devices, low recycling is found to be a requirement for producing the highest performance, and the improved deuterium recycling and impurity control properties of the W-shaped divertor have been found to be important in this respect. Fig. 12.4.13 illustrates the evolution of a 2.4 MA/4.3 T plasma with  $q_{95} \approx 3$  which attained the highest fusion triple product,  $1.5 \times 10^{21} \text{ keV sm}^{-3}$ , equivalent to  $Q_{DT} \approx 0.4$ . Initially a high- $\beta_p$  regime, characterized by an internal transport barrier at typically  $r/a \sim 0.7$ , is formed. A transition to an ELM-free H-mode then occurs, leading to an increase in the edge parameters and a further improvement in confinement. The phase of highest fusion performance is terminated at  $\beta_N = 2$  by a disruption caused by the rapid ( $10 \mu\text{s}-1 \text{ ms}$ ) growth of  $n = 1$  kink-balloon modes. At 1.5 MA/3.7 T this regime can be sustained in quasi-steady-state conditions for periods of between 4.5 s and 9 s with  $Q_{DT} \sim 0.16-0.11$ .

Central deposition of the neutral beam power in these plasmas produces very peaked plasma profiles, resulting in  $T_i(0) \sim 40 \text{ keV}$  and  $n(0) \sim 6 \times 10^{19} \text{ m}^{-3}$ . The existence of an internal transport barrier, identified by the formation of a steep ion temperature gradient at  $r/a > 0.5$  (Fig. 12.4.14), is a crucial aspect of the confinement properties. Measurements of the  $q$ -profile indicate that the barrier often lies close to the  $q = 2$  or  $q = 3$  surface and that its location could be related to the position at which  $s \sim 1$ . Analysis of the heat transport in the plasma core shows that the ion and electron thermal diffusivity fall by almost

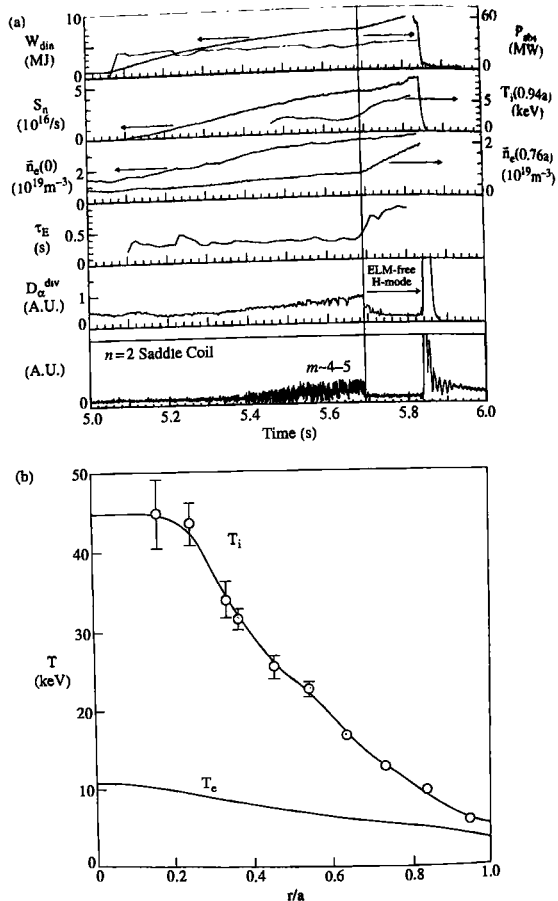


**Fig. 12.4.13** Overview of the high- $\beta_p$  H-mode with the highest fusion triple product. Shown are: (a) the diamagnetic stored energy,  $W_{\text{dia}}$ , the absorbed heating power,  $P_{\text{abs}}$ , the neutron emission,  $S_n$ , the edge ion temperature,  $T_i(0.94a)$ , the line averaged electron density,  $\bar{n}_e$ , along chords at  $r/a = 0$  and  $r/a = 0.76$ , the energy confinement time,  $t_E$ , the  $D_\alpha^{\text{div}}$  emission from the divertor region, and the signal from a saddle coil system for detecting mhd modes with  $n = 2$ ; (b) the radial ion and electron temperature profiles,  $T_i$  and  $T_e$  respectively, at the time of peak fusion performance [from Ishida, S. et al. *Fusion Energy 1996* (Proc. 16th Int. Conf., Montreal, 1996) Vol 1, 315. L.A.E.A., Vienna (1997)].

an order of magnitude on the formation of the barrier, reaching values commensurate with the neoclassical value of the ion thermal diffusivity in the plasma centre. The peaked profiles in this regime resemble those of TFR supershots, and an analysis of data from the two tokamaks has shown that the neutron yield follows the same scaling with respect to the absorbed power, plasma volume and peaking factor of the NBI fuelling.

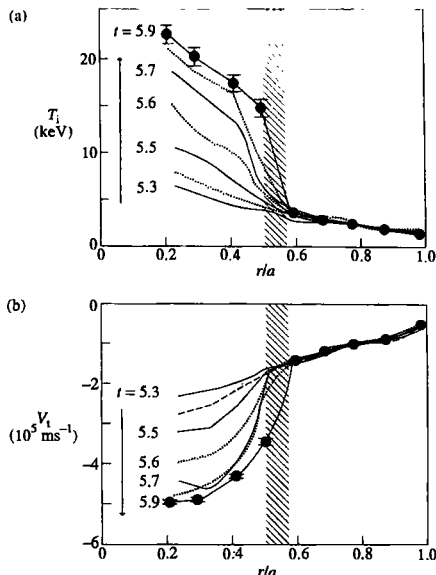


**Fig. 12.4.14** Development of steep gradients in the profiles of (a) ion temperature,  $T_i$ , and (b) toroidal rotation velocity,  $v_t$ , at the internal transport barrier, indicated by the vertical shaded region, in a high- $\beta_B$  H-mode such as that illustrated in Fig. 12.4.13 [Koide, Y. et al. *Plasma Physics and Controlled Nuclear Fusion Research 1994* (Proc. 15th Int. Conf., Seville, 1994) Vol 1, 199. I.A.E.A., Vienna (1995)].

Reversed shear plasmas are extensively exploited in the JT-60U programme. One of the more remarkable achievements is the establishment of core electron temperatures of 26 keV, though at a density of  $0.5 \times 10^{19} \text{ m}^{-3}$ , by the injection of 3 MW of centrally deposited electron cyclotron resonance heating power into a reversed shear plasma sustained by neutral beam injection and lower hybrid current drive. High fusion performance is established by injecting moderate neutral beam power, 10–15 MW, into a low density target plasma,  $\bar{n} \sim 1 \times 10^{19} \text{ m}^{-3}$ , early in the current rise. A central region of reversed shear develops during the current ramp and an internal transport barrier expands radially, eventually reaching  $r/a \sim 0.7\text{--}0.8$ , while the plasma edge remains in L-mode. The ion temperature rises to almost 20 keV throughout the plasma core and the core density reaches values of  $\sim 8 \times 10^{19} \text{ m}^{-3}$  (Fig. 12.4.15). The large volume encompassed by the transport barrier leads to significant enhancement of the energy confinement, with  $\tau_E \sim 1 \text{ s}$  ( $\sim 3 \tau_{ITER89-P}$ ), yielding  $n_D(0)T_i(0)\tau_E = 8.6 \times 10^{20} \text{ keV m}^{-3}$ , equivalent to  $Q_{DT} = 1.25$ , in the best pulse.

The highest fusion performance is attained under transient conditions, often with a disruptive termination at moderate values of  $\beta_N$  (<2) when

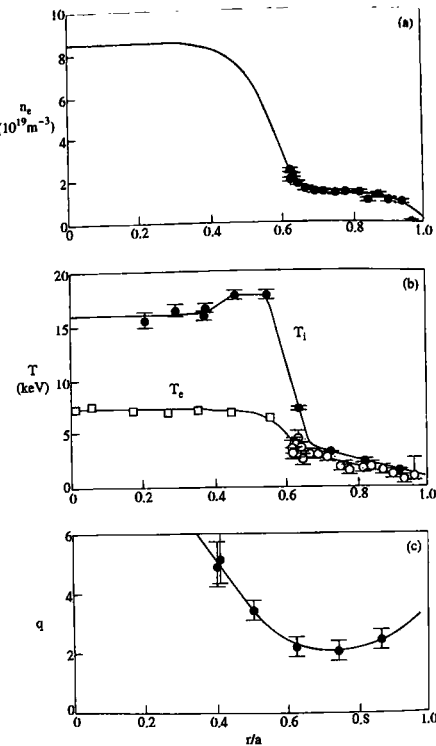


**Fig. 12.4.15** Radial profiles from a 2.6 MA/4.4 T (deuterium) reversed shear discharge with fusion performance corresponding to the highest estimated equivalent value of  $Q_{DT}$ : (a) electron density,  $n_e$ , (b) ion temperature,  $T_i$ , and electron temperature,  $T_e$ , (c) safety factor,  $q$  (from Ishida, S. et al. *Nuclear Fusion* 39, 1211 (1999)).

$q_{\min} \sim 2$ . Electron cyclotron emission measurements show a rapidly growing ( $\gamma^{-1} \sim 10 \mu\text{s}$ ) precursor mode to the disruption and mhd stability analysis indicates that the plasma is close to the ideal stability limit for low- $n$  ideal kink ballooning modes. This level of fusion performance has been reproduced in plasmas with similar global parameters in which a current hole develops. These discharges also terminate disruptively, in contrast to the current hole regime at higher values of  $q_{95}(\sim 5)$ . Careful programming of the auxiliary heating system to control the development of the plasma pressure has allowed  $n_D(0)T_i(0)r_E = 4 \times 10^{20} \text{ keV sm}^{-3}$ , equivalent to  $Q_{DT} = 0.5$ , to be sustained for 0.8 s in a reversed shear plasma. In this case the plasma disrupted at the modest value of  $\beta_N = 1.1$  and mhd stability analysis indicates that resistive interchange modes could be involved in the initial phase of the termination.

**12.5****DIII-D—General Atomics, San Diego, USA**

DIII-D was developed from the Doublet III tokamak, which had been designed to investigate the properties of doublet shaped plasmas, in which a waist is created in the midplane of an elongated equilibrium. The Doublet III experiment was more successful when operated with a conventional plasma geometry having an 'expanded boundary' divertor, that is with an internal magnetic separatrix but without a divertor chamber. It was, therefore, decided to rebuild the tokamak within the existing toroidal field coil set so as to maximize the volume available for this configuration (Fig. 12.5.1), at the same time increasing the shaping capability.

The resultant device, which began operating in early 1986, has an aspect ratio similar to that of JET,  $R/a = 1.67/0.67$ , a maximum toroidal field of 2.2 T, and is designed to achieve plasma currents of up to 3.5 MA with a diverted plasma, and 5 MA in the limiter configuration. Deuterium neutral beam injection provides up to 20 MW of heating power with ion energies of up to 80 keV, while the ion cyclotron radiofrequency system, operating at 60 and 83 MHz, has provided up to 4.4 MW and the electron

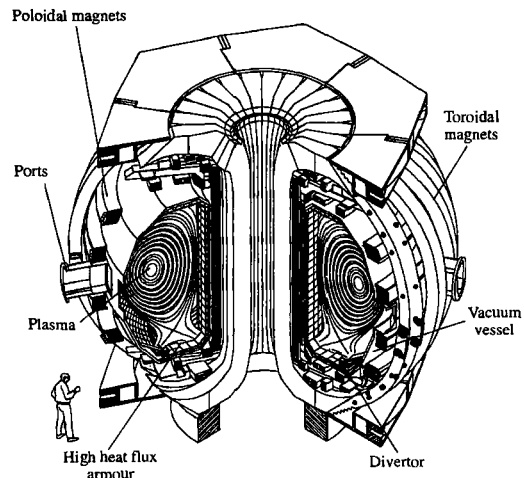


**Fig. 12.5.1** Layout of the DIII-D experiment.

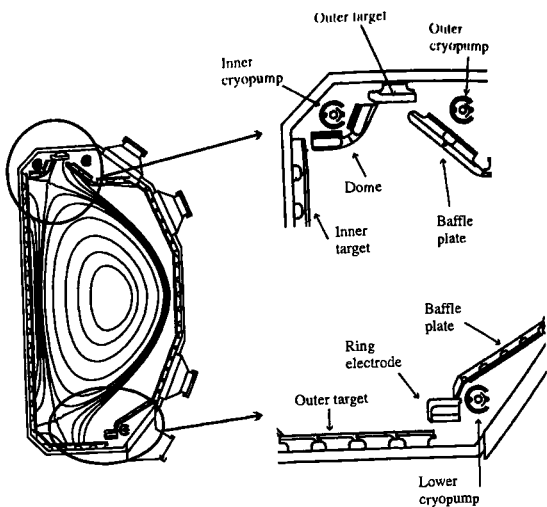


**Fig. 12.5.2** Cross-section of the DIII-D vacuum vessel showing the main elements of the upper and lower pumped divertors.

cyclotron resonance heating system, operating at 110 GHz, has injected up to 3 MW, though this system is being developed towards a 6 MW capability.

Initially the inconel vacuum vessel had a limited coverage of graphite tiles, but this was gradually extended, so that by the early 1990s the internal surface of the vessel was completely covered by graphite. A variety of techniques has been used to condition the vessel and reduce the recycling of hydrogen isotopes. Among these are baking of the vacuum vessel up to 400 °C, deuterium and helium glow discharge cleaning, carbonization, and boronization, the last two being of particular importance in limiting metallic sputtering from the vessel walls. Routine helium glow discharge cleaning between discharges is regarded as a valuable aid to achieving good H-modes, while the low recycling conditions obtained after boronization are exploited in producing the highest performance.

The power and particle control capabilities have been significantly improved by the introduction of pumped divertors at the top and bottom of the vessel (Fig. 12.5.2). In the period 1990 to 1993, a lower divertor with a rather open configuration was installed. This not only permits active pumping of the divertor region, using a liquid helium cooled cryopump, but also allows radial flows to be generated by application of an external electric field at the outer divertor strike point. Between 1997 and 2000 a closed divertor, with inboard and outboard cryopumps, was installed in the upper vessel with the aim of providing particle control for more highly shaped plasmas.

### Confinement and H-mode studies

Extensive investigations of the H-mode have contributed substantially both to the characterization of its confinement properties and to the understanding of the physics underlying the transition from L- to H-mode. As well as demonstrating H-modes with neutral beam injection, electron cyclotron heating, and fast magnetosonic wave heating in the ion cyclotron frequency range, experiments have produced ohmically heated H-modes and H-modes in plasmas limited on the inner wall. Energy confinement has been enhanced beyond the normal H-mode level by a number of methods and this is discussed in the next subsection.

The introduction of boronization and the installation of graphite tiles over the entire area of the first wall have facilitated routine operation in H-mode, and access to the regime follows similar patterns to those observed in other tokamaks. In NBI heated single null plasmas, the power threshold for the H-mode scales linearly with toroidal field, but more weakly with plasma density. In addition, when the ion VB drift is away from the X-point, the threshold power can be up to a factor of 5 greater than that required when the ion drift is towards the X-point. The dependence on toroidal field and density is absent in the double null configuration, but the strong relationship between the threshold power and the direction of the ion VB drift with respect to the dominant X-point persists. A displacement of only a few centimetres vertically, so that the ion drift is in the direction opposite to that of the dominant X-point, rather than towards it, increases the threshold power by more than a factor of 3. Considerable efforts have been made to characterize the H-mode access conditions in terms of local parameters at the plasma edge, within the pedestal region. It appears unlikely that a critical edge temperature is involved, as demonstrated most clearly by experiments in which H-modes were triggered by deuterium pellet injection at input powers > 20% below the normal H-mode power threshold. It has been suggested on the basis of experimental measurements that the temperature and pressure gradients within the pedestal are more likely control parameters for the L to H transition.

H-modes usually exhibit some form of ELM activity and the possible forms have been classified into three broad categories. Type I, or 'giant', ELMs increase in frequency with input power and can cause energy and particle losses of more than 10% of the total plasma content. Their importance in controlling edge parameters, in particular particle confinement, is illustrated by the achievement of H-modes with durations of up to 10 s in which near steady-state density, energy, and impurity content were maintained. Analysis of edge profiles in deuterium plasmas heated by hydrogen beams suggested that such ELMs occurred when the plasma edge was at the first ideal ballooning limit, and it was inferred that they were triggered by ballooning modes. Later experiments showed, however, that type I ELMs could persist at edge pressure gradients which exceeded the first stability limit by up to a factor of 2 in plasmas in which the edge region was in the second stability regime for ballooning modes. It has subsequently been proposed that type I ELMs in DIII-D are caused by

low to intermediate  $n$  ( $n = 5\text{--}10$ ) kink/ballooning modes, a conclusion supported by detailed stability analyses of plasmas in which the triangularity and squareness were varied. This confirmed that the edge pressure gradient at which type I ELMs occurred increased with triangularity and was highest at moderate squareness as expected.

Type II, or 'grassy', ELMs have higher frequency and lower amplitude. They have been observed in plasmas with low to moderate currents,  $I(\text{MA})/B(T) < 0.5$ , corresponding to values of  $s/q_{95}^2 < 0.15$ , where  $s = d(\ln q)/d(\ln \psi)$  is the shear,  $\psi$  being the enclosed poloidal flux. Type III, or 'transition', ELMs have small amplitude and occur when the input power is just above the transition threshold. Their frequency decreases as the power increases until, at moderate power, the plasma eventually becomes ELM-free. Coherent mhd precursor activity with  $4 \leq n \leq 13$  is a characteristic feature of type III ELMs. A further type of edge behaviour has been discovered in which the plasma edge parameters remain in steady-state, with values corresponding to those of an equivalent type I ELM discharge, but ELMs do not occur. The maintenance of quasi-steady-state conditions distinguishes this regime from ELM-free H-modes. In this 'quiescent' H-mode, discussed in more detail in the following subsection, the edge pedestal parameters appear to be controlled by an edge harmonic oscillation, in which multiple harmonics, with toroidal mode numbers ranging from  $n = 1$  to  $n = 10$ , persist throughout the H-mode.

Studies in DIII-D and other tokamaks have defined the conditions under which H-mode confinement can be obtained, but understanding the fundamental cause of the apparent bifurcation in confinement has proved more challenging. A series of experiments in limiter tokamaks, in which H-mode-like transitions were provoked by inserting an electrically biased probe into the plasma, coincided with theoretical developments which considered the influence of electric fields on transport processes. These insights have been pursued vigorously and substantial evidence has accumulated that the H-mode transition is associated with a change in the radial electric field at the plasma edge.

The essential concept which has emerged from theoretical investigations is that the electrostatic flute-like modes, commonly supposed to be responsible for anomalous transport in L-mode plasmas, can be stabilized in the presence of a sheared fluid flow deriving from a gradient in the  $E \times B$  drift velocity. The dominant role is played by the radial component of the electric field,  $E_r$ , which can be deduced from the lowest order radial force balance equation for a single ion species,

$$E_r = (Zen_z)^{-1} dp_z/dr - v_\theta B_\phi + v_\phi B_\theta, \quad 12.5.1$$

where the species has an ionic charge  $Z$ , density  $n_z$ , pressure  $p_z$ , and poloidal and toroidal rotation velocities  $v_\theta$  and  $v_\phi$ . Analysis of the characteristics of plasma turbulence and the influence of  $E \times B$  drifts on flute-like modes has allowed the derivation of a working criterion that complete stabilization of the turbulence should occur when the  $E \times B$

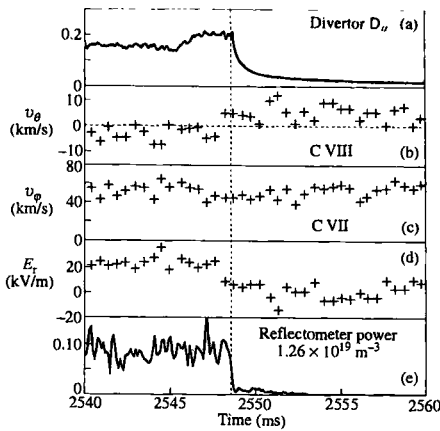


**Fig. 12.5.3** Time history across the L to H transition of (a)  $D_\alpha$  emission from the lower divertor of the DIII-D vessel, (b) the poloidal rotation velocity measured by an active CXRS channel located within 1 cm of the separatrix, (c) the toroidal rotation velocity from an active CXRS channel located within 1 cm of the separatrix, (d) the radial electric field measured at the same location as (b) and (c), (e) the power of a density reflectometer signal integrated from 75 to 800 kHz for a channel with a reflection layer within 2 cm of the separatrix, corresponding to an electron density of  $1.26 \times 10^{19} \text{ m}^{-3}$ . The dashed line indicates the initial fall of the  $D_\alpha$  signal, conventionally used to indicate the onset of the H-mode [from Gohil, P. et al. Nuclear Fusion 34, 1057 (1994)].

shearing rate for the modes,  $\omega_{E \times B}$ , is  $\sim \gamma_{\max}$ , the maximum linear growth rate of the modes.

Analysis of impurity emission in the visible region permits the three contributions to the radial electric field in equation 12.5.1 to be determined with submillisecond time resolution. The critical quantities are the radial profiles of poloidal and toroidal ion velocity and those of ion temperature and density. Initially, passive emission measurements were employed, but subsequently active charge exchange recombination spectroscopy, which exploits charge exchange reactions between plasma ions and the auxiliary heating beams, has been preferred. These measurements have shown that a negative radial electric field is established in a region within 1–2 cm of the plasma edge, virtually simultaneously with the drop in  $D_\alpha$  emission which accompanies the H-mode transition (Fig. 12.5.3). Similar phenomena occur in H-modes produced by neutral beam, electron cyclotron and ohmic heating, as well as in H-modes obtained in plasmas limited on the graphite tiles on the high magnetic field side of the torus.

Langmuir probe measurements at the plasma edge also show that the plasma floating potential becomes more negative, and that the ion saturation current falls in a manner consistent with the formation of a steep density gradient. Moreover, the amplitude of density fluctuations, measured by microwave reflectometry and far-infrared scattering, decreases rapidly within 100  $\mu$ s of the L to H transition in a layer of width 2–3 cm at the separatrix. The region in which these changes are observed corresponds to that commonly identified with the edge transport barrier,

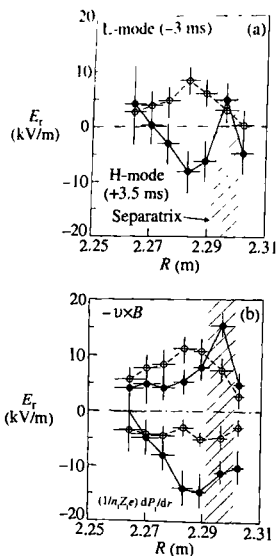


**Fig. 12.5.4** (a)  $E_r$  as a function of major radius,  $R$ , in the region close to the separatrix (shaded area) at two times: one in the L-mode, 3 ms before the L to H transition, and one in the H-mode, 3.5 ms after the L to H transition. (b) The  $v \times B$  and pressure gradient terms which sum to the  $E_r$  given in (a). The open circles correspond to the L-mode measurement and the solid circles to the H-mode measurement, while the shaded region indicates the experimental uncertainty in the determination of the location of the separatrix [Burrell, K.H. et al. *Physics of Plasmas* 1, 1536 (1994)].

which is regarded as a characteristic feature of the H-mode. A region of improved confinement then penetrates inwards on a timescale of tens of milliseconds following the transition, and is accompanied by increasing shear in the radial electric field and a reduced level of density fluctuations. The experimental evidence indicates that the change in the electric field precedes other signatures of the H-mode, supporting the contention that this is a primary cause, rather than a consequence, of the L to H transition.

In helium plasmas the radial electric field can be evaluated from the parameters of the majority ions, rather than impurity ions. Although the time resolution,  $\sim 7$  ms, is poorer than that attainable when using impurity ions, the development of a negative radial electric field at the plasma edge has been confirmed. Nevertheless, the contributions of the individual terms in the radial force balance equation are rather different (Fig. 12.5.4). In particular, measurements of the velocity of the helium majority ions made 3.5 ms after the transition show that they rotate in the ion diamagnetic drift direction, whereas the impurity ions are found to rotate in the electron diamagnetic drift direction. The magnitude of the rotation is much less than the ion diamagnetic drift, however, again implying a large negative radial electric field.

The confinement characteristics of H-modes have been studied extensively, with the general conclusion that access to the H-mode and global energy confinement are independent of heating method. Typical confinement enhancement factors of  $\sim 2$  relative to L-mode plasmas are obtained in deuterium H-modes heated by deuterium NBI, but, as in other tokamaks, the H-mode confinement enhancement factor usually falls as the density is raised towards the Greenwald value. In certain low power discharges,  $P_{NB} \leq 4$  MW, fuelled by gas puffing, it has been found that the density profile becomes more peaked and it is possible to maintain the quality of H-mode confinement, with  $\tau_E \sim 2\tau_E^{ITER89-P}$ , at densities  $\sim 1.4n_{GW}$ . Further improvement in the quality of H-mode confinement has been achieved in plasmas with neon puffing, where  $\tau_E \sim 3\tau_E^{ITER89-P}$  has been attained. It has been proposed that the enhancement in confinement beyond normal H-mode levels is associated with the stabilization of high wave number drift waves by the presence of impurities.

By preparing NBI heated L- and H-mode plasmas in which the global parameters were very similar, it was demonstrated that the local heat diffusivity in an H-mode is lower by a factor of up to 3 than in an L-mode, and that the edge transport barrier accounts for only a small fraction,  $\sim 15\%$ , of the improved energy confinement. More detailed analysis of the local transport properties of H-mode plasmas has been performed in dimensionless scaling experiments which have investigated the dependence of local thermal diffusivity on  $\beta$ ,  $v_*$  and  $\rho_*$  ( $= r/a$ ). Ion and electron thermal diffusivities exhibit a gyro-Bohm scaling, so that  $\chi_e$  and  $\chi_i$  have a linear variation with  $\rho_*$ , but have a weak dependence on  $\beta$ . The observed dependence of the effective (single fluid) thermal diffusivity on collisionality,  $\chi_{eff} \propto v_*^{0.49 \pm 0.08}$ , is ascribed in part to the unavourable influence of neoclassical ion thermal diffusivity, which is within a factor of 3 of the anomalous diffusivity in H-mode plasmas. Comparisons of

dimensionally similar plasmas between DIII-D and JET also showed that when the globally averaged values of key dimensionless parameters were carefully matched, the normalized thermal confinement time,  $B\tau_{E,h}$ , in the two devices agreed to within 7%, confirming the validity of the dimensionless parameter scaling approach to transport analysis. Experiments have also studied the dependence of local transport on the ratio  $T_i/T_e$ , finding that both ion and electron thermal diffusivities increase as the ratio decreases, independently of whether the ion or electron temperature is varied. It has been suggested that this can be explained by the sensitivity of the critical ion temperature gradient for the destabilization of ion temperature gradient turbulence to the ratio of ion and electron temperatures.

Basic transport processes in L-mode plasmas have been investigated by exploiting the localized power deposition of electron cyclotron resonance heating. Transport analysis of plasmas in which the electron cyclotron resonance was displaced significantly off-axis, by approximately half of the minor radius, found that a negative effective thermal diffusivity was required in the electron channel to explain the form of the electron temperature profile, which remained peaked. This implied the existence of a non-diffusive component of thermal transport to support the central peaking of the profile. However, heat losses through the ion channel ensured that the total heat flux was outwards, so that the second law of thermodynamics was not violated. Other L-mode experiments involving both ECRH and NBI heating have allowed the dependence of ion and electron heat transport on  $\rho_*$  to be separated for the first time. Electrons have a gyro-Bohm behaviour,  $\chi_e \propto \rho_*$ , but the ions behave in a manner described as 'Goldston-like', with  $\chi_i \propto \rho_*^{-1/2}$ . It has been suggested that the Bohm-like behaviour usually observed in other experiments can be understood as a single fluid average of these two scalings.

### Enhanced confinement and high performance

Developments in several areas have contributed to increases in the level of plasma performance achieved in DIII-D: gradual improvements in wall conditioning methods and particle control have lowered recycling levels and reduced impurity influxes, while the realization of techniques for modification of the current profile and the exploitation of plasma shaping, particularly higher triangularity, have provided access to higher confinement and improved stability. Studies have focussed on the development of plasmas in which energy confinement is further enhanced relative to the H-mode, while plasma pressure is maximized, so as to optimize the fusion gain,  $\beta \times \tau_E$ . Conventionally, figures of merit such as  $\beta_N H_{99}$ , where  $H_{99} = \tau_E/\tau_E^{\text{ITER89-P}}$ , and  $\beta_N H_{98}$ , where  $H_{98} = \tau_{E,h}/\tau_E^{\text{IPB98(y,z)}}$ , are used to provide normalized measures of the plasma performance in these experiments. Regimes with high figures of merit tend also towards high bootstrap current fractions, which is a desirable feature of steady-state plasmas.

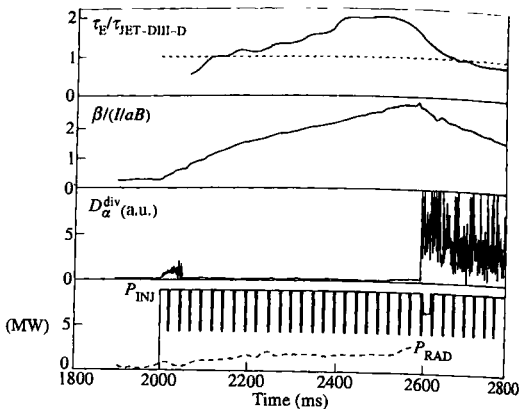


**Fig. 12.5.5** Typical waveforms for a VH-mode discharge. The ratio of the thermal energy confinement time to the JET/DIII-D scaling expression,  $\tau_E/\tau_{JET-DIII-D}$ , increases to  $\sim 2$  during the VH-mode. Also shown are the normalized toroidal beta,  $\beta/(I/aB)$ , the divertor  $D_\alpha$  emission, the injected NBI power,  $P_{INJ}$ , and the radiated power,  $P_{RAD}$  [from DIII-D Team (presented by R. D. Stambaugh) *Plasma Physics and Controlled Nuclear Fusion Research 1994* (Proc. 15th Int. Conf., Seville, 1994) Vol 1, 83. I.A.E.A., Vienna (1995)].

The VH-mode is a regime of very high confinement accessible in conditions of low recycling and low impurity influxes, particularly metallic influxes. It was first obtained following boronization of the vacuum vessel, but was later established without boronization after the first wall of the torus had been completely covered with graphite tiles. The regime was originally observed in double null plasmas with high triangularity,  $\delta_X \sim 0.8$ , and high input power,  $P > 8$  MW, using low target densities. This produced plasmas with unusually low radiated power fractions,  $P_{rad}/P \sim 30\%$ , and thermal energy confinement times up to a factor of 2 above those predicted by H-mode scaling. As illustrated in Fig. 12.5.5, the VH-mode develops after several hundred milliseconds of ELM-free conditions and is characterized by an enhanced confinement relative to H-mode levels, with an energy confinement time which can continue to rise throughout the ELM-free period. Core toroidal angular momentum also increases and bulk plasma density fluctuations fall. Ion temperatures range up to 20 keV, the fusion triple product has reached  $5 \times 10^{20} \text{ keV sm}^{-3}$ , and the performance is ultimately limited by mhd instability. Values of  $\beta$  as high as 12.5% have been achieved, the highest value attained in a tokamak plasma at conventional aspect-ratio.

Strong plasma shaping, especially high triangularity, is essential for peak performance in the VH-mode. Confinement enhancement is highest for  $4 \leq q_{95} \leq 5$ , and part of the confinement improvement at high elongation and high triangularity arises from the increase in  $q_{95}$  which is obtained for fixed plasma current. In addition, neutral beam driven and bootstrap currents cause  $q(0)$  to rise above unity initially, suppressing sawteeth. The high triangularity then promotes low magnetic shear in the plasma centre so that these plasmas satisfy the Mercier criterion, introduced in

Section 6.12, and have access to the second regime of ideal ballooning mode stability in the core. High triangularity also provides access to second stability at the plasma edge, and this feature is considered to be necessary for the suppression of ELM activity. These enhanced stability properties are believed to play a major role in determining the duration of the VH-mode: the phase during which confinement is significantly enhanced above H-mode scaling lasts for up to  $\sim 1$  s and is terminated by a global mhd event, which typically occurs with  $2.5 < \beta_N < 3.5$ . This returns the plasma to an ELMy H-mode with lower energy confinement. The mhd event is generally associated with modes having toroidal numbers in the range 1–5 which grow on a timescale of 20–50  $\mu$ s. This is consistent with mhd stability analysis, which indicates that, close to the termination, the region just inside the plasma edge,  $0.8 < \rho < 0.9$ , is marginally stable to ideal kink modes due to the high pressure and edge current gradients typical of the regime. Coupling to central mhd modes appears to influence the extent of the energy loss at the termination.

The region of improved confinement extends beyond that which has access to second stability, and it has been proposed that increased shear in the  $E \times B$  rotation velocity is responsible. As the energy confinement rises above the H-mode scaling prediction, the toroidal rotation velocity increases in the core plasma and falls at radii close to the plasma edge,  $r/a > 0.8$ . From equation 12.5.1, it follows that the radial electric field increases in the plasma core and a region with greater shear in the  $E \times B$  rotation velocity forms. The importance of this effect was explored in an experiment in which an error field, produced by an external coil, was used to slow the plasma rotation by magnetic braking in the vicinity of the  $q = 2$  surface. Fig. 12.5.6 compares the relevant profiles from

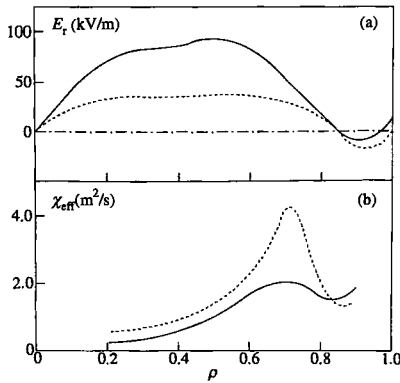


**Fig. 12.5.6** (a)  $E_r$  profiles in two discharges, one with (dashed line) and one without (solid line) magnetic braking. (b) single fluid thermal diffusivity,  $\zeta_{\text{eff}}$ , as a function of position for these discharges.  $\rho$  is the toroidal magnetic flux function [From Burreli, K.H. et al., *Plasma Physics and Controlled Nuclear Fusion Research 1994* (Proc. 15th Int. Conf., Seville, 1994) Vol. 1, 221, I.A.E.A., Vienna (1995)].

a representative VH-mode with a case in which magnetic braking was applied. In the latter case, the toroidal rotation, which is not shown, decreased, the radial electric field gradient in the region  $0.6 < \rho < 0.8$  decayed, and the thermal diffusivity increased.

Observations from several tokamaks have shown that the almost universal relationship between energy confinement time and plasma current can be broken in experiments in which the plasma current profile is modified. In DIII-D experiments where peaked current profiles were produced, either by increasing the elongation, or decreasing the current, the energy confinement enhancement relative to the H-mode scaling expression exhibited a close correlation with the plasma internal inductance. In cases in which the elongation was raised from 1.2 to 2 in  $\sim 200$  ms at constant current and neutral beam power, an H-mode transition occurred and  $\ell_i$  reached values of  $\sim 2$ . At the same time, the plasma energy confinement time initially rose, then fell as  $\ell_i$  relaxed. Plasmas in which the current was reduced from 2 to 1 MA at rates of up to  $-4$  MAs $^{-1}$  yielded similar results. A magnetic braking experiment similar to that described above showed that the confinement enhancement was correlated with the toroidal rotation velocity, again suggesting that  $E \times B$  shear suppression of turbulence contributed to the reduced transport. Despite the beneficial effects of current profile peaking, self-consistent equilibria with such peaked profiles are difficult to maintain in steady-state, as there is a substantial bootstrap current at high- $\beta$ , which tends to broaden the current profile, thereby reducing  $\ell_i$ .

Simultaneously with TFR enhanced reversed shear experiments, enhanced confinement was observed in plasmas in which the current rise and NBI heating phases were programmed to produce a region of negative central shear. In such discharges an internal transport barrier develops, more usually in the ion temperature profile, in L-mode, ELM-free H-mode, and ELMy H-mode regimes. Ion thermal transport is reduced significantly in the region of negative shear, and in some H-mode discharges the ion thermal diffusivity falls to neoclassical levels over most of the plasma. Strongly peaked pressure profiles can develop, with  $p(0)/(p) \sim 2-5$ , ion temperatures of up to 20 keV are obtained, and the fusion triple product has reached  $6.2 \times 10^{20}$  keVsm $^{-3}$ , equivalent to  $Q_{DT} = 0.32$  and the highest value attained in DIII-D. These plasmas have reached global energy confinement times of up to  $4.5 t_{E}^{\text{ITER89-P}}$ , and values of  $\beta_N \sim 5$  have been achieved by careful control of the discharge evolution to limit the pressure profile peaking while maintaining a high internal inductance. Many aspects of stability associated with high shaping discussed in relation to the VH-mode are equally relevant to the optimization of performance in discharges with negative central shear.

As discussed in Section 12.2, several factors can contribute to the reduction of anomalous transport in plasmas with negative central shear. However, analysis has shown that, in common with other enhanced confinement regimes established in DIII-D, stabilization of drift wave turbulence by shear in the  $E \times B$  rotation velocity appears to play a dominant role. Details of the current and pressure profiles, together with

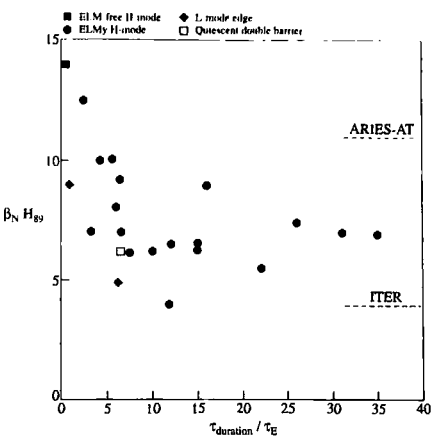


**Fig. 12.5.7** Plot of highest values of the performance figure of merit,  $\beta_N H_{89}$ , achieved in DIII-D plasmas as a function of the duration of the high performance phase normalized to the energy confinement time,  $\tau_{\text{duration}} / \tau_E$ . Pulses with the highest figures of merit at all values of  $\tau_{\text{duration}} / \tau_E$  were initially formed with negative central shear. The quiescent double barrier point relates to the mode illustrated in Fig. 12.5.8. Projected values for ITER reference (inductive) operation and for a proposed steady-state fusion power plant, ARIES-AT, are indicated [from Allen, S.L., et al. *Fusion Energy 2000* (Proc. 18th Int. Conf., Sorrento, 2000) paper I.A.E.A.-CN-77/OV 1/3. I.A.E.A., Vienna (2001)].

plasma shaping, determine the stability characteristics of the regime, the duration of the high confinement phase and the level of performance achieved. Limiting mhd activity can take a number of forms:  $n = 1$  ideal kinks, which can trigger disruptions in plasmas with an L-mode edge, Alfvén eigenmodes, neoclassical tearing modes, low to moderate- $n$  ideal kinks considered to be responsible for type I ELMs, and resistive wall modes.

As in other devices, it has proved possible to extend the initially transient improvements in confinement and stability and to develop quasi-stationary negative shear plasmas with enhanced plasma performance. Significant non-inductive current fractions have been obtained in such discharges, although with the limited profile control capability available, evolution of the current profile generally causes  $q(0)$  to fall towards unity. Nevertheless, sawtooth-free plasmas with  $q_{\min} \sim 1.05$  have been established at 1.2 MA/1.7 T and  $q_{95} = 4.4$  in which  $\beta_N H_{89} = 7$  has been maintained for 6.3 s, equivalent to  $3\tau_E$  and  $>30\tau_E$ . Higher performance discharges have been produced at similar current and toroidal field in which  $\beta_N H_{89} = 9$  was sustained for 2 s, equivalent to  $16\tau_E$ , where 50% of the current was driven by the bootstrap effect and 25% by neutral beams. Figure 12.5.7 illustrates the performance levels which have been achieved in DIII-D experiments as a function of normalized discharge duration. The envelope of pulses with the highest values of  $\beta_N H_{89}$  consists of plasmas which were established as negative central shear discharges.

In experiments in which negative central shear is generated with counter-NBI, a regime with internal and edge transport barriers forms in which the edge (H-mode) barrier is not modulated by ELMs, but

the plasma is nevertheless sustained in quasi-steady-state conditions. Denoted the quiescent double barrier mode, the regime combines enhanced confinement characteristics of an internal transport barrier with the quiescent H-mode edge discussed previously. This mode of operation avoids degradation of the transport barrier by ELMs and also eliminates the pulsed power and particle loads produced on divertor targets by type I ELMs. The regime has been observed over a wide range of plasma current and toroidal field, with  $3.7 \leq q_{95} \leq 4.6$ , but access appears to require a minimum injected power of  $\sim 3$  MW, low target densities, in the range  $2-3 \times 10^{19} \text{ m}^{-3}$ , which is achieved by strong divertor pumping, and the maintenance of a gap of at least 10 cm to the outer wall, possibly associated with large edge excursions of some fast ion orbits in counter-injection. These plasmas form peaked temperature and density profiles (Fig. 12.5.8), with edge pedestal parameters characteristic of an H-mode with type I ELMs. Transport analysis indicates that the ion thermal diffusivity is commensurate with neoclassical values in the transport barrier regions in the edge and core of the plasma (Fig. 12.5.8) and that the suppression of turbulent transport can be explained by  $E \times B$  velocity shear. The regime has been sustained for up to 3.8 s ( $26\tau_E$ ), a duration limited only by experimental considerations, and values of  $\beta_N H_{99} \sim 7$  have been sustained for periods of up to 1.6 s ( $10\tau_E$ ). Although accumulation of high-Z impurities during the quiescent phase leads to a gradual increase in  $Z_{eff}$  to values of around 6, initial experiments with central electron cyclotron heating and current drive indicate that this can reduce both peaking of the density profile and central impurity accumulation.

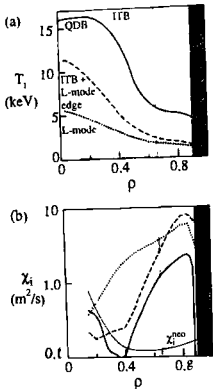


**Fig. 12.5.8** Comparison of plasma profiles from quiescent double barrier (QDB) mode (solid line), L-mode with ITB (dashed line), and L-mode plasmas (dotted line): (a) ion temperature,  $T_i$ , (b) ion thermal diffusivity,  $\chi_i$ , together with the calculated neoclassical value for the QDB case,  $\chi_i^{ne}$  [from Doyle, E.J. et al. *Plasma Physics and Controlled Fusion* 43, A95 (2001)].

### Mhd studies

In DIII-D, as in JET and JT-60U, the operational limitations imposed by the axisymmetric vertical displacement instability are a key issue. Equilibrium analysis using a rigid body treatment of axisymmetric plasma displacements indicated that the control system should be capable of maintaining stable plasmas for elongations of up to  $\kappa = 3$ . However, experiments revealed that plasmas became unstable at  $\kappa = 2.5$ , the lower limit being associated with non-rigid plasma displacements. More detailed calculations showed that, at maximum elongation, plasmas were within a few percent of the ideal stability limit. As expected, the limiting elongation was also found to be a function of the plasma current profile, with the maximum stable value of elongation failing with increasing internal inductance (Fig. 12.5.9). During vertical instabilities, halo currents have been observed with a magnitude of up to 40% of the plasma current, consistent with the mechanical forces experienced by the vacuum vessel.

Disruptions are triggered by a variety of causes and a range of techniques has been investigated to mitigate their consequences. Killer pellet injection, using cryogenic pellets of neon or argon, is effective in reducing

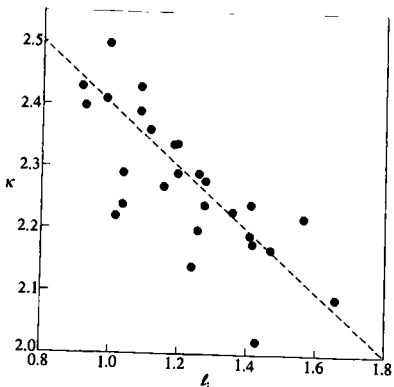
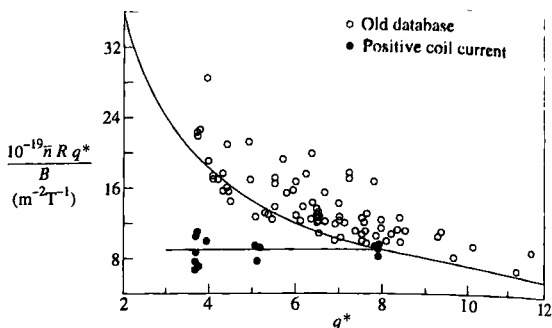


**Fig. 12.5.9** Maximum experimentally achieved elongation,  $\kappa$ , for plasmas near the ideal axisymmetric instability limit, as a function of the plasma internal inductance,  $l_i$ . The broken line indicates the dependence of the maximum achieved value of  $\kappa$  on  $l_i$  [Taylor, T.S. et al. *Plasma Physics and Controlled Nuclear Fusion Research 1990* (Proc. 13th Int. Conf., Washington, 1990) Vol 1, 177, I.A.E.A., Vienna (1991)].

thermal and electromechanical loads, but leads to the generation of runaway electrons. Injection of high pressure neon or argon gas, however, has successfully demonstrated complete radiative dissipation of the total plasma thermal and magnetic energy, within experimental uncertainties, and reduced halo currents and toroidal asymmetries, by a factor of 2–4 compared to unmitigated vertical instabilities, without generating significant runaway electron currents. Experiments were performed using a 7 MPa reservoir at room temperature, which injected  $\sim 4 \times 10^{22}$  particles, resulting in a gas-jet with a ram pressure of  $\sim 30$  kPa at the plasma edge, several times the volume averaged electron pressure of  $\sim 7$  kPa. Extrapolation of the relevant parameters to ITER suggests that this is a viable technique for mitigation of the consequences of disruptions at the reactor scale.

Disruptions produced by modes destabilized by external error fields have been of particular concern, since they impose substantial constraints on the accessible density range. This phenomenon, first identified in DIII-D, involves the growth of non-rotating  $n = 1$  modes, with  $m = 1, 2, 3$  components, which are induced by error fields arising from departures from axisymmetry in the poloidal field circuit. Contributions from many coils sum to an effective radial field component of 7 G in the  $m/n = 2/1$  helicity, equivalent to that produced by a horizontal displacement of a single poloidal field coil by 6 mm. The influence of this error field also depends on safety factor, so that the operational space was initially restricted to the region  $q^* D = q^*(10^{-19} \bar{n} R q^*/B) > 72 \text{ m}^{-2} \text{ T}^{-1}$ , where  $q^*$  is an analytic approximation to the edge safety factor and  $D$  is the usual density limit parameter (Fig. 12.5.10). As in JET, these modes can be suppressed by driving plasma rotation with NBI. However, this approach failed at high- $\beta$ , as the critical  $m/n = 2/1$  error field,  $B_r$ , required to

**Fig. 12.5.10** Plot of the lower limit of the operating region which is stable against locked  $n = 1$  modes induced by error fields in the  $10^{-19} \bar{n} R q^* / B$  vs  $q^*$  plane. The open circles represent points from experiments without error field correction system, with the upper line illustrating the operating boundary  $q^* D = 72 \text{ m}^{-2} \text{ T}^{-1}$ , where  $D = 10^{-19} \bar{n} R q^* / B$ . The solid circles correspond to experiments using a simple  $n = 1$  correction coil and the lower line shows the improved operating boundary  $D = 9 \text{ m}^{-2} \text{ T}^{-1}$  [Scoville, J.T. et al. Nuclear Fusion 31, 875 (1991)].



destabilize an  $n = 1$  mode decreased from  $(B_r/B)_{r=a} = 5 \times 10^{-4}$  at  $\beta = 2\%$  to  $(B_r/B)_{r=a} = 2 \times 10^{-4}$  at  $\beta = 5\%$ . To expand the operating regime, an *ad hoc* coil was added above the plasma in one toroidal location to enable the dominant  $n = 1$  component of the error field to be cancelled. This was successful and the operating limit was reduced to  $D = 9$  for  $q^* > 3$ , as illustrated in Fig. 12.5.10. A more sophisticated correction system, the 'C-coil', consisting of 6 external saddle coils distributed around the equatorial plane and capable of cancelling the error field more precisely, has subsequently been installed and is in routine use.

As noted previously, optimization of plasma shape, current distribution and pressure profile has contributed significantly to increasing the maximum attainable  $\beta$ , allowing global values of  $\beta$  of up to 12.5%, with axial values as high as 44%. Values of  $\beta \sim 8\%$  have been sustained in quasi-steady-state for periods of  $\sim 1$  s, but higher values are maintained only transiently, typically for times of  $\sim 100$  ms, and are limited by various forms of MHD activity. At  $q_{95} < 3$ , disruptions are observed for  $\beta_N$  as low as 3. These are preceded by an  $n = 1$  mode with a rapid growth rate,  $\sim 100 \mu\text{s}$ . At higher values of  $q_{95}$ , DIII-D plasmas readily attain values of  $\beta_N \sim 4$ , and can reach  $\beta_N \sim 6$ . The dependence of  $\beta$ -limiting instabilities on current and pressure profiles is well known from theoretical considerations, and is implicit in the scaling  $\beta \sim I/aB$ , which is calculated for 'optimized' profiles. When the current profile dependence is included explicitly through  $\ell_i$ , the  $\beta$ -limit in DIII-D is, with few exceptions, well described by  $\beta(\%) < 4\ell_i I(\text{MA})/aB$  (Fig. 12.5.11).

In many discharges neoclassical tearing modes, commonly destabilized by seed islands produced by sawteeth, fishbones, or ELMs, determine the limiting  $\beta_N$ . Modes with  $n = 2$  or  $n = 1$  are associated with a measurable degradation of confinement, with the latter producing major disruptions. In some cases the 2/1 mode has been observed to develop as the result of a descending cascade of modes with  $m/n = 5/4, 4/3, 3/2$ , and finally 2/1. Experiments in collaboration with JET and ASDEX Upgrade have confirmed that the critical  $\beta_N$  for the growth of  $m = 3/n = 2$

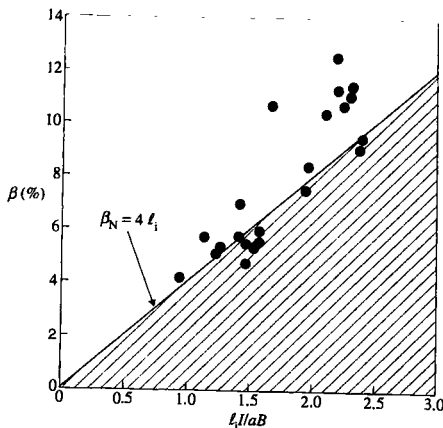


**Fig. 12.5.11** Scaling of the usual  $\beta$ -limit in DIII-D plasmas, indicated by the line  $\beta_N = 4 L_i$ . The solid circles indicate individual discharges from an experiment designed to test whether wall stabilization could be exploited to achieve higher  $\beta$  values. Several of these discharges lie above the usual limit and have exceeded the predicted stability limits in the absence of wall stabilization [from Turnbull, A.D. et al. *Plasma Physics and Controlled Nuclear Fusion Research 1994* (Proc. 15th Int. Conf., Seville, 1994) Vol 1, 705. I.A.E.A., Vienna (1995)].

modes scales as  $\rho_*$ , as expected theoretically. Long duration pulses, with  $q_{min} \sim 1.05$ ,  $\beta_N = 2.8$ , and  $\beta_{NH95} = 7$ , have nevertheless been sustained for over 6 s in the presence of a small  $m = 3/n = 2$  neoclassical tearing mode.

To optimize performance in long pulse operation, suppression of neoclassical tearing modes is required, and two possible approaches have been demonstrated in DIII-D. First, localized ECCD has been used, as in ASDEX Upgrade, to fully suppress an  $m = 3/n = 2$  mode. In addition, observations in ASDEX Upgrade showed that the growth of a second neoclassical tearing mode with different helicity from a pre-existing mode can effectively suppress the growth of the first mode, prompting the suggestion that an externally applied non-resonant helical field might produce the same result. The C-coil saddle set, discussed above, was therefore used to apply a static, non-resonant (predominantly  $m = 1, 2$ )  $n = 3$  helical field before the usual onset time of an  $m = 3/n = 2$  neoclassical tearing mode in a plasma with  $\beta_N \sim 2$ . This completely suppressed the mode until the termination of the externally applied field. However, a significant loss of toroidal momentum was observed, possibly due to ripple damping of the beam driven toroidal rotation.

As  $\beta$  increases, so does the bootstrap current, leading to a broadening of the plasma current profile, which tends to lower the instability threshold for ideal kink modes at the plasma edge. With a resistive wall, ideal kink modes take the form of a 'resistive wall mode', which was originally believed to be unstable on the wall penetration time. However, it is expected that if sufficient plasma rotation can be maintained, for example,

by neutral beam injection, these modes can be 'wall stabilized'. Initial evidence for such an effect was advanced on the basis of experiments in DIII-D in which the usual limit  $\beta(\%) < 4\ell_i l/(MA)/aB$  was exceeded by up to 50% for periods in excess of 10 wall penetration times,  $\tau_w$ . In these discharges, represented by the experimental points in Fig. 12.5.11, the high- $\beta$  phase terminated in a collapse, or disruption, caused by the growth of slowly rotating, or locked,  $n = 1$  modes with low  $m$ . Both the growth time,  $\gamma^{-1} \sim$  several milliseconds, and the structure of these modes were in agreement with those expected for the resistive wall mode.

As noted above, the critical error field for the growth of an  $n = 1$  mode falls with increasing  $\beta$ . Theoretical analysis suggests that this can be caused by the resonant excitation of a rotationally stabilized resistive wall mode by the error field when  $\beta_N$  is above the 'no-wall'  $\beta$ -limit, that is the  $\beta$ -limit predicted when the plasma is not enclosed within a conducting wall. In experiments in which the C-coil system was used to correct the error field, either in preprogrammed mode, or in a feedback mode based on the detection of the resonant response of the resistive wall mode, operation at  $\beta_N$  values of up to 50% above the no-wall limit was maintained for periods of  $>1$  s ( $>200\tau_w$ ) by sustaining rotational stabilization of the resistive wall mode. It is also predicted that these modes can be stabilized in the absence of plasma rotation by active magnetic feedback. Preliminary experiments, using the C-coil system and an external set of magnetic detection coils, have demonstrated the feasibility of active feedback control of the mode (Fig. 12.5.12) and have

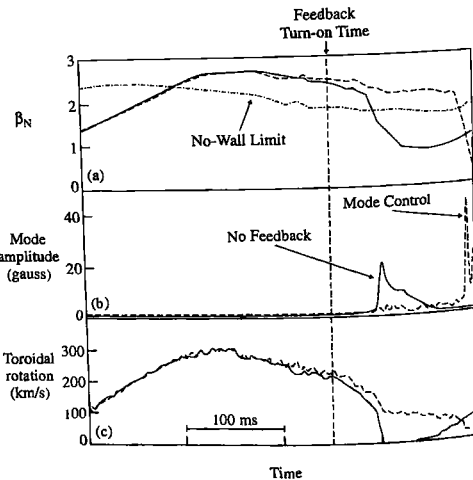


**Fig. 12.5.12** Comparison of (a)  $\beta_N$ , (b) resistive wall mode amplitude, (c) plasma toroidal rotation for pulses with  $\beta_N$  above the no-wall  $\beta$ -limit. Two cases are shown, no active feedback control of the resistive wall mode (solid line) and active feedback control using a 'mode control' algorithm (dashed line), illustrating the extension of the pulse duration at high- $\beta_N$  with active magnetic feedback [from Garofalo, A.M. et al. Fusion Energy 2000 (Proc. 18th Int. Conf., Sorrento, 2000) paper IAEA-CN-77/EXP3/01(R), I.A.E.A., Vienna (2001)].

maintained stable operation above the no-wall  $\beta$ -limit for periods of up to 50 $t_{\text{tw}}$ . Subsequently, an optimized system of sensors and feedback coils has been installed.

In DIII-D the density limit does not increase with input power, but is better described by the empirical Greenwald limit. A region of high density is observed in the X-point region, and there the maximum density does scale with the net power flowing across the separatrix. In ohmic and L-mode plasmas, the density limit occurs at high radiated power fractions, >75%, and is normally followed by a major disruption. This general behaviour is also true of ELMs in H-modes, but they return to the L-mode before disrupting.

The sawtooth collapse in DIII-D is usually associated with a full reconnection and exhibits a growing  $m = n = 1$  precursor, though, as in many tokamaks, the collapse time is shorter than the Kadomtsev value by an order of magnitude. From a statistical analysis of the current profile, derived from motional Stark effect and magnetic measurements, it was concluded that the average value of  $q(0)$  was  $0.96 \pm 0.08$  just before the sawtooth collapse and  $1.02 \pm 0.1$  just after the collapse. This supports the interpretation that the sawtooth produces full magnetic reconnection during the collapse and contributes to a pattern of experimental results in which measurements of the central safety factor in some tokamaks yield  $q(0) \sim 1$ , while similar measurements in others find  $q(0) \sim 0.7$ .

Magnetic fluctuations with frequencies in the range 50–200 kHz and with characteristics of TAE modes have been detected in discharges at low toroidal fields,  $\sim 1$  T, heated by high power NBI. Detailed studies of the activity have confirmed that the mode frequency, when properly corrected for Doppler shifts, exhibits the predicted variation with density and toroidal field. The fast ion velocity parallel to the magnetic field is somewhat lower than  $V_A$ , but is still within the range expected theoretically to excite TAE modes. Evidence of fast ion losses associated with this activity is seen, for example, in neutron emission measurements. These show that the losses scale linearly with the mode amplitude (Fig. 12.5.13) and that, in discharges with strong TAE activity, up to 70% of the NBI power, equivalent to  $\sim 10$  MW, can be lost. This is corroborated by bolometric observations of fast ion losses and by damage to optical components on the vessel wall.

### Current drive

Full non-inductive current drive was demonstrated in neutral beam heating experiments with plasma currents in the range 0.3–0.5 MA. The earliest experiments focused on NBI current drive in helium plasmas at 0.34 MA, establishing H-modes with  $\beta_p = 3.5$ . 80% of the plasma current was attributed to NBI driven current, with the remainder arising from the bootstrap current. In subsequent studies, with plasma currents in the range 0.4–0.5 MA, full current drive was again achieved, though with the proportions due to NBI current drive and bootstrap current reversed.

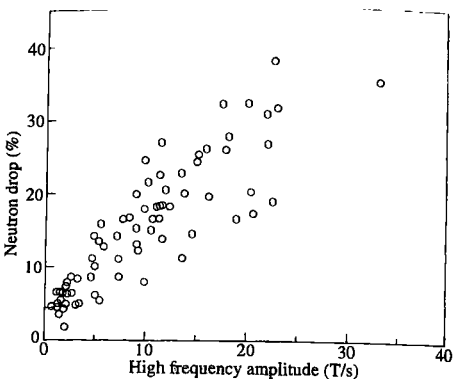


**Fig. 12.5.13** Fraction of fast ions lost during TAE activity, expressed as the fractional drop in neutron emission, as a function of the RMS amplitude of high frequency,  $f > 75$  kHz, mhd activity [Duong, H.H. et al. *Nuclear Fusion* 33, 749 (1993)].

In these experiments, with  $\beta_p$  values of up to 5.1, a spontaneous improvement of confinement was observed as the current profile broadened under the influence of the bootstrap current and  $q(0)$  rose above 2. The highest absolute levels of non-inductive current drive were obtained with NBI at plasma currents of  $\sim 1.2$  MA where the non-inductive current reached 700 kA, divided equally between NBI current drive and bootstrap current drive.

Radio frequency approaches to current drive include both fast Alfvén waves (FWCD) and electron cyclotron waves (ECCD). FWCD experiments used antennas operating at 60 and 83 MHz to couple powers of up to 2 MW into L- and H-mode plasmas heated by NBI and ECRH to increase the electron  $\beta$ , on which the FWCD efficiency depends. Up to 110 kA of FWCD was produced, with current drive efficiencies of up to  $0.54 \times 10^{19} \text{ Am}^{-2} \text{ W}^{-1}$ . The centrally peaked nature of the driven current profile was confirmed (Fig. 12.5.14a) and the current drive efficiency was found to increase with electron temperature, as expected from theory, though a significant reduction of the efficiency was observed in H-modes with high frequency ( $> 100$  Hz) ELMs.

Studies of ECCD have used steerable mirrors on the torus outboard side to launch waves at 110 GHz so as to couple to the second harmonic resonance in the extraordinary mode. Using up to 2 MW of microwave power in L- and H-mode plasmas, driven currents of up to 120 kA have been obtained at current drive efficiencies which are in good agreement with Fokker-Planck calculations. Detailed comparisons of the off-axis current drive profile, as determined from motional Stark effect measurements, with calculations have shown that the localization of the driven current agrees well with theory, the driven current profile having a full width of  $\Delta r/a \sim 0.1$  ( $\sim 7$  cm), as illustrated in Fig. 12.5.14b. Although off-axis current drive is known to be less efficient than central current

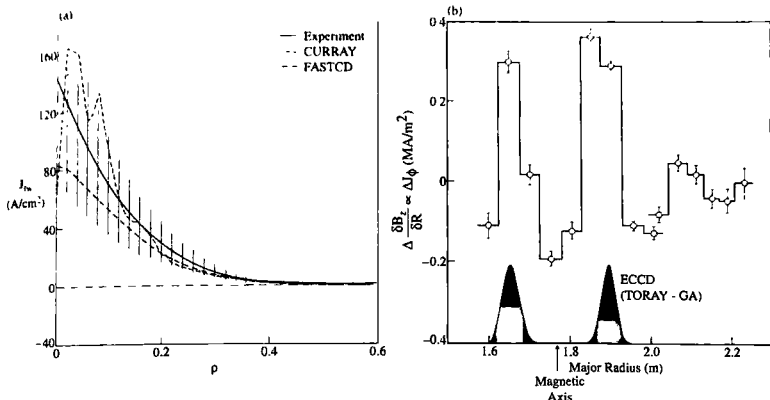


**Fig. 12.5.14** (a) Comparison of measured FWCD profile in a VH-mode plasma with calculations by two codes, CURRAY (ray tracing with multiple pass absorption), and FASTCD (ergodic limit of weakly damped rays), using different formalisms [Petty, C.C. *et al.* *Nuclear Fusion* **39**, 1421 (1999)]. (b) Measured profile of ECCD in an L-mode plasma, represented by the quantity  $\Delta(1/\mu_0) \partial B_z / \partial R$  derived from MSE measurements, compared with a calculation of the driven current profile using the TORAY-GA code [Petty, C.C. *et al.* *Radio Frequency Power in Plasmas* (Proc. 14th Top. Conf., Oxnard, 2001) 275. A.I.P., Melville (2001)].

drive due to absorption by trapped particles, the current drive efficiency is found to depend on the local electron  $\beta$ , an effect which mitigates the extent to which the current drive efficiency falls with increasing minor radius. This is understood in terms of wave absorption by electrons with higher  $v_{\parallel}$  as  $\beta$  increases, leading to a reduction in the fraction of electrons which cross the passing/trapped boundary in velocity space. As noted previously, the very localized nature of the ECCD profile has allowed the stabilization of neoclassical tearing modes.

### Divertor performance

Initial experiments at high current, that is above 2 MA, were restricted by excessive nickel influxes, and several steps were taken to address this problem. Carbonization of the first wall was used to deposit a thin,  $\sim 100$  nm, carbon film on plasma-facing surfaces. This reduced nickel line radiation by a factor of up to 30 in H-mode discharges, permitting operation at plasma currents of up to 3 MA. The effects of the carbon layer, which also included reduction in oxygen radiation by up to a factor of 6, lasted for  $\sim 100$  pulses. Boronization produced additional improvements in impurity control and decreased hydrogen recycling. This process, which was developed in TEXTOR and is discussed in Section 9.6, involves the deposition of a  $\sim 100$  nm layer of boron on plasma-facing surfaces. Advances in performance associated with this

technique include the discovery of the VH-mode. Further improvements in recycling and impurity control have been associated with complete coverage of the vessel by carbon and the installation of the upper and lower pumped divertors.

The relative importance of radiation and SOL conduction in power exhaust has been analyzed in some detail. In single null ELM H-modes with the ion VB drift towards the X-point, asymmetries of order 5 in the ratio of the peak power loading of the outer and inner strike points have been observed. This asymmetry disappears when the direction of the ion drift is reversed. Although ELMs can raise the peak heat flux to the target by two orders of magnitude, with the power lost predominantly to the inner strike point, they generally contribute <10% of the time averaged power to the divertor. The power deposition profile is therefore determined mainly by the steady-state transport between ELMs. A power balance for the normal ion VB drift direction shows that ~20% of the input power is lost as radiation from within the separatrix and ~30% is radiated from the X-point and divertor regions. The latter comes predominantly, ~65%, from the inner divertor leg, so that the target heating asymmetry is largely explained by the radiation imbalance. Measured losses account for 80–90% of the input power, which is within experimental uncertainties for the total power accountability and is typical for such discharges in large tokamaks.

Asymmetries between power deposition at the upper and lower divertors were investigated in a highly triangular quasi double null H-mode plasma in which the distance between the separatrices corresponding to the upper and lower X-points was varied. This showed that at low to moderate densities,  $n/n_{GW} \leq 0.7$ , a small change in the distance between the separatrices at the midplane,  $\delta R_{sep} = \pm 0.4$  cm, effectively changed the power deposition entirely from one divertor to the other. This was interpreted as being consistent with the width of the power decay length in the scrape-off layer. The transfer of ELM power from one divertor to the other was found to be more gradual, corresponding to  $\delta R_{sep} = \pm 1.9$  cm. At higher densities, where the plasma returned to L-mode and the divertor detached, the change occurred very gradually,  $\delta R_{sep} \sim \pm 4$  cm, which was of the same order as the scale length for the changeover in particle fluxes at lower density. It has been suggested that divertor, rather than scrape-off layer, processes are responsible for determining this scale length.

Several methods for decreasing the power conducted to the target have been investigated by exploiting the flexibility of the lower and upper pumped divertors (Fig. 12.5.2). Active pumping by the cryopumps has allowed considerably higher gas injection rates to be used in quasi-steady-state conditions in high power ELM H-modes (Fig. 12.5.15). The increased radiation reduces the peak divertor heat flux by a factor of 4, leading to the formation of a partially detached divertor, while leaving global energy confinement unaffected. Thomson scattering measurements in the divertor region show that the detached phase is characterized by an electron temperature of 1–2 eV, indicating that

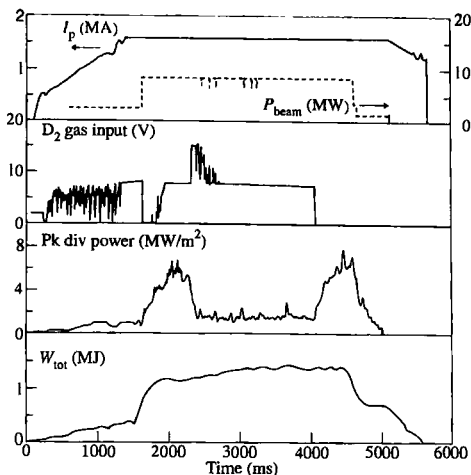
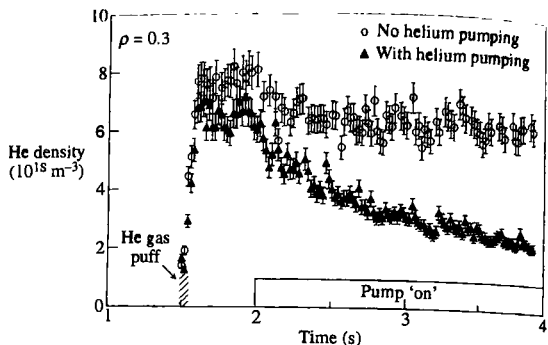


**Fig. 12.5.15** Overview of an ELM-My H-mode pulse in which strong deuterium injection was used to reduce the peak heat flux to the divertor target. Shown are the plasma current,  $I_p$ , the NBI power,  $P_{beam}$ , the  $D_2$  gas input, the peak heat flux to the divertor, 'Pk div power', and the total stored energy,  $W_{tot}$ . [From Hill, D.N. et al. *Plasma Physics and Controlled Nuclear Fusion Research 1994* (Proc. 15th Int. Conf., Seville, 1994) Vol 1, 499. IAEA, Vienna (1995).]

volume recombination of hydrogenic species is playing a significant role in the detachment process, as expected theoretically. In addition, analysis of the radiation and temperature distribution suggests that convection is the dominant energy transport mechanism in the divertor during this phase.

Control of the plasma density in ELM-My H-modes became possible for the first time following installation of the lower divertor cryopump, which has a measured speed of  $40 \text{ m}^3 \text{ s}^{-1}$  at a  $D_2$  pressure of 5 mtorr. This allows the density of ELM-My H-mode plasmas to be varied by up to a factor of 2. Particle exhaust rates have been enhanced, by up to a factor of 2, by divertor biasing, which generates an  $E \times B$  flow, sweeping plasma particles towards the entrance to the pump. The cryopump can also control the gas inventory of the vessel wall, providing an additional conditioning technique. In ELM-My H-modes fuelled only by NBI, the particle removal rate can exceed the beam fuelling rate, implying that gas is removed from the first wall. 'Puff and pump' experiments, involving deuterium puffing at rates of  $\sim 200 \text{ torr.l.s}^{-1}$ , together with active pumping, have demonstrated that injected argon can be enriched in the divertor plasma by up to a factor of 17 relative to the core plasma, suggesting that divertor impurity retention improves in the presence of induced scrape-off layer flows. Comparison of particle control with the lower open and upper closed divertors indicates very similar levels of performance, although the core ionization rate is found to be a factor of 2.6 lower with the latter, indicating an influence of the closed geometry on particle fluxes from the divertor into the main chamber.

**Fig. 12.5.16** Helium density at  $\rho = 0.3$ , as measured by active CXRS, as a function of time for discharges with and without active helium pumping. A short, 50 ms, helium puff is injected at 1.5 s and the pumping is 'switched on' at 2 s by changing the radial position of the outer divertor strike point. In the case with active helium pumping, provided by argon frosting of the cryopump, the helium concentration of the core plasma decays on a timescale of  $\sim 1$  s [Hillis, D.L. *et al.*, *Plasma Physics and Controlled Fusion* 36, A171 (1994)].



Investigations of helium transport and exhaust are an important element of the DIII-D programme. Gas puffing experiments producing a final helium concentration of  $\sim 10\%$  showed that in L-mode, ELM-free H-mode, and VH-mode the helium density profile relaxed within 1 s to that of the electron density profile. This suggests that the transport of helium is very similar to that of deuterium and that there is no preferential accumulation of helium in the plasma centre. As found in TFTR, the ratio of the helium particle diffusivity to the single fluid heat diffusivity is of order unity. Moreover, a dimensionless scaling analysis of helium transport in ELM-free H-modes determined that both the helium particle and effective thermal diffusivities scaled in a gyro-Bohm manner.

Condensing argon on the cryopump, 'argon frosting', creates a cryogenic layer capable of pumping helium. In DIII-D the measured pumping speed of the fresh layer on the lower cryopump is in the range  $12\text{--}18 \text{ m}^3 \text{ s}^{-1}$ , although this deteriorates in the course of a plasma pulse due to absorption of deuterium by the layer. Measurements of helium transport and exhaust have been performed both with gas puffing and with central helium fuelling from NBI. Figure 12.5.16 compares the time evolution of the helium concentration in the plasma core for ELM-free H-modes with and without argon frosting on the cryopump. In both cases the pump was 'switched on' by moving the outer strike point to the pump entrance at 2 s, following a helium gas puff at 1.5 s. Only in the discharge with argon frosting did the helium concentration decay, with an exhaust efficiency of  $\sim 5\%$  being achieved. Analysis of core helium transport in these experiments confirmed previous results. In addition, the ratio of the residence time for helium in the plasma chamber to the global energy confinement time was found to lie in the range  $8 < \tau_{\text{He}}^* / \tau_E < 14$ , which is considered to be acceptable for a reactor.

**12.6****ASDEX Upgrade—Max-Planck-Institut für  
Plasmaphysik, Garching, Germany**

The ASDEX Upgrade design is based on the Axial Symmetric Divertor EXperiment, ASDEX. The divertor concept of ASDEX was adapted with ASDEX Upgrade to the technical requirements of a fusion reactor. In a burning reactor plasma the poloidal field coils forming the divertor shape of the plasma with an X-point have to be located outside the vacuum vessel. For this reason, the divertor chambers are no longer separated from the plasma vessel by narrow slits but are wide open. Essential plasma properties, primarily the plasma density and the wall load have been adapted to the conditions expected in a fusion reactor. Sufficiently high heating power up to 28 MW ensures that the energy fluxes through the scrape off layer are equivalent to those in a reactor. ASDEX Upgrade thus serves for studying plasma wall interactions under reactor like scrape off layer conditions. Furthermore the experiment was so dimensioned that, enlarged to reactor size, there would be space for the blanket and first wall inside the main field magnetic coils. The physics studies also cover core plasma behaviour and confinement improvement.

The first plasma in ASDEX Upgrade was produced on 21 March 1991 after nearly 10 years of planning, design, and construction. The reference values for the ASDEX Upgrade design are given in Table 12.6.1. Figure 12.6.1 shows a 3D cut away view of ASDEX Upgrade with two different divertor geometries. Major modifications were made to expand the experimental possibilities of ASDEX Upgrade and to contribute to the discussion of the ITER design:

**Table 12.6.1 Main parameters of ASDEX Upgrade**

Major plasma radius	$R_0$	1.65 m
Minor plasma radius	$a$	0.5 m
Plasma height	$b$	0.85 m
Triangularity	$\delta$	$\leq 0.5$
Plasma current	$I_p$	$\leq 1.4$ MA
Toroidal magnetic field at magnetic axis	$B_0$	$\leq 3.9$ T
Current flat top duration	$t_D$	10 s
Installed auxiliary heating power	$P_H$	28 MW
Neutral beam heating 60 keV		10 MW
100 keV		10 MW
Ion cyclotron heating (30–90 MHz)		6 MW
Electron cyclotron heating (140 GHz)		2 MW

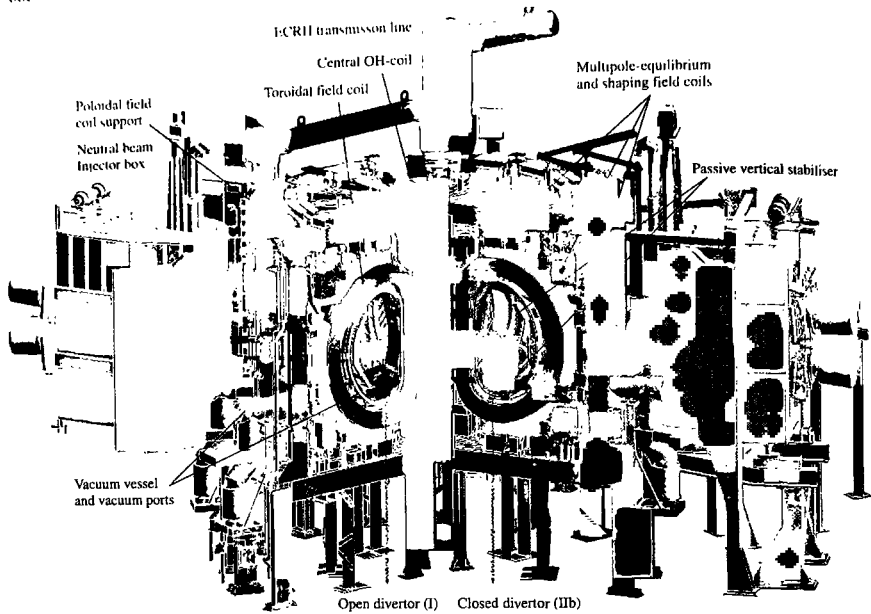


**Fig. 12.6.1** 3D cut away view of ASDEX Upgrade with neutral beam injector boxes and DIV I (left) and DIV IIb (right) divertor configuration.

- 1996 installation of tungsten-coated divertor plates
- 1997 closed lyre-shaped divertor and cryo pump
- 1997 second neutral beam injector with 100 keV beams and 10 MW heating power
- 2001 tangential neutral beam injection for off-axis current drive experiments
- 2001 adaptation of the closed lyre-shaped divertor to plasma configurations with a high triangularity shape. The three divertor designs which have been used are illustrated in Fig. 12.6.2.

A large set of diagnostics to characterize the core, edge, and divertor plasma conditions provide for the physics programme with the following main objectives:

- Particle and energy transport in the core plasma, operation boundaries, and confinement
- Conventional and 'advanced' tokamak scenarios for performance improvement
- Physics of plasma instabilities and their active stabilization
- Plasma edge and divertor physics as well as first wall materials.

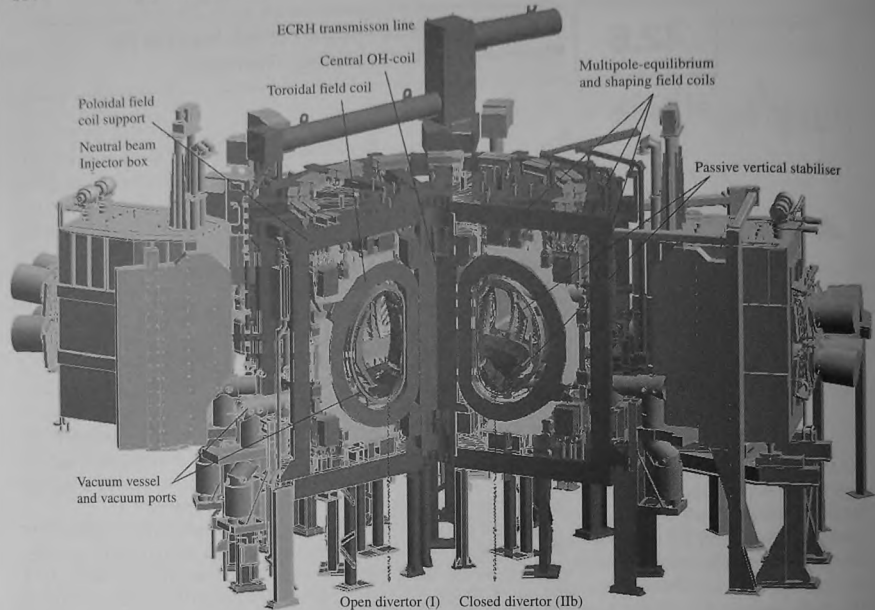


**Fig. 12.6.1** 3D cut away view of ASDEX Upgrade with neutral beam injector boxes and DIV I (left) and DIV IIb (right) divertor configuration.

- 1996 installation of tungsten-coated divertor plates
- 1997 closed lyre-shaped divertor and cryo pump
- 1997 second neutral beam injector with 100 keV beams and 10 MW heating power
- 2001 tangential neutral beam injection for off-axis current drive experiments
- 2001 adaptation of the closed lyre-shaped divertor to plasma configurations with a high triangularity shape. The three divertor designs which have been used are illustrated in Fig. 12.6.2.

A large set of diagnostics to characterize the core, edge, and divertor plasma conditions provide for the physics programme with the following main objectives:

- Particle and energy transport in the core plasma, operation boundaries, and confinement
- Conventional and 'advanced' tokamak scenarios for performance improvement
- Physics of plasma in-stabilities and their active stabilization
- Plasma edge and divertor physics as well as first wall materials.

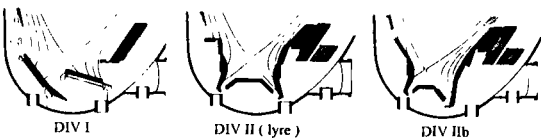


**Fig. 12.6.2** Evolution of divertor configurations in ASDEX Upgrade. DIV I (1991–1997), DIV II (1997–2000), DIV IIb adapted to higher triangularity plasmas.

### Divertor physics

A principal purpose of ASDEX Upgrade is to test concepts for power and particle exhaust. ASDEX Upgrade came into operation with the open divertor configuration, DIV I, characterized by flat horizontal divertor plates made from fine grain graphite. The outer divertor plate was put close to the X-point to benefit from the large flux expansion in that region. It had only a small pumping baffle in the outer divertor, which nevertheless was quite important for good particle exhaust. DIV I was replaced by the fairly closed lyre-shaped divertor, DIV II, to test the physics underlying the proposed ITER divertor, in particular the problem of exhausting power and particles while maintaining good core confinement. In parallel the heating power was increased to 20 MW by installing a second neutral beam injector box.

The target plates and the roof baffle of DIV II were shaped to influence the detachment properties by increasing the ionization of hydrogen neutrals around the separatrix and reducing the target heat flux, especially close to the separatrix. Experiments with the DIV II divertor show that the maximum heat flux at the divertor plates is reduced by a factor of 2 compared with the open DIV I divertor. This reduction of the power flow results from an increased radiative power loss, which is concentrated in the divertor region. With DIV II, about 45% of the input power is radiated below the X-point. Most of the divertor radiation is concentrated in a small emission zone along the separatrix. This had been predicted by modelling with a computer code, and a comparison with experimental results is shown in Fig. 12.6.3.

The enhanced divertor radiation is not caused by a stronger influx of carbon but is due to an increased radiation efficiency of carbon and hydrogen in the divertor plasma. Carbon cools the scrape off layer plasma down to the 5 eV region, where the hydrogen losses become significant.

DIV II was also optimized for particle compression, which is the ratio between the neutral density in the pump duct and the averaged ion mid-plane density near to the separatrix, as well as for impurity enrichment, defined as the ratio of impurity compression to hydrogen compression. The compression is of particular interest because it determines the pumping efficiency and the degree of particle control. Hydrogen and helium compression is much larger in DIV II than in the open divertor DIV I as predicted by modelling. The resulting enrichment ratio for helium is practically unchanged and the ratio of helium and energy replacement

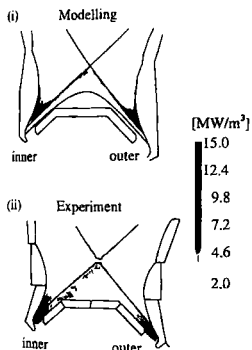


**Fig. 12.6.3** (i) Computer modelling of the radiation pattern predicts radiation bands between X-point and strike points. (ii) The reconstructed radiation pattern using virtual lines of sight during a vertical shift of the plasma reveals a narrow radiation zone from the inner strike point to the X-point. A corresponding band at the outer strike point cannot be detected due to missing bolometer lines of sight.

times, which has to be below 10 to 15 for a burning plasma not to be extinguished by the helium ash, is between 4 and 6.

DIV II was designed to fit plasma configurations with low triangularity into the narrow divertor legs. Configurations with higher triangularities could be run with the outer plasma fan at the top of the roof baffle, thereby losing the benefits of the lyre-shaped configuration, especially the power handling capacity and the pumping capability. During operation of the lyre-shaped divertor the interest in higher triangularity plasmas increased because of the improved confinement at higher density and the possible access to a confinement regime with reduced ELM size. To overcome the restriction DIV IIb was introduced to accommodate a larger variety of plasma shapes with higher triangularities.

### Plasma wall interactions and first wall material

One of the most difficult design issues for ITER is the choice of plasma facing materials, in particular for the divertor components. In most present-day tokamaks carbon is used as divertor material due to the good heat flux handling capacity combined with the relatively low  $Z$ . It has, however, disadvantages, which might be unacceptable in a future fusion device. Graphite suffers from an enhanced erosion by chemical processes even at low temperatures resulting in deposited layers around the vessel which incorporate up to 40% of hydrogen isotopes. The corresponding tritium enrichment would be too high for a reactor. Tungsten exhibits much more favourable properties with respect to erosion and other physical properties. In addition, there is good evidence that physical sputtering rates are lowered by prompt redeposition due to the gyro motion in the local magnetic field. On the other hand, the high self-sputtering rates make the use of tungsten feasible only for low plasma temperature, high density divertor conditions. Due to the high radiation power of tungsten, its fractional abundance in the main plasma should be substantially below  $10^{-4}$ . To investigate the suitability of tungsten in a divertor tokamak under reactor relevant conditions, the power receiving fine grain graphite plates of the open divertor DIV I were coated with a 0.5 mm thick layer of tungsten. The major points of interest were the investigation of erosion and deposition processes, the transport of tungsten into and within the bulk plasma, as well as the effect on the plasma performance. The discharges used cover almost the full operational space of plasma current, density, and auxiliary heating power. The averaged power load at the divertor plates reached  $6 \text{ MW/m}^2$  whereas the peak power load during type I ELMs was a factor of 3 higher.

The tungsten concentration in the confined plasma was investigated spectroscopically. Over 90% of the investigated discharges show concentrations below  $2 \times 10^{-5}$ . The tungsten concentration was strongly dependent on transport properties and generally decreased with an increase of additional heating power. A few discharges with counter neutral beam injection, strongly peaked density profiles, or low energy neutral

beam heating show tungsten accumulation due to a strong inwards drift compared with the anomalous transport.

Erosion and redeposition was measured by exposing target tile probes by means of a manipulator system and by post mortem investigation of long term probes exposed to the divertor and the scrape-off layer plasma. The migration pattern for an ohmic discharge is shown in Fig. 12.6.4. The low sputtering yield for plasma temperatures below 20 eV and the high retention leads to low erosion and negligible migration of tungsten into the main plasma.

The density and the  $\beta$  limits remain unchanged and no deterioration in the energy confinement occurs. The H-mode threshold and the radiating boundary scenarios are also unaffected. These results are encouraging for high-Z plasma facing components to be used in a future device. ASDEX Upgrade started in 1999 with a programme to replace inner vessel carbon tiles by tungsten. In three steps the lower, the upper, and then the central part of the inner heat protection shield were covered with tungsten. Discharges in all major plasma regimes were performed and specially dedicated limiter discharges were produced with the closest possible distance to the tungsten tiles. Generally the tungsten concentration stayed below  $10^{-5}$ , except discharge types revealing a strong peaking of the background density profile. With these encouraging results it was decided to expand the tungsten covered area step by step towards a full tungsten covered inner wall.

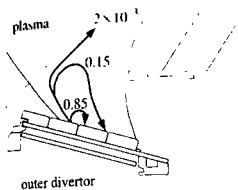


Fig. 12.6.4 Migration pattern for an ohmic discharge with a density of  $2.5 \times 10^{19} \text{ m}^{-3}$  and a tungsten concentration of about  $10^{-5}$ . Only the fraction  $2 \times 10^{-3}$  of the initially sputtered tungsten can leave the divertor region. 85% are promptly redeposited and about 15% stay in the divertor due to the divertor retention.

### Plasma edge related operation boundaries

It has been shown that various operation boundaries have their cause at the plasma edge. With a well equipped diagnostic configuration investigations were made of the physics of the H-mode transport barrier at the plasma edge, the causes for the density limit, the physics of ELMs and the connection of edge parameters and the overall plasma confinement. The edge operational limits can be summarized by combining the edge parameter dependence of various operational regimes in a single diagram. In the so called 'edge operation diagram' shown in Fig. 12.6.5 various operation areas with respect to electron density and electron temperature can be distinguished and scalings for critical parameters can be derived.

The operational space in this diagram is limited at high edge pressure gradients by ideal instabilities. A lower temperature limit is given by the onset of MARFE thermal instability below  $T_e \approx 90 \text{ eV}$ , which occurs at sufficiently high edge density. The L-H threshold in terms of local parameters represented by a critical temperature is:

$$T_e^{\text{thresh}}(eV) = 145 \left( \frac{n_{\text{edge}}}{10^{19}} \right)^{-0.3} B_t^{0.8} I_p^{0.5} \quad I_p \text{ in MA.}$$

The type of ELMs observed varies along the ideal pressure limit from type III to type I with a small ELM free region.

**Fig. 12.6.5** Edge operational diagram showing regime boundaries for discharges with  $I_p = 1$  MA,  $B_t = 2.5$  T,  $\delta = 0.2$ .  $T_e$  and  $n_e$  were taken at a position 2 cm inside the separatrix in order to represent absolute values as well as gradients in the steep gradient region. The dashed line marks the ideal ballooning limit at a normalized electron pressure gradient of  $\alpha_e = 1.2$ , and assuming a gradient length  $p/\nabla p = 3$  cm to convert the pressure gradient to the electron temperature in this diagram.

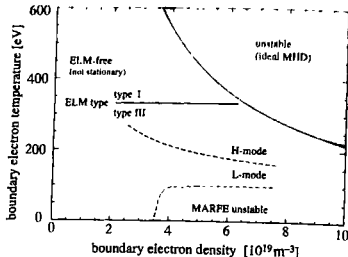
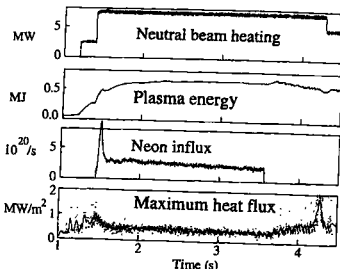


**Fig. 12.6.6** Completely detached H-mode discharge. During the Neon gas puff the divertor detaches as indicated by the reduced heat flux, and the type I ELMs vanish. This reduction of the maximum heat flux to the outer divertor is achieved without a reduction of plasma stored energy.



Type I ELMs are expected to cause an intolerable energy impact onto the divertor of next step fusion experiments. A favourable operational point in this diagram would be with the occurrence of type III ELMs near to the ideal pressure limit. The boundary temperature should be low enough to avoid non-stationary ELM-free H-phases. Type III ELMs are obtained either by low heating power just above the H-mode threshold or, at high power flux, by feedback-controlled impurity radiation using for example neon as a seed. This latter scenario is found in completely detached H-mode discharges, which in addition to favourable small ELMs exhibits full detachment of the divertor, as shown in Fig. 12.6.6. The level of confinement in this regime may crucially depend on whether a complete determination of bulk temperature and density profiles by edge stability limits can be avoided.

An operational window which avoids type I ELMs but keeps good confinement at high density has been established. This H-mode regime with type II ELMs was obtained for  $q_{95} > 3.5$  and an averaged triangularity  $\delta \geq 0.42$ . The magnetic configuration was close to double null and the density could be kept just at the empirical Greenwald limit. For these plasma conditions steady state type II H-modes without any type I ELM were observed, limited only by the length of the plasma-current flat top phase. The energy confinement is close to that of type I ELMs. H-mode and H-factors of  $H_{H95y} = 0.95$  have been achieved. The target

load during type II ELM phases as measured with thermography shows no large temporal variations and is comparable to the averaged target load measured in type I ELM discharges.

The experiments indicate that the consequences of edge stability limits go beyond mere changes of edge parameters such as the edge pedestal shape or transport across the edge barrier. For a given ideal ballooning limit, it is observed that core temperature profiles of electron and ion temperature differ only by an approximately constant factor for a wide range of plasma parameters. This stiffness of temperature profiles, together with very flat density profiles typically achieved with edge fuelling by gas puffing in conventional scenarios, links the edge pressure gradient to the stored energy and hence the global confinement. Consequently, the favourable density and magnetic field dependence of ITER H-mode scalings seems to be modified. A confinement improvement can be achieved in magnetic configurations with higher triangularity which have higher values for the ideal ballooning limit due to the increased magnetic shear.

### Confinement and transport studies

Confinement studies of conventional L- and H-modes indicate that the ion and electron temperature profiles are generally limited by a critical value of the temperature gradient length,  $(\nabla T/T)^{-1}$ . The resulting stiffness of the profiles is reflected by the proportionality between core and edge (or pedestal) temperatures. This means that the temperature profiles plotted on a logarithmic scale keep the same shape and are shifted vertically according to the edge temperature as shown in Fig. 12.6.7. Clearly, for stiff profiles, the edge temperature is an essential parameter for the profile behaviour and consequently for confinement. The observation that the temperature profiles are stiff was studied in more detail after upgrading one neutral beam injection line to a higher beam voltage of 93 kV. At high plasma densities the 60 and 93 kV neutral beams result in rather different deposition profiles at otherwise unchanged parameters. The reaction of the plasma transport to these different heating power profiles was investigated. The measured temperature profiles are unaffected by the change in the beam energy, shown in Fig. 12.6.7. The power balance analysis shows that the heat flux is significantly higher for the 93 kV compared to the 60 kV beam, owing to the deeper beam penetration. At midradius the difference amounts to a factor of almost 2. This leads to quite different effective heat diffusivities, despite the same temperature and density profiles. It is clear that the heat conductivity adjusts itself to maintain the observed stiff temperature profiles.

Analysis indicates that the physical mechanism causing such a profile self-organization is plasma turbulence driven by ion temperature gradient modes, trapped electron modes, and possibly electron temperature gradient modes, which causes a strong increase of the heat transport for temperature gradient length below the critical value. This mechanism is not necessarily valid in the plasma centre, where the profiles are

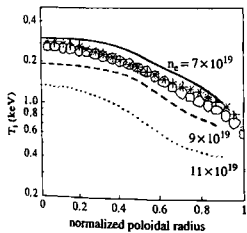


Fig. 12.6.7 H-mode ion temperature profiles measured during a density scan (lines) and for on- and off-axis heat deposition (symbols) are stiff with a constant temperature gradient length  $T/\nabla T$  in the confinement region between 0.3 and 0.8 of normalized poloidal radius.

determined by sawtooth activity and at the edge, where the temperature is so low that other turbulent modes are expected to dominate.

In discharges with pure electron heating, the local heat diffusivity for electrons,  $\chi_e$ , was measured with  $T_e$  modulation by heat pulse experiments using the ECRH heating system and the electron cyclotron emission diagnostic. The propagation of modulated ECRH power deposited at a fixed radius inside the plasma is analysed using the standard method based on Fourier transform of the  $T_e$  modulation, and the corresponding transport coefficient  $\chi_e$  is deduced.  $\nabla T_e/T_e$  at the fixed radial position was varied by a power scan. The result shows clearly a threshold in  $\nabla T_e/T_e$  where already a small increase in  $\nabla T_e/T_e$  results in a strong increase of  $\chi_e$  by about one order of magnitude.

### Particle transport, fuelling and density profile

Density control by strong gas puffing from the plasma edge is accompanied by a reduction of the edge temperature and, through profile stiffness, by confinement degradation. Central plasma refilling can avoid the temperature degradation and, in addition, may lead to peaked density profiles and a confinement improvement. Experiments with a moderate gas puff also reveals the option to increase the confinement by density peaking without deterioration of the edge parameters (see Fig. 12.6.8).

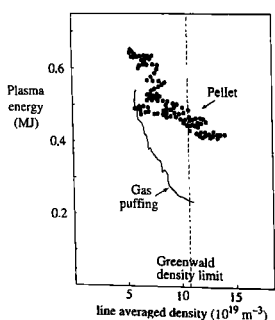


**Fig. 12.6.8** The strong degradation of stored plasma energy with increasing density build up in discharges with gas puffing (solid line) could be mitigated by pellet fuelling with high field side pellet injection (dots). The temporal evolution is into the direction of higher density.

The effect of pellet injection with different systems on the plasma density and performance was intensively investigated. Density feedback control was achieved at levels well above the empirical Greenwald density limit with injection from the low-field side. But it turned out that the high pellet particle fluxes result in a degradation of the particle confinement time. This effect is enhanced by ELMs triggered for each single pellet during H-mode phases. With the high particle fluxes and the particles expelled by the pellet-triggered ELM the energy stored by these particles is also lost from the plasma. Consequently, strong pellet refuelling at low refuelling efficiency, can cause high convective losses and confinement degradation. The refuelling efficiency of pellets coming from the low-field side decreases with increasing heating power, since in hot plasmas the material ablated by the pellets is rapidly shifted to the plasma edge and even partially expelled from the plasma. This is because the ablation cloud of a pellet sucks energy and a localized plasmoid with high internal pressure is formed. This diamagnetic plasmoid represents an extremely localized perturbation that is, subjected to a magnetic field gradient, drifting towards lower fields. This drift is beneficial if the pellet is injected from the magnetic high field side because it pushes the plasmoid to the plasma centre. As a result plasma particle and energy losses are reduced due to the nearly perfect absorption of the pellet material.

As found for low-field side pellet injection the high-field side pellets also trigger an ELM but the related energy and particle losses are much smaller. The fuelling efficiency increases with the penetration depth.

which depends on the pellet velocity. The ELM burst losses are of transient nature with a timescale for plasma energy recovery after a pellet sequence significantly shorter than the particle confinement time. This allows transient operation at enhanced density without confinement loss in respect of the initial conditions on a timescale of particle confinement time after the last pellet. A further increase in pellet speed results in pellet induced density ramps suffering less reduction of confined energy and approaching an adiabatic fuelling behaviour with density increase moving along an isobar. A first step towards this goal was made by upgrading the pellet guiding system to cope with pellet speeds up to  $1000 \text{ m s}^{-1}$  in 1999.

High density H-mode discharges with moderate constant gas puff and off-axis heating both with ICRH and NBI show a slowly evolving density peaking which yields high central density values at unchanged edge density and electron temperature. The energy confinement is therefore increased compared to discharges with flat density profiles. A peculiarity of such scenarios is that the equilibration time for peaked profiles is much longer than the energy confinement time. This means that these long time constants have to be considered for determination of a steady state situation and not the energy confinement time which is commonly used. The degradation of confinement in phases with increasing gas puff may be due to such non equilibrated density profiles as long as the confinement regime is not changed. The equilibrium shape of the density profiles depends on the heat flux profile in the core plasma. This, and the rate of peaking, could be modelled supposing that energy and particle transport due to turbulence is coupled to a certain extent and the neoclassical inward pinch is active. The ratio of particle and energy diffusivity of 0.1–0.2 derived from the model calculations corresponds well to the observation that the density equilibration time is much longer than the energy confinement time. The density peaking is strongly reduced by central heating with ICRH. This is due to the increase of the central heat diffusivity which, according to the model, also causes an increase of the particle transport. As a consequence, flat density profiles are expected in a reactor with central heating.

#### Advanced scenarios and internal transport barriers

The confinement performance of plasma discharges with stiff temperature profiles and flat H-mode density profiles is mainly fixed by the edge pedestal pressure. Tailoring of the density profile, by density peaking, allows an optimization of the plasma stored energy. A more effective procedure is to suppress the turbulent radial transport and to break the temperature profile stiffness. This results in so-called internal transport barriers inside the bulk plasma. These barriers yield a surplus of plasma energy inside the barrier compared with the presence of a single edge barrier. Additional conditions for these high confinement scenarios are that they are mhd-stable at these higher plasma pressures and that they can be maintained in a stationary state. Basically a reactor with such features

can be more compact than with a conventional concept. This has led to the study of the possibilities for stationary tokamak operation with such advanced scenarios combined with full non-inductive current drive by the internal bootstrap current and external driven currents.

Steady state improved H-mode plasmas have been approached by a combination of improved core confinement through density peaking with an ELMH mode edge and stiff temperature profiles. While the pressure gradients are distinctly enhanced in these cases, the overall performance and the pulse length was increased. Quasi steady-state high performance discharges were obtained by applying moderate neutral beam heating in the current ramp-up, in order to reduce current diffusion and hence generating flat current profiles to delay the formation of an  $m = 1, n = 1$  resonant  $q$ -surface. On approaching  $q = 1$  in the core, strong  $m = 1, n = 1$  fishbone instabilities, driven by trapped particles from neutral injections occur, preventing sawtooth activity and triggering the build-up of a peaked density profile. The impurity concentration is regulated by the core fishbones and ELMs at the edge. The high performance phase lasts for 6 s or 40 energy confinement times, only limited by the duration of the NBI. The highest fusion product obtained is  $n_0 T_0 \tau_E = 1.1 \times 10^{20} \text{ m}^{-3} \text{ keVs}$  and  $\beta_N \times H_{ITER89-P} = 7.5$ , which serves as a figure of merit for stability and confinement, have been achieved at a triangularity of  $\delta = 0.3$ . A further performance increase is prevented by neoclassical tearing modes which are the limiting instability for monotonic  $q$ -profiles.

Special discharge scenarios were developed to extend the stable operation without neoclassical tearing modes leading to H-mode plasmas with  $\beta_N > 3.5$  and good confinement with  $H_{ITER89-P} = 2.2$  in steady state for several seconds as shown in Fig. 12.6.9. The plasma configuration for these experiments have maximum shaping with a triangularity of about  $\delta = 0.42$  and a near double null plasma configuration. The electron density could be increased up to 90% of the Greenwald density without a significant loss in confinement. The ELM characteristic changes significantly from type I to type II ELMs, the ELM energy loss being reduced from about 3% of plasma stored energy to 0.5% during the near double null phase.

The fraction of inductively driven current in a tokamak plasma can be reduced by increasing the fraction of bootstrap current generated by the pressure gradient. To achieve this, the poloidal  $\beta$  was maximized by operation at low plasma current and sufficiently high heating power. Values of  $\beta_p \approx 3$  have been attained in H-mode plasmas at a plasma current of 400 kA ( $B_t = 2$  T) and with up to 10 MW neutral beam heating. With strong gas fuelling in the initial phase of the discharge and the low plasma current the high  $\beta_p$  plasmas reach the Greenwald density while keeping the H-mode confinement. The resulting performance value is  $\beta_N \times H_{ITER89-P} = 5$  at a triangularity of  $\delta = 0.2$ . The fraction of non-inductive driven current from the combination of large fraction of bootstrap current and neutral beam driven current is nearly 100%.

Most of the internal transport barriers were obtained through non-ohmic heating with up to 15 MW neutral beam injection, in the current

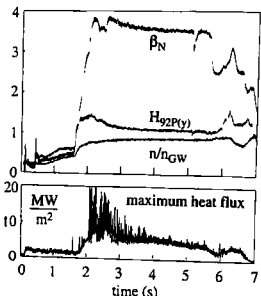


Fig. 12.6.9 High  $\beta_N$  discharge with reduced ELM activity as seen in a reduction of the maximum heat flux.

ramp up phase, and mhd-stable current profiles with an L- or H-mode edge both in limiter or divertor discharges. The magnetic shear is transiently reversed in the centre, and internal transport barriers form with central ion temperatures up to 20 keV and ion temperature gradient lengths much smaller than those of the H- or L-mode. However this internal transport barrier regime is limited by continuous evolution of the current profile which, without an off-axis current drive method, could not be prevented. This finally leads to a termination of the barrier by mhd instabilities in the core or edge. Compared with the high performance H-mode discharges described above, these discharges with internal transport barrier are limited in performance partly by the L-mode edge and in general by the low density achievable. However, by combining neutral beam heating and electron cyclotron current drive, counter to the plasma current direction, it was possible to simultaneously achieve reactor relevant temperatures of 10 keV for both electrons and ions. Pure internal electron transport barriers were obtained with electron heating by electron cyclotron current drive, counter to the plasma current direction, in low density discharges yielding thermal electron core temperatures above 20 keV.

### Magnetohydrodynamic stability

Magnetohydrodynamic instabilities impose a sensitive limit on the accessible operation areas, and in particular on the confined plasma pressure. The understanding of the physical mechanism of the instabilities is an important precondition for the development of efficient, stable confinement scenarios. The instability with most impact on plasma performance in H-mode discharges with positive magnetic shear profiles is the neoclassical tearing mode. This pressure-driven instability limits the confined plasma pressure by the formation of magnetic islands with a flat pressure profile inside, thus reducing the efficiency of the magnetic confinement. The impact of the neoclassical tearing mode on the discharge depends on the mode numbers: (4,3) modes have only small influence on confinement with less than 10% degradation, whereas (3,2) modes can reduce the confinement by 10–30% of the original value. The existence of (2,1) modes generally leads to an unacceptable loss of about 50% and, at  $q_{95} < 3$ , to a disruptive termination. An understanding of neoclassical tearing mode physics is essential for predicting their occurrence and for developing adequate tools for avoiding or stabilizing these modes. The critical normalized beta,  $\beta/(I/aB)$ , for the onset of neoclassical tearing modes has been found to scale proportionally to the normalized ion gyroradius,  $\rho/a$ , with a very weak dependence on the normalized collisionality,  $v_{ii}/\omega_e^*$ .

Since neoclassical tearing modes set the  $\beta$  limit in discharges with positive shear, a method of removing or avoiding them is of great importance. A demonstration of the stabilization of neoclassical tearing modes was performed with electron cyclotron current drive experiments. At beta normalized values between 2.2 and 2.5, a (3,2) mode could be completely stabilized by applying electron cyclotron current drive power of about 10%

of the total heating power, corresponding to 15–20 kA of helical current driven within the island, as shown in Fig. 12.6.10. Once the mode is stabilized, the normalized beta can be raised above the onset value if the total heating power is increased and the electron cyclotron current drive is on.

Extensive modelling of the mode stabilization by electron cyclotron current drive has been done using a cylindrical non-linear tearing mode code. In particular, the modelling has shown that the main stabilizing effect comes from direct generation of helical current within the island by current drive.

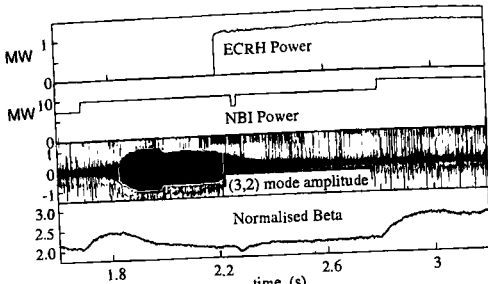


**Fig. 12.6.10** Stabilization of neoclassical tearing modes with electron cyclotron current drive as indicated by the amplitude of the  $m = 3, n = 2$  magnetic perturbations.  $\beta_N = 2.6$  was achieved in steady state without these modes by raising the neutral beam power.

## Bibliography

Much of the material discussed in this chapter has been presented at the biennial international conferences sponsored by the I.A.E.A., and at the annual conferences sponsored by the European Physical Society and the American Physical Society. Details of these meetings are given in the bibliography to Chapter 11 and individual references arising from these conferences will not be listed here. In addition, references given in figure captions will not be repeated.

### TFTR

Initial confinement results:

Ethimion, P.C. *et al.* Initial confinement studies of ohmically heated plasmas in the Tokamak Fusion Test Reactor. *Physical Review Letters* **52**, 1492 (1984).

Observation of neoclassical resistivity in TFTR:

Zarnstorff, M.C. *et al.* Parallel electric resistivity in the TFTR tokamak. *Physics of Fluids B* **2**, 1852 (1990).

Scaling of confinement with major and minor radius in L-mode plasmas:

Grisham, L.R. *et al.* Scaling of confinement with major and minor radius in the Tokamak Fusion Test Reactor. *Physical Review Letters* **67**, 66 (1991).

Limiter conditioning for supershot plasmas:

Dylla, H.F. *et al.* Conditioning of the graphite bumper limiter for enhanced confinement discharges in TFTR. *Nuclear Fusion* **27**, 1221 (1987).

Achievement of the supershot regime:

Strachan, J.D. *et al.* High-temperature plasmas in the Tokamak Fusion Test Reactor. *Physical Review Letters* **58**, 1004 (1987).

Limiter H-modes in TFTR:

Bush, C.E. *et al.* Peaked density profiles in circular-limiter H-modes on the TFTR tokamak. *Physical Review Letters* **65**, 424 (1990).

Analysis of the carbon bloom in high power heating experiments:

Ulrickson, M. *et al.* A review of carbon blooms on JET and TFTR. *Journal of Nuclear Materials* **176&177**, 44 (1990).

- Influence of low  $m/n$  mhd activity on supershot performance  
Thang, J. et al. Transport effects of low  $(m,n)$  mhd modes  
on TFTR supershots. *Nuclear Fusion* **34**, 1309 (1994).
- Identification of non-local neoclassical pressure gradient-driven tearing modes in supershots  
Chang, Z. et al. Observation of nonlinear neoclassical pressure gradient driven tearing modes in TFTR. *Physical Review Letters* **74**, 4663 (1995).
- Analysis of turbulence suppression by radial electric field shear in TFTR ERS plasmas  
Synakowski, E.J. et al. Role of electric field shear and Shafranov shift in sustaining high confinement in enhanced reversed shear plasmas on the TFTR tokamak. *Physical Review Letters* **78**, 2872 (1997).
- Observation of Kadomtsev-like sawtooth collapse:  
Nagayama, Y. et al. Analysis of sawtooth oscillations using simultaneous measurements of electron cyclotron emission imaging and X-ray tomography on TFTR. *Physical Review Letters* **67**, 3527 (1991).
- Measurement of  $q(0) \sim 0.7$  during sawtooth activity:  
Yamada, M. et al. Investigation of magnetic reconnection during a sawtooth crash in a high-temperature tokamak plasma. *Physics of Plasmas* **1**, 3269 (1994).
- Comparison of sawtooth and sawtooth-free plasmas with theoretical stability criterion:  
Leviton, F.M. et al. Stabilization and onset of sawteeth in TFTR. *Physical Review Letters* **72**, 2895 (1994).
- Observation of medium-L ballooning modes:  
Nagayama, Y. et al. Observation of ballooning modes in high-temperature tokamak plasmas. *Physical Review Letters* **69**, 2376 (1992).
- Evidence for TAE modes in NBI heated plasmas:  
Wong, K.L. et al. Excitation of Toroidal Alfvén Eigenmodes in TFTR. *Physical Review Letters* **66**, 1874 (1991).
- Determination that local transport has Bohm-like behaviour in L-mode plasmas:  
Perkins, F.W. et al. Nondimensional transport scaling in the Tokamak Fusion Test Reactor: is tokamak transport Bohm or gyro-Bohm? *Physics of Fluids* **B5**, 477 (1993).
- Initial sawtooth heat pulse propagation studies in TFTR:  
Fredrickson, E.D. et al. Heat pulse propagation studies in TFTR. *Nuclear Fusion* **26**, 849 (1986).
- Observation of ballistic component of heat pulse propagation:  
Fredrickson, E.D. et al. Ballistic contributions to heat-pulse propagation in the TFTR tokamak. *Physical Review Letters* **65**, 2869 (1990).
- Investigation of the temperature dependence of local transport coefficients:  
Efstathion, P.C. et al. Observation of temperature-dependent transport in the TFTR tokamak. *Physical Review Letters* **66**, 421 (1991).
- Application of beam emission spectroscopy to determine the characteristics of plasma turbulence:  
Durst, R.D. et al. Observation of a localized transition from edge to core density turbulence in the TFTR tokamak. *Physical Review Letters* **71**, 3135 (1993).
- Determination of local transport coefficients of helium:  
Synakowski, E.J. et al. Measurements of radial profiles of  $\text{He}^{2+}$  transport coefficients on the TFTR tokamak. *Physical Review Letters* **65**, 2255 (1990).
- First results of experiments with D-T mixtures in TFTR:  
Strachan, J.D. et al. Fusion power production from TFTR plasmas fueled with deuterium and tritium. *Physical Review Letters* **72**, 3526 (1994).
- Hawryluk, R.J. et al. Confinement and heating of a deuterium-tritium plasma. *Physical Review Letters* **72**, 3530 (1994).
- Evidence for electron heating by  $\alpha$ -particles:  
Taylor, G. et al. Fusion heating in a deuterium-tritium tokamak plasma. *Physical Review Letters* **76**, 2722 (1996).
- Use of lithium conditioning to improve fusion performance in D-T supershots:  
Mansfield, D.K. et al. Enhanced performance of deuterium-tritium-fueled supershots using extensive lithium conditioning in the Tokamak Fusion Test Reactor. *Physics of Plasmas* **2**, 4252 (1995).
- ICRF heating of D-T plasmas:  
Wilson, J.R. et al. Ion cyclotron range of frequency heating of a deuterium-tritium plasma via the second-harmonic tritium cyclotron resonance. *Physical Review Letters* **75**, 842 (1995).
- Measurements of fast confined  $\alpha$ -particles in D-T plasmas:  
McKee, G. et al. Confined alpha distribution measurements in a deuterium-tritium tokamak plasma. *Physical Review Letters* **75**, 649 (1995).
- Fisher, R.K. et al. Measurements of fast confined alphas on TFTR. *Physical Review Letters* **75**, 846 (1995).
- Losses of  $\alpha$ -particles due to kinetic ballooning modes:  
Chang, Z. et al. First observation of alpha particle loss induced by kinetic ballooning modes in TFTR deuterium-tritium experiments. *Physical Review Letters* **76**, 1071 (1996).
- Measurements of TAE modes excited by  $\alpha$ -particles:  
Nazikian, R. et al. Alpha-particle-driven toroidal Alfvén eigenmodes in the Tokamak Fusion Test Reactor. *Physical Review Letters* **78**, 2976 (1997).
- Overview of TFTR experiments in D-T plasmas:  
Hawryluk, R.J. Results from deuterium-tritium tokamak confinement experiments. *Reviews of Modern Physics* **70**, 537 (1998).

## JET

A summary of the scientific work on JET is given in the book:  
Wesson, J. *The Science of JET. JET Joint Undertaking*  
(2000)

Analysis of ohmic energy confinement:

Bartlett, D.V. *et al.* Energy confinement in JET ohmically heated plasmas. *Nuclear Fusion* 28, 73 (1988).

Observation of neoclassical resistivity in JET:

Campbell, D.J. *et al.* Plasma resistivity and field penetration in JET. *Nuclear Fusion* 28, 981 (1988).

First observation of H-modes in JET:

Tanga, A. *et al.* Magnetic separatrix experiments in JET. *Nuclear Fusion* 27, 1877 (1987).

Production of long steady-state H-modes:

Campbell, D.J. *et al.* H-modes under steady-state conditions in JET. *Plasma Physics and Controlled Fusion* 36, A255 (1994).

The density limiter and disruptions:

Wesson, J.A. *et al.* Disruptions in JET. *Nuclear Fusion* 29, 641 (1989).

Error field modes:

Fishpool, G.M., Haynes, P.S. Field error instabilities in JET. *Nuclear Fusion* 34, 109 (1994).

Reduction of forces at disruptions by control of pre-disruptive elongation:

Tanga, A. *et al.* Study of plasma disruptions in JET and its implications on engineering requirements. *Fusion Engineering* (Proc. 14th Symp., San Diego, 1991) Vol 1, 201. I.E.E., New York (1992).

Analysis of asymmetric vertical displacement events:

Riccardo, V. *et al.* Parametric analysis of asymmetric vertical displacement events at JET. *Plasma Physics and Controlled Fusion* 42, 29 (2000).

Observation of a very rapid sawtooth collapse:

Campbell, D.J. *et al.* Sawtooth activity in ohmically heated JET plasmas. *Nuclear Fusion* 26, 1085 (1986).

Wesson, J.A. *et al.* Spontaneous  $m = 1$  instability in the JET sawtooth collapse. *Nuclear Fusion* 31, 111 (1991).

Analysis of the sawtooth collapse showing significant differences from the full reconnection model of Kadomtsev:

Edwards, A.W. *et al.* Rapid collapse of a plasma sawtooth oscillation in the JET tokamak. *Physical Review Letters* 57, 210 (1986).

Variation of  $q(0)$  during sawtooth activity:

O'Rourke, J. The change in the safety factor profile at a sawtooth collapse. *Plasma Physics and Controlled Fusion* 33, 289 (1991).

First observation of sawtooth stabilization associated with fast particle populations:

Campbell, D.J. *et al.* Stabilization of sawteeth with additional heating in the JT-T tokamak. *Physical Review Letters* 60, 2148 (1988).

Control of sawtooth activity by minority ion fast wave current drive:

Bhatnagar, V.P. *et al.* Local magnetic shear control in a tokamak via fast wave minority ion current drive: theory and experiments in JET. *Nuclear Fusion* 34, 1579 (1994).

Suppression of onset of neoclassical tearing modes by control of sawtooth period:

Sauter, O. *et al.* Control of neoclassical tearing modes by sawtooth control. *Physical Review Letters* 88, 105001 (2002).

Studies of heat and particle transport using sawtooth temperature and density perturbations:

Tubbing, B.J.D. *et al.* Tokamak heat transport—a study of heat pulse propagation in JET. *Nuclear Fusion* 27, 1843 (1987).

de Haas, J.C.M. *et al.* Interpretation of heat and density pulse measurements in JET in terms of coupled transport. *Nuclear Fusion* 31, 1261 (1991).

First observation of PEP H-modes:

Tubbing, B.J.D. *et al.* H-mode confinement in JET with enhanced performance by pellet peaked density profiles. *Nuclear Fusion* 31, 839 (1991).

Rapid change of the electron thermal conductivity over a significant fraction of the minor radius at the L-H transition:

Cordey, J.G. *et al.* The evolution of the transport through the L-H transition in JET. *Nuclear Fusion* 35, 505 (1995).

Response of the local heat flux to negative temperature gradients:

Balet, B. *et al.* Heat transport with strong off-axis heating. *Nuclear Fusion* 32, 1261 (1992).

Analysis of  $\rho^*$  scaling of local transport in L-mode plasmas:

Christiansen, J.P. *et al.* The scaling of transport with normalized Larmor radius in JET. *Nuclear Fusion* 33, 863 (1993).

Isotope scaling of L-mode energy confinement:

Tibone, F. *et al.* Dependence of L-mode confinement on plasma ion species in JET. *Nuclear Fusion* 33, 1319 (1993).

Influence of triangularity on energy confinement in ELMy H-modes:

Saibene, G. *et al.* The influence of isotope mass, edge magnetic shear and input power on high density ELMy H-modes in JET. *Nuclear Fusion* 39, 1133 (1999).

Use of beryllium in JET:

The vast majority of results relating to the use of beryllium has been reported at the biennial conferences on plasma surface listed in the bibliography to Chapter 9. Highlights have

also been presented in invited and contributed papers given at the various international conferences noted previously.

#### Divertor experiments in JT-60

Results from the pumped divertor have been extensively reported in the literature at major international conferences listed in the bibliography to Chapter 11 and at international conferences on plasma surface interactions listed in the bibliography to Chapter 9. Three companion papers summarizing many of the key results are:

Horton, L.D. et al. Studies in JET divertors of varied geometry I: non-seeded plasma operation. *Nuclear Fusion* **30**, 1 (1990).

Matthews, G.F. et al. Studies in JET divertors of varied geometry II: impurity seeded plasmas. *Nuclear Fusion* **30**, 19 (1990).

McCracken, G.M. et al. Studies in JET divertors of varied geometry III: intrinsic impurity behaviour. *Nuclear Fusion* **30**, 41 (1990).

ICRF heated high- $\beta_p$  plasmas with high bootstrap current fraction:

Challis, C.D. et al. High bootstrap current ICRH plasmas in JET. *Nuclear Fusion* **33**, 1097 (1993).

Quasi-stationary operation with internal transport barriers:

Crisanti, F. et al. JET Quasistationary internal-transport-barrier operation with active control of the pressure profile. *Physical Review Letters* **88**, 145004 (2002).

Demonstration of 60kW of fusion power from D- $^3$ He reactions:

Boyd, D.A. et al.  $^3$ He-D fusion rate measurements during fast-wave heating experiments in JET. *Nuclear Fusion* **29**, 593 (1989).

First observations of high fusion performance in X-point plasmas in JET:

Balet, B. et al. High temperature L- and H-mode confinement in JET. *Nuclear Fusion* **30**, 2029 (1990).

Mhd activity associated with the termination of the high performance phase of hot ion H-modes:

Nave, M.F.F. et al. An overview of MHD activity at the termination of JET hot ion H-modes. *Nuclear Fusion* **37**, 809 (1997).

Rapid change in plasma transport associated with the hot ion H-mode termination:

Wesson, J.A. and Balet, B. Abrupt changes in confinement in the JET tokamak. *Physical Review Letters* **77**, 5214 (1996).

Results of deuterium-tritium experiments in JET:

The results of the PTE and DTEI experiments have been extensively reported in the refereed literature and at international conferences. The March 1999 (Vol 39) issue of Nuclear Fusion contained 10 papers detailing many of the key studies performed during DTEI. Two additional papers which summarize the major results are:

Keilhacker, M. et al. High fusion performance from deuterium-tritium experiments in JET. *Nuclear Fusion* **39**, 209 (1999).

Jacquinot, J. et al. Overview of ITER physics deuterium-tritium experiments in JET. *Nuclear Fusion* **39**, 235 (1999).

#### JT-60/JT-60U

H-mode experiments with diverted plasmas in JT-60:

Nakamura, H. et al. H-mode experiments with outer and lower divertors in JT-60. *Nuclear Fusion* **30**, 235 (1990). Improved confinement with pellet injection in JT-60:

Kamada, Y. et al. Improved confinement characteristics of pellet fuelled discharges on JT-60. *Nuclear Fusion* **29**, 1785 (1989).

Ozeki, T. et al. Ideal mhd stability of pellet fuelled plasmas in JT-60. *Nuclear Fusion* **31**, 51 (1991).

Many experimental results from JT-60 and JT-60U on 'remote radiative cooling', impurity seeded H-modes and divertor performance with the W-shaped divertor were presented at the conferences on plasma surface interactions listed in the bibliography to Chapter 9.

Impurity and radiation losses in JT-60U:

Kubo, H. et al. Study of impurity and radiative losses in divertor plasmas with absolutely calibrated VUV spectrometers in JT-60U. *Nuclear Fusion* **33**, 1427 (1993).

Helium exhaust measurements in JT-60:

Nakamura, H. et al. Helium ash exhaust studies with core fueling by a helium beam: L-mode divertor discharges with neutral-beam heating in the JT-60 tokamak. *Physical Review Letters* **67**, 2658 (1991).

Measurement of SOL flows in JT-60U:

Asakura, N. et al. Measurement of natural plasma flows along the field lines in the scrape-off layer on the JT-60U divertor tokamak. *Physical Review Letters* **84**, 3093 (2000).

Measurement of heat and particle fluxes at ELMs:

Asakura, N. et al. Fast measurement of ELM heat and particle fluxes, and plasma flow in the scrape-off layer of the JT-60U tokamak. *Plasma Physics and Controlled Fusion* **44**, A313 (2002).

High confinement impurity seeded H-modes:

Kubo, H. et al. High radiation and high density experiments in JT-60U. *Nuclear Fusion* **41**, 227 (2001).

Helium transport in reversed shear plasmas:

Takenaga, H. et al. Particle confinement and transport in JT-60U. *Nuclear Fusion* **39**, 1917 (1999).

Increase of lower hybrid current drive efficiency with electron temperature:

Ushigusa, K. et al. Lower hybrid current drive efficiency in the JT-60 tokamak. *Nuclear Fusion* **29**, 1052 (1989).

- Power loading of divertor during LHCD experiments:  
 Ushigusa, K. et al. Direct loss of energetic electrons during lower hybrid current drive in JT-60U. *Nuclear Fusion* **32**, 1977 (1992).
- Volt-second saving by LHCD during current ramp-up:  
 Naito, O. et al. Volt-second saving by lower hybrid current drive in JT-60. *Nuclear Fusion* **30**, 1137 (1990).
- Analysis of bootstrap current and neoclassical resistivity in JT-60:  
 Kikuchi, M. et al. Bootstrap current during perpendicularly neutral injection in JT-60. *Nuclear Fusion* **30**, 343 (1990).
- Current drive using negative ion based NBI:  
 Oikawa, T. et al. Heating and non-inductive current drive by negative ion based NBI in JT-60U. *Nuclear Fusion* **40**, 435 (2000).
- Establishment of electron transport barrier in reversed shear plasmas:  
 Fujita, T. et al. Internal transport barrier for electrons in JT-60U reversed shear discharges. *Physical Review Letters* **78**, 2377 (1997).
- Fully non-inductive reversed shear plasmas:  
 Fujita, T. et al. Quasisteady high-confinement reversed shear plasma with large bootstrap current fraction under full noninductive current drive conditions in JT-60U. *Physical Review Letters* **87**, 85001 (2001).
- Density limit studies in JT-60:  
 Kamada, Y. et al. Study of the density limit with pellet fuelling in JT-60. *Nuclear Fusion* **31**, 1827 (1991).
- Stabilization of current rise locked modes:  
 Ninomiya, H. et al. Large  $m = 3/n = 1$  locked mode in JT-60 and its stabilization. *Nuclear Fusion* **28**, 1275 (1988).
- Determination of the 'null point' for vertical instabilities:  
 Yoshino, R. et al. Avoidance of VDEs during plasma current quench in JT-60U. *Nuclear Fusion* **36**, 295 (1996).
- Control of runaway electrons following disruptions:  
 Yoshino, R. et al. Generation and termination of runaway electrons at major disruptions in JT-60U. *Nuclear Fusion* **39**, 151 (1999).
- Observation of beta collapse in JT-60 high- $\beta_p$  plasmas:  
 Ishida, S. et al. Observation of a fast beta collapse during high poloidal-beta discharges in JT-60. *Physical Review Letters* **68**, 1531 (1992).
- Suppression of neoclassical tearing modes by electron cyclotron heating and current drive:  
 Isayama, A. et al. Complete stabilization of a tearing mode in steady state high- $\beta_p$  H-mode discharges by the first harmonic electron cyclotron heating/current drive on JT-60U. *Plasma Physics and Controlled Fusion* **42**, L37 (2000).
- Observation of non-circularity induced Alfvén eigenmodes with ICRF heating:  
 Kramer, G.J. et al. Noncircularity and ellipticity induced Alfvén eigenmodes observed in JT-60U. *Physical Review Letters* **80**, 2594 (1998).
- Steady-state plasmas at high- $\beta_N$  and high- $\beta_p$ :  
 Kamada, Y. et al. Non-inductively current driven H mode with high  $\beta_N$  and high  $\beta_p$  values in JT-60U. *Nuclear Fusion* **34**, 1605 (1994).
- Observation of grassy ELMs in high triangularity H-modes:  
 Kamada, Y. et al. Disappearance of giant ELMs and appearance of minute grassy ELMs in JT-60U high-triangularity discharges. *Plasma Physics and Controlled Fusion* **42**, A247 (2000).
- High fusion reactivity experiments in high- $\beta_p$  H-modes:  
 Mori, M. et al. Achievement of high fusion triple product in the JT-60U high  $\beta_p$  H mode. *Nuclear Fusion* **34**, 1045 (1994).
- Nishitani, T. et al. Attainment of high fusion reactivity under high bootstrap current fraction in JT-60U. *Nuclear Fusion* **34**, 1069 (1994).
- Observation of internal transport barrier in high- $\beta_p$  H-modes:  
 Koide, Y. et al. Internal transport barrier on  $q = 3$  surface and poloidal plasma spin up in JT-60U high- $\beta_p$  discharges. *Physical Review Letters* **72**, 3662 (1994).
- High fusion reactivity experiments in reversed shear discharges:  
 Ishida, S. et al. Achievement of high fusion performance in JT-60U reversed shear discharges. *Physical Review Letters* **79**, 3917 (1997).

### DIII-D

- First observation of H-modes in DIII-D:  
 Burrell, K.H. et al. Observation of an improved energy-confinement regime in neutral-beam-heated divertor discharges in the DIII-D tokamak. *Physical Review Letters* **59**, 1432 (1987).
- Observation of ohmic H-modes:  
 Osborne, T.H. et al. Observation of the H-mode in ohmically heated divertor discharges on DIII-D. *Nuclear Fusion* **30**, 2023 (1990).
- Production of long steady-state H-modes:  
 Luxon, J.L. et al. Recent results from DIII-D and their implications for next generation tokamaks. *Plasma Physics and Controlled Fusion* **32**, 869 (1990).
- H-mode threshold dependence:  
 Carlstrom, T.N. et al. Experimental survey of the L-H transition conditions in the DIII-D tokamak. *Plasma Physics and Controlled Fusion* **36**, A147 (1994).
- H-modes triggered by pellet injection:  
 Gohil, P. et al. Investigations of H-mode plasmas triggered directly by pellet injection in the DIII-D tokamak. *Physical Review Letters* **86**, 644 (2001).

- Analysis of giant LMs as an edge ballooning limit  
Gohil, P. et al. Study of giant edge localized modes in DIII-D and comparison with ballooning theory. *Physical Review Letters* **61**, 1603 (1988).
- Observation of changes in the edge electric field shear at the L to H transition  
Groebner, R.J. et al. Role of edge electric field and poloidal rotation in the L-H transition. *Physical Review Letters* **64**, 3015 (1990).
- Use of majority ions for edge electric field measurements:  
Kim, J. et al. Rotation characteristics of main ions and impurity ions in H-mode tokamak plasma. *Physical Review Letters* **72**, 2199 (1994).
- Analysis of local transport in L-and H-mode plasmas:  
Jahns, G.L. et al. Comparison of transport in H- and L-phase discharges in the DIII-D tokamak. *Nuclear Fusion* **29**, 1271 (1989).
- Influence of safety factor on H-mode energy confinement in DIII-D:  
Schissel, D.P. et al. Examination of energy confinement in DIII-D at small values of the plasma safety factor. *Nuclear Fusion* **32**, 107 (1992).
- Off-axis ECR heating experiments exhibiting a negative effective thermal diffusivity:  
Luce, T.C. et al. Inward energy transport in tokamak plasmas. *Physical Review Letters* **68**, 52 (1992).
- Dimensionless scaling of electron and ion transport in L-mode plasmas:  
Petty, C.C. et al. Gyroradius scaling of electron and ion transport. *Physical Review Letters* **74**, 1763 (1995).
- First observation of the VH-mode:  
Jackson, G.L. et al. Regime of very high confinement in the boronized DIII-D tokamak. *Physical Review Letters* **67**, 3098 (1991).
- Confinement and stability properties of VH-modes:  
Osborne, T.H. et al. Confinement and stability of VH mode discharges in the DIII-D tokamak. *Nuclear Fusion* **35**, 23 (1995).
- Observation of enhanced confinement in plasmas with high internal inductance:  
Lao, L.L. et al. High internal inductance improved confinement H-mode discharges obtained with an elongation ramp technique in the DIII-D tokamak. *Physical Review Letters* **70**, 3435 (1993).
- Improved confinement in plasmas with negative central shear:  
Strait, E.J. et al. Enhanced confinement and stability in DIII-D discharges with reversed magnetic shear. *Physical Review Letters* **75**, 4421 (1995).
- High fusion performance in highly shaped negative shear plasmas:  
Lazarus, E.A. et al. Higher fusion power gain with current and pressure profile control in strongly shaped DIII-D tokamak plasmas. *Physical Review Letters* **77**, 2714 (1996).
- Quiescent double barrier regime:  
Greenfield, C.M. et al. Quiescent double barrier regime in the DIII-D tokamak. *Physical Review Letters* **86**, 4544 (2001).
- Studies of vertical stability with plasma elongation up to 2.5:  
Lister, J.B. et al. Experimental study of the vertical stability of high decay index plasmas in the DIII-D tokamak. *Nuclear Fusion* **30**, 2349 (1990).
- Disruption mitigation by high pressure gas injection:  
Whyte, D.G. et al. Mitigation of tokamak disruptions using high-pressure gas injection. *Physical Review Letters* **89**, 55001 (2002).
- Influence of rotation and  $\beta$  on error field modes:  
La Haye, R.J. et al. Non-linear instability to low  $m, n = 1$  error fields in DIII-D as a function of plasma fluid rotation and beta. *Nuclear Fusion* **32**, 2119 (1992).
- Initial experiments achieving  $\beta > 6\%$ :  
Taylor, T.S. et al. Achievement of reactor-relevant  $\beta$  in low-q divertor discharges in the Doublet III-D tokamak. *Physical Review Letters* **62**, 1278 (1989).
- Strait, E.J. et al. MHD instabilities near the  $\beta$  limit in the Doublet III-D tokamak. *Physical Review Letters* **62**, 1282 (1989).
- Influence of current profile on  $\beta$  limit:  
Lao, L.L. et al. Effects of current profile on the ideal ballooning mode. *Physics of Fluids B* **4**, 232 (1992).
- Observation of rotational stabilization of resistive wall mode:  
Strait, E.J. et al. Wall stabilization of high beta tokamak discharges in DIII-D. *Physical Review Letters* **74**, 2483 (1995).
- Garofalo, A.M. et al. Direct observation of the resistive wall mode in a tokamak and its interaction with plasma rotation. *Physical Review Letters* **82**, 3811 (1999).
- Density limit experiments:  
Petrie, T.W. et al. Plasma density limits during ohmic L mode and ELMing H mode operation in DIII-D. *Nuclear Fusion* **33**, 929 (1993).
- Observation of  $q(0) \sim 1$  during sawtooth oscillations:  
Wróblewski, D., Snider, R.T. Evidence of the complete magnetic reconnection during a sawtooth collapse in a tokamak. *Physical Review Letters* **71**, 859 (1993).
- Observation of TAE modes in NBI heated plasmas:  
Heidbrink, W.W. et al. An investigation of beam driven Alfvén instabilities in the DIII-D tokamak. *Nuclear Fusion* **31**, 1635 (1991).

- 100% non inductive current drive with NBI heating:  
 Simonen, T.C. *et al.* Neutral-beam current-driven high-polyoidal-beta operation of the DIII-D tokamak. *Physical Review Letters* **61**, 1720 (1988).
- Measurement of FWCD efficiency:  
 Petty, C.C. *et al.* Fast wave and electron cyclotron current drive in the DIII-D tokamak. *Nuclear Fusion* **35**, 773 (1995).
- First measurements of localized ECCD:  
 Luce, T.C. *et al.* Generation of noninductive current by electron cyclotron waves on the DIII-D tokamak. *Physical Review Letters* **83**, 4550 (1999).
- Experience with various approaches to wall conditioning, including boronization, and operational experience with the advanced divertor were the subject of many presentations at the conferences on plasma surface interactions listed in the bibliography to Chapter 9.
- DIII-D power handling experience:  
 Lasnier, C.J. *et al.* Survey of target plate heat flux in diverted DIII-D tokamak discharges. *Nuclear Fusion* **38**, 1225 (1998).
- Control of density in ELMy steady-state H-modes:  
 Stambaugh, R.D. *et al.* Divertor pumping and other reactor application issues for H-mode. *Plasma Physics and Controlled Fusion* **36**, A249 (1994).
- Control of extrinsic impurities by scrape-off layer flows:  
 Schaffer, M.J. *et al.* Impurity reduction during 'puff and pump' experiments on DIII-D. *Nuclear Fusion* **35**, 1000 (1995).
- Helium exhaust studies in ELMy H-modes:  
 Wade, M.R. *et al.* Helium exhaust studies in H-mode discharges in the DIII-D tokamak using an argon-frosted divertor cryopump. *Physical Review Letters* **74**, 2702 (1995).
- Scrape off-layer transport:**  
 Neuhauser, J. *et al.* Transport into and across the Scrape-off Layer in the ASDEX Upgrade Divertor Tokamak. *Plasma Phys. Controlled Fusion* **44**, 855 (2002).
- Divertor detachment and H-mode behaviour:**  
 Gruber, O. *et al.* Observation of continuous divertor detachment in H-mode discharges in ASDEX Upgrade. *Physical Review Letters* **74**, 4217–4220 (1995).
- Plasma performance with tungsten covered surfaces:**  
 Neu, R. *et al.* New results from the tungsten programme at ASDEX Upgrade. *Journal of Nuclear Materials* **313**, 116 (2003).
- Rohde, V. *et al.* Operation of ASDEX Upgrade with tungsten tiles at the central column. *Controlled Fusion and Plasma Physics (Proceedings of the 27th European Conference, Budapest, 2000)*.
- Confinement and core transport studies:**  
 Ryter, F. *et al.* Confinement and transport studies of conventional scenarios in ASDEX Upgrade. *Nuclear Fusion* **41**, 537–550 (2001).
- Pellet fuelling:**  
 Lang, P. *et al.* High density operation in H mode discharges by inboard launch pellet refuelling. *Nuclear Fusion* **40**, 245–260 (2000).
- H-mode discharges at high density:**  
 Stober, J. *et al.* Optimization of confinement, stability and power exhaust of the elmy H-mode in ASDEX Upgrade. *Plasma Physics Controlled Fusion* **43**, A39–A53 (2001).
- Advanced tokamak discharges and internal transport barrier:**  
 Gruber, O. *et al.* Steady state H mode and  $T_e \gg T_i$  operation with internal transport barrier in ASDEX Upgrade. *Nuclear Fusion* **40**, 1145–1155 (2000).
- Wolf, R. *et al.* Performance heating and current drive scenarios of ASDEX Upgrade advanced tokamak discharges. *Nuclear Fusion* **41**, 1259–1271 (2001).
- Active mhd-mode stabilization:**  
 Zohm, H. *et al.* The physics of neoclassical tearing modes and their stabilisation by ECCD in ASDEX Upgrade. *Nuclear Fusion* **41**, 197–202 (2001).
- Disruption recognition and mitigation:**  
 Pautasso, G. *et al.* Prediction and mitigation of disruptions in ASDEX Upgrade. *Journal of Nuclear Materials* **290–293**, 1045–1051 (2001).

**13**

## **The future**

**13.1****Status**

In Section 1.1 the success of tokamak research was demonstrated in a simple way by presenting a graph showing the progress in achieving values of the parameter  $nT\tau_E$ . It is appropriate here to give a somewhat fuller account using a more precise parameter,  $Q_{DT}$ , together with the plasma temperature.

Recalling from Section 1.5 that  $Q$  is the ratio of the thermonuclear power,  $P_{Th}$ , to the heating power supplied,  $Q_{DT}$  is defined for a deuterium plasma as the value of  $Q$  which would be obtained if half of the deuterium were replaced by tritium at the same density and temperature. In addition to the greatly increased reaction rate there would also be a reduction of the required applied heating power as a result of the contribution from  $\alpha$ -particle heating. Thus the required applied heating power would be reduced from  $P_H$  to  $P_H - P_\alpha$  and so,

$$Q_{DT} = \frac{\frac{1}{4}\overline{n^2(\sigma v)_{DT}}\mathcal{E}V}{P_H - \frac{1}{20}\overline{n^2(\sigma v)_{DT}}\mathcal{E}V}, \quad 13.1.1$$

where  $\mathcal{E} = 17.6$  MeV,  $P_\alpha = \frac{1}{3}P_{Th}$ , the bars indicate spatial averages, and  $V$  is the plasma volume.

The relation of  $Q_{DT}$  to  $nT\tau_E$  is obtained using the energy balance equation,  $P_H = 3\bar{n}\bar{T}V/\tau_E$ , to replace  $P_H$  in eqn 13.1.1. Thns, taking  $n$  and  $T$  to be parabolic with peak values  $\hat{n}$  and  $\hat{T}$

$$Q_{DT} = \frac{1}{1.0 \times 10^{-3} \frac{T^2}{(\sigma v)_{DT}} \frac{1}{(\hat{n}\hat{T}\tau_E)} - \frac{1}{5}}, \quad T \text{ and } \hat{T} \text{ in KeV} \quad 13.1.2$$

$T^2/(\sigma v)$  being a slowly varying function of temperature (see eqn 1.5.4). In Fig. 13.1.1 contours for effective break-even ( $Q_{DT} = 1$ ) and ignition ( $Q_{DT} \rightarrow \infty$ ) are plotted in the  $(\hat{n}\hat{T}\tau_E, \hat{T})$  plane together with the values achieved over the years by a number of tokamaks. This makes clear the experimental progress culminating in  $Q_{DT} \approx 1$ . Furthermore, as described in Chapter 12, experiments using D-T mixtures have produced actual fusion powers of several megawatts. In addition to this direct progress in terms of achieved parameters there has been a vast accumulation of information on the behaviour of tokamak plasmas, the principal aspects of which have formed the content of this book.

Having reached this point in the development of tokamaks the question arises as to how to proceed. This matter is addressed in the remaining sections, where the plans for the future are described.

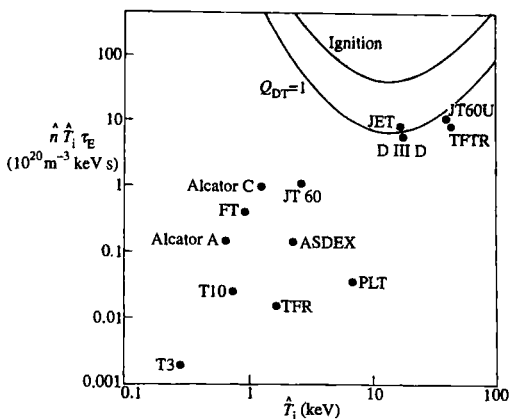


**Fig. 13.1.1** Contours for effective break-even ( $Q_{DT} = 1$ ) and ignition ( $Q_{DT} \rightarrow \infty$ ) in the  $(\hat{n}\hat{T}_i\tau_E, \hat{T}_i)$  plane, together with values obtained in several tokamaks.

## 13.2 Strategy

The successful development of tokamaks over four decades has brought the subject to the point where a reactor is in sight. This is not to say that the case for a commercial reactor has been proven, but rather that the general requirements and features of an experimental reactor can be seen. Of course there are problems and uncertainties, it could not be otherwise. However none of these appear to present insoluble difficulties and it is now necessary to choose the best way forward.

The obvious way to identify the issues to be resolved is to attempt the design of an experimental reactor. In addition to an enumeration of the questions to be answered, such a procedure provides a deeper insight into the true problems.

This was the strategy adopted by the 'fusion community'. It was recognized that the level of support available meant that the sensible way to proceed would be through international collaboration. As a result, an agreement was reached between four partners—the European Community, Japan, the USSR (later the Russian Federation) and the USA. Their decision was to design a tokamak which would ignite and produce fusion power in the GW range. The name given to this tokamak is ITER, the International Thermonuclear Experimental Reactor.

The Conceptional Design Activity (CDA) for ITER was started in 1988 and completed in 1990. This was followed by the Engineering Design

Activity (EDA), carried out on three sites—San Diego in the USA, Naka in Japan, and Garching in Germany which produced a design for ITER in 1998.

The estimated construction cost of ITER was 6 billion (1989) dollars. This cost was found to be unacceptable at the present stage and it was decided to proceed to the design of a less expensive device which would address the same issues at the original design but would not necessarily reach ignition. The target for the new design would be a ratio,  $Q$ , of fusion power to input power of 10 rather than the infinite values of  $Q$  implied by ignition. A further development was the withdrawal of the United States from the partnership in 1998. They rejoined in 2003 together with new partners China and South Korea.

The following sections outline first the design issues and then briefly describe the physics and engineering parameters of both 'Ignition ITER' and 'High- $Q$ -ITER'.

## 13.3

### Reactor requirements

The principal areas which determine the design are

- (1) confinement
- (2) disruptions
- (3) exhaust
- (4) technology

and these will be discussed in turn.

#### Confinement

The influence of confinement on the requirement for an ignited tokamak was discussed in Section 1.7. It was shown there that the plasma current required is  $I = 30/H(\text{MA})$  where  $H$  is the confinement improvement factor over L-mode scaling. This immediately raises the matter of the confidence in the scaling and the practicality of the regimes of enhanced confinement. These are matters of uncertainty and this uncertainty imposes a conservative design, with a current greater than 20 MA.

A new confinement issue arises in a reactor. What happens to the  $\alpha$ -particles produced in the fusion reaction? The  $\alpha$ -particles are confined by the magnetic field, and the number which can be tolerated in the plasma is limited. For a given confined energy each  $\alpha$ -particle reduces the number of reacting deuterons and tritons. The rate of production of  $\alpha$ -particles is given by  $P_\alpha/\delta_\alpha$  where  $P_\alpha$  is the thermonuclear power in the  $\alpha$ -particles and  $\delta_\alpha$  ( $= 3.5 \text{ MeV}$ ) is the energy of each  $\alpha$ -particle. This is equal to the

loss rate  $N_\alpha/\tau_\alpha$  where  $N_\alpha$  is the total number of  $\alpha$ -particles in the plasma and  $\tau_\alpha$  their confinement time. Thus

$$N_\alpha = \frac{P_\alpha \tau_\alpha}{\mathcal{E}_\alpha}. \quad 13.3.1$$

The power is related to the energy confinement time through

$$P_\alpha = \frac{3NT}{\tau_E}, \quad 13.3.2$$

where  $N$  is the total number of electrons and  $\tau_E$  the energy confinement time. Combining eqns 13.2.1 and 13.2.2 gives

$$\frac{N_\alpha}{N} = \frac{3T}{\mathcal{E}_\alpha} \frac{\tau_\alpha}{\tau_E}. \quad 13.3.3$$

For  $T = 14$  keV, eqn 13.3.3 becomes

$$\frac{N_\alpha}{N} = 0.012 \frac{\tau_\alpha}{\tau_E}.$$

The tolerable level of  $N_\alpha/N$  is not a precise figure but it is clear that  $\tau_\alpha$  must not be very much greater than  $\tau_E$ . To keep the  $\alpha$ -particle concentration below 10% requires  $\tau_\alpha \lesssim 8\tau_E$ .

The subject of  $\alpha$ -particle confinement is linked to the general confinement question through the behaviour of impurities in H-modes. It is found that impurities tend to accumulate in the best confined H-mode plasmas and relief is only obtained when the confinement is reduced by ELM activity. There is therefore a conflict between the requirement of good confinement and the need to minimize impurities and to expel  $\alpha$ -particles.

### Disruptions

Disruptions have three types of implication for a reactor. In the first place the existence of disruptions limits the operating space. In the second they give rise to large forces in the vacuum vessel and other components as discussed in Section 7.9. Thirdly there is the question, particularly for the longer term, as to the extent to which disruptions can be avoided.

In present tokamaks disruptions limit the edge density and the edge value of  $q$ . The low  $q$  limit is around  $q_{95} = 2$  and this limit can be avoided by operating at a value which leaves a margin of safety, say  $q_{95} = 3$ .

It is possible therefore, by choosing the operating conditions, to avoid systematic disruptions. However, in practice disruptions also occur away from the operation boundaries. These disruptions are usually due to an unsatisfactory time development of the profiles and, with care, can be avoided. A further type of disruption often results when there is a vertical plasma displacement following the loss of feedback control of the vertical instability described in Section 7.12. Other disruptions are due to

transient impurity influx or falling fragments of solid material. Whether such disruptions can be completely avoided is at present a matter for conjecture.

The effect of  $q$  constraints was discussed in Section 1.7 where the approximate requirement  $RB_\varphi \gtrsim (65/H)$  mT was obtained. Thus a toroidal magnetic field in the plasma of 6T implies a major radius of 9m for a confinement enhancement factor of one, and a proportionately smaller radius as  $H$  is increased.

### Exhaust

The problem of heat exhaust arises from the need to unload the  $\alpha$ -particle heating. The  $\alpha$ -particle heating amounts to 20% of the fusion power and, being deposited in the plasma, must be transmitted to material surfaces outside the plasma. These can, in principle, be either surfaces facing the main plasma or surfaces within a divertor system. The requirement of minimizing the introduction of impurities into the plasma seems to favour the divertor solution.

However the divertor is subject to a severe difficulty arising from the narrowness of the scrape-off layer channel which transmits an enormous heat flux density to the divertor.

The heat flux into the scrape-off layer, per unit toroidal length, can be written

$$h \simeq -2\pi a n \chi \frac{dT}{dr} \simeq \frac{2\pi a n \chi T}{\lambda}, \quad 13.3.4$$

where  $\lambda$  is the scrape-off layer thickness. This must equal the heat flux along the scrape-off layer to the divertor, which can be written

$$h \simeq 3nT \left( \frac{a}{L} c_s \right) \lambda, \quad 13.3.5$$

where  $L$  is the connection length along the magnetic field and  $c_s$  is the sound speed. The quantity  $(a/L)c_s$  can be thought of as the component of the parallel flow speed in the poloidal plane. From eqns 13.3.4 and 13.3.5 the scrape-off thickness is given by

$$\lambda \simeq \left( \frac{2\chi L}{c_s} \right)^{1/2}. \quad 13.3.6$$

For  $L = 30$  m,  $\chi = 2 \text{ m}^2 \text{s}^{-1}$  and  $c_s = 10^5 \text{ m s}^{-1}$  the scrape-off layer thickness  $\lambda \sim 3$  cm.

Taking 3 GW of fusion power the thermal heat flux is 600 MW. Thus for a toroidal circumference of 50 m and hence a scrape-off area of  $2 \times 50 \times 0.03 \text{ m}^2 = 3 \text{ m}^2$ , the power load would be  $200 \text{ MW m}^{-2}$ . This is a completely unacceptable power load to a material surface and presents a major design problem for a reactor. Possible sources of amelioration are inclined surfaces which spread the load, plasma radiation to reduce the surface heating, and the use of a gas target to protect the material surface.

by diffusing the heat flux. A further problem is the erosion of heat loaded surfaces as a result of sputtering and evaporation.

### Technology

The first wall will need to be maintained at a temperature around 600 °C, and to receive and survive the neutron flux associated with a GW power level. The blanket will have a cooling system to remove the deposited power and must have a tritium breeding capability with an associated tritium handling system.

To avoid the unacceptable ohmic heating losses of normal conductors the toroidal field coils must be superconducting with a magnetic field in the coil  $\sim 13$  T. Even higher fields have been proposed. The production of massive coils with these properties has required substantial development. The coils must carry the large magnetic stresses of normal operation and also be able to accept the transient forces which would arise from a disruption.

The plasma current must be maintained, preferably in a steady state but possibly for long pulses. Steady state current drive would require an RF system. This would have to be supplied with electrical power and the consequent recirculating power fraction constitutes a drain on the efficiency of the reactor. However, the current drive requirement can be much reduced by the existence of the internally driven bootstrap current.

Many components of the reactor will require control systems. The plasma position is intrinsically unstable and requires feedback control, and the fuelling must be adjusted to control the burning plasma. Furthermore a wide range of systems need to be monitored and fault control systems need to be installed to reduce the effect of unplanned events such as disruptions.

During the ITER engineering design phase there has been a large amount of technology development with the production of prototypes of all the major components and their maintenance systems. Although designed specifically for ITER, these prototypes demonstrate the viability of fusion technology more generally.

**Table 13.4.1** Principal parameters of the Outline Design for Ignition ITER. The values of fusion power and burn time are nominal values

Fusion power	1.5 GW
Burn time	1000 s
Plasma current	21 MA
Major radius	8.14 m
Plasma minor radius	2.8 m
Elongation	1.6
Divertor	Single null
Toroidal field (at major radius)	5.7 T
Toroidal field ripple at edge	±2%

The guiding design principles were (i) to minimize the number of components, (ii) to simplify each component, (iii) to increase the reliability of key systems, (iv) to design for intrinsic safety and flexibility, and (v) to favour reactor relevant technologies.

The principal design parameters of Ignition ITER are set out in Table 13.4.1 and drawings of the layout are given in Figs 13.4.1 and 13.4.2.

In the design, the toroidal field is produced by 20 superconducting coils. The field at the coils is 13 T and this would require niobium-tin technology. To limit the nuclear heating and insulation degradation in the coils the minimum thickness of the blanket-shield and vacuum vessel is ~1.3 m.

Some additional heating would be required to reach ignition, and around 100 MW was planned, the type of heating not being decided. At ignition the plasma would have an average temperature ~10 keV and a density  $\sim 10^{20} \text{ m}^{-3}$ .

The nominal fusion power was 1.5 GW. For stationary burn conditions with ~15%. He ash the D-T burn-up rate was  $\sim 10 \text{ mg s}^{-1}$ . The fusion power level would be feedback controlled through a combination of the fuel input rate, the auxilliary heating and the helium pumping rate. Possible fuel injection methods include a shallow pellet injection and gas fuelling.

The confinement required for sustained ignition was within that predicted by the H-mode scaling law.

It would be necessary to design a divertor which would reduce the steady power flux to solid surfaces to below  $10 \text{ MW m}^{-2}$ . It was thought that this could be achieved by arranging that the energy exhaust along the scrape-off layer terminated in a cold dense plasma cooled by line radiation and interaction with a neutral gas. The concepts involved required further development and the problem of transient heat pulses, arising for example from mhd instabilities, needed to be addressed.

The efficiency of current drive techniques in the high density operation of ITER is low and only a few MA could be driven by this means. A current drive scenario would only be of value if it were associated with a low

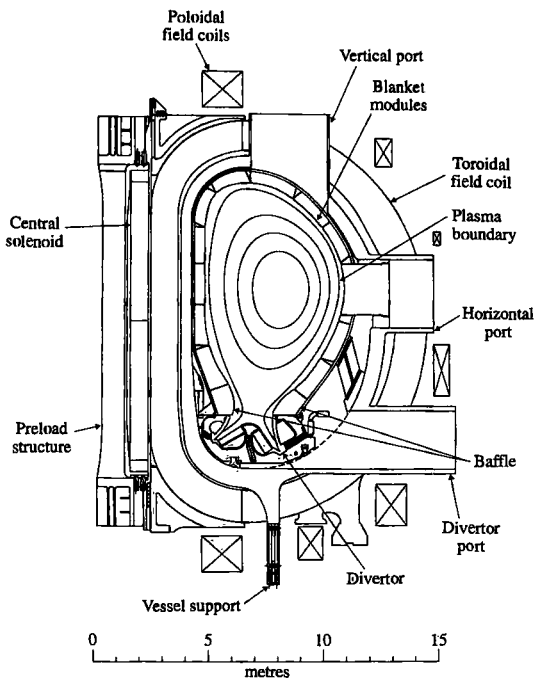


Fig. 13.4.1 Cross-sectional drawing showing the major components of Ignition ITER.

**Table 13.4.2 Ignition ITER Outline Design estimated construction costs (1989 million dollars)**

Superconducting magnet systems	1910
Vacuum vessel, blanket, divertor	760
Cryostat, cryoplant, vacuum and heat transport	640
Heating, fuelling, power supply and other plant	1090
Building and structures	1040
Assembly equipment and assembly	430
<b>TOTAL</b>	<b>5870</b>

plasma current, with a high beta poloidal providing a large bootstrap current.

Remote handling would be required for three types of operation, (i) planned introduction of a new component, (ii) renewal of components

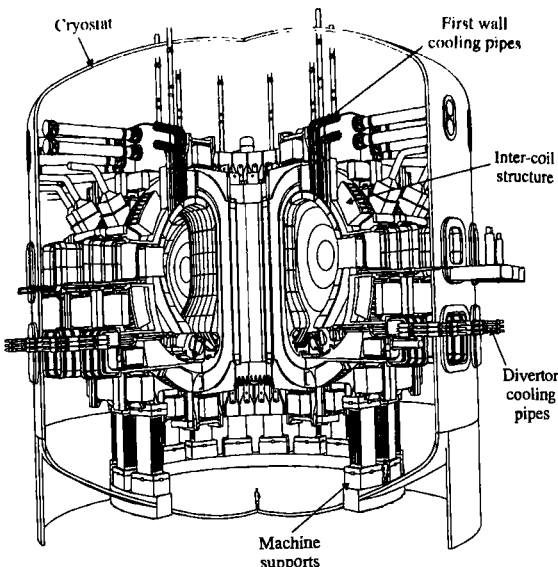


**Fig. 13.4.2** Drawing giving an overall view of the layout of Ignition ITER.

eroded by the plasma, and (iii) repair of faults. This last requirement should be minimized by high reliability components and duplication of vulnerable components with difficult access.

The estimated costs are summarized in Table 13.4.2.

### High- $Q$ ITER

The design of High- $Q$  ITER did not preclude the possibility of ignition but the objective was that the device should achieve extended burn with a ratio of fusion power to auxiliary heating power of at least 10 and with a duration sufficient to reach stationary conditions on the characteristic timescales of the plasma. The design also aims at demonstrating steady-state operation using non-inductive current drive with  $Q > 5$ .

On the engineering side the device would demonstrate the implementation of superconducting coils and remote maintenance. It would also test components for a future reactor and explore tritium breeding concepts. The plasma performance requirements call for an inductively driven flat-top current capability during burn of 300–500 s. To carry out nuclear and high heat flux testing requires an average neutron power load on the first wall of  $0.5 \text{ MW m}^{-2}$ . It is envisaged that the device would operate over a period of approximately 20 years with up to 30,000 pulses.

Much sophistication has gone into assessing the requirements for achieving  $Q = 10$ . However it is possible to illustrate the basic analysis using the simple model introduced in Section 1.5. Thus, the definition

$$Q = \frac{\frac{1}{4}n^2(\sigma v)\mathcal{E}V}{P_H}$$

and the power balance equation 1.5.7 for  $P_H$  give

$$Q = \frac{5}{\frac{60T}{n\tau_E(\sigma v)\mathcal{E}} - 1}. \quad 13.4.1$$

With the approximation for  $(\sigma v)$  given by eqn 1.5.4 and the allowance for plasma profiles used in Section 1.5, eqn 13.4.1 becomes

$$Q = \frac{5}{\frac{5 \times 10^{21}}{\hat{n}\hat{T}\tau_E} - 1} \quad \hat{T} \text{ in keV} \quad 13.4.2$$

giving ignition,  $Q \rightarrow \infty$ , at  $\hat{n}\hat{T}\tau_E = 5 \times 10^{21} \text{ m}^{-3} \text{ keVs}$ .

Equation 13.4.2 specifies the confinement time required at a given  $\hat{n}$  and  $\hat{T}$  to achieve the desired  $Q$ . The target value of  $Q = 10$  calls for an  $\hat{n}\hat{T}\tau_E$  value which is 2/3 of that needed for ignition. Using the large amount of data on the scaling of energy confinement time it was decided that to achieve  $Q = 10$  would require a plasma current of 15 MA. The principal design parameters are set out in Table 13.4.3.

**Table 13.4.3** Principal parameters for High- $Q$  ITER

Fusion power	500 MW
Burn time	$\geq 400$ s
Plasma current	15 MA
Major radius	6.2 m
Plasma minor radius	2.0 m
Elongation	1.70/1.85
Plasma volume	$837 \text{ m}^3$
Toroidal field	5.3 T at major radius 12 T on conductor
Heating/current drive power	73 MW (up to 110 MW)

The device has superconducting coils, the toroidal field coils and central solenoid using niobium-tin cooled to 4.5 K by supercritical helium and the poloidal field coils using niobium-titanium. The single null divertor is made of tungsten with carbon plasma-facing components. The water cooling system is designed to extract 750 MW of heat and the entire tokamak is enclosed in a cryostat. Plasma fueling is provided by gas injection and solid hydrogen pellets.

The shielding blanket is divided into two parts. The front part has 1 cm thick beryllium armour, 1 cm thick copper to diffuse heat, and around 5 cm of steel. The back part is a 35 cm thick shield made of steel and water.

It is planned that once the flat top current is reached, with an inductively driven current of 15 MA, subsequent fuelling and plasma heating for  $\sim 100$  s will produce a high- $Q$  D-T run with a fusion power of 500 MW. Then with non-inductive current drive the burn duration is envisaged to be extended to 1 hour.

Figures 13.4.3 gives a cross-sectional drawing showing the major components of High- $Q$  ITER and Fig. 13.4.4 gives an overall view.

The estimated costs are summarized in Table 13.4.4 which uses 1989 dollars to facilitate a comparison with the expected cost of Ignition ITER. The 2755 million (1989) dollar cost of High- $Q$  ITER is about half that of Ignition ITER. Using an inflation factor of 1.39 for 1989/2000 gives a cost estimate in year 2000 prices of 3829 million dollars.

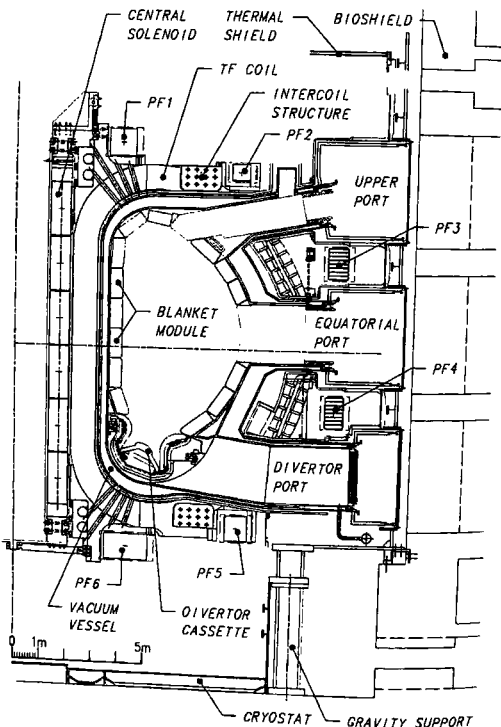


**Fig. 13.4.3** Cross-sectional drawing showing the main components of High- $Q$  ITER. PF and TF refer to the poloidal and toroidal field coils.

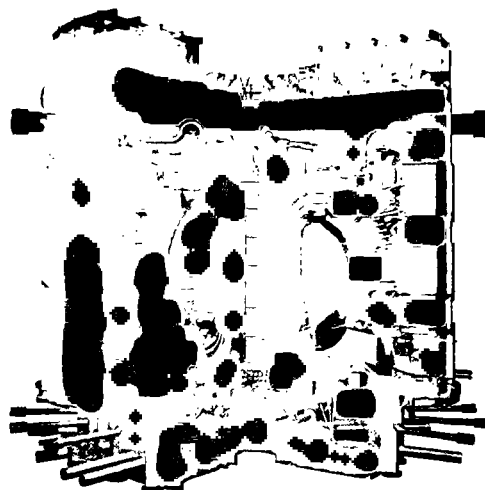


Fig. 13.4.4 Cutaway view of High-*Q* ITER.

**Table 13.4.4** Estimated capital costs of High-*Q* ITER (million (1989) dollars).

Magnet systems	762
Vacuum vessel, blanket, divertor	471
Other core components	139
Assembly	93
	1465
Buildings	380
Power supplies	215
Cooling water systems	131
Cryoplant	89
Other auxiliaries	101
	916
Heating and current drive	206
Diagnostics and CODAC	168
TOTAL	2755



**Fig. 13.4.4** Cutaway view of High-*Q* ITER.

**Table 13.4.4** Estimated capital costs of High-*Q* ITER (million (1989) dollars).

Magnet systems	762
Vacuum vessel, blanket, divertor	471
Other core components	139
Assembly	93
	1465
Buildings	380
Power supplies	215
Cooling water systems	131
Cryoplant	89
Other auxiliaries	101
	916
Heating and current drive	206
Diagnostics and CODAC	168
<b>TOTAL</b>	<b>2755</b>

## 13.5

## Prospects

### Power plant

In moving from ITER to a demonstration power-plant, the main step will be the integration of the physics and technology developments. Most of the physics issues will be the same as in ITER with limited extrapolation, but the issues of operating continuously, or semi-continuously will come to the fore. A power plant must produce power most of the time, not in pulses interspersed by significant downtime. This factor would already have been explored in ITER but will become very important in demonstrating fusion's ability to produce electricity in a dependable way. In a tokamak power plant this will require either an efficient form of current drive, which looks feasible but remains to be adequately demonstrated, or operation in long pulses with a high duty cycle.

The main technology development will be the use of a full power-plant blanket. This will perform the dual function of generating tritium for use in the plasma (through the transmutation of lithium) and providing the structure containing the coolant which carries the heat away to generate electricity. Although tests will inevitably be carried out in advance, this will be the real demonstration of the integration of blanket technology in the environment characteristic of a fusion power plant.

The step to a demonstration power plant is a key one, which must combine all the developments in establishing, sustaining, and controlling plasmas, with all the technology of superconducting magnets, power handling, and tritium generation. This must be achieved without compromising the passive safety features and good environmental properties that can be achieved in a fusion power plant, and must still allow the power to be generated in an economically viable way. Conceptual designs of such power plants exist and appear to be feasible, however it will only be by building such a device that the establishment of fusion power as a commercial reality will be established. This remains a goal for the future—the near term goal for the development of fusion power is the building of ITER or a similar device with a high power gain.

In considering the various power producing systems available additional weight is now given to the potential harm to future generations resulting from the deterioration that they may cause to the natural environment. This supports the development of future energy supplies with reduced levels of pollution. The present trend in the future energy market towards lower polluting, more sustainable energy sources lends support to the need for fusion research.

Estimates of the costs of a future power plant, use conceptual designs based on our present knowledge, making some allowance for

developments that are foreseen in the coming decades. The likely errors will result from unexpected technological developments, for instance the development of a cheap, room-temperature superconductor which could be used for the magnets, seen at present to be the biggest single cost item in a fusion power plant. However, using conventional materials in the designs, it should be possible to make reasonable estimates of the costs. In practice, it seems most sensible to consider a range of power plant designs, with different degrees of assumed developments, to give a likely range for the cost of electricity. This approach is supported by looking at the cost of electricity around the world at the present day, which shows variations by a factor of more than two between countries even when the same technology is employed. Since the present cost of electricity lies in such a wide range, it does not seem reasonable to expect a single figure for a future cost of electricity of a power source that is still under development.

The costing of conceptual fusion power plants gives, as expected, different results in different countries. The overall outcome, however, is that fusion costs lie in a range comparable to the range for projections for other power sources. This means that, using present conceptual designs, fusion is not ruled out on the basis of costs.

An alternative view of the economics of fusion can be gained from looking at the development of the cost of experimental devices. Although these will tend to be high because they are one-off devices with high levels of diagnostics, they give an indication of the level of costs to be expected. This approach suggests that a prototype plant in the gigawatt range will have a commercially acceptable cost.

### Outlook

The development of fusion power is at an important decision point where the commitment to move to a next generation of experiment is required. With the prospect of fusion as an energy source coming closer to technical demonstration, the role that fusion could play in the future energy market becomes an important issue.

Although commercial viability will depend primarily on the direct costs of fusion, the market in which fusion would have to compete is uncertain. Increasing weight is being given to the external costs of energy generation associated with safety and environmental issues, and these will move market conditions favourably for fusion.

Overall the potential value of a future energy option, capable of supplying a large fraction of mankind's energy needs, is so high that it would seem unwise to neglect it. Rather, the potential for success and the potential rewards should be used as input to determine the level of expenditure that is justified. Expenditure on energy research and development is a very small fraction of the total energy spend, and so seems to be clearly justifiable. Since it appears likely that the option of a power source for future generations can be secured without excessive cost, the sensible choice is to press ahead.

## Bibliography

---

A description of Ignitor ITER is given in Technical basis for the ITER interior design report, cost review and safety analysis; ITER EDA Documentation Series No. 7, IAEA, Vienna, 1996.

High-Q ITER is described in ITER Design Activities Summary of the ITER Final Design Report, ITER EDA Documentation Series No. 22 IAEA, Vienna 2001.

**14**

# **Appendix**

**14.1****Vector relations**

- (1)  $\mathbf{A} \cdot (\mathbf{B} \times \mathbf{C}) = \mathbf{B} \cdot (\mathbf{C} \times \mathbf{A}) = \mathbf{C} \cdot (\mathbf{A} \times \mathbf{B})$
- (2)  $\mathbf{A} \times (\mathbf{B} \times \mathbf{C}) = (\mathbf{A} \cdot \mathbf{C})\mathbf{B} - (\mathbf{A} \cdot \mathbf{B})\mathbf{C}$
- (3)  $\nabla \cdot (\phi \mathbf{A}) = \phi \nabla \cdot \mathbf{A} + \mathbf{A} \cdot (\nabla \phi)$
- (4)  $\nabla \times (\phi \mathbf{A}) = \phi \nabla \times \mathbf{A} + (\nabla \phi) \times \mathbf{A}$
- (5)  $\nabla \cdot (\mathbf{A} \times \mathbf{B}) = \mathbf{B} \cdot \nabla \times \mathbf{A} - \mathbf{A} \cdot \nabla \times \mathbf{B}$
- (6)  $\nabla(\mathbf{A} \cdot \mathbf{B}) = \mathbf{A} \times (\nabla \times \mathbf{B}) + (\mathbf{A} \cdot \nabla) \mathbf{B} + \mathbf{B} \times (\nabla \times \mathbf{A}) + (\mathbf{B} \cdot \nabla) \mathbf{A}$
- (7)  $\nabla \times (\mathbf{A} \times \mathbf{B}) = \mathbf{A}(\nabla \cdot \mathbf{B}) - \mathbf{B}(\nabla \cdot \mathbf{A}) - (\mathbf{A} \cdot \nabla) \mathbf{B} + (\mathbf{B} \cdot \nabla) \mathbf{A}$
- (8)  $\nabla \times (\nabla \times \mathbf{A}) = \nabla(\nabla \cdot \mathbf{A}) - \nabla^2 \mathbf{A}$
- (9)  $\nabla \cdot (\nabla \phi) = 0$
- (10)  $\nabla \cdot (\nabla \times \mathbf{A}) = 0.$

In cylindrical coordinates the components of  $(\mathbf{A} \cdot \nabla) \mathbf{B}$  are

$$(\mathbf{A} \cdot \nabla \mathbf{B})_r = \mathbf{A} \cdot \nabla B_r - \frac{A_\theta B_\theta}{r}$$

$$(\mathbf{A} \cdot \nabla \mathbf{B})_\theta = \mathbf{A} \cdot \nabla B_\theta + \frac{A_\theta B_r}{r}$$

$$(\mathbf{A} \cdot \nabla \mathbf{B})_z = \mathbf{A} \cdot \nabla B_z.$$

$$\text{Gauss' Theorem: } \int \nabla \cdot \mathbf{A} \, d\tau = \int \mathbf{A} \cdot dS$$

where  $dS$  is outward from the volume  $\tau$  and normal to the bounding surface  $S$ .

$$\text{Stoke' Theorem: } \int (\nabla \times \mathbf{A}) \cdot dS = \int \mathbf{A} \cdot dl$$

where  $dl$  is along the curve bounding the surface  $S$ .

$$\text{Green's Theorem: } \int (u \nabla^2 v - v \nabla^2 u) \, d\tau = \int (u \nabla v - v \nabla u) \cdot dS.$$

**14.2****Differential operators**

In an orthogonal coordinate system with coordinates  $u_1$ , and  $u_2$ , and  $u_3$ , the line element  $ds$  is given by

$$ds^2 = h_1^2 du_1^2 + h_2^2 du_2^2 + h_3^2 du_3^2$$

and if the unit vector is  $i$

$$\nabla \phi = \frac{1}{h_1} \frac{\partial \phi}{\partial u_1} i_1 + \frac{1}{h_2} \frac{\partial \phi}{\partial u_2} i_2 + \frac{1}{h_3} \frac{\partial \phi}{\partial u_3} i_3$$

$$\nabla \cdot A = \frac{1}{h_1 h_2 h_3} \left[ \frac{\partial}{\partial u_1} (h_2 h_3 A_1) + \frac{\partial}{\partial u_2} (h_3 h_1 A_2) + \frac{\partial}{\partial u_3} (h_1 h_2 A_3) \right]$$

$$\nabla \times A = \frac{1}{h_2 h_3} \left[ \frac{\partial}{\partial u_2} (h_3 A_3) - \frac{\partial}{\partial u_3} (h_2 A_2) \right] i_1$$

$$+ \frac{1}{h_3 h_1} \left[ \frac{\partial}{\partial u_3} (h_1 A_1) - \frac{\partial}{\partial u_1} (h_3 A_3) \right] i_2$$

$$+ \frac{1}{h_1 h_2} \left[ \frac{\partial}{\partial u_1} (h_2 A_2) - \frac{\partial}{\partial u_2} (h_1 A_1) \right] i_3$$

$$\nabla^2 \phi = \frac{1}{h_1 h_2 h_3} \left[ \frac{\partial}{\partial u_1} \left( \frac{h_2 h_3}{h_1} \frac{\partial \phi}{\partial u_1} \right) + \frac{\partial}{\partial u_2} \left( \frac{h_3 h_1}{h_2} \frac{\partial \phi}{\partial u_2} \right) \right.$$

$$\left. + \frac{\partial}{\partial u_3} \left( \frac{h_1 h_2}{h_3} \frac{\partial \phi}{\partial u_3} \right) \right].$$

In cylindrical coordinates  $r, \theta, z$ ,

$$ds^2 = dr^2 + r^2 d\theta^2 + dz^2$$

$$\nabla \phi = \frac{\partial \phi}{\partial r} i_r + \frac{1}{r} \frac{\partial \phi}{\partial \theta} i_\theta + \frac{\partial \phi}{\partial z} i_z$$

$$\nabla \cdot A = \frac{1}{r} \frac{\partial}{\partial r} (r A_r) + \frac{1}{r} \frac{\partial A_\theta}{\partial \theta} + \frac{\partial A_z}{\partial z}$$

$$\nabla \times A = \left( \frac{1}{r} \frac{\partial A_z}{\partial \theta} - \frac{\partial A_\theta}{\partial z} \right) i_r + \left( \frac{\partial A_r}{\partial z} - \frac{\partial A_z}{\partial r} \right) i_\theta$$

$$+ \left( \frac{1}{r} \frac{\partial}{\partial r} (r A_\theta) - \frac{1}{r} \frac{\partial A_r}{\partial \theta} \right) i_z$$

$$\nabla^2 \phi = \frac{1}{r} \frac{\partial}{\partial r} \left( r \frac{\partial \phi}{\partial r} \right) + \frac{1}{r^2} \frac{\partial^2 \phi}{\partial \theta^2} + \frac{\partial^2 \phi}{\partial z^2}.$$

**14.3****Units—conversions**

Physical quantity	Symbol	m.k.s. unit	Conversion factor —multiply→ ←divide—	Gaussian unit (c.g.s.)
Capacitance	<i>C</i>	farad (F)	$9 \times 10^{11}$	cm
Charge	<i>q</i>	coulomb (C)	$3 \times 10^9$	statcoulomb
Electrical conductivity	<i>σ</i>	ohm <sup>-1</sup> m <sup>-1</sup>	$9 \times 10^9$	sec <sup>-1</sup>
Current	<i>I</i>	ampere (A)	$3 \times 10^9$	statampere
Electric field	<i>E</i>	volt m <sup>-1</sup>	$\frac{1}{3} \times 10^{-4}$	statvolt cm <sup>-1</sup>
Electric potential	<i>ϕ</i>	volt (V)	$\frac{1}{3} \times 10^{-2}$	statvolt
Energy	<i>W</i>	joule (J)	$10^7$	erg
Force	<i>F</i>	newton (N)	$10^5$	dyne
Inductance	<i>L</i>	henry (H)	$\frac{1}{9} \times 10^{-11}$	sec <sup>2</sup> cm <sup>-1</sup>
Magnetic field	<i>B</i>	tesla (T)	$10^4$	gauss
Magnetic flux	<i>Φ</i>	weber (Wb)	$10^8$	maxwell
Magnetic intensity	<i>H</i>	ampere m <sup>-1</sup>	$4\pi \times 10^{-3}$	oersted
Power	<i>P</i>	watt (W)	$10^7$	erg sec <sup>-1</sup>
Pressure	<i>p</i>	pascal (Pa)	$10$	dyne cm <sup>-2</sup>
Resistance	<i>R</i>	ohm ( $Ω$ )	$\frac{1}{9} \times 10^{-11}$	sec cm <sup>-1</sup>
Resistivity	$η$	ohm m	$\frac{1}{9} \times 10^{-9}$	sec
Thermal conductivity	<i>K</i>	m <sup>-1</sup> s <sup>-1</sup>	$10^{-2}$	cm <sup>-1</sup> sec <sup>-1</sup>
Thermal diffusivity	<i>X</i>	m <sup>2</sup> s <sup>-1</sup>	$10^4$	cm <sup>2</sup> sec <sup>-1</sup>
Vector potential	<i>A</i>	weber m <sup>-1</sup>	$10^6$	gauss cm
Viscosity-dynamic	$η$	kg m <sup>-1</sup> s <sup>-1</sup>	$10$	poise
Viscosity-kinematic	<i>v</i>	m <sup>2</sup> s <sup>-1</sup>	$10^4$	cm <sup>2</sup> sec <sup>-1</sup>
Voltage	<i>V</i>	volt (V)	$\frac{1}{3} \times 10^{-2}$	statvolt

Value expressed in m.k.s. units × conversion factor = value expressed in Gaussian units.

$$1 \text{ pascal} = 1 \text{ N m}^{-2}$$

$$1 \text{ millibar (mb)} = 100 \text{ N m}^{-2}$$

$$\text{Atmospheric pressure} = 1013 \text{ mb} = 1.013 \times 10^5 \text{ N m}^{-2}$$

(760 mm Hg, } 0^\circ\text{C})

$$\begin{aligned} 1 \text{ torr} &= \text{pressure at } 1 \text{ mm Hg} \\ &= \frac{1}{760} \text{ atmospheric pressure} \\ &= 133 \text{ N m}^{-2} \end{aligned}$$

**14.4****Physical constants**

Electron charge	$e$	$1.6022 \times 10^{-19}$ coulomb
Electron mass	$m_e$	$9.1096 \times 10^{-31}$ kg
Proton mass	$m_p$	$1.6726 \times 10^{-27}$ kg
Velocity of light	$c$	$2.9979 \times 10^8$ m s <sup>-1</sup>
Planck's constant	$h$	$6.626 \times 10^{-34}$ joule s
Proton-electron mass ratio	$m_p/m_e$	1836.1
Fine structure constant	$e^2/2\epsilon_0 hc$	1/137.04
Classical electron radius	$e^2/4\pi\epsilon_0 m_e c^2$	$2.817 \times 10^{-15}$ m
Gravitational acceleration	$g$	$9.807$ m s <sup>-2</sup>
Boltzmann's constant	$k$	$1.3806 \times 10^{-23}$ joule K <sup>-1</sup>
1 electron volt (eV)		$1.6022 \times 10^{-19}$ joule
1 eV temperature		$1.1605 \times 10^4$ K
1 joule		$0.6241 \times 10^{19}$ eV
Energy of electron rest mass		0.511 MeV
Atomic mass unit		$1.6605 \times 10^{-27}$ kg
$\mu_0$		$4\pi \times 10^{-7}$ N m <sup>-1</sup>
$\epsilon_0$		$8.854 \times 10^{-12}$ F m <sup>-1</sup>
$\mu_0\epsilon_0 c^2$		1
Atmospheric particle density (760 mm Hg, 0°C)		$2.69 \times 10^{25}$ m <sup>-3</sup>

**14.5****Coulomb logarithm**

The classical Coulomb logarithm arises from the integral over collision impact parameters as described in Section 2.8. With a Coulomb potential the integral diverges at large impact parameters, but Debye shielding removes the divergence by effectively removing collisions for impact parameters greater than the Debye length  $\lambda_D$ . The resulting form of  $\ln \Lambda$  is

$$\ln \Lambda = \int_0^{\lambda_D} \frac{r \, dr}{r_0^2 + r^2} \quad 14.5.1$$

where

$$r_0 = \frac{e_1 e_2}{4\pi\epsilon_0 \mu v^2}$$

$e_1$  and  $e_2$  being the charges of the colliding particles and  $\mu$  their reduced mass,  $m_1 m_2 / (m_1 + m_2)$ . Thus

$$\ln \Lambda = \frac{1}{2} \ln(1 + (r/r_0)^2) \Big|_0^{\lambda_D}$$

and since  $r_0 \ll \lambda_D$ ,

$$\ln \Lambda = \ln \frac{\lambda_D}{r_0}. \quad 14.5.2$$

Introducing the temperature through

$$\frac{1}{2} \mu v^2 = \frac{3}{2} T \quad 14.5.3$$

the expressions required for eqn 14.5.2 are

$$\lambda_D = \left( \frac{\epsilon_0 T}{n_e e^2} \right)^{1/2}, \quad r_0 = \frac{e_1 e_2}{12\pi \epsilon_0 T}.$$

However, under some circumstances quantum mechanical effects intervene and modify  $\ln \Lambda$ . In tokamaks this principally affects collisions involving electrons. The numerical consequences of the modification will be discussed first and then a brief description of the nature of the quantum mechanical effect will be given.

Equation 14.5.2 is changed if  $r_0$  is less than  $\lambda_{qm}/2\pi$  where  $\lambda_{qm}$  is the de Broglie wavelength given by

$$\lambda_{qm} = \frac{\hbar}{\mu v}.$$

This occurs for

$$\frac{v}{c} \gtrsim |Z_1 Z_2| \alpha \quad 14.5.4$$

where  $Z_1 = e_1/e$ ,  $Z_2 = e_2/e$  and the fine structure constant

$$\alpha = \frac{e^2}{2\epsilon_0 h c} = \frac{1}{137}.$$

Using relation 14.5.3, the condition 14.5.4 for the applicability of the classical formula for singly charged particles becomes

$$T \lesssim \frac{\mu c^2}{5 \times 10^4}.$$

Since the rest mass energy of electron,  $m_e c^2$ , is 0.5 MeV the critical temperature for collisions involving electrons is  $\sim 10$  eV, so that for temperatures of interest the quantum mechanical correction is necessary. For ions the critical temperature is about 10 keV for protons and is correspondingly higher for higher masses. For present purposes therefore any quantum mechanical correction for ion-ion collisions will be small and

consequently it is usually adequate to use the classical formula for ion-ion collisions. Precise calculations for these cases lead to the following formulas:

*electron-electron collisions*

$$\ln \Lambda = 14.9 - \frac{1}{2} \ln(n_e/10^{20}) + \ln T_e, \quad T_e \text{ in keV}$$

*electron-ion collisions ( $T \gtrsim 10 \text{ eV}$ )*

$$\ln \Lambda = 15.2 - \frac{1}{2} \ln(n_e/10^{20}) + \ln T_e, \quad T_e \text{ in keV}$$

*ion-ion collisions (singly charged ions,  $T \lesssim 10(m_i/m_p) \text{ keV}$ )*

$$\ln \Lambda = 17.3 - \frac{1}{2} \ln(n_e/10^{20}) + \frac{3}{2} \ln T, \quad T \text{ in keV.}$$

Values of  $\ln \Lambda$  for electron-ion collisions are given in Fig. 14.5.1. Given the low level of accuracy which is generally possible in plasma physics it is usually inappropriate to take account of the slow variation of  $\ln \Lambda$  with  $n$  and  $T$ . The value  $\ln \Lambda = 17$  is accurate for electron-ion collision to within 10% between  $n_e = 2 \times 10^{18} \text{ m}^{-3}$  and  $2 \times 10^{21} \text{ m}^{-3}$  at  $T = 5 \text{ keV}$ , and between  $T = 600 \text{ eV}$  and  $18 \text{ keV}$  for  $n_e = 3 \times 10^{19} \text{ m}^{-3}$ .

To see the relation between the classical and quantum mechanical cases it is convenient to rewrite eqn 14.5.1 in terms of the scattering angle  $\chi$

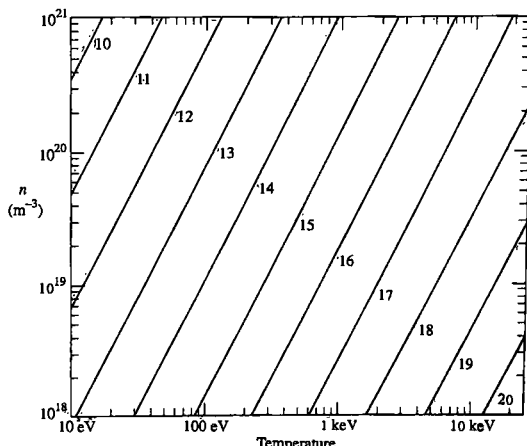


Fig. 14.5.1 Values of the Coulomb logarithm,  $\ln \Lambda$ , for electron-ion collisions plotted against electron density and temperature.

## 14.5 Coulomb logarithm

which, classically, is related to the impact parameter by

$$\sin^2 \chi/2 = \frac{r_0^2}{r^2 + r_0^2}.$$

Thus classically

$$\ln \Lambda = \int_{(r_0/\lambda_D)^2}^1 \frac{d \sin^2 \chi/2}{2 \sin^2 \chi/2}.$$

Turning now to the quantum mechanical behaviour, the first point to note is that (ignoring spin) the quantum mechanical and classical differential cross-sections for Coulomb collisions are the same. The difference arises through the effect of Debye shielding, the Debye shielded potential taking the form

$$\phi \sim \frac{e^{-r/\lambda_D}}{r}.$$

For the collision to appear classical it requires that the uncertainty,  $\Delta \chi$ , in scattering angle be much less than the scattering angle itself

$$\Delta \chi \ll \chi \quad 14.5.5$$

and the uncertainty in position,  $\Delta r$ , be much less than the impact parameter

$$\Delta r \ll r. \quad 14.5.6$$

Writing  $\Delta \chi = \Delta p_\perp / p$  and  $\chi = \delta p_\perp / \rho$ , where  $\Delta p_\perp$  is the uncertainty and  $\delta p_\perp$  is the change in transverse momentum, inequality 14.5.5 becomes  $\Delta p_\perp \ll \delta p_\perp$ , that is

$$\Delta p_\perp \ll 2\mu\nu \frac{rr_0}{r^2 + r_0^2}. \quad 14.5.7$$

From Heisenberg's uncertainty principle  $\Delta p_\perp \Delta r \sim \hbar$  and so, using inequalities 14.5.6 and 14.5.7, the collision will appear classical if

$$2\mu\nu \frac{r^2 r_0}{r^2 + r_0^2} \gg \hbar$$

or

$$\frac{\lambda_{qm}}{4\pi} \ll \frac{r_0}{1 + r_0^2/r^2}.$$

Thus if  $(\lambda_{qm}/4\pi) > r_0$  this condition cannot be satisfied and the collisions will not be classical for any scattering angle.

Using the Born approximation the quantum mechanical expression for  $\ln \Lambda$  is

$$\ln \Lambda = \int_0^1 \frac{\sin^2 \chi/2 d \sin^2 \chi/2}{2 \left[ \left( \frac{1}{4\pi} \frac{\lambda_{qm}}{\lambda_D} \right)^2 + \sin^2 \chi/2 \right]^2}. \quad 14.5.8$$

It is seen from eqn 14.5.8 that for  $\lambda_{qm} \ll \lambda_D$  the contributions from large angle scatters are unaffected by quantum effects but that small angle contributions with  $\sin \chi/2 < \lambda_{qm}/4\pi\lambda_D$  are essentially removed. Thus effectively

$$\ln \Lambda = \int_{(\lambda_{qm}/4\pi\lambda_D)^2}^1 \frac{d \sin^2 \chi/2}{2 \sin^2 \chi/2}$$

and so

$$\ln \Lambda = \ln \left( 4\pi \frac{\lambda_D}{\lambda_{qm}} \right). \quad 14.5.9$$

## 14.6

### Collision times

The *electron collision time* characterizing electron collisions with ions is

$$\tau_e = \frac{12\pi^{3/2}}{\sqrt{2}} \frac{\epsilon_0^2 m_e^{1/2} T_e^{3/2}}{n_i Z^2 e^4 \ln \Lambda}.$$

For singly charged ions

$$\begin{aligned} \tau_e &= 1.09 \times 10^{16} \frac{T_e^{3/2}}{n \ln \Lambda} \text{ s, } \quad T_e \text{ in keV,} \\ &= 6.4 \times 10^{14} \frac{T_e^{3/2}}{n} \text{ s, } \quad \ln \Lambda = 17, \quad T_e \text{ in keV.} \end{aligned} \quad 14.6.1$$

The values of  $\tau_e$  given by eqn 14.6.1 are plotted in Fig. 14.6.1.

The rate of energy transfer from electrons to ions is given by

$$\frac{\frac{3}{2} n (T_e - T_i)}{\tau_{ex}}$$

where the *energy exchange time*

$$\tau_{ex} = \frac{m_i}{2\bar{m}_e} \tau_e.$$

This time may therefore also be obtained using Fig. 14.6.1.

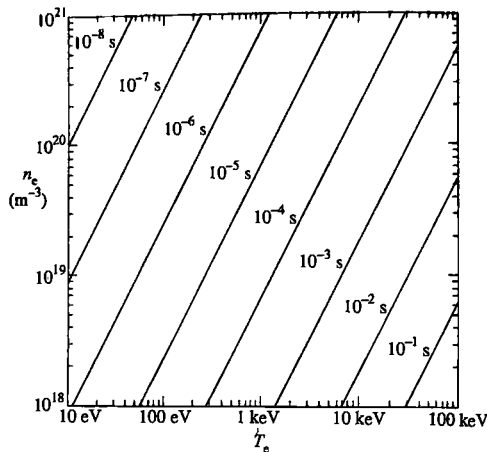


**Fig. 14.6.1** Values of  $\tau_e$  plotted against electron density and electron temperature. (Equation 14.6.1 with the precise values of  $\ln \Lambda$ .)

The *ion collision time* is

$$\tau_i = 12\pi^{3/2} \frac{e_0^2 m_i^{1/2} T_i^{3/2}}{n_i Z^4 e^4 \ln \Lambda_i}$$

and for singly charged ions

$$\tau_i = 6.60 \times 10^{17} \left( \frac{m_i}{m_p} \right)^{1/2} \frac{T_i^{3/2}}{n \ln \Lambda_i} \text{ s}, \quad T_i \text{ in keV.} \quad 14.6.2$$

The Coulomb logarithm for ions is approximated by  $\ln \Lambda_i = 1.1 \ln \Lambda$  to within 10% over the range covered by Fig. 14.6.1. Using this relation, eqns 14.6.1 and 14.6.2 give the following approximations for  $\tau_i$  putting  $T_i = T_e$ :

$$\text{ions } (Z=1) \quad \tau_i \simeq \frac{1}{1.1} \left( \frac{2m_i}{m_e} \right)^{1/2} \tau_e$$

$$\text{protons} \quad \tau_p \simeq 55 \tau_e$$

$$\text{deuterons} \quad \tau_d \simeq 78 \tau_e$$

$$\text{tritons} \quad \tau_t \simeq 95 \tau_e.$$

Using these relations approximate values of the ion collision time may be obtained from Fig. 14.6.1.

**14.7****Lengths****Debye length**

$$\lambda_D = \left( \frac{\epsilon_0 T_e}{n_e e^2} \right)^{1/2}$$

$$= 2.35 \times 10^5 (T_e/n_e)^{1/2} \text{ m}, \quad T_e \text{ in keV.} \quad 14.7.1$$

**Larmor radius (thermal particle,  $v_{\perp}^2 = 2v_T^2$ )**  
electron

$$\rho_e = \frac{v_{\perp e}}{\omega_{ce}} = \frac{\left(2m_e T_e\right)^{1/2}}{eB}$$

$$= 1.07 \times 10^{-4} \frac{T_e^{1/2}}{B} \text{ m} \quad T_e \text{ in keV,} \quad 14.7.2$$

ion

$$\rho_i = \frac{v_{\perp i}}{\omega_{ci}} = \frac{\left(2m_i T_i\right)^{1/2}}{eB}$$

$$= 4.57 \times 10^{-3} \left( \frac{m_i}{m_p} \right)^{1/2} \frac{T_i^{1/2}}{B} \text{ m,} \quad T_i \text{ in keV,}$$

proton

$$\rho_p = 4.57 \times 10^{-3} \frac{T_p^{1/2}}{B} \text{ m,} \quad T_p \text{ in keV,}$$

deuteron

$$\rho_d = 6.46 \times 10^{-3} \frac{T_d^{1/2}}{B} \text{ m,} \quad T_d \text{ in keV,} \quad 14.7.3$$

triton

$$\rho_t = 7.92 \times 10^{-3} \frac{T_t^{1/2}}{B} \text{ m,} \quad T_t \text{ in keV,}$$

 $\alpha$ -particle

$$\rho_\alpha = 4.55 \times 10^{-3} \frac{T_\alpha^{1/2}}{B} \text{ m,} \quad T_\alpha \text{ in keV,}$$

 $\alpha$ -particle with perpendicular energy  $\varepsilon_{\perp}$ 

$$\rho_\alpha = 1.44 \times 10^{-1} \frac{\varepsilon_{\perp}^{1/2}}{B} \text{ m,} \quad \varepsilon_{\perp} \text{ in MeV.}$$

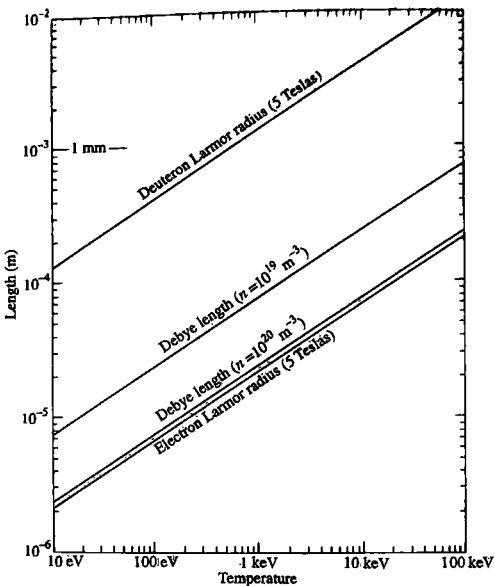


Fig. 14.7.1 Graphs of Larmor radius and Debye length against temperature (eqns 14.7.1, 14.7.2, and 14.7.3).

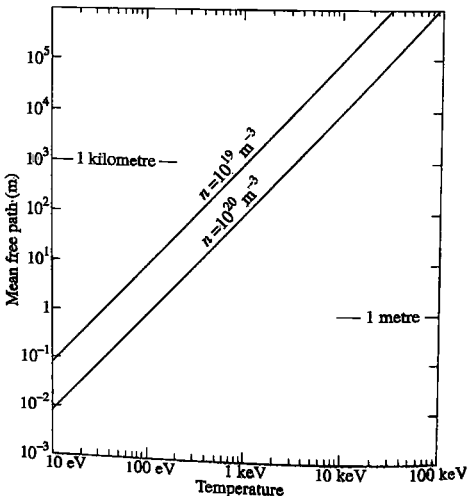


Fig. 14.7.2 Graphs of electron mean free path against temperature (eqn 14.7.4). The ion mean free path is approximately equal to the electron mean path at the same temperature.

**Mean free path ( $v_T \times$  collision time) ( $Z = 1$ )**

electron

$$\begin{aligned}\lambda_e &= v_{Te} \tau_e = \left( \frac{T_e}{m_e} \right)^{1/2} \tau_e \\ &= 1.44 \times 10^{23} \frac{T_e^2}{n \ln \Lambda} \text{ m}, \quad T_e \text{ in keV} \\ &= 8.5 \times 10^{21} \left( \frac{T_e^2}{n} \right) \text{ m}, \quad \ln \Lambda = 17, \quad T_e \text{ in keV.} \quad 14.7.4\end{aligned}$$

At a given temperature the ion mean free path  $\lambda_i \simeq \lambda_e$  since

$$\lambda_i = v_{Ti} \tau_i \simeq v_{Te} \tau_e = \lambda_e.$$

## 14.8

### Frequencies

**Plasma frequency**

electron

$$\omega_{pe} = \left( \frac{n_e e^2}{m_e \epsilon_0} \right)^{1/2} = 56.4 n_e^{1/2} \text{ s}^{-1},$$

$$f_{pe} = \frac{\omega_{pe}}{2\pi} = 8.98 n_e^{1/2} \text{ Hz,}$$

ion ( $Z = 1$ )

$$\omega_{pi} = \left( \frac{n_i e^2}{m_i \epsilon_0} \right)^{1/2} = 1.32(n_i/A)^{1/2} \text{ s}^{-1},$$

$$f_{pi} = \frac{\omega_{pi}}{2\pi} = 0.210(n_i/A)^{1/2} \text{ Hz.}$$

**Gyrofrequency**

electron

$$\omega_{ce} = \frac{eB}{m_e} = 0.176 \times 10^{12} B \text{ s}^{-1},$$

$$f_{ce} = \frac{\omega_{ce}}{2\pi} = 28.0 \times 10^9 B \text{ Hz,}$$

ion

$$\omega_{ci} = \frac{ZeB}{m_i} = 95.5 \times 10^6 \frac{Z}{A} B \text{ s}^{-1},$$

$$f_{ci} = \frac{\omega_{ci}}{2\pi} = 15.2 \times 10^6 \frac{Z}{A} B \text{ Hz}.$$

**Lower hybrid frequency**

$$\omega_{lh}^2 = \left( \frac{1}{\omega_{ci}^2 + \omega_{pi}^2} + \frac{1}{\omega_{ce}\omega_{ci}} \right)^{-1}.$$

**Upper hybrid frequency**

$$\omega_{uh}^2 = \omega_{ce}^2 + \omega_{pe}^2.$$

**Trapped particle bounce frequency**

$$\omega_b = \left( \frac{r}{2R_0} \right)^{1/2} \frac{v_\perp}{qR_0}.$$

**14.9****Velocities****Thermal velocity**

electron ion proton deuteron triton	$v_{Tj} = (T_j/m_j)^{1/2}$ $v_{Te} = 1.33 \times 10^7 T_e^{1/2}$ $v_{Ti} = 3.09 \times 10^5 (T_i/A)^{1/2}$ $v_{Tp} = 3.09 \times 10^5 T_p^{1/2}$ $v_{Td} = 2.19 \times 10^5 T_d^{1/2}$ $v_{Tt} = 1.79 \times 10^5 T_t^{1/2}$	$\text{m s}^{-1}$ $\text{m s}^{-1}$ $\text{m s}^{-1}$ $\text{m s}^{-1}$ $\text{m s}^{-1}$
---	---	---

$T$  in keV

**Alfvén velocity**

$$V_A = \frac{B}{(\mu_0 n_i m_i)^{1/2}} = 2.18 \times 10^{16} \frac{B}{(n_i A)^{1/2}} \text{ m s}^{-1}.$$

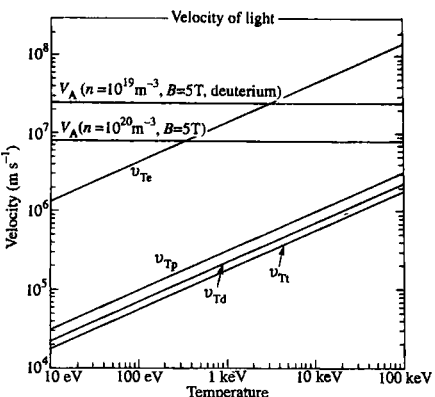


Fig. 14.9.1 Values of electron and ion thermal velocities and the Alfvén velocity.

## 14.10 Resistivity

The resistivity of a hydrogen plasma is discussed in Section 2.16. The value of the resistivity parallel to a magnetic field given by eqn 2.16.2 is

$$\eta_s = \eta_{\parallel} = 1.65 \times 10^{-9} \ln \Lambda / T_e^{3/2} \text{ ohm m}, \quad T_e \text{ in keV.} \quad 14.10.1$$

The resistivity is given as a function of temperature in Fig. 14.10.1. There is a weak dependence on density through  $\ln \Lambda$  and values are given for  $n = 10^{19} \text{ m}^{-3}$  and  $10^{20} \text{ m}^{-3}$ . The perpendicular resistivity,  $\eta_{\perp}$ , is larger by a factor 1.97.

In a plasma with ions of charge  $Z$  the resistivity is larger than in a plasma with singly charged ions. It is seen from eqn 2.15.1 that the collision frequency is proportional to  $Z^2$ , so the drag on an electron is increased by a factor  $Z^2$ . However, the number of electrons is  $n_e Z$ , so the number of current carriers per ion is proportional to  $Z$ . Consequently the resistivity is roughly proportional to  $Z$ . The precise form is

$$\eta_{\parallel}(Z) = N(Z) Z \eta_{\parallel}(1) \quad 14.10.2$$

where  $\eta_{\parallel}(1)$  is the resistivity given by eqn 14.10.1 and  $N$  is a numerical factor depending on  $Z$ . Calculations by Spitzer and Härn lead to the values of  $N$  given in Table 14.10.1.

In an impure hydrogen plasma the situation is complicated because of the multiplicity of levels of ionization of the impurity. An empirical

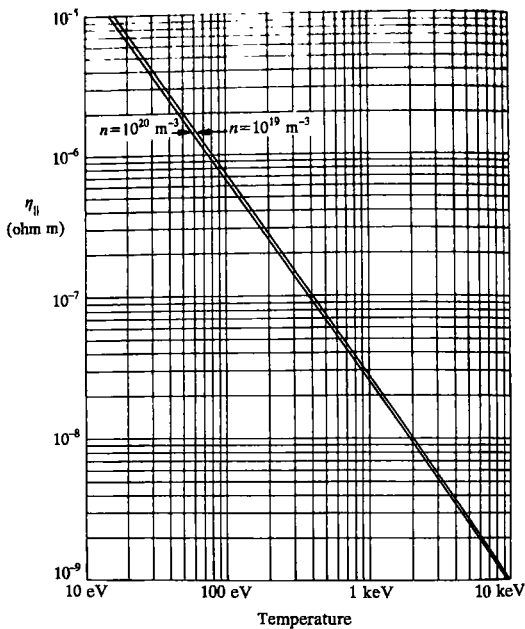


**Fig. 14.10.1** Spitzer resistivity against electron temperature for a hydrogen plasma.

**Table 14.10.1** Resistivity factor  $N(Z)$  of eqn 14.10.2

Z	1	2	4	16	$\infty$
$N$	1	0.85	0.74	0.63	0.58

formula which has the correct limiting forms is

$$\eta_{||}(Z_{\text{eff}}) = N(Z_{\text{eff}}) Z_{\text{eff}} \eta_{||}(1)$$

the effective value of  $Z$  being given by

$$Z_{\text{eff}} = \frac{1 + f \bar{Z}^2}{1 + f \bar{Z}}$$

where  $f$  is the ratio of impurity ions to hydrogen ions and  $\bar{Z}$  and  $\bar{Z}^2$  are averages over the impurity ions.

When trapped electrons exist these electrons do not carry a current and the plasma conductivity is reduced to its neoclassical value. An approximate formula is

$$\eta_n = \frac{\eta_{||}}{(1 - (r/R_0)^{1/2})^2}.$$

More generally the neoclassical resistivity is a function of the collision frequency and  $Z_{\text{eff}}$ . An approximate formula is

$$\eta = \eta_s \frac{Z_{\text{eff}}}{(1 - \phi)(1 - C\phi)} \frac{1 + 0.27(Z_{\text{eff}} - 1)}{1 + 0.47(Z_{\text{eff}} - 1)}$$

where

$$\phi = \frac{f_T}{1 + (0.58 + 0.20Z_{\text{eff}})\nu_{*e}}$$

$$C = \frac{0.56}{Z_{\text{eff}}} \left( \frac{3.0 - Z_{\text{eff}}}{3.0 + Z_{\text{eff}}} \right)$$

$$\nu_{*e} = \varepsilon^{-3/2} \frac{Rq}{v_{Te}\tau_e}$$

$R$  is the major radius of the plasma,  $q$  is the safety factor,  $\varepsilon^{-1}$  is the aspect ratio  $R/a$ ,  $v_{Te} = (T_e/m_e)^{1/2}$ ,  $f_T$  is the fraction of electrons trapped (for  $\nu_{*e} = 0$ )

$$f_T = 1 - \frac{(1 - \varepsilon)^2}{(1 - \varepsilon^2)^{1/2}(1 + 1.46\varepsilon^{1/2})}$$

and

$$\tau_e = 3(2\pi)^{3/2} \frac{\varepsilon_0^2 m_e^{1/2} T_e^{3/2}}{n_e e^4 \ln \Lambda}.$$

## 14.11

### Chang-Hinton formula for $\chi_i$

Because there are circumstances in which ion neoclassical thermal transport is comparable with experimental values it is appropriate to give an

expression for  $\chi_i$  which extends the formula of eqn 4.6.22 to incorporate finite aspect-ratio effects, and interpolates between banana, plateau, and Pfirsch-Schlüter regimes allowing for the effects of impurities. Thus, with  $q_i = -n_i \chi_i dT_i/dr$ , this expression is

$$q_i = \frac{\varepsilon^{-3/2} q^2 \rho_{\perp}^2}{\tau_i} \left\{ \left[ \frac{0.66(1 + 1.54\alpha) + (1.88\varepsilon^{1/2} - 1.54\varepsilon)(1 + 3.75\alpha)}{1 + 1.03\mu_{*i}^{t/2} + 0.31\mu_{*i}} \right] f_1 + \frac{0.59\mu_{*i}\varepsilon}{(1 + 0.74\mu_{*i}\varepsilon^{3/2})} \left[ 1 + \frac{1.33\alpha(1 + 0.60\alpha)}{1 + 1.79\alpha} \right] (f_1 - f_2) \right\} \quad 14.11.1$$

where  $\varepsilon = r/R$ ,  $\rho_i = (2T_i/m_i)^{1/2}/\omega_{ci}$ ,  $\alpha = n_i Z_i^2/n_i Z_{\perp}^2$  measures the effect of impurity ions with charge  $Z_i$  and density  $n_i$ , and  $\mu_{*i} = v_{*i}(1 + 1.54\alpha)$  with  $v_{*i} = v_i R q / \varepsilon^{3/2} v_{Ti}$ , a collisionality parameter allowing the interpolation between collision regimes. The first term in eqn 14.11.1 contains a factor  $f_1$  where

$$f_1 = \frac{1 + \frac{3}{2}(\varepsilon^2 + \varepsilon\Delta') + \frac{3}{8}\varepsilon^3\Delta'}{1 + \frac{1}{2}\varepsilon\Delta'},$$

$\Delta' = d\Delta/dr$  being the derivative of the Shafranov shift (see Section 3.6). This term describes the neoclassical contributions from the banana and plateau regimes and the transition between them as  $\mu_{*i}$  varies. The corrections proportional to  $\varepsilon^{1/2}$  and  $\varepsilon$  represent the effects of energy scattering terms in the collision operator which play a role at finite aspect ratio when the fraction of trapped particles is not small. The second term in eqn 14.11.1, which has a factor  $f_1 - f_2$  where

$$f_2 = \frac{\sqrt{1 - \varepsilon^2} \left( 1 + \frac{\varepsilon\Delta'}{2} \right)}{1 + \frac{\Delta'}{\varepsilon} (\sqrt{1 - \varepsilon^2} - 1)}$$

represents the Pfirsch-Schlüter contribution when  $\mu_{*i}\varepsilon^{3/2} > 1$ .

## 14.12

### Bootstrap current

An introductory account of the bootstrap current was given in Section 4.9. In that description collisions were neglected and only a limited range of

aspect-ratio was covered. The need to calculate the dependence of the bootstrap current on these parameters calls for an equation which covers their full range.

The equation given below gives one such form. The gradients are expressed in terms of the poloidal flux  $\psi$ . In a large aspect-ratio circular approximation these are related to the radial gradients by

$$y'(\psi) = \frac{1}{RB_\theta} \frac{dy}{dr}.$$

In terms of the inverse aspect-ratio,  $\varepsilon = r/R$ , and the collisionality

$$\nu_{*j} = \frac{\nu_j}{\varepsilon \omega_{bj}}$$

where  $\nu_e = \tau_e^{-1}$  and  $\nu_i = \tau_i^{-1}$ ,  $\tau_e$  and  $\tau_i$  being given by eqns 2.15.1 and 2.15.2, and  $\omega_{bj} = \varepsilon^{1/2}(T_j/m_j)^{1/2}/Rq$ , the bootstrap current is given by

$$(j_b \cdot B) = \frac{\mu_0 f(\psi) x p_e}{D(x)} \left( c_1 \frac{p'_e}{p_e} + c_2 \frac{p'_i}{p_i} + c_3 \frac{T'_e}{T_e} + c_4 \frac{T'_i}{T_i} \right)$$

where  $f(\psi)$  is the equilibrium flux function  $RB_\phi/\mu_0$  (see Section 3.2),  $x$  is the ratio of the number of trapped to circulating particles ( $\simeq \sqrt{2}\varepsilon^{1/2}$  for small  $\varepsilon$ ),  $p_j(\psi)$  and  $T_j(\psi)$  are the pressure and temperature of species  $j$ ,

$$D(x) = 2.4 + 5.4x + 2.6x^2$$

$$c_1 = \frac{4.0 + 2.6x}{\left(1 + 1.02\nu_{*e}^{1/2} + 1.07\nu_{*e}\right)\left(1 + 1.07\varepsilon^{3/2}\nu_{*e}\right)}$$

$$c_2 = \frac{T_i}{T_e} c_1$$

$$c_3 = \frac{7.0 + 6.5x}{\left(1 + 0.57\nu_{*e}^{1/2} + 0.61\nu_{*e}\right)\left(1 + 0.61\varepsilon^{3/2}\nu_{*e}\right)} - \frac{5}{2}c_1$$

and

$$c_4 = \left( \frac{d + 0.35\nu_{*i}^{1/2}}{1 + 0.7\nu_{*i}^{1/2}} + 2.1\varepsilon^3\nu_{*i}^2 \right) \frac{1}{\left(1 - \varepsilon^3\nu_{*i}^2\right)\left(1 + \varepsilon^3\nu_{*e}^2\right)} c_2$$

where

$$d = -\frac{1.17}{1 + 0.46x}.$$

The average  $\langle \rangle$  is defined by

$$\langle \mu \rangle = \oint \mu \frac{dl}{B_p} \oint \frac{dl}{B_p}$$

where  $dl$  is a poloidal line element in the magnetic surface and  $B_p$  is the poloidal magnetic field.

**14.13****Confinement scaling relations**

The international activity associated with ITER has generated a number of scaling expressions for the energy confinement time,  $\tau_E$ , in both L- and H-mode. These have been gradually refined as the quality of the multi-tokamak database has improved. Nevertheless some of the older versions are often quoted in the literature and new experimental data is frequently expressed in terms of them. A number of expressions are tabulated here for reference purposes. They all have the generic form

$$\tau_E = C I^{\alpha_I} B^{\alpha_B} P^{\alpha_P} \left( \frac{n}{10^{20}} \right)^{\alpha_n} A^{\alpha_A} R^{\alpha_R} \epsilon^{\alpha_\epsilon} \kappa^{\alpha_\kappa} s$$

where  $C$  is a constant,  $I$  is in MA and  $P$  in MW.

For L-mode, the well established standard scaling is ITER89-P, but a more recent one for thermal energy confinement is known as  $\tau_{E,\text{th}}^L$ . The constant  $C$  and exponents  $\alpha_I$ ,  $\alpha_B$  etc are tabulated in Table 14.13.1

In H-mode, early expressions for thermal energy confinement were given for both ELM<sub>y</sub> and ELM free cases. These were known as ITER H92-P ( $y$ ) and ITER H93-P for ELM<sub>y</sub> and ELM free, respectively. More recently, the scalings IPB98(y) and IPB98(y,2) have been derived for ELM<sub>y</sub> H-mode, the latter using a different definition of  $\kappa$  to account for the bean-shaped tokamak PBX-M. In addition a newer ELM free expression,  $\tau_{E,\text{th}}^{\text{ELM free}}$ , has been introduced. These ELM<sub>y</sub> and ELM free scaling expressions are tabulated in Tables 14.13.2 and 14.13.3.

**Table 14.13.1** L-Mode confinement time scalings.

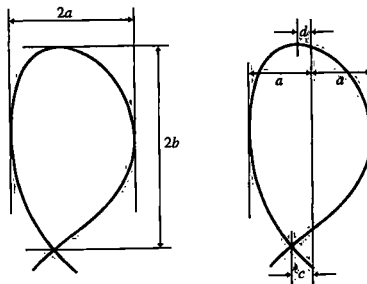
$\tau_E$	$C$	$\alpha_I$	$\alpha_B$	$\alpha_P$	$\alpha_n$	$\alpha_A$	$\alpha_R$	$\alpha_\epsilon$	$\alpha_\kappa$
$\tau_E^{\text{ITER89-P}}$	0.048	0.85	0.2	-0.5	0.1	0.5	1.5	0.3	0.5
$\tau_{E,\text{th}}^L$	0.058	0.96	0.03	-0.73	0.40	0.20	1.83	-0.06	0.64

**Table 14.13.2** ELM<sub>y</sub> H-mode confinement time scalings.

$\tau_E$	$C$	$\alpha_I$	$\alpha_B$	$\alpha_P$	$\alpha_n$	$\alpha_A$	$\alpha_R$	$\alpha_\epsilon$	$\alpha_\kappa$
$\tau_E^{\text{ITERH92-P}(y)}$	0.068	0.90	0.05	-0.65	0.30	0.40	2.1	0.20	0.80
$\tau_E^{\text{IPB98}(y)}$	0.094	0.97	0.08	-0.63	0.41	0.20	1.93	0.23	0.67
$\tau_E^{\text{IPB98}(y,2)}$	0.145	0.93	0.15	-0.69	0.41	0.19	1.97	0.58	0.78

**Table 14.13.3 ELM free H-mode confinement time scalings.**

$\tau_E$	$C$	$\alpha_I$	$\alpha_B$	$\alpha_P$	$\alpha_n$	$\alpha_A$	$\alpha_R$	$\alpha_\epsilon$	$\alpha_\kappa$
$\tau_{\text{ITER93-P}}$	0.053	1.06	0.32	-0.67	0.17	0.41	1.79	-0.11	0.66
$\tau_E^{\text{ELM free}}$	0.068	0.94	0.27	-0.68	0.34	0.43	1.98	0.10	0.68
$\tau_{E,\text{th}}$									

**14.14****Plasma shape****Fig. 14.14.1** Definitions of plasma dimensions

The elongation and triangularity of the plasma are defined using the dimensions shown in Fig. 14.14.1.

**Elongation**

$$\kappa = b/a.$$

**Triangularity**

$$\delta = \frac{(c+d)/2}{a}.$$

The vertical and horizontal limit of the plasma are defined either by tangents to the plasma edge or by the X-point of a separatrix.

**14.15****Formulae**

Maxwellian distribution function

$$f_j(v) = n_j \left( \frac{m_j}{2\pi T_j} \right)^{3/2} \exp \left( -\frac{m_j v^2}{2T_j} \right)$$

Force between two charges, separation  $d$

$$F = \frac{e_1 e_2}{4\pi \epsilon_0 d^2}.$$

Inductance per unit length of a uniform current of radius  $a$  with a coaxial return at radius  $b$  (energy =  $\frac{1}{2}LI^2$ )

$$L = \frac{\mu_0}{2\pi} \left( \frac{1}{4} + \ln \frac{b}{a} \right).$$

Inductance of a circular uniform current of radius  $a$  in a circular loop of radius  $R$

$$L = \mu_0 R \left( \ln \frac{8R}{a} - \frac{7}{4} \right).$$

Resistive skin depth in the surface of a conductor of conductivity  $\sigma$  for oscillations with angular frequency  $\omega$  (oscillations decay as  $\exp(-x/\delta)$ )

$$\delta = \left( \frac{2}{\mu_0 \sigma \omega} \right)^{1/2}.$$

Average value over a circular cross-section,  $r \leq a$ , of  $y = y_0(1-r^2/a^2)^v$

$$\bar{y} = \frac{y_0}{v+1}.$$

Definition of error function

$$\begin{aligned} \text{erf}(x) &= \frac{2}{\sqrt{\pi}} \int_0^x e^{-z^2} dz \\ \int_0^\infty e^{-\alpha x^2} dx &= \frac{1}{2} \left( \frac{\pi}{\alpha} \right)^{1/2} \\ \int x e^{-\alpha x^2} dx &= -\frac{1}{2\alpha} e^{-\alpha x^2} \\ \int_0^\infty x^2 e^{-\alpha x^2} dx &= \frac{1}{4} \left( \frac{\pi}{\alpha^3} \right)^{1/2} \\ \int x^3 e^{-\alpha x^2} dx &= -\frac{1}{2\alpha} \left( \frac{1}{\alpha} + x^2 \right) e^{-\alpha x^2}. \end{aligned}$$

**14.16****Symbols**

The following is a list of symbols in this book which are used without repeated definition.

**Geometry**

$(R, \phi, z)$	Cylindrical coordinates based on the major axis of the torus, $z = 0$ being the median plane
$(r, \theta)$	Polar coordinates in the minor cross-section
$R_0$ (or $R$ )	Major radius of the plasma
$a$	Minor-radius, half-width, of the plasma
$b$	Half-height of the plasma
$m$	Poloidal mode number
$n$	Toroidal mode number
$\varepsilon$	Inverse aspect ratio, $r/R$
$\kappa$	The elongation of the plasma, $b/a$

**Magnetic field**

$B_\phi$	Toroidal magnetic field
$B_p$	Poloidal magnetic field
$B_\theta$	Poloidal magnetic field for large aspect-ratio circular cross-section
$q$	Safety factor
$q_0$	$q$ at the magnetic axis
$q_a$	$q$ at the plasma surface

**Particles**

Particle types are denoted by subscripts e (electron), i (ion), p (proton), d (deuteron), t (triton).

$e_j$	Electric charge
$m_j$	Mass
$Z_j$ (or $Z$ )	Charge/ $e$
$A_j$ (or $A$ )	Atomic mass
$v_{Tj}$	Thermal velocity, $(T_j/m_j)^{1/2}$
$\omega_{cj}$	Cyclotron frequency, $e_j B / m_j$
$\rho_j$	Larmor radius, $v_{\perp j} / \omega_{cj}$ or $\sqrt{2} v_{Tj} / \omega_{cj}$
$v_{\parallel}$	Velocity parallel to the magnetic field
$v_{\perp}$	Velocity perpendicular to the magnetic field

**Plasma**

Species denoted by subscripts

$T_j$	Temperature
$T$	Temperature when $T_e$ is taken to be equal to $T_i$

$n_j$	Particle density
$n$	Electron density in pure hydrogen plasma (= ion density)
$\nu$	Collision frequency
$\tau_E$	Energy confinement time
$\lambda_D$	Debye length
$\omega_p$	Plasma frequency

## Bibliography

There is a more complete collection of plasma physics formulas and data in  
 Book, D.L. NRL Memorandum Report 3332, Naval Research Laboratory, Washington D.C.  
 and in a condensed form in  
 Book, D.L. *NRL Plasma Formulary*, Naval Research Laboratory, Washington D.C. (1977).

### Coulomb logarithm

Calculation of the Coulomb logarithm is described in  
 Sivukhin, D.V. Coulomb collisions in a fully ionized plasma,  
*Reviews of plasma physics* (ed. Leontovich, M.A.) Vol. 4,  
 Consultants Bureau, New York (1966).

### Resistivity

Values of  $\bar{Z}$  and  $\bar{Z}^2$  may be obtained from  
 Post, D.E., Jensen, R.V., Tarter, C.B., Grasberger, W.H.,  
 and Lokke, W.A., Steady-state radiative cooling rates for

low-density, high-temperature plasmas. *Atomic Data and Nuclear Data Tables* **20**, 397 (1977).  
 The approximate formula for the neoclassical resistivity is from  
 Hirshman, S.P., Hawryluk, R.J., and Birge, B. Neoclassical conductivity of a tokamak plasma. *Nuclear Fusion* **17**, 611 (1977).

### Chang-Hinton formula

Chang, C.S. and Hinton, F.L. Effect of impurity particles on the finite aspect-ratio neoclassical ion thermal conductivity in a tokamak. *Physics of Fluids* **29**, 3314 (1986).

### Bootstrap current

The equation for the bootstrap current is a corrected form from  
 Wilson, H.R. UKAEA Report Fus 271 (1994).

# Index

- Abel transform 509  
AC operation 621  
adiabatic compression 239, 598  
adiabatic equation 80  
adiabatic invariants 49  
adsorption 461  
Alcator scaling 567  
Alfvén wave 98  
alpha particle  
  heating 9, 617, 641  
  losses 616  
  TAE excitation 616  
Ampère's law 80  
anomalous transport 150  
  candidate modes 213  
arcing 473  
Artimovich 562  
  scaling 563  
aspect-ratio expansion 117  
atomic processes 457  
axisymmetric instability 342
- backscattering, surface 454  
baking, vacuum vessel 463  
ballooning modes 337  
  in TFFT 605  
banana diffusion 159  
banana orbits 130  
banana regime 159  
beam emission spectroscopy 611  
beryllium surfaces 633  
  effect on density limit 624  
beta,  $\beta$ , 115  
  in DIII-D 678  
  poloidal 116  
beta limit 343  
  scaling in DIII-D 347, 678  
binding energy, surface 466  
blanket 18  
Bohm scaling 194  
bolometry 541  
bootstrap current 172  
  general formula 738  
  in DIII-D 681  
  in JET 637  
  in JT-60/JT-60U 654  
  in TFFT 605  
boronization 465, 580
- bounce frequency 129  
bounce point 127  
Braginskii equations 88  
bremsstrahlung 227  
  measurement 537  
bucket source 254
- canonical momentum 125  
carbon bloom  
  in JET 642  
  in TFFT 601  
carbonization 465  
  in DIII-D 683  
  in TEXTOR 580  
centrifugal effects 133  
Chang-Hinton formula for  $x_i$  737  
charge exchange 255, 457  
  neutrals 523  
  recombination spectroscopy 530  
cleaning, discharge 463  
Clemmow-Mullaly-Allis diagram 291  
coils, layout 17  
collisions 51  
  momentum and energy change 53  
collision times 69  
compressional heating 240, 598  
conditioning of wall 461  
conductivity, neoclassical 173, 737  
confinement 150  
  in DIII-D 667  
  in JET 629  
  in JT-60 647  
  in JT-60U 659  
  in TFFT 608  
  momentum 197  
confinement modes and scaling 180  
  Goldston scaling 20, 152, 182  
  H-mode 184, 185  
  improved ohmic 181  
  ITER 89-P scaling 183  
  ITER H93-P scaling 184  
  L-mode 182  
  PEP 184  
  radiatively improved 185  
  supershot 184  
  V-H modes 185  
confinement time  
  definition 9, 150  
  particle 537
- $\frac{1}{2}r_p^2$  scaling 17, 563  
*see also* confinement; confinement  
  modes and scaling  
continuity equation 78, 89  
Cordey pass 13  
coronal equilibrium 230, 532  
Coulomb barrier 4  
Coulomb logarithm 53, 725  
critical gradients 217  
cross-sections  
  charge exchange 245  
  fusion 5  
  ionization by ions 245  
cryopump 666  
current drive 136  
  DIII-D 681  
  electron cyclotron 143  
  fast wave, electron 142  
  fast wave, minority ion 144  
JET 637  
JT-60/JT-60U 652  
lower hybrid 139  
neutral beam 137  
current moments 503  
current penetration 364  
current profile  
  hollow 181  
  model 119  
current quench, disruption 376  
cyclotron frequency 40  
cyclotron radiation 229
- Debye length 36  
Debye shielding 35  
  in collisions 53  
decay index, magnetic field 343  
deflection time, particle 65  
density limit  
  in DIII-D 681  
  in JET 623  
  in JT-60/JT-60U 656  
desorption 462  
deuterium, abundance 25  
deuterium-tritium experiments  
  in JET 640  
  in TFFT 612  
diamagnetic frequency 421  
diamagnetic loop 501  
diamagnetism 84

- diagnostics 498  
 dielectric tensor 76, 94  
 diffusion, plasma 552  
 diffusion tensor 58  
 discharge cleaning 463  
 dispersion relation 94  
 disruptions 374  
   causes 376  
   current decay 387  
 density limit 378  
   in DIII-D 676  
   in JET 623  
   in JT-60U 655  
   low  $q$  377  
 physics 382  
 reactor 709  
 runaway electrons 387  
   in TFTR 605  
     vacuum vessel currents 389  
 dissociative ionization 458  
 dissociative recombination 458  
 divertor experiments  
   in ASDEX 578  
   in ASDEX upgrade 689  
   in DIII-D 683  
   in JET 633  
   JT-60/JT-60U 649  
 divertors 19, 477  
   bundle 570  
   design considerations 487  
   flow 485  
   heat flux 489  
   one-dimensional model of SOL 479  
   volume power losses 483  
 Doppler broadening 539  
 Doppler shift 539  
 Dreicer electric field 74  
 drift instabilities 418  
 drift kinetic equation 58  
 drifts, particle 44  
   curvature 46  
    $E \times B$  44  
   polarization 47  
    $\nabla B$  45  
 drift surfaces 126  
 drift wave 420  
 dynamic friction 58, 64
- ECE, measurement of  $T_e$  518  
 economics, tokamak 26  
 ECRH 290  
 edge localized modes 409  
 electric fields 123  
   sheared 210  
 electromagnetic waves 96
- electromagnetism 75  
 electron cyclotron emission, measurement  
   of  $T_e$  518  
 electron cyclotron heating 290  
 electron density measurement 507, 511  
 electron drift mode 425  
   toroidal 426  
 electron drift wave 421  
 electron temperature gradient  
   mode 429  
 electron temperature measurement 514  
 ELMs 409  
 energy balance equation 92  
 energy confinement time,  
   definition 9, 148  
 energy consumption, world 25  
 energy loss 9  
 energy principle 309  
 energy resources, world 26  
 entropy conservation 80  
 equation of motion 78  
 equilibrium 106  
 ergodicity 397  
 ergodic magnetic field 353, 398  
   transport 204  
 erosion, arc 473  
 error field instability 394  
   experiment 583, 677  
 error function 742  
 evaporation 489
- Fabry-Perot interferometer 520  
 Faraday rotation 510  
 feedback control of instability 571  
 field particles 65  
 fishbone instability 399  
 fluctuations  
   correlation with transport 200  
   L-H transition 202  
   measurement 551  
   observations 199  
   transport 199  
 fluid equations 77  
 flux functions 108  
 Fokker-Planck equation 56, 57  
   for a Maxwellian distribution 62  
   for a plasma 60  
 Fourier transform spectrometer 520  
 friction force 90  
 'frozen in' magnetic field 83  
 fuel resources 24  
 fusion cross-sections 5  
 fusion reactions 3
- gap mode 403  
 gauge transformation 77
- Gauß factor 228, 538  
 Gauss' theorem 722  
 gettering 463  
 Goldston scaling 20, 152, 182  
 Grad-Shafranov equation 109  
 Green's theorem 722  
 Greenwald limit 377  
 gyro-averaged equations 58  
 gyro-Bohm scaling 194  
 gyrofrequency (cycotron frequency) 40  
 gyro-kinetic equation 59  
 gyrotron 291
- halo current 396  
   in experiment 620, 676  
 Hamilton's equations 55  
 heat exchange 93  
   time 67  
 heating 238  
   ECRH 290  
   ICRH 270  
   lower hybrid 286  
   neutral beam 243  
   ohmic 240  
 heat transfer in solid 489  
 heavy ion beam probe 552  
 helical magnetic field 366  
 helical magnetic flux 366  
 helium transport 612, 650, 686  
 high  $\beta$ , in DIII-D 678  
 H-modes 185  
   edg localized modes 189  
 hoop force 107, 155  
 Hugill diagram 377
- ICRH 270  
 ideal mhd modes 304  
 ignition 10, 12  
 impact parameter 53  
 impurities 23  
   coronal equilibrium 461  
   ionization 459  
   measurement 525  
 impurity radiation 229  
 impurity transport 219  
 incompressibility 80  
 inductance, plasma 120  
   measurement 503  
 instabilities 352  
   axisymmetric 342, 396  
   ballooning 337  
 collisionless trapped particle 431  
 dissipative trapped particle 432  
 dissipative trapped electron 434  
 edge localized modes, ELMs 410  
 electron drift 420

- error field 104  
 fishbone 399  
 internal kink 329  
 ion temperature gradient 428  
 kink 313  
 localized 336  
 $m = t$  tearing 334  
 MARFE 406  
 microinstabilities 417  
 micro-tearing 435  
 Mirov 362  
 modes for transport 213  
 passing particle 422  
 resistive  $m = 1$  332  
 sawtooth oscillations 365  
 tearing 318  
 thermonuclear 13  
 toroidal Alfvén 402  
 trapped particle 430  
 trapped ion mode 433  
 unified  $m = 1$  theory 336  
 vertical 396  
 interferometry 507  
 internal inductance,  $\ell_i$  120  
     measurement 503  
 internal kink instability 329  
 internal transport barriers 189, 226  
 inward pinch 196  
 ion cyclotron heating 270  
     experiments 285  
 ionization, dissociative 458  
 ionization, molecular 458  
 ion source 253  
 ion temperature gradient  
     mode 428  
 ion temperature measurement 522  
 ITER 711  
     costs 713, 717  
  
 kinetic equations 55  
     gyro-averaged 58  
 kink instability  
     internal 329  
     resistive  $m = 1$  332  
     surface 313  
  
 Lagrangian 311  
 Landau collision integral 61  
 Landau contour 101  
 Landau damping 100  
 Langmuir probes 546  
     measurements 669  
 large aspect-ratio expansion 117  
 Larmor orbits 40  
 Larmor radius 41  
 laser diagnostics 514  
  
 Lawson criterion 12  
 L-H transition  
     in ASDEX 577  
     in DIII-D 667  
     fluctuations 202  
     in JET 226  
     radial extent 225  
 LiDAR 516  
 limiter 475  
 linearization 306  
 $\ell_i$ , internal inductance 122  
 lithium 24  
     blanket 18  
     reserves 24  
 ln  $\Lambda$  53, 725  
 localized modes 336  
 loop voltage, measurement 502  
 lower hybrid frequency 734  
 lower hybrid heating 286  
  
 Mach-Zehnder interferometer 507  
 magnetic islands 354  
     overlap 397  
     width 355  
 magnetic measurements 500  
 magnetic moment 49  
 magnetic reconnection 354  
     sawtooth 366  
 magnetic shear 107  
 magnetic surfaces 108  
 magnetohydrodynamics (mhd) 79  
 magnetohydrodynamic waves 97  
 magnetosonic waves 99  
 MARFEs 406  
     measured radiation 541  
 mass deficit 4  
 Maxwell distribution function 6  
 Maxwell's equations 75  
 mean free path 733  
 melting 491  
 Mercier criterion 337  
 metallic films 464  
 mhd stability  
     axisymmetric modes 342  
     ballooning modes 337  
      $\beta$ -limit 343  
     effect of conducting  
         wall 326  
     energy principle 309  
     growth rates 307  
     internal kink 329  
     kink instability 313  
     large aspect-ratio expansion 312  
     linearization 306  
     localized modes 336  
 $m = 1$  tearing mode 334  
  
 quasi-interchange 331  
 resistive  $m = 1$  332  
 tearing mode 318  
 tokamak instabilities 311  
 unified  $m = 1$  theory 336  
 microinstabilities 418  
 micro-tearing mode 419, 435  
 Mirov oscillations 362  
 mirror effect 43  
 mirror force, tokamak 127  
 mode locking 390  
 molecular ionization 458  
 momentum equation 89  
 motional Stark effect 557  
     measurements 605, 681  
 Murakami parameter 377  
  
 neoclassical resistivity 173  
     formula 737  
     measurement 598  
 neoclassical tearing mode 359  
 neoclassical transport  
     banana 159  
     Firsch-Schlüter 158  
     plateau 167  
 neutral beam  
     experiments 251  
     heating 243, 246  
     injection 243  
     from negative ions 256  
     production 253  
     slowing 248  
 neutral particles  
     measurement of  $T_i$  524  
     production 523  
 neutron emission, measurement  
     of  $T_i$  526  
 $nTg$  for ignition 10  
 $nTg$ , triple product 11  
     improvement in 3  
  
 Ohkawa current 571  
 ohmic heating 240  
 Ohm's law 80  
 O-point 355  
 optical depth 519  
 optimized shear 181, 190  
  
 particle motion  
     along  $B$  42  
     drifts 44  
 particle orbits 124  
     trapped 129  
     potato 131  
 particle trapping 127  
     conditions for 128

- passing particle instabilities 422  
 passing particles 124  
 pedestals 217  
 pellet injection  
     Alcator C 567  
     JET 625, 638  
     TFTR 598  
 PEPs, pellet enhanced plasmas 184, 638  
 permeability 76  
 Pfirsch-Schlüter current 155  
 Pfirsch-Schlüter diffusion 159  
 pick-up coils 500  
     instability measurements 505  
 plasma current  
     measurement 501  
     reactor 21  
 plasma elongation, axisymmetric modes 342  
 plasma energy, measurement 503  
 plasma frequency 38, 95  
 plasma oscillations 95  
 plasma parameter 38  
 plasma rotation 133  
 plasma sheath 446  
 plasma-surface interactions 444  
 plasma waves 94  
 plateau regime 167  
 plateau transport 167  
 polarimetry 509  
 polarization 84  
 poloidal magnetic field 16  
 potato orbits 131  
 power balance 8, 10  
 Poynting vector 77  
 precursors, disruption 375  
 pressure, anisotropic 83  
 pressure tensor 82  
 primary coils 17  
 probes, Langmuir 546  
     profile stiffness 693  
 pump limiter 580
- $Q$ , power ratio 12  
      $Q_{\text{cr}}$  706  
 $q$ , safety factor 111  
     cylindrical 114  
     experiment 372, 674  
     profile determination 556  
     profiles 113  
 quasi-linear theory, turbulence 206  
 quasi-neutrality 36  
 quench, current 376
- radiation from plasmas 531  
     bolometry 541  
     bremsstrahlung 227  
     impurity 229
- measurement 536  
 power 229  
 soft X-rays 542  
 radiation losses  
     bremsstrahlung 227  
     cyclotron 229  
     impurity 229  
 radiation shield 19  
 radio-frequency heating 258  
 rational surfaces 305  
 reactor economics 25  
 reactor parameters 19  
 reactor power 22  
 reactor requirements 708  
 Rehut-Lallia-Watkins model in JET  
     transport 216  
 recombination, dissociative 45g  
 recombination radiation 539  
 reconnection, magnetic 354, 367  
 recycling 453  
 reduced mass 6  
 reflectrometry 511  
 refractive index 94  
 relaxation processes 65  
 resistive diffusion 152  
 resistive instabilities 304  
 resistive layer, tearing mode 320  
 resistive skin-depth 742  
 resistive wall  
     axisymmetric modes 342  
     instability 679  
     mode locking 390  
 resistivity 70  
     experiment 59g  
     neoclassical 175  
     Spitzer 71  
 resonant surface 305  
 ripple transport 175  
     collisional 179  
     collisional well trapping 176  
     experiment 179  
     fast particles 177  
     stochastic 179  
 Rogowski coil 501  
 Rosenbluth potentials 61  
 rotation, plasma 133  
 rotational transform 113  
 runaway electron current 387  
 runaway electrons 72  
     in disruptions 387  
     mechanisms 72, 74  
 Rutherford scattering 52
- safety factor,  $q$ , 111  
 Sakharov 562
- sawtooth oscillations 365  
     collapse time 370  
     first observation 565  
     heat pulse 610  
     in JET 625  
     Kadomtsev's model 366  
     quasi-interchange 371  
     ramp phase 373  
     soft X-ray measurement 521  
     spontaneous onset 373  
     stabilization 627  
     in TEXTOR 373  
     in TFTR 605  
     thermal collapse 374  
     value of  $q_0$  372  
 scaling laws, confinement 191  
     Artsimovitch 563  
     Bohm scaling 194  
     Connor-Taylor constraint 191  
     Goldston 20  
     gyro-Bohm scaling 194  
     identity experiments 194  
     Kadomtsev constraint 191  
     tables 192, 739  
 scrape-off layer, SOL 449  
     one-dimensional model 479  
     parallel transport 452  
 Shafranov shift 119  
 shear damping 421  
 shear magnetic 107, 340  
     electric field 210  
 sheath, plasma 446  
 shield, neutron 19  
 skin-depth, resistive 742  
 slideaway regime 567  
 stowing-down time 65  
 small aspect-ratio tokamaks 586  
 snake 625  
 soft X-rays 542  
 SOL, *see* scrape-off layer  
 sound waves 96  
 spectroscopy 536  
 Spitzer resistivity 71  
 sputtering 466  
 Stark effect, motional 557  
 Stix-Golant accessibility condition 288  
 Stoke's theorem 84  
 stress tensor 92  
 superconducting coils 16  
 supershots-577  
 switch-off experiment 224  
 synchrotron (cyclotron) radiation 229
- TAE  
     in DIII-D 681  
     in JET 626

- in JT-60U 659
- in TFR 608
- Tamm 562
- tearing mode
  - in disruptions 383
  - linear theory 318
  - micro- 435
  - neoclassical 359
  - non-linear 356
  - stability 333
- temperature pedestals 217
- test particle 65
- thermal conductivity 88, 93
- thermal force 90
- thermal stability 13
- thermal velocity 734
- thermonuclear fusion 5
- thermonuclear power density 8
- thermonuclear reaction rate 5, 11
- Thomson scattering 514
  - measurement of  $T_e$  562
- tokamak, name 27
- tokamak plasma 34
- tokamak reactor 18
  - costs 26
  - economics 25
  - electricity production 19
- tokamak research, history 27
- tomography 544
- toroidal Alfvén eigenmodes, TAE 402
- toroidal field coils 16
- transformer action 16
- transport
  - anomalous 150
  - banana regime 159
  - barriers 189
  - classical, cylinder 153
  - coefficients 195
  - electric field shear 210
  - fluctuations 199
  - H-mode 152
  - impurity 219
  - instability modes 213
  - L-mode 152
  - neoclassical 151
  - Pfirsch-Schlüter 158
  - plateau regime 167
  - Rebut-Lallia-Watkins 216
  - ripple 175
  - turbulence-induced 202
- transport coefficients 195
  - banana regime 166
  - plateau regime 169
- trapped particle instabilities 430
  - collisionless 431
  - dissipative 432
  - dissipative trapped electron 434
  - trapped ion 433
- trapped particles 124
  - bounce frequency 129
  - instabilities 430
  - orbits 129
  - trapping, condition for 128
- tritium
  - behaviour in surfaces 492
  - breeding 18
  - inventory 492
- tritium experiments
  - in JET 640
  - in TFR 612
- turbulence
  - electrostatic 203
  - magnetic 204
  - quasi-linear theory 206
  - saturation 208
  - simulations 217
  - stochastic 204
  - transport 192
- unipolar arc 473
- units xiif
- 'universal' trapped electron instability 419, 421
- vacuum magnetic field 121
- vacuum vessel
  - baking 463
  - forces 389
- vapour pressure 490
- vector potential 76
- vertical instability 396, 342
  - in JET 620
- vertical magnetic field 123
- VH-mode 672
- viscosity 92
- Vlasov equation 56
- voltage, loop 502
- wall conditioning 461
- wall stabilization 680
- Ware pinch 169
- waves, plasma 94
- X-event 223
- X-point 115
  - magnetic island 355
- X-rays, soft 542
- Zeta 562
- Zeeman effect 557
- $Z_{\text{eff}}$ 
  - definition 72
  - in JET 633
  - measurement 534, 538